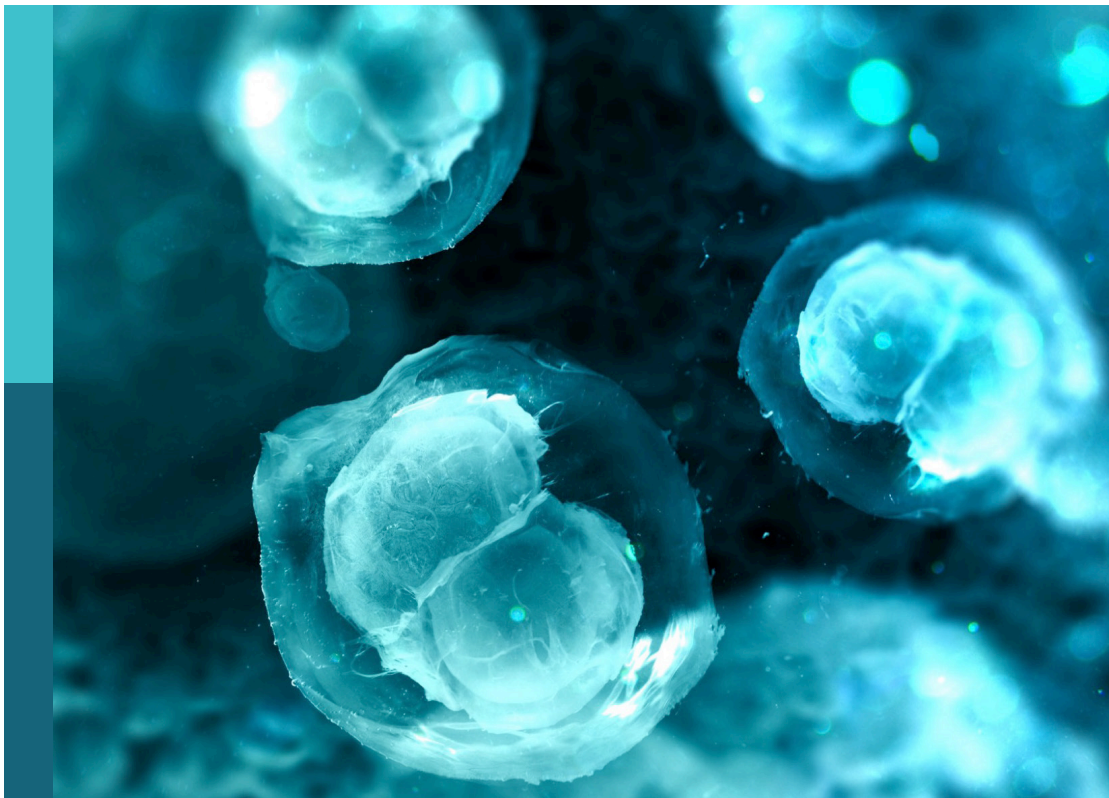
frontiers | Research Topics

Regulation of adult stem cells fate and function in natural and artificial microenvironments

Edited by
Pavel Makarevich, Andrei S. Chagin and Yu-Chen Hu

Published in
Frontiers in Cell and Developmental Biology
Frontiers in Genetics



FRONTIERS EBOOK COPYRIGHT STATEMENT

The copyright in the text of individual articles in this ebook is the property of their respective authors or their respective institutions or funders. The copyright in graphics and images within each article may be subject to copyright of other parties. In both cases this is subject to a license granted to Frontiers.

The compilation of articles constituting this ebook is the property of Frontiers.

Each article within this ebook, and the ebook itself, are published under the most recent version of the Creative Commons CC-BY licence. The version current at the date of publication of this ebook is CC-BY 4.0. If the CC-BY licence is updated, the licence granted by Frontiers is automatically updated to the new version.

When exercising any right under the CC-BY licence, Frontiers must be attributed as the original publisher of the article or ebook, as applicable.

Authors have the responsibility of ensuring that any graphics or other materials which are the property of others may be included in the CC-BY licence, but this should be checked before relying on the CC-BY licence to reproduce those materials. Any copyright notices relating to those materials must be complied with.

Copyright and source acknowledgement notices may not be removed and must be displayed in any copy, derivative work or partial copy which includes the elements in question.

All copyright, and all rights therein, are protected by national and international copyright laws. The above represents a summary only. For further information please read Frontiers' Conditions for Website Use and Copyright Statement, and the applicable CC-BY licence.

ISSN 1664-8714
ISBN 978-2-83251-086-5
DOI 10.3389/978-2-83251-086-5

About Frontiers

Frontiers is more than just an open access publisher of scholarly articles: it is a pioneering approach to the world of academia, radically improving the way scholarly research is managed. The grand vision of Frontiers is a world where all people have an equal opportunity to seek, share and generate knowledge. Frontiers provides immediate and permanent online open access to all its publications, but this alone is not enough to realize our grand goals.

Frontiers journal series

The Frontiers journal series is a multi-tier and interdisciplinary set of open-access, online journals, promising a paradigm shift from the current review, selection and dissemination processes in academic publishing. All Frontiers journals are driven by researchers for researchers; therefore, they constitute a service to the scholarly community. At the same time, the *Frontiers journal series* operates on a revolutionary invention, the tiered publishing system, initially addressing specific communities of scholars, and gradually climbing up to broader public understanding, thus serving the interests of the lay society, too.

Dedication to quality

Each Frontiers article is a landmark of the highest quality, thanks to genuinely collaborative interactions between authors and review editors, who include some of the world's best academicians. Research must be certified by peers before entering a stream of knowledge that may eventually reach the public - and shape society; therefore, Frontiers only applies the most rigorous and unbiased reviews. Frontiers revolutionizes research publishing by freely delivering the most outstanding research, evaluated with no bias from both the academic and social point of view. By applying the most advanced information technologies, Frontiers is catapulting scholarly publishing into a new generation.

What are Frontiers Research Topics?

Frontiers Research Topics are very popular trademarks of the *Frontiers journals series*: they are collections of at least ten articles, all centered on a particular subject. With their unique mix of varied contributions from Original Research to Review Articles, Frontiers Research Topics unify the most influential researchers, the latest key findings and historical advances in a hot research area.

Find out more on how to host your own Frontiers Research Topic or contribute to one as an author by contacting the Frontiers editorial office: frontiersin.org/about/contact

Regulation of adult stem cells fate and function in natural and artificial microenvironments

Topic editors

Pavel Makarevich — Lomonosov Moscow State University, Russia

Andrei S. Chagin — Karolinska Institutet (KI), Sweden

Yu-Chen Hu — National Tsing Hua University, Taiwan

Citation

Makarevich, P., Chagin, A. S., Hu, Y.-C., eds. (2023). *Regulation of adult stem cells fate and function in natural and artificial microenvironments*.

Lausanne: Frontiers Media SA. doi: 10.3389/978-2-83251-086-5

Table of contents

06 Editorial: Regulation of Adult Stem Cells Fate and Function in Natural and Artificial Microenvironments
Pavel I. Makarevich and Yu-Chen Hu

10 The Development of Controllable Magnetic Driven Microphysiological System
Jia-Wei Yang, Yu-Wei Chen, Pei-Yi Ho, Liane Jiang, Kuan Yu Hsieh, Sheng-Jen Cheng, Ko-Chih Lin, Huai-En Lu, Hsien-Yi Chiu, Shien-Fong Lin and Guan-Yu Chen

20 Epiphyseal Cartilage Formation Involves Differential Dynamics of Various Cellular Populations During Embryogenesis
Yi Zhang, Karl Annusver, Kazunori Sunadome, Polina Kameneva, Steven Edwards, Guanghua Lei, Maria Kasper, Andrei S. Chagin, Igor Adameyko and Meng Xie

33 Site-Dependent Lineage Preference of Adipose Stem Cells
Tingliang Wang, Ryan C. Hill, Monika Dzieciatkowska, Lian Zhu, Aniello M. Infante, Gangqing Hu, Kirk C. Hansen and Ming Pei

49 Development of a Novel Hanging Drop Platform for Engineering Controllable 3D Microenvironments
Chin-Yi Cho, Tzu-Hsiang Chiang, Li-Hung Hsieh, Wen-Yu Yang, Hsiang-Hao Hsu, Chih-Kuang Yeh, Chieh-Cheng Huang and Jen-Huang Huang

60 A Testis-Derived Hydrogel as an Efficient Feeder-Free Culture Platform to Promote Mouse Spermatogonial Stem Cell Proliferation and Differentiation
Yan Yang, Qilian Lin, Chengxing Zhou, Quan Li, Ziyi Li, Zhen Cao, Jinlian Liang, Hanhao Li, Jiaxin Mei, Qihao Zhang, Qi Xiang, Wei Xue and Yadong Huang

74 Three-Dimensional Compaction Switches Stress Response Programs and Enhances Therapeutic Efficacy of Endometrial Mesenchymal Stem/Stromal Cells
Alisa Domnina, Julia Ivanova, Larisa Alekseenko, Irina Kozhukharova, Aleksandra Borodkina, Natalia Pugovkina, Irina Smirnova, Olga Lyublinskaya, Irina Fridlyanskaya and Nikolay Nikolsky

88 Niches for Skeletal Stem Cells of Mesenchymal Origin
Anastasiia D. Kurenkova, Ekaterina V. Medvedeva, Phillip T. Newton and Andrei S. Chagin

105 Hox-Positive Adult Mesenchymal Stromal Cells: Beyond Positional Identity
Maria Kulebyakina and Pavel Makarevich

114 Inhibiting Heat Shock Protein 90 Protects Nucleus Pulposus-Derived Stem/Progenitor Cells From Compression-Induced Necroptosis and Apoptosis
Binwu Hu, Shuo Zhang, Weijian Liu, Peng Wang, Songfeng Chen, Xiao Lv, Deyao Shi, Kaige Ma, Baichuan Wang, Yongchao Wu and Zengwu Shao

134 Novel Glial Cell Functions: Extensive Potency, Stem Cell-Like Properties, and Participation in Regeneration and Transdifferentiation
Valentin Milichko and Vyacheslav Dyachuk

145 Extracellular Matrix and Cellular Plasticity in Musculoskeletal Development
Sophia Ka Yan Ma, Andy Shing Fung Chan, Aqsa Rubab, Wilson Cheuk Wing Chan and Danny Chan

165 Building an Artificial Cardiac Microenvironment: A Focus on the Extracellular Matrix
Olivia Pagliarosi, Vittorio Picchio, Isotta Chimenti, Elisa Messina and Roberto Gaetani

173 Integrated Analyses of Mouse Stem Cell Transcriptomes Provide Clues for Stem Cell Maintenance and Transdifferentiation
Li-Juan Wang, Xiao-Xiao Li, Jie Hou, Xin-Hua Song, Wen-Hai Xie and Liang Shen

192 Effects of Recombinant Spidroin rS1/9 on Brain Neural Progenitors After Photothrombosis-Induced Ischemia
Mikhail M. Moisenovich, Denis N. Silachev, Anastasia M. Moysenovich, Anastasia Yu. Arkhipova, Konstantin V. Shaitan, Vladimir G. Bogush, Vladimir G. Debabov, Alexander V. Latanov, Irina B. Pevzner, Ljubava D. Zorova, Valentina A. Babenko, Egor Y. Plotnikov and Dmitry B. Zorov

209 Extracellular Vesicles Released by Tumor Endothelial Cells Spread Immunosuppressive and Transforming Signals Through Various Recipient Cells
Tatiana Lopatina, Enrica Favaro, Ludmila Danilova, Elana J. Fertig, Alexander V. Favorov, Luciane T. Kagohara, Tiziana Martone, Benedetta Bussolati, Renato Romagnoli, Roberto Albera, Giancarlo Pecorari, Maria Felice Brizzi, Giovanni Camussi and Daria A. Gaykalova

223 Mesenchymal Stromal Cell-Produced Components of Extracellular Matrix Potentiate Multipotent Stem Cell Response to Differentiation Stimuli
Ekaterina Novoseletskaya, Olga Grigorieva, Peter Nimiritsky, Nataliya Basalova, Roman Eremichev, Irina Milovskaya, Konstantin Kulebyakin, Maria Kulebyakina, Sergei Rodionov, Nikolai Omelyanenko and Anastasia Efimenko

248 Influence of Human Platelet Lysate on Extracellular Matrix Deposition and Cellular Characteristics in Adipose-Derived Stem Cell Sheets
Nai-Chen Cheng, Yuan-Kun Tu, Ning-Hsu Lee and Tai-Horng Young

263 The Bone-Forming Properties of Periosteum-Derived Cells Differ Between Harvest Sites
Lisanne C. Groeneveldt, Tim Herpelinck, Marina Maréchal, Constantinus Politis, Wilfred F. J. van IJcken, Danny Huylebroeck, Liesbet Geris, Eskeatnaf Mulugeta and Frank P. Luyten

280 The Duo of Osteogenic and Angiogenic Differentiation in ADSC-Derived Spheroids
Anastasiya A. Gorkun, Daria P. Revokatova, Irina M. Zurina, Denis A. Nikishin, Polina Y. Bikmulina, Peter S. Timashev, Anastasiya I. Shpichka, Nastasia V. Kosheleva, Tamara D. Kolokoltsova and Irina N. Saburina

294 Novel Functional Genes Involved in Transdifferentiation of Canine ADMSCs Into Insulin-Producing Cells, as Determined by Absolute Quantitative Transcriptome Sequencing Analysis
Pengxiu Dai, Jiakai Li, Yijing Chen, Luwen Zhang, Xinke Zhang, Jinglu Wang, Guixiang Qi and Yihua Zhang

311 Characterized the Adipogenic Capacity of Adipose-Derived Stem Cell, Extracellular Matrix, and Microenvironment With Fat Components Grafting
Wenqing Jiang, Junrong Cai, Jingyan Guan, Yunjun Liao, Feng Lu, Jingjing Ma, Jianhua Gao and Yuteng Zhang

frontiers | Frontiers in Cell and Developmental Biology

EDITORIAL
published: 17 August 2022
doi: 10.3389/fcell.2022.955568

Editorial: Regulation of Adult Stem Cells Fate and Function in Natural and Artificial Microenvironments

Pavel I. Makarevich[1,2]* *and Yu-Chen Hu*[3]

[1]*Laboratory of Gene and Cell Therapy, Institute for Regenerative Medicine, Lomonosov Moscow State University, Moscow, Russia,* [2]*Chair of Biochemistry and Molecular Medicine, Faculty of Medicine, Lomonosov Moscow State University, Moscow, Russia,* [3]*Department of Chemical Engineering, National Tsing Hua University, Hsinchu, Taiwan*

Keywords: stem cell niche, tissue engineering, extracellular matrix, mesenchymal stem cells, differentiation

Editorial on the Research Topic

Regulation of Adult Stem Cells Fate and Function in Natural and Artificial Microenvironments

CHALLENGING NATURE OF ADULT STEM CELL FATE CONTROL MECHANISM FOR A RESEARCHER

The stem cells of an adult organism possess an amazing ability to support tissue renewal throughout life and take part in a complex framework of events after damage, where they present a valuable source of tissue "spare" elements. Their shift from quiescence towards differentiation or self-renewal is controlled by a *niche* microenvironment that provides an interface. The latter "filters and amplifies" incoming signals to generate a multifaceted yet unambiguous instruction for residing stem cells. As a theoretical basis, the concept of the stem cell niche is a robust model describing the general principle of stem cell fate control. However, modeling the stem cell fate and its time-course apart from native tissue is complicated. In some cases (stromal niches) even the entity itself is described as a dynamic focus of stimuli and can hardly be localized for investigation.

In this Research Topic, the majority of researchers focus on chosen objects to hypothesize their role in stem cell control and put them to experimental tests to conclude on their importance in cell fate definition. Studied objects in this field range from matrix proteins and cytokines to transcription factors or synthetic biomaterials that mimic the tissue conditions or at least some of them.

EXTRACELLULAR MATRIX: ROLE BEYOND STRUCTURAL SUPPORT

After a seminal work by Hauschka and Konigsberg (1966), the extracellular matrix (ECM) was considered more than a network of fibrillar proteins providing structural support for cells. The development of decellularization to obtain dECM samples from cultured cells and organs opened a new field extensively studied in recent decades. Investigation of the role of ECM in the control of stem cell differentiation and reprogramming is a growing field and the majority of works in this Research Topic are related to ECM and stem cell fate.

Summary of recent data on ECM in control of cardiac renewal and regeneration has been presented by Pagliarosi et al. from the R. Gaetani group. They present a very original view of ECM as a complex bioactive network that facilitates, regulates, and may control cell fate is presented and

OPEN ACCESS

Edited and Reviewed by:
Valerie Kouskoff, The University of Manchester, United Kingdom

***Correspondence:**
Pavel I. Makarevich
pmakarevich@mc.msu.ru

Specialty section:
This article was submitted to Stem Cell Research, a section of the journal Frontiers in Cell and Developmental Biology

Received: *28 May 2022*
Accepted: *01 June 2022*
Published: *17 August 2022*

Citation:
Makarevich PI and Hu Y-C (2022) Editorial: Regulation of Adult Stem Cells Fate and Function in Natural and Artificial Microenvironments. Front. Cell Dev. Biol. 10:955568. doi: 10.3389/fcell.2022.955568

supported by strong data including findings by the authors. Stromal/supporting cells, mechanical stimuli, presence of soluble factors, and cellular cross-talk are covered with an accent made to each component's role in the generation of the microenvironment of the cardiac tissue matrix. Based on these, the authors proposed the application of recent knowledge on the 3D culture and artificial tissues that may reproduce native control of differentiation. A similar level of rigor is found in a review by Ma et al. covering the concept and role of ECM in musculoskeletal plasticity. ECM is pointed to as a critical component of musculoskeletal niches, allowing stem cell entry and exit, transitional niche formation, or modulation of niche composition/environment. This overview of the role of ECM stresses that besides progenitor cell fate, the ECM takes plays an active role in reprogramming mature cells, especially in changing conditions (e.g., damage).

Jiang et al. found that dECM facilitated mesenchymal-to-endothelial phenotype switch in seeded adipose-derived mesenchymal stromal/stem cells (MSC), which correlated with an influx of pro-regenerative M2-macrophages. In contrast, dECM alone was widely invaded by M1-macrophages associated with damage and inflammation. Respectively, MSC-seeded dECM has shown active adipogenesis outcomes in nude mice while dECM alone has failed to provide mature fat at the site of implantation. This is one of few reports on dECM inducing active reprogramming of stromal cells to endothelial ones.

The work of Yang et al. supports the role of ECM in stem cell differentiation control, demonstrating that testis-derived decellularized ECM (dECM) alone was a sufficient platform for mouse spermatogonial stem cell long-term culture and differentiation to spermatids once being induced properly. Besides providing a feasible culture model using dECM hydrogel authors highlight the importance of SSC contact with tissue-specific ECM to function properly. Similar findings using the dECM approach were reported by Novoseletskaya et al., who found that human MSC enhances differentiation potency to 3 lineages (adipose, bone, and cartilage) once cultured on dECM obtained from long-term cultured MSC to obtain cell sheets. These findings suggest the importance of ECM-controlled stiffness and integrin signaling support in the function of stromal-type niches.

Finally, recombinant proteins from non-mammalian species may provide an interesting biomimetic approach to induce and support neural progenitor cells (NPC) *in situ*. Moisenovich et al. used recombinant spidroin 1 (rS 1/9)—an insoluble insect scleroprotein (much resembling animal collagens) to successfully activate nestin-positive NPCs at the site of brain damage in mice. The putative mechanism included activating the influence of rS 1/9 degradation products on resident NPCs. Thus, a xenogeneic protein was successfully used to invoke pro-regenerative and survival effects in mammalian resident NPC.

TISSUE-AND SITE-SPECIFICITY DEFINING STEM CELLS AND MSC PROPERTIES

A cell's origin provides a significant bias even when it is isolated and cultured for a significant period of time. Epigenetic and transcriptomic fingerprints defined by tissue and developmental environment still influence how the cell acts and functions *in vitro* making them autonomous properties of these cell cultures. This becomes especially important when we isolate primary MSC or stem cells for the needs of regenerative medicine (cell therapy or tissue engineering). In that case, both efficacy and safety may be impacted by tissue and site of origin.

The autonomous properties of cells driving their regenerative potency and cell fate are the focus of a hypothesis paper by Kulebyakina and Makarevich, who suggests that resident MSC retaining high expression of *Hox* genes after birth might be the "pro-regenerative" subpopulation responding to damage differently from *Hox*-negative MSC. Furthermore, they draw attention to the regenerative capacities of human endometrium and speculate on the role of HOXA10 and HOXA11 in the mediation of numerous healings without scarring that occurs in every menstrual cycle. Thus, a novel role of *Hox* genes (widely known as the cell's positional "bar-code") has been proposed in tissue renewal which involves cyclic damage of endometrium.

A good example of site-specificity influence on stem cell fate is provided by Groeneveldt et al. Comparative analysis of skeletal stem and progenitor cells (SSPC) from the periosteum of maxilla, mandible, or tibia demonstrated that despite the large extent of similarity, anatomic origin has a great impact on osteogenic properties of periosteal SSPC. For example, in ectopic bone formation animal test maxilla-derived periosteal SSPC failed to generate bone while cells from the mandible were as effective as tibial ones. This highlighted that even cells of similar tissue origin possess site-dependent features which should be evaluated and taken into account for regenerative medicine and tissue engineering implication of those.

Wang et al. focused on the site-dependent profile of adipose-derived MSC isolated from subcutaneous fat or infrapatellar fat pads trying to imply a concept of tissue-specific lineage preference during differentiation. Using transcriptomic and proteomic analyses they successfully identified a significant discrepancy between these cell types depending on their source. They demonstrated that cells from the subcutaneous compartment showed higher proliferation and an incline towards adipogenic differentiation compared to their infrapatellar fat counterparts that were pro-chondorgenic. One of the putative reasons for autonomous properties might be a significant difference in local ECM environments highlighted in other papers in this Research Topic.

DEVELOPMENT-DRIVEN APPROACH FOR UNDERSTANDING STEM CELL FATE REGULATION MECHANISMS

Cell fate shifts during the development of an organism are a well-studied field in embryology and is a fruit field for investigation of adult stem cells' properties and modes of operation under different settings.

Zhang et al. provide a cutting-edge development-driven study, shedding light on the asymmetrical pattern of growth in cartilage

formation that eventually allows the formation of sophisticated shapes in these elements of the human skeleton. Lineage tracing experiments of Col2+, Prrx1+, and Gli1+ cells provided an important point that a switch between cell division and cell influx exists immediately after joint cavitation to form epiphyseal cartilage. These findings contribute to understanding of factors that control the shape of organs and tissues and make way to further targeted investigation of mechanisms that govern these cells' subpopulations and their cross-talk.

A review by Kurenkova et al. from the A Chagin Group focuses on the above-mentioned SSPC, with a focus on their niches in different compartments. A thorough summary of current literature proposes that all described niches have a site-specific repertoire of signals that can be divided into *primary* or *modulating* depending on their role: maintaining basic SSPC functions (renewal or progeny generation) or adaptation to a change of conditions respectively. Eventually, among a myriad of signaling molecules Wnt, hedgehog, and inflammatory cytokines were highlighted as indispensable regulators in all described niches of SSPC of mesenchymal origin.

A review by Milichko and Dyachuk provides insights into the function of glial cells, focusing on the recently discovered heterogeneity of Schwann cells, stemness of certain sub/populations of the human nervous system, and their origin in development. Extensive comparative and descriptive analysis of both embryonic and adult Schwann cells and their potency draws attention to their future use to stimulate nerve system renewal or regeneration.

DEVELOPING MODELS, SOPHISTICATED TECHNIQUES, AND 3D CULTURES TO CONTROL STEM CELL FATE AND VIABILITY

Significant attention has also been paid to techniques and models that can be implied for stem cell research, disease modeling, or used to support stem cells' properties *in vitro*. Yang et al. developed an original model implying a magnetically-driven dynamic system to culture alveolar cells in circulating flow, providing mechanical stimuli for adequate long-term culture and distribution of cells. Furthermore, the authors have demonstrated that silica particles uptake to validate functional properties and obtained a controllable and highly reproducible model that allows investigation of lung physiology and disease in a tissue-like environment.

The "Hanging drop" model was developed by Cho et al. using a sophisticated model of this classic approach involving a pressure-assisted network for droplet accumulation (PANDA). The tunable and robust generation of artificial niches was demonstrated and 3D microtissues from MSC and podocytes were obtained to eventually suggest their use in tissue-mimicking with the expansion of PANDA application to other niches and cell types. An approach for cell sheet generation has been proposed by Cheng et al., who used human platelet lysate (HPL) to obtain thicker cell sheets enriched with connective tissue and demonstrated the anti-fibrotic and pro-angiogenic properties of their secretome. The soluble factors of HPL might find use in the generation of tissue-engineered constructs for tissue repair and replacement.

The spatial status of cells and compaction are highlighted by Domnina et al. in their study, which used endometrial MSC in spheroids and found that compaction resulted in cell protection from oxidative stress. Interestingly, compaction decreased anti-apoptotic and anti-autophagy genes suggesting a pathway to programmed elimination of damaged cells in 3D culture. The authors demonstrated a HIF-1α-dependent increase in the therapeutic efficacy of secretome samples obtained from spheroids compared to routine culture. Thus, a switch to a 3D environment altered the MSC viability control program and regenerative capacity. A paper by Hu et al. also focused on cell viability control and showed that apo- and necroptosis in nucleus pulposus-derived stem cells due to compression may be activated via heat shock protein 90 (HSP90). Beyond a basic understanding of a widely spread degenerative disease, this study provided an interesting therapeutic target for future drug development.

THE TWIST OF FATE: PAVING THE WAY TO CELLULAR REPROGRAMMING

Cell fate and control are associated with many amazing phenomena including rapid change of cellular identity from one type to another or induction of pluripotency *in vitro*. For many researchers and translational scientists working in regenerative medicine controlled reprogramming of adult cells it remains a goal to be reached and the current Research Topic covers certain endeavors in the field.

A bioinformatic study by Wang et al. involved a wide array of stem cells from mouse embryo adult testis, brain, and bone marrow using a MEF cell line as control. Their transcriptomic analysis provided an array of genes (*Itgam, Cxcr6,* and *Agtr2*) that might overlap and bridge between cell type-specific regions and thus in the future may provide targets for reprogramming control or stimulation of SC renewal. Seeking molecular pathways and targets that may induce cell transdifferentiation has led Dai et al. to a study where canine adipose MSC and insulin-producing cells (IPC) were screened, and eventually *Foxa1, Pbx1* and *Rfx3* were validated to provide prospective targets for induction of MSC-to-IPC reprogramming in future experimental protocols and cell-replacement therapy.

Among soluble factors that regulate cell fate extracellular vesicles (EVs) were in the spotlight and our Research Topic included a work by Lopatina et al. who convincingly demonstrated that EVs released from tumor endothelial cells are mediators of non-metastatic carcinogenesis. A potent ability of tumor-derived EVs to "corrupt" local immunity via reprogramming of stromal and immune cells by factors carried in tumor-generated EVs have been shown.

CONCLUDING REMARKS

The articles collected in this Research Topic indicate that contemporary understating of how a cell "commits and performs" implies the existence of a complicated network of

signals, stimuli, and interactions that guide towards maturation, putting it to a halt or even reverse. Researchers investigating how stem cell fate is defined will endeavor to evaluate each known element's role and impact. Futures challenges will soon need to be addressed, such as when we try to understand how the integral complex system of cell fate definition works.

Despite these challenges, we believe that a precise description of the crucial factors that control and comprise the niche and provide tissue-specific features accompanied by the development of new techniques to investigate cell fate will eventually build a new understanding of how stem cells are controlled in different settings.

AUTHOR CONTRIBUTIONS

PM, AC, and Y-CH equally contributed as Guest Editors of this Research Topic and interacted throughout the editorial process, by defining the scope and focus of the topic, inviting leaders in research fields to contribute, and acting as handling editors of the submitted manuscripts. All authors equally contributed to the Editorial and approved the submitted version.

FUNDING

PM is supported by the Russian Science Foundation grant №19-75-30007.

ACKNOWLEDGMENTS

We thank the Editorial Office of Frontiers in Cell and Developmental Biology for their assistance throughout the editorial process. We express gratitude for support to our coeditor AC who refused a co-author credit for this Editorial due to his extremely occupied schedule and wish him good luck in further studies.

REFERENCES

Hauschka, S. D., and Konigsberg, I. R. (1966). The Influence of Collagen on the Development of Muscle Clones. *Proc. Natl. Acad. Sci. U. S. A.* 55 (1), 119–126. doi:10.1073/pnas.55.1.119

Conflict of Interest: The authors declare that the research was conducted in the absence of any commercial or financial relationships that could be construed as a potential conflict of interest.

Publisher's Note: All claims expressed in this article are solely those of the authors and do not necessarily represent those of their affiliated organizations, or those of the publisher, the editors and the reviewers. Any product that may be evaluated in this article, or claim that may be made by its manufacturer, is not guaranteed or endorsed by the publisher.

Copyright © 2022 Makarevich and Hu. This is an open-access article distributed under the terms of the Creative Commons Attribution License (CC BY). The use, distribution or reproduction in other forums is permitted, provided the original author(s) and the copyright owner(s) are credited and that the original publication in this journal is cited, in accordance with accepted academic practice. No use, distribution or reproduction is permitted which does not comply with these terms.

frontiers in Cell and Developmental Biology

ORIGINAL RESEARCH
published: 07 November 2019
doi: 10.3389/fcell.2019.00275

The Development of Controllable Magnetic Driven Microphysiological System

*Jia-Wei Yang[1,2], Yu-Wei Chen[2], Pei-Yi Ho[2], Liane Jiang[2,3], Kuan Yu Hsieh[1,2], Sheng-Jen Cheng[1,2], Ko-Chih Lin[1,2], Huai-En Lu[4], Hsien-Yi Chiu[5,6,7], Shien-Fong Lin[1,2] and Guan-Yu Chen[2,8]**

[1] Department of Electrical and Computer Engineering, College of Electrical and Computer Engineering, National Chiao Tung University, Hsinchu, Taiwan, [2] Institute of Biomedical Engineering, College of Electrical and Computer Engineering, National Chiao Tung University, Hsinchu, Taiwan, [3] Centre for Ophthalmology, Section for Experimental Ophthalmic Surgery and Refractive Surgery, University of Stuttgart, Stuttgart, Germany, [4] Bioresource Collection and Research Center, Food Industry Research and Development Institute, Hsinchu, Taiwan, [5] Department of Dermatology, National Taiwan University Hospital Hsin-Chu Branch, Hsinchu, Taiwan, [6] Department of Dermatology, College of Medicine, National Taiwan University, Taipei, Taiwan, [7] Department of Dermatology, National Taiwan University Hospital, Taipei, Taiwan, [8] Department of Biological Science and Technology, National Chiao Tung University, Hsinchu, Taiwan

OPEN ACCESS

Edited by:
Pavel Makarevich, Lomonosov Moscow State University, Russia

Reviewed by:
Jason Chia-Hsun Hsieh, Chang Gung Memorial Hospital, Taiwan
Johnson Chung, University of Wollongong, Australia

***Correspondence:**
Guan-Yu Chen
guanyu@nctu.edu.tw

Specialty section:
This article was submitted to Stem Cell Research, a section of the journal Frontiers in Cell and Developmental Biology

Received: *16 September 2019*
Accepted: *25 October 2019*
Published: *07 November 2019*

Citation:
Yang J-W, Chen Y-W, Ho P-Y, Jiang L, Hsieh KY, Cheng S-J, Lin K-C, Lu H-E, Chiu H-Y, Lin S-F and Chen G-Y (2019) The Development of Controllable Magnetic Driven Microphysiological System. Front. Cell Dev. Biol. 7:275. doi: 10.3389/fcell.2019.00275

Current research has enabled the use of microphysiological systems and creation of models for alveolar and pulmonary diseases. However, bottlenecks remain in terms of medium- and long-term regulation of cell cultures and their functions in microchannel systems, as well as in the enhancement of *in vitro* representation of alveolar models and reference values of the data. Currently used systems also require on-chip manufacturing of complex units, such as pumps, tubes, and other cumbersome structures for maintaining cells in culture. In addition, system simplification and minimization of all external and human factors major challenges facing the establishment of *in vitro* alveolar models. In this study, a magnetically driven dynamic alveolus cell-culture system has been developed to use controlled magnetic force to drive a magnetic film on the chip, thereby directing the fluid within it to produce a circulating flow. The system has been confirmed to be conducive with regard to facilitating uniform attachment of human alveolar epithelial cells and long-term culture. The cell structure has been recapitulated, and differentiation functions have been maintained. Subsequently, reactions between silica nanoparticles and human alveolar epithelial cells have been used to validate the effects and advantages of the proposed dynamic chip-based system compared to a static environment. The innovative concept of use of a magnetic drive has been successfully employed in this study to create a simple and controllable yet dynamic alveolus cell-culture system to realize its functions and advantages with regard to *in vitro* tissue construction.

Keywords: magnetic driven, microphysiological systems, human alveolar epithelial cells, barrier function, silica nanoparticles

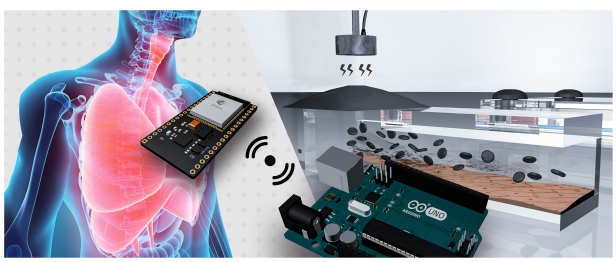
INTRODUCTION

The physiological and biological functions of alveolar epithelial type II (AEII) cells involve synthesizing, secreting, and recycling of all surfactant components to regulate surface tension within the entire alveolus (Fehrenbach, 2001; Mason, 2006). Although AEII cells only account for approximately 5% of the total alveolar surface area, they comprise 60% of the total number of alveolar cells (Crapo et al., 1982; Fehrenbach, 2001). They therefore play an essential role in maintaining the overall function of alveoli, thereby serving as progenitors of alveolar epithelial cells (Barkauskas et al., 2013; Hogan, 2018; Nabhan et al., 2018; Zacharias et al., 2018). Although isolation techniques and collection pipelines for primary alveolar cells have been well established, primary AEII cells tend to differentiate into AEI cells when employing common dish-culture methods (Fujino et al., 2012; Nikolic et al., 2017; Zheng et al., 2017). In addition, many studies have confirmed the difficulty involved in maintaining AEII cells with surfactant producing functions using *in vitro* culture methods (Mao et al., 2015). Consequently, cell-growth and differentiation regulation, representativeness enhancement of *in vitro* alveolar models, enhancement of reference data values, and complete recapitulation of functions of the human alveolus have become important research topics in recent times (Bove et al., 2014; Jain et al., 2015; Mao et al., 2015).

Cell culture techniques employing microfluidic devices have become increasingly popular, and microfluidic systems, over the years, have realized versatility, miniaturization, and automation of biochemical processes (Halldorsson et al., 2015; Chiu et al., 2017). Flexibly designing a chip device for each experiment or cell, using different parameters during each experiment to improve operational flexibility, performing perfusion cell culture, and reducing reagent consumption have all become possible (Mark et al., 2010; Byun et al., 2014). Extant researchers have indicated that alveolar epithelial cells can be cultured on a film placed on a microchip, and differences in gas pressures can be used to simulate the respiratory motion of the human body (Huh et al., 2010; Stucki et al., 2015a; Guenat and Berthiaume, 2018). It has also been determined that differences exist in the molecular penetration rate, wherein a higher penetration rate can be observed in dynamic environments compared to static environments (Huh et al., 2012; Esch et al., 2015). The secretion of cytokine is also much higher in dynamic environments compared to that in static environments (Stucki et al., 2015b). Researchers have also investigated the culture of AEII cells in dynamic systems and observed that differences in the flow rate greatly affect cell morphology and activity as well as proteins secreted by them (Grek et al., 2009; Stucki et al., 2018). Different results have been observed for different cells, albeit at the same flow rate, and it has been observed that quick and convenient control of dynamic culture environment parameters and the corresponding flow rate greatly assist the functioning of alveolar epithelial cells while also facilitating microenvironment construction (Douville et al., 2011; Freund et al., 2012).

In current microfluidics fluid-control practices, however, the principal driving method involves driving the medium through a syringe or peristaltic pump to provide a state of stable laminar flow inside on-chip channels. The main purpose of this state is to simulate fluid flow within human body tissues, thereby providing a fluidic environment that simulates the human body (Tehranirokh et al., 2013; Kim et al., 2014; Kimura et al., 2018). For example, in the recently developed lung modeling technology, alveolar cells are constructed on a chip with the objective of replacing studies involving animal subjects while also generating more accurate and reliable preclinical data (Benam et al., 2015, 2016; Ronaldson-Bouchard and Vunjak-Novakovic, 2018). However, creation of such a pump system requires many tubes to be interconnected, and a syringe and many converters are required to connect the chip with a medium reservoir (Temiz et al., 2015). Channel pretreatment is also complicated, requiring high-temperature sterilization. In addition, peristaltic pumps are to be squeezed, thereby resulting in brittleness and instability of channels. Further, the more the channels are used, the greater is the difference between the theoretical and actual flow rates on a chip. Such a system often requires use of numerous auxiliary devices, and therefore, placement of these auxiliary components to minimize the effect of all external and human factors currently constitutes a major challenge facing the development of the technology pertaining to alveolar cell culture on microfluidic systems.

To enhance the *in vitro* physiological function of alveolar cells, the design of a physical environment capable of simulating real life conditions is crucial to ensure that cell growth occurs under culture conditions that are as close as possible to *in vivo* conditions in terms of spatial parameters. In this study, a magnetically driven alveolar cell chip-based system has been developed equipped with a magnetic film. Integration of the thin magnetic film and controllable magnetic output with a microchannel system provides a simple and controllable fluid dynamic environment that recapitulates cell structures, physical and chemical microenvironments, and biomimetic nature of fluid flow. It also offers advantages pertaining to *in vitro* analysis of tissue functions and alveolar environmental activity (**Scheme 1**). This system is also expected to realize the advantages of device simplification by way of removal of complicated structures, such as pumps and tubes. Moreover, nanoparticles



SCHEME 1 | The magnetically driven dynamic alveolus cell-culture system facilitates selection of magnetically controllable output modes, and employs a magnetic film as a medium to control fluid circulation through on-chip microchannel.

were introduced and the toxicological effects were compared between dynamic and static environments via use of the proposed alveolar system, thereby validating its potential for use in future bionic engineering applications concerning tissue and organ chips.

MATERIALS AND METHODS

Design of Proposed Magnetic Driven Chip

The PDMS material used in this study contained Sylgard 184A base and Sylgard 184B curing agent. In this study, the PDMS chips were prepared at base-to-curing agent ratios of 10:1 to 15:1 for use in subsequent experiments (Dardik et al., 2005). The overall structure of the proposed magnetic driven chip can be primarily divided into two parts – (i) a PDMS-based three-layer chip comprising a top layer, middle layer (microchannel), and glass slide (bottom layer) and (ii) a chip fixture comprising an upper cover and mounting base. The layers in the first part are bonded to each other by oxygen-plasma-activated bonding. The upper layer of the chip is a rectangular cuboid measuring 75 mm (L) × 25 mm (W) × 5 mm (H) and contains square slots measuring 20 mm (L) × 20 mm (W) × 5 mm (H) and 5 mm (L) × 5 mm (W) × 5 mm (H). These empty slots are primarily used to hold the cell medium. The second layer is a 55 mm (L) × 1.5 mm (W) × 0.2 mm (H) microchannel layer while the third layer is a 75 mm (L) × 25 mm (W) × 1 mm (H) glass slide. After the second and third layers are bonded, a microchannel measuring 55 mm (L) × 1.5 mm (W) × 0.2 mm (H) is formed to constitute the area for cell culture. The upper cover of the second part measures 86 mm (L) × 36 mm (W) × 2 mm (H) in outer dimensions, and its periphery contains an M6 hole (a hole with diameter measuring 6 mm and containing a thread). In addition, two square areas [measuring 19 mm (L) × 19 mm (W) and 7 mm (L) × 7 mm (W)] are carved of the inside. Likewise, the base has external dimensions of 86 mm (L) × 36 mm (L) × 8 mm (W), and its periphery contains an M6 hole.

Magnetic Film Preparation

The CI-powder (44890, Sigma–Aldrich) used in this study had a particle size distribution of 5–9 μm, a density of 7.86 g/mL, and a purity of 99.5%, with a color that was pale to dark gray. The magnetic film was prepared by blending a specific ratio of PDMS solution (a 15:1 ratio of Sylgard 184A base to Sylgard 184B curing agent) (Royet et al., 2017). PDMS solution was next added at CI-powder-to-PDMS weight ratios of 2:1, 1:1, 2:1, and 4:1 (CI:PDMS), and was stirred thoroughly for 10 min until uniform. The CI–PDMS mixture was then poured into the mold, and the membrane containing CI–PDMS was placed in a vacuum plate for 10 min to remove air from the CI–PDMS. It was next placed in an oven at 80°C for 2 h for curing, and the preparation of the magnetic film was completed. The magnetic film was next washed with 70% alcohol, and the remaining liquid was removed using nitrogen gas.

Electromagnet System and Support Bracket

Mechanical 3D computer-aided design software (Solidworks, 2015, Concord, MA, United States) was used to draw the system support bracket, which primarily consisted of a rectangular cuboid with dimensions of 100 mm (L) × 50 mm (W) × 35 mm (H). The left side had a rectangular slot of 75 mm (L) × 27 mm (W) × 30 mm (H) where the magnetic driven chip placed, and an area on top was designed to allow the electromagnet to be mounted above the chip. A 3D printer was then used to output the completed object. The constant current LED driver module (LuxDrive BuckPuck 3021, Randolph, VT, United States) contained six pins: high output voltage DC (LED+), low output voltage DC (LED−), control pin voltage (CTL), and reference regulator current (REF), high input voltage DC (VIN+), and low input voltage DC (VIN−). The suction-cup electromagnet (HCNE1-P30/22) was wired by connecting to the output voltage DC of driver module. The input voltage DC was connected to the DC 12V switching power supply adapter (APV-35-12, Mean Well Enterprises Co., Ltd.). After the CTL was connected to the pin specified by the code of the Arduino, the signal was transmitted to the driver module and run according to the logic of the code.

Code Writing and Control

The CTL pins of driver module were connected to the PIN_3, 5, 6, 9, 10, and 11 (pulse width modulation, PWM) on the Arduino UNO R3 development board, to complete pre-operation (Badamasi, 2014). For program coding, the pins were first arranged in a void setup(), and the pin was set to OUTPUT. Next, two loop function were written in the void loop() to control the increase and decrease of the magnetic force. The first loop was for controlling the increase in magnetic force. In the first loop, the variable *a* was set to a value of 0 and incremented by 1 after each loop. In addition, the delay() syntax was used to control the time. The loop terminated when the variable *a* equaled 255. The second loop was then executed using the same principle in reverse to control the decrease in magnetic force, thus completing the coding of the magnetic system.

Measurement of Magnetic Film Deformation

The electromagnet was placed under the magnetic film, and then the electromagnet was opened to deform the film. The deformation of the film was recorded using a 3D shape measuring instrument (S neox non-contact 3D optical profiler, Sensofar). An image of the magnetic film as well as the 3D reconstructed image and film deformation were obtained directly from the measurement results. In addition, the deformation values were directly measured and the data were plotted using OriginLab and GraphPad Prism software.

Measurements of Flow Rate in a Microchannel

The 2 mL of polystyrene particles having a particle size of 19.2 μm and a concentration of 2×10^5 beads/mL were injected into

the magnetic driven chip. The chip was then placed on the Electromagnet System, and Arduino was used to program the magnetic regulation of the particle flow rate in the microchannels. The flow rate measurement was divided into sinusoidal and stepped sinusoidal signals cyclic flows. First, a sinusoidal function generator was used to generate 8 bits (0–255) for a total of 256 values. Next, a matrix with a capacity of 256 values was coded in Arduino, and then the same loop was used to iterate the initial value from 0 to 255. Thus, a complete sine wave signal could be obtained, and the rate of flow could be adjusted by delaying the time of each iteration. Finally, a microscope was used to observe the flow of particles in the microchannels, and video was captured using the recording mode of the microscope software at 60 fps. The flow velocity (μm/s) of the particles was inferred from the recorded video using the tracker video analysis and modeling tool[1]. After the flow velocity (μm/s) was determined and then converted to the volumetric flow rate (μL/min) in the microchannels in different modes for continuous cell culture.

Cell Culture and Analysis

The human pulmonary alveolar epithelial cells (HPAEpiC) used in this study were obtained from ScienCell Research Laboratories (Catalog #3200). First, 2 μg/cm^2 poly-L-lysine (Sigma–Aldrich) was added to a T-75 flask (75 cm^2) before inoculation of the cells. Next, cells were inoculated at a density of 10,000–15,000 cells/cm^2 into the culture dish with alveolar epithelial cell medium (AEpiCM, ScienCell), epithelial cell growth supplement (EpiCGS, ScienCell), fetal bovine serum (FBS, ScienCell), and penicillin/streptomycin solution (P/S, ScienCell), and then cultured at 37°C and 5% CO_2. The culture medium was changed every other day, and then every 3 days until the confluent state was reached. In subsequent analytical experiments, live and dead cells were detected by staining with green and red fluorescence, respectively, using a LIVE/DEAD assay (GeneCopoeia™), and cell viability was verified by fluorescence microscopy. Next, we added the primary antibody SPC (AB3786, Millipore) at a concentration of 1:1000, a Cy3-fluorescence labeled goat anti-rabbit secondary antibody (2707846, Cell signal) at a concentration of 1:200, and Alexa Fluor® 488-labeled phalloidin (A12379, Invitrogen) at a concentration of 1:200. After immunofluorescence staining, protein expression was observed with a fluorescence microscope (Ti-U, Nikon).

ELISA Assays

For detecting the release of interleukin 6 (IL-6), the human IL-6 ELISA kit from Invitrogen (Thermo Fisher Scientific) was

[1]https://physlets.org/tracker/

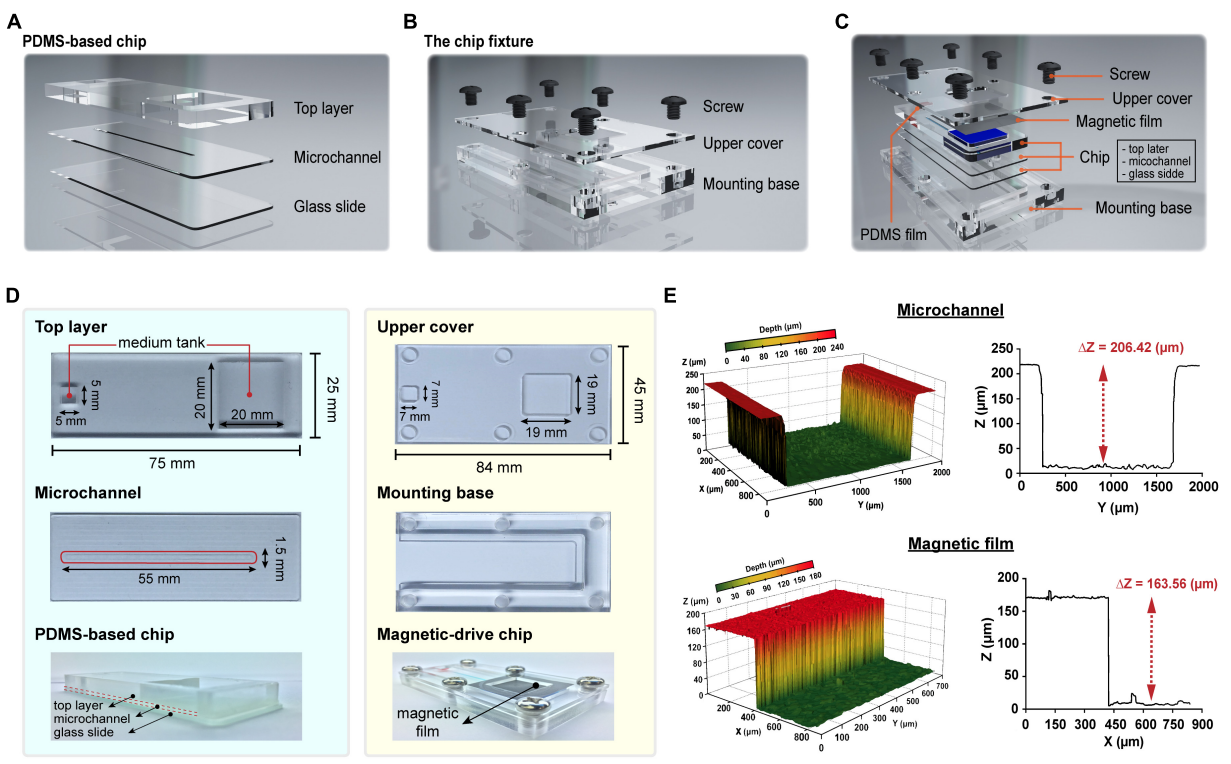


FIGURE 1 | Design and fabrication of the magnetic driven chip. **(A)** Schematic of PDMS-based three-layer chip containing top layer, microchannel, and glass slide. **(B)** Schematic of chip fixture containing upper cover and mounting base. **(C)** Designing an assembly drawing of magnetic driven chip and its components (PDMS-based chip, chip fixture, and PDMS/magnetic film). **(D)** Fabrication of a magnetic driven chip includes a chip with process combining PDMS and glass slide (left side) and chip fixture of transparent acrylic plastic plates (right side). **(E)** The 3D surface morphology measurement of microchannels and magnetic films. *Z*-axis depth analysis showed that the height of the chip microchannel was 206.42 μm and the film thickness was 163.56 μm.

utilized. The supernatant of the plate cell culture wells was aspirated after the set exposure time to the treatments. The supernatant of the microfluidic chips was aspirated out of the medium. The test was carried out by following the protocol.

Statistical Analysis

The data were analyzed via Student's *t*-test or one-way ANOVA using the GraphPad Prism software and expressed as the mean ± standard deviation based on observations of the 10 representative fluorescent images obtained from three independent experiments. *P*-values <0.05 were considered statistically significant.

RESULTS AND DISCUSSION

Fabrication of the Magnetic Driven Chip

The overall structure of the proposed magnetic driven chip can be primarily divided into two parts – (i) a PDMS-based three-layer chip comprising a top layer, middle layer (microchannel), and glass slide (bottom layer) (**Figure 1A** and **Supplementary Figure S1**) and (ii) a chip fixture comprising an upper cover and mounting base (**Figure 1B**). The layers in the first part are bonded to each other by oxygen plasma activated bonding. The upper layer of the chip is a rectangular cuboid contains two square slots. These empty slots are primarily used to hold the cell medium. The second layer is a microchannel layer while the third layer is a glass slide. After the second and third layers are bonded, a microchannel is formed to constitute the area for cell culture. Finally, the magnetic and PDMS films are placed on the cell-culture-medium container slot formed on the chip, respectively. The upper cover and mounting base of the second part both contain six M6 holes (a hole with diameter measuring 6 mm and containing a thread) (**Figure 1C**). In addition, two square areas are carved of the upper cover. The area inside the fixture is responsible for fabricating the said three-layer chip (**Figure 1D**). The thickness of the magnetic film and chip-microchannel height were measured to be 163.56 and 206.42 μm, respectively, using a 3-D shape measuring instrument (**Figure 1E** and **Supplementary Figure S2**). The chip and fixture were sealed via fixation using a 1.5 N.m torque screw, thereby completing the assembly of the entire magnetic driven chip system (**Supplementary Video S1**).

Manipulation of the Magnetic Driven Chip

To facilitate performing cell culture experiments on the proposed magnetic driven chip, the said magnetic chip was first set

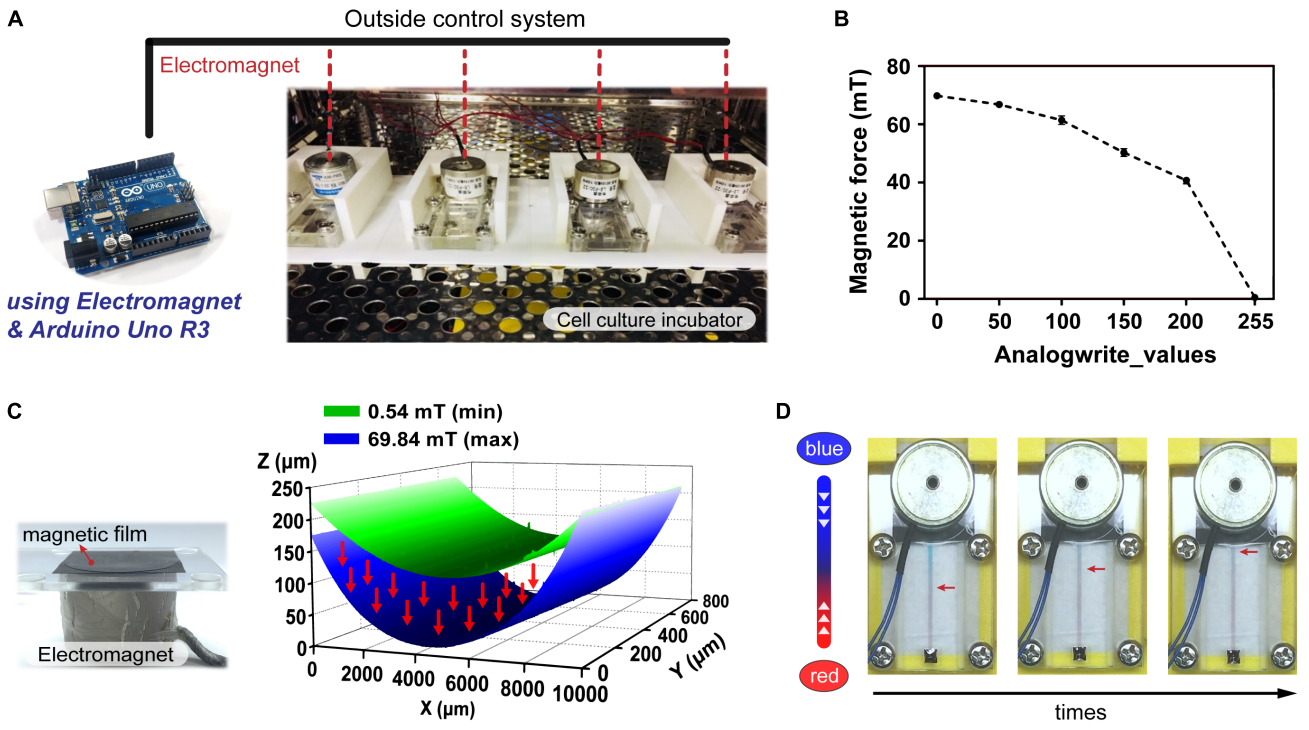


FIGURE 2 | Operation and control of the magnetic driven chip. **(A)** Actual image of a magnetic driven chip used for cell culture. The electromagnetism (magnetic force) and elastically deformed magnetic film of magnetic driven chip inside an incubator at 37°C was controlled by an external Arduino control board. **(B)** Measurement and analysis of the change in magnetic force of the electromagnet. The magnetic field corresponding to different analogWrite() values recorded by the magnetic field Gauss meter in the Arduino program ranged from 0.54 to 69.84 mT (n = 5). **(C)** Deformation of the magnetic film after being subjected to different magnetic fields. The 3D surface morphology measurement results showed that the distance of magnetic film deformation corresponding to magnetic fields of 0.54–69.84 mT could reach 203.49 μm. **(D)** Status of the fluid during long-term fluid flow. Two liquids with different colors (red/blue) had no leakage and maintained a stable flow field.

firmly along with an electromagnetic module inside a constant temperature incubator maintained at 37°C (**Figure 2A**). When the electromagnetic module was placed above the magnetic film, the film underwent different types of deformations depending on the magnetic force magnitude. The said magnitude could be used to control the electromagnetic module that transmits electrical signals to the incubator through a connecting wire using an Arduino control board (**Supplementary Figure S3**). To determine the limit of the magnetic force in this system, we divided the magnetic force into 0–255 equal parts, which were recorded using a magnetic field Gauss meter. The magnetic force can be sequentially controlled in PWM mode, with the analogWrite() function which analog value – 0, 50, 100, 200, and 255. For analogWrite() = 255, the magnetic force of the electromagnet was observed to be minimum, and its maximum values equaled approximately 69.84 mT for analogWrite() = 0 (**Figure 2B**). **Figure 2C** demonstrates that when the magnetic force equals 69.84 mT, the film-shape variable measures 203.49 μm. This serves to effectively drive the liquid through flow channels, thereby resulting in dynamic flow. **Figure 2D** demonstrates that upon injection of two colored dyes into the flow, the system continues to operate stably for a considerable duration without occurrence of any dye leakage. As can be observed in the figure, driving the magnetic film using a magnet makes the red-colored dye flow onto the other side owing to difference in pressure. Flow of the dye on the chip demonstrates feasibility of the magnetically driven chip system to sustain stable dynamic flow (**Supplementary Video S2**).

Programmable Control of the Magnetic Driven Chip

An important advantage of the proposed system is that it does not require use of complicated structures, such as pumps and tubes, and that it is simple to implement. Arduino controls the magnetic force-induced deformation of the magnetic film, thereby establishing a simple and controllable fluid dynamic environment (**Figure 3A**). To further elucidate the feasibility of controlling the flow rate within a microchannel, nanoparticles were introduced into the flowing liquid, and the flow velocity of particles within the channel was calculated using the tracker video analysis and modeling tool (see text footnote 1). Subsequently, the liquid flow rate (μm/s) was converted to volumetric flow rate (μL/min) (**Supplementary Table S1**). **Figure 3B** demonstrates that for analogWrite() values of 0, 50, 100, 150, and 200, the corresponding volumetric flow rates equal 18.18, 18.14, 12.53, 8.18, and 3.88 μL/min, respectively, thereby indicating that the magnetically driven chip system can not only drive liquid flow but also dynamically change the flow rate within channels in real time by making adjustments to the magnetic force and magnetic film deformation parameter. In addition, the Arduino program can be used to control the magnetic force by using different signal output methods, such as sinusoidal

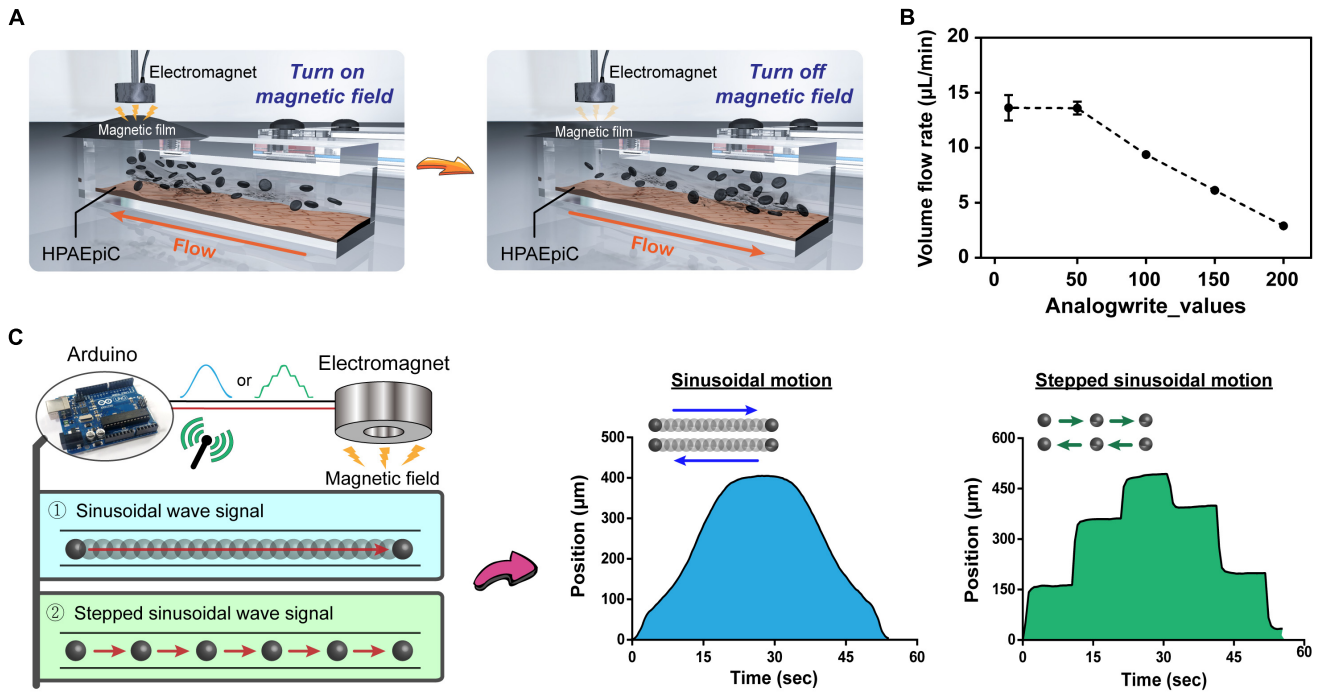


FIGURE 3 | Programmable control of fluid flow patterns and rates. **(A)** Schematic of immediate control of changes in the magnetic film. The chip system does not contain any microfluidic tubing device, and the flow of liquid can be rapidly and easily changed through programmed changes in the magnetic field using Arduino. **(B)** Fluid flow rates corresponding to the magnitude of the magnetic field. Adding nanoparticles to the liquid allowed for visual observation and calculation through microscopy, with flow rates ranging from 2.90 to 13.64 μL/min (n = 3). **(C)** Evaluation of changes in magnetic fields by different signal patterns, sinusoidal and stepped sinusoidal signals were used for cyclical flow in the microchannel, and the non-linear flow rate (non-fixed value) could be adjusted flexibly to meet various conditions in the body.

and stepped sinusoidal signals to control the cyclic flow of liquid within flow channels (**Figure 3C** and **Supplementary Videos S3, S4**). Compared to straight line linear flow systems, the fluid demonstrates not only a fixed but also an adjustable flow pattern, thereby provides new options for performing microfluidic cell cultures.

Magnetic Driven Chip for Modeling the Alveolar

To further understand advantages of the proposed method for use in cell culture and future tissue chip applications, HPAEpiCs were cultured using the proposed magnetically driven dynamic system with collagen coating being used as the chip–substrate interface material (**Figure 4A**). The cell concentration inoculated on the chip was set as 2×10^6 cells/mL (**Supplementary Figure S4**), and the effects of liquid circulation on cell culture were observed using different output signals, such as sinusoidal and stepped sinusoidal signals. Results of this investigation demonstrated the cells to be in their best condition after 5 days of cell proliferation when fluid flow was controlled using a stepped sinusoidal signal (**Figure 4B**). Additionally, the shear stress and nutrient exchange functions realized by the flow rate were deemed to be most suitable for cell culture. **Figure 4C** demonstrates that observation of the cells via LIVE/DEAD assay revealed no obvious cell death in the chip after 7 days of dynamic culture. Recapitulation of the effect on cell viability within channels revealed the cells to remain intact and uniform when cultured using the proposed on-chip system. Fluorescence staining facilitated clear observation of the tight-junction marker zonula occludens-1 (ZO-1), produced by tight junctions of the cell in real time, along with the specific surfactant protein C (SPC) secreted by AEII cells (**Figure 4D**). This implies that the proposed culture method not only leads to uniform cell culture on-chip but also maintains the barrier function and differentiation ability of AEII cells. In view of these advantages, microchannel cell culture, such as that performed on cell or organ chips, is no longer dependent on only a single parameter for flow rate control, and that use of a magnetic drive effectively controls the fluid flow pattern in the step-signal-output mode. The frequency and shear stresses generated within the chip tend to rapidly adjust optimum growth conditions for the cells (**Supplementary Table S2**), thereby recapitulating the cell structure and maintaining the cell-differentiation ability. This helps us realize the advantages of *in vitro* analysis of the tissue function and cell-biochemical activity.

Functionality of the Magnetic Driven Alveolus Cell-Culture Chip

To thoroughly compare the differences in cellular response between the proposed magnetic driven system and generic

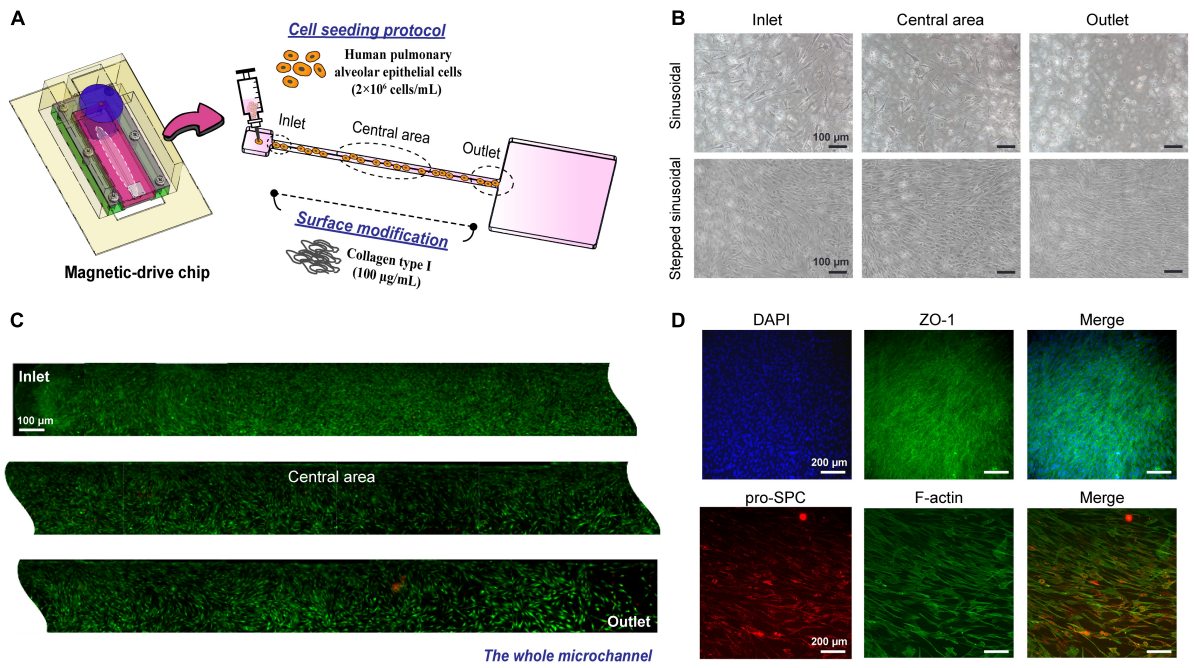


FIGURE 4 | HPAEpiC cells cultured in a dynamic magnetic driven chip. **(A)** Schematic of cell seeding in the chip. First, the substrate was treated with collagen, and cell suspension with a concentration of 2×10^6 cells/mL was injected into the microchannel. **(B)** Effect of magnetic field signaling mode on cell growth. Cells were cultured for 5 days using the sinusoidal signal and stepped sinusoidal signal, and the stepped sinusoidal had the optimal cell density and morphology. Stepped sinusoidal signals were thus used in subsequent experiments. Scale bar is 100 μm. **(C)** Fluorescence of viable cells cultured in a dynamic flow environment. After 7 days of continuous perfusion flow field driven by the magnetic film, it was observed by LIVE/DEAD assay that the entire flow channel exhibited good cell viability and sufficient growth. Scale bar is 100 μm. **(D)** The functional characterization of cells cultured in a dynamic flow environment. Immunofluorescence image of a monolayer formed by HPAEpiC cells after 7 days of culture, which included a barrier function (tight junction protein 1, ZO-1) and specific pro-surfactant protein C (pro-SPC) secreted by HPAEpiC. Scale bar is 200 μm.

static culture methods, a stimulation was performed using silica nanoparticles (Si-NPs) at a concentration of 50 μg/mL and identical cell density (**Figure 5A**). **Figure 5B** demonstrates that cells grown using static culture methods exhibit considerable cell death after 24 h of stimulation, whereas minimal cell death can be in cells grown using the magnetic driven system. **Figure 5C** illustrates a significant difference in the IL-6 inflammatory response of Si-NPs between static and dynamic systems. The IL-6 concentration expressed after performing the Si-NPs stimulation in a static environment was observed to be much higher with a tendency to increase with increase in stimulation time. A similar phenomenon was observed when comparing results obtained through use of a conventional peristaltic pump with static cells. Silica-treated cells in the dynamic system were, in general, observed to be healthy with a few dead cells spreading over the cell complex (Rothbauer et al., 2015; Yazdimamaghani et al., 2018). Thus, regarding to device simplification, use of the proposed magnetic driven system not only provides advantages but also facilitates on-chip fluid flow to be controlled using the magnetic-output mode, which in turn facilitates rapid attainment of optimum growth conditions for cells in a feasible manner. Comparing the results of cytotoxicity and immune reactions obtained via Si-NPs stimulation also demonstrates that use of the proposed system results in occurrence of a smaller number of inflammatory reactions compared to the static cell culture system. This result is similar to that obtained using a dynamic system driven by a conventional peristaltic pump (**Supplementary Figure S5**). In order to further investigate the difference in reactions stimulated by Si-NPs between the dynamic and static cell-culture environments, cell cultures were performed using blue fluorescent polystyrene particles (blue particles) in identical concentrations for 24 h in using either the magnetic driven system or static culture environment (**Figures 5D,E**). Corresponding results demonstrated that compared to the static environment, polystyrene particles were less likely to adhere to cells in the dynamic environment (Rothbauer et al., 2015). Thus, cell deaths and inflammatory reactions caused by the particles may not be significant (**Figure 5F**). This result is also consistent with dynamic environment phenomena occurring inside the human body (Björnmalm et al., 2016). In addition to demonstrating the feasibility of using a magnetic driven system for cell culture and stimulation within a dynamic

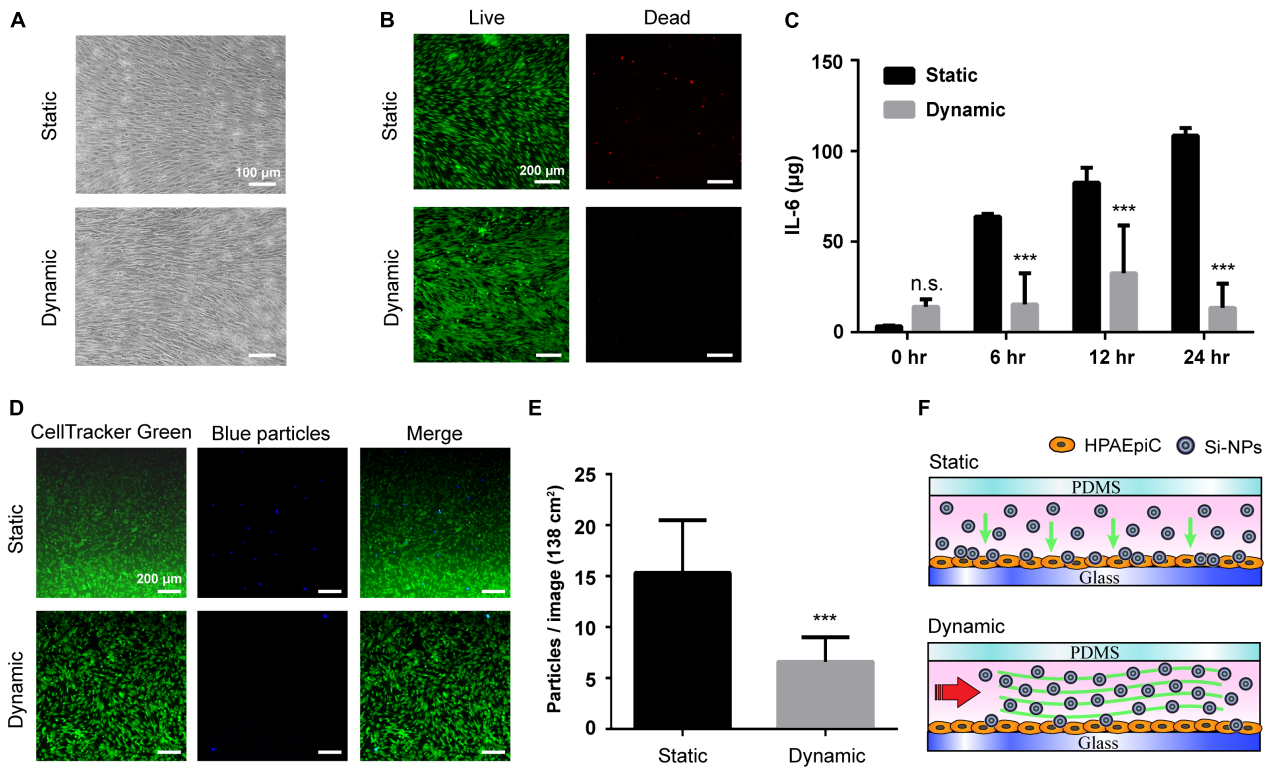


FIGURE 5 | Magnetic driven chip applied to inflammatory reactions to stimuli. **(A)** Bright field images of cells cultured on static and dynamic environment after exposure to Si-NPs at a concentration of 50 μg/mL for 24 h. Scale bar is 100 μm. **(B)** After 24 h treatment of Si-NPs, the cells were observed by LIVE/DEAD assay staining that cell viability in the static culture was significantly lower than in the dynamic culture. Scale bar is 200 μm. **(C)** Comparison of the immune response after Si-NPs stimulation. The concentration of IL-6 produced by cells in the static environment was much higher, and the concentration increased as the time of exposure increased (*** $p < 0.001$; $n = 3$). **(D)** Fluorescence of particles deposited in dynamic and static environments. After adding blue fluorescent particles (blue particles), the number of particles deposited in the cells in the static environment after 24 h was significantly higher than in the dynamic environment. Scale bar is 200 μm. **(E)** Quantification of the number of blue particles deposited on the cells. The particles deposited on the cells were calculated from fluorescent signals, and the results showed that the number in the static environment was twice that in the dynamic environment (***$p < 0.001$; $n = 10$). **(F)** Schematic of the particle deposition process when exposing Si-NPs that is added in the magnetic driven chip with static and dynamic environment.

environment, these results also demonstrate that magnetic driven systems mimics the dynamic environment of the human body more closely, thereby generating a relatively greater amount of meaningful data.

CONCLUSION

The present study describes the development of a new type of magnetically driven chip. The proposed system facilitates selection of magnetically controllable output modes, and employs a magnetic film as a medium to control fluid circulation through on-chip microchannels, thereby overcoming bottlenecks associated with primary on-chip human cell culture while also addressing problems pertaining to uniform and long-term on-chip culture of alveolar cells along with recapitulation of the cell structure and cell differentiation functions (**Supplementary Figure S6**). Reactions between human alveolar epithelial cells and Si-NPs were assessed to validate differences between the dynamic environment produced by the chip and conventional static environments, thereby realizing functions and advantages of *in vitro* tissue construction. Numerous techniques have been developed in recent years to construct organs and/or tissues on chips to resolve the enormous differences between animal experiments and clinical trials (Capulli et al., 2014; Ahadian et al., 2018).

However, representing individualized differences on chips yet remains a major challenge. The proposed system does not only not require complicated structures, such as pumps and tubes, thereby simplifying device construction, but also greatly reduces external factors derived from equipment requirements and human influenced factors during experiments. The system also possesses a wireless connection system capable of collecting breathing signals of individuals. It can simulate the most realistic individualized breathing models by converting parameters, such as individual respiratory rate and respiratory force. This helps facilitate collection of more realistic and effective information with regard to drug screening as well as establishment of individualized disease models. In view of these advantages, the system demonstrates great potential for use in applications related to bionic engineering of tissue and organ chips.

DATA AVAILABILITY STATEMENT

All datasets generated for this study are included in the article/**Supplementary Material**.

AUTHOR CONTRIBUTIONS

J-WY, Y-WC, and G-YC contributed to the conception of the study. J-WY, Y-WC, P-YH, and LJ carried out the experiments. KH, S-JC, and K-CL helped perform the analysis with constructive discussions. H-EL, H-YC, S-FL, and G-YC supervised the research design. J-WY and G-YC wrote the manuscript. All authors listed have made a substantial, direct and intellectual contribution to the work, and approved it for publication.

FUNDING

G-YC would like to acknowledge financial support from the National Chiao Tung University (106W970, 107W970), the Ministry of Science and Technology (MOST 106-EPA-F006-001, MOST 107-2622-E-009-023-CC1, MOST 107-2218-E-080-001-, MOST 108-2218-E-080-001, MOST-107-EPA-F-007-002, and MOST 108-2636-E-009-007-), the National Health Research Institutes (NHRI-EX107-10714EC and NHRI-EX108-10714EC), and the Higher Education Sprout Project of the National Chiao Tung University and the Ministry of Education, Taiwan.

SUPPLEMENTARY MATERIAL

The Supplementary Material for this article can be found online at: https://www.frontiersin.org/articles/10.3389/fcell.2019.00275/full#supplementary-material

REFERENCES

Ahadian, S., Civitarese, R., Bannerman, D., Mohammadi, M. H., Lu, R., Wang, E., et al. (2018). Organ-on-a-chip platforms: a convergence of advanced materials. *Cells Microscale Technol.* 7:1700506. doi: 10.1002/adhm.201700506

Badamasi, Y. A. (2014). "The working principle of an Arduino," in *Proceedings of the 11th International Conference on Electronics, Computer and Computation (ICECCO)*, Nigeria, 1–4.

Barkauskas, C. E., Cronce, M. J., Rackley, C. R., Bowie, E. J., Keene, D. R., Stripp, B. R., et al. (2013). Type 2 alveolar cells are stem cells in adult lung. *J. Clin. Invest.* 123, 3025–3036. doi: 10.1172/JCI68782

Benam, K. H., Novak, R., Nawroth, J., Hirano-Kobayashi, M., Ferrante, T. C., Choe, Y., et al. (2016). Matched-comparative modeling of normal and diseased human airway responses using a microengineered breathing lung chip. *Cell Syst.* 3:456–466e4.

Benam, K. H., Villenave, R., Lucchesi, C., Varone, A., Hubeau, C., Lee, H.-H., et al. (2015). Small airway-on-a-chip enables analysis of human lung inflammation and drug responses in vitro. *Nat. Methods* 13, 151–157. doi: 10.1038/nmeth.3697

Björnmalm, M., Faria, M., Chen, X., Cui, J., and Caruso, F. (2016). Dynamic flow impacts cell–particle interactions: sedimentation and particle shape effects. *Langmuir* 32, 10995–11001. doi: 10.1021/acs.langmuir.6b03216

Bove, P. F., Dang, H., Cheluvaraju, C., Jones, L. C., Liu, X., O'Neal, W. K., et al. (2014). Breaking the in vitro alveolar type II cell proliferation barrier while retaining ion transport properties. *Am. J. Respir. Cell Mol. Biol.* 50, 767–776. doi: 10.1165/rcmb.2013-0071OC

Byun, C. K., Abi-Samra, K., Cho, Y.-K., and Takayama, S. (2014). Pumps for microfluidic cell culture. *Electrophoresis* 35, 245–257. doi: 10.1002/elps.201300205

Capulli, A. K., Tian, K., Mehandru, N., Bukhta, A., Choudhury, S. F., Suchyta, M., et al. (2014). Approaching the in vitro clinical trial: engineering organs on chips. *LChip* 14, 3181–3186. doi: 10.1039/c4lc00276h

Chiu, D. T., deMello, A. J., Di Carlo, D., Doyle, P. S., Hansen, C., Maceiczyk, R. M., et al. (2017). Small but perfectly formed? successes, challenges, and

opportunities for microfluidics in the chemical and biological sciences. *Chem* 2, 201–223. doi: 10.1016/j.chempr.2017.01.009

Crapo, J. D., Barry, B. E., Gehr, P., Bachofen, M., and Weibel, E. R. (1982). Cell number and cell characteristics of the normal human lung. *Am. Rev. Respir. Dis.* 126, 332–337.

Dardik, A., Chen, L., Frattini, J., Asada, H., Aziz, F., Kudo, F. A., et al. (2005). Differential effects of orbital and laminar shear stress on endothelial cells. *J. Vasc. Surg.* 41, 869–880. doi: 10.1016/j.jvs.2005.01.020

Douville, N. J., Zamankhan, P., Tung, Y. C., Li, R., Vaughan, B. L., Tai, C. F., et al. (2011). Combination of fluid and solid mechanical stresses contribute to cell death and detachment in a microfluidic alveolar model. *Lab. Chip* 11, 609–619. doi: 10.1039/c0lc00251h

Esch, E. W., Bahinski, A., and Huh, D. (2015). Organs-on-chips at the frontiers of drug discovery. *Nat. Rev. Drug Discov.* 14, 248–260. doi: 10.1038/nrd4539

Fehrenbach, H. (2001). Alveolar epithelial type II cell: defender of the alveolus revisited. *Respir. Res.* 2, 33–46.

Freund, J. B., Goetz, J. G., Hill, K. L., and Vermot, J. (2012). Fluid flows and forces in development: functions, features and biophysical principles. *Development* 139, 1229–1245. doi: 10.1242/dev.073593

Fujino, N., Kubo, H., Ota, C., Suzuki, T., Suzuki, S., Yamada, M., et al. (2012). A novel method for isolating individual cellular components from the adult human distal lung. *Am. J. Respir. Cell Mol. Biol.* 46, 422–430. doi: 10.1165/rcmb.2011-0172OC

Grek, C. L., Newton, D. A., Qiu, Y., Wen, X., Spyropoulos, D. D., and Baatz, J. E. (2009). Characterization of alveolar epithelial cells cultured in semipermeable hollow fibers. *Exp. Lung Res.* 35, 155–174. doi: 10.1080/01902140802495870

Guenat, O. T., and Berthiaume, F. (2018). Incorporating mechanical strain in organs-on-a-chip: lung and skin. *Biomicrofluidics* 12:042207. doi: 10.1063/1.5024895

Halldorsson, S., Lucumi, E., Gomez-Sjoberg, R., and Fleming, R. M. T. (2015). Advantages and challenges of microfluidic cell culture in polydimethylsiloxane devices. *Biosens. Bioelectron.* 63, 218–231. doi: 10.1016/j.bios.2014.07.029

Hogan, B. (2018). Stemming lung disease? *N. Engl. J. Med.* 378, 2439–2440. doi: 10.1056/nejmcibr1803540

Huh, D., Leslie, D. C., Matthews, B. D., Fraser, J. P., Jurek, S., Hamilton, G. A., et al. (2012). A human disease model of drug toxicity-induced pulmonary edema in a lung-on-a-chip microdevice. *Sci. Transl. Med.* 4:ra147. doi: 10.1126/scitranslmed.3004249

Huh, D., Matthews, B. D., Mammoto, A., Montoya-Zavala, M., Hsin, H. Y., and Ingber, D. E. (2010). Reconstituting organ-level lung functions on a chip. *Science* 328, 1662–1668. doi: 10.1126/science.1188302

Jain, R., Barkauskas, C. E., Takeda, N., Bowie, E. J., Aghajanian, H., Wang, Q., et al. (2015). Plasticity of Hopx(+) type I alveolar cells to regenerate type II cells in the lung. *Nat. Commun.* 6:6727. doi: 10.1038/ncomms7727

Kim, D., Wu, X., Young, A. T., and Haynes, C. L. (2014). Microfluidics-based in vivo mimetic systems for the study of cellular biology. *Acc. Chem. Res.* 47, 1165–1173. doi: 10.1021/ar4002608

Kimura, H., Sakai, Y., and Fujii, T. (2018). Organ/body-on-a-chip based on microfluidic technology for drug discovery. *Drug Metab. Pharmacokinet.* 33, 43–48. doi: 10.1016/j.dmpk.2017.11.003

Mao, P., Wu, S., Li, J., Fu, W., He, W., Liu, X., et al. (2015). Human alveolar epithelial type II cells in primary culture. *Physiol. Rep.* 3:e12288. doi: 10.14814/phy2.12288

Mark, D., Haeberle, S., Roth, G., von Stetten, F., and Zengerle, R. (2010). Microfluidic lab-on-a-chip platforms: requirements, characteristics and applications. *Chem. Soc. Rev.* 39, 1153–1182. doi: 10.1039/b820557b

Mason, R. J. (2006). Biology of alveolar type II cells. *Respirology* 11(Suppl.1), S12–S15.

Nabhan, A. N., Brownfield, D. G., Harbury, P. B., Krasnow, M. A., and Desai, T. J. (2018). Single-cell Wnt signaling niches maintain stemness of alveolar type 2 cells. *Science* 359, 1118–1123. doi: 10.1126/science.aam6603

Nikolic, M. Z., Caritg, O., Jeng, Q., Johnson, J. A., Sun, D., Howell, K. J., et al. (2017). Human embryonic lung epithelial tips are multipotent progenitors that can be expanded in vitro as long-term self-renewing organoids. *eLife* 6:e26575. doi: 10.7554/eLife.26575

Ronaldson-Bouchard, K., and Vunjak-Novakovic, G. (2018). Organs-on-a-chip: a fast track for engineered human tissues in drug development. *Cell Stem Cell* 22, 310–324. doi: 10.1016/j.stem.2018.02.011

Rothbauer, M., Praisler, I., Docter, D., Stauber, R., and Ertl, P. J. B. (2015). Microfluidic impedimetric cell regeneration assay to monitor the enhanced cytotoxic effect of nanomaterial perfusion. *Biosensors* 5, 736–749. doi: 10.3390/bios5040736

Royet, D., Hériveaux, Y., Marchalot, J., Scorretti, R., Dias, A., Dempsey, N. M., et al. (2017). Using injection molding and reversible bonding for easy fabrication of magnetic cell trapping and sorting devices. *JMMM* 427, 306–313. doi: 10.1016/j.jmmm.2016.10.102

Stucki, A. O., Stucki, J. D., Hall, S. R., Felder, M., Mermoud, Y., Schmid, R. A., et al. (2015a). A lung-on-a-chip array with an integrated bio-inspired respiration mechanism. *Lab. Chip* 15, 1302–1310. doi: 10.1039/c4lc01252f

Stucki, A. O., Stucki, J. D., Hall, S. R. R., Felder, M., Mermoud, Y., Schmid, R. A., et al. (2015b). A lung-on-a-chip array with an integrated bio-inspired respiration mechanism. *LChip* 15, 1302–1310. doi: 10.1039/c4lc01252f

Stucki, J. D., Hobi, N., Galimov, A., Stucki, A. O., Schneider-Daum, N., Lehr, C.-M., et al. (2018). Medium throughput breathing human primary cell alveolus-on-chip model. *Sci. Rep.* 8:14359. doi: 10.1038/s41598-018-32523-x

Tehranirokh, M., Kouzani, A. Z., Francis, P. S., and Kanwar, J. R. (2013). Microfluidic devices for cell cultivation and proliferation. *Biomicrofluidics* 7:51502. doi: 10.1063/1.4826935

Temiz, Y., Lovchik, R. D., Kaigala, G. V., and Delamarche, E. (2015). Lab-on-a-chip devices: how to close and plug the lab? *MiEng* 132, 156–175. doi: 10.1016/j.mee.2014.10.013

Yazdimamaghani, M., Barber, Z. B., Hadipour Moghaddam, S. P., and Ghandehari, H. (2018). Influence of silica nanoparticle density and flow conditions on sedimentation, cell uptake, and cytotoxicity. *Mol. Pharm.* 15, 2372–2383. doi: 10.1021/acs.molpharmaceut.8b00213

Zacharias, W. J., Frank, D. B., Zepp, J. A., Morley, M. P., Alkhaleel, F. A., Kong, J., et al. (2018). Regeneration of the lung alveolus by an evolutionarily conserved epithelial progenitor. *Nature* 555, 251–255. doi: 10.1038/nature25786

Zheng, D., Soh, B. S., Yin, L., Hu, G., Chen, Q., Choi, H., et al. (2017). Differentiation of club cells to alveolar epithelial cells in vitro. *Sci. Rep.* 7:41661. doi: 10.1038/srep41661

Conflict of Interest: The authors declare that the research was conducted in the absence of any commercial or financial relationships that could be construed as a potential conflict of interest.

Copyright © 2019 Yang, Chen, Ho, Jiang, Hsieh, Cheng, Lin, Lu, Chiu, Lin and Chen. This is an open-access article distributed under the terms of the Creative Commons Attribution License (CC BY). The use, distribution or reproduction in other forums is permitted, provided the original author(s) and the copyright owner(s) are credited and that the original publication in this journal is cited, in accordance with accepted academic practice. No use, distribution or reproduction is permitted which does not comply with these terms.

frontiers in Cell and Developmental Biology

ORIGINAL RESEARCH
published: 05 March 2020
doi: 10.3389/fcell.2020.00122

Epiphyseal Cartilage Formation Involves Differential Dynamics of Various Cellular Populations During Embryogenesis

Yi Zhang[1,2], Karl Annusver[3], Kazunori Sunadome[2], Polina Kameneva[2], Steven Edwards[4], Guanghua Lei[1], Maria Kasper[3], Andrei S. Chagin[2,5], Igor Adameyko[2,6] and Meng Xie[2]**

[1] Department of Orthopaedics, Xiangya Hospital, Central South University, Changsha, China, [2] Department of Physiology and Pharmacology, Karolinska Institutet, Solna, Sweden, [3] Department of Biosciences and Nutrition, Karolinska Institutet, Huddinge, Sweden, [4] Light Sheet Microscopy Pilot Facility at SciLifeLab, KTH Royal Institute of Technology, Stockholm, Sweden, [5] Institute for Regenerative Medicine, I.M. Sechenov First Moscow State Medical University, Moscow, Russia, [6] Department of Molecular Neurosciences, Medical University of Vienna, Vienna, Austria

OPEN ACCESS

Edited by:
Katiucia Batista Silva Paiva, University of São Paulo, Brazil

Reviewed by:
Maurizio Pacifici, Children's Hospital of Philadelphia, United States
Noriaki Ono, University of Michigan, United States

***Correspondence:**
Igor Adameyko
igor.adameyko@ki.se
Meng Xie
meng.xie@ki.se

Specialty section:
This article was submitted to Stem Cell Research, a section of the journal Frontiers in Cell and Developmental Biology

Received: *20 November 2019*
Accepted: *12 February 2020*
Published: *05 March 2020*

Citation:
Zhang Y, Annusver K, Sunadome K, Kameneva P, Edwards S, Lei G, Kasper M, Chagin AS, Adameyko I and Xie M (2020) Epiphyseal Cartilage Formation Involves Differential Dynamics of Various Cellular Populations During Embryogenesis. Front. Cell Dev. Biol. 8:122. doi: 10.3389/fcell.2020.00122

A joint connects two or more bones together to form a functional unit that allows different types of bending and movement. Little is known about how the opposing ends of the connected bones are developed. Here, applying various lineage tracing strategies we demonstrate that progenies of Gdf5-, Col2-, Prrx1-, and Gli1-positive cells contribute to the growing epiphyseal cartilage in a spatially asymmetrical manner. In addition, we reveal that cells in the cartilaginous anlagen are likely to be the major sources for epiphyseal cartilage. Moreover, Gli1-positive cells are found to proliferate along the skeletal edges toward the periarticular region of epiphyseal surface. Finally, a switch in the mechanism of growth from cell division to cell influx likely occurs in the epiphyseal cartilage when joint cavitation has completed. Altogether, our findings reveal an asymmetrical mechanism of growth that drives the formation of epiphyseal cartilage ends, which might implicate on how the articular surface of these skeletal elements acquires their unique and sophisticated shape during embryonic development.

Keywords: joint, cartilage, clonal tracing, asymmetrical, dynamics, embryonic development

INTRODUCTION

Synovial joints are structures located between adjacent skeletal elements, allowing different types of locomotion. The joint surface is covered by articular cartilage and is mechanically stabilized by ligaments that connect the skeletal elements together. Early limb formation starts from a continuous and uninterrupted Y-shaped cartilaginous anlagen (Hamrick, 2001). The developing limb buds consist of undifferentiated mesenchyme that express Paired related homeobox 1 (Prrx1) (Martin and Olson, 2000). The first sign that marks the initiation of the joint formation process is the accumulation of a condensed mesenchymal cell population at the future joint site within the anlagen, so-called the interzone. Cells within the interzone express a new set of genes, including the growth differentiation factor 5 (Gdf5) and serve as joint progenitors by generating a continuous influx of newly produced cells into the developing joint (Koyama et al., 2008; Shwartz et al., 2016).

Synovial joints are often uniquely shaped with complex surfaces of adjusted bones matching each other. How this unique morphogenesis is achieved is not clear.

Generally, joint shape morphogenesis begins once the cavitation and synovial space formation initiate (Pacifici et al., 2005), however, one study provided evidence that the process precedes cavitation during hip joint development in chicken (Nowlan and Sharpe, 2014). This remarkable process that defines a variety of distinct joint shapes specific for individual anatomical sites remains the least understood aspect of joint formation. It has been proposed that the proximal and distal ends of the connected skeletal elements might grow simultaneously to complement each other into an interlocking and reciprocally shaped structure (Pacifici et al., 2005). At the cellular level, knee joint development involves cells from the initial anlagen that express collagen type 2 (Col2) and later become interzone cells that turn off Col2 expression, as well as Col2-negative mesenchymal cells recruited from the surroundings that later differentiate into Col2-positive chondrocytes (Hyde et al., 2008).

Hedgehog (Hh) signaling is an evolutionarily conserved pathway that plays important roles in limb development (Tickle and Towers, 2017). There are three Hh homologous proteins in mammals: Sonic hedgehog (Shh), Indian hedgehog (Ihh), and Desert hedgehog (Dhh). When Hh ligands bind to their binding partner Patched (Ptch) at the cell surface it relieves the inhibition of Ptc on another transmembrane protein, Smoothened (Smo) (Corbit et al., 2005; Rohatgi et al., 2007); leading to its phosphorylation by various kinases that eventually activates the Gli transcription factors to promote transcription of Hh target genes (Humke et al., 2010). During embryonic limb development, Shh is expressed in the zone of polarizing activity (ZPA), located in the posterior edge of the limb bud (Wang et al., 2000); where it patterns the anteroposterior axis of the future limb (Kicheva et al., 2012). Chondrocyte-specific overexpression of Shh during murine joint development leads to joint fusion (Tavella et al., 2004). Ihh ligands are important regulators for growth plate chondrocyte proliferation and differentiation (St-Jacques et al., 1999).

In this study, we show that the epiphyseal cartilage grows in an asymmetrical manner that involves differential dynamics of various cellular population.

MATERIALS AND METHODS

Mice

All animal work was permitted by the Ethical Committee on Animal Experiments (Stockholm North committee and Linköping Animal Ethics Committee) and conducted according to The Swedish Animal Agency's Provisions and Guidelines. Genetic recombination in pregnant female mice was induced by intraperitoneal (ip) injection of tamoxifen (Sigma #T5648). Tamoxifen was dissolved in corn oil at a concentration of 20 mg/ml. 2–5 mg of tamoxifen was injected into the pregnant dam. For plug checking, male and female mice were put together in the evening and vaginal plug was checked early next morning. The day when the plug was observed was considered as E0.5.

The Col2a1-CreERT2 (Nakamura et al., 2006), Prx1-CreERT2 (Kawanami et al., 2009), Gdf5-CreERT2 (Shwartz et al., 2016), Gli1-CreERT2 (Ahn and Joyner, 2004), and R26RConfetti (Snippert et al., 2010) mice have been previously described.

Chemical Injection

Ethynyl deoxyuridine (Life Technologies #E10187) was dissolved in PBS at a concentration of 1 mg/ml and ip injected into the pregnant dam.

Epiphyseal Cartilage and Joint Surface Region Definition and Cell Density Quantification

Knee and elbow joint surfaces on images of 2D tissue sections were defined using the ImageJ software. Sagittal sections are collected from about 200 to 300 μm or 100 to 200 μm of the middle regions along the medial-lateral axis, for the knee and elbow joints, respectively. At least, four sections were analyzed per embryo. The ends of epiphyseal cartilage were outlined along the edge of the proximal or distal ends of the four skeletal elements and connected with a straight line between the two ending points of the condyles. The dorsal, middle and ventral regions were defined by equally dividing the connecting straight line into three parts and drawing two straight lines at the dividing points upward to the surface. Number of clones was counted in each region and divided by the total area in mm^2 to obtain the clonal density. Periarticular region were defined as the cells within the top 50 μm of the epiphyseal cartilage. Length between the dorsal and ventral condylar regions of tibia and radius is defined as the longest distance between the dorsal and ventral sides.

3D Analysis of Confetti Clones

3D quantification of the proximal ends of tibia and radius was performed using the Imaris software.

Tissue Preparation and Immunohistochemistry

Embryos were collected and fixed in 4% PFA for 2–5 h at 4°C. Samples were then washed in PBS at 4°C for 1 h before being placed into 30% sucrose 4°C overnight to eliminate the remaining PFA. Tissues were subsequently embedded in OCT (Tissue-Tek #25608-930) and sectioned into 30–50 μm-thick sections at −20°C. Sections were equilibrated in PBS at room temperature prior to imaging. Primary antibodies (anti-Sox9, Sigma #HPA001758; anti-Col2, Invitrogen #MA5-12789) were applied to the sections for overnight incubation at 4°C. Samples were washed in PBST prior to incubation in secondary fluorescent antibodies for 1 h at room temperature. Images were acquired with an LSM880 confocal microscope.

Alcian Blue and Eosin Staining

Sections were post fixed in 4% PFA for 5 min at room temperature and then washed with distill water. 0.1% Alcian blue (Sigma #A5268)/0.1 M HCL (Sigma # H1758) solution was applied

for 3 min at room temperature, followed by staining in 0.02% eosin for 2 min.

EDU Retrieval

Frozen sections were used for EdU detection with a click reaction in a mixture of 0.1 M Tris pH 7.5, 2 mM CuSO4, 0.1 M ascorbic acid, and 2 μM Alexa Fluor Azide 647 (Invitrogen #A10277) for 30 min at room temperature, protected from light.

RESULTS

Gdf5-Positive Cells Contribute Asymmetrically to the Developing Epiphyseal Cartilage

Appearance of the interzone at the site of future joint formation marks the initiation of the joint formation process, where the interzone cells start to express a new set of genes, including Gdf5 (Storm et al., 1994; Guo et al., 2004). To investigate how these cells contribute to the developing epiphyseal cartilage ends of the knee and elbow joints during embryogenesis, we used a recently described Gdf5-CreERT2;R26R-Tomato mouse strain that recombines in the interzone mesenchyme (Shwartz et al., 2016). Since joint cavitation takes place between embryonic day (E) 12.5 and E13.5 in the knee and elbow (**Supplementary Figure S1**), we injected tamoxifen at E11.5, E12.5, E13.5 or E14.5 and collected the samples at E17.5 to reveal the dynamics of Gdf5-positive cells before and after the cavitation process. The overall contribution of the Gdf5-positive cells to the epiphyseal cartilage is rather minor (**Figures 1A–H**). We noticed that the Gdf5-positive cells specified at all the time points tested, except at E14.5 for the elbow joint, exhibited an uneven distribution pattern between the two opposing ends of the knee and elbow joints; where significantly more Gdf5-traced cells and their progenies were observed in the epiphyseal cartilage of the distal end of femur/humerus compared to the proximal end of tibia/radius (**Figures 1A–I** and **Supplementary Figures S2A–I**). In addition, the density of Gdf5-positive cell progenies behaved as a factor of time of tamoxifen injection, which consistently decreased at the distal ends of femur (**Figures 1A–D,I**) and humerus (**Supplementary Figures S2A–D,I**) as joint cavitation proceeds; indicating that the interzone cells become a less important player for epiphyseal cartilage construction after cavitation has completed. The density of Gdf5-positive cells at the proximal epiphyseal ends of tibia and radius was too low for any obvious distribution pattern to be reliably detected (**Figures 1E–I** and **Supplementary Figures S2E–I**).

We also checked the spatial distribution of the Gdf5-positive cells in the femur and humerus epiphyseal cartilage along the dorsal-ventral axis during E11.5 or E12.5–E17.5 tracings, where the highest amount of Gdf5-positive cells were found in these structures. For the sagittally sectioned samples, we divided the epiphyseal end into three regions of similar size (see section "Materials and Methods") and referred to as ventral condyle (V), intercondylar eminence (I), and dorsal condyle (D) regions, respectively (**Figures 1A,B** and **Supplementary Figures S2A,B**). Then, we quantified the density of Gdf5-positive cells in each region and found that it decreased along the dorsal-ventral or ventral-dorsal axis of the femur and humerus epiphyseal cartilage, respectively, during both tracing periods (**Figure 1J** and **Supplementary Figure S2J**). One-day tracing from E12.5 to E13.5 revealed that the labeled cells were mainly present around the joint forming region (**Supplementary Figures S2K–N**).

Taken together, these results show that the Gdf5-positive cells specified before joint cavitation contribute to the epiphyseal cartilage of knee and elbow joints in an asymmetrical manner both along the longitudinal axis between the two opposing ends and the dorsal-ventral axis within the femur and humerus epiphyseal ends.

Epiphyseal Cartilage Is Mainly Derived From the Cells Initially Located in the Cartilaginous Anlagen in an Asymmetrical Manner

The *Col2a1* gene has been shown to be robustly expressed in chondrogenic lineage during early embryonic limb development (Cheah et al., 1985). To label the epiphyseal cartilage progenitors, we then employed the Col2a1-CreERT2 mouse strain that labels the chondrogenic and cartilaginous cells (Nakamura et al., 2006) and coupled it to the R26R-Confetti mouse strain to color-code individual clones (Snippert et al., 2010). The Col2a1-positive clones (referred to as Col2 from here onward) specified at all four time points covered the majority of the epiphyseal cartilage at E17.5 in both the knee (**Figures 2A–H**) and elbow (**Supplementary Figures S3A–H**) joints. We also noticed that the later the tracing was initiated the higher overall density of Col2-positive clones was observed in the epiphyseal cartilage, especially when tracing was initiated at E14.5 (**Figure 2M** and **Supplementary Figure S3M**). Similar outcome was obtained when analyzing at the 3D level (**Supplementary Figures S4A–D**). This likely reflects the increase in Col2 expression and suggests maturation of chondrocytes after the completion of joint cavitation.

To examine the cell populations that were labeled by the Col2CreERT2 before and after joint cavitation, we performed 1-day tracings that were initiated at either E12.5 or E13.5. During E12.5–E13.5 tracing, most of the Col2-positive clones were observed in the cartilaginous anlagen of femur, tibia, humerus and radius, especially on the diaphyseal side; and only a few positive clones were observed in the joint-forming region and the surrounding tissues (**Figures 2I,J** and **Supplementary Figures S3I–J**). During E13.5–E14.5 tracing, Col2-positive clones were also mainly located in the cartilaginous anlagen, with a more even distribution (**Figures 2K,L** and **Supplementary Figures S3K,L**). Since the epiphyseal ends of the knee and elbow joints were largely covered by Col2-positive clones during E12.5 or E13.5–E17.5 tracings (**Figures 2B,C,F,G** and **Supplementary Figures S3B,C,F,G**), these results suggest that the epiphyseal cartilage is likely derived from the Col2-positive cells initially located in the cartilaginous anlagen. However, since there is still a few Col2-positive clones labeled outside the anlagen, we cannot completely rule out their roles in epiphyseal cartilage formation.

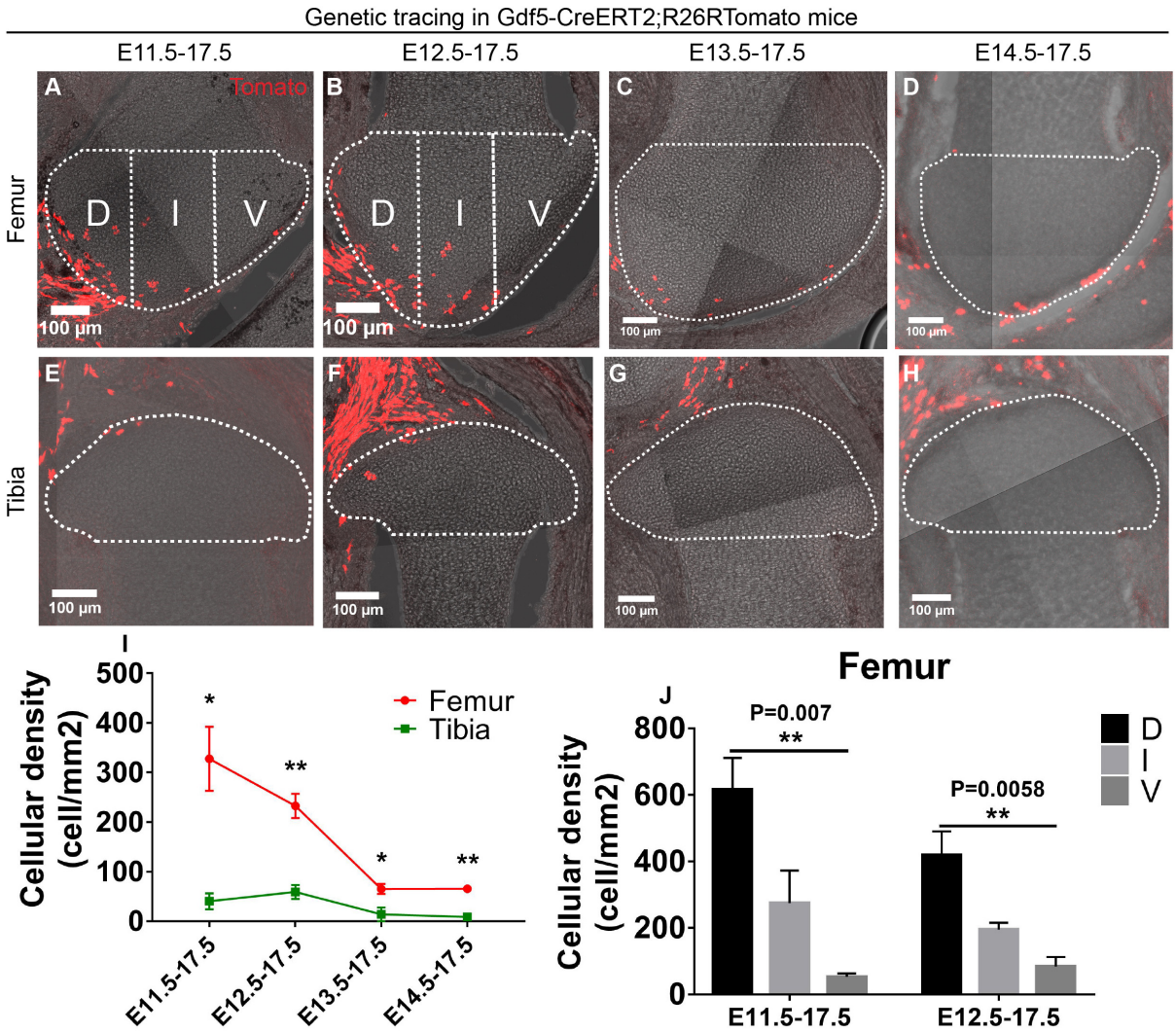


FIGURE 1 | Gdf5-expressing cells contribute asymmetrically to the epiphyseal cartilage development. **(A–H)** Example images showing the distribution of traced Gdf5-expressing cells in the epiphyseal cartilage of knee joint. D, I, and V refer to dorsal condyle, intercondylar eminence and ventral condyle regions, respectively. **(I)** Quantification of the cellular density distribution among the four tracing periods revealed an asymmetrical contribution of the Gdf5-expressing cells to the epiphyseal cartilage of femur and tibia. **(J)** Quantification of the cellular density distribution in the D, I, and V regions during E11.5–E17.5 and E12.5–E17.5 tracings revealed an asymmetrical contribution of the Gdf5-expressing cells to the femoral epiphyseal cartilage along the dorsal-ventral axis. Clonal density represents the number of traced clones over cartilage area (mm^2). Data represent mean ± SEM, where at least five embryos were analyzed. The white dashed lines outline the epiphyseal cartilage in **(A–H)**. $^*P < 0.05$, $^{**}P < 0.01$.

Unlike the Gdf5-tracings, no difference in clonal density was observed between the two opposing ends of the knee joint and elbow during most of the tracing periods (**Figure 2M** and **Supplementary Figure S3M**). We also analyzed the distribution pattern of Col2-positive clones along the dorsal-ventral axis of the epiphyseal ends at both joints. For each skeletal element, the Col2-positive clones exhibited a unique and asymmetrical pattern of distribution during many of the above-mentioned tracing periods (**Figures 2N,O** and **Supplementary Figures S3N,O**). In addition, analysis of the entire epiphyseal cartilage at the proximal ends of tibia and radius at the 3D-level demonstrated similar pattern of asymmetrical distribution (**Supplementary Figures S4E,F** and **Supplementary Videos S1–S8**).

Taken together, these results show that increasing amount of Col2-positive clones are recruited from the cartilaginous anlagen to the epiphyseal cartilage in an asymmetrical manner along the dorsal-ventral axis.

Prrx1 Expression Is Down Regulated in Epiphyseal Cartilage Progenitors as Joint Cavitation Proceeds

After checking the contribution of interzone and chondrogenic cells, we then wondered how the earlier cell populations, i.e., the limb mesenchymal cells, contribute to the developing epiphyseal cartilage. Therefore, we employed the Prrx1-CreERT2 mouse

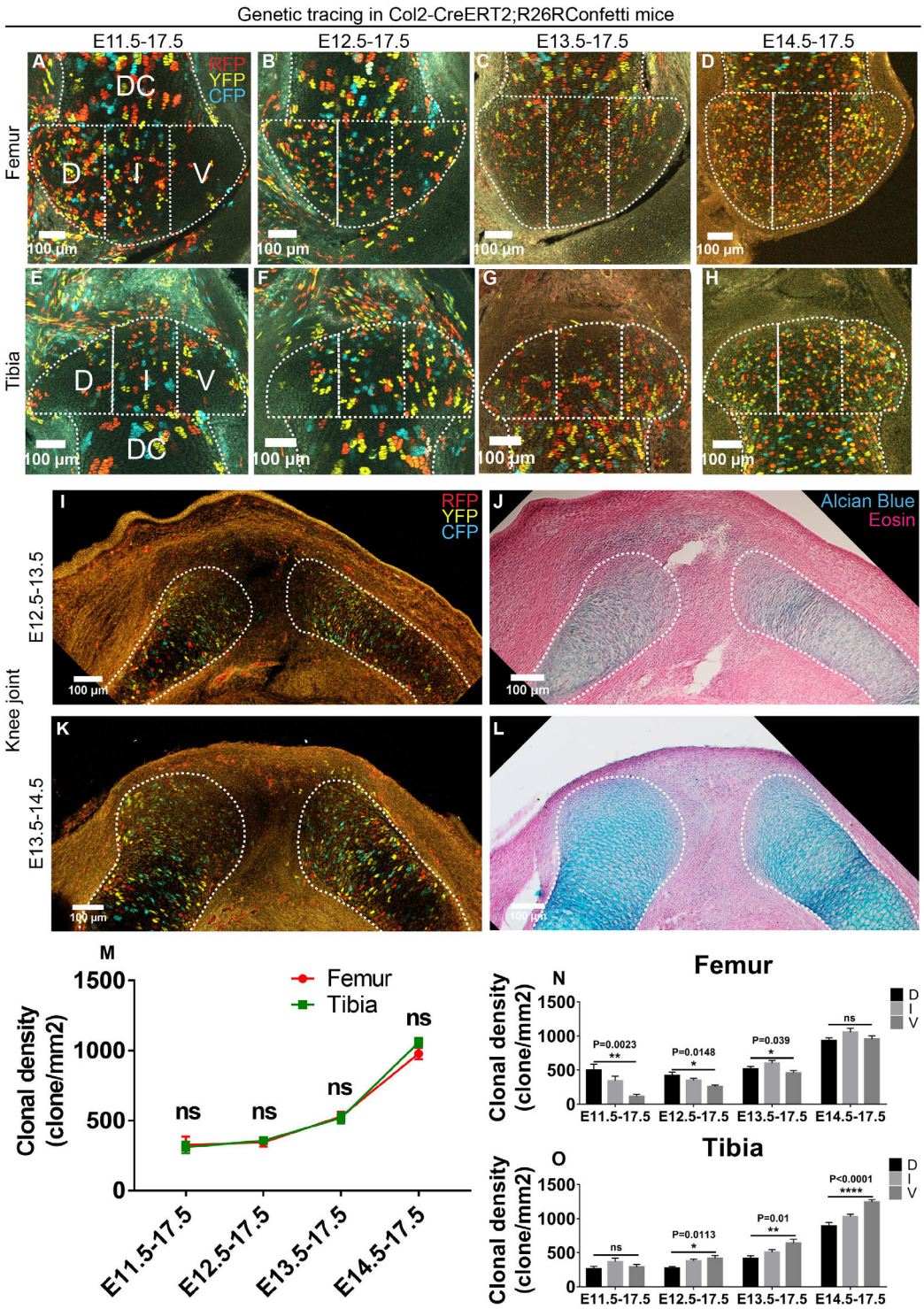


FIGURE 2 | Cells in the cartilaginous anlagen are the major contributors to epiphyseal cartilage development in an asymmetrical manner. **(A–H)** Example images illustrating the distribution of traced Col2-expressing clones in the epiphyseal cartilage of knee joint. D, I, and V refer to dorsal condyle, intercondylar eminence, and ventral condyle regions, respectively. **(I–L)** 1-day tracings of the Col2-expressing cells from E12.5 to E13.5 and E13.5 to E14.5 mainly labeled the cells in the diaphyseal side of the cartilaginous anlagen. **(J)** and **(L)** are alcian blue and eosin staining of the same tissue section on the left. **(M)** Quantification of the clonal density distribution revealed an ascending trend in the epiphyseal cartilage among the four tracing periods. **(N,O)** Quantification of the clonal density distribution in the D, I, and V regions revealed an asymmetrical contribution of the Col2-expressing clones to the femoral and tibial epiphyseal cartilage along the dorsal-ventral axis during many of the analyzed tracing periods. Clonal density represents the number of traced clones over cartilage area (mm^2). Data represent mean ± SEM, where at least five embryos were analyzed. The white dashed lines outline the epiphyseal and diaphyseal cartilage (DC). $^*P < 0.05$, $^{**}P < 0.01$, $^{****}P < 0.001$, ns, not significant.

strain to label the mesenchymal progenitor cells of the limb bud (Kawanami et al., 2009) and coupled it with the R26R-Confetti strain. Contrary to the Col2-tracings, a reversed trend in the stage-dependent clonal density distribution was observed for the Prrx1-positive clones, i.e., the later the tracing started, the less Prrx1-positive clones were observed in the epiphyseal cartilage of both the knee (**Figures 3A–H,M**) and elbow joints (**Supplementary Figures S5A–H,M**). This suggests that Prrx1 expression is down-regulated in the epiphyseal progenitors as joint cavitation proceeds, likely correlates with the differentiation of these cells into mature chondrocytes.

We also performed 1-day tracings to find out the cell populations that were actually labeled in the knee and elbow joints before (E12.5) and after (E13.5) cavitation. During both tracings, Prrx1-CreERT2 labeled most of the cells in the joint forming region and the epiphysis of the cartilaginous anlagen, as well as some of the chondrocytes in the diaphysis (**Figures 3I–L** and **Supplementary Figures S5I–L**). Considering the diminished role of Prrx1-positive cells at the epiphyseal ends as joint cavitation proceeds (**Figure 3M** and **Supplementary Figure S5M**), it is likely that the intensively labeled Prrx1-positive cells in the joint cavity and the surroundings only make minor contribution to the epiphyseal cartilage. The Prrx1-positive cells in the cartilaginous anlagen are likely the same population of the Col2-positive cells that give rise to the epiphyseal cartilage.

Unlike the Col2-tracings, significantly more Prrx1-positive clones were observed in the tibial epiphyseal cartilage compared to the femoral side during all tracing periods (**Figure 3M**), which is completely opposite to the distribution pattern of the Gdf5-traced cells between the two ends (**Figure 1I**). Intriguingly, such difference was not detected at the elbow joint (**Supplementary Figure S5M**). In addition, asymmetrical distribution of the Prrx1-positive clones was also observed along the dorsal-ventral axis of the epiphyseal cartilage of both the knee and elbow joints during many of the tracing periods (**Figures 3N,O** and **Supplementary Figures S5N,O**). Such spatial differences in the distribution pattern of Col2- and Prrx1-positive clones were not observed in the developing diaphyseal cartilage during all four tracing periods (**Supplementary Figure S6**), indicating that construction of the epiphyseal and diaphyseal cartilage involves differential cellular dynamics.

Taken together, these results further suggest that the epiphyseal cartilage are not formed via an even cellular contribution, but rather employs an asymmetrical mechanism of growth along the longitudinal and dorsal-ventral axes.

Epiphyseal Cartilage Formation After Joint Cavitation Involves Newly Recruited Col2-Positive Clones

Color-coding of individual clones with the R26R-Confetti reporter allows us to quantify the number of cells in each Col2- and Prrx1-positive clone and analyze the clonal dynamics based on their size distribution among all tracing periods in the epiphyseal cartilage. At the knee joint, the average size of Col2-positive clones remained at about five cells per clone during E11.5, E12.5 or E13.5–E17.5 tracings; however, it dropped sharply to only two cells per clone when tracing was initiated at E14.5 (**Figures 4A,B**). This is opposite to the trend of Col2-positive clonal density, where a sharp increase was observed when traced at E14.5 (**Figure 2M**). To confirm that the sharp reduction in clonal size traced at E14.5 was a result of reduced cell division, we assessed the proliferation status of the epiphyseal cells by injecting ethynyl deoxyuridine (EDU) at E13.5 or E14.5 and collected at E15.5 for analysis. Indeed, significantly more EDU-positive cells were observed in the knee and elbow epiphyseal cartilage, but not the diaphyseal cartilage, of the E13.5 injected embryos than the E14.5 injected ones (**Figures 4E–H** and **Supplementary Figures S7E–H**); further suggesting that the reduced clonal size is a result of decreased cell division. Therefore, proliferation of the epiphyseal cartilage is likely not a result of even proliferation of chondrocytes, in which case both the clonal density and size would simply be bigger for animals injected at earlier stages. On the other hand, these observations can be explained by the *de novo* appearance of Col2-positive clones that are formed after joint cavitation, i.e., Col2-positive cells that are labeled at E14.5.

Taken together, when labeled at E11.5, E12.5 or E13.5, density of the Col2-positive clones steadily increases while the clonal size remains consistent, suggesting a continuous mechanism of epiphyseal cartilage development as joint cavitation proceeds. At E14.5, an increased amount of Col2-positive cells are recruited to the epiphyseal cartilage, where they divide much less actively than the ones specified earlier; indicating that the mechanism of epiphyseal cartilage formation may switch from cell division to cell influx when joint cavitation has completed.

For the Prrx1-positive clones, the average clonal size steadily decreased from approximately seven cells per clone to three cells per clone in a two-cell interval during E11.5, E12.5 or E13.5–E17.5 tracings and remained at the same size during E14.5–E17.5 tracing (**Figures 4C,D**), suggesting that the Prrx1-positive cells specified before joint cavitation divide at a relatively constant rate, whereas the ones specified after joint cavitation divide much less actively. Similar trends of clonal size distribution were observed at the elbow joints for both Col2- and Prrx1-positive clones with an overall slightly more smooth decrease compared to the corresponding knee joints (**Supplementary Figures S7A–D**).

Gli1-Positive Cells Proliferate Along the Skeletal Edges to Cover the Periarticular Region of Epiphyseal Surface

Next, we sought to explore the signaling pathways and responsive cell types that govern the formation of epiphyseal cartilage. Given that Hh acts as a major morphogen in limb bud and cartilage patterning during murine embryonic development (Wang et al., 2000; Kicheva et al., 2012), we obtained the Gli1-CreERT2;R26R-Tomato mouse strain that labels Hh-responsive cells upon tamoxifen injection (Ahn and Joyner, 2004) to check their tracing patterns during the four above-mentioned tracing periods at the epiphyseal ends of the knee and elbow joints. At the knee joint, we found that the surrounding cells along the dorsal and ventral edges of both skeletal elements and some perichondrial cells were consistently labeled in all conditions (**Figures 5A–H**). In

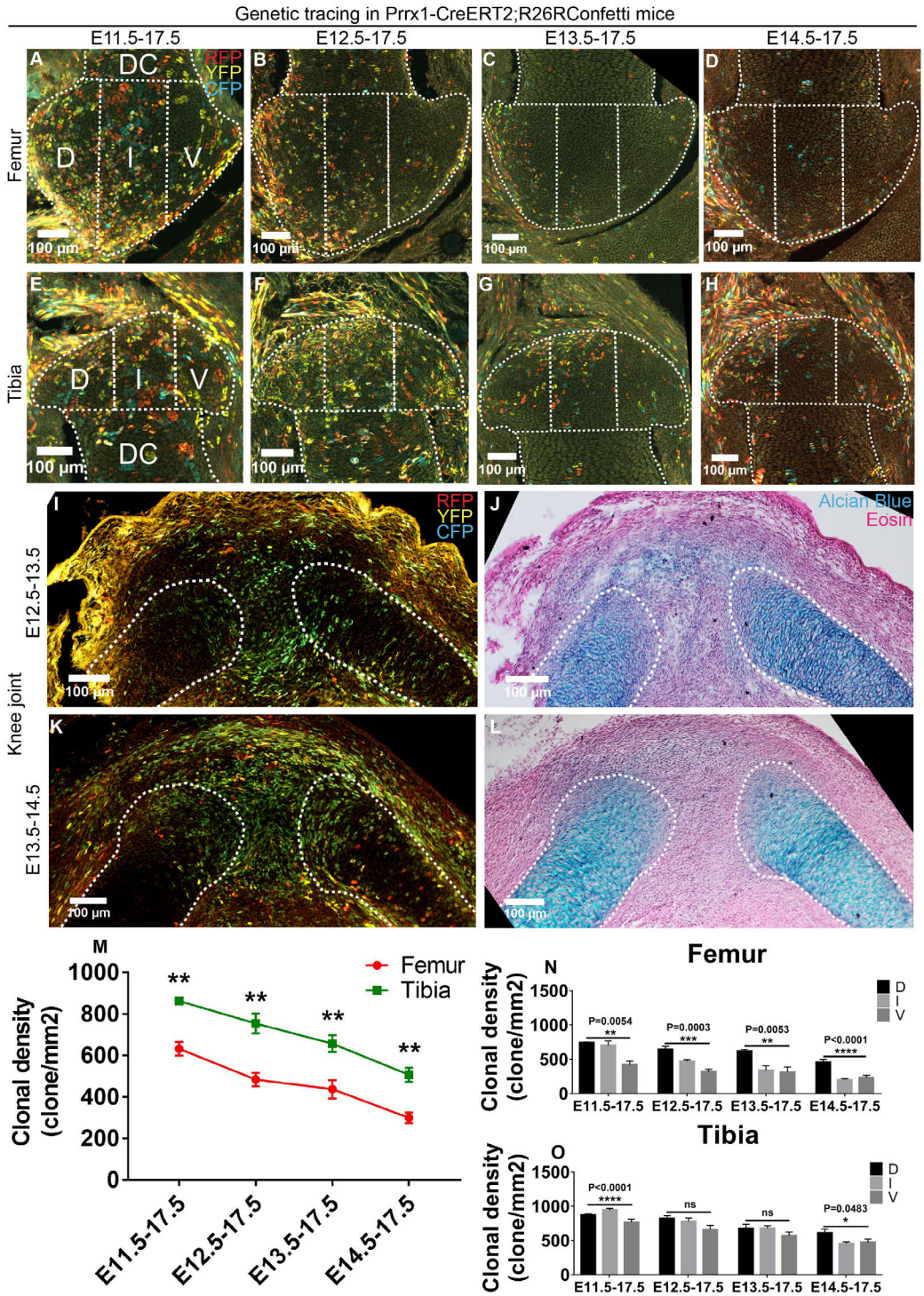


FIGURE 3 | Prrx1 expression decreases in epiphyseal progenitors as joint cavitation proceeds. **(A–H)** Example images illustrating the distribution of traced Prrx1-expressing clones in the epiphyseal cartilage of knee joint. D, I, and V refer to dorsal condyle, intercondylar eminence, and ventral condyle regions, respectively. **(I–L)** 1-day tracings of the Prrx1-expressing cells from E12.5 to E13.5 and E13.5 to E14.5 mainly labeled the cells in the joint forming region and epiphyseal side of the cartilaginous anlagen. **(J)** and **(L)** are alcian blue and eosin staining of the same tissue section on the left. **(M)** Quantification of the clonal density distribution revealed a descending trend in the epiphyseal cartilage among the four tracing periods and an asymmetrical contribution to the femoral and tibial epiphyseal ends. **(N,O)** Quantification of the clonal density distribution in the D, I, and V regions revealed an asymmetrical contribution of the Prrx1-expressing clones to the femoral and tibial epiphyseal cartilage along the dorsal-ventral axis during many of the analyzed tracing periods. Clonal density represents the number of traced clones over cartilage area (mm^2). Data represent mean ± SEM, where at least five embryos were analyzed. The white dashed lines outline the epiphyseal and diaphyseal cartilage (DC). $^*P < 0.05$, $^{**}P < 0.01$, $^{***}P < 0.005$, $^{****}P < 0.001$, ns, not significant.

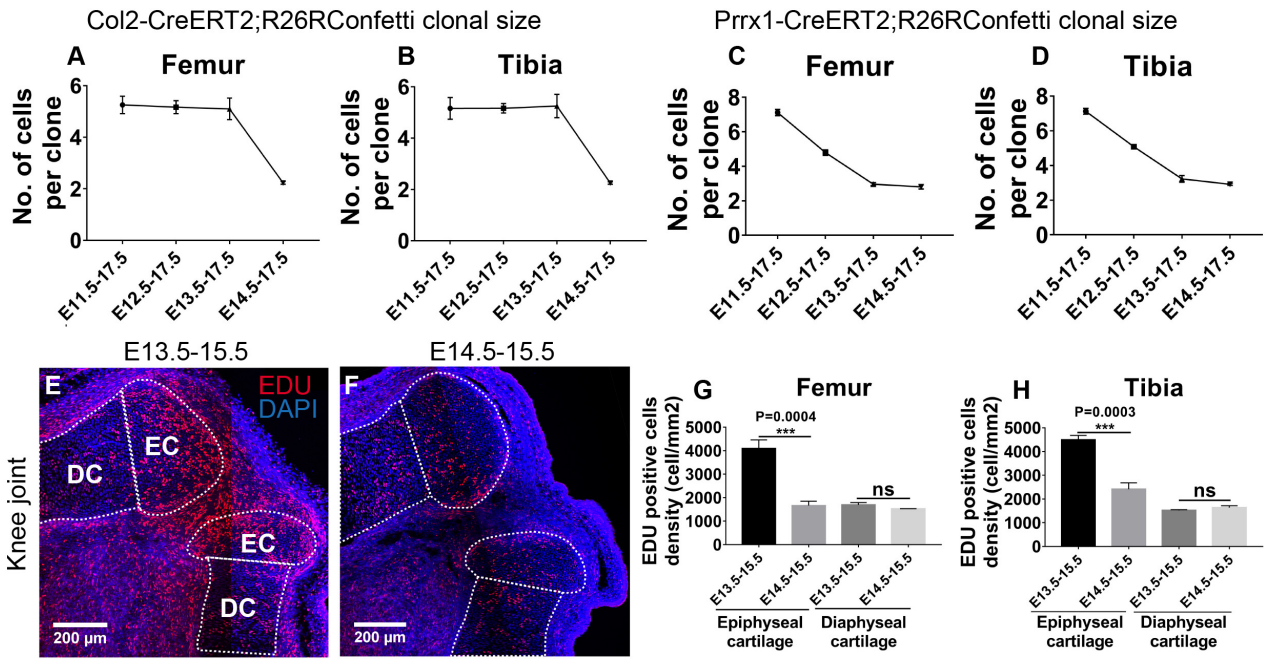


FIGURE 4 | Epiphyseal cartilage formation involves influx of Col2-expressing cells post joint cavitation. **(A,B)** Size of the traced Col2-expressing clones was significantly reduced in the femoral and tibial epiphyseal cartilage during E14.5–E17.5 tracing. **(C,D)** Size of the traced Prrx1-expressing clones gradually decreased as the tracing was initiated at later stages. **(E,F)** Example EDU staining images of knee joint in wild type mice injected with EDU at E13.5 or E14.5. **(G,H)** More EDU-positive cells were found in the epiphyseal cartilage, but not the underneath growth plate, of both femur and tibia when EDU was injected at E13.5 compared to injection at E14.5. EDU-positive cell density represents the number of EDU-positive cells over cartilage area (mm^2). Data represent mean ± SEM, where at least three embryos were analyzed. The white dashed lines outline the epiphyseal cartilage (EC) and diaphyseal cartilage (DC). ***$P < 0.005$, ns, not significant.

addition, the density of Gli1-positive cells in the periarticular region of the epiphyseal surface [defined as the 4–6 layers of chondrocytes within the top 50 μm of the epiphyseal surface (Tong et al., 2019)] was significantly increased when tracing was initiated at later time points, especially at E13.5 and E14.5 where majority of the periarticular region was covered by Gli1-positive cells (**Figures 5A–H,M,N**). These results suggest that the Hh-responsive cells specified after joint cavitation are the major contributors to the periarticular region of the knee joint. Chondrocytes were counterstained with Sox9 to better define the cartilage (Ng et al., 1997; Zhao et al., 1997).

To further dissect the cellular mechanism underlying the formation of the periarticular region, we performed 1-day tracing from E13.5 to E14.5 and E14.5 to E15.5 to assess the initial location of the Gli1-positive cells. Employing the same spatial analysis strategy for the epiphyseal cartilage, we divided the periarticular region into three sub-regions, i.e., ventral condyle (V), intercondylar eminence (I), and dorsal condyle (D), to quantify the density of Gli1-positive cells in each sub-region (**Figures 5I–L**). With 1-day tracing starting from either E13.5 or E14.5, more Gli1-positive cells were found in the V and D sub-regions compared to the I sub-region (**Figures 5O,P**). However, with longer tracing until E17.5, more Gli1-positive cells were found in the I sub-region, compared to the other two (**Figures 5O,P**). In addition, the overall density of Gli1-positive cells within the periarticular region was much higher with tracings started from E14.5, compared to tracings started from E13.5 (**Figures 5O,P**). These results suggest that chondrocytes within the periarticular region are mostly derived from the Gli1-positive cells along the dorsal and ventral edges of the femur and tibia, where they likely proliferate along the edges toward the plateau to eventually cover the entire periarticular region. When tracing from E15.5 to E17.5, significantly less periarticular cells were labeled compared to the E14.5–E17.5 tracing (**Supplementary Figure S9**), suggesting that these cells respond less to the Hh signaling from E15.5.

Intriguingly, tracing pattern of the Gli1-positive cells at the elbow joint appeared to be rather random. Surrounding and perichondrial cells were not consistently labeled (**Supplementary Figures S8A–L**) and the density of Gli1-positive cells in the periarticular region varies among the four tracing periods (**Supplementary Figures S8M,N**). No obvious distribution pattern was recognized among the three sub-regions either (**Supplementary Figures S8O,P**). This suggests that the Gli1-positive cells may have differential roles in the development of elbow and knee epiphyseal surface.

DISCUSSION

Previous study using Col2-Cre;R26R mice showed that the Col2-positive anlagen proliferate until the presence of interzone cells at the future joint site, where they no longer express Col2 and start to express Gdf5 (Hyde et al., 2008). In addition, a continuous

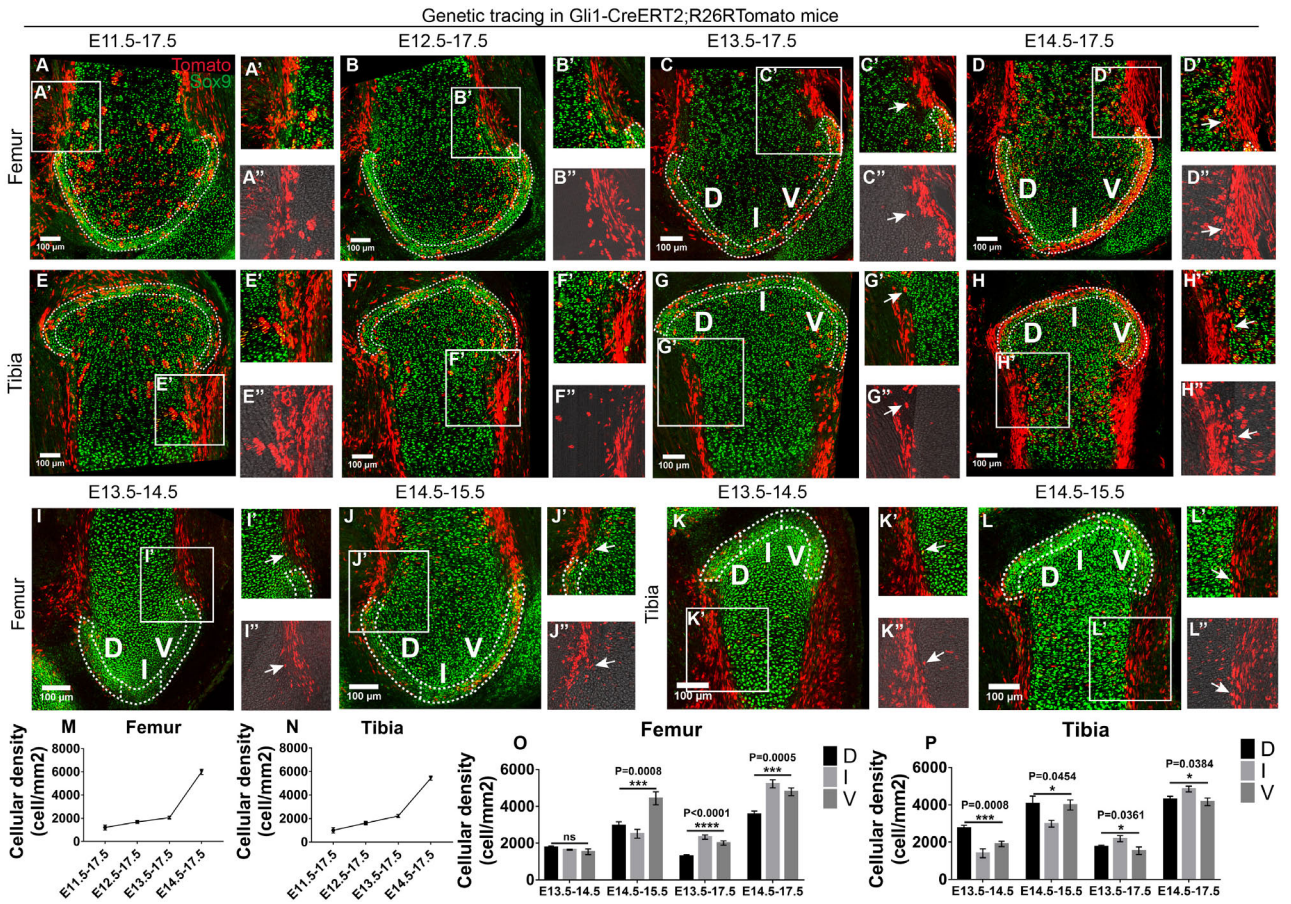


FIGURE 5 | Gli1-expressing cells along the skeletal edges give rise to the periarticular region of epiphyseal surface. **(A–L)** Example images of lineage tracings in Gli1-CreERT2;R26RTomato mice at the knee joint surface. Sox9 staining was added to help define the cartilage. **(M,N)** Increased density of Gli1-positive cells were found in the periarticular region when tracing was started at later time points. **(O,P)** Gli1-positive cells proliferate from the dorsal (D) and ventral (V) edges of the epiphyseal surface toward the intercondylar eminence (I) when cavitation has completed. Data represent mean ± SEM where at least four embryos were analyzed. The white dashed lines outline the periarticular region of the epiphyseal surface. Arrows in the insets of **(C,D,G–L)** point to the Tomato and Sox9 double positive perichondrial cells. Insets labeled with double apostrophe marks show Tomato only **(A–L)**. $^{*}P < 0.05$, $^{***}P < 0.005$, $^{****}P < 0.001$, ns, not significant.

influx of Gdf5-positive cells has been shown to contribute to the formation of various joint structures, including the articular surface where they start to express Col2 again and become mature chondrocytes (Shwartz et al., 2016). Using various lineage tracing strategies, our work builds on top of the existing influx model of joint development to quantitatively demonstrate the asymmetrical engagement of progenies of the Gdf5-, Col2-, Prrx1-, and Gli1-positive cells into the generation of new cartilage at the epiphyseal ends.

When labeled before joint cavitation at E12.5, Col2-positive cells were mainly present in the cartilaginous anlagen toward the diaphyseal side; whereas Prrx1-positive cells occupied a decent fraction of the joint forming region and the epiphyseal side of the anlagen, as well as part of the diaphysis (**Figure 6A**). At E17.5, the developing epiphyseal cartilage is largely covered by both the Col2- and the Prrx1-positive clones of similar size in an asymmetrical manner (**Figure 6B**). Therefore, the epiphyseal cartilage is likely constructed by an overlapping population of Col2- and Prrx1-positive cells specified before joint cavitation. Based on the 1-day tracing pattern of both strains, the only major overlapping population is the cells located on the diaphyseal side of the anlagen, hinting the cellular origin of the epiphyseal cartilage. When labeled after joint cavitation at E13.5, Col2-positive cells were still mainly located in the cartilaginous anlagen, whereas Prrx1 was expressed in almost all cells of the joint forming region and the epiphyseal side of the anlagen, but only in some of the diaphyseal cells (**Figure 6C**). Meanwhile, Gli1-positive cells were observed along the edges of the anlagen, likely proliferating toward the periarticular region of epiphyseal surface (**Figure 6C**). At E17.5, the developing cartilage was mainly occupied by the Col2-positive clones, but to a much lesser extent by the Prrx1-positive clones; and the entire periarticular region was covered by the Gli1-positive cells (**Figure 6D**). This further excludes the Prrx1-positive cells in the joint forming region and the epiphyseal side of the anlagen as the progenitors for epiphyseal cartilage growth, in which case their density should be increased or maintained at E17.5. Thus, cells in the cartilaginous anlagen might be the major cellular

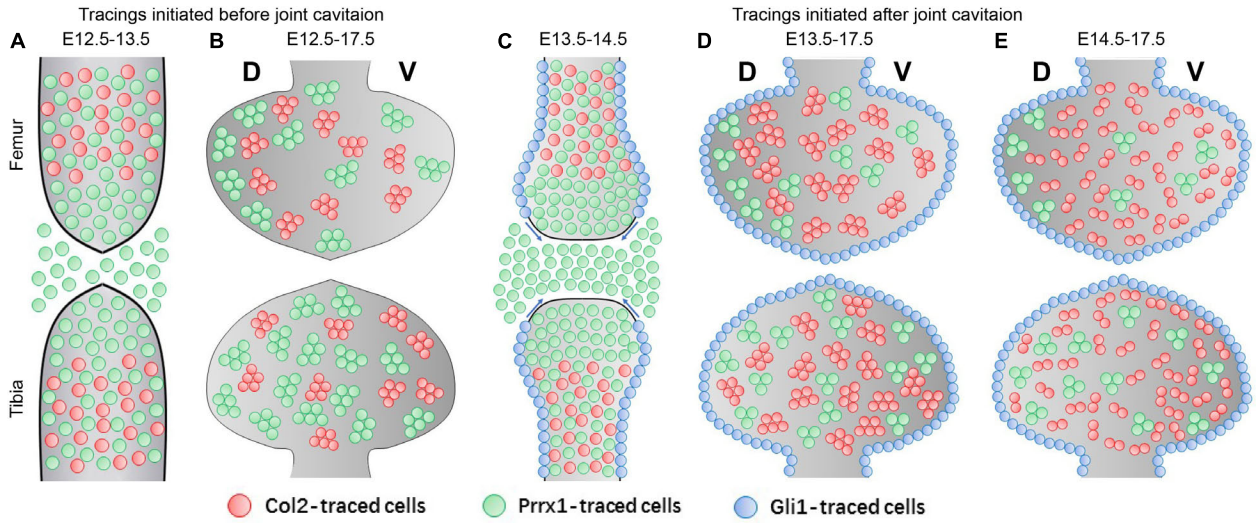


FIGURE 6 | A model for epiphyseal cartilage development at the knee joint surface. **(A)** When labeled before joint cavitation, Col2 is mainly expressed in the cells of the diaphyseal part of the cartilaginous anlagen, whereas Prrx1 is expressed in cells located in the joint forming region, the epiphyseal part of the cartilaginous anlagen and the surround tissues, as well as the diaphyseal anlagen. **(B)** Both the traced Col2- and Prrx1-positive clones occupy majority of the epiphyseal cartilage at E17.5. **(C)** When labeled after joint cavitation, Col2 is mainly expressed in the cells of the cartilaginous anlagen, whereas Prrx1-expressing cells mark almost the entire joint forming region and the epiphyseal anlagen. At the meantime, Gli1-expressing cells lineup along the dorsal and ventral edge of the anlagen, likely migrating toward the periarticular region of epiphyseal surface. **(D,E)** The epiphyseal cartilage is almost entirely composed of the Col2-traced clones at E17.5, whereas the Prrx1-traced clones are found at a much lesser extent. New Col2-expressing cells are recruited to the epiphyseal cartilage when labeled at E14.5 as reflected by the significant drop in their clonal size. Meanwhile, the Gli1-traced cells cover the entire periarticular region during this time. The asymmetrical distribution of the Col2- and Prrx1-traced clones along both the longitudinal axis between the two opposing ends and the dorsal-ventral axis within each skeletal element is also reflected in **(B,D,E)**.

source for epiphyseal cartilage growth. At E14.5, the major developing mechanism of epiphyseal cartilage likely switches from cell division to cell influx, where the traced Col2-positive clones becomes significantly smaller in size, accompanied by a dramatic increase in density (**Figure 6E**); although we cannot fully exclude the influence from the difference in the length of tracing periods.

It is worth noting that the mouse lines used in this study likely label overlapping cell populations, although each strain has a relatively unique labeling pattern based on the 1-day tracings. Therefore, the contribution patterns observed for different lineage tracings likely involve overlapping cellular populations, especially for the labeled cells in the cartilaginous anlagen, many of which are positive for both Col2 and Prrx1. We cannot completely exclude the effects of tamoxifen administration and distribution, CreERT2 efficiency and transgene nature and expression on the outcome of the tracing experiments. However, based on the stable clonal size and unique clonal distribution observed in different embryos for each tracing period, as well as the decent Cre recombination efficiency in all tested strains as reflected by the amount of labeled cells; these technical issues should not produce any profound interference on our conclusions.

Previous studies show that the Gdf5-positive cells contribute to joint formation in a temporally different manner, where the early specified Gdf5-positive cells make the most contribution to the epiphysis (Storm and Kingsley, 1999; Shwartz et al., 2016). Consistently, we also observed a decreasing trend in Gdf5-positive cell density in the epiphyseal cartilage along the induction time line. It is worth noting that although the overall level of Gdf5-positive cell in the epiphyseal cartilage is relatively low, it does not truly reflect the recombination efficiency of Gdf5CreERT2. Our recent findings show that the cruciate ligament is highly labeled in the same strain, especially during the E11.5–E17.5 and E12.5–E17.5 tracings (Zhang et al., 2020). On top, our data indicate that from E12.5 onward the Col2-positive cells in the cartilaginous anlagen likely become the major contributors to the epiphyseal cartilage. A temporal switch in the major mechanism of epiphyseal cartilage formation from influx of the Gdf5-positive cells to proliferation of the Col2-positive cells might exist as cells in the anlagen become mature chondrocytes. Our observation is in line with another previous study using EDU and BrdU incorporation methods to show that the embryonic articular cartilage cells originate from the proliferating chondrocytes located in the distal anlagen (Ray et al., 2015).

Early limb develops from a single piece of uninterrupted mesenchymal condensation, which later goes through a cavitation process to physically separate into zeugopod and stylopod. Current understanding of joint cavitation believes that cell death plays a major role in the separation of the continuous skeletal anlagen (Mitrovic, 1978; Nalin et al., 1995; Kimura and Shiota, 1996; Abu-Hijleh et al., 1997), albeit it has been challenged by other studies (Ito and Kida, 2000). Gli1 has recently been identified as a marker for osteogenic progenitors in murine long bone formation (Shi et al., 2017) and for mesenchymal

stem cells within the suture mesenchyme for craniofacial bone development (Zhao et al., 2015). Constitutive activation of Hh signaling specifically in the interzone cells caused severe morphological changes in murine knee joint (Rockel et al., 2016). Overexpression of Shh in chondrocytes abolished the joint cavity due to disrupted cell apoptosis and proliferation (Tavella et al., 2004). Our observation that the Gli1-positive cells labeled at E13.5 or E14.5, time points when joint cavitation has just accomplished, are mainly present along the edges of the developing femur and tibia and proliferate toward the periarticular region of epiphyseal surface that eventually give rise to the entire structures further hints a potential role of these cells in the cavitation process. Convergence of the Gli1-positive cells from the two sides might mark the end point of the joint cavitation process. Influx of the surrounding cells might be an additional source for periarticular cartilage formation since some of them also express Gli1 during the tracings. This complies with the previous finding that articular cartilage continually express Gdf5 during multiple embryonic tracings (Shwartz et al., 2016).

Shape of the epiphyseal cartilage is one of the main factors that determines joint stability. The architecture of joint shape is extensively related to the pathogenesis of osteoarthritis. Many studies have suggested that tibial and femoral bone morphology at the knee joint is a risk factor for anterior cruciate ligament (ACL) injury (Lansdown and Ma, 2018; Vasta et al., 2018) and medial meniscus tears (Barber et al., 2017), especially the tibial plateau slope (Wang et al., 2017). Not only to the susceptibility to ACL injury, post trauma recovery is also linked to the bone shape differences (Lansdown et al., 2017). In the present study, we analyzed the spatial distribution, density and size of Gdf5-, Col2-, Prrx1-, and Gli1-positive cells/clones to investigate how the epiphyseal cartilage is developed when recombination is induced at different time points, which can be cross-compared. It seems that epiphyseal cartilage does not proliferate via continuous expansion of the pre-existing chondrocyte clones, in which case the clonal density and size would simply be bigger for embryos injected at earlier stages. Alternatively, increasing amount of Col2-positive chondrogenic clones are asymmetrically recruited to the epiphyseal cartilage at a relatively late time point, i.e., post joint cavitation. These clones are small in term of clonal size and stable in term of clonal geometry, most of which contain only two cells. Our data support and extend the previously established cell influx model for joint development (Shwartz et al., 2016) by showing how many chondrogenic cells are engaged into generation of new cartilage in the epiphyseal cartilage and how asymmetrically they are distributed during this process. Our data suggest that the proliferation of pre-existing cartilage is limited and rather uniform, whereas the asymmetrical influx and proliferation of pro-chondrogenic cells likely accounts for the asymmetrically developed epiphyseal ends. Such a temporally (before and after joint cavitation) and spatially (along the dorsal-ventral and longitudinal axes) asymmetrical growth mechanism of epiphyseal cartilage might provide indications on the cellular dynamics underlying the development of various shaping features of the joint ends. In addition, we uncover the differential contribution of several known cellular sources for the epiphyseal cartilage during embryonic development, which might impinge on the cellular and molecular target selection for the development of novel treatment against clinical conditions as a result of abnormal fetal joint morphogenesis, such as hip dysplasia.

DATA AVAILABILITY STATEMENT

The datasets generated for this study are available on request to the corresponding author.

ETHICS STATEMENT

The animal study was reviewed and approved by the Stockholm North or Linköping Ethical Committee.

AUTHOR CONTRIBUTIONS

MX, IA, and YZ designed the study. YZ performed all the experiments, except those specified below. KA and MK provided the Gli1-CreERT2;R26R-Tomato mouse strain and performed the genetic tracings and embryo collection. PK and MX helped with mouse embryonic tracing experiments. SE helped with light sheet microscopic imaging for 3D clonal analysis. AC, KS, and GL provided intellectual input into the manuscript. MX and IA wrote the manuscript.

FUNDING

This study was supported by the Swedish Research Council (Project Numbers 2016-02835 for ASC, 2018-02713 for IA, and 2018-02963 for MK), Swedish Cancer Society (MK), Karolinska Institute (AC, IA, and MX), and the Russian Foundation for Basic Research (Grant #19-29-04115 to AC). MX was supported by the EMBO long-term postdoc fellowship and Stiftelsen Frimurare Barnhuset I Stockholm. YZ was supported by the Chinese Scholarship Council (student ID: 201706370196) and the Fundamental Research Funds for the Central Universities of Central South University (2017zzts233). KA was supported by Karolinska Institutet Ph.D. (KID) funding. The Gdf5-CreERT2 mouse strain is a gift from Dr. Elazar Zelzer, Weizmann Institute of Science, Israel.

SUPPLEMENTARY MATERIAL

The Supplementary Material for this article can be found online at: https://www.frontiersin.org/articles/10.3389/fcell.2020.00122/full#supplementary-material

FIGURE S1 | Alcian blue **(A–D)**, Col2 and Sox9 **(E–P)** staining of the knee and elbow joint during at E12.5 and E13.5. The white dashed lines outline the cartilage.

FIGURE S2 | (A–H) Example images showing the distribution of traced Gdf5-expressing cells in the epiphyseal cartilage of elbow joint. D, I, and V refer to dorsal condyle, intercondylar eminence, and ventral condyle regions, respectively. **(I)** Quantification of the cellular density distribution among the four tracing periods

revealed an asymmetrical contribution of the Gdf5-expressing cells to the epiphyseal cartilage of humerus and radius. **(J)** Quantification of the cellular density distribution in the D, I, and V regions during E11.5–E17.5 and E12.5–E17.5 tracings revealed an asymmetrical contribution of the Gdf5-expressing cells to the humerus epiphyseal cartilage along the dorsal-ventral axis. **(K–N)** 1-day tracings of the Gdf5-expressing cells from E12.5 to E13.5 in knee **(K,L)** and elbow **(M,N)** joints mainly labeled the cells around the joint forming region. **(L)** and **(N)** are alcian blue and eosin staining of the same tissue section on the left. Clonal density represents the number of traced clones over cartilage area (mm^2). Data represent mean ± SEM, where at least five embryos were analyzed. The white dashed lines outline the epiphyseal cartilage. $^{**}P < 0.01$, $^{***}P < 0.005$, $^{****}P < 0.001$.

FIGURE S3 | (A–H) Example images illustrating the distribution of traced Col2-expressing clones in the epiphyseal cartilage of elbow joint. D, I, and V refer to dorsal condyle, intercondylar eminence and ventral condyle regions, respectively. **(I–L)** 1-day tracings of the Col2-expressing cells from E12.5 to E13.5 and E13.5 to E14.5 mainly labeled the cells in the diaphyseal side of the cartilaginous anlagen. **(J)** and **(L)** are alcian blue and eosin staining of the same tissue section on the left. **(M)** Quantification of the clonal density distribution revealed an ascending trend in the epiphyseal cartilage among the four tracing periods. **(N,O)** Quantification of the clonal density distribution in the D, I, and V regions revealed an asymmetrical contribution of the Col2-expressing clones to the humerus and radius epiphyseal cartilage along the dorsal-ventral axis during many of the analyzed tracing periods. Clonal density represents the number of traced clones over cartilage area (mm^2). Data represent mean ± SEM, where at least five embryos were analyzed. The white dashed lines outline the epiphyseal and diaphyseal cartilage (DC). $^{*}P < 0.05$, $^{**}P < 0.01$, $^{***}P < 0.005$, $^{****}P < 0.001$.

FIGURE S4 | (A–D) 3D analysis of traced Col2-expressing clonal density in the entire epiphyseal cartilage of the four skeletal elements. **(E,F)** Distribution of traced Col2-expressing clones in dorsal condyle (D), intercondylar eminence (I), and ventral condyle (V) regions of the entire tibia and radius epiphyseal cartilage at the 3D level. Clonal density represents the number of traced clones over cartilage area (mm^2). Data represent mean ± SEM, where at least five embryos were analyzed. $^{*}P < 0.05$, $^{**}P < 0.01$.

FIGURE S5 | (A–H) Example images illustrating the distribution of traced Prrx1-expressing clones in the epiphyseal cartilage of elbow joint. D, I, and V refer to dorsal condyle, intercondylar eminence and ventral condyle regions, respectively. **(I–L)** 1-day tracings of the Prrx1-expressing cells from E12.5 to E13.5 and E13.5 to E14.5 mainly labeled the cells in the joint forming region and epiphyseal side of the cartilaginous anlagen. **(J)** and **(L)** are alcian blue and eosin staining of the same tissue section on the left. **(M)** Quantification of the clonal density distribution revealed a descending trend in the epiphyseal cartilage among the four tracing periods. **(N,O)** Quantification of the clonal density distribution in the D, I, and V regions revealed an asymmetrical contribution of the Prrx1-expressing clones to the humerus and radius epiphyseal cartilage along the dorsal-ventral axis during many of the analyzed tracing periods. Clonal density represents the number of traced clones over cartilage area (mm^2). Data represent mean ± SEM, where at least five embryos were analyzed. The white dashed lines outline the epiphyseal and diaphyseal cartilage (DC). $^{*}P < 0.05$.

FIGURE S6 | (A–H) The Col2- and Prrx1-traced clones distribute evenly in the dorsal condyle (D), intercondylar eminence (I), and ventral condyle (V) regions of the diaphyseal cartilage of the four skeletal elements. Clonal density represents the number of traced clones over cartilage area (mm^2). Data represent mean ± SEM, where at least five embryos were analyzed.

FIGURE S7 | (A,B) Size of the traced Col2-expressing clones dropped sharply in the humerus and radius epiphyseal cartilage during E14.5–E17.5 tracing. **(C,D)** Size of the traced Prrx1-expressing clones gradually decreased as the tracing was initiated at later stages. **(E,F)** Example EDU staining images of elbow joint in wild type mice injected with EDU at E13.5 or E14.5. **(G,H)** More EDU-positive cells were found in the epiphyseal cartilage, but not the underneath growth plate, of both humerus and radius when EDU was injected at E13.5 compared to injection at E14.5. EDU-positive cell density represents the number of EDU-positive cells over cartilage area (mm^2). Data represent mean ± SEM, where at least three embryos were analyzed. The white dashed lines outline the epiphyseal cartilage (EC) and diaphyseal cartilage (DC). $^{***}P < 0.005$, $^{****}P < 0.001$.

FIGURE S8 | (A–L) Example images of lineage tracings in Gli1-CreERT2;R26RTomato mice at the elbow joint surface. **(M–P)** No obvious pattern was observed for Gli1-tracings at the elbow joint periarticular region. Data represent mean ± SEM where at least four embryos were analyzed. The white dashed lines outline the periarticular region of epiphyseal surface. D, I, and V refer to dorsal condyle, intercondylar eminence and ventral condyle sub-regions, respectively. $^{*}P < 0.05$, $^{**}P < 0.01$.

FIGURE S9 | (A–H) Gli1-positive cell density dropped sharply in the periarticular region of epiphyseal surface of knee and elbow joint during E15.5–E17.5 tracing compared to E14.5–E17.5 tracing. Data represent mean ± SEM where at least four embryos were analyzed. The white dashed lines outline the periarticular region of epiphyseal surface. $^{***}P < 0.005$, $^{****}P < 0.001$.

VIDEOS S1–S8 | 3D scans of the knee (S1, S3, S5, S7) and elbow (S2, S4, S6, S8) joints of Col2-CreERT2;R26RConfetti mice traced from E11.5, E12.5, E13.5 or E14.5 to E17.5. The upper skeletal elements are femur or humerus and the lower ones are tibia or radius in all videos.

REFERENCES

Abu-Hijleh, G., Reid, O., and Scothorne, R. J. (1997). Cell death in the developing chick knee joint: I. Spatial and temporal patterns. *Clin. Anat.* 10, 183–200. doi: 10.1002/(sici)1098-2353(1997)10:3<183::aid-ca4>3.0.co;2-v

Ahn, S., and Joyner, A. L. (2004). Dynamic changes in the response of cells to positive hedgehog signaling during mouse limb patterning. *Cell* 118, 505–516. doi: 10.1016/j.cell.2004.07.023

Barber, F. A., Getelman, M. H., and Berry, K. L. (2017). Complex medial meniscus tears are associated with a biconcave medial tibial plateau. *Arthroscopy* 33, 783–789. doi: 10.1016/j.arthro.2016.09.027

Cheah, K. S., Stoker, N. G., Griffin, J. R., Grosveld, F. G., and Solomon, E. (1985). Identification and characterization of the human type II collagen gene (COL2A1). *Proc. Natl. Acad. Sci. U.S.A.* 82, 2555–2559. doi: 10.1073/pnas.82.9.2555

Corbit, K. C., Aanstad, P., Singla, V., Norman, A. R., Stainier, D. Y., and Reiter, J. F. (2005). Vertebrate Smoothened functions at the primary cilium. *Nature* 437, 1018–1021. doi: 10.1038/nature04117

Guo, X., Day, T. F., Jiang, X., Garrett-Beal, L., Topol, L., and Yang, Y. (2004). Wnt/beta-catenin signaling is sufficient and necessary for synovial joint formation. *Genes Dev.* 18, 2404–2417. doi: 10.1101/gad.1230704

Hamrick, M. W. (2001). Primate origins: evolutionary change in digital ray patterning and segmentation. *J. Hum. Evol.* 40, 339–351. doi: 10.1006/jhev.2001.0467

Humke, E. W., Dorn, K. V., Milenkovic, L., Scott, M. P., and Rohatgi, R. (2010). The output of Hedgehog signaling is controlled by the dynamic association between Suppressor of Fused and the Gli proteins. *Genes Dev.* 24, 670–682. doi: 10.1101/gad.1902910

Hyde, G., Boot-Handford, R. P., and Wallis, G. A. (2008). Col2a1 lineage tracing reveals that the meniscus of the knee joint has a complex cellular origin. *J. Anat.* 213, 531–538.

Ito, M. M., and Kida, M. Y. (2000). Morphological and biochemical re-evaluation of the process of cavitation in the rat knee joint: cellular and cell strata alterations in the interzone. *J. Anat.* 197(Pt 4), 659–679. doi: 10.1046/j.1469-7580.2000.19740659.x

Kawanami, A., Matsushita, T., Chan, Y. Y., and Murakami, S. (2009). Mice expressing GFP and CreER in osteochondro progenitor cells in the periosteum. *Biochem. Biophys. Res. Commun.* 386, 477–482. doi: 10.1016/j.bbrc.2009.06.059

Kicheva, A., Cohen, M., and Briscoe, J. (2012). Developmental pattern formation: insights from physics and biology. *Science* 338, 210–212. doi: 10.1126/science.1225182

Kimura, S., and Shiota, K. (1996). Sequential changes of programmed cell death in developing fetal mouse limbs and its possible roles in limb morphogenesis.

J. Morphol. 229, 337–346. doi: 10.1002/(sici)1097-4687(199609)229:3<337::aid-jmor8>3.0.co;2-v

Koyama, E., Shibukawa, Y., Nagayama, M., Sugito, H., Young, B., Yuasa, T., et al. (2008). A distinct cohort of progenitor cells participates in synovial joint and articular cartilage formation during mouse limb skeletogenesis. *Dev. Biol.* 316, 62–73. doi: 10.1016/j.ydbio.2008.01.012

Lansdown, D., and Ma, C. B. (2018). The Influence of Tibial and Femoral Bone Morphology on Knee Kinematics in the Anterior Cruciate Ligament Injured Knee. *Clin. Sports Med.* 37, 127–136. doi: 10.1016/j.csm.2017.07.012

Lansdown, D. A., Pedoia, V., Zaid, M., Amano, K., Souza, R. B., Li, X., et al. (2017). Variations in knee kinematics after ACL injury and after reconstruction are correlated with bone shape differences. *Clin. Orthop. Relat. Res.* 475, 2427–2435. doi: 10.1007/s11999-017-5368-8

Martin, J. F., and Olson, E. N. (2000). Identification of a prx1 limb enhancer. *Genesis* 26, 225–229. doi: 10.1002/(sici)1526-968x(200004)26:4<225::aid-gene10>3.0.co;2-f

Mitrovic, D. (1978). Development of the diarthrodial joints in the rat embryo. *Am. J. Anat.* 151, 475–485. doi: 10.1002/aja.1001510403

Nakamura, E., Nguyen, M. T., and Mackem, S. (2006). Kinetics of tamoxifen-regulated Cre activity in mice using a cartilage-specific CreER(T) to assay temporal activity windows along the proximodistal limb skeleton. *Dev. Dyn.* 235, 2603–2612. doi: 10.1002/dvdy.20892

Nalin, A. M., Greenlee, T. K. Jr., and Sandell, L. J. (1995). Collagen gene expression during development of avian synovial joints: transient expression of types II and XI collagen genes in the joint capsule. *Dev. Dyn.* 203, 352–362. doi: 10.1002/aja.1002030307

Ng, L. J., Wheatley, S., Muscat, G. E., Conway-Campbell, J., Bowles, J., Wright, E., et al. (1997). SOX9 binds DNA, activates transcription, and coexpresses with type II collagen during chondrogenesis in the mouse. *Dev. Biol.* 183, 108–121. doi: 10.1006/dbio.1996.8487

Nowlan, N. C., and Sharpe, J. (2014). Joint shape morphogenesis precedes cavitation of the developing hip joint. *J. Anat.* 224, 482–489. doi: 10.1111/joa.12143

Pacifici, M., Koyama, E., and Iwamoto, M. (2005). Mechanisms of synovial joint and articular cartilage formation: recent advances, but many lingering mysteries. *Birth Defects Res. C Embryo. Today* 75, 237–248. doi: 10.1002/bdrc.20050

Ray, A., Singh, P. N., Sohaskey, M. L., Harland, R. M., and Bandyopadhyay, A. (2015). Precise spatial restriction of BMP signaling is essential for articular cartilage differentiation. *Development* 142, 1169–1179. doi: 10.1242/dev.110940

Rockel, J. S., Yu, C., Whetstone, H., Craft, A. M., Reilly, K., Ma, H., et al. (2016). Hedgehog inhibits beta-catenin activity in synovial joint development and osteoarthritis. *J. Clin. Invest.* 126, 1649–1663. doi: 10.1172/jci80205

Rohatgi, R., Milenkovic, L., and Scott, M. P. (2007). Patched1 regulates hedgehog signaling at the primary cilium. *Science* 317, 372–376. doi: 10.1126/science.1139740

Shi, Y., He, G., Lee, W. C., Mckenzie, J. A., Silva, M. J., and Long, F. (2017). Gli1 identifies osteogenic progenitors for bone formation and fracture repair. *Nat. Commun.* 8:2043.

Shwartz, Y., Viukov, S., Krief, S., and Zelzer, E. (2016). Joint development involves a continuous influx of Gdf5-positive cells. *Cell Rep.* 15, 2577–2587. doi: 10.1016/j.celrep.2016.05.055

Snippert, H. J., Van Der Flier, L. G., Sato, T., Van Es, J. H., Van Den Born, M., Kroon-Veenboer, C., et al. (2010). Intestinal crypt homeostasis results from neutral competition between symmetrically dividing Lgr5 stem cells. *Cell* 143, 134–144. doi: 10.1016/j.cell.2010.09.016

St-Jacques, B., Hammerschmidt, M., and Mcmahon, A. P. (1999). Indian hedgehog signaling regulates proliferation and differentiation of chondrocytes and is essential for bone formation. *Genes Dev.* 13, 2072–2086. doi: 10.1101/gad.13.16.2072

Storm, E. E., Huynh, T. V., Copeland, N. G., Jenkins, N. A., Kingsley, D. M., and Lee, S. J. (1994). Limb alterations in brachypodism mice due to mutations in a new member of the TGF beta-superfamily. *Nature* 368, 639–643. doi: 10.1038/368639a0

Storm, E. E., and Kingsley, D. M. (1999). GDF5 coordinates bone and joint formation during digit development. *Dev. Biol.* 209, 11–27. doi: 10.1006/dbio.1999.9241

Tavella, S., Biticchi, R., Schito, A., Minina, E., Di Martino, D., Pagano, A., et al. (2004). Targeted expression of SHH affects chondrocyte differentiation, growth plate organization, and Sox9 expression. *J. Bone Miner Res.* 19, 1678–1688. doi: 10.1359/jbmr.040706

Tickle, C., and Towers, M. (2017). Sonic hedgehog signaling in limb development. *Front. Cell Dev. Biol.* 5:14. doi: 10.3389/fcell.2017.00014

Tong, W., Tower, R. J., Chen, C., Wang, L., Zhong, L., Wei, Y., et al. (2019). Periarticular mesenchymal progenitors initiate and contribute to secondary ossification center formation during mouse long bone development. *Stem Cells* 37, 677–689. doi: 10.1002/stem.2975

Vasta, S., Andrade, R., Pereira, R., Bastos, R., Battaglia, A. G., Papalia, R., et al. (2018). Bone morphology and morphometry of the lateral femoral condyle is a risk factor for ACL injury. *Knee Surg. Sports Traumatol. Arthrosc.* 26, 2817–2825. doi: 10.1007/s00167-017-4761-x

Wang, B., Fallon, J. F., and Beachy, P. A. (2000). Hedgehog-regulated processing of Gli3 produces an anterior/posterior repressor gradient in the developing vertebrate limb. *Cell* 100, 423–434. doi: 10.1016/s0092-8674(00)80678-9

Wang, Y. L., Yang, T., Zeng, C., Wei, J., Xie, D. X., Yang, Y. H., et al. (2017). Association between tibial plateau slopes and anterior cruciate ligament injury: a meta-analysis. *Arthroscopy* 33:e1244.

Zhang, Y., Kameneva, P., Annusver, K., Kasper, M., Chagin, A. S., Adameyko, I., et al. (2020). Cruciate ligament, patellar tendon, and patella formation involves differential cellular sources and dynamics as joint cavitation proceeds. *Dev. Dyn.* [Epub ahead of print]

Zhao, H., Feng, J., Ho, T. V., Grimes, W., Urata, M., and Chai, Y. (2015). The suture provides a niche for mesenchymal stem cells of craniofacial bones. *Nat. Cell Biol.* 17, 386–396. doi: 10.1038/ncb3139

Zhao, Q., Eberspaecher, H., Lefebvre, V., and De Crombrugghe, B. (1997). Parallel expression of Sox9 and Col2a1 in cells undergoing chondrogenesis. *Dev. Dyn.* 209, 377–386. doi: 10.1002/(sici)1097-0177(199708)209:4<377::aid-aja5>3.0.co;2-f

Conflict of Interest: The authors declare that the research was conducted in the absence of any commercial or financial relationships that could be construed as a potential conflict of interest.

Copyright © 2020 Zhang, Annusver, Sunadome, Kameneva, Edwards, Lei, Kasper, Chagin, Adameyko and Xie. This is an open-access article distributed under the terms of the Creative Commons Attribution License (CC BY). The use, distribution or reproduction in other forums is permitted, provided the original author(s) and the copyright owner(s) are credited and that the original publication in this journal is cited, in accordance with accepted academic practice. No use, distribution or reproduction is permitted which does not comply with these terms.

frontiers in Cell and Developmental Biology

ORIGINAL RESEARCH
published: 15 April 2020
doi: 10.3389/fcell.2020.00237

Site-Dependent Lineage Preference of Adipose Stem Cells

*Tingliang Wang[1,2], Ryan C. Hill[3], Monika Dzieciatkowska[3], Lian Zhu[2], Aniello M. Infante[4], Gangqing Hu[4,5], Kirk C. Hansen[3] and Ming Pei[1,6]**

[1] Stem Cell and Tissue Engineering Laboratory, Department of Orthopedics, West Virginia University, Morgantown, WV, United States, [2] Department of Plastic and Reconstructive Surgery, Shanghai Ninth People's Hospital Affiliated with Shanghai Jiao Tong University School of Medicine, Shanghai, China, [3] Department of Biochemistry and Molecular Genetics, University of Colorado Denver, Aurora, CO, United States, [4] Bioinformatics Core Facility, West Virginia University, Morgantown, WV, United States, [5] Department of Microbiology, Immunology and Cell Biology, School of Medicine, West Virginia University, Morgantown, WV, United States, [6] WVU Cancer Institute, Robert C. Byrd Health Sciences Center, West Virginia University, Morgantown, WV, United States

OPEN ACCESS

Edited by:
Pavel Makarevich, Lomonosov Moscow State University, Russia

Reviewed by:
Egor Plotnikov, Lomonosov Moscow State University, Russia
Elena Andreeva, Russian Academy of Sciences, Russia
Dmitry Traktuev, University of Florida, United States

***Correspondence:**
Ming Pei
mpei@hsc.wvu.edu

Specialty section:
This article was submitted to Stem Cell Research, a section of the journal Frontiers in Cell and Developmental Biology

Received: *13 December 2019*
Accepted: *20 March 2020*
Published: *15 April 2020*

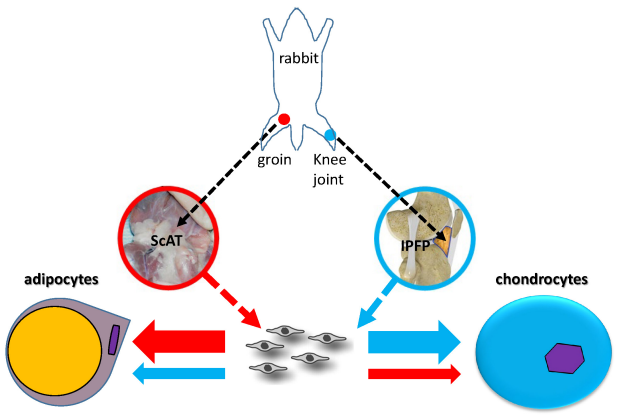
Citation:
Wang T, Hill RC, Dzieciatkowska M, Zhu L, Infante AM, Hu G, Hansen KC and Pei M (2020) Site-Dependent Lineage Preference of Adipose Stem Cells. Front. Cell Dev. Biol. 8:237. doi: 10.3389/fcell.2020.00237

Adult stem cells have unique properties in both proliferation and differentiation preference. In this study, we hypothesized that adipose stem cells have a depot-dependent lineage preference. Four rabbits were used to provide donor-matched adipose stem cells from either subcutaneous adipose tissue (ScAT) or infrapatellar fat pad (IPFP). Proliferation and multi-lineage differentiation were evaluated in adipose stem cells from donor-matched ScAT and IPFP. RNA sequencing (RNA-seq) and proteomics were conducted to uncover potential molecular discrepancy in adipose stem cells and their corresponding matrix microenvironments. We found that stem cells from ScAT exhibited significantly higher proliferation and adipogenic capacity compared to those from donor-matched IPFP while stem cells from IPFP displayed significantly higher chondrogenic potential compared to those from donor-matched ScAT. Our findings are strongly endorsed by supportive data from transcriptome and proteomics analyses, indicating a site-dependent lineage preference of adipose stem cells.

Keywords: adipogenesis, adipose stem cell, chondrogenesis, infrapatellar fat pad, osteogenesis, subcutaneous adipose tissue

INTRODUCTION

Adult stem cells, found in varied tissues such as bone marrow, adipose, and synovium, have the capacity for proliferation and differentiation and are important cell sources for clinical therapy (Brown et al., 2019). However, adult stem cells from different sources have different capacities for proliferation and tissue-specific differentiation (Pizzute et al., 2015). This discrepancy even exists in a single tissue, for example, adipose tissue. Recent evidence indicates that, compared with subcutaneous adipose tissue (ScAT), infrapatellar fat pad (IPFP) is a unique adipose tissue with some distinct features (Sun et al., 2018). ScAT, a fat pad beneath the skin, is becoming an attractive stem cell source for tissue regeneration due to its ease of harvest in large quantities with a minimally invasive procedure (Chu et al., 2019). IPFP, located inside the knee joint and outside the synovial membrane, is becoming a promising stem cell source for cartilage engineering and regeneration (Sun et al., 2018).



GRAPHICAL ABSTRACT | Lineage preference of adult stem cells might be influenced by local matrix microenvironment. In this study, stem cells from subcutaneous adipose tissue (ScAT) had more adipogenic capacity and those from infrapatellar fat pad (IPFP) possessed advantageous chondrogenic potential; these findings are fully endorsed by molecular evidence from RNA Seq and proteomic analyses.

In osteoarthritis, IPFP exhibits both anti-inflammatory and pro-inflammatory characteristics (Alegre-Aguarón et al., 2012). Increasing evidence indicates the superiority of IPFP-derived stem cells (IPFSCs) over subcutaneous adipose stem cells (ScASCs) in chondrogenic differentiation capacity (Alegre-Aguarón et al., 2012; Lopa et al., 2014); however, most reports are not donor-matched studies, leading to an uncertain conclusion unless large-scale samples are used. In this study, donor-matched IPFSCs and ScASCs isolated from four New Zealand white rabbits were used for comparison in cell proliferation and tri-lineage differentiation capacities. We hypothesized that adipose stem cells have a depot-dependent lineage preference. Transcriptome and proteome analyses were used to facilitate an in-depth understanding of site-dependent variations of lineage preference.

MATERIALS AND METHODS

Cell Culture and Proliferation and Surface Phenotype Evaluation

Donor-matched inguinal ScAT and IPFP were obtained from four 4-month-old male New Zealand white rabbits. This project was approved by our Institutional Animal Care and Use Committee (IACUC). The harvested tissues were finely minced and digested using 0.1% collagenase P (Roche, Indianapolis, IN, United States) for 90 min at 37°C in a shaking water bath. The collected cells were cultured in growth medium containing alpha-minimum essential medium (αMEM), 10% fetal bovine serum, 100 U/mL penicillin, 100 μg/mL streptomycin, and 0.25 μg/mL fungizone (Invitrogen, Carlsbad, CA, United States) in a 37°C, 5% CO_2, humidified incubator. After reaching 80% confluence, ScASCs and IPFSCs were detached and counted (n = 4) using a hemocytometer, then seeded on T175 flasks at a density of 3000/cm^2 for expansion. The cells were counted for three passages after harvesting. Cell population doubling time (PD time) was then calculated based on the formula "PD time = T*log (2) / (log (N_1) – log (N_0))". T stands for incubation time, N_1 stands for harvesting cell number, and N_0 stands for seeding cell number.

Passage 1 ScASCs and IPFSCs from four donors were used to perform EdU (5-ethynyl-2′-deoxyuridine) cell proliferation assay (cat no. C1024; Invitrogen) according to manufacturer's protocols. Briefly, the cells were seeded at a density of 3000/cm^2, grew to 40% confluence, and then were incubated with 10 μM EdU solution for 3 h before detaching, fixing, permeabilizing, and staining the cells. EdU fluorescence was detected and analyzed by FACSCalibur (BD Biosciences, San Jose, CA, United States) using FCS Express 5 software (De Novo Software, Los Angeles, CA, United States).

A CD146 assay was performed on passage 1 ScASCs and IPFSCs from four donors. Briefly, 3 × 10^5 cells (n = 4) were incubated with CD146 antibody conjugated with phycoerythrin (cat no. 12-1469-42; Thermo Fisher Scientific, Milford, MA, United States) in darkness for 30 min. The fluorescence was analyzed by FACSCalibur using FCS Express 5 software (De Novo Software, Los Angeles, CA, United States).

Stemness and Senescence Gene Expression

Expanded cells were evaluated using real-time quantitative polymerase chain reaction (qPCR) for differences between ScASCs and IPFSCs in stemness and senescence-related gene expression. Total RNA was extracted from passage 1 cells of all four donors using TRIzol (Invitrogen). Then cDNA was synthesized from mRNA by reverse transcriptase using a High-Capacity cDNA Archive Kit (Thermo Fisher Scientific). Primers of stemness-related genes, senescence-related genes, and an endogenous reference gene (**Table 1**) were customized from Integrated DNA Technologies (IDT, Coralville, IA, United States) as Sybr green gene expression assay using their qPCR tool. qPCR was performed with iCycler iQ^{TM} Multicolor RT-PCR Detection and calculated by computer software (PerkinElmer, Wellesley, MA, United States).

Chondrogenic Induction and Evaluation

Passage 2 expanded cells (4 × 10^5) were centrifuged at 300 g for 7 min in a 15-ml polypropylene tube to form a pellet. After 24 h incubation (day 0), the pellets were cultured with serum free medium containing high-glucose Dulbecco's modified Eagle's medium, 40 μg/mL proline, 0.1 μM ascorbic acid-2-phosphate, 100 nM dexamethasone, 1 × ITS premix (BD Biosciences),100 U/mL penicillin, 100 μg/mL streptomycin, 0.25 μg/mL fungizone, and 10 ng/mL recombinant human transforming growth factor beta3 (TGFβ3, PeproTech Inc., Rocky Hill, NJ, United States) in a 37°C, 5% CO_2, humidified incubator for up to 18 days.

Total RNA from ScASCs and IPFSCs (n = 4) was extracted from pellets using an RNase-free pestle in TRIzol, and other

TABLE 1 | Primers for qPCR.

Gene name	Full name	TaqMan Assay ID or IDT primers
Stemness-related genes		
NANOG	Nanog homeobox	Forward: TCAACTGCGGAGATGAAGTG; Reverse: GTTTGCTGTGCTGTGTTCTG
REX1	ZFP42 zinc finger protein	Forward: AGCCCAGCAGGCAGAAATGGAA; Reverse: TGGTCAGTCTCACAGGGCACAT
NES	nestin	Forward: AGAATTCCCGGCTTCAGACA; Reverse: TCTTCAGAAAGGCTGGCACA
SOX2	SRY-box2	Forward: TGAAGGAGCACCCGGATTAT; Reverse: GCAGCGTGTACTTATCCTTCTT
Senescence-related genes		
CDKN1A	Cyclin dependent kinase inhibitor 1A	Forward: ACCTCTCAGGGTCGGAAA; Reverse: GGATTACGGCTTCCTCTTGG
TP53	Tumor protein 53	Forward: CGTGCGGAGTATTTGGATGA; Reverse: TGGATGGTGGTACAGTCAGA
Chondrogenesis-related genes		
SOX9	SRY-box 9	Oc04096872_m1
COL2A1	Collagen type II alpha 1 chain	Oc03396132_g1
ACAN	Aggrecan	Forward: CTACGGAGACAAGGATGAGTTC; Reverse: CGTAAAAGACCTCACCCTCCAT
COL10A1	Collagen type X alpha 1 chain	Oc04097225_s1
MMP13	Matrix metallopeptidase 13	Oc03396895_m1
Adipogenesis-related genes		
ADIPOQ	Adiponectin, C1Q and collagen domain containing	Oc03823307_s1
PPARG	Peroxisome proliferator activated receptor gamma	Oc03397329_m1
LEP	Leptin	Oc03395809_s1
LPL	Lipoprotein lipase	Forward: GCAAGACCTTCGTGGTGAT; Reverse: GTTGGAGTCTGGTTCTCTCTTG
Osteogenesis-related genes		
BGLAP	Bone gamma-carboxyglutamate protein	ARMFW6N
SPP1	Secreted phosphoprotein 1	Oc04096883_g1
DCN	Decorin	Oc03398037_m1
SPARC	Secreted protein acidic and cysteine rich	Oc03395844_m1
Endogenous control gene		
GAPDH	Glyceraldhyde-3-phosphate dehydrogenase	Forward: TTCCACGGCACGGTCAAGGC; Reverse: GGGCACCAGCATCACCCCAC

qPCR procedures were the same as described above. Primers for chondrogenic-related genes and the endogenous control gene (**Table 1**) were customized as TaqMan® gene expression assay from Applied Biosystems (Foster City, CA, United States). *ACAN* primer was customized as Sybr green gene expression assay from IDT (**Table 1**).

Adipogenic Induction and Evaluation

When passage 2 cells grew to 90% confluence, they were cultured in adipogenic medium consisting of growth medium supplemented with 1 μM dexamethasone, 10 μM insulin (Biovendor, Asheville, NC, United States), 0.5 mM 3-isobutyl-1-methylxanthine, and 200 μM indomethacin in a 37°C, 5% CO_2, humidified incubator for as long as 21 days. Primers for qPCR analysis (n = 4) of adipogenic-related genes (**Table 1**) were customized as TaqMan® gene expression assay from Applied Biosystems. *LPL* primer was customized as Sybr green gene expression assay from IDT (**Table 1**).

Adipogenic induced cell samples were dissolved in lysis buffer with protease inhibitors. Total protein was quantified by a NanoDrop Spectrophotometer. Twenty micrograms of proteins (n = 4) were separated on a 12% polyacrylamide gel and transferred to nitrocellulose membrane (30 V, overnight at 4°C). Membranes were blocked with 5% non-fat milk in TBS (Tris-buffered saline) and probed with primary adiponectin (ADIPOQ) monoclonal antibody (cat no. MA1-054; Thermo Fisher Scientific) followed by secondary antibody conjugated with HRP (horseradish peroxidase) (cat no. RK244131; Thermo Fisher Scientific). Next, a chemiluminescence kit (GE Healthcare, Chicago, IL, United States) was used for developing; the blot was imaged using a GE gel documentation. Anti-β actin antibody (Invitrogen) was used to normalize the loading amounts.

Osteogenic Induction and Evaluation

When passage 2 cells grew to 90% confluence, they were cultured with osteogenic medium consisting of growth medium supplemented with 0.01 μM dexamethasone, 50 mg/L ascorbic acid-2-phosphate, and 10 mM β-glycerophosphate in a 37°C, 5% CO_2, humidified incubator for as long as 21 days. Primers for qPCR analysis (n = 4) of osteogenic-related genes (**Table 1**) were customized as TaqMan® gene expression assays from Applied Biosystems.

Protein extracts were assayed for osteocalcin using Osteocalcin (OCN) assay kit (cat no. MBS2019743; MyBioSource, San Diego, CA, United States) following manufacturer's instructions. Briefly, protein samples (n = 4) were added to wells with pre-coated osteocalcin antibody and incubated at room temperature for 1 h. Upon incubation, 100 uL of detection reagent A was added to the microwells and incubated at 37°C for 1 h. Microwells were washed and incubated with 100 μL of detection reagent B at 37°C for 30 min. Upon washing, 90 μL of 3,3',5,5'- tetramethylbenzidine substrate solution was added and the sample was incubated at 37°C for 30 min. The reaction was stopped by the addition of 50 μL of stop solution. This enzyme-linked immunosorbent assay (ELISA) was quantitatively measured using a microplate reader at 450 nm.

RNA-Seq Analysis

The total RNA samples collected from donor-matched passage 1 IPFSCs ($n = 4$) and ScASCs ($n = 4$) underwent an initial quality control (QC) check. When samples were deemed high quality [RIN (RNA Integrity Number) > 8], a Next Generation Library was built followed by a final QC check, which involved Qubit quantification and size estimation on the Agilent Bioanalyzer using a High Sensitivity DNA chip. The completed libraries were sequenced on their HiSeq 2500 (Illumina, Inc., San Diego, CA, United States). FastQC[1] and multiQC (Ewels et al., 2016) were used to confirm that the read quality was good and no trimming was required. We mapped the pair-end RNA-Seq reads to the reference genome of Oryctolagus cuniculus (OryCun2.0) from Ensembl (Zerbino et al., 2018) using the Subread aligner (Liao et al., 2013). The number of read counts corresponding to gene transcripts annotated by Ensembl (OryCun2.0.98) were summarized by the featureCounts function from the Rsubread package (Liao et al., 2019). Gene expression levels were quantified by Reads Per Kilobase of transcript, per Million mapped reads (RPKM) with in-house script. We applied Edger3 (McCarthy et al., 2012) to call differentially expressed genes with the following criteria: fold change (FC) > 2, false discovery rate (FDR) < 0.05, and an average expression (RPKM) higher than one in at least one condition.

Proteomics Analysis of Donor-Matched Cells and Their Deposited Matrices

Donor-matched passage 1 IPFSCs ($n = 4$; C-IPFSC) and ScASCs ($n = 4$; C-ScASC) as well as the decellularized extracellular matrices (dECM) deposited by passage 1 IPFSCs ($n = 4$; E-IPFSC) and ScASCs ($n = 4$; E-ScASC) were used for this analysis. dECM was prepared following our previous protocol (Li and Pei, 2018). Briefly, 0.2% gelatin solution was used to coat a tissue culture plastic (TCP) flask for 1 h, followed by treatment with 1% glutaraldehyde and 1M ethanolamine for 30 min each. Both cells were cultured in the above-treated TCP flasks using growth medium until 100% confluence followed by supplementation with 250 μM L-ascorbic acid phosphate magnesium salt for 10 days and then treatment with Extraction Buffer (0.5% Triton X-100 and 20 mM NH_4OH in phosphate buffered saline) (Pizzute et al., 2016). Cell lysates (50 μg) were diluted in 8 M urea in 100 mM ammonium bicarbonate (ABC) pH 8.5 for digestion according to the Filter Aided Sample Preparation (FASP) protocol. dECMs were processed as previously described (Barrett et al., 2017). Briefly, samples were lyophilized, and digested with 100 mM cyanogen bromide (CNBr). The resultant digest was solubilized in 8 M urea and FASP digested with sequencing grade trypsin (Wiśniewski et al., 2009). Liquid chromatography tandem mass spectrometry (LC-MS/MS) was performed on an Eksigent 2D nano LC coupled to an LTQ-Orbitrap Velos mass spectrometer. MS acquisition parameters were detailed previously (Hill et al., 2015). Raw files were directly loaded into Proteome Discoverer 2.2 3 (Thermo Fisher Scientific) and searched against mouse SwissProt database using an in-house Mascot^{TM} server (Version 2.5, Matrix Science). Mass tolerances were +/- 10ppm for MS peaks, and +/- 0.6 Da for MS/MS fragment ions. CNBr /Trypsin specificity was used allowing for 1 missed cleavage. Met oxidation, proline hydroxylation, protein N-terminal acetylation, and peptide N-terminal pyroglutamic acid formation were allowed for variable modifications while carbamidomethyl of Cys was set as a fixed modification. Label Free Quantifications were done using the Minora Feature detector for peak intensity based abundance. Protein thresholds of 1% FDR were used to filter for high confidence identifications. Results were directly exported into Microsoft Excel. Statistical enumeration of the data was achieved through Metaboanalyst (v3.6) (Xia and Wishart, 2016) and pathway analysis was done using the Reactome (Fabregat et al., 2018).

Statistical Analyses

For the data from flow analysis, ELISA, and qPCR, results are presented as the mean and the standard deviation of the mean; the *t*-test was used to assess data between two groups. All statistical analyses were performed with SPSS 13.0 statistical software (SPSS, Inc., Chicago, IL, United States). $p < 0.05$ was considered statistically significant.

RESULTS

Stem Cell Proliferation and Surface Marker Expression

ScASCs and donor-matched IPFSCs showed similar fibroblast-like morphology (**Figure 1A**). Population doubling (PD) time of ScASCs was significantly shorter than IPFSCs (**Figure 1B**) and relative EdU incorporation of ScASCs was higher than IPFSCs (**Figure 1C**), indicating that ScASCs were superior to donor-matched IPFSCs in cell proliferation. Surface phenotype assay showed that CD146 expression was negligible in ScASCs with an average of 0.39% ($n = 4$) while in donor-matched IPFSCs, the average CD146 expression was 4.52% ($n = 4$), significantly higher than ScASCs (**Figure 1D**). Due to the commercial unavailability of surface marker antibodies targeting rabbit CD44, CD73, CD90, and CD105, RNA-seq was used to measure these surface marker expressions at mRNA levels including *CD44* (Log2FC from IPFSCs to ScASCs was 1.20, *FDR = 9.22E-09*), *NT5E* (5′-Nucleotidase Ecto for CD73) (Log2FC from IPFSCs to ScASCs was −0.99, *FDR = 1.69E-05*), *THY1* (Thy-1 Cell Surface Antigen for CD90) (Log2FC from IPFSCs to ScASCs was 0.39, *FDR = 1.00E+00*), and *ENG* (Endoglin for CD105) (Log2FC from IPFSCs to ScASCs was −0.67, *FDR = 1.32E-01*) (**Figure 1E**). Interestingly, qPCR data showed that there were no significant differences in stemness-related genes *NANOG*, *REX1*, *NES*, and *SOX2*, and senescence-related genes *CDKN1A* and *TP53* in donor-matched adipose stem cells (**Figure 1F**).

Adaptation of Transcription Factors During Differentiation Induction

To determine the adaptation of transcription factors in ScASCs and donor-matched IPFSCs, qPCR was used to

[1]https://www.bioinformatics.babraham.ac.uk/projects/fastqc/

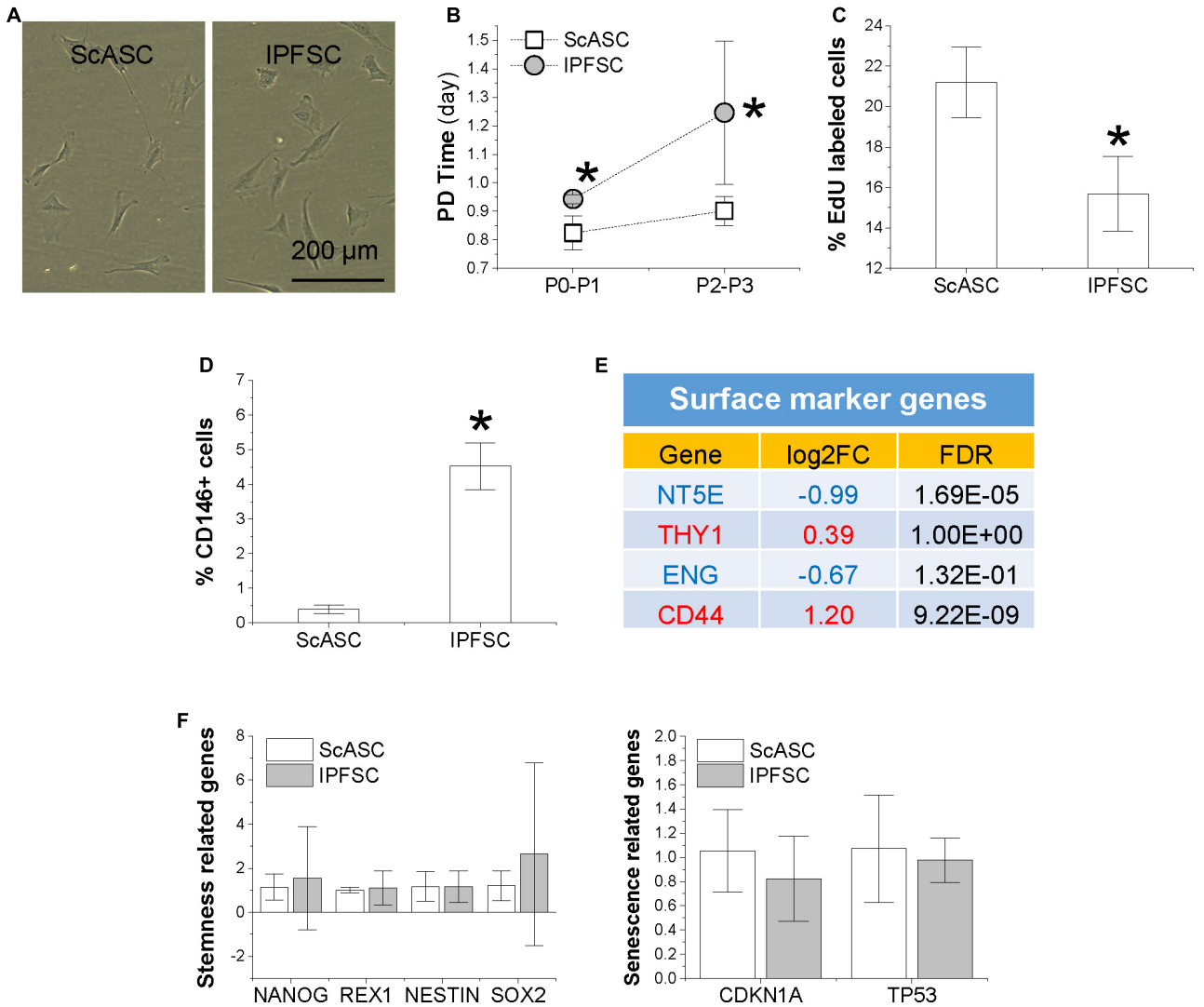


FIGURE 1 | Comparison of proliferation capacity between ScASCs (n = 4) and donor-matched IPFSCs (n = 4) in **(A)** cell morphology; **(B)** cell population doubling (PD) time calculated by cell counting; **(C)** relative EdU incorporation; **(D)** CD146 surface marker expression level evaluated by flow cytometry analysis; **(E)** other surface marker gene expression levels evaluated by RNA-seq, in which a positive value in log2FC means higher expression in IPFSCs (in red) and a negative value means higher expression in ScASCs (in blue); and **(F)** stemness-related genes *NANOG*, *REX1*, *NESTIN*, and *SOX2* and senescence-related genes *CDKN1A* and *TP53* measured by qPCR. Data are shown as bar charts. * indicates a significant difference compared to the corresponding control group ($p < 0.05$).

evaluate *SOX9* for chondrogenesis, *PPARG* for adipogenesis, and *RUNX2* for osteogenesis during differentiation induction. Before induction, only *SOX9* expression was significantly higher in IPFSCs compared with ScASCs (**Figure 2A**). After an 18-day chondrogenic induction, *SOX9* expression was maintained at a higher level in IPFSCs similar to day 0 while *PPARG* expression was significantly lower than ScASCs despite a remarkable increase of *PPARG* in both cells (**Figures 2B,C**). After 21-day adipogenic induction, the difference in *SOX9* expression between groups was diminished; interestingly, both *PPARG* and *RUNX2* expression in IPFSCs were significantly lower than donor-matched ScASCs (**Figure 2D**). After a 21-day osteogenic induction, the difference in *SOX9* expression decreased but IPFSCs still had a higher level than ScASCs; intriguingly, IPFSCs exhibited a higher expression level in *PPARG* than ScASCs (**Figure 2E**).

Development of Differentiation Factors During Induction

To further explore the differentiation preference of donor-matched adipose stem cells, qPCR was used to evaluate *COL2A1* and *ACAN* as markers of chondrogenesis, *ADIPOQ* and *LPL* for adipogenesis, and *BGLAP* and *SPP1* for osteogenesis during induction. Before induction, IPFSCs had significantly higher expression of *COL2A1* and *ACAN* than ScASCs (**Figure 3A**), in line with *SOX9* expression (**Figure 2A**). The advantageous expression of *COL2A1* and *ACAN* was further strengthened

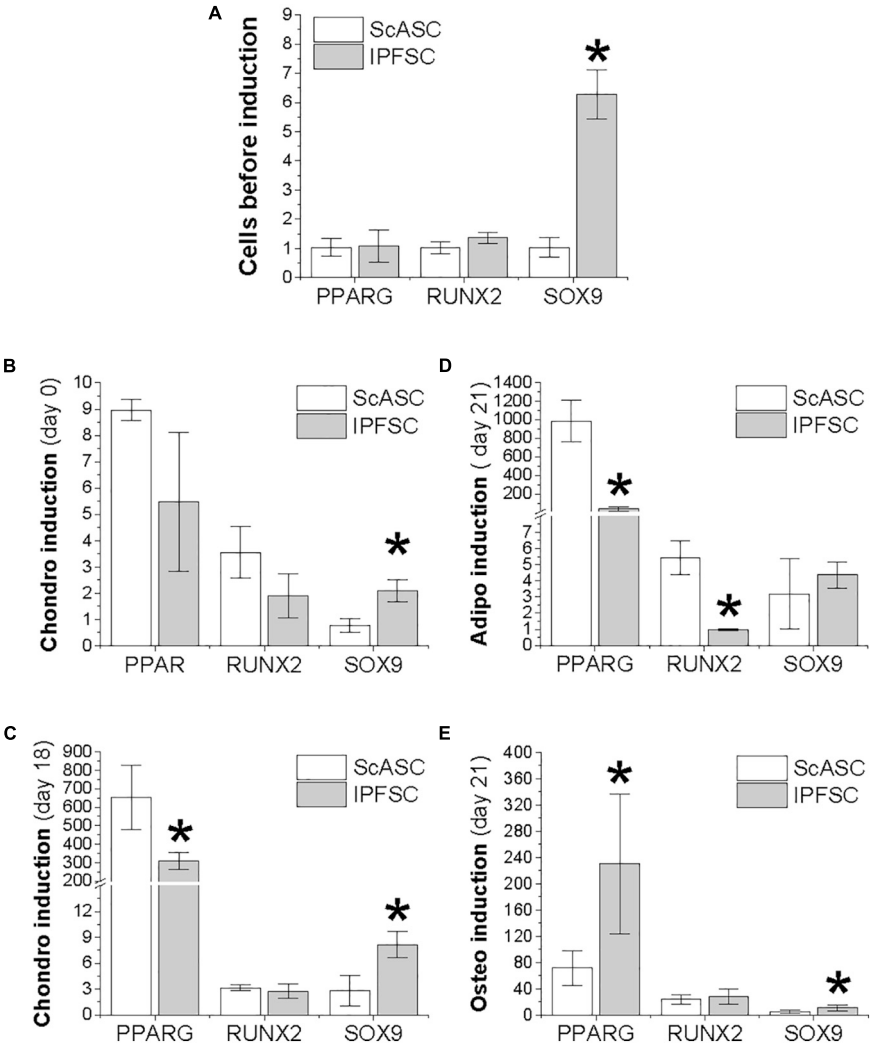


FIGURE 2 | Expression of transcription factors in ScASCs (n = 4) and donor-matched IPFSCs (n = 4) measured by qPCR. *SOX9*, *PPARG*, and *RUNX2* were used to represent chondrogenesis, adipogenesis, and osteogenesis, respectively. Expanded cells were evaluated before induction **(A)** and after induction **(B–E)**: **(B)** 24 h after centrifugation to form a pellet but before chondrogenic induction; **(C)** 18 days after chondrogenic induction; **(D)** 21 days after adipogenic induction; and **(E)** 21 days after osteogenic induction. Data are shown as bar charts. Expression of each target gene in undifferentiated IPFSCs **(A)** and differentiated ScASCs/IPFSCs **(B–E)** is plotted against undifferentiated ScASCs **(A)**, which is set as "1". * indicates a significant difference compared to the corresponding control group ($p < 0.05$).

during chondrogenic induction (**Figure 3B**). No significant difference of *COL10A1* expression was observed between groups; however, we found that *MMP13* expression was more than 1000 times higher in IPFSCs compared with ScASCs before induction, which became comparable between groups after chondrogenic induction (**Figure 3C**).

Before induction, ScASCs exhibited higher expression of *ADIPOQ* and *LPL* than IPFSCs (**Figure 3D**), despite no significant difference in transcription factor *PPARG* expression (**Figure 2A**). The dominant expression of *ADIPOQ* and *LPL* became dramatically increased during adipogenic induction along with differentiation gene *LEP* and transcription factor *PPARG* expression (**Figure 3E**). Moreover, higher expression of adiponectin (ADIPOQ) in ScASCs than donor-matched IPFSCs was also confirmed in Western blot analysis (**Figure 3F**).

For osteogenic differentiation, despite no difference in *BGLAP* expression before induction, IPFSCs displayed a higher expression of *SPP1* than ScASCs (**Figure 3G**), which became comparable after 21-day osteogenic induction along with other differentiation genes *BGLAP*, *DCN*, and *SPARC* expression (**Figure 3H**). Furthermore, comparable expression of OCN between ScASCs and IPFSCs was also confirmed in ELISA analysis (**Figure 3I**).

Transcriptome Difference Between ScASCs and Donor-Matched IPFSCs

We applied RNA-seq data analysis to explore the difference in gene expression levels between ScASCs and IPFSCs. Principal coordinate analysis on gene expression across all genes revealed

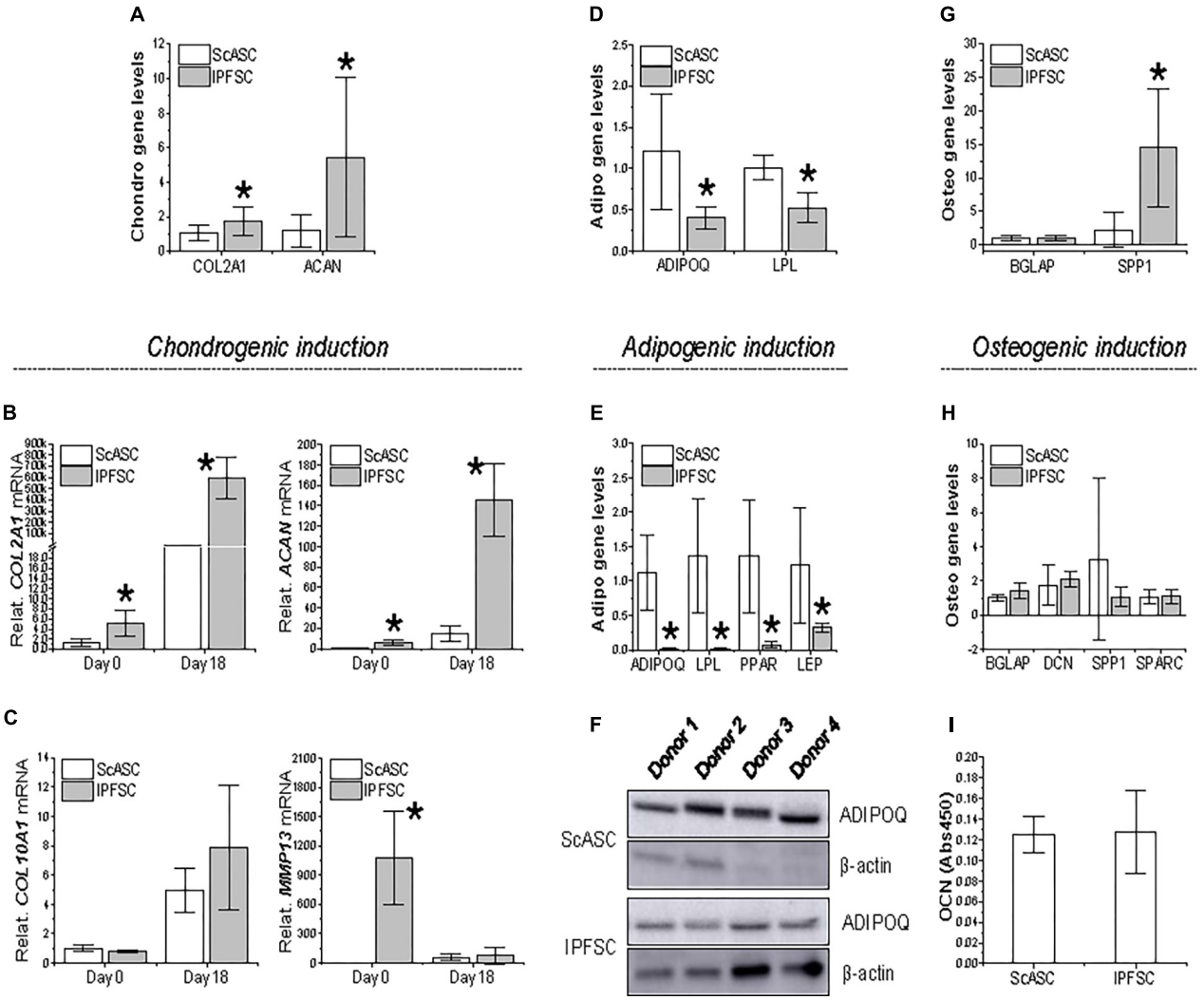


FIGURE 3 | Expression of differentiation genes in ScASCs (n = 4) and donor-matched IPFSCs (n = 4) before and after induction. For chondrogenic differentiation, typical markers, *COL2A1* and *ACAN*, were evaluated using qPCR before **(A)** and after chondrogenic induction **(B)**. Hypertrophic markers *COL10A1* and *MMP13* were also measured after chondrogenic induction **(C)**. For adipogenic differentiation, typical markers, *ADIPOQ* and *LPL*, were evaluated using qPCR before **(D)** and after adipogenic induction **(E)**. *LEP* expression was also measured after induction **(E)**. Adiponectin (ADIPOQ) expression was confirmed using Western blot analysis with β-actin as an internal control **(F)**. For osteogenic differentiation, typical markers, *BGLAP* and *SPP1*, were evaluated using qPCR before **(G)** and after osteogenic induction **(H)**. Expression of *DCN* and *SPARC* were also measured after induction **(H)**. Osteocalcin (OCN) expression was confirmed using ELISA analysis **(I)**. Expression of each target gene in IPFSCs is plotted against the corresponding ScASCs, which is set as "1", but for those in chondrogenic induction **(B/C)**, expression in day 0 is plotted as "1". Data are shown as bar charts. * indicates a significant difference compared to the corresponding control group ($p < 0.05$).

that samples from ScASCs and IPFSCs were from two distinctive clusters on the first dimension (**Figure 4A**). By applying EdgeR (McCarthy et al., 2012) with stringent thresholds [FC > 2 and FDR < 0.05], we identified 359 and 277 protein-coding genes upregulated and downregulated from the ScASC samples to the IPFSC samples, respectively (**Figure 4B**). Intriguingly, differentially expressed genes were enriched in those encoding transcription factors (**Figure 4C**), including the Homeobox (HOX) gene family related to stem cell differentiation (Seifert et al., 2015; **Figure 4D**).

We next examined the expression changes on particular groups of genes known to function in chondrogenesis and/or adipogenesis. The data were presented as Log2FC of expression and FDR. Functional annotation clustering was categorized (**Figure 5**) including (A) HOX gene family; (B) T (the brachyury gene)-box (TBX) gene family; (C) TGFβ (TGFB) gene family; (D) SOX gene family; (E) Bone morphogenetic protein (BMP) gene family; (F) Wingless/integrase-1 (WNT) gene signals; (G) Collagen (COL) gene family; (H) Lysyl oxidase (LOX) gene family; (I) Genes coding for Basement membrane proteins; (J)

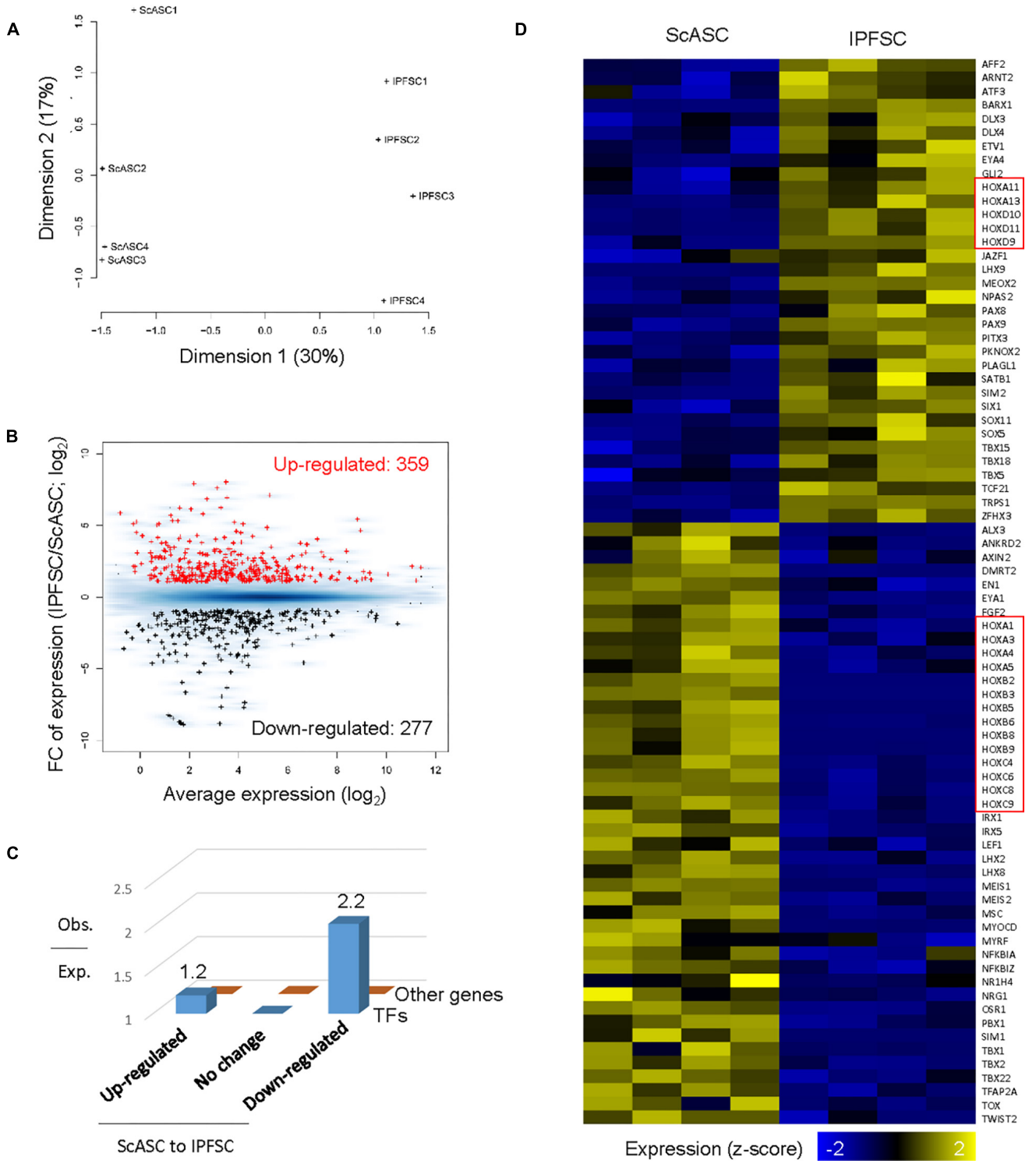


FIGURE 4 | Differentially expressed gene analysis of ScASCs and donor-matched IPFSCs from four rabbits (n = 4). **(A)** Principal coordinates analysis on gene expression for RNA-Seq samples from ScASCs and IPFSCs. **(B)** MA plot showing the average and fold change (FC) of gene expression for differentially expressed genes between ScASCs and IPFSCs. Red: genes upregulated from ScASCs to IPFSCs; Black: genes downregulated from ScASC to IPFSCs; Blue background: all expressed genes. **(C)** Bar plot showing the ratio of observed number to the expected number of genes for transcription factor genes and for other genes grouped based on their expression changes between ScASCs and IPFSCs. **(D)** Heat map showing the expression changes between ScASCs and IPFSCs for differentially expressed transcription factors. Genes sorted first by their expression changes and then by names. Red rectangles: Homeobox (HOX) genes.

A HOX gene family

Gene	log2FC	FDR
HOXD10	6.79	1.3E-62
HOXD11	5.28	3.5E-26
HOXD9	2.70	3.6E-13
HOXA11	1.37	1.8E-07
HOXA10	0.64	2.1E-02
HOXC10	-0.64	5.2E-06
HOXA4	-1.11	5.8E-08
HOXC9	-1.14	1.3E-10
HOXA5	-1.25	7.5E-14
HOXA3	-1.33	8.6E-06
HOXA1	-1.59	3.7E-04
HOXC6	-1.61	5.8E-27
HOXC4	-1.74	1.1E-22
HOXC8	-3.04	1.2E-50
HOXB6	-7.73	1.9E-85
HOXB3	-8.78	4.0E-39
HOXB2	-8.85	4.4E-40
HOXB9	-8.89	2.0E-85

B TBX gene family

Gene	log2FC	FDR
TBX5	1.24	2.5E-05
TBX15	1.14	9.9E-17
TBX18	1.03	2.7E-12
TBX22	-1.09	1.4E-03
TBX2	-1.69	3.8E-11
TBX1	-6.70	2.9E-38

C TGFB gene family

Gene	log2FC	FDR
TGFB3	2.16	1.1E-17
TGFB2	1.07	4.4E-04
LTBP1	0.81	7.4E-02

D SOX gene family

Gene	log2FC	FDR
SOX11	3.51	8.2E-17
SOX6	3.12	1.5E-07
SOX5	2.95	3.6E-27
SOX9	0.77	6.3E-06

E BMP gene family

Gene	log2FC	FDR
BMP4	3.96	1.9E-32
BMPR2	-0.36	3.8E-02
BMPER	-1.09	6.0E-12
BMP3	-8.37	5.4E-30

F WNT signals

Gene	log2FC	FDR
SFRP5	2.42	2.6E-06
SFRP2	2.09	5.7E-23
FZD1	1.31	1.8E-18
FZD5	1.04	2.9E-08
GREM2	0.59	7.2E-03
LRP6	0.38	1.4E-02
PIAS3	-0.35	4.9E-02
RYK	-0.53	7.7E-04
ROR2	-0.53	3.4E-04
NFATC4	-0.53	1.5E-02
FZD2	-1.14	2.2E-04
AXIN2	-1.22	2.7E-03
FZD7	-1.46	3.7E-11
WNT4	-2.01	1.8E-06

G COL gene family

Gene	log2FC	FDR
COL11A1	4.58	2.2E-03
COL8A2	2.45	2.2E-06
COL26A1	2.25	1.3E-14
COLEC12	2.04	1.6E-02
COL8A1	1.65	1.4E-12
PCOLCE2	1.31	1.2E-18
COL2A1	-0.54	1.3E-04
COL1A1	-0.55	6.5E-03
COL1A2	-0.56	8.0E-03
COL3A1	-0.85	3.2E-04
COL14A1	-1.56	3.5E-08
COL4A5	-3.54	2.4E-19
COL21A1	-4.21	6.4E-23

H LOX gene family

Gene	log2FC	FDR
LOXL3	1.66	4.5E-04
LOXL4	1.53	2.4E-03
LOXL2	1.08	2.8E-13
LOXL1	0.86	4.3E-10
LOX	0.71	1.9E-04

I Basement membrane

Gene	log2FC	FDR
LAMA3	2.45	6.9E-04
LAMA1	2.39	5.1E-07
NID2	-0.62	9.3E-04
COL4A5	-3.54	2.4E-19

J Matrix turnover enzymes

Gene	log2FC	FDR
MMP13	7.45	1.4E-16
ADAMTSL3	4.52	1.3E-08
ADAMTS17	2.60	6.0E-07
TIMP3	0.70	2.9E-02
ADAMTS14	-0.37	8.2E-02
ADAMTS12	-0.77	2.1E-06
IL1A	-4.15	1.1E-61
ADAMTS19	-7.01	9.0E-69

K ITG gene family

Gene	log2FC	FDR
ITGA7	1.69	1.6E-02
ITGB8	1.61	2.2E-31
ITGA6	1.03	3.8E-06
ITGA3	0.82	5.9E-02
ITGA4	0.76	4.0E-03
ITGA8	-2.48	2.6E-12

L AQP gene family

Gene	log2FC	FDR
AQP1	3.74	2.9E-36
AQP4	1.79	2.5E-04
AQP11	1.77	8.6E-09
AQP3	1.05	7.3E-11

M Chondrogenic genes

Gene	log2FC	FDR
TNC	5.38	6.1E-10
MATN2	5.04	2.9E-17
SMOC1	4.43	1.9E-32
GALNT5	4.38	1.8E-12
HAPLN1	4.32	2.2E-08
CYTL1	4.16	8.2E-57
TRPS1	3.98	5.1E-91
PRELP	3.61	5.0E-62
PAX9	3.41	1.7E-07
THBS4	3.28	1.9E-43
IGF1	3.11	1.4E-04
CHST15	2.87	4.5E-20
MCAM	2.62	5.7E-07
ACAN	2.59	8.5E-08
ITM2A	2.48	4.7E-09
FMOD	2.31	9.2E-05
SOD3	2.10	3.9E-09
FBLN7	2.00	5.9E-22
CSPG4	1.92	1.2E-46
GPC3	1.88	5.6E-20
FGFR2	1.70	3.9E-08
CCL2	1.69	2.1E-05
LUM	1.61	8.8E-10
TLR2	1.61	8.4E-14
ITIH3	1.42	3.1E-08
FGF10	1.40	1.2E-05
MATN3	1.36	6.3E-04
UST	1.33	9.7E-03
CD44	1.20	9.2E-09
ALCAM	1.15	1.6E-01
CHST11	1.02	5.6E-04
MDFI	0.96	5.5E-02
ZEB1	0.91	2.4E-08
ECM2	0.87	1.4E-03
SDC4	0.81	1.9E-08
JAG1	0.79	3.8E-03
DSE	0.78	8.6E-06
LAYN	0.70	2.2E-05
CYP26B1	0.67	1.3E-04
HYAL1	0.67	7.8E-06
UXS1	0.63	6.0E-06
NDST1	0.55	2.4E-03
SDC2	0.54	1.2E-02
BGN	0.44	3.9E-02
FSTL1	0.42	1.9E-02

N Adipogenic genes

Gene	log2FC	FDR
ALDH1A2	7.04	3.5E-33
TGFA	5.05	3.3E-09
TCF21	2.13	3.0E-13
FABP3	1.55	7.7E-04
LPL	1.52	1.4E-04
SMOC2	1.50	5.6E-04
ETV1	1.38	6.0E-03
FABP5	1.13	1.7E-07
LPIN1	0.96	1.4E-03
ECM1	0.93	3.7E-04
DOK1	0.89	7.6E-02
PPARD	0.86	3.7E-06
JAG1	0.79	3.8E-03
IL11RA	0.77	6.9E-06
LIFR	0.74	1.5E-02
KLF5	0.70	4.7E-05
SLC29A1	0.66	3.1E-06
GREM2	0.59	7.2E-03
TRIB2	0.52	4.9E-03
LRP6	0.38	1.4E-02
PIAS3	-0.35	4.9E-02
OSBPL11	-0.49	3.0E-02
NFATC4	-0.53	1.5E-02
ACSF2	-0.69	1.4E-03
SIK2	-0.76	3.9E-02
FZD2	-1.14	2.2E-04
ACSL5	-1.80	5.8E-12
WNT4	-2.01	1.8E-06
ABCD2	-2.22	2.5E-06
IGF2BP1	-2.32	8.6E-02
HPGD	-4.45	7.7E-06
LHX8	-5.29	1.9E-68

FIGURE 5 | Expression changes between IPFSCs and ScASCs for selected groups of genes with function in chondrogenesis and/or adipogenesis: **(A)** Homeobox (HOX) gene family; **(B)** T (the brachyury gene)-box (TBX) gene family; **(C)** TGFβ (TGFB) gene family **(D)** SOX gene family; **(E)** Bone morphogenetic protein (BMP) gene family; **(F)** Wingless/integrase-1 (WNT) gene signals; **(G)** Collagen (COL) gene family; **(H)** Lysyl oxidase (LOX) gene family; **(I)** Genes coding for Basement membrane proteins; **(J)** Genes coding Matrix turnover enzymes; **(K)** Integrin (ITG) gene family; **(L)** Aquaporin (AQP) gene family; **(M)** Chondrogenic-related genes; and **(N)** Adipogenic-related genes. Green shaded FDR indicates favorable effect of the gene on chondrogenesis **(M)** or adipogenesis **(N)**. A positive value in log2FC means higher expression in IPFSCs (in red), and a negative value means higher expression in ScASCs (in blue). Orange shaded FDR: > 0.05.

Genes coding Matrix turnover enzymes; (K) Integrin (ITG) gene family; (L) Aquaporin (AQP) gene family; (M) Chondrogenic-related genes; and (N) Adipogenic-related genes.

Proteome Difference Between ScASCs and Donor-Matched IPFSCs

Both cells and deposited proteins were interrogated with bottom-up mass spectrometry-based proteomics to monitor differences in protein abundance (**Figure 6A**). The pathway analysis highlighted that the matrix proteins deposited by ScASCs mapped to more cell cycle regulators than traditional ECM proteins (**Figures 6B,C**), such as the uptick in fibril associated collagens with interrupted triple helices (FACIT collagens) including COL12A1 (FC = 2.26, p = 0.010) and COL14A1 (FC = 4.73, p = 0.002), Thrombospondin 1 (THBS1) (FC = 4.60, p = 0.008), THBS2 (FC = 8.37, p = 0.009), Asporin (ASPN, FC = 9.70, p = 0.002), Podocan (PODN, FC = 1.70, p = 0.009), and Versican (VCAN, FC = 3.10, p = 0.001). These proteins did not seem to be laying down as much ECM in general as those deposited by IPFSCs as shown by both the pathway analysis and the relatively lower amount of structural ECM.

In contrast, the matrix proteins enriched from IPFSCs include numerous basement membrane components (**Figures 6B,C**), such as nidogen 1 (NID1) (FC = 0.27, p = 0.008), heparin sulfate proteoglycan 2 (HSPG2)/perlecan (FC = 0.54, p = 0.001), laminin subunits including LAMA5 (FC = 0.10, p = 0.030), LAMB1 (FC = 0.40, p = 0.033), LAMB2 (FC = 0.28, p = 0.004), and LAMG1 (FC = 0.34, p = 0.005). Of relevance, and consistent with the mRNA level, the integrin A6 subunit (ITGA6) that forms a laminin receptor was also significantly increased (FC = 0.03, p = 0.005). In addition, various isoforms of fibronectin (FN) were significantly higher. Interestingly, compared to those secreted by ScASCs, collagen modifying enzymes, such as LOX and tissue

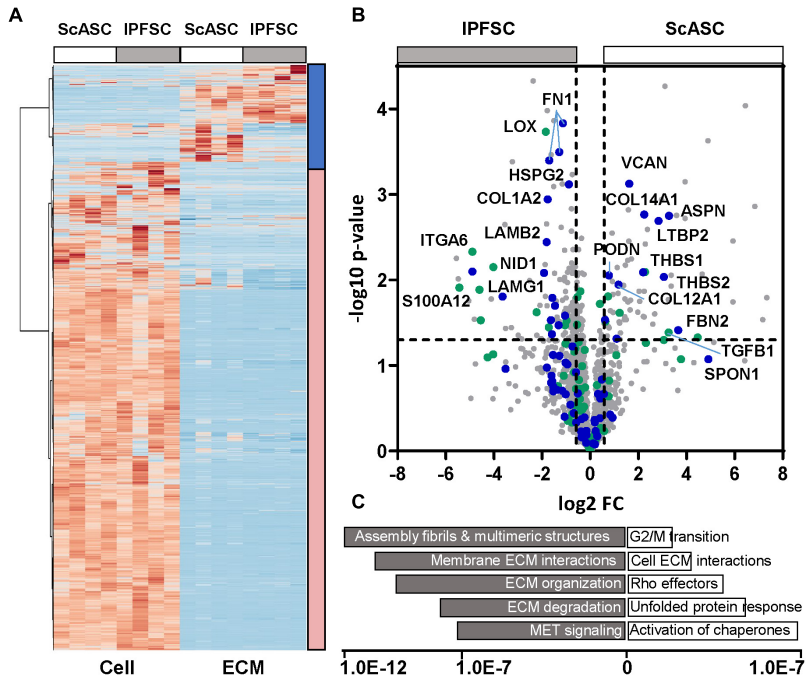


FIGURE 6 | Proteomic results of cells and ECMs from ScASCs versus IPFSCs of four donor-matched rabbits. **(A)** Heatmap for global representation of protein differences (Z score used). The blue bar on the left indicates the region highly enriched in ECM components, the red bar indicates the region that contains primarily intracellular proteins. **(B)** Volcano plot with the *Y*-axis indicating -log10 *p*-value and the *X*-axis of the fold change (FC) in log2. Core ECM proteins are indicated in blue and Matrisome associated proteins are in green. **(C)** Gene enrichment analysis (top pathways, Reactome) is shown with the *X*-axis indicating the statistical significance based on false discovery rates using the Benjamani_hochberg method.

transglutaminase (TG2, FC = 0.49, p = 0.050), accompanying fibrillar collagens, such as COL5A1 (FC = 0.36, p = 0.020) and COL5A3 (FC = 0.48, p = 0.030), were significantly upregulated in the matrix proteins deposited by IPFSCs. Consistent with the measured mRNA levels, LOX was significantly increased (FC = 0.27, p = 0.000) in matrix proteins deposited by IPFSCs, with similar trends in LOX-like 1 (LOXL1) (FC = 0.30, p = 0.036) and LOXL4 (FC = 0.48, p = 0.030).

DISCUSSION

Adult stem cells have the ability to differentiate into varied lineages. Increasing evidence indicates that adult stem cells from different tissues do not have equivalent ability toward a specific lineage differentiation (Jones and Pei, 2012; Pizzute et al., 2015). However, there is a lack of comparable studies using donor-matched adult stem cells and their matrix microenvironment. In this study, we found that, despite both deriving from adipose tissue, ScASCs and IPFSCs isolated from different depots of four donor-matched rabbits exhibited significant divergence in both proliferation and differentiation potential. Transcriptome and proteomics data provide robust evidence to support our hypothesis that there are site-dependent variations in lineage potential and preference of stem cells from adipose tissue.

Our proliferation data showed that ScASCs grew faster than donor-matched IPFSCs, which might result from higher levels of COL12A1, COL14A1, THBS1, THBS2, and VCAN expression in the matrix proteins deposited by ScASCs. These matrix proteins trend higher in tumor microenvironments and tissues to support proliferative or structurally rigid phenotypes (Wight et al., 2014; Subramanian and Schilling, 2015; Belotti et al., 2016). We also found that IPFSCs expressed significantly higher CD146 than donor-matched ScASCs, which was in line with the gene expression level in RNA-seq data (Log2FC from IPFSCs to ScASCs in CD146/*MCAM* was 2.62, *FDR* = 5.7E-07). Regardless of the role as a perivascular marker for adult stem cells (Crisan et al., 2008), a higher level of CD146 expression in adult stem cells might be associated with an advantage in chondrogenic differentiation (Hagmann et al., 2014; Su et al., 2015). Despite the failure to measure expression of surface markers CD90 and CD105 using flow cytometry on both ScASCs and IPFSCs (data not shown), our RNA-seq data indicated that the genes (*NT5E*, *THY1*, *ENG*, and *CD44*) encoding surface marker proteins (CD73, CD90, CD105, and CD44) were expressed in both cells with *NT5E* preferentially expressed in ScASCs and *CD44* advantageously expressed in IPFSCs. We also found no statistical difference in measured stemness-related genes (*NANOG*, *REX1*, *NESTIN*, and *SOX2*), indicating that these genes expressed in the donor-matched IPFSCs and ScASCs might not contribute to the discrepancy of a specific lineage differentiation found in this study.

Our differentiation data indicated that IPFSCs exhibited a significantly higher level of chondrogenic markers compared

with donor-matched ScASCs. RNA-seq data showed that advantageous genes in IPFSCs can be categorized into several clusters based on functional annotation clustering. For example, the HOX gene, an evolutionarily highly conserved gene family, determines lineage specific differentiation of adult stem cells once tissue damage occurs (Seifert et al., 2015). In this study, HOXD genes, including *HOXD9-11* and *HOXA10/11*, were only dominantly expressed in IPFSCs over donor-matched ScASCs. HOXD genes, one of four grouped HOX clusters (HOXA, HOXB, HOXC, and HOXD) in vertebrates, are suggested to play a role in stem cell based chondrogenesis (Jung and Tsonis, 1998; González-Martín et al., 2014). *HOXA11* and *HOXD11* double mutant mice had shorter limb formation (Boulet and Capecchi, 2004). Compared with IPFSCs, however, donor-matched ScASCs exhibited robust expression of other HOX genes, such as *HOXA4*, *HOXA5*, *HOXC4*, and *HOXC8*, which are closely associated with adipogenesis rather than osteogenesis (Levi et al., 2010). An exception is *HOXC8* which does not inhibit but retards chondrogenesis, resulting in a boost of proliferating precursor cells and a negative influence on chondrogenesis (Yueh et al., 1998; Cormier et al., 2003).

Another group of conservative transcription factors, TBX family genes, also plays crucial roles throughout development. Our RNA-seq data showed that *TBX5*, *TBX15*, and *TBX18* were highly expressed in IPFSCs compared to donor-matched ScASCs. TBX5 was reported to activate WNT and fibroblast growth factor (FGF) signaling in upper limb development (Takeuchi et al., 2003). Overexpression of *TBX15* in 3T3-L1 preadipocytes impeded adipocyte differentiation and reduced triglyceride content (Gesta et al., 2011). *TBX15* and *TBX18* co-expressed in the limb mesenchyme indicate their functions during limb development (Tanaka and Tickle, 2004; Singh et al., 2005). Recently, *TBX18* was reported to co-express with *SOX9* in chondrogenic progenitors and differentiating chondrocytes (Haraguchi et al., 2015). In contrast, *TBX1* was reported to be preferentially expressed in the inducible pool of brown adipocytes (beige cells) present in white fat of the inguinal depot (Wu et al., 2012). The above findings indicate that two fat depots, ScAT and IPFP, exhibit distinct HOX and TBX conservative gene expression profiles that likely influence their differentiation preference.

The TGFβ superfamily is composed of two subfamilies; the TGFβ subfamily mainly includes TGFβs (1, 2, and 3) and the BMP subfamily mainly includes BMPs (2, 4-10) (Wang et al., 2014). A considerable amount of *in vitro* data indicate that TGFβ signaling pathways promote mesenchymal condensation (Barry et al., 2001; Tuli et al., 2003) and the early stages of chondrocyte differentiation, but restrain terminal hypertrophy (Mueller and Tuan, 2008; Shintani et al., 2013). In this study, we found that all TGFβ isotypes (*TGFB1*, *TGFB2*, and *TGFB3*) and latent-TGFB-binding protein 1 (*LTBP1*) were preferentially expressed in IPFSCs rather than donor-matched ScASCs. However, the protein level showed an opposite trend for TGFB1 and LTBP2, indicating that, while ScASCs have more available bound ligand, IPFSCs may have more free ligand, which needs to be further confirmed. This finding is in line with the advantageous expression in IPFSCs of the combination of *SOX5*, *SOX6*, and *SOX9* (the SOX trio) that supplies signals sufficient to induce permanent cartilage (Ikeda et al., 2004) and of *SOX11* that contributes to the regulation of growth/differentiation factor 5 (GDF5) in joint maintenance (Kan et al., 2013). Our data also showed that only *BMP4* exhibited a statistically higher level of expression in IPFSCs compared with donor-matched ScASCs. BMP4 plays an important role in retaining chondrogenic phenotype, through both increasing matrix production and suppressing the production of collagen type X (Reddi, 2001; Steinert et al., 2003). Another important BMP isotype in chondrogenesis, *BMP2*, was expressed at a higher level in IPFSCs than in donor-matched ScASCs despite no significant difference (*FDR* = 5.9E-01). Interestingly, *BMP3*, which was reported to inhibit bone formation by hindering BMP2 activity (Bahamonde and Lyons, 2001), was significantly expressed in ScASCs compared with donor-matched IPFSCs. These findings indicate that IPFSCs have an expression profile consistent with endochondral bone formation over donor-matched ScASCs. The above data support that TGFβ signaling cooperated with BMP signaling in stimulating articular cartilage regeneration (Wang et al., 2014).

Increasing evidence indicates that the canonical Wnt signaling pathway inhibits adipogenesis while the noncanonical Wnt pathway promotes adipogenesis by antagonizing the Wnt/β-catenin pathway (Christodoulides et al., 2009). In accordance with the above findings, we found that preferential expression favoring Wnt/β-catenin signaling genes such as SPARC-related modular calcium binding protein 2 (*SMOC2*) (Nie and Sage, 2009), low-density lipoprotein receptor-related protein 6 (*LRP6*) (Peröbner et al., 2012), and Gremlin 2 (*GREM2*) (Wu et al., 2015) in IFPSCs might be responsible for the inhibition of adipogenesis and the enhancement of chondrogenesis. In contrast, expression inhibiting Wnt/β-catenin signaling genes such as *WNT4* (Liu et al., 2016) and nuclear factor of activated T-cells 4 (*NFATC4*) (Yang et al., 2006) in ScASCs might be responsible for promoting adipogenesis and blocking chondrogenesis (Church et al., 2002).

Interestingly, we found FACIT collagen, such as *COL14A1* and *COL21A1*, was expressed at a higher level in ScASCs rather than IPFSCs. We also found that, despite collagen modifying enzymes detectable in both cells, IPFSCs exhibited significantly higher expression of LOX isoforms and tissue transglutaminase (Log2FC from IPFSCs to ScASCs for *TGM2* was 3.68, *FDR* = 4.9E-06) at both mRNA and protein levels than ScASCs, along with fibrillar collagens COL5A1 and COL5A3, which participate in the formation of a fibrillar collagen network and the regulation of fibrillogenesis (Imamura et al., 2000; Malfait et al., 2005; Lincoln et al., 2006). These findings indicate that IPFSCs are more suitable adipose stem cells for chondrogenesis compared to donor-matched ScASCs. During chondrogenesis, the contents of collagen type II and of non-reducible collagen cross-links were positively linked with tensile biomechanical properties and the functional integrity of cartilage tissues (Williamson et al., 2003). LOX family enzyme activities catalyze the eventual enzymatic conversion that is needed for the generation of biosynthetic collagen cross-links. For example, knockdown studies demonstrated that LOXL2 expression is required for mouse ATDC5

chondroprogenitors' differentiation toward chondrocytes through regulation of *SNAIL* and *SOX9*, two important transcription factors for chondrogenesis (Iftikhar et al., 2011). Interestingly, hypoxia increased LOX gene expression, which promoted pyridinoline cross-links in engineered cartilage (Makris et al., 2013).

Regarding the matrix components, we found that IPFSCs deposited more basement membrane proteins compared to ScASCs, including *LAMA1*, *LAMA3*, and *HSPG2* at an mRNA level and LAMA5, LAMB1, LAMB2, LAMG1, NID1, and HSPG2 at a protein level. In contrast, *NID2* and *COL4A5* were significantly more highly expressed in ScASCs compared to donor-matched IPFSCs. Given the function of *HSPG2* encoding perlecan as the "factotum" in cartilage (Melrose et al., 2008) and the role of laminins in cartilage regeneration (Sun et al., 2017), *NID2* and *COL4A5* expression might be associated with adipogenic differentiation, which remains to be elucidated.

Interestingly, matrix turnover enzymes were uniquely preferentially expressed in IPFSCs or ScASCs. For example, matrix metallopeptidase 13 (MMP13), known as collagenase 3, was found exclusively in IPFSCs. The enzyme's initial role is in tissue remodeling, especially during embryonic development, but it is also highly active in some pathological processes such as osteoarthritis and cancer (Inada et al., 2004; Tardif et al., 2004). In osteoarthritis, *MMP13* was highly expressed in chondrocytes and synovial cells responsible for the degradation of cartilage matrix (Inada et al., 2004; Davidson et al., 2006; van den Berg, 2011). However, little is known about *MMP13* expression in IPFP, either in healthy donors or in the pathological process. In this study, qPCR data showed that *MMP13* was expressed more than 1000-fold higher in IPFSCs than donor-matched ScASCs during cell condensation (day 0 pellet), in accordance with RNA-seq data of cell samples (Log2FC from IPFSCs to ScASCs in *MMP13* was 7.45, *FDR = 1.4E-16*). Interestingly, after an 18-day chondrogenic induction, IPFSCs exhibited a comparable expression of *MMP13* to donor-matched ScASCs. From the proteomics analysis, A disintegrin and metalloproteinase with thrombospondin motifs 5 (ADAMTS5) and ADAMTS1 were identified as significantly higher levels in IPFSCs versus a much higher level of ADAMTSL1 (ADAMTS like 1) in ScASCs. The protease profile is likely important for key processing events associated with the physiological role of IPFP in support of the remodeling of articular cartilage, which requires further investigation.

Integrin, a transmembrane receptor, facilitates cell-ECM adhesion. Interestingly, more integrins were advantageously expressed in IPFSCs including *ITGA3*, *ITGA4*, *ITGA6*, *ITGA7*, and *ITGB8* compared to *ITGA8*, which was superiorly expressed in donor-matched ScASCs. Another transmembrane protein, aquaporin, called the "the plumbing system for cells", was found to serve as a water channel to rapidly move water through cells. Chondrocytes from articular cartilage are unique due to their sensitivity to water transfer and ionic and osmotic adjustments from the extracellular environment and are responsible for the creation of synovial fluid. A recent report showed that the expression of AQP1 and AQP3 were upregulated during chondrogenic induction of human adipose stem cells, indicative of physiological modification of functionally mature chondrocytes to the local environment (Graziano et al., 2018). This finding was consistent with our data, in which all statistically significant AQP gene expression was advantageously found in IPFSCs rather than donor-matched ScASCs, not only *AQP1* and *AQP3* but also *AQP4* and *AQP11*.

Furthermore, we found that important clusters associated with cartilage matrix were preferentially expressed in IPFSCs over donor-matched ScASCs. For instance, one of the clusters is glycosaminoglycan (GAG) metabolic and biosynthetic process, including N-Deacetylase And N-Sulfotransferase 1 (*NDST1*), Polypeptide N-Acetylgalactosaminyltransferase 5 (*GALNT5*), Biglycan (*BGN*), Carbohydrate Sulfotransferase 11 (*CHST11*), Dermatan-sulfate epimerase (*DSE*), Hyaluronidase-1 (*HYAL1*), and Inter-alpha-trypsin inhibitor heavy chain H3 (*ITIH3*), along with GAG binding function cluster, genes of *CD44*, *ACAN*, *BGN*, *BMP4*, Chemokine (C-C motif) ligand 2 (*CCL2*), Extracellular matrix protein 2 (*ECM2*), *FGF10*, *FGFR2*, Fibulin 7 (*FBLN7*), Follistatin-like 1 (*FSTL1*), Hyaluronan and proteoglycan link protein 1 (*HAPLN1*), Layilin (*LAYN*), *LPL*, procollagen C-endopeptidase enhancer 2 (*PCOLCE2*), Proline/arginine-rich end leucine-rich repeat protein (*PRELP*), Superoxide dismutase 3 (*SOD3*), *THBS4*, and Toll-like receoptor 2 (*TLR2*). The CD44 receptor transduces signals on chondrocytes, which is an important mediator of cell-matrix interactions, especially the homeostasis maintained by hyaluronan-CD44 interactions (Knudson and Loeser, 2002). Another crucial cluster is chondroitin sulfate proteoglycan and its metabolic process of which the advantageously expressed genes in IPFSCs include *ACAN*, *BGN*, Fibromodulin (*FMOD*), *HSPG2*, Syndecan 2 (*SDC2*), *SDC4*, *IGFI*, Cytokine-like 1 (*CYTL1*), *CHST11*, *CHST15*, Chondroitin sulfate N-acetylgalactosaminyltransferase 2 (*CSGALNACT2*), *DSE*, and Uronyl 2-sulfotransferase (*UST*). *IGFI* encodes insulin-like growth factor-I, which is the predominant anabolic growth factor and decreases matrix catabolism for articular cartilage (Jenniskens et al., 2006). Apparently, IPFSCs naturally express abundant genes involved in the chondrogenesis pathway by modulating cartilage development and cartilage ECM while ScASCs show no significant correlation with chondrogenesis.

Both ScASCs and donor-matched IPFSCs expressed plenty of genes related to lipid and fatty acid in their biosynthetic, catabolic, binding, and homeostasis processes. Among these differentially expressed genes, none of them showed a distinct tendency toward the brown adipose tissue due to either nondetectable expression of Uncoupling protein-1 (*UCP1*), Peroxisome proliferator-activated receptor-γ coactivator 1-α (*PGC1A*), and Forkhead box protein C2 (*FOXC2*), or comparable expression of Cell death inducing DFFA-like effector A (*CIDEA*) (Log2FC from IPFSCs to ScASCs was −1.45, *FDR* = 7.1E-01), a core set of brown adipose genes (Harms and Seale, 2013). Given the preferential expression of *PPARG*, a master regulator of adipogenesis (Kawai and Rosen, 2010), in ScASCs, most privileged associated genes favored adipogenesis, including but not limited to ATP Binding Cassette Subfamily G Member 1 (*ABCG1*) (Frisdal et al., 2015), Fibrillin-1 (*FBN1*) (Davis et al., 2016), *NFATC4* (Yang et al., 2006), Oxysterol-binding

protein-related protein 11 (*OSBPL11*) (Zhou et al., 2012), Paternally expressed gene-10 (*PEG10*) (Hishida et al., 2007), Salt inducible kinase 2 (*SIK2*) (Henriksson et al., 2015), and *WNT4* (Christodoulides et al., 2009). Protein inhibitor of activated STAT 3 (*PIAS3*) did not favor adipogenesis (Deng et al., 2006). In contrast, excluding a few genes favoring adipogenesis, such as Docking protein 1 (*DOK1*) (Hosooka et al., 2008), *ECM1* (Challa et al., 2015), and Leukemia inhibitor factor receptor alpha (*LIFR*) (Aubert et al., 1999), most related genes inhibited adiogenic differentiation in IPFSCs, including but not limited to Fatty acid binding protein 4 (*FABP4*) (Garin-Shkolnik et al., 2014), *GREM2* (Wu et al., 2015), Jagged canonical NOTCH ligand 1 (*JAG1*) (Ugarte et al., 2009), *LRP6* (Peröbner et al., 2012), *SMOC2* (Nie and Sage, 2009), and Tribbles homolog 2 (*TRIB2*) (Naiki et al., 2007). The above findings indicate that, compared with ScASCs, donor-matched IPFSCs exhibit less potential to differentiate toward adipose tissue.

Our study did not find a significant difference in expression levels of osteogenic markers between ScASCs and donor-matched IPFSCs after induction. It has long been speculated that IPFSCs have a higher chondrogenic potential than other fat depots in the body (Sun et al., 2018), which might be due to the IPFP's anatomic site that is closer to synovium and cartilage; it is regarded as a special form of fibro-adipose tissue (Macchi et al., 2016), or a continuation of synovium. IPFSCs may share some common characteristics with synovium-derived stem cells, a tissue-specific stem cell for chondrogenesis (Jones and Pei, 2012). A study comparing IPFSCs with near knee joint ScASCs from donor-matched osteoarthritis patients found that IPFSCs had a superior chondrogenic potential; ScASCs were superior in osteogenesis while both were similar in adipogenic capacity (Lopa et al., 2014). In this study with donor-matched normal adipose stem cells, we observed clear superiority of IPFSCs for chondrogenesis. However, we obtained divergent results on adipogenic and osteogenic potential. There were two possible explanations for the discrepancy; first, species differences between humans and rabbits can lead to considerable diversity, and secondly, Lopa et al. harvested IPFSCs from aged patients affected by osteoarthritis (Lopa et al., 2014) while we harvested from young healthy rabbits. The adult stem cell profile could be greatly affected by disease and aging (Li and Pei, 2012; Lynch and Pei, 2014).

Taken together, by donor-matched comparison and high throughput assay of transcriptome and proteomics, this study investigated the variance of depot-specific adult stem cells from adipose tissues. The findings might shed some light on the hypothesis that adipose stem cells have a depot-dependent lineage preference. Here, we have profiled RNA and protein levels to identify unique transcriptional programs, signaling components, and matrix environments that reveal novel insights into the higher chondrogenic potential of IPFSCs.

DATA AVAILABILITY STATEMENT

The RNA-Seq datasets generated for this study can be found in the GEO, under the accession number GSE142626, https://www.ncbi.nlm.nih.gov/geo/query/acc.cgi?acc=GSE142626. The data that support the findings of this study are available from the corresponding author upon reasonable request.

ETHICS STATEMENT

The animal study was reviewed and approved by IACUC of West Virginia University, protocol number 1608003840.

AUTHOR CONTRIBUTIONS

TW contributed to the conception and design, collection and/assembly of data, data analysis and interpretation, manuscript writing, and final approval of the manuscript. RH and MD contributed to the collection and/assembly of data, data analysis and interpretation, manuscript writing, and final approval of the manuscript. AI, GH, LZ, and KH contributed to the data analysis and interpretation, manuscript writing, and final approval of the manuscript. MP contributed to the conception and design, financial support, data analysis and interpretation, manuscript writing, and final approval of the manuscript.

FUNDING

This work was supported by Research Grants from the Musculoskeletal Transplant Foundation (MTF) and the National Institutes of Health (1R01AR067747-01A1) to MP. We also would like to acknowledge the WVU Flow Cytometry and Single Cell Core Facility and the grants that support the facility, TME CoBRE grant P20GM131322 and the WV CTSI grant GM104942. The work was also partially supported by the National Institute of General Medical Sciences Grant 5U54GM104942-04 to G.H. and P20 GM103434 to AI.

ACKNOWLEDGMENTS

We thank Suzanne Danley for editing the manuscript.

REFERENCES

Alegre-Aguarón, E., Desportes, P., García-Álvarez, F., Castiella, T., Larrad, L., and Martínez-Lorenzo, M. J. (2012). Differences in surface marker expression and chondrogenic potential among various tissue-derived mesenchymal cells from elderly patients with osteoarthritis. *Cells Tissues Organs* 196, 231–240. doi: 10.1159/000334400

Aubert, J., Dessolin, S., Belmonte, N., Li, M., McKenzie, F. R., Staccini, L., et al. (1999). Leukemia inhibitory factor and its receptor promote adipocyte differentiation via the mitogen-activated protein kinase cascade. *J. Biol. Chem.* 274, 24965–24972. doi: 10.1074/jbc.274.35.24965

Bahamonde, M. E., and Lyons, K. M. (2001). BMP3: to be or not to be a BMP. *J. Bone Joint Surg. Am.* 83A(Pt 1), S56–S62.

Barrett, A. S., Wither, M. J., Hill, R. C., Dzieciatkowska, M., D'Alessandro, A., Reisz, J. A., et al. (2017). Hydroxylamine chemical digestion for insoluble extracellular matrix characterization. *J. Proteome Res.* 16, 4177–4184. doi: 10.1021/acs.jproteome.7b00527

Barry, F., Boynton, R. E., Liu, B., and Murphy, J. M. (2001). Chondrogenic differentiation of mesenchymal stem cells from bone marrow: differentiation-dependent gene expression of matrix components. *Exp. Cell Res.* 268, 189–200. doi: 10.1006/excr.2001.5278

Belotti, D., Capelli, C., Resovi, A., Introna, M., and Taraboletti, G. (2016). Thrombospondin-1 promotes mesenchymal stromal cell functions via TGFβ and in cooperation with PDGF. *Matrix Biol.* 55, 106–116. doi: 10.1016/j.matbio.2016.03.003

Boulet, A. M., and Capecchi, M. R. (2004). Multiple roles of Hoxa11 and Hoxd11 in the formation of the mammalian forelimb zeugopod. *Development* 131, 299–309. doi: 10.1242/dev.00936

Brown, C., McKee, C., Bakshi, S., Walker, K., Hakman, E., Halassy, S., et al. (2019). Mesenchymal stem cells: cell therapy and regeneration potential. *J. Tissue Eng. Regen. Med.* 13, 1738–1755. doi: 10.1002/term.2914

Challa, T. D., Straub, L. G., Balaz, M., Kiehlmann, E., Donze, O., Rudofsky, G., et al. (2015). Regulation of de novo adipocyte differentiation through cross talk between adipocytes and preadipocytes. *Diabetes* 64, 4075–4087. doi: 10.2337/db14-1932

Christodoulides, C., Lagathu, C., Sethi, J. K., and Vidal-Puig, A. (2009). Adipogenesis and WNT signalling. *Trends Endocrinol. Metab.* 20, 16–24. doi: 10.1016/j.tem.2008.09.002

Chu, D. T., Nguyen Thi Phuong, T., Tien, N. L. B., Tran, D. K., Minh, L. B., Thanh, V. V., et al. (2019). Adipose tissue stem cells for therapy: an update on the progress of isolation, culture, storage, and clinical application. *J. Clin. Med.* 8:E917. doi: 10.3390/jcm8070917

Church, V., Nohno, T., Linker, C., Marcelle, C., and Francis-West, P. (2002). Wnt regulation of chondrocyte differentiation. *J. Cell Sci.* 115(Pt 24), 4809–4818. doi: 10.1242/jcs.00152

Cormier, S. A., Mello, M. A., and Kappen, C. (2003). Normal proliferation and differentiation of Hoxc-8 transgenic chondrocytes *in vitro*. *BMC Dev. Biol.* 3:4. doi: 10.1186/1471-213x-3-4

Crisan, M., Yap, S., Casteilla, L., Chen, C. W., Corselli, M., Park, T. S., et al. (2008). A perivascular origin for mesenchymal stem cells in multiple human organs. *Cell Stem Cell* 3, 301–313. doi: 10.1016/j.stem.2008.07.003

Davidson, R. K., Waters, J. G., Kevorkian, L., Darrah, C., Cooper, A., Donell, S. T., et al. (2006). Expression profiling of metalloproteinases and their inhibitors in synovium and cartilage. *Arthritis Res. Ther.* 8:R124.

Davis, M. R., Arner, E., Duffy, C. R., De Sousa, P. A., Dahlman, I., Arner, P., et al. (2016). Expression of FBN1 during adipogenesis: relevance to the lipodystrophy phenotype in Marfan syndrome and related conditions. *Mol. Genet. Metab.* 119, 174–185. doi: 10.1016/j.ymgme.2016.06.009

Deng, J., Hua, K., Caveney, E. J., Takahashi, N., and Harp, J. B. (2006). Protein inhibitor of activated STAT3 inhibits adipogenic gene expression. *Biochem. Biophys. Res. Commun.* 339, 923–931. doi: 10.1016/j.bbrc.2005.10.217

Ewels, P., Magnusson, M., Lundin, S., and Käller, M. (2016). MultiQC: summarize analysis results for multiple tools and samples in a single report. *Bioinformatics* 32, 3047–3048. doi: 10.1093/bioinformatics/btw354

Fabregat, A., Jupe, S., Matthews, L., Sidiropoulos, K., Gillespie, M., and Garapati, P. (2018). The reactome pathway knowledgebase. *Nucleic Acids Res.* 46, D649–D655. doi: 10.1093/nar/gkx1132

Frisdal, E., Le Lay, S., Hooton, H., Poupel, L., Olivier, M., Alili, R., et al. (2015). Adipocyte ATP-binding cassette G1 promotes triglyceride storage, fat mass growth, and human obesity. *Diabetes* 64, 840–855. doi: 10.2337/db14-0245

Garin-Shkolnik, T., Rudich, A., Hotamisligil, G. S., and Rubinstein, M. (2014). FABP4 attenuates PPARgamma and adipogenesis and is inversely correlated with PPARgamma in adipose tissues. *Diabetes* 63, 9009–9011. doi: 10.2337/db13-0436

Gesta, S., Bezy, O., Mori, M. A., Macotela, Y., Lee, K. Y., and Kahn, C. R. (2011). Mesodermal developmental gene Tbx15 impairs adipocyte differentiation and mitochondrial respiration. *Proc. Natl. Acad. Sci. U.S.A.* 108, 2771–2776. doi: 10.1073/pnas.1019704108

González-Martín, M. C., Mallo, M., and Ros, M. A. (2014). Long bone development requires a threshold of Hox function. *Dev. Biol.* 392, 454–465. doi: 10.1016/j.ydbio.2014.06.004

Graziano, A. C. E., Avola, R., Pannuzzo, G., and Cardile, V. (2018). Aquaporin1 and 3 modification as a result of chondrogenic differentiation of human mesenchymal stem cell. *J. Cell Physiol.* 233, 2279–2291. doi: 10.1002/jcp.26100

Hagmann, S., Frank, S., Gotterbarm, T., Dreher, T., Eckstein, V., and Moradi, B. (2014). Fluorescence activated enrichment of CD146+ cells during expansion of human bone-marrow derived mesenchymal stromal cells augments proliferation and GAG/DNA content in chondrogenic media. *BMC Musculoskelet. Disord.* 15:322. doi: 10.1186/1471-2474-15-322

Haraguchi, R., Kitazawa, R., and Kitazawa, S. (2015). Epigenetic regulation of Tbx18 gene expression during endochondral bone formation. *Cell Tissue Res.* 359, 503–512. doi: 10.1007/s00441-014-2028-0

Harms, M., and Seale, P. (2013). Brown and beige fat: development, function and therapeutic potential. *Nat. Med.* 19, 1252–1263. doi: 10.1038/nm.3361

Henriksson, E., Säll, J., Gormand, A., Wasserstrom, S., Morrice, N. A., Fritzen, A. M., et al. (2015). SIK2 regulates CRTCs, HDAC4 and glucose uptake in adipocytes. *J. Cell Sci.* 128, 472–486. doi: 10.1242/jcs.153932

Hill, R. C., Calle, E. A., Dzieciatkowska, M., Niklason, L. E., and Hansen, K. C. (2015). Quantification of extracellular matrix proteins from a rat lung scaffold to provide a molecular readout for tissue engineering. *Mol. Cell Proteomics* 14, 961–973. doi: 10.1074/mcp.M114.045260

Hishida, T., Naito, K., Osada, S., Nishizuka, M., and Imagawa, M. (2007). peg10, an imprinted gene, plays a crucial role in adipocyte differentiation. *FEBS Lett.* 581, 4272–4278. doi: 10.1016/j.febslet.2007.07.074

Hosooka, T., Noguchi, T., Kotani, K., Nakamura, T., Sakaue, H., Inoue, H., et al. (2008). Dok1 mediates high-fat diet-induced adipocyte hypertrophy and obesity through modulation of PPAR-gamma phosphorylation. *Nat. Med.* 14, 188–193. doi: 10.1038/nm1706

Iftikhar, M., Hurtado, P., Bais, M. V., Wigner, N., Stephens, D. N., Gerstenfeld, L. C., et al. (2011). Lysyl oxidase-like-2 (LOXL2) is a major isoform in chondrocytes and is critically required for differentiation. *J. Biol. Chem.* 286, 909–918. doi: 10.1074/jbc.M110.155622

Ikeda, T., Kamekura, S., Mabuchi, A., Kou, I., Seki, S., Takato, T., et al. (2004). The combination of SOX5, SOX6, and SOX9 (the SOX trio) provides signals sufficient for induction of permanent cartilage. *Arthritis Rheum.* 50, 3561–3573. doi: 10.1002/art.20611

Imamura, Y., Scott, I. C., and Greenspan, D. S. (2000). The pro-alpha3(V) collagen chain. Complete primary structure, expression domains in adult and developing tissues, and comparison to the structures and expression domains of the other types V and XI procollagen chains. *J. Biol. Chem.* 275, 8749–8759. doi: 10.1074/jbc.275.12.8749

Inada, M., Wang, Y., Byrne, M. H., Rahman, M. U., Miyaura, C., López-Otín, C., et al. (2004). Critical roles for collagenase-3 (Mmp13) in development of growth plate cartilage and in endochondral ossification. *Proc. Natl. Acad. Sci. U.S.A.* 101, 17192–17197. doi: 10.1073/pnas.0407788101

Jenniskens, Y. M., Koevoet, W., de Bart, A. C., Weinans, H., Jahr, H., Verhaar, J. A., et al. (2006). Biochemical and functional modulation of the cartilage collagen network by IGF1. TGFbeta2 and FGF2. *Osteoarthritis Cartilage* 14, 1136–1146. doi: 10.1016/j.joca.2006.04.002

Jones, B., and Pei, M. (2012). Synovium-derived stem cells: a tissue-specific stem cell for cartilage tissue engineering and regeneration. *Tissue Eng. Part B Rev.* 18, 301–311. doi: 10.1089/ten.teb.2012.0002

Jung, J. C., and Tsonis, P. A. (1998). Role of 5' HoxD genes in chondrogenesis *in vitro*. *Int. J. Dev. Biol.* 42, 609–615.

Kan, A., Ikeda, T., Fukai, A., Nakagawa, T., Nakamura, K., Chung, U. I., et al. (2013). SOX11 contributes to the regulation of GDF5 in joint maintenance. *BMC Dev. Biol.* 13:4. doi: 10.1186/1471-213X-13-4

Kawai, M., and Rosen, C. J. (2010). PPARgamma: a circadian transcription factor in adipogenesis and osteogenesis. *Nat. Rev. Endocrinol.* 6, 629–636. doi: 10.1038/nrendo.2010.155

Knudson, W., and Loeser, R. F. (2002). CD44 and integrin matrix receptors participate in cartilage homeostasis. *Cell Mol. Life Sci.* 59, 36–44. doi: 10.1007/s00018-002-8403-0

Levi, B., James, A. W., Glotzbach, J. P., Wan, D. C., Commons, G. W., and Longaker, M. T. (2010). Depot-specific variation in the osteogenic and adipogenic potential of human adipose-derived stromal cells. *Plast. Reconstr. Surg.* 126, 822–834. doi: 10.1097/PRS.0b013e3181e5f892

Li, J., and Pei, M. (2012). Cell senescence: a challenge in cartilage engineering and regeneration. *Tissue Eng. Part B Rev.* 18, 270–287. doi: 10.1089/ten.TEB.2011.0583

Li, J., and Pei, M. (2018). A protocol to prepare decellularized stem cell matrix for rejuvenation of cell expansion and cartilage regeneration. *Methods Mol. Biol.* 1577, 147–154. doi: 10.1007/7651_2017_27

Liao, Y., Smyth, G. K., and Shi, W. (2013). The Subread aligner: fast, accurate and scalable read mapping by seed-and-vote. *Nucleic Acids Res.* 41:e108. doi: 10.1093/nar/gkt214

Liao, Y., Smyth, G. K., and Shi, W. (2019). The R package Rsubread is easier, faster, cheaper and better for alignment and quantification of RNA sequencing reads. *Nucleic Acids Res.* 47:e47. doi: 10.1093/nar/gkz114

Lincoln, J., Florer, J. B., Deutsch, G. H., Wenstrup, R. J., and Yutzey, K. E. (2006). ColVa1 and ColXIa1 are required for myocardial morphogenesis and heart valve development. *Dev. Dyn.* 235, 3295–3305. doi: 10.1002/dvdy.20980

Liu, R., Li, N., Lin, Y., Wang, M., Peng, Y., Lewi, K., et al. (2016). Glucagon like peptide-1 promotes adipocyte differentiation via the Wnt4 mediated sequestering of beta-catenin. *PLoS One* 11:e0160212. doi: 10.1371/journal.pone.0160212

Lopa, S., Colombini, A., Stanco, D., de Girolamo, L., Sansone, V., and Moretti, M. (2014). Donor-matched mesenchymal stem cells from knee infrapatellar and subcutaneous adipose tissue of osteoarthritic donors display differential chondrogenic and osteogenic commitment. *Eur. Cell Mater.* 27, 298–311. doi: 10.22203/ecm.v027a21

Lynch, K., and Pei, M. (2014). Age associated communication between cells and matrix: a potential impact on stem cell-based tissue regeneration strategies. *Organogenesis* 10, 289–298. doi: 10.4161/15476278.2014.970089

Macchi, V., Porzionato, A., Sarasin, G., Petrelli, L., Guidolin, D., Rossato, M., et al. (2016). The infrapatellar adipose body: a histotopographic study. *Cells Tissues Organs* 201, 220–231. doi: 10.1159/000442876

Makris, E. A., Hu, J. C., and Athanasiou, K. A. (2013). Hypoxia-induced collagen crosslinking as a mechanism for enhancing mechanical properties of engineered articular cartilage. *Osteoarthritis Cartilage* 21, 634–641. doi: 10.1016/j.joca.2013.01.007

Malfait, F., Coucke, P., Symoens, S., Loeys, B., Nuytinck, L., and De Paepe, A. (2005). The molecular basis of classic Ehlers-Danlos syndrome: a comprehensive study of biochemical and molecular findings in 48 unrelated patients. *Hum. Mutat.* 25, 28–37. doi: 10.1002/humu.20107

McCarthy, D. J., Chen, Y., and Smyth, G. K. (2012). Differential expression analysis of multifactor RNA-Seq experiments with respect to biological variation. *Nucleic Acids Res.* 40, 4288–4297. doi: 10.1093/nar/gks042

Melrose, J., Hayes, A. J., Whitelock, J. M., and Little, C. B. (2008). Perlecan, the "jack of all trades" proteoglycan of cartilaginous weight-bearing connective tissues. *Bioessays* 20, 457–469. doi: 10.1002/bies.20748

Mueller, M. B., and Tuan, R. S. (2008). Functional characterization of hypertrophy in chondrogenesis of human mesenchymal stem cells. *Arthritis Rheum.* 58, 1377–1388. doi: 10.1002/art.23370

Naiki, T., Saijou, E., Miyaoka, Y., Sekine, K., and Miyajima, A. (2007). TRB2, a mouse Tribbles ortholog, suppresses adipocyte differentiation by inhibiting AKT and C/EBPbeta. *J. Biol. Chem.* 282, 24075–24082. doi: 10.1074/jbc.m701409200

Nie, J., and Sage, E. H. (2009). SPARC inhibits adipogenesis by its enhancement of beta-catenin signaling. *J. Biol. Chem.* 284, 1279–1290. doi: 10.1074/jbc.M808285200

Peröbner, I., Karow, M., Jochum, M., and Neth, P. (2012). LRP6 mediates Wnt/β-catenin signaling and regulates adipogenic differentiation in human mesenchymal stem cells. *Int. J. Biochem. Cell Biol.* 44, 1970–1982. doi: 10.1016/j.biocel.2012.07.025

Pizzute, T., Lynch, K., and Pei, M. (2015). Impact of tissue-specific stem cells on lineage specific differentiation: a focus on musculoskeletal system. *Stem Cell Rev. Rep.* 11, 119–132. doi: 10.1007/s12015-014-9546-8

Pizzute, T., Zhang, Y., He, F., and Pei, M. (2016). Ascorbate-dependent impact on cell-derived matrix in modulation of stiffness and rejuvenation of infrapatellar fat derived stem cells toward chondrogenesis. *Biomed. Mater.* 11:045009. doi: 10.1088/1748-6041/11/4/045009

Reddi, A. H. (2001). Bone morphogenetic proteins: from basic science to clinical applications. *J. Bone Joint Surg. Am.* 83A Suppl 1(Pt 1), S1–S6.

Seifert, A., Werheid, D. F., Knapp, S. M., and Tobiasch, E. (2015). Role of Hox genes in stem cell differentiation. *World J. Stem Cells* 7, 583–595. doi: 10.4252/wjsc.v7.i3.583

Shintani, N., Siebenrock, K. A., and Hunziker, E. B. (2013). TGF-ß1 enhances the BMP-2-induced chondrogenesis of bovine synovial explants and arrests downstream differentiation at an early stage of hypertrophy. *PLoS One* 8:e53086. doi: 10.1371/journal.pone.0053086

Singh, M. K., Petry, M., Haenig, B., Lescher, B., Leitges, M., and Kispert, A. (2005). The T-box transcription factor Tbx15 is required for skeletal development. *Mech. Dev.* 122, 131–144. doi: 10.1016/j.mod.2004.10.011

Steinert, A., Weber, M., Dimmler, A., Julius, C., Schütze, N., Nöth, U., et al. (2003). Chondrogenic differentiation of mesenchymal progenitor cells encapsulated in ultrahigh-viscosity alginate. *J. Orthop. Res.* 21, 1090–1097. doi: 10.1016/s0736-0266(03)00100-1

Su, X., Zuo, W., Wu, Z., Chen, J., Wu, N., Ma, P., et al. (2015). CD146 as a new marker for an increased chondroprogenitor cell sub-population in the later stages of osteoarthritis. *J. Orthop. Res.* 33, 84–91. doi: 10.1002/jor.22731

Subramanian, A., and Schilling, T. F. (2015). Tendon development and musculoskeletal assembly: emerging roles for the extracellular matrix. *Development* 142, 4191–4204. doi: 10.1242/dev.114777

Sun, Y., Chen, S., and Pei, M. (2018). Comparative advantages of infrapatellar fat pad: an emerging stem cell source for regenerative medicine. *Rheumatology* 57, 2072–2086. doi: 10.1093/rheumatology/kex487

Sun, Y., Wang, T. L., Toh, W. S., and Pei, M. (2017). The role of laminins in cartilaginous tissues: from development to regeneration. *Eur. Cell Mater.* 34, 40–54. doi: 10.22203/eCM.v034a03

Takeuchi, J. K., Koshiba-Takeuchi, K., Suzuki, T., Kamimura, M., Ogura, K., and Ogura, T. (2003). Tbx5 and Tbx4 trigger limb initiation through activation of the Wnt/Fgf signaling cascade. *Development* 130, 2729–2739. doi: 10.1242/dev.00474

Tanaka, M., and Tickle, C. (2004). Tbx18 and boundary formation in chick somite and wing development. *Dev. Biol.* 268, 470–480. doi: 10.1016/j.ydbio.2003.12.036

Tardif, G., Reboul, P., Pelletier, J. P., and Martel-Pelletier, J. (2004). Ten years in the life of an enzyme: the story of the human MMP-13 (collagenase-3). *Mod. Rheumatol.* 14, 197–204. doi: 10.3109/s10165-004-0292-7

Tuli, R., Tuli, S., Nandi, S., Huang, X., Manner, P. A., Hozack, W. J., et al. (2003). Transforming growth factor-beta-mediated chondrogenesis of human mesenchymal progenitor cells involves N-cadherin and mitogen-activated protein kinase and Wnt signaling cross-talk. *J. Biol. Chem.* 278, 41227–41236. doi: 10.1074/jbc.m305312200

Ugarte, F., Ryser, M., Thieme, S., Fierro, F. A., Navratiel, K., Bornhäuser, M., et al. (2009). Notch signaling enhances osteogenic differentiation while inhibiting adipogenesis in primary human bone marrow stromal cells. *Exp. Hematol.* 37, 867–875. doi: 10.1016/j.exphem.2009.03.007

van den Berg, W. B. (2011). Osteoarthritis year 2010 in review: pathomechanisms. *Osteoarthritis Cartilage* 19, 338–341. doi: 10.1016/j.joca.2011.01.022

Wang, R. N., Green, J., Wang, Z., Deng, Y., Qiao, M., Peabody, M., et al. (2014). Bone Morphogenetic Protein (BMP) signaling in development and human diseases. *Genes Dis.* 1, 87–105.

Wight, T. N., Kinsella, M. G., Evanko, S. P., Potter-Perigo, S., and Merrilees, M. J. (2014). Versican and the regulation of cell phenotype in disease. *Biochim. Biophys. Acta* 1840, 2441–2451. doi: 10.1016/j.bbagen.2013.12.028

Williamson, A. K., Chen, A. C., Masuda, K., Thonar, E. J., and Sah, R. L. (2003). Tensile mechanical properties of bovine articular cartilage: variations with growth and relationships to collagen network components. *J. Orthop. Res.* 21, 872–880. doi: 10.1016/s0736-0266(03)00030-5

Wiśniewski, J. R., Zougman, A., Nagaraj, N., and Mann, M. (2009). Universal sample preparation method for proteome analysis. *Nat. Methods* 6, 359–362. doi: 10.1038/nmeth.1322

Wu, J., Boström, P., Sparks, L. M., Ye, L., Choi, J. H., Giang, A. H., et al. (2012). Beige adipocytes are a distinct type of thermogenic fat cell in mouse and human. *Cell* 150, 366–376. doi: 10.1016/j.cell.2012.05.016

Wu, Q., Tang, S. G., and Yuan, Z. M. (2015). Gremlin 2 inhibits adipocyte differentiation through activation of Wnt/β-catenin signaling. *Mol. Med. Rep.* 12, 5891–5896. doi: 10.3892/mmr.2015.4117

Xia, J., and Wishart, D. S. (2016). Using MetaboAnalyst 3.0 for comprehensive metabolomics data analysis. *Curr. Protoc. Bioinformatics* 55, 14.10.1-14.10.91,

Yang, T. T., Suk, H. Y., Yang, X., Olabisi, O., Yu, R. Y., Durand, J., et al. (2006). Role of transcription factor NFAT in glucose and insulin homeostasis. *Mol. Cell Biol.* 26, 7372–7387. doi: 10.1128/mcb.00580-06

Yueh, Y. G., Gardner, D. P., and Kappen, C. (1998). Evidence for regulation of cartilage differentiation by the homeobox gene Hoxc-8. *Proc. Natl. Acad. Sci. U.S.A.* 95, 9956–9961. doi: 10.1073/pnas.95.17.9956

Zerbino, D. R., Achuthan, P., Akanni, W., Amode, M. R., Barrell, D., Bhai, J., et al. (2018). Ensembl 2018. *Nucleic Acids Res.* 46, D754–D761. doi: 10.1093/nar/gkx1098

Zhou, Y., Robciuc, M. R., Wabitsch, M., Juuti, A., Leivonen, M., Ehnholm, C., et al. (2012). OSBP-related proteins (ORPs) in human adipose depots and cultured adipocytes: evidence for impacts on the adipocyte phenotype. *PLoS One* 7:e45352. doi: 10.1371/journal.pone.0045352 doi: 10.1371/journal.pone.0045352

Conflict of Interest: The authors declare that the research was conducted in the absence of any commercial or financial relationships that could be construed as a potential conflict of interest.

Copyright © 2020 Wang, Hill, Dzieciatkowska, Zhu, Infante, Hu, Hansen and Pei. This is an open-access article distributed under the terms of the Creative Commons Attribution License (CC BY). The use, distribution or reproduction in other forums is permitted, provided the original author(s) and the copyright owner(s) are credited and that the original publication in this journal is cited, in accordance with accepted academic practice. No use, distribution or reproduction is permitted which does not comply with these terms.

frontiers in Cell and Developmental Biology

ORIGINAL RESEARCH
published: 07 May 2020
doi: 10.3389/fcell.2020.00327

Development of a Novel Hanging Drop Platform for Engineering Controllable 3D Microenvironments

Chin-Yi Cho[1†], Tzu-Hsiang Chiang[1†], Li-Hung Hsieh[2], Wen-Yu Yang[2,3], Hsiang-Hao Hsu[4,5], Chih-Kuang Yeh[3], Chieh-Cheng Huang[2] and Jen-Huang Huang[1*]*

[1] Department of Chemical Engineering, National Tsing Hua University, Hsinchu, Taiwan, [2] Institute of Biomedical Engineering, National Tsing Hua University, Hsinchu, Taiwan, [3] Department of Biomedical Engineering and Environmental Sciences, National Tsing Hua University, Hsinchu, Taiwan, [4] Department of Nephrology, Kidney Research Center, Linkou Chang Gung Memorial Hospital, Taoyuan, Taiwan, [5] College of Medicine, School of Medicine, Chang Gung University, Taoyuan, Taiwan

OPEN ACCESS

Edited by:
Pavel Makarevich,
Lomonosov Moscow State University, Russia

Reviewed by:
Nastasia V. Kosheleva,
Lomonosov Moscow State University, Russia
Huaping Wang,
Beijing Institute of Technology, China

***Correspondence:**
Chieh-Cheng Huang
chiehcheng@mx.nthu.edu.tw
Jen-Huang Huang
jenhuang@mx.nthu.edu.tw

[†] These authors have contributed equally to this work

Specialty section:
This article was submitted to Stem Cell Research, a section of the journal Frontiers in Cell and Developmental Biology

Received: 26 February 2020
Accepted: 16 April 2020
Published: 07 May 2020

Citation:
Cho C-Y, Chiang T-H, Hsieh L-H, Yang W-Y, Hsu H-H, Yeh C-K, Huang C-C and Huang J-H (2020) Development of a Novel Hanging Drop Platform for Engineering Controllable 3D Microenvironments. Front. Cell Dev. Biol. 8:327. doi: 10.3389/fcell.2020.00327

Conventional biomedical research is mostly performed by utilizing a two-dimensional monolayer culture, which fails to recapitulate the three-dimensional (3D) organization and microenvironment of native tissues. To overcome this limitation, several methods are developed to fabricate microtissues with the desired 3D microenvironment. However, they tend to be time-consuming, labor-intensive, or costly, thus hindering the application of 3D microtissues as models in a wide variety of research fields. In the present study, we have developed a pressure-assisted network for droplet accumulation (PANDA) system, an easy-to-use chip that comprises a multichannel fluidic system and a hanging drop cell culture module for uniform 3D microtissue formation. This system can control the desired artificial niches for modulating the fate of the stem cells to form the different sizes of microtissue by adjusting the seeding density. Furthermore, a large number of highly consistent 3D glomerulus-like heterogeneous microtissues that are composed of kidney glomerular podocytes and mesenchymal stem cells have been formed successfully. These data suggest that the developed PANDA system can be employed as a rapid and economical platform to fabricate microtissues with tunable 3D microenvironment and cellular heterogeneity, thus can be employed as tissue-mimicking models in various biomedical research.

Keywords: hanging drop, array, microtissue, glomerulus, podocyte

INTRODUCTION

Native tissues are comprised of multiple micro-scaled subunits that are characterized by distinct cellular heterogeneity, well-defined three-dimensional (3D) architectures, and tissue-specific niches (Liu et al., 2014; Todhunter et al., 2015; Kuo et al., 2017). Until now, the majority of our knowledge of cell behaviors and how they are modulated are learned through observations *in vitro* (Zakrzewski et al., 2019). However, current biomedical research is mostly carried out using two-dimensional

(2D) cultured cells, which fail to faithfully recreate the complexity of the 3D microenvironment in living tissues (Ranga et al., 2014). As a result, it is not surprising that the observed cellular behavior and responses in such settings cannot appropriately reflect those *in vivo*. This dramatically hinders the progress in several research domains, including cell biology, drug discovery/development, disease modeling, and regenerative medicine (Fatehullah et al., 2016).

In recent years, techniques to engineer the 3D microenvironment *in vitro* have attracted considerable attention. This is because the cells cultivated in 3D configuration are exposed to the milieu that is more similar to *in vivo* tissues compared to that grown in conventional 2D configuration (Oliveira et al., 2018). More specifically, 3D-cultured cells exhibit several *in vivo*-like characteristics in terms of the morphology, behavior, metabolism, cellular heterogeneity, and cell-to-cell or cell-to-matrix interactions, which are all diminished in the 2D-cultivated cells (Kuo et al., 2017; Oliveira et al., 2018; Kim et al., 2019). Therefore, cells cultured in 3D configuration and engineered to micro-scaled tissues represent a better *in vitro* model that recapitulates the physiological conditions of native tissues and has emerged as powerful tools for biomedical applications.

Currently, several approaches (hanging drop, centrifugal pellet, spinner flask, patterned surface, and magnetic or acoustic levitation of cells) and materials (non-adhesive substrates, superhydrophobic/superhydrophilic surfaces, and porous 3D scaffolds) have been developed as culture platforms for 3D microtissue fabrication (Lin and Chang, 2008; Achilli et al., 2012; Cui et al., 2017; Yu et al., 2020). Despite these being proven to be useful for generating 3D microtissues, each of these methods may have some limitations that hinder their widespread application in various biomedical domains. The conventional hanging drop technique is labor-intensive and requires a second manipulation for transferring the formed microtissue into a different culture vessel for the subsequent assays (Fang and Eglen, 2017). Additionally, the formed microtissues may exhibit various sizes and morphologies (Ouyang et al., 2015). However, even though microtissues with a relatively uniform geometry can be obtained by using external forces to aggregate cells, the subtle cellular responses toward the applied physical forces can affect the biochemical and physiological functions of the cells, thus altering their behavior or even viability (Skiles et al., 2013). Using novel materials as substrates for 3D microtissue cultivation can be highly efficient but extremely expensive, thus not being cost-effective for mass production (Liao et al., 2019). Therefore, developing a 3D microtissue culture platform that has a high level of reproducibility and consistency along with it being economical and easy to operate, would be highly favored to advance the laboratory proof-of-concepts to develop clinically usable tools.

To address the above-mentioned drawbacks of the existing approaches, we present a pressure-assisted network for droplet accumulation (PANDA) system to form a consistent and uniform hanging drop array for fast and massive production of native-like 3D microtissues, enabling the easy establishment of controllable and adjustable 3D microenvironments *in vitro* for further applications. As a proof of concept, the PANDA system was employed for the fabrication and study of the kidney glomerular microtissues that were composed of podocytes and mesenchymal stem cells (MSCs). The podocytes were post-mitotic and specialized glomerular epithelial cells that contribute to renal filtration barrier (May et al., 2014; Hale et al., 2018), while the MSCs could differentiate into mesangial cells that are crucial pericytes in glomeruli (Imasawa et al., 2001; Wong et al., 2014). Drug-induced nephrotoxicity, which leads to podocyte loss, glomerular scarring, and thus, acute or chronic kidney injury, remains a challenging issue in clinical settings and preclinical drug development (Kandasamy et al., 2015; Musah et al., 2017). Using the developed PANDA chip, a large number of kidney microtissues with a uniform composition, which is an essential criterion for the reproducibility of high-throughput screening, could be generated easily. Therefore, the PANDA chip developed in this study holds significant potential to serve as a rapid and economical platform for the growth of highly consistent microtissues with precisely controlled and tunable 3D microenvironments for use in cell biology research, drug screening, therapeutic effect prediction, and engineering implantable tissues.

PRINCIPLE

The major goal of this study is to form consistent hanging drops spontaneously by using a cost-effective approach for the generation of 3D microtissues in a controllable manner. To achieve this goal, a mechanism based on the pressure difference between the surrounding environment and the system was applied to spontaneously pull the cell suspension toward the internal chamber to form the hanging drops (**Figure 1A**). The pressure difference was generated by withdrawing the air from the internal air chamber through air permeable tubing. Initially, the pressure inside the air chamber (P) was the same as the atmosphere pressure (P_{atm}). Once the air was withdrawn from the air chamber, the P was less than P_{atm}, which led to the cell suspension located on the well plate overcoming the capillary force and entering the internal chamber through the through-hole. The penetrated cell suspension could spontaneously form a spherical droplet due to the cohesive force and adhered to the wall because of the surface tension. The pulling force combined with the pressure-driven force and gravity force was required to be less than the adhesive force to prevent the dripping of the droplet. On the contrary, an insufficient pulling force would not be able to overcome the capillary force to form the hanging drop which served as a microenvironment for cell growth. Therefore, a high adhesive force generated from the holding layer was essential to balance the pulling force and to maintain the hanging status of the droplet. This could be achieved by manipulating the hydrophilic properties between the well plate and the holding layer. In general, highly hydrophilic materials can hold the droplet without dripping but may lead to more liquid residue remaining on the wells or flatten the edge of the hanging drop. Once the droplet was formed, the withdrawal of air was stopped, and the outlet of the system was closed to finish

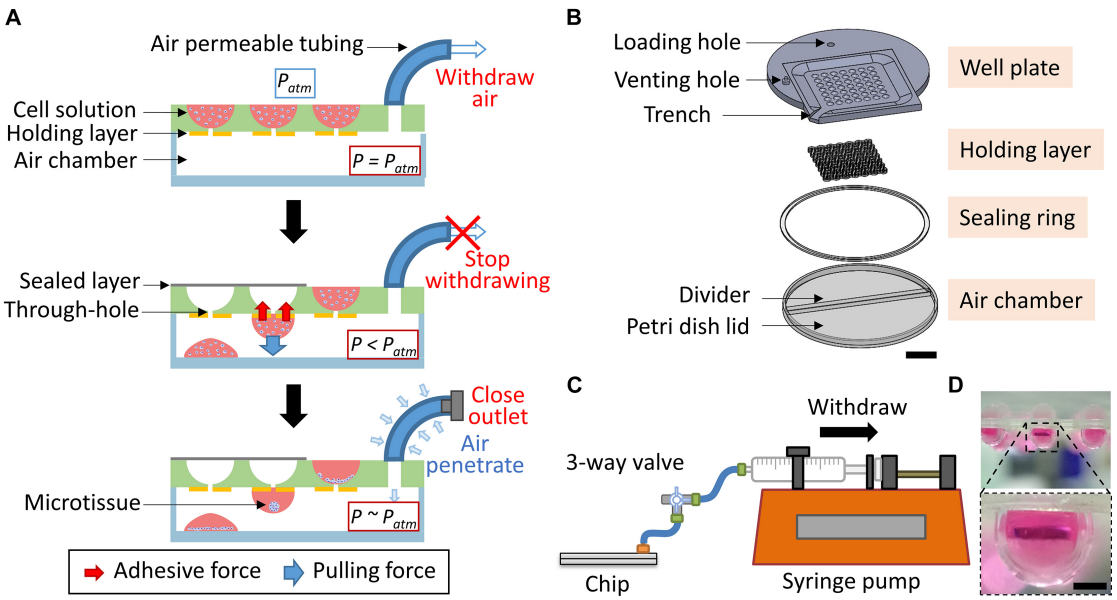


FIGURE 1 | The PANDA system. **(A)** Schematic of the PANDA principle. The internal air of the system is withdrawn from the air chamber, leading to the pressure of the air chamber (*P*) being less than the atmosphere pressure (P_{atm}). The pressure difference allows the cell solution located on the well plate to enter into the air chamber. The cohesive force causes the cell solution to form a droplet while the adhesive force from the holding layer prevents the droplet from dripping that eventually forms the hanging drop. The PANDA system can be placed in the incubator and each hanging drop can allow the cells to spontaneously form the spheroid (or microtissue). The air can gradually penetrate through a gas permeable tubing to balance the internal pressure and the surrounding pressure. **(B)** The exploded view of the PANDA system. Scale bar represents 2 cm. **(C)** The schematic of the PANDA system connected to a syringe pump. **(D)** The hanging drops formed after using the PANDA system. Scale bar represents 1 mm.

the forming procedure. The PANDA system could be placed on the incubator, therefore, the *P* could gradually equal P_{atm} due to more air entering into the internal chamber through a gas permeable tubing connected to the PANDA system. This ensured that the whole system provided a normal culturing condition for the growth of the cells. Compared to the conventional hanging drop method, the PANDA system contributed to the development of an efficient method to culture the cells using the hanging drop method.

MATERIALS AND METHODS

Design and Fabrication of the PANDA System

To balance the pulling force and the adhesive force, an air-sealed chamber, and a material with a slightly high hydrophilic surface were two critical aspects of the PANDA system. The PANDA system consisted of four major parts: the well plate, holding layer, sealing ring, and air chamber (**Figure 1B**). Each part was designed using a 3D CAD design software (SolidWorks 2019, Dassault Systèmes, United States) and followed the same design logic similar to the previous study (Lin et al., 2019). The shell-shaped well plate contained a circular region with a diameter of 85 mm and a square with each side 70 mm. The thickness of the well plate was set to 4.5 mm and the diameter of each well was 4.6 mm, thus allowing to hold more medium for the long-term growth of cell culture. For the region generating the hanging drop, the well plate was scooped in a 45.4 mm square area with 1.5 mm depth to gather extra liquid when pouring the medium on the plate. In the square groove, 49 wells with a diameter of 4.6 mm were designed to accommodate cell suspension. At the bottom of the well, a penetrating channel of 1.2 mm diameter was designed to keep the cell suspension in the well but allow it to penetrate when the pressure difference was generated. Furthermore, a trench was designed to connect to the square-shaped groove at the edge of the plate to discharge the excess cell suspension. The well plate was constructed by engraving a 4.5 mm thick polycarbonate (PC) sheet (Formosa Idemitsu Petrochemical Corporation, Taiwan) using a CNC milling machine (Roland MDX-40A Benchtop CNC Mill, United States). A venting hole of 4 mm diameter was engraved on the top of the well plate so that the tubing adaptor (BDMR210-9, Nordson MEDICAL, United States) could be installed and fixed with epoxy glue to facilitate the assembling of the chip.

The holding layer was designed to have a connecting ring structure corresponding to the position of the wells on the well pate. Once the holding layer was assembled with the well plate, only the hydrophilic rings could hold the droplets while other regions prevented the spread of the formed droplets (Hsiao et al., 2012). To investigate the adhesive force of the holding layer, we focused on the geometry and hydrophilicity of the ring. We chose polyethylene terephthalate (PET, Formosa Idemitsu Petrochemical Corporation, Taiwan) as the material for the holding layer because it had higher hydrophilicity (contact angle = 72.5°) than PC (contact angle = 82°). Therefore, when

the droplets formed under the chip, the hydrophilic property of PET stabilized the droplets, preventing them from dripping. The holding layer was generated by alternatively assembling the upper part (named as U) and the lower part (named as L) to study the influence of the microstructure. The ring structure of the upper part had 4.6 mm outer diameter and 1.2 mm inner diameter while the ring structure of the lower part had 4.6 mm outer diameter and 2.6 mm inner diameter (**Supplementary Figure S1**). Both parts were designed using the Solid Edge 2D software package (ST9, Siemens, United States) and fabricated using a layer-by-layer stacking technique on the PET sheets (Ni et al., 2019). The PET sheets were pre-laminated with double-sided adhesive tape (9122, 3M Company, United States) and machined using a laser cutting machine (PLS6.75, Universal Laser System, United States) so that the holding layer could be assembled with the well plate to generate specialized geometries.

A 90 mm diameter petri dish lid (66-1501, Biologix, China) was used as the air chamber of the PANDA system. A customized divider (76 mm length) was cut from the PC sheet by using the CNC milling machine and inserted into the petri dish cap to create the air chamber and phosphate-buffered saline (PBS) loading reservoir. The sealing ring was cut from the 0.1 mm thick PET sheet pre-laminated with the double-sided adhesive tape by using the laser cutter to obtain the ring structure with 88 mm inner diameter and 96 mm outer diameter (**Supplementary Figure S2A**). The PANDA chip was prepared by placing the well plate on the air chamber and sealing with the sealing ring to avoid leakage during the air withdrawal process. The sealing sheet of size 46 × 46 mm for covering the well plate, was cut from the PET sheet (0.1 mm thickness) pre-laminated with the adhesive tape using the laser cutter (**Supplementary Figure S2B**). All the devices and connecting components used for the preparation of the cell culture were sterilized following the standard autoclave procedure.

Setup of the PANDA System

As shown in **Figure 1C**, the PANDA system was set up by connecting the well plate and a syringe (10 mL, Becton Dickinson, United States) installed in a syringe pump (NE-4000, New Era Pump Systems, United States) through a silicone tubing (1/16 inch inner diameter, EW-95802-02, Cole-Parmer, United States) to generate a constant and steady withdrawal of air from the PANDA chip. The connection between the silicone tubing and syringe was made using a female Luer fitting (FTLL210-9, Nordson MEDICAL, United States). A Luer 3-way valve (Guangzhou JU Plastic Fitting Technology, China) was installed between the PANDA chip and syringe pump, allowing the disconnection of the PANDA chip from the syringe pump after the formation of the hanging drops.

Analysis of Internal Pressure

The internal pressure of the chamber was analyzed by using a pressure sensor system. Briefly, another 3-way valve (serving as a venting valve) was connected after the original 3-way valve (serving as a connection valve) that had been connected to the PANDA chip (**Supplementary Figure S3**). A differential pressure transmitter (984, Beck Sensors, Germany) was connected to the venting valve to monitor the internal pressure within the system in real-time. All the connections were made using Luer lock adaptors and silicone tubing. The real-time data of the internal pressure was acquired by a portable data acquisition module (USB-4718, Advantech, Taiwan), which could transfer and record the data in the computer for analysis later.

Measurement of Success Rate

The successful and consistent formation of the hanging drops is critical for establishing a stable microenvironment to culture the cells. Failures in the formation of hanging drops such as dripping, flatting, and even non-response may influence the other drops or reduce the testing samples for further experiments. To verify the various assembling and operating conditions of the PANDA system, the success rate of hanging drop formation was estimated by using Equation 1 as follows.

$$\text{Success rate (\%)} = \frac{\text{Number of drops attached on the plate}}{\text{Number of the wells}} \times 100 \quad (1)$$

Cell Culture

Conditionally immortalized mouse podocytes, derived by Endlich's group, which were transfected with a temperature-sensitive T antigen and green fluorescent protein (GFP), were used in this study (Schiwek et al., 2004; Chen et al., 2018). The podocytes were maintained at 33 °C in RPMI 1640 medium (Thermo Fisher Scientific, United States) and supplemented with 10% fetal bovine serum (FBS; GE Healthcare Bio-Sciences, United States), 10 U/mL mouse interferon (IFN)-γ (PeproTech, United States) that drove the T-antigen application (Chen et al., 2018). To deactivate the T antigen and promote podocyte differentiation, cells were incubated at 37°C, and their culture medium was changed to that without IFN-γ (Chen et al., 2018).

Human umbilical cord blood-derived MSCs that were transfected with red fluorescence protein (RFP) were obtained from the Bioresource Collection and Research Center, Food Industry Research and Development Institute, Hsinchu, Taiwan (Hung et al., 2010). The MSCs were cultured in α-minimum essential medium (Thermo Fisher Scientific, United States) supplemented with 20% FBS and 4 ng/mL basic fibroblast growth factor (PeproTech, United States).

Fabrication and Characterization of the 3D Microtissues Using PANDA System

For the formation of 3D kidney microtissues, the confluent podocytes and MSCs were harvested from culture dishes using 0.05% trypsin and mixed with 1:1 ratio of cell density. The cell mixture was then transferred into a PANDA chip followed by the hanging drop formation procedure to culture the cells. The grown microtissues were observed daily under a fluorescence microscope (Olympus, Japan) to measure the diameter of the 3D microtissues. Alternatively, the 3D microtissues were collected and processed for immunofluorescence staining. Samples were fixed in 4% paraformaldehyde, permeabilized with 0.1% Triton

X-100, and incubated with a blocking buffer for 1 h followed by primary antibody against P-cadherin (1:200 dilution; Abcam, United States) staining at 4°C overnight. Alexa Fluor 633-conjugated secondary antibody (1: 200 dilution; Thermo Fisher Scientific, United States) was used to detect the primary antibody. The nuclei were visualized by counterstaining with 4',6-diamidino-2-phenylindole (DAPI; 1 μg/mL; Thermo Fisher Scientific, United States). The mounted samples were imaged under a laser scanning confocal microscope (LSM 780, Carl Zeiss, Germany). Additionally, a Live/Dead Viability/Cytotoxicity Kit (Thermo Fisher Scientific, United States) was used to evaluate the viability of the cells grown within 3D microtissue according to the manufacturer's instruction. In order to prevent crosstalk of fluorescence, the podocytes and MSCs that were not expressing fluorescence proteins were employed for the live/dead assay.

Statistical Analysis

Data were obtained from three independent experiments and analyzed through one-way ANOVA with Bonferroni correction using GraphPad Prism (Version 8.3, GraphPad Software, United States). The data are expressed as mean ± standard deviation. Results were considered significant when $^{*}P < 0.05$ and $^{****}P < 0.001$.

RESULTS AND DISCUSSION

Manipulation of PANDA System

The hanging drop technique has been widely employed to form microtissues from primary cells or stem cells due to its simplicity and ease of operation without using specialized equipment (Laschke and Menger, 2017; Shri et al., 2017). Furthermore, this approach can achieve the desired uniform size of the microtissues, which is a critical factor to reproduce the experimental results for drug screening compared to other approaches (Mehta et al., 2012). However, the extremely labor-intensive operating procedure limits the development of this technique for high throughput experiments (Amaral et al., 2017). Manually loading the cell suspension on the hanging drop plate has been verified with high size variation of the produced microtissues, although the variation is still relatively low (SD ∼10%). Although this tedious operating procedure that requires careful handling has been overcome by introducing robotic liquid handling equipment (Drewitz et al., 2011; Tung et al., 2011), this complicated and costly instrument is essential to obtain consistent results. Here, we have introduced the PANDA system to produce the hanging drop array spontaneously and consistently using only a commercially available syringe pump. The operating procedure for the PANDA system is straightforward. There is total of eight major steps to form the hanging drops for the growth of microtissues (**Figure 2**). Step 1: Add the cell suspension on the well plate by using a pipette. Similar to other approaches for microtissue formation, the cell concentration that controls the size of the microtissue can be determined at this step. Step 2: Pour the excess cell suspension into a centrifuge tube. The collected cell suspension can be used in the next chip. Step 3: Use a scraper to remove the residue. Notably, this step should be repeated until the level of the solution in the well is uniform and can ensure that each well retains the same amount of cell suspension to obtain the uniform size of the hanging drops. Step 4: Fill the reservoir with PBS through the loading hole to retain moisture inside the air chamber during the cell culture. Step 5: Seal the loading hole to enclose the whole system so that air can only be withdrawn from the venting hole. Step 6: Connect with the syringe pump to initiate the withdrawal of air. The hanging drops are formed individually with time and can be visualized from the top view (**Supplementary Video S1**). When the last hanging drop is formed, stop the syringe pump. Over-withdrawal of air triggers the dripping of the hanging drops. Step 7: Seal the wells using the sealing sheet to prevent the hanging drops from evaporating, so that the air chamber can maintain lower pressure and prevent the backflow of the cell suspension. After switching off the 3-way valve, the PANDA chip can be disconnected and placed in the cell culture incubator until the microtissues are formed. Step 8: After removal from the cell culture, disassemble the chip and collect the hanging drops using a pipette. The hanging drops can be collected individually or collectively for further experiments. The size of the hanging drops from the 49-wells PANDA chip was measured to be 13.75 ± 0.24 μL, demonstrating the uniform formation of hanging drops using the procedure developed in this study.

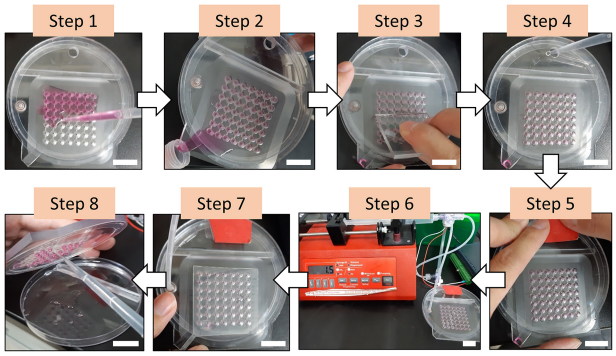


FIGURE 2 | The procedure of forming the hanging drops using the PANDA system. **Step 1**: Add the cell suspension on the well plate. **Step 2**: Pour the excess cell suspension into a centrifuge tube. **Step 3**: Use a scraper to remove the residue. **Step 4**: Fill the reservoir with PBS through the loading hole. **Step 5**: Seal the loading hole. **Step 6**: Connect with the syringe pump to initiate the withdrawal of air and wait until all hanging drops are formed. **Step 7**: Seal the wells using the sealing sheet. The PANDA system is now ready for cell culture. **Step 8**: After cell culture, disassemble the chip and collect the hanging drops using a pipette for further experiments. All scale bar represent 2 cm.

Adhesion Capability of Holding Layer

The formation of the hanging drops is based on the air pressure-driven force to pull the cell suspension entering the through-hole, while the adhesive force from the holding layer holds the hanging drops and prevents dripping. There are two major factors to maintain the high adhesive force of the

holding layer: hydrophilicity and surface geometry. A high hydrophilic surface can be achieved by coating the surface with hydrophilic materials such as polydopamine (Lee et al., 2007; Kang et al., 2012), but the additional coating step and cost limit the use in further applications and for mass production. Most importantly, these materials may interfere with the growth of the cells during cell culture. High hydrophilicity of the holding layer can prevent the hanging drop from dripping but it can also trigger the spreading of the liquid on the surface, leading to failure to form a spherical droplet. The micro-topographical features of the surface have been reported to stabilize the droplet arrays without spreading on the surface and spheroids have been successfully formed inside the hanging drops (Hsiao et al., 2012). To enhance the adhesion capability of the holding layer, we generated five different microstructures using a more hydrophilic material such as PET compared to the material of the well plate (PC). Both the upper and lower parts of the holding layer had a thickness of 0.1 mm and 0.25 mm so that the combinations of the holding structure were $U_{0.25}$, $U_{0.25}/L_{0.1}$, $U_{0.25}/L_{0.25}$, $U_{0.1}/L_{0.1}$, and $U_{0.1}/L_{0.25}$. Based on the results from **Figure 3A**, the holding layer design with $U_{0.25}/L_{0.1}$ had an almost 100% success rate while the other designs had success rates ranging from 78 to 90%. The upper part with 0.25 mm thickness resulted in a high success rate compared to the upper part with 0.1 mm thickness, suggesting that the upper part played a major role in contributing high adhesive force even without the lower part. Therefore, the holding layer with $U_{0.25}/L_{0.1}$ microstructure was chosen in the following experiment.

Influence of Flow Rate

Although providing a constant withdrawal of air is sufficient to accomplish the formation of hanging drops, the flow rate controlled by the syringe pump can determine the total operation time in the whole process. To investigate the influence of the flow rate, the success rates at five different flow rates were measured. When the PANDA system was operated to form the hanging drop array, only the flow rate at 3 mL/min had a success rate of 93% while the other flow rates had success rates up to 100% (**Figure 3B**). This flow rate generated a sudden change of air pressure that led to a high pressure-driven force to pull the liquid. However, it also caused the liquid to have insufficient time to spread on the hydrophilic surface of the holding layer. Therefore, we observed that 2–3 out of 49 wells were not able to attach firmly on the chip. We observed that one well failed to hold the hanging drop at the flow rate equal to 0.6 mL/min. This is because the pressure-driven force was slowly generated in the air chamber, leading to the unstable formation of the hanging drops. Furthermore, we investigated the processing time to completely generate the 49 hanging drop arrays at different flow rates and studied whether the operating process was efficient in forming the hanging drops compared to the conventional pipette based approach. The operating time was defined as the interval from the start of the syringe pump to the formation of the last droplet. **Figure 3C** demonstrates that at a low flow rate of 0.6 mL/min, the processing time was approximately 117 s to form 49 hanging drop arrays, while

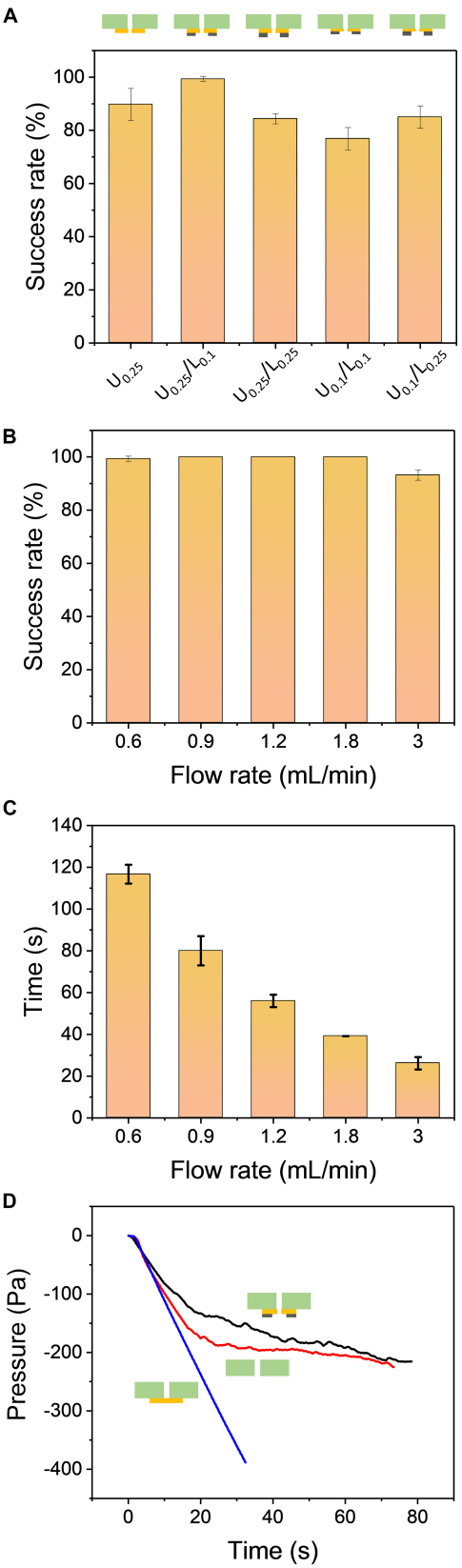


FIGURE 3 | Continued

FIGURE 3 | (A) The comparison of the hanging drop formation success rate using five different combinations of the holding layers: $U_{0.25}$, $U_{0.25}/L_{0.1}$, $U_{0.25}/L_{0.25}$, $U_{0.1}/L_{0.1}$, $U_{0.1}/L_{0.25}$. The flow rate of air withdrawal was set to 0.9 mL/min. **(B)** The comparison of the success rate for different flow rates. The design of the holding layer was $U_{0.25}/L_{0.1}$. **(C)** The processing time of hanging drop formation when using various flow rates. All results were repeated three times ($N = 3$). **(D)** The internal pressure of the air chamber during operation of the PANDA system at different holding conditions: sealed holding layer (blue line), without holding layer (red line), and $U_{0.25}/L_{0.1}$ design of the holding layer (black line). The flow rate of air withdrawal was set to 0.9 mL/min.

at a high flow rate up to 3 mL/min it required only 26 s to complete the formation process. We tested the processing time to manually load 48 wells of 20 μL liquid in a 96-well plate using an 8-channel pipette. It required 60–90 s of processing time depending on the number of persons. Thus, the PANDA system not only generated a uniform hanging drop array, but also increased the operational efficiency and reduced the human errors in manual operation.

Internal Pressure of the PANDA System

The one-by-one formation process of hanging drops can be visualized from the top of the chip with naked eyes. It can also be used to determine the end of the operation process by observing the formation of the last hanging drop. This approach is sufficient when a few hanging drops are to be determined but may become tedious when a large number of hanging drops are formed. To decide when to stop the syringe pump, it is more effective to analyze the internal pressure of the air chamber in real-time. **Figure 3D** demonstrates that the internal pressure of the air chamber changed with time during the air withdrawal process. Three different conditions were compared in the PANDA system: sealed holding layer, without holding layer, and the holding layer with $U_{0.25}/L_{0.1}$ design. Initially, the internal pressure at three different conditions all decreased when the syringe pump began to withdraw the air at a constant flow rate. The pressure linearly decreased to −350 Pa at 30 s for the condition with the sealed holding layer. It is reasonable that when the air is constantly removed from an enclosed system, the pressure linearly decreases with time. Although this vacuum-driven process was relatively weak (∼0.3% pressure loss after 30 s) compared to other approaches (e.g., vacuum pump), the mild process was suitable for the PANDA system without generating a high pulling force due to the sudden change of pressure. The result without using the holding layer indicated that the pressure gradually reached a plateau after 30 s of constant withdrawal of air. Simultaneously, we observed that most of the hanging drops failed to adhere to the bottom surface of the well plate due to the lack of the holding layer. The empty wells allowed more air to enter into the air chamber, balancing the pressure loss generated from the vacuum. Unlike the well plate without the holding layer, the pressure in the holding layer with $U_{0.25}/L_{0.1}$ design gradually decreased with time and reached to −220 Pa when all 49 hanging drops were formed. Interestingly, the fluctuation of the curve was observed after 15 s of constant withdrawal. To further investigate these fluctuations during the air withdrawal process, we fabricated a 9-well PANDA system and followed the same operation procedure for the formation of the hanging drops (**Supplementary Figure S4**). The internal pressure inside the 9-well air chamber was found to follow a similar trend as the 49-well chip, resulting in a reduction of the pressure with time. Furthermore, the change in the fluctuations was found to be more obvious than in the 49-well chip. A total of 9 peaks was observed from the pressure curve, indicating that the internal pressure slightly increased and decreased again due to the capillary force of the well during the formation process. These peaks were corresponding to the individual formation of the 9 hanging drops. The internal pressure eventually decreased to −220 Pa, demonstrating the same condition as the 49-well chip to form the last hanging drop. Therefore, the measurement of internal pressure in the PANDA system may become another tool to monitor the hanging drop formation process in real-time.

Fabrication of 3D Kidney Microtissues Using PANDA Chip

To validate the application of the PANDA chip, 3D kidney microtissues that were composed of GFP-expressed podocytes and RFP-expressed MSCs in 1:1 ratio were formed. We first analyzed the effect of the cell number in each droplet on the formed microtissues. Within 24 h, cells within the droplet arrays assembled into 3D microtissues. According to the fluorescence images in **Figure 4A**, both GFP and RFP signals were detected from the obtained microtissues, demonstrating that the seeded podocytes and MSCs formed the 3D microtissues together.

Analysis of the assembled microtissues revealed a positive correlation between the number of cells in each droplet and the diameter of the 3D microtissues (**Figure 4B**). When the cell seeding density was relatively low (<6,000 cells per droplet), cells within one droplet tended to aggregate into multiple microtissues with various sizes and morphologies. Conversely, a higher cell seeding density (>8,000 cells per droplet) resulted in the formation of a single large microtissue in a droplet. Importantly, these microtissues exhibited a high consistency of diameters, which is critical for developing a drug screening platform. It is worth noting that in the group that contained 10,000 cells within each droplet, the podocytes within the assembled microtissues were distributed uniformly, suggesting enhanced interaction between podocytes and MSCs. Thereby, such a condition was chosen for fabricating 3D kidney microtissues for the following experiments.

During prolonged culture, an increase in the diameter of the microtissues up to ∼500 μm was observed after 3 days of culture (**Figures 4C,D**), suggesting that both podocytes and MSCs within the microtissues proliferated continuously. The similar result was also observed when only MSCs were cultured in the hanging drops for 3 days (**Supplementary Figure S5**). Owing to the diffusion limitation of oxygen (typically around 200–250 μm), a hypoxic core may develop within 3D multicellular microtissues, thus inducing cell death (Potapova et al., 2007; Kaully et al., 2009). To assess the viability of the prepared 3D microtissues, a live/dead assay that stains living cells with green fluorescence owing to

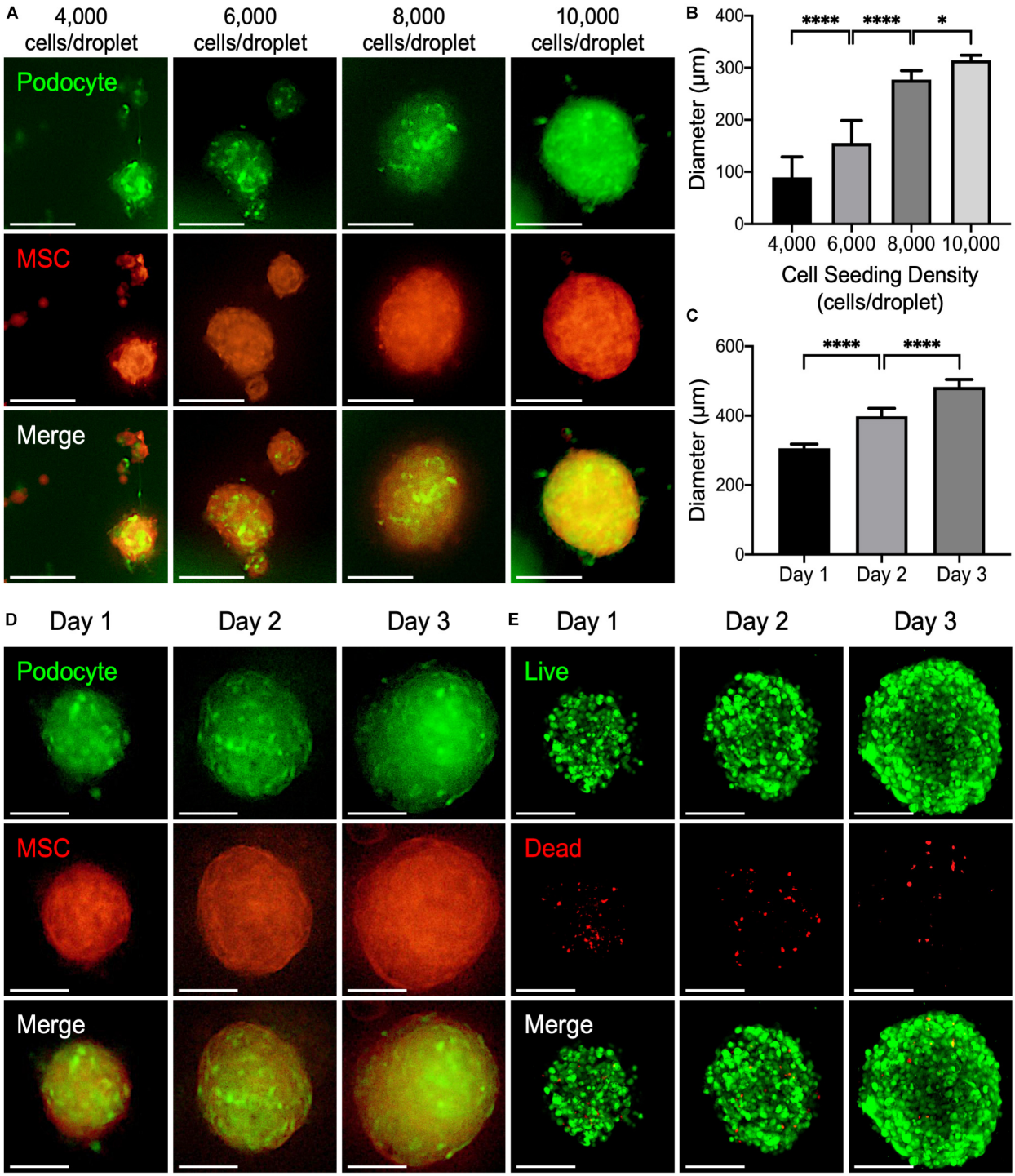


FIGURE 4 | (A) Representative fluorescence images of 3D kidney microtissues comprised of podocyte (green) and mesenchymal stem cells (MSCs; red) fabricated using a PANDA chip. The microtissues were formed within 24 h. **(B)** The diameters of the formed 3D microtissues after 1 day of culture (*$P < 0.05$; ****$P < 0.001$; $N = 20$). **(C)** The diameters of the formed 3D microtissues cultured on different days (****$P < 0.001$. $N = 20$). **(D)** Representative fluorescence images of 3D kidney microtissues cultivated for various periods. **(E)** Confocal images of live (green) and dead (red) cells. All scale bars represent 200 μm.

the hydrolysis of calcein acetoxymethyl ester and dead cells with red fluorescence by ethidium homodimer was conducted. As indicated by the fluorescence images in **Figure 4E**, most cells grown within the 3D microtissues were alive during the entire culture period according to the prevalent green fluorescence emitted from the living cells.

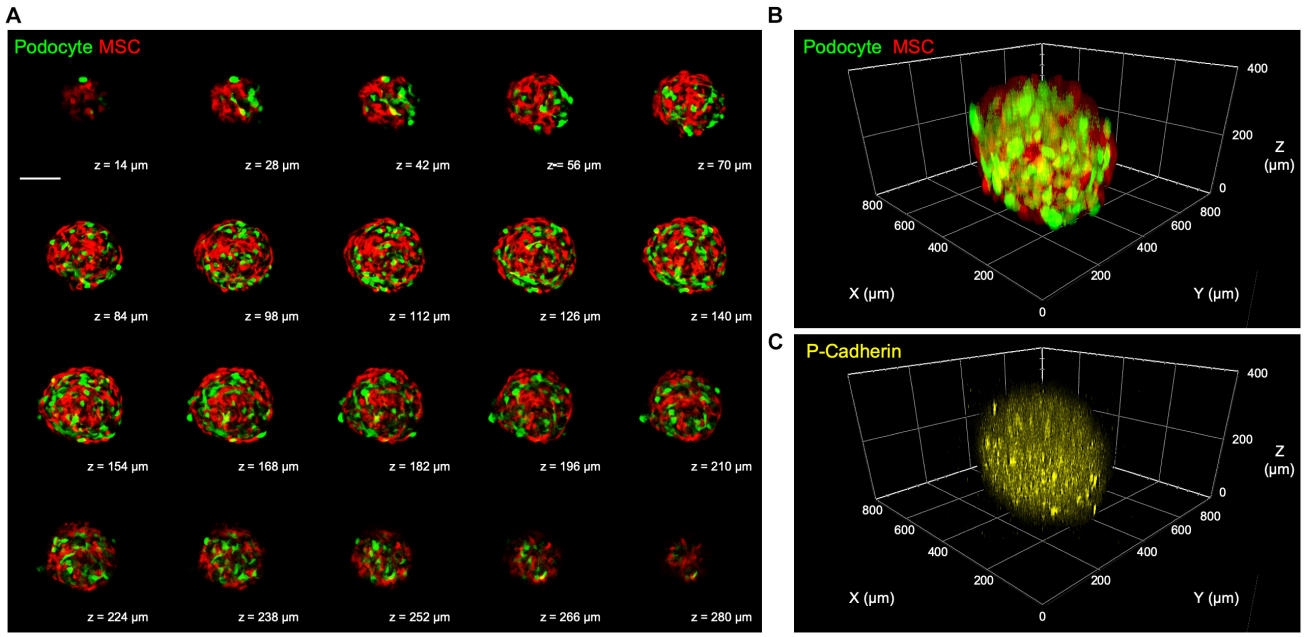


FIGURE 5 | (A) Representative confocal Z-stack images showing mixed podocytes and MSCs in the fabricated 3D kidney microtissues after a 3-day culture. Scale bar represents 200 μm. **(B)** Reconstructed 3D confocal images showing the distribution of the two cell types and **(C)** the podocyte-specific P-cadherin.

After a 3-day culture, the 3D microtissues were processed for confocal microscopy. According to the obtained confocal Z-stack images, the harvested 3D kidney microtissues were composed of mixed podocytes and MSCs, as indicated by the signals of GFP and RFP, respectively, in each optical section (**Figure 5A**) and the 3D reconstructed image (**Figure 5B** and **Supplementary Video S2**). Additionally, podocyte-specific marker P-cadherin was identified throughout the whole 3D microtissues (**Figure 5C**), demonstrating the formation of kidney-like tissues.

To bridge the gap between *in vitro* cell-based assays and *in vivo* studies, a model that can appropriately reflect the complexities of the 3D microenvironment is highly warranted. It has been demonstrated that the cells grown within multicellular microtissues are exposed to a native-mimicking and heterogeneous microenvironment in terms of their interaction with neighboring cells and extracellular matrix, the acquisition of oxygen and nutrients, and the elimination of metabolic waste (Lin and Chang, 2008). The developed PANDA system can be employed to generate 3D microtissues with tunable cellular compositions and microenvironments, thus offering a platform that can engineer the desired artificial niches for modulating cell behaviors or elucidating cellular and molecular mechanisms. For example, by adjusting the density of cells seeded into a PANDA chip, the size of the formed microtissues and thus the internal heterogenous microenvironment with gradients of oxygen and nutrients can be established and precisely controlled, thereby providing a highly reproducible model for further analysis. Moreover, the successful incorporation of multiple cell types into a single microtissue demonstrates the potential to develop PANDA system for engineering cellular heterogeneity, an important characteristic of native tissue.

CONCLUSION

In conclusion, we have demonstrated a new approach for fast and effective production of a hanging drop array with a consistent droplet volume using the PANDA system driven by withdrawing the air to generate pressure difference in the chip. An array of highly consistent 3D kidney microtissues were successfully fabricated using the PANDA system from composing kidney glomerular podocytes and mesenchymal stem cells, suggesting a potential application to serve as a rapid and economical platform to generate desired 3D microenvironments for exploring and harnessing cellular behaviors and responses. We envision that the PANDA system may be adopted to prepare various types of 3D microtissues, which can be employed as *in vivo*-mimicking models for a wide variety of biomedical research fields.

DATA AVAILABILITY STATEMENT

All datasets generated for this study are included in the article/**Supplementary Material**.

AUTHOR CONTRIBUTIONS

C-YC, T-HC, and J-HH contributed to the conception of the study. C-YC, T-HC, W-YY, and L-HH carried

out the experiments. C-YC and W-YY helped perform the analysis with constructive discussions. C-CH and J-HH supervised the research design and wrote the manuscript. All authors approved the final version of the manuscript.

FUNDING

This work was supported by the Ministry of Science and Technology (MOST) in Taiwan under grant 107-2221-E-007-041-MY3 (J-HH) and 109-2636-B-007-001 (C-CH).

ACKNOWLEDGMENTS

The authors thank the technical assistant of Biomedical Science and Engineering Center, National Tsing Hua University, Taiwan for help with the confocal laser scanning microscopy.

SUPPLEMENTARY MATERIAL

The Supplementary Material for this article can be found online at: https://www.frontiersin.org/articles/10.3389/fcell.2020.00327/full#supplementary-material

REFERENCES

Achilli, T. M., Meyer, J., and Morgan, J. R. (2012). Advances in the formation, use and understanding of multi-cellular spheroids. *Expert Opin. Biol. Ther.* 12, 1347–1360. doi: 10.1517/14712598.2012.707181

Amaral, R. L. F., Miranda, M., Marcato, P. D., and Swiech, K. (2017). Comparative analysis of 3D bladder tumor spheroids obtained by forced floating and hanging drop methods for drug screening. *Front. Physiol.* 8:605. doi: 10.3389/fphys.2017.00605

Chen, T. H., Chen, J. S., Ko, Y. C., Chen, J. W., Chu, H. Y., Lu, C. S., et al. (2018). A microfluidic platform for investigating transmembrane pressure-induced glomerular leakage. *Micromachines* 9:228. doi: 10.3390/mi9050228

Cui, X., Hartanto, Y., and Zhang, H. (2017). Advances in multicellular spheroids formation. *J. R. Soc. Interface* 14:20160877. doi: 10.1098/rsif.2016.0877

Drewitz, M., Helbling, M., Fried, N., Bieri, M., Moritz, W., and Lichtenberg, J. (2011). Towards automated production and drug sensitivity testing using scaffold-free spherical tumor microtissues. *Biotechnol. J.* 6, 1488–1496. doi: 10.1002/biot.201100290

Fang, Y., and Eglen, R. M. (2017). Three-dimensional cell cultures in drug discovery and development. *SLAS Discov.* 22, 456–472. doi: 10.1177/1087057117696795

Fatehullah, A., Tan, S. H., and Barker, N. (2016). Organoids as an in vitro model of human development and disease. *Nat. Cell. Biol.* 18, 246–254. doi: 10.1038/ncb3312

Hale, L. J., Howden, S. E., Phipson, B., Lonsdale, A., Ghobrial, I., Hosawi, S., et al. (2018). 3D organoid-derived human glomeruli for personalised podocyte disease modelling and drug screening. *Nat. Commun.* 9:5167. doi: 10.1038/s41467-018-07594-z

Hsiao, A. Y., Tung, Y. C., Kuo, C. H., Mosadegh, B., Bedenis, R., Pienta, K. J., et al. (2012). Micro-ring structures stabilize microdroplets to enable long term spheroid culture in 384 hanging drop array plates. *Biomed Microdev.* 14, 313–323. doi: 10.1007/s10544-011-9608-5

Hung, C.-J., Yao, C.-L., Cheng, F.-C., Wu, M.-L., Wang, T.-H., and Hwang, S.-M. (2010). Establishment of immortalized mesenchymal stromal cells with red fluorescence protein expression for in vivo transplantation and tracing in the rat model with traumatic brain injury. *Cytotherapy* 12, 455–465. doi: 10.3109/14653240903555827

Imasawa, T., Utsunomiya, Y., Kawamura, T., Zhong, Y., Nagasawa, R., Okabe, M., et al. (2001). The potential of bone marrow-derived cells to differentiate to glomerular mesangial cells. *J. Am. Soc. Nephrol.* 12, 1401–1409.

Kandasamy, K., Chuah, J. K. C., Su, R., Huang, P., Eng, K. G., Xiong, S. J., et al. (2015). Prediction of drug-induced nephrotoxicity and injury mechanisms with human induced pluripotent stem cell-derived cells and machine learning methods. *Sci. Rep.* 5:12337. doi: 10.1038/srep12337

Kang, S. M., Hwang, N. S., Yeom, J., Park, S. Y., Messersmith, P. B., Choi, I. S., et al. (2012). One-step multipurpose surface functionalization by adhesive catecholamine. *Adv. Funct. Mater.* 22, 2949–2955. doi: 10.1002/adfm.201200177

Kaully, T., Kaufman-Francis, K., Lesman, A., and Levenberg, S. (2009). Vascularization–the conduit to viable engineered tissues. *Tissue Eng. Part B Rev.* 15, 159–169. doi: 10.1089/ten.teb.2008.0193

Kim, S.-J., Park, J., Byun, H., Park, Y.-W., Major, L. G., Lee, D. Y., et al. (2019). Hydrogels with an embossed surface: an all-in-one platform for mass production and culture of human adipose-derived stem cell spheroids. *Biomaterials* 188, 198–212. doi: 10.1016/j.biomaterials.2018.10.025

Kuo, C.-T., Wang, J.-Y., Lin, Y.-F., Wo, A. M., Chen, B. P. C., and Lee, H. (2017). Three-dimensional spheroid culture targeting versatile tissue bioassays using a PDMS-based hanging drop array. *Sci. Rep.* 7:4363. doi: 10.1038/s41598-017-04718-1

Laschke, M. W., and Menger, M. D. (2017). Life is 3D: boosting spheroid function for tissue engineering. *Trends Biotechnol.* 35, 133–144. doi: 10.1016/j.tibtech.2016.08.004

Lee, H., Dellatore, S. M., Miller, W. M., and Messersmith, P. B. (2007). Mussel-inspired surface chemistry for multifunctional coatings. *Science* 318, 426–430. doi: 10.1126/science.1147241

Liao, W., Wang, J. Q., Xu, J. C., You, F. Y., Pan, M. X., Xu, X. P., et al. (2019). High-throughput three-dimensional spheroid tumor model using a novel stamp-like tool. *J. Tissue Eng.* 10:2041731419889184. doi: 10.1177/2041731419889184

Lin, C. K., Hsiao, Y. Y., Nath, P., and Huang, J. H. (2019). Aerosol delivery into small anatomical airway model through spontaneous engineered breathing. *Biomicrofluidics* 13:044109. doi: 10.1063/1.5121188

Lin, R.-Z., and Chang, H.-Y. (2008). Recent advances in three-dimensional multicellular spheroid culture for biomedical research. *Biotechnol. J.* 3, 1172–1184. doi: 10.1002/biot.200700228

Liu, W., Li, Y., Feng, S., Ning, J., Wang, J., Gou, M., et al. (2014). Magnetically controllable 3D microtissues based on magnetic microcryogels. *Lab Chip* 14, 2614–2625. doi: 10.1039/c4lc00081a

May, C. J., Saleem, M., and Welsh, G. I. (2014). Podocyte dedifferentiation: a specialized process for a specialized cell. *Front. Endocrinol.* 5:148. doi: 10.3389/fendo.2014.00148

Mehta, G., Hsiao, A. Y., Ingram, M., Luker, G. D., and Takayama, S. (2012). Opportunities and challenges for use of tumor spheroids as models to test drug delivery and efficacy. *J. Control. Release* 164, 192–204. doi: 10.1016/j.jconrel.2012.04.045

Musah, S., Mammoto, A., Ferrante, T. C., Jeanty, S. S. F., Hirano-Kobayashi, M., Mammoto, T., et al. (2017). Mature induced-pluripotent-stem-cell-derived human podocytes reconstitute kidney glomerular-capillary-wall function on a chip. *Nat. Biomed. Eng.* 1:69. doi: 10.1038/s41551-017-0069

Ni, B. S., Tzao, C., and Huang, J. H. (2019). Plug-and-play *in vitro* metastasis system toward recapitulating the metastatic cascade. *Sci. Rep.* 9:18110. doi: 10.1038/s41598-019-54711-z

Oliveira, N. M., Martins-Cruz, C., Oliveira, M. B., Reis, R. L., and Mano, J. F. (2018). Coculture of spheroids/2D cell layers using a miniaturized patterned platform as a versatile method to produce scaffold-free tissue engineering building blocks. *Adv. Biosyst.* 2:1700069.

Ouyang, L. L., Yao, R., Mao, S. S., Chen, X., Na, J., and Sun, W. (2015). Three-dimensional bioprinting of embryonic stem cells directs highly uniform embryoid body formation. *Biofabrication* 7:044101. doi: 10.1088/1758-5090/7/4/044101

Potapova, I. A., Gaudette, G. R., Brink, P. R., Robinson, R. B., Rosen, M. R., Cohen, I. S., et al. (2007). Mesenchymal stem cells support migration, extracellular matrix invasion, proliferation, and survival of endothelial cells in vitro. *Stem Cells* 25, 1761–1768. doi: 10.1634/stemcells.2007-0022

Ranga, A., Gjorevski, N., and Lutolf, M. P. (2014). Drug discovery through stem cell-based organoid models. *Adv. Drug Deliv. Rev.* 69-70, 19–28. doi: 10.1016/j.addr.2014.02.006

Schiwek, D., Endlich, N., Holzman, L., Holthöfer, H., Kriz, W., and Endlich, K. (2004). Stable expression of nephrin and localization to cell-cell contacts in novel murine podocyte cell lines. *Kidney Int.* 66, 91–101. doi: 10.1111/j.1523-1755.2004.00711.x

Shri, M., Agrawal, H., Rani, P., Singh, D., and Onteru, S. K. (2017). Hanging drop, a best three-dimensional (3D) culture method for primary buffalo and sheep hepatocytes. *Sci. Rep.* 7:1203. doi: 10.1038/s41598-017-01355-6

Skiles, M. L., Sahai, S., Rucker, L., and Blanchette, J. O. (2013). Use of culture geometry to control hypoxia-induced vascular endothelial growth factor secretion from adipose-derived stem cells: optimizing a cell-based approach to drive vascular growth. *Tissue Eng. Part A* 19, 2330–2338. doi: 10.1089/ten.TEA.2012.0750

Todhunter, M. E., Jee, N. Y., Hughes, A. J., Coyle, M. C., Cerchiari, A., Farlow, J., et al. (2015). Programmed synthesis of three-dimensional tissues. *Nat. Methods* 12, 975–981.

Tung, Y. C., Hsiao, A. Y., Allen, S. G., Torisawa, Y. S., Ho, M., and Takayama, S. (2011). High-throughput 3D spheroid culture and drug testing using a 384 hanging drop array. *Analyst* 136, 473–478. doi: 10.1039/c0an00609b

Wong, C.-Y., Tan, E.-L., and Cheong, S.-K. (2014). In vitro differentiation of mesenchymal stem cells into mesangial cells when co-cultured with injured mesangial cells. *Cell Biol. Int.* 38, 497–501. doi: 10.1002/cbin.10231

Yu, C.-P., Juang, J.-H., Lin, Y.-J., Kuo, C.-W., Hsieh, L.-H., and Huang, C.-C. (2020). Enhancement of subcutaneously transplanted β cell survival using 3d stem cell spheroids with proangiogenic and prosurvival potential. *Adv. Biosyst.* 4:1900254. doi: 10.1002/adbi.201900254

Zakrzewski, W., Dobrzyński, M., Szymonowicz, M., and Rybak, Z. (2019). Stem cells: past, present, and future. *Stem Cell Res. Ther.* 10:68.

Conflict of Interest: The authors declare that the research was conducted in the absence of any commercial or financial relationships that could be construed as a potential conflict of interest.

Copyright © 2020 Cho, Chiang, Hsieh, Yang, Hsu, Yeh, Huang and Huang. This is an open-access article distributed under the terms of the Creative Commons Attribution License (CC BY). The use, distribution or reproduction in other forums is permitted, provided the original author(s) and the copyright owner(s) are credited and that the original publication in this journal is cited, in accordance with accepted academic practice. No use, distribution or reproduction is permitted which does not comply with these terms.

frontiers in Cell and Developmental Biology

ORIGINAL RESEARCH
published: 19 May 2020
doi: 10.3389/fcell.2020.00250

A Testis-Derived Hydrogel as an Efficient Feeder-Free Culture Platform to Promote Mouse Spermatogonial Stem Cell Proliferation and Differentiation

*Yan Yang[1,2†], Qilian Lin[1†], Chengxing Zhou[1], Quan Li[1], Ziyi Li[1], Zhen Cao[1], Jinlian Liang[1], Hanhao Li[3], Jiaxin Mei[1], Qihao Zhang[1], Qi Xiang[1,4], Wei Xue[2] and Yadong Huang[1,3]**

[1] Guangdong Provincial Key Laboratory of Bioengineering Medicine, Department of Cell Biology, Jinan University, Guangzhou, China, [2] Department of Biomedical Engineering, Jinan University, Guangzhou, China, [3] Department of Pharmacology, Jinan University, Guangzhou, China, [4] Biopharmaceutical Research & Development Center of Jinan University, Guangzhou, China

OPEN ACCESS

Edited by:
Yu-Chen Hu,
National Tsing Hua University, Taiwan

Reviewed by:
Chao-Ling Yao,
Yuan Ze University, Taiwan
Ji Bao,
Sichuan University, China

***Correspondence:**
Yadong Huang
tydhuang@jnu.edu.cn

† These authors have contributed equally to this work

Specialty section:
This article was submitted to Stem Cell Research, a section of the journal Frontiers in Cell and Developmental Biology

Received: 12 February 2020
Accepted: 24 March 2020
Published: 19 May 2020

Citation:
Yang Y, Lin Q, Zhou C, Li Q, Li Z, Cao Z, Liang J, Li H, Mei J, Zhang Q, Xiang Q, Xue W and Huang Y (2020) A Testis-Derived Hydrogel as an Efficient Feeder-Free Culture Platform to Promote Mouse Spermatogonial Stem Cell Proliferation and Differentiation. Front. Cell Dev. Biol. 8:250. doi: 10.3389/fcell.2020.00250

Fertility preservation and assisted reproductive medicine require effective culture systems for the successful proliferation and differentiation of spermatogonial stem cells (SSCs). Many SSC culture systems require the addition of feeder cells at each subculture, which is tedious and inefficient. Here, we prepared decellularized testicular matrix (DTM) from testicular tissue, which preserved essential structural proteins of testis. The DTM was then solubilized and induced to form a porous hydrogel scaffold with randomly oriented fibrillar structures that exhibited good cytocompatibility. The viability of SSCs inoculated onto DTM hydrogel scaffolds was significantly higher than those inoculated on Matrigel or laminin, and intracellular gene expression and DNA imprinting patterns were similar to that of native SSCs. Additionally, DTM promoted SSC differentiation into round spermatids. More importantly, the DTM hydrogel supported SSC proliferation and differentiation without requiring additional somatic cells. The DTM hydrogel scaffold culture system provided an alternative and simple method for culturing SSCs that eliminates potential variability and contamination caused by feeder cells. It might be a valuable tool for reproductive medicine.

Keywords: testicular extracellular matrix, hydrogel, spermatogonial stem cells, proliferation, differentiation

INTRODUCTION

Spermatogenesis is the proliferation and differentiation of spermatogonial stem cells (SSCs) called germ-line stem cells, within the seminiferous tubules of the testes, resulting in haploid, free-swimming spermatozoa. Maintenance of SSCs and induction of spermiogenesis *in vitro* will facilitate the study of reproductive biology, including assisted reproductive medicine and genetic modification (Stukenborg et al., 2009). SSCs are extremely rare (0.02–0.03%) in the testis (de Rooij and Russell, 2000); it is valuable to develop protocols for SSC propagation and differentiation *in vitro*.

SSCs located in the seminiferous tubules require complex endocrine and auto-/paracrine regulation as well as cellular interactions to proliferate and differentiate (de Rooij, 2009). SSC propagation requires growth factors, including glial cell line-derived neurotrophic factor (GDNF), secreted from Sertoli cells, basic fibroblast growth factor (bFGF), and epidermal growth factor (EGF) (Simon et al., 2007; Hofmann, 2008; Takashima et al., 2015). The widely adopted approach for SSC propagation was a two-dimensional culture system relying on cytokines of feeder cell layers. Mouse embryonic fibroblasts (MEFs) and Sertoli cells were the most frequently used feeder cells (Kanatsu-Shinohara et al., 2003; Nasiri et al., 2012; Song and Wilkinson, 2014). However, the preparation of subcultures for SSCs is tedious and variable. It is necessary to establish an efficient and practical method to propagate SSCs. Kanatsu-Shinohara et al. reported that laminin could maintain SSC activity when the medium was supplemented with GDNF, fetuin, and lipid-associated molecules (Kanatsu-Shinohara et al., 2011). However, the proliferative frequency of SSCs was lower (0.4–1.0%). Subsequently, Kinarm Ko et al. developed a Matrigel-based feeder-free culture system for long-term propagation of SSCs using the StemPro-34 SFM medium containing numerous factors for SSCs (Choi et al., 2014). Besides, it was reported that soft agar culture system (SACS) (Stukenborg et al., 2008) and collagen gel matrix (Khajavi et al., 2014) could mimic germ cell niche formation in the seminiferous tubules to permit mouse spermatogenesis *in vitro*. However, in these culture systems, somatic cells have a critical role in meiotic and postmeiotic differentiation of SSCs. Therefore, establishing an alternative culture condition that mimics testis niche is important for SSC proliferation and differentiation *in vitro*.

The extracellular matrix (ECM) consists of structural and functional molecules secreted by the resident cells, which provides biochemical and biomechanical signaling cues to influence the surrounding cells' behavior dynamically (Agmon and Christman, 2016). It was used in tissue engineering. Thereinto, tissue-specific ECM scaffolds derived from homologous tissue may be more effective in producing desired cell phenotypes than non-homologous tissues (Zhang et al., 2009; Aamodt and Grainger, 2016; Spang and Christman, 2018). The ECM are available in sheets, powders, and hydrogels (Aamodt and Grainger, 2016; Saldin et al., 2017; Spang and Christman, 2018). The hydrogel is able to fill a different space with a homogeneous concentration. In the proper composition, the ECM hydrogel scaffolds can promote mesenchymal stem cell differentiation into a neural lineage (DeQuach et al., 2011), hepatocytes (Park et al., 2016). Recently, it has been reported that decellularized testicular matrix (DTM) may be a suitable material for the generation of the testicular organoids; however, the ability of DTM hydrogels to support SSC proliferation and differentiation in the absence of testicular cells remains unknown (Baert et al., 2015, 2017; Murdock et al., 2019; Rezaei Topraggaleh et al., 2019).

In this study, we produced a soluble DTM using an acid–pepsin solution, which self-assembled to form a hydrogel scaffold. The DTM-derived hydrogel scaffold could provide a microenvironment to support SSCs proliferation and differentiation *in vitro*.

MATERIALS AND METHODS

Animals

Mice used in experiments were purchased from the Experimental Animal Center of Guangdong Province, China. Animals were maintained under a 12-h light/dark cycle and a controlled temperature (24 ± 2°C) with relative humidity (50–60%). The standard rodent diet and drinking water were freely accessible. All experiments were conducted according to the National Institute of Health guidelines for the care and use of animals and approved by the Institutional Animal Care and Use Committee of Jinan University.

Decellularization of Testicular Tissue

Testes were obtained from male mice and decapsulated. Testicular fragments were decellularized as previously described (Baert et al., 2015). Briefly, tissues were rinsed in 1 × phosphate-buffered saline (PBS) to remove residual blood and subsequently stirred in 1% sodium dodecyl sulfate (SDS) in PBS solution for 18 h. Following the decellularization, the tissue was washed using PBS for 24 h, and PBS was renewed six times to remove the cellular fragment and remaining detergents. The decellularized testis-derived ECM, referred to as DTM, was lyophilized, and stored in −20°C until use.

Assessment of Cellular Contents

Native and decellularized samples were fixed in 4% paraformaldehyde for 24 h, then embedded in paraffin, and serially sectioned at 5 μm thickness. The cell nuclei residues were determined by hematoxylin and eosin (H&E) staining or 4′,6-diamidino-2-phenylindole (DAPI) (Sigma, Poole, Dorset, United Kingdom) staining.

For quantitative analysis of the DNA content, DNA was extracted from native or DTM tissues using the HiPure Tissue DNA Mini Kit (Magen, Shanghai, China) according to the manufacturer's instructions. The concentration of the total DNA was determined using a Nano Drop ND-2000 spectrophotometer (2000C, Thermo Fisher Scientific, United States) and normalized for sample weight.

Immunohistochemistry

Retention of collagen I, collagen IV, fibronectin, and laminin in DTM was studied by immunohistochemistry. Sections were deparaffinized and rehydrated. Endogenous peroxidases were quenched using 0.3% H_2O_2. After blocking with 3% bovine serum albumin (BSA), sections were incubated with primary antibodies at 4°C overnight, followed by incubation using a horseradish peroxidase (HRP)-conjugated secondary antibody at 37°C for 1 h. The peroxidase activity was visualized with 3,3-diaminobenzidine (DAB) for 5 min, and the slides were counterstained with hematoxylin. Normal rabbit immunoglobulin G (IgG) was used for isotype controls. The following antibodies were used: rabbit

anticollagen I (Affinity Biosciences, Changzhou, China), rabbit anticollagen IV (Affinity Biosciences, Changzhou, China), rabbit antifibronectin (Affinity Biosciences, Changzhou, China), and rabbit antilaminin (Affinity Biosciences, Changzhou, China).

Preparation of DTM Hydrogel

DTM hydrogels were prepared according to previously described protocols (Pati et al., 2014). Briefly, lyophilized DTM powder was sterilized by e-beam irradiation at 22 kGy and stored at room temperature. Then, the sterilized DTM powder was digested in a solution of 0.5 M acetic with 10 mg of pepsin (Sigma, Poole, Dorset, United Kingdom) for 100 mg DTM and stirred at 4°C for 72 h to form a pregel solution under sterile condition. The solution was centrifuged to remove the particles. The pepsin–acetic DTM solution was neutralized to pH 7.0 with dropwise addition of cold 1 M sodium hydroxide (Sigma, Poole, Dorset, United Kingdom). To form the hydrogel, the neutralized pregel was incubated at 37°C for 60 min.

Rheological Measurement

Rheological characterizations of DTM hydrogel were determined using a Physica MCR 301 rheometer (Anton Paar, Hertford, United Kingdom) as previously described (Paduano et al., 2017). Briefly, the pH of the DTM digest was neutralized to 7.0 and diluted to 2.5, 5, or 10 mg DTM/ml. The diluted pregel solutions at 4°C were placed between 50 mm parallel plates separated by a 0.2-mm measuring gap. The plates were precooled within a humidified chamber to 4°C and were then warmed to 37°C during the first 75 s of each measurement run. A 30-min time course experiment was performed, during which the samples were subjected to an oscillatory strain of 1% at a constant angular frequency of 1 rad/s (0.159 Hz) and rapidly increased temperature from 4 to 37°C to induce gelation as indicated by a sharp increase and plateauing of the storage modulus (G'), and the loss modulus (G'') ($n = 3$).

Turbidity Gelation Kinetics Assay

Turbidimetric gelation kinetics was determined as previously described (Medberry et al., 2013). In brief, the neutralized DTM solution was diluted to 2.5, 5, and 10 mg/ml and placed into a 96-well plate (100 μl/well). The plate was placed in a preheated (37°C) plate reader, and the optical density (OD) was read at 405 nm every 2 min for 90 min. Data were collected using GraphPad prism and normalized using **Equation (1)**, where A is the absorbance at a given time, A_0 is the lowest absorbance (time zero), and $A_{\max}$ is the maximum absorbance. According to the fitting curve, the following values can be obtained: the time required to 50% ($t_{1/2}$) and 95% (t_{95}) maximum absorbance. The lag phase (t_{lag}) was defined as the point where a line representing the slope at log $t_{1/2}$ intersects the turbidimetry baseline with 0% absorbance. The turbidimetric speed (S) was determined by calculating the slope of the curve at $t_{1/2}$.

$$\text{Normalized absorbance (NA)} = \frac{A - A_0}{A\ max - A_0} \quad (1)$$

Scanning Electron Microscopy

DTM hydrogels were frozen at −80°C and lyophilized overnight. Subsequently, the lyophilized hydrogel was dried in a critical point dryer and sputter coated with gold/palladium. Images were taken under a LEO 1530 scanning electron microscope. The average pore size of DTM was determined by the measurement of two perpendicular dimensions of at least 10 randomly selected pores using ImageJ software (ImageJ, United States).

Spermatogonial Stem Cell Culture

Testicular tissue was obtained from 6-day-old male mice. To obtain SSC suspension from the tissue, a two-step enzymatic digestion protocol was applied (Guan et al., 2009). Briefly, decapsulated testes were treated with collagenase type IV (1 mg/ml) for 15 min at 37°C, followed by digestion in 0.25% trypsin and 1 mM ethylenediaminetetraacetic acid (EDTA) for 10 min at 37°C. The singly dissociated cells were incubated overnight in dish coated with gelation to removed somatic cells. Non-adherent and weakly adherent cells were collected and then labeled with CD326 (EpCAM) MicroBeads by Mini MACS Starting Kit (Miltenyi Biotec, Stevenage, United Kingdom) according to the manufacturer's protocol. Cells were rinsed with PBS containing 0.5% BSA (Sigma, Poole, Dorset, United Kingdom), and the CD326-positive cells were collected. The CD326-positive cells were plated onto DTM hydrogel, Matrigel (10 mg/ml) hydrogel, or laminin (2 mg/ml) coated plates with SSC culture medium. The SSC medium was composed of Dulbecco's modified Eagle's medium (DMEM), 15% fetal bovine serum (FBS, Thermo Fisher Scientific, Waltham, MA, United States), 50 μM-mercaptoethanol (Thermo Fisher Scientific, Waltham, MA, United States), 1 × minimal essential medium (MEM) non-essential amino acids (Thermo Fisher Scientific, Waltham, MA, United States), and 10 ng/ml mouse GDNF (Peprotech, Rocky Hill, United States).

Live/Dead Staining

Five hundred microliters of DTM hydrogel (2.5, 5, and 10 mg/ml), 10 mg/ml Matrigel growth factor reduced basement membrane matrix (Corning, New York, United States), and 2 mg/ml laminin (Sigma, Poole, Dorset, United Kingdom) were added to six-well plates and incubated at 37°C for 2 h to form scaffold. SSCs were seeded on laminin, DTM hydrogel, and Matrigel hydrogel for 7 days. The live/dead cells were visualized by Calcein-AM/PI Double Stain Kit (Yeasen, Shanghai, China). Samples were imaged under a microscope. Live (green) and dead (red) cells were counted using Image J software.

Alkaline Phosphatase Reactivity

Cells were washed with PBS three times and fixed with 4% paraformaldehyde for 3 min. Alkaline phosphatase (ALP) (Leagene, Beijing, China) was added to the plate and incubated for 30 min and then washed with PBS three times. The samples were photographed under a microscope within 3 h.

Reverse Transcription PCR

Reverse transcription PCR (RT-PCR) was performed to assess the expression of SSC-specific marker genes in colonies. RNA was extracted from the cell pellet by Trizol reagent (Sigma, Poole, Dorset, United Kingdom). Reverse transcription was performed using Prime Script^{TM} RT Master Mix (Takara, Dalian, China) following manufacturer's instructions. The primers are listed in **Supplementary Table S1**.

Flow Cytometric Analysis

To determine the expression of SSC-specific surface markers, SSCs were resuspended in cold PBS supplemented with 0.5% FBS at density of 1×10^6 cells/ml and stained with primary antibodies, CD326 (EpCAM), CD49f (Intergrin α6), CD29 (Intergrin β1), and CD117 (c-kit) (all from EBioscience, Thermo Fisher Scientific, Waltham, MA, United States), at 4°C for 30 min. Rabbit IgG1-PE was used as isotype control. Flow cytometry was performed using CellQuest software (BD Biosciences).

Genomic DNA Methylation Analysis

Genomic DNA of SSCs was isolated using the HiPure Tissue DNA Mini Kit (Magen, Shanghai, China) according to the manufacturer's protocol. The methylation levels of the *H19* and *Igf2r* gene of genomic DNA were determined by bisulfite sequencing PCR. The primers are shown in **Supplementary Table S1**.

Spermatogonial Stem Cell Transplantation

Transplantation was performed as previously described (Ko et al., 2009). Briefly, 4-week-old male mice were treated with 25 mg/kg busulfan by intraperitoneal injection. After 1 month, these mice were used as SSC recipients. SSCs cultured on DTM were collected and labeled with carboxyfluorescein diacetate succinimidyl ester (CFDA-SE) following manufacturer's instructions. Then, the single-cell suspensions (approximately 1×10^5 cells in 10 μl of PBS) were injected into the seminiferous tubules of recipient mice through the efferent ducts using a micropipette (40–50 μm diameter tips). The mice were euthanized 1 month later, and testes were collected and examined.

Spermatogonial Stem Cell Differentiation

SSCs were plated on laminin, Matrigel, and DTM hydrogel scaffolds with SSC differentiation medium composed of DMEM, 10% FBS, minimal essential medium (MEM) non-essential amino acids (Thermo Fisher Scientific, Waltham, MA, United States), 10 μM testosterone (Cayman, Michigan, United States), 100 ng/ml follicle stimulating hormone (FSH) (ProSpec, Rocky Hill, United States), and 100 ng/ml retinoic acid (RA) (Sigma, Poole, Dorset, United Kingdom) at 34°C under 5% CO_2. The culture medium was changed every 2 days.

Quantitative Real-Time PCR

RNA was extracted from the cell pellet by Trizol reagent (Sigma, Poole, Dorset, United Kingdom). Reverse transcription was performed with the complementary DNA (cDNA) synthesis kit (TaKaRa Taq^{TM} Version 2.0 plus dye). Gene expression was analyzed quantitatively using the ChamQ SYBR® qPCR Master Mix (Vazyme, Nanjing, China). The PCR data were recorded by Bio-Rad CFX Manager Software (version 2.0). Gene expression data were normalized to the *Gapdh* as housekeeping gene. The primers are listed in **Supplementary Table S2**.

Immunofluorescence

Cells were fixed in 4% paraformaldehyde for 30 min and washed three times in PBS. The cells were treated in 0.2% Triton-X for 10 min. Non-specific adhesion sites were blocked with 3% BSA (Sigma, Poole, Dorset, United Kingdom) for 30 min at room temperature. The primary and secondary antibodies were diluted in a solution of PBS containing 3% BSA, 1% horse serum, and 0.1% Triton X-100. Cells were incubated with primary antibodies Acrosin (Santa, CA, United States) overnight at 4°C, followed by incubation with secondary antibodies for 2 h at room temperature. Nuclei were stained with DAPI (Thermo Fisher Scientific, Waltham, MA, United States). Stained samples were visualized, and images were captured using a LSM710 confocal microscope (Zeiss) and analyzed by the Image J software.

DNA Content Analysis

Flow cytometry was performed to measure the DNA content of SSCs. In brief, cells were washed twice in PBS and fixed in cold 70% ethanol for 4 h. Cells were then stained with propidium iodide at 2–8°C for 10 min and analyzed within 3 h by FACSCalibur system (BD Bioscience).

Statistical Analyses

All experiments were repeated at least three times, and data were expressed as the mean ± one standard deviation around the mean (SD). Statistical analyses were performed by Prism software (GraphPad Software, San Diego, CA, United States). Statistical analyses were performed with an unpaired Student's *t* test or one-way ANOVA for more than two groups. A two-tailed value of $p < 0.05$ was considered statistically significant.

RESULTS

Macroscopic Appearance of Decellularized Testicular Matrix

Testes were collected and the tunica albuginea was removed. The exposed testicular tissues were treated with 1% SDS to generate a DTM (**Figures 1A,B**). H&E staining displayed the absence of cells and cell debris in the matrix after decellularization (**Figures 1C,D**). DAPI staining also confirmed the absence of residual nuclei in the DTM when compared with the native testicular tissue (**Figures 1E,F**). The residual DNA content in the DTM, 11.37 ± 0.84 ng/mg, was significantly lower than that of the native testes tissue (545.20 ± 37.21 ng/mg) (**Figure 1G**), indicating that 97.91% of DNA was removed from the tissue. The minimal residual cell debris and DNA indicated that the testicular tissue was successfully decellularized. We then evaluated the retention

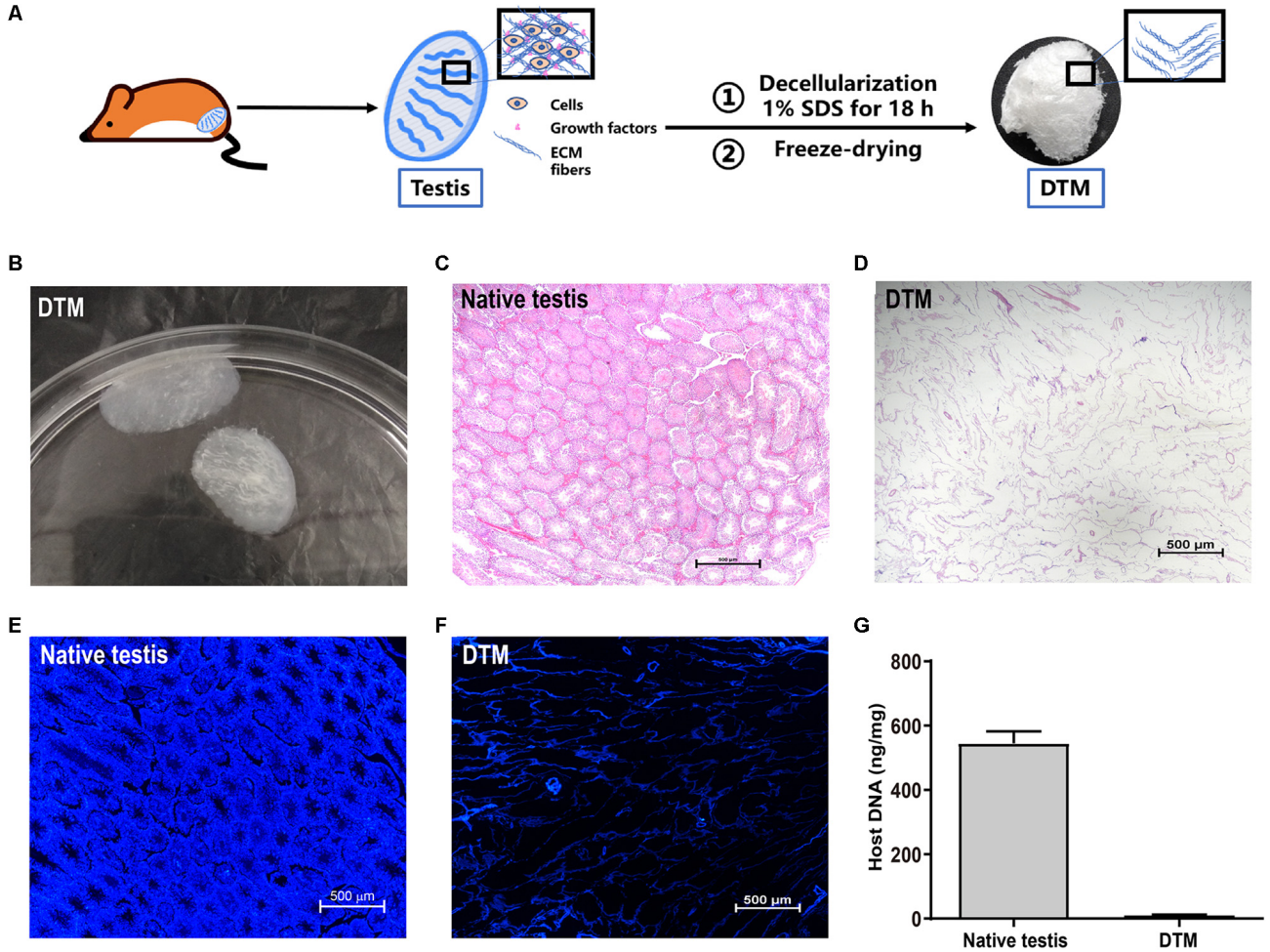


FIGURE 1 | Characterization of native testes and decellularized testicular matrix (DTM). **(A)** Schematic illustration showing the process of DTM generation. **(B)** Macroscopic appearance of DTM. **(C,D)** H&E staining of testis section before decellularization and DTM. Scale bar, 500 μm. **(E,F)** 4′,6-Diamidino-2-phenylindole (DAPI) staining for residual DNA content in testis section before decellularization and DTM. Scale bar, 500 μm. **(G)** DNA quantification of native testis and DTM.

of structural components in DTM following decellularization. Immunohistochemical analysis revealed that the expression of laminin, fibronectin, collagen type I, and collagen type IV were significantly reduced after decellularization. However, the presence of laminin, fibronectin, collagen type I, and collagen type IV in DTM indicated that the essential components of testicular ECM were preserved in DTM after decellularization (**Figure 2**).

Characterization of Decellularized Testicular Matrix Hydrogel

The lyophilized DTM was digested in pepsin solution; then, the DTM solution was thermally induced to form DTM hydrogels (**Figure 3A**). The hydrogels with a low DTM concentration (2.5 mg/ml) were extremely delicate. Hydrogels with DTM concentration of 5 and 10 mg/ml had a rigid structure with defined edges (**Figure 3B**). The rheological characteristics of the DTM hydrogels were determined using a parallel plate rheometer. After incubating the pregels at 37°C, their behavior was like that of a cross-linked gel and exhibited greater storage modulus (G') than loss modulus (G''). Results displayed that pregel with a DTM concentration of 10 mg/ml had the highest storage modulus exhibiting solid-like behavior (**Figure 3C**).

The fiber network topology revealed that DTM hydrogels possessed a randomly oriented fibrillar structure (**Figures 3D–F**), and average fiber diameter did not vary with DTM concentration (**Figure 3G**). The pore size of the hydrogels with a DTM concentration of 10 mg/ml was 0.5 μm, which was significantly smaller than the pore size of hydrogels at DTM concentration of 5 mg/ml (0.70 μm) and 2.5 mg/ml (0.94 μm) (**Figure 3H**).

The turbidimetric gelation kinetic curves for the hydrogels were sigmoidal at different DTM concentrations. Hydrogels formed after a lag period. The half time of gelation ($t_{1/2}$) for the hydrogels was not dependent on DTM concentration: 2.5 mg/ml DTM, 30 min; 5 mg/ml DTM, 27 min; and 10 mg/ml DTM, 30 min. Similarly, no significant difference was found in either

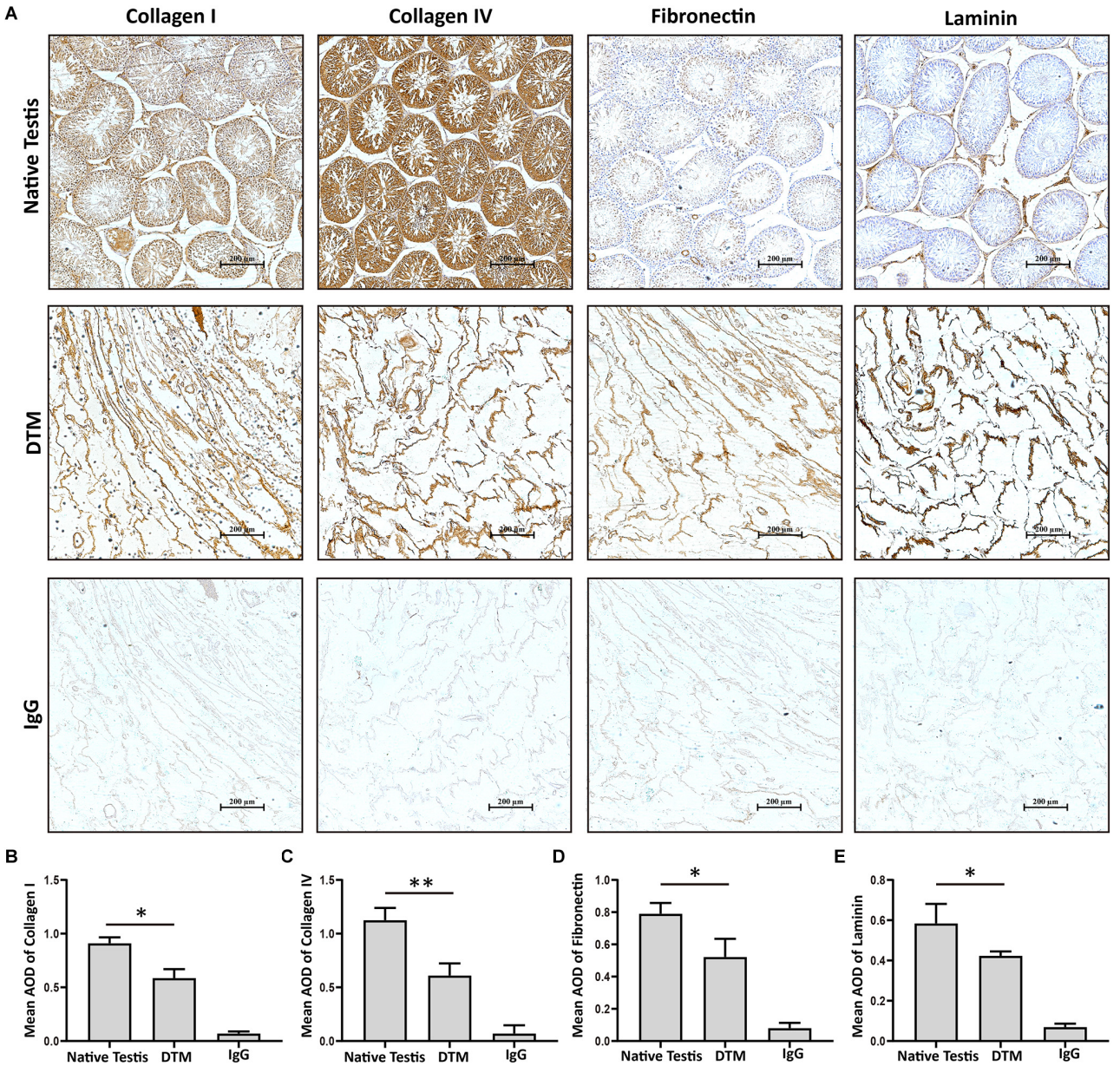


FIGURE 2 | Immunohistochemical staining of native testis and decellularized testicular matrix (DTM). **(A)** Immunohistochemical validation of the essential extracellular matrix proteins of the native testis (laminin, collagen type I, collagen type IV, and fibronectin) in the DTM. Scale bar, 200 μm. **(B–E)** Relative quantity of collagen I, collagen IV, fibronectin, and laminin. ImageJ software was used to determine the average optical density (AOD). Data were shown as mean ± SD, $n = 8$. Differences were considered statistically significant at $^{*}p < 0.05$, $^{**}p < 0.01$.

time of 95% gelation (t_{95}) or lag time (t_{lag}) at various DTM concentrations (**Figure 3I**).

Decellularized Testicular Matrix Hydrogel Enhanced SSC Survival

The effect of DTM hydrogel on the adherence and proliferation of SSC was investigated. SSCs were plated on DTM hydrogel (2.5, 5, and 10 mg/ml) scaffold, Matrigel scaffold, and laminin-coated dish for 7 days (**Figure 4A**). At the first day, SSCs spontaneously formed aggregates on all concentrations of DTM hydrogels and Matrigel scaffold but not on laminin-coated dish (**Figure 4B**). The number of SSC colonies formed on the 10 mg/ml DTM hydrogel was significantly higher than the other groups after the third day (**Figure 4C**).

After 7 days, calcein-AM and propidium iodide double staining revealed that most of the SSCs on the 10 mg/ml DTM hydrogels displayed high viability, indicated by green dots, and expanded on the surface of the scaffold. Additionally, there was very few dead

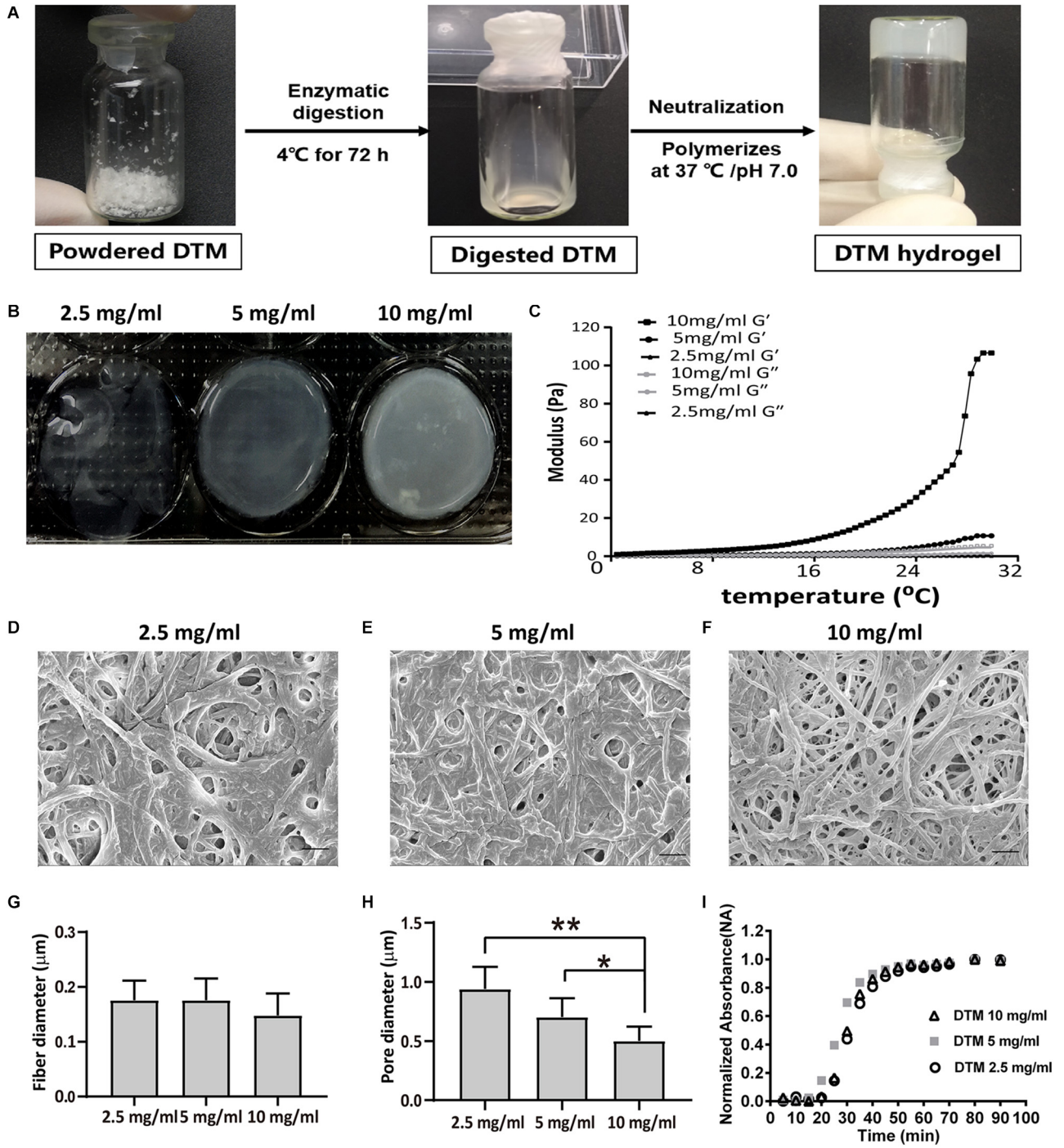


FIGURE 3 | Characterization of decellularized testicular matrix (DTM) hydrogel with DTM concentrations of 2.5, 5, and 10 mg/ml. **(A)** Schematic illustration showing the production of DTM hydrogel. **(B)** Macroscopic view of pH-neutralized DTM digests injected into 1.38 cm diameter rings at 37°C for 1 h. **(C)** Rheological characterization of DTM hydrogels. The gelation kinetics were determined by monitoring changes in the storage modulus (*G′*) and loss modulus (*G″*) after inducing gelation. Data represent the means for three independent experiments. **(D–F)** Scanning electron microscopy (SEM) images of DTM derived hydrogels formed at DTM concentrations of 2.5, 5, and 10 mg/ml. The scale bars represent 1 μm. **(G,H)** Fiber diameter and pore size of DTM hydrogels at concentrations of 2.5, 5, and 10 mg/ml. SEM images were analyzed using an automated fiber-tracking algorithm to determine the average fiber diameter and pore size of each concentration. Data were shown as mean ± SD, $n = 6$. Differences were considered statistically significant at $^{*}p < 0.05$, $^{**}p < 0.01$. **(I)** Turbidimetric gelation kinetics of DTM hydrogel at DTM concentrations of 2.5, 5, and 10 mg/ml. After DTM pepsin digests were pH neutralized, DTM were inoculated into a 96-well plate at 37°C to induce gelation. The absorbance at 405 nm was measured at 5-min intervals and normalized between 0 (the initial absorbance) and 1 (the maximum absorbance).

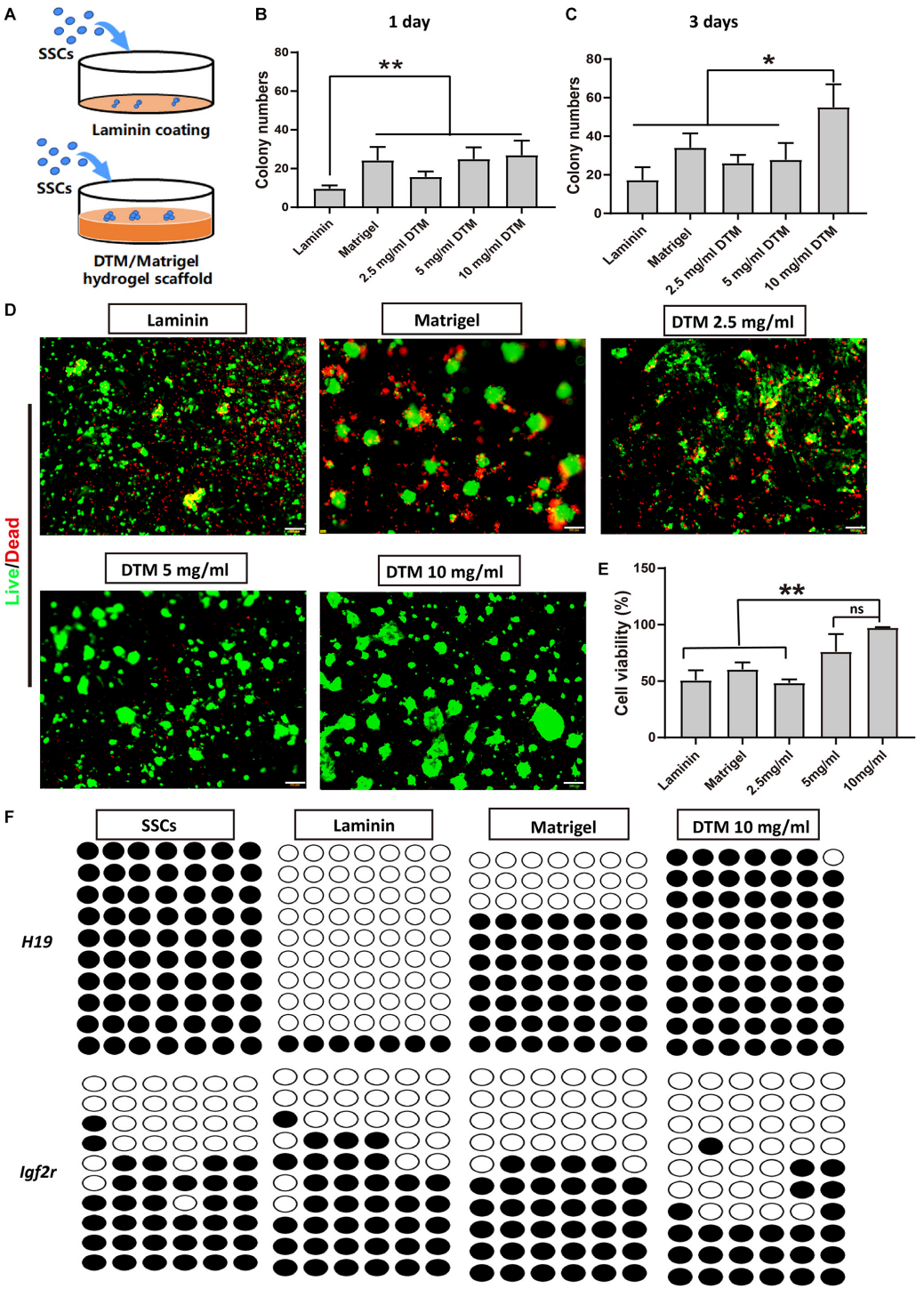


FIGURE 4 | Decellularized testicular matrix (DTM) hydrogel enhances spermatogonial stem cell (SSC) survival. **(A)** Schematic diagram of the experimental design. **(B,C)** The number of SSC colonies were analyzed at days 1 and 3. SSC cultured on the DTM hydrogels (2.5, 5, and 10 mg/ml) scaffold, Matrigel scaffold, and laminin-coated dish with SSC medium treatment. The number of colonies were measured by ImageJ software at a sample size of 100–500 μm^2 at the end of the first and third day. **(D)** Live/dead assays revealing the morphologies of SSC cultured on the DTM hydrogels with DTM concentrations of 2.5, 5, and 10 mg/ml, Matrigel, and laminin-coated dishes after 7 days. Green indicates live cells, and red indicates dead cells. Scale bar, 100 μm. **(E)** Cell survival rates of SSC were analyzed at day 7. Data are shown as mean ± SD, $n = 6$. Differences were considered statistically significant at $^{**}p < 0.01$. ns, no significant. **(F)** DNA methylation pattern of *H19* and *Igf2r* gene in SSCs. The DNA methylation status of paternally imprinted (*H19*) and maternally imprinted (*Igf2r*) genes in SSCs cultured on 10 mg/ml DTM hydrogels, Matrigel scaffold, and laminin-coated dish at day 7 were analyzed by bisulfite sequencing. Black circles represent methylated CpG sites, and white circles represent unmethylated CpG sites. CpG, 5′-C-phosphate-G-3′.

cells on 10 mg/ml DTM hydrogel, as indicated by red dots (**Figure 4D**). The percentage of viable SSC, 96.19 ± 3.11%, was significantly higher on 10 mg/ml DTM hydrogels than on laminin (50.71 ± 7.21%) or Matrigel (60.31 ± 5.06%) (**Figure 4E**).

Besides, the epigenetic stability of SSCs cultured on 10 mg/ml DTM hydrogels, Matrigel, and laminin was analyzed by bisulfite sequencing to determine the genomic imprinting pattern of the SSCs. Differentially methylated regions (DMRs) of the paternally imprinted *H19* gene and maternally imprinted *Igf2r* gene were examined. The level of *H19* methylation and *Igf2r* demethylation in SSCs seeded on DTM hydrogels was closer to native SSCs when compared with laminin and Matrigel. SSCs on Matrigel and laminin had decreased *H19* methylation, and the hypomethylation level of *Igfr2* was elevated (**Figure 4F**). Taken together, these results indicated that 10 mg/ml DTM hydrogel scaffolds provided a better environment to support SSC survival and maintain the native DNA methylation patterns of SSC; therefore, this concentration was used for further study.

Decellularized Testicular Matrix Maintains Stemness of SSCs

SSCs cultured on 10 mg/ml DTM hydrogels for 7 days displayed good adherence and colony formation (**Figure 5A**). Alkaline phosphatase activity was positive in the colonies formed on the DTM hydrogels (**Figure 5B**). SSCs cultured on DTM hydrogels expressed the SSC-specific gene markers (*Gfra1*, *c-Ret-1*, *c-Ret-2*, *Plzf*, and *Oct4*) (**Figure 5C**). There was no significant difference between SSC cultured on DTM and native SSC in expression (**Figures 5D,E**). SSC-specific surface proteins, integrin α6 (CD49f), integrin β6, and EpCAM (CD326) were positive in SSCs seeded on DTM hydrogel, while c-kit was negative (**Figure 5F**). However, the percentage of CD49f, integrin β6, and CD326 significantly decreased when SSC was seeded on laminin or Matrigel (**Supplementary Figure S1**). Therefore, the levels of genes and surface proteins of SSCs cultured on DTM hydrogels were similar to those of the native SSCs.

A spermatogonial transplantation assay was performed to determine the stem cell activity of SSCs cultured on DTM hydrogel. The SSCs were labeled with CFDA-SE, a fluorescent green dye, and transplanted into the seminiferous tubules of busulfan-treated adult mice through their efferent ducts (**Figure 6A**). One month after transplantation, the mice were euthanized, and their testes were removed and examined for expression of CFDA-SE. SSCs were observed along the rim of the tubules, indicating that they had settled into their designated niche, the basal compartment of the seminiferous tubules (**Figure 6B**). Histological analyses displayed that some meiotic and postmeiotic cells labeled with CFDA-SE were observed in the tubules of SSC-transplanted mice. Only spermatogonia were present in the control (**Figures 6C,D**). These results suggested that the DTM hydrogel scaffold could maintain stemness of SSCs *in vitro*, and these SSCs could colonize into testicular tubules and differentiate after transplantation.

DTM Hydrogel Promoted SSC Differentiation Into Round Spermatids

The influence of 10 mg/ml DTM hydrogels on SSC differentiation was evaluated by the addition of differentiation medium containing DMEM supplemented with FBS, testosterone, FSH, and RA for 7 days. Matrigel scaffold and laminin-coated dishes were used as controls (**Figure 7A**). The genes involved in spermatogonial differentiation or meiosis, *c-Kit*, *Stra8*, *Sycp3*, *Crem*, *Prm1*, and *Acrosin* were detected by quantitative RT-PCR (qRT-PCR). DTM hydrogel and Matrigel significantly promoted cells to express *c-Kit*, *Stra8*, and *Sycp3*. Meanwhile, the expression level of postmeiotic genes (*Crem*, *Prm1*, and *Acrosin*) in cells cultured on DTM hydrogel was greater than that on Matrigel and laminin (**Figure 7B**). Immunofluorescence revealed that more cells expressed acrosin, a protein of spermatids, in DTM compared to the Matrigel and laminin (**Figure 7C** and **Supplementary Figure S2**).

Furthermore, ploidy of SSCs on DTM, Matrigel, and laminin was assessed by flow cytometry. Round or elongated spermatids should be haploid (1N) as the result of two consecutive meiotic divisions; spermatogonia, secondary spermatocytes; somatic cells should be diploid (2N); and primary spermatocytes should be tetraploid (4N). On an average, the percentage of haploid cells was 40.4% in DTM greater than that of Matrigel. The cells cultured on laminin largely consisted of 2N and 4N subpopulations with a negligible amount of 1N cells, indicating cell arrest at the 2N or 4N stage (**Figures 7D,E**). Collectively, DTM hydrogel scaffold induced SSC differentiation into round spermatids without requiring the additional somatic cells. DTM hydrogel scaffolds may support SSC differentiation better than Matrigel and laminin.

DISCUSSION

In vivo, the functionality of SSCs is maintained by the testicular microenvironment (Dores et al., 2012). Tissue-specific ECM mimics the microenvironment of native tissue, which is important in stem cell proliferation and differentiation. It has been reported that ECMs were potential substrates for expansion of retinal progenitor cells (Kundu et al., 2016) and mesenchymal stem cells (Lin et al., 2012; Ng et al., 2014). To determine whether the testicular ECM supported SSCs' viability and proliferation effectively, we prepared DTM from the testicular tissue. After decellularization, 97.91% of cellular materials (DNA, cytosolic proteins) were removed. An immunohistochemistry analysis revealed that the essential proteins (collagen I, collagen IV, fibronectin, and laminin) that confer the structural and functional properties of the testis were preserved.

Since three-dimensional hydrogel scaffolds have a complex structure, they absorb and retain large volumes of water and exhibit plasticity similar to that of the microstructure of native extracellular matrix (Tibbitt and Anseth, 2009; Geckil et al., 2010), which greatly influence cell behavior (Lee et al., 2017; Romero-Lopez et al., 2017). The lyophilized DTM was solubilized by pepsin digestion and subsequently thermal induced to form porosity hydrogel scaffold. The hydrogel scaffolds possessed a

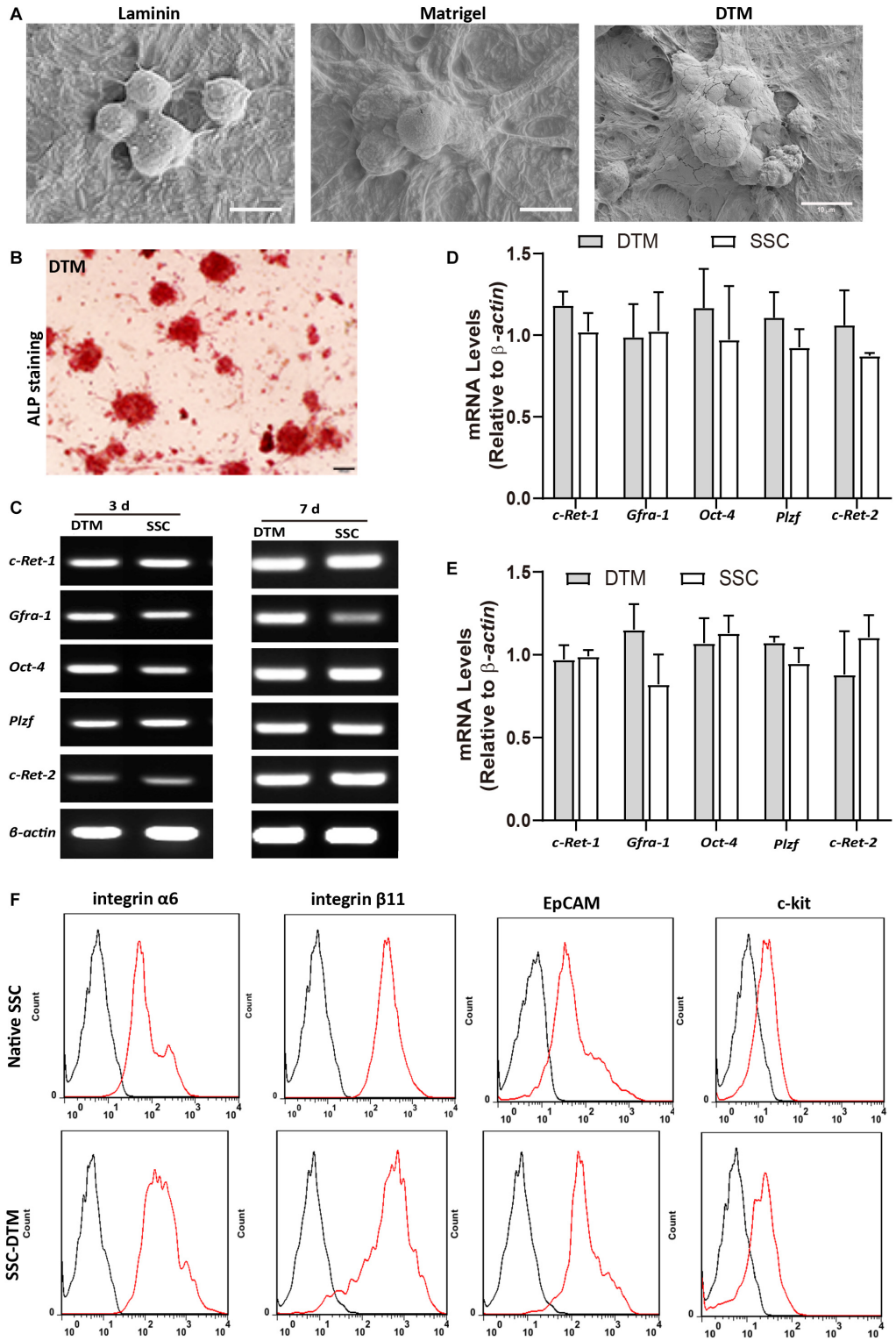


FIGURE 5 | Decellularized testicular matrix (DTM) hydrogel maintains stemness of spermatogonial stem cells (SSCs). **(A)** Scanning electron microscopy (SEM) image of SSCs seeded on 10 mg/ml DTM hydrogel at day 7. Scale bar, 10 μm. **(B)** Alkaline phosphatase activity of SSCs seeded onto 10 mg/ml DTM hydrogels at day 7. Scale bar, 100 μm. **(C)** Reverse transcription PCR (RT-PCR0 analysis of SSC-specific gene expression after 3 and 7 days of culture on 10 mg/ml DTM hydrogel scaffold. **(D,E)** The amount of relative expression was normalized to that of β-actin. **(F)** Fluorescence-activated cell sorting (FACS) analysis of the expression of SSC surface proteins after 7 days of culture on 10 mg/ml DTM hydrogel scaffold. The red histograms represent the cell count for the specific antibody, and the back histograms represent the fluorescence of the negative control.

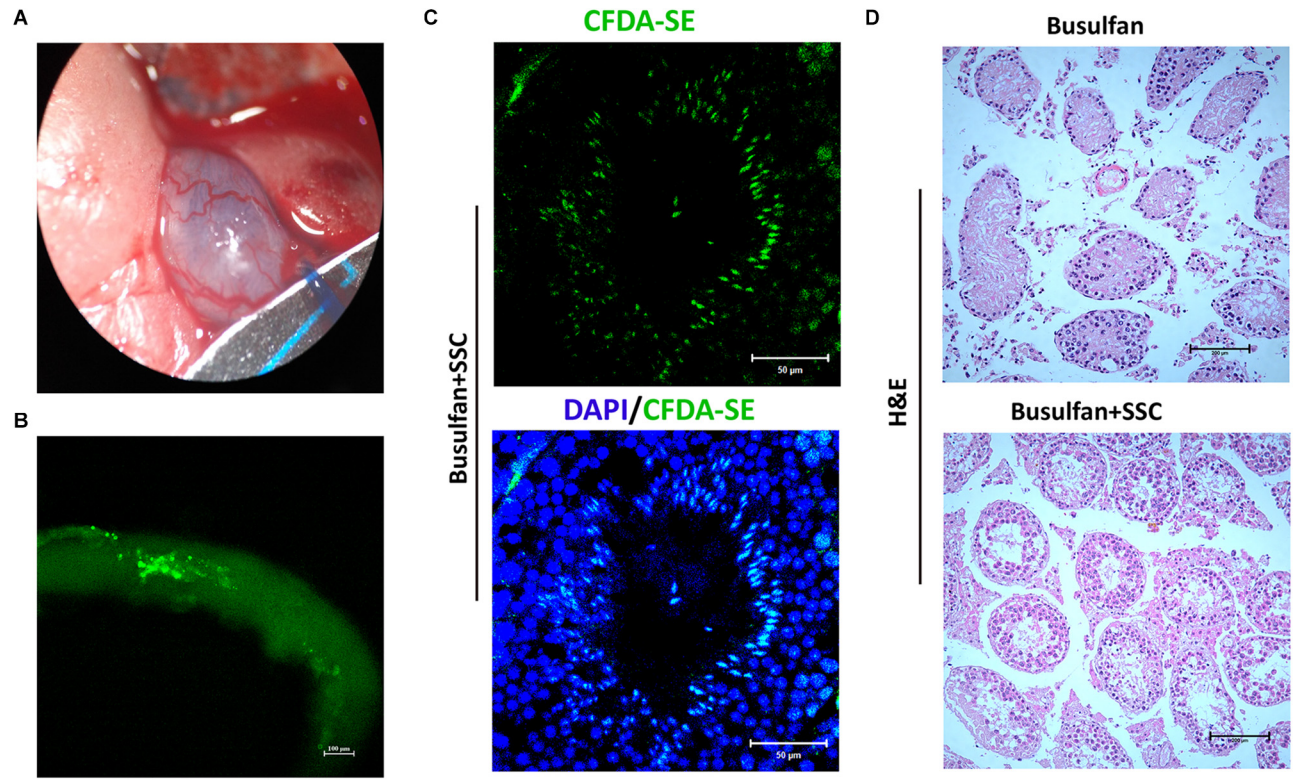


FIGURE 6 | Spermatogonial stem cell (SSC) transplants into testicular tubules. **(A)** Schematic illustration of SSC transplantation. Approximately 5×10^5 SSCs cultured on decellularized testicular matrix (DTM) hydrogels were micropipetted into the seminiferous tubules of mice 1 month after busulfan treatment (40 mg/kg). **(B)** Image of the recipient testicular tubule with fluorescence staining 35 days after SSC transplantation. **(C)** The testes were sectioned and stained with 4′,6-diamidino-2-phenylindole (DAPI) (blue) and examined under a fluorescent microscopy. Scale bars, 50 μm. **(D)** H&E staining of non-transplanted and transplanted recipient testis. The scale bars represent 200 μm.

randomly oriented fibrillar structure, and the pore size decreased with increased DTM concentrations, and exhibited sigmoidal gelation kinetics, which consistent with a nucleation and growth mechanism (Zhu et al., 2018). Previous studies (Kanatsu-Shinohara et al., 2011; Choi et al., 2014) have demonstrated that Matrigel and laminin supported SSC proliferation, but in this case, special SSC culture medium components, such as StemPro supplement, GDNF, fibroblast growth factor 2 (FGF2), stromal cell-derived factor-1 (SDF-1), EGF, and fetuin, were required. The medium was relatively complex, expensive, and time consuming to prepare. In our study, when SSCs were cultured on DTM hydrogel, it was able to attach and proliferate without DNA imprinting pattern changing in the absence of StemPro supplement and fetuin. However, laminin and Matrigel could not maintain the DNA imprinting pattern of SSC without StemPro supplement and fetuin. Besides, SSC propagated on DTM hydrogels displayed significantly higher cell viability and number of adherent colonies than that on Matrigel and laminin. The purity of SSC increased when the culture time extended. As a result, the gene expression of *Gfra-1* increased at day 7. These results indicated that DTM contained some factors that could maintain SSC activity and gene expression. The reason might be that pepsin cleaves the peptide bonds of the collagen triple helix structure to unravel collagen fibril aggregates (Miller, 1972) and produces a broad variety of bioactive peptides (Wu et al., 2015), which might play major roles in regulating cell proliferation, gene expression, and differentiation *in vitro*.

Regarding the differentiation of SSC, collagen gel matrixes (Lee et al., 2006, 2007), 3D soft agar culture system (SACS) (Stukenborg et al., 2008, 2009; Mahmoud, 2012), and 3D methylcellulose culture system (MCS) (Stukenborg et al., 2008; Khajavi et al., 2014; Huleihel et al., 2015) could induce murine male premeiotic germ cell differentiation into postmeiotic germ cell. However, these procedures depended on Sertoli cells. In our study, the hydrogel of DTM maintained SSCs' properties and promoted SSC differentiation into round spermatids without somatic cells, and the number of haploid cells in the DTM hydrogels was significantly higher than that in Matrigel and laminin. This result was in agreement with previous observations showing that native ECM hydrogel scaffolds directed stem cells to differentiate into a specific lineage, including osteogenic cells (Pati et al., 2015) and adipose stem cells (Yang et al., 2013). Native ECM hydrogel could provide a favorable environment for stem differentiation (Hoshiba et al., 2016; Saldin et al., 2017; Spang and Christman, 2018). Although we did not have a detailed description on the composition of the DTM, survival and

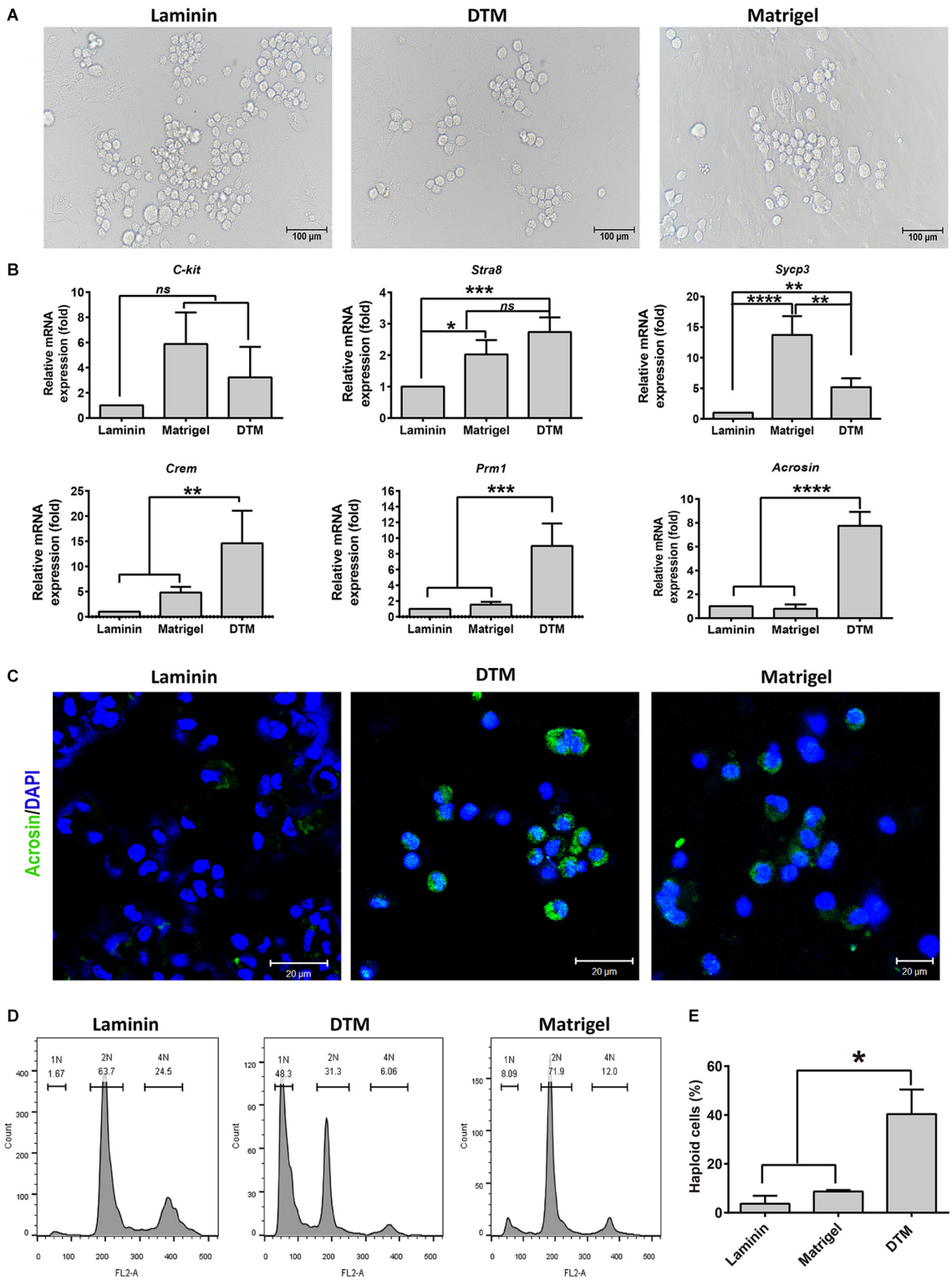


FIGURE 7 | Assessment of the spermatogonial stem cell (SSC) differentiation in decellularized testicular matrix (DTM) hydrogel culture system. **(A)** Images of cell differentiation under a phase contrast microscope. Scale bar, 100 μm. **(B)** Real-time PCR analysis of the gene expression involved in spermatogonial differentiation or meiosis. **(C)** Immunofluorescence showing the expression of Acrosin in the differentiated cells from SSCs. The scale bars represent 20 μm. **(D)** Flow cytometry showing DNA content in the differentiated cells from SSCs. **(E)** The percentage of haploid cells. SSCs cultured on DTM hydrogel, Matrigel scaffold, and laminin-coated dish with SSC differentiation medium treatment for 7 days. All quantitative data were obtained from three independent experiments and are presented as mean ± SD; differences were considered statistically significant at $^{***}p < 0.001$, $^{**}p < 0.01$, and $^{*}p < 0.05$.

meiosis occurrence in the DTM hydrogel scaffold were observed. The DTM hydrogel might support some bioactive substances to promote SSC differentiation into round spermatids, while Matrigel and laminin lack the complex organic components of testicular ECM. Therefore, the composition of the DTM deserves careful study in the future.

In summary, we found that hydrogel scaffolds containing 10 mg/ml DTM mimicked the testicular microenvironment, providing an alternative feeder-free culture system for SSC proliferation and differentiation. The hydrogel scaffold culture systems could provide us an efficient model to study the survival, proliferation, and meiosis of SSCs *in vitro*. Compared with the feeder culture system, the DTM hydrogel eliminates potential variability and contamination caused by feeder cells, and the process of testis-derived hydrogel was easier to standardize. This would contribute important knowledge to the fields of reproductive and cellular biology.

CONCLUSION

DTM was prepared from testicular tissues and induced to form porosity hydrogel scaffolds that possessed a randomly oriented fibrillar structure. Hydrogel scaffold containing 10 mg/ml DTM maintained the properties of SSCs at the molecular and cellular levels and promoted SSCs differentiating into round spermatids in the absence of somatic cells. The DTM hydrogel scaffold culture system is a simple and efficient feeder-free culture system and may provide a better environment to support SSC proliferation and differentiation. It might be a valuable tool for reproductive medicine.

DATA AVAILABILITY STATEMENT

The data that support the findings of this study are available from the corresponding author upon reasonable request.

ETHICS STATEMENT

The animal study was reviewed and approved by Institutional Animal Care and Use Committee of Jinan University. Written informed consent was obtained from the owners for the participation of their animals in this study.

AUTHOR CONTRIBUTIONS

YY, QiL, and CZ conducted the experiments. QuL, ZL, CZ, JL, HL, and JM analyzed the data. QZ, QX, and WX interpreted the data. YY and YH designed the research and wrote the manuscript. All authors reviewed, edited, and approved the manuscript.

FUNDING

This work received financial support from National Natural Science Foundation of China (81871150 and 31801235), Natural Science Foundation of Guangdong Province (2018A030313473), the Science and Technology Plan Project of Guangzhou (201508020001, 2016A020214013, 201803010044, and 201704YG066), Major Scientific and Technological Special Project of Administration of Ocean and Fisheries of Guangdong Province (to YH, 2017), and China Postdoctoral Science Foundation funded project (2017M622914).

SUPPLEMENTARY MATERIAL

The Supplementary Material for this article can be found online at: https://www.frontiersin.org/articles/10.3389/fcell.2020.00250/full#supplementary-material

REFERENCES

Aamodt, J. M., and Grainger, D. W. (2016). Extracellular matrix-based biomaterial scaffolds and the host response. *Biomaterials* 86, 68–82. doi: 10.1016/j.biomaterials.2016.02.003

Agmon, G., and Christman, K. L. (2016). Controlling stem cell behavior with decellularized extracellular matrix scaffolds. *Curr. Opin. Solid State Mater. Sci.* 20, 193–201. doi: 10.1016/j.cossms.2016.02.001

Baert, Y., De Kock, J., Alves-Lopes, J. P., Soder, O., Stukenborg, J. B., and Goossens, E. (2017). Primary human testicular cells self-organize into organoids with testicular properties. *Stem Cell Rep.* 8, 30–38. doi: 10.1016/j.stemcr.2016.11.012

Baert, Y., Stukenborg, J. B., Landreh, M., De Kock, J., Jornvall, H., Soder, O., et al. (2015). Derivation and characterization of a cytocompatible scaffold from human testis. *Hum. Reprod.* 30, 256–267. doi: 10.1093/humrep/deu330

Choi, N. Y., Park, Y. S., Ryu, J. S., Lee, H. J., Arauzo-Bravo, M. J., Ko, K., et al. (2014). A novel feeder-free culture system for expansion of mouse spermatogonial stem cells. *Mol. Cells* 37, 473–479. doi: 10.14348/molcells.2014.0080

de Rooij, D. G. (2009). The spermatogonial stem cell niche. *Microsc. Res. Tech.* 72, 580–585. doi: 10.1002/jemt.20699

de Rooij, D. G., and Russell, L. D. (2000). All you wanted to know about spermatogonia but were afraid to ask. *J. Androl.* 21, 776–798.

DeQuach, J. A., Yuan, S. H., Goldstein, L. S., and Christman, K. L. (2011). Decellularized porcine brain matrix for cell culture and tissue engineering scaffolds. *Tissue Eng. Part A* 17, 2583–2592. doi: 10.1089/ten.TEA.2010.0724

Dores, C., Alpaugh, W., and Dobrinski, I. (2012). From in vitro culture to in vivo models to study testis development and spermatogenesis. *Cell Tissue Res.* 349, 691–702. doi: 10.1007/s00441-012-1457-x

Geckil, H., Xu, F., Zhang, X., Moon, S., and Demirci, U. J. N. (2010). Engineering hydrogels as extracellular matrix mimics. *Nanomedicine* 5, 469–484. doi: 10.2217/nnm.10.12

Guan, K., Wolf, F., Becker, A., Engel, W., Nayernia, K., and Hasenfuss, G. (2009). Isolation and cultivation of stem cells from adult mouse testes. *Nat. Protoc.* 4, 143–154. doi: 10.1038/nprot.2008.242

Hofmann, M.-C. (2008). Gdnf signaling pathways within the mammalian spermatogonial stem cell niche. *Mol. Cell. Endocrinol.* 288, 95–103. doi: 10.1016/j.mce.2008.04.012

Hoshiba, T., Chen, G., Endo, C., Maruyama, H., Wakui, M., Nemoto, E., et al. (2016). Decellularized extracellular matrix as an in vitro model to study the comprehensive roles of the ECM in stem cell differentiation. *Stem Cells Int.* 2016:6397820. doi: 10.1155/2016/6397820

Huleihel, M., Nourashrafeddin, S., and Plant, T. M. (2015). Application of three-dimensional culture systems to study mammalian spermatogenesis, with an

emphasis on the rhesus monkey (*Macaca mulatta*). *Asian J. Androl.* 17, 972–980. doi: 10.4103/1008-682X.154994

Kanatsu-Shinohara, M., Inoue, K., Ogonuki, N., Morimoto, H., Ogura, A., and Shinohara, T. (2011). Serum- and feeder-free culture of mouse germline stem cells. *Biol. Reprod.* 84, 97–105. doi: 10.1095/biolreprod.110.086462

Kanatsu-Shinohara, M., Ogonuki, N., Inoue, K., Miki, H., Ogura, A., Toyokuni, S., et al. (2003). Long-term proliferation in culture and germline transmission of mouse male germline stem cells. *Biol. Reprod.* 69, 612–616. doi: 10.1095/biolreprod.103.017012

Khajavi, N., Akbari, M., Abolhassani, F., and Dehpour, A. R. (2014). Role of somatic testicular cells during mouse spermatogenesis in three-dimensional collagen gel culture system. *Cell J.* 16, 79–90.

Ko, K., Tapia, N., Wu, G., Kim, J. B., Bravo, M. J. A., Sasse, P., et al. (2009). Induction of pluripotency in adult unipotent germline stem cells. *Cell Stem Cell* 5, 87–96. doi: 10.1016/j.stem.2009.05.025

Kundu, J., Michaelson, A., Talbot, K., Baranov, P., Young, M. J., and Carrier, R. L. (2016). Decellularized retinal matrix: natural platforms for human retinal progenitor cell culture. *Acta Biomater.* 31, 61–70. doi: 10.1016/j.actbio.2015.11.028

Lee, H., Han, W., Kim, H., Ha, D. H., Jang, J., Kim, B. S., et al. (2017). Development of liver decellularized extracellular matrix bioink for three-dimensional cell printing-based liver tissue engineering. *Biomacromolecules* 18, 1229–1237. doi: 10.1021/acs.biomac.6b01908

Lee, J. H., Gye, M. C., Choi, K. W., Hong, J. Y., Lee, Y. B., Park, D. W., et al. (2007). In vitro differentiation of germ cells from nonobstructive azoospermic patients using three-dimensional culture in a collagen gel matrix. *Fertil. Steril.* 87, 824–833. doi: 10.1016/j.fertnstert.2006.09.015

Lee, J. H., Kim, H. J., Kim, H., Lee, S. J., and Gye, M. C. (2006). In vitro spermatogenesis by three-dimensional culture of rat testicular cells in collagen gel matrix. *Biomaterials* 27, 2845–2853. doi: 10.1016/j.biomaterials.2005.12.028

Lin, H., Yang, G., Tan, J., and Tuan, R. S. (2012). Influence of decellularized matrix derived from human mesenchymal stem cells on their proliferation, migration and multi-lineage differentiation potential. *Biomaterials* 33, 4480–4489. doi: 10.1016/j.biomaterials.2012.03.012

Mahmoud, H. (2012). Concise review: spermatogenesis in an artificial three-dimensional system. *Stem Cells* 30, 2355–2360. doi: 10.1002/stem.1238

Medberry, C. J., Crapo, P. M., Siu, B. F., Carruthers, C. A., Wolf, M. T., Nagarkar, S. P., et al. (2013). Hydrogels derived from central nervous system extracellular matrix. *Biomaterials* 34, 1033–1040. doi: 10.1016/j.biomaterials.2012.10.062

Miller, E. J. (1972). Structural studies on cartilage collagen employing limited cleavage and solubilization with pepsin. *Biochemistry* 11, 4903–4909. doi: 10.1021/bi00776a005

Murdock, M. H., David, S., Swinehart, I. T., Reing, J. E., Tran, K., Gassei, K., et al. (2019). Human testis extracellular matrix enhances human spermatogonial stem cell survival in vitro. *Tissue Eng. Part A* 25, 663–676. doi: 10.1089/ten.TEA.2018.0147

Nasiri, Z., Hosseini, S. M., Hajian, M., Abedi, P., Bahadorani, M., Baharvand, H., et al. (2012). Effects of different feeder layers on short-term culture of prepubertal bovine testicular germ cells in-vitro. *Theriogenology* 77, 1519–1528. doi: 10.1016/j.theriogenology.2011.11.019

Ng, C. P., Sharif, A. R., Heath, D. E., Chow, J. W., Zhang, C. B., Chan-Park, M. B., et al. (2014). Enhanced ex vivo expansion of adult mesenchymal stem cells by fetal mesenchymal stem cell ECM. *Biomaterials* 35, 4046–4057. doi: 10.1016/j.biomaterials.2014.01.081

Paduano, F., Marrelli, M., Alom, N., Amer, M., White, L. J., Shakesheff, K. M., et al. (2017). Decellularized bone extracellular matrix and human dental pulp stem cells as a construct for bone regeneration. *J. Biomater. Sci. Polym. Ed.* 28, 730–748. doi: 10.1080/09205063.2017.1301770

Park, K. M., Hussein, K. H., Hong, S. H., Ahn, C., Yang, S. R., Park, S. M., et al. (2016). Decellularized liver extracellular matrix as promising tools for transplantable bioengineered liver promotes hepatic lineage commitments of induced pluripotent stem cells. *Tissue Eng. Part A* 22, 449–460. doi: 10.1089/ten.TEA.2015.0313

Pati, F., Jang, J., Ha, D. H., Won Kim, S., Rhie, J. W., Shim, J. H., et al. (2014). Printing three-dimensional tissue analogues with decellularized extracellular matrix bioink. *Nat. Commun.* 5:3935. doi: 10.1038/ncomms4935

Pati, F., Song, T. H., Rijal, G., Jang, J., Kim, S. W., and Cho, D. W. (2015). Ornamenting 3D printed scaffolds with cell-laid extracellular matrix for bone tissue regeneration. *Biomaterials* 37, 230–241. doi: 10.1016/j.biomaterials.2014.10.012

Rezaei Topraggaleh, T., Rezazadeh Valojerdi, M., Montazeri, L., and Baharvand, H. (2019). A testis-derived macroporous 3D scaffold as a platform for the generation of mouse testicular organoids. *Biomater. Sci.* 7, 1422–1436. doi: 10.1039/c8bm01001c

Romero-Lopez, M., Trinh, A. L., Sobrino, A., Hatch, M. M., Keating, M. T., Fimbres, C., et al. (2017). Recapitulating the human tumor microenvironment: colon tumor-derived extracellular matrix promotes angiogenesis and tumor cell growth. *Biomaterials* 116, 118–129. doi: 10.1016/j.biomaterials.2016.11.034

Saldin, L. T., Cramer, M. C., Velankar, S. S., White, L. J., and Badylak, S. F. (2017). Extracellular matrix hydrogels from decellularized tissues: structure and function. *Acta Biomater.* 49, 1–15. doi: 10.1016/j.actbio.2016.11.068

Simon, L., Ekman, G. C., Tyagi, G., Hess, R. A., Murphy, K. M., and Cooke, P. S. (2007). Common and distinct factors regulate expression of mRNA for ETV5 and GDNF, Sertoli cell proteins essential for spermatogonial stem cell maintenance. *Exp. Cell Res.* 313, 3090–3099. doi: 10.1016/j.yexcr.2007.05.002

Song, H. W., and Wilkinson, M. F. (2014). Transcriptional control of spermatogonial maintenance and differentiation. *Semin. Cell Dev. Biol.* 30, 14–26. doi: 10.1016/j.semcdb.2014.02.005

Spang, M. T., and Christman, K. L. (2018). Extracellular matrix hydrogel therapies: in vivo applications and development. *Acta Biomater.* 68, 1–14. doi: 10.1016/j.actbio.2017.12.019

Stukenborg, J. B., Schlatt, S., Simoni, M., Yeung, C. H., Elhija, M. A., Luetjens, C. M., et al. (2009). New horizons for *in vitro* spermatogenesis? An update on novel three-dimensional culture systems as tools for meiotic and post-meiotic differentiation of testicular germ cells. *Mol. Hum. Reprod.* 15, 521–529. doi: 10.1093/molehr/gap052

Stukenborg, J. B., Wistuba, J., Luetjens, C. M., Elhija, M. A., Huleihel, M., Lunenfeld, E., et al. (2008). Coculture of spermatogonia with somatic cells in a novel three-dimensional soft-agar-culture-system. *J. Androl.* 29, 312–329. doi: 10.2164/jandrol.107.002857

Takashima, S., Kanatsu-Shinohara, M., Tanaka, T., Morimoto, H., Inoue, K., Ogonuki, N., et al. (2015). Functional differences between GDNF-dependent and FGF2-dependent mouse spermatogonial stem cell self-renewal. *Stem Cell Rep.* 4, 489–502. doi: 10.1016/j.stemcr.2015.01.010

Tibbitt, M. W., and Anseth, K. S. (2009). Hydrogels as extracellular matrix mimics for 3D cell culture. *Biotechnol. Bioeng.* 103, 655–663. doi: 10.1002/bit.22361

Wu, J., Ding, Q., Dutta, A., Wang, Y., Huang, Y. H., Weng, H., et al. (2015). An injectable extracellular matrix derived hydrogel for meniscus repair and regeneration. *Acta Biomater.* 16, 49–59. doi: 10.1016/j.actbio.2015.01.027

Yang, G., Rothrauff, B. B., Lin, H., Gottardi, R., Alexander, P. G., and Tuan, R. S. (2013). Enhancement of tenogenic differentiation of human adipose stem cells by tendon-derived extracellular matrix. *Biomaterials* 34, 9295–9306. doi: 10.1016/j.biomaterials.2013.08.054

Zhang, Y., He, Y., Bharadwaj, S., Hammam, N., Carnagey, K., Myers, R., et al. (2009). Tissue-specific extracellular matrix coatings for the promotion of cell proliferation and maintenance of cell phenotype. *Biomaterials* 30, 4021–4028. doi: 10.1016/j.biomaterials.2009.04.005

Zhu, S., Yuan, Q., Yin, T., You, J., Gu, Z., Xiong, S., et al. (2018). Self-assembly of collagen-based biomaterials: preparation, characterizations and biomedical applications. *J. Mater. Chem. B* 6, 2650–2676. doi: 10.1039/c7tb02999c

Conflict of Interest: The authors declare that the research was conducted in the absence of any commercial or financial relationships that could be construed as a potential conflict of interest.

Copyright © 2020 Yang, Lin, Zhou, Li, Li, Cao, Liang, Li, Mei, Zhang, Xiang, Xue and Huang. This is an open-access article distributed under the terms of the Creative Commons Attribution License (CC BY). The use, distribution or reproduction in other forums is permitted, provided the original author(s) and the copyright owner(s) are credited and that the original publication in this journal is cited, in accordance with accepted academic practice. No use, distribution or reproduction is permitted which does not comply with these terms.

frontiers in Cell and Developmental Biology

ORIGINAL RESEARCH
published: 16 June 2020
doi: 10.3389/fcell.2020.00473

Three-Dimensional Compaction Switches Stress Response Programs and Enhances Therapeutic Efficacy of Endometrial Mesenchymal Stem/Stromal Cells

Alisa Domnina, Julia Ivanova, Larisa Alekseenko, Irina Kozhukharova, Aleksandra Borodkina, Natalia Pugovkina, Irina Smirnova, Olga Lyublinskaya, Irina Fridlyanskaya and Nikolay Nikolsky*

Department of Intracellular Signaling and Transport, Institute of Cytology of the Russian Academy of Sciences, Saint Petersburg, Russia

OPEN ACCESS

Edited by:
Andrei S. Chagin, Karolinska Institutet (KI), Sweden

Reviewed by:
Chao-Ling Yao, Yuan Ze University, Taiwan
Shanti Gurung, Hudson Institute of Medical Research, Australia

***Correspondence:**
Olga Lyublinskaya
o.lyublinskaya@mail.ru

Specialty section:
This article was submitted to Stem Cell Research, a section of the journal Frontiers in Cell and Developmental Biology

Received: *02 March 2020*
Accepted: *20 May 2020*
Published: *16 June 2020*

Citation:
Domnina A, Ivanova J, Alekseenko L, Kozhukharova I, Borodkina A, Pugovkina N, Smirnova I, Lyublinskaya O, Fridlyanskaya I and Nikolsky N (2020) Three-Dimensional Compaction Switches Stress Response Programs and Enhances Therapeutic Efficacy of Endometrial Mesenchymal Stem/Stromal Cells. Front. Cell Dev. Biol. 8:473. doi: 10.3389/fcell.2020.00473

Mesenchymal stem cells are currently tested as a promising tool for the treatment of a wide range of human diseases. Enhanced therapeutic potential of spheroids formed from these cells has been proved in numerous studies, however, the fundamental basics of this effect are still being discussed. In this work, we showed that endometrial mesenchymal stem/stromal cells (eMSCs) assembled in spheroids possess a higher therapeutic efficacy compared to cells grown in monolayer in the treatment of the defects that are non-specific for eMSC tissue origin – skin wounds. With the purpose to elucidate the possible causes of superior spheroid potency, we compared the tolerance of eMSC cultivated in spheres and monolayer to the stress insults. Using genetically encoded hydrogen peroxide biosensor HyPer, we showed that three-dimensional configuration (3D) helped to shield the inner cell layers of spheroid from the external H_2O_2-induced oxidative stress. However, the viability of oxidatively damaged eMSCs in spheroids appeared to be much lower than that of monolayer cells. An extensive analysis, which included administration of heat shock and irradiation stress, revealed that cells in spheroids damaged by stress factors activate the apoptosis program, while in monolayer cells stress-induced premature senescence is developed. We found that basal down-regulation of anti-apoptotic and autophagy-related genes provides the possible molecular basis of the high commitment of eMSCs cultured in 3D to apoptosis. We conclude that predisposition to apoptosis provides the programmed elimination of damaged cells and contributes to the transplant safety of spheroids. In addition, to investigate the role of paracrine secretion in the wound healing potency of spheroids, we exploited the *in vitro* wound model (scratch assay) and found that culture medium conditioned by eMSC spheroids accelerates the migration of adherent cells. We showed that 3D eMSCs upregulate transcriptional activator, hypoxia-inducible factor (HIF)-1, and secret ten-fold more HIF-1-inducible pro-angiogenic factor VEGF

(vascular endothelial growth factor) than monolayer cells. Taken together, these findings indicate that enhanced secretory activity can promote wound healing potential of eMSC spheroids and that cultivation in the 3D cell environment alters eMSC vital programs and therapeutic efficacy.

Keywords: mesenchymal stem cells, endometrial stem/stromal cells, spheroids, therapeutic potential, oxidative stress, heat shock, apoptosis, stress response

INTRODUCTION

Mesenchymal stem/stromal cells (MSCs) are the subject of numerous fundamental and applied research due to their unique biological properties and high therapeutic potential, proven by clinical trials (Bernardo et al., 2012; Fitzsimmons et al., 2018; Hoogduijn and Lombardo, 2019). Initially, in the mid-60s of the 20th century, MSCs were isolated from bone marrow (Friedenstein et al., 1970). Further, this type of cells was found in almost all connective tissues of the body – adipose tissue, umbilical blood, placenta, amniotic fluid, dental pulp, and endometrium (Andrzejewska et al., 2019). According to the criteria established by the International Society for Cellular Therapy (Dominici et al., 2006), cultured MSCs express surface markers CD90, CD105, and CD73, but do not show hematopoietic markers expression; possess the high adhesion capacity to plastic surfaces, fibroblast-like morphology, as well as ability to differentiate into adipocytes, chondrocytes and osteoblasts. Due to their immunomodulatory and pro-angiogenic properties proven in patients (Petinati et al., 2018), MSCs are currently considered to be an effective tool for the treatment of degenerative, autoimmune, and inflammatory diseases, as well as injuries and strokes (Wang et al., 2012). The majority of clinical trials use the cellular suspension of MSCs as the therapeutic agent. However, the latest research suggests putting into practice the MSCs, incorporated into various three-dimensional (3D) and tissue-like structures (Baptista et al., 2018; Nimiritsky et al., 2019; Yao et al., 2020). The imitation of tissue-like cell organization *in vitro* has become possible with the development of 3D models of cell growth, such as scaffolds based on different synthetic or natural materials and seeded with cells, as well as scaffold-free models – cell spheroids (Han et al., 2019).

Spheroids, originally emerged as 3D aggregates of tumor cells, have long been used in cell biology as a model for studying the hierarchical structure of tumors and their microenvironment, as well as for testing various antitumor drugs (Sant and Johnston, 2017). Later on, this model of cell growth has become applicable for the cultivation of MSCs isolated from different tissues (Bartosh et al., 2010; Baraniak and McDevitt, 2012; Lee et al., 2016; Cui et al., 2017; Domnina et al., 2018). When culturing in 3D configuration the plasticity of MSCs leads to the phenotype shifts and acquirement of the features unusual for their two-dimensional (2D) cultures (Yeh et al., 2014; Forte et al., 2017; Han et al., 2019). For instance, generation of the hypoxic zone in the center of spheroid causes the expression of hypoxia-associated genes, such as the key transcription factor induced by hypoxia, HIF-1 (hypoxia-inducible factor 1), which enhances the synthesis of pro-survival proteins and increase the adaptive abilities of cells. Cultivation in spheroids augmentes the angiogenic potential of MSCs due to increased secretion of growth factors (VEGF, HGF, and FGF2), enhances anti-inflammatory and anti-apoptotic MSC properties due to the upregulation of such genes as TSG-6 (TNFα-induced gene/protein 6), STC-1 (staniocalcin-1), and PGE2 (prostaglandin E2; Bartosh et al., 2010; Madrigal et al., 2014; Lee et al., 2016; Murphy et al., 2017). In addition, 3D MSC substantially enhance secretion of chemokines and cytokines, as well as expression of their receptors, such as CXCR4 (CXC chemokine receptor 4) and CMKLR1 (chemokine-like receptor 1) that stimulate their immunomodulatory and "homing" capacities (Zhang et al., 2012; Madrigal et al., 2014).

Changes in the molecular and functional properties of MSCs cultivated in spheroids open up the new prospects for the clinical use of these cells. Currently, numerous preclinical studies with the use of MSC spheres are conducted, aimed at the correction of various human diseases, such as skeletal system diseases, ischemic and cardiovascular disorders and wound healing (Wang et al., 2009; Amos et al., 2010; Bhang et al., 2012; Zhang et al., 2012; Emmert et al., 2013). We have previously demonstrated that transplantation of spheroids from human endometrial MSCs (eMSCs) can be used in the treatment of infertility (Domnina et al., 2018). Using a model of Asherman's syndrome in rats (a model of infertility caused by replacement of the normal endometrium with connective tissue as a result of damage), we showed that the intrauterine administration of eMSCs in spheroids results in a better therapeutic effect than the administration of eMSCs after cultivation in a monolayer. The therapeutic effect was assessed by the offspring number and by the number of offspring pregnancy in model animals (Domnina et al., 2018). In the current study, we use eMSC spheroids to heal the defects that are non-specific for eMSC tissue origin – skin wounds. We show that spheroid transplantation stimulates wound healing in experimental animals more efficiently than transplanting a suspension of cells cultured in a monolayer, and discuss the possible causes of the enhanced therapeutic potential of 3D eMSCs.

RESULTS

eMSC Spheroid Transplantation Stimulates Skin Wound Healing

We evaluated the effect of 3D eMSC transplantation on the wound healing process of experimental animals (rats). In these experiments, pieces of full-thickness skin (1.5 cm × 1.5 cm) on the rat back were excised to create a skin wounds

(**Figure 1A**). Immediately after, monolayer eMSC in suspension (4×10^6 cells/per wound) and eMSC spheroids (4×10^6 cells in total/per wound) were injected in PBS solution around the prepared full-thickness skin wounds. The administration of PBS was used as a negative control. On the day of surgery and every day thereafter the open wounds were photographed and the reduction of the wound size was analyzed (**Supplementary Figure S1A**). On day 10 (see **Figure 1A**), the rate of the wound closure was as follows: the wounds treated with eMSC spheroids were almost closed (85 ± 3%); the wounds treated with monolayer eMSCs were partly closed with new tissue (77 ± 2%); in control animals, where PBS solution was administered, wound closure was low (57 ± 4%). Moreover, on day 7 after transplantation, the thickness of granulation tissue and the length of the regenerating epithelium in histological sections were higher in the case of eMSC spheroids application compared to the control wounds (see **Figure 1B** and **Supplementary Figure S1B**). Complete wound healing was observed: on day 12 – for eMSC spheroids, on day 14 – for eMSC, cultivated in monolayer, on day 16 – for non-treated wounds (PBS).

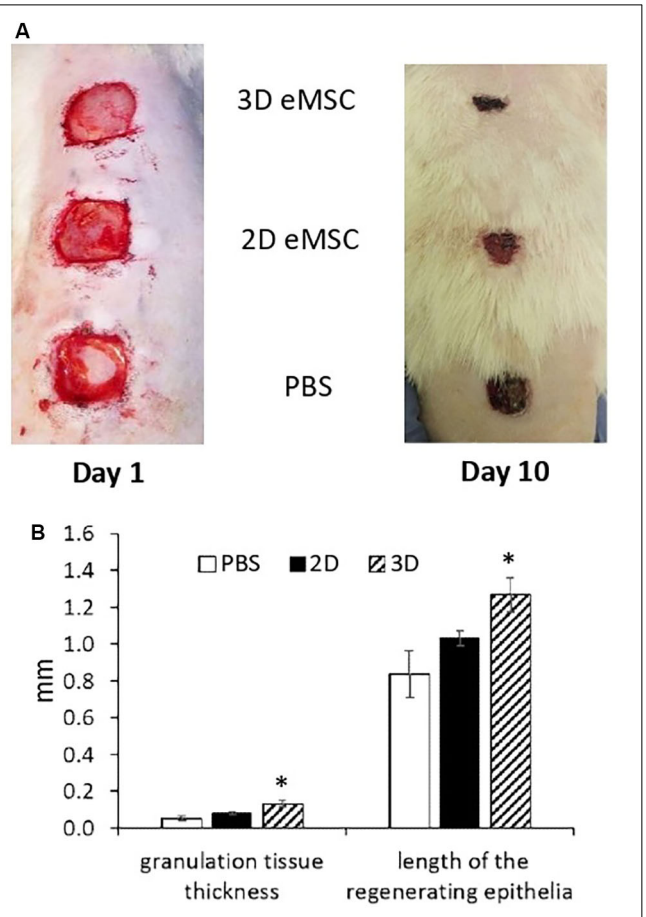


FIGURE 1 | Wound closure in rat after 2D and 3D eMSC transplantation. **(A)** Day 1 (left image) and 10 (right image) after eMSC (passage 7) transplantation. **(B)** Granulation tissue thickness and length of the regenerating epithelia in the rat wound on the seventh day after eMSC transplantation. Data are shown as mean ± SD. Two-tailed Student's *t*-test was utilized for pairwise comparison. $^*p < 0.05$ vs. PBS and 2D eMSCs.

The results presented in this section showed that eMSC spheroids can be applied to stimulate skin regeneration and that 3D eMSCs potentiate wound healing more effectively than 2D eMSCs. Next, we attempted to figure out which properties determine the high regenerative potential of spheroids.

Outer Cell Layers Protect a Spheroid Core From Oxidative Stress

The protection of inner cell layers in spheroids from the harmful impacts during transplantation is often considered as one of the possible causes of their high therapeutic potential.

Since the processes of tissue regeneration, including wound healing, are often accompanied by the local oxidative stress, we analyzed the response of cells cultivated in spheroids to H_2O_2-induced oxidative damage. We used eMSC line with stable expression of genetically encoded hydrogen peroxide biosensor HyPer-cyto (Belousov et al., 2006). This sensor is localized in cell cytosol and its ratiometric fluorescence signal is used as a measure of intracellular peroxide concentration.

Analysis of the dynamic changes in the HyPer fluorescence signal after addition of H_2O_2 (200 μM) to the spheroid culture medium showed that peroxide permeated only the outer layers of spheroids (**Figure 2A**). After 4 h of incubation, H_2O_2 was completely metabolized by the outer cells, and the HyPer signal returned to its basal level. In contrast to 3D eMSCs, cells in the monolayer culture, exposed to the same concentration of H_2O_2, were all subjected to peroxide oxidation (**Figure 2B**). DNA integrity test, carried out 1 h after H_2O_2 exposure revealed much more cells (83 ± 7% of total cell population) with histone H2AX phosphorylation foci (γH2AX foci) in the eMSC monolayer in comparison with cells, cultured in 3D (10 ± 3% of total cell population) (**Figures 2C–E**). This data confirm the shielding effect of the outer cell layers against the hydrogen peroxide damage in spheroids.

3D eMSCs Respond to Stress by Activating the Apoptosis Program

In the next batch of experiments, we investigated the fate of oxidatively damaged cells and compared the viability of 2D and 3D eMSCs treated with H_2O_2. Annexin V assay showed that H_2O_2-damaged spheroid cells appeared to be more prone to the activation of apoptotic program than monolayer cells. One day after treatment of eMSC spheroids with non-cytotoxic for monolayer eMSCs doses of peroxide (100–200 μM), a substantial fraction of the late apoptotic (AnV+/DAPI+) cells was detected in spheroids (**Figure 3A**). Due to the protection of the inner layers of spheroids from the action of peroxide by the outer cells, the dose of H_2O_2 which is consumed by each outer cell in a sphere is higher than the dose per one monolayer cell. This fact may explain the increased level of apoptosis in spheroids observed after the peroxide exposure. To find out whether spheroid cells damaged by other stress insults activate the apoptotic program as well, we performed experiments with the heat shock (45°C, 30 min). Annexin V test carried out 24 h after cell heating

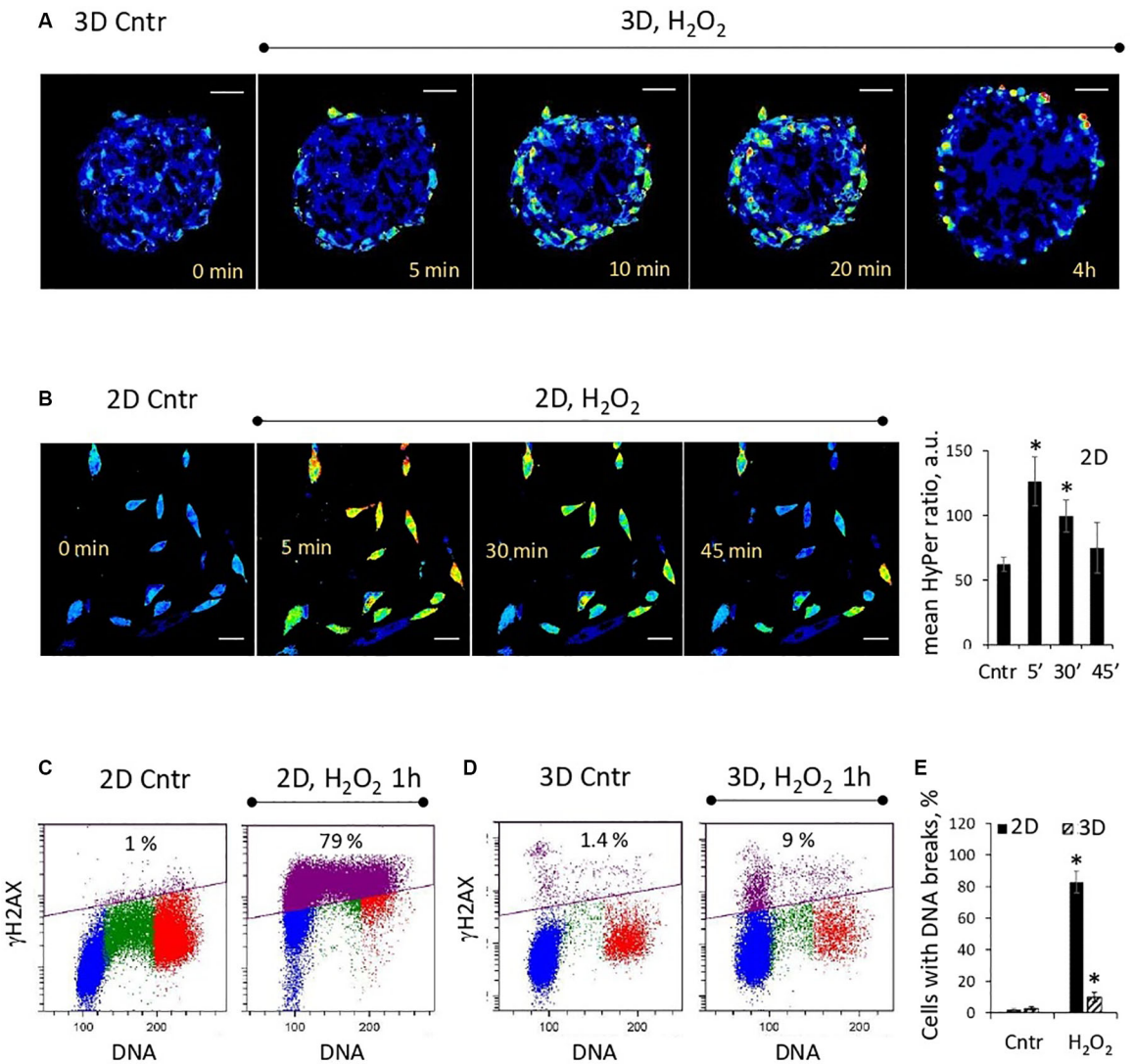


FIGURE 2 | Outer cell layers protect the inner cell mass of the spheroid from the damaging effects of oxidative stress. **(A)** Weak penetration of H_2O_2 inside the spheroids: ratiometric images of HyPer-expressing spheroids just after adding H_2O_2 (200 μM) to the cell medium. **(B)** Dynamics of H_2O_2 consumption by monolayer cells (passage 11): ratiometric images of HyPer-expressing cells just after adding H_2O_2 (200 μM) to the cell medium (left) and quantification of the mean HyPer ratio signal per cell (right). Data are shown as mean ± SD ($N = 15$). *$p < 0.05$ vs. the control values. **(C,D)** Flow cytometry assay for DNA breaks in 2D and 3D eMSCs (passage 12): test for γH2AX-positive cells, performed after 1-h exposition to 200 μM of H_2O_2. Blue, green and red markings correspond to cells in the G_0/G_1, S, and G_2/M phases of the cell cycle, respectively. Violet color marks γH2AX-positive cells. **(E)** Fraction of γH2AX-positive cells in 2D and 3D eMSCs treated with 200 μM of H_2O_2 for 1 h. Data are shown as mean ± SD ($N = 3$). *$p < 0.05$ vs. the control values. Scale bar: 50 μm. Cntr, control cells.

indicated the presence of both late (AnV+/DAPI+) and early (AnV+/DAPI−) apoptotic cell fractions in 3D eMSC samples (**Figure 3B**). Moreover, the early apoptosis, revealed by both the Annexin V binding assay (see **Figure 3B** and flow cytometry histograms in **Supplementary Figure S2**) and tests for active 3/7 caspase (**Figures 3D,E**), was detected in 3D cells within a few hours after the heat shock (3–6h). In contrast to spheroid cells, tests for apoptosis performed at different time points after heating of the monolayer cells did not show any signs of apoptotic program activation. In addition to experiments with heat shock and peroxide, we performed a series of experiments with irradiation of cells. Similar to other stresses, exposure of spheroids to 10 Gy induced apoptosis, detected one day after the insult, while monolayer cells almost did not change their viability after irradiation (**Figure 3C**).

To check the distribution of the dead cells in the spheres exposed to different stresses, we stained H_2O_2-treated spheroids with a vital dye, propidium iodide (PI), and compare the staining pattern with that observed after the sphere heating (**Figure 3F**). In H_2O_2-exposed spheroids, dead cells were located only in the outer layers, whilst after the heat shock, dead cells were distributed evenly. This data additionally proves that 3D arrangement protects the inner cells of the spheres from the oxidative damage and death.

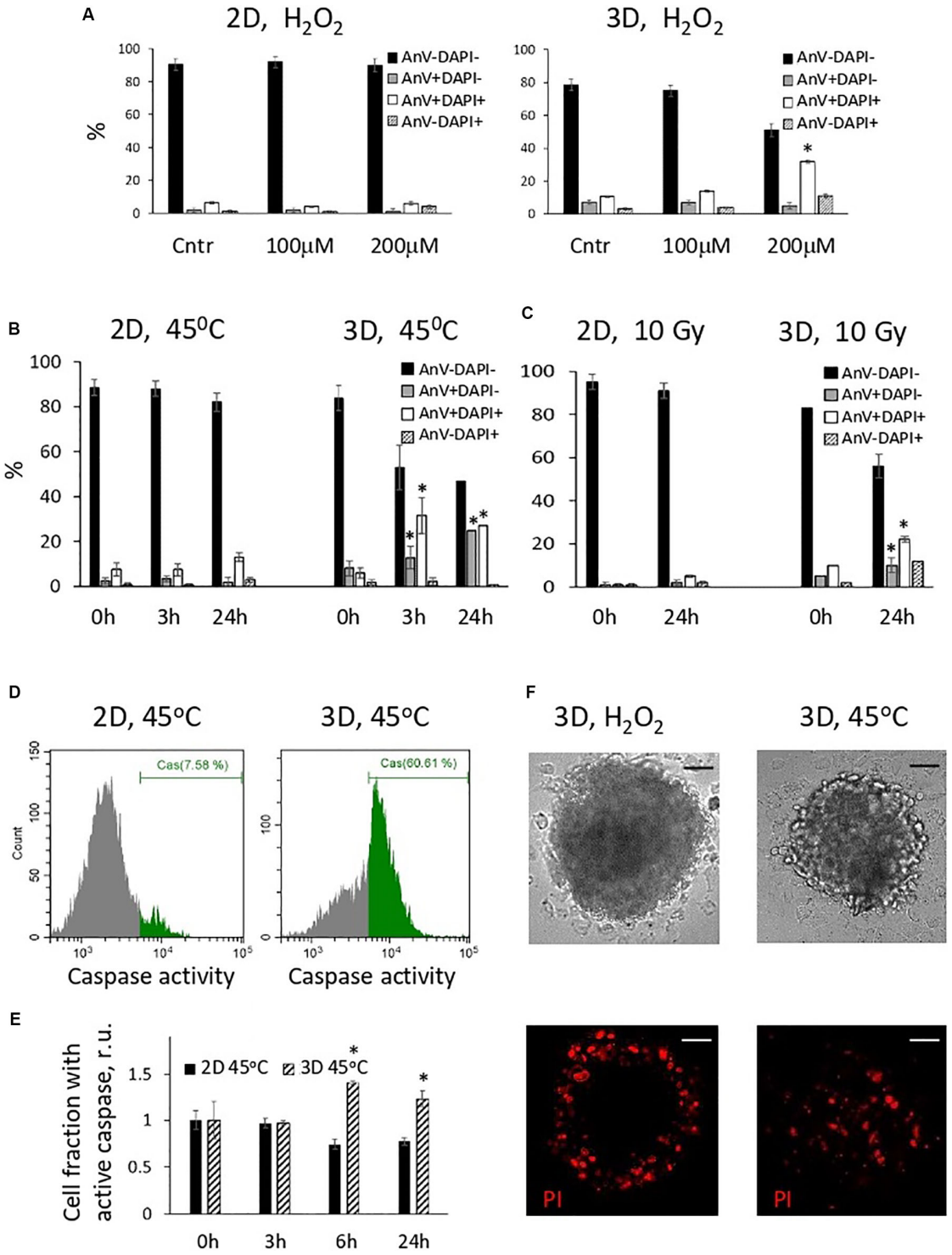


FIGURE 3 | Cells in spheroids, in contrast to monolayer eMSCs, activate apoptotic program in response to stress-induced damaging effects. **(A–C)** Quantification of apoptotic cell fractions in 2D and 3D eMSCs exposed to oxidative stress **(A)**, heat shock **(B)**, and irradiation stress **(C)**; data are derived from the Annexin-V/DAPI flow cytometry assay performed 24 h **(A,C)**, or 3, and 24 h **(B)** after the stress insults. Data are shown as mean ± SD ($N = 3$). For early (AnV+/DAPI−) and late (AnV+/DAPI+) apoptotic cell fractions: $^*p < 0.05$ vs. the control values ($t = 0$ h). **(D)** Flow cytometry assay for 3/7 caspase activation in 2D and 3D eMSCs (passage 8) exposed to heat shock reveals cell fraction with caspase activity in 3D sample (test is performed 6 h after cell heating). **(E)** Quantification of cell fraction with active caspase in 2D and 3D eMSCs after the heating. Data are normalized to the control values ($t = 0$ h) and shown as mean ± SD ($N = 3$). $^*p < 0.05$ vs. the control. **(F)** Cell death in spheroids was confirmed by the propidium iodide staining performed 4 h after H_2O_2 (left) or heat treatments (right). Scale bar: 50 μm. Cntr, control cells; r.u., relative units; PI, propidium iodide.

Next, with the purpose to analyze the reasons for the high tendency of spheroids to the activation of apoptosis program under stressors, we tracked the activation of the stress response programs in eMSC spheroids and eMSC monolayer after heating. We compared the expression of the genes responsible for the activation of HSR (Heat Shock Response): molecular chaperones HSP70 and HSP90, DNAJB9 [DnaJ Heat Shock Protein Family (HSP40) Member B9], as well as the transcription factor that activates the expression of chaperon genes, HSF1. RT-PCR analysis (**Figure 4A**) revealed strong upregulation of HSR genes 3 h after heating of both 2D and 3D cells, but the expression pattern in 2D and 3D eMSCs was different. A significant (about 100-fold) increase in HSP70 expression was observed in heated vs. control 3D eMSCs, accompanied by the induction of HSP70 key regulator, HSF1. In contrast, heated 2D eMSCs upregulated HSP90 gene. The expression level of DNAJB9, the co-chaperone involved in endoplasmic reticulum-associated degradation of misfolded proteins, increased slightly in both 2D and 3D eMSCs. Basing on these observations, we supposed that the reason for low survival rate of eMSCs in spheroids exposed to stress was not a deficiency of protective mechanisms, but a high capacity for activation of the apoptosis program. To check this point, we analyzed the levels of both heat-stress-induced and basal expression of genes related to apoptosis in 2D and 3D cultures. After the heat treatment, 3D eMSCs upregulated pro-apoptotic genes (Bax and PUMA) and down-regulated anti-apoptotic Bcl-xL gene, whilst 2D eMSCs upregulated Bcl-xL. In addition, we found low basal level of anti-apoptotic Bcl-xL gene expression in eMSC spheroids in comparison to monolayer cells (**Figure 4B**). As autophagy process is often considered as a protective mechanism that prevents cells from undergoing apoptosis, we checked the basal expression of autophagy-related (ATG3 and BECN1) genes, which appeared to be about 2 times lower in eMSC spheroids than in eMSC monolayer (**Figure 4C**).

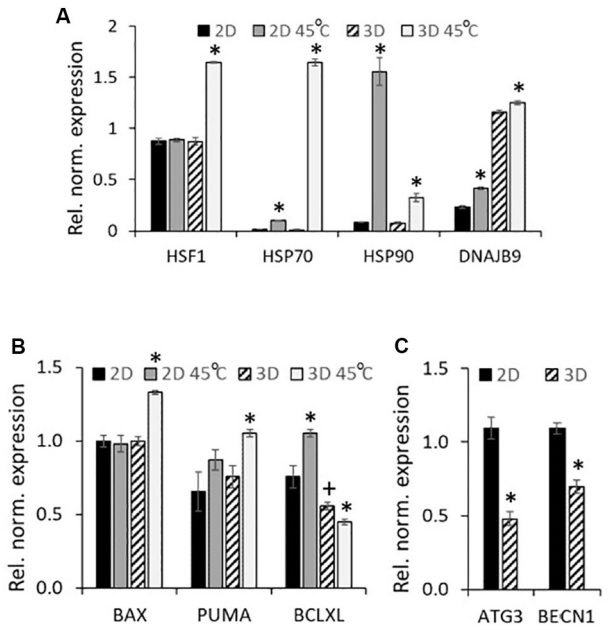


FIGURE 4 | eMSC heat shock-induced gene expression profiles: upregulation of HSR genes (2D and 3D eMSCs), pro-apoptotic genes (3D eMSCs) and anti-apoptotic genes (2D eMSCs). **(A,B)** Expression of heat shock response **(A)**, as well as pro- and anti-apoptotic **(B)** genes in 2D and 3D eMSCs exposed to heating (3 h after the treatment). **(C)** Basal expression of autophagy-related genes in 2D and 3D eMSCs. Data **(A–C)** are shown as mean ± SD ($N = 3$). $^{*}p < 0.05$ vs. the appropriate non-heated cells **(A,B)**, or vs. 2D eMSCs **(C)**. $^{+}p < 0.05$ vs. the 2D eMSC control **(B)**.

Taken together, these findings point out to the high commitment of 3D MSCs to apoptosis activated by the cell damage caused by various stresses (thermal, oxidative stress and cell irradiation). The next part of our work was devoted to the analysis of 2D and 3D eMSC progeny cells, survived after stress administration.

2D eMSCs Respond to Stress by Activating the Stress-Induced Premature Senescence Program

In our previous studies, we found that activation of the stress-induced premature senescence (SIPS) program is a typical response of 2D eMSCs to sublethal stresses (Alekseenko et al., 2014; Borodkina et al., 2014; Domnina et al., 2016; Kozhukharova et al., 2018; Kornienko et al., 2019). Here, we analyzed 2D eMSCs that survived incubation with 200 μM hydrogen peroxide (exposure causing apoptosis in 3D eMSC) and found signs of SIPS several days after H_2O_2 administration. As shown in **Figure 5**, H_2O_2-treated monolayer eMSCs stopped proliferating, as evidenced by cell growth curves. Moreover, flow cytometric analysis revealed in these cells a significant increase in the forward scatter signal (reflects the cell size), as well as in the ROS level measured using H_2DCFDA probe. We also found in H_2O_2-treated eMSCs activation of the classical p53/p21/Rb signaling pathway that causes cell cycle arrest. Finally, the activity of senescence-associated β-galactosidase was detected 5 days after H_2O_2 exposure. Our findings indicate the development of premature senescence in monolayer cells induced by H_2O_2 treatment.

In addition to oxidative stress, we traced the fate of 2D cells that survived the heat shock. In contrast to the apoptotic reaction of 3D eMSC, heat shock induced a stop in the proliferation of damaged monolayer cells (**Figure 6A**), which was accompanied by a prolonged S-G_2/M cell cycle block (**Figure 6C**) and expression of active senescence-associated β-galactosidase (**Figure 6D**). These results confirmed our previously published data and gave evidence about the induction of the SIPS program in 2D eMSC cultures that survived sublethal thermal stress (Alekseenko et al., 2014, 2018). To check whether 3D eMSCs that survived heat shock undergo stress-induced senescence, heated spheroids were dissociated 3 h after the stress, plated, and then were further cultured under adhesive monolayer conditions. Within a few days after the heat shock, we analyzed daily the distribution of the cell cycle phases and counted the number of 3D-derived eMSCs. Our experiments (**Figure 6C**) showed that one day after the stress, the descendants of both heated and control non-heated 3D eMSCs remained predominantly in the G_0/G_1 phase, in the state of the proliferation block which is

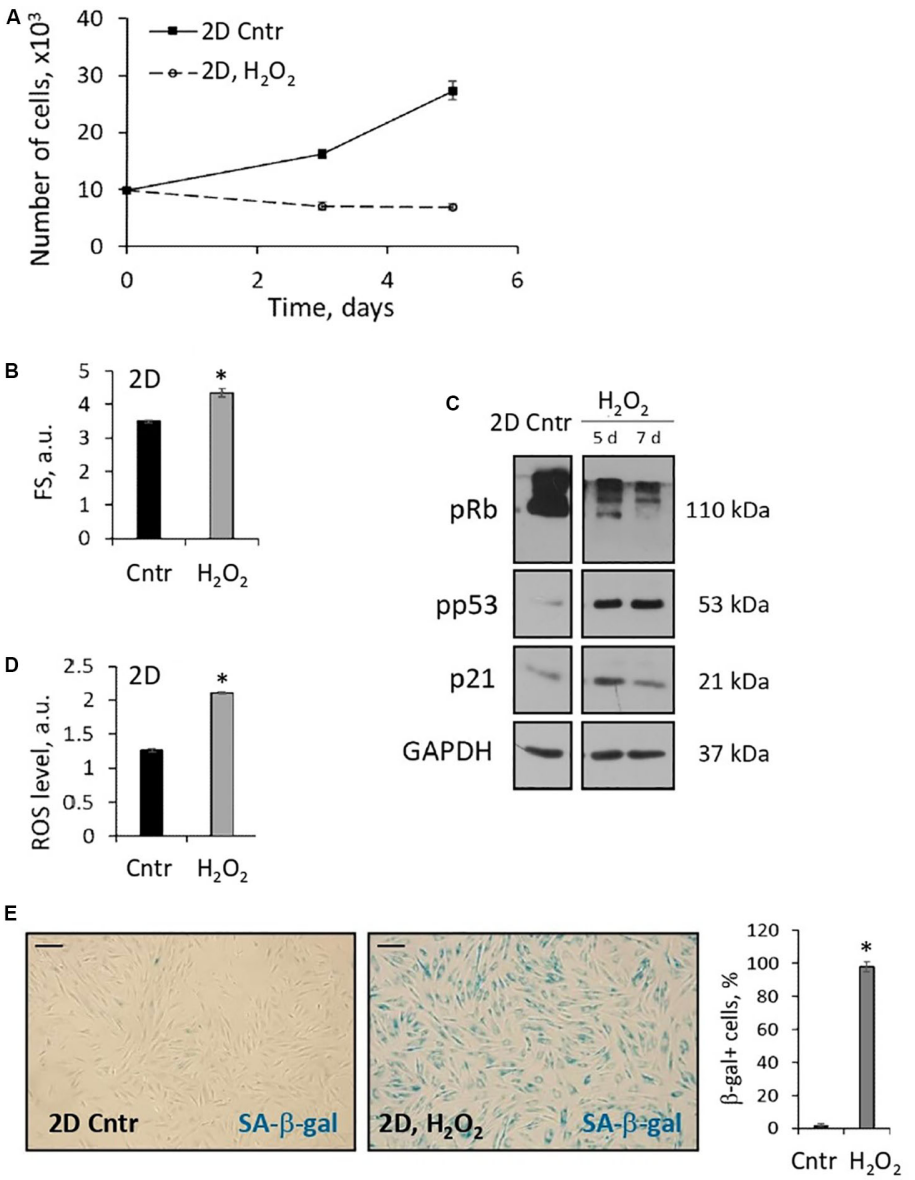


FIGURE 5 | 2D eMSCs respond to oxidative stress-induced damage by activation of premature senescence program. **(A)** Growth curves of H_2O_2-treated 2D eMSCs (passage 11) measured after the treatment. **(B)** Increase in the mean size of the H_2O_2-treated cells revealed by the forward scatter flow cytometry measurements (5 days after the treatment). **(D)** Increase of the ROS level in the H_2O_2-treated cells detected by flow cytometry analysis of H_2DCFDA stained cells (5 days after the treatment). **(C)** Expression of the molecular markers of cell senescence revealed in H_2O_2-treated cells by Western blotting (5 and 7 days after the treatment). **(E)** Activity of SA-β-gal in H_2O_2-treated cells (5 days after the treatment): images and quantification of SA-β-gal + cell fraction. Data in panels **(A–D)** are shown as mean ± SD ($N = 3$). *$p < 0.05$ vs. the control cells. Scale bar: 100 μm. Cntr, control cells; a.u., arbitrary units; FS, forward scattering; ROS, reactive oxygen species; SA-β-gal, senescence associated β-galactosidase.

typical for eMSCs cultured in spheroids (Domnina et al., 2018). At the same time, the amount of cells survived heating was significantly lower than the control values. Nevertheless, after several days, the survived descendants resumed division and did not differ in proliferation rates (**Figure 6B**) and cell cycle dynamics (**Figure 6C**) from the control 3D-derived eMSCs.

Thus, the results presented in this section show that eMSCs cultivated in monolayer respond to different types of stress by activating the SIPS program, while eMSCs cultivated in the configuration of spheroids are prone to stress-induced apoptosis, but not susceptible to the development of the premature senescence.

Secretory Capacity of eMSCs Cultivated in Spheroids

One more specificity of eMSCs cultured in spheroids that can contribute to their high regenerative potential may be the shift in

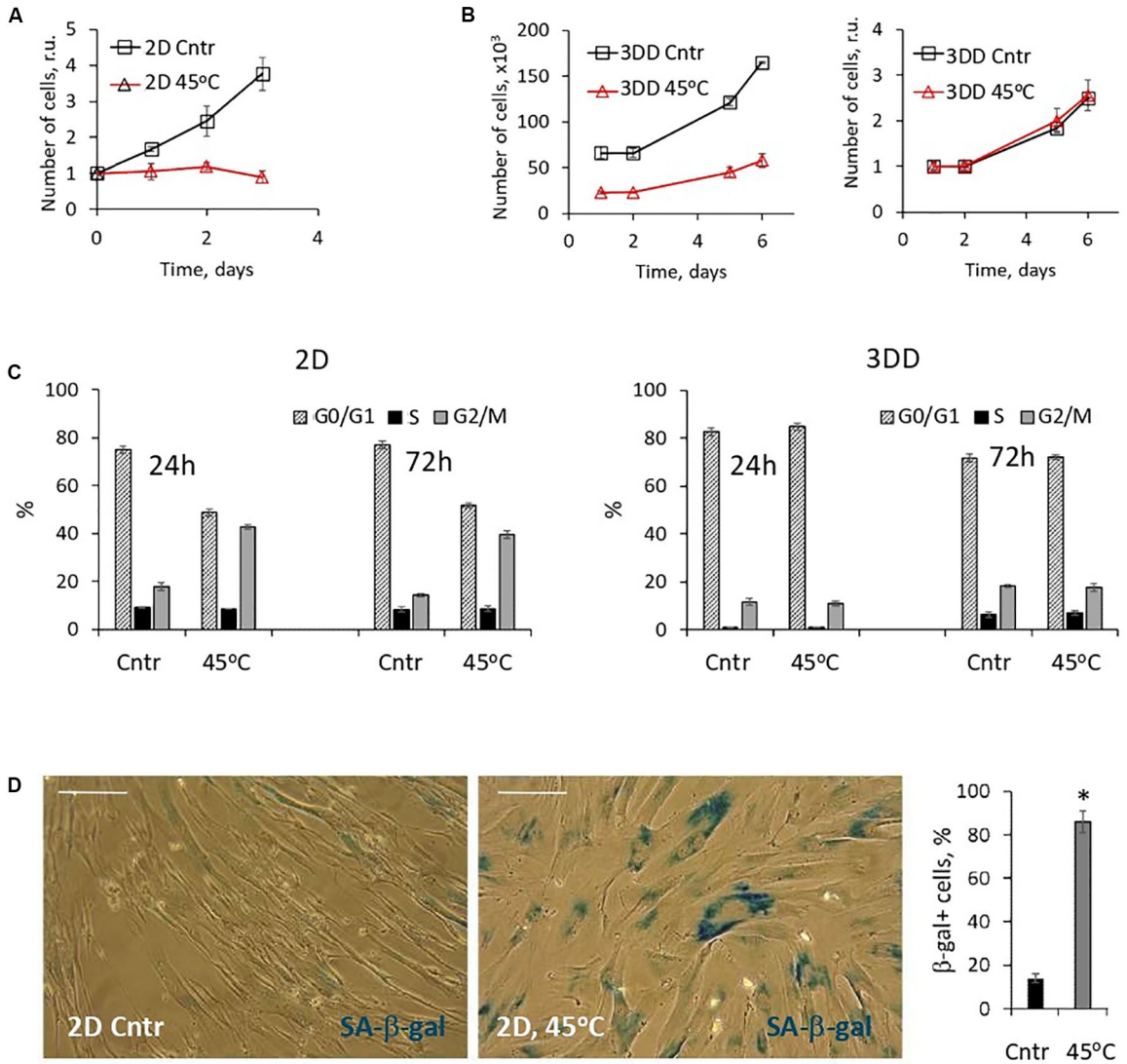


FIGURE 6 | 2D eMSCs, in contrast to 3D eMSCs, respond to the heat shock by activation of premature senescence program. **(A)** Growth curves of 2D eMSCs (passage 7) measured after the heat treatment. Data are normalized to the initial values. **(B)** Growth curves of 3DD eMSCs: cells were derived by trypsinization from the control spheroids and spheroids exposed to the heat shock, seeded as 2D culture, and after that counted daily. Curves reflect either the absolute number of cells in a dish (left), or relative numbers normalized to the initial values (right). Spheroids in this experiment were formed from eMSCs at passage 9. **(C)** Cell cycle phase distribution of 2D and 3DD eMSCs measured 24 and 72 h after the heat treatment. **(D)** Activity of SA-β-gal in 2D cells exposed to heating (5 days after the treatment): images and quantification of SA-β-gal + cell fraction. Data **(A–D)** are shown as mean ± SD ($N = 3$). Scale bar: 40 μm. Cntr, control cells; 3DD, 3D-derived cells; r.u., relative units; SA-β-gal, senescence associated β-galactosidase.

the cell secretory phenotype. In our previous work, we showed that cultivation in spheroids increases the expression of anti-inflammatory eMSC genes (Domnina et al., 2018). At the same time, the literature data indicates that in the case of MSCs from adipose tissue, bone marrow, and umbilical cord blood cultivated in spheroids, the secretion of angiogenic factors, such as vascular endothelial growth factor (VEGF), also increases (Madrigal et al., 2014). Using enzyme-linked immunosorbent assay (ELISA), we compared the basal level of VEGF-A secretion in eMSCs at different passages seeded both in3D and 2D configuration. In 2D eMSCs, VEGF secretion has been significantly reduced after cell passaging; however, 72-h culturing of eMSC in 3D structures markedly increased VEGF secretion at each cell passage (**Figure 7A**).

Vascular endothelial growth factor is known to be a cytokine whose secretion increases with hypoxia. Using the RT-PCR, we found that the high level of VEGF secretion in eMSC spheroids was accompanied by enhanced expression of the VEGF-A genes and the hypoxia-inducible factor HIF-1α, which controls the transcriptional activity of VEGF (**Figure 7B**).

To investigate the effect of soluble factors secreted by 3D eMSCs on wound healing, we carried out a scratch assay,

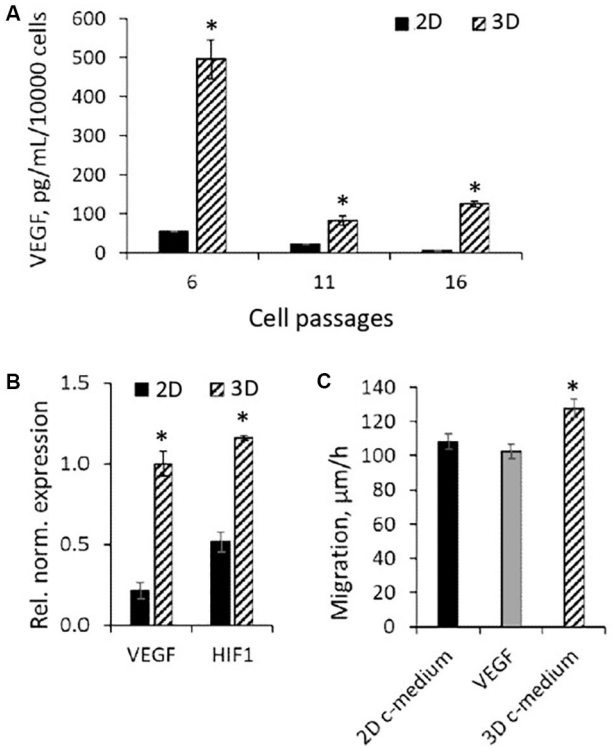


FIGURE 7 | Secretory activity of 3D eMSCs. **(A)** VEGF level measured by ELISA in the growth medium of eMSC spheroids formed from eMSCs of different passages. **(B)** Upregulation of HIF1 and VEGF genes in spheroids in comparison to monolayer grown eMSCs (passage 8). **(C)** Rate of eMSC (passage 9) migration into the cell-free area in the dish with growth medium conditioned by 3D and 2D eMSCs (passage 8), as well as medium supplemented with 10 ng of recombinant human VEGF. Data **(A–C)** are shown as mean ± SD ($N = 3$). *$p < 0.05$ vs. 2D eMSCs. 2D c-medium, growth medium conditioned by 2D eMSCs; 3D c-medium, growth medium conditioned by 3D eMSCs; VEGF [in panel (C)], growth medium supplemented with 10 ng of VEGF.

using condition medium from spheroids and monolayer as potential stimulators of cell migration (**Figure 7C**). The medium obtained from spheroids significantly increased the rate of scratch healing in comparison with 2D eMSCs, which indicates the stimulating effect of spheroid-secreted paracrine factors on cell motility during wound closure. At the same time, the addition of exogenous recombinant VEGF to the 2D eMSC medium did not enhance cell migration that points out to the complex character of the eMSC wound healing potency.

DISCUSSION

When developing cell technologies for the correction of various human pathologies, it is worth taking into account that cell therapeutic potential is determined by a whole range of functional and molecular characteristics of cells. This includes immune tolerance, resistance to stress, which prevents cell death during transplantation, the ability to secrete specific factors necessary for the treatment of pathologies, etc. Each of these characteristics deserves a detailed study for each type of pathology and type of transplanted material. In this article, using eMSCs as an example, we have proven the ability of these cells, cultured as spheroids and as monolayer, to correct defects that are non-specific for eMSC tissue origin – skin wounds. The therapeutic potential of spheroids turned out to be higher than that of cells cultured in a monolayer. By analyzing the possible causes of high therapeutic potency of eMSC spheroids, we compared the resistance of 3D and 2D eMSCs to the cytotoxic effect of stress insults, and evaluated the secretory properties of eMSCs cultivated in 2D and 3D cell environment.

In a comparative analysis of the 3D and 2D eMSC resistance to stress, we investigated cell response to different types of damaging effects. First, we studied the oxidative stress induced by exogenous hydrogen peroxide. H_2O_2 is a source of local oxidative stress that accompanies the process of inflammation in the regenerating tissues of the body. Our *ex vivo* experiments have shown that the outer cell layers in spheroids shield the damaging effects of exogenous H_2O_2. The antioxidant system of these cells effectively eliminates H_2O_2 and serves as a protective barrier that leaves the inner layers of cells intact. As a result, the number of cells with DNA damage in H_2O_2-treated spheroids is lower than that in the monolayer culture exposed to peroxide. It is worth noting that, in addition to the screening effect, the low level of DNA damage in spheroids observed in our experiments can be explained by the low proliferative index of 3D cells. Our analysis of the 3D eMSC cell cycle (Domnina et al., 2018) showed that cells in spheroids do not proliferate that means they are less susceptible to the DNA-damaging stress factors. In contrast to eMSCs from spheroids, actively proliferating monolayer cells are more sensitive to the genotoxic effect of stress (Alekseenko et al., 2018).

Further, we investigated the fate of cells damaged by oxidative stress. It turned out that under the same H_2O_2-treatment conditions, damaged cells of the outer layer of spheroids activated the apoptosis program and died, while 2D cells with damaged DNA survived. In addition, we compared the viability of 3D and 2D eMSCs after exposure to heat shock and irradiation. In all cases, stress led to the emergence of a high percentage of apoptotic cells in spheroids, while no apoptosis was detected in 2D eMSCs. To find out, whether the higher sensitivity of spheroid cells to stress can be an attribute of only eMSCs, we conducted experiments with 2D and 3D adipose MSCs and obtained similar results (not shown here): heat shock induced apoptosis in 3D MSCs, but did not lead to the death of monolayer cells.

Analysis of the HSR gene expression revealed significant upregulation of the chaperone genes in both 3D and 2D eMSCs after the heat stress, which demonstrates the high efficiency of the cell defense molecular mechanisms. Interestingly, the pattern of HSR gene expression in 3D and 2D eMSCs was different, which indicates diverse pathways of the protective response to stress.

Taken together, these data suggest that stress-induced death of cells in eMSC spheroids is not due to the deficiency of protective mechanisms, but due to the high commitment of 3D eMSCs to apoptosis. This assumption is further confirmed by the low basal expression of anti-apoptotic gene Bcl-xL and autophagy-controlling genes (ATG3 and BECN1). It is well

known that upon activation of apoptosis pathways in cells, an autophagy program that performs a cytoprotective function is often suppressed (Gordy and He, 2012), and we suppose that basal suppression of autophagy-controlling genes in 3D eMSCs may evidence about the predisposition to apoptosis even under the normal physiological conditions. It should be noted that our data are in a good agreement with the results obtained for cell spheroids consisting of the other types of MSCs (Bartosh et al., 2013). According to these studies, caspase activity observed in MSC spheroids stimulates the secretion of interleukins, which determines their anti-inflammatory properties and is thus one of the key fundamental properties of 3D MSCs that affect their therapeutic potential.

Next, our studies have shown, that in contrast to the apoptosis program, which is activated in damaged 3D eMSCs, a program of premature senescence of cells is initiated in 2D eMSC cultures exposed to stress. It is known that cells of different origin can respond differently to stressful insults. We previously showed that stress induces premature senescence in mesenchymal stem cells, but apoptosis in embryonic stem cells (Alekseenko et al., 2012, 2014). The results obtained in this work prove that 3D cultivation is able to switch the programs of eMSC stress response, cancel the activation of senescence pathways and activate the apoptotic program. We suggest that this effect can be associated with phenotypic shift, which is accompanied by the enhanced expression of the key pluripotent transcription factors Nanog and Sox observed in 3D cultured eMSC (Domnina et al., 2018). Summarizing our studies on the stress response of 3D eMSCs, in spite of the shielding effect of the outer cell layers in spheroids against some types of the cell damage (such as external oxidative stress), spheroid therapeutic potency is not related to maintaining high cell viability in case of damage during transplantation. Instead, we conclude that predisposition to apoptosis provides the programmed elimination of damaged cells that may contribute to the therapeutic efficiency and transplant safety of spheroids. Recently, it has been shown that damaged cells undergoing SIPS can be less effective and even dangerous in clinical applications. Senescent cells possess attenuated angiogenic potential (Ratushnyy et al., 2020), and when injected into an organism for the therapeutic needs, can induce inflammation and oncological transformation of healthy tissues due to the potentially harmful secretory phenotype (Turinetto et al., 2016).

In contrast, secretome of 3D-cultured cells can be considered in itself as a potent therapeutic agent. In our previous works on the use of eMSC spheroids for the treatment of infertility, we found that 3D cultivation of eMSCs significantly increases the expression of genes responsible for the anti-inflammatory factors secretion (Domnina et al., 2018). In the present work, we compared the ability of eMSCs cultured in 3D and 2D geometry to secrete VEGF, an endothelial vascular growth factor with angiogenic, trophic, and anti-apoptotic properties. We found that similar to spheroids from MSCs of adipose tissue, bone marrow, and umbilical cord blood, eMSC spheroids increase the level of VEGF secretion ten-fold compared to the eMSC monolayer. Using *in vitro* model of wound healing (scratch assay), we have shown that administration of conditioned 3D eMSC medium increases cell mobility and the rate of scratch closure to a greater extent than conditioned 2D eMSC medium, proving that enhanced secretory activity can promote wound healing potential of eMSC spheroids. At the same time, supplementation the culture medium with recombinant VEGF did not increase cell mobility that proves that high therapeutic potency of 3D cells is not due to high VEGF secretion only but instead is determined by the full repertoire of released molecules (such as chemokines, growth factors, miRNAs, etc.).

CONCLUSION

Transplantation of human eMSCs cultured as spheroids or as a monolayer into rats contributes to the treatment of skin wounds – the defects that are non-specific for the tissue origin of eMSCs. The therapeutic effect of eMSCs from spheroids exceeds the effect of eMSCs cultured in the monolayer configuration. In spite of the shielding effect of the outer cell layers in spheroids against some types of the cell damage (such as external oxidative stress), spheroid therapeutic potency is not related to maintaining high cell viability in case of damaging during transplantation. Cells in spheroids respond to damage induced by various stress insults by activating the apoptosis program, in contrast to monolayer cells in which a program of premature senescence is induced. In the *in vitro* wound healing model, administration of the conditioned 3D eMSC medium increases cell mobility and the rate of scratch closure to a greater extent than conditioned 2D eMSC medium, proving that enhanced secretory activity can promote wound healing potential of eMSC spheroids. Thus, cultivation in 3D cell environment alters eMSC vital programs and therapeutic efficacy.

MATERIALS AND METHODS

Cell Cultures

Human endometrial mesenchymal stem cell lines (eMSCs) were derived from a desquamated endometrium of menstrual blood from healthy donors (Zemel'ko et al., 2011). Endometrial MSCs express CD13, CD29, CD44, CD73, CD90, CD146, and CD105 surface markers and are negative for the hematopoietic markers CD34 and CD45, they possess the ability to differentiate into adipocytes, chondrocytes and osteoblasts (Zemel'ko et al., 2011). Cells were cultivated in DMEM/F12 growth medium (Gibco) containing 10% fetal bovine serum (FBS, HyClone), 1% L-glutamine (Gibco) and 1% penicillin-streptomycin (Gibco). Endometrial MSCs were maintained at 37°C in a humidified chamber with 5% CO_2 and subcultured twice per week. In this study we used cells from 3 to 12 passage. The experiments were approved by the Ethics Committee of the Almazov National Medical Research Centre (Saint Petersburg, Russia) and performed in accordance with the institutional guidelines. All cell donors signed an informed consent for voluntary participation.

Spheroid Formation

Spheroids (3D cultures) were formed from monolayer eMSCs (2D cultures) using the hanging drop technique. Seven thousand

cells per 35 μL of DMEM/F-12 medium containing 10% of FBS were placed in drops on the cover of 10-cm Petri dishes (Corning) and inverted. During the next 48 h, cells spontaneously aggregated in hanging drops and formed spheres, which were transferred then to dishes coated with 2-hydroxyethyl methacrylate (HEMA, Sigma) and cultured in 2 ml of full growth medium for 24 h.

Cell Treatments

Within this study cells were subjected to different stress insults – oxidative, thermal, and cell irradiation stresses. In each experiment, the cell count was equal (100,000 cells maintained as 2D or 3D culture in 2 ml of medium per 3 cm-diameter Petri dish). Oxidative stress was induced by incubation of eMSCs with hydrogen peroxide solution in the FBS free medium. To perform the heat shock experiments, dishes with 2D and 3D eMSC cultures were incubated at 45°C for 30 min in the water bath. For cell irradiation experiments eMSCs were exposed to 10 Gy doses of irradiation using a stationary X-ray device (0.49 Gy/min).

Live Cell Microscopy

Two-dimensional eMSCs and already formed eMSC spheroids, which both expressed genetically encoded biosensor of hydrogen peroxide HyPer, were placed in 4-well chambered coverglass plate (Thermo Fisher Scientific) with 750 μl of full growth medium per well. Cells were left overnight to ensure either the formation of monolayer (in the case of 2D cultures), or attachment and immobility of spheroids (in the case of 3D cultures). On the next day before the experiment, the complete medium was changed to serum-free DMEM/F-12, and the plate was placed to the confocal microscopy chamber (Olympus FV3000) maintained at 37°C. Two-hundred microliter of hydrogen peroxide was then added to each well and the consecutive shots in 405 nm and 488 nm channel were taken each 5 min. The obtained images were then processed using ImageJ software as described in Mishina et al. (2013). Image processing yields a ratiometric HyPer signal that visualize the hydrogen peroxide concentration profile inside individual cell. The similar image processing was applied for 2D eMSCs. Visualization of the dead cells in the spheres exposed to oxidative stress or heat treatment was achieved using PI staining (40 μg/ml, 20 min at 37°C) performed 4 h after the stress insults.

Apoptosis Assay

For detection of apoptosis in cells exposed to stress insults, 3, 6, or 24 h after the treatments both 2D and 3D cell cultures were trypsinized, suspended in the buffer solution and double-stained with 4′,6-diamidino-2-phenylindole (DAPI) and Annexin V Alexa Fluor 647 conjugate (Invitrogen^{TM}) according to the manufacturer's instructions. Cell samples were analyzed with CytoFLEX flow cytometer (Beckman Coulter, 405/633 nm lasers).

For detection of the caspase activity, 6 h after the treatments 2D and 3D cells were trypsinized, suspended in the growth medium and stained with CellEvent Caspase-3/7 Green Detection Reagent (Invitrogen^{TM}) for 20 min at 37°C. After the staining procedure, cell samples were analyzed with CytoFLEX flow cytometer (Beckman Coulter, 488 nm laser).

Cell Proliferation Assay

For analysis of the proliferative activity of cells exposed to stress insults, 2 h after the treatments, 2D and 3D cultures were trypsinized and plated as adherent cultures. Cells derived from the spheres are referred to as 3D-derived (3DD) cells. After seeding, once a day, 2D and 3DD cells were detached, counted, permeabilized with 0.1% Triton X-100 and stained for 5 min with 2 μg/ml of DAPI to perform the cell cycle analysis. Cell cycle phase distribution was measured with CytoFLEX S flow cytometer (Beckman Coulter, 375 nm laser).

DNA Damage Assay

One hour after H_2O_2 exposure, 2D and 3D cultures were trypsinized, washed twice with PBS, and then fixed/permeabilized using Nuclear Factor Fix and Perm Buffer Set (BioLegend). For specific detection of γH2AX foci accumulation, cells were incubated with anti-γH2AX antibodies (1:200, Abcam) for 1 h at room temperature in the dark. After washing with PBS, cells were incubated with 1:500 solution of goat-anti-mouse (GAM) Alexa Fluor 488 secondary antibodies and 1 μg/ml of DAPI for 30 min at room temperature in the dark. The γH2AX foci accumulation, as well as its distribution among the cell cycle phases, were then analyzed with CytoFLEX flow cytometer (Beckman Coulter, 405/488 nm lasers).

In vivo Wound Healing Assay

Twelve adult albino male Wistar rats with 230–250 g weight were used in experiments. The animals were maintained in the designated animal care facility with free access to tap water and food. All manipulations were done under aseptic conditions. Animals were anesthetized by intramuscular injection of Zoletil 100 (Virbac) in dose 5 mg/kg weight. The animal backs were shaved and disinfected with 70% alcohol. Three pieces of full-thickness skin (1.5 cm × 1.5 cm) on central side of the back were excised to create three skin wounds. Immediately after, monolayer eMSC in suspension (4×10^6 cells/per wound) and eMSC spheroids (4×10^6 cells in total/per wound) were implanted in 100 μl PBS solution around the prepared full-thickness skin wounds. The same volume of PBS without cells was used for the control wound. Finally, each animal was covered with bandage. On the day of surgery and every day thereafter the open wounds were photographed. The wound area was measured by tracing the wound margin and calculating pixel area using the image analyzer ImageJ (Rasband, 2012). The time of wound closure was defined as the time at which the wound bed was completely reepithelialized. The percentage of wound closure was calculated as follows: (area of original wound - area of actual wound)/area of original wound × 100% (Santos et al., 2015). A wound was considered completely closed when wound area was equal to zero. Some rats were sacrificed 7 days after surgery for histological examination. Collected skin tissue was fixed in 10% buffered formalin for 24 h and embedded in paraffin. The tissue blocks were cut into 5-mm-thickness sections followed by routine hematoxylin and eosin staining. Epithelialization (length of the regenerating epithelia) and granulation tissue thickness were assessed by the light microscopy.

All experimental procedures with animals were performed according to the Institutional guidelines for the care and use of laboratory animals. All studies on animals were performed after approval by the Institutional Animal Care and Use Committee of Institute of Cytology RAS (Assurance Identification number F18-00380).

In vitro Wound Healing Assay

For *in vitro* wound healing assay a standard *in vitro* technique for probing collective cell migration was used according to the recommendations (Jonkman et al., 2014).

We compared the dynamics of the migration into the cell-free area of 2D eMSCs, treated with culture medium, containing 1% FBS and 10 ng recombinant human VEGF (Gibco Life Technologies, United States) or conditioned growth medium from 2D and 3D eMSCs, containing 1% FBS. Two-well silicone insert (Ibidi) in a 24-well plates were used for gap creation. Twenty-five thousand cells in growth medium were seeded on both sides of the insert and incubated overnight after a confluent monolayer was formed. The next day inserts were removed, cells were washed and compared samples of medium were added to the wells. Photographs of the cells were taken at 0, 8 and 24 h to monitor the gap close. The gap size was measured as a function of time using Fiji/ImageJ software package.

Enzyme Linked Immunosorbent Assay

The concentration of VEGF in the cell medium was measured using ELISA kit DuoSet Human VEGF (R&D-system, United States) following the manufacturer's instructions. Quantification was performed by building a standard curve using known concentrations of human VEGF. Cell medium was collected from the same number of 2D and 3D cells incubated for 3 days in the growth medium with 1% FBS.

Detection of Cell Senescence

Three to five days after the stress insults, cells that express senescence associated β-galactosidase were detected in 2D cultures with the use of senescence β-galactosidase staining kit (Cell Signaling Technology, United States) according to the manufacturer's instructions. For each experimental point not less than 100 randomly selected cells were analyzed. Besides, the increase in the cell size and reactive oxygen species (ROS) production in the senescent cell cultures was assessed. For this purpose, 2D cells were incubated in the 5 μM staining solution of ROS-sensitive probe 2′,7′-dichlorodihydrofluorescein diacetate (H2DCFDA, Invitrogen, D399) in the serum-free medium for 30 min in the dark at 37°C. After that, cells were harvested, suspended in the fresh medium and immediately analyzed with CytoFLEX flow cytometer (Beckman Coulter, 488 nm laser). To evaluate the increase in the cell size which accompanies the senescence, forward scatter signal was monitored in the parallel experiments.

Western Blotting

Western blotting was performed as described previously (Borodkina et al., 2014). SDS-PAGE electrophoresis, transfer

TABLE 1 | The primers and conditions for qRT-PCR.

Symbol	Primer sequence	Amplification conditions	PCR product size (bp)	NCBI Reference Sequence
VEGF	F: 5′-CTACCTCCACCATGCCAAGT-3′ R: 5′-GATAGACATCCATGAACTTCACCA-3′	93°C, 20 s, 59°C, 20 s, 72°C, 30 s	95	NM_001025366.3
ATG3	F: 5′-GTGGCAGCGAGGACATTTTC-3′ R: 5′-CCATGTTGGACAGTGGTGGA-3′	93°C, 20 s, 60°C, 20 s, 72°C, 30 s	250	NM_001278712.2
Becn1	F: 5′-GGCTGAGAGACTGGATCAGG-3′ R: 5′-CTGCGTCTGGGCATAACG-3′	93°C, 20 s, 60°C, 20 s, 72°C, 30 s	127	NM_001313998.2
HIF1	F: 5′-CCGCCCGCTTCTCTCTAGT-3′ R: 5′-TGGCTGCATCTCGAGACTTT-3′	93°C, 20 s, 60°C, 20 s72°C 30 s	240	NM_181054.3
HSF1	F: 5′-CAGCTGATGAAGGGGAAGCA-3′ R: 5′-ACTGTCGTTCAGCATCAGGG-3′	93°C, 20 s, 60°C, 20 s, 72°C, 30 s	216	NM_005526.4
HSP70	F: 5′-ATGCGGCCAAGAACCAGGTG-3′ R: 5′-GCGCTGCGAGTCGTTGAAGT-3′	93°C, 20 s, 61°C, 20 s, 72°C, 30 s	307	NM_005345.5
HSP90	F: 5′-AATCGGAAGAAGCTTTCAGA-3′ R: 5′-GTGCTTGTGACAATACAGCA-3′	93°C, 20 s, 55°C, 20 s, 72°C, 30 s	446	NM_005348.3
HSP40	F: 5′-AGTCGGAGGGTGCAGGATATT-3′ R: 5′-TTGATTTGGCGCTCTGATGC-3′	93°C, 20 s, 60°C, 20 s, 72°C, 30 s	153	NM_012328.3
BclXl	F: 5′-GCTTGGATGGCCACTTACCT-3′ AS: 5′-GGGAGGGTAGAGTGGATGGT-3′	93°C, 20 s, 60°C, 20 s, 72°C, 30 s	231	NM_001317919.2
PUMA	F: 5′-GAC CTC AAC GCA CAG TAC GA-3′ R: 5′-CAC CTA ATT GGG CTC CAT CT-3′	93°C, 20 s, 60°C, 20 s, 72°C, 30 s	147	XM_006723141.3
BAX	F: 5′-GGG TTG TCG CCC TTT TCT-3′ R: 5′-CAG CCC ATG ATG GTT CTG ATC AG-3′	93°C, 20 s, 60°C, 20 s, 72°C, 30 s	91	NM_138763.4
GAPDH	F: 5′-GAGGTCAATGAAGGGGTCAT-3′ R: 5′-AGTCAACGGATTTGGTCGTA-3′	93°C, 20 s, 60°C, 20 s, 72°C, 30 s	100	NM_001357943.2

to nitrocellulose membrane and immunoblotting with ECL (Thermo Fisher Scientific, United States) detection were performed according to standard manufacturer's protocols (Bio-Rad Laboratories, United States). Antibodies against the following proteins were used: glyceraldehyde-3-phosphate dehydrogenase (GAPDH) (clone 14C10) (1:1000, #2118, Cell Signaling Technology, United States), phospho-p53 (Ser15) (clone 16G8) (1:700, #9286, Cell Signaling Technology, United States), p21Waf1/Cip1 (clone 12D1) (1:1000, #2947, Cell Signaling Technology, United States), phospho-Rb (Ser 807/811) (1:1000, #8516, Cell Signaling Technology, United States), well as horseradish peroxidase-conjugated goat anti-rabbit IG (GAR-HRP, Cell Signaling Technology, United States) (1:10000).

qRT-PCR Assays

To analyze gene expression, total RNA was isolated with RNeasy Micro Kit (Qiagen) according to the manufacturer's instructions. RNA concentration was quantified using NanoDrop ND-1000 Spectrophotometer (NanoDrop Technologies, Inc, Wilmington, DE, United States). cDNA was obtained by reverse transcription of 500 ng RNA using the RevertAid H Minus First Strand cDNA Synthesis Kit (Fermentas) according to the manufacturer's instructions. It was subsequently amplified with specific primers, using DreamTaq^{TM} PCR Master Mix (2X) (Thermo Fisher Scientific) with Cyclo Temp Amplificator. cDNA was amplified with specific primers, using EvaGreen® dye (Biotium) and DreamTaq^{TM} PCR Master Mix (2X) (Thermo Fisher Scientific) in the BioRad CFX-96 real time system (BioRad, CA, United States), according to the kit's enclosed protocol. The volume of PCR reactions was 20 μl. Expression of target genes was normalized to GAPDH gene. Primers and reaction conditions are presented in the **Table 1**. All amplification reactions were performed in triplicates. Each gene expression was calculated using Real-Time PCR Analysis Software BioRad, CA, United States. Experiments were repeated at least three times.

Statistical Analysis

All data are presented as the mean values of at least three independent experiments with standard deviations. Statistical significance was calculated using either ANOVA-Tukey test in case of multiple comparisons or Student's *t*-test in case of pair comparisons. p-values < 0.05 were considered significant.

DATA AVAILABILITY STATEMENT

All datasets generated for this study are included in the article/**Supplementary Material**.

ETHICS STATEMENT

The experiments were approved by the Ethics Committee of the Almazov National Medical Research Centre (Saint Petersburg, Russia) and performed in accordance with the institutional guidelines. All cell donors signed an informed consent for voluntary participation.

AUTHOR CONTRIBUTIONS

JI, AD, LA, IK, AB, IF, and OL wrote the main manuscript text and prepared figures. JI, AD, LA, IK, AB, IF, IS, NP, and OL performed experimental part of the work and analyzed data. NN and IF supervised the work. All authors reviewed the manuscript.

FUNDING

This work was supported by Russian Science Foundation grant #19-14-00108.

SUPPLEMENTARY MATERIAL

The Supplementary Material for this article can be found online at: https://www.frontiersin.org/articles/10.3389/fcell.2020.00473/full#supplementary-material

REFERENCES

Alekseenko, L. L., Shilina, M. A., Lyublinskaya, O. G., Kornienko, J. S., Anatskaya, O. V., Vinogradov, A. E., et al. (2018). Quiescent human mesenchymal stem cells are more resistant to heat stress than cycling cells. *Stem Cells Int.* 2018:3753547. doi: 10.1155/2018/3753547

Alekseenko, L. L., Zemelko, V. I., Domnina, A. P., Lyublinskaya, O. G., Zenin, V. V., Pugovkina, N. A., et al. (2014). Sublethal heat shock induces premature senescence rather than apoptosis in human mesenchymal stem cells. *Cell Stress Chaperones.* 19, 355–366. doi: 10.1007/s12192-013-0463-6

Alekseenko, L. L., Zemelko, V. I., Zenin, V. V., Pugovkina, N. A., Kozhukharova, I. V., Kovaleva, Z. V., et al. (2012). Heat shock induces apoptosis in human embryonic stem cells but a premature senescence phenotype in their differentiated progeny. *Cell Cycle* 11, 3260–3269. doi: 10.4161/cc.21595

Amos, P. J., Kapur, S. K., Stapor, P. C., Shang, H., Bekiranov, S., Khurgel, M., et al. (2010). Human adipose-derived stromal cells accelerate diabetic wound healing: impact of cell formulation and delivery. *Tissue Eng. Part A* 16, 1595–1606. doi: 10.1089/ten.TEA.2009.0616

Andrzejewska, A., Lukomska, B., and Janowski, M. (2019). Concise review: mesenchymal stem Cells: from roots to boost. *Stem Cells* 37, 855–864. doi: 10.1002/stem.3016

Baptista, L. S., Kronemberger, G. S., Côrtes, I., Charelli, L. E., Matsui, R. A. M., Palhares, T. N., et al. (2018). Adult stem cells spheroids to optimize cell colonization in scaffolds for cartilage and bone tissue engineering. *Int. J. Mol. Sci.* 19:1285. doi: 10.3390/ijms19051285

Baraniak, P. R., and McDevitt, T. C. (2012). Scaffold-free culture of mesenchymal stem cell spheroids in suspension preserves multilineage potential. *Cell Tissue Res.* 347, 701–711. doi: 10.1007/s00441-011-1215-5

Bartosh, T. J., Ylöstalo, J. H., Bazhanov, N., Kuhlman, J., and Prockop, D. J. (2013). Dynamic compaction of human mesenchymal stem/precursor cells into spheres self-activates caspase-dependent IL1 signaling to enhance secretion of modulators of inflammation and immunity (PGE2, TSG6, and STC1). *Stem Cells* 31, 2443–2456. doi: 10.1002/stem.1499

Bartosh, T. J., Ylöstalo, J. H., Mohammadipoor, A., Bazhanov, N., Coble, K., Claypool, K., et al. (2010). Aggregation of human mesenchymal stromal cells (MSCS) into 3d spheroids enhances their antiinflammatory properties. *Proc. Natl. Acad. Sci. U.S.A.* 107, 13724–13729. doi: 10.1073/pnas.1008117107

Belousov, V. V., Fradkov, A. F., Lukyanov, K. A., Staroverov, D. B., Shakhbazov, K. S., Terskikh, A. V., et al. (2006). Genetically encoded fluorescent indicator for intracellular hydrogen peroxide. *Nat. Methods* 3, 281–286. doi: 10.1038/nmeth866

Bernardo, M. E., Pagliara, D., and Locatelli, F. (2012). Mesenchymal stromal cell therapy: a revolution in regenerative medicine. *Bone Marrow Transplant.* 47, 164–171. doi: 10.1038/bmt.2011.81

Bhang, S. H., Lee, S., Shin, J. Y., Lee, T. J., and Kim, B. S. (2012). Transplantation of cord blood mesenchymal stem cells as spheroids enhances vascularization. *Tissue Eng. Part A* 18, 2138–2147. doi: 10.1089/ten.TEA.2011.0640

Borodkina, A., Shatrova, A., Abushik, P., Nikolsky, N., and Burova, E. (2014). Interaction between ROS dependent DNA damage, mitochondria and P38 MAPK underlies senescence of human adult stem cells. *Aging* 6, 481–495. doi: 10.18632/aging.100673

Cui, X., Hartanto, Y., and Zhang, H. (2017). Advances in multicellular spheroids formation. *J. R. Soc. Interface* 14:20160877. doi: 10.1098/rsif.2016.0877

Dominici, M., Blanc, K. L., Mueller, I., Slaper-Cortenbach, I., Marini, F., Krause, D., et al. (2006). Minimal criteria for defining multipotent mesenchymal stromal cells. The international society for cellular therapy position statement. *Cytotherapy* 8, 315–317. doi: 10.1080/14653240600855905

Domnina, A., Novikova, P., Obidina, J., Fridlyanskaya, I., Alekseenko, L., Kozhukharova, I., et al. (2018). Human mesenchymal stem cells in spheroids improve fertility in model animals with damaged endometrium. *Stem Cell Res. Ther.* 9:50. doi: 10.1186/s13287-018-0801-9

Domnina, A. P., Novikova, P. V., Lyublinskaya, O. G., Zenin, V. V., Fridlyanskaya, I. I., Mikhailov, V. M., et al. (2016). Mesenchymal stem cells with irreversibly arrested proliferation stimulate decidua development in rats. *Exp. Ther. Med.* 12, 2447–2454. doi: 10.3892/etm.2016.3671

Emmert, M. Y., Wolint, P., Wickboldt, N., Gemayel, G., Weber, B., Brokopp, C. E., et al. (2013). Human stem cell-based three-dimensional microtissues for advanced cardiac cell therapies. *Biomaterials* 34, 6339–6354. doi: 10.1016/j.biomaterials.2013.04.034

Fitzsimmons, R. E. B., Mazurek, M. S., Soos, A., and Simmons, C. A. (2018). Mesenchymal stromal/stem cells in regenerative medicine and tissue engineering. *Stem Cells Int.* 2018:8031718. doi: 10.1155/2018/8031718

Forte, E., Chimenti, I., Rosa, P., Angelini, F., Pagano, F., Calogero, A., et al. (2017). EMT/MET at the Crossroad of stemness, regeneration and oncogenesis: the ying-yang equilibrium recapitulated in cell spheroids. *Cancers* 9:98. doi: 10.3390/cancers9080098

Friedenstein, A. J., Chailakhjan, R. K., and Lalykina, K. S. (1970). THE DEVELOPMENT OF FIBROBLAST COLONIES IN MONOLAYER CULTURES OF GUINEA–PIG BONE MARROW AND SPLEEN CELLS. *Cell Prolif.* 3, 393–403. doi: 10.1111/j.1365-2184.1970.tb00347.x

Gordy, C., and He, Y. W. (2012). The crosstalk between autophagy and apoptosis: where does this lead? *Protein Cell* 3, 17–27. doi: 10.1007/s13238-011-1127-x

Han, H.-W., Asano, S., and Hsu, S.-H. (2019). Cellular spheroids of mesenchymal stem cells and their perspectives in future healthcare. *Appl. Sci.* 9:627. doi: 10.3390/app9040627

Hoogduijn, M. J., and Lombardo, E. (2019). Mesenchymal stromal cells anno 2019: dawn of the therapeutic era? Concise review. *Stem Cells Transl. Med.* 8, 1126–1134. doi: 10.1002/sctm.19-0073

Jonkman, J. E. N., Cathcart, J. A., Xu, F., Bartolini, M. E., Amon, J. E., Stevens, K. M., et al. (2014). An introduction to the wound healing assay using live-cell microscopy. *Cell Adh. Migr.* 8, 440–451. doi: 10.4161/cam.36224

Kornienko, J., Smirnova, I. S., Pugovkina, N. A., Ivanova, J. S., Shilina, M. A., Grinchuk, T. M., et al. (2019). High doses of synthetic antioxidants induce premature senescence in cultivated mesenchymal stem cells. *Sci. Rep.* 9:1296. doi: 10.1038/s41598-018-37972-y

Kozhukharova, I., Zemelko, V., Kovaleva, Z., Alekseenko, L., Lyublinskaya, O., and Nikolsky, N. (2018). Therapeutic doses of doxorubicin induce premature senescence of human mesenchymal stem cells derived from menstrual blood, bone marrow and adipose tissue. *Int. J. Hematol.* 107, 286–296. doi: 10.1007/s12185-017-2346-6

Lee, J. H., Han, Y. S., and Lee, S. H. (2016). Long-duration three-dimensional spheroid culture promotes angiogenic activities of adipose-derived mesenchymal stem cells. *Biomol. Ther.* 24, 260–267. doi: 10.4062/biomolther.2015.146

Madrigal, M., Rao, K. S., and Riordan, N. H. (2014). A review of therapeutic effects of mesenchymal stem cell secretions and induction of secretory modification by different culture methods. *J. Transl. Med.* 12:260. doi: 10.1186/s12967-014-0260-8

Mishina, N. M., Markvicheva, K. N., Bilan, D. S., Matlashov, M. E., Shirmanova, M. V., Liebl, D., et al. (2013). Visualization of intracellular hydrogen peroxide with HyPer, a genetically encoded fluorescent probe. *Methods Enzymol.* 526, 45–59. doi: 10.1016/B978-0-12-405883-5.00003-X

Murphy, K. C., Whitehead, J., Falahee, P. C., Zhou, D., Simon, S. I., and Leach, J. K. (2017). Multifactorial experimental design to optimize the anti-inflammatory and proangiogenic potential of mesenchymal stem cell spheroids. *Stem Cells* 35, 1493–1504. doi: 10.1002/stem.2606

Nimiritsky, P. P., Eremichev, R. Y., Alexandrushkina, N. A., Efimenko, A. Y., Tkachuk, V. A., and Makarevich, P. I. (2019). Unveiling mesenchymal stromal cells' organizing function in regeneration. *Int. J. Mol. Sci.* 20:823. doi: 10.3390/ijms20040823

Petinati, N., Drize, N., Sats, N., Risinskaya, N., Sudarikov, A., Drokov, M., et al. (2018). Recovery of donor hematopoiesis after graft failure and second hematopoietic stem cell transplantation with intraosseous administration of mesenchymal stromal cells. *Stem Cells Int.* 2018:6495018. doi: 10.1155/2018/6495018

Rasband, W. S. (2012). *ImageJ*. Bethesda, MD: U. S. National Institutes of Health.

Ratushnyy, A., Ezdakova, M., and Buravkova, L. (2020). Secretome of senescent adipose-derived mesenchymal stem cells negatively regulates angiogenesis. *Int. J. Mol. Sci.* 21:1802. doi: 10.3390/ijms21051802

Sant, S., and Johnston, P. A. (2017). The production of 3D tumor spheroids for cancer drug discovery. *Drug Discov. Today Technol.* 23, 27–36. doi: 10.1016/j.ddtec.2017.03.002

Santos, J. M., Camões, S. P., Filipe, E., Cipriano, M., Barcia, R. N., Filipe, M., et al. (2015). Three-dimensional spheroid cell culture of umbilical cord tissue-derived mesenchymal stromal cells leads to enhanced paracrine induction of wound healing. *Stem Cell Res. Ther.* 6:90. doi: 10.1186/s13287-015-0082-5

Turinetto, V., Vitale, E., and Giachino, C. (2016). Senescence in human mesenchymal stem cells: functional changes and implications in stem cell-based therapy. *Int. J. Mol. Sci.* 17:1164. doi: 10.3390/ijms17071164

Wang, C. C., Chen, C. H., Hwang, S. M., Lin, W. W., Huang, C. H., Lee, W. Y., et al. (2009). Spherically symmetric mesenchymal stromal cell bodies inherent with endogenous extracellular matrices for cellular cardiomyoplasty. *Stem Cells* 27, 724–732. doi: 10.1634/stemcells.2008-0944

Wang, S., Qu, X., and Zhao, R. C. (2012). Clinical applications of mesenchymal stem cells. *J. Hematol. Oncol.* 5:19. doi: 10.1186/1756-8722-5-19

Yao, B., Wang, R., Wang, Y., Zhang, Y., Hu, T., Song, W., et al. (2020). Biochemical and structural cues of 3D-printed matrix synergistically direct MSC differentiation for functional sweat gland regeneration. *Sci. Adv.* 6:eaaz1094. doi: 10.1126/sciadv.aaz1094

Yeh, H. Y., Liu, B. H., Sieber, M., and Hsu, S. H. (2014). Substrate-dependent gene regulation of Self-assembled human MSC spheroids on chitosan membranes. *BMC Genomics* 15:10. doi: 10.1186/1471-2164-15-10

Zemel'ko, V. I., Grinchuk, T. M., Domnina, A. P., Artsybasheva, I. V., Zenin, V. V., Kirsanov, A. A., et al. (2011). Multipotent mesenchymal stem cells of desquamated endometrium: isolation, characterization, and application as a feeder layer for maintenance of human embryonic stem cells. *Tsitologiia* 53, 919–929.

Zhang, Q., Nguyen, A. L., Shi, S., Hill, C., Wilder-Smith, P., Krasieva, T. B., et al. (2012). Three-dimensional spheroid culture of human gingiva-derived mesenchymal stem cells enhances mitigation of chemotherapy-induced oral mucositis. *Stem Cells Dev.* 21, 937–947. doi: 10.1089/scd.2011.0252

Conflict of Interest: The authors declare that the research was conducted in the absence of any commercial or financial relationships that could be construed as a potential conflict of interest.

Copyright © 2020 Domnina, Ivanova, Alekseenko, Kozhukharova, Borodkina, Pugovkina, Smirnova, Lyublinskaya, Fridlyanskaya and Nikolsky. This is an open-access article distributed under the terms of the Creative Commons Attribution License (CC BY). The use, distribution or reproduction in other forums is permitted, provided the original author(s) and the copyright owner(s) are credited and that the original publication in this journal is cited, in accordance with accepted academic practice. No use, distribution or reproduction is permitted which does not comply with these terms.

frontiers in Cell and Developmental Biology

REVIEW
published: 10 July 2020
doi: 10.3389/fcell.2020.00592

Niches for Skeletal Stem Cells of Mesenchymal Origin

*Anastasiia D. Kurenkova[1], Ekaterina V. Medvedeva[1], Phillip T. Newton[2] and Andrei S. Chagin[1,3]**

[1] Institute for Regenerative Medicine, I.M. Sechenov First Moscow State Medical University (Sechenov University), Moscow, Russia, [2] Department of Women's and Children's Health, Karolinska Institutet, Stockholm, Sweden, [3] Department of Physiology and Pharmacology, Karolinska Institutet, Stockholm, Sweden

With very few exceptions, all adult tissues in mammals are maintained and can be renewed by stem cells that self-renew and generate the committed progeny required. These functions are regulated by a specific and in many ways unique microenvironment in stem cell niches. In most cases disruption of an adult stem cell niche leads to depletion of stem cells, followed by impairment of the ability of the tissue in question to maintain its functions. The presence of stem cells, often referred to as mesenchymal stem cells (MSCs) or multipotent bone marrow stromal cells (BMSCs), in the adult skeleton has long been realized. In recent years there has been exceptional progress in identifying and characterizing BMSCs in terms of their capacity to generate specific types of skeletal cells *in vivo*. Such BMSCs are often referred to as skeletal stem cells (SSCs) or skeletal stem and progenitor cells (SSPCs), with the latter term being used throughout this review. SSPCs have been detected in the bone marrow, periosteum, and growth plate and characterized *in vivo* on the basis of various genetic markers (i.e., Nestin, Leptin receptor, Gremlin1, Cathepsin-K, etc.). However, the niches in which these cells reside have received less attention. Here, we summarize the current scientific literature on stem cell niches for the SSPCs identified so far and discuss potential factors and environmental cues of importance in these niches *in vivo*. In this context we focus on (i) articular cartilage, (ii) growth plate cartilage, (iii) periosteum, (iv) the adult endosteal compartment, and (v) the developing endosteal compartment, in that order.

Keywords: skeletal stem cells, progenitors, osteoblasts, chondrocytes, MSCs, stem cell niche

OPEN ACCESS

Edited by:
So-ichiro Fukada, Osaka University, Japan

Reviewed by:
Yuuki Imai, Ehime University, Japan
Nedime Serakinci, Near East University, Cyprus
Christa Maes, KU Leuven, Belgium

***Correspondence:**
Andrei S. Chagin
andrei.chagin@ki.se

Specialty section:
This article was submitted to Stem Cell Research, a section of the journal Frontiers in Cell and Developmental Biology

Received: *29 February 2020*
Accepted: *17 June 2020*
Published: *10 July 2020*

Citation:
Kurenkova AD, Medvedeva EV, Newton PT and Chagin AS (2020) Niches for Skeletal Stem Cells of Mesenchymal Origin. Front. Cell Dev. Biol. 8:592. doi: 10.3389/fcell.2020.00592

INTRODUCTION

The Concept of a Stem Cell Niche

A stem cell niche is a dynamic and specialized microenvironment with a specific architecture that regulates self-renewal of stem cells, the balance between their quiescent and proliferative states, as well as their choice of fate and differentiation of their progeny. These functions are coordinated through communication between the stem cells and local environment, including neighboring cells, components of the extracellular matrix, and local gradients of morphogens and cytokines, in combination with physical factors such as oxygen tension, temperature, shear stress, etc. (Schofield, 1978; Wong et al., 2012; Ceafalan et al., 2018; Singh et al., 2019). Thus, to be comprehensive, studies

on stem cells should take their appropriate niche into consideration as well. The several stem cell niches identified to date harbor hematopoietic (HSCs), neural, intestinal, epithelial, and muscle stem cells, among many others. Only some of these have so far been characterized extensively.

The Hematopoietic Stem Cell (HSC) Niche Exemplifies the Complexity of These Microenvironments

The influence of the local environment on the behavior of the HSC niche (also called the bone marrow niche), which is among the most well-characterized, was first demonstrated by transplanting HSCs from intact to RARγ-deficient mice (Walkley et al., 2007). The HSC niche is now known to contain predominantly mesenchymal stromal and vascular endothelial cells and to receive signals from osteoblasts, macrophages, megakaryocytes, sympathetic nerve fibers and non-myelinated Schwann cells (Crane et al., 2017). The balance between differentiation of HSCs toward the myeloid or lymphoid lineage is regulated via signaling through the pathway involving delta-like canonical Notch ligand 4 (Dll4) in vascular endothelial cells (Tikhonova et al., 2019). Mesenchymal cells and their progeny control the size of this niche and, thus, the number of HSCs (Calvi et al., 2003; Zhang et al., 2003; Méndez-Ferrer et al., 2010) via the Notch, Bone Morphogenetic Protein (BMP) and Wnt signaling pathways (Calvi et al., 2003; Zhang et al., 2003; Fleming et al., 2008).

The major factors that promote homing of HSCs to their niche include angiogenin, stem cell factor (SCF, encoded by *Kitl*), stroma derived factor-1 (SDF1, also known as Cxcl12 and encoded by *Cxcl12*), angiopoetin, interleukin 7 (IL-7), Wnt5 and Dll4 (Calvi et al., 2003; Fleming et al., 2008; Crane et al., 2017). Recently, single-cell transcriptional profiling of bone marrow cells identified the cellular sources for these factors with a resolution higher than ever achieved previously: SCF, SDF1, angiogenin and membrane-bound Dll4 are produced by vascular endothelial cells; the highest levels of SDF1, SCF, and IL-7β are detected in mesenchymal cells; while Wnt5a is secreted by osteoblasts (Tikhonova et al., 2019). All these factors play a role in regulating the number of HSCs and their rate of renewal, as well as their mobilization and/or the direction in which they differentiate.

Historical Perspective on Mesenchymal Stem Cells (MSCs) and Issues of Terminology

In addition to providing a home for HSCs, the skeleton gives fundamental structural support, facilitates locomotion and serves as an endocrine organ (DiGirolamo et al., 2012). Like all other adult tissues, skeletal tissues require a constant supply of cells for their renewal and maintenance throughout life. Friedenstein et al. (1968) identified a heterogeneous fibroblast-like cell population (colony-forming fibroblasts) in the bone marrow and spleen. In culture these colony-forming fibroblasts are capable of attaching to plastic, forming colonies and differentiating spontaneously into osteoblasts in culture; whereas when transplanted into guinea pigs they formed multiple skeletal tissues, such as bone, cartilage, muscle, and tendon (Friedenstein et al., 1970, 1974; Friedenstein, 1990).

This discovery remained largely unnoticed for two decades until Maureen Owen proposed that these colony-forming fibroblasts are bone marrow stromal stem cells (Owen and Friedenstein, 1988). Meanwhile, using limb bud mesenchymal cells from chick embryos, Arnold Caplan and colleagues were exploring mechanisms underlying osteo- and chondrogenic differentiation, coining the term mesenchymal stem cells (MSCs) for the first time (reviewed in Caplan, 1991). MSCs were reported to reside in the bone marrow, periosteum and muscle connective tissue, and could be expanded and differentiated into bone and cartilage both *in vitro* cultures, as well as in diffusion chambers implanted into mice (Caplan, 1991).

It should be emphasized here that the dogma in the 1980's and early 1990's was that the adult body only contained one type of stem cells, namely, hematopoietic stem cells. Accordingly, these initial discoveries of bone marrow stromal stem cells/MSCs were recognized and appreciated primarily by investigators interested in experimental hematology. However, this was changed by the publication by Pittenger (1999) of a protocol for the isolation, phenotypic characterization and expansion of human MSCs, which was well received in the atmosphere of excitement generated by the discovery of human embryonic stem cells.

Unfortunately, during subsequent decades the pronounced heterogeneity of MSCs, in combination with the wide variety of experimental approaches employed to isolate and culture these cells, led to confusion in this field. It also became clear that the term "mesenchymal stem cells" is inappropriate, since it does not reflect their properties accurately (Dominici et al., 2006; Bianco et al., 2008). Even Caplan, the inventor of this term, made pleas that it be changed (Caplan, 2010, 2017). In 2006 the International Society of Cellular Therapies recommended the terminology "multipotent mesenchymal stromal cells" instead, defining these as clonogenic, multipotent, self-renewing cells that express CD105, CD73, and CD90, but not CD45, CD34, CD14, CD11b, CD79α, or HLA-DR, and are capable of osteogenic, chondrogenic and adipogenic differentiation (Dominici et al., 2006). Nonetheless, the term MSCs is utilized so widely by researchers around the globe that it is unclear when, or even if this terminology will be clarified, an issue that continues being discussed (Bianco and Robey, 2015; Caplan, 2017; Ambrosi et al., 2019).

In the present review we focus almost exclusively on *in vivo* characterization of MSCs, which are often referred to as skeletal stem cells (SSCs) (Bianco and Robey, 2015; Ambrosi et al., 2019). Since in many cases these cell populations are characterized on the basis of genetic markers which actually label heterogenous populations (Debnath et al., 2018; Tikhonova et al., 2019), below we will use the term skeletal stem and progenitor cells (SSPCs).

In recent years several types of SSPCs at different locations within the skeleton and with different functions and markers have been described (Sacchetti et al., 2007; Méndez-Ferrer et al., 2010; Ding et al., 2012; Greenbaum et al., 2013;

Zhou B.O. et al., 2014; Chan et al., 2015; Li et al., 2017; Mizuhashi et al., 2018, 2019; Newton et al., 2019). However, our understanding of the local microenvironment in which these various SSPCs reside and the factors involved in regulating their behavior is still evolving. Below, on the basis of what is known to date, we make some suggestions concerning the nature of each particular niche. We have arranged our comments in the order of the following anatomical locations: articular cartilage, epiphyseal cartilage, periosteum, adult endosteal compartment and developing endosteal compartment.

SSPCs IN THE ARTICULAR CARTILAGE AND THEIR MAINTENANCE

The superficial zone of articular cartilage contains chondroprogenitors capable of generating chondrocytes, both *ex vivo* (Dowthwaite et al., 2004) and *in vivo* (Kozhemyakina et al., 2015) and also capable of reconstituting the entire articular cartilage (i.e., the middle and deep zone chondrocytes) in postnatal mice (Li et al., 2017). These cells have the following characteristics:

(i) Expression of several markers commonly utilized for the identification of SSPCs (BMSCs//MSCs), including CD105, vascular cell adhesion protein 1 (Vcam1, also known as CD106), CD166, Notch1, Stro, Dkk3, Tenascin C, Erg, CD73, CD34 and smooth muscle actin (Dowthwaite et al., 2004; Jiang and Tuan, 2015; Kozhemyakina et al., 2015; Li et al., 2017).
(ii) The ability to form colonies and differentiate into chondrocytes, osteoblasts and adipocytes *in vitro* (Alsalameh et al., 2004; Dowthwaite et al., 2004; Jiang and Tuan, 2015).
(iii) A cell cycle that is slower than that of their progeny (Li et al., 2017).

Kozhemyakina et al. (2015) showed that superficial cells expressing proteoglycan 4 (Prg4, also called lubricin) *in vivo* give rise to articular chondrocytes while themselves remaining at the surface of the articular cartilage for at least one year, suggesting that they are capable of renewal. To address this question directly, we utilized these same Prg4-CreERT2 transgenic mice in combination with clonal analysis *in vivo* and found that, indeed, these superficial cells can divide asymmetrically, generating one daughter cell that remains at the surface while the other undergoes further differentiation (Li et al., 2017). We have also observed symmetrical division of these superficial cells, following which both daughter cells remain at the cartilage surface, continue to express stem cell markers and exhibit characteristic flat morphology (Li et al., 2017). These observations indicate renewal of chondroprogenitors and, therefore, we refer to these superficial Prg4+ chondroprogenitors as articular SSPCs (art-SSPCs).

The microenvironment in which art-SSPCs reside is quite unique – there is no vascularization, no innervation, the cells are exposed to the synovial fluid and, in connection with locomotion, are frequently subjected to mechanical stress. Surgical translocation of hypertrophic chondrocytes from the growth plate to the articular surface leads to their gradual adoption of a phenotype resembling that of art-SSPCs (Chau, 2014), lending support to the concept that this unique microenvironment promotes art-SSPC properties.

Synovial fluid is enriched in lubricin, a large proteoglycan product of the *Prg4* gene and hyaluronic acid, which, together with phosphatidylcholine, form a stable boundary layer that minimizes the shear stress associated with locomotion (Seror et al., 2015). Both this layer and other molecular components of the synovial fluid might be involved in creating the appropriate microenvironment. In addition, synovial fluid transports oxygen and nutrients, along with soluble factors secreted by the art-SSPCs, chondrocytes and cells of the synovial membrane, all of which might also play a role in creation of the microenvironment required for the maintenance and renewal of art-SSPCs.

In connection with movements, joints are regularly subjected to mechanical forces and mechanical stimuli influence the fates of various types of stem cells (Engler et al., 2006; Guilak et al., 2009). Although the principal component of stress might be similar for art-SSPCs and underlying chondrocytes, shear stress is obviously higher at the surface, where art-SSPCs are located. Indeed, mechanical loading and shear stress might actually be part of the microenvironment required by art-SSPCs.

This possibility is supported by the finding that fluid flow shear stress enhances the expression of *Prg4* by art-SSPCs through a mechanism dependent on prostaglandin-endoperoxide synthase 2 (Cox2) and cAMP response element-binding protein (CREB) (Ogawa et al., 2014) and perhaps also on Wnt/β-catenin (Xuan et al., 2019). Furthermore, mechanical stress may elevate expression of Gremlin-1 (an antagonist of BMP signaling) by cells in the middle zone (Chang et al., 2019). Intra-articular injection of recombinant Gremlin-1 promotes the development of osteoarthritis, and blocking this factor improves healing (Chang et al., 2019). BMPs are involved in the restoration of cartilage destroyed by osteoarthritis, apparently by stimulating the proliferation and differentiation of chondrocytes (Deng et al., 2018). BMP7 is produced primarily by the cells of the superficial zone (Chubinskaya et al., 2000), and if this process is inhibited, less aggrecan is produced (Söder et al., 2005).

Further support for an impact of mechanical stress on art-SSPCs is provided by the finding that in connection with destruction of articular cartilage by immobilizing a joint, cells at the cartilage surface (the location of art-SSPCs) are lost first (Hagiwara et al., 2009; Correa Maldonado et al., 2013). However, this observation must be interpreted with care, since immobilization not only reduces mechanical stress, but also limits circulation of the synovial fluid, potentially impairing respiration by the cells in cartilage and limiting their access to nutrients.

In contrast to the underlying chondrocytes located in an extracellular matrix rich in type II collagen and negatively charged proteoglycans, the extracellular matrix surrounding art-SSPCs is rich in type XXII collagen and thrombospondin 4 (*Thbs4*) and contains only low amounts of proteoglycans (Gray et al., 2001; Feng et al., 2019). Gene array analysis has revealed that the art-SSPCs themselves exhibit low expression of typical components of the cartilage matrix, including aggrecan

(*Acan*), collagen II (*Col2a1*), collagen IX (*Col9a1*), collagen XI (*Col11a1*), and matrilin-1 (*Matn1*), while expressing tenascin C (*Tnc*) and CD44 (*Cd44*) (Yasuhara et al., 2011) at high levels. Thus, art-SSPCs are surrounded by an extracellular matrix that differs substantially in composition from the one surrounding chondrocytes. Since the extracellular matrix plays a role in regulating the behavior of SSPCs (Engler et al., 2006; Guilak et al., 2009; Ferreira et al., 2018), this unique composition may be part of the specific microenvironment required for the maintenance and renewal of art-SSPCs.

Due to their unique location, art-SSPCs are not in direct contact with any other types of cells and even become gradually separated from their progeny by abundant extracellular matrix. Nevertheless, committed progeny and cells of the synovial membrane are probably the only cells capable of communicating with art-SSPCs, although communication with macrophages and other blood cells that infiltrate into the synovial space cannot be excluded, especially in connection with pathological processes.

As described for various niches in which epithelial or hematopoietic stem cells reside, interplay between stem cells and their progeny is common (Ferraro et al., 2010). Such interplay between mesenchymal cells is exemplified by the niche in the mouse incisor, where committed progeny signal back to the stem cells via interaction between delta like non-canonical Notch ligand 1 (Dlk1) and Notch (Walker et al., 2019). In mouse articular cartilage Notch ligands and receptors are expressed in a distinct spatiotemporal pattern, with *Notch1* being expressed by neonatal art-SSPCs (Hayes et al., 2003; Dowthwaite et al., 2004). With the exception of the superficial zone, other Notch receptors (Notch 2, 3, and 4) and ligands (Jagged 1 and 2) are distributed throughout the articular cartilage (Hayes et al., 2003).

Attenuation of Notch with DAPT, an inhibitor of gamma-secretase, prevents the proliferation of chondroprogenitors, thereby depleting the number of progeny cells and leading to a region poor in cells beneath the superficial zone (Dowthwaite et al., 2004). The depletion of Notch signaling in the entire adult articular cartilage employing Aggrecan-CreERT transgenic mice results in progressive degeneration of the extracellular matrix, including loss of proteoglycan, along with fibrosis in the articular cartilage and altered chondrocyte morphology (Liu et al., 2016). Thus, as in the mouse incisor (Walker et al., 2019), the Notch signaling pathway may participate in regulating mouse art-SSPCs. At the same time, it is worth mentioning that Notch1 has been detected immunohistochemical in all zones of human articular cartilage (Ustunel et al., 2008; Grogan et al., 2009) or, in one case, only during osteoarthritis (Mahjoub et al., 2012), but that the existence of putative human art-SSPCs remains to be established.

In addition to Notch, art-SSPCs express members of other signaling pathways that have been evolutionarily conserved and play crucial roles during development, including members of the Wnt family, BMPs, and members of the family of transforming growth factors, their receptors and modulators (Yasuhara et al., 2011; Grogan et al., 2013). Wnt/β-catenin signaling has been detected in the superficial zone of the articular cartilage of adult mice, but not in the chondrocytes of the middle and deep zones (Xuan et al., 2019). Using transgenic mice mutated specifically with respect to cartilage (i.e., collagen type II- or type XI-driven transcripts), Yasuhara et al. (2011) found that activation of Wnt/β-catenin signaling enhances the number of slowly dividing art-SSPCs, whereas deletion of β-catenin stimulates chondrogenic differentiation and induces complete loss of art-SSPCs (Yasuhara et al., 2011). Mice in which β-catenin has been knocked-out specifically in the superficial zone develop osteoarthritis early than controls (8 weeks after surgical induction of this condition), in combination with reduced expression of lubricin and destruction of the superficial zone (Xuan et al., 2019). In contrast, Prg4-Cre-driven stabilization of β-catenin enhances resistance against osteoarthritis, as well as expression of the *Prg4* gene in the superficial zone of articular cartilage (Xuan et al., 2019).

Analysis of the gene expression profiles revealed that the expression of both canonical and non-canonical Wnt ligands (*Wnt2b, Wnt4, Wnt5a, Wnt11*, and *Wnt16*) by art-SSPCs differs significantly from that by chondrocytes (Yasuhara et al., 2011). The relatively high levels of mRNA encoding the non-canonical Wnt ligands *Wnt5a, Wnt5b, Wnt9a*, and *Wnt16* in art-SSPCs were later confirmed (Xuan et al., 2019). Treatment of cultured art-SSPCs with non-canonical Wnt5a or Wnt5b elevated their expression of *Prg4*, but also caused canonical responses, i.e., elevations in the expression of *Ctnnb1* (β-catenin-coding gene) and *Axin2* genes (Xuan et al., 2019). Activation of the canonical β-catenin pathway with Wnt3a elevates the number of art-SSPCs during their first two passages in culture (Yasuhara et al., 2011), although inhibitors of this pathway pose no effect in these *in vitro* experiments (Yasuhara et al., 2011). Altogether, findings both *in vivo* and *in vitro* indicate that β-catenin signaling in the superficial zone contributes to the homeostasis and maintenance of the art-SSPCs phenotype in articular cartilage, but the exact nature of its involvement remains to be further elucidated.

Altogether, the microenvironment supporting the maintenance of art-SSPCs and the generation of articular chondrocytes probably involves signaling from underlying chondrocytes (e.g., through Notch ligands), a unique set of proteins in the extracellular matrix (e.g., collagen type XXII and thrombospondin-4) and mechanical stress (**Figure 1A**).

THE STEM CELL NICHE IN THE EPIPHYSEAL GROWTH PLATE

Recently, it was shown that the resting zone of the postnatal epiphyseal growth plate of mice harbors slowly cycling stem cells that express parathyroid hormone-related protein (PTHrP) and are capable of generating epiphyseal chondrocytes (Mizuhashi et al., 2018). These stem cells can be detected a year after labeling at 6 days of postnatal age. Here, to emphasize their location, we will refer to them as epiphyseal skeletal stem progenitor cells (ep-SSPCs).

In vitro these ep-SSPCs can directly differentiate into osteoblasts, chondrocytes and, to a lesser extent, adipocytes (Mizuhashi et al., 2018); whereas *in vivo* they generate chondrocytes, which then undergo hypertrophy and

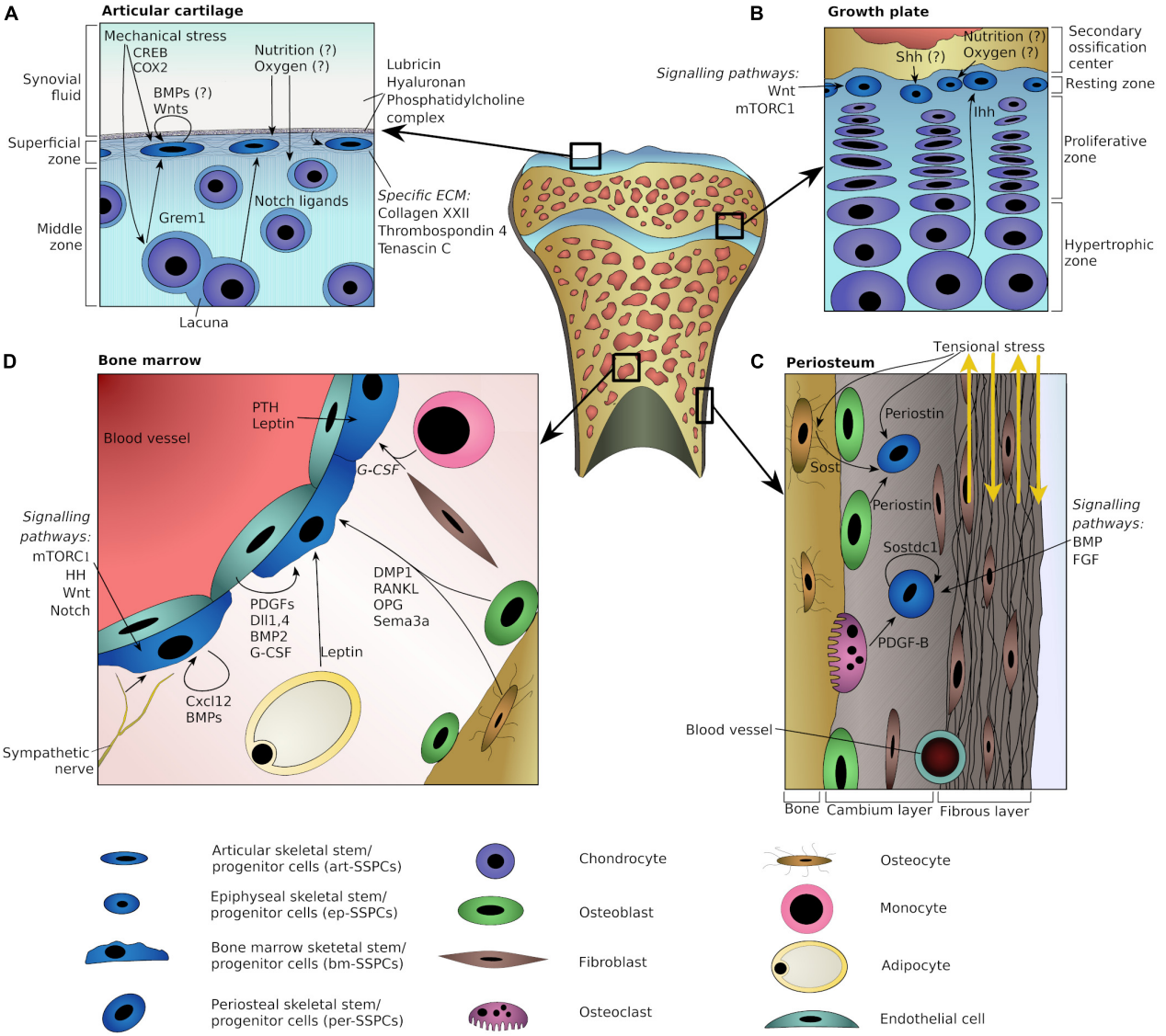


FIGURE 1 | Schematic representation of plausible niche components at various skeletal locations. Potential niche components are shown for articular cartilage **(A)**, epiphyseal growth plate **(B)**, periosteum **(C)**, and adult bone marrow **(D)**. Arrows indicate directions of interactions or point toward specific cells. Question marks indicate potential players with the lack of strong direct evidences.

transdifferentiate into osteoblasts and stromal cells (Mizuhashi et al., 2018). During the juvenile period of growth, additional ep-SSPCs probably move from the perichondrium into the periphery of the resting zone, as revealed by genetic tracing of Axin2-positive perichondrial cells (Usami et al., 2019).

One key feature that distinguishes stem cells from their progenitors is their ability to maintain their own population and, at the same time, generate committed progeny via asymmetric cell division (Post and Clevers, 2019). This implies that clones of stem cells are stable, whereas those of their progenitor cells are only temporary. Indeed, labeling of all chondrocytes within the growth plate of mice revealed the formation of stable clones between 3 and 4 weeks (Newton et al., 2019). This coincides with the maturation of the secondary ossification center (SOC), which may constitute a part of the stem cell niche responsible for the renewal of ep-SSPCs (Newton et al., 2019). In line with this observation, tracing of PTHrP+ cells in mice from 6 days of age revealed that temporary clones are formed initially, whereas the formation of stable clones is observed only after 25 days of age (Mizuhashi et al., 2018).

Thus, PTHrP+ cells within the growth plate may act as slowly cycling chondroprogenitors that acquire the ability to self-renew only upon formation of the niche. This proposal is supported by the phenotypic and functional changes that these cells undergo at the time of niche formation, i.e., expression of stem cell markers such as CD73 and CD49e, among other changes in their transcriptional profile (Newton et al., 2019), as well as development of differential responsiveness to activation

of hedgehog (HH) signaling (based on comparison of Mizuhashi et al., 2018 and Newton et al., 2019; see also below). Interestingly, in line with earlier indications (Ferraro et al., 2010), these findings suggest that the niche not only maintains stem cells, but also primes their phenotypic and functional properties.

The stem cell niche in the growth plate, which we refer to as the epiphyseal stem cell niche (Chagin and Newton, 2019), is probably formed by the SOC when it has matured so that bone cells and extracellular matrix is close to the ep-SSPCs (Newton et al., 2019). The variety of cells present in the SOC include osteocytes, osteoblasts, stromal cells, mesenchymal cells, and hematopoietic cells of the bone marrow, as well as nerve fibers and the cells that form blood vessels. Furthermore, appearance of the SOC alters local mechanical loading (Xie et al., 2019a) and, since the blood vessels from the SOC are near the avascular cartilage, probably nutrition and oxygenation as well.

Thus, the number of potential actors in connection with formation of the epiphyseal niche is quite high. We found that several types of cells in the SOC produce Sonic hedgehog (Shh) (Newton et al., 2019), a diffusible morphogen that can participate in the formation of a stem cell niche (Lai et al., 2017). In theory, Shh could diffuse from the SOC to the resting zone of the growth plate to help achieve this formation. Indeed, pharmacological inhibition of HH signaling results in fusion of the growth plate (Kimura et al., 2008; Newton et al., 2019). At the same time, the Indian hedgehog (Ihh) protein, another member of hedgehog family, is expressed by pre-hypertrophic and hypertrophic chondrocytes and then diffuses through the growth plate to stimulate the expression of PTHrP (encoded by *Pthlh*) by chondroprogenitors (Vortkamp et al., 1996). It is important to stress that specific genetic ablation of Ihh within the growth plate induces premature fusion (Maeda et al., 2007).

Moreover, activation of HH through either systemic or intra-articular injection of smoothened agonist (SAG) promotes the proliferation of ep-SSPCs (Newton et al., 2019). Interestingly, SAG has this effect only after formation of the SOC, actually inhibiting the expansion of ep-SSPCs if injected earlier (Mizuhashi et al., 2018). Altogether, hedgehog signaling clearly plays major roles in the epiphyseal stem cell niche, such as sustaining renewal of the stem cells, but the detailed role of each hedgehog ligand in the niche remains to be elucidated.

It is important to emphasize that at the same time as pre-hypertrophic chondrocytes are an important source of Ihh, they are also descendants of the ep-SSPCs. Thus, it can be said that the descendants of the ep-SSPCs participate in the formation of the stem cell niche. In this context it is worth mentioning that ablation of parathyroid hormone receptor 1 (PTHR1, encoded by *Pthr1*), which brings the region in which Ihh is expressed and the ep-SSPCs closer together, triggers apoptosis in slowly dividing (label-retaining) chondrocytes in the resting zone of 4-week old mice (Chagin et al., 2014). However, upon niche formation there is very little overlap between these label-retaining and the column-forming cells, which thus may appear to be different populations (Newton et al., 2019).

The observation that HH influences ep-SSPCs in different ways before and after the onset of the niche indicates that their response is dependent on the present state of their microenvironment. Accordingly, these cells may also respond to other morphogens and signaling in a different manner before and after the onset of the niche. If so, this will complicate use of the results of many genetic manipulations (which are often performed on fetal/neonatal growth plate, long before the onset of the niche) in unraveling the mechanisms underlying juvenile growth.

In connection with these mechanisms, the Wnt/β-catenin pathway affects slowly cycling cells in the resting zone. Specifically, transient activation of this pathway in the growth plate of 2–3-week-old mice results in fusion of this structure 7 weeks later (Yuasa et al., 2009). Furthermore, excessive β-catenin signaling causes hypertrophic chondrocytes to undergo apoptosis (Yuasa et al., 2009), potentially an indirect mechanism of action on ep-SSPCs. On the other hand, ablation of β-catenin from the entire growth plate of 4–6-day-old mice employing Col2-CreERT causes loss of the label-retaining cells from the resting zone at 4 weeks of age (Candela et al., 2014). At the same time, a deficiency in β-catenin does not impair the size and functions of hypertrophic cells, but rather their transdifferentiation into osteoblasts (Houben et al., 2016). These observations, together with the well-established role of the β-catenin pathway in other stem cell niches (Clevers and Nusse, 2012), indicate that β-catenin may well play a key role in the epiphyseal stem cell niche, although direct evidence for this is still lacking.

The mammalian target of rapamycin complex 1 (mTORC1), another signaling pathway that has been conserved throughout evolution, may also be involved in regulating the behavior of ep-SSPCs in the epiphyseal niche. Activation of this pathway, by ablation of the tuberous sclerosis complex 1 (*Tsc1*) gene, shifts the division of colony-forming cells within the growth plate from symmetric to asymmetric; whereas inactivation by ablation of the regulatory associated protein of mTORC1 (Raptor) (encoded by the *Rptor* gene) leads to the loss of the clones within the growth plate (Newton et al., 2018, 2019). In these experiments genetic ablation was performed in 3-day-old mice, and although no phenotype in the growth plate is observed until the SOC is formed (Newton et al., 2018, 2019) indirect effects cannot be excluded entirely. Altogether, it appears likely that mTORC1 signaling regulates the balance between symmetric and asymmetric division of ep-SSPCs.

In summary, components of the SOC and gradients of the two HH morphogens Shh and Ihh appear to play important roles in the epiphyseal stem cell niche. In addition, mTORC1 and Wnt/β-catenin signaling pathways are likely to be involved in the regulation of ep-SSPCs (**Figure 1B**).

THE PERIOSTEAL STEM CELL NICHE

The periosteum is a thin membrane covering the external surface of numerous skeletal elements. In the case of long bones, this membrane is formed in connection with embryonic bone formation, when the core of the mesenchymal condensation differentiates into chondrocytes (forming a cartilaginous skeletal element) and the surrounding layer of mesenchymal cells forms

a tight membrane-like structure with cells of characteristic flat morphology called the perichondrium. When mineralized bone starts to form at the expense of the cartilage anlagen, this perichondrium lining newly formed bone is re-designated as the periosteum, while the lining around cartilage is still called the perichondrium (Dwek, 2010).

The presence of SSPCs in the perichondrium/periosteum was indicated by surgical observations already 250 years ago. In 1779 Michele Troja observed the osteogenic capacity of the periosteum and Ollier (1867), confirmed that the inner layer of the isolated periosteum (cambium) can produce bone and is essential for transversal bone growth. Since these early discoveries, the presence of stem/progenitor cells in the periosteum has been confirmed and described in greater detail in numerous clinical observations (Lazzeri et al., 2009). Moreover, Caplan and colleagues (Nakahara et al., 1990a,b, 1991a,b) have shown that cells in the periosteum possess chondro- and osteogenic capacity *in vitro*.

The genetic identification and detailed characterization of periosteum *in vivo* was not performed until later, including by recent lineage tracing strategies in mice using a variety of drivers. Tracing of α-smooth muscle actin (α-SMA)-positive cells revealed their periosteal location, as well as their osteo- and chondrogenic capacities and contribution to the healing of bone fractures (Grcevic et al., 2012). However, it turned out that the α-SMA promoter is active in several different cell types (Yuan, 2015; Alarcon-Martinez et al., 2018; Ge et al., 2018), making this initial observation ambiguous.

Subsequently, the finding that Cathepsin K (*Ctsk* gene), generally employed as a marker for osteoclasts, can also be used to label periosteal cells allowed detailed characterization of the cellular hierarchy within the periosteum, including identification of CtsK+CD200+ cells as periosteal stem cells (here per-SSPCs) (Debnath et al., 2018). Under normal physiological conditions in the adult periosteum, per-SSPCs differentiate into cells of the osteoblast lineage (Debnath et al., 2018), whereas during healing of a non-stabilized fracture, these cells also differentiate into chondrocytes (Colnot, 2009; Colnot et al., 2012; Ortinau et al., 2019). Interestingly, single-cell analysis of CtsK-traced cells from both the perichondrium and periosteum of 6-day-old pups revealed four different subpopulations with: (i) expression of the α-SMA gene *Acta2* at high levels, (ii) high levels of Sca1 (encoded by *Ly6a*), (iii) expression of the chondrocyte markers *Col2a1* and *Sox9*, and (iv) expression of *Bglap* and *Alpl*, markers for osteoblasts. Finally, a subpopulation of α-SMA+ cells also expressing MX dynamin-like GTPase 1 (Mx1) was recently shown to behave like per-SSPCs, contributing to cells of the osteoblast lineage, participating in the healing of fractures, and restoring their own populating following serial transplantations (Ortinau et al., 2019).

At present it is not entirely clear to what degree these populations of CtsK+ and Mx1+α-SMA+ cells overlap. During neonatal life, CtsK+ cells probably contain a subpopulation of α-SMA+ cells (subpopulation 4, Figure 3h in Debnath et al., 2018), but the situation in the adult periosteum is more complicated: CtsK+ cells do not express the leptin receptor (LepR) or CD140a, whereas Mx1+α-SMA+ cells do (Debnath et al., 2018; Ortinau et al., 2019). Nonetheless, in both of these studies the per-SSPCs were found to be located close to the surface of bone, potentially in their own stem cell niche.

The robustness of the periosteum is provided by its collagen, while the elasticity of this structure is based on fibers of elastin reinforced by collagenous Sharpey's fibers anchored to the bone at an angle of 45°. This structural arrangement maintains the periosteal tissue in a state of anisotropic tensional pre-stress (Knothe Tate et al., 2016). Changes in this stress following bone fracture and periosteal lesion leads to deformation of the structural collagen fibrils and cellular nuclei, as well as rapid emigration of cells (Yu et al., 2017).

Such observations have led to the proposal that the periosteal tissue acts as a mechanosensor and it is assumed that the normal state of stress promotes quiescence in the periosteal stem cell niche (Knothe Tate et al., 2016; Yu et al., 2017). Theoretically, this quiescence could be achieved through the action of different proteins such as periostin (*Postn*) on per-SSPCs. Indeed, using immunofluorescence periostin+ cells have been detected in the inner layer of the periosteum located along the cortex of bone, but not in the bone marrow or endosteum (Duchamp de Lageneste et al., 2018). Furthermore, after fracture, expression of periostin in the periosteum is elevated and, in addition, if this protein is knocked out, bone regeneration and callus size and quality are all reduced (Duchamp de Lageneste et al., 2018). Transplantation of wild-type periosteal cells into periostin-KO mice improve fracture healing in these animals to a remarkable degree (Duchamp de Lageneste et al., 2018). Thus, both mechanical forces and proteins of the extracellular matrix appear likely to be involved in the formation of a stem cell niche for per-SSPCs.

In response to mechanical stimulation the levels of both periostin mRNA and protein in total-bone extracts increase, an effect mediated by a reduction in expression of the sclerostin (*Sost*) gene by osteocytes (Bonnet et al., 2009). Interestingly, through interaction with the integrin αVβ3 receptor, periostin inhibits *Sost* expression directly (Bonnet et al., 2012). In a similar manner, periostin is required for the anabolic effects of parathyroid hormone (PTH) on cortical bone (Bonnet et al., 2012).

A paralog of *Sost*, the Sclerostin domain-containing protein 1 (*Sostdc1*, also known by S*ost-Like, Wise, Ectodin* and *Usag-1*) is expressed primarily in the periosteum (Collette et al., 2016) and contributes to limb morphogenesis (Collette et al., 2013). Sostdc1 has been described as an antagonist of BMP signaling (Yanagita, 2005) and both Sostdc1 and Sost inhibit Wnt signaling via lipoprotein receptor-related proteins (LRP) co-receptors (Li et al., 2005; Semenov et al., 2005). The cells in the periosteum that express Sostdc1 also express Nestin (encoded by *Nes*) and α-SMA, suggesting that these are osteochondral progenitor cells which participate actively in callus formation during bone repair (Collette et al., 2016). Absence of Sostdc1 hastens the expansion and differentiation of a subpopulation of per-SSPCs during bone healing (Collette et al., 2016). Such findings indicate that both Sostdc1 and periostin promote and maintain the quiescence of per-SSPCs in the periosteal niche, either directly and/or by modulating Wnt/β-catenin signaling.

Healing of bone fractures involves a well-orchestrated series of biological events, including hematoma, inflammation, revascularization, bone formation and remodeling (Bahney et al., 2019). Interestingly, a subpopulation of per-SSPCs that express both Mx1 and α-SMA (Mx1+α-SMA+ per-SSPCs) migrate toward the site of injury *in vivo* (Ortinau et al., 2019). These cells, which express the chemokine receptors *Ccr5* and *Ccr3* on their surface, migrate toward the injury along a gradient of Ccl5 (encoded by *Ccl5, Rantes*), a ligand for these receptors (Ortinau et al., 2019). In response to inflammation Ccl5 is synthesized by a number of different cells, including CD8+ T-cells, NK-cells, macrophages, epithelial cells, fibroblasts and platelets. Following bone injury in both *Ccl5*- and *Ccr5*-deficient mice, formation of new bone is impaired and the volume of the external callus reduced, indicating the importance of this migratory mechanism for regeneration (Ortinau et al., 2019) and suggesting that per-SSPCs or their immediate progeny must leave their niche in order to take part in bone regeneration.

In addition to the markers described above, per-SSPCs were recently reported in the outer layer of the periosteum of mice and found to express Nestin during the early postnatal period as well as being positive for LepR tracing in adulthood (Gao et al., 2019). Deficiency in cytokine colony stimulating factor 1 (CSF-1) in mononuclear cells, macrophages and osteoclasts leads to a significant reduction in the numbers of osteoprogenitor cells expressing Nestin, Osterix (Osx, also known as Sp7 transcription factor) as well as LepR-traced cells, possibly indicating that cells of the macrophage lineage play an important role in supporting periosteal niches (Gao et al., 2019). In addition, platelet-derived growth factor subunit B (PDGF-B), secreted by tartrate-resistant acid phosphatase (TRAP)-positive cells, stimulates the expression of *Postn* by cells derived from the periosteum. Furthermore, ablation of the receptor for PDGF-B, PDGFRβ, in cells of the LepR-lineage impairs their recruitment to the bone surface, as well as the formation of new bone tissue both during active bone growth and bone repair (Gao et al., 2019).

Although there is evidence that BMP, Fibroblast Growth Factor (FGF), hedgehog and Notch signaling are all involved in bone regeneration mediated by the periosteum, their direct involvement in regulation of per-SSPCs not yet been demonstrated. Ablation of *Bmp2* prior to fracture (utilizing the ubiquitous R26-CreERT strain coupled with *Bmp2* floxed mice) eliminates formation of the callus, with only undifferentiated cells being observed at the site of the injury (Wang et al., 2011). Insertion of a bone graft from *Bmp2*-deficient mice into the wild-type host fails to rescue differentiation, but administration of exogenous BMP2 partially improved healing (Wang et al., 2011). At the same time, the level of expression of *Bmp4* and *Bmp7* in mice deficient in *Bmp2* does not change in response to bone fracture (Tsuji et al., 2006). These observations indicate that BMP2 has an important role to play in connection with the healing of bone fractures, but whether this factor regulates the behavior of per-SSPCs directly remains to be determined.

The role of the FGF family of proteins in stimulating osteogenesis in connection with fracture healing is well established (Charoenlarp et al., 2017). Although *Fgf4, 8* and *20* are not expressed in the callus, expression of *Fgf2, 9, 16*, and *18* in this structure is elevated temporarily in response to bone fracture, a response important for the healing process (Schmid et al., 2009). At the same time, expression of the FGF receptor 1 (*Fgfr1*) by periosteal osteoprogenitor cells is enhanced in response to fracture (Nakajima et al., 2001), suggesting that FGF proteins may be involved in the regulation of osteogenesis by per-SSPCs.

Following bone damage, expression of the Notch ligands Jagged1 (*Jag1*) *Notch2* and *Hes1* in the callus rises with time (Dishowitz et al., 2012). Ablation of Jagged1 (*Jag1*) or inhibition of canonical Notch signaling in osteochondral progenitors by the dominant-negative mastermind-like (dnMAML) protein in the paired related homeobox 1 (Prx1)-Cre mouse strain causes periosteal expansion of cortical bone, while simultaneously lowering the expression of osteogenic genes (Youngstrom et al., 2016).

Ihh is expressed by pre-hypertrophic chondrocytes in the callus (Le et al., 2001) and may also be involved in the healing of fractures by periosteal cells. *In vitro* activation of HH signaling promotes the osteo- and chondrogenic differentiation of periosteal mesenchymal cells (Wang et al., 2010). Deletion of Smoothened (frizzled class receptor gene *Smo*), an intracellular member of the HH pathway, utilizing ubiquitous R26-CreER mice attenuates the recovery of bone mass after fracture and diminishes cell proliferation in the callus (Wang et al., 2010).

In summary, the periosteal niche may encompass its unique extracellular matrix (of which periostin is an important component), mechanosensing mechanisms, and signaling cues from cells of the osteo- and macrophage lineages. The signaling molecules likely to participate in regulation of the per-SSPCs include Sost, Sostdc1, and PDGFs, as well as members of the BMP and FGF families. Inflammatory chemokines, and in particular Ccl5, may cause per-SSPCs to leave their niche (**Figure 1C**).

THE PERIVASCULAR NICHE IN ADULT BONE

Classical bone marrow derived stromal cells (BMSCs) have been described as fibroblast-like and adherent and capable of forming colonies cells obtained from adult bone marrow (Friedenstein et al., 1970). Similarly, human BMSCs are most often obtained from adult bone marrow (Sacchetti et al., 2007). Accordingly, we first discuss a potential niche for adult BMSCs, referred to here as bone marrow skeletal stem and progenitor cells (bm-SSPCs), both to highlight their predominant characteristics *in vivo* and in alignment with the terminology discussed in section "Historical Perspective on Mesenchymal Stem Cells (MSCs) and Issues of Terminology" above.

Among the various genetic markers utilized to characterize adult bm-SSPCs *in vivo*, the leptin receptor (LepR) is among those studied most extensively, primarily employing transgenic LepR-Cre mice (Ding et al., 2012; Zhou B.O. et al., 2014; Tikhonova et al., 2019). LepR-traced cells contribute little to bone formation during the early postnatal period, but as mice age, most osteoblasts and osteocytes are derived from LepR+ cells (Zhou B.O. et al., 2014). The progeny of LepR+ cells also differentiate into bone marrow adipocytes, but not into chondrocytes of the

growth plate under normal physiological conditions. However, during fracture healing the progeny of LepR+ cells constitute almost half of the chondrocytes in the callus (Zhou B.O. et al., 2014). LepR+ cells also express markers for bm-SSPCs such as Prx1 (*Prrx1)*, PDGFRα (*Pdgfra*) and CD51 (*Itgav)* and can form colonies and differentiate into cells of three different lineages *in vitro* (Zhou B.O. et al., 2014). At the same time, the population of cells marked by LepR-Cre is heterogeneous, consisting of two adipocyte-bias and two osteoblast-bias subpopulations, of which it is mainly the former that have the ability to form colonies (Tikhonova et al., 2019).

LepR+ bm-SSPCs are localized in close proximity to the sinusoids and arterioles of the bone marrow (Ding et al., 2012; Zhou B.O. et al., 2014). Therefore, it seems likely that endothelial cells and circulating hormones participate in the formation and/or regulation of the stem cell niche for LepR+ bm-SSPCs. Indeed, it has been proposed that leptin regulates the balance between the osteo- and adipogenic differentiation of bm-SSPCs (Yue et al., 2016). Specifically, activation of Janus kinase 2 (Jak2), an intracellular downstream effector of LepR, in the mesenchyme of the limb bud (in Prx1-Cre:Jak2V617F mice) reduces the trabecular bone mass and increases the number of adipocytes (Yue et al., 2016). Ablation of LepR using Prx1-Cre enhances the expression of markers of osteogenesis (i.e., *Wnt4*), while attenuating the levels of markers of adipogenesis (i.e., *Socs3* and *Cebra*) (Yue et al., 2016). However, these observations must be interpreted with care, since non-inducible Prx1-Cre is active at the limb bud stage (from embryonic day (E) 9.5) and when employed for genetic alterations will induce them in all cells of mesenchymal origin in the limb, including stromal cells, chondrocytes, osteoblasts, osteocytes, and adipocytes (Logan et al., 2002). Thus, the phenotypes observed may be generated indirectly.

It is also unclear whether systemic leptin or leptin secreted by adipocytes in the bone marrow is involved in the regulation of LepR+ bm-SSPCs (Fellows et al., 2016). Adipocytes derived from a CD45-CD31-Sca1+CD24+ mesenchymal-like population of cells, which also express LepR and Cxcl12, secrete dipeptidyl peptidase-4 (Dpp4), which promotes the adipogenic differentiation of CD45-CD31-Sca1+CD24+ cells, forming a positive feedback loop (Ambrosi et al., 2017). *In vitro* sitagliptin, an inhibitor of Dpp4 used clinically to treat diabetes mellitus type 2, promotes osteogenesis, but does not affect the angiogenesis of either CD45-CD31-Sca1+CD24+ cells or CD45-CD31-Sca1-PDGFRα+ osteochondroprogenitors. *In vivo* both sitagliptin and another inhibitor of Dpp4, the tripeptide diprotin A, raise the number of osteochondroprogenitors, lower the number of adipocytes, and promote fracture healing (Ambrosi et al., 2017). On the other hand, single-cell RNA sequencing (scRNAseq) of cells traced with either LepR or vascular endothelial cadherin (VE-Cadherin, also known as CD144) revealed that they do not express *Dpp4* (Tikhonova et al., 2019). Thus, the nature of the Dpp4-dependent interaction between adipocytes and LepR+ bm-SSPCs requires further clarification. Since Dpp4 cleaves a number of chemokines and cytokines, including SDF1 (Zhong and Rajagopalan, 2015), the role of this peptidase in controlling the behavior of stem cells may turn out to be quite complex.

As mentioned above, the close proximity of LepR+ bm-SSPCs to blood vessels suggests that endothelial cells can contribute to the SSPCs niche, as they in fact do to the HSC niche (Winkler et al., 2012; Itkin et al., 2016). Indeed, LepR+ cells express both PDGFRα (*Pdgfra*) and PDGFRβ (*Pdgfrb*) (Sugiyama et al., 2006; Zhou B.O. et al., 2014), whose ligands PDGF-B and PDGF-D are produced by endothelial cells (and pre-osteoclasts) (Xie et al., 2014; Böhm et al., 2019). The existence of such crosstalk is supported by the recent finding that ablation of PDGFRβ from Osx-Cre-positive cells has no effect on bone formation, but lowers the contribution of Osx-traced cells to fracture healing and impaired vascularization of the callus (Böhm et al., 2019).

In addition, endothelial cells and LepR+ bm-SSPCs may interact via the Notch and BMP pathways. Endothelial cells express the Notch ligands *Dll4* and *Dll1*, while LepR+ cells express the *Notch3* receptor (Tikhonova et al., 2019). In addition, LepR+ cells secrete BMP4, while endothelial cells express the *Bmpr2* receptor (Tikhonova et al., 2019). Altogether, these observations suggest that extensive interactions between endothelial cells and bm-SSPCs may contribute to the niche microenvironment.

Of the intracellular signaling pathways likely to be involved in the regulation of LepR+ bm-SSPCs, PI3K/Akt/mTORC1 signaling appears to be a highly plausible candidate. Ablation of the phosphatase and tensin homolog (Pten) in LepR+ cells forces them to differentiate toward the adipogenic lineage (Zhou B.O. et al., 2014). Since Pten counteracts the activity of PI3K, this finding suggests that endocrine/paracrine modulators of the PI3K/Akt/mTORC1 pathway, such as insulin and insulin-like growth factors, may participate in creating a niche appropriate for bm-SSPCs.

Healing of fractures begins in an inflammatory environment. Interestingly, chronic inflammation connected to aging reduces the number of LepR+ bm-SSPCs, as well as their capacity to participate in repair; whereas blocking chronic inflammation with non-steroidal anti-inflammatory drugs (NSAIDs) improves bone regeneration and elevates the number of bm-SSPCs (Josephson et al., 2019). These effects probably involve inhibition of the nuclear factor kappa-light-chain-enhancer in activated B cells (NF-κB), which is otherwise stimulated by SASP (senescence-associated secretory phenotype) (Josephson et al., 2019).

Several other intracellular factors appear to influence the functionality of bm-SSPCs. For instance, ablation of Hox11 (T-cell leukemia homeobox protein 1, *Tlx1* gene) impairs differentiation of bm-SSPCs into cells of the chondrogenic lineage during repair of fractured zeugopod bones, compromising healing or abrogating this process entirely (Rux et al., 2016, 2017). Specific ablation of the forkhead box C1 gene *Foxc1* in LepR+ cells and their progeny (employing LepR-Cre mouse strain) increases the number of adipocytes in the bone marrow, suggesting that *Foxc1* inhibits the adipogenic differentiation of bm-SSPCs (Omatsu et al., 2014). Finally, deletion of the Ebf1 and Ebf3 transcription factors in LepR-targeted cells promotes osteogenesis, suggesting that these factors are required for inhibiting the osteogenic differentiation of bm-SSPCs (Seike et al., 2018).

Other Genetic Markers and Strains of Mice Employed to Characterize Adult bm-SSPCs

All four subpopulations of LepR+ cells express high levels of *Cxcl12* (Tikhonova et al., 2019). The reciprocal analysis of cells targeted in Cxcl12-CreERT mice reported recently (Matsushita et al., 2020) demonstrated that under normal physiological conditions the labeled cells express LepR strongly and are relatively quiescent, contributing predominantly to adipogenesis and only negligibly to the generation of trabecular osteoblasts (Matsushita et al., 2020). This is in contrast to LepR+ bm-SSPCs that produce as much as 90% of the cells of the osteo-lineage with age (Zhou B.O. et al., 2014), a difference that may reflect the fact that in transgenic Cxcl12-CreERT mice only a subset of Cxcl12+ cells is labeled genetically (Matsushita et al., 2020).

Interestingly, in connection with perturbations such as drilling into the bone or the healing of transverse fractures in the tibia, Cxcl12-traced cells contribute a large proportion of the chondrocytes in the fracture callus, as well as the vast majority of the osteoblasts/osteocytes in the formed cortical bone. The selective ablation of β-catenin in this Cxcl12-positive population of cells impairs their osteoblastic differentiation and ability to participate in fracture healing (Matsushita et al., 2020). Thus, in theory at least, bm-SSPCs labeled with Cxcl12-CreERT may represent a subpopulation of LepR+ cells that is activated specifically in response to pathological conditions and β-catenin pathway is involved either in their activation or subsequent functions.

LepR+ bm-SSPCs also express Prx1 (Zhou B.O. et al., 2014, Tikhonova et al., 2019) and activation of hedgehog signaling in Prx1+ cells in 2-week-old Prx1-CreERT mice (Kawanami et al., 2009) promotes their osteogenic differentiation, both *in vivo* and *in vitro* (Deng et al., 2019). Thus, hedgehog signaling may be required for the proper functioning of bm-SSPCs.

In addition to the use LepR as a genetic marker, the bm-SSPCs of adult mice can also be labeled on the basis of their expression of *Grem1*, utilizing the inducible Grem1-CreERT mouse strain (Worthley et al., 2015). Although the populations of LepR+ and Grem1+ bm-SSPCs do not necessarily overlap, scRNAseq analysis revealed expression of *Grem1* by the peri-sinusoidal fraction of LepR-traced cells destined preferentially to become adipocytes (Tikhonova et al., 2019). At the same time, Grem1+ cells in adult mice are predominantly osteogenic (Worthley et al., 2015), suggesting that there exists a subset of Grem1+ cells distinct from the LepR+ population. Grem1+ cells in adult mice are characterized by high expression of *Bmp2*, *Bmp5*, and *Bmp6*, as well as pronounced BMP signaling (Worthley et al., 2015) that may be involved in regulating bm-SSPCs. It is noteworthy that the KEGG (Kyoto Encyclopedia of Genes and Genomes) analysis shows high levels of activities for the extracellular matrix-receptor interaction, PI3K/Akt/mTORC1 and focal adhesion pathways in Grem1+ cells (Worthley et al., 2015).

Another marker utilized to identify adult bm-SSPCs is the glioma-associated oncogene homolog zinc finger protein 1 (Gli1) (Shi et al., 2017). Adult Gli1+ cells characterized employing inducible Gli1-CreERT:tdTomato mice, when labeled at one month of age generate osteoblasts and bone marrow adipocytes with time and, if analyzed 24 h after the labeling, about 60% of these cells are found to express PDGFRα and 10% LepR (Shi et al., 2017). However, 5 months later already 50% of the Tomato+ cells express LepR (Shi et al., 2017). It remains to be determined whether this finding reflects a hierarchical relationship between Gli1+ and LepR+ bm-SSPCs or age-dependent expression of LepR.

Ablation of the HH pathway in adult Gli1+ cells impairs their osteogenic differentiation (Shi et al., 2017), in good agreement with the observation (described in more detail above) that activation of this pathway promotes the osteogenic differentiation of Prx1+ bm-SSPCs (Deng et al., 2019). Some evidences also indicate that β-catenin-dependent Wnt signaling is involved in the regulation of adult bm-SSPCs. Specifically, inactivation of β-catenin in adult Gli1+ cells favors their adipogenic differentiation (Shi et al., 2017). This aligns well with the previous observation that Osx-Cre mediated ablation of β-catenin causes a shift of the fate of targeted cells to the adipogenic line (Song et al., 2012). However, in this context it should not be forgotten that Osx-Cre targets a number of different types of cells, including osteoprogenitors, pericytes and bm-SSPCs (Mizoguchi et al., 2014; Böhm et al., 2019).

These observations indicate that the HH, BMP, Wnt, and mTORC1 pathways are all involved in determining the fate of adult bm-SSPCs and, accordingly, external effectors of these pathways may be involved in creating a niche designed for bm-SSPCs.

Characterization of bm-SSPCs Using the Nestin-GFP and Non-inducible Prx1-Cre Mouse Strains

The Nestin-GFP and non-inducible Prx1-Cre mouse strains are often used to characterize adult bm-SSPCs but have some limitations. An early, highly influential article identified Nestin (*Nes*) as a key marker of bm-SSPCs (referred to as MSCs in that publication), largely on the basis of analysis of Nestin-GFP transgenic mice (Méndez-Ferrer et al., 2010). However, later investigations revealed that the expression of transgenic Nestin-GFP does not reflect the expression of endogenous Nestin or of the transgenic Nestin-Cre construct (Ding et al., 2012; Zhou B.O. et al., 2014), which complicates interpretation of numerous observations considerably. Employing another Nestin-CreERT strain, Worthley et al. (2015) were able to target only 4% of the Nestin-GFP cells, which revealed no contribution to the osteoblast lineage. Furthermore, LepR+ bm-SSPCs do not express the *Nes* gene (Zhou B.O. et al., 2014, Tikhonova et al., 2019) and the population of Grem1+ cells is distinct from that of Nestin-GFP cells (Worthley et al., 2015). At the same time, other investigators have reported detection of low levels of Nestin-GFP in LepR-targeted cells, so called Nestin-GFP^{dim} cells, located close to sinusoids (Ding et al., 2012; Kunisaki et al., 2013). Moreover, 87% of sorted adult Nestin-GFP^{high} cells have been reported to express *Lepr* (Li et al., 2016). Thus, there is a considerable confusion in the scientific

literature concerning the use of Nestin-GFP as a marker for bm-SSPCs cells. To complicate this situation even more, the limited overlap between the Nestin-GFP and Nestin-CreERT transgenic strains of mice (Worthley et al., 2015) makes it difficult to use these as model systems to explore the contribution of Nestin-GFP^{high} cells to the generation of adipocytes, chondrocytes and osteoblasts *in vivo*.

In the case of Prx1-Cre mice, it has been reported that in 10-week-old animals LepR+ cells express *Prx1* (Zhou B.O. et al., 2014, Tikhonova et al., 2019) and 87–89% of the Prx1-Cre-traced cells express LepR in adult mice (Yue et al., 2016). On other hand, cells of the Prx1-Cre-traced subpopulation within the PDGFRα+Sca1+lin-CD45 cells form colonies, but do not express *Nes* or *Lepr* (Greenbaum et al., 2013). Thus, it seems likely that the Prx1-traced cells comprise bm-SSPCs, including LepR+ bm-SSPCs. However, as mentioned above, it must be remembered in this context that the non-inducible Prx1-Cre causes recombination in the limb bud mesenchyme from day E9.5 onward (Logan et al., 2002).

Nevertheless, numerous interesting observations are made with Nestin-GFP and non-inducible Prx1-Cre mice and can shed light on the composition of the adult bm-SSPCs niche and will, therefore, be discussed below.

Sympathetic nerve fibers connected to perivascular stromal cells regulate Nestin-GFP cells. More specifically, chemical neurectomy increases the proliferative activity of Nestin-GFP^{high} cells, whereas treatment with β3 adrenergic receptor agonists inhibits the osteogenic differentiation of these same cells in culture (Méndez-Ferrer et al., 2010). Expression of the gap junction proteins gamma 1 (connexin-45, encoded by *Gjc1*) and alpha 1 (connexin 43, encoded by *Gja1*) by Nestin-GFP^{high} cells suggest that they may have an electromechanical connection to noradrenergic nerve fibers (Méndez-Ferrer et al., 2010). In addition, with aging the bone marrow becomes less innervated and the number of Nestin-GFP^{high} cells, but not Nestin-GFP^{dim} cells rises (Maryanovich et al., 2018).

Furthermore, a functional sympathetic nervous system is required for the anti-osteogenic action of leptin (Takeda et al., 2002). In another model, elevated production of IL-1β by HSCs due to a constitutive mutation in Jak2 (mutation *p.V617F*) results in neuronal damage and decreases the number of Schwann cells, which in turn causes the death of Nestin-GFP^{dim} cells; and this effect is attenuated by an antagonist of β3-adrenoceptors, BRL37344 (Arranz et al., 2014). In this connection it is worth mentioning that sympathetic nerve fibers are involved in regulating a niche for HSCs through secretion of norepinephrine (Katayama et al., 2006), as well as in regulation of the stem cell niche in hair follicles via secretion of Shh (Brownell et al., 2011). This apparent involvement of sympathetic nerve fibers in the bm-SSPCs niche certainly warrants further investigation.

Intermittent treatment of bone with parathyroid hormone (PTH) or PTH-related peptide (PTHrP) exerts a well-known anabolic effect (Osagie-Clouard et al., 2017). After PTH treatment of mice, Nestin-GFP^{high} cells isolated from these animals demonstrate enhanced proliferation and differentiation into osteoblasts in culture (Méndez-Ferrer et al., 2010; Ding et al., 2012). Genetic ablation of the PTH/PTHrP Receptor (*Pth1r*) in Prx1-targeted cells enhances bone adiposity, whereas treatment of isolated bm-SSPCs with PTH1-34 promotes osteogenic differentiation (Fan et al., 2017). The chemokine Cxcl12, which is secreted in considerable amounts by stromal and mesenchymal cells and is known play a role in maintaining the HSC niche (Sugiyama et al., 2006), appears to be involved in supporting the bm-SSPCs niche as well. Targeted deletion of *Cxcl12* in Prx1-targeted cells reduces the mass and elevates the adiposity of bone (Tzeng et al., 2018). Since Prx1-specific ablation of the Cxcl12 receptor Cxcr4 (*Cxcr4*) reduces bone mass without affecting marrow adiposity, it remains unclear whether the effect is autonomous for bm-SSPCs (Tzeng et al., 2018).

Granulocyte colony-stimulating factor (G-CSF or Csf3) secreted by monocytes, fibroblasts and endothelial cells inhibits both the expansion of Nestin-GFP^{high} cells and their differentiation toward the osteoblast lineage (Méndez-Ferrer et al., 2010).

The receptor activator of nuclear factor kappa-B ligand (RANKL) is secreted not only by osteoblasts, but also by bm-SSPCs (Fan et al., 2017; Chen et al., 2018). In addition to regulating osteoclastogenesis (Lacey et al., 1998), RANKL attenuates the differentiation of bm-SSPCs into cells of the osteogenic lineage (Cao, 2018; Chen et al., 2018). This inhibition is probably mediated by activation of NF-κB, with subsequent inhibition of Wnt/β-catenin signaling (Chen et al., 2018).

Furthermore, both osteocytes and osteoblasts secrete osteoprotegerin (OPG), a soluble decoy receptor for RANKL (Kramer et al., 2010), and it appears plausible that a balance between RANKL and OPG may regulate the behavior of bm-SSPCs, creating a feedback signal. Another regulatory link between bm-SSPCs and their progeny may involve Semaphorin 3A (Sema3a), which is secreted by osteoblasts and osteocytes and may promote osteogenic differentiation of bm-SSPCs (Hayashi et al., 2012; Qiao et al., 2018). Altogether, PTH, Cxcl12, G-CSF, the RANKL/OPG ratio and Sema3a may potentially contribute to the formation and regulation of the bm-SSPCs niche in an endocrine/paracrine/autocrine fashion. Further research will establish precise roles played by these different factors.

Clearly, the extracellular matrix plays a role in the regulation of bm-SSPCs *in vitro* (Hoshiba et al., 2016), as well as in the regulation of other stem cell niches *in vivo* (Gattazzo et al., 2014). However, *in vivo* evidence for an involvement of the extracellular matrix in the regulation of adult bm-SSPCs is rather limited. Overexpression of dentin matrix protein 1 (DMP1) under the transcriptional control of the *Nes* promoter attenuates the proliferation and osteogenic differentiation of Nestin+ cells, leading subsequently to a reduction in bone mass (Pan et al., 2017). In contrast, Prx1-dependent ablation of *Dmp1* enhances bone mass and the number of osteoblasts *in vivo* and promotes the *ex vivo* osteogenic differentiation of cells expressing Prx1 (Zhang et al., 2018). Thus, DMP1 may be one of the components of the extracellular matrix involved in niche formation.

In this context it is worth noting that DMP1 is secreted primarily by the progeny of bm-SSPCs, i.e., late osteoblasts and

osteocytes (Fan et al., 2017; Chen et al., 2018). Interestingly concerning the extracellular matrix, a classic test for bone formation involving injection of bm-SSPCs under the kidney capsule shows that these cells can form bone only when co-injected either with their progeny (Chan et al., 2015) or matrigel (Debnath et al., 2018), the extracellular matrix of mouse sarcoma. Thus, their progeny and/or the extracellular matrix are key components of the niche required for maintenance of bm-SSPCs.

In summary, our understanding of the adult bm-SSPCs niche is still evolving. Key components of this niche probably include their immediate progeny, the progeny of HSCs (e.g., monocytes and osteoclasts), adjoining endothelial cells, sympathetic nerve fibers, the extracellular matrix and various hormones coming both from the bloodstream, as well as acting in a paracrine manner (**Figure 1D**).

SKELETAL STEM AND PROGENITOR CELLS IN DEVELOPING BONE

Different genetic markers and/or various other approaches have been utilized to characterize several populations of skeletal stem cells in fetal, neonatal or early postnatal bones. Some of these have already been mentioned above (e.g., Prx1+, Gli1+, Grem1+, Nestin+) and others include Sox9+ SSPCs (Akiyama et al., 2005; He et al., 2017), Col2+ SSPCs (Ono et al., 2014b), Osx+ SSPCs (Greenbaum et al., 2013; Mizoguchi et al., 2014; Tzeng et al., 2018) and Lin-AlphaV+CD200+ SSPCs (Short et al., 2009). Genetic labeling reveals that some of these give rise to others during development (i.e., cells expressing Prx1 begin expressing Osx, Sox9, and Col2), while other populations overlap partially (i.e., Sox9+ and Col2+ cells, Osx+ and Prx1+ cells). In addition, essentially every mouse strain mentioned above targets perichondrium (i.e., Prx1, Nestin-GFP, Sox9, Col2, Grem1, Gli1, and Osx markers) and/or the growth plate chondrocytes (i.e., Prx1, Sox9, Col2, Gremlin, and Gli1 markers). It is important to emphasize that during development the perichondrium gives rise to bone marrow stroma (Maes et al., 2010) and, as discussed above, retains SSPCs into adulthood (Yang et al., 2013; Debnath et al., 2018). Moreover, *trans*-differentiation of hypertrophic chondrocytes of the growth plate into various mesenchymal-type cells of the bone marrow is well established (Yang G. et al., 2014, Yang L. et al., 2014; Zhou X. et al., 2014) and particularly intensive during the early stages of longitudinal bone growth (Li et al., 2017; Mizuhashi et al., 2018; Newton et al., 2019).

The potential influx of new stem/progeny cells from other sources [e.g., Schwann and endoneurial fibroblasts (Carr et al., 2019; Xie et al., 2019b)] makes the development of the skeleton even more complex. From our perspective, the information presently available is indicative of phenotypic plasticity of cells of mesenchymal original and high developmental dynamics during neonatal growth. FACS-based characterization of SSPCs such as Lin-AlphaV+CD200+ SSPCs (Chan et al., 2015, 2018) obtained from surgical samples of fetal or neonatal growth plate surrounded by innervated perichondrium may resolve this issue by identifying *bona fide* skeletal stem cells. However, this approach does not reveal their exact location or the nature of their microenvironment and allows only limited manipulation of these cells in their natural *milieu*.

Of course, every population of SSPCs identified provides valuable information, but, at the same time, little insight can be made into location or composition of the niche during this period. Indeed, *in vivo* identification and localization of the progeny of any specific type of SSPCs is virtually impossible in this dynamic setting. Nevertheless, one pattern is becoming clear.

Several markers – including Grem1 (Worthley et al., 2015), Gli1 (Shi et al., 2017), LepR (Zhou B.O. et al., 2014), Osx (at its multipotency stage, Mizoguchi et al., 2014), PDGFRβ (Böhm et al., 2019), Prx1 (Greenbaum et al., 2013), Nestin-GFP (Ono et al., 2014a), and Col2 (Ono et al., 2014b) – reveal the presence of putative stem cells in the region of the primary spongiosa, immediately below the growth plate. The primary spongiosa is a unique area characterized by intensive bone formation and tissue remodeling. Its distinct extracellular matrix is comprised of remnants of calcified cartilage enriched in type X collagen and osteopontin and containing high levels of matrix metalloproteinases such as MMP9, MMP13, and MMP14, highly active osteoclasts, active *trans*-differentiation of hypertrophic chondrocytes, active angiogenesis and unique arrangements of endothelial cells into hemospheres (Wang et al., 2013).

Furthermore, hypertrophic chondrocytes express a variety of cytokines, including vascular endothelial growth factor (VEGF), RANKL, OPG, and Ihh (Houben et al., 2016), which also may participate in creating a proper microenvironment for SSPCs. For example, ablation of *Ihh* in the growth plate employing Col2-Cre attenuates both Wnt signaling and the maturation of osteoblasts within the primary spongiosa (Maeda et al., 2007). Thus, this combination of features may be the key to creating and maintaining the SSPC niche in growing bones.

However, detailed determination of the components of this niche and their roles in the regulation of individual populations of SSPCs within the primary spongiosa will probably require approaches that are more advanced and sophisticated than those been utilized to date. Moreover, it is important to remember that in humans the growth plate fuses (disappears) during late puberty, in association with the cessation of growth, whereas in mice the growth plate remains open while these animals continue growing into adulthood (Emons et al., 2011; Chagin and Newton, 2019). Accordingly, findings on mice must be applied to humans only with care.

CONCLUSION

Our present knowledge concerning stem cell niches comes mainly from studies on the epithelial and hematopoietic niches, while stem cell niches for SSPCs have been characterized much less extensively. Above, we summarize known information and our own current ideas about the composition of such niches

within bones and the key regulatory pathways that may be involved in establishing and maintaining them.

Each stem cell niche is a complex microenvironment, with an influx of converging signals that influence the behavior of stem cells. We propose that these signals can be categorized as either primary or modulating, with the former being responsible for maintaining basic functions, such as the renewal of stem cells and generation of their progeny, whereas the latter adapt stem cell behavior to changing conditions. Identification of these signals associated with niches for mesenchymal-type cells could be of considerable value in connection with various regenerative therapeutic approaches.

In summary, all of the skeletal stem cell niches discussed here have three features in common: (i) feedback from committed or differentiated progeny, (ii) interaction with the extracellular matrix, and (iii) responsiveness to mechanical and chemical stimuli. Moreover, hedgehog and Wnt signaling, along with inflammatory signals appear to be most common regulators for niches of mesenchymal-type cells (see also **Figure 1**). Clearly, a better understanding of the microenvironments provided by such niches can suggest novel therapeutic approaches based on the regulation of SSPCs.

AUTHOR CONTRIBUTIONS

AC and AK conceived the study. All authors contributed to reviewing the literature, intellectual discussion of the findings, and drafting the manuscript.

FUNDING

This study was supported financially by the Russian Scientific Foundation (RSF, grant #19-15-00241 to AC), the Swedish Research Council (grants #2016-02835 to AC and #2019-01919 to PN), the Karolinska Institutet (AC and PN) including a SFO Stem/Regen junior grant to AC, and the Sechenov University (within the framework of Russian Academic Excellence Project 5-100).

ACKNOWLEDGMENTS

We are grateful to these funding bodies and universities for their support.

REFERENCES

Akiyama, H., Kim, J.-E., Nakashima, K., Balmes, G., Iwai, N., Deng, J. M., et al. (2005). Osteo-chondroprogenitor cells are derived from Sox9 expressing precursors. *Proc. Natl. Acad. Sci. U.S.A.* 102, 14665–14670. doi: 10.1073/pnas.0504750102

Alarcon-Martinez, L., Yilmaz-Ozcan, S., Yemisci, M., Schallek, J., Kılıç, K., Can, A., et al. (2018). Capillary pericytes express α-smooth muscle actin, which requires prevention of filamentous-actin depolymerization for detection. *eLife* 7:e034861. doi: 10.7554/eLife.34861

Alsalameh, S., Amin, R., Gemba, T., and Lotz, M. (2004). Identification of mesenchymal progenitor cells in normal and osteoarthritic human articular cartilage. *Arthrit. Rheum.* 50, 1522–1532. doi: 10.1002/art.20269

Ambrosi, T. H., Longaker, M. T., and Chan, C. K. F. (2019). A revised perspective of skeletal stem cell biology. *Front. Cell Dev. Biol.* 7:189. doi: 10.3389/fcell.2019.00189

Ambrosi, T. H., Scialdone, A., Graja, A., Gohlke, S., Jank, A.-M., Bocian, C., et al. (2017). Adipocyte accumulation in the bone marrow during obesity and aging impairs stem cell-based hematopoietic and bone regeneration. *Cell Stem Cell* 20, 771–784. doi: 10.1016/j.stem.2017.02.009

Arranz, L., Sánchez-Aguilera, A., Martín-Pérez, D., Isern, J., Langa, X., Tzankov, A., et al. (2014). Neuropathy of haematopoietic stem cell niche is essential for myeloproliferative neoplasms. *Nature* 512, 78–81. doi: 10.1038/nature13383

Bahney, C. S., Zondervan, R. L., Allison, P., Theologis, A., Ashley, J. W., Ahn, J., et al. (2019). Cellular biology of fracture healing. *J. Orthop. Res.* 37, 35–50. doi: 10.1002/jor.24170

Bianco, P., and Robey, P. G. (2015). Skeletal stem cells. *Development* 142, 1023–1027. doi: 10.1242/dev.102210

Bianco, P., Robey, P. G., and Simmons, P. J. (2008). Mesenchymal stem cells: revisiting history, concepts, and assays. *Cell Stem Cell* 2, 313–319. doi: 10.1016/j.stem.2008.03.002

Böhm, A. M., Dirckx, N., Tower, R. J., Peredo, N., Vanuytven, S., Theunis, K., et al. (2019). Activation of skeletal stem and progenitor cells for bone regeneration is driven by PDGFRβ signaling. *Dev. Cell* 51, 236–254. doi: 10.1016/j.devcel.2019.08.013

Bonnet, N., Conway, S. J., and Ferrari, S. L. (2012). Regulation of beta catenin signaling and parathyroid hormone anabolic effects in bone by the matricellular protein periostin. *Proc. Natl. Acad. Sci. U. S. A.* 109, 15048–15053. doi: 10.1073/pnas.1203085109

Bonnet, N., Standley, K. N., Bianchi, E. N., Stadelmann, V., Foti, M., Conway, S. J., et al. (2009). The matricellular protein periostin is required for sost inhibition and the anabolic response to mechanical loading and physical activity. *S. J. Biol. Chem.* 284, 35939–35950. doi: 10.1074/jbc.M109.060335

Brownell, I., Guevara, E., Bai, C. B., Loomis, C. A., and Joyner, A. L. (2011). Nerve-derived sonic hedgehog defines a niche for hair follicle stem cells capable of becoming epidermal stem cells. *Cell Stem Cell* 8, 552–565. doi: 10.1016/j.stem.2011.02.021

Calvi, L. M., Adams, G. B., Weibrecht, K. W., Weber, J. M., Olson, D. P., Knight, M. C., et al. (2003). Osteoblastic cells regulate the haematopoietic stem cell niche. *Nature* 425, 841–846. doi: 10.1038/nature02040

Candela, M. E., Cantley, L., Yasuaha, R., Iwamoto, M., Pacifici, M., and Enomoto-Iwamoto, M. (2014). Distribution of slow-cycling cells in epiphyseal cartilage and requirement of β-catenin signaling for their maintenance in growth plate. *J. Orthop. Res.* 32, 661–668. doi: 10.1002/jor.22583

Cao, X. (2018). RANKL-RANK signaling regulates osteoblast differentiation and bone formation. *Bone Res.* 6, 1–2. doi: 10.1038/s41413-018-0040-9

Caplan, A. I. (1991). Mesenchymal stem cells. *J. Orthop. Res.* 9, 641–650. doi: 10.1002/jor.1100090504

Caplan, A. I. (2010). What's in a Name? *Tissue Eng. Part A* 16, 2415–2417. doi: 10.1089/ten.tea.2010.0216

Caplan, A. I. (2017). Mesenchymal stem cells: time to change the name. *Stem Cells Transl. Med.* 6, 1445–1451. doi: 10.1002/sctm.17-0051

Carr, M. J., Toma, J. S., Johnston, A. P. W., Frankland, P. W., Kaplan, D. R., and Miller, F. D. (2019). Mesenchymal precursor cells in adult nerves contribute to mammalian tissue repair and regeneration. *Stem Cell* 24, 1–17. doi: 10.1016/j.stem.2018.10.024

Ceafalan, L. C., Enciu, A. M., Fertig, T. E., Popescu, B. O., Gherghiceanu, M., Hinescu, M. E., et al. (2018). Heterocellular molecular contacts in the mammalian stem cell niche. *Eur. J. Cell Biol.* 97, 442–461. doi: 10.1016/j.ejcb.2018.07.001

Chagin, A. S., and Newton, P. T. (2019). Postnatal skeletal growth is driven by the epiphyseal stem cell niche: potential implications to pediatrics. *Pediatr. Res.* 87, 986–990. doi: 10.1038/s41390-019-0722-z

Chagin, A. S., Vuppalapati, K. K., Kobayashi, T., Guo, J., Hirai, T., Chen, M., et al. (2014). G-protein stimulatory subunit alpha and Gq/11α G-proteins are both required to maintain quiescent stem-like chondrocytes. *Nat. Commun.* 5:3673. doi: 10.1038/ncomms4673

Chan, C. K. F., Gulati, G. S., Sinha, R., Tompkins, J. V., Lopez, M., Carter, A. C., et al. (2018). Identification of the human skeletal stem cell. *Cell* 175, 43–56. doi: 10.1016/j.cell.2018.07.029

Chan, C. K. F., Seo, E. Y., Chen, J. Y., Lo, D., McArdle, A., Sinha, R., et al. (2015). Identification and specification of the mouse skeletal stem cell. *Cell* 160, 285–298. doi: 10.1016/j.cell.2014.12.002

Chang, S. H., Mori, D., Kobayashi, H., Mori, Y., Nakamoto, H., Okada, K., et al. (2019). Excessive mechanical loading promotes osteoarthritis through the gremlin-1–NF-κB pathway. *Nat. Commun.* 10, 1–5. doi: 10.1038/s41467-019-09491-5

Charoenlarp, P., Rajendran, A. K., and Iseki, S. (2017). Role of fibroblast growth factors in bone regeneration. *Inflamm. Regen.* 37, 1–7. doi: 10.1186/s41232-017-0043-8

Chau, M. M. (2014). *Regulation of Growth Plate And Articular Chondrocyte Differentiation: Implications For Longitudinal Bone Growth And Articular Cartilage Formation*. Sweden: Karolinska University Hospital.

Chen, X., Zhi, X., Wang, J., and Su, J. (2018). RANKL signaling in bone marrow mesenchymal stem cells negatively regulates osteoblastic bone formation. *Bone Res.* 6, 1–8. doi: 10.1038/s41413-018-0035-6

Chubinskaya, S., Merrihew, C., Cs-Szabo, G., Mollenhauer, J., McCartney, J., Rueger, D. C., et al. (2000). Human articular chondrocytes express osteogenic protein-1. *J. Histochem. Cytochem.* 48, 239–250. doi: 10.1177/002215540004800209

Clevers, H., and Nusse, R. (2012). Wnt/β-catenin signaling and disease. *Cell* 149, 1192–1205. doi: 10.1016/j.cell.2012.05.012

Collette, N. M., Yee, C. S., Hum, N. R., Murugesh, D. K., Christiansen, B. A., Xie, L. Q., et al. (2016). Sostdc1 deficiency accelerates fracture healing by promoting the expansion of periosteal mesenchymal stem cells. *Bone* 88, 20–30. doi: 10.1016/j.bone.2016.04.005

Collette, N. M., Yee, C. S., Murugesh, D., Sebastian, A., Taher, L., Gale, N. W., et al. (2013). Sost and its paralog Sostdc1 coordinate digit number in a Gli3-dependent manner. *Dev. Biol.* 383, 90–105. doi: 10.1016/j.ydbio.2013.08.015

Colnot, C. (2009). Skeletal cell fate decisions within periosteum and bone marrow during bone regeneration. *J. Bone Miner. Res.* 24, 274–282. doi: 10.1359/jbmr.081003

Colnot, C., Zhang, X., and Tate, M. L. K. (2012). Current insights on the regenerative potential of the periosteum: molecular, cellular, and endogenous engineering approaches. *J. Orthop. Res.* 30, 1869–1878. doi: 10.1002/jor.22181

Correa Maldonado, D., Cavenaghi Pereira da Silva, M., and El-Razi Neto, S. (2013). The effects of joint immobilization on articular cartilage of the knee in previously exercised rats. *J. Anat.* 222, 518–525. doi: 10.1111/joa.12036

Crane, G. M., Jeffery, E., and Morrison, S. J. (2017). Adult haematopoietic stem cell niches. *Nat. Rev. Immunol.* 17, 573–590. doi: 10.1038/nri.2017.53

Debnath, S., Yallowitz, A. R., McCormick, J., Lalani, S., Zhang, T., Xu, R., et al. (2018). Discovery of a periosteal stem cell mediating intramembranous bone formation. *Nature* 562, 133–139. doi: 10.1038/s41586-018-0554-8

Deng, Q., Li, P., Che, M., Liu, J., Biswas, S., Ma, G., et al. (2019). Activation of hedgehog signaling in mesenchymal stem cells induces cartilage and bone tumor formation via Wnt/β-Catenin. *eLife* 8:e50208. doi: 10.7554/eLife.50208

Deng, Z. H., Li, Y. S., Gao, X., Lei, G. H., and Huard, J. (2018). Bone morphogenetic proteins for articular cartilage regeneration. *Osteoarthr. Cartil.* 26, 1153–1161. doi: 10.1016/J.JOCA.2018.03.007

DiGirolamo, D. J., Clemens, T. L., and Kousteni, S. (2012). The skeleton as an endocrine organ. *Nat. Rev. Rheumatol.* 8, 674–683. doi: 10.1038/nrrheum.2012.157

Ding, L., Saunders, T. L., Enikolopov, G., and Morrison, S. J. (2012). Endothelial and perivascular cells maintain haematopoietic stem cells. *Nature* 481, 457–462. doi: 10.1038/nature10783

Dishowitz, M. I., Terkhorn, S. P., Bostic, S. A., and Hankenson, K. D. (2012). Notch signaling components are upregulated during both endochondral and intramembranous bone regeneration. *J. Orthop. Res.* 30, 296–303. doi: 10.1002/jor.21518

Dominici, M., Le Blanc, K., Mueller, I., Slaper-Cortenbach, I., Marini, F., Krause, D., et al. (2006). Minimal criteria for defining multipotent mesenchymal stromal cells. The international society for cellular therapy position statement. *Cytotherapy* 8, 315–317. doi: 10.1080/14653240600855905

Dowthwaite, G. P., Bishop, J. C., Redman, S. N., Khan, I. M., Rooney, P., Evans, D. J. R., et al. (2004). The surface of articular cartilage contains a progenitor cell population. *J. Cell Sci.* 117, 889–897. doi: 10.1242/jcs.00912

Duchamp de Lageneste, O., Julien, A., Abou-Khalil, R., Frangi, G., Carvalho, C., Cagnard, N., et al. (2018). Periosteum contains skeletal stem cells with high bone regenerative potential controlled by periostin. *Nat. Commun.* 9:773. doi: 10.1038/s41467-018-03124-z

Dwek, J. R. (2010). The periosteum: What is it, where is it, and what mimics it in its absence? *Skelet. Radiol.* 39, 319–323. doi: 10.1007/s00256-009-0849-9

Emons, J., Chagin, A. S., Sävendahl, L., Karperien, M., and Wit, J. M. (2011). Mechanisms of growth plate maturation and epiphyseal fusion. *Horm. Res. Paediatr.* 75, 383–391. doi: 10.1159/000327788

Engler, A. J., Sen, S., Sweeney, H. L., and Discher, D. E. (2006). Matrix elasticity directs stem cell lineage specification. *Cell* 126, 677–689. doi: 10.1016/j.cell.2006.06.044

Fan, Y., Hanai, J., Le, P. T., Bi, R., Maridas, D., DeMambro, V., et al. (2017). Parathyroid Hormone directs bone marrow mesenchymal cell fate. *Cell Metab.* 25, 661–672. doi: 10.1016/j.cmet.2017.01.001

Fellows, C. R., Matta, C., Zakany, R., Khan, I. M., and Mobasheri, A. (2016). Adipose, bone marrow and synovial joint-derived mesenchymal stem cells for cartilage repair. *Front. Genet.* 7:213. doi: 10.3389/fgene.2016.00213

Feng, C., Chan, W. C. W., Lam, Y., Wang, X., Chen, P., Niu, B., et al. (2019). Lgr5 and Col22a1 mark progenitor cells in the lineage toward juvenile articular chondrocytes. *Stem Cell Rep.* 8, 290–304. doi: 10.1016/j.stemcr.2019.08.006

Ferraro, F., Celso, C., and Scadden, D. (2010). Adult stem cels and their niches. *Adv. Exp. Med. Biol.* 695, 155–168. doi: 10.1007/978-1-4419-7037-4_11

Ferreira, S. A., Motwani, M. S., Faull, P. A., Seymour, A. J., Yu, T. T. L., Enayati, M., et al. (2018). Bi-directional cell-pericellular matrix interactions direct stem cell fate. *Nat. Commun.* 9:4049. doi: 10.1038/s41467-018-06183-4

Fleming, H. E., Janzen, V., Lo Celso, C., Guo, J., Leahy, K. M., Kronenberg, H. M., et al. (2008). Wnt signalling in the niche enforces hematopoietic stem cell quiescence and is necessary to preserve self-renewal in vivo. *Cell Stem Cell* 2, 274–283. doi: 10.1016/j.stem.2008.01.003

Friedenstein, A. (1990). "Osteogenic stem cells in bone marrow," in *Bone and Mineral Research*, eds J. Heersche and J. Kanis (Amsterdam: Elsevier), 243–272. doi: 10.1016/b978-0-444-81371-8.50012-1

Friedenstein, A., Deriglasova, U., Kulagina, N., Panasuk, A., Rudakowa, S., Luriá, E., et al. (1974). Precursors for fibroblasts in different populations of hematopoietic cells as detected by the in vitro colony assay method. *Exp. Hematol.* 2, 83–92.

Friedenstein, A., Petrakova, K., Kurolesova, A., and Frolova, G. (1968). Heterotopic of bone marrow. Analysis of precursor cells for osteogenic and hematopoietic tissues. *Transplantation* 6, 230–247.

Friedenstein, A. J., Chailakhjan, R. K., and Lalykina, K. S. (1970). The development of fibroblast colonies in monolayer cultures of guinea-pig bone marrow and spleen cells. *Cell Tissue Kinet.* 3, 393–403. doi: 10.1111/j.1365-2184.1970.tb00347.x

Gao, B., Deng, R., Chai, Y., Chen, H., Hu, B., Wang, X., et al. (2019). Macrophage-lineage TRAP+ cells recruit periosteum-derived cells for periosteal osteogenesis and regeneration. *J. Clin. Invest.* 129, 2578–2594. doi: 10.1172/JCI98857

Gattazzo, F., Urciuolo, A., and Bonaldo, P. (2014). Extracellular matrix: a dynamic microenvironment for stem cell niche. *Biochim. Biophys. Acta Gen. Subj.* 1840, 2506–2519. doi: 10.1016/J.BBAGEN.2014.01.010

Ge, J., Burnier, L., Adamopoulou, M., Kwa, M. Q., Schaks, M., Rottner, K., et al. (2018). RhoA, Rac1, and Cdc42 differentially regulate αSMA and collagen I expression in mesenchymal stem cells. *J. Biol. Chem.* 293, 9358–9369. doi: 10.1074/jbc.RA117.001113

Gray, M. L., Burstein, D., and Xia, Y. (2001). Biochemical (and functional) imaging of articular cartilage. *Semin. Musculoskelet. Radiol.* 05, 329–344. doi: 10.1055/s-2001-19043

Grcevic, D., Pejda, S., Matthews, B. G., Repic, D., Wang, L., Li, H., et al. (2012). In vivo fate mapping identifies mesenchymal progenitor cells. *Stem Cells* 30, 187–196. doi: 10.1002/stem.780

Greenbaum, A., Hsu, Y.-M. S., Day, R. B., Schuettpelz, L. G., Christopher, M. J., Borgerding, J. N., et al. (2013). CXCL12 in early mesenchymal progenitors is required for haematopoietic stem-cell maintenance. *Nature* 495, 227–230. doi: 10.1038/nature11926

Grogan, S. P., Duffy, S. F., Pauli, C., Koziol, J. A., Su, A. I., D'Lima, D. D., et al. (2013). Zone-specific gene expression patterns in articular cartilage. *Arthrit. Rheum.* 65, 418–428. doi: 10.1002/art.37760

Grogan, S. P., Miyaki, S., Asahara, H., D'Lima, D. D., and Lotz, M. K. (2009). Mesenchymal progenitor cell markers in human articular cartilage: normal distribution and changes in osteoarthritis. *Arthrit. Res. Ther.* 11:R85. doi: 10.1186/ar2719

Guilak, F., Cohen, D. M., Estes, B. T., Gimble, J. M., Liedtke, W., and Chen, C. S. (2009). Cell stem cell review control of stem cell fate by physical interactions with the extracellular matrix. *Stem Cell* 5, 17–26. doi: 10.1016/j.stem.2009.06.016

Hagiwara, Y., Ando, A., Chimoto, E., Saijo, Y., Ohmori-Matsuda, K., and Itoi, E. (2009). Changes of articular cartilage after immobilization in a rat knee contracture model. *J. Orthop. Res.* 27, 236–242. doi: 10.1002/jor.20724

Hayashi, M., Nakashima, T., Taniguchi, M., Kodama, T., Kumanogoh, A., and Takayanagi, H. (2012). Osteoprotection by semaphorin 3A. *Nature* 485, 69–74. doi: 10.1038/nature11000

Hayes, A. J., Dowthwaite, G. P., Webster, S. V., and Archer, C. W. (2003). The distribution of Notch receptors and their ligands during articular cartilage development. *J. Anat.* 202, 495–502. doi: 10.1046/j.1469-7580.2003.00185.x

He, X., Bougioukli, S., Ortega, B., Arevalo, E., Lieberman, J. R., and McMahon, A. P. (2017). Sox9 positive periosteal cells in fracture repair of the adult mammalian long bone. *Bone* 103, 12–19. doi: 10.1016/j.bone.2017.06.008

Hoshiba, T., Chen, G., Endo, C., Maruyama, H., Wakui, M., Nemoto, E., et al. (2016). Decellularized extracellular matrix as an in vitro model to study the comprehensive roles of the ECM in stem cell differentiation. *Stem Cells Int.* 2016, 1–10. doi: 10.1155/2016/6397820

Houben, A., Kostanova-Poliakova, D., Weissenböck, M., Graf, J., Teufel, S., von der Mark, K., et al. (2016). β-catenin activity in late hypertrophic chondrocytes locally orchestrates osteoblastogenesis and osteoclastogenesis. *Development* 143, 3826–3838. doi: 10.1242/dev.137489

Itkin, T., Gur-Cohen, S., Spencer, J. A., Schajnovitz, A., Ramasamy, S. K., Kusumbe, A. P., et al. (2016). Distinct bone marrow blood vessels differentially regulate haematopoiesis. *Nature* 532, 323–328. doi: 10.1038/nature17624

Jiang, Y., and Tuan, R. S. (2015). Origin and function of cartilage stem/progenitor cells in osteoarthritis. *Nat. Rev. Rheumatol.* 11, 206–212. doi: 10.1038/nrrheum.2014.200

Josephson, A. M., Bradaschia-Correa, V., Lee, S., Leclerc, K., Patel, K. S., Lopez, E. M., et al. (2019). Age-related inflammation triggers skeletal stem/ progenitor cell dysfunction. *Proc. Natl. Acad. Sci. U.S.A.* 116, 6995–7004. doi: 10.1073/pnas.1810692116

Katayama, Y., Battista, M., Kao, W. M., Hidalgo, A., Peired, A. J., Thomas, S. A., et al. (2006). Signals from the sympathetic nervous system regulate hematopoietic stem cell egress from bone marrow. *Cell* 124, 407–421. doi: 10.1016/j.cell.2005.10.041

Kawanami, A., Matsushita, T., Chan, Y. Y., and Murakami, S. (2009). Mice expressing GFP and CreER in osteochondro progenitor cells in the periosteum. *Biochem. Biophys. Res. Commun.* 386, 477–482. doi: 10.1016/j.bbrc.2009.06.059

Kimura, H., Ng, J. M. Y., and Curran, T. (2008). Transient inhibition of the hedgehog pathway in young mice causes permanent defects in bone structure. *Cancer Cell* 13, 249–260. doi: 10.1016/j.ccr.2008.01.027

Knothe Tate, M. L., Yu, N. Y. C., Jalilian, I., Pereira, A. F., and Knothe, U. R. (2016). Periosteum mechanobiology and mechanistic insights for regenerative medicine. *Bonekey Rep.* 5:857. doi: 10.1038/bonekey.2016.70

Kozhemyakina, E., Zhang, M., Ionescu, A., Ayturk, U. M., Ono, N., Kobayashi, A., et al. (2015). Identification of a Prg4-expressing articular cartilage progenitor cell population in mice. *Arthrit. Rheumatol.* 67, 1261–1273. doi: 10.1002/art.39030

Kramer, I., Halleux, C., Keller, H., Pegurri, M., Gooi, J. H., Weber, P. B., et al. (2010). Osteocyte Wnt/β-catenin signaling is required for normal bone homeostasis. *Mol. Cell. Biol.* 30, 3071–3085. doi: 10.1128/mcb.01428-09

Kunisaki, Y., Bruns, I., Scheiermann, C., Ahmed, J., Pinho, S., Zhang, D., et al. (2013). Arteriolar niches maintain haematopoietic stem cell quiescence. *Nature* 502, 637–643. doi: 10.1038/nature12612

Lacey, D. L., Timms, E., Tan, H. L., Kelley, M. J., Dunstan, C. R., Burgess, T., et al. (1998). Osteoprotegerin ligand is a cytokine that regulates osteoclast differentiation and activation. *Cell* 93, 165–176. doi: 10.1016/S0092-8674(00)81569-X

Lai, C.-M., Lin, K.-Y., Kao, S.-H., Chen, Y.-N., Huang, F., and Hsu, H.-J. (2017). Hedgehog signaling establishes precursors for germline stem cell niches by regulating cell adhesion. *J. Cell Biol.* 216:1439. doi: 10.1083/JCB.201610063

Lazzeri, D., Gatti, G. L., Romeo, G., Balmelli, B., and Massei, A. (2009). Bone regeneration and periosteoplasty: a 250-year-long history Cleft Palate. *Craniofac. J.* 46, 621–628. doi: 10.1597/08-085.1

Le, A. X., Miclau, T., Hu, D., and Helms, J. A. (2001). Molecular aspects of healing in stabilized and non-stabilized fractures. *J. Orthop. Res.* 19, 78–84. doi: 10.1016/S0736-0266(00)00006-1

Li, C., Zhen, G., Chai, Y., Xie, L., Crane, J. L., Farber, E., et al. (2016). RhoA determines lineage fate of mesenchymal stem cells by modulating CTGF-VEGF complex in extracellular matrix. *Nat. Commun.* 7:11455. doi: 10.1038/ncomms11455

Li, L., Newton, P. T., Bouderlique, T., Sejnohova, M., Zikmund, T., Kozhemyakina, E., et al. (2017). Superficial cells are self-renewing chondrocyte progenitors, which form the articular cartilage in juvenile mice. *FASEB J.* 31, 1067–1084. doi: 10.1096/fj.201600918R

Li, X., Zhang, Y., Kang, H., Liu, W., Liu, P., Zhang, J., et al. (2005). Sclerostin binds to LRP5/6 and antagonizes canonical Wnt signaling. *J. Biol. Chem.* 280, 19883–19887. doi: 10.1074/jbc.M413274200

Liu, Z., Ren, Y., Mirando, A. J., Wang, C., Zuscik, M. J., O'Keefe, R. J., et al. (2016). Notch signaling in postnatal joint chondrocytes, but not subchondral osteoblasts, is required for articular cartilage and joint maintenance. *Osteoarthr. Cartil.* 24, 740–751. doi: 10.1016/j.joca.2015.10.015

Logan, M., Martin, J. F., Nagy, A., Lobe, C., Olson, E. N., and Tabin, C. J. (2002). Expression of Cre recombinase in the developing mouse limb bud driven by aPrxl enhancer. *Genesis* 33, 77–80. doi: 10.1002/gene.10092

Maeda, Y., Nakamura, E., Nguyen, M.-T., Suva, L. J., Swain, F. L., Razzaque, M. S., et al. (2007). Indian Hedgehog produced by postnatal chondrocytes is essential for maintaining a growth plate and trabecular bone. *Proc. Natl. Acad. Sci. U.S.A.* 104, 6382–6387. doi: 10.1073/pnas.0608449104

Maes, C., Kobayashi, T., Selig, M. K., Torrekens, S., Roth, S. I., Mackem, S., et al. (2010). Osteoblast precursors, but not mature osteoblasts, move into developing and fractured bones along with invading blood vessels. *Dev. Cell* 19, 329–344. doi: 10.1016/j.devcel.2010.07.010

Mahjoub, M., Sassi, N., Driss, M., Laadhar, L., Allouche, M., Hamdoun, M., et al. (2012). Expression patterns of Notch receptors and their ligands in human osteoarthritic and healthy articular cartilage. *Tissue Cell* 44, 182–194. doi: 10.1016/j.tice.2012.03.001

Maryanovich, M., Zahalka, A. H., Pierce, H., Pinho, S., Nakahara, F., Asada, N., et al. (2018). Adrenergic nerve degeneration in bone marrow drives aging of the hematopoietic stem cell niche. *Nat. Med.* 24, 782–791. doi: 10.1038/s41591-018-0030-x

Matsushita, Y., Nagata, M., Kozloff, K. M., Welch, J. D., Mizuhashi, K., Tokavanich, N., et al. (2020). A Wnt-mediated transformation of the bone marrow stromal cell identity orchestrates skeletal regeneration. *Nat. Commun.* 11:332. doi: 10.1038/s41467-019-14029-w

Méndez-Ferrer, S., Michurina, T. V., Ferraro, F., Mazloom, A. R., MacArthur, B. D., Lira, S. A., et al. (2010). Mesenchymal and haematopoietic stem cells form a unique bone marrow niche. *Nature* 466, 829–834. doi: 10.1038/nature09262

Mizoguchi, T., Pinho, S., Ahmed, J., Kunisaki, Y., Hanoun, M., Mendelson, A., et al. (2014). Osterix marks distinct waves of primitive and definitive stromal progenitors during bone marrow development. *Dev. Cell* 29, 340–349. doi: 10.1016/j.devcel.2014.03.013

Mizuhashi, K., Nagata, M., Matsushita, Y., Ono, W., and Ono, N. (2019). Growth plate borderline chondrocytes behave as transient mesenchymal precursor cells. *J. Bone Miner. Res.* 34, 1387–1392. doi: 10.1002/jbmr.3719

Mizuhashi, K., Ono, W., Matsushita, Y., Sakagami, N., Takahashi, A., Saunders, T. L., et al. (2018). Resting zone of the growth plate houses a unique class of skeletal stem cells. *Nature* 563, 254–258. doi: 10.1038/s41586-018-0662-5

Nakahara, H., Bruder, S. P., Goldberg, V. M., and Caplan, A. I. (1990a). In vivo osteochondrogenic potential of cultured cells derived from the periosteum. *Clin. Orthop. Relat. Res.* 259, 223–232. doi: 10.1097/00003086-199010000-00032

Nakahara, H., Bruder, S. P., Haynesworth, S. E., Holecek, J. J., Baber, M. A., Goldberg, V. M., et al. (1990b). Bone and cartilage formation in diffusion chambers by subcultured cells derived from the periosteum. *Bone* 11, 181–188. doi: 10.1016/8756-3282(90)90212-H

Nakahara, H., Dennis, J. E., Bruder, S. P., Haynesworth, S. E., Lennon, D. P., and Caplan, A. I. (1991a). In vitro differentiation of bone and hypertrophic cartilage from periosteal-derived cells. *Exp. Cell Res.* 195, 492–503. doi: 10.1016/0014-4827(91)90401-F

Nakahara, H., Goldberg, V. M., and Caplan, A. I. (1991b). Culture-expanded human periosteal-derived cells exhibit osteochondral potential in vivo. *J. Orthop. Res.* 9, 465–476. doi: 10.1002/jor.1100090402

Nakajima, A., Nakajima, F., Shimizu, S., Ogasawara, A., Wanaka, A., Moriya, H., et al. (2001). Spatial and temporal gene expression for fibroblast growth factor type I receptor (FGFR1) during fracture healing in the rat. *Bone* 29, 458–466. doi: 10.1016/S8756-3282(01)00604-4

Newton, P. T., Li, L., Zhou, B., Schweingruber, C., Hovorakova, M., Xie, M., et al. (2019). A radical switch in clonality reveals a stem cell niche in the epiphyseal growth plate. *Nature* 567, 234–238. doi: 10.1038/s41586-019-0989-6

Newton, P. T., Xie, M., Medvedeva, E. V., Sävendahl, L., and Chagin, A. S. (2018). Activation of mTORC1 in chondrocytes does not affect proliferation or differentiation, but causes the resting zone of the growth plate to become disordered. *Bone Rep.* 8, 64–71. doi: 10.1016/j.bonr.2018.02.006

Ogawa, H., Kozhemyakina, E., Hung, H.-H., Grodzinsky, A. J., and Lassar, A. B. (2014). Mechanical motion promotes expression of Prg4 in articular cartilage via multiple CREB-dependent, fluid flow shear stress-induced signalling pathways. *Genes Dev.* 28, 127–139. doi: 10.1101/gad.231969.113

Ollier, L. (1867). *Traite Experimental Et Clinque De La Regeneration Des Os Et De La Production Artificiialle Du Tissosseaux*. Paris: Masson & Fils.

Omatsu, Y., Seike, M., Sugiyama, T., Kume, T., and Nagasawa, T. (2014). Foxc1 is a critical regulator of haematopoietic stem/progenitor cell niche formation. *Nature* 508, 536–540. doi: 10.1038/nature13071

Ono, N., Ono, W., Mizoguchi, T., Nagasawa, T., Frenette, P. S., and Kronenberg, H. M. (2014a). Vasculature-associated cells expressing nestin in developing bones encompass early cells in the osteoblast and endothelial lineage. *Dev. Cell* 29, 330–339. doi: 10.1016/j.devcel.2014.03.014

Ono, N., Ono, W., Nagasawa, T., and Kronenberg, H. M. (2014b). A subset of chondrogenic cells provides early mesenchymal progenitors in growing bones. *Nat. Cell Biol.* 16, 1157–1167. doi: 10.1038/ncb3067

Ortinau, L. C., Wang, H., Lei, K., Deveza, L., Jeong, Y., Hara, Y., et al. (2019). Identification of functionally distinct Mx1+αSMA+ periosteal skeletal stem cells. *Cell Stem Cell* 25, 784–796. doi: 10.1016/j.stem.2019.11.003

Osagie-Clouard, L., Sanghani, A., Coathup, M., Briggs, T., Bostrom, M., and Blunn, G. (2017). Parathyroid hormone 1-34 and skeletal anabolic action: the use of parathyroid hormone in bone formation. *Bone Res.* 6, 14–21. doi: 10.1302/2046-3758.61.BJR-2016-0085.R1

Owen, M., and Friedenstein, A. J. (1988). Stromal stem cells: marrow-derived osteogenic precursors. *Ciba Found. Symp.* 136, 42–60. doi: 10.1002/9780470513637.ch4

Pan, M., Weng, Y., and Sun, Y. (2017). Overexpression of dentin matrix protein 1 in Nestin+ cells causes bone loss in mouse long bone. *Biochem. Biophys. Res. Commun.* 490, 356–363. doi: 10.1016/j.bbrc.2017.06.048

Pittenger, M. F. (1999). multilineage potential of adult human mesenchymal stem cells. *Science* 284, 143–147. doi: 10.1126/science.284.5411.143

Post, Y., and Clevers, H. (2019). Defining adult stem cell function at its simplest: the ability to replace lost cells through mitosis. *Cell Stem Cell* 25, 174–183. doi: 10.1016/j.stem.2019.07.002

Qiao, Q., Xu, X., Song, Y., Song, S., Zhu, W., and Li, F. (2018). Semaphorin 3A promotes osteogenic differentiation of BMSC from type 2 diabetes mellitus rats. *J. Mol. Histol.* 49, 369–376. doi: 10.1007/s10735-018-9776-1

Rux, D. R., Song, J. Y., Pineault, K. M., Mandair, G. S., Swinehart, I. T., Schlientz, A. J., et al. (2017). Hox11 function is required for region-specific fracture repair. *J. Bone Miner. Res.* 32, 1750–1760. doi: 10.1002/jbmr.3166

Rux, D. R., Song, J. Y., Swinehart, I. T., Pineault, K. M., Schlientz, A. J., Trulik, K. G., et al. (2016). Regionally restricted hox function in adult bone marrow multipotent mesenchymal stem/Stromal cells. *Dev. Cell* 39, 653–666. doi: 10.1016/j.devcel.2016.11.008

Sacchetti, B., Funari, A., Michienzi, S., Di Cesare, S., Piersanti, S., Saggio, I., et al. (2007). Self-renewing osteoprogenitors in bone marrow sinusoids can organize a *Hematopoietic* microenvironment. *Cell* 131, 324–336. doi: 10.1016/j.cell.2007.08.025

Schmid, G. J., Kobayashi, C., Sandell, L. J., and Ornitz, D. M. (2009). Fibroblast growth factor expression during skeletal fracture healing in mice. *Dev. Dyn.* 238, 766–774. doi: 10.1002/dvdy.21882

Schofield, R. (1978). The relationship between the spleen colony-forming cell and the haemopoietic stem cell. A hypothesis. *Blood Cells* 4, 7–25.

Seike, M., Omatsu, Y., Watanabe, H., Kondoh, G., and Nagasawa, T. (2018). Stem cell niche-specific Ebf3 maintains the bone marrow cavity. *Genes Dev.* 32, 359–372. doi: 10.1101/gad.311068.117

Semenov, M., Tamai, K., and He, X. (2005). SOST is a ligand for LRP5/LRP6 and a Wnt signaling inhibitor. *J. Biol. Chem.* 280, 26770–26775. doi: 10.1074/jbc.M504308200

Seror, J., Zhu, L., Goldberg, R., Day, A. J., and Klein, J. (2015). Supramolecular synergy in the boundary lubrication of synovial joints. *Nat. Commun.* 6:6497. doi: 10.1038/ncomms7497

Shi, Y., He, G., Lee, W.-C., McKenzie, J. A., Silva, M. J., and Long, F. (2017). Gli1 identifies osteogenic progenitors for bone formation and fracture repair. *Nat. Commun.* 8:2043. doi: 10.1038/s41467-017-02171-2

Short, B. J., Brouard, N., and Simmons, P. J. (2009). Prospective isolation of mesenchymal stem cells from mouse compact bone. *Methods Mol. Biol.* 482, 259–268. doi: 10.1007/978-1-59745-060-7_16

Singh, A., Yadav, C. B., Tabassum, N., Bajpeyee, A. K., and Verma, V. (2019). Stem cell niche: dynamic neighbor of stem cells. *Eur. J. Cell Biol.* 98, 65–73. doi: 10.1016/j.ejcb.2018.12.001

Söder, S., Hakimiyan, A., Rueger, D. C., Kuettner, K. E., Aigner, T., and Chubinskaya, S. (2005). Antisense inhibition of osteogenic protein 1 disturbs human articular cartilage integrity. *Arthrit. Rheum.* 52, 468–478. doi: 10.1002/art.20856

Song, L., Liu, M., Ono, N., Bringhurst, F. R., Kronenberg, H. M., and Guo, J. (2012). Loss of wnt/β-catenin signalling causes cell fate shift of preosteoblasts from osteoblasts to adipocytes. *J. Bone Miner. Res.* 27, 2344–2358. doi: 10.1002/jbmr.1694

Sugiyama, T., Kohara, H., Noda, M., and Nagasawa, T. (2006). Maintenance of the hematopoietic stem cell pool by CXCL12-CXCR4 chemokine signaling in bone marrow stromal cell niches. *Immunity* 25, 977–988. doi: 10.1016/j.immuni.2006.10.016

Takeda, S., Elefteriou, F., Levasseur, R., Liu, X., Zhao, L., Parker, K. L., et al. (2002). Leptin regulates bone formation via the sympathetic nervous system. *Cell* 111, 305–317. doi: 10.1016/S0092-8674(02)01049-8

Tikhonova, A. N., Dolgalev, I., Hu, H., Sivaraj, K. K., Hoxha, E., Cuesta-Domínguez, A., et al. (2019). The bone marrow microenvironment at single-cell resolution. *Nature* 569, 222–228. doi: 10.1038/s41586-019-1104-8

Tsuji, K., Bandyopadhyay, A., Harfe, B. D., Cox, K., Kakar, S., Gerstenfeld, L., et al. (2006). BMP2 activity, although dispensable for bone formation, is required for the initiation of fracture healing. *Nat. Genet.* 38, 1424–1429. doi: 10.1038/ng1916

Tzeng, Y. S., Chung, N. C., Chen, Y. R., Huang, H. Y., Chuang, W. P., and Lai, D. M. (2018). Imbalanced osteogenesis and adipogenesis in mice deficient in the chemokine Cxcl12/Sdf1 in the bone mesenchymal stem/progenitor cells. *J. Bone Miner. Res.* 33, 679–690. doi: 10.1002/jbmr.3340

Usami, Y., Gunawardena, A. T., Francois, N. B., Otsuru, S., Takano, H., Hirose, K., et al. (2019). Possible contribution of wnt-responsive chondroprogenitors to the postnatal murine growth plate. *J. Bone Miner. Res.* 34, 964–974. doi: 10.1002/jbmr.3658

Ustunel, I., Ozenci, A. M., Sahin, Z., Ozbey, O., Acar, N., Tanriover, G., et al. (2008). The immunohistochemical localization of notch receptors and ligands in human articular cartilage, chondroprogenitor culture and ultrastructural characteristics of these progenitor cells. *Acta Histochem.* 110, 397–407. doi: 10.1016/j.acthis.2007.12.005

Vortkamp, A., Lee, K., Lanske, B., Segre, G. V., Kronenberg, H. M., and Tabin, C. J. (1996). Regulation of rate of cartilage differentiation by indian hedgehog and PTH-related protein. *Science* 273, 613–622. doi: 10.1126/science.273.5275.613

Walker, J. V., Zhuang, H., Singer, D., Illsley, C. S., Kok, W. L., Sivaraj, K. K., et al. (2019). Transit amplifying cells coordinate mouse incisor mesenchymal stem cell activation. *Nat. Commun.* 10:3596. doi: 10.1038/s41467-019-11611-0

Walkley, C. R., Olsen, G. H., Dworkin, S., Fabb, S. A., Swann, J., McArthur, G. A., et al. (2007). A microenvironment-induced myeloproliferative syndrome caused by retinoic acid receptor γ deficiency. *Cell* 129, 1097–1110. doi: 10.1016/j.cell.2007.05.014

Wang, L., Benedito, R., Bixel, M. G., Zeuschner, D., Stehling, M., Sävendahl, L., et al. (2013). Identification of a clonally expanding haematopoietic compartment in bone marrow. *EMBO J.* 32, 219–230. doi: 10.1038/emboj.2012.308

Wang, Q., Huang, C., Xue, M., and Zhang, X. (2011). Expression of endogenous BMP-2 in periosteal progenitor cells is essential for bone healing. *Bone* 48, 524–532. doi: 10.1016/j.bone.2010.10.178

Wang, Q., Huang, C., Zeng, F., Xue, M., and Zhang, X. (2010). Activation of the hh pathway in periosteum-derived mesenchymal stem cells induces bone formation in vivo: Implication for postnatal bone repair. *Am. J. Pathol.* 177, 3100–3111. doi: 10.2353/ajpath.2010.100060

Winkler, I. G., Barbier, V., Nowlan, B., Jacobsen, R. N., Forristal, C. E., Patton, J. T., et al. (2012). Vascular niche E-selectin regulates hematopoietic stem cell dormancy, self renewal and chemoresistance. *Nat. Med.* 18, 1651–1657. doi: 10.1038/nm.2969

Wong, V. W., Levi, B., Rajadas, J., Longaker, M. T., and Gurtner, G. C. (2012). Stem cell niches for skin regeneration. *Int. J. Biomater.* 2012, 1–8. doi: 10.1155/2012/926059

Worthley, D. L., Churchill, M., Compton, J. T., Tailor, Y., Rao, M., Si, Y., et al. (2015). Gremlin 1 identifies a skeletal stem cell with bone, cartilage, and reticular stromal potential. *Cell* 160, 269–284. doi: 10.1016/j.cell.2014.11.042

Xie, H., Cui, Z., Wang, L., Xia, Z., Hu, Y., Xian, L., et al. (2014). PDGF-BB secreted by preosteoclasts induces CD31hi Emcnhi vessel subtype in coupling osteogenesis. *Nat. Med.* 20, 1270–1278. doi: 10.1038/nm.3668

Xie, M., Gol'din, P., Herdina, A. N., Estefa, J., Medvedeva, E. V., Li, L., et al. (2019a). Evolution of the growth plate into a spatially separated structure allows bone growth on land. *bioRxiv* [Preprint], doi: 10.1101/571612

Xie, M., Kamenev, D., Kaucka, M., Kastriti, M. E., Zhou, B., Artemov, A. V., et al. (2019b). Schwann cell precursors contribute to skeletal formation during embryonic development in mice and zebrafish. *Proc. Natl. Acad. Sci. U.S.A.* 116, 15068–15073. doi: 10.1073/PNAS.1900038116

Xuan, F., Yano, F., Mori, D., Chijimatsu, R., Maenohara, Y., Nakamoto, H., et al. (2019). Wnt/β-catenin signaling contributes to articular cartilage homeostasis through lubricin induction in the superficial zone. *Arthrit. Res. Ther.* 21:247. doi: 10.1186/s13075-019-2041-5

Yanagita, M. (2005). BMP antagonists: their roles in development and involvement in pathophysiology. *Cytokine Growth. Factor. Rev.* 16, 309–317. doi: 10.1016/j.cytogfr.2005.02.007

Yang, G., Zhu, L., Hou, N., Lan, Y., Wu, X.-M., Zhou, B., et al. (2014). Osteogenic fate of hypertrophic chondrocytes. *Cell Res.* 24, 1266–1269. doi: 10.1038/cr.2014.111

Yang, L., Tsang, K. Y., Tang, H. C., Chan, D., and Cheah, K. S. E. (2014). Hypertrophic chondrocytes can become osteoblasts and osteocytes in endochondral bone formation. *Proc. Natl. Acad. Sci. U.S.A.* 111, 12097–12102. doi: 10.1073/pnas.1302703111

Yang, W., Wang, J., Moore, D. C., Liang, H., Dooner, M., Wu, Q., et al. (2013). Ptpn11 deletion in a novel progenitor causes metachondromatosis by inducing hedgehog signalling. *Nature* 499, 491–495. doi: 10.1038/nature12396

Yasuhara, R., Ohta, Y., Yuasa, T., Kondo, N., Hoang, T., Addya, S., et al. (2011). Roles of b-catenin signaling in phenotypic expression and proliferation of articular cartilage superficial zone cells. *Lab. Investig.* 91, 1739–1752. doi: 10.1038/labinvest.2011.144

Youngstrom, D. W., Dishowitz, M. I., Bales, C. B., Carr, E., Mutyaba, P. L., Kozloff, K. M., et al. (2016). Jagged1 expression by osteoblast-lineage cells regulates trabecular bone mass and periosteal expansion in mice. *Bone* 91, 64–74. doi: 10.1016/j.bone.2016.07.006

Yu, N. Y. C., O'Brien, C. A., Slapetova, I., Whan, R. M., and Knothe Tate, M. L. (2017). Live tissue imaging to elucidate mechanical modulation of stem cell niche quiescence. *Stem Cells Transl. Med.* 6, 285–292. doi: 10.5966/sctm.2015-0306

Yuan, S.-M. (2015). α-smooth muscle actin and ACTA2 gene expressions in vasculopathies. *Rev. Bras. Circ. Cardiovasc.* 30, 644–649. doi: 10.5935/1678-9741.20150081

Yuasa, T., Kondo, N., Yasuhara, R., Shimono, K., Mackem, S., Pacifici, M., et al. (2009). Transient Activation of Wnt/β-catenin signaling induces abnormal growth plate closure and articular cartilage thickening in postnatal mice. *Am. J. Pathol.* 175, 1993–2003. doi: 10.2353/ajpath.2009.081173

Yue, R., Zhou, B. O., Shimada, I. S., Zhao, Z., and Morrison, S. J. (2016). Leptin receptor promotes adipogenesis and reduces osteogenesis by regulating mesenchymal stromal cells in adult bone marrow. *Cell Stem Cell* 18, 782–796. doi: 10.1016/j.stem.2016.02.015

Zhang, J., Niu, C., Ye, L., Huang, H., He, X., Tong, W.-G., et al. (2003). Identification of the haematopoietic stem cell niche and control of the niche size. *Nature* 425, 836–841. doi: 10.1038/nature02041

Zhang, S., Wan, H., Wang, P., Liu, M., Li, G., Zhang, C., et al. (2018). Extracellular matrix protein DMP1 suppresses osteogenic differentiation of mesenchymal stem cells. *Biochem. Biophys. Res. Commun.* 501, 968–973. doi: 10.1016/j.bbrc.2018.05.092

Zhong, J., and Rajagopalan, S. (2015). Dipeptidyl peptidase-4 regulation of SDF-1/CXCR4 axis: implications for cardiovascular disease. *Front. Immunol.* 6:477. doi: 10.3389/fimmu.2015.00477

Zhou, B. O., Yue, R., Murphy, M. M., Peyer, J. G., and Morrison, S. J. (2014). Leptin-receptor-expressing mesenchymal stromal cells represent the main source of bone formed by adult bone marrow. *Cell Stem Cell* 15, 154–168. doi: 10.1016/j.stem.2014.06.008

Zhou, X., von der Mark, K., Henry, S., Norton, W., Adams, H., and de Crombrugghe, B. (2014). Chondrocytes transdifferentiate into osteoblasts in endochondral bone during development, postnatal growth and fracture healing in mice. *PLoS Genet.* 10:e1004820. doi: 10.1371/journal.pgen.1004820

Conflict of Interest: The authors declare that the research was conducted in the absence of any commercial or financial relationships that could be construed as a potential conflict of interest.

Copyright © 2020 Kurenkova, Medvedeva, Newton and Chagin. This is an open-access article distributed under the terms of the Creative Commons Attribution License (CC BY). The use, distribution or reproduction in other forums is permitted, provided the original author(s) and the copyright owner(s) are credited and that the original publication in this journal is cited, in accordance with accepted academic practice. No use, distribution or reproduction is permitted which does not comply with these terms.

frontiers in Cell and Developmental Biology

HYPOTHESIS AND THEORY
published: 31 July 2020
doi: 10.3389/fcell.2020.00624

Hox-Positive Adult Mesenchymal Stromal Cells: Beyond Positional Identity

Maria Kulebyakina[1] *and Pavel Makarevich*[1,2]*

[1] *Department of Biochemistry and Molecular Medicine, Faculty of Medicine, Lomonosov Moscow State University, Moscow, Russia,* [2] *Laboratory of Gene and Cell Therapy, Institute for Regenerative Medicine, Lomonosov Moscow State University, Moscow, Russia*

Homeotic genes *(Hox)* are universal regulators of the body patterning process in embryogenesis of metazoans. The *Hox* gene expression pattern *(Hox* code) retains in adult tissues and serves as a cellular positional identity marker. Despite previously existing notions that the *Hox* code is inherent in all stroma mesenchymal cells as a whole, recent studies have shown that the *Hox* code may be an attribute of a distinct subpopulation of adult resident mesenchymal stromal cells (MSC). Recent evidence allows suggesting a "non-canonical" role for *Hox* gene expression which is associated with renewal and regeneration in postnatal organs after damage. In tissues with high regenerative capacity, it has been shown that a special cell population is critical for these processes, a distinctive feature of which is the persistent expression of tissue-specific *Hox* genes. We believe that in the postnatal period Hox-positive subpopulation of resident MSC may serve as a unique regenerative reserve. These cells coordinate creation and maintenance of the correct structure of the stroma through a tissue-specific combination of mechanisms. In this article, we summarize data on the role of resident MSC with a tissue-specific pattern of *Hox* gene expression as regulators of correct tissue reconstruction after injury.

Keywords: *Hox* genes, mesenchymal stem/stromal cells, postnatal morphogenesis, regeneration, stroma, tissue renewal

OPEN ACCESS

Edited by:
Darius Widera,
University of Reading,
United Kingdom

Reviewed by:
Philippe Bourin,
Independent Researcher, Toulouse, France
Aleksandra Borodkina,
Institute of Cytology (RAS), Russia
Francesco De Francesco,
Azienda Ospedaliero Universitaria Ospedali Riuniti, Italy
Oleg Gusev,
RIKEN, Japan

***Correspondence:**
Pavel Makarevich
pmakarevich@mc.msu.ru

Specialty section:
This article was submitted to Stem Cell Research, a section of the journal Frontiers in Cell and Developmental Biology

Received: *04 May 2020*
Accepted: *22 June 2020*
Published: *31 July 2020*

Citation:
Kulebyakina M and Makarevich P (2020) Hox-Positive Adult Mesenchymal Stromal Cells: Beyond Positional Identity. Front. Cell Dev. Biol. 8:624. doi: 10.3389/fcell.2020.00624

INTRODUCTION

Homeotic genes (designated as *Hox* in mice and *HOX* in humans) is a family of homeotic genes encoding transcription factors known to function as master regulators of cell identity and fate during embryonic development of vertebrates. In mammals, *Hox* genes regulate patterning of the embryo along the body axis ranging from the anterior boundary of hindbrain till the tail end of the body. *Hox* genes are highly conserved among species and encode a set of proteins that share a high degree of structural similarity. In mammals, 39 *Hox* gene family members are organized into four clusters labeled A, B, C, and D – each cluster located on a separate chromosome – namely 7, 17, 12, and 2, respectively.

Each complex occupies a similar position in the harboring chromosome and its genes are numbered ranging from 1 to 13 according to their location from 3′ to 5′ terminus. However, not each group has all 13 genes, – some numbers may be missing (*e.g.*, *Hoxd* subgroup

has nine genes). Genes of the same number (*e.g.*, *Hoxa9*, *Hoxb9*, *Hoxc9*, and *Hoxd9*) represent paralogues and demonstrate two unique features of *Hox* genes:

- *Spatial collinearity* which means that in the embryo their expression is activated in anteroposterior direction in the same order they are located on the chromosome, starting from 3′. For example, genes of paralogous group 3 are expressed posteriorly to genes of group 2 and all the way further to group 13.
- *Temporal collinearity* which means that during development 3′ genes are expressed earlier than 5′ genes. In vertebrates limb development is determined by posterior *Hox* genes (*Hox9-13*) reflecting the principle of collinearity – indeed, the development of distal body parts correlates with expression of "late-numbered" *Hox* genes. *E.g.*, within a developing limb *Hox9* genes are expressed in the most proximal portion while *Hox13* genes – in the most distal.

In adult organism cells can retain expression of *Hox* genes to form the distinct *Hox* expression pattern known as "*Hox* code" that strictly matches the *Hox* spectrum this part of the body demonstrated during embryonic development (Kmita and Duboule, 2003; Lappin et al., 2006; Svingen and Tonissen, 2006). *Hox* expression patterns are formed at the stage of mesoderm segmentation and subsequently remain unchanged reflecting positional affiliation of cells (Chang et al., 2002; Ackema and Charité, 2008; Picchi et al., 2013). *Hox* code is maintained throughout life in both – stromal and parenchymal cells, but the functional role of postnatal *Hox* gene expression in stroma remains highly enigmatic.

Further, we shall present an overview that will guide to a putative role of postnatal *Hox* expression in subpopulations of stromal cells as a feature required for tissue repair after damage in mammals (including human).

REDUNDANCY OF *Hox* GENES AND STRUCTURAL ANOMALIES CAUSED BY THEIR DISRUPTION

From the functional point of view, Hox proteins are DNA-binding transcription factors that can act as an activator for certain target genes and a repressor for others. The specificity of Hox transcription factors binding to a DNA sequence is determined by protein cofactors from other families (Moens and Selleri, 2006). The main targets of Hox are proteins involved in chromatin remodeling and transcription factors which in summary suggests a major role of Hox in the regulation of genome expression through epigenetic and transcriptional control.

Thus, it is no surprise that a critical role of *Hox*-encoded proteins has been established in a great variety of cellular functions: cell growth, differentiation, migration, invasion, adhesion, etc. (Seifert et al., 2015). At the same time known regulators of *Hox* gene expression are scarce yet recent data suggests that *Hox* expression during embryogenesis is regulated by BMP, Wnt, and retinoic acid pathways. In the adult organism, several *Hox* regulators are found including vitamin D and steroid hormones which shall be discussed in detail below (Seifert et al., 2015; Du and Taylor, 2015).

Despite *Hox* genes' pivotal role in embryo patterning, loss of function in a single *Hox* gene does not always lead to body structural malformation. This matches the existence of paralogous groups mentioned above although the molecular functions of genes among paralogous groups do not fully overlap. In other words, *Hox* genes are characterized by *functional redundancy*.

To date, several dozen mouse strains have been created carrying knockouts of different *Hox* genes. Many of these strains demonstrate profound inborn defects of organs and tissues while some (*e.g.*, with mutant *Hoxc5* or *Hoxa7*) do not display any developmental anomalies. A comprehensive analysis of deviations characteristic for these knockout mice strains can be found in the review by Quinonez and Innis (2014).

In humans, a dozen of developmental anomalies caused by mutations in *HOX* family genes have been described (Quinonez and Innis, 2014). For example, patients with a *HOXA2* gene mutation have microtia, a shortened and narrowed auditory tunnel and cleft palate (Alasti et al., 2008); hereditary hand-food-genital syndrome is a result of *HOXA13* mutations as well (Mortlock and Innis, 1997; Goodman et al., 2000).

POSTNATAL EXPRESSION OF *Hox* IN STROMAL CELLS: MEMORIZING LOCATION AND SUPPORTING REGENERATIVE POTENCY

Stromal cells of mesodermal origin, such as mesenchymal stromal cells (MSC), fibroblasts, smooth muscle cells (Chi et al., 2007), and preadipocytes (Gesta et al., 2006), have a mechanism to memorize their topographic location in the form of their *Hox* code.

Indeed, fibroblasts isolated from topographically different body regions are characterized by a stable *Hox* code reflecting initial localization (Chang et al., 2002; Ackema and Charité, 2008). Moreover, the pattern of *Hox* gene expression in the postnatal period resembles that during development. For example, *Hox* codes in fibroblasts from different tissues coincide with *Hox* codes of mesoangioblasts of respective somites during embryogenesis (Ackema and Charité, 2008).

Lineage tracing data shows that in the postnatal period certain Hox-positive MSC (for example, expressing *Hoxa11*) do not arise from Hox-negative ones, but originate from pre-existed mesoangioblasts (Pineault et al., 2019). Thus, the expression of *Hox* genes in tissue-resident MSC does not seem to "turn on" in the postnatal period but rather remains unrepressed in some cells after birth. This is consistent with a confirmed postulate that in embryonic development *Hox* genes are repressed irreversibly and recapitulation of their expression seems impossible under physiological conditions (Wang et al., 2009). In this case, MSC

inhere *Hox* code of their progenitors and retain it throughout life. This data supports a predisposition that in the postnatal period, tissues may contain subpopulations of Hox-positive MSC originating from embryonic progenitors and retaining their *Hox* code.

The *Hox* code of MSC reflects not only their location and harbor within the body but also serves as a "fingerprint" of tissue from which the cells were isolated. Hox-positive status is a very stable characteristic of a cell: it persists *in vitro* after prolonged culture, during differentiation, and in presence of soluble factors secreted by cells with another *Hox* code (Ackema and Charité, 2008). Expression of *Hox* in MSC is strongly resistant to the influence of exogenous factors (soluble molecules, hypoxia, stress, cell-to-cell contacts, etc.).

It was shown (Leucht et al., 2008) that the *Hox* code in stem cells is preserved even after transplantation to a Hox-negative organ or tissue within the host. In contrast, Hox-negative cells can adopt the *Hox*-code from the Hox-positive environment and this may occur after their heterotopic transplantation, as well as *in vitro* after co-culture with Hox-positive cells. Human unrestricted somatic stem cells (USSC) isolated from cord blood are characterized by the absence of *HOX* expression yet they readily acquire a *HOX* code when co-cultured with Hox-positive MSC (Liedtke et al., 2013).

Pronounced stability of the *Hox* code in the postnatal period may be important for proper healing and tissue regeneration. *Hox* gene expression is locally enhanced at the site of healing cutaneous wound (Uyeno et al., 2001) or bone fracture (Rux et al., 2017), supporting the proposed importance of *Hox* gene expression in these processes. Indeed, *Hox* gene upregulation in the site of injury strongly correlates with the regeneration outcome. Recent work by Qu et al. (2020) on murine digit tip regeneration demonstrated that only the successful regeneration is accompanied by temporary upregulation of *Hoxa13* and *Hoxd13* genes – ones that regulate digit development in embryogenesis. Furthermore, *Hox* gene expression is critical for fibroblast-dependent mechanisms of wound healing. It was demonstrated by Hansen et al. (2003) using transgenic diabetic mice that exhibit diminished wound healing. Exogenous delivery of *Hoxd3* gene to wound bed by plasmid injections accelerated wound closure in these mice which was mediated by robust increase of collagen production by fibroblasts.

Data from in *vivo* experiments suggest that a mismatch between expression patterns of *Hox* genes in the graft and its surroundings may lead to decreased graft survival (Dani et al., 2017). This was accurately demonstrated in a model of bone regeneration after heterologous transplantation (Leucht et al., 2008). In this study, fates of Hoxa11-positive MSC from the tibia and Hox-negative neural crest stem cells from the mandibula were investigated after transplantation either to a Hox-positive (tibia) or Hox-negative environment (mandibula). It was established that transplantation of Hox-negative stem cells to a Hoxa11-positive region led to the acquisition of Hoxa11-positive status by transplanted cells followed by successful healing. In contrast, transplantation of Hox11-positive cells to a Hox-negative microenvironment resulted in a drastic reduction of bone tissue regeneration.

Thus, the contribution of *Hox*-code in resident stromal cells to tissue repair becomes a basis for further assumptions on potential objects and mechanisms to be investigated in this field. We should notice that the role of *Hox* gene expression in regeneration/repair is expected to be the most prominent in tissues with strong regeneration capacity which will be discussed below.

AMONG MSCs, THERE ARE SUBPOPULATIONS EXPRESSING *Hox*, AND THEY DIFFER IN PROPERTIES FROM THOSE THAT DO NOT EXPRESS *Hox*

There is evidence that Hox-positive and Hox-negative subpopulations of stem or stromal cells may reside within the same tissue/organ. It was shown that these subpopulations, although residing in the same compartment, show distinct patterns of properties, for instance, specific *in vitro* differentiation abilities. Particularly, it has been shown that cord blood stem cells contain a subpopulation of USSC that do not express *Hox* and a pool of bone marrow-derived MSC that express *Hox* genes (*HOXA9*, *HOXB7*, *HOXC10*). This finding was concordant with unrestricted potency of USSC that can differentiate into cells of all three germ layers while cord blood MSC are limited to tissues of mesodermal origin (Liedtke et al., 2010). *Vice versa* bone marrow (HOX-positive) MSC, but not USSC (HOX-negative), readily undergo adipogenic differentiation in routine laboratory tests (Kögler et al., 2009).

Thus, it seems that the role of *Hox* gene expression in adult stromal and stem cells is not limited to storing positional information. Since *Hox* genes are master regulators of many processes, *Hox* code affects cell phenotype and, therefore, functional characteristics of a cell which allows claiming that Hox-positive and Hox-negative cells represent two distinct subpopulations. This is consistent with results (Bradaschia-Correa et al., 2019) that Hox status accurately defines transcriptomic differences and differentiation potential between periosteal MSC obtained from Hox-positive and Hox-negative anatomic sites. Recent findings by Rux et al. (2016) highlight a subpopulation of periosteal Hoxa11-positive MSC that was characterized as a progenitor-enriched subpopulation. The role of *Hox11* genes in bone repair will be discussed below supporting this remarkable finding by animal tests in a model of bone fracture.

Another example of the *Hox* gene that serves as a discerning marker within one anatomic region is *HOXC10*. The placenta contains both decidua-derived MSC in which *HOXC10* is highly expressed and amnion-derived MSC that lack its expression (Hwang et al., 2009). These two cell types demonstrate the dramatic difference in their potency and secretome composition (Kögler et al., 2004, 2005) supporting that presence or absence of a specific Hox may be used as a marker to discern between subpopulations of functionally different cells. Indeed, both MSC – from decidua and amnion – show a typical CD73/90/105 immunophenotype and fully comply with other criteria of MSC.

We have mentioned above that fibroblasts isolated from various regions of the body are characterized by different *Hox* codes reflecting their origin. This characteristic of cultured cells retains *in vitro* for a substantial period of time. However, this data was obtained by evaluation of *Hox* expression in a fibroblast culture after several passages (or after a 2-week colony formation assay), which raises a concern on whether a true physiological pattern of *Hox* expression can be reproduced in such kind of experiment. Isolation of MSC is a stress factor similar to tissue damage that affects the status of isolated cells including expression of key transcription factors. It was demonstrated that the phenotype of cultured MSC does not fully reflect the heterogeneity (including functional) of the cell population that existed *in situ* prior to isolation (Sacchetti et al., 2016). Indeed, selective conditions of culture medium may result in a proliferation of one subpopulation and loss of minor pools of cells or ones that fail to adapt to culture medium composition. Thus, over several passages, the composition and ratio of cellular subpopulations may change dramatically and where one may gain advantage another may be marginally eliminated. In addition, we have also mentioned that Hox-negative cells are able to "adopt" *Hox* expression patterns from surrounding cells both – *in vivo* and *in vitro* via an unestablished mechanism (Leucht et al., 2008; Liedtke et al., 2013). Therefore, it is possible that the entire primary culture, previously heterogeneous in *Hox* expression, may acquire a Hox-positive status over time *in vitro*.

RESIDENT Hox-POSITIVE MSC DETERMINE THE STRUCTURE AND ORGANIZATION OF STROMA

Bone

Recent studies have revealed an important role of Hox11-positive stromal cells subpopulation in limb bone regeneration. During embryogenesis, *Hox11* paralogues regulate the development of bones in the forearms and lower legs (zeugopod). In the postnatal period, a subset of Hoxa11-positive MSC resides in these parts of the skeleton. After a fracture, the expression of *Hoxa11* drastically increases at the site of injury. It has been established that *Hox11* genes are necessary for successful fracture healing both in early stages when *Hox11* function is essential for maturation of chondrocytes and in later healing periods when remodeling of the extracellular matrix has been shown to be *Hox11*-dependent (Rux et al., 2016, 2017). *Hox11* genes play an important role not only in fracture healing but also in normal bone turnover: *Hox11*-expressing MSC regulate osteocyte renewal, promoting maturation of osteoblasts and maintaining natural spatial organization of collagen fibrils in the bone (Song et al., 2020).

Loss-of-function experiments show that bone MSC lacking expression of *Hox11* genes fail to completely differentiate to the osteogenic and chondrogenic lineages *in vitro* (Rux et al., 2017; Song et al., 2020). Bone marrow MSC isolated from different parts of the skeleton and therefore having a different *Hox* code also differ by the efficiency of adipogenic and osteogenic differentiation (Ackema and Charité, 2008). Thus, in MSC their *Hox* code does not only carry information about positional identity but also determines specific "bias" of multipotency in cells from different anatomical regions.

In mouse tibia, *Hoxa11* paralogues are expressed exclusively in a subpopulation of periosteal MSC with a PDGFRα+/CD51+/LepR+ immunophenotype (Rux et al., 2016) and it was established that these Hoxa11-positive MSC are essential for normal fracture healing (Rux et al., 2017) supporting that this subpopulation is functionally distinct from Hoxa11-negative MSC of the tibia.

Thus, Hox-positive MSC are necessary for both normal bone renewal and fracture healing. Moreover, we may speculate that during fracture healing Hox-positive MSC may temporarily induce *Hox* expression in other cell subpopulations as these characteristics of Hox-positive-to-Hox-negative cells crosstalk were described *in vitro* in multiple types of stromal cells from other tissue.

Spleen

In recent study, Ueno et al. (2019) characterized a Hoxa11-positive subpopulation of MSC in neonatal mouse spleen. Experiments with ectopic transplantation of an embryonic spleen showed that MSC of this subpopulation differentiate into all three types of splenic stromal cells. After stroma formation, it undergoes repopulation by hematopoietic cells of the host finalizing ectopic spleen to a fully operational organ.

In humans, structural elements of the spleen also show a vivid potential to form heterotopically. There are reported cases of splenosis – a condition when autologous heterotransplantation of splenic cells occurs after the rupture of the organ's capsule. Eventually, it results in ectopic formation of spleen tissue – typically in the abdominal cavity (Fremont and Rice, 2007). It is likely that HOXA11-positive MSC of the spleen may be crucial for the development of splenosis in humans via creating an ectopic stromal harbor for other cell types to build organ *ex situ*. This claim is supported by data in mice that Hoxa11-positive MSC can give rise to all types of spleen stromal cells.

Thus, *Hoxa11* gene expression may be a marker of MSC that function as splenic stroma organizers, and their potency to rebuild spleen's stromal portion is a strong intrinsic feature realized via a specific *Hox*-dependent gene expression profile.

Endometrium

Besides spleen, the human body has another structure that can "take root," rebuild and function after autologous heterotransplantation – endometrium, the inner layer of the uterus.

Endometrium undergoes deep desquamation during every menstrual cycle and regenerates with a remarkable rapidity (within several days). This extraordinary ability of endometrium results in up to 200–300 cycles of complete regeneration over a woman's lifespan and is mediated by specific properties of its stromal cells (endometrial MSC).

The capability of human endometrium to grow outside the uterus also underlies a serious condition known as endometriosis, in which endometrial tissue is ectopically formed in the abdominal cavity, on the surface of ovaries or even umbilicus. Endometriosis leads to hormonal disorders, infertility, and

bleedings since ectopic tissue may undergo desquamation during the menstrual cycle (Vercellini et al., 2013).

Data on the potential role of *Hox* genes in endometrial renewal and ectopy are accumulated during recent decades and deserve an overview within the scope of this communication.

The development of the female reproductive system from the Mullerian duct is controlled by *HOXA9-HOXA13* genes. In particular, morphogenesis of the uterus is strongly regulated by *HOXA10* and *HOXA11*. In mice, impaired function of any of these genes leads to defects in a part of the reproductive system which they control during development (Taylor, 2000). In human development dysregulation of *HOXA10* expression may occur under the influence of a nonsteroidal estrogen medication – diethylstilbestrol (DES) and xenoestrogens, such as methoxychlor and bisphenol A. Both latter substances were widely spread for common purposes like protection of livestock from insect parasites (methoxychlor) or plasticware manufacture (bisphenol A). Influence of these xenobiotics on the developing embryo leads to abnormalities of the reproductive system mediated by persistent impairment of *Hox* gene expression (Ma et al., 1998; Fei et al., 2005; Smith and Taylor, 2007).

In the postnatal period *HOX* expression, specifically *HOXA10* and *HOXA11*, is retained in endometrium and in its resident MSC. Furthermore, there is a remarkable feature of endometrial MSC in which expression of *HOXA10* and *HOXA11* is regulated by steroid sex hormones: estrogen and progesterone.

During the menstrual cycle, plasma concentrations of estrogen and progesterone vary to regulate the switch of its phases. Expression of *HOXA10* and *HOXA11* in endometrial MSC also changes concordantly with undulations of hormone concentration (**Figure 1**). Expression of *HOXA10* and *HOXA11* factors is relatively low in the proliferative phase but increases and reaches its peak in the secretory phase and persists throughout menstruation (Taylor et al., 1998; Tang et al., 2006).

After menstruation, an extensively vascularized wound surface is formed. Menstrual discharge blood has decreased coagulation leading to the absence of granulations and rapid epithelisation followed by formation of the endometrial stroma. The latter is possible due to the proliferation and differentiation of endometrial MSC accompanied by intensive vascularization of tissue layers. We hypothesize that increased *HOXA10* and *HOXA11* expression in MSC during menstruation is an evolutionary established response required for quick and efficient regeneration.

Decidualization and embryo implantation that require the adequate function of the endometrium are *Hox*/*HOX*-dependent processes as well (Du and Taylor, 2015). Subsequently, most reviews of *HOX* genes' role in endometrial function mainly focus on the relation of *HOX* family to female fertility.

We would like to draw attention to another aspect of *HOX* gene expression that can be stipulated as a putatively pivotal role of HOX-positive stromal cells in regeneration of the endometrium. It should be noted that the female reproductive system is one of the few regions in the adult organism that is characterized by a relatively high basal *HOX* gene expression compared to other body parts (Taylor, 2000). We suppose that elevated basal *HOXA* expression in the endometrium may reflect a specific higher threshold for enhanced control of regeneration and retainment of cell program during multiple cycles of its renewal throughout life.

No genetic disease caused by mutations of the *HOXA10/11* genes is known in humans, but there is evidence that a

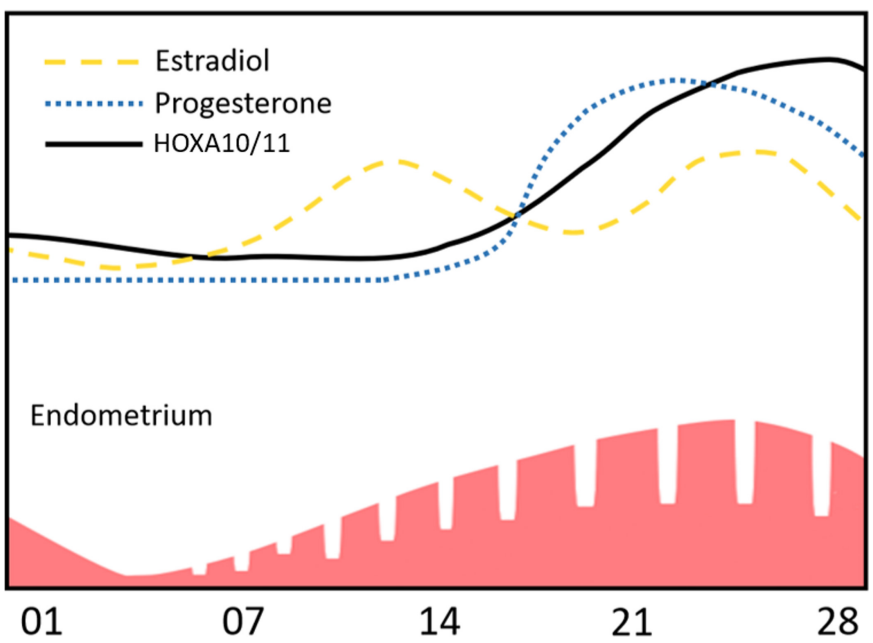


FIGURE 1 | *HOXA10* and *HOXA11* expression dynamic is concordant to changes of estradiol and progesterone levels during the menstrual cycle.

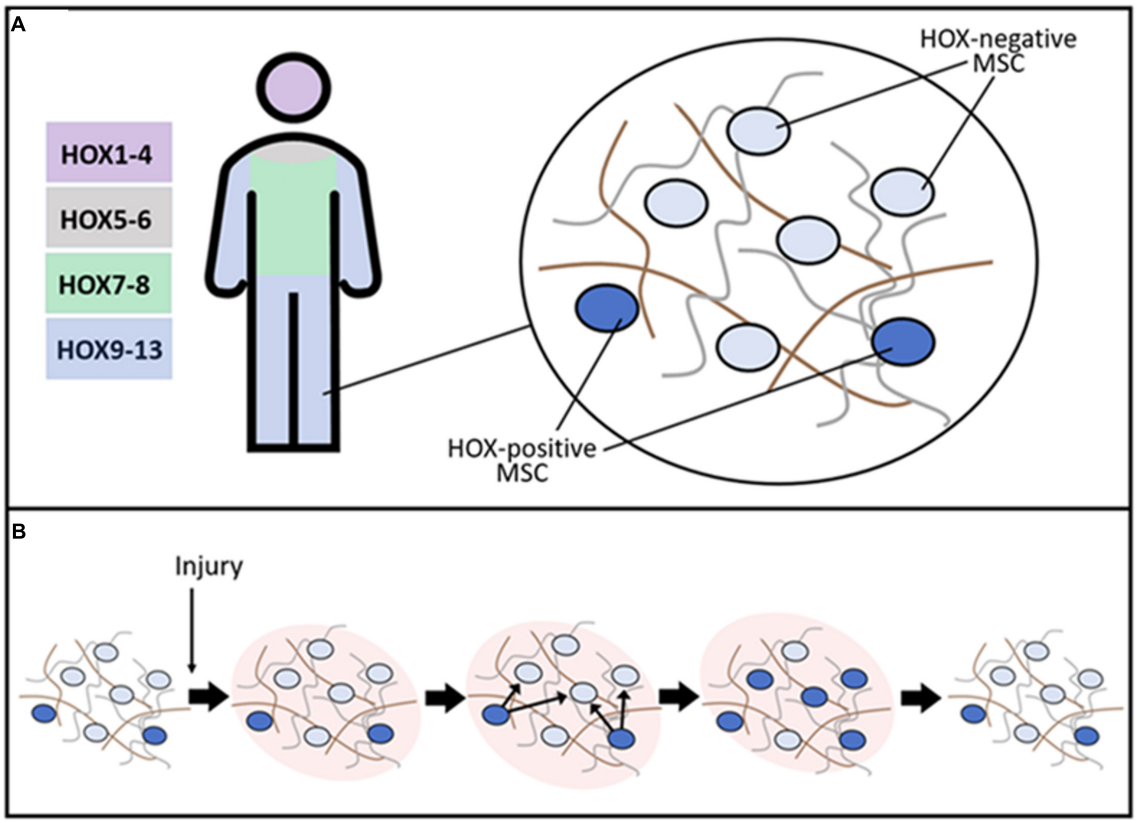


FIGURE 2 | Putative role of resident HOX-positive MSC in the maintenance of stroma tissue-specific structure. **(A)** After embryogenesis, *HOX* gene expression is conserved in a distinct subpopulation of MSC. The schematic representation of *HOX* codes in distinct body parts is present. In normal tissue, a small HOX-positive subpopulation of MSC coordinates matrix turnover processes supporting normal architecture of stroma during physiological tissue renewal. **(B)** After damage, HOX-positive MSC are activated and induce expression of *HOX* genes in neighboring cells leading to the restoration of the initial structure of tissue stroma and facilitating regeneration.

number of diseases of the female reproductive system such as hydrosalpinx, polycystic ovary syndrome and endometriosis are accompanied by decreased expression of *HOXA10* and *HOXA11* in the endometrium. Remarkably numerous and accurate studies show this for endometriosis (Wu et al., 2005; Du and Taylor, 2015). We want to pay special attention to the relation of impaired expression of *HOXA10* and *HOXA11* to endometriosis since this disease involves the ability of the endometrial stroma to self-organize ectopically, i.e., to "ignore" conditions of an ectopic environment.

We suggest that decreased expression of *HOXA10*/*HOXA11* in endometrial stromal cells may be a causal factor in the development of endometriosis. According to data on the interaction between a graft and a host with different *Hox* codes, lack of *Hox* expression in the transplant allows it to successfully engraft – either in a Hox-positive or Hox-negative host environment. Therefore, decreased expression of *HOXA10*/*HOXA11* genes results in partial loss of *HOX* code "identity" in endometrial cells facilitating its ectopy. It is of particular interest that the suppression of *HOXA10* results in increased autophagy proteins (beclin-1 and LC3-II) expression in endometrial tissue (Zheng et al., 2018). We suppose that it reflects a protective mechanism for clearance of cells with "loss of identity", and that its failure results in the survival of ectopic endometrial cells with suppressed *HOXA10*/*11*. Being moved into the abdominal cavity they may adopt local HOX conditions and by unknown means avoid intrinsically activated autophagy to form endometrial tissue in an ectopic location.

Due to findings on Hoxa11-positive periosteum MSC, it is known that *Hox* gene functioning in stromal cells is of great importance for maintaining the normal structure of the stroma. In patients with endometriosis, the architecture of eutopic endometrium is impaired, including increased surface epithelium heterogeneity and reduced endometrial thickness (reviewed in Sharpe-Timms, 2001), which can also be caused or mediated by altered *HOX* expression in stromal cells of the endometrium.

Thus, available data suggests that the expression of *HOXA* genes in MSC of the endometrium ensures its normal functioning and regeneration during the menstrual cycle. We suggest that a HOXA-positive MSC subpopulation in the endometrium is critical for controlling its physiological regeneration after damage, as well as for maintaining the normal structure.

CONCLUSION

Homeobox genes are critical during embryonic development of many animals. Expression of *Hox* is known to persist in many tissues in the postnatal period suggesting the role of these genes not only during development but also for the functioning of tissues throughout life. The tissue-specific pattern of *Hox* gene expression is inherent in stromal/stem cells of mesenchymal origin whose role in physiological renewal and regeneration is well-established in recent decades (**Figure 2**).

We believe that the generally adopted *Hox* code hypothesis and the role of these genes in supporting postnatal cell identity might lead us to a particularly important direction in the study of human regenerative biology. Key points of this hypothetical direction are summarized below:

1. In adult organisms, resident MSC represent a highly heterogeneous cell population with variable differentiation potency, sensitivity to regulatory stimuli, and genome expression. Recent studies demonstrated the existence of specific subpopulations of MSC necessary for the organization of normal tissue stroma with its tissue-specific features. Presumably, subpopulations of MSC retaining *Hox* expression may take specialized functions associated with the organization of the tissue-specific structure of the stroma. Our hypothesis relies on the expression of *Hox* genes as a specific feature of this subpopulation as far as resident MSC include cells of both types – highly expressing *Hox* genes and cells that lack *Hox* expression.
2. In humans, HOX-positive MSC subpopulations are crucial for maintaining and reconstructing stroma and have been identified within tissues that demonstrate a remarkable ability for regeneration (bone and spleen). We suggest that resident Hox-positive MSC are leading *organizers* of stroma renewal and tissue regeneration in other tissues as well and highlight a direction of research focused on the endometrium.
3. The peculiar feature of spleen and endometrium is ectopic growth which indicates a potent ability of cells within these tissues to rebuild a functional environment and give rise to organs (*e.g.*, splenosis). We suggest that *Hox* expression in a certain subpopulation of MSC in these tissues mediates their ectopic growth and efficient regeneration. Probably, identification of this subpopulation might be within reach in the endometrium as a feasible model object undergoing massive desquamation and reconstruction several hundred times. Data has been accumulated in favor of the assumption that Hox-positive stromal cells of the endometrium are important for its successful regeneration. Study of *Hox* patterns and their role in endometrial regeneration will allow more detailed insight into the functions of Hox-positive MSC and will expand our understanding of postnatal morphogenesis.

From a methodological point of view identification of crucial *Hox* genes using knockout or transgenic models may be a complicated mission due to functional redundancy of *Hox* paralogues. One may fail to exactly define an *in vivo* role of a given *Hox* using its knockout. To achieve a "loss of function" status with an obvious morphological outcome, a strain of animals with mixed knockouts and lacking several *Hox* genes may be required. In addition, conditional loss-of-function models are often obligatory – otherwise, it will be impossible to separate the effects of *Hox* disruption in embryonic development from defects that occur due to *Hox* gene suppression in the same structures in the postnatal period.

We expect our communication to trigger a certain amount of discussion and invite other authors and peers to comment on the potential of proposed direction of research and shall endeavor to decipher the role of *Hox* genes in regeneration using available models within our expertise (Eremichev et al., 2018; Nimiritsky et al., 2019).

AUTHOR CONTRIBUTIONS

MK: conception and drafting of the manuscript. PM: editing the manuscript, proofing, and funding acquisition. Both authors contributed to the article and approved the submitted version.

FUNDING

This work has been supported by the Russian Science Foundation grants #19-75-00067 (figure preparation and access to publications) and #19-75-30007 (publisher fee).

ACKNOWLEDGMENTS

Authors express their gratitude to Dr. Ivan Kulakovskiy for fruitful discussion on bioinformatical approaches that may be used in further studies and to Mr. Mikhail Arbatskiy for assistance in bioinformatics surveys during manuscript revision.

REFERENCES

Ackema, K. B., and Charité, J. (2008). Mesenchymal stem cells from different organs are characterized by distinct topographic Hox codes. *Stem Cells Dev.* 17, 979–1091. doi: 10.1089/scd.2007.0220

Alasti, F., Sadeghi, A., Sanati, M. H., Farhadi, M., Stollar, E., Somers, T., et al. (2008). A mutation in HOXA2 is responsible for autosomal-recessive microtia in an Iranian family. *Am. J. Hum. Genet.* 82, 982–991. doi: 10.1016/j.ajhg.2008.02.015

Bradaschia-Correa, V., Leclerc, K., Josephson, A. M., Lee, S., Palma, L., Litwa, H. P., et al. (2019). Hox gene expression determines cell fate of adult periosteal stem/progenitor cells. *Sci. Rep.* 9:5043. doi: 10.1038/s41598-019-41639-7

Chang, H. Y., Chi, J.-T., Dudoit, S., Bondre, C., van de Rijn, M., Botstein, D., et al. (2002). Diversity, topographic differentiation, and positional memory in human fibroblasts. *Proc. Natl. Acad. Sci. U.S.A.* 99, 12877–12882. doi: 10.1073/pnas.162488599

Chi, J.-T., Rodriguez, E. H., Wang, Z., Nuyten, D. S. A., Mukherjee, S., van de Rijn, M., et al. (2007). Gene expression programs of human smooth muscle cells: tissue-specific differentiation and prognostic significance in breast cancers. *PLoS Genet.* 3:164. doi: 10.1371/journal.pgen.0030164

Dani, C., Foissac, R., Ladoux, A., and Chignon-Sicard, B. (2017). Autologous fat grafts: can we match the donor fat site and the host environment for better postoperative outcomes and safety? *Curr. Surg. Rep.* 5:14. doi: 10.1007/s40137-017-0178-1

Du, H., and Taylor, H. S. (2015). The role of Hox genes in female reproductive tract development, adult function, and fertility. *Cold Spring Harb. Perspect. Med.* 6:023002. doi: 10.1101/cshperspect.a023002

Eremichev, R. Y., Makarevich, O. A., Alexandrushkina, N. A., Kulebyakin, K. Y., Dyikanov, D. T., and Makarevich, P. I. (2018). Menstrual-blood serum displays an antifibrotic effect on human endometrial mesenchymal stromal cells. *Cell Tiss. Biol.* 12, 281–288. doi: 10.1134/S1990519X1804003X

Fei, X., Chung, H., and Taylor, H. S. (2005). Methoxychlor disrupts uterine Hoxa10 gene expression. *Endocrinology* 146, 3445–3451. doi: 10.1210/en.2005-0341

Fremont, R. D., and Rice, T. W. (2007). Splenosis: a review. *South Med. J.* 100, 589–593. doi: 10.1097/SMJ.0b013e318038d1f8

Gesta, S., Blüher, M., Yamamoto, Y., Norris, A. W., Berndt, J., Kralisch, S., et al. (2006). Evidence for a role of developmental genes in the origin of obesity and body fat distribution. *Proc. Natl. Acad. Sci. U.S.A.* 103, 6676–6681. doi: 10.1073/pnas.0601752103

Goodman, F. R., Bacchelli, C., Brady, A. F., Brueton, L. A., Fryns, J. P., Mortlock, D. P., et al. (2000). Novel HOXA13 mutations and the phenotypic spectrum of hand-foot-genital syndrome. *Am. J. Hum. Genet.* 67, 197–202. doi: 10.1086/302961

Hansen, S. L., Myers, C. A., Charboneau, A., Young, D. M., and Boudreau, N. (2003). HoxD3 accelerates wound healing in diabetic mice. *Am. J. Pathol.* 163, 2421–2431. doi: 10.1016/S0002-9440(10)63597-3

Hwang, J. H., Seok, O. S., Song, H. R., Jo, J. Y., and Lee, J. K. (2009). HOXC10 as a potential marker for discriminating between amnion- and decidua-derived mesenchymal stem cells. *Cloning Stem. Cells* 11, 269–279. doi: 10.1089/clo.2008.0068

Kmita, M., and Duboule, D. (2003). Organizing axes in time and space; 25 years of colinear tinkering. *Science* 301, 331–333. doi: 10.1126/science.1085753

Kögler, G., Critser, P., Trapp, T., and Yoder, M. (2009). Future of cord blood for non-oncology uses. *Bone Marrow Transplant.* 44, 683–697. doi: 10.1038/bmt.2009.287

Kögler, G., Radke, T. F., Lefort, A., Sensken, S., Fischer, J., Sorg, R. V., et al. (2005). Cytokine production and hematopoiesis supporting activity of cord blood-derived unrestricted somatic stem cells. *Exp. Hematol.* 33, 573–583. doi: 10.1016/j.exphem.2005.01.012

Kögler, G., Sensken, S., Airey, J. A., Trapp, T., Müschen, M., Feldhahn, N., et al. (2004). A new human somatic stem cell from placental cord blood with intrinsic pluripotent differentiation potential. *J. Exp. Med.* 200, 123–135. doi: 10.1084/jem.20040440

Lappin, T. R., Grier, D. G., Thompson, A., and Halliday, H. L. (2006). HOX genes: seductive science, mysterious mechanisms. *Ulster Med. J.* 75, 23–31.

Leucht, P., Kim, J. B., Amasha, R., James, A. W., Girod, S., and Helms, J. A. (2008). Embryonic origin and Hox status determine progenitor cell fate during adult bone regeneration. *Development* 135, 2845–2854. doi: 10.1242/dev.023788

Liedtke, S., Buchheiser, A., Bosch, J., Bosse, F., Kruse, F., Zhao, X., et al. (2010). The HOX code as a "biological fingerprint" to distinguish functionally distinct stem cell populations derived from cord blood. *Stem Cell Res.* 5, 40–50. doi: 10.1016/j.scr.2010.03.004

Liedtke, S., Freytag, E. M., Bosch, J., Houben, A. P., Radke, T. F., Deenen, R., et al. (2013). Neonatal mesenchymal-like cells adapt to surrounding cells. *Stem Cell Res.* 11, 634–646. doi: 10.1016/j.scr.2013.04.001

Ma, L., Benson, G. V., Lim, H., Dey, S. K., and Maas, R. L. (1998). Abdominal B (AbdB) Hoxa genes: regulation in adult uterus by estrogen and progesterone and repression in mullerian duct by the synthetic estrogen diethylstilbestrol (DES). *Dev. Biol.* 197, 141–154. doi: 10.1006/dbio.1998.8907

Moens, C. B., and Selleri, L. (2006). Hox cofactors in vertebrate development. *Dev. Biol.* 291, 193–206. doi: 10.1016/j.ydbio.2005.10.032

Mortlock, D. P., and Innis, J. W. (1997). Mutation of HOXA13 in hand-foot-genital syndrome. *Nat. Genet.* 15, 179–180. doi: 10.1038/ng0297-179

Nimiritsky, P. P., Eremichev, R. Y., Alexandrushkina, N. A., Efimenko, A. Y., Tkachuk, V. A., and Makarevich, P. I. (2019). Unveiling mesenchymal stromal Cells'. organizing function in regeneration. *Int. J. Mol. Sci.* 20:823. doi: 10.3390/ijms20040823

Picchi, J., Trombi, L., Spugnesi, L., Barachini, S., Maroni, G., Brodano, G. B., et al. (2013). HOX and TALE signatures specify human stromal stem cell populations from different sources. *J. Cell Physiol.* 228, 879–889. doi: 10.1002/jcp.24239

Pineault, K. M., Song, J. Y., Kozloff, K. M., Lucas, D., and Wellik, D. M. (2019). Hox11 expressing regional skeletal stem cells are progenitors for osteoblasts, chondrocytes and adipocytes throughout life. *Nat. Commun.* 10:3168. doi: 10.1038/s41467-019-11100-4

Qu, F., Palte, I. C., Gontarz, P. M., Zhang, B., and Guilak, F. (2020). Transcriptomic analysis of bone and fibrous tissue morphogenesis during digit tip regeneration in the adult mouse. *FASEB J.* 10 doi: 10.1096/fj.202000330R [Epub ahead of print].

Quinonez, S. C., and Innis, J. W. (2014). Human HOX gene disorders. *Mol. Genet. Metab.* 111, 4–15. doi: 10.1016/j.ymgme.2013.10.012

Rux, D. R., Song, J. Y., Pineault, K. M., Mandair, G. S., Swinehart, I. T., Schlientz, A. J., et al. (2017). Hox11 function is required for region-specific fracture repair. *J. Bone Miner. Res.* 32, 1750–1760. doi: 10.1002/jbmr.3166

Rux, D. R., Song, J. Y., Swinehart, I. T., Pineault, K. M., Schlientz, A. J., Trulik, K. G., et al. (2016). Regionally restricted Hox function in adult bone marrow multipotent mesenchymal stem/stromal cells. *Dev. Cell* 39, 653–666. doi: 10.1016/j.devcel.2016.11.008

Sacchetti, B., Funari, A., Remoli, C., Giannicola, G., Kögler, G., Liedtke, S., et al. (2016). No identical "mesenchymal stem cells" at different times and sites: human committed progenitors of distinct origin and differentiation potential are incorporated as adventitial cells in microvessels. *Stem Cell Rep.orts* 6, 897–913. doi: 10.1016/j.stemcr.2016.05.011

Seifert, A., Werheid, D. F., Knapp, S. M., and Tobiasch, E. (2015). Role of Hox genes in stem cell differentiation. *World J. Stem Cells* 7, 583–595. doi: 10.4252/wjsc.v7.i3.583

Sharpe-Timms, K. L. (2001). Endometrial anomalies in women with endometriosis. *Ann. N. Y. Acad. Sci.* 943, 131–147. doi: 10.1111/j.1749-6632.2001.tb03797.x

Smith, C., and Taylor, H. S. (2007). Xenoestrogen exposure imprints expression of genes (Hoxa10) required for normal uterine development. *FASEB J.* 21, 239–246. doi: 10.1096/fj.06-6635com

Song, J. Y., Pineault, K. M., Dones, J. M., Raines, R. T., and Wellik, D. M. (2020). Hox genes maintain critical roles in the adult skeleton. *Proc. Natl. Acad. Sci. U.S.A* 117, 7296–7304. doi: 10.1073/pnas.1920860117

Svingen, T., and Tonissen, K. F. (2006). Hox transcription factors and their elusive mammalian gene targets. *Heredity* 97, 88–96. doi: 10.1038/sj.hdy.6800847

Tang, Y., Wang, L., Lv, L., Su, B., Feng, X., Wang, N., et al. (2006). Differential expression of HOXA11 in human endometrial glandular epithelial and stromal cells. *Reprod. Contracept.* 11.

Taylor, H. S. (2000). The role of HOX genes in the development and function of the female reproductive tract. *Semin. Reprod. Med.* 18, 81–89. doi: 10.1055/s-2000-13478

Taylor, H. S., Arici, A., Olive, D., and Igarashi, P. (1998). HOXA10 is expressed in response to sex steroids at the time of implantation in the human endometrium. *J. Clin. Invest.* 101, 1379–1384. doi: 10.1172/JCI1057

Ueno, Y., Fujisaki, K., Hosoda, S., Amemiya, Y., Okazaki, S., Notsu, C., et al. (2019). Transcription factor Tlx1 marks a subset of lymphoid tissue organizer-like mesenchymal progenitor cells in the neonatal spleen. *Sci. Rep.* 9:20408.

Uyeno, L. A., Newman-Keagle, J. A., Cheung, I., Hunt, T. K., Young, D. M., and Boudreau, N. (2001). Hox D3 expression in normal and impaired wound healing. *J. Surg. Res.* 100, 46–56. doi: 10.1006/jsre.2001.6174

Vercellini, P., Viganò, P., Somigliana, E., and Fedele, L. (2013). Endometriosis: pathogenesis and treatment. *Nat. Rev. Endocrinol.* 10, 261–275. doi: 10.1038/nrendo.2013.255

Wang, K., Helms, J., and Chang, H. (2009). Regeneration, repair and remembering identity: the three Rs of Hox gene expression. *Trends Cell Biol.* 19, 268–275. doi: 10.1016/j.tcb.2009.03.007

Wu, Y., Halverson, G., Basir, Z., Strawn, E., Yan, P., and Guo, S. W. (2005). Aberrant methylation at HOXA10 may be responsible for its aberrant expression in the endometrium of patients with endometriosis. *Am. J. Obstet. Gynecol.* 193, 371–380. doi: 10.1016/j.ajog.2005.01.034

Zheng, J., Luo, X., Bao, J., Huang, X., Jin, Y., Chen, L., et al. (2018). Decreased expression of HOXA10 may activate the autophagic process in ovarian endometriosis. *Reprod. Sci.* 25, 1446–1454.

Conflict of Interest: The authors declare that the research was conducted in the absence of any commercial or financial relationships that could be construed as a potential conflict of interest.

Copyright © 2020 Kulebyakina and Makarevich. This is an open-access article distributed under the terms of the Creative Commons Attribution License (CC BY). The use, distribution or reproduction in other forums is permitted, provided the original author(s) and the copyright owner(s) are credited and that the original publication in this journal is cited, in accordance with accepted academic practice. No use, distribution or reproduction is permitted which does not comply with these terms.

frontiers in Cell and Developmental Biology

ORIGINAL RESEARCH
published: 07 August 2020
doi: 10.3389/fcell.2020.00685

Inhibiting Heat Shock Protein 90 Protects Nucleus Pulposus-Derived Stem/Progenitor Cells From Compression-Induced Necroptosis and Apoptosis

Binwu Hu[1†], Shuo Zhang[1†], Weijian Liu[1], Peng Wang[1], Songfeng Chen[2], Xiao Lv[1], Deyao Shi[1], Kaige Ma[1], Baichuan Wang[1], Yongchao Wu[1] and Zengwu Shao[1]*

[1] Department of Orthopaedics, Union Hospital, Tongji Medical College, Huazhong University of Science and Technology, Wuhan, China, [2] Department of Orthopaedic Surgery, The First Affiliated Hospital of Zhengzhou University, Zhengzhou, China

OPEN ACCESS

Edited by:
Pavel Makarevich, Lomonosov Moscow State University, Russia

Reviewed by:
Gelina Kopeina, Lomonosov Moscow State University, Russia
Xiaolei Zhang, Second Affiliated Hospital and Yuying Children's Hospital of Wenzhou Medical University, China

***Correspondence:**
Zengwu Shao
szwpro@163.com

[†] These authors have contributed equally to this work

Specialty section:
This article was submitted to Molecular Medicine, a section of the journal Frontiers in Cell and Developmental Biology

Received: 23 March 2020
Accepted: 06 July 2020
Published: 07 August 2020

Citation:
Hu B, Zhang S, Liu W, Wang P, Chen S, Lv X, Shi D, Ma K, Wang B, Wu Y and Shao Z (2020) Inhibiting Heat Shock Protein 90 Protects Nucleus Pulposus-Derived Stem/Progenitor Cells From Compression-Induced Necroptosis and Apoptosis. Front. Cell Dev. Biol. 8:685. doi: 10.3389/fcell.2020.00685

Nucleus pulposus-derived stem/progenitor cells (NPSCs) provide novel prospects for the regeneration of degenerated intervertebral disc (IVD). Nevertheless, with aging and degeneration of IVD, the frequency of NPSCs markedly decreases. Excessive cell death could be the main reason for declined frequency of NPSCs, however, the exact mechanisms remain elusive. Thus, the present study was undertaken to explore the mechanisms of compression-induced NPSCs death, and the effects of heat shock protein 90 (HSP90) on NPSCs survival. Here, we found that compression could trigger receptor-interacting protein kinase 1 (RIPK1)/receptor-interacting protein kinase 3 (RIPK3)/mixed lineage kinase domain-like protein (MLKL)-mediated necroptosis of NPSCs. Furthermore, we found that elevated expression of HSP90 was involved in compression-induced NPSCs death, and inhibiting HSP90 could dramatically attenuate compression-induced necroptosis of NPSCs via regulating the expression and activity of RIPK1/RIPK3/MLKL, and alleviating the mitochondrial dysfunction (mitochondrial membrane potential loss and ATP depletion) and oxidative stress [production of mitochondrial reactive oxygen species (ROS), cellular total ROS and malondialdehyde, and downregulation of superoxide dismutase 2]. Besides necroptosis, compression-induced apoptosis of NPSCs was also attenuated by HSP90 inhibition. In addition, we found that enhanced expression of HSP70 contributed to the cytoprotective effects of inhibiting HSP90. More encouragingly, our results demonstrated that inhibiting HSP90 could also mitigate the exhaustion of NPSCs *in vivo*. In conclusion, RIPK1/RIPK3/MLKL-mediated necroptosis participates in compression-induced NPSCs death. Furthermore, targeting HSP90 to simultaneously inhibit necroptosis and apoptosis of NPSCs might be an efficient strategy for preventing the death of NPSCs, thus rescuing the endogenous repair capacity of NP tissue.

Keywords: nucleus pulposus-derived stem/progenitor cells, heat shock protein 90, necroptosis, apoptosis, intervertebral disc degeneration, compression

INTRODUCTION

Intervertebral disc (IVD) degeneration (IVDD) has been widely considered as the paramount etiology for low back pain, leading to heavy socio-economic burden due to lost productivity and increasing health care costs (Maetzel and Li, 2002; Freemont, 2009). Accumulating evidence has demonstrated that dysregulation of the function and quantity of nucleus pulposus (NP) cells accounts for the initiation of IVDD (Buckwalter, 1995; Li et al., 2018b). Therefore, many treatments aiming at retarding or reversing disc degeneration, including cell transplantation, growth factors supplementation and gene therapy, mainly focus on reviving the function and quantity of NP cells (Smith et al., 2011). However, these established methods have limitations more or less (Zhao et al., 2007). Recently, many studies have proven the existence of NP-derived stem/progenitor cells (NPSCs) (Risbud et al., 2007; Hu and He, 2018). It is reported that NPSCs could secrete extracellular matrix and differentiate toward NP cells (Tao et al., 2015). Furthermore, the co-culture of NP cells and NPSCs could enhance cell proliferation and the expression of chondrogenic-associated genes under hypertonicity condition (Tao et al., 2013). Thus, NPSCs might provide novel prospects for the regeneration of degenerated IVD. However, with aging and degeneration of IVD, the frequency of NPSCs markedly decreases, indicating the exhaustion of NPSCs (Sakai et al., 2012). Excessive cell death could be the main reason for the exhaustion of NPSCs. Previous studies have demonstrated that many adverse microenvironment factors, such as high osmolarity, low pH, oxidative stress and mechanical loading, could induce NPSCs death (Hu and He, 2018; Nan et al., 2019). Nevertheless, the precise mechanisms have not yet been fully elucidated.

Mechanical loading has long been recognized as the leading cause of IVDD (Neidlinger-Wilke et al., 2014). Our previous studies demonstrate that programmed cell death, such as apoptosis and necroptosis, participates in compression-induced NP cells death (Ding et al., 2012; Chen et al., 2017). Meanwhile, we found that compression could also trigger apoptosis of NPSCs (Li et al., 2018a). However, it has not been fully elucidated whether other types of programmed cell death are involved in compression-induced NPSCs death. Necroptosis is a newly defined form of regulated necrosis, which is mainly mediated by receptor-interacting protein kinase 1 (RIPK1)/receptor-interacting protein kinase 3 (RIPK3)/mixed lineage kinase domain-like protein (MLKL) signaling pathway (Hu et al., 2018). It has been reported that necroptosis contributes to various pathophysiological conditions, including systemic inflammation, ischemic reperfusion injury and neurodegeneration (Zhou and Yuan, 2014; Galluzzi et al., 2017). Therefore, unraveling the role of necroptosis in compression-induced NPSCs death, and its regulatory mechanisms might provide novel targets for preventing NPSCs death.

Heat shock protein 90 (HSP90) is a widely-expressed molecular chaperone, which is involved in numerous physiological processes such as signal transduction, intracellular transport, and protein degradation (Li and Buchner, 2013). Generally, HSP90 is thought to maintain cell viability and prevent apoptosis. It is reported that HSP90 could directly promote cell survival through the activation of nuclear factor-kappa B, indirectly promote cell survival via HSP90-Akt complexes, and modulate the intrinsic pathway of apoptosis (Arya et al., 2007). On the contrary, elevated expression of HSP90 could also exert pro-death roles under some circumstances (Hooven et al., 2004; Wang et al., 2011; Ma et al., 2015). Correspondingly, inhibiting HSP90 by specific inhibitors or siRNAs is able to downregulate some cell death-related pathways, such as the IKK/IκB/p65 pathway, as well as activate multiple cell survival pathways, including induction of heat shock protein 70 (HSP70) and the phosphorylation of Akt, extracellular signal regulated kinase 1/2 and glycogen synthase kinase 3β, ultimately attenuating cell death in many pathological process (Wang et al., 2011; Alani et al., 2014; Li J. et al., 2015; Liu Q. et al., 2016). Traditionally, decreased cell death caused by HSP90 inhibition is mainly attributed to reduced cell apoptosis, recent studies also reveal that RIPK1, RIPK3, and MLKL, the critical components of necroptosis signaling pathway, are client proteins of HSP90 (Lewis et al., 2000; Li D. et al., 2015; Zhao et al., 2016). Inhibiting HSP90 could block necroptosis by modulating the stability and function of RIPK1, RIPK3, and MLKL (Yang and He, 2016). Thus, HSP90 could simultaneously regulate apoptosis and necroptosis, which might be a wonderful target for preventing cell death. However, the roles of HSP90 in compression-induced NPSCs death have not been determined yet.

Mitochondrial dysfunction and reactive oxygen species (ROS) are critical in the execution of necroptosis (Marshall and Baines, 2014). Furthermore, they could also trigger cell apoptosis through mitochondrial apoptosis pathway (Feng et al., 2017). Our group has demonstrated that mitochondrial dysfunction and oxidative stress contribute greatly to compression-induced NP cells apoptosis and necroptosis (Ding et al., 2012; Chen et al., 2018). Furthermore, we found that compression could also trigger mitochondrial dysfunction and oxidative stress of NPSCs, leading to cell apoptosis (Li et al., 2018a). Therefore, suppressing mitochondrial dysfunction and oxidative stress might be efficient methods for preventing compression-induced NPSCs apoptosis and necroptosis.

In present study, we first investigated the involvement of necroptosis in compression-induced death of NPSCs. Subsequently, we determined the roles of HSP90 in compression-induced NPSCs death and explored relevant mechanisms. In addition, we also evaluated whether inhibiting HSP90 alleviated the exhaustion of NPSCs *in vivo*. Our study provides novel insights into the mechanisms of compression-induced NPSCs death as well as experimental evidence of a possible target for protecting NPSCs.

MATERIALS AND METHODS

Samples Collection

Experimental protocols for this study were approved by medical ethics committee of Tongji Medical College, Huazhong University of Science and Technology. Written informed consent was obtained from all patients. Human NP tissues were obtained from patients undergoing routine surgery for

lumbar and separated by an experienced surgeon in the Department of Orthopaedics, Union Hospital (Wuhan, China). Magnetic resonance images were used to evaluate the degree of IVDD according to Pfirrmann magnetic resonance images-grade system, and the samples of Pfirrmann grade I and II were regarded as non-degenerated (Pfirrmann et al., 2001). All samples were sectioned for the following experiments: (1) for histological analysis, tissues were fixed in 4% formaldehyde and embedded in paraffin, and (2) for cell culture, tissues were immediately immersed in phosphate-buffered saline (PBS).

Isolation and Culture of Human NPSCs

Human NPSCs were isolated and cultured in accordance with previously established protocols (Liu et al., 2017; Li et al., 2018a; Liang et al., 2018). Briefly, after being washed with PBS for three times, NP tissues were carefully examined using a dissecting microscope to remove any adherent tissues such as the annulus fibrosus, cartilage endplate and ligaments. Subsequently, the NP tissues were minced into small fragments and digested in 0.2% (m/v) type II collagenase (Sigma, St. Louis, MO, United States) for 12 h at 37°C. Then, the mixture was centrifuged at 300 g for 5 min. The obtained cells and partially digested tissues were resuspended in complete medium for mesenchymal stem cells (Cyagen Biosciences Inc., Guangzhou, China) and cultured at 37°C in a humidified atmosphere containing 5% CO_2. The culture medium was changed every 3 days, and cells were passaged on reaching 80–90% confluence. The NPSCs of second and third passage were used in following experiments.

Cell Treatment

To mimic the *in vivo* compression environment, a stainless-steel pressure vessel was utilized following the protocols previously established by our group (Chen et al., 2017, 2018; Li et al., 2018a; Wang W. et al., 2018). NPSCs which were cultured in cell culture dishes or plates as monolayer were placed on the bracket in the pressure apparatus and exposed to 1.0 MPa pressure for different time periods. The pressure vessel was supplied with a small quantity of double distilled water at the bottom to maintain moisture and placed in an incubator at 37°C.

The HSP90 inhibitor BIIB021, RIPK1 inhibitor Necrostatin-1 (Nec-1), RIPK3 inhibitor GSK′872, MLKL inhibitor Necrosulfonamide (NSA), proteasome inhibitor MG132, and HSP70 inhibitor Ver155008 (Ver) were all purchased from Selleck Chemicals (Houston, TX, United States). For all experiments, NPSCs were pretreated with inhibitors for 2 h before compression treatment, while control groups were given isopyknic dimethylsulfoxide as vehicle control.

Cell Viability Assay

Cell viability was examined using the cell counting kit 8 (CCK-8; Dojindo, Kyushu Island, Japan) following the manufacturer's instructions. Briefly, NPSCs were seeded in 96-well culture plates at a density of 5×10^3 cells per well and treated as above. At indicated time points, the culture medium was discarded, and 100 μL of DMEM/Ham's F-12 (DMEM/F-12; Thermo Fisher Scientific, Waltham, MA, United States) and 10 μL of CCK-8 reagent were added to each well. Then, the absorbance was detected after incubation for 3 h at 37°C at a wavelength of 450 nm on a microplate reader (Biotek, Winooski, VT, United States).

Lactate Dehydrogenase (LDH) Release Assay

Cells were seeded in 96-well culture plates at a density of 5×10^3 cells per well and treated as above. The release of LDH from NPSCs to culture medium was examined using the LDH Cytotoxicity Assay Kit (Beyotime, Shanghai, China) according to manufacturer's instructions. The absorbance was detected at a wavelength of 490 nm using a microplate reader (Biotek).

Transmission Electron Microscopy (TEM)

The ultrastructure of NPSCs was observed using TEM following previously described methods (Chen et al., 2017, 2018). Briefly, after indicated treatments, cells were collected and pelleted by centrifugation at 1000 g for 15 min. The pellets were then fixed with 2.5% glutaraldehyde in PBS for 2 h and post-fixed with 1% osmium tetroxide for 2 h at room temperature. Next, the pellets were dehydrated in a graded series of ethanol and embedded in epon 812. Ultrathin sections were stained with uranyl acetate and lead citrate, and were examined utilizing the Tecnai G2 12 transmission electron microscope (FEI Company, Holland).

Live and Dead Cell Staining

The membrane permeable probe Calcein-AM (Santa Cruz Biotechnology, lnc., Dallas, TX, United States) and propidium iodide (PI) (Nanjing Keygen Biotech, Nanjing, China) were used to label the live and dead cells, respectively. After indicated treatments, the NPSCs were washed twice with PBS. Then, the cells were incubated with Calcein-AM (2 μM) at 37°C for 20 min in the dark. After being gently rinsed twice with PBS, cells were further stained with PI according to manufacturer's instructions. The live (green fluorescence) and dead (red fluorescence) cells were imaged by fluorescence microscopy (Olympus IX71, Japan).

Transfection of siRNA

The siRNAs for HSP90α and HSP90β were published previously and synthesized by RiboBio Co (Guangzhou, China) (Shang and Tomasi, 2006). The target sequences of siRNAs were as follows: HSP90α, 5′-CCCAGUUGAUGUCAUUGAUCAUCAA-3′; HSP90β, 5′-GGCAGAGGAAGAGAAAGGUGAGAAA-3′. The negative control (NC) siRNA was also purchased from RiboBio Co. The transfection was performed utilizing the Lipofectamine 3000 (Thermo Fisher Scientific) according to manufacturer's instructions, and the transfection efficacy was tested by real-time PCR (RT-PCR) and Western blot (WB).

Immunofluorescence Staining

NPSCs which were seeded on glass coverslips were washed with PBS, and fixed by 4% paraformaldehyde for 15 min. Cells were then permeabilized with 0·5% Triton X-100 (Beyotime) for 15 min at room temperature (for staining of Tie2, the permeabilization was not performed), and blocked with goat serum albumin for 1 h. Next, samples were washed with

PBS and incubated with the mixture of mouse anti-HSP90 antibody (1:200, Santa Cruz Biotechnology) and rabbit anti-phosphorylated MLKL (P-MLKL) antibody (Ser358, 1:200, Affinity Biosciences, OH, United States), the rabbit anti-HSP70 antibody (1:500, ABclonal, Wuhan, China), or rabbit anti-Tie2 antibody (1:100, Proteintech Group, Wuhan, China) at 4°C overnight, followed by incubation with fluorophore-conjugated secondary antibody (1:200, Proteintech Group). Finally, the nuclei were stained with 4′-6-diamidino-2-phenylindole (DAPI). Fluorescence images were observed using fluorescence microscope (Olympus IX71).

Annexin V and PI Staining

The Annexin V-fluorescein isothiocyanate (FITC)/PI Apoptosis Detection Kit (Nanjing Keygen Biotech), and the Cell Apoptosis Detection Kit (PI) (Nanjing Keygen Biotech) were used to quantify the apoptotic and necrotic ratio of NPSCs, respectively. Briefly, after compression treatment, cells were harvested by trypsinization and washed twice with PBS. Then, the cells were stained according to manufacturer's instructions. All samples were subsequently analyzed by flow cytometry (BD LSR II, Becton Dickinson).

Terminal Deoxynucleotidyl Transferase Biotin-dUTP Nick end Labeling (TUNEL) Assay

TUNEL assays were performed using the One Step TUNEL Apoptosis Assay Kit (Beyotime) following manufacturer's instructions. Briefly, cells were fixed with 4% formaldehyde for 30 min and permeabilized by 0.3% Triton X-100 for 5 min. Subsequently, the cells were incubated with TUNEL reaction mixture for 1 h at 37°C in the dark, counterstained with DAPI and observed under a fluorescence microscope (Olympus IX71). The cells with green fluorescence were defined as apoptotic cells.

Evaluation of Mitochondrial Membrane Potential (MMP)

After compression treatment, NPSCs were stained with the fluorescent probe 5,5′,6,6′-tetrachloro-1,1′,3,3′-tetraethyl-benzimidazolylcarbocyanine iodide (JC-1, Nanjing Keygen Biotech) according to manufacturer's instructions. Then, the stained cells were analyzed by flow cytometry (BD LSRII, Becton Dickinson) and observed using fluorescence microscope (Olympus IX71).

ATP Production Assay

The ATP content was assessed using the Enhanced ATP Assay Kit (Beyotime). Briefly, after compression treatment, NPSCs were lysed with the ATP lysis buffer. Then, the supernatant was collected by centrifugation at 12,000 g for 5 min and reacted with the ATP detection working dilution. The luminescence activity was detected by luminescence spectrometry (EnSpire, United States). The ATP level was normalized to cellular protein concentration.

Mitochondrial ROS (mtROS) Analysis

The mtROS was measured using MitoSOX Red (Thermo Fisher Scientific) staining according to manufacturer's instructions. After compression treatment, the NPSCs were incubated with 5 μM MitoSOX Red for 10 min at 37°C. The NPSCs were then washed twice and counterstained with DAPI at 37°C for 10 min. Images were acquired using fluorescence microscope (Olympus IX71).

Measurement of Cellular ROS

The intracellular ROS level was measured using the ROS Assay Kit (Beyotime) according to manufacturer's instructions. The NPSCs were harvested and washed twice with PBS. Then, cells were incubated with 2′-7′-dihydrodichlorofluoroscein diacetate (DCFH-DA) in the dark at 37°C for 20 min. After being washed with DMEM/F-12 for three times, the fluorescence intensity was detected using flow cytometry (BD LSR II, Becton Dickinson). Intracellular ROS level in NPSCs was also observed under a fluorescence microscope (Olympus IX71).

Malondialdehyde (MDA) Detection

The MDA concentration was determined using the Lipid Peroxidation MDA Assay Kit (Beyotime). NPSCs were washed with PBS, lysed with lysis buffer and centrifuged at 120,00 g for 10 min. Then, the supernatant was collected and reacted with the thiobarbituric acid. After centrifugation, the absorbance of supernatant was measured using spectrophotometer (EnSpire) at a wavelength of 532 nm. The MDA concentration was normalized to cellular protein concentration.

WB Analysis

Total protein of cells was extracted using radioimmunoprecipitation assay buffer (Beyotime) containing the protease and phosphatase inhibitors. The protein concentration was determined utilizing the Enhanced BCA Protein Assay Kit (Beyotime). Equal amount of protein was electrophoresed in 8–12% sodium dodecyl sulfate-polyacrylamide gel and transferred onto polyvinylidene difluoride membranes (EMD Millipore, Billerica, MA, United States). After being blocked with 5% bovine serum albumin in Tris Buffered Saline with Tween 20 (TBST) buffer for 1 h at room temperature, the polyvinylidene difluoride membranes were incubated overnight at 4°C with primary antibodies against: HSP90 (1:500), RIPK1 (1:1000, Abcam, Cambridge, MA, United States), phosphorylated RIPK1 (P-RIPK1) (Ser166, 1:1000, Cell Signaling Technology, Danvers, MA, United States), RIPK3 (1:1000, Abcam), phosphorylated RIPK3 (P-RIPK3) (Ser227, 1:1000, Abcam), MLKL (1:1000, Abcam), P-MLKL (1:1000), Bcl-2 (1:1000, Abcam), Bax (1:500, Proteintech Group), Caspase-3 (1:500, Proteintech Group), poly ADP-ribose polymerase (PARP) (1:500, Proteintech Group), HSP70 (1:500), c-jun-N-terminal kinase (JNK) (1:1000, Cell Signaling Technology), phosphorylated JNK (P-JNK) (Thr183/Tyr185, 1:1000, Cell Signaling Technology), superoxide dismutase 2 (SOD2) (1:500, Proteintech Group), HSP90α (1:1000, ABclonal), HSP90β (1:500, ABclonal), GAPDH (1:2000,

Affinity Biosciences). Subsequently, the membranes were washed three times with TBST and incubated with corresponding horseradish peroxidase-conjugated secondary antibodies for 1 h at room temperature. The protein bands were detected using enhanced chemiluminescence reagent system (Affinity Biosciences) following the manufacturer's instructions.

RT-PCR

Total RNA was extracted from NPSCs using the TRIzol reagent (Thermo Fisher Scientific) according to manufacturer's instructions. Then, the concentration and purity of the total RNA were determined using the NanoDrop 2000. The isolated RNA was reverse-transcribed into corresponding cDNA using the reverse transcriptional kit (TaKaRa Bio, Tokyo, Japan). Quantitative RT-PCR was performed using the SYBR PrimeScript RT-PCR Kit (TaKaRa Bio) on the Step One Plus Real-Time PCR system (Thermo Fisher Scientific). *GAPDH* was used as the endogenous control, and relative mRNA expression levels of target genes were calculated using the $2^{-\Delta\Delta Ct}$ method. The primer sequences were designed and synthesized as follows: *HSP90AA1*, F: 5′-TCTCCACAGGGCTTGTTTTCC-3′, R: 5′-CATTTTTGGCACTAACTGTCATCC-3′; *HSP90AB1*, F: 5′-CCAGGCACTTCGGGACAAC-3′, R: 5′-TCAAACAGCAGCACCACCAG- 3′; *GAPDH*, F: 5′-AATCCCATCACCATCTTCCAG-3′, R: 5′-GAGCCCCAGCCTTCTCCAT-3′.

Surgical Procedure of Animal Experiments

All animal procedures were performed under the approval of the animal experimentation committee of Huazhong University of Science and Technology. Twenty skeletally mature 12-week-old male Sprague-Dawley rats, ranging from 380 to 450 g, were obtained from the Experimental Animal Center of Huazhong University of Science and Technology. A previously reported rat tail model of disc degeneration induced by mechanical loading was employed in current study (Yurube et al., 2014; Yan et al., 2017). Rats were anesthetized by intraperitoneal injection of 50 mg/kg pentobarbital. The disc levels in rat tail were located by palpation on the coccygeal vertebrae. Then, rat tails were fixed with an Ilizarov-type apparatus. In brief, two cross 0.80 mm diameter Kirschner wires were inserted percutaneously into the 8th and 10th caudal vertebral bodies perpendicular to the tail's axis, respectively. The Kirschner wires were subsequently attached to stainless steel rings which were connected longitudinally with four threaded rods. After instrumentation, axial force was generated utilizing four calibrated springs (0.50 N/mm) installed over each rod. In present study, the compressive stress of 1.3 MPa which was in accordance with the transient disc loading force produced by lifting a moderate weight in human lumbar spine was used to induce the disc degeneration of rat tail (Lotz and Chin, 2000). Rat tails with the compressive apparatus unloaded were regarded as the sham group. Following surgery, the caudal segments 8/9 and 9/10 were injected with vehicle in sham group, or randomly injected with BIIB021 (1000 nM/L) and vehicle in loaded group, respectively. To avoid disc degeneration induced by puncture, a micro-syringe attached to a 30-gauge needle (Hamilton Bonaduz AG, Bonaduz, Switzerland) was used, and the injection volume was 2 μL (Zou et al., 2013; Yurube et al., 2014). Following surgery, all animals were supplied with antibiotics and allowed unrestricted food, water and activity. The injections were conducted every 4 days. After 20 days, the rats were euthanized, and the discs were harvested, fixed in 4% paraformaldehyde, decalcified in 10% ethylenediaminetetraacetic acid and embedded in paraffin.

Immunohistochemistry (IHC)

The paraffin-embedded tissue samples were cut into 4-μm thickness sections. The sections were then deparaffinized, rehydrated and incubated in 3% H_2O_2 for 20 min at room temperature to block the endogenous peroxidase activity. Antigen retrieval was performed by pressure cooking in 10 mmol/L citrate buffer, pH 6. Subsequently, the sections were blocked with 10% goat serum albumin for 30 min at room temperature, followed by incubation with rabbit anti-Tie2 polyclonal antibody (1:100), mouse anti-HSP90 antibody (1:50) at 4°C overnight. After being washed, the sections were labeled with horseradish peroxidase-linked goat anti-rabbit secondary antibody at 37°C for 1 h, and counterstained with hematoxylin.

Statistical Analysis

All experiments were repeated at least three times, and data were presented as mean ± SD. Statistical analysis was performed using SPSS statistical software program 20·0 (IBM, Armonk, NY, United States). Differences between groups were analyzed by Student's *t*-test or one-way analysis of variance (ANOVA) followed by Bonferroni *post hoc* test. $P < 0{\cdot}05$ was considered statistically significant.

RESULTS

Compression Induced Necrotic Cell Death of NPSCs

We first detected the presence of NPSCs in human non-degenerated and degenerated NP tissues. Tie2, the specific surface marker for NPSCs, was used to label cells in tissue samples (Sakai et al., 2012; Tekari et al., 2016). In present study, we also used Tie2 to identify the purity of NPSCs (**Supplementary Figure S1**). The IHC showed that NPSCs existed in human non-degenerated and degenerated NP tissues. However, in degenerated NP tissues, the frequency of Tie2 positive cells declined dramatically, indicating the exhaustion of NPSCs (**Figure 1A**). We subsequently examined the influence of compression on viability of NPSCs. The CCK-8 assays demonstrated that cell viability of NPSCs was reduced by compression treatment in time-dependent manner (**Figure 1B**). Furthermore, prolonged compression treatment also led to increased LDH release (**Figure 1C**). We then determined whether compression induced necrosis of NPSCs. As expected, the flow cytometric analyses of PI staining showed that there was a marked increase in PI-positive cells in response to compression, indicating increased cellular necrosis (**Figures 1D,E**). In addition,

we also utilized the TEM to observe the ultrastructure of NPSCs. As shown in **Figure 1F**, after exposure to compression for 48 h, the ultrastructure of cells was extensively damaged, as manifested by severe vacuolation, swelling of organelles and disruption of the plasma membrane. Taken together, above results suggested that compression could induce necrotic cell death of NPSCs.

RIPK1/RIPK3/MLKL-Mediated Necroptosis Was Involved in Compression-Induced Death of NPSCs

To investigate whether necroptosis was involved in compression-induced NPSCs death, we first examined the expression of key proteins of necroptosis signaling pathway. The WB results demonstrated that the expression levels of RIPK1, P-RIPK1, RIPK3, P-RIPK3, MLKL, and P-MLKL were all increased by compression treatment (**Figures 2A,B**). To further confirm the involvement of necroptosis in compression-induced NPSCs death, we used different concentrations of RIPK1 inhibitor Nec-1, RIPK3 inhibitor GSK′872 or MLKL inhibitor NSA to treat NPSCs, respectively. The results of CCK-8 assays showed that inhibiting RIPK1, RIPK3, or MLKL could also preserve the viability of NPSCs in response to compression (**Figure 2C**). In addition, pretreatment of NPSCs with NSA could also decrease the ratio of PI positive cells caused by compression (**Figures 2D,E**). Collectively, these results indicated that RIPK1/RIPK3/MLKL-mediated necroptosis was involved in compression-induced death of NPSCs.

Inhibition of HSP90 Attenuated Compression-Induced NPSCs Death

To investigate the roles of HSP90 in compression-induced NPSCs death, we first detected the expression of HSP90 in human NP tissues. The IHC results demonstrated that HSP90 expression was elevated in degenerated NP tissues, indicating the involvement of HSP90 in the process of IVDD (**Supplementary Figure S2**). We further evaluated the expression levels of HSP90 in NPSCs in response to compression. The RT-PCR results demonstrated that the expression levels of *HSP90AA1* and *HSP90AB1* were elevated by compression treatment, which peaked at 48 h and 24 h, respectively (**Figures 3A,B**). In addition, the protein expression of HSP90 was also increased in a time-dependent manner (**Figure 3C**). We subsequently pretreated NPSCs with different concentrations of HSP90 inhibitor BIIB021. As shown in **Figure 3D**, pretreating NPSCs with BIIB021 attenuated the loss of viability caused by compression treatment. Since the cytoprotective effect was most prominent in concentration of 100 nM, therefore, the BIIB021 concentration of 100 nM was chosen for the following experiments. We then detected the influence of BIIB021 treatment on the expression of HSP90. The WB results showed that 100 nM of BIIB021 treatment could promote the expression of HSP90 in NPSCs under compression (**Supplementary Figure S3**). We further observed the survival of NPSCs using the live/dead cell staining. Consistently, live/dead cell staining displayed that the number of dead cells (red fluorescence) decreased, while the number of live cells (green fluorescence) increased in BIIB021 groups compared to that in control groups (**Figure 3E**).

To further verify the cytoprotective effects of inhibiting HSP90, HSP90 specific siRNAs were used. The transfection efficacy was validated by RT-PCR and WB, and the expression of HSP90 was dramatically downregulated at both protein and mRNA levels (**Supplementary Figures S4A,B**). Then, the CCK-8 assays were employed to examine the effects of HSP90 specific siRNAs on NPSCs viability. Interestingly, only when NPSCs were transfected with HSP90β siRNA could the loss of viability be attenuated (**Figure 3F**). In the meanwhile, transfection of NPSCs with HSP90α siRNA didn't have significant influence on cell viability (**Supplementary Figure S4C**). Furthermore, co-transfection of NPSCs with HSP90β (10 nM) siRNA and different concentrations of HSP90α siRNAs also failed to rescue the loss of viability (**Supplementary Figure S4D**). These evidences demonstrated that HSP90 exerted pro-death roles in compression-induced NPSCs death, and inhibiting rather than silencing HSP90 could effectively attenuate compression-induced NPSCs death.

Enhanced Expression of HSP70 Contributed to the Cytoprotective Effects of Inhibiting HSP90

Previous studies have revealed that inhibition of HSP90 could result in increased HSP70 synthesis, which might be the reason for the protective effects of inhibiting HSP90 (Alani et al., 2014). Thus, we next evaluated the expression levels of HSP70 in NPSCs. As expected, the WB results showed that compression increased the expression of HSP70 protein in time-dependent manner, while the inhibition of HSP90 further promoted the expression of HSP70 (**Figure 4A**). Consistently, the immunofluorescence results displayed that inhibition of HSP90 notably enhanced the fluorescence intensity of HSP70 both in nuclei and cytoplasm (**Figure 4B**). HSP70 exerts its cytoprotective effects mainly by inhibiting JNK (Gabai et al., 1998). Therefore, we next examined the activity of JNK. The WB results showed that the expression of P-JNK was reduced by BIIB021 treatment at 24 and 36 h, indicating the decreased activity of JNK (**Figure 4C**). We further used HSP70 inhibitor Ver to treat NPSCs. The CCK-8 results showed that Ver treatment partially abolished the cytoprotective effects of HSP90 inhibitor (**Figure 4D**). Collectively, these results indicated that enhanced expression of HSP70 induced by HSP90 inhibitor contributed to the cytoprotective effects of inhibiting HSP90.

Inhibiting HSP90 Suppressed Compression-Induced Necroptosis of NPSCs

HSP90 is recently found to modulate the stability and function of RIPK1, RIPK3, and MLKL, indicating the regulatory effects of HSP90 on necroptosis (Yang and He, 2016). Using immunofluorescence, we observed that compression could elevate the expression of HSP90 and P-MLKL simultaneously (**Figure 5A**). More interestingly, we found that in cells which expressed higher levels of P-MLKL, the expression of HSP90

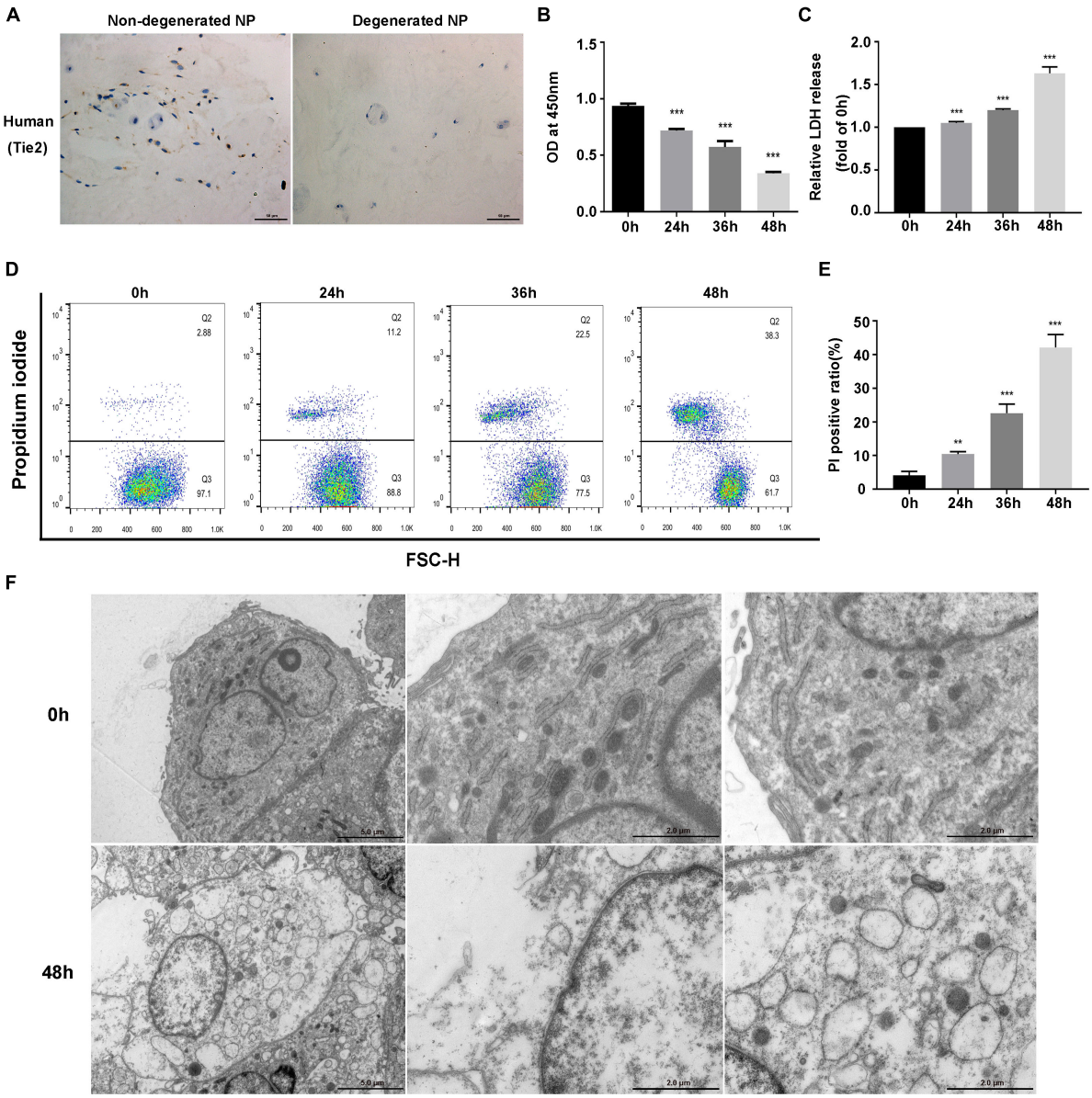


FIGURE 1 | Compression induced necrotic cell death of NPSCs. **(A)** IHC staining of Tie2 for marking NPSCs in non-degenerated (37 years old, male, grade II) and degenerated (43 years old, male, grade IV) human NP tissues (original magnification: ×400). **(B)** Cell viability of NPSCs examined by CCK-8 assays. **(C)** The relative release of LDH at different time points. **(D)** Representative dot plots of PI staining obtained from flow cytometry analysis of NPSCs. **(E)** The statistical analysis of PI positive ratio of NPSCs. **(F)** The morphological ultrastructural appearance of NPSCs observed by TEM. The NPSCs exposed to 48 h of compression displayed necrotic morphological changes, such as severe vacuolation, swelling of organelles and disruption of the plasma membrane. The data were expressed as mean ± SD from at least three independent experiments, and they were analyzed by a two-tailed *t*-test or ANOVA. (**$P < 0.01$, ***$P < 0.001$ vs. 0 h).

was also stronger, indicating that HSP90 might be associated with compression-induced necroptosis of NPSCs (**Figure 5A**). Therefore, we subsequently examined whether inhibiting HSP90 suppressed compression-induced necroptosis of NPSCs. The flow cytometric analyses showed that the proportion of PI positive cells was significantly decreased by BIIB021 treatment, indicating alleviated cellular necrosis (**Figures 5B,C**). The TEM results further confirmed that the necrotic ultrastructure features, such as the swelling of organelles and disruption of the plasma membrane, were alleviated by BIIB021 treatment (**Figure 5D**). Furthermore, we found that the expression of RIPK1, P-RIPK1, RIPK3, P-RIPK3, and P-MLKL were all dramatically inhibited by HSP90 inhibitor (**Figures 5E,F**). However, the inhibitory effect of BIIB021 on MLKL was significant only in 48 h group (**Figures 5E,F**). Then, we used HSP90 specific siRNAs to further verify the regulatory effects of HSP90 on necroptosis. Consistently, downregulation of HSP90 could also reduce the expression of RIPK1, P-RIPK1, RIPK3, P-RIPK3, MLKL, and

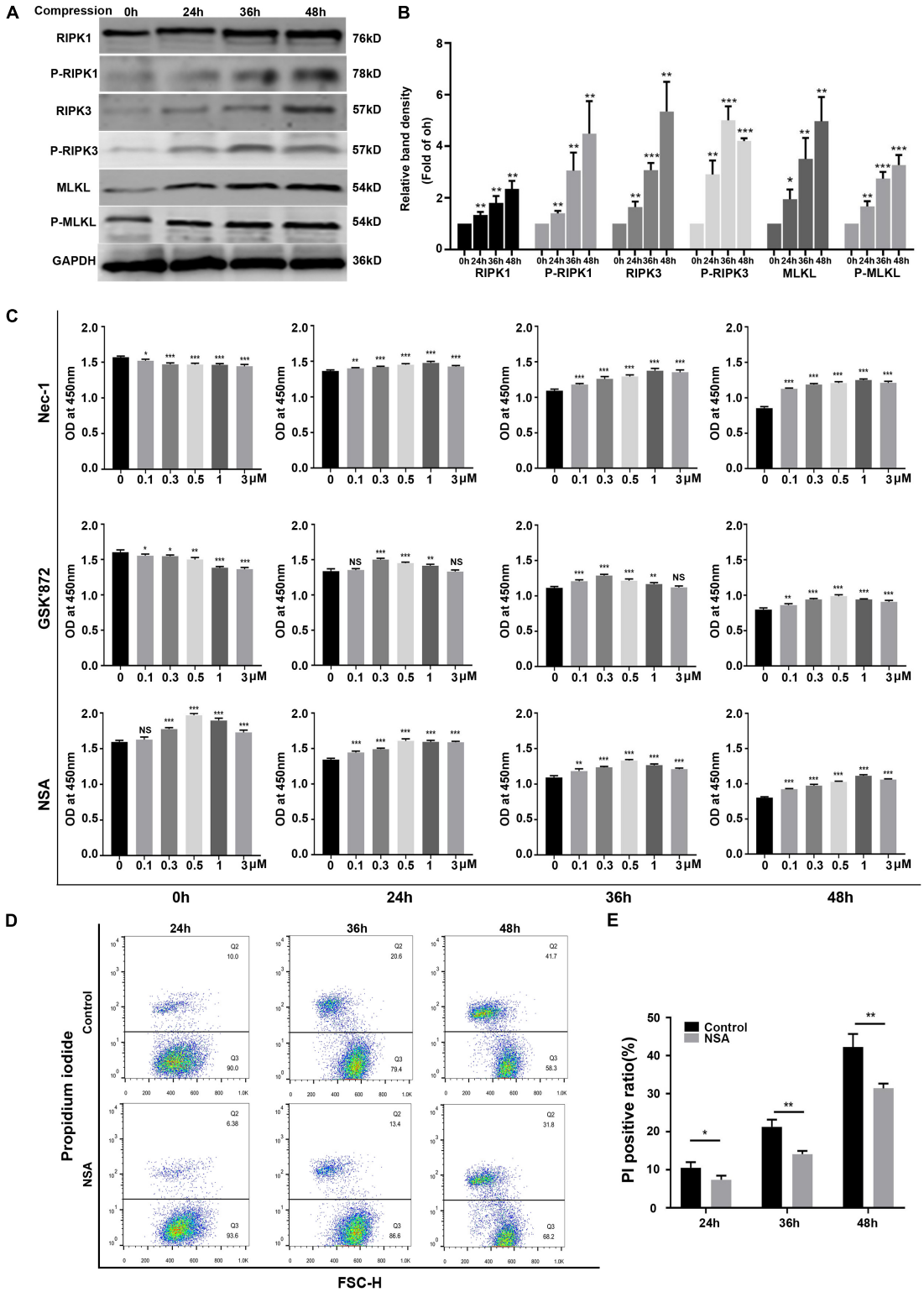


FIGURE 2 | RIPK1/RIPK3/MLKL-mediated necroptosis was involved in compression-induced death of NPSCs. **(A)** Representative WB graphs of the expression of RIPK1, P-RIPK1, RIPK3, P-RIPK3, MLKL, and P-MLKL. **(B)** Quantitation of the expression levels of RIPK1, P-RIPK1, RIPK3, P-RIPK3, MLKL, and P-MLKL. **(C)** The effects of different concentrations of Nec-1, GSK′872 and NSA on cell viability of NPSCs exposed to 0, 24, 36, and 48 h compression measured by CCK-8 assays. **(D)** Representative dot plots of PI staining obtained from flow cytometry analysis of NPSCs. **(E)** The statistical analysis of PI positive ratio of NPSCs. The data were expressed as mean ± SD from at least three independent experiments, and they were analyzed by a two-tailed *t*-test. (*$P < 0.05$, **$P < 0.01$, ***$P < 0.001$ vs. 0 h, 0 μM or control, NS, not significant).

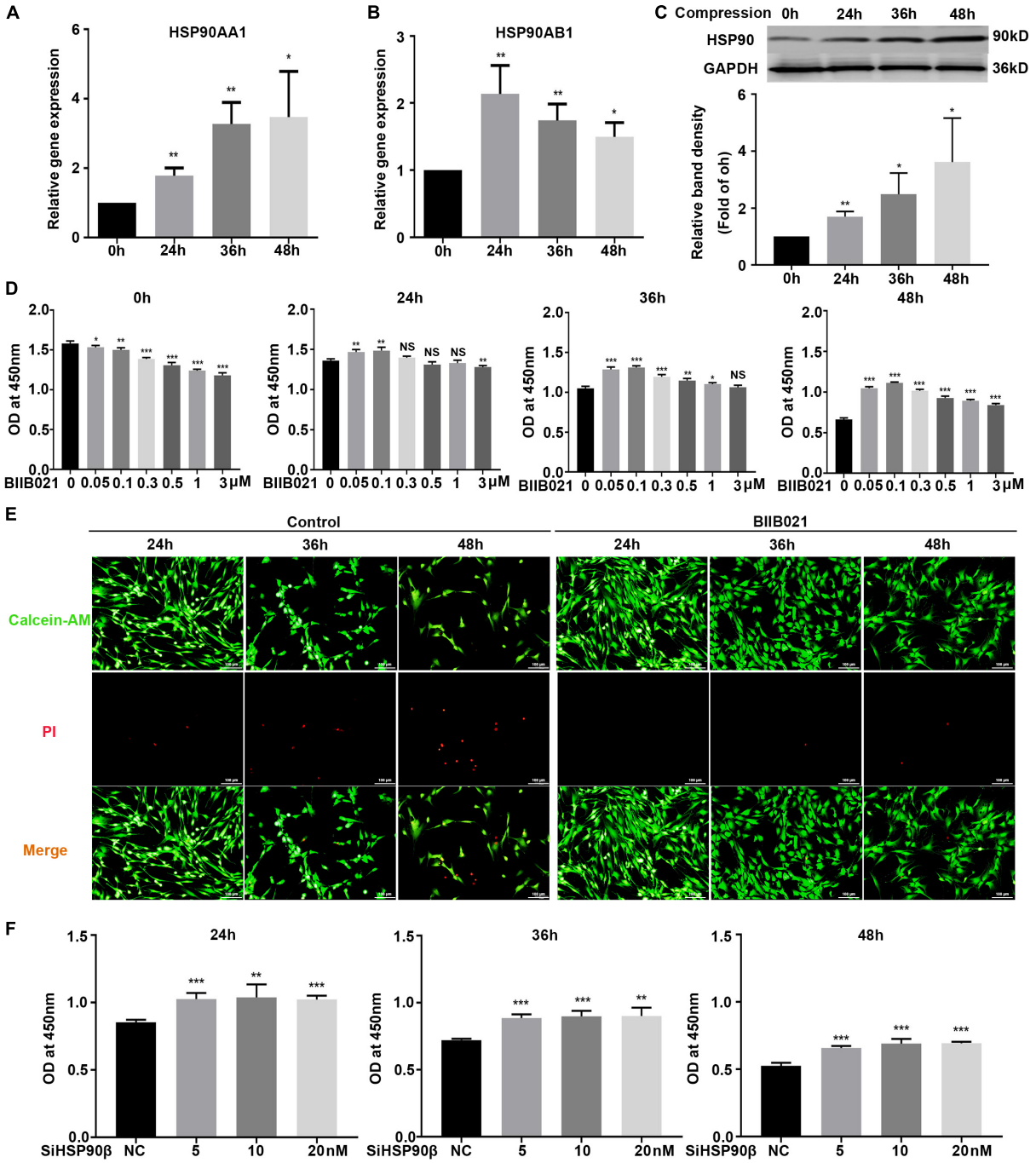


FIGURE 3 | Inhibition of HSP90 attenuated compression-induced NPSCs death. **(A,B)** The expression levels of *HSP90AA1* **(A)** and *HSP90AB1* **(B)** measured by RT-PCR in human NPSCs. Data were normalized to *GAPDH*. **(C)** Representative WB graphs and quantitation of the expression level of HSP90. **(D)** The effects of different concentrations of BIIB021 on cell viability of NPSCs exposed to 0, 24, 36, and 48 h compression measured by CCK-8 assays. **(E)** Typical fluorescence photomicrograph of live/dead cell staining of NPSCs. Green fluorescent signaling (Calcien-AM) indicates live cells and red fluorescent signaling (PI) indicates dead cells (original magnification: ×200). **(F)** The effects of SiHSP90β on cell viability of NPSCs exposed to 24, 36, and 48 h compression measured by CCK-8 assays. The data were expressed as mean ± SD from at least three independent experiments, and they were analyzed by a two-tailed *t*-test. (*$P < 0.05$, **$P < 0.01$, ***$P < 0.001$ vs. 0 h, 0 μM or NC, NS, not significant).

P-MLKL (**Supplementary Figures S5A,B**). Previous studies have reported that HSP90 regulates necroptosis mainly by modulating the stability and function of RIPK1, RIPK3, and MLKL via ubiquitin–proteasome pathway (Yang and He, 2016). We then used proteasome inhibitor MG132 to explore whether HSP90 regulated the degradation of above proteins in NPSCs under

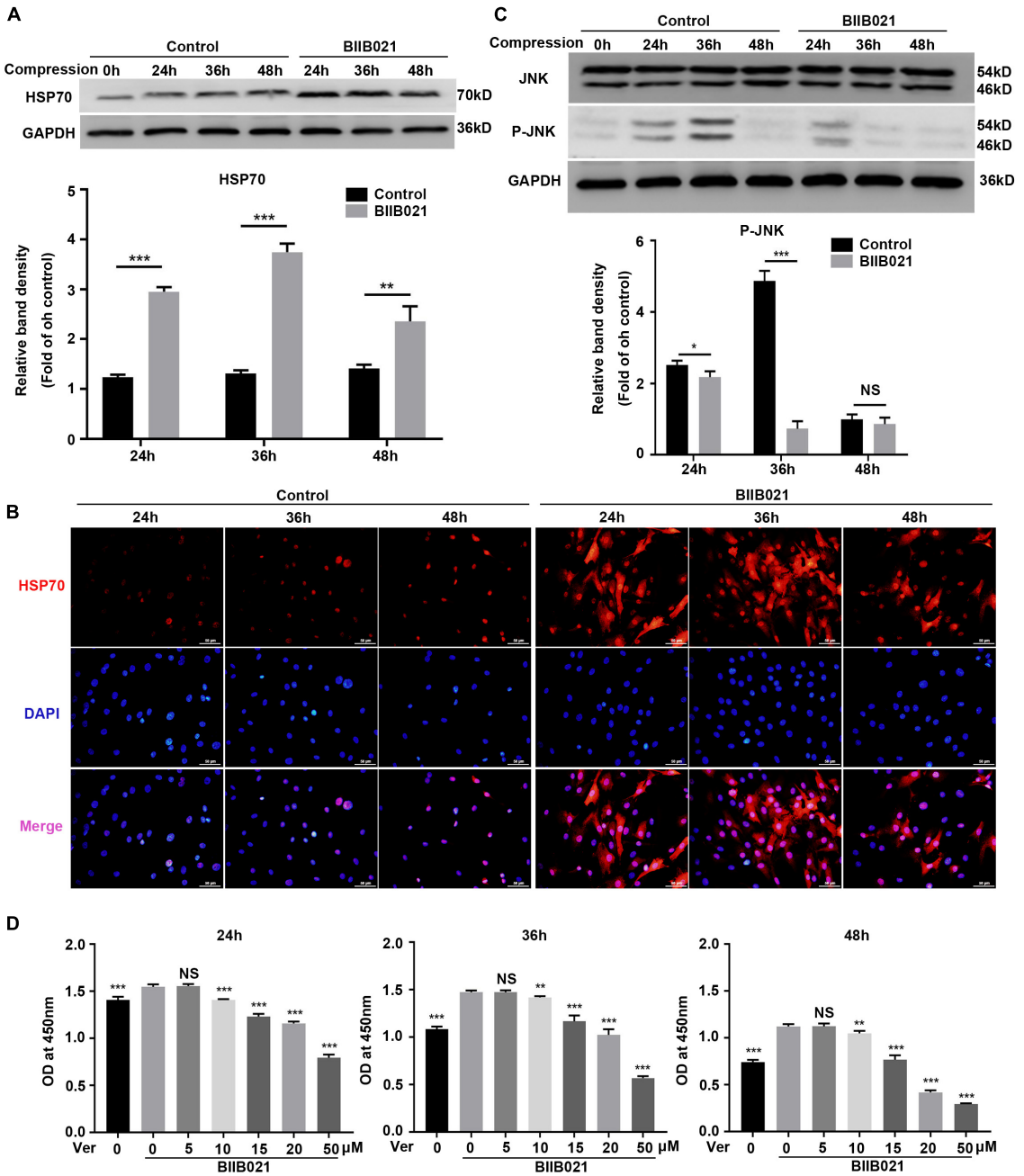


FIGURE 4 | Enhanced expression of HSP70 contributed to the cytoprotective effects of inhibiting HSP90. **(A)** Representative WB graphs and quantitation of the expression levels of HSP70. **(B)** The representative fluorescence photomicrograph of HSP70 expression detected by immunofluorescence staining (original magnification: ×400). **(C)** Representative WB graphs and quantitation of the expression levels of JNK and P-JNK. **(D)** Ver partly reversed the protective effects of BIIB021 on NPSCs exposed to 24, 36, and 48 h compression measured by CCK-8 assay. The data were expressed as mean ± SD from at least three independent experiments, and they were analyzed by a two-tailed *t*-test. (*$P < 0.05$, **$P < 0.01$, ***$P < 0.001$ vs. control or Ver 0 nM+BIIB021 100 nM group, NS, not significant).

compression. The WB results demonstrated that treatment of NPSCs with MG132 blocked the decline in the expression of RIPK1, P-RIPK1, RIPK3, P-RIPK3, MLKL, and P-MLKL induced by BIIB021 (**Figures 5G,H**). Collectively, these results indicated that inhibiting HSP90 could effectively suppress compression-induced necroptosis of NPSCs.

Inhibiting HSP90 Attenuated Compression-Induced Mitochondrial Dysfunction of NPSCs

Mitochondrial dysfunction and ROS are critical in the execution of necroptosis (Marshall and Baines, 2014). Thus, to further confirm the inhibition of necroptosis by BIIB021, we investigated

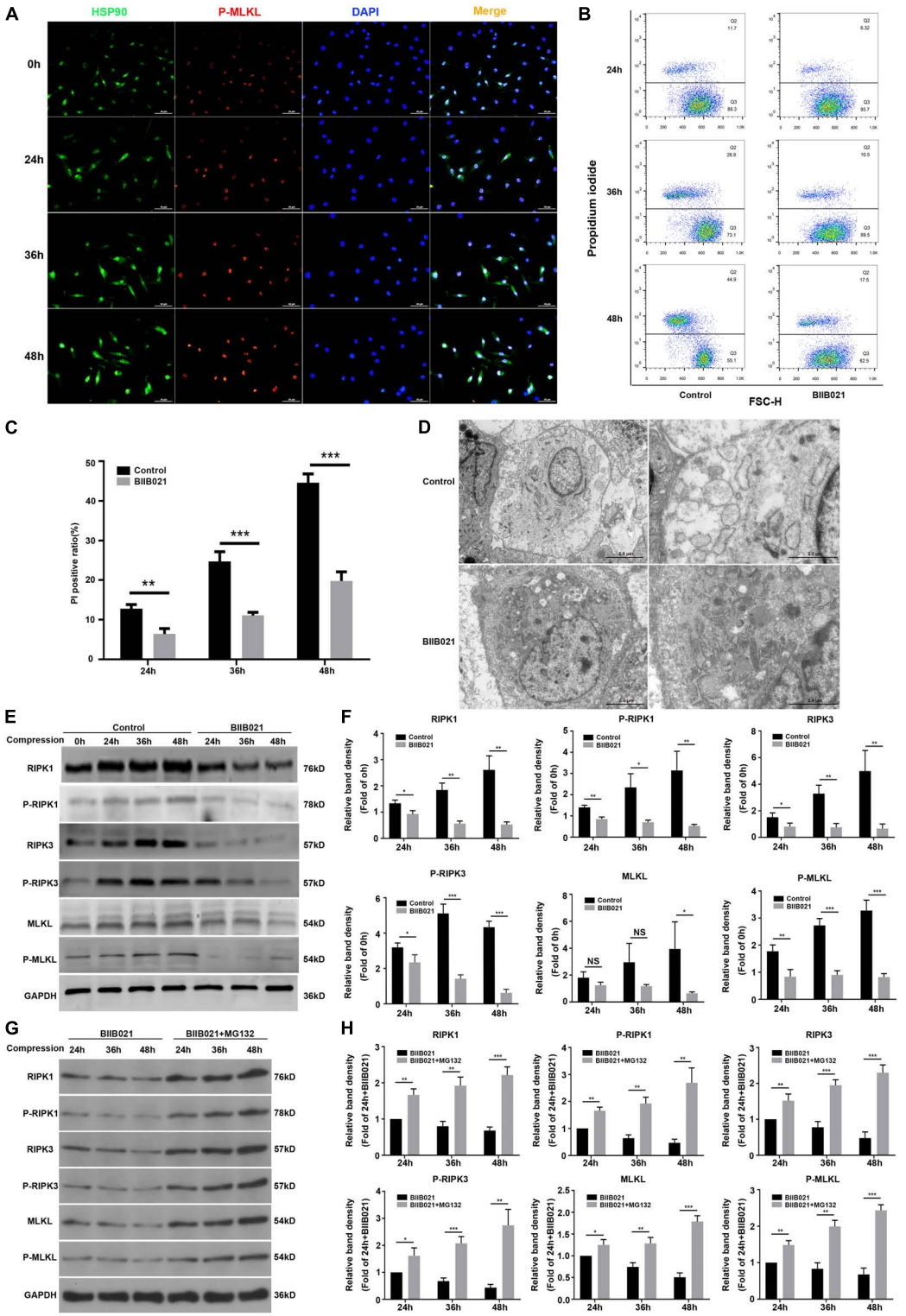


FIGURE 5 | Inhibiting HSP90 suppressed compression-induced necroptosis of NPSCs. **(A)** The representative fluorescence photomicrograph of HSP90 and P-MLKL expression detected by immunofluorescence staining (original magnification: ×400). **(B)** Representative dot plots of PI staining obtained from flow cytometry analysis of NPSCs. **(C)** The statistical analysis of PI positive ratio of NPSCs. **(D)** The morphological ultrastructural appearance of NPSCs exposed to 48 h compression observed by TEM. **(E,F)** Representative WB graphs and quantitation of the expression levels of RIPK1, P-RIPK1, RIPK3, P-RIPK3, MLKL, and P-MLKL. **(G,H)** Representative WB graphs and quantitation of the expression levels of RIPK1, P-RIPK1, RIPK3, P-RIPK3, MLKL, and P-MLKL. The data were expressed as mean ± SD from three independent experiments, and they were analyzed by a two-tailed *t*-test. [$^{*}P < 0.05$, $^{**}P < 0.01$, $^{***}P < 0.001$ vs. control or BIIB021 **(G,H)**].

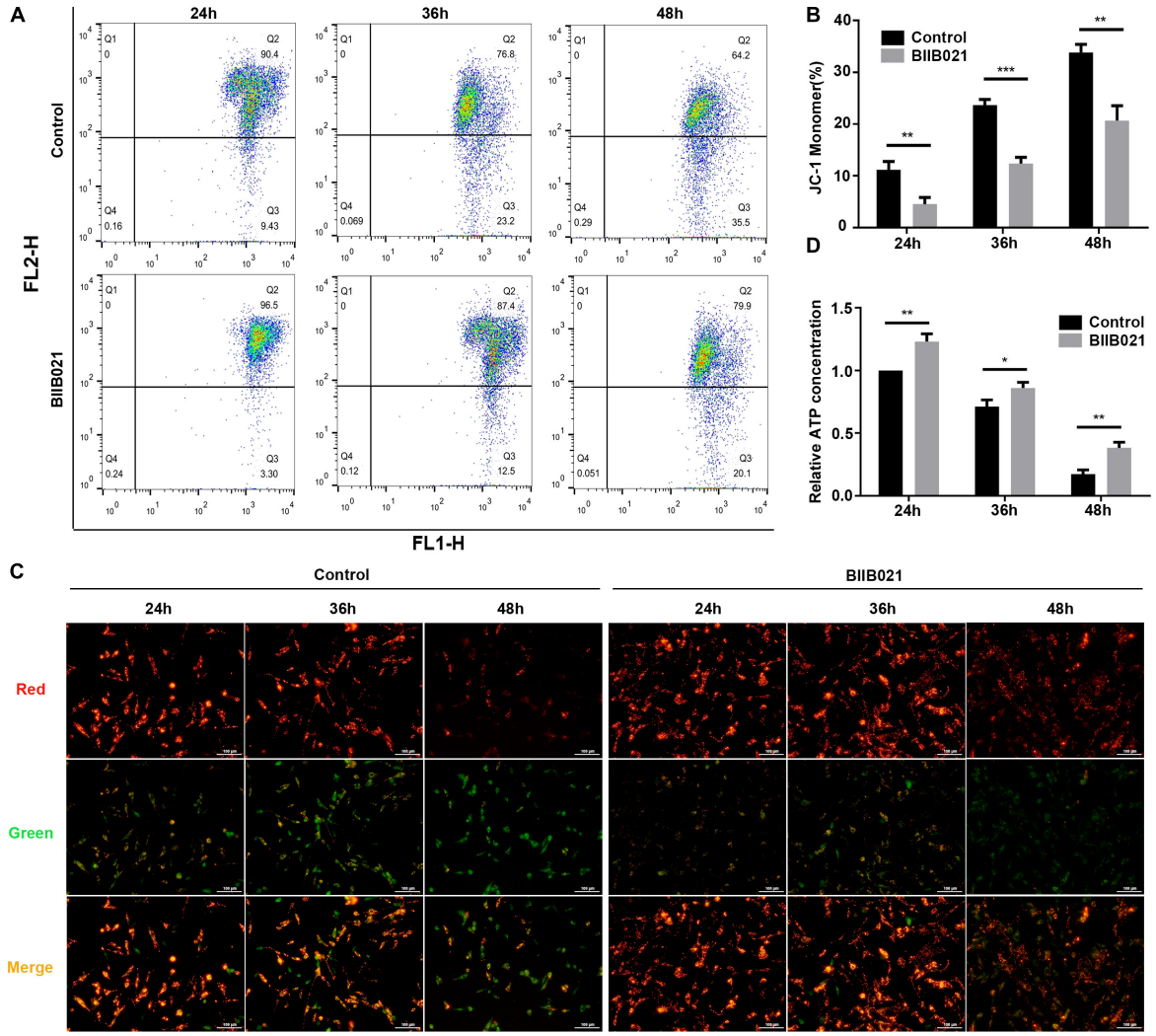


FIGURE 6 | Inhibiting HSP90 attenuated compression-induced mitochondrial dysfunction of NPSCs. **(A)** Representative dot plots of JC-1 staining obtained from flow cytometry analysis of NPSCs for detecting the MMP. **(B)** The statistical analysis of MMP which was expressed as the ratio of JC-1 monomer. **(C)** Typical fluorescence photomicrograph of JC-1 staining in NPSCs (original magnification: ×200). **(D)** The protective effects of BIIB021 on compression-induced ATP depletion of NPSCs. The data were expressed as mean ± SD from three independent experiments, and they were analyzed by a two-tailed *t*-test. (**P* < 0.05, ***P* < 0.01, ****P* < 0.001 vs. control).

the effects of inhibiting HSP90 on mitochondria. Loss of MMP is regarded as the indicator of mitochondrial dysfunction. The flow cytometric analyses of JC-1 staining showed that inhibiting HSP90 notably alleviated the loss of MMP, as indicated by decreased ratio of JC-1 monomer in BIIB021 groups (**Figures 6A,B**). Additionally, the fluorescence imaging of JC-1 staining also confirmed the rescue effects of inhibiting HSP90 on MMP loss, as demonstrated by increased red fluorescence and decreased green fluorescence (**Figure 6C**). Further, we evaluated the intracellular ATP level of NPSCs. Our results showed that compression caused time-dependent decline of intracellular ATP, while the treatment of BIIB021 attenuated the depletion of intracellular ATP in NPSCs (**Figure 6D**). These data indicated that inhibiting HSP90 attenuated compression-induced mitochondrial dysfunction of NPSCs.

Inhibiting HSP90 Alleviated Compression-Induced Oxidative Stress of NPSCs

We first utilized the MitoSOX Red to evaluate the mtROS levels. As demonstrated by fluorescence images, an increasing production of mtROS was observed in compression-treated NPSCs, while BIIB021 treatment reduced the mtROS level (**Figure 7A**). Furthermore, we also used the DCFH-DA probe to label the intracellular total ROS. As indicated by flow cytometric analyses, inhibiting HSP90 could also largely attenuate the level of intracellular total ROS (**Figures 7B,C**). In addition, the fluorescence images also demonstrated the same tendency (**Figure 7D**). MDA is an indicator of lipid peroxidation, and SOD2 is an antioxidant enzyme. Corresponding to above results,

we also found that inhibiting HSP90 decreased the MDA content and promoted the expression of SOD2 in NPSCs (**Figures 7E,F**). These results suggested that inhibiting HSP90 could efficiently alleviate compression-induced oxidative stress of NPSCs.

Inhibiting HSP90 Protected NPSCs From Compression-Induced Apoptosis

Since mitochondrial dysfunctional and ROS could trigger cell apoptosis through mitochondrial apoptosis pathway, we then determined whether HSP90 regulated compression-induced apoptosis of NPSCs (Feng et al., 2017). The flow cytometric analyses illustrated that inhibition of HSP90 alleviated compression-induced apoptosis of NPSCs in comparison with control groups (**Figures 8A,B**). In addition, the proportion of TUNEL-positive cells (green fluorescence) was also decreased in the presence of BIIB021, which intuitively confirmed the inhibitory effects of inhibiting HSP90 on apoptosis of NPSCs (**Figure 8C**). To further verify HSP90 inhibition-mediated blockage of apoptosis, we evaluated the expression levels of apoptosis-related proteins. The WB results demonstrated that inhibition of HSP90 could alleviate the decrease of Bcl-2/Bax ratio, and block the up-regulation of pro-apoptotic factors cleaved-caspase 3 and cleaved-PARP (**Figures 8D,E**). These multiple lines of evidences implied that besides necroptosis, inhibiting HSP90 could also attenuate compression-induced apoptosis of NPSCs.

Inhibiting HSP90 Attenuated the Exhaustion of NPSCs *in vivo*

The aforementioned results demonstrated that inhibiting HSP90 could protect NPSCs from compression-induced death *in vitro*. To further explore whether inhibition of HSP90 exerted cytoprotective effects *in vivo*, a rat tail model of disc degeneration induced by mechanical loading was employed. As shown in **Figure 9**, the HE staining illustrated the degeneration of IVD in compression-treated group. Furthermore, as demonstrated by IHC, the frequency of Tie2-positive cells in NP tissue was decreased in compression-loaded groups compared to that in sham-operated group, indicating the exhaustion of NPSCs *in vivo* (**Figure 9**). Furthermore, compared to control group, the decline in the frequency of Tie2-positive cells in NP tissue was attenuated in BIIB021-injected group, which indicated the inhibition of NPSCs exhaustion (**Figure 9**). Together, these results suggested that compression could trigger the exhaustion of NPSCs, and inhibiting HSP90 could attenuate the exhaustion of NPSCs *in vivo*.

DISCUSSION

NPSCs provide novel prospects for the regeneration of degenerated IVD (Hu and He, 2018). However, with aging and degeneration, the frequency of NPSCs markedly decreases, indicating the exhaustion of NPSCs (Sakai et al., 2012). The precise mechanisms underlying the exhaustion of NPSCs have not yet been fully elucidated. As shown in **Figure 10**, in current study, we identified that compression could trigger RIPK1/RIPK3/MLKL-mediated necroptosis of NPSCs. Furthermore, we found that elevated expression of HSP90 was involved in compression-induced NPSCs death, and inhibiting HSP90 could dramatically attenuate compression-induced necroptosis of NPSCs via regulating the expression and activity of RIPK1/RIPK3/MLKL, and alleviating the mitochondrial dysfunction and oxidative stress. Besides necroptosis, compression-induced apoptosis of NPSCs was also attenuated by HSP90 inhibition. In addition, we found that enhanced expression of HSP70 also contributed to the cytoprotective effects of inhibiting HSP90. More encouragingly, our results demonstrated that inhibiting HSP90 could also mitigate the exhaustion of NPSCs *in vivo*. To our knowledge, this is the first study to identify the implication of necroptosis as well as the roles of HSP90 in compression-induced NPSCs death.

Cell death is the common characteristic for the pathology of various human diseases (Zhou and Yuan, 2014). Our group has demonstrated that compression could induce the apoptosis of NPSCs, which could partially explain the exhaustion of NPSCs (Li et al., 2018a). In present study, we found that compression could also trigger the necrotic cell death of NPSCs, as indicated by increased PI positive cells and the necrotic morphological features revealed by TEM. These results are in accordance with previous discovery which shows that the necrotic cells gradually increase with aging, and even 80% of total cells are necrotic in elderly people (Buckwalter, 1995). Necrosis is traditionally regarded as unregulated accidental cell death process. Recently, accumulating evidence reveals that a subset of necrosis, referred to as necroptosis, could occur in controlled and regulated manner (Hu et al., 2018). Our previous study proves that compression could induce RIPK1/RIPK3/MLKL-mediated necroptosis of NP cells (Chen et al., 2017). For NPSCs, our data showed that the expression levels and activity of RIPK1, RIPK3, and MLKL were increased by compression treatment. In addition, all of the Nec-1, GSK′872 and NSA could attenuate compression-induced viability loss of NPSCs. The flow cytometric analyses further confirmed that NSA could decrease the proportion of PI positive cells. Altogether, these results indicate that RIPK1/RIPK3/MLKL-mediated necroptosis is involved in compression-induced NPSCs death.

HSP90 is an abundantly expressed molecular chaperone, which plays important roles in many cellular processes (Jackson, 2013). Many kinds of adverse stimuli, such as the mechanical loading, oxidative stress and oxygen-glucose deprivation, could induce the expression of HSP90 (Siebelt et al., 2013; Chooi and Chan, 2016; Liu Q. et al., 2016; Wang Z. et al., 2018). We also detected that compression could increase the expression of HSP90 at both protein and mRNA levels in NPSCs. Our findings are consistent with former study which demonstrates that mechanical loading could upregulate the expression of HSP90 in NP cells encapsulated in 3D collagen constructs (Chooi and Chan, 2016). We then determined the effects of HSP90 on compression-induced NPSCs death. Our results demonstrated that inhibiting HSP90 with BIIB021

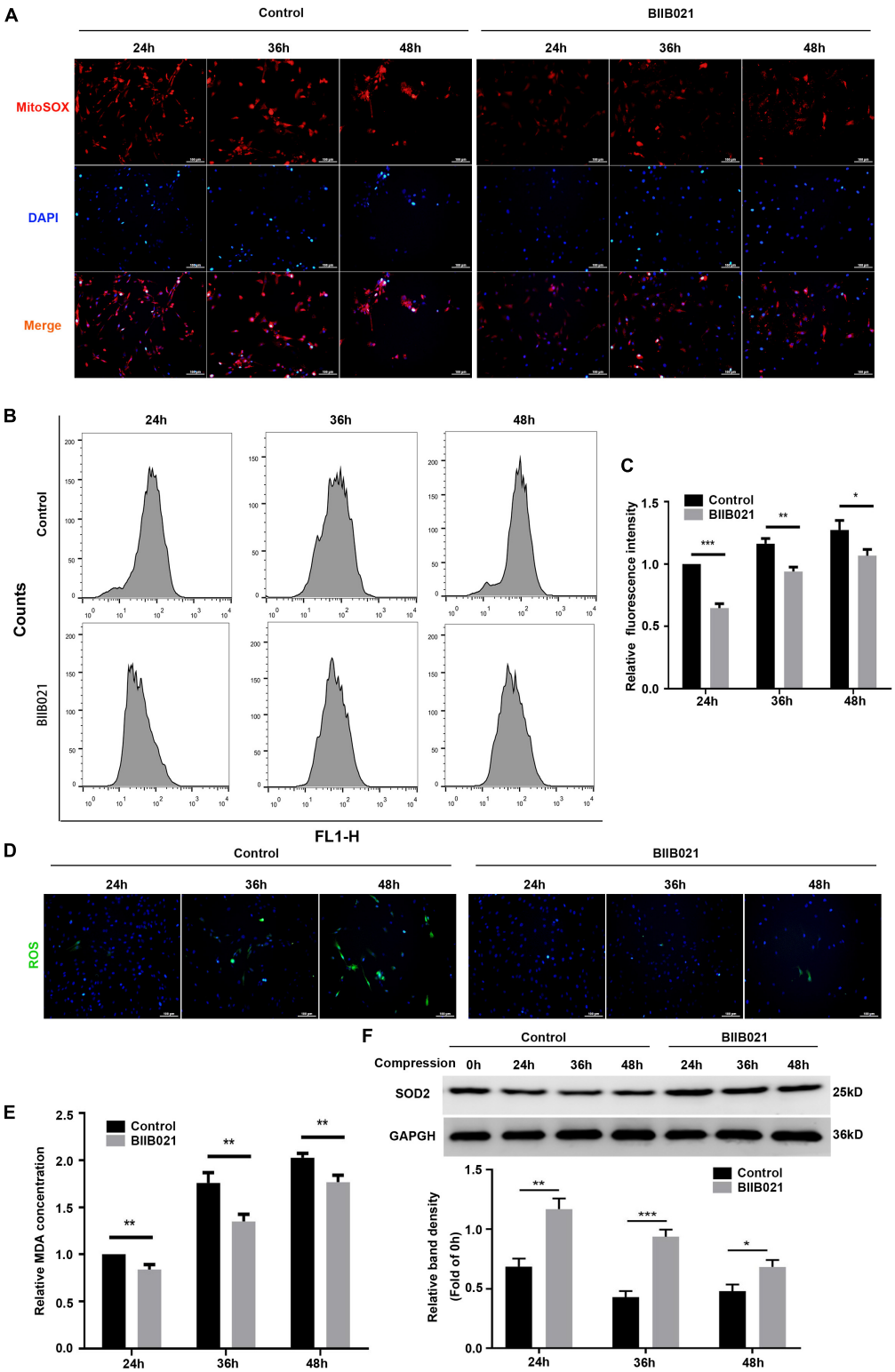


FIGURE 7 | Inhibiting HSP90 alleviated compression-induced oxidative stress of NPSCs. **(A)** Typical fluorescence photomicrograph of mtROS in NPSCs probed by MitoSOX red (original magnification: ×200). **(B)** Representative dot plots of DCFH-DA staining obtained from flow cytometry analysis of NPSCs for detecting cellular ROS. **(C)** The statistical analysis of cellular ROS. **(D)** Typical fluorescence photomicrograph of cellular ROS in NPSCs (original magnification: ×200). **(E)** The relative content of intracellular MDA. **(F)** Representative WB graphs and quantitation of the expression levels of SOD2. The data were expressed as mean ± SD from three independent experiments, and they were analyzed by a two-tailed *t*-test. (*$P < 0.05$, **$P < 0.01$, ***$P < 0.001$ vs. control).

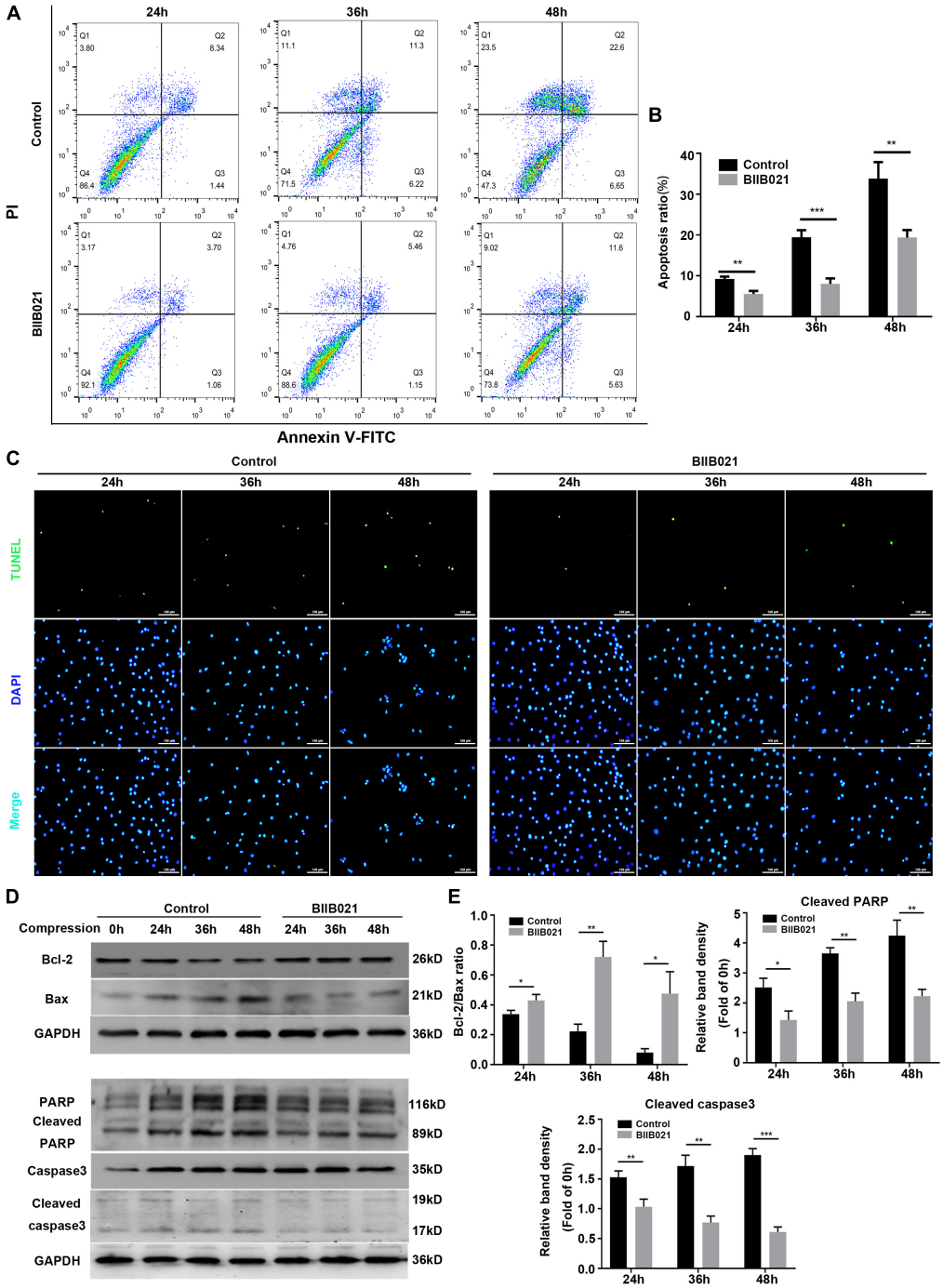


FIGURE 8 | Inhibiting HSP90 protected NPSCs from compression-induced apoptosis. **(A)** Representative dot plots of Annexin V-FITC/PI staining obtained from flow cytometry analysis of NPSCs. The Annexin + /PI- and Annexin + /PI+ represent apoptotic cells. **(B)** The statistical analysis of apoptosis ratio of NPSCs. **(C)** Typical fluorescence photomicrograph of TUNEL staining of NPSCs (original magnification: ×200). **(D)** Representative WB graphs of the expression of Bcl-2, Bax, PARP, cleaved PARP, caspase3, and cleaved caspase3. **(E)** Quantitation of the ratio of Bcl-2/Bax and the expression levels of cleaved PARP, and cleaved caspase3. The data were expressed as mean ± SD from three independent experiments, and they were analyzed by a two-tailed *t*-test. (*$P < 0.05$, **$P < 0.01$, ***$P < 0.001$ vs. control, NS, not significant).

dramatically suppressed the death of NPSCs, indicating the pro-death role of HSP90 in compression-induced NPSCs death. Our findings are consistent with some former studies which show that HSP90 exerts pro-death functions in some pathological processes, such as traumatic brain injury and eye degeneration (Hooven et al., 2004; Ma et al., 2015). Furthermore,

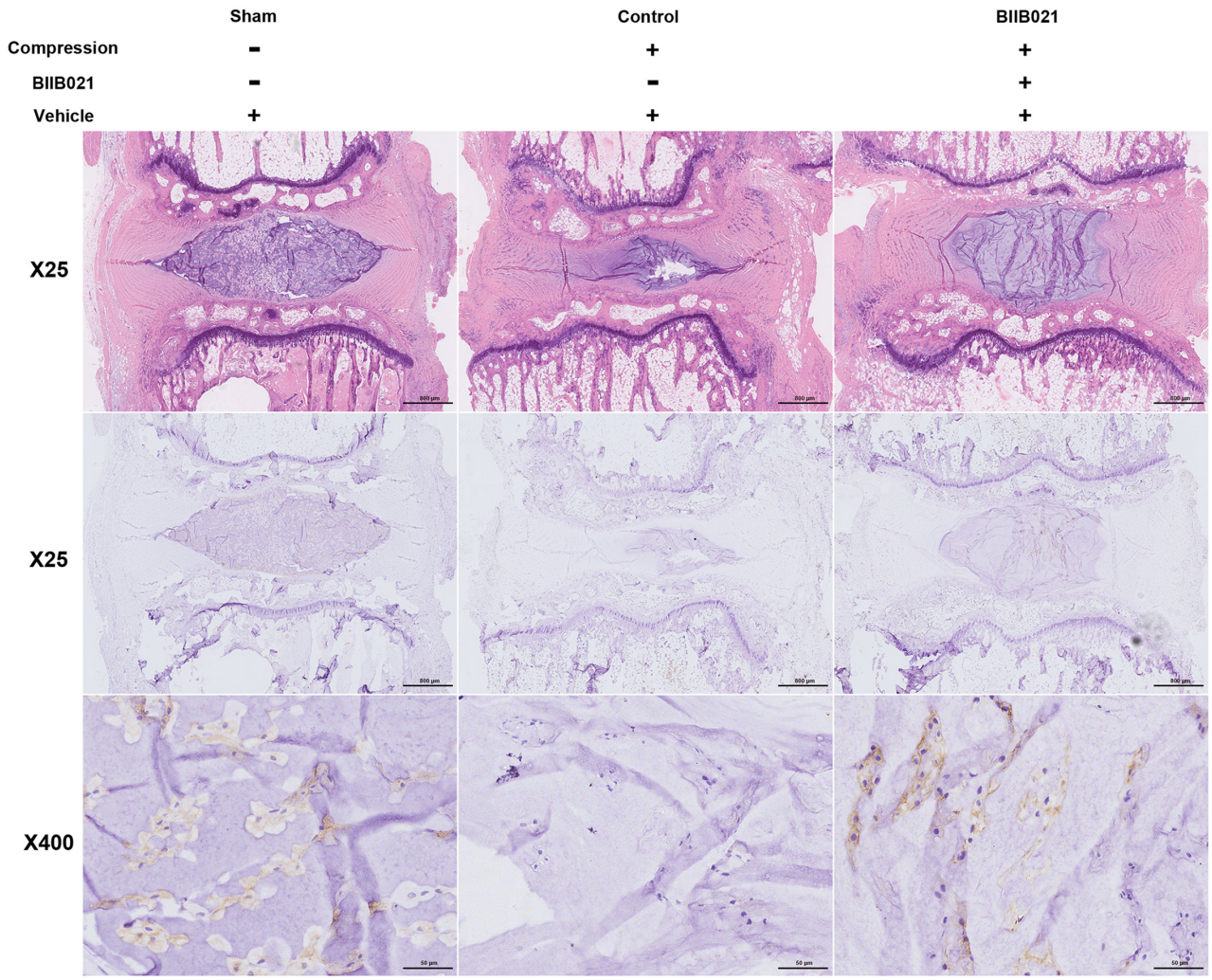


FIGURE 9 | Inhibiting HSP90 attenuated the exhaustion of NPSCs *in vivo*. Hematoxylin and eosin staining (original magnification: ×25) and the IHC staining of Tie2 (original magnification: ×25 and 400) for labeling endogenous NPSCs of IVDs.

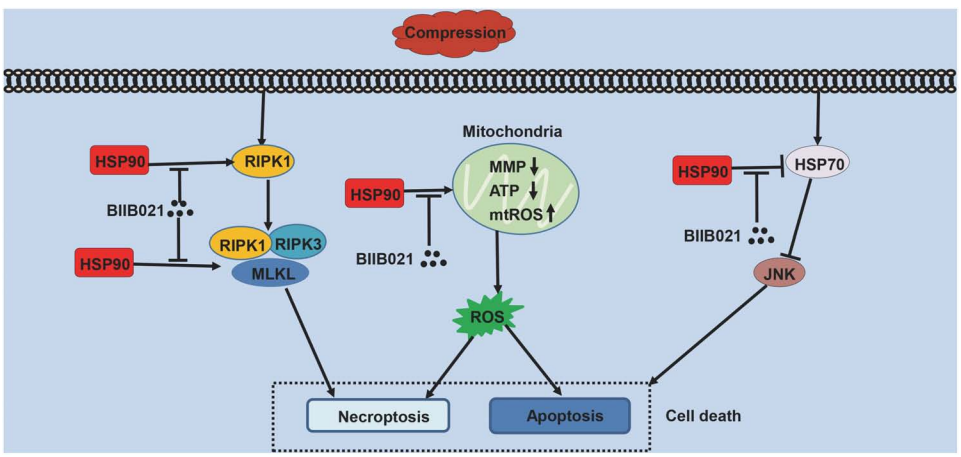


FIGURE 10 | The schematic representation of the effects of HSP90 on compression-induced NPSCs death.

the cytoprotective effects of inhibiting HSP90 have also been proven in plenty of studies (Alani et al., 2014; Ma et al., 2015; Yin et al., 2017). However, we must notice that there are also studies supporting the pro-survival roles of HSP90 (Arya et al., 2007). We speculated that the discrepant effects of HSP90 on cell death might be due to different activity of the pro-survival and pro-death signaling pathways. HSP90 could interact with a wide spectrum of client proteins, which indicates that HSP90 participates in the regulation of numerous signaling pathways, including both the pro-survival and pro-death signaling pathways (Pearl and Prodromou, 2000). Thus, the different activity of the pro-survival and pro-death signaling pathways caused by HSP90 under different circumstance and cell types might result in different cell fate. However, this hypothesis needs to be verified in further studies. In present study, we used HSP90α and HSP90β specific siRNAs to further validate the protective effects of inhibiting HSP90. However, only the transfection of HSP90β siRNA could improve the viability of NPSCs, while the transfection of HSP90α siRNA or simultaneous transfection of both the HSP90α and HSP90β siRNAs had no influence on cell viability. Our findings imply that HSP90α and HSP90β might have different effects on NPSCs death, which needs further exploration.

In present study, we found that compression-induced necroptosis of NPSCs was dramatically attenuated by HSP90 inhibitor. We observed that inhibition of HSP90 decreased PI positive cells and alleviated necrotic ultrastructure features of NPSCs. We also found that the expression of core necroptosis regulators RIPK1, P-RIPK1, RIPK3, P-RIPK3 and P-MLKL were all dramatically inhibited by HSP90 inhibitor or HSP90 specific siRNAs. However, the inhibitory effect of BIIB021 on MLKL was significant only in 48 h group, which might be because that HSP90 mainly modulates the function of MLKL rather than simply controls its stability (Yang and He, 2016). Previous studies have revealed that HSP90 regulates necroptosis by modulating the stability and function of RIPK1, RIPK3, and MLKL via ubiquitin–proteasome pathway (Yang and He, 2016). We also observed that MG132 blocked the decline in the expression of core necroptosis regulators induced by BIIB021, which indicated that HSP90 regulated compression-induced necroptosis of NPSCs via modulating the stability of core necroptosis regulators. The regulatory effects of HSP90 on necroptosis are just recently established, and much of our knowledge comes from models based on the stimulation of tumor necrosis factor (Yang and He, 2016). Only (Wang Z. et al., 2018) have manifested the regulatory effects of HSP90 on necroptosis in the background of specific disease. Thus, our results provide novel evidence for the regulatory effects of HSP90 on necroptosis.

In addition to regulating the expression and activity of RIPK1, RIPK3, and MLKL, we found that inhibiting HSP90 could also alleviate the mitochondrial dysfunction and oxidative stress of NPSCs. Our results demonstrated that inhibiting HSP90 could mitigate the loss of MMP and the depletion of ATP. Moreover, inhibition of HSP90 reduced compression-induced production of mtROS, cellular total ROS and MDA, and promoted the expression of SOD2. Our results are consistent with former study which shows that silence of HSP90 could alleviate 6-hydroxydopamine-induced oxidative stress of PC12 cells via upregulation of NRF-2 (Alani et al., 2014). In addition, it is reported that inhibiting HSP90 could overcome hydrogen peroxide-induced death of neural stem cells, which also implies the anti-oxidative stress role of inhibiting HSP90 (Liu Q. et al., 2016). Mitochondrial dysfunction and ROS are critical in the execution of necroptosis (Marshall and Baines, 2014). Our group has demonstrated that mitochondrial dysfunction and oxidative stress contribute greatly to compression-induced NP cells necroptosis (Chen et al., 2018). Thus, alleviated mitochondrial dysfunction and oxidative stress could further confirm the inhibitory effect of HSP90 inhibitors on necroptosis. Mitochondrial dysfunction and ROS could also trigger cell apoptosis. Consistently, we observed that apoptosis of NPSCs induced by compression was alleviated by BIIB021 treatment. Consistent with our results, many studies have shown that HSP90 could exert pro-apoptotic effects in some diseases, such as traumatic brain injury, neurodegenerative disease and eye degeneration (Hooven et al., 2004; Alani et al., 2014; Ma et al., 2015). Furthermore, the inhibition of apoptosis by HSP90 inhibitors or siRNAs has also been established in many studies (Wang et al., 2011; Alani et al., 2014; Ma et al., 2015; Yin et al., 2017). In a word, the above results demonstrate that the apoptosis and necroptosis of NPSCs induced by compression could be simultaneously suppressed by HSP90 inhibitor. It is widely accepted that inhibiting apoptosis could enhance the necroptosis. Thus, simultaneous inhibition of apoptosis and necroptosis might be more efficient in protecting cells from death, and this concept has been proven in our previous study conducted in NP cells (Chen et al., 2018). Therefore, inhibiting HSP90 might be a promising potent strategy for preventing cells from death.

The induction of HSP70 by HSP90 inhibitors, which is associated with the activation of heat shock factor 1, has been documented in many studies (Siebelt et al., 2013; Alani et al., 2014; Kim et al., 2015). We also observed that inhibition of HSP90 notably augmented the expression of HSP70 in NPSCs. HSP70 is a ubiquitous molecular chaperone, which could regulate the intrinsic and extrinsic apoptotic pathways, thus protecting cells against various cellular stresses (Kumar et al., 2016). Besides apoptosis, some recent studies propose that HSP70 could also inhibit necroptosis via suppressing autophagy or RIPK1 activity (Liu X. et al., 2016; Srinivasan et al., 2018). Thus, enhanced expression of HSP70 is generally considered to be responsible for the cytoprotective effects of inhibiting HSP90. Consistently, we found that HSP70 inhibitor Ver could impair the cytoprotective effects of inhibiting HSP90. Furthermore, HSP70 is known to repress the activation of JNK (Gabai et al., 1998). Herein, we identified that the activation of JNK was inhibited by BIIB021 treatment. There are studies manifesting that activated JNK is extensively involved in apoptosis and programmed necrosis, such as necroptosis, pyroptosis and ferroptosis (Dhanasekaran and Reddy, 2017). Thus, in line with

previous studies, above evidences strongly support that elevated expression of HSP70 contributes greatly to the cytoprotective effects of BIIB021 in NPSCs.

We also verified the cytoprotective effects of inhibiting HSP90 *in vivo* using a rat tail model of disc degeneration induced by mechanical loading. The *in vivo* results showed that compression treatment decreased the frequency of Tie2 positive cells, which further confirmed that compression was responsible for the exhaustion of NPSCs. BIIB021 treatment partially prevented the decline in the frequency of Tie2 positive cells, indicating the inhibition of NPSCs exhaustion. Our results are consistent with some previous studies which demonstrate that inhibiting HSP90 could protect the neural progenitor cells and intestinal stem cell niche (Wang et al., 2011; Joly et al., 2016). Currently, there are many HSP90 inhibitors being tested in clinical trials for antitumor therapy (Dickson et al., 2013; Muhammad Wasif et al., 2014; Piotrowska et al., 2018). Except for cancers, HSP90 inhibitors are also promising in treating osteoarthritis, traumatic brain injury, neurodegenerative disease et al. (Siebelt et al., 2013; Alani et al., 2014; Ma et al., 2015). Although some HSP90 inhibitors are well-tolerated and effective in treating cancers, we must notice that HSP90 inhibitors-associated dose-limiting toxicities are not accepted in treating IVDD. In present research, we proved that local administration of BIIB021 was effective in attenuating compression-induced exhaustion of NPSCs, which provides potential strategy for attenuating systemic side effects of HSP90 inhibitors. Thus, it might be possible for the translation of our results into the clinical therapy for IVDD.

CONCLUSION

In conclusion, our results prove that RIPK1/RIPK3/MLKL-mediated necroptosis participates in compression-induced NPSCs death. Furthermore, we demonstrate that HSP90 plays pivotal roles in compression-induced NPSCs death. Inhibiting HSP90 could dramatically reduce the death of NPSCs via suppressing the cell apoptosis and necroptosis. Furthermore, our study might provide promising strategy for preventing the exhaustion of NPSCs, thus delaying or even reversing the degeneration of IVD.

DATA AVAILABILITY STATEMENT

The raw data supporting the conclusions of this article will be made available by the authors, without undue reservation.

ETHICS STATEMENT

The studies involving human participants were reviewed and approved by The Medical Ethics Committee of the Tongji Medical College, Huazhong University of Science and Technology. The patients/participants provided their written informed consent to participate in this study. The animal study was reviewed and approved by The Animal Experimentation Committee of the Huazhong University of Science and Technology.

AUTHOR CONTRIBUTIONS

BH, SZ, and ZS designed the study and experiments. BH, SZ, WL, PW, XL, and DS conducted the experiments. BH, SZ, SC, BW, and YW drafted and edited the manuscript. KM, BW, and ZS supervised the experiments. All authors approved the final version of the manuscript.

FUNDING

This study was supported by grants from the National Key Research and Development Program of China (No. 2016YFC1100100), grants from the Major Research Plan of National Natural Science Foundation of China (No. 91649204), and grants from the National Natural Science Foundation of China (No. 81974352).

SUPPLEMENTARY MATERIAL

The Supplementary Material for this article can be found online at: https://www.frontiersin.org/articles/10.3389/fcell.2020.00685/full#supplementary-material

REFERENCES

Alani, B., Salehi, R., Sadeghi, P., Zare, M., Khodagholi, F., Arefian, E., et al. (2014). Silencing of Hsp90 chaperone expression protects against 6-hydroxydopamine toxicity in PC12 cells. *J. Mol. Neurosci.* 52, 392–402. doi: 10.1007/s12031-013-0163-9

Arya, R., Mallik, M., and Lakhotia, S. C. (2007). Heat shock genes - integrating cell survival and death. *J. Biosci.* 32, 595–610. doi: 10.1007/s12038-007-0059-3

Buckwalter, J. A. (1995). Aging and degeneration of the human intervertebral disc. *Spine* 20, 1307–1314. doi: 10.1097/00007632-199506000-00022

Chen, S., Lv, X., Hu, B., Shao, Z., Wang, B., Ma, K., et al. (2017). RIPK1/RIPK3/MLKL-mediated necroptosis contributes to compression-induced rat nucleus pulposus cells death. *Apoptosis* 22, 626–638. doi: 10.1007/s10495-017-1358-2

Chen, S., Lv, X., Hu, B., Zhao, L., Li, S., Li, Z., et al. (2018). Critical contribution of RIPK1 mediated mitochondrial dysfunction and oxidative stress to compression-induced rat nucleus pulposus cells necroptosis and apoptosis. *Apoptosis* 23, 299–313. doi: 10.1007/s10495-018-1455-x

Chooi, W. H., and Chan, B. P. (2016). Compression loading-induced stress responses in intervertebral disc cells encapsulated in 3D collagen constructs. *Sci. Rep.* 6:26449. doi: 10.1038/srep26449

Dhanasekaran, D. N., and Reddy, E. P. (2017). JNK-signaling: a multiplexing hub in programmed cell death. *Genes Cancer* 8, 682–694. doi: 10.18632/genesandcancer.155

Dickson, M. A., Okuno, S. H., Keohan, M. L., Maki, R. G., D'Adamo, D. R., Akhurst, T. J., et al. (2013). Phase II study of the HSP90-inhibitor BIIB021 in gastrointestinal stromal tumors. *Ann. Oncol.* 24, 252–257. doi: 10.1093/annonc/mds275

Ding, F., Shao, Z., Yang, S., Wu, Q., Gao, F., and Xiong, L. (2012). Role of mitochondrial pathway in compression-induced apoptosis of nucleus pulposus cells. *Apoptosis* 17, 579–590. doi: 10.1007/s10495-012-0708-3

Feng, C., Yang, M., Lan, M., Liu, C., Zhang, Y., Huang, B., et al. (2017). ROS: crucial intermediators in the pathogenesis of intervertebral disc degeneration. *Oxid. Med. Cell. Longev.* 2017:5601593. doi: 10.1155/2017/5601593

Freemont, A. J. (2009). The cellular pathobiology of the degenerate intervertebral disc and discogenic back pain. *Rheumatology* 48, 5–10. doi: 10.1093/rheumatology/ken396

Gabai, V. L., Meriin, A. B., Yaglom, J. A., Volloch, V. Z., and Sherman, M. Y. (1998). Role of Hsp70 in regulation of stress-kinase JNK: implications in apoptosis and aging. *FEBS Lett.* 438, 1–4. doi: 10.1016/s0014-5793(98)01242-3

Galluzzi, L., Kepp, O., Chan, F. K., and Kroemer, G. (2017). Necroptosis: mechanisms and relevance to disease. *Annu. Rev. Pathol.* 12, 103–130. doi: 10.1146/annurev-pathol-052016-100247

Hooven, T. A., Yamamoto, Y., and Jeffery, W. R. (2004). Blind cavefish and heat shock protein chaperones: a novel role for hsp90alpha in lens apoptosis. *Int. J. Dev. Biol.* 48, 731–738. doi: 10.1387/ijdb.041874th

Hu, B., and He, R. (2018). Intervertebral disc-derived stem/progenitor cells as a promising cell source for intervertebral disc regeneration. *Stem Cells Intern.* 2018:7412304. doi: 10.1155/2018/7412304

Hu, B., Shi, D., Lv, X., Chen, S., Huang, Q., Xie, M., et al. (2018). Prognostic and clinicopathological significance of MLKL expression in cancer patients: a meta-analysis. *BMC Cancer* 18:736. doi: 10.1186/s12885-018-4655-4

Jackson, S. E. (2013). Hsp90: structure and function. *Top Curr. Chem.* 328, 155–240. doi: 10.1007/128_2012_356

Joly, A. L., Deepti, A., Seignez, A., Goloudina, A., Hebrard, S., Schmitt, E., et al. (2016). The HSP90 inhibitor, 17AAG, protects the intestinal stem cell niche and inhibits graft versus host disease development. *Oncogene* 35, 2842–2851. doi: 10.1038/onc.2015.242

Kim, N., Kim, J. Y., and Yenari, M. A. (2015). Pharmacological induction of the 70-kDa heat shock protein protects against brain injury. *Neuroscience* 284, 912–919. doi: 10.1016/j.neuroscience.2014.11.010

Kumar, S., Stokes, J. III, Singh, U. P., Scissum Gunn, K., Acharya, A., Manne, U., et al. (2016). Targeting Hsp70: a possible therapy for cancer. *Cancer Lett.* 374, 156–166. doi: 10.1016/j.canlet.2016.01.056

Lewis, J., Devin, A., Miller, A., Lin, Y., Rodriguez, Y., Neckers, L., et al. (2000). Disruption of hsp90 function results in degradation of the death domain kinase, receptor-interacting protein (RIP), and blockage of tumor necrosis factor-induced nuclear factor-kappaB activation. *J. Biol. Chem.* 275, 10519–10526. doi: 10.1074/jbc.275.14.10519

Li, D., Xu, T., Cao, Y., Wang, H., Li, L., Chen, S., et al. (2015). A cytosolic heat shock protein 90 and cochaperone CDC37 complex is required for RIP3 activation during necroptosis. *Proc. Natl. Acad. Sci. U.S.A.* 112, 5017–5022. doi: 10.1073/pnas.1505244112

Li, J., Yang, F., Guo, J., Zhang, R., Xing, X., and Qin, X. (2015). 17-AAG post-treatment ameliorates memory impairment and hippocampal CA1 neuronal autophagic death induced by transient global cerebral ischemia. *Brain Res.* 1610, 80–88. doi: 10.1016/j.brainres.2015.03.051

Li, J., and Buchner, J. (2013). Structure, function and regulation of the hsp90 machinery. *Biomed. J.* 36, 106–117. doi: 10.4103/2319-4170.113230

Li, Z., Chen, S., Ma, K., Lv, X., Lin, H., Hu, B., et al. (2018a). CsA attenuates compression-induced nucleus pulposus mesenchymal stem cells apoptosis via alleviating mitochondrial dysfunction and oxidative stress. *Life Sci.* 205, 26–37. doi: 10.1016/j.lfs.2018.05.014

Li, Z., Li, X., Chen, C., Li, S., Shen, J., Tse, G., et al. (2018b). Long non-coding RNAs in nucleus pulposus cell function and intervertebral disc degeneration. *Cell Prolif.* 51:e12483. doi: 10.1111/cpr.12483

Liang, H., Chen, S., Huang, D., Deng, X., Ma, K., and Shao, Z. (2018). Effect of compression loading on human nucleus pulposus-derived mesenchymal stem cells. *Stem Cells Int.* 2018, 1481243. doi: 10.1155/2018/1481243

Liu, J., Tao, H., Wang, H., Dong, F., Zhang, R., Li, J., et al. (2017). Biological behavior of human nucleus pulposus mesenchymal stem cells in response to changes in the acidic environment during intervertebral disc degeneration. *Stem Cells Dev.* 26, 901–911. doi: 10.1089/scd.2016.0314

Liu, Q., Li, Y., Jiang, W., Li, Y., Zhou, L., Song, B., et al. (2016). Inhibition of HSP90 promotes neural stem cell survival from oxidative stress through attenuating NF-kappaB/p65 activation. *Oxid. Med. Cell. Longev.* 2016:3507290. doi: 10.1155/2016/3507290

Liu, X., Zhang, C., Zhang, C., Li, J., Guo, W., Yan, D., et al. (2016). Heat shock protein 70 inhibits cardiomyocyte necroptosis through repressing autophagy in myocardial ischemia/reperfusion injury. *Vitro Cell Dev. Biol. Anim.* 52, 690–698. doi: 10.1007/s11626-016-0039-8

Lotz, J. C., and Chin, J. R. (2000). Intervertebral disc cell death is dependent on the magnitude and duration of spinal loading. *Spine* 25, 1477–1483. doi: 10.1097/00007632-200006150-00005

Ma, L., Li, Z., Liu, Z., Li, M., Sui, D., Liu, Y., et al. (2015). 17AAG improves histological and functional outcomes in a rat CCI model through autophagy activation and apoptosis attenuation. *Neurosci. Lett.* 599, 1–6. doi: 10.1016/j.neulet.2015.05.004

Maetzel, A., and Li, L. (2002). The economic burden of low back pain: a review of studies published between 1996 and 2001. *Best Pract. Res. Clin. Rheumatol.* 16, 23–30. doi: 10.1053/berh.2001.0204

Marshall, K. D., and Baines, C. P. (2014). Necroptosis: is there a role for mitochondria? *Front. Physiol.* 5:323. doi: 10.3389/fphys.2014.00323

Muhammad Wasif, S., Chris, T., Monica, M., Udai, B., Nicole, L., Januario, C., et al. (2014). A phase 1, dose-escalation, pharmacokinetic and pharmacodynamic study of BIIB021 administered orally in patients with advanced solid tumors. *Clin. Cancer Res.* 20, 445–455. doi: 10.1158/1078-0432.ccr-13-1257

Nan, L. P., Wang, F., Ran, D., Zhou, S. F., Liu, Y., Zhang, Z., et al. (2019). Naringin alleviates H2O2-induced apoptosis via the PI3K/Akt pathway in rat nucleus pulposus-derived mesenchymal stem cells. *Connect. Tissue Res.* 1–14. doi: 10.1080/03008207.2019.1631299

Neidlinger-Wilke, C., Galbusera, F., Pratsinis, H., Mavrogonatou, E., Mietsch, A., Kletsas, D., et al. (2014). Mechanical loading of the intervertebral disc: from the macroscopic to the cellular level. *Eur. Spine J.* 23(Suppl. 3), S333–S343. doi: 10.1007/s00586-013-2855-9

Pearl, L. H., and Prodromou, C. (2000). Structure and in vivo function of Hsp90. *Curr. Opin. Struct. Biol.* 10, 46–51. doi: 10.1016/s0959-440x(99)00047-0

Pfirrmann, C. W., Metzdorf, A., Zanetti, M., Hodler, J., and Boos, N. (2001). Magnetic resonance classification of lumbar intervertebral disc degeneration. *Spine* 26, 1873–1878. doi: 10.1097/00007632-200109010-00011

Piotrowska, Z., Costa, D. B., Oxnard, G. R., Huberman, M., Gainor, J. F., Shaw, A. T., et al. (2018). Activity of the Hsp90 inhibitor luminespib among non-small-cell lung cancers harboring EGFR exon 20 insertions. *Ann. Oncol.* 29, 2092–2097. doi: 10.1093/annonc/mdy336

Risbud, M. V., Guttapalli, A., Tsai, T. T., Lee, J. Y., Danielson, K. G., Vaccaro, A. R., et al. (2007). Evidence for skeletal progenitor cells in the degenerate human intervertebral disc. *Spine* 32, 2537–2544. doi: 10.1097/BRS.0b013e318158dea6

Sakai, D., Nakamura, Y., Nakai, T., Mishima, T., Kato, S., Grad, S., et al. (2012). Exhaustion of nucleus pulposus progenitor cells with ageing and degeneration of the intervertebral disc. *Nat. Commun.* 3:1264. doi: 10.1038/ncomms2226

Shang, L., and Tomasi, T. B. (2006). The heat shock protein 90-CDC37 chaperone complex is required for signaling by types I and II interferons. *J. Biol. Chem.* 281, 1876–1884. doi: 10.1074/jbc.M509901200

Siebelt, M., Jahr, H., Groen, H. C., Sandker, M., Waarsing, J. H., Kops, N., et al. (2013). Hsp90 inhibition protects against biomechanically induced osteoarthritis in rats. *Arthrit. Rheum* 65, 2102–2112. doi: 10.1002/art.38000

Smith, L. J., Nerurkar, N. L., Choi, K. S., Harfe, B. D., and Elliott, D. M. (2011). Degeneration and regeneration of the intervertebral disc: lessons from development. *Dis. Model. Mech.* 4, 31–41. doi: 10.1242/dmm.006403

Srinivasan, S. R., Cesa, L. C., Li, X., Julien, O., Zhuang, M., Shao, H., et al. (2018). Heat shock protein 70 (Hsp70) suppresses RIP1-dependent apoptotic and necroptotic cascades. *Mol. Cancer Res.* 16, 58–68. doi: 10.1158/1541-7786.mcr-17-0408

Tao, Y., Zhou, X., Liang, C., Li, H., Han, B., Li, F., et al. (2015). TGF-beta3 and IGF-1 synergy ameliorates nucleus pulposus mesenchymal stem cell differentiation towards the nucleus pulposus cell type through MAPK/ERK signaling. *Growth Fact.* 33, 326–336. doi: 10.3109/08977194.2015.1088532

Tao, Y. Q., Liang, C. Z., Li, H., Zhang, Y. J., Li, F. C., Chen, G., et al. (2013). Potential of co-culture of nucleus pulposus mesenchymal stem cells and nucleus pulposus cells in hyperosmotic microenvironment for intervertebral disc regeneration. *Cell Biol. Int.* 37, 826–834. doi: 10.1002/cbin.10110

Tekari, A., Chan, S. C. W., Sakai, D., Grad, S., and Gantenbein, B. (2016). Angiopoietin-1 receptor Tie2 distinguishes multipotent differentiation capability in bovine coccygeal nucleus pulposus cells. *Stem Cell Res. Ther.* 7:75. doi: 10.1186/s13287-016-0337-9

Wang, G., Krishnamurthy, K., and Tangpisuthipongsa, D. (2011). Protection of murine neural progenitor cells by the Hsp90 inhibitor 17-allylamino-17-demethoxygeldanamycin in the low nanomolar concentration range. *J. Neurochem.* 117, 703–711. doi: 10.1111/j.1471-4159.2011.07239.x

Wang, W., Qing, X., Wang, B., Ma, K., Wei, Y., and Shao, Z. (2018). Tauroursodeoxycholic acid protects nucleus pulposus cells from compression-induced apoptosis and necroptosis via inhibiting endoplasmic reticulum stress. *Evid. Based Complem. Alternat. Med.* 2018:6719460. doi: 10.1155/2018/6719460

Wang, Z., Guo, L. M., Wang, Y., Zhou, H. K., Wang, S. C., Chen, D., et al. (2018). Inhibition of HSP90alpha protects cultured neurons from oxygen-glucose deprivation induced necroptosis by decreasing RIP3 expression. *J. Cell Physiol.* 233, 4864–4884. doi: 10.1002/jcp.26294

Yan, Z., Pan, Y., Wang, S., Cheng, M., Kong, H., Sun, C., et al. (2017). Static compression induces ECM remodeling and integrin alpha2beta1 expression and signaling in a rat tail caudal intervertebral disc degeneration model. *Spine* 42, E448–E458. doi: 10.1097/brs.0000000000001856

Yang, C. K., and He, S. D. (2016). Heat shock protein 90 regulates necroptosis by modulating multiple signaling effectors. *Cell Death Dis.* 7:e2126. doi: 10.1038/cddis.2016.25

Yin, X. H., Han, Y. L., Zhuang, Y., Yan, J. Z., and Li, C. (2017). Geldanamycin inhibits Fas signaling pathway and protects neurons against ischemia. *Neurosci. Res.* 124, 33–39. doi: 10.1016/j.neures.2017.05.003

Yurube, T., Hirata, H., Kakutani, K., Maeno, K., Takada, T., Zhang, Z., et al. (2014). Notochordal cell disappearance and modes of apoptotic cell death in a rat tail static compression-induced disc degeneration model. *Arthrit. Res. Ther.* 16:R31. doi: 10.1186/ar4460

Zhao, C. Q., Wang, L. M., Jiang, L. S., and Dai, L. Y. (2007). The cell biology of intervertebral disc aging and degeneration. *Ageing Res. Rev.* 6, 247–261. doi: 10.1016/j.arr.2007.08.001

Zhao, X. M., Chen, Z., Zhao, J. B., Zhang, P. P., Pu, Y. F., Jiang, S. H., et al. (2016). Hsp90 modulates the stability of MLKL and is required for TNF-induced necroptosis. *Cell Death Dis.* 7:e2089. doi: 10.1038/cddis.2015.390

Zhou, W., and Yuan, J. (2014). Necroptosis in health and diseases. *Semin. Cell Dev. Biol.* 35, 14–23. doi: 10.1016/j.semcdb.2014.07.013

Zou, F., Jiang, J., Lu, F., Ma, X., Xia, X., Wang, L., et al. (2013). Efficacy of intradiscal hepatocyte growth factor injection for the treatment of intervertebral disc degeneration. *Mol. Med. Rep.* 8, 118–122. doi: 10.3892/mmr.2013.1450

Conflict of Interest: The authors declare that the research was conducted in the absence of any commercial or financial relationships that could be construed as a potential conflict of interest.

Copyright © 2020 Hu, Zhang, Liu, Wang, Chen, Lv, Shi, Ma, Wang, Wu and Shao. This is an open-access article distributed under the terms of the Creative Commons Attribution License (CC BY). The use, distribution or reproduction in other forums is permitted, provided the original author(s) and the copyright owner(s) are credited and that the original publication in this journal is cited, in accordance with accepted academic practice. No use, distribution or reproduction is permitted which does not comply with these terms.

frontiers in Cell and Developmental Biology

REVIEW
published: 18 August 2020
doi: 10.3389/fcell.2020.00809

Novel Glial Cell Functions: Extensive Potency, Stem Cell-Like Properties, and Participation in Regeneration and Transdifferentiation

Valentin Milichko[1] *and Vyacheslav Dyachuk*[1,2]*

[1] Department of Nanophotonics and Metamaterials, ITMO University, St. Petersburg, Russia, [2] National Scientific Center of Marine Biology, Far Eastern Branch, Russian Academy of Sciences, Vladivostok, Russia

Glial cells are the most abundant cells in both the peripheral and central nervous systems. During the past decade, a subpopulation of immature peripheral glial cells, namely, embryonic Schwann cell-precursors, have been found to perform important functions related to development. These cells have properties resembling those of the neural crest and, depending on their location in the body, can transform into several different cell types in peripheral tissues, including autonomic neurons. This review describes the multipotent properties of Schwann cell-precursors and their importance, together with innervation, during early development. The heterogeneity of Schwann cells, as revealed using single-cell transcriptomics, raises a question on whether some glial cells in the adult peripheral nervous system retain their stem cell-like properties. We also discuss how a deeper insight into the biology of both embryonic and adult Schwann cells might lead to an effective treatment of the damage of both neural and non-neural tissues, including the damage caused by neurodegenerative diseases. Furthermore, understanding the potential involvement of Schwann cells in the regulation of tumor development may reveal novel targets for cancer treatment.

Keywords: Schwann cell precursors, peripheral glial cells, heterogeneity, plasticity and multipotency, reprogramming, neurological diseases, carcinogenesis

OPEN ACCESS

Edited by:
Andrei S. Chagin, Karolinska Institutet (KI), Sweden

Reviewed by:
Raul R. Gainetdinov, Saint Petersburg State University, Russia
Johannes F. W. Greiner, Bielefeld University, Germany

***Correspondence:**
Vyacheslav Dyachuk
slavad83@gmail.com

Specialty section:
This article was submitted to Stem Cell Research, a section of the journal Frontiers in Cell and Developmental Biology

Received: *26 April 2020*
Accepted: *31 July 2020*
Published: *18 August 2020*

Citation:
Milichko V and Dyachuk V (2020) Novel Glial Cell Functions: Extensive Potency, Stem Cell-Like Properties, and Participation in Regeneration and Transdifferentiation. Front. Cell Dev. Biol. 8:809. doi: 10.3389/fcell.2020.00809

INTRODUCTION

Peripheral glial cells encompass a wide variety of cell types, including myelinating Schwann cells, non-myelinating Schwann (Remak) cells (Jessen and Mirsky, 2010), glia of the enteric nervous system (Ochoa-Cortes et al., 2016), satellite glial cells of peripheral ganglia, and perisynaptic Schwann cells (PSCs) located in neuromuscular junctions (Alvarez-Suarez et al., 2020). In addition, boundary cap cells give rise to terminal glia associated with dermal nerve endings (Zujovic et al., 2011; Gresset et al., 2015). Moreover, researchers have described other small subpopulations of glial cells, such as olfactory ensheathing cells that envelop bundles of axons in the olfactory bulb (Su and He, 2010) and specialized subtypes of glial cells in sensory organs (Ruffini endings, Krause end bulbs, and Meissner's and Pacinian corpuscles) (Byers, 1985; Maeda et al., 1999; Kastriti and Adameyko, 2017).

Classically, peripheral glial cells have been viewed as multifunctional, nourishing, supporting and protecting neurons, myelinating axons, regulating synaptic connectivity and sensory function, and participating in the maintenance and regeneration of the peripheral nervous system (Barres, 2008). In recent decades, researchers have discovered that glial cells also play additional novel and unexpected roles, both during development and in adult animals (Adameyko et al., 2009; Dyachuk et al., 2014; Kaukua et al., 2014; Abdo et al., 2019; Xie et al., 2019), including participation in diseases (diabetes, tunnel syndrome, nerve paralysis, Guillain-Barre syndrome) (Gonçalves et al., 2018).

Involvement of Schwann Cell Populations in Development

Traditionally, terminally differentiated peripheral glial cells (or Schwann) cells (SCs) have been thought to derive directly from multipotent neural crest cells (NCCs), which appear for only a short time during early mammalian development, and then give rise to a variety of other cell types (Le Douarin and Kalcheim, 1999). However, this concept has been challenged by several recent studies involving lineage tracing that have revealed the existence of Schwann cell precursors (SCPs) with transcriptional profiles similar to those of SCs and NCCs (Adameyko et al., 2009; Kastriti and Adameyko, 2017). These SCPs can differentiate into an extraordinary variety of cell types, including immature Schwann cells, which subsequently differentiate into the myelinating and non-myelinating Schwann cells, associated with peripheral nerves. Recent data, showed that embryonic Schwann cells are able to differentiate into endoneurial fibroblasts (Joseph, 2004), pigment cells (Adameyko et al., 2009), parasympathetic neurons (Dyachuk et al., 2014), mesenchymal dental cells (Kaukua et al., 2014), enteric neurons (Espinosa-Medina et al., 2017), chromaffin cells of the adrenal gland (Furlan et al., 2017), cells of the Zuckerkandl organ (Kastriti et al., 2019), chondrocytes, and osteocytes (Xie et al., 2019; **Figure 1**).

Are Schwann cell precursors needed, in association with early development, when a population of NCCs, that appears earlier, can produce a wide range of cell types? One fundamental difference between these two types of cells is that NCCs migrate along a concentration gradient of growth factors released by neighboring tissues during a specific 24 h period, whereas SCPs are continuously associated with rapidly growing embryonic nerves, migrating together with them to quickly reach, even distant, regions of the body. The relatively large size of mouse and chicken embryos requires a rapid and appropriately timed delivery of undifferentiated cells to various locations where they give rise to several specialized types of cells, a function that SCPs are capable of performing.

In this context, the mechanism(s) by which SCPs attach and detach from growing nerves and the temporal and spatial regulation of these mechanism(s) remain(s) unclear. It is known that the signals released by axons, as well as the actual physical interaction of axons with SCPs, are involved in the survival and differentiation of SCPs (Birchmeier and Nave, 2008), influencing their subsequent differentiation into specialized cell types (Dyachuk et al., 2014). The signaling pathway involving the neuregulin–ErbB heteromeric receptor plays crucial roles in both SCP migration and in the survival of glial cells (Birchmeier, 2009). For example, in teleost fish, the association of SCPs with nerves and their glial commitment are controlled by this pathway (Garratt et al., 2000; Honjo et al., 2008). Moreover, similar mechanisms are active in the mammalian peripheral nervous system (Britsch et al., 1998; Jessen and Mirsky, 2005; Dyachuk et al., 2014), as demonstrated by the observation that, in mice in which *ErbB2* has been genetically ablated, no SCPs are associated with the developing nerves, ultimately resulting in the widespread death of both motor and sensory neurons. *Sox10, ErbB3,* or *Nrg1* genes are responsible for the survival of SCPs, and the inactivation of these genes led to the degeneration of motor and sensory neurons (Riethmacher et al., 1997; Wolpowitz et al., 2000; Britsch et al., 2001). Genetic ablation of peripheral nerves in mouse embryos or the pharmacological impairment in zebrafish larvae depleted SCPs nerve-associated SCPs, thereby preventing the appearance of neurons of the PNS and of melanophore stem cells (Dooley et al., 2013).

Comparative single-cell transcriptomic analysis of NCCs and SCPs has revealed that these two embryonic cell populations express many common transcription factors (TF) (Kastriti and Adameyko, 2017; Soldatov et al., 2019). As shown before, during early differentiation, SCPs programming is downregulated, while neuronal, neuroendocrine (e.g., chromaffin cells), or mesenchymal (odontoblasts, chondrocytes, and osteocytes) traits are upregulated (Dyachuk et al., 2014; Kaukua et al., 2014; Furlan et al., 2017; Xie et al., 2019). What determines the specialization direction in which a SCP will develop remains unclear. Are the different nerve and body locations of SCPs involved in their type of specialization? Perhaps the specific signals released by cells in the innervated target organs help to determine the fate of SCPs. Appropriately designed experiments are required to answer these fascinating questions.

Natural (Adaptive) Reprogramming of Schwann Cells

Differentiated definitive somatic cells can be reprogrammed by enhancing the levels of the Yamanaka factors (Takahashi and Yamanaka, 2006). At the same time, specialized cells in certain adult mammalian tissues can be naturally reprogrammed in response to an injury (Merrell and Stanger, 2016). The most well-known example of such an adaptive reprogramming is the transformation of myelin cells into cells with a non-myelinating Schwann cell phenotype, following certain types of injuries of the nervous system. Schwann cells have a unique capacity to promote the recovery of axons. After detaching from their axons, these cells release neurotrophic factors that improve the axonal survival. Moreover, by radically changing the local signaling environment, they participate in the autophagy of myelin and in the expression of cytokines, being also able to attract macrophages for myelin clearance. Finally, SCs proliferate to replace the lost cells and differentiate to elongate, branch, and form regeneration tracks (Bungner bands) (Jessen et al., 2015; **Figure 2**). The molecular profiling of glia cells following

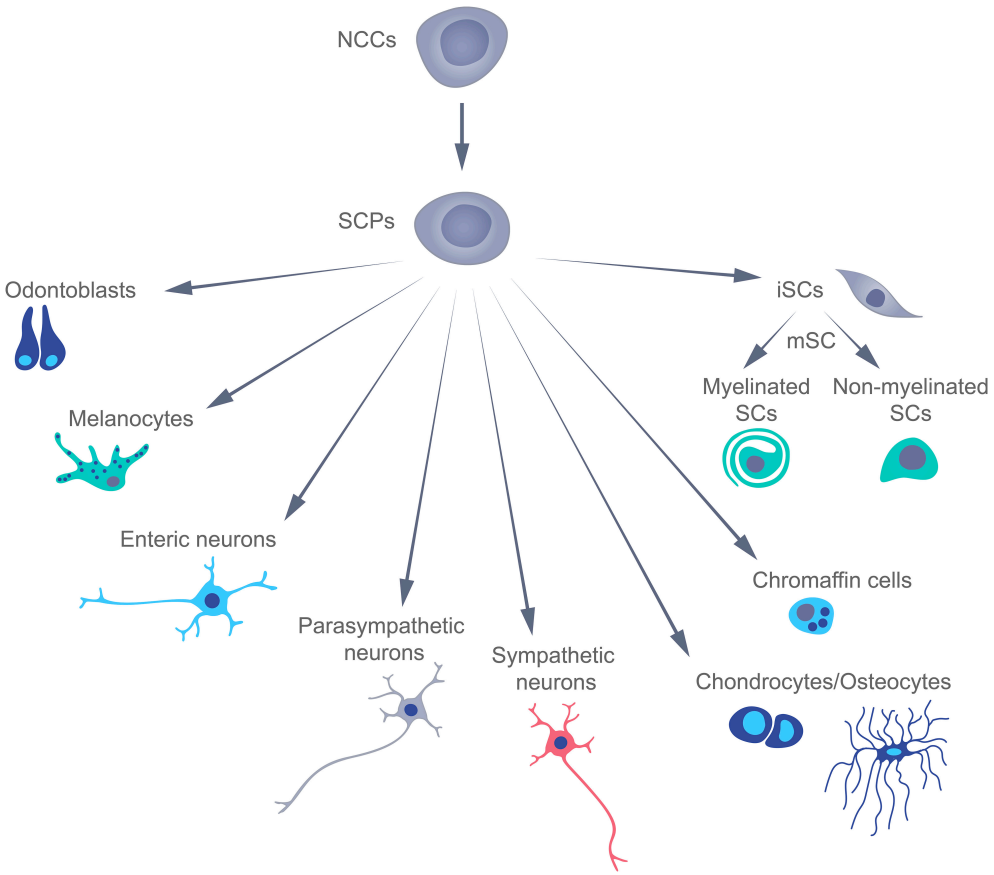


FIGURE 1 | The multipotency of Schwann cell precursors during early mammalian development.

injury is now receiving considerable attention, in order to determine their status.

Transcriptional profiling indicates that, following injury, Schwann cells acquire some properties of immature SCs, with concomitant repression of genes encoding proteins involved in the production of myelin (BrosiusLutz and Barres, 2014; Jessen and Mirsky, 2016). It should be emphasized that this transformation of mature Schwann cells into reparative Schwann cells is not actually dedifferentiation, although this process has been designated as such, previously. Indeed, this process involves the *de novo* expression of genes (*Shh* and *Olig1*) that are never expressed by embryonic Schwann cells, and whose expression is a unique aspect of the response to injury (Arthur-Farraj et al., 2012; Lin et al., 2015). At the same time, the transcription factor SOX2, a marker of developing SCPs, becomes upregulated as part of this reprogramming (Johnston et al., 2016).

The key molecular molecules that participate in this reprogramming of SCs include both certain transcription factors (e.g., c-JUN, SOX2) and signaling pathways (ERK, NOTCH). Moreover, the molecular characterization of bridge and distal stumps of transected nerves indicates that, during reprogramming, SCs acquire mesenchymal traits, i.e., this process is somewhat similar to an epithelial-to-mesenchymal transition (EMT) (Arthur-Farraj et al., 2017; Clements et al., 2017).

Epigenomic changes in Schwann cells play an important role in differentiation and in their myelination (Woodhoo et al., 2009; Arthur-Farraj et al., 2012; Napoli et al., 2012; Jessen et al., 2015; Ma et al., 2016). However, epigenomic reprogramming of SCs in response to injury has not yet been characterized in detail. For example, HDAC-mediated deacetylation of promyelinating transcription factor NF-κB is essential for the differentiation and myelination of SCs *in vitro* (Nickols et al., 2003; Chen et al., 2011). In contrast, the activation of NF-κB is not required for myelination of SCs *in vivo* (Morton et al., 2013). This discrepancy may indicate that the myelination of SCs during development, and following injury, is regulated by different transcriptional programs. Although NF-κB appears to regulate EMT genes, as shown for several human cancers (Pires et al., 2017), the underlying mechanism of the action NF-κB in glia development and myelination remains unknown.

Moreover, the findings concerning the levels of expression of TFs by SCs following injury are also in disagreement, sometimes. For example, some researchers have observed no changes in the levels of SC markers (Jessen et al., 2015), while others have found a decreased expression of transcription factors (Clements et al., 2017). Such discrepancies raise questions concerning the true nature of SCs during reprogramming. On the one hand,

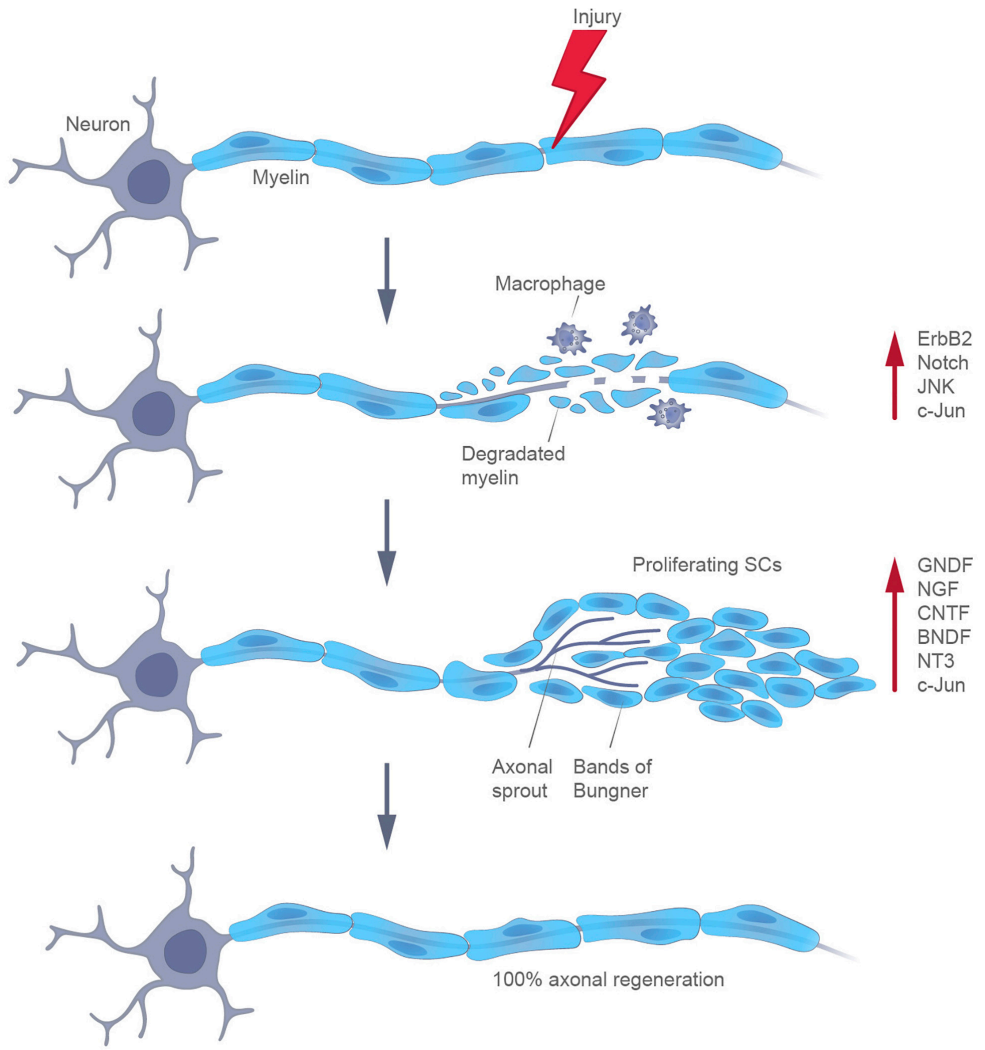


FIGURE 2 | Participation of Schwann cells in the regeneration of peripheral axons, following injury.

an upregulation through a transcriptional program orchestrated by c-JUN re-programs cells to become "repair" glial cells, with their own specific molecular signature (Arthur-Farraj et al., 2012); while on the other hand, the similarity of expression of transcription factors that is characteristic of EMT and of reprogrammed SCs after injury indicates their relationship to neural crest stem cells and/or to their own progenitors, SCPs or immature SCs.

Of course, there is also the possibility that there are subpopulations of SCs that have been reprogrammed in different ways (mesenchymal, immature glial, and neural crest) at different sites of injury (**Figure 3A**).

Another function performed by SCs in adults is the participation in the regeneration of the tips of the digits. After injury of the ends of fingers or toes, the transcription factor SOX2 is upregulated in the SCs associated with the damaged nerves. These cells, then, detach from their axons and migrate into the regenerating region, where they secrete paracrine growth factors that induce the proliferation of the resident mesenchymal precursors (Johnston et al., 2016). Accordingly, genetic ablation of *Sox2* in SCs and denervation impairs the regeneration of nails and bones in mice and this regeneration can be rescued by transplantation of neonatal SCs (expressing SOX2) cultured *in vitro* into the injured digits (Le et al., 2005; Taranova et al., 2006; Johnston et al., 2016).

The skin is often used as a model system for research on regeneration, containing many different types of cells, including stem and progenitor cells. The skin of mice and humans is permeated by dense axons of a small diameter that are often severely damaged, in association with injuries of various kinds. In general, the recovery of thin axons in the skin resembles the analogous processes that occur in other parts of the PNS.

In injured skin, SCs detach from the nerves and undergo reprogramming and, later, division, in order to restore lost cells (Johnston et al., 2013). SCs expressing the glial markers SOX2 and S100b actively migrate into the healing dermis to aid in

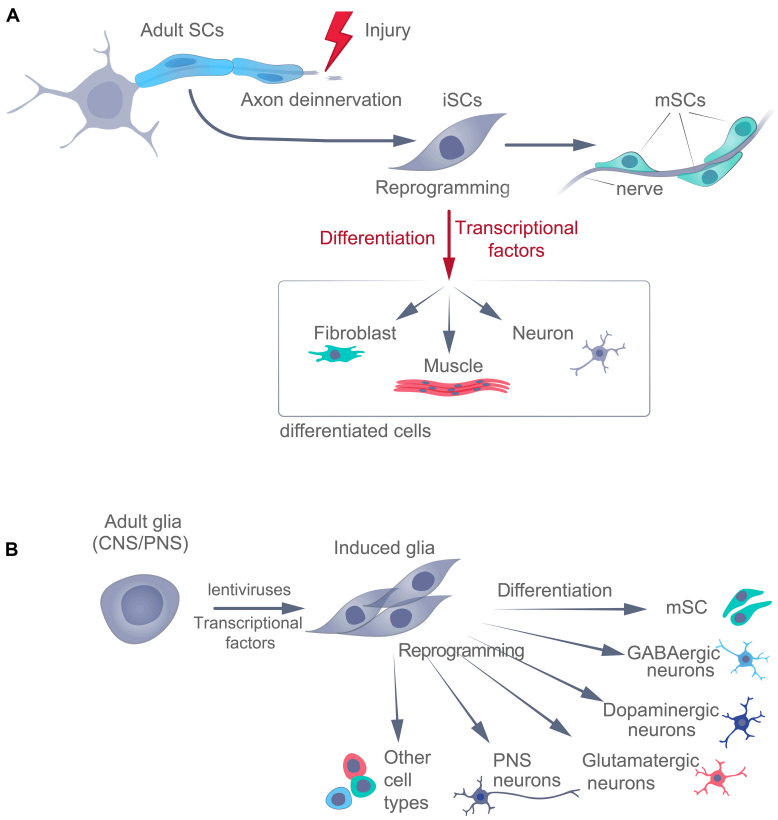


FIGURE 3 | Naturally occurring (adaptive) **(A)** and experimental **(B)** reprogramming of adult glial cells, following injury. SCs, Schwann cells; iSC, immature Schwann cells; mSC, mature Schwann cells.

its repair, probably by forcing mesenchymal cells to proliferate (Johnston et al., 2013). DTA-dependent ablation of SOX2^{+}-glial cells reduces the proliferation of dermal and epidermal cells, thereby impairing wound healing (Johnston et al., 2016).

Interestingly, SOX2/S100b/P75^{+} glial cells, which may participate in dermal maintenance and wound-healing, attach to axons surrounding the hair follicles (Hunt et al., 2008; Biernaskie et al., 2009), but this still remains unclear. Peripheral glial cells activated in response to injury can promote wound healing in the skin of adult mice. Such repairing SCs detach from the injured nerves and move into the granulation tissue, where they are reprogrammed into invasive mesenchymal-like cells and drive peripheral nerve regeneration (Clements et al., 2017; Parfejevs et al., 2018).

These examples of the participation of Schwann cells, together with axons, in the regeneration of nerves and target tissues, make these cells attractive for regenerative therapies. However, a more in-depth molecular understanding of these processes is required before clinical application can be considered.

Moreover, in zebrafish, Müller glia in the retina can differentiate into neurons in response to lesions (Raymond et al., 2006) through a process dependent on TF ASCL1 (Ramachandran et al., 2010). Thus, in addition to helping restore small damaged axons, forcing the proliferation of mesenchymal cells, and participating in dermal maintenance and wound healing, as well as in the regeneration of nails and bones, glial cells may be involved in adult neurogenesis. Reprogrammed iSCs may even be sources of other types of cells in adult vertebrates, in response to damage (**Figure 3A**).

Experimental Reprogramming of Schwann Cells

Terminally differentiated somatic cells can be induced to become pluripotent (dedifferentiation) or switch to a different specialized phenotype (transdifferentiation). Experimental differentiation of SCs into neurons in adults is complicated and time-consuming and has not yet been standardized. Transdifferentiation involves reprogramming the cell, which directly switches the cellular phenotype to that of another somatic cell type (**Figure 3B**), e.g., the conversion of glial cells into neurons. This can be achieved experimentally, both *in vitro* and *in vivo,* using many different approaches – either indirectly (via iPSCs using TF or via iNPCs using TF^{+} differentiation factors) or directly (using pro-neuronal TF^{+} differentiation and maturation factors or chemicals), each with its own advantages and disadvantages. For example, in cell culture, a chemical cocktail containing inhibitors of HDACs, GSK-3 kinases, and TGF-β-mediated pathways, in combination with hypoxia, can reprogram fibroblasts into neuroprogenitor cells (Cheng et al., 2014). In addition, fibroblasts can be reprogrammed directly into neurons using small molecules

alone (Li et al., 2014; Hu et al., 2015). In connection with these promising procedures for the transformation of somatic cells, the cells obtained still need to be genetically and functionally characterized, and these experimental protocols require standardization.

To reprogram cells using regulatory factors, bacterial or viral vectors are introduced into cells to cause an overexpression of key transcription factors, and thereby, initiate transdifferentiation (Patel and Yang, 2010; Grath and Dai, 2019); CRISPR/Cas9 gene editing can also employed to alter the pattern of gene expression directly (Rubio et al., 2016); or drugs that target transcription factors can be used to give rise to epigenetic remodeling (e.g., for transdifferentiation of human fibroblasts into endothelial cells, cardiac cells into skeletal myocytes, and mesenchymal stem cells into cardiomyocytes) (Naeem et al., 2013; Kaur et al., 2014; Sayed et al., 2015). Of these three approaches, the direct reprogramming of neuronal cells by introduction of lentiviral vectors that results in an overexpression of specific transcription factors is the most popular and effective, at present. Examples of cells that have been transdifferentiated into neurons, to date, include glia (Heins et al., 2002), mouse and human fibroblasts (Vierbuchen et al., 2010; Yoo et al., 2011; Adler et al., 2012), and fibroblasts and astrocytes (Addis et al., 2011; Caiazzo et al., 2011; Rivetti Di Val Cervo et al., 2017).

The transcription factor PAX6 is a key determinant of the neurogenic potential of glial cells from the cortex (Heins et al., 2002). In the case of transformation of glia (astrocytes) from the CNS into neurons, both *in vitro* and *in vivo*, the most common approach involves TFs, such as NEUROG2, BRN4, NEUROD1, ASCL1, DLX2, and/or SOX2 (Addis et al., 2011; Guo et al., 2014; Liu et al., 2015; Brulet et al., 2017; **Table 1**).

In general, SCs that support the repair of damaged nerves are too short-lived to complete this process successfully. Consequently, considerable research is now focused on genetic reprogramming designed to allow SCs to retain their ability to repair damaged axons. Adenoviral vectors were the first to be successfully utilized to transduce Schwann cells in a peripheral nerve (Shy et al., 1995) and, later, lentiviral vectors were found to be even better for this purpose (Naldini et al., 1996).

Lentiviral-mediated overexpression of the trophic factor GDNF by both the intact and lesioned rat sciatic nerve elevates the density of the present SCs, but, at the same time, the morphology of these cells becomes abnormal and myelination of axons is severely impaired (Eggers et al., 2013). Moreover, although GDNF promotes the growth of local axons, the trapping of axons in the nerve ("candy store" effect) is detrimental to regeneration (Eggers et al., 2013; Santosa et al., 2013).

By employing a lentiviral vector to induce the overexpression of the neurotrophin NGF in SCs of the rat sciatic nerve, 2 weeks after injury, elevated the number of axons expressing NF200, ChAT, and CGRP and improved axonal regeneration (Shakhbazau et al., 2012). When SCs were induced to express BDNF, CNTF, or NT3, in an attempt to repair unilateral 1-cm defects in rat peroneal nerves, the differential effects on the morphology of peripheral nerve grafts, the number and type of regenerating axons, myelination, and locomotor function were observed, 10 weeks later (Godinho et al., 2013).

TABLE 1 | Transcription factors utilized for *in vivo* reprogramming of glial cells into neurons in the CNS.

Type of CNS cells reprogrammed	Transcription factors	Other factors added	Cells generated	References
Astrocytes	PAX6	None	Neurogenic cells	Heins et al., 2002
Astrocytes	NEURO2	FGF+EGF	Dopaminergic/ glutaminergic neurons	Grande et al., 2013
Reactive astrocytes and NG2 glia	NEUROD1	None	Glutaminergic neurons	Guo et al., 2014
NG2 glia	SOX2	None	GABAergicneurons	Heinrich et al., 2010
Astrocytes	ASCL1	None	Glutamatergic and GABAergic neurons	Liu et al., 2015
NG2 glia	ASCL1 + LMX1a + NURR1	None	Glutamatergic and GABAergic neurons	Torper et al., 2013
Astrocytes	NEUROD1 + ASCL1 + LMX1a	miR218	Dopaminergic neurons	Rivetti Di Val Cervo et al., 2017
Astrocytes	NEUROD1	None	Neurons	Brulet et al., 2017
Astrocytes	SOX2	VPA	GABAergic neurons	Su et al., 2014
Astrocytes	SOX2	VPA + BDNF + NOGGIN	GABAergic, glycinergic, serotonergic, cholinergic neurons	Wang et al., 2016

In general, glial cells are readily available and apparently suitable for direct reprogramming into neurons. Since the neurons and glia in the CNS originate from the same neural population, their epigenetic profiles are, presumably, the same. It is highly likely that experimenting with many more different types of adult cells and transcription factors will increase the yields of the target cells and, at the same time, lower the cost of future therapies.

Glial Reprogramming *in vivo* in the Context of Neurological Diseases

At present, the progressive damage and death of neurons, which are post-mitotic and do not regenerate, is incurable. The source of the differentiated cells to be reprogrammed is important. Parenchymal astrocytes and $NG2^+$ glia have been successfully reprogrammed into $NEUN^+$ dopaminergic, glutaminergic, and GABA neurons of the striatum and cortex, using lentiviral vectors. These vectors have encoded a single TF (NEUROD, SOX2, or ASCL1) (Heinrich et al., 2010; Guo et al., 2014; Liu et al., 2015) or a mixture of these factors (ASCL1 + BRN2 + MYT1 or NEUROD + ASCL1 + LMX1a + miR218 or SOX2, together with the neurotrophic factors BDNF + NOGGIN, or NEUROG2 with FGF + EGF) (Grande et al., 2013; Torper et al., 2013; Rivetti Di Val Cervo et al., 2017; **Table 1**). Moreover, astrocytes from the spinal cord can be transdifferentiated into GABA-, glycin-, serotonin-, and cholinergic neurons through the

overexpression of *Sox2*, together with the addition of valproic acid (which inhibits histone deacetylase), BDNF, and NOGGIN (Su et al., 2014; Wang et al., 2016; **Table 1**).

As indicated above, despite recent progress in increasing the yield of neurons from transformed glia, relatively few neurons have been obtained and these have survived only for a short period of time. These limitations may be overcome through the addition of other growth factors (e.g., FGF2, EGF) or/and chemicals (calcitriol, α-tocotrienol) (Grande et al., 2013; Gascón et al., 2016). In addition, appropriate alterations of the microenvironment (e.g., through co-expression of BDNF and NOG, or the presence of VPA) might also influence the maturation and survival of neurons *in vivo* (Niu et al., 2015; Wang et al., 2016).

In this context, reprogramming of glial cells, for example, in order to obtain new neurons during development, might also offer a viable approach to treatment *in vivo* (Bertrand et al., 2002; Dyachuk et al., 2014). One example of how this strategy has already been utilized successfully is in the transformation of spiral ganglion glial cells into auditory neurons to restore hearing (Noda et al., 2018). Direct conversion of glial cell into neurons of the CNS may eventually provide an effective treatment for various neurodegenerative diseases, such as ALS, Alzheimer's (AD), and Parkinson's (PD) disease. For example, in mice with PD, the treatment of astrocytes with a lentiviral vector that induced the overexpression of the transcription factors NEUROD1, ASCL1, LMX1A, and miR218, increased their numbers of dopaminergic neurons and led to the recovery of motor function, 5 weeks after treatment (Rivetti Di Val Cervo et al., 2017). In addition, in AD animal models, reactive glial cells can produce the transcription factor NEUROD1, which leads to the reprogramming of astrocytes into glutamatergic neurons, and of NG2 glial cells into glutamatergic and GABAergic neurons (Guo et al., 2014).

These examples of the reprogramming of glial cells into functional neurons are promising for the restoration of lost neurons, due to neurological damage or disease. In fact, *in vivo* reprogramming has several major advantages over *in vitro* approaches, including the maintenance of natural microenvironments, absence of complications associated with cell grafting, and a more efficient transdifferentiation. However, many questions remain unanswered. For example, whether transdifferentiation may be used to treat the cognitive and behavioral deficits that are becoming more common worldwide. Moreover, the problem of finding a more suitable source of cells with pronounced plasticity, rapid growth, and the ability to produce different types of neurons, still remains.

If reprogrammed cells are to be used successfully to treat neurodegenerative diseases, the neurons obtained must connect with other neurons to form functional pathways. In this context a significant achievement has been glial reprogramming into excitatory glutamatergic, inhibitory GABAergic, and dopaminergic neurons, which exhibit the electrophysiological properties of mature neurons, including action potential and synaptic connections (Grande et al., 2013; Torper et al., 2013; Guo et al., 2014; Su et al., 2014; Liu et al., 2015; Wang et al., 2016; Brulet et al., 2017; Rivetti Di Val Cervo et al., 2017).

In fact, although integration of "newborn" neurons into networks has been convincingly shown in several investigations, the full recovery of lost or damaged neuronal networks remains to be demonstrated. Clearly, much more insight into the mechanisms underlying neuronal transformation is required and single-cell deep sequencing, bioinformatics, and electrophysiological data should be of considerable value in this context.

Reprogramming of SCs in the Tumor Milieu

For a long period, SCs were considered to not be involved in carcinogenesis and research on the promotion of cancer development, both *in vivo* and *in vitro*, has focused primarily on innervation by peripheral axons (Magnon et al., 2013). However, it is now clear that a dedifferentiated SCs phenotype, strongly reminiscent of those which arise in response to nerve injury, enables cancer progression (Deborde et al., 2016). In fact, SCs promote infiltration of peripheral nerves by cancer cells (perineural invasion, PNI) by establishing an early contact with these cells, thereby attracting them to the location of SCs (Demir et al., 2014; **Figure 4**).

More specifically, the motility and invasiveness of cancer cells depends on the secretion of chemokines by SCs and on the expression of the corresponding receptors on tumor cells (Deborde et al., 2016; Zhou et al., 2018). Moreover, SCs can degrade the extracellular matrix to form tunnels or bands coated with laminin, along which cancer cells migrate (Deborde and Wong, 2017). In addition, the release of BDNF by SCs promotes EMT in cancer cells, together with the loss of E-cadherin and the upregulation of NCAM1, thereby facilitating migration and invasion (Azam and Pecot, 2016; Deborde et al., 2016; Shan et al., 2016). Accordingly, SCs first attract cancer cells, and later, promote their invasion into nerves (**Figure 4**).

Interestingly, to promote their own perineural invasion, cancer cells exploit some of the canonical functions and features of SCs (plasticity, the ability to dedifferentiate in response to injury, alterations in the ECM), otherwise involved in neuronal repair and regulation. Genes expressed by pre-myelinating SCs, such as *Gfap, Ncam, L1-cam, P75, and Sox2*, have been implicated in this invasion (Demir et al., 2014, 2016). Thus, cancer cells can reprogram mature myelinated SCs into iSCs, which are more flexible and mobile (Jessen and Mirsky, 2019a). Moreover, as shown by Deborde et al. (2016), *Gfap* is expressed at high levels by dedifferentiated SCs, being closely associated with cancer cells, but not, at all, by differentiated Schwann cells, similarly, to the involvement of SCs in the repair of nerves (Jessen and Mirsky, 2019a).

At the same time, cancer cells interact with other types of normal cells as well, including immune cells that infiltrate the tumor and modulate its invasion (Shurin, 2012). Such recruitment of immune cells, which accelerates tumorigenesis, can be aided by SCs, in an analogous manner to the recruitment of immune cells during nerve repair (Deborde and Wong, 2017; Jessen and Mirsky, 2019b). Moreover, SCs modulate the activity of the immune cells that are, thus, recruited. For

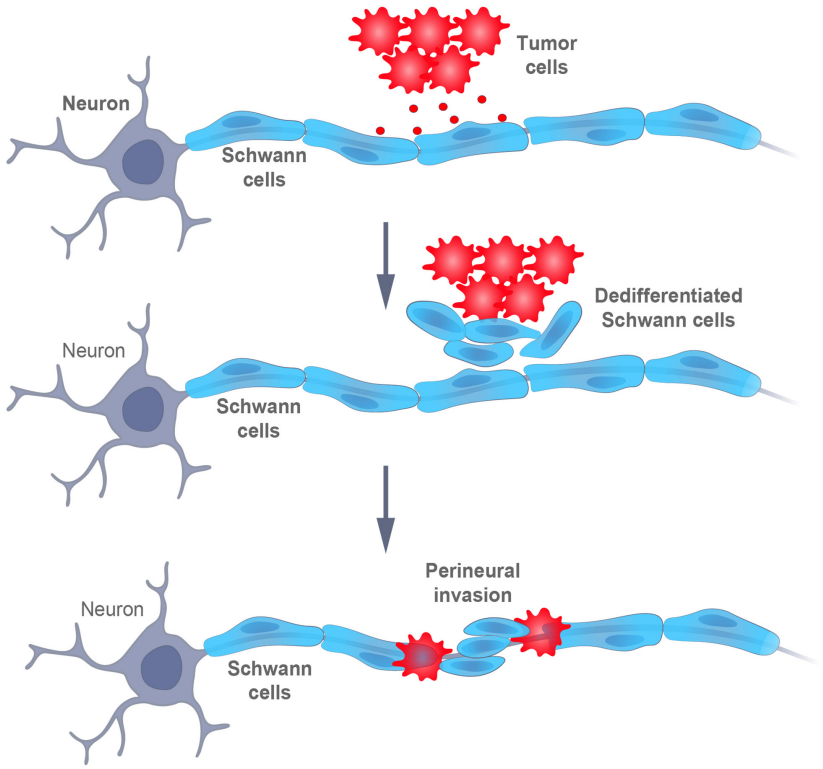


FIGURE 4 | Schematic representation of the interaction between tumor and Schwann cells. Signals from the cancer cells promote the dedifferentiation of Schwann cells, which, then, intermingle with the cancer cells and promote their dispersal and, finally, perineural invasion (i.e., infiltration within or around the nerves).

example, SCs exposed to melanoma cells *in vitro* enhance the ability of myeloid-derived suppressor cells (MDSCs) to suppress T cell proliferation (Martyn et al., 2019). In addition, the exposure of SCs to tumor cells elevates their expression of myelin-associated glycoprotein (MAG), which inhibits axonal growth and influences glia-axon interactions (Quarles, 2007). Indeed, MAG itself increases the immunosuppressive potential of MDSCs in a T cell inhibitory assay in a similar manner to that through which SCs are exposed to tumor cells (Martyn et al., 2019). Thus, factors released by cancer cells exert effects on SCs, which attract immune cells, that participate in the formation of the microenvironment which determines the course of tumor development.

CONCLUSION

The findings summarized here indicate that SCs can be transformed into different types of cells, both ontogenetically under natural conditions and experimentally in the laboratory. The multipotent properties of early populations of SC precursors make them attractive candidates for correcting various developmental pathologies. Furthermore, the adaptive reprogramming of SCs, in connection with axonal regeneration, gives rise to glia that can be transformed experimentally into different cell types, opens up new approaches to regenerative therapy of traumatic brain and spinal cord injuries, as well as neurodegenerative diseases.

In addition, a more detailed understanding of the molecular mechanisms underlying the promotion of carcinogenesis by SCs, primarily by facilitating perineural invasion and dissemination, may allow the treatment designed to suppress the initial stages of cancer development. Such an approach could also provide an alternative to anti-cancer therapies that target nerve fibers, which are usually quite toxic. Finally, our evolving understanding of the role played by SCs in carcinogenesis may promote the development of efficient approaches to managing cancer pain syndrome.

AUTHOR CONTRIBUTIONS

VM and VD were responsible for the intellectual content of this work. VD wrote the manuscript. Both authors contributed to the article and approved the submitted version.

FUNDING

This study was financially supported by the Russian Science Foundation (Grant 18-75-10005), RFBR (Grant 19-29-04035), and the Government of the Russian Federation through an ITMO Fellowship and the Professorship Program.

REFERENCES

Abdo, H., Calvo-Enrique, L., Lopez, J. M., Song, J., Zhang, M. D., Usoskin, D., et al. (2019). Specialized cutaneous schwann cells initiate pain sensation. *Science* 365, 695–699. doi: 10.1126/science.aax6452

Adameyko, I., Lallemend, F., Aquino, J. B., Pereira, J. A., Topilko, P., Müller, T., et al. (2009). Schwann cell precursors from nerve innervation are a cellular origin of melanocytes in skin. *Cell* 139, 366–379. doi: 10.1016/j.cell.2009.07.049

Addis, R. C., Hsu, F. C., Wright, R. L., Dichter, M. A., Coulter, D. A., and Gearhart, J. D. (2011). Efficient conversion of astrocytes to functional midbrain dopaminergic neurons using a single polycistronic vector. *PLoS One* 6:e28719. doi: 10.1371/journal.pone.0028719

Adler, A. F., Grigsby, C. L., Kulangara, K., Wang, H., Yasuda, R., and Leong, K. W. (2012). Nonviral direct conversion of primary mouse embryonic fibroblasts to neuronal cells. *Mol. Ther. Nucleic Acids.* 1:e32. doi: 10.1038/mtna.2012.25

Alvarez-Suarez, P., Gawor, M., and Prószyński, T. J. (2020). Perisynaptic schwann cells – the multitasking cells at the developing neuromuscular junctions. *Semin. Cell Dev. Biol.* 104, 31–38. doi: 10.1016/j.semcdb.2020.02.011

Arthur-Farraj, P. J., Latouche, M., Wilton, D. K., Quintes, S., Chabrol, E., Banerjee, A., et al. (2012). c-Jun reprograms schwann cells of injured nerves to generate a repair cell essential for regeneration. *Neuron* 75, 633–647. doi: 10.1016/j.neuron.2012.06.021

Arthur-Farraj, P. J., Morgan, C. C., Adamowicz, M., Gomez-Sanchez, J. A., Fazal, S. V., Beucher, A., et al. (2017). Changes in the coding and non-coding transcriptome and DNA methylome that define the schwann cell repair phenotype after nerve injury. *Cell Rep.* 20, 2719–2734. doi: 10.1016/j.celrep.2017.08.064

Azam, S. H., and Pecot, C. V. (2016). Cancer's got nerve: schwann cells drive perineural invasion. *J. Clin. Invest.* 126, 1242–1244. doi: 10.1172/JCI86801

Barres, B. A. (2008). The mystery and magic of glia: a perspective on their roles in health and disease. *Neuron* 60, 430–440. doi: 10.1016/j.neuron.2008.10.013

Bertrand, N., Castro, D. S., and Guillemot, F. (2002). Proneural genes and the specification of neural cell types. *Nat. Rev. Neurosci.* 3, 517–530. doi: 10.1038/nrn874

Biernaskie, J., Paris, M., Morozova, O., Fagan, B. M., Marra, M., Pevny, L., et al. (2009). SKPs derive from hair follicle precursors and exhibit properties of adult dermal stem cells. *Cell Stem Cell* 5, 610–623. doi: 10.1016/j.stem.2009.10.019

Birchmeier, C. (2009). ErbB receptors and the development of the nervous system. *Exp. Cell Res.* 315, 611–618. doi: 10.1016/j.yexcr.2008.10.035

Birchmeier, C., and Nave, K.-A. (2008). Neuregulin-1, a key axonal signal that drives Schwann cell growth and differentiation. *Glia* 56, 1491–1497. doi: 10.1002/glia.20753

Britsch, S., Goerich, D. E., Riethmacher, D., Peirano, R. I., Rossner, M., Nave, K. A., et al. (2001). The transcription factor Sox10 is a key regulator of peripheral glial development. *Genes Dev.* 15, 66–78. doi: 10.1101/gad.186601

Britsch, S., Li, L., Kirchhoff, S., Theuring, F., Brinkmann, V., Birchmeier, C., et al. (1998). The ErbB2 and ErbB3 receptors and their ligand, neuregulin-1, are essential for development of the sympathetic nervous system. *Genes Dev.* 12, 1825–1836. doi: 10.1101/gad.12.12.1825

BrosiusLutz, A., and Barres, B. A. (2014). Contrasting the glial response to axon injury in the central and peripheral nervous systems. *Dev. Cell* 28, 7–17. doi: 10.1016/j.devcel.2013.12.002

Brulet, R., Matsuda, T., Zhang, L., Miranda, C., Giacca, M., Kaspar, B. K., et al. (2017). NEUROD1 instructs neuronal conversion in non-reactive astrocytes. *Stem Cell Rep.* 8, 1506–1515. doi: 10.1016/j.stemcr.2017.04.013

Byers, M. R. (1985). Sensory innervation of periodontal ligament of rat molars consists of unencapsulated Ruffini-like mechanoreceptors and free nerve endings. *J. Comp. Neurol.* 231, 500–518. doi: 10.1002/cne.902310408

Caiazzo, M., Dell'Anno, M. T., Dvoretskova, E., Lazarevic, D., Taverna, S., Leo, D., et al. (2011). Direct generation of functional dopaminergic neurons from mouse and human fibroblasts. *Nature* 476, 224–227. doi: 10.1038/nature10284

Chen, Y., Wang, H., Yoon, S. O., Xu, X., Hottiger, M. O., Svaren, J., et al. (2011). HDAC-mediated deacetylation of NF-κB is critical for Schwann cell myelination. *Nat. Neurosci.* 14, 437–441. doi: 10.1038/nn.2780

Cheng, L., Hu, W., Qiu, B., Zhao, J., Yu, Y., Guan, W., et al. (2014). Generation of neural progenitor cells by chemical cocktails and hypoxia. *Cell Res.* 24, 665–679. doi: 10.1038/cr.2014.32

Clements, M. P., Byrne, E., Camarillo Guerrero, L. F., Cattin, A. L., Zakka, L., Ashraf, A., et al. (2017). The wound microenvironment reprograms schwann cells to invasive mesenchymal-like cells to drive peripheral nerve regeneration. *Neuron* 96, 98–114.e7. doi: 10.1016/j.neuron.2017.09.008

Deborde, S., Omelchenko, T., Lyubchik, A., Zhou, Y., He, S., McNamara, W. F., et al. (2016). Schwann cells induce cancer cell dispersion and invasion. *J. Clin. Invest.* 126, 1538–1554. doi: 10.1172/JCI82658

Deborde, S., and Wong, R. J. (2017). How Schwann cells facilitate cancer progression in nerves. *Cell. Mol. Life Sci.* 74, 4405–4420. doi: 10.1007/s00018-017-2578-x

Demir, I. E., Boldis, A., Pfitzinger, P. L., Teller, S., Brunner, E., Klose, N., et al. (2014). Investigation of schwann cells at neoplastic cell sites before the onset of cancer invasion. *J. Natl. Cancer Inst.* 106:dju184. doi: 10.1093/jnci/dju184

Demir, I. E., Tieftrunk, E., Schorn, S., Saricaoglu, ÖC., Pfitzinger, P. L., Teller, S., et al. (2016). Activated Schwann cells in pancreatic cancer are linked to analgesia via suppression of spinal astroglia and microglia. *Gut* 65, 1001–1014. doi: 10.1136/gutjnl-2015-309784

Dooley, C. M., Mongera, A., Walderich, B., and Nusslein-Volhard, C. (2013). On the embryonic origin of adult melanophores: the role of ErbB and Kit signalling in establishing melanophore stem cells in zebrafish. *Development* 140, 1003–1013. doi: 10.1242/dev.087007

Dyachuk, V., Furlan, A., Shahidi, M. K., Giovenco, M., Kaukua, N., Konstantinidou, C., et al. (2014). Parasympathetic neurons originate from nerve-associated peripheral glial progenitors. *Science* 345, 82–87. doi: 10.1126/science.1253281

Eggers, R., de Winter, F., Hoyng, S. A., Roet, K. C. D., Ehlert, E. M., Malessy, M. J. A., et al. (2013). Lentiviral vector-mediated gradients of GDNF in the injured peripheral nerve: effects on nerve coil formation, schwann cell maturation and myelination. *PLoS One.* 8:e71076. doi: 10.1371/journal.pone.0071076

Espinosa-Medina, I., Jevans, B., Boismoreau, F., Chettouh, Z., Enomoto, H., Müller, T., et al. (2017). Dual origin of enteric neurons in vagal Schwann cell precursors and the sympathetic neural crest. *Proc. Natl. Acad. Sci. U.S.A.* 114, 11980–11985. doi: 10.1073/pnas.1710308114

Furlan, A., Dyachuk, V., Kastriti, M. E., Calvo-Enrique, L., Abdo, H., Hadjab, S., et al. (2017). Multipotent peripheral glial cells generate neuroendocrine cells of the adrenal medulla. *Science* 357:eaal3753. doi: 10.1126/science.aal3753

Garratt, A. N., Britsch, S., and Birchmeier, C. (2000). Neuregulin, a factor with many functions in the life of a Schwann cell. *BioEssays* 22, 987–996. doi: 10.1002/1521-1878(200011)22:11<987::aid-bies5>3.0.co;2-5

Gascón, S., Murenu, E., Masserdotti, G., Ortega, F., Russo, G. L., Petrik, D., et al. (2016). Identification and successful negotiation of a metabolic checkpoint in direct neuronal reprogramming. *Cell Stem Cell* 18, 396–409. doi: 10.1016/j.stem.2015.12.003

Godinho, M. J., Teh, L., Pollett, M. A., Goodman, D., Hodgetts, S. I., Sweetman, I., et al. (2013). Immunohistochemical, ultrastructural and functional analysis of axonal regeneration through peripheral nerve grafts containing schwann cells expressing BDNF, CNTF or NT3. *PLoS One* 8:e69987. doi: 10.1371/journal.pone.0069987

Gonçalves, N. P., Vægter, C. B., and Pallesen, L. T. (2018). Peripheral glial cells in the development of diabetic neuropathy. *Front. Neurol.* 9:268. doi: 10.3389/fneur.2018.00268

Grande, A., Sumiyoshi, K., López-Juárez, A., Howard, J., Sakthivel, B., Aronow, B., et al. (2013). Environmental impact on direct neuronal reprogramming in vivo in the adult brain. *Nat. Commun.* 4:2373. doi: 10.1038/ncomms3373

Grath, A., and Dai, G. (2019). Direct cell reprogramming for tissue engineering and regenerative medicine. *J. Biol. Eng.* 13:14. doi: 10.1186/s13036-019-0144-9

Gresset, A., Coulpier, F., Gerschenfeld, G., Jourdon, A., Matesic, G., Richard, L., et al. (2015). Boundary caps give rise to neurogenic stem cells and terminal glia in the skin. *Stem Cell Rep.* 5, 278–290. doi: 10.1016/j.stemcr.2015.06.005

Guo, Z., Zhang, L., Wu, Z., Chen, Y., Wang, F., and Chen, G. (2014). In vivo direct reprogramming of reactive glial cells into functional neurons after brain injury and in an Alzheimer's disease model. *Cell Stem Cell* 14, 188–202. doi: 10.1016/j.stem.2013.12.001

Heinrich, C., Blum, R., Gascón, S., Masserdotti, G., Tripathi, P., Sánchez, R., et al. (2010). Directing astroglia from the cerebral cortex into subtype

specific functional neurons. *PLoS Biol.* 8:e1000373. doi: 10.1371/journal.pbio.1000373

Heins, N., Malatesta, P., Cecconi, F., Nakafuku, M., Tucker, K. L., Hack, M. A., et al. (2002). Glial cells generate neurons: the role of the transcription factor Pax6. *Nat. Neurosci.* 5, 308–315. doi: 10.1038/nn828

Honjo, Y., Kniss, J., and Eisen, J. S. (2008). Neuregulin-mediated ErbB3 signaling is required for formation of zebrafish dorsal root ganglion neurons. *Development* 135, 2615–2625. doi: 10.1242/dev.022178

Hu, W., Qiu, B., Guan, W., Wang, Q., Wang, M., Li, W., et al. (2015). Direct conversion of normal and Alzheimer's disease human fibroblasts into neuronal cells by small molecules. *Cell Stem Cell* 17, 204–212. doi: 10.1016/j.stem.2015.07.006

Hunt, D. P. J., Morris, P. N., Sterling, J., Anderson, J. A., Joannides, A., Jahoda, C., et al. (2008). A highly enriched niche of precursor cells with neuronal and glial potential within the hair follicle dermal papilla of adult skin. *Stem Cells* 26, 163–172. doi: 10.1634/stemcells.2007-0281

Jessen, K. R., and Mirsky, R. (2005). The origin and development of glial cells in peripheral nerves. *Nat. Rev. Neurosci.* 6, 671–682. doi: 10.1038/nrn1746

Jessen, K. R., and Mirsky, R. (2010). Control of schwann cell myelination. *F1000 Biol. Rep*. 2:19. doi: 10.3410/B2-19

Jessen, K. R., and Mirsky, R. (2016). The repair Schwann cell and its function in regenerating nerves. *J. Physiol.* 594, 3521–3531. doi: 10.1113/JP270874

Jessen, K. R., and Mirsky, R. (2019a). Schwann cell precursors; multipotent glial cells in embryonic nerves. *Front. Mol. Neurosci.* 12:69. doi: 10.3389/fnmol.2019.00069

Jessen, K. R., and Mirsky, R. (2019b). The success and failure of the schwann cell response to nerve injury. *Front. Cell. Neurosci.* 13:33. doi: 10.3389/fncel.2019.00033

Jessen, K. R., Mirsky, R., and Lloyd, A. C. (2015). Schwann cells: development and role in nerve repair. *Cold Spring Harb. Perspect. Biol.* 7:a020487. doi: 10.1101/cshperspect.a020487

Johnston, A. P. W., Naska, S., Jones, K., Jinno, H., Kaplan, D. R., and Miller, F. D. (2013). Sox2-mediated regulation of adult neural crest precursors and skin repair. *Stem Cell Rep.* 1, 38–45. doi: 10.1016/j.stemcr.2013.04.004

Johnston, A. P. W., Yuzwa, S. A., Carr, M. J., Mahmud, N., Storer, M. A., Krause, M. P., et al. (2016). Dedifferentiated schwann cell precursors secreting paracrine factors are required for regeneration of the mammalian digit tip. *Cell Stem Cell* 19, 433–448. doi: 10.1016/j.stem.2016.06.002

Joseph, N. M. (2004). Neural crest stem cells undergo multilineage differentiation in developing peripheral nerves to generate endoneurial fibroblasts in addition to Schwann cells. *Development* 131, 5599–5612. doi: 10.1242/dev.01429

Kastriti, M. E., and Adameyko, I. (2017). Specification, plasticity and evolutionary origin of peripheral glial cells. *Curr. Opin. Neurobiol.* 47, 196–202. doi: 10.1016/j.conb.2017.11.004

Kastriti, M. E., Kameneva, P., Kamenev, D., Dyachuk, V., Furlan, A., Hampl, M., et al. (2019). Schwann cell precursors generate the majority of chromaffin cells in zuckerkandl organ and some sympathetic neurons in paraganglia. *Front. Mol. Neurosci.* 12:6. doi: 10.3389/fnmol.2019.00006

Kaukua, N., Shahidi, M. K., Konstantinidou, C., Dyachuk, V., Kaucka, M., Furlan, A., et al. (2014). Glial origin of mesenchymal stem cells in a tooth model system. *Nature* 513, 551–554. doi: 10.1038/nature13536

Kaur, K., Yang, J., Eisenberg, C. A., and Eisenberg, L. M. (2014). 5-Azacytidine promotes the transdifferentiation of cardiac cells to skeletal myocytes. *Cell. Reprogram.* 16, 324–330. doi: 10.1089/cell.2014.0021

Le, N., Nagarajan, R., Wang, J. Y. T., Araki, T., Schmidt, R. E., and Milbrandt, J. (2005). Analysis of congenital hypomyelinating Egr2Lo/Lo nerves identifies Sox2 as an inhibitor of Schwann cell differentiation and myelination. *Proc. Natl. Acad. Sci. U.S.A.* 102, 2596–2601. doi: 10.1073/pnas.0407836102

Le Douarin, N., and Kalcheim, C. (1999). *The Neural Crest*. Cambridge: Cambridge University Press.

Li, K., Zhu, S., Russ, H. A., Xu, S., Xu, T., Zhang, Y., et al. (2014). Small molecules facilitate the reprogramming of mouse fibroblasts into pancreatic lineages. *Cell Stem Cell* 14, 228–236. doi: 10.1016/j.stem.2014.01.006

Lin, H.-P., Oksuz, I., Hurley, E., Wrabetz, L., and Awatramani, R. (2015). Microprocessor complex subunit DiGeorge syndrome critical region gene 8 (Dgcr8) is required for schwann cell myelination and myelin maintenance. *J. Biol. Chem.* 290, 24294–24307. doi: 10.1074/jbc.M115.636407

Liu, Y., Miao, Q., Yuan, J., Han, S., Zhang, P., Li, S., et al. (2015). Ascl1 converts dorsal midbrain astrocytes into functional neurons In Vivo. *J. Neurosci.* 35, 9336–9355. doi: 10.1523/JNEUROSCI.3975-14.2015

Ma, K. H., Hung, H. A., and Svaren, J. (2016). Epigenomic regulation of schwann cell reprogramming in peripheral nerve injury. *J. Neurosci.* 36, 9135–9147. doi: 10.1523/JNEUROSCI.1370-16.2016

Maeda, T., Ochi, K., Nakakura-Ohshima, K., Youn, S. H., and Wakisaka, S. (1999). The ruffini ending as the primary mechanoreceptor in the periodontal ligament: its morphology, cytochemical features, regeneration, and development. *Crit. Rev. Oral Biol. Med.* 10, 307–327. doi: 10.1177/10454411990100030401

Magnon, C., Hall, S. J., Lin, J., Xue, X., Gerber, L., Freedland, S. J., et al. (2013). Autonomic nerve development contributes to prostate cancer progression. *Science* 341:1236361. doi: 10.1126/science.1236361

Martyn, G. V., Shurin, G. V., Keskinov, A. A., Bunimovich, Y. L., and Shurin, M. R. (2019). Schwann cells shape the neuro-immune environs and control cancer progression. *Cancer Immunol. Immunother.* 68, 1819–1829. doi: 10.1007/s00262-018-02296-3

Merrell, A. J., and Stanger, B. Z. (2016). Adult cell plasticity in vivo: de-differentiation and transdifferentiation are back in style. *Nat. Rev. Mol. Cell Biol.* 17, 413–425. doi: 10.1038/nrm.2016.24

Morton, P. D., Dellarole, A., Theus, M. H., Walters, W. M., Berge, S. S., and Bethea, J. R. (2013). Activation of NF-κB in Schwann cells is dispensable for myelination In vivo. *J. Neurosci.* 33, 9932–9936. doi: 10.1523/JNEUROSCI.2483-12.2013

Naeem, N., Haneef, K., Kabir, N., Iqbal, H., Jamall, S., and Salim, A. (2013). DNA methylation inhibitors, 5-azacytidine and zebularine potentiate the transdifferentiation of rat bone marrow mesenchymal stem cells into cardiomyocytes. *Cardiovasc. Ther.* 31, 201–209. doi: 10.1111/j.1755-5922.2012.00320.x

Naldini, L., Blomer, U., Gallay, P., Ory, D., Mulligan, R., Gage, F. H., et al. (1996). In vivo gene delivery and stable transduction of nondividing cells by a lentiviral vector. *Science* 272, 263–267. doi: 10.1126/science.272.5259.263

Napoli, I., Noon, L. A., Ribeiro, S., Kerai, A. P., Parrinello, S., Rosenberg, L. H., et al. (2012). A central role for the ERK-signaling pathway in controlling schwann cell plasticity and peripheral nerve regeneration in vivo. *Neuron* 73, 729–742. doi: 10.1016/j.neuron.2011.11.031

Nickols, J. C., Valentine, W., Kanwal, S., and Carter, B. D. (2003). Activation of the transcription factor NF-κB in Schwann cells is required for peripheral myelin formation. *Nat. Neurosci.* 6, 161–167. doi: 10.1038/nn995

Niu, W., Zang, T., Smith, D. K., Vue, T. Y., Zou, Y., Bachoo, R., et al. (2015). SOX2 reprograms resident astrocytes into neural progenitors in the adult brain. *Stem Cell Rep.* 4, 780–794. doi: 10.1016/j.stemcr.2015.03.006

Noda, T., Meas, S. J., Nogami, J., Amemiya, Y., Uchi, R., Ohkawa, Y., et al. (2018). Direct reprogramming of spiral ganglion non-neuronal cells into neurons: toward ameliorating sensorineural hearing loss by gene therapy. *Front. Cell Dev. Biology.* 6:16. doi: 10.3389/fcell.2018.00016

Ochoa-Cortes, F., Turco, F., Linan-Rico, A., Soghomonyan, S., Whitaker, E., Wehner, S., et al. (2016). Enteric Glial Cells. *Inflamm. Bowel Dis.* 22, 433–449. doi: 10.1097/MIB.0000000000000667

Parfejevs, V., Debbache, J., Shakhova, O., Schaefer, S. M., Glausch, M., Wegner, M., et al. (2018). Injury-activated glial cells promote wound healing of the adult skin in mice. *Nat. Commun.* 9:236. doi: 10.1038/s41467-017-01488-2

Patel, M., and Yang, S. (2010). Advances in reprogramming somatic cells to induced pluripotent stem cells. *Stem Cell Rev. Rep.* 6, 367–380. doi: 10.1007/s12015-010-9123-8

Pires, B. R. B., Mencalha, A. L., Ferreira, G. M., de Souza, W. F., Morgado-Díaz, J. A., Maia, A. M., et al. (2017). NF-kappaB is involved in the regulation of EMT genes in breast cancer cells. *PLoS One* 12:e0169622. doi: 10.1371/journal.pone.0169622

Quarles, R. H. (2007). Myelin-associated glycoprotein (MAG): past, present and beyond. *J. Neurochem.* 100, 1431–1448. doi: 10.1111/j.1471-4159.2006.04319.x

Ramachandran, R., Fausett, B. V., and Goldman, D. (2010). Ascl1a regulates Müller glia dedifferentiation and retinal regeneration through a Lin-28-dependent, let-7 microRNA signalling pathway. *Nature Cell Biology.* 12, 1101–1107. doi: 10.1038/ncb2115

Raymond, P. A., Barthel, L. K., Bernardos, R. L., and Perkowski, J. J. (2006). Molecular characterization of retinal stem cells and their niches in adult zebrafish. *BMC Dev. Biol.* 6:36. doi: 10.1186/1471-213X-6-36

Riethmacher, D., Sonnenberg-Riethmacher, E., Brinkmann, V., Yamaai, T., Lewin, G. R., and Birchmeier, C. (1997). Severe neuropathies in mice with targeted mutations in the ErbB3 receptor. *Nature* 389, 725–730. doi: 10.1038/39593

Rivetti Di Val Cervo, P., Romanov, R. A., Spigolon, G., Masini, D., Martín-Montañez, E., Toledo, E. M., et al. (2017). Induction of functional dopamine neurons from human astrocytes in vitro and mouse astrocytes in a Parkinson's disease model. *Nat. Biotechnol.* 35, 444–452. doi: 10.1038/nbt.3835

Rubio, A., Luoni, M., Giannelli, S. G., Radice, I., Iannielli, A., Cancellieri, C., et al. (2016). Rapid and efficient CRISPR/Cas9 gene inactivation in human neurons during human pluripotent stem cell differentiation and direct reprogramming. *Sci. Rep.* 6:37540. doi: 10.1038/srep37540

Santosa, K. B., Jesuraj, N. J., Viader, A., Macewan, M., Newton, P., Hunter, D. A., et al. (2013). Nerve allografts supplemented with schwann cells overexpressing glial-cell-line-derived neurotrophic factor. *Muscle Nerve* 47, 213–223. doi: 10.1002/mus.23490

Sayed, N., Wong, W. T., Ospino, F., Meng, S., Lee, J., Jha, A., et al. (2015). Transdifferentiation of human fibroblasts to endothelial cells role of innate immunity. *Circulation* 131, 300–309. doi: 10.1161/CIRCULATIONAHA.113.007394

Shakhbazau, A., Kawasoe, J., Hoyng, S. A., Kumar, R., van Minnen, J., Verhaagen, J., et al. (2012). Early regenerative effects of NGF-transduced Schwann cells in peripheral nerve repair. *Mol. Cell. Neurosci.* 50, 103–112. doi: 10.1016/j.mcn.2012.04.004

Shan, C., Wei, J., Hou, R., Wu, B., Yang, Z., Wang, L., et al. (2016). Schwann cells promote EMT and the Schwann-like differentiation of salivary adenoid cystic carcinoma cells via the BDNF/TrkB Axis. *Oncol. Rep.* 35, 427–435. doi: 10.3892/or.2015.4366

Shurin, M. (2012). Cancer as an immune-mediated disease. *ImmunoTargets Ther.* 1, 1–6. doi: 10.2147/ITT.S29834

Shy, M. E., Tani, M., Shi, Y. −J., Whyatt, S. A., Chbihi, T., Scherer, S. S., et al. (1995). An adenoviral vector can transfer lacZ expression into schwann cells in culture and in sciatic nerve. *Ann. Neurol.* 38, 429–436. doi: 10.1002/ana.410380313

Soldatov, R., Kaucka, M., Kastriti, M. E., Petersen, J., Chontorotzea, T., Englmaier, L., et al. (2019). Spatiotemporal structure of cell fate decisions in murine neural crest. *Science* 364:eaas9536. doi: 10.1126/science.aas9536

Su, Z., and He, C. (2010). Olfactory ensheathing cells: biology in neural development and regeneration. *Prog. Neurobiol.* 92, 517–532. doi: 10.1016/j.pneurobio.2010.08.008

Su, Z., Niu, W., Liu, M. L., Zou, Y., and Zhang, C. L. (2014). In vivo conversion of astrocytes to neurons in the injured adult spinal cord. *Nat. Commun.* 5:3338. doi: 10.1038/ncomms4338

Takahashi, K., and Yamanaka, S. (2006). Induction of pluripotent stem cells from mouse embryonic and adult fibroblast cultures by defined factors. *Cell* 126, 663–676. doi: 10.1016/j.cell.2006.07.024

Taranova, O. V., Magness, S. T., Fagan, B. M., Wu, Y., Surzenko, N., Hutton, S. R., et al. (2006). SOX2 is a dose-dependent regulator of retinal neural progenitor competence. *Genes Dev.* 20, 1187–1202. doi: 10.1101/gad.1407906

Torper, O., Pfisterer, U., Wolf, D. A., Pereira, M., Lau, S., Jakobsson, J., et al. (2013). Generation of induced neurons via direct conversion in vivo. *Proc. Natl. Acad. Sci. U.S.A.* 110, 7038–7043. doi: 10.1073/pnas.1303829110

Vierbuchen, T., Ostermeier, A., Pang, Z. P., Kokubu, Y., Südhof, T. C., and Wernig, M. (2010). Direct conversion of fibroblasts to functional neurons by defined factors. *Nature* 8:207. doi: 10.1038/nature08797

Wang, L.-L., Su, Z., Tai, W., Zou, Y., Xu, X.-M., and Zhang, C.-L. (2016). The p53 pathway controls SOX2-mediated reprogramming in the adult mouse spinal cord. *Cell Rep.* 17, 891–903. doi: 10.1016/j.celrep.2016.09.038

Wolpowitz, D., Mason, T. B. A., Dietrich, P., Mendelsohn, M., Talmage, D. A., and Role, L. W. (2000). Cysteine-rich domain isoforms of the neuregulin-1 gene are required for maintenance of peripheral synapses. *Neuron* 25, 79–91. doi: 10.1016/S0896-6273(00)80873-9

Woodhoo, A., Alonso, M. B. D., Droggiti, A., Turmaine, M., D'Antonio, M., Parkinson, D. B., et al. (2009). Notch controls embryonic Schwann cell differentiation, postnatal myelination and adult plasticity. *Nat. Neurosci.* 12, 839–847. doi: 10.1038/nn.2323

Xie, M., Kamenev, D., Kaucka, M., Kastriti, M. E., Zhou, B., Artemov, A. V., et al. (2019). Schwann cell precursors contribute to skeletal formation during embryonic development in mice and zebrafish. *Proc. Natl. Acad. Sci. U.S.A.* 116, 15068–15073. doi: 10.1073/pnas.1900038116

Yoo, A. S., Sun, A. X., Li, L., Shcheglovitov, A., Portmann, T., Li, Y., et al. (2011). MicroRNA-mediated conversion of human fibroblasts to neurons. *Nature* 476, 228–231. doi: 10.1038/nature10323

Zhou, Y., Shurin, G. V., Zhong, H., Bunimovich, Y. L., Han, B., and Shurin, M. R. (2018). Schwann cells augment cell spreading and metastasis of lung cancer. *Cancer Res.* 78, 5927–5939. doi: 10.1158/0008-5472.CAN-18-1702

Zujovic, V., Thibaud, J., Bachelin, C., Vidal, M., Deboux, C., Coulpier, F., et al. (2011). Boundary cap cells are peripheral nervous system stem cells that can be redirected into central nervous system lineages. *Proc. Natl. Acad. Sci. U.S.A.* 108, 10714–10719. doi: 10.1073/pnas.1018687108

Conflict of Interest: The authors declare that the research was conducted in the absence of any commercial or financial relationships that could be construed as a potential conflict of interest.

The handling editor declared a past co-authorship with one of the authors VD.

Copyright © 2020 Milichko and Dyachuk. This is an open-access article distributed under the terms of the Creative Commons Attribution License (CC BY). The use, distribution or reproduction in other forums is permitted, provided the original author(s) and the copyright owner(s) are credited and that the original publication in this journal is cited, in accordance with accepted academic practice. No use, distribution or reproduction is permitted which does not comply with these terms.

frontiers in Cell and Developmental Biology

REVIEW
published: 25 August 2020
doi: 10.3389/fcell.2020.00781

Extracellular Matrix and Cellular Plasticity in Musculoskeletal Development

*Sophia Ka Yan Ma[1], Andy Shing Fung Chan[1], Aqsa Rubab[1], Wilson Cheuk Wing Chan[1,2,3] and Danny Chan[1,3]**

[1] School of Biomedical Sciences, The University of Hong Kong, Hong Kong, China, [2] Department of Orthopedics Surgery and Traumatology, The University of Hong Kong-Shenzhen Hospital, Shenzhen, China, [3] The University of Hong Kong Shenzhen Institute of Research and Innovation (HKU-SIRI), Shenzhen, China

Cellular plasticity refers to the ability of cell fates to be reprogrammed given the proper signals, allowing for dedifferentiation or transdifferentiation into different cell fates. *In vitro,* this can be induced through direct activation of gene expression, however this process does not naturally occur *in vivo*. Instead, the microenvironment consisting of the extracellular matrix (ECM) and signaling factors, directs the signals presented to cells. Often the ECM is involved in regulating both biochemical and mechanical signals. In stem cell populations, this niche is necessary for maintenance and proper function of the stem cell pool. However, recent studies have demonstrated that differentiated or lineage restricted cells can exit their current state and transform into another state under different situations during development and regeneration. This may be achieved through (1) cells responding to a changing niche; (2) cells migrating and encountering a new niche; and (3) formation of a transitional niche followed by restoration of the homeostatic niche to sequentially guide cells along the regenerative process. This review focuses on examples in musculoskeletal biology, with the concept of ECM regulating cells and stem cells in development and regeneration, extending beyond the conventional concept of small population of progenitor cells, but under the right circumstances even "lineage-restricted" or differentiated cells can be reprogrammed to enter into a different fate.

Keywords: extracellular matrix, plasticity, development, limb regeneration, chondrocyte, hypertrophic chondrocyte, joint formation, muscle

OPEN ACCESS

Edited by:
Andrei S. Chagin, Karolinska Institutet (KI), Sweden

Reviewed by:
Noriaki Ono, University of Michigan, United States
Shiwu Dong, School of Biomedical Engineering, Third Military Medical University, China

***Correspondence:**
Danny Chan
chand@hku.hk

Specialty section:
This article was submitted to Stem Cell Research, a section of the journal Frontiers in Cell and Developmental Biology

Received: *29 May 2020*
Accepted: *27 July 2020*
Published: *25 August 2020*

Citation:
Ma SKY, Chan ASF, Rubab A, Chan WCW and Chan D (2020) Extracellular Matrix and Cellular Plasticity in Musculoskeletal Development. Front. Cell Dev. Biol. 8:781. doi: 10.3389/fcell.2020.00781

INTRODUCTION

Over the past couple of decades, cellular reprogramming or plasticity has gained traction as a means to address different areas of research, ranging from the understanding of disease progression, to manipulating cells *in vitro* (Gilbert et al., 2010; Madl et al., 2018), and as a potential target for direct regeneration (Blau and Pomerantz, 2011). The idea of cellular plasticity was first described as a concept by Helen Blau in the 1980s (Blau et al., 1985) which proposed that differentiated cells were not a terminal endpoint, and should be regarded as a cellular "state" (Zipori, 2004) that had to be actively maintained by co-ordination of both intrinsic and extrinsic factors. Cell states could

therefore be altered depending on the signals they receive, changing gene expression profiles, and behavior (Blau et al., 2001; Estrov, 2009; Merrell and Stanger, 2016).

Several key studies have demonstrated this between the 1980s and early 2000s, including cloning of "Dolly the sheep" by somatic nuclear transfer (Wilmut et al., 1997), expression of muscle related genes in heterokaryons (Blau et al., 1983) and the identification of the "Yamanaka factors" to induce pluripotent stem cells from fibroblasts (Takahashi and Yamanaka, 2006). Other studies also demonstrated that trans-differentiation of mature cells into a different cell types can be achieved by one or several key transcription factors (Davis et al., 1987; Zhou et al., 2008; Ieda et al., 2010; Vierbuchen et al., 2010).

While these studies demonstrate the role of transcription factors in determining cell fate, cells independently altering their gene expression profiles does not occur naturally in living organisms. Instead, the surrounding microenvironment of cells will dictate how they respond and behave under normal physiological conditions. For stem cell populations, a highly specialized microenvironment, the stem cell niche, is composed of the extracellular matrix (ECM), signaling factors, and niche cells that provides coordinated signals to direct specific outcomes (Voog and Jones, 2010).

THE ECM INTEGRATES BOTH BIOCHEMICAL AND MECHANICAL SIGNALING IN THE STEM CELL NICHE

In the native environment, the role of the ECM in the stem cell niche is as important as biochemical signals. In addition to providing mechanical force, the ECM also regulates biochemical signals, as it binds and localizes signaling molecules (Wang et al., 2008; Shi et al., 2011), and presentation to cell under mechanical loading or ECM remodeling (Davis et al., 2000). Therefore, the ECM can be considered as a multifaceted component of the niche that can integrate both biochemical and mechanical cues to regulate cells.

The study by Engler et al. (2006) first highlighted the importance of mechanical force, such as matrix stiffness in directing mesenchymal stem cell differentiation, which can act independently of transcription factors. This study and others have demonstrated how the ECM, which was once regarded as a primarily structural component, can actively regulate cells through what is known as mechanotransduction (Pelham and Wang, 1997; Lo et al., 2000; McBeath et al., 2004; Gilbert et al., 2010; Wang et al., 2012; Urciuolo et al., 2013; Mao et al., 2016; Watt, 2016). Thus, mechanical forces are translated through signaling cascades, to affect changes that occur in the nucleus and gene expression. This is achieved through ECM-binding receptors such as integrins, mechanosensitive channels, G-coupled protein receptors, and growth factor receptors, which are involved in translating the various signals provided by the ECM (**Figure 1A**; Orr et al., 2006; Wang et al., 2009; Vining and Mooney, 2017; Jahed and Mofrad, 2019).

Furthermore, studies have shown that the structure of the actin-cytoskeleton network as a response to the outside environment can lead to enhanced reprogramming of cells. For example, reducing the stiffness of the matrix alone is sufficient to increase expression of *Oct4* and *Nanog* in HEK 293 cells without additional transcription factors (Guo et al., 2014). Moreover, combining both substrate stiffness and transcription factors can lead to an increase in euchromatic and fewer heterochromatic nuclear DNA regions, and results in enhanced iPSC conversion (Gerardo et al., 2019), indicating that alteration of chromatin state as a result of mechanical signaling can work synergistically with transcription factors that can improve the efficiency of reprogramming events. These are just a few examples of how current research are uncovering the potential of the extracellular matrix, working together with the correct combination of signaling factors as a means of directing cell fate.

CELLULAR REPROGRAMMING *IN VIVO*

A recent review highlighted studies of cellular reprogramming that occurs in development, or as a response to stress (Merrell and Stanger, 2016). Cells in each tissue tend to have a specialized niche specific to that tissue (Voog and Jones, 2010), and how these niches are maintained and remodeled will be context dependent. Changes to this niche will affect the outcome of cell behavior that can lead to either favorable (repair, regeneration) (Jopling et al., 2010; Mercer et al., 2013), or detrimental events such as fibrosis or degeneration (Moyer and Wagner, 2011; Bryant et al., 2017).

It is now clear that there are resident progenitor cells present in practically all mammalian tissues which serve to maintain turnover of cells during homeostasis (Voog and Jones, 2010). However, if this system is challenged in mammalians due to significant stress, it often fails to recover sufficiently, leading to permanent tissue damage (Kaur et al., 2015; Rockey et al., 2015; Talman and Ruskoaho, 2016). On the other hand, there are regenerative model organisms that are able to overcome this hurdle and effectively remodel the microenvironment to allow for complete regeneration. This can be achieved through employing cellular reprogramming, such as dedifferentiation or re-entry into the cell cycle, in order to regenerate tissues such as the heart (Jopling et al., 2010), an entire limb (Tanaka et al., 1997; Kumar et al., 2000), or any missing part of the body in planarians (Ivankovic et al., 2019). Understanding how these niches are formed and remodeled *in vivo*, and how they function under different biological contexts, will therefore provide insights into how to better develop tools needed to improve the directed-regulation of cells *in vitro* or enhance these processes *in vivo*.

While cells can encounter different environments under various scenarios, this review will focus on three main concepts: (1) a stationary cell in a changing environment (**Figure 1B**), (2) a migratory cell encountering a new environment (**Figure 1C**), (3) and a cell in a transitional environment during tissue regeneration, and returning to homeostatic conditions upon completion (**Figure 1D**). In the stationary cell model, cells are responding to changes that occur in the surrounding environment, as they or other cells modify the properties of this environment, and subsequently acquire different fates as the ECM changes over time. In the second scenario, cells undergoing

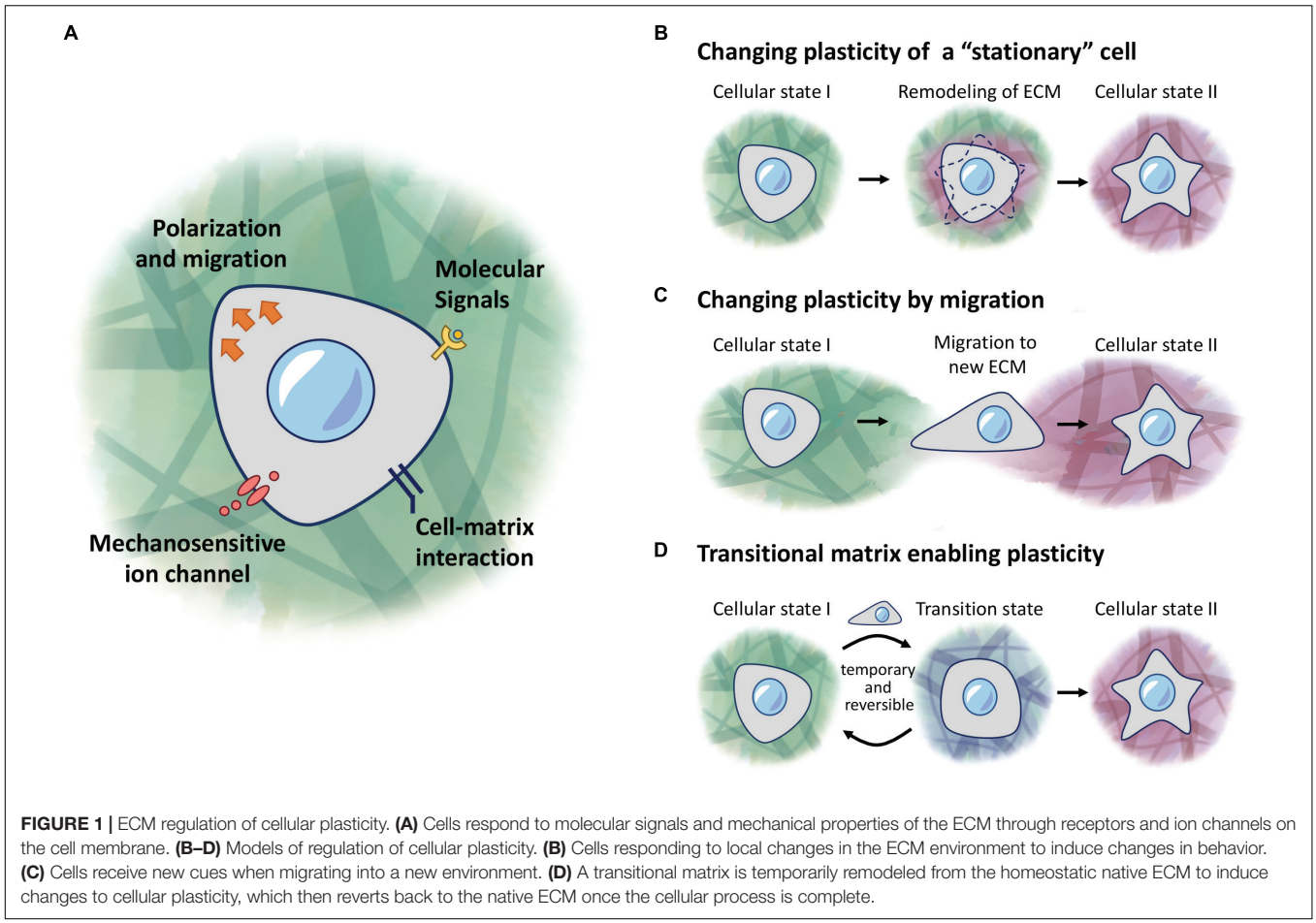


FIGURE 1 | ECM regulation of cellular plasticity. **(A)** Cells respond to molecular signals and mechanical properties of the ECM through receptors and ion channels on the cell membrane. **(B–D)** Models of regulation of cellular plasticity. **(B)** Cells responding to local changes in the ECM environment to induce changes in behavior. **(C)** Cells receive new cues when migrating into a new environment. **(D)** A transitional matrix is temporarily remodeled from the homeostatic native ECM to induce changes to cellular plasticity, which then reverts back to the native ECM once the cellular process is complete.

migration may encounter a different environment from their original location, and hence will respond depending on what new signals are presented to these cells. Lastly, we describe the concept of a transitional matrix which is transiently remodeled, during the process of regeneration, followed by restoration of the native/homeostatic niche, once the entire process is completed.

Quite often these processes cooperate with each other during developmental and regenerative processes, and serve to achieve different outcomes at different stages of these processes. We will address these from the context of musculoskeletal development, repair and regeneration, and cells that contribute to the formation of the skeletal and muscle tissues.

FATE OF A CHONDROCYTE: THE CHANGING PLASTICITY OF A "STATIONARY" CELL

The journey of a chondrocyte well illustrates the concept of changing cell plasticity. This cell, derived from the mesodermal lineage is the primary cell for the making of cartilage, a semi-solid hydrated tissue containing mostly of ECM. In development, chondrocytes play key roles in formation of the skeleton. Indeed, the axial and appendicular bones are all formed through the process of endochondral ossification, in which a cartilage template of the future bone is first made, and then are converted into bone. In this journey, the chondrocytes will undergo hypertrophy, and then transdifferentiate into osteoblasts. Further, synovial joints are formed within these cartilage templates that involves a dedifferentiation process, reprogramming chondrocytes back to multipotent progenitor cells within the joint forming region, that will give rise to all the structures of the joint (Wang et al., 2016). Thus, chondrocytes trapped in their own matrix undergo numerous changes, modifying their ECM microenvironment sequentially, providing the niche needed for cell-matrix interaction and availability of signaling molecules for cell maintenance, proliferation, differentiation, dedifferentiation and transdifferentiation.

Chondrocyte Dedifferentiation in Synovial Joint Formation

During early limb development, condensed mesenchymal forming cartilage templates of the future bones are primed to the chondrocyte lineage, expressing a potent chondrocyte transcription factor Sox9, and producing typical cartilage ECM such as collagen II (**Figure 2A**). At the site of the future joint (the interzone), changes in molecular signals and ECM occur to facilitate a conversion of the rounded

chondrocytes into more flattened interzone cells (Mitrovic, 1978). This process has been described as dedifferentiation as the early "committed chondrocytes" revert to a progenitor status, regaining differentiation potency (Garciadiego-Cazares et al., 2004; Seemann et al., 2005). However, it is also possible that this represents a normal lineage divergence in differentiation in the formation of joints. While the precise signals that drive this process is not clear, patterning genes such as the Hox genes, Wnt and BMP signals are involved (Davis et al., 1995; Storm and Kingsley, 1999; Guo et al., 2004). However, changes in the ECM environment and cell-matrix interaction appear to be sufficient to initiate a joint forming process. For example, inhibition of α5β1 integrin at an ectopic site in a developing limb interrupted cell-matrix interaction of chondroprogenitors, and an ectopic joint is formed at that site (Garciadiego-Cazares et al., 2004). Thus, altering cell-matrix contact is part of the "dedifferentiation" initiation events.

With "dedifferentiation" and formation of the interzone, the ECM environment changes, creating a "softer" structure containing proteoglycans and glycosaminoglycan such as hyaluronic acid (HA), creating an open network structure (Edwards et al., 1994). Binding of HA to its receptor CD44 is essential for normal joint development and cavitation (Dowthwaite et al., 1998). Proliferation of interzone cells are limited, and the interzone expands through further recruitment of the mesenchymal cells from the surrounding mesenchyme (Shwartz et al., 2016). Importantly, the microenvironment is now conducive to direct the differentiation of the incoming mesenchymal cells into interzone cells.

At the molecular level, dedifferentiated interzone cells express high levels of *Gdf5*, and is an earlier gene marker for these cells (Storm and Kingsley, 1999; Seemann et al., 2005), and later, a stem cell marker *Lgr5* (Feng et al., 2019). Cell lineage tracing showed that interzone cells can become cells in the meniscus and cruciate ligaments, and chondrocytes in the articular cartilage (Koyama et al., 2008; Feng et al., 2019). Within the interzone, cells begin to produce a different set of ECM and remodel the microenvironment with the downregulation of *Sox9* and *Col2a1* (Amarilio et al., 2007), and initiate the production of *Cilp* and *Col22a1* (Feng et al., 2019).

Interzone cells at different locations of a developing joint receive their unique differentiation cues and further segregate and differentiate into different compartments. Collagen XXII (*Col22a1*) is a novel maker for late interzone cells as the interzone cells further differentiate to an articular chondrocyte lineage (Feng et al., 2019). Its expression is maintained in the forming meniscus and articular cartilage but absent in the forming cruciate ligaments. The role of collagen XXII in the interzone is not clear, but its expression remains in the most superficial layer of the future mouse articular cartilage (Feng et al., 2019), providing a unique niche for cells residing in this layer. *Col22a1* is expressed at other sites, but limited to cells at tissue junctions or boundaries (Koch et al., 2004). Articular chondrocytes sense changes of mechanical stimuli from the environment and produce *Prg4* (lubricin), an ECM protein that functions to reduce shear at the cartilage joint surfaces (Ogawa et al., 2014). Cellular turnover and ECM remodeling in the articular cartilage is limited, an acceleration of which will cause cartilage destruction, and cellular changes leading to osteoarthritis (van der Kraan and van den Berg, 2012).

Transdifferentiation of a Chondrocyte to an Osteoblast

The other journey of a chondrocyte in the developing cartilage template is in the process of endochondral ossification (**Figure 2B**), occurring in the initiation of primary and secondary ossification centers, and establishment the cartilage growth plates at the ends of long bones for linear growth. Thus, articular and growth plate chondrocytes are differentiated through a divergence in their fate (**Figure 2C**). While they are similarly controlled by the expression of *Sox9* and producing similar ECM at the macroscopic level, they differ in terms of cell state and function that are likely to be controlled by subtle variations at the pericellular level within the different compartments of the articular or growth plate cartilages.

Conceptually, growth plate chondrocytes can be considered as transitional cells for bone elongation, changing and remodeling the ECM in the process. Chondrocytes in the growth plate undergo "scheduled" hypertrophy in this transition to osteoblasts. Interestingly, this is not the case for articular cartilage chondrocytes, except in degenerative conditions such as osteoarthritis (van der Kraan and van den Berg, 2012). Of interest, a recent study showed collagen II suppresses articular chondrocyte hypertrophy and osteoarthritis progression by promoting β1-integrin-SMAD1 interaction, thus inhibiting BMP-SMAD1-mediated chondrocyte hypertrophy (Lian et al., 2019). Therefore, changing the collagen II-containing environment may be a prerequisite condition for hypertrophy, and this is the case in chondrocyte hypertrophy in the growth plate, with the down-regulation of *Col2a1* and up-regulation of *Col10a1*, followed by a complete change in the ECM composition.

The major function of the growth plate cartilage is for the linear growth of long bones. Traditionally, the process of endochondral ossification process has been described in a linear progression, from the activation of chondrocyte proliferation to a hypertrophic stage conducive for mineralization and vascularization (Kronenberg, 2003). The hypertrophic chondrocytes are described as terminally differentiated cells that undergo apoptosis, and the mineralized cartilage matrix is converted to bone, through the action of incoming osteoblasts and progenitor cells. However, this concept has been challenged recently, as a number of cell-fate mapping studies of chondrocytes showed not all the hypertrophic chondrocytes undergo apoptosis, but can transitioned to become osteoblasts, contributing to the bone forming process (Ono et al., 2014; Yang G. et al., 2014; Yang L. et al., 2014; Zhou et al., 2014; Park et al., 2015). This sequence of event indeed demonstrates the plasticity of chondrocytes and hypertrophic chondrocytes that changes in coordination with the ECM. While such changes in plasticity do occur in other systems (Dityatev and Schachner, 2003; Urciuolo et al., 2013; Poltavets et al., 2018), the unique example here is

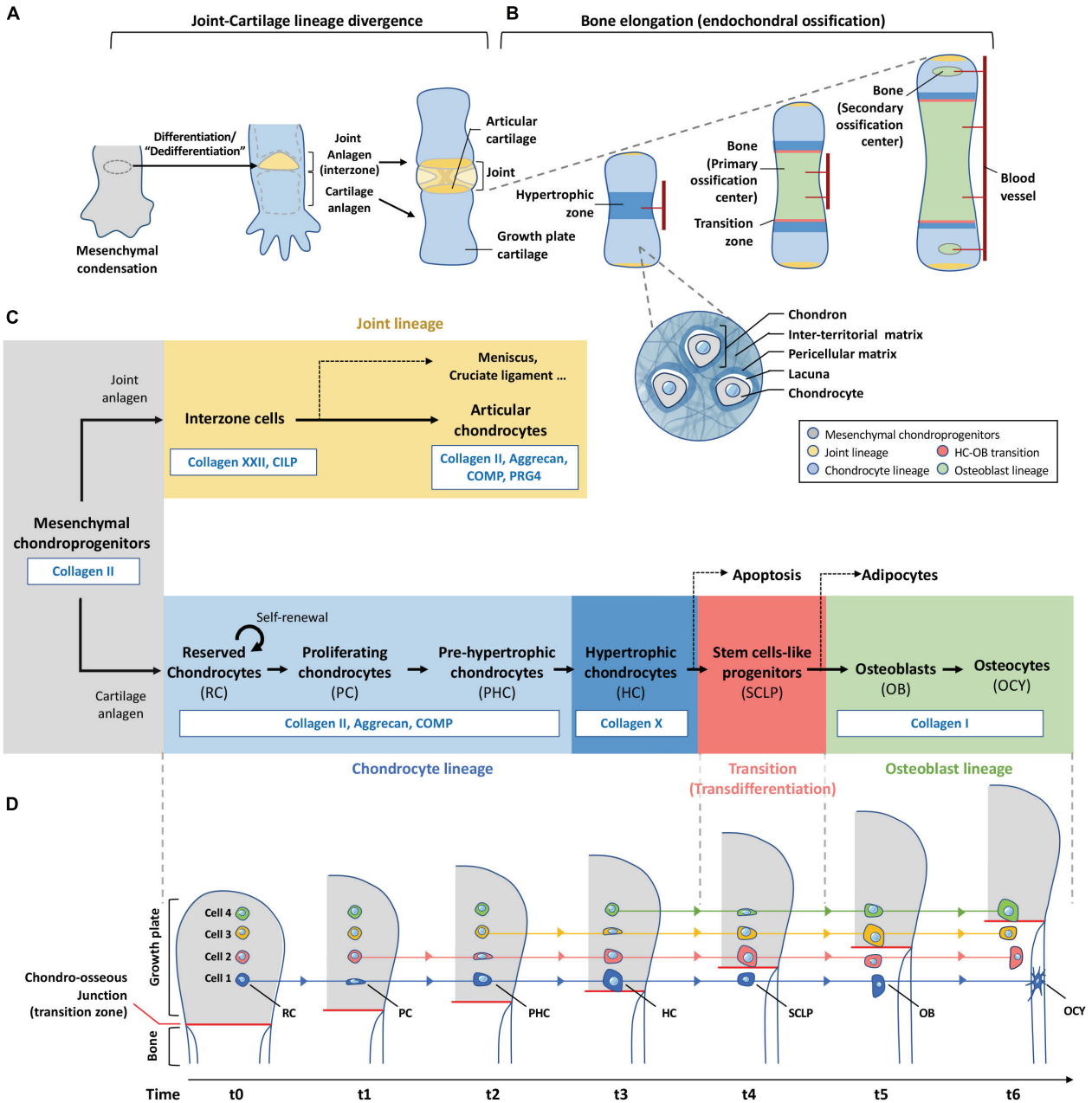


FIGURE 2 | Plasticity of chondrocytes in differentiation, de-differentiation and transdifferentiation. **(A)** Mesenchymal condensation contains progenitor cells for both joint and growth plate cartilage formation. Cells at the site of future joint undergo dedifferentiation to form the interzone which eventually give rise to different joint components including the articular cartilage. **(B)** Chondroprogenitors outside the interzone become part of the growth plate cartilage and differentiate into chondrocytes which are located inside individual lacunae and bound with pericellular matrix. Each of these cocoon-like structures is called a "chondron." Bones elongate through a developmental event called endochondral ossification. Chondrocytes at the central region of the cartilage analgen first undergo hypertrophy. Blood vessels are invaded to induce remodeling of cartilage matrix to mineralized bone matrix. Cartilage is then separated by the primary ossification center into the distal and proximal parts where the growth plates are formed. Before the end of puberty, chondrocytes in the growth plate actively undergo programmed differentiation and transdifferentiation as shown in **(C,D)**, contributing to the formation and elongation of bones. Invasion of blood vessels in-between the articular surface and the growth plates leads to hypertrophy of cells and hence formation of secondary ossification centers at bone ends of a long bone. **(C)** This roadmap shows the changes of matrix production with the differentiation status of chondroprogenitors-descendant cells. Same color scheme is applied in **(A–C)** to indicate the fate of each lineage in skeletal tissues. **(D)** Chondrocytes are not actively migrating to the ossification front during endochondral ossification. Instead, they stay at the same position receiving external cues at specific moment to differentiate and remodel its surrounding matrix. Hypertrophic chondrocytes at the chondro-osseous junction produce enzymes to remove matrix and release themselves to the bone marrow, and transit to stem-cell like progenitors for osteoblasts which will finally differentiate into osteocytes buried in bone. RC, reserved chondrocyte; PC, proliferating chondrocyte; PHC, Pre-hypertrophic chondrocyte; HC, Hypertrophic chondrocyte; SCLP, Stem cells-like progenitors; OB, Osteoblast; OCY, Osteocyte.

the spatial location of a chondrocyte that is entrapped within a rigid and dense cartilage matrix environment that gradually changes without a physical movement in modifying the ECM to produce a permissive change in the niche of the chondrocytes in the transition process.

Plasticity Transiting in a Designated Spatial Location

Traditional illustrations show proliferative chondrocytes expanding downwards, and then differentiating into hypertrophic chondrocytes, giving the impression that the cells have moved in their relative spatial position, but in reality, they remained static. In **Figure 2D**, we present the biological process of endochondral ossification as cartilage is converted to bone, and in the case of a growth plate, there is a continual supply of new cartilage through chondrocyte proliferation, from a switch of "reserved" chondrocytes to a proliferative stage that progresses to the hypertrophic stage (Kronenberg, 2003). Here, there are number of interesting cellular changes from the perspective of ECM cellular states that can be related to the concept of "transition of a stationary cell" (**Figure 2D**).

In the reserved cartilage, there are chondrocytes embedded in a "sea" of ECM often refer to as rich in collagen II, IX, XI and proteoglycans such as aggrecan, decorin and fibromodulin, and many other cartilage-related ECM including cartilage oligomeric matrix protein (COMP) and matrillins (Myllyharju, 2014). These matrix proteins organize into a functional cartilage structure. Cells within this cartilage are far apart, and the position of the matrix in relation to their distance to the cell and between cells serve different functions. Matrix occupying the space between cells is referred to as the inter-territorial matrix, and is more likely to be structural in nature, whereas matrix closer to each individual is the territorial matrix, linking the inter-territorial matrix to the pericellular matrix (PCM) of the cell, which is immediate to the cell, and presenting as the matrix niche of the cell (**Figure 2B**).

It was generally accepted that the reserved cartilage contains "quiescent" chondrocytes. Some serve as stem cells, while others closer to the proliferative zone will receive signals for cell cycle reentry for active cell divisions. How these different types of cells are kept in close proximity to each other is not well understood, but likely to fall within the concept of differential microenvironments built within and between chondrocytes. Recent studies have shed light on the potential stem cell niche within the reserved zone in postnatal life (Mizuhashi et al., 2018; Newton et al., 2019). For example, skeletal stem cells appear to be among PTHrP-positive chondrocytes, and PTHrP-positive chondrocytes expressed markers for skeletal stem and progenitor cells (Mizuhashi et al., 2018). In addition, some of these stem cells undergo asymmetric cell division for self-renewal and the other daughter cell contributes to proliferative chondrocytes forming the characteristic columns (Newton et al., 2019). PTHrP-positive chondrocytes response to Indian hedgehog (IHH) signaling, a morphogen gradient that is regulated by HSPG; thus the level of HSPG in the territorial and inter-territorial matrix will have a role.

Transition to Active Proliferation and Formation of Chondrocyte Columns

While the precise signals that activate the proliferation of chondrocyte forming column of cells is not clear, various growth factors are involved, including mitogenic signals such as insulin like growth factor (IGF), Indian hedgehog (IHH), and anti-mitogenic FGF signaling through FGFR3 (Samsa et al., 2017); all of which are regulated by the ECM in terms of availability and presentation. As indicated earlier, the IHH gradient along the proximal-distal axis of the growth plate, in which heparan sulfate proteoglycans (HSPGs) have a role in establishing this gradient, has differential short- and long-range effects that is concentration dependent, and interacts with the PTHrP/PPR signaling pathway (Kobayashi et al., 2002). Further, membrane bound HSPGs function as a co-factor for FGF receptors in the presentation of FGF ligands to chondrocytes. Indeed, altered range of IHH signaling was observed in mice deficient of *Ext1*, one of the heparan sulfate (HS) polymerizing enzymes, causing growth plate dysmorphology (Koziel et al., 2004).

As the chondrocyte enters the active cell cycle stage, the formation of a column of cells reorganizes the ECM environment. Although it is thought that the overall cartilage component has not changed much, the spatial orientation of the cells in relation to the matrix has changed dramatically, with cell-cell contact along the proximal-distal axis, while there is cell-matrix contact at the peripheral of the column of chondrocytes, entrapped in a cocoon-like structure referred to as a "chondron" (**Figure 2B**). This is a highly organized and unique structure that is necessary for the elongation of long bones. The importance of chondrocyte stacking is well illustrated in a mouse model lacking β1-integrin (Aszodi et al., 2003), a cell surface receptor necessary for cell-matrix interaction. It is shown that a chondrocyte divides perpendicular to the long axis of the cell, and a mechanical event that allows the sliding of the daughter cells to be stacked along longitudinal axis is controlled by cell-matrix interaction. The stiffer matrix in the longitudinal septum separating the columns restricts the rotating direction of the daughter cells and hence the cell stack formation (Prein et al., 2016). Flattening of proliferating chondrocytes is also correlated with the gradual increase of collagen density and matrix stiffness from embryonic stage to early postnatal stages (Prein et al., 2016).

Transition to Osteoblasts via Hypertrophy

Hypertrophy of chondrocytes involves a series of phenotypic and cell state changes. At the "prehypertropic" stage, the cells are exiting the cell cycle and the ECM begins to change with down-regulation of much of "cartilage" ECM markers such as *Col2a1* and its transcriptional regulator *Sox9,* while *Col10a1* and *Ihh* expression are increased. Sox9 plays a central regulatory role in chondrocyte hypertrophy. Sox9 has an inhibitory role on *Col10a1* expression in proliferating chondrocytes through the Gli factors (Leung et al., 2011). In early hypertrophic chondrocytes, Sox9 interacts with another transcription factor Mef2c to activate *Col10a1* expression (Dy et al., 2012). However, the ectopic expression of *Sox9* in hypertrophic chondrocytes can

suppress *Col10a1* expression (Leung et al., 2011). Members of AP-1 families such as Jun and Fosl2 have also been shown to act together with Sox9 to promote chondrocyte hypertrophy (He et al., 2016). *Col10a1* is a marker for hypertrophic chondrocytes but the function of Collagen X is not clear, as hypertrophy occurs normally in *Col10a1*-null mice with normal growth plate morphology (Kwan et al., 1997). It is proposed to facilitate mineralization of hypertrophic cartilage, ready to be converted to bone (Kwan et al., 1997).

The need for cellular hypertrophy at this stage of endochondral ossification is not clear. A contribution to bone elongation is proposed, and the degree of cell enlargement could be correlated with the rate of bone growth (Cooper et al., 2013). For example, larger hypertrophic chondrocytes were found in rapidly elongating proximal tibia; whereas smaller ones were found in slower elongating proximal radius (Wilsman et al., 1996). However, it is also possible that this change is part of the preparation for the final transitional stage of a chondrocyte to become an osteoblast. Hypertrophy in a confined space requires room for expansion, and thus the need to remodel the ECM for this purpose, and at the same time, could alter the cell-matrix interaction and the cellular architecture in reprogramming the chondrocyte. While the term "hypertrophic chondrocyte" described the origin of these cells, it has none of the molecular characteristics of a chondrocyte; it is a very different cell. In fact, it bears more resemblance with an osteoblast as it expresses *Runx2*, a "master" regulator initiating osteoblast differentiation (Schroeder et al., 2005). Thus, these hypertrophic cells in this new environment is preparing their next journey, and the hypertrophy process alters again the plasticity and the potential of these cells for further dedifferentiation or transdifferentiation.

End of a Plasticity Journey: The Final Act of a Chondrocyte

The transition of a hypertrophic chondrocyte to an osteoblast was a major discovery that has provided much interest in deciphering the molecular mechanism and the role of hypertrophic chondrocyte in bone formation. This was achieved by using various Cre-drivers marking chondrocytes (Col2a1-Cre) and hypertrophic chondrocytes (Col10a1-Cre) specifically, and follow their fate (Ono et al., 2014; Yang G. et al., 2014; Yang L. et al., 2014; Zhou et al., 2014; Park et al., 2015). While this transition is now well accepted, the mechanism by which this takes place is not clear. However, it is clear that this takes place at the ossification front or the chondro-osseous junction, where there is yet another major switch in ECM, and the environment in which transiting cells encounters. An ECM switch is evident by the high expression level of MMP13 at the chondro-osseous junction, that would actively degrade ECM components (Stickens et al., 2004), and assisted with degradative enzymes from the incoming osteoclasts with the invading vasculature (Gerber et al., 1999), will released the hypertrophic chondrocytes from their enclosed environment of a chondron. This renewed "freedom" sets these cells to reprogram into a multipotent status in cellular plasticity.

This "out of jail" concept is supported by decades-old observations that chondrocyte isolated from their ECM environment, cultured in monolayer dedifferentiate with proliferation and passage; changing morphology and gene expression profiles from *Col2a1*/*Col10a1* expressing cells to mesenchymal like cells expressing *Col1a1* (von der Mark et al., 1977), and stem cell markers (Jiang et al., 2016). Entrapping chondrocytes within a 3D cartilage ECM can maintain the chondrocyte phenotype *in vitro*, and reducing dedifferentiation (Mao et al., 2019), as further support of the role of ECM in the niche. Interestingly, a re-entry into the cell cycle may contribute to reprogramming, inducing the expression mesenchymal stem cell surface marker such as *Sca1* in mice (Park et al., 2015) or zebrafish (Giovannone et al., 2019). Further, osteoblasts and bone marrow adipocytes have been identified as descendants of these Sca1 + cells as evidence for multipotency (Giovannone et al., 2019). In bone fracture repair that involves the formation of a cartilaginous callus, chondrocyte descendent cells marked with *Acan*-CreERT2 and *Col2a1*-CreERT inducible Cre mice showed these cells also transit to become osteoblasts (Zhou et al., 2014; Hu et al., 2017). It was further demonstrated that hypertrophic chondrocytes in the callus transition zone re-entered cell cycles and expressed pluripotency genes such as Sox2, Oct4, and Nanog (Hu et al., 2017).

The long journey of chondrocytes illustrates the relationship between progressive matrix remodeling and cell plasticity (**Figures 2A–C**). Hypertrophic chondrocytes in this context seem to be highly plastic, acting as progenitors for adipocytes, chondrocytes, osteoblasts, and probably have similar roles at key tissue junction sites, as such cells are found at the insertion site of cartilage endplate to the annulus fibrosus of an intervertebral disc (Roberts et al., 1998), or tendon to bone insert sites (Galatz et al., 2007) where these cell can be identified.

CHANGING PLASTICITY BY MIGRATION: LIMB BUD OUTGROWTH

Cells can alter their state through movement out of an old niche and into a new environment, undergoing exposure to new molecular and mechanical signals, and thus new cell behavior. This occurs frequently in the context of the development such that this change in environment is necessary and sufficient for directing the formation of new tissues during embryogenesis. Here, we will discuss events occurring in early limb bud formation to illustrate this concept, where progenitor cells undergo numerous changes and reprogramming for migration, proliferation, and differentiation to the required cell types.

Key Processes and Compartments of an Early Limb Bud

During limb development, the earliest event is the delamination of cells from the somatopleure epithelium covering the lateral plate mesoderm through epithelial-to-mesenchymal transition (EMT) to form the limb mesenchyme as it buds out (**Figure 3A**). This process is initiated by transcription factors *Tbx5* (fore limb) and its downstream target, *Fgf10*, whereby FGF10 induces the formation at the ectoderm, the apical ectodermal ridge (AER) that expresses *Fgf8* (**Figure 3B**). Through a feed-forward

relationship between FGF10 and FGF8 signals, the progress zone is established with active proliferation of mesenchymal cells (Crossley and Martin, 1995; Ohuchi et al., 1997). Cells at these early stages in the limb mesenchyme maintain their undifferentiated state and undergo migration and proliferation which contributes to directed outgrowth of the limb bud (Gros and Tabin, 2014; Jin et al., 2019). Thus, the somatopleure cells undergo extensive reprogramming and eventually all change from an epithelial state to a migratory and proliferative state of the mesenchymal cells (Xu et al., 1998, 1999; Gros et al., 2010). As the limb bud grows, these cells will contribute to the skeletal elements of the limb (Zuniga, 2015) while the myogenic precursors for muscle formation migrate in from the myotome (Deries and Thorsteinsdóttir, 2016).

The ECM landscape of the early limb bud dictates how signaling factors such as FGFs and SHH are presented and activated. It also provides a suitable matrix for cells to move and change shape, while suppressing differentiation. Current knowledge shows this is achieved through differential HS sulfation patterns, and enrichment of HA around the progress zone beneath the AER (Kosher and Savage, 1981; Nogami et al., 2004; Li et al., 2007; **Figure 3C**). Distribution of laminin (Godfrey and Gradall, 1998; Gros and Tabin, 2014) glucosaminoglycans (Li et al., 2007), fibronectin (FN) (Zhu et al., 2020), nidogen (Böse et al., 2006), also support functional compartmentalization of ECM components in the regulation of these early processes.

Limb Bud Outgrowth: Cell Transformation and Migration Into a New Environment

Somatopleure cells are attached to the epithelium via laminin on the basal side. FGF10 induced EMT is accompanied by the breakdown of the laminin layer (**Figure 3D**), and dispersal of laminin fragments throughout the limb mesenchyme (Gros and Tabin, 2014). Inhibition of *Tbx5* and *Fgf10* not only inhibits the progression of EMT in the mouse forelimb, but also leads to the accumulation of dense regions of laminin around the somatopleure epithelium (Gros and Tabin, 2014). Detachment of cells through degradation of the laminin enriched layer is necessary for cells to transition from an epithelial phenotype to a mesenchymal migratory phenotype. Once detached, these cells react to signaling cues in the mesenchymal space, leading to migration and proliferation in the limb bud, resulting in expansion of the mesenchyme and formation of the progress zone (**Figure 3E**). Although laminins have been shown to be involved during later stages of muscle development in the limb (Godfrey and Gradall, 1998), whether these punctate laminin deposits observed at the earlier stages have a direct role in the subsequent proliferation and migration of early mesenchymal limb cells remains to be seen.

Migration and Proliferation of Cells in the Limb Bud Mesenchyme: Role of Sulfation Patterns on HSPG

Following EMT, the proliferation and migration of cells entering the nascent limb bud continue to rely on FGF signaling in this new environment of the forming mesenchyme (Gros et al., 2010; Gros and Tabin, 2014). FGF signaling is highly dependent on its binding to HSPGs for presentation to the appropriate receptors (reviewed in Matsuo and Kimura-Yoshida, 2013). This is one of the prime examples of how ECM can act to regulate signaling gradients at the cell surface, driving cellular processes and tissue patterning during development. FGF10 and FGF8 target different cell populations with high specificity in the AER and limb mesenchymal cells, respectively. This selective binding of FGF to the appropriate FGF receptor (FGFR) is achieved through HSPG on the cell surface such that FGF10, but not FGF8, will interact with cells at the AER in the zebrafish limb bud (Sun et al., 2002; Norton et al., 2005; Lu et al., 2011). Whereas, CD44 expressed by AER cells binds FGF8 and presenting this to the underlying mesenchymal cells (Sherman et al., 1998; **Figure 3E**).

The specificity of FGF binding to HSPG is further fine-tuned by the O-sulfation pattern of glucosaminoglycans, achieved through differential expression of sulfate modifying enzymes. In the developing chicken limb bud, it was shown that expression of heparan sulfate 2-O-sulfotransferase (*HS2ST*) and heparan sulfate 6-O-sulfotransferase isoforms (*HS6ST-1* and *-2*) were expressed in different regions with different substrate specificities. *HS2ST* expression was detected throughout the mesenchymal region, with lower expression in the ectoderm in both wing and leg buds. *HS6ST-1* was enriched at the anterior proximal regions of the wing and leg bud, with weak expression at the posterior proximal region. In contrast *HS6ST-2* was mainly expressed in the posterior region of the mesenchyme (Nogami et al., 2004; **Figure 3C**).

FGF10 requires 6-O-sulfated structures for bind to HSPG, and the expression pattern of the sulfotransferases suggests a higher level of high 6-O-sulfated HSPG in the proximal region than the distal region of the limb bud. This in turn would direct FGF10 signal toward the AER (Nogami et al., 2004). Indeed, functional analysis in chick limb bud development confirmed that FGF10 signaling is dependent on 6-O-sulfated HSPG mediated by *HS6ST-2* (Kobayashi et al., 2010). While the expression pattern of *HS6ST* orthologs (*6OST-1*, *-2,* and *-3*) in the mouse embryo is slightly different to the chick embryo, with *6OST-1* expressed in the mesenchyme and AER, *6OST-2* in the mesenchyme, and *6OST-3* in the distal mesenchyme and epithelium, their expression patterns still consistent with the directed signaling of FGF10 toward the AER (Sedita et al., 2004).

While FGF signaling directs the proximal/distal patterning and outgrowth, the anterior/posterior patterning is controlled another feed-forward loop between FGF4 and SHH signaling in limb development (Laufer et al., 1994). *Shh* is expressed at the zone of polarizing activity (ZPA) located at the anterior region (**Figure 3C**) that provides a patterning morphogen gradient along the anterior/posterior axis. Here, the activity of SHH is regulated by its binding to 2-O sulfated HSPG as such binding will restrict its cleavage to the soluble form by ADAM17, thereby regulating signaling capacity along this axis in limb patterning such as the number and identity of the digits (Dierker et al., 2009; **Figure 3C**). Together, these fine-tuning of

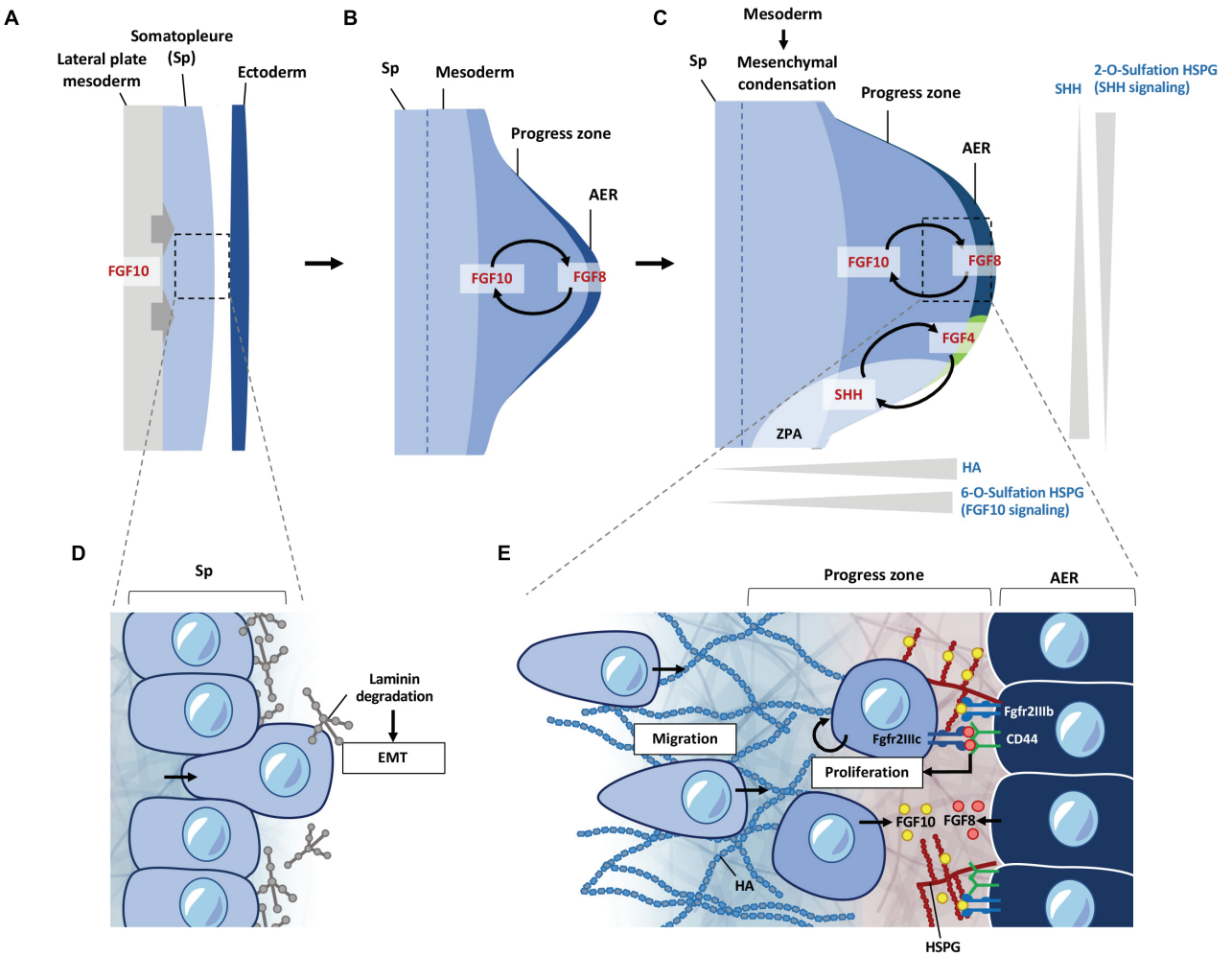


FIGURE 3 | ECM regulation of signals during early limb bud formation. **(A)** FGF10 signaling from the lateral plate mesoderm induces EMT of somatopleure cells toward the ectoderm. **(B)** FGF10 induces formation of the AER from the overlying ectoderm, inducing FGF8 expression at the AER. FGF10 and FGF8 form a feed-forward signaling loop. FGF signaling induces proliferation and migration of cells in the progress zone leading to outgrowth of the limb bud. **(C)** HSPG sulfation patterns regulate diffusion of FGF and SHH signaling. 6-O sulfation regulates FGF10 binding to HSPG leading to enhanced FGF10 signaling at the progress zone/AER boundary. FGF8 first induces SHH expression at the ZPA, which is then later maintained by a feed-forward loop of FGF4-SHH signaling. 2-O sulfation of HSPG negatively regulates SHH signaling from the ZPA at the posterior regions of the limb bud, limiting diffusion of SHH at the posterior regions. HA is present at higher levels at the progress zone but absent from the AER. HA is also reduced during initiation of mesenchymal condensation in the limb bud. **(D)** Somatopleure cells are attached to laminin on the basal side. Laminin is degraded upon induction of EMT, liberating cells to migrate to form the limb bud mesenchyme. **(E)** FGF10 from the limb mesenchyme binds to 6-O sulfated HSPG and is presented to the Fgfr2b receptor on the AER cells, which induces *FGF8* to be produced by the AER cells. FGF8 secreted by the AER is bound by CD44, which presents FGF8 to the Fgfr2c receptor to cells in the progress zone, leading to proliferation of cells in the progress zone during early limb bud formation. FGF8 also induces *FGF10* expression, leading to a feed-forward loop of FGF10-FGF8 signaling. EMT, epithelial mesenchymal transition; Sp, somatopleure; AER, apical ectodermal ridge; ZPA, zone of polarizing activity; HA; hyaluronic acid; HSPG, heparan sulfate proteoglycan.

FGF and SHH signaling by the sulfation pattern of HSPG at the cell surface indicate that cells within the mesenchyme and the AER responds to their environment, and in turn modify its pericellular niche by differential expression of ECM and modifying genes, and cells will act accordingly as they enter into that local environment. In this case, the undifferentiated cells in the progress zone maintain proliferation and migration through exposure to FGFs localized to this region via HSPGs, while also responding to patterning cues from SHH signaling. Differentiation and condensation into skeletal elements initiates when cells leave the influence of this progress zone, which is in part is enabled by changes in hyaluronic acid (HA) levels (Li et al., 2007; **Figure 3C**).

An Environment for Cell Proliferation and Migration: Role of Hyaluronic Acid

The ECM within the limb progress zone needs to provide a proper environment for migrating cells to maintain proliferation and their progenitor state. HA as a large unsulfated glycosaminoglycan contributes to this permissive environment. HA is known to regulate cell proliferation and migration

(Toole, 2001; Solis et al., 2012), and is produced by the enzyme HA synthase 2 (*Has2*). *Has2* is highly expressed at the distal posterior subridge mesoderm in the chick limb bud, but not in the AER (Li et al., 2007). Thus, there is an increasing gradient of HA in the progress zone along the proximal to distal axis that also correlates with the state of cellular differentiation along this axis (Kosher and Savage, 1981). The lack of HA is suggested to promote physical interaction between the AER and the underlying mesenchymal cells. In addition, CD44 localization in cells of the AER could induce endocytosis and subsequent intracellular degradation of HA (Culty et al., 1992; Hua et al., 1993); thus maintaining a HA-free region between the mesenchymal progress zone and AER (Yu et al., 1996).

Cell proliferation needs a permissive ECM and space, in part related to the stiffness and hydration property of the microenvironment in the limb bud mesenchyme (Wells, 2008; Bott et al., 2010; Notari et al., 2018; Sun et al., 2018). HA could regulate these processes (Li et al., 2007), as it can generate a hydrated PCM with its high affinity for water, separating cells from each other, and providing space needed for changes in cell shape and migration (Toole, 2001). Importantly, HA also has a role in maintaining the limb mesenchymal cells in an undifferentiated state in their journey toward the AER, shielding cells from incoming signals that would otherwise induce a differentiation. Thus with the reducing level of HA and *Has2* expression in the proximal mesenchyme with limb bud outgrowth, precartilage mesenchymal condensations are formed in the proximal central core of the limb bud (Knudson and Toole, 1985; Li et al., 2007). This is consistent with a much-reduced coat of HA around the PCM of cells during mesenchymal condensation, such that cells in the chondrogenic and myogenic regions lacked HA in the PCM (Knudson and Toole, 1985). Further, as in the AER, HA interaction with CD44 at the condensing region will mediated endocytosis of HA leading to degradation of HA, promoting cell-cell contact (Hua et al., 1993; Rousche and Knudson, 2002). Conversely, maintaining Has2 expression will lead to malformation or loss of skeletal elements in the limb (Li et al., 2007).

While HSPG and HA represent the more extensively studied examples of the role of the ECM in regulating the environment in the developing limb, recent studies are beginning to uncover the role of other ECM proteins in limb bud formation and outgrowth such as FN (Zhu et al., 2020) and nidogen (Böse et al., 2006).

Durotaxis in Limb Bud Formation: Fibronectin and Wnt5a in Establishing a Tissue Stiffness Gradient

Directional migration of cells can act through chemical attractants (chemotaxis) or mechanical stiffness (durotaxis) (Pelham and Wang, 1997). In durotaxis, cells tend to migrate toward stiffer substrates; hence directional movement can be achieved along an increasing stiffness gradient in the tissue controlled by the ECM (Vincent et al., 2013). Recently, a 3D stiffness gradient in the mouse limb bud was revealed, raising the possibility that durotaxis may be involved (Zhu et al., 2020). Interestingly, this corresponded to a domain of Wnt5a-dependent expression of FN and stiffness of the limb mesenchyme. Wnt5a is involved in planar cell polarity (PCP) (Witze et al., 2008) and this would be consistent with a stiffness dependent polarization leading to durotaxis, contributed by a gradient of FN. Thus, a loss of Wnt5a signaling leads to decreased stiffness in the tissue and loss of directional movement (Zhu et al., 2020). A role of the AER is suggested as activation of directional motility toward the AER via Wnt5a signaling acts through FGF8 (Gros et al., 2010). As FN is assembled at the cell surface, with development it is also possible that this Wnt5a/FN/durotaxis relationship continues to function in shaping the limb bud through condensation of precursor sites of skeletal elements and mechanosensing of the cells (Zhu et al., 2020).

Plasticity of Cells and ECM Dynamics Contributing to Limb Bud Formation

It is clear that the ECM dynamics in this scenario 2 (**Figure 1C**) is key in controlling cellular plasticity in directing cell movement, maintaining cellular status in the process, and activating differentiation on arrival of their new home. Our review of the early stages of limb bud formation highlighted some of these relationships. However our understanding is limited and needs to be expanded to gain insight into tissue organization, and the spatial relationship of the cells with their own PCM to the structure. The role of additional ECM components need to come into play, such as the importance of nidogen in maintaining basement membrane integrity, an impairment of which leads to altered range of FGF8 signaling from the AER (Böse et al., 2006), or the identification of new differentially expressed ECM genes with developmental time such as *Col12a1* using single cell transcriptomic approaches (Tejedor et al., 2020). Further changes to this ECM at the later stages of limb bud development then facilitate the differentiation of tissues such as cartilage and muscle (Hurle et al., 1994; Godfrey and Gradall, 1998; Arteaga-Solis et al., 2001; McCulloch et al., 2009; Nandadasa et al., 2014).

TRANSITIONAL MATRIX ENABLING PLASTICITY: THE BLASTEMA IN LIMB REGENERATION

Regeneration requires detailed coordination of events to guide cells to repair the tissue. Urodeles such as axolotls and newts are able to regenerate complete limbs which makes them an attractive model to study the mechanics of complex tissue regeneration. Inevitably, this process would involve remodeling of the ECM and changes to the signals that cells receive. The existing ECM needs to be altered to form a permissive environment for cells to proliferate, migrate and differentiate in a coordinated manner. While there are many similarities with events during limb development, the regenerative process does not initiate in an embryonic environment and will need to intercalate the old and new tissues. This requires the additional activation of differentiated cells close to the wound, to transiently gain plasticity, proliferative and migratory characteristics. This process can be described through three major events: (1)

wound healing and activation of resident cell populations; (2) recruitment and proliferation of progenitor cells to form the blastema; and (3) differentiation and integration of new tissue (**Figures 4A–E**). During this process a transitional ECM, which is a transient extracellular environment that is different from the native ECM, is remodeled over time to enable different but coordinated cellular processes to occur over the course of regeneration.

Cellular Landscape of an Early Regenerating Limb

Urodele limb regeneration involves a complex coordination of events that allows for mobilization and activation of cells from the stump tissue (reviewed in Stocum, 2017), which will migrate and accumulate to form a blastema. This blastema grows from recruitment and proliferation of progenitor cells, which then differentiate into tissue cells to build the missing parts, while intercalating with the old tissue to regain a functional limb (**Figures 4A–D**). The blastema in part resembles the embryonic limb bud as it recapitulates many of the developmental processes of limb formation. However, significant reorganization is needed at the old and new tissue junction to integrate both tissues.

Upon injury, FGF (FGF2 and FGF8) and BMP (BMP2 and BMP7) signals from injured nerves (Makanae et al., 2014) and the apical ectodermal cap (AEC) (Han et al., 2001; Giampaoli et al., 2003), are required for blastema formation, and growth is through activation of cells around the wound site (**Figure 4C**). There is evidence of conserved signaling pathways activated during limb regeneration. For example in *Xenopus*, the FGF10 and FGF8 signaling loop found in the developing limb bud (**Figure 3B**), is conserved during limb regeneration (Yokoyama et al., 2000), and FGF10 is also upregulated within 24 h in the axolotl blastema (Knapp et al., 2013). Similarly, FGFs contribute to proliferative cues during regeneration, while SHH is also involved in anterior-posterior patterning during axolotl limb regeneration (**Figure 4E**; Nacu et al., 2016).

Briefly, migration of epithelial keratinocytes is needed to form the wound epithelium, which then initiates formation of the blastema, initially consisting of primarily fibroblasts of dermal and periskeletal origin. These fibroblasts constitute over 40% of the blastema cell population (Muneoka et al., 1986), and will contribute to connective tissue cells and skeletal morphogenesis (Currie et al., 2016; Gerber et al., 2018). Other lineage restricted progenitors such as mononucleated myoblasts arising from dedifferentiated myofibers, *Pax7* + satellite cells, and neural progenitors also migrate into the blastema to regenerate the missing tissues (Stocum, 2017). This is similar to the embryonic limb bud, where muscle progenitors migrate in from the myotome (Deries and Thorsteinsdóttir, 2016), and skeletal elements differentiate from cells arising from the somatopleure in the limb mesenchyme (Zuniga, 2015). The blastema therefore consists of a heterogonous pool of mainly lineage-restricted progenitor cells that contribute to the different lineages, with dermal and periskeletal fibroblasts possessing a greater level of plasticity as it contributes to both connective tissue and skeletal elements (Gerber et al., 2018). Much like the AER, the AEC is proposed to provide signals that maintain cells in their undifferentiated state while promoting migration and proliferation, while neurons also provide proliferative signals to sustain growth of the blastema (Stocum, 2017).

ECM Landscape of an Early Regenerating Limb

Like the limb bud, the blastema ECM also has roles in regulation of patterning by providing a permissive environment for cell migration and proliferation to occur, while maintaining cells in an undifferentiated state. Here, we discuss the role of a transitional matrix present at the stump tissue and blastema during muscle regeneration in the limb in regulating the earlier stages of regeneration. Although regeneration of a limb recapitulates many developmental processes, a transitional matrix is needed to enable recruitment of differentiated cells and reprogram them into a progenitor state, which is not required during development. This transitional matrix serves as an "incubator" region for progenitors cells, priming them to the specified lineages (**Figures 4D,E**). Towards the end of regeneration, the new tissue needs to seamlessly integrate with the original tissue by downregulating components of the transitional matrix. This enables restoration of the native ECM which is described in the example of the regenerating limb muscle (**Figure 4F**).

Building the Transitional Matrix at the Wound Site: The Role of MMPs

Initiation of limb regeneration requires formation of a wound epithelium, which is achieved through migration of keratinocytes to cover the amputated limb within 24 h (**Figure 4B**). Keratinocytes delaminate from the wound epithelium, proliferate and migrate across the injury site over a fibrin and FN network (Donaldson and Mahan, 1983; Donaldson et al., 1989). This requires activation of MMP9 activity (**Figure 4B**), enabling filopodia formation to occur (Ferris et al., 2010). From this, an AEC is formed that serves similar functions as the limb bud AER, providing essential FGF signals to the underlying blastemal cells (**Figure 4C**; Campbell and Crews, 2008). A striking difference is the AEC consists of several layers of cells that covers the entire amputated stump, whereas the AER protrudes as a ridge that is located at the dorsal ventral boundary of the limb bud. This difference may reflect the need for a larger number of cells at the AEC to sustain a broader morphogen range and patterning of information to direct the differentiation of cells to build the niche to reconstruct the missing part.

The early AEC lacks an underlying basement membrane structure (Repesh and Oberpriller, 1980; Neufeld and Day, 1996). Thus, facilitating interactions between the AEC and the underlying blastemal cells (Neufeld and Day, 1996). With blastema outgrowth, cells at the AEC express additional MMPs (nCol, MMP9, MMP3/10a, and MMP3/10b), to enable active and efficient ECM remodeling at this critical phase of regeneration (**Figure 4C**; Vinarsky et al., 2005). Thus, inhibition of MMPs at this stage will lead to failure of blastema formation, as a thick collagen layer under the epithelium impaired the required

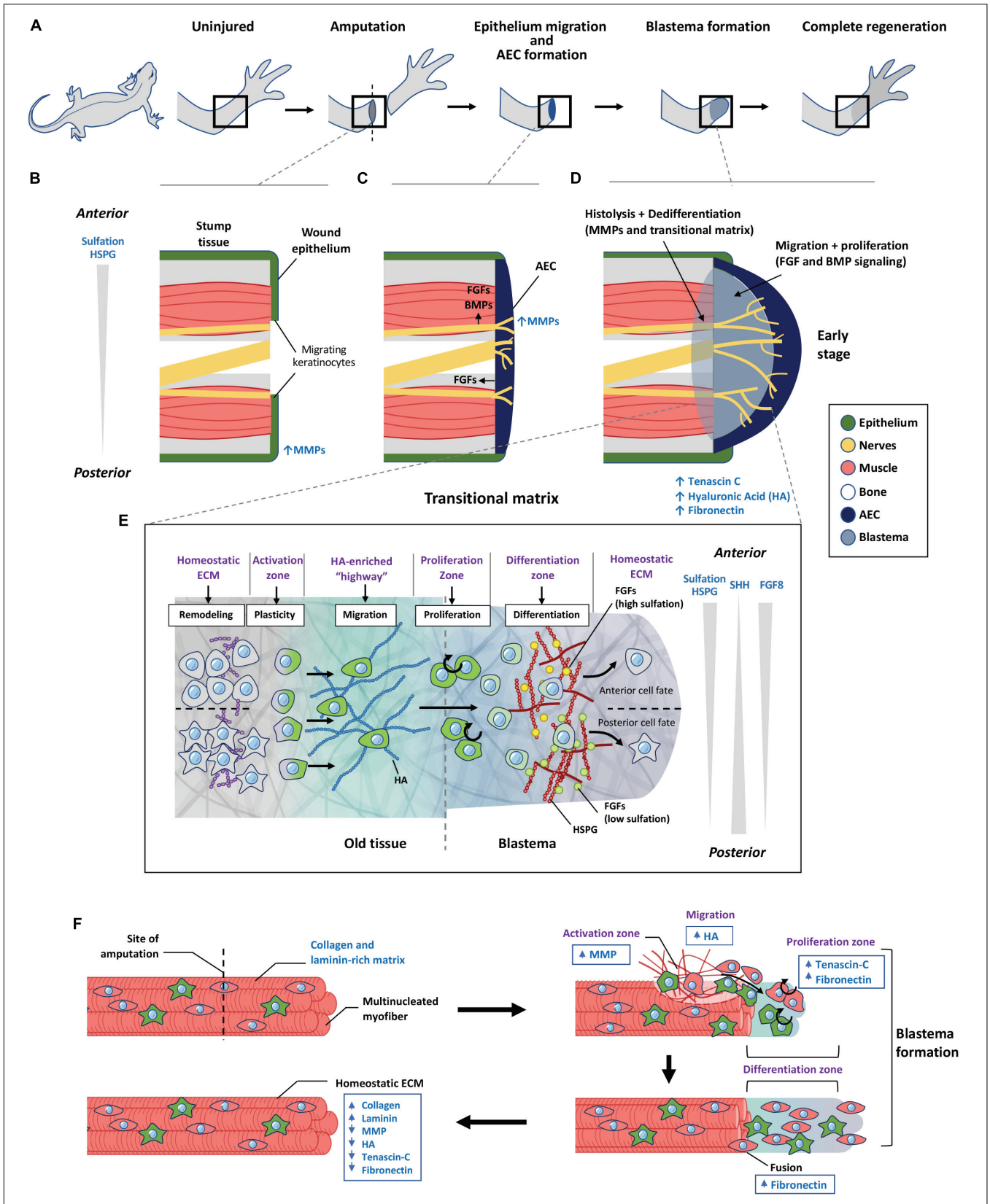


FIGURE 4 | Continued

FIGURE 4 | The role of transitional matrix during limb regeneration. **(A)** Overview of limb regeneration. **(B)** After amputation, a wound epithelium is formed through migration of keratinocytes across the wound stump along with the upregulation of MMPs to facilitate degradation of the collagen and laminin-rich ECM. **(C)** As more cells migrate from the epithelium, the wound epithelium is transformed into the multi-cell layered AEC covering the entire wound stump. The AEC and neurons provide essential FGF and BMP signals to initiate blastema formation. MMP expression remains high during this initial stage of blastema formation. **(D)** Formation of the blastema requires remodeling of the ECM to form a transitional matrix. TNC, HA, and FN are upregulated in the distal stump and blastema mesenchyme which enhances dedifferentiation of myofibers, followed by migration and proliferation which depend on FGFs and BMPs to sustain the outgrowth of the blastema. **(E)** ECM regulation of cellular events that occur over during regeneration. Remodeling of the ECM in the old tissue activates cellular reprogramming and migration to form the blastema. Here cells undergo proliferation and differentiation to form the missing tissue. Differences in sulfation levels of HSPG spatially regulate FGF signaling to direct anterior and posterior positional identities. Similar to the limb bud, SHH and FGF8 gradients regulate anterior posterior polarity during later stages of limb regeneration. **(F)** Model of transitional matrix regulation of muscle regeneration. Upon injury, an upregulation of MMPs degrades the native ECM, while upregulation of TNC, HA in the distal stump and blastema promotes dedifferentiation and migration of muscle. Upregulation of FN in the blastema enhances proliferation and fusion of muscle progenitors into myofibers. When regeneration is complete, the transitional matrix components are downregulated, while collagen and laminin is upregulated. The resulting environment therefore returns to the original native ECM of the uninjured muscle. AEC, apical ectodermal cap; HSPG, heparan sulfate proteoglycan; MMP, matrix metalloproteinase; HA, hyaluronic acid.

communication of signals between the AEC with the underlying cells (Vinarsky et al., 2005). Later in regeneration, the AEC begins to build its own ECM niche including FN (Christensen and Tassava, 2000), laminin (Del Rio-Tsonis et al., 1992), collagen IV (Del Rio-Tsonis et al., 1992), and collagen XII (Wei et al., 1995) in its reconstruction of the basement membrane.

MMPs are also activated in the old tissue near the wound site to degrade the existing ECM and to rebuild an integrative boundary between the old and new tissues. MMPs deposited by the wound epithelium and invading macrophages digest the collagen-rich ECM (**Figures 4B,C**), allowing cells to migrate away from their original environment through a process called histolysis (Godwin et al., 2013; Stocum, 2017). With this, the collagen II matrix in differentiated muscle is reduced (Mailman and Dresden, 1976; Gulati et al., 1983a), as well as major basement membrane components including collagen IV and laminins (Mailman and Dresden, 1976; Gulati et al., 1983a; Rao et al., 2009). The boundary between the old and new tissues is a critical site of the transitional matrix where histolysis and cellular dedifferentiation take place concomitantly (**Figure 4D**).

Within the old tissue, this change in the ECM environment will alter the niche of specific progenitor cells to proliferate and migrate, or activate dedifferentiation of specific tissue cell types, to be mobilized to build the permissive transitional matrix within the growing blastema. It is also possible that specific MMP-derived cryptic signals from the degradation of ECM molecules could contribute to new cell signaling driving the cellular processes (Schenk and Quaranta, 2003). For example, in the newt limb blastema, the degraded matrix is then replaced by a TNC, FN, and HA-rich matrix (**Figures 4D,F**; Calve et al., 2010), resembling the limb bud environment that will encourage cellular dedifferentiation, proliferation, and migration.

Transitional Matrix Enhances Cellular Dedifferentiation, Proliferation, and Migration

FGF and BMP signals presented to the injured tissues initiate blastema formation and blastema growth, which depends on dedifferentiation and recruitment of progenitor cells from the stump tissue into the forming blastema. The properties of the ECM present during this stage is similar in nature to the ECM in the developing limb, providing a hydrated and soft matrix for cells to navigate and maintain their progenitor state at early stages of limb regeneration. Initial activation of myofiber dedifferentiation also resembles the first concept of a stationary cell (**Figure 1B**) responding to signals and changes that occur in the ECM, resulting in fragmentation and migration out of the old tissue into the blastema (Calve et al., 2010). Here, we provide an example for muscle regeneration where the transitional matrix likely supports plasticity, proliferation, and migration that can apply to other cell types found in the blastema (Calve et al., 2010).

After amputation, the ECM surrounding muscle fibers in the stump region is remodeled from a collagen and laminin rich matrix, to a TNC and HA rich matrix, preceding cellular proliferation with the induction of DNA synthesis (**Figure 4F**; Calve et al., 2010). TNC is normally localized to defined tissues such as tendons and myotendinous junctions. During regeneration TNC becomes widely distributed throughout the regenerating blastema with a higher level at the distal portion of the stump tissue (Calve et al., 2010). HA is has a similar distribution in a normal blastema (Calve et al., 2010). The dynamic change of HA is similar to limb bud formation, facilitating proliferation and migration. TNC promotes proliferation through its anti-substrate adhesive property as it binds to cells (Murphy-Ullrich, 2001).

TNC can also trigger a series of myogenic programming through two master regulators myoG and myoD, and proliferation through cyclin A upregulation (Fluck et al., 2008). An enrichment of TNC and HA surrounding muscle fibers could therefore support dedifferentiation through fragmentation into mononucleate myoblasts, which then migrate toward the blastema and undergo proliferation (Kumar et al., 2000; Calve et al., 2010; **Figure 4F**). With dedifferentiation, cells may express embryonic-like antigens that could be targeted by circulating immune cells such as lymphocytes and macrophages. It is thought that deposition of HA in the PCM can prevent an undesired immune response, protects migrating blastemal cells by masking embryonic-like antigens (Alibardi, 2017). As regeneration proceeds to the formation of skeletal elements, both TNC and HA expression is downregulated in regions of condensing cartilage anlagens, allowing cellular aggregation and tissue morphogenesis to be initiated (Calve et al., 2010).

The mechanical property of the transitional matrix is less stiff compared to the stump tissue, that in part contributes myoblast plasticity during regeneration. It has been shown that a soft

TNC matrix enhances myofiber fragmentation and migration, while myoblast fusion is promoted in stiffer laminin or FN matrix (Calve and Simon, 2012). FN is less dynamically expressed compared to TNC and HA, but is upregulated together with TNC and HA under the wound epidermis (Christensen and Tassava, 2000; Calve et al., 2010). As regeneration proceeds, there is an increase in FN in the blastema mesenchyme (Gulati et al., 1983b; Nace and Tassava, 1995) which could promote proliferation, and also serve to enhance redifferentiation of myoblasts and fusion to form myotubes (**Figure 4F**; Calve et al., 2010; Calve and Simon, 2012). Thus, in the limb blastema, the dynamic changes in transitional matrix also fine tunes the mechanical environment contributing to cellular reprogramming and re-differentiation.

A Return to the "Native" ECM and Homeostatic Cell Niche

As regeneration proceeds, the ECM composition eventually changes to support differentiation and integration of the old and new tissue by a gradual transition back to the original matrix which is indistinguishable from the previously uninjured tissue. For this to occur, inhibition of MMPs in the regenerating tissue is suppressed by the upregulation of tissue inhibitors of metalloproteinases (TIMPS) (Stocum, 2017), together with upregulation of ECM proteins including laminins and other basal lamina components which promotes myoblast differentiation (Calve et al., 2010; Calve and Simon, 2012). Similarly, expressions of TNC and HA are downregulated (Calve and Simon, 2012) such that the muscle microenvironment no longer promotes dedifferentiation, proliferation and migration of cells (**Figure 4F**). Eventually, plasticity of cells is suppressed as the transitional matrix is further remodeled toward a differentiation inducing environment to complete the regenerative process, resetting all systems back to an original native ECM and homeostatic cell niche (Gulati et al., 1983a; Neufeld and Day, 1996; Mescher, 2004).

ECM REMODELING DURING MAMMALIAN SKELETAL MUSCLE REGENERATION

Mammalians are unable to fully regenerate limbs, however, there are certain tissues such as the skin, liver, and skeletal muscle that are able to undergo repairs that can be considered as "regeneration." In mammalian skeletal muscle, regeneration does not involve dedifferentiation, but rather recruitment of muscle progenitor satellite cells (Relaix and Zammit, 2012). Skeletal muscle regeneration is less complex than limb regeneration, but similar concepts apply for the need to recruit progenitor cells through remodeling of the ECM. Here we can observe how each of the 3 concepts described above are applied during this process.

Under homeostatic conditions, satellite cells are kept in a quiescent state until the muscle is damaged and disruption to their surrounding basement membrane leads to activation of these cells (Blanco-Bose et al., 2001; Dumont et al., 2015; Feige et al., 2018; **Figure 1B**). The ECM niche of satellite cells is located between the sarcolemma and basal lamina of mature muscle fibers (Mauro, 1961). The basal side of the cell attaches to the basal lamina by α7β1 integrin and dystroglycan (Blanco-Bose et al., 2001; Dumont et al., 2015; Feige et al., 2018), which establishes a "polarized niche" that promotes satellite cells to enter a quiescent state (Dumont et al., 2015). Satellite cells contribute to their own niche by depositing basal lamina components such as HSPG Syndecan-3 and Syndecan-4 (Cornelison et al., 2001), which is an example of the stationary cell model (**Figure 1B**).

Activation of cells to undergo proliferation required remodeling of the ECM, as a form of a simplified transitional matrix (**Figure 1D**). Here, FGF2 is also involved in directing proliferation of satellite cells, which is regulated by an increase in 6-O and 2-O-sulfation of HS chains, as genetic ablation of HSPGs leads to impaired muscle regeneration in mice (Cornelison et al., 2004). Hence, sulfation of HSPG appears to be a common regulator in activating cells in directing tissue outgrowth, repair and regeneration.

Lastly, differentiation is regulated by the ECM the migrating satellite cell encounters at the site of injury (**Figure 1C**). Following activation, the muscle progenitor cell migrates along the longitudinal axis of the injured myofiber, along the remnant basal lamina known as a "ghost fiber" (Vracko and Benditt, 1972; Webster et al., 2016) and differentiates into nascent myofibers (Webster et al., 2016). Migrating myoblast-ghost fiber interaction is likely to promote cell fusion into multinucleated fibers, as demonstrated by seeding myoblasts on Matrigel in culture (Melo et al., 1996). Although the detailed mechanism is not known, proteoglycans, FN and laminins are involved in this process (Melo et al., 1996). Disrupted integrin binding to the RGD (arg-gly-asp) domain on FN, collagens, and laminins in culture leads to impaired myoblast fusion (Menko and Boettiger, 1987). These findings are similar to axolotl limb blastema where laminins and FN facilitates formation of new muscle fibers.

This demonstrates how different components of ECM serve to regulate each stage of repair, and that the similarity of ECM proteins involved in both limb and skeletal muscle regenerative processes, including cell activation and differentiation, indicates an evolutionary conserved role of the ECM in controlling the fates of muscle progenitor.

DISCUSSION

The plasticity of cells is now accepted as a common paradigm whereby the fate of a cell is no longer defined by a differentiated end point, but rather a potentially dynamic state that can be altered given the right microenvironment or niche, to be maintained or changed for a specific outcome. Clearly, our definition of cells need to be revised and as we consider the journey of cells in developmental and regenerative processes, and how they may be recruited in addition to the stem cell pool. The hypertrophic chondrocyte is an example of a cell that may falls into such a category of being capable of existing as a type of "multiple potent progenitor cell."

While the examples given in this review describe events that happen in different context, in reality, the different scenarios can occur within a specific tissue or different stages of process of development and regeneration. The activation stage depends on local microenvironment changes to activate a local cell population to change, while the migration of cells then brings them into a new environment to proliferate and migrate to the target sites. In regeneration, a transitional matrix is likely to be involved during the entire process, first by creating an environment permissive for proliferation and/or migration, followed by deposition of new ECM that will direct the construction of the missing structures.

The concept of ECM holding positional cues in regulating tissue patterning is exemplified in the axolotl accessory limb model, where the ability to induce the formation and patterning of a blastema on an anterior wound region of the limb by decellularized skin grafts, is dependent on the original anterior or posterior location of the graft (Phan et al., 2015). This in turn is related to the differential sulfation pattern of HSPG present in the anterior or posterior skin grafts, contributing to spatial regulation of FGF signaling (Phan et al., 2015; **Figure 4E**), analogous to the AER and mesenchymal relationship in normal development of a limb bud (Nogami et al., 2004; Sedita et al., 2004). Interestingly, such positional cues do exist in neonate mammalian skin, such that the graft of a decellularized mouse skin from posterior limb of newborn mice can induce some level of blastema pattern in the accessory limb model that is lost by postnatal day 9 (Phan et al., 2015). Consistently, there is a differential sulfation pattern of HSPG between anterior and posterior skin that is lost by postnatal day 9 (Phan et al., 2015).

Finally, a recent concept of a moving cell population together with a mobile ECM in shaping tissues is intriguing (Loganathan et al., 2016; Hopyan, 2017), raising the potential of need to consider and capture the molecular cues into the world of tissue engineering for repair of regeneration of missing tissues, whereby engineered tissues with cells are implanted, to direct migration of relevant structures together with cells in facilitating the integration and repair process.

Given the ever-growing importance of the ECM, the use of native or biomimetic scaffolds is an area of continuous development, with studies aiming to engineer fully customizable and tunable scaffolds which are biocompatible with native tissues, that can then guide progenitor cells or resident cells toward specific outcomes. Development of tools (Jenkins and Little, 2019), such as electrospinning, 3D bioprinting, lithography, and even a hybrid of different techniques (Dalton et al., 2020), enable the construction of increasingly detailed structures that can better mimic the *in vivo* environment.

For example, scaffolds such as the self-assembling peptide amphiphiles (Sato et al., 2018) developed in recent years is an example of how these scaffolds can be specifically designed to suit regeneration of different tissues such as muscle (Sleep et al., 2017) and nerves (Cheng et al., 2013; Matsuoka et al., 2017). In these studies, peptides mimicking various ECM proteins, such as collagen (Gore et al., 2001; Luo and Tong, 2011), laminin (Cheng et al., 2013), heparin (Mammadov et al., 2011), and TNC (Sever et al., 2014), were incorporated into peptide amphiphiles. These provide signals to cells that interact with this matrix, promoting behaviors such as proliferation and differentiation of cells which aids in repairing tissues such as muscle and can be degraded and remodeled over time with native ECM (Sleep et al., 2017).

Scaffolds have also been designed for bone related regeneration (Donnaloja et al., 2020), which can incorporate key ECM proteins such as collagen (Zhang et al., 2018) and HA (Zhai et al., 2020), or a combination of synthetic polymers with inorganic materials such as hydroxyapatite (Villa et al., 2015) and calcium phosphate (Sauerova et al., 2019). While significant advances have been made over the last two decades, the ideal scaffold for bone tissue regeneration has yet to be developed (Donnaloja et al., 2020). Therefore, a better understanding of the native ECM in bone biology together with improved scaffold fabrication technology will be of importance to make advances in field of bone tissue regeneration (Donnaloja et al., 2020).

The complexity of tissue and cell specific ECM highlights the relevance to precise matching and modifications of ECM proteins required to coordinate and converge mechanical and biochemical signals to the resident cells. It is important to understand how different ECM components function together in future development of biomimetic scaffolds, and to capture the critical cell and ECM information of tissue development and regeneration processes needed for specific temporal and spatial requirements.

AUTHOR CONTRIBUTIONS

All authors contributed to the conception, planning, and writing of the manuscript.

FUNDING

This work was supported by the Collaborative Research Fund (C7030-18G), Research Grants Council of Hong Kong, and an endowment fund (SY and HY Cheng Professor in Stem Cell Biology and Regenerative Medicine).

REFERENCES

Alibardi, L. (2017). Hyaluronic acid in the tail and limb of amphibians and lizards recreates permissive embryonic conditions for regeneration due to its hygroscopic and immunosuppressive properties. *J. Exp. Zool. B Mol. Dev. Evol.* 328, 760–771. doi: 10.1002/jez.b.22771

Amarilio, R., Viukov, S. V., Sharir, A., Eshkar-Oren, I., Johnson, R. S., and Zelzer, E. (2007). HIF1alpha regulation of Sox9 is necessary to maintain differentiation of hypoxic prechondrogenic cells during early skeletogenesis. *Development* 134, 3917–3928. doi: 10.1242/dev.008441

Arteaga-Solis, E., Gayraud, B., Lee, S. Y., Shum, L., Sakai, L., and Ramirez, F. (2001). Regulation of limb patterning by extracellular microfibrils. *J. Cell Biol.* 154, 275–282. doi: 10.1083/jcb.200105046

Aszodi, A., Hunziker, E. B., Brakebusch, C., and Fassler, R. (2003). Beta1 integrins regulate chondrocyte rotation, G1 progression, and cytokinesis. *Genes Dev.* 17, 2465–2479. doi: 10.1101/gad.277003

Blanco-Bose, W. E., Yao, C. C., Kramer, R. H., and Blau, H. M. (2001). Purification of mouse primary myoblasts based on alpha 7 integrin expression. *Exp. Cell Res.* 265, 212–220. doi: 10.1006/excr.2001.5191

Blau, H., Pavlath, G., Hardeman, E., Chiu, C., Silberstein, L., Webster, S., et al. (1985). Plasticity of the differentiated state. *Science* 230, 758–766. doi: 10.1126/science.2414846

Blau, H. M., Brazelton, T. R., and Weimann, J. M. (2001). The evolving concept of a stem cell: entity or function? *Cell* 105, 829–841. doi: 10.1016/s0092-8674(01)00409-3

Blau, H. M., Chiu, C.-P., and Webster, C. (1983). Cytoplasmic activation of human nuclear genes in stable heterocaryons. *Cell* 32, 1171–1180. doi: 10.1016/0092-8674(83)90300-8

Blau, H. M., and Pomerantz, J. H. (2011). Re"evolutionary" Regenerative medicine. *JAMA* 305, 87–88.

Böse, K., Nischt, R., Page, A., Bader, B. L., Paulsson, M., and Smyth, N. (2006). Loss of nidogen-1 and-2 results in syndactyly and changes in limb development. *J. Biol. Chem.* 281, 39620–39629. doi: 10.1074/jbc.m607886200

Bott, K., Upton, Z., Schrobback, K., Ehrbar, M., Hubbell, J. A., Lutolf, M. P., et al. (2010). The effect of matrix characteristics on fibroblast proliferation in 3D gels. *Biomaterials* 31, 8454–8464. doi: 10.1016/j.biomaterials.2010.07.046

Bryant, D. M., Sousounis, K., Payzin-Dogru, D., Bryant, S., Sandoval, A. G. W., Fernandez, J. M., et al. (2017). Identification of regenerative roadblocks via repeat deployment of limb regeneration in axolotls. *NPJ Regen. Med.* 2, 1–15.

Calve, S., Odelberg, S. J., and Simon, H. G. (2010). A transitional extracellular matrix instructs cell behavior during muscle regeneration. *Dev. Biol.* 344, 259–271. doi: 10.1016/j.ydbio.2010.05.007

Calve, S., and Simon, H. G. (2012). Biochemical and mechanical environment cooperatively regulate skeletal muscle regeneration. *FASEB J.* 26, 2538–2545. doi: 10.1096/fj.11-200162

Campbell, L., and Crews, C. (2008). Wound epidermis formation and function in urodele amphibian limb regeneration. *Cell. Mol. Life Sci. CMLS* 65, 73–79. doi: 10.1007/s00018-007-7433-z

Cheng, T.-Y., Chen, M.-H., Chang, W.-H., Huang, M.-Y., and Wang, T.-W. (2013). Neural stem cells encapsulated in a functionalized self-assembling peptide hydrogel for brain tissue engineering. *Biomaterials* 34, 2005–2016. doi: 10.1016/j.biomaterials.2012.11.043

Christensen, R. N., and Tassava, R. A. (2000). Apical epithelial cap morphology and fibronectin gene expression in regenerating axolotl limbs. *Dev. Dyn.* 217, 216–224. doi: 10.1002/(sici)1097-0177(200002)217:2<216::aid-dvdy8>3.0.co;2-8

Cooper, K. L., Oh, S., Sung, Y., Dasari, R. R., Kirschner, M. W., and Tabin, C. J. (2013). Multiple phases of chondrocyte enlargement underlie differences in skeletal proportions. *Nature* 495, 375–378. doi: 10.1038/nature11940

Cornelison, D. D., Filla, M. S., Stanley, H. M., Rapraeger, A. C., and Olwin, B. B. (2001). Syndecan-3 and syndecan-4 specifically mark skeletal muscle satellite cells and are implicated in satellite cell maintenance and muscle regeneration. *Dev. Biol.* 239, 79–94. doi: 10.1006/dbio.2001.0416

Cornelison, D. D., Wilcox-Adelman, S. A., Goetinck, P. F., Rauvala, H., Rapraeger, A. C., and Olwin, B. B. (2004). Essential and separable roles for Syndecan-3 and Syndecan-4 in skeletal muscle development and regeneration. *Genes Dev.* 18, 2231–2236. doi: 10.1101/gad.1214204

Crossley, P. H., and Martin, G. R. (1995). The mouse Fgf8 gene encodes a family of polypeptides and is expressed in regions that direct outgrowth and patterning in the developing embryo. *Development* 121, 439–451.

Culty, M., Nguyen, H. A., and Underhill, C. B. (1992). The hyaluronan receptor (CD44) participates in the uptake and degradation of hyaluronan. *J. Cell Biol.* 116, 1055–1062. doi: 10.1083/jcb.116.4.1055

Currie, J. D., Kawaguchi, A., Traspas, R. M., Schuez, M., Chara, O., and Tanaka, E. M. (2016). Live imaging of axolotl digit regeneration reveals spatiotemporal choreography of diverse connective tissue progenitor pools. *Dev. Cell* 39, 411–423. doi: 10.1016/j.devcel.2016.10.013

Dalton, P. D., Woodfield, T. B., Mironov, V., and Groll, J. (2020). Advances in hybrid fabrication toward hierarchical tissue constructs. *Adv. Sci.* 2020:1902953. doi: 10.1002/advs.201902953

Davis, A. P., Witte, D. P., Hsieh-Li, H. M., Potter, S. S., and Capecchi, M. R. (1995). Absence of radius and ulna in mice lacking hoxa-11 and hoxd-11. *Nature* 375, 791–795. doi: 10.1038/375791a0

Davis, G. E., Bayless, K. J., Davis, M. J., and Meininger, G. A. (2000). Regulation of tissue injury responses by the exposure of matricryptic sites within extracellular matrix molecules. *Am. J. Pathol.* 156, 1489–1498. doi: 10.1016/s0002-9440(10)65020-1

Davis, R. L., Weintraub, H., and Lassar, A. B. (1987). Expression of a single transfected cDNA converts fibroblasts to myoblasts. *Cell* 51, 987–1000. doi: 10.1016/0092-8674(87)90585-x

Del Rio-Tsonis, K., Washabaugh, C. H., and Tsonis, P. A. (1992). The mutant axolotl Short toes exhibits impaired limb regeneration and abnormal basement membrane formation. *Proc. Natl. Acad. Sci. U.S.A.* 89, 5502–5506. doi: 10.1073/pnas.89.12.5502

Deries, M., and Thorsteinsdóttir, S. (2016). Axial and limb muscle development: dialogue with the neighbourhood. *Cell. Mol. Life Sci.* 73, 4415–4431. doi: 10.1007/s00018-016-2298-7

Dierker, T., Dreier, R., Petersen, A., Bordych, C., and Grobe, K. (2009). Heparan sulfate-modulated, metalloprotease-mediated sonic hedgehog release from producing cells. *J. Biol. Chem.* 284, 8013–8022. doi: 10.1074/jbc.m806838200

Dityatev, A., and Schachner, M. (2003). Extracellular matrix molecules and synaptic plasticity. *Nat. Rev. Neurosci.* 4, 456–468. doi: 10.1038/nrn1115

Donaldson, D. J., and Mahan, J. T. (1983). Fibrinogen and fibronectin as substrates for epidermal cell migration during wound closure. *J. Cell Sci.* 62, 117–127.

Donaldson, D. J., Mahan, J. T., Amrani, D., and Hawiger, J. (1989). Fibrinogen-mediated epidermal cell migration: structural correlates for fibrinogen function. *J. Cell Sci.* 94, 101–108.

Donnaloja, F., Jacchetti, E., Soncini, M., and Raimondi, M. T. (2020). Natural and synthetic polymers for bone scaffolds optimization. *Polymers* 12:905. doi: 10.3390/polym12040905

Dowthwaite, G. P., Edwards, J. C., and Pitsillides, A. A. (1998). An essential role for the interaction between hyaluronan and hyaluronan binding proteins during joint development. *J. Histochem. Cytochem.* 46, 641–651. doi: 10.1177/002215549804600509

Dumont, N. A., Wang, Y. X., Von Maltzahn, J., Pasut, A., Bentzinger, C. F., Brun, C. E., et al. (2015). Dystrophin expression in muscle stem cells regulates their polarity and asymmetric division. *Nat. Med.* 21, 1455–1463. doi: 10.1038/nm.3990

Dy, P., Wang, W., Bhattaram, P., Wang, Q., Wang, L., Ballock, R. T., et al. (2012). Sox9 directs hypertrophic maturation and blocks osteoblast differentiation of growth plate chondrocytes. *Dev. Cell* 22, 597–609. doi: 10.1016/j.devcel.2011.12.024

Edwards, J. C., Wilkinson, L. S., Jones, H. M., Soothill, P., Henderson, K. J., Worrall, J. G., et al. (1994). The formation of human synovial joint cavities: a possible role for hyaluronan and CD44 in altered interzone cohesion. *J. Anat.* 185(Pt 2), 355–367.

Engler, A. J., Sen, S., Sweeney, H. L., and Discher, D. E. (2006). Matrix elasticity directs stem cell lineage specification. *Cell* 126, 677–689. doi: 10.1016/j.cell.2006.06.044

Estrov, Z. (2009). Stem cells and somatic cells: reprogramming and plasticity. *Clin. Lymphoma Myeloma* 9(Suppl. 3), S319–S328.

Feige, P., Brun, C. E., Ritso, M., and Rudnicki, M. A. (2018). Orienting muscle stem cells for regeneration in homeostasis, aging, and disease. *Cell Stem Cell* 23, 653–664. doi: 10.1016/j.stem.2018.10.006

Feng, C., Chan, W. C. W., Lam, Y., Wang, X., Chen, P., Niu, B., et al. (2019). Lgr5 and Col22a1 mark progenitor cells in the lineage toward juvenile articular chondrocytes. *Stem Cell Rep.* 13, 713–729. doi: 10.1016/j.stemcr.2019.08.006

Ferris, D. R., Satoh, A., Mandefro, B., Cummings, G. M., Gardiner, D. M., and Rugg, E. L. (2010). Ex vivo generation of a functional and regenerative wound epithelium from axolotl (Ambystoma mexicanum) skin. *Dev. Growth Diff.* 52, 715–724. doi: 10.1111/j.1440-169x.2010.01208.x

Fluck, M., Mund, S. I., Schittny, J. C., Klossner, S., Durieux, A. C., and Giraud, M. N. (2008). Mechano-regulated tenascin-C orchestrates muscle repair. *Proc. Natl. Acad. Sci. U.S.A.* 105, 13662–13667. doi: 10.1073/pnas.0805365105

Galatz, L., Rothermich, S., Vanderploeg, K., Petersen, B., Sandell, L., and Thomopoulos, S. (2007). Development of the supraspinatus tendon-to-bone insertion: localized expression of extracellular matrix and growth factor genes. *J. Orthop. Res.* 25, 1621–1628. doi: 10.1002/jor.20441

Garciadiego-Cazares, D., Rosales, C., Katoh, M., and Chimal-Monroy, J. (2004). Coordination of chondrocyte differentiation and joint formation by alpha5beta1 integrin in the developing appendicular skeleton. *Development* 131, 4735–4742. doi: 10.1242/dev.01345

Gerardo, H., Lima, A., Carvalho, J., Ramos, J. R., Couceiro, S., Travasso, R. D., et al. (2019). Soft culture substrates favor stem-like cellular phenotype and facilitate reprogramming of human mesenchymal stem/stromal cells (hMSCs) through mechanotransduction. *Sci. Rep.* 9, 1–18.

Gerber, H. P., Vu, T. H., Ryan, A. M., Kowalski, J., Werb, Z., and Ferrara, N. (1999). VEGF couples hypertrophic cartilage remodeling, ossification and angiogenesis during endochondral bone formation. *Nat. Med.* 5, 623–628. doi: 10.1038/9467

Gerber, T., Murawala, P., Knapp, D., Masselink, W., Schuez, M., Hermann, S., et al. (2018). Single-cell analysis uncovers convergence of cell identities during axolotl limb regeneration. *Science* 362:eaaq0681. doi: 10.1126/science.aaq0681

Giampaoli, S., Bucci, S., Ragghianti, M., Mancino, G., Zhang, F., and Ferretti, P. (2003). Expression of FGF2 in the limb blastema of two Salamandridae correlates with their regenerative capability. *Proc. R. Soc. Lond. Ser. B Biol. Sci.* 270, 2197–2205. doi: 10.1098/rspb.2003.2439

Gilbert, P. M., Havenstrite, K. L., Magnusson, K. E., Sacco, A., Leonardi, N. A., Kraft, P., et al. (2010). Substrate elasticity regulates skeletal muscle stem cell self-renewal in culture. *Science* 329, 1078–1081. doi: 10.1126/science.1191035

Giovannone, D., Paul, S., Schindler, S., Arata, C., Farmer, D. T., Patel, P., et al. (2019). Programmed conversion of hypertrophic chondrocytes into osteoblasts and marrow adipocytes within zebrafish bones. *eLife* 8:e42736.

Godfrey, E., and Gradall, K. S. (1998). Basal lamina molecules are concentrated in myogenic regions of the mouse limb bud. *Anat. Embryol.* 198, 481–486. doi: 10.1007/s004290050198

Godwin, J. W., Pinto, A. R., and Rosenthal, N. A. (2013). Macrophages are required for adult salamander limb regeneration. *Proc. Natl. Acad. Sci. U.S.A.* 110, 9415–9420. doi: 10.1073/pnas.1300290110

Gore, T., Dori, Y., Talmon, Y., Tirrell, M., and Bianco-Peled, H. (2001). Self-assembly of model collagen peptide amphiphiles. *Langmuir* 17, 5352–5360. doi: 10.1021/la010223i

Gros, J., Hu, J. K.-H., Vinegoni, C., Feruglio, P. F., Weissleder, R., and Tabin, C. J. (2010). WNT5A/JNK and FGF/MAPK pathways regulate the cellular events shaping the vertebrate limb bud. *Curr. Biol.* 20, 1993–2002. doi: 10.1016/j.cub.2010.09.063

Gros, J., and Tabin, C. J. (2014). Vertebrate limb bud formation is initiated by localized epithelial-to-mesenchymal transition. *Science* 343, 1253–1256. doi: 10.1126/science.1248228

Gulati, A. K., Reddi, A. H., and Zalewski, A. A. (1983a). Changes in the basement membrane zone components during skeletal muscle fiber degeneration and regeneration. *J. Cell. Biol.* 97, 957–962. doi: 10.1083/jcb.97.4.957

Gulati, A. K., Zalewski, A. A., and Reddi, A. H. (1983b). An immunofluorescent study of the distribution of fibronectin and laminin during limb regeneration in the adult newt. *Dev. Biol.* 96, 355–365. doi: 10.1016/0012-1606(83)90173-2

Guo, J., Wang, Y., Sachs, F., and Meng, F. (2014). Actin stress in cell reprogramming. *Proc. Natl. Acad. Sci. U.S.A.* 111, E5252–E5261.

Guo, X., Day, T. F., Jiang, X., Garrett-Beal, L., Topol, L., and Yang, Y. (2004). Wnt/beta-catenin signaling is sufficient and necessary for synovial joint formation. *Genes Dev.* 18, 2404–2417. doi: 10.1101/gad.1230704

Han, M. J., An, J. Y., and Kim, W. S. (2001). Expression patterns of Fgf-8 during development and limb regeneration of the axolotl. *Dev. Dyn.* 220, 40–48. doi: 10.1002/1097-0177(2000)9999:9999<::aid-dvdy1085>3.0.co;2-8

He, X., Ohba, S., Hojo, H., and Mcmahon, A. P. (2016). AP-1 family members act with Sox9 to promote chondrocyte hypertrophy. *Development* 143, 3012–3023. doi: 10.1242/dev.134502

Hopyan, S. (2017). Biophysical regulation of early limb bud morphogenesis. *Dev. Biol.* 429, 429–433. doi: 10.1016/j.ydbio.2017.06.034

Hu, D. P., Ferro, F., Yang, F., Taylor, A. J., Chang, W., Miclau, T., et al. (2017). Cartilage to bone transformation during fracture healing is coordinated by the invading vasculature and induction of the core pluripotency genes. *Development* 144, 221–234. doi: 10.1242/dev.130807

Hua, Q., Knudson, C. B., and Knudson, W. (1993). Internalization of hyaluronan by chondrocytes occurs via receptor-mediated endocytosis. *J. Cell Science* 106, 365–375.

Hurle, J. M., Corson, G., Daniels, K., Reiter, R. S., Sakai, L. Y., and Solursh, M. (1994). Elastin exhibits a distinctive temporal and spatial pattern of distribution in the developing chick limb in association with the establishment of the cartilaginous skeleton. *J. Cell Sci.* 107, 2623–2634.

Ieda, M., Fu, J.-D., Delgado-Olguin, P., Vendatham, V., Hayashi, Y., Bruneau, B. G., et al. (2010). Direct reprogramming of fibroblasts into functional cardiomyocytes by defined factors. *Cell* 142, 375–386. doi: 10.1016/j.cell.2010.07.002

Ivankovic, M., Haneckova, R., Thommen, A., Grohme, M. A., Vila-Farré, M., Werner, S., et al. (2019). Model systems for regeneration: planarians. *Development* 146:dev167684. doi: 10.1242/dev.167684

Jahed, Z., and Mofrad, M. R. (2019). The nucleus feels the force, LINCed in or not! *Curr. Opin. Cell Biol.* 58, 114–119. doi: 10.1016/j.ceb.2019.02.012

Jenkins, T. L., and Little, D. (2019). Synthetic scaffolds for musculoskeletal tissue engineering: cellular responses to fiber parameters. *NPJ Regen. Med.* 4, 1–14.

Jiang, Y., Cai, Y., Zhang, W., Yin, Z., Hu, C., Tong, T., et al. (2016). Human cartilage-derived progenitor cells from committed chondrocytes for efficient cartilage repair and regeneration. *Stem Cells Transl. Med.* 5, 733–744. doi: 10.5966/sctm.2015-0192

Jin, L., Wu, J., Bellusci, S., and Zhang, J.-S. (2019). Fibroblast growth factor 10 and vertebrate limb development. *Front. Genet.* 9:705. doi: 10.3389/fgene.2018.00705

Jopling, C., Sleep, E., Raya, M., Martí, M., Raya, A., and Belmonte, J. C. I. (2010). Zebrafish heart regeneration occurs by cardiomyocyte dedifferentiation and proliferation. *Nature* 464, 606–609. doi: 10.1038/nature08899

Kaur, S., Siddiqui, H., and Bhat, M. H. (2015). Hepatic progenitor cells in action: liver regeneration or fibrosis? *Am. J. Pathol.* 185, 2342–2350.

Knapp, D., Schulz, H., Rascon, C. A., Volkmer, M., Scholz, J., Nacu, E., et al. (2013). Comparative transcriptional profiling of the axolotl limb identifies a tripartite regeneration-specific gene program. *PLoS One* 8:e61352. doi: 10.1371/journal.pone.0061352

Knudson, C. B., and Toole, B. P. (1985). Changes in the pericellular matrix during differentiation of limb bud mesoderm. *Dev. Biol.* 112, 308–318. doi: 10.1016/0012-1606(85)90401-4

Kobayashi, T., Chung, U. I., Schipani, E., Starbuck, M., Karsenty, G., Katagiri, T., et al. (2002). PTHrP and Indian hedgehog control differentiation of growth plate chondrocytes at multiple steps. *Development* 129, 2977–2986.

Kobayashi, T., Habuchi, H., Nogami, K., Ashikari-Hada, S., Tamura, K., Ide, H., et al. (2010). Functional analysis of chick heparan sulfate 6-O-sulfotransferases in limb bud development. *Dev. Growth Diff.* 52, 146–156. doi: 10.1111/j.1440-169x.2009.01148.x

Koch, M., Schulze, J., Hansen, U., Ashwodt, T., Keene, D. R., Brunken, W. J., et al. (2004). A novel marker of tissue junctions, collagen XXII. *J. Biol. Chem.* 279, 22514–22521. doi: 10.1074/jbc.m400536200

Kosher, R. A., and Savage, M. P. (1981). Glycosaminoglycan synthesis by the apical ectodermal ridge of chick limb bud. *Nature* 291, 231–232. doi: 10.1038/291231a0

Koyama, E., Shibukawa, Y., Nagayama, M., Sugito, H., Young, B., Yuasa, T., et al. (2008). A distinct cohort of progenitor cells participates in synovial joint and articular cartilage formation during mouse limb skeletogenesis. *Dev. Biol.* 316, 62–73. doi: 10.1016/j.ydbio.2008.01.012

Koziel, L., Kunath, M., Kelly, O. G., and Vortkamp, A. (2004). Ext1-dependent heparan sulfate regulates the range of Ihh signaling during endochondral ossification. *Dev. Cell.* 6, 801–813. doi: 10.1016/j.devcel.2004.05.009

Kronenberg, H. M. (2003). Developmental regulation of the growth plate. *Nature* 423, 332–336. doi: 10.1038/nature01657

Kumar, A., Velloso, C. P., Imokawa, Y., and Brockes, J. P. (2000). Plasticity of retrovirus-labelled myotubes in the newt limb regeneration blastema. *Dev. Biol.* 218, 125–136. doi: 10.1006/dbio.1999.9569

Kwan, K. M., Pang, M. K., Zhou, S., Cowan, S. K., Kong, R. Y., Pfordte, T., et al. (1997). Abnormal compartmentalization of cartilage matrix components in mice lacking collagen X: implications for function. *J. Cell. Biol.* 136, 459–471. doi: 10.1083/jcb.136.2.459

Laufer, E., Nelson, C. E., Johnson, R. L., Morgan, B. A., and Tabin, C. (1994). Sonic hedgehog and Fgf-4 act through a signaling cascade and feedback loop to integrate growth and patterning of the developing limb bud. *Cell* 79, 993–1003. doi: 10.1016/0092-8674(94)90030-2

Leung, V. Y., Gao, B., Leung, K. K., Melhado, I. G., Wynn, S. L., Au, T. Y., et al. (2011). SOX9 governs differentiation stage-specific gene expression in growth

plate chondrocytes via direct concomitant transactivation and repression. *PLoS Genet.* 7:e1002356. doi: 10.1371/journal.pgen.1002356

Li, Y., Toole, B. P., Dealy, C. N., and Kosher, R. A. (2007). Hyaluronan in limb morphogenesis. *Dev. Biol.* 305, 411–420. doi: 10.1016/j.ydbio.2007.02.023

Lian, C., Wang, X., Qiu, X., Wu, Z., Gao, B., Liu, L., et al. (2019). Collagen type II suppresses articular chondrocyte hypertrophy and osteoarthritis progression by promoting integrin beta1-SMAD1 interaction. *Bone Res.* 7:8.

Lo, C.-M., Wang, H.-B., Dembo, M., and Wang, Y.-L. (2000). Cell movement is guided by the rigidity of the substrate. *Biophys. J.* 79, 144–152. doi: 10.1016/s0006-3495(00)76279-5

Loganathan, R., Rongish, B. J., Smith, C. M., Filla, M. B., Czirok, A., Bénazéraf, B., et al. (2016). Extracellular matrix motion and early morphogenesis. *Development* 143, 2056–2065. doi: 10.1242/dev.127886

Lu, P., Takai, K., Weaver, V. M., and Werb, Z. (2011). Extracellular matrix degradation and remodeling in development and disease. *Cold Spring Harb. Perspect. Biol.* 3:a005058. doi: 10.1101/cshperspect.a005058

Luo, J., and Tong, Y. W. (2011). Self-assembly of collagen-mimetic peptide amphiphiles into biofunctional nanofiber. *ACS Nano* 5, 7739–7747. doi: 10.1021/nn202822f

Madl, C. M., Heilshorn, S. C., and Blau, H. M. (2018). Bioengineering strategies to accelerate stem cell therapeutics. *Nature* 557, 335–342. doi: 10.1038/s41586-018-0089-z

Mailman, M. L., and Dresden, M. H. (1976). Collagen metabolism in the regenerating forelimb of Notophthalmus viridescens: synthesis, accumulation, and maturation. *Dev. Biol.* 50, 378–394. doi: 10.1016/0012-1606(76)90159-7

Makanae, A., Mitogawa, K., and Satoh, A. (2014). Co-operative Bmp-and Fgf-signaling inputs convert skin wound healing to limb formation in urodele amphibians. *Dev. Biol.* 396, 57–66. doi: 10.1016/j.ydbio.2014.09.021

Mammadov, R., Mammadov, B., Toksoz, S., Aydin, B., Yagci, R., Tekinay, A. B., et al. (2011). Heparin mimetic peptide nanofibers promote angiogenesis. *Biomacromolecules* 12, 3508–3519. doi: 10.1021/bm200957s

Mao, A. S., Shin, J.-W., and Mooney, D. J. (2016). Effects of substrate stiffness and cell-cell contact on mesenchymal stem cell differentiation. *Biomaterials* 98, 184–191. doi: 10.1016/j.biomaterials.2016.05.004

Mao, Y., Block, T., Singh-Varma, A., Sheldrake, A., Leeth, R., Griffey, S., et al. (2019). Extracellular matrix derived from chondrocytes promotes rapid expansion of human primary chondrocytes in vitro with reduced dedifferentiation. *Acta Biomater.* 85, 75–83. doi: 10.1016/j.actbio.2018.12.006

Matsuo, I., and Kimura-Yoshida, C. (2013). Extracellular modulation of Fibroblast Growth Factor signaling through heparan sulfate proteoglycans in mammalian development. *Curr. Opin. Genet. Dev.* 23, 399–407. doi: 10.1016/j.gde.2013.02.004

Matsuoka, A. J., Sayed, Z. A., Stephanopoulos, N., Berns, E. J., Wadhwani, A. R., Morrissey, Z. D., et al. (2017). Creating a stem cell niche in the inner ear using self-assembling peptide amphiphiles. *PLoS One* 12:e0190150. doi: 10.1371/journal.pone.0190150

Mauro, A. (1961). Satellite cell of skeletal muscle fibers. *J. Biophys. Biochem. Cytol.* 9, 493–495. doi: 10.1083/jcb.9.2.493

McBeath, R., Pirone, D. M., Nelson, C. M., Bhadriraju, K., and Chen, C. S. (2004). Cell shape, cytoskeletal tension, and RhoA regulate stem cell lineage commitment. *Dev. Cell* 6, 483–495. doi: 10.1016/s1534-5807(04)00075-9

McCulloch, D. R., Nelson, C. M., Dixon, L. J., Silver, D. L., Wylie, J. D., Lindner, V., et al. (2009). ADAMTS metalloproteases generate active versican fragments that regulate interdigital web regression. *Dev. Cell* 17, 687–698. doi: 10.1016/j.devcel.2009.09.008

Melo, F., Carey, D. J., and Brandan, E. (1996). Extracellular matrix is required for skeletal muscle differentiation but not myogenin expression. *J. Cell. Biochem.* 62, 227–239. doi: 10.1002/(sici)1097-4644(199608)62:2<227::aid-jcb11>3.0.co;2-i

Menko, A. S., and Boettiger, D. (1987). Occupation of the extracellular matrix receptor, integrin, is a control point for myogenic differentiation. *Cell* 51, 51–57. doi: 10.1016/0092-8674(87)90009-2

Mercer, S. E., Odelberg, S. J., and Simon, H.-G. (2013). A dynamic spatiotemporal extracellular matrix facilitates epicardial-mediated vertebrate heart regeneration. *Dev. Biol.* 382, 457–469. doi: 10.1016/j.ydbio.2013.08.002

Merrell, A. J., and Stanger, B. Z. (2016). Adult cell plasticity in vivo: de-differentiation and transdifferentiation are back in style. *Nat. Rev. Mol. Cell Biol.* 17:413. doi: 10.1038/nrm.2016.24

Mescher, A. L. (2004). The cellular basis of limb regeneration in urodeles. *Int. J. Dev. Biol.* 40, 785–795.

Mitrovic, D. (1978). Development of the diarthrodial joints in the rat embryo. *Am. J. Anat.* 151, 475–485. doi: 10.1002/aja.1001510403

Mizuhashi, K., Ono, W., Matsushita, Y., Sakagami, N., Takahashi, A., Saunders, T. L., et al. (2018). Resting zone of the growth plate houses a unique class of skeletal stem cells. *Nature* 563, 254–258. doi: 10.1038/s41586-018-0662-5

Moyer, A. L., and Wagner, K. R. (2011). Regeneration versus fibrosis in skeletal muscle. *Curr. Opin. Rheumatol.* 23, 568–573. doi: 10.1097/bor.0b013e32834bac92

Muneoka, K., Fox, W., and Bryant, S. (1986). Cellular contribution from dermis and cartilage to the regenerating limb blastema in axolotls. *Dev. Biol.* 116, 256–260. doi: 10.1016/0012-1606(86)90062-x

Murphy-Ullrich, J. E. (2001). The de-adhesive activity of matricellular proteins: is intermediate cell adhesion an adaptive state? *J. Clin. Invest.* 107, 785–790. doi: 10.1172/jci12609

Myllyharju, J. (2014). Extracellular matrix and developing growth plate. *Curr. Osteoporos. Rep.* 12, 439–445. doi: 10.1007/s11914-014-0232-1

Nace, J. D., and Tassava, R. A. (1995). Examination of fibronectin distribution and its sources in the regenerating newt limb by immunocytochemistry and in situ hybridization. *Dev. Dyn.* 202, 153–164. doi: 10.1002/aja.1002020207

Nacu, E., Gromberg, E., Oliveira, C. R., Drechsel, D., and Tanaka, E. M. (2016). FGF8 and SHH substitute for anterior–posterior tissue interactions to induce limb regeneration. *Nature* 533, 407–410. doi: 10.1038/nature17972

Nandadasa, S., Foulcer, S., and Apte, S. S. (2014). The multiple, complex roles of versican and its proteolytic turnover by ADAMTS proteases during embryogenesis. *Matrix Biol.* 35, 34–41. doi: 10.1016/j.matbio.2014.01.005

Neufeld, D. A., and Day, F. A. (1996). Perspective: a suggested role for basement membrane structures during newt limb regeneration. *Anat. Rec.* 246, 155–161. doi: 10.1002/(sici)1097-0185(199610)246:2<155::aid-ar1>3.0.co;2-0

Newton, P. T., Li, L., Zhou, B., Schweingruber, C., Hovorakova, M., Xie, M., et al. (2019). A radical switch in clonality reveals a stem cell niche in the epiphyseal growth plate. *Nature* 567, 234–238. doi: 10.1038/s41586-019-0989-6

Nogami, K., Suzuki, H., Habuchi, H., Ishiguro, N., Iwata, H., and Kimata, K. (2004). Distinctive expression patterns of heparan sulfate O-sulfotransferases and regional differences in heparan sulfate structure in chick limb buds. *J. Chem.* 279, 8219–8229. doi: 10.1074/jbc.m307304200

Norton, W. H., Ledin, J., Grandel, H., and Neumann, C. J. (2005). HSPG synthesis by zebrafish Ext2 and Extl3 is required for Fgf10 signalling during limb development. *Development* 132, 4963–4973. doi: 10.1242/dev.02084

Notari, M., Ventura-Rubio, A., Bedford-Guaus, S. J., Jorba, I., Mulero, L., Navajas, D., et al. (2018). The local microenvironment limits the regenerative potential of the mouse neonatal heart. *Sci. Adv.* 4:eaao5553. doi: 10.1126/sciadv.aao5553

Ogawa, H., Kozhemyakina, E., Hung, H. H., Grodzinsky, A. J., and Lassar, A. B. (2014). Mechanical motion promotes expression of Prg4 in articular cartilage via multiple CREB-dependent, fluid flow shear stress-induced signaling pathways. *Genes Dev.* 28, 127–139. doi: 10.1101/gad.231969.113

Ohuchi, H., Nakagawa, T., Yamamoto, A., Araga, A., Ohata, T., Ishimaru, Y., et al. (1997). The mesenchymal factor, FGF10, initiates and maintains the outgrowth of the chick limb bud through interaction with FGF8, an apical ectodermal factor. *Development* 124, 2235–2244.

Ono, N., Ono, W., Nagasawa, T., and Kronenberg, H. M. (2014). A subset of chondrogenic cells provides early mesenchymal progenitors in growing bones. *Nat. cell biol.* 16, 1157–1167. doi: 10.1038/ncb3067

Orr, A. W., Helmke, B. P., Blackman, B. R., and Schwartz, M. A. (2006). Mechanisms of mechanotransduction. *Dev. Cell* 10, 11–20.

Park, J., Gebhardt, M., Golovchenko, S., Perez-Branguli, F., Hattori, T., Hartmann, C., et al. (2015). Dual pathways to endochondral osteoblasts: a novel chondrocyte-derived osteoprogenitor cell identified in hypertrophic cartilage. *Biol. Open* 4, 608–621. doi: 10.1242/bio.201411031

Pelham, R. J., and Wang, Y.-L. (1997). Cell locomotion and focal adhesions are regulated by substrate?flexibility. *Proc. Natl. Acad. Sci. U.S.A.* 94, 13661–13665. doi: 10.1073/pnas.94.25.13661

Phan, A. Q., Lee, J., Oei, M., Flath, C., Hwe, C., Mariano, R., et al. (2015). Positional information in axolotl and mouse limb extracellular matrix is mediated via heparan sulfate and fibroblast growth factor during limb regeneration in the axolotl (*Ambystoma mexicanum*). *Regeneration* 2, 182–201. doi: 10.1002/reg2.40

Poltavets, V., Kochetkova, M., Pitson, S. M., and Samuel, M. S. (2018). The role of the extracellular matrix and its molecular and cellular regulators in cancer cell plasticity. *Front. Oncol.* 8:431. doi: 10.3389/fonc.2018.00431

Prein, C., Warmbold, N., Farkas, Z., Schieker, M., Aszodi, A., and Clausen-Schaumann, H. (2016). Structural and mechanical properties of the proliferative zone of the developing murine growth plate cartilage assessed by atomic force microscopy. *Matrix Biol.* 50, 1–15. doi: 10.1016/j.matbio.2015.10.001

Rao, N., Jhamb, D., Milner, D. J., Li, B., Song, F., Wang, M., et al. (2009). Proteomic analysis of blastema formation in regenerating axolotl limbs. *BMC Biol.* 7:83. doi: 10.1186/1741-7007-7-83

Relaix, F., and Zammit, P. S. (2012). Satellite cells are essential for skeletal muscle regeneration: the cell on the edge returns centre stage. *Development* 139, 2845–2856. doi: 10.1242/dev.069088

Repesh, L. A., and Oberpriller, J. C. (1980). Ultrastructural studies on migrating epidermal cells during the wound healing stage of regeneration in the adult newt, *Notophthalmus viridescens*. *Am. J. Anat.* 159, 187–208. doi: 10.1002/aja.1001590207

Roberts, S., Bains, M. A., Kwan, A., Menage, J., and Eisenstein, S. M. (1998). Type X collagen in the human invertebral disc: an indication of repair or remodelling? *Histochem. J.* 30, 89–95.

Rockey, D. C., Bell, P. D., and Hill, J. A. (2015). Fibrosis—a common pathway to organ injury and failure. *N. Engl. J. Med.* 372, 1138–1149. doi: 10.1056/nejmra1300575

Rousche, K. T., and Knudson, C. B. (2002). Temporal expression of CD44 during embryonic chick limb development and modulation of its expression with retinoic acid. *Matrix Biol.* 21, 53–62. doi: 10.1016/s0945-053x(01)00189-5

Samsa, W. E., Zhou, X., and Zhou, G. (2017). Signaling pathways regulating cartilage growth plate formation and activity. *Semin. Cell Dev. Biol.* 62, 3–15. doi: 10.1016/j.semcdb.2016.07.008

Sato, K., Hendricks, M. P., Palmer, L. C., and Stupp, S. I. (2018). Peptide supramolecular materials for therapeutics. *Chem. Soc. Rev.* 47, 7539–7551. doi: 10.1039/c7cs00735c

Sauerova, P., Suchy, T., Supova, M., Bartos, M., Klima, J., Juhasova, J., et al. (2019). Positive impact of dynamic seeding of mesenchymal stem cells on bone-like biodegradable scaffolds with increased content of calcium phosphate nanoparticles. *Mol. Biol. Rep.* 46, 4483–4500. doi: 10.1007/s11033-019-04903-7

Schenk, S., and Quaranta, V. (2003). Tales from the crypt [ic] sites of the extracellular matrix. *Trends Cell Biol.* 13, 366–375. doi: 10.1016/s0962-8924(03)00129-6

Schroeder, T. M., Jensen, E. D., and Westendorf, J. J. (2005). Runx2: a master organizer of gene transcription in developing and maturing osteoblasts. *Birth Defects Res. C Embryo Today* 75, 213–225. doi: 10.1002/bdrc.20043

Sedita, J., Izvolsky, K., and Cardoso, W. V. (2004). Differential expression of heparan sulfate 6-O-sulfotransferase isoforms in the mouse embryo suggests distinctive roles during organogenesis. *Dev. Dyn.* 231, 782–794. doi: 10.1002/dvdy.20173

Seemann, P., Schwappacher, R., Kjaer, K. W., Krakow, D., Lehmann, K., Dawson, K., et al. (2005). Activating and deactivating mutations in the receptor interaction site of GDF5 cause symphalangism or brachydactyly type A2. *J. Clin. Invest.* 115, 2373–2381. doi: 10.1172/jci25118

Sever, M., Mammadov, B., Guler, M. O., and Tekinay, A. B. (2014). Tenascin-C mimetic peptide nanofibers direct stem cell differentiation to osteogenic lineage. *Biomacromolecules* 15, 4480–4487. doi: 10.1021/bm501271x

Sherman, L., Wainwright, D., Ponta, H., and Herrlich, P. (1998). A splice variant of CD44 expressed in the apical ectodermal ridge presents fibroblast growth factors to limb mesenchyme and is required for limb outgrowth. *Genes Dev.* 12, 1058–1071.

Shi, M., Zhu, J., Wang, R., Chen, X., Mi, L., Walz, T., et al. (2011). Latent TGF-β structure and activation. *Nature* 474, 343–349.

Shwartz, Y., Viukov, S., Krief, S., and Zelzer, E. (2016). Joint development involves a continuous influx of Gdf5-positive cells. *Cell Rep.* 15, 2577–2587.

Sleep, E., Cosgrove, B. D., Mcclendon, M. T., Preslar, A. T., Chen, C. H., Sangji, M. H., et al. (2017). Injectable biomimetic liquid crystalline scaffolds enhance muscle stem cell transplantation. *Proc. Natl. Acad. Sci. U.S.A.* 114, E7919–E7928.

Solis, M. A., Chen, Y.-H., Wong, T. Y., Bittencourt, V. Z., Lin, Y.-C., and Huang, L. L. (2012). Hyaluronan regulates cell behavior: a potential niche matrix for stem cells. *Biochem. Res. Int.* 2012:346972.

Stickens, D., Behonick, D. J., Ortega, N., Heyer, B., Hartenstein, B., Yu, Y., et al. (2004). Altered endochondral bone development in matrix metalloproteinase 13-deficient mice. *Development* 131, 5883–5895.

Stocum, D. L. (2017). Mechanisms of urodele limb regeneration. *Regeneration* 4, 159–200.

Storm, E. E., and Kingsley, D. M. (1999). GDF5 coordinates bone and joint formation during digit development. *Dev. Biol.* 209, 11–27.

Sun, M., Chi, G., Li, P., Lv, S., Xu, J., Xu, Z., et al. (2018). Effects of matrix stiffness on the morphology, adhesion, proliferation and osteogenic differentiation of mesenchymal stem cells. *Int. J. Med. Sci.* 15, 257–268.

Sun, X., Mariani, F. V., and Martin, G. R. (2002). Functions of FGF signalling from the apical ectodermal ridge in limb development. *Nature* 418, 501–508.

Takahashi, K., and Yamanaka, S. (2006). Induction of pluripotent stem cells from mouse embryonic and adult fibroblast cultures by defined factors. *Cell* 126, 663–676.

Talman, V., and Ruskoaho, H. (2016). Cardiac fibrosis in myocardial infarction—from repair and remodeling to regeneration. *Cell Tissue Res.* 365, 563–581.

Tanaka, E. M., Gann, A. A., Gates, P. B., and Brockes, J. P. (1997). Newt myotubes reenter the cell cycle by phosphorylation of the retinoblastoma protein. *J. Cell Biol.* 136, 155–165.

Tejedor, G., Laplace-Builhé, B., Luz-Crawford, P., Assou, S., Barthelaix, A., Mathieu, M., et al. (2020). Whole embryo culture, transcriptomics and RNA interference identify TBX1 and FGF11 as novel regulators of limb development in the mouse. *Sci. Rep.* 10, 1–15.

Toole, B. P. (2001). Hyaluronan in morphogenesis. *Semin. Cell Dev. Biol.* 12, 79–87.

Urciuolo, A., Quarta, M., Morbidoni, V., Gattazzo, F., Molon, S., Grumati, P., et al. (2013). Collagen VI regulates satellite cell self-renewal and muscle regeneration. *Nat. Commun.* 4, 1–13.

van der Kraan, P. M., and van den Berg, W. B. (2012). Chondrocyte hypertrophy and osteoarthritis: role in initiation and progression of cartilage degeneration? *Osteoarthr. Cartilage* 20, 223–232.

Vierbuchen, T., Ostermeier, A., Pang, Z. P., Kokubu, Y., Südhof, T. C., and Wernig, M. (2010). Direct conversion of fibroblasts to functional neurons by defined factors. *Nature* 463, 1035–1041.

Villa, M. M., Wang, L., Huang, J., Rowe, D. W., and Wei, M. (2015). Bone tissue engineering with a collagen–hydroxyapatite scaffold and culture expanded bone marrow stromal cells. *J. Biomed. Mater. Res. B Appl. Biomater.* 103, 243–253.

Vinarsky, V., Atkinson, D. L., Stevenson, T. J., Keating, M. T., and Odelberg, S. J. (2005). Normal newt limb regeneration requires matrix metalloproteinase function. *Dev. Biol.* 279, 86–98.

Vincent, L. G., Choi, Y. S., Alonso-Latorre, B., Del Álamo, J. C., and Engler, A. J. (2013). Mesenchymal stem cell durotaxis depends on substrate stiffness gradient strength. *Biotechnol. J.* 8, 472–484.

Vining, K. H., and Mooney, D. J. (2017). Mechanical forces direct stem cell behaviour in development and regeneration. *Nat. Rev. Mol. Cell Biol.* 18, 728–742.

von der Mark, K., Gauss, V., Von Der Mark, H., and Muller, P. (1977). Relationship between cell shape and type of collagen synthesised as chondrocytes lose their cartilage phenotype in culture. *Nature* 267, 531–532.

Voog, J., and Jones, D. L. (2010). Stem cells and the niche: a dynamic duo. *Cell Stem Cell* 6, 103–115.

Vracko, R., and Benditt, E. P. (1972). Basal lamina: the scaffold for orderly cell replacement. Observations on regeneration of injured skeletal muscle fibers and capillaries. *J. Cell. Biol.* 55, 406–419.

Wang, N., Tytell, J. D., and Ingber, D. E. (2009). Mechanotransduction at a distance: mechanically coupling the extracellular matrix with the nucleus. *Nat. Rev. Mol. Cell Biol.* 10, 75–82.

Wang, X., Chan, W. C. W., and Chan, D. (2016). "Joint development," in *Cartilage: Physiology and Development*, eds S. Grässel and A. Aszódi (Switzerland: Springer International Publishing), 169–189.

Wang, X., Harris, R. E., Bayston, L. J., and Ashe, H. L. (2008). Type IV collagens regulate BMP signalling in *Drosophila*. *Nature* 455, 72–77.

Wang, Y.-K., Yu, X., Cohen, D. M., Wozniak, M. A., Yang, M. T., Gao, L., et al. (2012). Bone morphogenetic protein-2-induced signaling and osteogenesis is regulated by cell shape, RhoA/ROCK, and cytoskeletal tension. *Stem Cells Dev.* 21, 1176–1186.

Watt, F. M. (2016). Engineered microenvironments to direct epidermal stem cell behavior at single-cell resolution. *Dev. Cell* 38, 601–609.

Webster, M. T., Manor, U., Lippincott-Schwartz, J., and Fan, C. M. (2016). Intravital imaging reveals ghost fibers as architectural units guiding myogenic progenitors during regeneration. *Cell Stem Cell* 18, 243–252.

Wei, Y., Yang, E. V., Klatt, K. P., and Tassava, R. A. (1995). Monoclonal antibody MT2 identifies the urodele α1 chain of type XII collagen, a developmentally regulated extracellular matrix protein in regenerating newt limbs. *Dev. Biol.* 168, 503–513.

Wells, R. G. (2008). The role of matrix stiffness in regulating cell behavior. *Hepatology* 47, 1394–1400.

Wilmut, I., Schnieke, A. E., Mcwhir, J., Kind, A. J., and Campbell, K. H. S. (1997). Viable offspring derived from fetal and adult mammalian cells. *Nature* 385, 810–813.

Wilsman, N. J., Farnum, C. E., Leiferman, E. M., Fry, M., and Barreto, C. (1996). Differential growth by growth plates as a function of multiple parameters of chondrocytic kinetics. *J. Orthop. Res.* 14, 927–936.

Witze, E. S., Litman, E. S., Argast, G. M., Moon, R. T., and Ahn, N. G. (2008). Wnt5a control of cell polarity and directional movement by polarized redistribution of adhesion receptors. *Science* 320, 365–369.

Xu, X., Li, C., Takahashi, K., Slavkin, H. C., Shum, L., and Deng, C.-X. (1999). Murine fibroblast growth factor receptor 1α isoforms mediate node regression and are essential for posterior mesoderm development. *Dev. Biol.* 208, 293–306.

Xu, X., Weinstein, M., Li, C., Naski, M., Cohen, R. I., Ornitz, D. M., et al. (1998). Fibroblast growth factor receptor 2 (FGFR2)-mediated reciprocal regulation loop between FGF8 and FGF10 is essential for limb induction. *Development* 125, 753–765.

Yang, G., Zhu, L., Hou, N., Lan, Y., Wu, X. M., Zhou, B., et al. (2014). Osteogenic fate of hypertrophic chondrocytes. *Cell. Res.* 24, 1266–1269.

Yang, L., Tsang, K. Y., Tang, H. C., Chan, D., and Cheah, K. S. (2014). Hypertrophic chondrocytes can become osteoblasts and osteocytes in endochondral bone formation. *Proc. Natl. Acad. Sci. U.S.A.* 111, 12097–12102.

Yokoyama, H., Yonei-Tamura, S., Endo, T., Belmonte, J. C. I., Tamura, K., and Ide, H. (2000). Mesenchyme with fgf-10 expression is responsible for regenerative capacity in *Xenopus* limb buds. *Dev. Biol.* 219, 18–29.

Yu, Q., Grammatikakis, N., and Toole, B. P. (1996). Expression of multiple CD44 isoforms in the apical ectodermal ridge of the embryonic mouse limb. *Dev. Dyn.* 207, 204–214.

Zhai, P., Peng, X., Li, B., Liu, Y., Sun, H., and Li, X. (2020). The application of hyaluronic acid in bone regeneration. *Int. J. Biol. Macromol.* 151, 1224–1239.

Zhang, D., Wu, X., Chen, J., and Lin, K. (2018). The development of collagen based composite scaffolds for bone regeneration. *Bioactive Mater.* 3, 129–138.

Zhou, Q., Brown, J., Kanarek, A., Rajagopal, J., and Melton, D. A. (2008). In vivo reprogramming of adult pancreatic exocrine cells to β-cells. *Nature* 455, 627–632.

Zhou, X., Von Der Mark, K., Henry, S., Norton, W., Adams, H., and De Crombrugghe, B. (2014). Chondrocytes transdifferentiate into osteoblasts in endochondral bone during development, postnatal growth and fracture healing in mice. *PLoS Genet.* 10:e1004820. doi: 10.1371/journal.pgen.1004820

Zhu, M., Tao, H., Samani, M., Luo, M., Wang, X., Hopyan, S., et al. (2020). Spatial mapping of tissue properties in vivo reveals a 3D stiffness gradient in the mouse limb bud. *Proc. Natl. Acad. Sci. U.S.A.* 117, 4781–4791.

Zipori, D. (2004). The nature of stem cells: state rather than entity. *Nat. Rev. Genet.* 5, 873–878.

Zuniga, A. (2015). Next generation limb development and evolution: old questions, new perspectives. *Development* 142, 3810–3820.

Conflict of Interest: The authors declare that the research was conducted in the absence of any commercial or financial relationships that could be construed as a potential conflict of interest.

Copyright © 2020 Ma, Chan, Rubab, Chan and Chan. This is an open-access article distributed under the terms of the Creative Commons Attribution License (CC BY). The use, distribution or reproduction in other forums is permitted, provided the original author(s) and the copyright owner(s) are credited and that the original publication in this journal is cited, in accordance with accepted academic practice. No use, distribution or reproduction is permitted which does not comply with these terms.

frontiers in Cell and Developmental Biology

MINI REVIEW
published: 04 September 2020
doi: 10.3389/fcell.2020.559032

Building an Artificial Cardiac Microenvironment: A Focus on the Extracellular Matrix

*Olivia Pagliarosi[1], Vittorio Picchio[2], Isotta Chimenti[2,3], Elisa Messina[4] and Roberto Gaetani[1,5]**

[1] Department of Molecular Medicine, Faculty of Pharmacy and Medicine, Sapienza University of Rome, Rome, Italy, [2] Department of Medical and Surgical Sciences and Biotechnology, Faculty of Pharmacy and Medicine, Sapienza University of Rome, Rome, Italy, [3] Mediterranea Cardiocentro, Naples, Italy, [4] Department of Maternal, Infantile, and Urological Sciences, "Umberto I" Hospital, Rome, Italy, [5] Department of Bioengineering, Sanford Consortium for Regenerative Medicine, University of California, San Diego, San Diego, CA, United States

OPEN ACCESS

Edited by:
Pavel Makarevich,
Lomonosov Moscow State University, Russia

Reviewed by:
Natalia Kalinina,
Lomonosov Moscow State University, Russia
Jinah Jang,
Pohang University of Science and Technology, South Korea

***Correspondence:**
Roberto Gaetani
roberto.gaetani@uniroma1.it

Specialty section:
This article was submitted to Stem Cell Research, a section of the journal Frontiers in Cell and Developmental Biology

Received: 04 May 2020
Accepted: 18 August 2020
Published: 04 September 2020

Citation:
Pagliarosi O, Picchio V, Chimenti I, Messina E and Gaetani R (2020) Building an Artificial Cardiac Microenvironment: A Focus on the Extracellular Matrix. Front. Cell Dev. Biol. 8:559032. doi: 10.3389/fcell.2020.559032

The increased knowledge in cell signals and stem cell differentiation, together with the development of new technologies, such as 3D bioprinting, has made the generation of artificial tissues more feasible for *in vitro* studies and *in vivo* applications. In the human body, cell fate, function, and survival are determined by the microenvironment, a rich and complex network composed of extracellular matrix (ECM), different cell types, and soluble factors. They all interconnect and communicate, receiving and sending signals, modulating and responding to cues. In the cardiovascular field, the culture of stem cells *in vitro* and their differentiation into cardiac phenotypes is well established, although differentiated cardiomyocytes often lack the functional maturation and structural organization typical of the adult myocardium. The recreation of an artificial microenvironment as similar as possible to the native tissue, though, has been shown to partly overcome these limitations, and can be obtained through the proper combination of ECM molecules, different cell types, bioavailability of growth factors (GFs), as well as appropriate mechanical and geometrical stimuli. This review will focus on the role of the ECM in the regulation of cardiac differentiation, will provide new insights on the role of supporting cells in the generation of 3D artificial tissues, and will also present a selection of the latest approaches to recreate a cardiac microenvironment *in vitro* through 3D bioprinting approaches.

Keywords: cardiac microenvironment, extracellular matrix, cardiac tissue engineering, cardiac differentiation, 3D bioprinting

INTRODUCTION

The regulation of cell proliferation, differentiation, and function is influenced by several factors, such as signaling molecules, cell-cell interaction, and the extracellular matrix (ECM), which are collectively defined as the microenvironment. Among their many functions in homeostasis, these factors play a fundamental role also in tissue development, turnover, and repair. The regulation

of stem cell behavior is a particularly delicate task: in fact, embryonic stem cells (ESCs) are the main players during embryogenesis, and are tightly regulated and coordinated to maintain their stemness, as well as their activation and functional differentiation. Moreover, the increasing use of induced pluripotent stem cells (iPSCs) to obtain differentiated cell types requires particular attention also on the signals regulating their biology. Indeed, this very specific microenvironment is now commonly defined as the stem cell "niche," and its understanding and modeling could boost advancements in the field of tissue engineering, and even subsequent *in vivo* therapeutic applications (Chimenti et al., 2017).

The most studied cell regulatory signals are mediated by growth factors (GFs) and soluble cues, widely used in *ex vivo* research to differentiate adult and ESCs into mature cells. The role of molecules such as insulin-like and fibroblast GFs (Bendall et al., 2007), Wnt proteins (Reya et al., 2003; Lie et al., 2005), and many other cytokines (Endele et al., 2014) have been extensively studied, while the role of the ECM in the regulation of the microenvironment and the niche still remains to be fully understood. The ECM is not an inert, structural scaffold, as once thought: it maintains indeed the structure and function of organs, participating in their development and remodeling. ECM allows cell-cell communication and it modulates cell motility, adhesion, survival, and proliferation (Miyamoto et al., 1996; Ross and Borg, 2001). The ECM is composed of structural proteins, such as collagens, and numerous non-structural regulatory proteins, such as proteoglycans (PGs). Within the niche, different ECM molecules can regulate stem cell behavior by direct interactions with integrin receptors expressed on the cellular membrane, by modulating tissue compliance and consequent cell response through the mechanosensing machinery, or through the binding of different GFs and their controlled spatiotemporal presentation to the neighboring cells.

In the heart, ECM proteins surround and protect all cell types: cardiomyocytes, fibroblasts, endothelial cells, pericytes, and smooth muscle cells. All together, proteins, cells, and their cross-talk, create an interconnected microenvironment, which promptly reacts to external changes and cues such as biochemical (GFs, cytokines, hormones), electrical and mechanical signals (such as changes in contraction, stretch, and pressure), necessary to maintain myocardial integrity and functional responsiveness, especially during development and physiological post-natal remodeling (Howard and Baudino, 2013). Cardiac ECM, in fact, is a dynamic structure, constantly undergoing synthesis and degradation, modifying its composition in space and time in response to contingencies, from early development to post-natal life, aging, and possibly diseased states (Schenke-Layland et al., 2012; Rienks et al., 2014).

In this review, we will focus on the role of the ECM in the regulation of the cardiac microenvironment, starting briefly from tissue development during embryogenesis, to the role of different ECM molecules in cardiac differentiation and proliferation, both *in vitro* and *in vivo*. Moreover, we will also address the role of supporting cells and describe the most promising approaches to recreate *in vitro* a physiologically relevant cardiac microenvironment through 3D bioprinting technology.

THE CARDIAC EXTRACELLULAR MATRIX

During embryogenesis, the heart is the first functional organ to develop, thanks to the proliferation, migration, and differentiation of cardiac precursor cells (CPCs). These cells migrate from the primitive streak in the embryo, organizing themselves into the mesoderm (Abu-issa and Kirby, 2007), from which the CPCs derive; then they differentiate into all the major cell types of the heart, including cardiomyocytes (CMs), smooth muscle cells, endothelial cells, and fibroblasts (Yustzey and Kirby, 2002; Kelly et al., 2014; Witman and Sahara, 2018). The primitive cardiac tube has an outer layer of myocardium and an inner one of endothelium, divided by an acellular space filled with a provisional ECM, also known as the cardiac jelly, which is essential for the maintenance of the tube structure during its transformation into the definite heart form (Huang et al., 1995). This matrix is enriched in hyaluronic acid (HA) and PGs, which render it highly hydrated and malleable (Bernanke and Markwald, 1984; Funderburg and Markwald, 1986). Cardiac jelly components sequester GFs and influence CPC movement and differentiation, and are extremely important during epithelial-to-mesenchymal transition (EMT), which is necessary for many ontological steps to generate adult tissues and organs (Butcher and Markwald, 2007; Thiery et al., 2009; Votteler et al., 2010). Cardiac jelly also contains fibronectin, laminin, different types of collagen, fibulin, and fibrillin, that are fundamental in orchestrating tissue growth, organization, and differentiation (Icardo and Manasek, 1983; Mjaatvedt et al., 1987; Little et al., 1989; Bouchey et al., 1996).

After birth, the heart undergoes remodeling to adapt to the mechanical, chemical, and electrical changes of the growing body. These alterations in organ geometry are accompanied by changes in ECM composition, and are necessary to maintain efficient cardiac function (Baudino et al., 2006). Many ECM components are involved. Collagen I is the most abundant in both developing and adult tissue. Still, in the latter, its density and crosslinking are higher, and a decrease in the ratio between collagen I and collagen III is observed (Thompson et al., 1979; Borg, 1982; Hanson et al., 2013; González et al., 2019). Fibronectin (FN), instead, decreases in the adult tissue (Kim et al., 1999; Lockhart et al., 2011) with a concomitant increase of elastin (Kim et al., 1999). These changes are generally associated with an increase in cardiac stiffness, with the heart tissue becoming less compliant during heart development and CM differentiation, as demonstrated by the threefold increase of left ventricle stiffness 5 days following birth, up to an elastic modulus of approximately 10–20 kPa (Jacot et al., 2008; Horn, 2015).

Extracellular matrix proteins not only act as anchored ligands: they are also reservoirs for GFs, cytokines, and

proteases, in particular matrix metalloproteinases (MMPs) and tissue inhibitor of metalloproteinases (TIMPS) (Hynes, 2009; Brizzi et al., 2012). MMPs degrade collagen (Daley et al., 2008), while simultaneously releasing small bioactive peptides and GFs stored within the matrix, releasing soluble ligands that participate in the homeostasis of the microenvironment. Indeed, FN, vitronectin, collagens, and PGs, avidly bind many GFs, such as FGFs and VEGFs, regulating their presentation, distribution, and activation (Brizzi et al., 2012; Nakayama et al., 2014). Likewise, collagen IV binds BMP4 (Wang et al., 2008).

ROLE OF THE ECM IN CARDIAC DIFFERENTIATION

As mentioned earlier, cells and ECM are directly connected, and the matrix can influence their growth, organization, and differentiation; similarly, the microenvironment regulates stem cell proliferation, hence the maintenance of potency or differentiation into a specific cell lineage (**Figure 1**).

Cells adhere to ECM proteins through integrin receptors, which activate intracellular signal transductions and are known to regulate many developmentally relevant processes (Wozniak et al., 2004; Saleem et al., 2009; Sa et al., 2014; Neiman et al., 2019). For example, the interaction between collagen type I and β1-integrin was studied in murine iPSC-derived embryoid bodies, and was shown to be important for cell growth and cardiac lineage commitment (Zeng et al., 2013). Collagen type I has been reported to support the maturation of murine (m) and human (h)iPSC-derived CMs, and to modulate intracellular calcium homeostasis and their electrophysiological properties (Lu et al., 2011; Edalat et al., 2019), while collagen type IV can increase the differentiation potential of m/hCPCs (Schenke-Layland et al., 2012). Both of them promote proliferation of CPCs and maintain the pluripotency of mESCs *in vitro* (Lu et al., 2017). It is worth mentioning that even with the same biochemical compositions (e.g., molecular collagen), different microstructures (e.g., fibrous versus porous) can nonetheless differentially affect the phenotype of cardiac cell types (Chimenti et al., 2011).

Similarly, Cheng et al. (2013) described that FN promotes mesodermal differentiation *via* β1-integrin through the

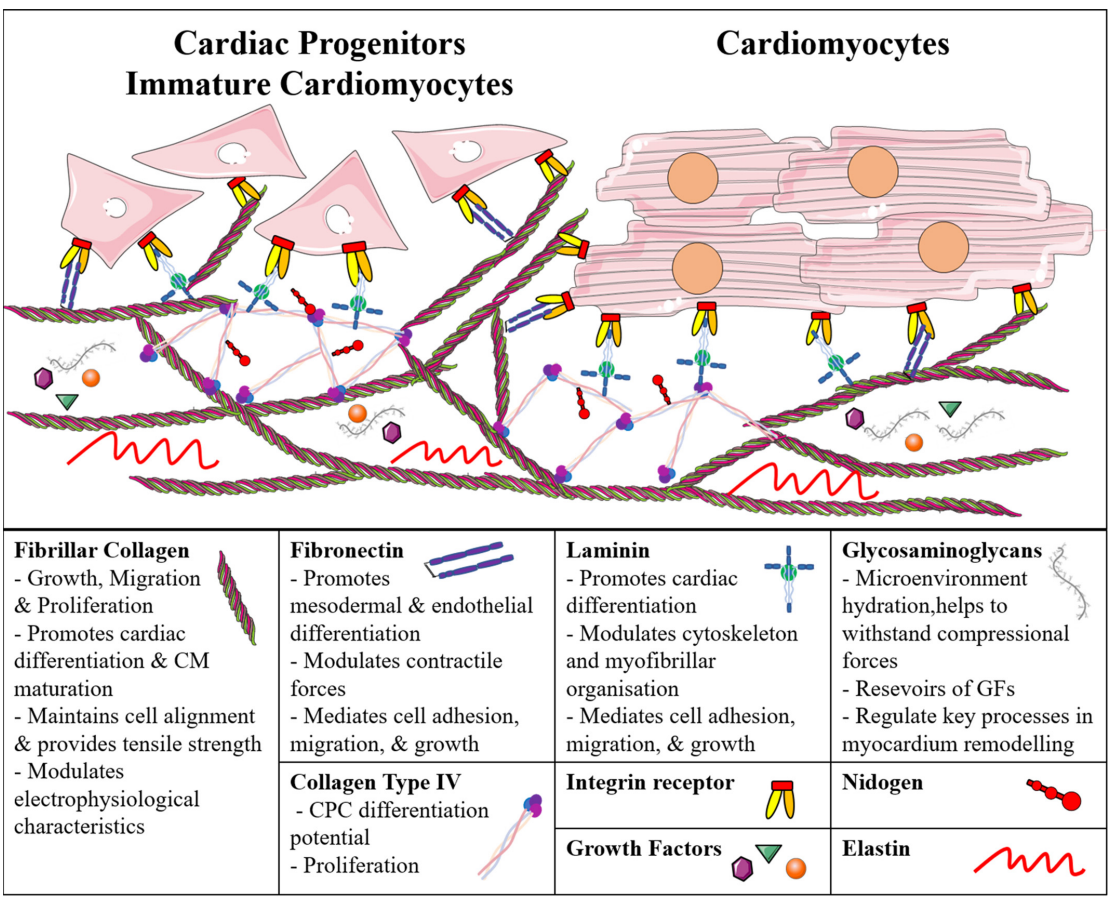


FIGURE 1 | Schematic representation of the main cardiac extracellular matrix components and their direct interaction with immature and adult cardiomyocytes. CM, Cardiomyocyte; CPC, Cardiac Progenitor Cell; GF, Growth Factor.

activation of the Wnt/β-catenin pathway in mESCs. Laminin (LM), instead, has been described to support ESC-derived CPC differentiation, and modulate the cytoskeleton and myofibrillar organization (Battista et al., 2005; Sa et al., 2014). Similar to single ECM components, culturing ESC-derived CPCs on matrices with different combinations of these ECM proteins has shown efficient cell attachment, cardiac differentiation, and survival (Battista et al., 2005; Jung et al., 2015; Lu et al., 2017). Sa et al. (2014) have investigated the effects of various ratios of FN and LN, and found that human ESCs differentiating on 70:30 FN:LN yielded CMs with higher efficiency compared to simple gelatin coatings. Several commercial ECM-based products are available for *in vitro* studies on substrates with multiple components. Matrigel^{TM}, a basement membrane-derived matrix, promotes EMT, generating precardiac mesoderm, and can promote CM differentiation (Zhang et al., 2012). Similarly, Cardiogel^{TM}, a mixture of collagen types I and III, LM, FN, and PGs derived from cardiac fibroblasts, leads to better adherence and maturation of CMs (Vanwinkle et al., 1996). Therefore, despite many studies have shown the importance of different ECM molecules in cardiac cell differentiation and functionality, in order to recreate the proper microenvironment *in vitro,* it is essential to provide the cells with all the ECM molecules present in the native tissue. For this reason, tissue-derived biomaterials are increasingly being used to culture both progenitor and differentiated CMs. Different decellularization and recellularization strategies of cardiac tissue or whole heart have been developed, using myocardium originating from rats (Ott et al., 2008; Carvalho et al., 2012; Wang et al., 2019), porcines (Singelyn and Christman, 2010; Ferng et al., 2017; Lee et al., 2017), bovines (Arslan et al., 2018), and even humans (Johnson et al., 2014; Sánchez et al., 2015; Guyette et al., 2016; Masumoto et al., 2016; Tang-Quan et al., 2018). Interestingly, cardiac progenitor stromal cells, isolated from newborn mice or human fetal heart, can increase their proliferative capacity and expression of key cardiac transcription factors when cultured in a cardiac-derived ECM hydrogel compared to collagen only, both in 2D (French et al., 2012) and 3D (Gaetani et al., 2016). Decellularized mouse hearts allow hiPSC-derived CPCs to migrate, proliferate, and differentiate into all cardiac cell types, exhibiting efficient spontaneous beating (Lu et al., 2013). Furthermore, human decellularized cardiac tissue has been shown to support miPSC and mESC viability and differentiation into CMs (Oberwallner et al., 2015). Other authors have exploited slices of decellularized human hearts; for example, Garreta et al. (2016) found that the electrical and mechanical functionality of hiPSC-derived CMs increased when grown on such slices, compared to Matrigel.

Besides biochemical signals, the ECM regulates cell behavior also by modulating the mechanical properties of the microenvironment. Cells respond to mechanical cues by altering their cytoskeletal organization, myofibril striation and alignment, by expressing specific combinations of cell adhesion molecules (CAMs), and activating signaling pathways and mechanosensitive ion channels (Ireland and Simmons, 2015; Tallawi et al., 2015). In fact, CMs differentiate better on substrates of stiffness similar to the native tissue (∼10 kPa) (Engler et al., 2008; Jacot et al., 2008; Bhana et al., 2010; Young and Engler, 2011; Tallawi et al., 2015). Indeed, when the substrate is too rigid or too soft, CMs overstrain themselves or do inefficient work, respectively; in both cases it results in an impaired contractile capacity.

NEW APPROACHES IN MODELING THE ARTIFICIAL MICROENVIRONMENT

As mentioned previously, the regulation of the microenvironment depends on multiple factors such as cell-cell and cell-ECM interaction, as well as GFs, cytokines, and small molecule signaling, that overall modulate cellular phenotypes. Under these premises, many groups have developed novel methods to grow cardiac progenitor and differentiated cells, creating new microenvironments through 3D culture systems, bioprinting, cardiac patches, and organoid chambers.

Among these approaches, 3D bioprinting can generate tissues using different cells or scaffolds simultaneously, thus having the potential to recreate *in vitro*, at least in part, the complex microenvironment of any given tissue through the accurate design of the biochemical properties and structure of biomaterials, together with the proper cellular composition. In the last years, many synthetic and biological materials have been used to make bioinks. Cardiac-derived primitive stromal cells, CPCs, and iPSC-derived CMs have been printed in many types of biomaterials, including alginate, HA, and gelatin, among others, and have been used for regenerative medicine and tissue modeling applications (Gaetani et al., 2012, 2015). As mentioned above, several studies have shown how using a single ECM component fails to recapitulate the complexity of the natural cardiac ECM, and thus cannot efficiently reproduce the innate cellular microenvironment (Gardin et al., 2020). Protocols for decellularized extracellular matrix (dECM) have been recently adapted to be used in conjunction with printing technology. They could represent a very promising scaffold for 3D cell culture, as they retain the complex biochemical composition of the native tissue. In this regard, Pati and Cho (2017) have designed a method to prepare dECM from porcine hearts as a bioink, and have used it to bioprint an MSC-laden construct by extrusion-based 3D printing technology. The resulting dECM had highly preserved levels of collagen and glycosaminoglycans, providing a native-like environment for the maintenance of a 3D structured tissue (Pati and Cho, 2017). The importance of cardiac ECM as a component of bioinks has been also highlighted by Jang et al. (2017), who used cardiac porcine dECM complexed with UV-treated vitamin B2 to prepare cardiac-specific hydrogels. These scaffolds were used in combination with human infant CPCs to fabricate 3D bioprinted cardiac constructs with a stiffness similar to the native myocardium, which enhanced viability, proliferation, and cardiac differentiation of CPCs (Jang et al., 2017). Similarly, Bejleri et al. (2018) have developed a 3D bioprinted patch containing heart dECM for the delivery of human pediatric

CPCs. The authors demonstrated that these dECM patches improved cardiogenic differentiation and angiogenic potential when compared to cells grown in gelatin-methacryloyl patches, highlighting the importance of the proper ECM composition in the microenvironment for physiologic cell behavior (Bejleri et al., 2018). Similarly, Yu et al. (2019) described a method to make cardiac dECM bioinks to fabricate patient-specific tissues, with high control over micro-architecture and mechanical properties using a digital light processing (DLP)-based 3D bioprinter. The results showed that dECM bioinks provide a suitable microenvironment to support maturation of hiPSC-derived CMs (Yu et al., 2019).

As mentioned previously, the microenvironment is also modulated by cellular diversity, including supporting cells, such as stromal primitive cells, pericytes, or fibroblasts (**Figure 2**; Castaldo and Chimenti, 2018; Forte et al., 2018). Several studies in 3D culture systems have shown the beneficial effects of fibroblasts co-culture on ESC- or iPSC-derived CM differentiation (Liau et al., 2011; Ou et al., 2011; Valls-Margarit et al., 2019). These beneficial effects are probably due to the secretion of GFs and deposition of new ECM, which in turn may increase the compaction of the artificial tissues, resulting in better cell-to-cell contact. Furthermore, these systems most likely allow more complex tissue mechanical properties, thereby enabling adequate mechanosensing signaling, which is a fundamental player for tissue maturation (Pesce et al., 2017).

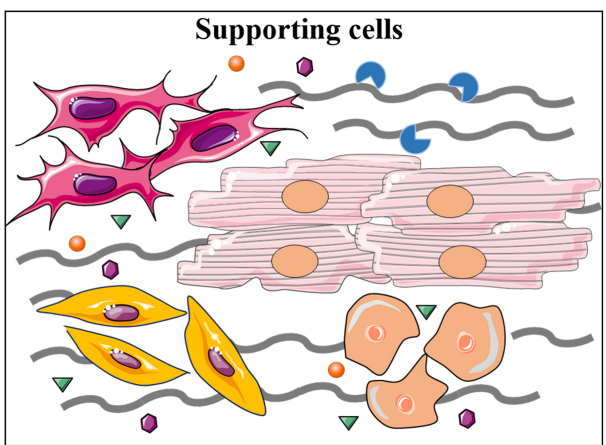


FIGURE 2 | Supporting cells and their function in the regulation of the cardiac microenvironment and generation of cardiac-like tissues.

Interestingly, Zhang et al. (2019) recently showed that co-culture of hiPSC-cardiac fibroblasts with hiPSC-CMs is beneficial for the electrophysiological properties of CMs compared to co-culture with dermal fibroblasts. The study highlighted the importance of tissue-specificity for boundary conditions in the microenvironment, and could be used not only to improve the maturation of cultured cells, but also to study potential specific mechanosensing signaling mediated by tissue specific cells (Zhang et al., 2019). Besides tissue-specificity, it is also important to consider phenotypic changes due to pathological conditions that may alter the behavior of resident fibroblasts and other stromal cells, and consequently the balance between cardiogenic and fibrotic signaling inside the microenvironment (Pagano et al., 2017). Similar to fibroblasts, also endothelial and smooth muscle cells have been shown to increase the structural or electrical maturation of hiPSC-derived CMs (Giacomelli et al., 2017; Pasquier et al., 2017; Vuorenpää et al., 2017). In fact, hiPSC-derived smooth muscle cells and pericytes could increase the structural maturation of iPSC-derived CMs in a 3D collagen I-matrigel scaffold (Masumoto et al., 2016). Recently, the group has reported a new personalized strategy to engineer immuno-compatible patient-specific cardiac patches. In detail, a biopsy of adipose tissue was isolated from patients, and the cellular and acellular components were separated. While the cells were reprogrammed to become pluripotent stem cells, the ECM was processed into a personalized hydrogel able to support hiPSC differentiation into cardiac cells *in vitro* (Edri et al., 2019). Afterward, the same groups made a more complex 3D model adding endothelial cells as a source of vascular structures, thus obtaining patient-specific vascularized cardiac patches (Noor et al., 2019).

Other examples to generate highly complex structures include the work of Li et al. (2018) that have created for the first time a human ventricle-like cardiac organoid chamber (hvCOC) to generate advanced models resembling cardiac geometry. HiPSC-derived CMs and dermal fibroblasts have been embedded in a collagen-based ECM, and transferred to an agarose mold with a centrally placed inflatable balloon. This allowed to form the hollow 3D hvCOC that enhanced the maturation of ventricular CMs, providing a unique microenvironment that could mimic fluid pumping, similar to a mature heart chamber (Li et al., 2018). Similarly, Macqueen's team created a tissue-engineered scale model of the human left ventricle with rat ventricle myocytes or hiPSC-derived CMs seeded on a FN-coated scaffold. The scaffold was made by pull spinning a mixture of PCL and gelatin onto a mandrel in the shape of an ellipsoidal ventricle to promote native-like anisotropic myocardial tissue genesis and chamber-level contractile function (Macqueen et al., 2018).

CONCLUSION

Reconstructing and mimicking the complexity of native tissues is a challenging objective of contemporary research. Biochemical composition, intercellular communication, co-culture of multiple

cell types, and mechanosensing represent key features, among many others, that need to be finely tuned in order to create physiologically relevant microenvironments for cell integration and differentiation. All these features can significantly affect the desired yield and the expected phenotype of artificial tissues and constructs. Increasing knowledge of the basic mechanisms regulating tissue homeostasis, together with advancements in biomaterial preparation and bioprinting, are gradually allowing the design and development of artificial microenvironments with in creasing complexity. This progress will provide innovative tools for *ex vivo* research, as well as new strategies for tissue repair in regenerative medicine.

AUTHOR CONTRIBUTIONS

RG, OP, and VP contributed to the text and figures. EM and IC contributed to the text and figure editing. All authors contributed to the article and approved the submitted version.

FUNDING

This project has received funding from the Euratom Research and Training Programme 2014–2018 under grant agreement no. 755523 and by grant #RG11916B85CDBF76 from Sapienza University of Rome to IC.

REFERENCES

Abu-issa, R., and Kirby, M. L. (2007). Heart field: from mesoderm to heart tube. *Annu. Rev. Cell Dev. Biol.* 23, 45–68. doi: 10.1146/annurev.cellbio.23.090506.123331

Arslan, Y. E., Galata, Y. F., Sezgin Arslan, T., and Derkus, B. (2018). Trans-differentiation of human adipose-derived mesenchymal stem cells into cardiomyocyte-like cells on decellularized bovine myocardial extracellular matrix-based films. *J. Mater. Sci. Mater. Med.* 29:127. doi: 10.1007/s10856-018-6135-4

Battista, S., Guarnieri, D., Borselli, C., Zeppetelli, S., Borzacchiello, A., Mayol, L., et al. (2005). The effect of matrix composition of 3D constructs on embryonic stem cell differentiation. *Biomaterials* 26, 6194–6207. doi: 10.1016/j.biomaterials.2005.04.003

Baudino, T. A., Carver, W., Giles, W., Borg, T. K., Troy, A., Carver, W., et al. (2006). Cardiac fibroblasts: friend or foe? *Am. J. Physiol. Heart Circ. Physiol.* 291, H1015–H1026. doi: 10.1152/ajpheart.00023.2006

Bejleri, D., Streeter, B. W., Nachlas, A. L. Y., Brown, M. E., Gaetani, R., Christman, K. L., et al. (2018). Bioprinted cardiac patch composed of cardiac-specific extracellular matrix and progenitor cells for heart repair. *Adv. Healthc. Mater.* 7:1800672. doi: 10.1002/adhm.201800672

Bendall, S. C., Stewart, M. H., Menendez, P., George, D., Vijayaragavan, K., Werbowetski-Ogilvie, T., et al. (2007). IGF and FGF cooperatively establish the regulatory stem cell niche of pluripotent human cells in vitro. *Nature* 448, 1015–1021. doi: 10.1038/nature06027

Bernanke, D. H., and Markwald, R. R. (1984). Effects of two glycosaminoglycans on seeding of cardiac cushion tissue cells into a collagen-lattice culture system. *Anat. Rec.* 210, 25–31. doi: 10.1002/ar.1092100105

Bhana, B., Iyer, R. K., Chen, W. L. K., Zhao, R., Sider, K. L., Likhitpanichkul, M., et al. (2010). Influence of substrate stiffness on the phenotype of heart cells. *Biotechnol. Bioeng.* 105, 1148–1160. doi: 10.1002/bit.22647

Borg, T. K. (1982). Development of the connective tissue network in the neonatal hamster heart. *Am. J. Anat.* 443, 435–443. doi: 10.1002/aja.1001650407

Bouchey, D., Argraves, W. S., and Little, C. D. (1996). Fibulin-1, vitronectin, and fibronectin expression during avian cardiac valve and septa development. *Anat. Rec.* 551, 540–551. doi: 10.1002/(sici)1097-0185(199604)244:4<540::aid-ar12>3.0.co;2-p

Brizzi, M. F., Tarone, G., and Defilippi, P. (2012). Extracellular matrix, integrins, and growth factors as tailors of the stem cell niche. *Curr. Opin. Cell Biol.* 24, 645–651. doi: 10.1016/j.ceb.2012.07.001

Butcher, J. T., and Markwald, R. R. (2007). Valvulogenesis: the moving target. *Philos. Trans. R. Soc. Lond. B Biol. Sci.* 362, 1489–1503. doi: 10.1098/rstb.2007.2130

Carvalho, J. L., de Carvalho, P. H., Gomes, D. A., and Goes, A. M. (2012). Characterization of decellularized heart matrices as biomaterials for regular and whole organ tissue engineering and initial in-vitro recellularization with ips cells. *Physiol. Behav.* 176, 139–148. doi: 10.1016/j.physbeh.2017.03.040

Castaldo, C., and Chimenti, I. (2018). Cardiac progenitor cells: the matrix has you. *Stem Cells Transl. Med.* 7, 506–510. doi: 10.1002/sctm.18-0023

Cheng, P., Andersen, P., Hassel, D., Kaynak, B. L., Limphong, P., Juergensen, L., et al. (2013). Fibronectin mediates mesendodermal cell fate decisions. *Development* 140, 2587–2596. doi: 10.1242/dev.089052

Chimenti, I., Massai, D., Morbiducci, U., Beltrami, A. P., Pesce, M., and Messina, E. (2017). Stem cell spheroids and ex vivo niche modeling: rationalization and scaling-up. *J. Cardiovasc. Transl. Res.* 10, 150–166. doi: 10.1007/s12265-017-9741-5

Chimenti, I., Rizzitelli, G., Gaetani, R., Angelini, F., Ionta, V., Forte, E., et al. (2011). Human cardiosphere-seeded gelatin and collagen scaffolds as cardiogenic engineered bioconstructs. *Biomaterials* 32, 9271–9281. doi: 10.1016/j.biomaterials.2011.08.049

Daley, W. P., Peters, S. B., and Larsen, M. (2008). Extracellular matrix dynamics in development and regenerative medicine. *J. Cell Sci.* 121, 255–264. doi: 10.1242/jcs.006064

Edalat, S. G., Jang, Y., Kim, J., and Park, Y. (2019). Collagen type I containing hybrid hydrogel enhances cardiomyocyte maturation in a 3D cardiac model. *Polymers* 11:687. doi: 10.3390/polym11040687

Edri, R., Gal, I., Noor, N., Harel, T., Fleischer, S., Adadi, N., et al. (2019). Personalized hydrogels for engineering diverse fully autologous tissue implants. *Adv. Mater.* 31:1803895. doi: 10.1002/adma.201803895

Endele, M., Etzrodt, M., and Schroeder, T. (2014). Instruction of hematopoietic lineage choice by cytokine signaling. *Exp. Cell Res.* 329, 207–213. doi: 10.1016/j.yexcr.2014.07.011

Engler, A. J., Carag-krieger, C., Johnson, C. P., Raab, M., Tang, H., Speicher, D. W., et al. (2008). Embryonic cardiomyocytes beat best on a matrix with heart-like elasticity : scar-like rigidity inhibits beating. *J. Cell Sci.* 121, 3794–3802. doi: 10.1242/jcs.029678

Ferng, A. S., Connell, A. M., Marsh, K. M., Qu, N., Medina, A. O., Bajaj, N., et al. (2017). Acellular porcine heart matrices: whole organ decellularization with 3D-bioscaffold & vascular preservation. *J. Clin. Transl. Res.* 3, 260–270. doi: 10.18053/jctres.03.201702.001

Forte, E., Furtado, M. B., and Rosenthal, N. (2018). The interstitium in cardiac repair: role of the immune–stromal cell interplay. *Nat. Rev. Cardiol.* 15, 601–616. doi: 10.1038/s41569-018-0077-x

French, K. M., Boopathy, A. V., Dequach, J. A., Chingozha, L., Lu, H., Christman, K. L., et al. (2012). A naturally derived cardiac extracellular matrix enhances cardiac progenitor cell behavior in vitro. *Acta Biomater.* 8, 4357–4364. doi: 10.1016/j.actbio.2012.07.033

Funderburg, F. M., and Markwald, R. R. (1986). Conditioning of native substrates by chondroitin sulfate proteoglycans during cardiac mesenchymal cell migration. *J. Cell Biol.* 103, 2475–2487. doi: 10.1083/jcb.103.6.2475

Gaetani, R., Doevendans, P. A., Metz, C. H. G., Alblas, J., Messina, E., Giacomello, A., et al. (2012). Cardiac tissue engineering using tissue printing technology and human cardiac progenitor cells. *Biomaterials* 33, 1782–1790. doi: 10.1016/j.biomaterials.2011.11.003

Gaetani, R., Feyen, D. A. M., Verhage, V., Slaats, R., Messina, E., Christman, K. L., et al. (2015). Epicardial application of cardiac progenitor cells in a 3D-printed gelatin/hyaluronic acid patch preserves cardiac function after myocardial infarction. *Biomaterials* 61, 339–348. doi: 10.1016/j.biomaterials.2015.05.005

Gaetani, R., Yin, C., Srikumar, N., Braden, R., Doevendans, P. A., Sluijter, J. P. G., et al. (2016). Cardiac-derived extracellular matrix enhances cardiogenic properties of human cardiac progenitor cells. *Cell Transplant.* 25, 1653–1663. doi: 10.3727/096368915X689794

Gardin, C., Ferroni, L., Latremouille, C., Chachques, J. C., Mitrečić, D., and Zavan, B. (2020). Recent applications of three dimensional printing in cardiovascular medicine. *Cells* 9:742. doi: 10.3390/cells9030742

Garreta, E., de Oñate, L., Fernández-Santos, M. E., Oria, R., Tarantino, C., Climent, A. M., et al. (2016). Myocardial commitment from human pluripotent stem cells: rapid production of human heart grafts. *Biomaterials* 98, 64–78. doi: 10.1016/j.biomaterials.2016.04.003

Giacomelli, E., Bellin, M., Sala, L., van Meer, B. J., Tertoolen, L. G. J., Orlova, V. V., et al. (2017). Three-dimensional cardiac microtissues composed of cardiomyocytes and endothelial cells co-differentiated from human pluripotent stem cells. *Development* 144, 1008–1017. doi: 10.1242/dev.143438

González, A., López, B., Ravassa, S., San José, G., and Díez, J. (2019). The complex dynamics of myocardial interstitial fibrosis in heart failure. Focus on collagen cross-linking. *Biochim. Biophys. Acta Mol. Cell Res.* 1866, 1421–1432. doi: 10.1016/j.bbamcr.2019.06.001

Guyette, J. P., Charest, J. M., Mills, R. W., Jank, B. J., Moser, P. T., Gilpin, S. E., et al. (2016). Bioengineering human myocardium on native extracellular matrix. *Physiol. Behav.* 176, 139–148. doi: 10.1016/j.physbeh.2017.03.040

Hanson, K. P., Jung, J. P., Tran, Q. A., Hsu, S. P. P., Iida, R., Ajeti, V., et al. (2013). Spatial and temporal analysis of extracellular matrix proteins in the developing murine heart: a blueprint for regeneration. *Tissue Eng. Part A* 19, 1132–1143. doi: 10.1089/ten.tea.2012.0316

Horn, M. A. (2015). Cardiac physiology of aging: extracellular considerations. *Compr. Physiol.* 5, 1069–1121. doi: 10.1002/cphy.c140063

Howard, C. M., and Baudino, T. A. (2013). Dynamic cell–cell and cell–ECM interactions in the heart. *J. Mol. Cell. Cardiol.* 70, 19–26. doi: 10.1016/j.yjmcc.2013.10.006

Huang, J., Potts, J. A. Y. D., Vincent, E. B., Weeks, D. L., and Runyanbf, R. B. (1995). Mechanisms of cell transformation in the embryonic heart. *Ann. N. Y. Acad. Sci.* 752, 317–330. doi: 10.1111/j.1749-6632.1995.tb17441.x

Hynes, R. O. (2009). Extracellular matrix: not just pretty fibrils. *Science* 326, 1216–1219. doi: 10.1126/science.1176009.Extracellular

Icardo, J. M., and Manasek, F. J. (1983). An indirect immunofluorescence study of the distribution of fibronectin during the formation of the cushion tissue mesenchyme in the embryonic heart. *Dev. Biol.* 101, 336–345. doi: 10.1016/0012-1606(84)90147-7

Ireland, R. G., and Simmons, C. A. (2015). Human pluripotent stem cell mechanobiology: manipulating the biophysical microenvironment for regenerative medicine and tissue engineering applications. *Stem Cells* 33, 3187–3196. doi: 10.1002/stem.2105

Jacot, J. G., McCulloch, A. D., and Omens, J. H. (2008). Substrate stiffness affects the functional maturation of neonatal rat ventricular myocytes. *Biophys. J.* 95, 3479–3487. doi: 10.1529/biophysj.107.124545

Jang, J., Park, H. J., Kim, S. W., Kim, H., Park, J. Y., Na, S. J., et al. (2017). 3D printed complex tissue construct using stem cell-laden decellularized extracellular matrix bioinks for cardiac repair. *Biomaterials* 112, 264–274. doi: 10.1016/j.biomaterials.2016.10.026

Johnson, T. D., Dequach, J. A., Gaetani, R., Ungerleider, J., Elhag, D., Nigam, V., et al. (2014). Human versus porcine tissue sourcing for an injectable myocardial matrix hydrogel. *Biomater. Sci.* 2, 735–744. doi: 10.1039/c3bm60283d

Jung, J. P., Hu, D., Domian, I. J., and Ogle, B. M. (2015). An integrated statistical model for enhanced murine cardiomyocyte differentiation via optimized engagement of 3D extracellular matrices. *Sci. Rep.* 5:18705. doi: 10.1038/srep18705

Kelly, R. G., Buckingham, M. E., and Moorman, A. F. (2014). Heart fields and cardiac morphogenesis. *Cold Spring Harb. Perspect. Med.* 4:a015750. doi: 10.1101/cshperspect.a015750

Kim, H. D., Yoon, C. S., Kim, H., and Rah, B. J. (1999). Expression of extracellular matrix components fibronectin and laminin in the human fetal heart. *Cell Struct. Funct.* 24, 19–26. doi: 10.1247/csf.24.19

Lee, P. F., Chau, E., Cabello, R., Yeh, A. T., Sampaio, L. C., Gobin, A. S., et al. (2017). Inverted orientation improves decellularization of whole porcine hearts. *Acta Biomater.* 49, 181–191. doi: 10.1016/j.actbio.2016.11.047

Li, R. A., Keung, W., Cashman, T. J., Backeris, P. C., Johnson, B. V., Bardot, E. S., et al. (2018). Bioengineering an electro-mechanically functional miniature ventricular heart chamber from human pluripotent stem cells HHS public access. *Biomaterials* 163, 116–127. doi: 10.1016/j.biomaterials.2018.02.024

Liau, B., Christoforou, N., Leong, K., and Bursac, N. (2011). Pluripotent stem cell-derived cardiac tissue patch with advanced structure and function. *Biomaterials* 32, 9180–9187. doi: 10.1038/jid.2014.371

Lie, D. C., Colamarino, S. A., Song, H. J., Désiré, L., Mira, H., Consiglio, A., et al. (2005). Wnt signalling regulates adult hippocampal neurogenesis. *Nature* 437, 1370–1375. doi: 10.1038/nature04108

Little, C. D., Piquet, D. M., Davis, L. A., Walters, L., and Drake, C. J. (1989). Distribution of laminin, collagen type IV, collagen type I, and fibronectin in chicken cardiac jelly/basement membrane. *Anat. Rec.* 224, 417–425. doi: 10.1002/ar.1092240310

Lockhart, M., Wirrig, E., Phelps, A., and Wessels, A. (2011). Extracellular matrix and heart development. *Birth Defects Res. Part A Clin. Mol. Teratol.* 91, 535–550. doi: 10.1002/bdra.20810

Lu, J., Kaestle, K., Huang, J., Liu, Q., Zhang, P., Gao, L., et al. (2017). Interactions of human embryonic stem cell-derived cardiovascular progenitor cells with immobilized extracellular matrix proteins. *J. Biomed. Mater. Res. Part A* 105, 1094–1104. doi: 10.1002/jbm.a.36005

Lu, T. Y., Lin, B., Kim, J., Sullivan, M., Tobita, K., Salama, G., et al. (2013). Repopulation of decellularized mouse heart with human induced pluripotent stem cell-derived cardiovascular progenitor cells. *Nat. Commun.* 4:2307. doi: 10.1038/ncomms3307

Lu, Y. Y., Chen, Y. C., Kao, Y. H., Wu, T. J., Chen, S. A., and Chen, Y. J. (2011). Extracellular matrix of collagen modulates intracellular calcium handling and electrophysiological characteristics of HL-1 cardiomyocytes with activation of angiotensin II type 1 receptor. *J. Card. Fail.* 17, 82–90. doi: 10.1016/j.cardfail.2010.10.002

Macqueen, L. A., Sheehy, S. P., Chantre, C. O., Zimmerman, J. F., Pasqualini, F. S., Liu, X., et al. (2018). A tissue-engineered scale model of the heart ventricle. *Nat. Biomed. Eng.* 2, 930–941. doi: 10.1038/s41551-018-0271-5

Masumoto, H., Nakane, T., Tinney, J. P., Yuan, F., Ye, F., Kowalski, W. J., et al. (2016). The myocardial regenerative potential of three-dimensional engineered cardiac tissues composed of multiple human iPS cell-derived cardiovascular cell lineages. *Sci. Rep.* 6:29933. doi: 10.1038/srep29933

Miyamoto, S., Teramoto, H., and Gutkind, J. S. (1996). Integrins can collaborate with growth factors for phosphorylation of receptor tyrosine kinases and MAP kinase activation: roles of integrin aggregation and occupancy of receptors. *J. Cell Biol.* 135, 1633–1642. doi: 10.1083/jcb.135.6.1633

Mjaatvedt, C. H., Lepera, R. C., and Markwald, R. R. (1987). Myocardial specificity for initiating endothelial-mesenchymal cell transition in embryonic chick heart correlates with a particulate distribution of fibronectin. *Dev. Biol.* 119, 59–67. doi: 10.1016/0012-1606(87)90206-5

Nakayama, K. H., Hou, L., and Huang, N. F. (2014). Role of extracellular matrix signaling cues in modulating cell fate commitment for cardiovascular tissue engineering. *Adv. Healthc. Mater.* 3, 628–641. doi: 10.1002/adhm.201300620

Neiman, G., Scarafía, M. A., La Greca, A., Velazque, N. L. S., Garate, X., Waisman, A., et al. (2019). Integrin alpha-5 subunit is critical for the early stages of human pluripotent stem cell cardiac differentiation. *Sci. Rep.* 9:18077.

Noor, N., Shapira, A., Edri, R., Gal, I., Wertheim, L., and Dvir, T. (2019). 3D printing of personalized thick and perfusable cardiac patches and hearts. *Adv. Sci.* 6:1900344. doi: 10.1002/advs.201900344

Oberwallner, B., Brodarac, A., Anić, P., Šarić, T., Wassilew, K., Neef, K., et al. (2015). Human cardiac extracellular matrix supports myocardial lineage commitment of pluripotent stem cells. *Eur. J. Cardiothorac. Surg.* 47, 416–425. doi: 10.1093/ejcts/ezu163

Ott, H. C., Matthiesen, T. S., Goh, S. K., Black, L. D., Kren, S. M., Netoff, T. I., et al. (2008). Perfusion-decellularized matrix: using nature's platform to engineer a bioartificial heart. *Nat. Med.* 14, 213–221. doi: 10.1038/nm1684

Ou, D. B., He, Y., Chen, R., Teng, J. W., Wang, H. T., Zeng, D., et al. (2011). Three-dimensional co-culture facilitates the differentiation of embryonic stem cells into mature cardiomyocytes. *J. Cell. Biochem.* 112, 3555–3562. doi: 10.1002/jcb.23283

Pagano, F., Angelini, F., Castaldo, C., Picchio, V., Messina, E., Sciarretta, S., et al. (2017). Normal versus pathological cardiac fibroblast-derived extracellular

matrix differentially modulates cardiosphere-derived cell paracrine properties and commitment. *Stem Cells Int.* 2017:7396462. doi: 10.1155/2017/7396462

Pasquier, J., Gupta, R., Rioult, D., Hoarau-Véchot, J., Courjaret, R., Machaca, K., et al. (2017). Coculturing with endothelial cells promotes in vitro maturation and electrical coupling of human embryonic stem cell–derived cardiomyocytes. *J. Hear Lung Transplant.* 36, 684–693. doi: 10.1016/j.healun.2017.01.001

Pati, F., and Cho, D. W. (2017). Bioprinting of 3D tissue models using decellularized extracellular matrix bioink. *Methods Mol. Biol.* 1612, 381–390. doi: 10.1007/978-1-4939-7021-6_27

Pesce, M., Messina, E., Chimenti, I., and Beltrami, A. P. (2017). Cardiac mechanoperception: a life-long story from early beats to aging and failure. *Stem Cells Dev.* 26, 77–90. doi: 10.1089/scd.2016.0206

Reya, T., Duncan, A. W., Ailles, L., Domen, J., Scherer, D. C., Willert, K., et al. (2003). A role for Wnt signalling in self-renewal of haematopoietic stem cells. *Nature* 423, 409–414. doi: 10.1038/nature01593

Rienks, M., Papageorgiou, A.-P., Frangogiannis, N. G., and Heymans, S. (2014). Myocardial extracellular matrix. *Circ. Res.* 114, 872–888. doi: 10.1161/CIRCRESAHA.114.302533

Ross, R. S., and Borg, T. K. (2001). Integrins and the myocardium. *Circ. Res.* 88, 1112–1119. doi: 10.1161/hh1101.091862

Sa, S., Wong, L., and McCloskey, K. E. (2014). Combinatorial fibronectin and laminin signaling promote highly efficient cardiac differentiation of human embryonic stem cells. *Biores. Open Access* 3, 150–161. doi: 10.1089/biores.2014.0018

Saleem, S., Li, J., Yee, S., Fellows, G. F., Goodyer, C. G., and Wang, R. (2009). β1 integrin/FAK/ERK signalling pathway is essential for human fetal islet cell differentiation and survival. *J. Pathol.* 219, 182–192. doi: 10.1002/path

Sánchez, P. L., Fernández-Santos, M. E., Costanza, S., Climent, A. M., Moscoso, I., Gonzalez-Nicolas, M. A., et al. (2015). Acellular human heart matrix: a critical step toward whole heart grafts. *Biomaterials* 61, 279–289. doi: 10.1016/j.biomaterials.2015.04.056

Schenke-Layland, K., Nsair, A., Van Handel, B., Angelis, E., Gluck, J. M., Votteler, M., et al. (2012). Recapitulation of the embryonic cardiovascular progenitor cell niche. *Biomaterials* 32, 2748–2756. doi: 10.1016/j.biomaterials.2010.12.046. Recapitulation

Singelyn, J. M., and Christman, K. L. (2010). Injectable materials for the treatment of myocardial infarction and heart failure: the promise of decellularized matrices. *J. Cardiovasc. Transl. Res.* 3, 478–486. doi: 10.1007/s12265-010-9202-x

Tallawi, M., Rai, R., Boccaccini, A. R., and Aifantis, K. E. (2015). Effect of substrate mechanics on cardiomyocyte maturation and growth. *Tissue Eng. Part B Rev.* 21, 157–165. doi: 10.1089/ten.teb.2014.0383

Tang-Quan, K. R., Mehta, N. A., Sampaio, L. C., and Taylor, D. A. (2018). Whole cardiac tissue bioscaffolds. *Adv. Exp. Med. Biol.* 1098, 59–83. doi: 10.1007/978-3-319-97421-7

Thiery, J. P., Acloque, H., Huang, R. Y. J., and Nieto, M. A. (2009). Epithelial-mesenchymal transitions in development and disease. *Cell* 139, 871–890. doi: 10.1016/j.cell.2009.11.007

Thompson, R. P., Fitzharris, T. P., Denslow, S., and LeRoy, E. C. (1979). Collagen synthesis in the developing chick heart. *Tex. Rep. Biol. Med.* 39, 305–319.

Valls-Margarit, M., Iglesias-García, O., Di Guglielmo, C., Sarlabous, L., Tadevosyan, K., Paoli, R., et al. (2019). Engineered macroscale cardiac constructs elicit human myocardial tissue-like functionality. *Stem Cell Rep.* 13, 207–220. doi: 10.1016/j.stemcr.2019.05.024

Vanwinkle, W. B., Snuggs, M. B., and Buja, L. M. (1996). Cardiogel: a biosynthetic extracellular matrix for cardiomyocyte culture. *Vitr. Cell. Dev. Biol. Anim.* 32, 478–485. doi: 10.1007/BF02723051

Votteler, M., Kluger, P. J., Walles, H., and Schenke-layland, K. (2010). Stem cell microenvironments - unveiling the secret of how stem cell fate is defined. *Macromol. Biosci.* 10, 1302–1315. doi: 10.1002/mabi.201000102

Vuorenpää, H., Penttinen, K., Heinonen, T., Pekkanen-Mattila, M., Sarkanen, J. R., Ylikomi, T., et al. (2017). Maturation of human pluripotent stem cell derived cardiomyocytes is improved in cardiovascular construct. *Cytotechnology* 69, 785–800. doi: 10.1007/s10616-017-0088-1

Wang, X., Harris, R. E., Bayston, L. J., and Ashe, H. L. (2008). Type IV collagens regulate BMP signalling in *Drosophila*. *Nature* 2, 313–315. doi: 10.1038/nature07214

Wang, Z., Long, D. W., Huang, Y., Chen, W. C. W., Kim, K., and Wang, Y. (2019). Decellularized neonatal cardiac extracellular matrix prevents widespread ventricular remodeling in adult mammals after myocardial infarction. *Acta Biomater.* 87, 140–151. doi: 10.1016/j.actbio.2019.01.062

Witman, N., and Sahara, M. (2018). Cardiac progenitor cells in basic biology and regenerative medicine. *Stem Cells Int.* 2018:8283648. doi: 10.1155/2018/8283648

Wozniak, M. A., Modzelewska, K., Kwong, L., and Keely, P. J. (2004). Focal adhesion regulation of cell behavior. *Biochim. Biophys. Acta Mol. Cell Res.* 1692, 103–119. doi: 10.1016/j.bbamcr.2004.04.007

Young, J. L., and Engler, A. J. (2011). Hydrogels with time-dependent material properties enhance cardiomyocyte differentiation in vitro. *Bone* 32, 1002–1009. doi: 10.1038/jid.2014.371

Yu, C., Ma, X., Zhu, W., Wang, P., Miller, K. L., Stupin, J., et al. (2019). Scanningless and continuous 3D bioprinting of human tissues with decellularized extracellular matrix. *Biomaterials* 194, 1–13. doi: 10.1016/j.biomaterials.2018.12.009

Yustzey, K. E., and Kirby, M. L. (2002). Wherefore heart thou? Embryonic origins of cardiogenic. *Dev. Dyn.* 320, 307–320. doi: 10.1002/dvdy.10068

Zeng, D., Ou, D. B., Wei, T., Ding, L., Liu, X. T., Hu, X. L., et al. (2013). Collagen/β1 integrin interaction is required for embryoid body formation during cardiogenesis from murine induced pluripotent stem cells. *BMC Cell Biol.* 14:5. doi: 10.1186/1471-2121-14-5

Zhang, J., Klos, M., Wilson, G. F., Herman, A. M., Lian, X., Raval, K. K., et al. (2012). Extracellular matrix promotes highly efficient cardiac differentiation of human pluripotent stem cells: the matrix sandwich method. *Circ. Res.* 111, 1125–1136. doi: 10.1161/CIRCRESAHA.112.273144

Zhang, J., Tao, R., Campbell, K. F., Carvalho, J. L., Ruiz, E. C., Kim, G. C., et al. (2019). Functional cardiac fibroblasts derived from human pluripotent stem cells via second heart field progenitors. *Nat. Commun.* 10:2238.

Conflict of Interest: The authors declare that the research was conducted in the absence of any commercial or financial relationships that could be construed as a potential conflict of interest.

Copyright © 2020 Pagliarosi, Picchio, Chimenti, Messina and Gaetani. This is an open-access article distributed under the terms of the Creative Commons Attribution License (CC BY). The use, distribution or reproduction in other forums is permitted, provided the original author(s) and the copyright owner(s) are credited and that the original publication in this journal is cited, in accordance with accepted academic practice. No use, distribution or reproduction is permitted which does not comply with these terms.

frontiers in Genetics

ORIGINAL RESEARCH
published: 04 September 2020
doi: 10.3389/fgene.2020.563798

Integrated Analyses of Mouse Stem Cell Transcriptomes Provide Clues for Stem Cell Maintenance and Transdifferentiation

Li-Juan Wang[1,2†], Xiao-Xiao Li[1,2†], Jie Hou[2], Xin-Hua Song[2], Wen-Hai Xie[1,2] and Liang Shen[1,2*]*

[1] Zibo Key Laboratory of New Drug Development of Neurodegenerative Diseases, Shandong Provincial Research Center for Bioinformatics Engineering and Technique, Institute of Biomedical Research, Shandong University of Technology, Zibo, China, [2] School of Life Sciences, Shandong University of Technology, Zibo, China

In vivo cell fate reprogramming has emerged as a new method for understanding cell plasticity and as potential treatment for tissue regeneration. Highly efficient and precise reprogramming requires fully understanding of the transcriptomes which function within different cell types. Here, we adopt weighted gene co-expression network analysis (WGCNA) to explore the molecular mechanisms of self-renewal in several well-known stem cell types, including embryonic stem cells (ESC), primordial germ cells (PGC), spermatogonia stem cells (SSC), neural stem cells (NSC), mesenchymal stem cells (MSC), and hematopoietic stem cells (HSC). We identified 37 core genes that were up-regulated in all of the stem cell types examined, as well as stem cell correlated gene co-expression networks. The validation of the co-expression genes revealed a continued protein-protein interaction network that included 823 nodes and 3113 edges. Based on the topology, we identified six densely connected regions within the continued protein-protein interaction network. The SSC specific genes *Itgam*, *Cxcr6*, and *Agtr2* bridged four densely connected regions that consisted primarily of HSC-, NSC-, and MSC-correlated genes. The expression levels of identified stem cell related transcription factors were confirmed consistent with bioinformatics prediction in ESCs and NSCs by qPCR. Exploring the mechanisms underlying adult stem cell self-renewal will aid in the understanding of stem cell pool maintenance and will promote more accurate and efficient strategies for tissue regeneration and repair.

Keywords: stem cell, transcriptomes, transdifferentiation, co-expression, network

OPEN ACCESS

Edited by:
Andrei S. Chagin, Karolinska Institutet (KI), Sweden

Reviewed by:
Toshiyuki Yamane, Mie University, Japan
Philippe Bourin, Independent Researcher, Toulouse, France

***Correspondence:**
Wen-Hai Xie
xiewenhai@sdut.edu.cn
Liang Shen
shen@sdut.edu.cn

† These authors have contributed equally to this work

Specialty section:
This article was submitted to Stem Cell Research, a section of the journal Frontiers in Genetics

Received: *19 May 2020*
Accepted: *17 August 2020*
Published: *04 September 2020*

Citation:
Wang L-J, Li X-X, Hou J, Song X-H, Xie W-H and Shen L (2020) Integrated Analyses of Mouse Stem Cell Transcriptomes Provide Clues for Stem Cell Maintenance and Transdifferentiation. Front. Genet. 11:563798. doi: 10.3389/fgene.2020.563798

INTRODUCTION

In mammals, different tissues and organs exhibit different capacities for regeneration that are based on the regenerative capacities of endogenous stem cells (Xia et al., 2018). ESCs are pluripotent stem cells that are able to differentiate into more than 220 cell types within the adult human body (Thomson et al., 1998). Since the initial isolation of embryonic stem cells (ESCs), stem cell biology has attracted increasing attention. Although the capacity of tissue regeneration in mammals is progressively lost during development, several tissues and organs still maintain stem cell niches that produce progeny cells which promote tissue regeneration (Adams and Scadden, 2006; Oatley et al., 2009). Accumulating evidence also indicates that the isolation of stem cells from others

tissue or organs, including the intestine, liver, and teeth, is feasible and that those stem cells can maintain the regeneration of their respective tissues under certain circumstances (Hosoya et al., 2020; Takahashi and Shiraishi, 2020). The best-characterized types of adult stem cells in mammals are hematopoietic (HSCs), neural (NSCs), mesenchymal (MSCs), and spermatogonia (SSCs) stem cells. HSCs, NSCs, and SSCs can be respectively differentiated into special lineage progeny cells such as bloods cells, neurons or glia cells, and spermatogonia. MSCs are multipotent adult stem cells that can differentiate into many kinds of tissues that include bone, cartilage, muscle, fat cells, and connective tissue (Prockop, 1997). Based on their diversity, multipotency and availability, MSCs have successfully attracted increasing attention for use in tissue repair and regeneration (Nimiritsky et al., 2019; Yin et al., 2019).

Certain tissue-derived stem cells can not only differentiate into destined progeny cells but also transdifferentiate into different stem cell lineages. ESC and MSC-derived neural precursors and neurons have been used in cell therapy strategies to cure neurodegenerative diseases (Lo Furno et al., 2018; Zhang et al., 2020). SSCs that are unipotent in regard to spermatogenesis have also been reprogrammed into pluripotent stem cells (Guan et al., 2006). Induced pluripotent stem cells (iPS) that were generated directly from fibroblasts have clarified the mechanisms underlying transdifferentiation and can provide an endless supply of cells for patient-specific or disease-specific cell therapy without the issue of ethical controversy (Takahashi and Yamanaka, 2006; Takahashi et al., 2007). As the transfection of inducing transcription factors typically requires the use of a retrovirus or lentivirus vector, an elevated risk for the formation of teratomas exists in iPS cell-based therapy. Non-integrating techniques for the generation of iPS have become available in recent years, and these include the use of mRNA (Sridhar et al., 2016), proteins (Nordin et al., 2017), and small chemical molecules (Hou et al., 2013). The risk of teratoma formation also exists when non-integrating techniques are used to generate iPS, and this risk is primarily due to the remainder undifferentiated pluripotent cells after transplantation (Knoepfler, 2009). Direct transdifferentiation, which involves the conversion of somatic cells into other terminal differentiated cell lineages, offers a safer and more attractive strategy for tissue repair (Gascon et al., 2017; Ghiroldi et al., 2017; Pereira et al., 2019). The exogenous expression of neural lineage-specific transcription factors *Ascl1*, *Brn2*, and *Myt1l* successful convert fibroblasts into neurons directly (Caiazzo et al., 2015). The use of another five-factors cocktail that included *Foxg1*, *Sox2*, *Ascl1*, *Dlx5*, and *Lhx6* also converted fibroblasts into induced GABAergic interneurons (Colasante et al., 2015). Human gingival fibroblasts could be induced to transdifferentiate into functional osteoblasts via epigenetic modification and the induction of osteogenic signaling *in vitro* and *in vivo* (Cho et al., 2017). Several pancreatic transcription factors have been found to induce liver transdifferentiation into pancreatic tissues (Luo et al., 2014). Small molecules could also convert fibroblasts into islet-like cells by allowing these cells to avoid a pluripotent state (Li et al., 2014). Studies focusing on liver regeneration have suggested endogenous reprogramming as a therapeutic strategy for cell repair. Ectopic expression of *Foxa3*, *Gata4*, *Hnf1a*, and *Hnf4a* can convert murine myofibroblasts into hepatocyte-like cells *in vivo* (Song et al., 2016; Cheng et al., 2019). Ectopic expression of *Sox2* is sufficient to convert astrocytes into ASCL1-positive neural progenitors (Niu et al., 2013). Further studies revealed that *Sox2*-dependent *in vivo* reprogramming is regulated by several transcription factors, such as *Ascl1*, *Nr2e1*, *p53* and *p21* (Islam et al., 2015; Wang et al., 2016). Brain glial cells can also be directly reprogrammed into neurons by ectopic expression of other transcription factors, such as *Brn2*, *Myt1l*, *Neurod1*, and *Neurog2* (Grande et al., 2013; Torper et al., 2013; Guo et al., 2014). *In vivo* cell fate reprogramming has emerged as a new means of understanding cell plasticity and as a potential treatment in tissue regeneration. A more comprehensive understanding of the mechanisms underlying cell fate reprogramming would promote the development of more accurate and efficient strategies for tissue regeneration and repair.

Based on the observation that terminally differentiated cells can be reprogrammed into different cell lineages, transdifferentiation of stem cells may also be feasible. Understanding mechanisms govern the special properties of stem cells will provide useful information for tissue repair and regeneration. To develop safety strategies for stem cell transdifferentiation *in vivo*, it is necessary to clarify the mechanisms underlying the regulation and function of different stem cell types. Comprehensive comparisons of transcriptome characteristics of adult stem cells remain relatively rare. Here, we focus on the underlying molecular mechanisms governing self-renewal in several well-known stem cell types. WGCNA can be used to identify co-expression networks associated with different cell types (Langfelder and Horvath, 2008; Yandim and Karakulah, 2019; Yang et al., 2019; Liao et al., 2020). The expression profiles of the six best-characterized types of stem cells (ESCs, HSCs, MSCs, SSCs, PGCs, and NSCs) were re-analyzed by WGCNA. Six stem cell correlated gene co-expression networks in conjunction with identified transcription factors were constructed, and 37 genes were identified as up-regulated genes in all of these stem cells. The validation of the co-expression gene networks resulted in construction of a continued protein-protein interaction network for stem cell transdifferentiation. The topology analysis of the continued protein-protein interaction network provided useful information in regard to stem cell maintenance and transdifferentiation. CTCF binding motif analyses indicated that stem cells occupy less CTCF, indicating that stem cells require chromosome opening activity to maintain stem cell-specific stemness properties. Clarifying the mechanisms underlying stem cell self-renewal will aid us in understanding of this process and will allow us to develop more accurate and efficient strategies for tissue regeneration and repair.

MATERIALS AND METHODS

Transcriptional Profiling of Stem Cells

The gene expression profiles of ESCs (Zhao et al., 2009), PGCs (Miyoshi et al., 2016), SSCs (Oatley et al., 2009), NSCs (Azim et al., 2015), MSCs (Wislet-Gendebien et al., 2012), and HSCs

(Kvinlaug et al., 2011) were downloaded from public database (Gene Expression Omnibus database, GEO). In order to obtain the stem cell up-regulated genes, mouse embryo fibroblast cells (MEF) were used as a control to remove genes that are common between stem cells and MEF. All datasets were hybridized on the Mouse Genome 430 2.0 array. The Affy package of R was used to process the initial datasets (Gautier et al., 2004). The RMA function was adopted to obtain the expression of probes. PCA of the datasets displayed different developmental potentials among the selected stem cell types. Respective stem cell correlated gene lists were obtained by comparing the expression profiles to those of MEFs based on linear models and empirical Bayes methods. Benjamini and Hochberg's method was used to control for the false discovery rate (FDR), and we used the adjusted *p*-values to control for the FDR. The FDR ratio was set as 5%. Adjusted *p*-values of <0.01 and log (Foldchange) of >1.5 were selected as the thresholds for the stem cell up-regulated genes. The UpSetR package was used to display the interactions among the stem cell up-regulated genes for all six of the stem cell types (Conway et al., 2017).

Weighted Gene Co-expression Network Analysis

The respective stem cell correlated genes were combined to form an expression matrix that was used for further research. WGCNA was employed to identify co-expression modules (Langfelder and Horvath, 2008). The power of 20 was adopted as soft-threshold for the analysis. Depending upon the resulting adjacency matrix, we calculated the topological overlap matrix to measure the interconnectedness of the co-expression network. The Dynamic Hybrid Tree Cut algorithm was used to define modules that were representative of the co-expression genes. Modules with a correlation of above 0.85 were merged together. After identifying the co-expression modules, we associated these modules with respective cell types. Modules with a correlation of >0.80 ($p < 0.01$) were designated as stem cell correlated modules.

Topological Analysis of Modules That Are Associated With Stem Cell Types

The genes within stem cell correlated modules that exhibit high connectivity may play similar roles in the maintenance of stem cell properties. Cytoscape (version 3.7.1) software was used to performed topological analysis of the co-expression network (Shannon et al., 2003). Hub genes were identified based on a high degree of connectivity among the genes in the respective modules. The Cytoscape plug-in MCODE was used to identify densely connected regions from the entire network (Bader and Hogue, 2003). We selected clusters exhibiting MCODE scores of >3.5, and greater than 10 nodes were used as candidate clusters. Transcription factor annotation was performed based on AnimalTFDB 3.0 (Hu et al., 2018).

Quantitative RT-PCR

Neural stem cells were isolated from E12.5 mouse embryonic cortex conserved in our lab. ESCs and MEF were gifts from Kang Zou. Total RNA from ESCs, NSCs and MEF were extracted using Trizol reagent (Invitrogen). Primescript Reverse Transcriptase (Thermo Fisher) was used to synthesize cDNA. The detection of genes expression was performed based on Real-time PCR with SYBR Green (BioTeke). The expression levels of all the genes tested were determined relative to β-actin transcript levels. Primer sequences are listed in **Supplmentary Table S1**.

Gene Ontology Analysis

Gene ontology analyses of identified modules and core genes were performed by DAVID (Huang da et al., 2009). The corrected FDR with a *p* value of <0.05 was selected as threshold for enriched GO terms.

CTCF Analysis of Respective Stem Cell-Specific Hub Genes

CTCF binding motif analysis was performed using CTCFBSDB 2.0 which was developed for CTCF binding sites and genome organization (Ziebarth et al., 2013). The top 20 hub genes within the respective stem cell-specific modules were analyzed for the presence of a CTCF binding motif. Random sampling was used to evaluate the genome wide CTCF binding sites. Random samplings of 20 genes were performed on the formed expression matrix. Random sampling was performed 100,000 times to reflect the random occupancy rates of the CTCF binding motif.

Cross-Species Annotation Between Mouse and Human Stem Cells Up-Regulated Genes

Human ESC, NSC, SSC, MSC, HSC, and fibroblast datasets that based on the microarray platform GPL570 from GEO database. Fibroblast datasets were used as a control to obtain human stem cell up-regulated genes. The parameters of human stem cell data analysis are the same as used in mouse data mining. The R package of homologene was used to cross-species annotation.

RESULTS

Transcription Profiles of Respective Stem Cell Types

Based on the different expression analysis, we obtained a list of genes that were up-regulated in specific stem cell types that included ESCs (1751), PGCs (2349), SSCs (2157), NSCs (2224), MSCs (551), and HSCs (2624) (**Figure 1A**). We also observed 64 intersections among these highly expressed specific stem cell genes. The highly expressed gene lists for each stem cell type are provided in **Supplementary Table S2**. The number of genes only in the respective stem cell was lower than 40%, in contrast to up-regulated genes (**Supplementary Figure S1**). The ESCs-only section was 24.4%. The proportions of ESCs, PGCs and SSCs were more than the other three adult stem cells. ESCs, PGCs, and SSCs shared 247 genes, as shown with a blue bar in **Figure 1A**; this was consistent with the pluripotency of ESCs, PGCs, and SSCs. Several studies have demonstrated that PGCs and SSCs possess a pluripotency similar to ESCs under

proper conditions (Matsui et al., 1992; Kanatsu-Shinohara et al., 2004; Seandel et al., 2007). Principal Component Analysis (PCA) revealed that ESCs, SSCs, and PGCs were more similar to each other than the other three types of stem cells (**Figure 1B**). Bone-derived MSCs was more related to mouse embryo fibroblast cells (MEF) than HSCs. The highest ratio of those six stem types was HSCs, which was coincident with the unipotent stem cell of HSCs. The intersect sizes of ESCs and the other five types of stem cells were 186 (PGC), 134 (SSC), 77 (NSC), 10 (MSC), and 50 (HSC), which are shown with the purple bar in **Figure 1A**. The Venn analysis revealed that the six stem cell types shared 37 common genes (**Figure 1A**). The relative expression values of those 37 core genes among stem cells and MEF are shown in **Supplementary Figure S2**. The clustering of the stem cell types was consistent with the result of PCA. ESCs, SSCs, and PGCs were more closely to each other. The 37 core genes were assigned to two large blocks based on heatmap analysis (**Supplementary Figure S2**). *Cdca5*, *Trim37*, *Mllt4*, and other 15 other genes were highly expressed compared to MEF. The expressions of the 37 highly expressed core genes are detailed in **Table 1**. The foldchanges of the respective types of stem cells were compared to MEF. The Gene Ontology (GO) analysis of the biological function of the 37 common up-regulated genes indicated that these genes were involved in DNA recombination, chromatin organization, and DNA metabolic processes (**Figure 1C**). *Trim37*, *Tle4*, *Dnmt1*, *Cdca5*, and *Brca1* were enriched with the molecular function of chromatin binding. This was consistent with the idea that stem cells that are actively maintaining self-renewal require higher mitotic activity and a greater number of cell divisions. The 37 core genes may play important roles in maintaining a more open chromatin conformation during self-renewal.

WGCNA Identified Stem Cell-Specific Co-expression Gene Modules

The respective stem cell-specific genes formed an expression matrix that included 6690 genes. WGCNA analysis was performed to isolate stem cell correlated co-expression genes modules based on the formed expression matrix. The soft threshold power for network construction was selected as 20 (**Figure 2A**). The eigengenes of modules correlated above 0.85

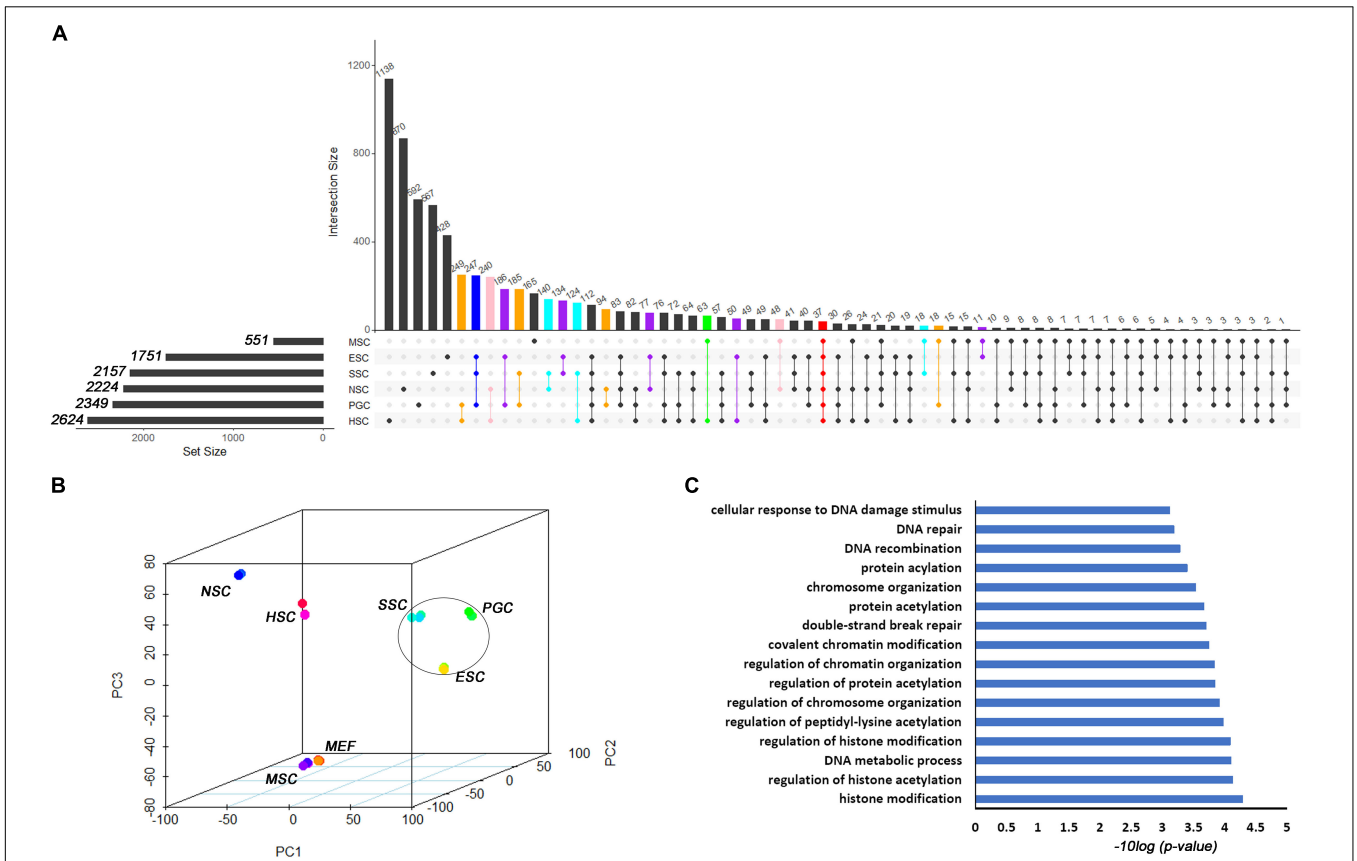


FIGURE 1 | Transcription profiles for ESCs, PGCs, SSCs, NSCs, MSCs, and HSCs. **(A)** The intersection of highly expressed genes from the six types of stem cells. Dots represents the intersections of the six types of stem cells in the Venn analysis. The bar represents the size of the individual intersections. Dots with lines show highly expressed genes shared by the lined stem cells types. Different intersections of those six types of stem cells are highlighted with different colors. The 37 commonly highly expressed genes among the six types of stem cells are highlighted with red bar. **(B)** PCA revealed differences among the six types of stem cells. **(C)** GO analysis of the biological function of the core 37 core commonly highly expressed genes. The benjamini-adjusted *p* value of <0.05 was selected as threshold for enrichment of GO_BP_FAT terms.

TABLE 1 | The 37 core highly expressed genes.

Gene Symbol	ESC		PGC		SSC		NSC		MSC		HSC	
	logFC	adj.P.Val	logFC	adj.P.Val	logFC	adj.P.Val	logFC	adj.P.Val	logFC	adj.P.Val	logFC	adj.P.Val
Cdca5	3.36	5.94E−08	3.34	9.93E−08	3.40	6.40E−07	3.20	3.80E−10	1.87	2.95E−06	2.39	1.96E−03
Trim37	1.57	2.33E−05	3.58	2.81E−07	3.25	2.31E−07	3.63	6.11E−10	1.82	1.02E−05	2.75	4.13E−05
Mllt4	2.39	1.58E−07	1.78	2.31E−06	2.49	1.30E−07	2.46	1.18E−08	1.86	1.44E−06	2.73	1.70E−05
Chek1	2.43	6.19E−08	2.72	1.08E−07	2.29	8.29E−06	2.45	1.22E−09	1.75	5.19E−07	2.05	5.84E−04
Brca1	3.69	1.82E−08	3.70	5.47E−08	3.42	1.33E−07	2.47	6.81E−10	2.08	6.92E−07	1.70	1.93E−03
Tle4	4.93	3.85E−08	5.02	3.54E−08	3.68	1.15E−07	3.48	6.98E−10	1.62	1.53E−05	5.39	2.26E−06
Rffl	2.59	3.58E−08	5.14	6.34E−09	3.76	1.01E−08	2.83	2.93E−10	1.85	3.15E−07	5.41	2.52E−06
Tab3	1.63	6.47E−07	3.40	3.79E−08	3.23	2.49E−08	2.77	1.94E−10	1.74	6.81E−07	2.86	9.80E−06
Psmc3ip	2.45	4.93E−07	4.03	1.08E−07	2.37	7.38E−05	3.11	7.67E−10	1.96	5.42E−06	3.57	7.79E−04
Cmss1	2.24	1.85E−07	2.62	1.73E−07	1.75	1.88E−06	2.59	8.82E−10	1.83	3.75E−06	2.30	2.94E−05
Plekha8	2.51	1.20E−07	3.30	1.11E−07	3.57	2.08E−08	2.18	2.48E−08	1.66	1.44E−06	1.61	3.86E−04
Dscc1	2.89	8.46E−08	3.36	1.18E−07	3.17	5.23E−06	3.52	1.46E−10	2.74	5.41E−07	2.29	1.31E−04
Dock9	2.14	1.19E−06	2.82	3.71E−07	4.05	3.95E−08	1.95	4.34E−08	2.10	1.46E−06	3.22	4.17E−05
Gsta4	6.86	4.30E−08	4.25	6.85E−07	5.38	8.06E−08	3.27	2.24E−08	3.45	2.07E−06	3.84	1.10E−04
Incenp	2.09	1.52E−07	3.17	4.06E−08	2.61	1.84E−06	2.45	1.62E−09	1.81	7.77E−07	2.77	7.76E−04
Dnmt1	2.07	1.65E−07	3.83	2.01E−08	2.91	5.57E−08	2.48	1.89E−08	1.85	3.01E−07	4.22	1.26E−05
Camk1d	3.36	4.94E−08	2.80	4.35E−07	3.17	6.50E−08	2.17	9.08E−09	3.38	7.90E−08	4.29	1.46E−05
Tmem170	2.50	4.25E−07	2.08	4.63E−05	1.83	1.53E−06	2.04	2.07E−08	1.87	2.31E−06	2.91	4.99E−05
Rad54b	3.32	2.75E−08	3.24	2.24E−07	3.63	1.31E−06	2.51	3.49E−08	2.11	3.68E−06	3.56	1.05E−05
Tmem243	2.50	6.47E−08	4.39	1.24E−08	2.41	2.10E−07	2.00	4.79E−09	2.28	2.13E−07	2.84	7.62E−03
Foxred2	2.44	9.71E−07	1.65	1.69E−05	1.99	2.23E−06	2.57	1.52E−08	2.07	1.38E−06	5.34	9.28E−05
Exoc6	3.24	4.59E−07	3.56	4.60E−07	2.76	1.34E−06	3.23	2.88E−09	1.93	9.27E−06	6.11	4.21E−06
Mis18bp1	2.97	3.58E−08	3.16	7.98E−07	2.82	1.75E−06	2.63	3.13E−09	1.75	1.93E−06	1.60	1.16E−03
Nav2	2.85	5.40E−07	2.29	1.87E−05	1.72	3.05E−05	2.57	3.55E−08	1.70	4.39E−05	4.40	4.72E−06
Rad51ap1	2.24	3.02E−07	1.84	1.16E−06	1.62	3.62E−05	1.86	5.61E−09	2.07	3.74E−06	2.16	8.17E−05
Ddb2	1.76	1.92E−06	3.90	4.36E−08	3.92	5.14E−08	3.10	2.36E−10	1.69	1.49E−06	4.79	7.74E−06
Cep70	2.55	3.68E−07	3.78	1.06E−07	3.27	5.16E−07	3.97	1.80E−10	1.88	4.35E−06	4.46	2.83E−06
Taf7	4.75	5.74E−09	4.84	2.08E−08	5.48	5.97E−09	1.63	5.81E−08	1.93	3.69E−07	3.74	7.01E−05
Kbtbd8	5.09	6.20E−09	5.96	1.11E−08	4.85	3.18E−08	3.91	5.36E−11	2.11	4.64E−06	2.57	3.87E−03
4930422N03Rik	2.17	1.96E−06	6.38	9.40E−09	5.34	8.81E−09	2.84	1.18E−09	1.66	3.63E−05	4.01	1.31E−05
Depdc1b	2.41	2.73E−05	1.61	3.61E−04	1.98	5.53E−05	3.01	8.87E−08	1.68	2.11E−04	1.72	5.66E−03
C2cd5	3.73	5.89E−09	5.03	6.04E−09	2.29	3.75E−07	3.42	4.39E−11	1.86	2.68E−07	3.50	5.27E−05
Ctnnal1	6.01	1.78E−08	2.97	8.81E−07	1.81	1.06E−03	3.44	1.80E−09	3.56	7.03E−07	4.29	1.05E−05
Rps6ka6	6.29	9.41E−08	4.76	4.13E−07	4.78	3.13E−07	6.22	1.83E−10	3.11	8.37E−06	2.50	3.28E−03
Rab6b	2.17	1.14E−05	4.00	4.56E−08	2.53	9.25E−08	5.65	5.49E−12	4.03	8.71E−09	1.57	4.90E−04
Cdkl5	1.99	2.48E−05	2.43	7.99E−06	2.78	4.02E−07	3.77	1.42E−10	2.67	7.33E−07	2.10	2.44E−03
Rps6ka5	1.55	2.44E−05	2.31	2.37E−07	2.53	8.16E−08	2.59	1.34E−09	2.64	4.85E−07	4.80	1.64E−06

were merged, and a heat map of the gene dendrogram was assigned to the six different subtypes of stem cells (**Figure 2B**). From the heatmap, we can easily obtain information of cluster genes which were highly expressed with stem cell types. Gene module eigengenes were classified into three groups by hierarchical clustering (**Figure 2C**). Modules correlated to stem cell types that possessed correlations of above 0.80 were selected for further study. We found 11 modules that were correlated to the six stem cell types based on the correlation between modules and respective stem cell types (**Figure 2D**). Specifically, purple was correlated to ESCs, brown was correlated to PGCs, yellow, light cyan, and dark gray modules were correlated to SSCs, turquoise and salmon modules were correlated to NSCs, the pink module was correlated to MSCs, and blue, bisque4, and indianred4 were correlated to HSCs. WGCNA identified stem cell special co-expression networks which make it possible to detail the mechanisms of stem cell maintenance.

Function Annotation of Stem Cells Types Respective Modules

Functional annotations of the respective types of stem cells correlated modules were performed by DAVID system. The enriched GO_BP terms were consistent with their respective stem cell characteristic properties. The purple module, which is related to ESCs, was involved in multicellular organism

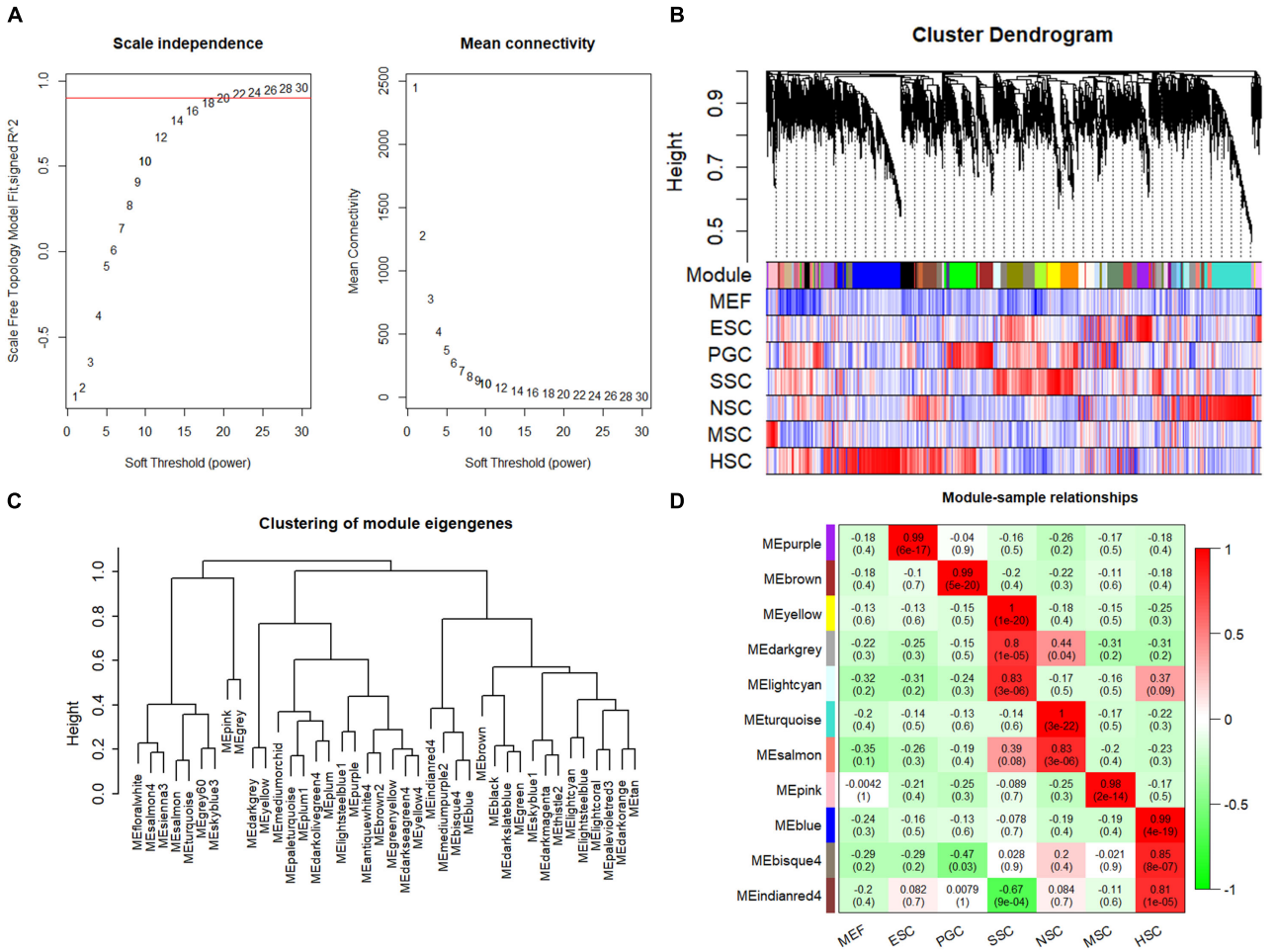


FIGURE 2 | WGCNA identified stem cell type-specific highly expressed genes. **(A)** Selection of soft thresholding powers for WGCNA. The red line corresponds to 0.9. As the lowest power that satisfies the approximate scale-free topology criterion, the number 20 was interpreted as a soft-threshold of the correlation matrix. **(B)** Heat map of the gene dendrogram that was assigned to the six different subtypes of stem cells. The colored row indicates the expression values of genes in the dendrogram. **(C)** The identified module eigengenes were classified into three groups by hierarchical clustering. **(D)** Heat map of the six different subtypes of stem cell-specific modules. Modules with a correlation of >0.80 ($p < 0.01$) were designated as stem cell-specific modules. Each row and column corresponded to the identified module and stem cell type. The correlations and *p*-values of the corresponding modules were labeled.

development, endoderm development, and the establishment of various organs and cells (**Figure 3A**). This was consistent with the multi-lineage differentiation potential of ESCs. Brown and yellow module genes were also involved in multicellular organism development, indicating that PGCs and SSCs could obtain ESC-like features and differentiate into progeny cells of three different germ layers (**Figures 3B,C**). SSCs correlated yellow module genes were involved in spermatogenesis-related processes, and SSCs possessed characteristic properties of adult germline stem cells. NSC correlated turquoise module genes were involved in neural system development, which was consistent with neural stem cell characteristic properties (**Figure 3D**). MSC correlated pink module genes were involved in T cell development, T cell mediated immunity, immune responses, and bone mineralization which exactly demonstrated the bone marrow derivation of MSCs (**Figure 3E**). HSC correlated blue module genes were involved in the immune response, and this was consistent with the characteristic properties of HSC (**Figure 3F**). Functional annotations of the respective types of stem cells correlated modules consistent with the stem cell properties means that the association of co-expression genes modules with respective stem cells is feasible.

Network Analysis of the Stem Cells Respective Modules

Given that the genes possessed high connectivity in stem cell correlated modules, these genes may play similar roles in maintenance of stem cell properties. A subsequent analysis was performed on these high-connectivity genes. The connectivity threshold of the edges between two genes was set at 0.4 for turquoise (253 genes), 0.3 for blue (363 genes), 0.2 for brown (148 genes), yellow (130 genes) and purple (127 genes), and at 0.05 for pink (125 genes). The genes within the respective

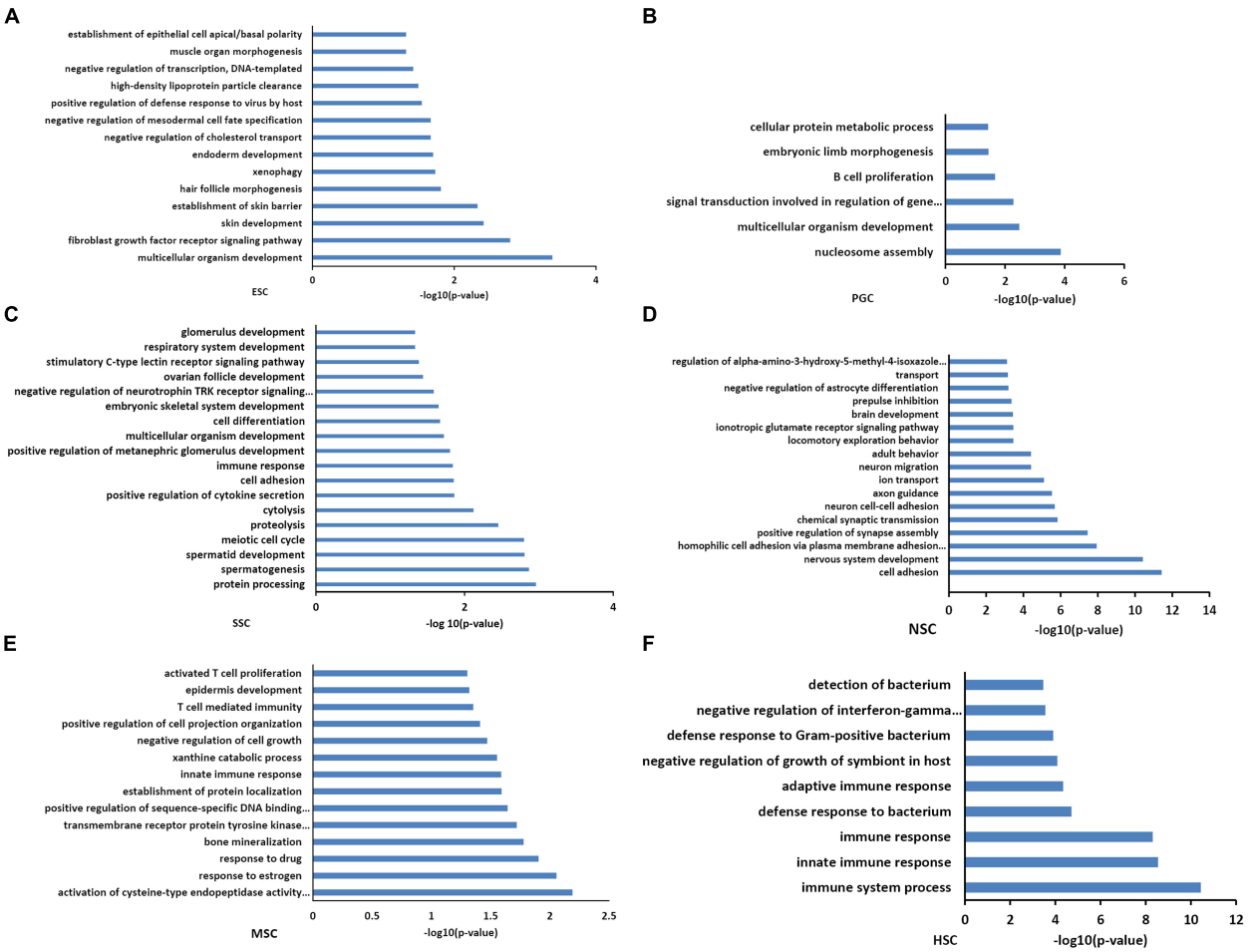


FIGURE 3 | Functional annotation of the six stem cell types correlated modules. GO analysis of genes in six stem cell types correlated modules were annotated by DAVID 7.8. ESC enriched GO terms included multicellular organism development, endoderm development, and the establishment of various organs and cells **(A)**. GO analysis of PGCs correlated modules genes were involved in multicellular organism development and embryonic limb morphogenesis **(B)**. SSC correlated module genes were involved in cell differentiation, spermatogenesis-related processes, and multicellular organism development **(C)**. NSC correlated module genes were involved in neural system development **(D)**. MSC correlated module genes were involved in T cell development, T cell mediated immunity, immune responses, and bone mineralization **(E)**. HSC correlated module genes were involved in the immune response **(F)**.

stem cell-specific modules are listed in **Supplementary Table S3**. The topological analysis of the co-expression network provided information for the maintenance of stem cell properties maintaining. According to topologic principles, hub genes with high degrees of connectivity played important roles in continuous network. We displayed the connections of those co-expression genes by Cytoscape software.

As transcriptional factors play important roles in maintaining cell types, we focused our studies on the genes within the connectivity network that were involved in transcriptional regulation. The results from this analysis are presented in **Figures 4–6**. Transcription related genes are highlighted in red. Hub genes that were within the top 10% of the high connectivity network are highlighted in blue, and these are presented in the respective module networks generated by topological analysis. The transcription factors *Foxd3* and *Zscan10* aligned with the hub genes within the purple module were required to maintain mouse ESCs (Hanna et al., 2002; Yamane et al., 2015; **Figure 4A**). The *Zscan10* was also found to be a key component of the ESC core transcriptional regulatory network formed by *Pou5f1* and *Sox2* (Yu et al., 2009). Transcriptional repressor *Prdm1* (Yamashiro et al., 2016), transcription factors *Rhox9*, and *Evx1* were aligned with the hub genes of the brown module means those transcription factors mayplay an essential role in PGC specification (**Figure 4B**). *Tcf21* was aligned with the hub genes of the yellow module (**Figure 5A**). The expression of *Tcf21* was higher in SSC that may be consistent with regulation of sex determining factor SRY. The transcription factor *Neurod6* was aligned with the hub genes within the turquoise module (**Figure 5B**). *Neurod6* is known to be involved in retina cell fate determination, differentiation, morphological development, and circuit formation (Cherry et al., 2011). *Hoxc13* was aligned with the hub genes of pink module (**Figure 6A**). The transcription factors *Nfe2* and *Gfi1* were aligned with the hub genes of the

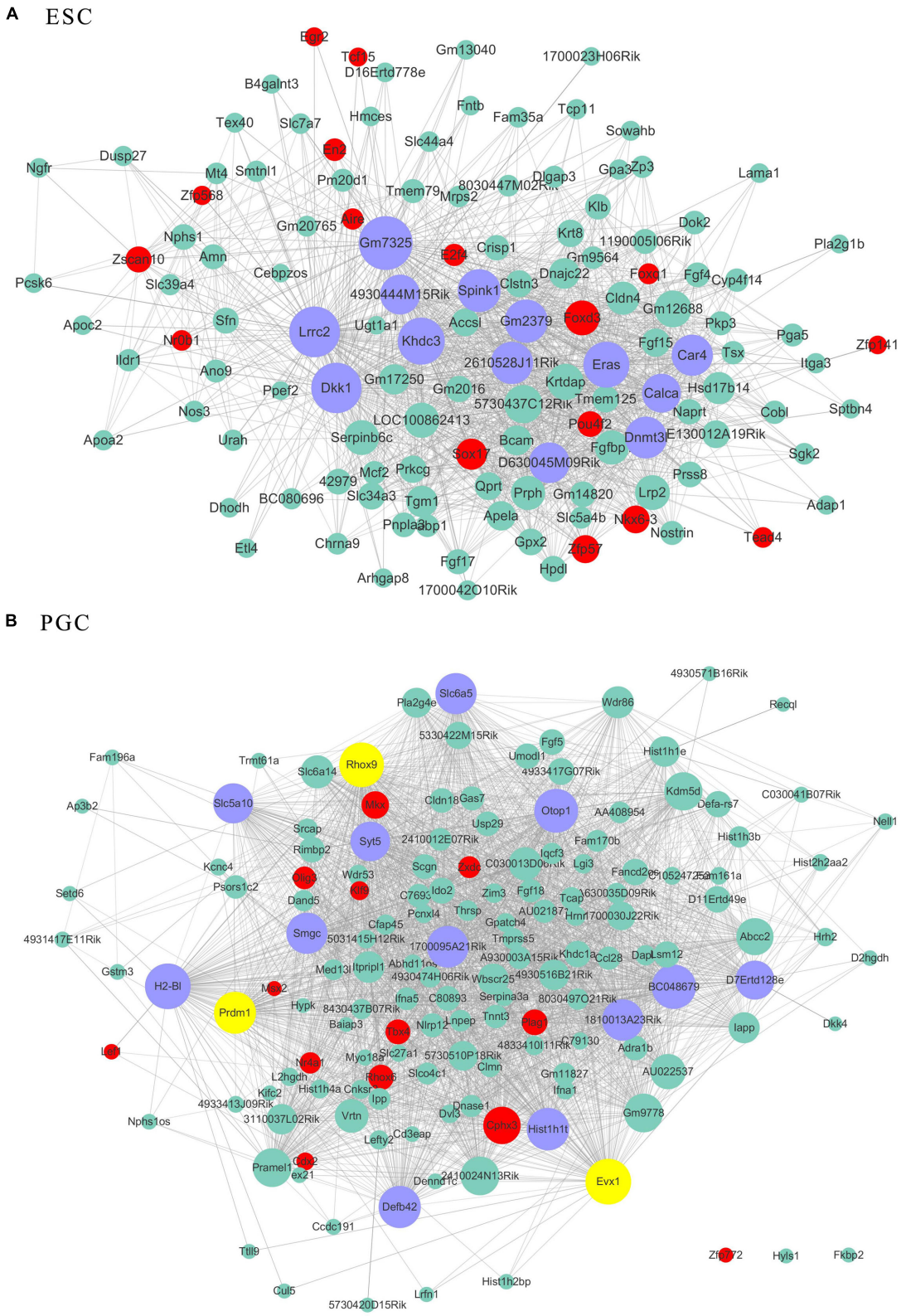


FIGURE 4 | The related co-expression networks of ESC and PGC. The co-expression networks of the ESC-correlated purple module **(A)**, PGC-correlated brown module **(B)**. The hub nodes are highlighted in blue within the co-expression networks. Transcription factors within the respective network are highlighted in red. Transcription factors that were included in the top 10% of nodes are highlighted in yellow within the respective networks. The size of the nodes corresponds to their degrees.

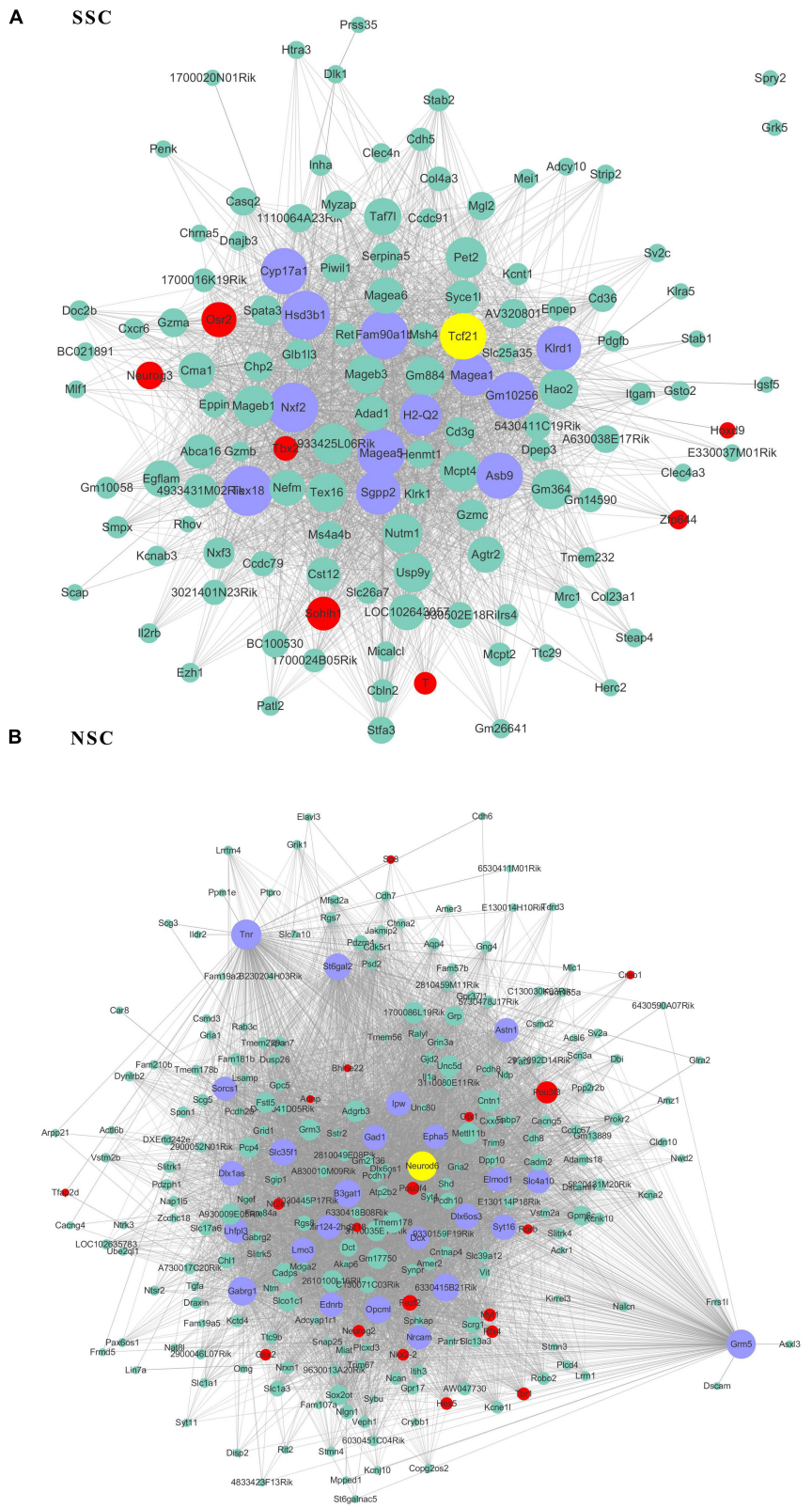


FIGURE 5 | The related co-expression networks of SSC and NSC. SSC-correlated yellow module **(A)**, NSC-correlated turquoise module **(B)**. The hub nodes are highlighted in blue within the co-expression networks. Transcription factors within the respective network are highlighted in red. Transcription factors that were included in the top 10% of nodes are highlighted in yellow within the respective networks. The size of the nodes corresponds to their degrees.

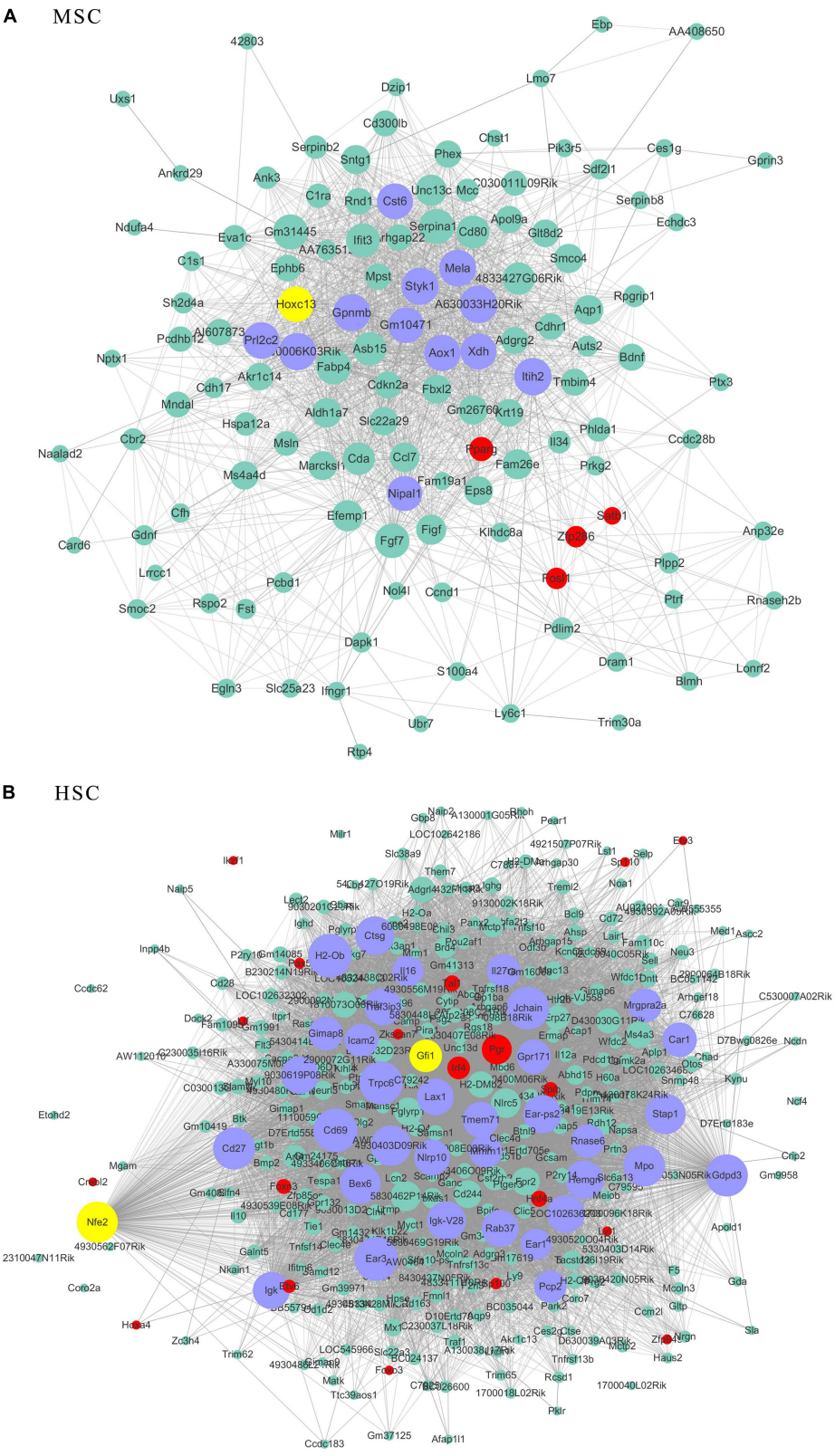


FIGURE 6 | The related co-expression networks of SSC and NSC. MSC-correlated pink module **(A)** and HSC-correlated blue module **(B)**. The hub nodes are highlighted in blue within the co-expression networks. Transcription factors within the respective network are highlighted in red. Transcription factors that were included in the top 10% of nodes are highlighted in yellow within the respective networks. The size of the nodes corresponds to their degrees.

blue module (**Figure 6B**), indicating that *Nfe2* and *Gfi1* are important for the maintenance of HSCs. *Nfe2* was found to be required for adult thrombocyte formation and function in zebrafish (Rost et al., 2018). Transiently expressed *Gfi1* could convert adult murine endothelial cells to hematopoietic stem cells (Barcia Duran et al., 2018). After topological analysis of the co-expression network, we will easily obtain useful clues for stem cell maintenance. Since *Foxd3* and *Zscan10* have been found playing important roles in maintaining mouse ESCs. There are reasons to speculate that *Zfp57*, *Pou4f2*, *Sox17,* and *Nkx6-3* which are the subsequent predicted transcription factors also vital to maintenance of mouse ESCs. In the same way, other predicted transcription factors in stem cell special co-expressed network would be critical for maintenance stem cell pool.

Considering the thousands of different expressed genes obtained from difference analysis, stem cell correlated co-expression network provide clues to detail regulatory networks of key transcription factors. We intend to detect the expression of the identified stem cell related genes by qPCR detection. Pluripotent transcription factor *Pou5f1* and NSCs special marker *Nestin* were used to confirm the respective identities of ESCs and NSCs. Both of them were lowly expressed in MEF. The identified ESC correlated transcription factors *Zfp57* and *Zscan10* were highly expressed in ESC compared to MEF. Both of *Zfp57* and *Zscan10* lowly expressed in NSC means that *Zfp57* and *Zscan10* may not be required in neurogenesis during embryo development (**Figures 7A,B**). We also detected *Hes5*, the Notch signaling effector which acts as a key regulator of maintenance of NSC was highly expressed in NSC (**Figure 7C**). NSC correlated transcription factors *Pou3f3*, *Pou3f4*, and *Zscan18* were also more highly expressed in NSC compared to MEF (**Figures 7D–F**). The expression levels of several identified stem cell related transcription factors were consistent with our prediction.

As Yamanaka factors are famous for promoting MEF transdifferentiated into iPS, we then attempted to determine whether or not the transcription factors listed in ESC are most correlated with the purple module. Unfortunately, the well-known transcription factors are not in the list of ESC's most correlated module genes. Although *Pou5f1 (Oct4)*, *Sox2*, *Nanog* are not listed in ESC most relevant modules, they are part of the respective modules that are relatively highly correlated to ESC. For example, Sox2 belongs to the module Plum1 with a correlation of 0.78 (p value = 6.36E-05). Nanog belongs to the module lightsteelblue1 with a correlation of 0.62 (p value = 0.0026). *Pou5f1* belongs to the module Yellow4 with a correlation of 0.57 (p value = 0.0064). Unfortunately, the other Yamanaka factors *Klf4* and *Myc* are in the modules brown2 and Lightcoral, with no significant correlation (brown2, cor = −0.1, p value = 0.7; Lightcoral, cor = 0.26, p value = 0.2). It is also worth mentioning that *Klf4* was listed in the PGC-correlated brown module with a correlation of 0.78 (p value = 3E-05). *Klf4* was found to be expressed at a high level in human PGCs, and transfection with both *Sox2* and *Pou5f1* resulted to inducing PGCs into iPS at a relatively high efficiency (Wei et al., 2009). The Yamanaka factors listed in different respective modules may reflect the different regulatory networks among those transcription factors. Several of those neighbor nodes were famous transcription factors related to the maintenance and transdifferentiation of ESC, such as *Sox2* interacted with *Dppa5a*, *Zic3*, and *Peg10* (**Figure 8A**). *Zic3* enhances the generation of mouse iPS depend on interact with *Pou5f1*, *Sox2* and *Klf4* (Declercq et al., 2013). Histone methyltransferase *Ezh2* that required for stable ESC self-renewal and differentiation also lists in the *Sox2* mediated network. *Nanog* interacted with *Prdm14, Nifx,* and *Rex2* (**Figure 8B**). *Prdm14* were found playing important roles in induced pluripotent stem sell reprogramming (Seki, 2018). *Pou5f1* interacted with *Sall4*, *Lin28a* (**Figure 8C**). *Pou5f1* interacted with *Sall4* formed a transcription regulation feedback loop governing the "stemness" of ES cells (Yang et al., 2010). The predicted transcription factors within the respective network of respective Yamanaka factors which highlighted in red may be playing important roles in maintenance and transdifferentiation of ESC.

Validation of Stem Cell-Specific Modules Based on STRING Database

To validate the co-expression connections of stem cells correlated modules genes, protein-protein interaction networks were detected by STRING v11 (Szklarczyk et al., 2019). The six types of stem cell correlated genes and the 37 core genes were imported into the STRING database to generate a continued protein-protein interaction network that was bridged by 25 other genes. The continued protein-protein interaction network contains 823 nodes and 3113 edges (**Supplementary Figure S3**).

Based on topology, we identified six densely connected regions within the continued protein-protein interaction network (**Figure 9**). Densely connected regions provide useful information with regard to the ability of stem cells to maintain their respective characteristic properties. Validated protein-protein interactions confirmed that co-expressed genes formed independent interaction modules. The identification of the interactions among different stem cell correlated genes would provide useful insights into the molecular mechanisms of transdifferentiation. The SSC correlated genes *Itgam*, *Cxcr6*, and *Agtr2* bridged four densely connected regions that consisted primarily of HSC, NSC, and MSC correlated genes (**Figure 9A**). As predicted transcription factors *Dnmt1* and *Prdm1* have been found essential for SSCs maintenance, those cell surface genes may participate in some signal pathway activating the expression of transcription factors. Those cell surface genes are essential to maintain stem cell niche.

The core genes *Chek1*, *Brca1*, *Cdca5*, *Rad51ap1*, *Mis18bp1*, *Incenp*, and *Dscc1* formed densely connected modules that were linked to the NSC correlated gene network via Mrc1 in **Figure 9C**. The majority of the seven genes were annotated with cell cycle and chromatin. *Zcchc18* acts as transcriptional factor within the NSC related gene interaction network. Wnt signaling plays an important role in stem cell maintenance by targeting various cadherin molecules such as *Cdh6*, *Cdh7* and *Cdh8* in NSCs, *Cdh5* in SSCs, and *Cdh17* in MSCs (**Figure 9E**). As indicated in **Figure 9F**, the neural related

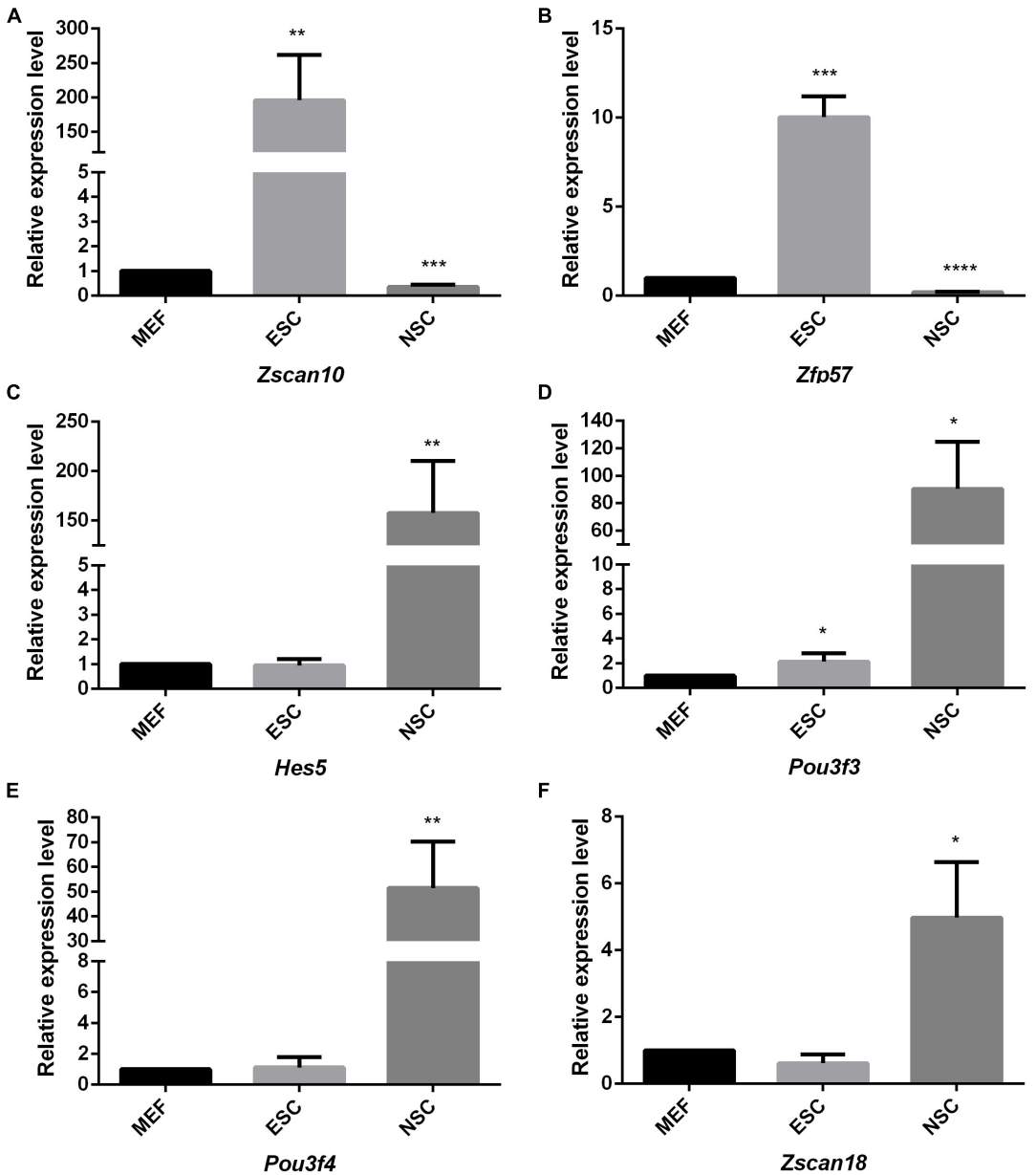


FIGURE 7 | The quantitative analysis of identified stem cell related genes based on qPCR **(A–F)**. The expression levels of identified stem cell related genes were detected in ESC and NSC. All data were normalized to the β-actin and are displayed as fold changes compared to MEF. Error bars are the standard deviation (SD) of at least three repeats. The significance of differences in multiple comparisons were determined by student's *t*-test. "*" means $p < 0.05$, "**" means $p < 0.01$, "****" means $p < 0.001$, and "****" means $p < 0.0001$.

genes *Hes5*, *Neurog2*, *Dcx*, *Fabp7*, and *Elavl3* form a densely connected region that may be critical for NSC maintenance. The connected network consisted of ESC, PGC, and SSC related genes. The dynamics expression of *Hes5* was correlated with cell fate determination during embryonic development (Munoz-Esquivel et al., 2019). *Hes5*, *Neurog3*, *Cdx2*, *Foxd3*, *Neurog2*, and *T* were the transcription factors that mediated the bulk of the downstream gene expression. Manipulating the expression of those transcription factors may provide useful information for stem cell transdifferentiation *in vivo*.

CCCTC-Binding Factor (CTCF) Motif Analysis Provide Clues for the Global Organization of Chromatic Architecture of Stem Cells

Various cell types and physiological states typically display different chromatin structures. Given the highly specific transcriptional activity of stem cells, chromatin structures within these stem cells may display different features. The GO analysis of the 37 common highly expressed core genes enriched in

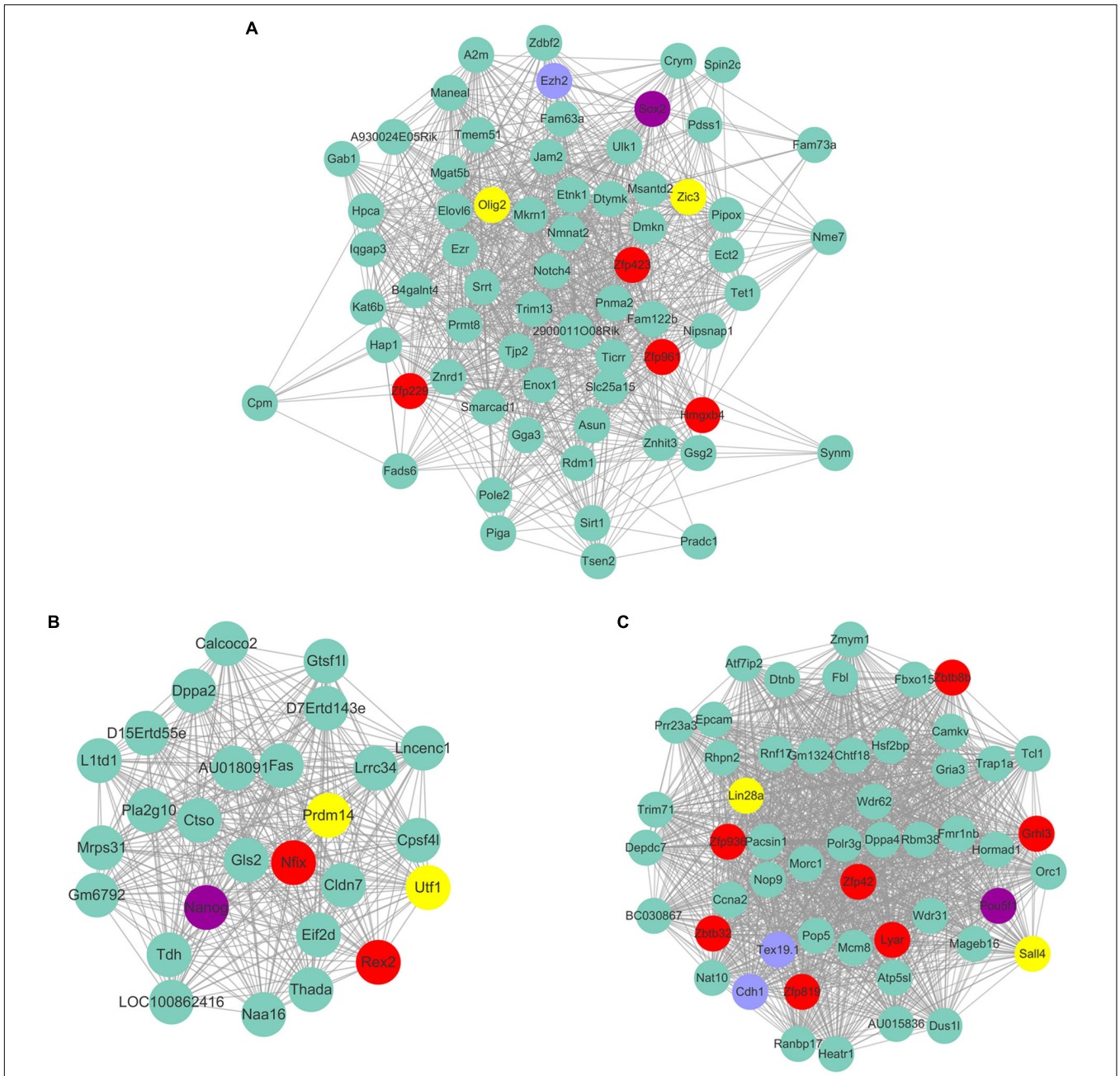


FIGURE 8 | The predicted co-expressed network of Yamanaka factors. The co-expression networks of Yamanaka factors Sox2 **(A)**, Nanog **(B)**, and Pou5f1 **(C)**. Yamanaka factors Sox2, Nanog and Pou5f1 are labeled in purple. Several well-known stemness transcription factors are marked in yellow and non-transcription factors were labeled as blue. The predicted transcription factors within the respective network of respective Yamanaka factors are highlighted in red. For clarity, the top 20% of the nodes of Nanog and Pou5f1 co-expressed genes were displayed according to node degree.

DNA recombination and chromatin organization indicated that CTCF regulates the structure of chromatin and defines the boundaries between active and heterochromatic DNA. This finding prompted us to evaluate the CTCF binding sites within those hub genes. As shown in **Figure 10**, the results indicated that 5–20% of the hub genes possessed a binding motif for CTCF, and this is relatively lower than the value of 33% that is expected for genome-wide CTCF binding sites (Holwerda and de Laat, 2013). Random samplings of 20 genes from the expression matrix displayed random occupancy rates of the genome-wide CTCF binding sites (**Supplementary Figure S4**). This indicates that stem cells require chromosome opening activity to successfully maintain stem cell-specific stemness properties. Highly expressed genes are typically located far from the boundaries between active and heterochromatic DNA. It is also possible that the few hub genes that possess CTCF binding sites may be more rigorously

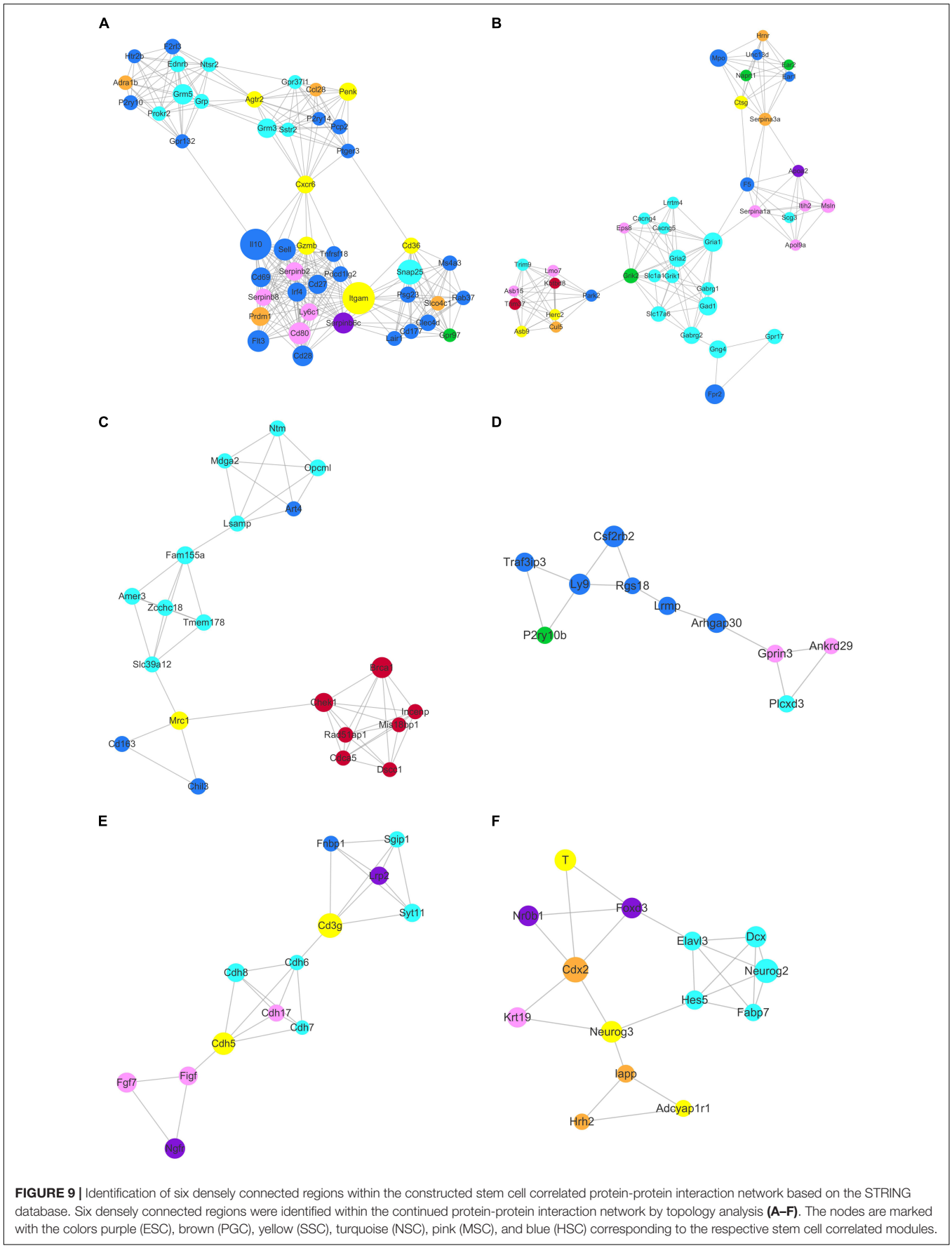


FIGURE 9 | Identification of six densely connected regions within the constructed stem cell correlated protein-protein interaction network based on the STRING database. Six densely connected regions were identified within the continued protein-protein interaction network by topology analysis **(A–F)**. The nodes are marked with the colors purple (ESC), brown (PGC), yellow (SSC), turquoise (NSC), pink (MSC), and blue (HSC) corresponding to the respective stem cell correlated modules.

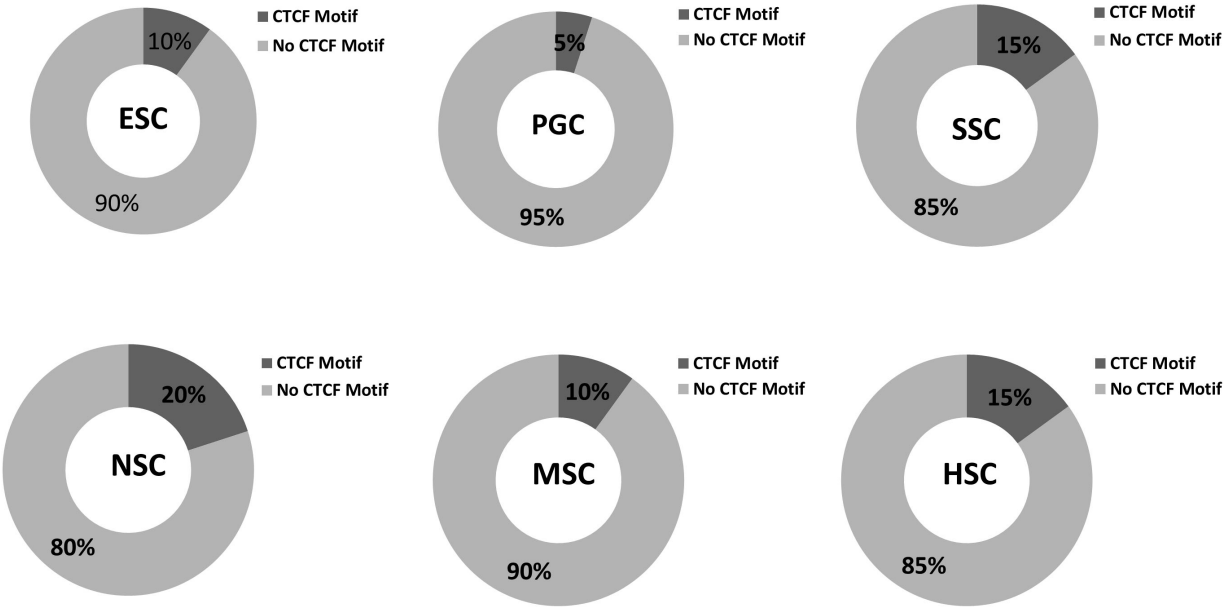


FIGURE 10 | CTCF binding sites in respective stem cell hub genes. The occupancy rates of the CTCF binding motif among the 20 hub genes within the respective stem cell specific modules. Dark gray shading indicates the percentages of CTCF binding motif among the 20 hub genes in the six stem cell types. Light gray corresponded to non- CTCF binding motifs.

regulated during stem cells differentiation. It is established that PGCs possess a special germ-line differentiation potential and exhibits the lowest number of CTCF binding motifs within their correlated hub genes. NSC correlated hub genes possess the highest number of CTCF binding motifs, suggesting that neural cell differentiation requires chromatin remodeling. This is consistent with the findings of a previous study that the activation of neuronal specific genes requires chromatin modification (Su et al., 2017).

ESC and NSC Shown More Conservative Than Other Types of Stem Cells Between Human and Mouse

As the 37 core genes co-expressed in multiple types of stem cell in mouse, we also detected the expression profiles of different types of stem cells in human. Further analysis found that only partial of mouse stem cell up-regulated genes were detected in human respective stem cells due to differences between species. There are 35 human homologous genes according to mouse core 37 genes. Whether or not of those core genes were up-regulated in the respective human stem cells were shown in **Supplementary Table S4**. Human ESC up-regulated genes contain 14 of 37 core genes and human NSC and SSC respective contain 8 and 12. CDCA5, DEPDC1B, RAD51AP1 and RAD54B were all up-regulated in human ESC, NSC, and SSC. To our surprise, none of the 37 core genes was up-regulated in human MSC. The percentages of common up-regulated genes both in mouse and human stem cells are different among the 5 types of human stem cells (**Supplementary Figure S5**). ESC and NSC shared more conservative between human and mouse. SSC and HSC are moderate conservative. Human MSC displays distinct signatures, only 27 genes were both up-regulated in mouse and human. That maybe explain none of the 37 core genes was up-regulated in human MSC. Higher common up-regulated genes both in mouse and human ESC and NSC may be explained by the conservative mechanism of mammalian embryo and neural system development. Most famous stem cell marker genes were conservative in both mouse and human. For example, homologous genes of famous ESC special transcription factor *Pou5f1*, *Lin28a*, *Nanog*, *Sox2* were also up-regulated in human ESC. NSC special genes *Sox2*, *Olig1* and *Pou3f3* were also up-regulated in human NSC. The same as SSC special genes were also up-regulated in human SSC, such as *Epcam*, *Ddx4*, *Tex14*, *Cdh1*, *PIWIL2* and so on. The relative expression foldchanges of those homologous genes were annotated in **Supplementary Table S5**.

Next, we also validated whether or not of those stem cell special genes which identified by WGCNA were also up-regulated in respective human stem cells. Almost half of mouse NSC special genes were also up-regulated in human NSC. As mouse NSC special turquoise module enrich 253 genes, there are 207 human homologous genes contains 97 genes that up-regulated in human NSC. The percentages of homologous genes in mouse NSC special modules was higher than common up-regulated genes shared by mouse and human (46.9% vs. 27.9%). Some identified transcription factors were also detected in corresponding human stem cells. For example, qPCR validated NSC correlated transcription factors *Pou3f3* was also up-regulated in human NSC. Other NSC special transcription factor *Hes5*, *Rfx4* and *Nkx2-2* were also up-regulated in human NSC. qPCR validated ESC correlated transcription factors *Zscan10* and ESC self-renewal related transcription factor *Foxd3* were

also up-regulated in human NSC. Further exploring function of identified conservative homologous genes may provide clues for detailing differences between species development. The percentages of homologous genes of mouse NSC special modules was higher than common up-regulated gene means that results of WGCNA data mining are credible. Those identified mouse stem cell special genes which also up-regulated in human stem cells were highlighted with yellow color in **Supplementary Table S3**.

DISCUSSION

In vivo cell fate reprogramming has emerged as a new method for understanding cell plasticity and as potential treatment for tissue regeneration. Understanding the underlying mechanism controlling cell fate reprogramming would promote the development of more accurate and efficient strategies for tissue regeneration and repair. Although there are many studies examining stem cell renewal, the specific mechanism underlying the maintenance of stemness in several adult stem types remains unknown. Here, we aimed to identify the key genes associated with ESCs, PGCs, SSCs, NSCs, MSCs, and HSCs. A total of 37 core genes were highly expressed in all of the above stem cells. These genes were identified, and stem cell correlated gene co-expression networks were obtained. The validation of the co-expression genes among different stem cells allowed us to construct a continued protein-protein interaction network that included 823 nodes and 3113 edges. Based on topology, six densely connected regions within this continued protein interaction network were found. Densely connected regions provide useful information with regard to the characteristic properties of stem cell maintenance. The interactions among different stem cell related genes provided useful information regarding the process of transdifferentiation. CTCF binding motif analysis revealed that the hub genes of respective stem cell modules occupy less CTCF. Clarifying the mechanisms underlying adult stem cell self-renewal will aid in our understanding of stem cell pool maintenance and will promote the development of more accurate and efficient strategies for tissue regeneration and repair.

The 37 core genes may play important roles in maintaining an open chromatin conformation during self-renewal. Those core genes may determine the difference between stem cells and terminally differentiated cells. *Trim37* monoubiquitinates histone H2A, and this process is associated with transcriptional repression (Bhatnagar et al., 2014). *Trim37* may repress various genes during stem cell self-renewal. The observation that the ubiquitin ligases BRCA1 and CHEK1 are both highly expressed within stem cells indicates that DNA repair mechanisms are highly active in the maintenance of stem cell self-renewal. The nucleotide excision repair protein DDB2 is highly expressed in the stem cells, suggesting that the nucleotide excision repair mechanism may also be essential for the maintenance of stem cell genome integrity. *Dnmt1* was also identified as one of the 37 core genes, indicating that DNA demethylation is essential for stem cell maintenance. The general transcription factor *Taf7* has been found to play an essential role in embryonic development (Gegonne et al., 2012). *Taf7* was included in the 37 core genes, which means that *Taf7* is also essential for SSC, NSC, MSC, HSC, and PGC maintenance.

Several of those neighbor nodes in Yamanaka factors belonged to modules were famous transcription factors related to the maintenance and transdifferentiation of ESC, such as *Sox2* interacted with *Dppa5a*, *Zic3*, and *Peg10*. *Nanog* interacted with *Prdm14*, *Nifx* and *Rex2*. *Pou5f1* interacted with *Sall4*, *Lin28a*. The expression levels of several identified stem cell related transcription factors were consistent with our prediction. Based on the bioinformatic prediction and qPCR detection, we think it is worth to reprogram MEF to ESC or NSC by overexpression of *Zfp57* or *Zscan18*.

HSC transplantation is well characterized as the first widely accepted adult stem cell within the hematopoietic system that could give rise to different types of blood cells. In recent years, studies have found that HSC transplantation can not only produce cells within the blood system but can also improve body function. Bone marrow cells migrate into the liver, and they fuse with hepatocytes to produce proliferating cells that are responsible for liver regeneration (Pedone et al., 2017). Transplanted bone marrow cells can also fused with neuronal cells in murine adult brains to protect and regenerate brain tissues (Weimann et al., 2003). Based on their diversity and differentiation potential, MSCs have gained increasing attention for their potential use in tissue repair and regeneration. The validation of the stem cell correlated modules that were generated based on the STRING database provided useful information regarding the characteristic properties of stem cell maintenance. Identifying the interactions among different stem cell correlated genes provided useful insights into the process of transdifferentiation. Although none common gene was shared in the all of the 5 types of human stem cells, ESC and NSC shown more conservative than others between human and mouse. Most of the ESC and NSC shared more conservative between human and mouse. The percentages of homologous genes of mouse NSC special modules was higher than common up-regulated gene means that results of WGCNA data mining are credible. Further detailing the conservative transcription factors between mouse and human may be provide clues for such as *Pou3f3*, *Hes5*, *Rfx4* and *Nkx2-2* for NSC, *Zscan10, Foxd3* for ESC. Manipulating the expression of those identified transcription factors may provide useful information that will allow for a greater understanding of stem cell transdifferentiation.

CONCLUSION

Highly efficient and precise reprogramming requires an understanding of the transcriptomes which function within different cell types. In this study, we focus on the underlying molecular mechanisms of self-renewal in several well-known stem cell types. We identified 37 core genes that were highly expressed in all of the stem cell types examined, and stem cell correlated gene co-expression networks were obtained based on WGCNA. The validation of the co-expression genes among different stem cell types revealed a continued protein-protein

interaction network that included 823 nodes and 3113 edges. Based on topology, densely connected regions provide useful information with regard to the ability of stem cells to maintain their respective characteristic properties.

CTCF binding motif analysis revealed that the hub genes of respective stem cell modules occupy less CTCF. Human stem cells display a distinct result from mouse stem cell. ESC and NSC shown more conservative than other types of stem cells between human and mouse. Clarifying the mechanisms underlying adult stem cell self-renewal will aid in the understanding of stem cell pool maintenance and will promote more accurate and efficient strategies for tissue regeneration and repair.

DATA AVAILABILITY STATEMENT

All datasets presented in this study are included in the article/**Supplementary Material**.

ETHICS STATEMENT

The animal study was reviewed and approved by Animal Ethics Committee of Shandong University of Technology.

AUTHOR CONTRIBUTIONS

W-HX and LS: conceptualization and supervision. L-JW, X-XL, and W-HX: methodology. L-JW, X-XL, and JH: software and formal analysis. L-JW, X-XL, JH, and X-HS: investigation. X-HS and W-HX: resources. L-JW and W-HX: data curation. L-JW and X-XL: writing-original draft preparation. W-HX: writing review and editing and project administration. L-JW, LS, and W-HX: funding acquisition. All authors contributed to the article and approved the submitted version.

FUNDING

This work was supported by the National Natural Science Foundation of China (81501316 and 31500086) and University Youth Innovation Team of Shandong Province (Grant No. 2019KJK017).

ACKNOWLEDGMENTS

We thank Kang Zou (Nanjing Agricultural University) for providing us with ESC and MEF cells.

SUPPLEMENTARY MATERIAL

The Supplementary Material for this article can be found online at: https://www.frontiersin.org/articles/10.3389/fgene.2020.563798/full#supplementary-material

FIGURE S1 | The number of genes only in the respective stem cell in contrast to up-regulated genes.

FIGURE S2 | Heatmap of the expression relative value of the 37 core genes in the respective stem cells and MEF.

FIGURE S3 | The continued protein-protein interaction network contains 823 nodes and 3113 edges. The nodes were painted as colors such as turquoise, blue, brown, yellow, purple, and pink corresponding to the stem cell-respective modules.

FIGURE S4 | Random occupancy rates of the CTCF binding motif. Random sampling was used to evaluate the genome-wide CTCF binding sites.

FIGURE S5 | The percentages of common up-regulated genes both in mouse and human stem cells are different among the 5 types of human stem cells. Mouse_homolog means the up-regulated genes of mouse respective stem cells corresponding to human homologous genes. The percentage was calculated by compared gene amount of respective sections to the sum of mouse and human up-regulated genes.

TABLE S1 | Primer sequences used in this study.

TABLE S2 | The highly expressed gene lists of each types of stem cell.

TABLE S3 | The gene lists of stem cells respective special modules. Those identified mouse stem cell special genes which also up-regulated in human stem cells were highlighted with yellow color.

TABLE S4 | Whether or not of those core genes were up-regulated in the respective human stem cells.

TABLE S5 | The relative expression foldchanges of those annotated homologous genes between mouse and human.

REFERENCES

Adams, G. B., and Scadden, D. T. (2006). The hematopoietic stem cell in its place. *Nat. Immunol.* 7, 333–337. doi: 10.1038/ni1331

Azim, K., Hurtado-Chong, A., Fischer, B., Kumar, N., Zweifel, S., Taylor, V., et al. (2015). Transcriptional hallmarks of heterogeneous neural stem cell niches of the subventricular zone. *Stem Cells* 33, 2232–2242. doi: 10.1002/stem.2017

Bader, G. D., and Hogue, C. W. V. (2003). An automated method for finding molecular complexes in large protein interaction networks. *BMC Bioinform.* 4:2. doi: 10.1186/1471-2105-4-2

Barcia Duran, J. G., Lis, R., Lu, T. M., and Rafii, S. (2018). In vitro conversion of adult murine endothelial cells to hematopoietic stem cells. *Nat. Protoc.* 13, 2758–2780. doi: 10.1038/s41596-018-0060-3

Bhatnagar, S., Gazin, C., Chamberlain, L., Ou, J., Zhu, X., Tushir, J. S., et al. (2014). TRIM37 is a new histone H2A ubiquitin ligase and breast cancer oncoprotein. *Nature* 516, 116–120. doi: 10.1038/nature13955

Caiazzo, M., Giannelli, S., Valente, P., Lignani, G., Carissimo, A., Sessa, A., et al. (2015). Direct conversion of fibroblasts into functional astrocytes by defined transcription factors. *Stem Cell Rep.* 4, 25–36. doi: 10.1016/j.stemcr.2014.12.002

Cheng, Z., He, Z., Cai, Y., Zhang, C., Fu, G., Li, H., et al. (2019). Conversion of hepatoma cells to hepatocyte-like cells by defined hepatocyte nuclear factors. *Cell Res.* 29, 124–135. doi: 10.1038/s41422-018-0111-x

Cherry, T. J., Wang, S., Bormuth, I., Schwab, M., Olson, J., and Cepko, C. L. (2011). NeuroD factors regulate cell fate and neurite stratification in the developing retina. *J. Neurosci.* 31, 7365–7379. doi: 10.1523/jneurosci.2555-10.2011

Cho, Y., Kim, B., Bae, H., Kim, W., Baek, J., Woo, K., et al. (2017). Direct gingival fibroblast/osteoblast transdifferentiation via epigenetics. *J. Dent. Res.* 96, 555–561. doi: 10.1177/0022034516686745

Colasante, G., Lignani, G., Rubio, A., Medrihan, L., Yekhlef, L., Sessa, A., et al. (2015). Rapid conversion of fibroblasts into functional forebrain GABAergic interneurons by direct genetic reprogramming. *Cell Stem Cell.* 17, 719–734. doi: 10.1016/j.stem.2015.09.002

Conway, J. R., Lex, A., and Gehlenborg, N. (2017). UpSetR: an R package for the visualization of intersecting sets and their properties. *Bioinformatics* 33, 2938–2940. doi: 10.1093/bioinformatics/btx364

Declercq, J., Sheshadri, P., Verfaillie, C. M., and Kumar, A. (2013). Zic3 enhances the generation of mouse induced pluripotent stem cells. *Stem Cells Dev.* 22, 2017–2025. doi: 10.1089/scd.2012.0651

Gascon, S., Masserdotti, G., Russo, G. L., and Gotz, M. (2017). Direct neuronal reprogramming: achievements, hurdles, and new roads to success. *Cell Stem Cell* 21, 18–34. doi: 10.1016/j.stem.2017.06.011

Gautier, L., Cope, L., Bolstad, B. M., and Irizarry, R. A. (2004). affy—analysis of Affymetrix GeneChip data at the probe level. *Bioinformatics* 20, 307–315. doi: 10.1093/bioinformatics/btg405

Gegonne, A., Tai, X., Zhang, J., Wu, G., Zhu, J., Yoshimoto, A., et al. (2012). The general transcription factor TAF7 is essential for embryonic development but not essential for the survival or differentiation of mature T cells. *Mol. Cell. Biol.* 32, 1984–1997. doi: 10.1128/mcb.06305-11

Ghiroldi, A., Piccoli, M., Ciconte, G., Pappone, C., and Anastasia, L. (2017). Regenerating the human heart: direct reprogramming strategies and their current limitations. *Basic Res. Cardiol.* 112:68.

Grande, A., Sumiyoshi, K., Lopez-Juarez, A., Howard, J., Sakthivel, B., Aronow, B., et al. (2013). Environmental impact on direct neuronal reprogramming in vivo in the adult brain. *Nat. Commun.* 4:2373.

Guan, K., Nayernia, K., Maier, L. S., Wagner, S., Dressel, R., Lee, J. H., et al. (2006). Pluripotency of spermatogonial stem cells from adult mouse testis. *Nature* 440, 1199–1203. doi: 10.1038/nature04697

Guo, Z., Zhang, L., Wu, Z., Chen, Y., Wang, F., and Chen, G. (2014). In vivo direct reprogramming of reactive glial cells into functional neurons after brain injury and in an Alzheimer's disease model. *Cell Stem Cell.* 14, 188–202. doi: 10.1016/j.stem.2013.12.001

Hanna, L. A., Foreman, R. K., Tarasenko, I. A., Kessler, D. S., and Labosky, P. A. (2002). Requirement for Foxd3 in maintaining pluripotent cells of the early mouse embryo. *Genes Dev.* 16, 2650–2661. doi: 10.1101/gad.1020502

Holwerda, S. J., and de Laat, W. (2013). CTCF: the protein, the binding partners, the binding sites and their chromatin loops. *Philos. Trans. R. Soc. Lond. Ser. B Biol. Sci.* 368:20120369. doi: 10.1098/rstb.2012.0369

Hosoya, A., Shalehin, N., Takebe, H., Shimo, T., and Irie, K. (2020). Sonic hedgehog signaling and tooth development. *Int. J. Mol. Sci.* 21:6.

Hou, P., Li, Y., Zhang, X., Liu, C., Guan, J., Li, H., et al. (2013). Pluripotent stem cells induced from mouse somatic cells by small-molecule compounds. *Science* 341, 651–654. doi: 10.1126/science.1239278

Hu, H., Miao, Y.-R., Jia, L.-H., Yu, Q.-Y., Zhang, Q., and Guo, A.-Y. (2018). AnimalTFDB 3.0: a comprehensive resource for annotation and prediction of animal transcription factors. *Nucleic Acids Res.* 47, D33–D38.

Huang da, W., Sherman, B. T., and Lempicki, R. A. (2009). Systematic and integrative analysis of large gene lists using DAVID. *Bioinform. Resour.* 4, 44–57. doi: 10.1038/nprot.2008.211

Islam, M. M., Smith, D. K., Niu, W., Fang, S., Iqbal, N., Sun, G., et al. (2015). Enhancer analysis unveils genetic interactions between TLX and SOX2 in neural stem cells and in vivo reprogramming. *Stem Cell Rep.* 5, 805–815. doi: 10.1016/j.stemcr.2015.09.015

Kanatsu-Shinohara, M., Inoue, K., Lee, J., Yoshimoto, M., Ogonuki, N., Miki, H., et al. (2004). Generation of pluripotent stem cells from neonatal mouse testis. *Cell* 119, 1001–1012.

Knoepfler, P. S. (2009). Deconstructing stem cell tumorigenicity: a roadmap to safe regenerative medicine. *Stem Cells* 27, 1050–1056. doi: 10.1002/stem.37

Kvinlaug, B. T., Chan, W. I., Bullinger, L., Ramaswami, M., Sears, C., Foster, D., et al. (2011). Common and overlapping oncogenic pathways contribute to the evolution of acute myeloid leukemias. *Cancer Res.* 71, 4117–4129. doi: 10.1158/0008-5472.can-11-0176

Langfelder, P., and Horvath, S. (2008). WGCNA: an R package for weighted correlation network analysis. *BMC Bioinform.* 9:559. doi: 10.1186/1471-2105-4-559

Li, K., Zhu, S., Russ, H. A., Xu, S., Xu, T., Zhang, Y., et al. (2014). Small molecules facilitate the reprogramming of mouse fibroblasts into pancreatic lineages. *Cell Stem Cell* 14, 228–236. doi: 10.1016/j.stem.2014.01.006

Liao, Y., Xiao, H., Cheng, M., and Fan, X. (2020). Bioinformatics analysis reveals biomarkers with cancer stem cell characteristics in lung squamous cell carcinoma. *Front. Genet.* 11:427. doi: 10.3389/fgene.2020.00427

Lo Furno, D., Mannino, G., and Giuffrida, R. (2018). Functional role of mesenchymal stem cells in the treatment of chronic neurodegenerative diseases. *J. Cell. Physiol.* 233, 3982–3999. doi: 10.1002/jcp.26192

Luo, H., Chen, R., Yang, R., Liu, Y., Chen, Y., Shu, Y., et al. (2014). Reprogramming of mice primary hepatocytes into insulin-producing cells by transfection with multicistronic vectors. *J. Diabetes Res.* 2014:716163.

Matsui, Y., Zsebo, K., and Hogan, B. L. (1992). Derivation of pluripotential embryonic stem cells from murine primordial germ cells in culture. *Cell* 70, 841–847. doi: 10.1016/0092-8674(92)90317-6

Miyoshi, N., Stel, J. M., Shioda, K., Qu, N., Odajima, J., Mitsunaga, S., et al. (2016). Erasure of DNA methylation, genomic imprints, and epimutations in a primordial germ-cell model derived from mouse pluripotent stem cells. *Proc. Natl. Acad. Sci. U.S.A.* 113, 9545–9550. doi: 10.1073/pnas.1610259113

Munoz-Esquivel, J., Gottle, P., Aguirre-Cruz, L., Flores-Rivera, J., Corona, T., Reyes-Teran, G., et al. (2019). Sildenafil inhibits myelin expression and myelination of oligodendroglial precursor cells. *ASN Neurol.* 11:1759091419832444.

Nimiritsky, P. P., Eremichev, R. Y., Alexandrushkina, N. A., Efimenko, A. Y., Tkachuk, V. A., and Makarevich, P. I. (2019). Unveiling mesenchymal stromal cells' organizing function in regeneration. *Int. J. Mol. Sci.* 20:823. doi: 10.3390/ijms20040823

Niu, W., Zang, T., Zou, Y., Fang, S., Smith, D. K., Bachoo, R., et al. (2013). In vivo reprogramming of astrocytes to neuroblasts in the adult brain. *Nat. Cell Biol.* 15, 1164–1175. doi: 10.1038/ncb2843

Nordin, F., Ahmad, R. N. R., and Farzaneh, F. (2017). Transactivator protein: an alternative for delivery of recombinant proteins for safer reprogramming of induced pluripotent stem cell. *Virus Res.* 235, 106–114. doi: 10.1016/j.virusres.2017.04.007

Oatley, J. M., Oatley, M. J., Avarbock, M. R., Tobias, J. W., and Brinster, R. L. (2009). Colony stimulating factor 1 is an extrinsic stimulator of mouse spermatogonial stem cell self-renewal. *Development* 136, 1191–1199. doi: 10.1242/dev.032243

Pedone, E., Olteanu, V. A., Marucci, L., Munoz-Martin, M. I., Youssef, S. A., de Bruin, A., et al. (2017). Modeling dynamics and function of bone marrow cells in mouse liver regeneration. *Cell Rep.* 18, 107–121. doi: 10.1016/j.celrep.2016.12.008

Pereira, M., Birtele, M., and Rylander Ottosson, D. (2019). Direct reprogramming into interneurons: potential for brain repair. *Cell. Mol. Life Sci.* 76, 3953–3967. doi: 10.1007/s00018-019-03193-3

Prockop, D. J. (1997). Marrow stromal cells as stem cells for nonhematopoietic tissues. *Science* 276, 71–74. doi: 10.1126/science.276.5309.71

Rost, M. S., Shestopalov, I., Liu, Y., Vo, A. H., Richter, C. E., Emly, S. M., et al. (2018). Nfe2 is dispensable for early but required for adult thrombocyte formation and function in zebrafish. *Blood Adv.* 2, 3418–3427. doi: 10.1182/bloodadvances.2018021865

Seandel, M., James, D., Shmelkov, S. V., Falciatori, I., Kim, J., Chavala, S., et al. (2007). Generation of functional multipotent adult stem cells from GPR125+ germline progenitors. *Nature* 449, 346–350. doi: 10.1038/nature06129

Seki, Y. (2018). PRDM14 is a unique epigenetic regulator stabilizing transcriptional networks for pluripotency. *Front. Cell Dev. Biol.* 6:12. doi: 10.3389/fgene.2020.00012

Shannon, P., Markiel, A., Ozier, O., Baliga, N. S., Wang, J. T., Ramage, D., et al. (2003). Cytoscape: a software environment for integrated models of biomolecular interaction networks. *Genome Res.* 13, 2498–2504. doi: 10.1101/gr.1239303

Song, G., Pacher, M., Balakrishnan, A., Yuan, Q., Tsay, H. C., Yang, D., et al. (2016). Direct reprogramming of hepatic myofibroblasts into hepatocytes in vivo attenuates liver fibrosis. *Cell Stem Cell.* 18, 797–808. doi: 10.1016/j.stem.2016.01.010

Sridhar, A., Ohlemacher, S. K., Langer, K. B., and Meyer, J. S. (2016). Robust differentiation of mRNA-reprogrammed human induced pluripotent stem cells toward a retinal lineage. *Stem Cells Transl. Med.* 5, 417–426. doi: 10.5966/sctm.2015-0093

Su, Y., Shin, J., Zhong, C., Wang, S., Roychowdhury, P., Lim, J., et al. (2017). Neuronal activity modifies the chromatin accessibility landscape in the adult brain. *Nat. Neurosci.* 20, 476–483. doi: 10.1038/nn.4494

Szklarczyk, D., Gable, A. L., Lyon, D., Junge, A., Wyder, S., Huerta-Cepas, J., et al. (2019). STRING v11: protein-protein association networks with increased

coverage, supporting functional discovery in genome-wide experimental datasets. *Nucleic Acids Res.* 47, D607–D613.

Takahashi, K., Tanabe, K., Ohnuki, M., Narita, M., Ichisaka, T., Tomoda, K., et al. (2007). Induction of pluripotent stem cells from adult human fibroblasts by defined factors. *Cell* 131, 861–872. doi: 10.1016/j.cell.2007.11.019

Takahashi, K., and Yamanaka, S. (2006). Induction of pluripotent stem cells from mouse embryonic and adult fibroblast cultures by defined factors. *Cell* 126, 663–676. doi: 10.1016/j.cell.2006.07.024

Takahashi, T., and Shiraishi, A. (2020). Stem cell signaling pathways in the small intestine. *Int. J. Mol. Sci.* 21:2032. doi: 10.3390/ijms21062032

Thomson, J. A., Itskovitz-Eldor, J., Shapiro, S. S., Waknitz, M. A., Swiergiel, J. J., Marshall, V. S., et al. (1998). Embryonic stem cell lines derived from human blastocysts. *Science* 282, 1145–1147. doi: 10.1126/science.282.5391.1145

Torper, O., Pfisterer, U., Wolf, D. A., Pereira, M., Lau, S., Jakobsson, J., et al. (2013). Generation of induced neurons via direct conversion in vivo. *Proc. Natl. Acad. Sci. U.S.A.* 110, 7038–7043. doi: 10.1073/pnas.1303829110

Wang, L. L., Su, Z., Tai, W., Zou, Y., Xu, X. M., and Zhang, C. L. (2016). The p53 pathway controls SOX2-mediated reprogramming in the adult mouse spinal cord. *Cell Rep.* 17, 891–903. doi: 10.1016/j.celrep.2016.09.038

Wei, Z., Yang, Y., Zhang, P., Andrianakos, R., Hasegawa, K., Lyu, J., et al. (2009). Klf4 interacts directly with Oct4 and Sox2 to promote reprogramming. *Stem Cells* 27, 2969–2978.

Weimann, J. M., Charlton, C. A., Brazelton, T. R., Hackman, R. C., and Blau, H. M. (2003). Contribution of transplanted bone marrow cells to Purkinje neurons in human adult brains. *Cell* 100, 2088–2093. doi: 10.1073/pnas.0337659100

Wislet-Gendebien, S., Laudet, E., Neirinckx, V., Alix, P., Leprince, P., Glejzer, A., et al. (2012). Mesenchymal stem cells and neural crest stem cells from adult bone marrow: characterization of their surprising similarities and differences. *Science* 69, 2593–2608. doi: 10.1007/s00018-012-0937-1

Xia, H., Li, X., Gao, W., Fu, X., Fang, R. H., Zhang, L., et al. (2018). Tissue repair and regeneration with endogenous stem cells. *Nat. Rev. Mater.* 3, 174–193. doi: 10.1038/s41578-018-0027-6

Yamane, M., Fujii, S., Ohtsuka, S., and Niwa, H. (2015). Zscan10 is dispensable for maintenance of pluripotency in mouse embryonic stem cells. *Biochem. Biophys. Res. Commun.* 468, 826–831. doi: 10.1016/j.bbrc.2015.11.039

Yamashiro, C., Hirota, T., Kurimoto, K., Nakamura, T., Yabuta, Y., Nagaoka, S. I., et al. (2016). Persistent requirement and alteration of the key targets of PRDM1 during primordial germ cell development in mice. *Biol. Reproduct.* 94:7.

Yandim, C., and Karakulah, G. (2019). Expression dynamics of repetitive DNA in early human embryonic development. *BMC Genom.* 20:439. doi: 10.1186/s12864-019-5803-1

Yang, J., Gao, C., Chai, L., and Ma, Y. (2010). A novel SALL4/OCT4 transcriptional feedback network for pluripotency of embryonic stem cells. *PLoS One* 5:e10766. doi: 10.1371/journal.pone.0010766

Yang, W., Xia, Y., Qian, X., Wang, M., Zhang, X., Li, Y., et al. (2019). Co-expression network analysis identified key genes in association with mesenchymal stem cell osteogenic differentiation. *Cell Tissue Res.* 378, 513–529. doi: 10.1007/s00441-019-03071-1

Yin, J. Q., Zhu, J., and Ankrum, J. A. (2019). Manufacturing of primed mesenchymal stromal cells for therapy. *Nat. Biomed. Eng.* 3, 90–104. doi: 10.1038/s41551-018-0325-8

Yu, H. B., Kunarso, G., Hong, F. H., and Stanton, L. W. (2009). Zfp206, Oct4, and Sox2 are integrated components of a transcriptional regulatory network in embryonic stem cells. *J. Biol. Chem.* 284, 31327–31335. doi: 10.1074/jbc.m109.016162

Zhang, L., Dong, Z. F., and Zhang, J. Y. (2020). Immunomodulatory role of mesenchymal stem cells in Alzheimer's disease. *Life Sci.* 246:117405. doi: 10.1016/j.lfs.2020.117405

Zhao, X. Y., Li, W., Lv, Z., Liu, L., Tong, M., Hai, T., et al. (2009). iPS cells produce viable mice through tetraploid complementation. *Nature* 461, 86–90. doi: 10.1038/nature08267

Ziebarth, J. D., Bhattacharya, A., and Cui, Y. (2013). CTCFBSDB 2.0: a database for CTCF-binding sites and genome organization. *Nucleic Acids Res.* 41, D188–D194.

Conflict of Interest: The authors declare that the research was conducted in the absence of any commercial or financial relationships that could be construed as a potential conflict of interest.

Copyright © 2020 Wang, Li, Hou, Song, Xie and Shen. This is an open-access article distributed under the terms of the Creative Commons Attribution License (CC BY). The use, distribution or reproduction in other forums is permitted, provided the original author(s) and the copyright owner(s) are credited and that the original publication in this journal is cited, in accordance with accepted academic practice. No use, distribution or reproduction is permitted which does not comply with these terms.

frontiers in Cell and Developmental Biology

ORIGINAL RESEARCH
published: 08 September 2020
doi: 10.3389/fcell.2020.00823

Effects of Recombinant Spidroin rS1/9 on Brain Neural Progenitors After Photothrombosis-Induced Ischemia

Mikhail M. Moisenovich[1†], Denis N. Silachev[2,3,4†], Anastasia M. Moysenovich[1], Anastasia Yu. Arkhipova[1], Konstantin V. Shaitan[1], Vladimir G. Bogush[5,6], Vladimir G. Debabov[5,6], Alexander V. Latanov[1], Irina B. Pevzner[2,3], Ljubava D. Zorova[2,3], Valentina A. Babenko[2,3], Egor Y. Plotnikov[2,3,7] and Dmitry B. Zorov[2,3]**

[1] Department of Biology, Lomonosov Moscow State University, Moscow, Russia, [2] Laboratory of Mitochondrial Structure and Function, A. N. Belozersky Institute of Physico-Chemical Biology, Lomonosov Moscow State University, Moscow, Russia, [3] V.I. Kulakov National Medical Research Center of Obstetrics, Gynecology, and Perinatology, Moscow, Russia, [4] Histology, Embryology and Cytology Department, Peoples' Friendship University of Russia, Moscow, Russia, [5] National Research Center "Kurchatov Institute" – GOSNIIGENETIKA, Moscow, Russia, [6] National Research Center "Kurchatov Institute", Moscow, Russia, [7] Institute of Molecular Medicine, I.M. Sechenov First Moscow State Medical University, Moscow, Russia

The existence of niches of stem cells residence in the ventricular–subventricular zone and the subgranular zone in the adult brain is well-known. These zones are the sites of restoration of brain function after injury. Bioengineered scaffolds introduced in the damaged loci were shown to support neurogenesis to the injury area, thus representing a strategy to treat acute neurodegeneration. In this study, we explored the neuroprotective activity of the recombinant analog of *Nephila clavipes* spidroin 1 rS1/9 after its introduction into the ischemia-damaged brain. We used nestin–green fluorescent protein (GFP) transgenic reporter mouse line, in which neural stem/progenitor cells are easily visualized and quantified by the expression of GFP, to determine the alterations in the dentate gyrus (DG) after focal ischemia in the prefrontal cortex. Changes in the proliferation of neural stem/progenitor cells during the first weeks following photothrombosis-induced brain ischemia and *in vitro* effects of spidroin rS1/9 in rat primary neuronal cultures were the subject of the study. The introduction of microparticles of the recombinant protein rS1/9 into the area of ischemic damage to the prefrontal cortex leads to a higher proliferation rate and increased survival of progenitor cells in the DG of the hippocampus which functions as a niche of brain stem cells located at a distance from the injury zone. rS1/9 also increased the levels of a mitochondrial probe in DG cells, which may report on either an increased number of mitochondria and/or of the mitochondrial membrane potential in progenitor cells. Apparently, the stimulation of progenitor cells was caused by formed biologically active products stemming from rS1/9 biodegradation which can also have an effect upon the growth of primary cortical neurons, their adhesion, neurite growth, and the formation of a neuronal network. The high biological activity of rS1/9 suggests it as an excellent

OPEN ACCESS

Edited by:
Andrei S. Chagin, Karolinska Institutet (KI), Sweden

Reviewed by:
Yongting Wang, Shanghai Jiao Tong University, China
Takayuki Nakagomi, Hyogo College of Medicine, Japan

***Correspondence:**
Egor Y. Plotnikov
plotnikov@genebee.msu.ru; plotnikov@belozersky.msu.ru
Dmitry B. Zorov
zorov@genebee.msu.ru; zorov@belozersky.msu.ru

† These authors have contributed equally to this work

Specialty section:
This article was submitted to Molecular Medicine, a section of the journal Frontiers in Cell and Developmental Biology

Received: *29 March 2020*
Accepted: *03 August 2020*
Published: *08 September 2020*

Citation:
Moisenovich MM, Silachev DN, Moysenovich AM, Arkhipova AY, Shaitan KV, Bogush VG, Debabov VG, Latanov AV, Pevzner IB, Zorova LD, Babenko VA, Plotnikov EY and Zorov DB (2020) Effects of Recombinant Spidroin rS1/9 on Brain Neural Progenitors After Photothrombosis-Induced Ischemia. Front. Cell Dev. Biol. 8:823. doi: 10.3389/fcell.2020.00823

material for therapeutic usage aimed at enhancing brain plasticity by interacting with stem cell niches. Substances formed from rS1/9 can also be used to enhance primary neuroprotection resulting in reduced cell death in the injury area.

Keywords: scaffold, fibroin, stroke, neural progenitors, mitochondria

INTRODUCTION

Acute focal brain damage can lead to impaired or lost cognitive, sensorimotor, and visceral functions. The main physiological mechanism of functional recovery of the brain after the damage is neuroplasticity that is, the ability of neuronal tissues to undergo adaptive changes, both at the structural and functional levels—from molecular and cellular changes to global rearrangements of the neural network. During reparation of other tissues, posttraumatic central nervous system (CNS) responses can be divided into three consecutive phases: cell death and inflammation, cell proliferation, and tissue remodeling. Some of these events such as cell death, recruitment of inflammatory and immune cells, the formation of a fibrin-collagen mesh, angiogenesis, and fibroblast proliferation, reflect classic responses to damage in any tissue, whereas others such as infiltration into the injury area of microglia cells, migration of neuronal progenitor cells, and the formation of a compact astroglial scar, are specific and unique to the CNS (Burda and Sofroniew, 2014). Currently, in experimental studies of acute cerebral pathologies, therapeutic strategies are based on approaches of primary neuroprotection aimed at reducing cell death in the damaged loci. However, despite the effectiveness of these approaches proven in preclinical studies, their translation into clinical practice is very difficult because of failures at the level of clinical trials (Moretti et al., 2015). The difficulty of implementation of primary neuroprotection is the limited length of the therapeutic window, which cannot go beyond 5–6 h after damage. On the other hand, approaches aimed at enhancing brain plasticity, i.e., those considering effects on the damaged brain independent on the pharmacologic therapeutic window, such as stem cell or extracellular vesicle transplantation (Bang and Kim, 2019; Borlongan, 2019), or scaffold transplantation (Gopalakrishnan et al., 2019) have shown high therapeutic efficiency.

Adult animal brain is known to have stem cell niches in the ventricular–subventricular zone and the subgranular zone in which new neurons and glial cells are continuously generated from neural stem/progenitor cells (Lazutkin et al., 2019; Obernier and Alvarez-Buylla, 2019). In the subgranular zone of the hippocampus, after exiting the cell cycle, new generations of cells locally migrate to the granular cell layer and turn into mature granular neurons (Lazutkin et al., 2019). There is also evidence of the presence of additional niches of neural progenitor cells associated with vessels, in particular with pericytes and such regionally activated stem cells also contribute to neural regeneration (Shimada et al., 2010, 2012; Nakagomi et al., 2011; Nakata et al., 2017). The balance between stem cell proliferation/differentiation in a cell niche depends on both intercellular interactions and the molecular environment (Obernier and Alvarez-Buylla, 2019). Pathological processes in the brain caused by ischemia or traumatic brain injury can affect the mechanisms of neurogenesis in stem niches (Arvidsson et al., 2002; Gao et al., 2009; Benner et al., 2013; Faiz et al., 2015) including the proliferation of neural stem/progenitor cells, which can be a potential resource for the restoration of damaged nerve tissue. However, in the case of natural regeneration, very few newly created neurons maturate and survive, which may be due to the lack of signals that stimulate the growth of neurites and the suboptimal availability or arrangement of subcellular machinery to enable growth cone reformation and axonal elongation (Bradke et al., 2012). In several studies, it has been shown that various biologically active compounds can enhance the proliferation, differentiation, migration, and subsequent survival of newly formed neuronal cells. For example, fibrinogen is a regulator of neural stem/progenitor cells–derived astrogenesis from the subventricular niche via the BMP receptor signaling pathway following injury (Pous et al., 2020).

The process of choosing strategies for restoration of brain function requires an understanding of how exactly neuroplastic processes occur in the brain in response to trauma and subsequent insertion of the scaffold into the brain lesion. The most modern and informative approach is the use of animal lines with a special reporter, in which stem and progenitor cells carry a genetically encoded construct associated with the expression of a specialized protein typical for this cell type. The most common marker used is nestin which is expressed in the brain stem cell niches of embryos and adult mammals, and it is not found in differentiated cells of neural tissue (Enikolopov et al., 2015; Mignone et al., 2016).

It became clear that the adult brain has a greater neuroplastic potential than previously thought (Chen et al., 2014); however, its ability to regenerate is still quite limited and unable to compensate for the loss of cells and to remodel the extracellular matrix in acute injuries such as focal traumatic injury and ischemic stroke (Moreau et al., 2012). Unlike healing of skin wounds and during other tissue injuries, when the CNS is damaged in the trauma area, there is no anatomical substrate, such as granulation tissue, which can support the migration of progenitor brain cells from stem cell niches to fill cell-free spaces. Thus, to provide the cells with an anatomical substrate for migration and axon guidance, additional scaffolds must be inserted into the injury area.

That is why a promising approach to restoring brain function after an injury can be the introduction of scaffolds supporting intrinsic neurogenesis and/or of those containing various substances that activate the proliferation of resident neural progenitor cells (Nih et al., 2018). Additionally, the matrix can act as a chemoattractant and/or as structural support

providing migration of progenitor cells to the area of damage (Volkov et al., 2020). At this time, several compounds have been proposed as scaffolds for the regeneration of nerve tissue which differ in both their composition and three-dimensional structure (Wang et al., 2018). Structural silk proteins from silkworms and spiders are considered as the most promising materials used for neural tissue engineering. They have a unique combination of physical and chemical properties and biological activity that ensure their biocompatibility and high regenerative activity (Magaz et al., 2018; Johari et al., 2020). Substrates based on silk fibroin from *Bombyx mori* are able to support adhesion, viability, and neuritogenesis of neuronal cells in different model systems (Hopkins et al., 2013). Some proteins of the spidroin family could be one of the promising agents for brain recovery after a stroke because of the expression of multiple repeats of a GRGGL sequence recognized by neural progenitors (An et al., 2015). Films made of recombinant spidroins have a more suitable surface charge and substrate stiffness for supporting the growth of primary rat cortical neurons than coatings made of fibroin and polylysine (An et al., 2015). In another study, Lewicka et al. (2012) showed that films made of 4RepCt support proliferation and neuronal differentiation of neural stem cells. Also, earlier it has been shown that the ability of a combined matrix containing recombinant analogs of spider dragline silk proteins–spidroin 1 (rS1/9) and spidroin 2 (rS2/12), polycaprolactone, and platelet-rich plasma supports the growth and neuronal differentiation of reprogrammed human nerve progenitor cells (Baklaushev et al., 2019).

Previously, we have explored the biological properties of substrates generated from the recombinant protein rS1/9 which is an analog of spidroin 1 from *Nephila clavipes*. The rS1/9 molecule has a molecular mass of 94 kDa and consists of nine repeating monomers, each of which contains four sequences called primary repeats (so-called initial repeats). Each of these repeats is enriched with GGL, GGY, and GGQ triplets and contains 1 polyalanine cluster consisting of five to eight amino acid residues. These repetitions are identical to the primary repeats residing in natural spidroin 1. Polyalanine clusters form β-sheets, which, in turn, form crystallites that provide a unique stability to the materials based on spidroins (Bogush et al., 2009). This protein also contains 18 repeats of the NCAM-binding sequence GRGGL, which is a signal for binding neuronal cells. Spidroin rS1/9 has been shown to promote cell proliferation, with both vascular and nerve sprouting inside three-dimensional spidroin structures (Moisenovich et al., 2012).

In this study, we used a transgenic reporter nestin–green fluorescent protein (GFP) expressed in a mouse line, in which neural stem/progenitor cells are easily visualized and quantified to assess the alterations in the dentate gyrus (DG) after focal ischemia in the prefrontal cortex. The recombinant analog of *N. clavipes* spidroin 1 rS1/9 with 18 GRGGL repeats was used to prepare microgels which was introduced into the damaged area of the mouse brain. We examined changes in the proliferation of neural stem/progenitor cells during the first weeks following photothrombosis-induced brain ischemia and also *in vitro* effects of spidroin rS1/9 in rat primary neuronal cultures.

MATERIALS AND METHODS

Scaffolds and Microparticles Assembly

Formation of Films

Using the protocols described earlier regenerated fibroin was obtained and later lyophilized (Nosenko et al., 2018). Recombinant protein rS1/9 produced by yeast cells carrying gene rS1/9 was isolated from lysed cells, purified by ion-exchange chromatography in fast protein liquid chromatography up to 95% purity and lyophilized. Fibroin or rS1/9 was dissolved in hexafluoroisopropanol (up to a concentration of 20 mg/mL). One hundred microliters of this solution was pipetted evenly onto a 24-mm cover glass and left for 2 h at room temperature to vaporize hexafluoroisopropanol. The resulting films were incubated for 24 h in 96% ethanol. The films were stored in 96% ethanol in a sealed container at +4°C, and before use, they were washed five times in phosphate-buffered saline (PBS).

Generation of Microparticles

Microparticles based on recombinant spidroin rS1/9 with sizes of 100 and 300 μm were obtained as described in Nosenko et al. (2018). Microparticles were stored in 70% ethanol and washed five times in PBS prior to use.

Scaffolds Surface Morphology Analysis

Preparation of films and microparticles for scanning electron microscopy (SEM) was performed according to standard protocol. Briefly, films or microparticles were fixed overnight using 2.5% glutaraldehyde in 0.1 M cacodylate buffer at +4°C. The samples were then washed three times in 0.1 M cacodylate buffer at pH7.2 for 5 min, followed by dehydration in a series of ethanol solutions with increasing concentrations and acetone (Chemmed, Russia). After critical point drying using Hitachi critical point dryer HCP-2 (Hitachi, Ltd., Japan), films or microparticles were metallized with a 20-nm-thick platinum layer using Ion Coater IB3 (Eiko Engineering Co., Japan). The resulting samples were analyzed with Camscan S2 microscope (Cambridge Instruments, United Kingdom) at 10-nm resolution and operating voltage −20 kV. Images were obtained using MicroCapture software (SMA, Russia).

Preparation of Conditioned Culture Medium by rS1/9

The sterilized rS1/9 microparticles were placed into 24-well plates, and 1 mL of cell culture medium was added to each well. The culture growth medium contained Neurobasal medium A (Gibco, United States) containing 2% serum-free supplement NeuroMax (PanEco, Russia) and 0.5 mM L-glutamine (PanEco). Microparticles were incubated for 1 week at 37°C and 5% CO_2. Then, medium with microparticles was transferred to sterile microcentrifuge tubes and centrifuged at 16,000 *g* for 30 min. The supernatant was collected and used immediately in the tests.

rS1/9 Hydrolysis

The 30 mg/mL rS1/9 microparticles were exposed to trypsin (PanEco) or thrombin (Instrumentation Laboratory Company, Bedford, MA, United States) at 37°C for 2 days, and proteolytic activities were inactivated by supplemented fetal bovine serum

(FBS). The solution with microparticles was transferred to sterile microcentrifuge tubes and centrifuged at 16,000 *g* for 30 min. The supernatant was collected and used immediately in the tests.

Cell Culture Experiments

All experimental procedures conformed to the Guidelines for Proper Control of Animal Experiments approved by the local ethics regulations. Primary cultures of neurons from the hippocampus or cortex were obtained from brains of Wistar rats (hippocampal cells) or BALB/c murine (cortical cells) embryos (E18). The cell suspension was obtained according to the previously published method (Brewer, 1995). Cortical cells were plated on fibroin (FB) or rS1/9 films with a density of 10,000 per 1 cm^2. The cells were allowed to sediment for 1 h at 37°C and 5% CO_2, and then non-attached cells were removed, and 1.5 mL of culture medium (Neurobasal medium A containing 2% serum-free supplement NeuroMax and 0.5 mM L-glutamine) was added. Hippocampal cells were plated on glass coated with poly-L-lysine (0.5 mg/mL). The cells were allowed to sediment for 1 h at 37°C and 5% CO_2, and then non-attached cells were removed, and 1.5 mL of Neurobasal medium A containing 2% serum-free supplement NeuroMax and 0.5 mM L-glutamine or conditioned with rS1/9 Neurobasal medium A containing 2% serum-free supplement NeuroMax and 0.5 mM L-glutamine were added. For cocultivation of microparticles and hippocampal cells, suspension of microparticles was placed in the Transwell cell culture plate inserts (Corning, United States) with pore size 0.4 μm. For experiments, cells were used at day 7 (cortical cells) or days 1, 4, and 8 (hippocampal cells) in culture.

For neural progenitor cell isolation, hippocampal tissues were cut into 1-mm^3 tissue blocks. Trypsin/EDTA (0.25%; PanEco) was used to digest the tissue at 37°C for 7 min. The digested tissue solution was collected and placed in a 15-mL centrifuge tube, and Dulbecco modified Eagle medium/F12 (DMEM/F12; 1:1; PanEco) containing 1% hiFBS (HyClone) was added to stop the digestion. Centrifugation was performed at 300 *g* for 4 min. The supernatant was discarded, and the cell suspension was resuspended using DMEM/F12 culture media supplemented with 2% NeuroMax (PanEco), 10 ng/mL basic fibroblast growth factor (PanEco), and 0.5 mmol/L Glutamax (Gibco; Thermo Fisher Scientific, Inc., United States). After 12 h, the medium was changed. After reaching 70–80% confluency, the cells were passaged using trypsin/EDTA (0.05%; PanEco). The second passage was seeded on cover slides coated with poly-L-lysine and cultured with the presence of thrombin- or trypsin-digested rS1/9 for 3 days. For BrdU incorporation assay cells were treated with BrdU at final concentration 10 μM for 4 h before fixation.

Immunofluorescence of Neural Cells

Immunofluorescence was used to visualize cortical cells grown on FB and rS1/9 films for 7 days, as well as to analyze the impact of rS1/9 conditioned medium or presence rS1/9 microparticles on hippocampal cells growth. In both cases, samples were fixed with 4% paraformaldehyde and treated with 0.1% Triton X-100 in PBS for 10 min. Then samples were incubated with 0.1% Tween 20, 0.3 M glycine, and 1% bovine serum albumin (BSA) in PBS for 2 h.

The cortical cells were labeled with anti-neural cell adhesion molecule (NCAM) monoclonal antibodies (56C04; Thermo Fisher Scientific) at 1:200 dilution in 0.1% Tween 20, 0.3 M glycine and 1% BSA in PBS and incubated overnight at 4°C and then labeled with rabbit anti–mouse immunoglobulin G (IgG) (H + L) secondary antibodies conjugated with Alexa Fluor® 546 (1:1,000; Thermo Fisher Scientific). To detect β3-tubulin, anti–β3-tubulin antibody conjugated with Alexa Fluor® 488, was used (1:800; BioLegend). For CD31 detection, sections were incubated with Alexa Fluor 667 conjugated anti-mouse CD31 antibodies (1:300, clone MEC113; BioLegend). Cell nuclei were visualized with Hoechst 33342 (Thermo Fisher Scientific). The images were obtained using an Eclipse Ti-E microscope with an A1 (Nikon Corporation, Japan) confocal module and a CFI Plan Apo VC 20×/0.75 objective. Image analysis was performed using NIS-Elements and ImageJ software.

The hippocampal cells were labeled with antinestin antibody (Rat-401; BioLegend) at 1:200 dilution in 0.1% Tween 20, 0.3 M glycine and 1% BSA in PBS and incubated overnight at 4°C and then labeled with rabbit anti–mouse IgG (H + L) secondary antibody conjugated with Alexa Fluor® 546 (1:1,000; Thermo Fisher Scientific). Cell nuclei were visualized with Hoechst 33342. Images were captured on an Eclipse Ti-E microscope with the A1 confocal module (Nikon Corporation) and a Plan fluor 40×1.3 objective. Image analysis was performed using NIS-Elements and ImageJ software.

The neural progenitor cells were incubated overnight with anti-BrdU antibodies (1:250; Abcam, United States). Unbound antibodies were washed five times with a mixture of PBS/1% FBS/0.1% Tween-20. Samples were treated for 1 h at room temperature with Cy3 conjugated secondary polyclonal antibodies (goat anti–rat IgG H + L, 1:750). Nestin was visualized using primary antinestin antibodies (Rat-401; BioLegend) at 1:200 dilution in 0.1% Tween 20, 0.3 M glycine, and 1% BSA in PBS and incubated overnight at 4°C followed by labeling with rabbit anti–mouse IgG (H + L) secondary antibodies conjugated with Alexa Fluor® 488 (1:1,000; Thermo Fisher Scientific). Nuclei were counterstained with Hoechst 33342. Images were captured on an Eclipse Ti-E microscope with the A1 confocal module (Nikon Corporation) and CFI Plan Apo VC 20×/0.75 objective.

Nestin-Based Reporter Transgenic Mice

C57BL/6 mice were bred at our facility and used with a 12-h light cycle at a constant temperature (22°C ± 2°C) with *ad libitum* access to food and water. The nestin-GFP mouse line was generated as described (Mignone et al., 2016) and kindly provided by Grigori Enikolopov. The experiments were conducted in accordance with the ethical standards and recommendations for accommodation and care of laboratory animals covered by the Council Directives of the European community 2010/63/EU on the use of animals for experimental studies. The animal protocols were approved by the institutional animal ethics committee (protocol 5/18 from May 14, 2018).

Induction of Photothrombotic Infarcts

Young male mice (17 ± 3 g) were used for the experiments. Focal cortical infarct was induced using the photothrombosis model as described by Watson et al. (1985) with modification. Under isoflurane anesthesia (2–2.5% in air) by SomnoSuite® system (Kent Scientific Corporation, Torrington, CT, United States), a mouse was placed in a stereotactic frame, and the skull was exposed through a midline incision cleared of connective tissue and dried. The rose Bengal dye (3% solution, 40 mg/kg; Sigma–Aldrich) dissolved in saline was injected into the jugular vein. A green light source (SDLaser 301) producing a 3-mm-diameter light beam was positioned on the region corresponding to the right prefrontal cortex. After 5 min of the dye injections, the brain was illuminated through the intact skull for 10 min. Rectal temperature was kept constant at 37.0°C ± 0.2°C using a heating pad. The animals were divided into following groups: control (n = 4), intact mice; Isch + saline (n = 12), mice with stroke induction that received intracranial (i/c) injection of saline; Isch + rS1/9 (n = 12), mice with stroke induction that received i/c injection of rS1/9 microparticles.

One day after photothrombotic stroke induction, the mice were placed in a stereotaxic frame, and under aseptic conditions, the sutures were removed, and the skull was exposed. In the ischemia + rS1/9 group of animals, suspension of spidroin microparticles in saline was transplanted into a single point in the center of lesion area of the prefrontal cortex using a Hamilton syringe with a needle (Microliter 702 LT). The stereotaxic coordinates for the injection of microparticles into the prefrontal cortex were as follows: +1.6 mm anterior to bregma, and 2.1 mm ventral to the skull surface. The syringe needle was inserted up to a depth of 1.0 ± 0.2 mm through the hole in the skull. The solution was then infused in a total volume of 2 μL at a rate of 0.25 μL/min using a microscrew in order to reduce the pressure on the surrounding tissue. When the solution was infused, the needle was pulled out with a rate of 0.25 mm/min. Group of mice "Isch + saline" received the same volume of saline.

Dissection of Hippocampal DG

Dissection of the hippocampal DG was made as described by Hagihara et al. (2009).

Magnetic Resonance Imaging Studies of the Brain Damage

Infarct volume was quantified by analyzing brain magnetic resonance imaging (MRI) scans obtained 7 days after the stroke induction as described previously (Silachev et al., 2009) on a 7-T magnet (Bruker BioSpec 70/30 USR; Bruker BioSpin, Ettlingen, Germany) using 86-mm volume resonator for radiofrequency transmission and a phased array mice head surface coil for a reception. Before scanning, the animals were anesthetized with isoflurane 2–2.5% in a mixture of oxygen and air. Mice were placed in a prone position on a water-heated bed. The heads of the mice were immobilized using a nose mask and masking tape. The imaging protocol included a T2-weighted image sequence (time to repetition = 4,500 ms, time to echo = 12 ms, slice thickness = 0.5 mm).

Flow Cytometry Assessment of Mitochondrial Transmembrane Potential

Comparative analysis of mitochondrial transmembrane potential in the cells was undertaken using a CyFlow cytometric analyzer (FACS Canto II; Becton Dickinson, BD, United States). The hippocampal DG was isolated as described above and placed in DMEM medium at room temperature in a Petri dish. The DG was dissected, and the tissue was incubated for 15 min in trypsin/EDTA (0.05%/0.02% wt/vol in PBS at 37°C). The cells were rinsed twice with PBS and once with DMEM medium without bicarbonate, dissociated by Pasteur pipette in DMEM, pelleted by centrifugation (210 g for 2 min at 21°C) and resuspended in DMEM. A cell suspension containing 1×10^5 cells was divided into two samples: unstained cells used as a negative control and loaded with tetramethylrhodamine ethyl ester (TMRE). The cell suspension was stained with 100 nM TMRE for 60 min at room temperature; 543-nm laser excitation was used, and emission beyond 560 nm was collected for evaluation of TMRE fluorescence. In total, 200,000 cells per sample were taken; each experiment included the usage of three animals. Target cells were allocated on dot plots based on the values of side and forward light scattering, as well as the intensity of TMRE fluorescence. The results were analyzed using FACS Diva 6.1 (Becton Dickinson) and Kaluza 2.1 (Beckman Coulter, United States) software.

Tissue Processing

Mice were deeply anesthetized with an overdose of chloral hydrate. Brains were excised after 4 and 7 postoperative days, fixed in 4% formaldehyde with PBS and sliced using a VibroSlice microtome (World Precision Instruments) into 100-μm-thick sections. The brain slices were studied using an LSM510 laser scanning confocal microscope (Carl Zeiss, Jena, Germany). Fluorescence analysis was performed in glass-bottom dishes with excitation at 488 and 543 nm and emission collected at 500 to 530 nm and >560 nm, respectively.

BrdU Administration

BrdU (100 mg/kg body weight) was administered by intraperitoneal (i.p.) injection. BrdU was diluted in sterile PBS to make a solution of 10 mg/mL.

Assessment of Cell Proliferation by BrdU Incorporation

For BrdU immunodetection, antigen retrieval was performed before blocking: the samples were kept overnight in Tris-buffer (pH 9) at 65°C and then washed with PBS for 15 min and incubated with 2N HCl for 2 h at 37°C, followed by 10-min neutralization in 0.1 M borate buffer (pH 8.5). Then slices were incubated in 0.1% Tween 20, 0.3 M glycine, and 1% BSA in PBS for 6 h. After blocking, samples were incubated overnight with an anti-BrdU antibody (1:250; Abcam). Non-bound antibodies were washed five times in PBS/1% FBS/0.1% Tween-20. Samples were treated for 2 h at room temperature with Cy3-conjugated secondary polyclonal antibodies (goat anti–rat IgG H + L, 1:750; Thermo Fisher Scientific). Nuclei were counterstained

with Hoechst 33342. Images were captured on an Eclipse Ti-E microscope with the A1 confocal module (Nikon Corporation) and a Plan Fluor 40×1.3 objective.

Western Blot Analysis

Western blotting was used for determination of the levels of βIII-tubulin, glial fibrillary acidic protein (GFAP), and NCAM in hippocampus homogenates prepared 4 days after stroke induction. The brain was isolated immediately after decapitation and cooled in PBS. Hippocampus was used for analysis; it was homogenized in 100 μL of PBS containing 1 mM protease inhibitor [phenylmethylsulfonyl fluoride (PMSF)]. Total protein concentration was measured in samples by bicinchoninic acid kit for protein determination (Sigma, United States). Ten micrograms of total protein in hippocampus homogenate samples were loaded on 12.5% polyacrylamide gel and separated under denaturing conditions. After electrophoresis, gels were blotted 30 min at 1 amp onto polyvinylidene fluoride membranes (Amersham Pharmacia Biotech, United Kingdom), which were blocked for 12 h at 4°C in Tris buffer by 5% non-fat milk and subsequently incubated with primary rabbit anti–βIII-tubulin (Abcam, 1:1,000), mouse anti-GFAP (DAKO, United States, 1:20,000), and mouse anti-NCAM (Invitrogen, United States, 1:400) antibodies. Membranes were processed with secondary antibodies conjugated with horseradish peroxidase (Imtek, Russia, 1:10,000). Detection was performed by a ChemiDoc^{TM} MP imaging system (Bio-Rad, United States) with a WesternBright^{TM} Enhanced Chemiluminescence kit (Advansta, United States).

Hippocampal GFP Level Assessment

Hippocampus was homogenized in PBS/PMSF buffer. Ten micrograms of total protein in hippocampus homogenate samples were loaded on 12.5% polyacrylamide gel and separated under native conditions. After electrophoresis, gels were visualized by a ChemiDoc^{TM} MP imaging system (Bio-Rad) with Alexa 488 filter.

Statistical Analysis

Statistical analyses were performed using Statistica 7.0 for Windows (StatSoft, Inc., United States). The normality of the parameter distribution was estimated using the Shapiro–Wilk criterion *W*. All data were presented as means ± standard error of means. Data were compared using Student *t*-test when 2 groups were compared and parametric analysis of variance when more than 2 groups were compared. Differences were considered significant at $p \leq 0.05$. $p < 0.05$ was considered as statistically significant.

RESULTS

The Structural Organization of Scaffolds

Two types of scaffolds were used in experiments – thin films and microparticles based on the recombinant spidroin rS1/9, a recombinant analog of N. clavipes spidroin 1. The surface structure of films and microparticles were analyzed using SEM

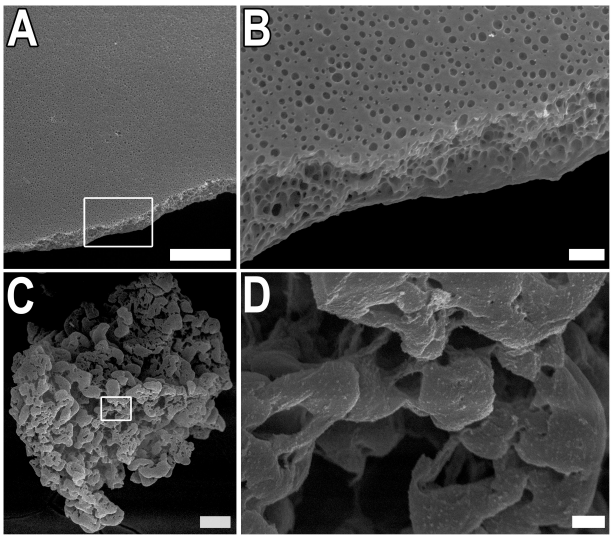


FIGURE 1 | Structure of rS1/9 films and microparticles. **(A,B)** SEM images of rS1/9 films. **(C,D)** SEM images of rS1/9 microparticles. **(A,C)** Scale bar 50 μm. White frames in **(A,C)** indicate the regions, enlarged in **(B,D)**, respectively. Scale bar 3 μm.

(**Figure 1**). The films were prepared by casting rS1/9 (see proper section in Section "Materials and Methods"). The thickness of the films varied from 10 to 20 μm. On the surface and cross-section of the rS1/9 film, spontaneously formed submicrostructures in the form of pores are visible (**Figures 1A,B**). The pore size varies from 1 to 500 nm on the surface and 10 to 1,000 nm on the cut. Microparticles were obtained as a result of the physical crushing of hydrogel and represent hydrogel particles with a complex surface. Surface elements include nanostructures with a diameter of 100 to 300 nm and microstructures with a size of 10 to 30 μm (**Figures 1C,D**).

The Effect of rS1/9 on the Neuronal Cultures Growth

To facilitate our studies of the potential effect of rS1/9 material on process formation cortical neurons, we established cultures of embryonic day 18 (E18) murine cortical neurons. The ability of films based on silk proteins to maintain neuronal cell adhesion, as well as the growth of neurites and the formation of a neuronal network, was assessed using immunofluorescence staining with antibodies against β3-tubulin, NCAM, and DAPI. On the seventh day of cultivation of cortical neurons, the number of nuclei on the rS1/9 film was significantly higher compared to FB, 196.5 ± 44.1 and 71.4 ± 28.3, respectively (**Figure 2A**). β3-Tubulin staining was chosen to evaluate the parameters of neurite outgrowth because it provides bright, specific, and reliable staining of embryonic neurons in the mouse cerebral cortex. To determine the specific parameters of neurite outgrowth affected by rS1/9 films, a comparative morphometric analysis of total neurite length, number of neurites, and the thickness of neurites of cortical neurons cultured on FB and rS1/9 films was performed for 7 days. Compared to cells cultured on a FB-based

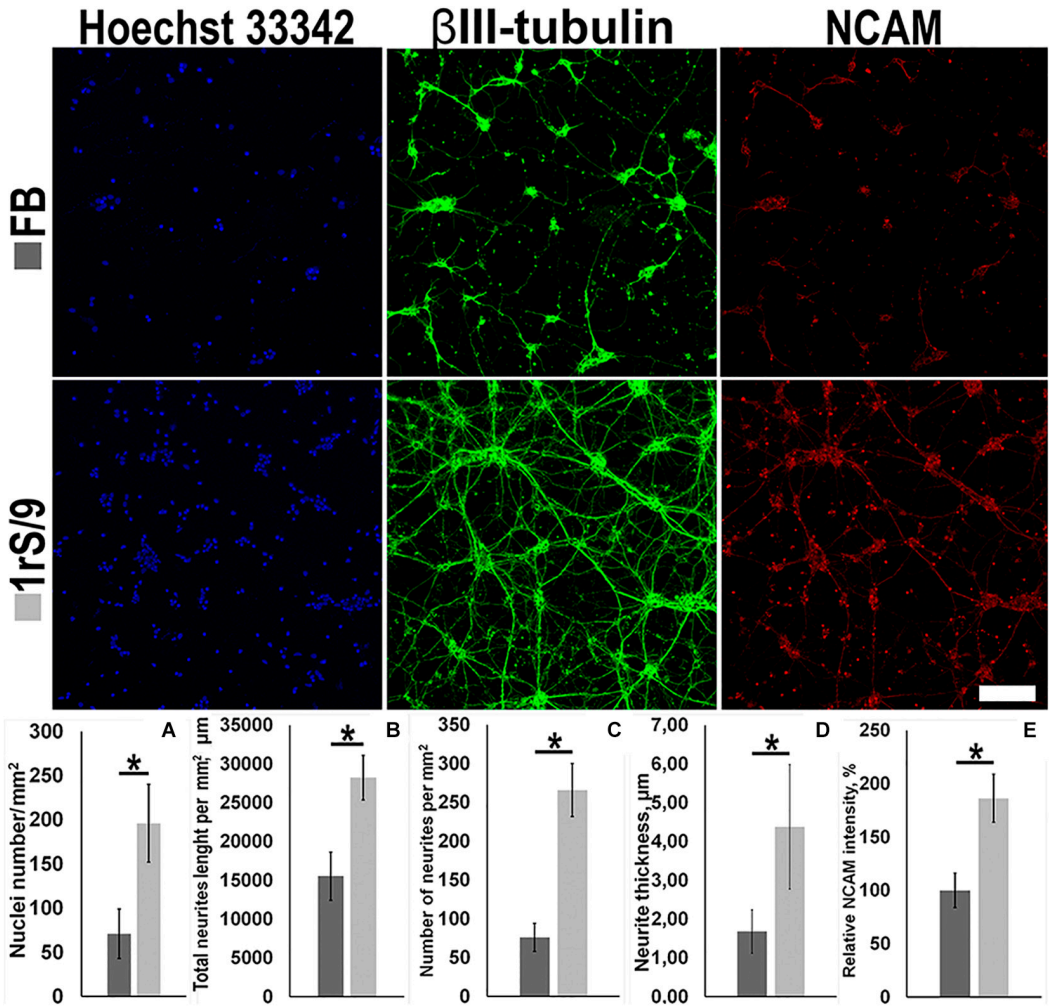


FIGURE 2 | Effect of fibroin films (top) and 1 rS/9 (bottom) on the number of neurons in the mouse cortex and on the morphology of their neurites on the seventh day of cultivation. The cells were treated with antibodies to βIII-tubulin (green) and NCAM (red), and the nuclei were detected by Hoechst 33342 (blue). Scale = 100 μm. **(A)** The number of nuclei per μm^2, **(B)** total length of neurites per mm^2, **(C)** number of neurites per mm^2, **(D)** thickness of neurites, and **(E)** relative intensity values of NCAM. *Significant difference between groups ($p < 0.05$).

substrate, total neurite length was significantly greater on rS1/9 (15,536.5 ± 3,102.6 μm and 28,226.6 ± 2,857.7 μm, respectively, **Figure 2B**). Also, rS1/9 material provided a significant increase in the total number of neurites and their thickness compared to FB was 266.2 ± 34.7 and 76.6 ± 18.3, respectively (**Figure 2C**) and 4.4 ± 1.6 and 1.7 ± 0.5 μm, respectively (**Figure 2D**). The relative pixel intensity values of NCAM indicate that NCAM expression is significantly higher on rS1/9 film, compared to FB (186.4% ± 22.6 and 100.0% ± 16.2%, respectively, **Figure 2E**).

Effects of rS1/9 on Outgrowth and Branching of Neurites

To determine the effect of rS1/9-based microparticles on the parameters of neurite outgrowth of hippocampal neurons, cultures of E18 rat hippocampal neurons were obtained. Because the injury zone is located at a distance of several millimeters from the hippocampus and direct contact of the injected scaffold with cells of this zone is unlikely, we used a model of *in vitro* cell culturing in the presence of rS1/9 microparticles without direct contact with cells in the Transwell system, as well as in an air-conditioned environment (it contains products of spontaneous hydrolysis of rS1/9 and does not contain rS1/9 itself). To obtain an air-conditioned environment, microparticles rS1/9 were incubated for a week at 37°C in complete growth media under sterile conditions. After this period, the conditioned medium of microparticles was collected and used to quantify neurite outgrowth. To create conditions in which rS1/9 is present in the culture system but does not have direct contact with cells, a suspension of rS1/9 microparticles was placed in a permeable polycarbonate membrane insert. Next, insert containing a suspension of microparticles was transferred to the wells of a 24-well plate with glass coated with poly-L-lysine, after which a suspension of cells was introduced into

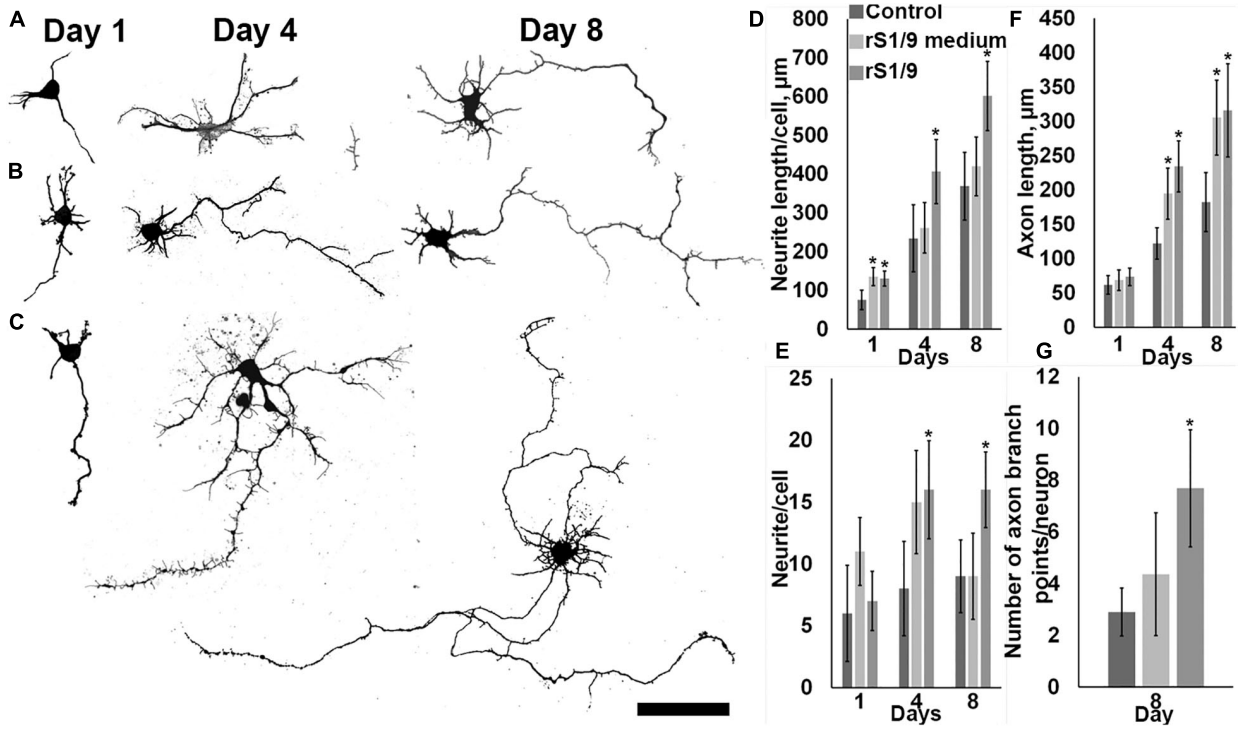


FIGURE 3 | Influence of the presence of rS1/9 microparticles on the cultivation of hippocampal neurons and a conditioned environment on the growth of neuronal sprout. **(A–C)** Binary inverted confocal image of nestin^{+} immunostained cells on days 1, 4, and 8 of cultivation. **(A)** Control, **(B)** hippocampal neurons cultured in a conditioned environment, **(C)** hippocampal neurons cultured in the presence of particles. The scale = 50 μm. **(D)** The length of neurites per cell, **(E)** the number of neurites per cell, **(F)** the length of the axon, and **(G)** the number of axon branch points per neuron. *Significant difference vs. control group ($p < 0.05$).

the well. As a control, cells growing in a standard culture medium on poly-L-lysine–coated glasses were used. The cells were fixed on days 1, 4, and 8 of culture and treated with antibodies to nestin, after which a morphometric analysis of the growth parameters of neurites was performed (**Figures 3A–C**). On the first and eighth days, the length of neurites of cells cultured in the presence of rS1/9 was significantly higher compared to the control group. On the other hand, the conditioned environment also contributed to the formation of longer neurites on the first day of cultivation, compared to the control, but this difference was not observed on the fourth day. On the first day of cultivation, the total length of neurites was 130.2 ± 19.1 μm (rS1/9), 135.4 ± 23.4 μm (conditioned medium), and 75.9 ± 24.9 μm (control), and on the eighth day of cultivation, 601.4 ± 89.3 μm (rS1/9) and 368.7 ± 87.2 μm (control) (**Figure 3D**). Cultivation of hippocampal neurons in the presence of microparticles also contributed to an increase in the number of neurites per cell on the fourth and eighth days of cultivation, compared to the control: on the fourth day of cultivation, the number of neurites was 16.19 ± 3.97 (rS1/9) and 8.04 ± 3.81 (control) and on the eighth day – 16.11 ± 3.07 (rS1/9) and 8.57 ± 2.95 (control). There was no statistically significant difference between the group receiving the conditioned environment and the control (**Figure 3E**). We observed an increase in the length of axons when of hippocampal neurons were cultured in the presence of microparticles starting from the fourth day *in vitro*. At the same time, an increase in the length of the axon in comparison with the control was also observed for cells cultured in a conditioned environment (**Figure 3F**). Thus, the values of axon length were 234.3 ± 37.1 μm (rS1/9), 194.6 ± 37.3 μm (conditioned medium), and 122.2 ± 22.8 μm (control) on the fourth day of cultivation, and 316.1 ± 67.8 μm (rS1/9), 305.4 ± 54.7 μm (conditioned medium), and 182.2 ± 41.5 μm (control) on the eighth day of cultivation. In addition, the axons of cells cultured in the presence of microparticles had more branching nodes compared to the control group, 7.7 ± 2.3 μm (rS1/9) and 2.9 ± 0.9 μm (control) (**Figure 3G**).

To get insight into the mechanisms of action of the rS1/9-conditioned medium (described above), we explored the effect of rS1/9 proteolytic degradation products on the proliferation of neural progenitor cells in culture. It is known that the brain contains several proteases capable to cleave rS1/9 at specific sites. In particular, among these proteases are trypsin IV and thrombin which presence has been demonstrated in the brain tissue (Wang et al., 2008). We exposed rS1/9 microparticles to trypsin or thrombin, added the resulting hydrolysate to the cell culture medium, and kept the culture of neural progenitor cells in the conditioned medium for 3 days. We found that this treatment induced a significant increase in the number of nestin-positive cells in the culture (**Figure 4**). Certainly, this increase was due

to the proliferation of neural stem/progenitor cells, because the majority of nestin-positive cells demonstrated positive BrdU staining.

We treated rS1/9 with trypsin or thrombin and added the obtained hydrolysate to the cell culture media. The addition of the proteolyzed spidroin caused a sharp increase in the number of nestin-positive cells in culture (**Figure 4**). This increase was associated with the proliferation of neural stem/progenitor cells, because many nestin-positive cells were also positively stained for BrdU.

Effects of rS1/9 on Neural Progenitors Proliferation in the Hippocampal DG

The object of the study was a genetically modified reporter line of mice in which stem and progenitor cells are characterized by the expression of a GFP located under the nestin promoter (nestin-GFP mice) (Mignone et al., 2016). Focal brain damage in the prefrontal cortex was modeled by a photo-induced occlusion of cortical vessels. As a result, a focal focus of ischemic damage was formed, including only the area of the prefrontal cortex (**Figures 5A,B**). The relationship between injured areas (in prefrontal cortex), rS1/9-injection site, and hippocampus is presented in serial MRI scans (**Supplementary Figure 1**). Intracerebral injection in the area of ischemic damage of rS1/9 microparticles in the volume of 2 μL or saline solution to control animals was performed 24 h after stroke simulation. Analysis of confocal images of brain slices on day 7 revealed the presence of GFP^+ cells in the area of the DG (**Figures 5D–F**). Based on the morphology of these cells, it was possible to identify resting neural progenitors [quiescent neural progenitors (QNPs)], which have a triangular soma and an expanding apical process that crosses the granular cell layer and ends in a set of small sprouts in the molecular layer of the DG (**Figure 5F**). It is known that because of asymmetric mitosis division, QNPs divide to form amplifying neural progenitors (ANPs) which have a round or oval shape and very short sprouts but also are GFP^+ (**Supplementary Figure 2**, red arrow). In the figure presented in **Supplementary Figure 2**, one can see that in some places it is very difficult to identify QNPs and ANPs based only on morphological criteria because of the close location of cells. The objective of this study was to qualitatively assess changes in the number of GFP^+ cells in the area of the stem cell niche—the DG, in response to brain damage followed by the transplantation of rS1/9 microparticles to the area of damage. An increase in GFP^+ cells in the subgranular zone of the hippocampus compared with the control group (**Figures 5C,E**) was observed in the group of animals that received rS1/9 injection in the area of ischemic injury (**Figures 5D,F**). Besides, we examined cell proliferation following a photothrombotic stroke when the mice received injections of BrdU (i.p., 100 μg/g body weight) 5 days after rS1/9 injection. The number of BrdU-positive cells in the DG of rS1/9-treated mice (**Figures 5C–F**) was significantly higher than in the control group mice (**Figure 5E**).

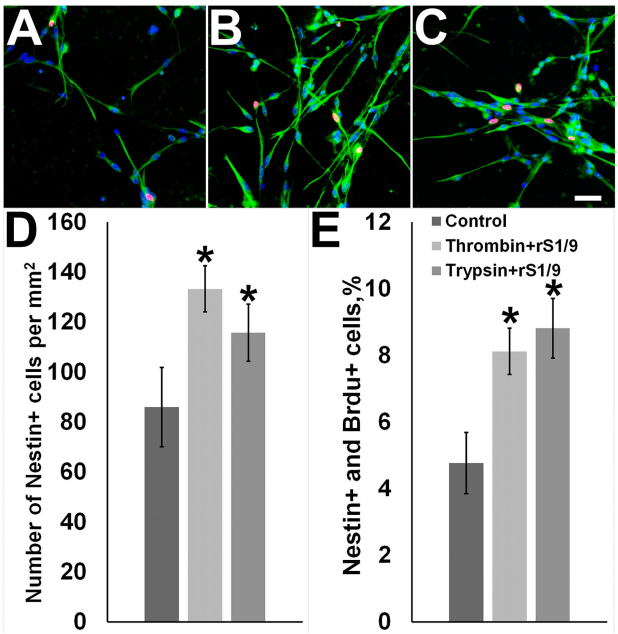


FIGURE 4 | Effects of rS1/9 proteolytic degradation products on cultured neural stem/progenitor cells. **(A)** Control cells, **(B)** cells incubated with thrombin-digested rS 1/9, **(C)** cells incubated with trypsin-digested rS1/9. Neural stem cells were cultured in selective medium and incubated with enzymatically processed rS1/9 for 3 days. The cells were exposed to antibodies to Nestin (green) and BrdU (red), and the nuclei were stained by Hoechst 33342 (blue). Scale = 50 microns. **(D)** The number of $Nestin^+$ cells per mm^2, **(E)** Percentages of $Nestin^+$ and $BrdU^+$ cells. Values are Mean ± SD of three independent experiments. *Significant difference vs. control group ($p < 0.05$).

The distribution of BrdU-positive cells in the subregions of the dentate gyrus was significantly different in both groups. BrdU-positive cells were located primarily in the granule cell layer and hilus of the dentate gyrus in rS1/9-treated mice (**Figures 5E,F**).

Additionally, we analyzed angiogenesis in the brain after the stroke and rS1/9 administration. The brain slices were stained with both BrdU (cell proliferation marker) and CD31 antibodies (vessel marker). We found that a significant part of nestin-positive cells (in all groups of animals) was colocalized in structures positively stained with antibodies to CD31. Thus, we can assume that some of the progenitor cells in the brain are derived from microvessel pericytes. Indeed, Nakata et al. (2017) also observed that $nestin^+$ cells were adjacent to $CD31^+$ cells in the ischemic zone suggesting the pericytic origin of neural progenitors. On the other hand, the majority of nestin-positive cells in the dentate gyrus area were not stained with CD31, so the stem cells located there did not belong to microvessels and pericytes. Analysis of $nestin^+$ and $BrdU^+$ cells revealed an increase in the proliferation of progenitor cells not only in the ipsilateral but also contralateral hemisphere (**Figure 6**). Quantitative analysis of $BrdU^+$, $nestin^+$, and $CD31^+$ cells revealed a significant increase in

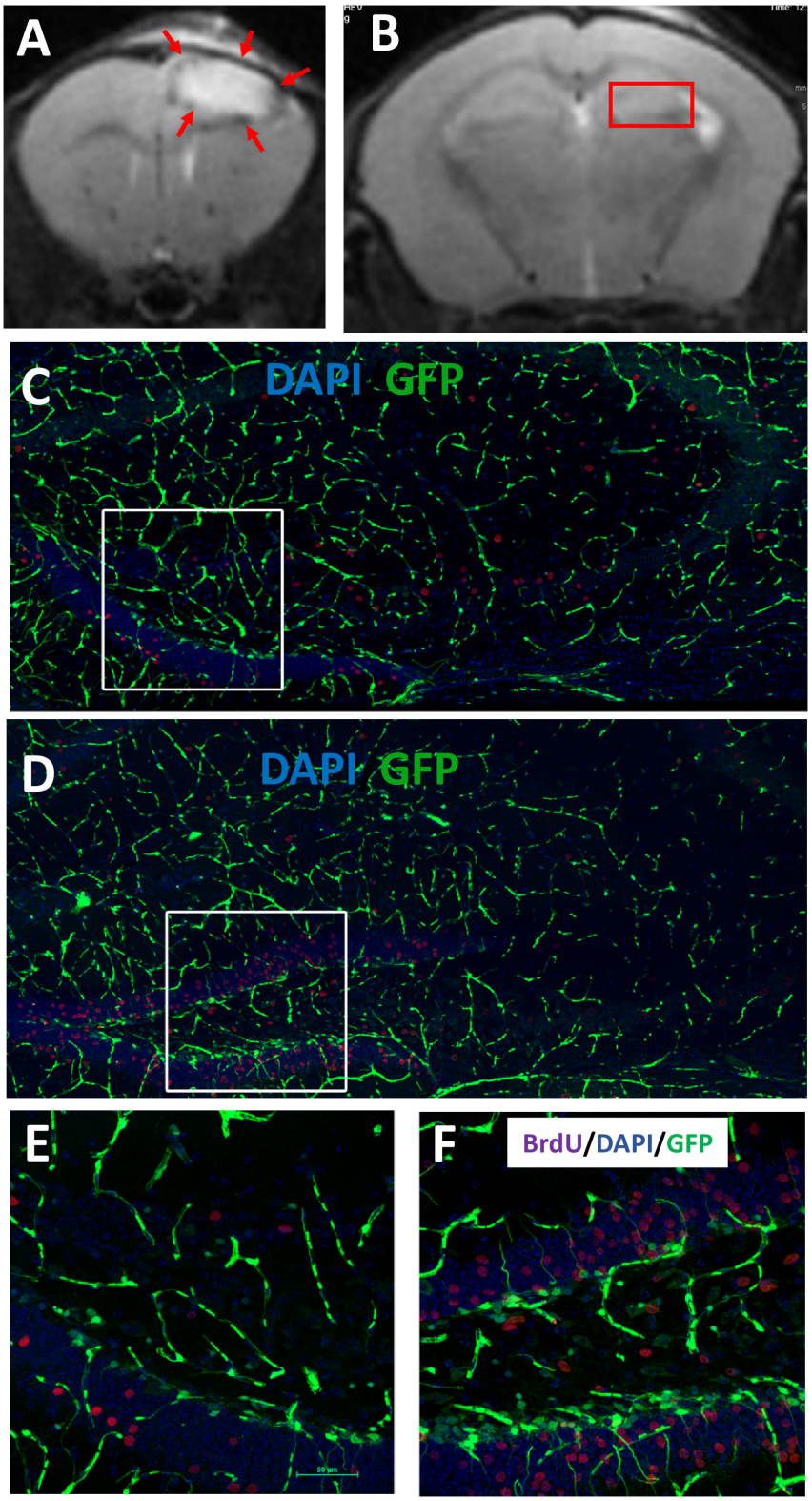


FIGURE 5 | Evaluation of cell proliferation in GFP$^+$ cells in the adult hippocampus 7 days after focal ischemia. T2-weighted MRI scans of coronal brains slices in the area of prefrontal cortex **(A)** and dentate gyrus **(B)** after 7 days' stroke induction. The red arrows indicate the ischemic region. The red frame marks the area of the dentate gyrus. Proliferation of GFP$^+$ cells in the hippocampus of control **(C)** or rS1/9-treated mice **(D)**. **(E,F)** Higher zoom of the area marked by a white box **(C,D)** presented in **(E,F)**. Nuclei were stained with DAPI (blue), immunostaining with antibody against BrdU (purple).

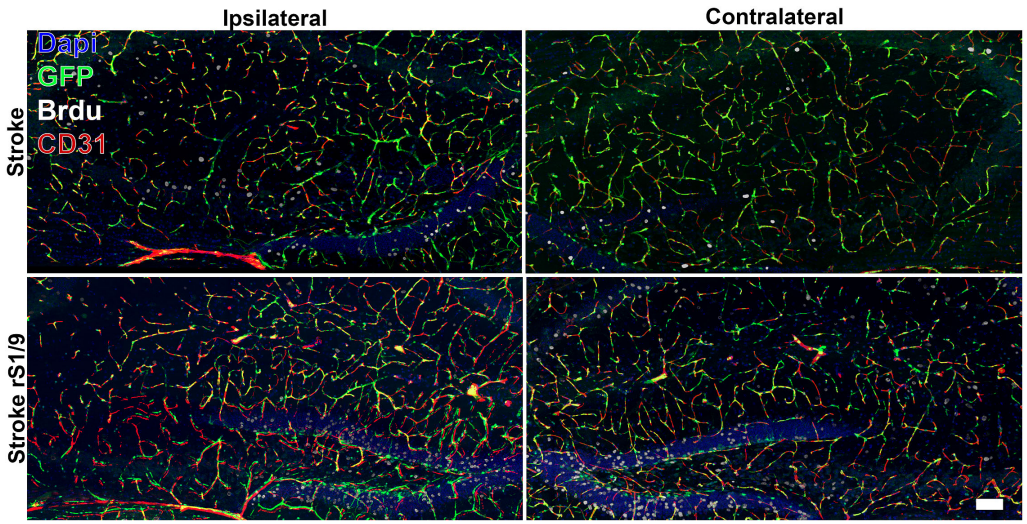


FIGURE 6 | Evaluation of GFP$^+$, CD31$^+$, and BrdU$^+$ cells in both contralateral and ipsilateral hippocampus 7 days after focal ischemia. Nuclei were stained with DAPI (blue), immunostaining with an antibody against BrdU (white) and CD31 (red), and nestin-GFP$^+$ cells are green.

BrdU$^+$/nestin$^+$ cells both in ipsilateral and contralateral hippocampus (**Supplementary Figures 3**, **4**) in brains treated with rS1/9. However, rS1/9 treatment did not cause any increase in BrdU$^+$/nestin$^+$ cells in the ischemic area in cortex, as well as in peri-ischemic zone (**Supplementary Figures 5**, **6**). Moreover, we found slight increase in CD31$^+$ cells in hippocampus (**Supplementary Figure 4**) and penumbra area (**Supplementary Figure 6**) in mice after ischemia with rS1/9 treatment.

Effect of rS1/9 Treatment on the Proportion of Different Types of Neural Cells in the Hippocampus

To determine alterations in the subtypes of cells in the hippocampus following brain ischemia and rS1/9 treatment, we analyzed the levels of a number of proteins that are markers of brain cells. Analysis of neuronal-specific tubulin showed no changes in the amount of βIII-tubulin in the hippocampus of mice on day 4 after brain ischemia. Injection of spidroin also did not affect the amount of tubulin, which indicates that there are no significant changes in the number of neurons in the DG of the hippocampus at these periods after ischemia (**Figure 7A**). At the same time, a significant increase in the number of GFAP (**Figure 7B**) was found which indicates the possible development of posttraumatic astrogliosis in the hippocampus region remote from the focus of ischemic damage. In the group of animals that received rS1/9, there was a tendency to decrease the number of GFAP signal, that is, a decrease in the pathological activation of astrocytes. The level of GFP also increased in groups of animals with ischemia or ischemia with spidroin treatment from 75.7 ± 1.6 in control to 122.1 ± 16.5 or 134.2 ± 15.8 a.u., correspondingly (**Figure 7C**, $p < 0.05$), which confirms our data on the increase in the number of neural progenitor cells obtained on brain slices in the hippocampus region. We analyzed the amount of NCAM in the hippocampus and found its significant increase after brain ischemia, as well as after injection of rS1/9 hydrogel in the area of ischemic damage (**Figure 7D**).

Impact of Brain Ischemia and rS1/9 on Mitochondria of Neural Cells

Mitochondria play a key role in the development of damage in the ischemic brain, and their normal functioning can be impaired by the action of damaging stimuli. Therefore, we analyzed the mitochondrial transmembrane potential in the hippocampus region of brain cells 7 days after ischemia. It was found that the intensity of the fluorescence of specific probe for the membrane potential, TMRE, significantly increases in cells isolated from the hippocampus after induction of photothrombosis in the prefrontal cortex compared to intact animals. However, when spidroin was administered to the area of ischemic injury, further enhancement of TMRE fluorescence was observed (**Figures 8A,B**). These changes may indicate either an increase in the transmembrane potential of mitochondria 7 days after ischemia or an increase in the number of mitochondria themselves. To distinguish these effects, we analyzed the levels of PGC1α, which is responsible for mitochondrial biogenesis and proliferation. It was found that the amount of this factor increases in hippocampal cells after brain ischemia from 31.9 ± 7.3 to 47.3 ± 8.6 a.u. (**Figure 8C**); thus, it gives evidence of a compensatory increase in mitochondrial biogenesis. The injection of spidroin enhanced this process (**Figure 8C**) and increased PGC1α levels up to 59.3 ± 9.8 a.u. Thus, an increase in the intensity of TMRE fluorescence in neural cells should be interpreted as an increase in the number of mitochondria, rather than as an increase in mitochondrial potential.

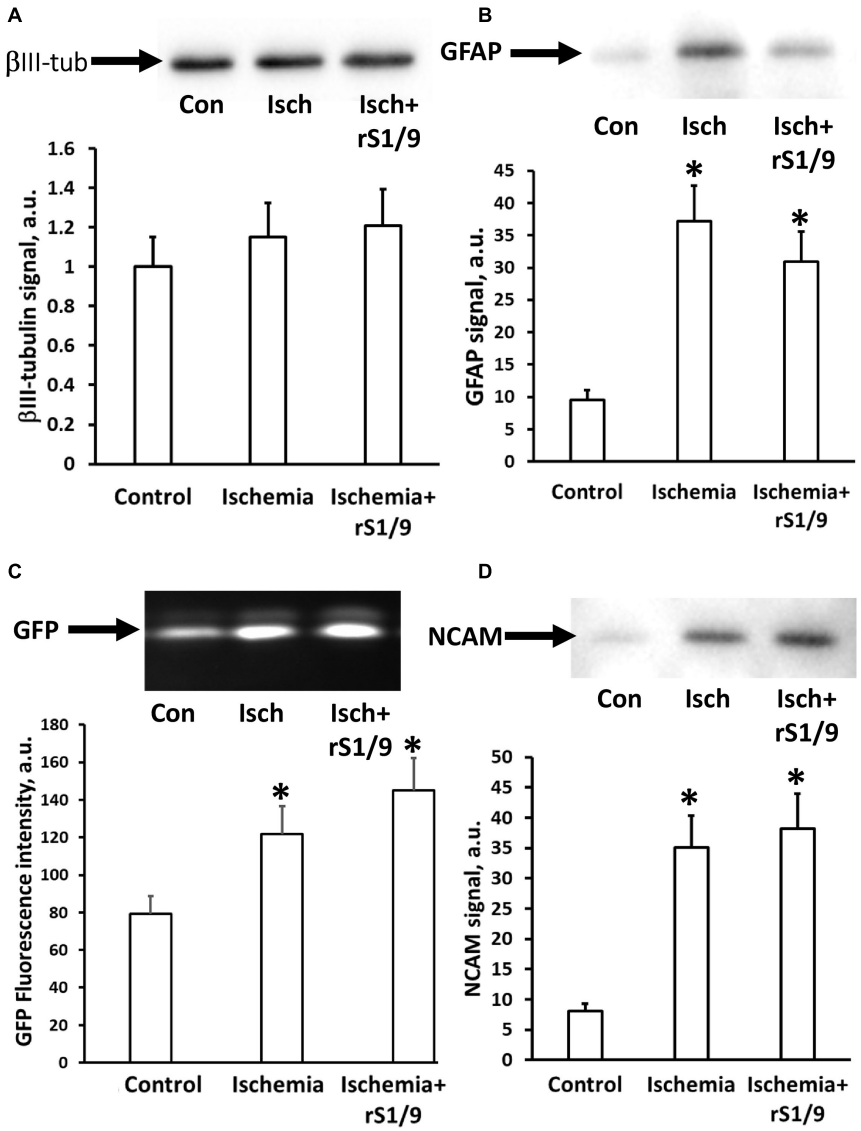


FIGURE 7 | Changing the neuronal cell types in the hippocampus after rS1/9 treatment on the fourth day of stroke induction. **(A)** The level of βIII-tubulin, **(B)** glial fibrillary acidic protein (GFAP), **(C)** green fluorescent protein (GFP), and **(D)** neural cell adhesion molecule (NCAM) in hippocampus homogenates. Representative Western blots with averaged corresponding densitometry are presented. Number of animals was $n = 4$ per each experimental group. $^*p < 0.05$, compared to control.

DISCUSSION

In this study, we analyzed the effect of microparticles from recombinant spidroin rS1/9 after its injection into the area of ischemic damage to the prefrontal cortex on the niche of stem cells in the DG of the hippocampus. It is well known that "new" (adult-born) neurons can be formed in the adult brain as a result of neurogenesis. In particular, such neurons were found in the DG of the hippocampus in rodents (Kempermann et al., 1997; Seki and Arai, 1999) and in humans (Knoth et al., 2010; Bergmann et al., 2015). These studies allow us to put forth a hypothesis about the possible participation of neurogenesis in the processes of brain plasticity and, as a result, in cognitive processes, as well as in the regeneration of brain tissue after damage. The peculiarity of "adult" neurogenesis is that the brain has already formed neurotransmitter systems that ensure the functioning of organized neural networks. The DG of the adult brain receives various direct and modulating neurotransmitter signals from several other structures including the prefrontal cortex (Jin and Maren, 2015; Nilssen et al., 2019). Damage to the prefrontal cortex is known to be associated with cognitive impairment due to impaired morphofunctional connections with the hippocampus (Hoover and Vertes, 2007; Silachev et al., 2009; Churchwell and Kesner, 2011; Bast et al., 2017). Activation of neurogenesis should promote functional recovery in this area of damage. We assumed that the delivery of a hydrogel based

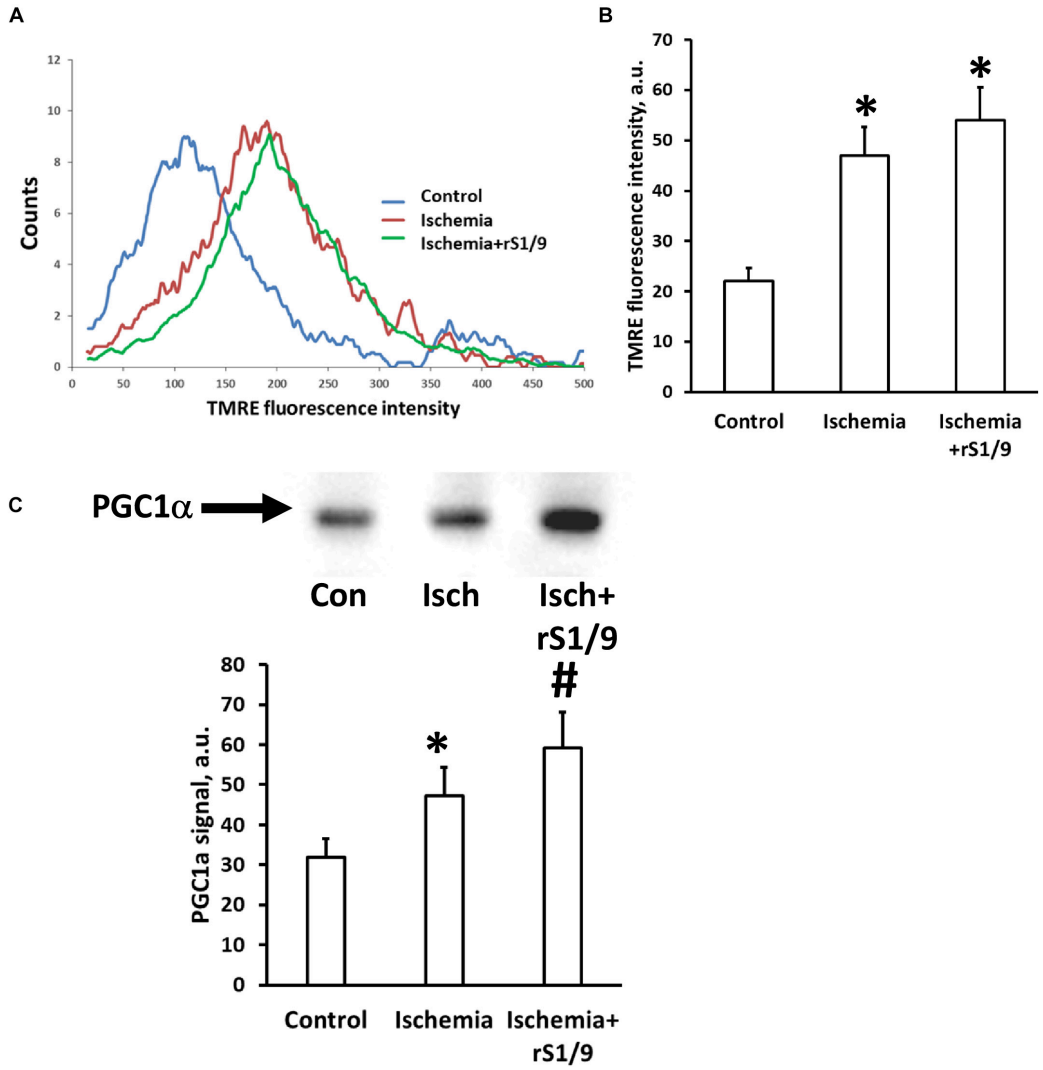


FIGURE 8 | Effects of rS1/9 spidroin treatment on mitochondria of rat brain hippocampus after ischemic stroke. Mitochondrial membrane potential was estimated by TMRE loading in isolated neural cells immediately after trypsin digestion of mouse brain. Representative histograms of flow cytometry analysis of cell suspension **(A)** and quantification of mean TMRE fluorescence intensity **(B)**. Analysis of mitochondria biogenesis indicated by PGC-1α factor levels in hippocampal tissue **(C)**. $^{*}p < 0.05$, compared to control, $^{\#}p < 0.05$, compared to ischemia.

on the biologically active substance spidroin to the area of ischemic damage would promote the proliferation and survival of progenitor cells in the niche of brain stem cells (the DG).

The efficiency of using structural silk proteins from *B. mori* and *N. clavipes* for creating a matrix for neural tissue engineering has been demonstrated in numerous studies (Magaz et al., 2018; Salehi et al., 2020). Biomaterials based on silkworm fibroin are able to maintain the adhesion of neurons without adversely affecting their proliferation, morphology, and migration (Qu et al., 2010; Wei et al., 2013). In addition, fibroin scaffolds not only can support the adhesion and viability of cortical neurons but also carry a neuroprotective role demonstrated in the oxygen–glucose deprivation model (Moisenovich et al., 2019). It is known that the inclusion of RGD, GFPGER, and other peptide sequences in the structure of the material that mimic cell-binding motives of fibronectin, collagen, laminin, and other extracellular matrix proteins can regulate cell adhesion and, as a result, neuronal growth (Qu et al., 2010). The interaction of cellular receptors with such sequences mediates the influence of the microenvironment on cellular behavior. Neuronal membranes contain not only classical cell adhesion molecules, such as integrins and cadherins, but also neuron-specific cell adhesion molecules, such as NCAM (Kiryushko et al., 2004). NCAM is highly expressed in the central and peripheral nervous systems, where it plays an important functional role in cell adhesion, cell migration, and axon proliferation. In addition, NCAM is involved in the regulation of synaptic plasticity and recovery after brain damage (Park et al., 2018). Located on the surface of neurons, NCAM induces intracellular signaling pathways and cytoskeletal rearrangements in response

to exposure to its extracellular domain (Wobst et al., 2015). Thus, NCAM-mediated cell adhesion is a critical step for triggering signaling events that lead to the growth of neurites (Maness and Schachner, 2007).

The recombinant analog of spidroin 1 rS1/9 used in our experiments contains 18 repeats of the NCAM-binding sequence GRGGL and is characterized by a high positive charge under physiological conditions, which is a critical property for NCAM-mediated adhesion (An et al., 2015). Films and microparticles obtained from rS1/9 were characterized by a complex surface and the presence of spontaneously formed micropores and submicropores (**Figures 1A–D**). It is known that the presence of pores can improve the diffusion of nutrients and oxygen in an artificial extracellular matrix. Also, during the formation of a neural network, the growth cone of the neurite is sensitive to surface elements, so that nanostructures and microstructure on the surface guide and modulate the growth of neurons. Moreover, it has been shown that neurites can penetrate pores with a diameter of 0.8–5 μm and extend the neurite coverage on the non-seeded side of the substrate, thereby increasing the volume of the neuronal network (George et al., 2018).

In our study, we demonstrated that rS1/9-based films provide better support for the growth of primary cortical neurons, including adhesion, neurite proliferation, and neural network formation, compared to fibroin-based films (**Figures 2A–D**). There was an increase in the intensity of NCAM-specific staining compared to fibroin (**Figure 2E**). This effect can be explained both by the content of a large number of NCAM-binding GRGGL sequences in the rS1/9 structure and a high positive charge and by the complex structure of the surface. These data are consistent with earlier studies that report a positive role of high charge and the presence of NCAM-binding motifs on the development of the neural network in cortical neuron culture (An et al., 2015). Thus, rS1/9-based materials can provide an attractive substrate for neurite germination and migration, which is one of the mechanisms of brain recovery after trauma (Park and Biederer, 2013).

It is known that solutions of silk proteins also carry biological activity and can interact not only with surface receptors but also penetrate the cell affecting the activation of signaling pathways, for example, the nuclear factor κB signaling pathway (Park et al., 2018). Based on the above facts, as well as taking into account the ability of rS1/9 to biodegrade in proteolytic (Krishnaji et al., 2013) and neutral (Moisenovich et al., 2011) conditions, we suggested that a suspension of microparticles added to damaged brain tissue may act as an intercellular matrix, and its products of hydrolysis may affect the growth of hippocampal nerve cells. To test this hypothesis, primary hippocampal neurons were cultured in a conditioned environment or in conditions where particles were isolated from direct contact with neurons by a membrane whose pore size prevented rS1/9 particles from directly entering the well with cells. In these experiments, we showed that the cultivation of hippocampal neurons in the presence of rS1/9 provides the formation of a larger number of longer neurites in terms of a cell, axon lengthening, and increasing its branching nodes (**Figures 3D–G**). The conditioned rS1/9 environment also had a positive effect on the length of neurites and axons but did not contribute to the formation of more neurites and axon branching points (**Figures 3D–G**). These results can be explained by the presence of products of hydrolysis of spidroin in the medium which carries multiple repeats of a neuron-specific GRGGL sequence recognized by neural progenitors (An et al., 2015). In case of culture in the Transwell culture system, neurons could receive rS1/9 hydrolysis products continuously formed from particles, in contrast to the conditioned environment, where the effect of dissolved spidroin or its hydrolysis products was bolus, which probably determined the difference in the results obtained. Thus, the injectable form of rS1/9 can affect neuronal growth without direct contact with cells, which is probably due to the formation of their biodegradation products, and it is important, given the distance of the injury zone from the hippocampus *in vivo*.

The next step of the work was to evaluate *in vivo* the effect of rS1/9 on the niche of progenitor cells in the DG. For this purpose, a reporter line of animals was used in which stem and progenitor cells were labeled with GFP associated with nestin expression which is a characteristic marker for this cell type (Bernal and Arranz, 2018). Nestin is expressed in the proliferative areas of the brain of embryos and adult mammals, and it is not found in differentiated cells of nervous tissue. Modeling of photothrombosis in the prefrontal cortex on day 7 led to an increase in the number of nestin-positive cells in the DG. Our data are consistent with a study in which with use of a similar line of mice it was demonstrated that traumatic brain injury in the sensorimotor cortex caused changes in proliferation of QNPs and ANPs in the acute phase following TBI (Gao et al., 2009). The hippocampus and prefrontal cortex are known to maintain functional interaction and anatomical connections and play a central role in various behavioral and cognitive functions. The ventral CA1 region of the hippocampus projects to the prelimbic medial prefrontal cortex and orbitomedial frontal cortex and the dorsal CA1 projects to the infralimbic and prelimbic parts of the prefrontal cortex (Sigurdsson and Duvarci, 2015). Because the prefrontal cortex has direct anatomical connections with the hippocampus (Jin and Maren, 2015), signal molecules such as rS1/9 and products of its degradation could directly enter the hippocampus and activate the processes of progenitor cell proliferation. Injection of rS1/9 microparticles into core ischemic damage resulted in a statistically significant increase in progenitor cell proliferation in the subgranular region of the DG. Additional labeling of proliferating BrdU cells on day 6 after rS1/9 injection revealed an increase in the content of $BrdU^+$ cells in the granular layer of the DG. We also detected single double-positive GFP^+ and $BrdU^+$ cells. It was previously shown that only a small portion of GFP^+ can be marked with BrdU after 24 h of pulse labeling (Filippov et al., 2003). We suggest that the injection of rS1/9 into the injury area can directly affect the proliferation of progenitor cells in the DG due to the diffusion of rS1/9 hydrolysis products from the injury area, which is consistent with our *in vitro* experiments.

As to the particular mechanisms of action of spidroin, it is necessary to keep in mind its effects on cell proliferation in contralateral DG where we found some increase in $BrdU^+$ cells, although it was not as pronounced as in the ipsilateral hemisphere. It is also important to note that the contralateral hemisphere of animals treated with spidroin contains more

$CD31^+$ cells in the hippocampus region while only a trend for the increase was observed in the ipsilateral hemisphere. We supposed that in the latter compartment, the effect of increasing in $CD31^+$ cells is similar to that in the contralateral hippocampus, but because of the more considerable variability of data apparently associated with the impact of ischemia, we were unable to achieve statistically significant values, contrary to the contralateral hemisphere which does not show high heterogeneity between samples. Also, the ipsilateral hemisphere contains much more nestin-positive and BrdU-positive cells. On the contrary, the contralateral hippocampus (since it was not exposed to damaging stimuli) mainly ignites neoangiogenesis caused by spidroin. These observations allow us to speculate that rS1/9 and its degradation products have not only a local, but also a systemic effect. Probably, these molecules are transported by the bloodstream to the contralateral hemisphere where they exert their influence on neurogenesis and angiogenesis. As has recently been shown, neural stem cells with their processes are directly in contact with the cells belonging to blood vessels and can capture substances from the blood (Licht et al., 2020).

We do not rule out that the injected spidroin gel could serve as a structural matrix through which progenitor cells could migrate to the area of damage. Reiner and Sapir (2018) showed that implanting a sponge coated with an adhesive factor in the injured neonatal brain supports the migration of neuroblasts and improves functional recovery. Additional analysis of markers of functional brain cells in the hippocampus by Western blotting showed that the marker of differentiated neurons βIII-tubulin remained unchanged. On the other hand, as a result of ischemic damage to the prefrontal cortex, the levels of GFAP increased, which may indicate the development of astrogliosis. Previously, remote cortical damage in the sensorimotor or prefrontal region has been shown to cause the proliferation of reactive astrocytes (Sandhir et al., 2008; Chin et al., 2013; Lee et al., 2020). Our results are also consistent with data from Gao and coauthors, who showed an increase in $GFAP^+$ cells in the granule cell layer and hilus zone (Gao et al., 2009) in a similar mouse line during TBI modeling.

An interesting finding was the effect of brain ischemia in the prefrontal cortex on the status of mitochondria in hippocampal cells, as well as the effect of hydrogel therapy with spidroin on them. As we have shown, the distant effect of ischemic damage is realized via the activation of proliferative processes in the DG of the hippocampus and possibly by reactive astrogliosis. In line with these changes, we can interpret the change in the accumulation of potential-dependent mitochondrial dye in the cells of the DG, which increases after ischemia and after spidroin. An increase in TMRE fluorescence can be considered either as an increase in the mitochondrial transmembrane potential or as an increase in the number of mitochondria themselves. A partial answer to the question of which process prevails is given by analyzing the levels of PGC1α, which is an activator of the signaling pathway leading to mitochondrial biogenesis (Scarpulla, 2011). We found that the levels of PGC1α in the hippocampus 4 days after photothrombosis were increased, which indicates the activation of mitochondrial proliferation. We can consider these changes as a compensatory increase in the number of mitochondria in response to damage of brain tissue necessary for the adequate energy supply of stem and progenitor cell proliferation and differentiation (Cheng et al., 2012; de Oliveira Bristot et al., 2019).

We conclude that the stimulation of progenitor cells by rS1/9 and its effects on the growth of primary cortical neurons, their adhesion, neurite growth, and the formation of a neuronal network make this substance an excellent material for developing therapeutic strategies aimed at enhancing brain plasticity by influencing stem cell niches. Scaffolds formed from rS1/9 can also be used in regenerative medicine to enhance primary neuroprotection, resulting in reduced cell death directly in the injury area.

DATA AVAILABILITY STATEMENT

All datasets generated for this study are included in the article/**Supplementary Material**.

ETHICS STATEMENT

The animal study was reviewed and approved by A. N. Belozersky Institute animal ethics committee (Protocol 5/18 from May 14, 2018).

AUTHOR CONTRIBUTIONS

MM, EP, DS, and DZ developed the concept, performed data analysis and manuscript writing, supervised the experiments, and analyzed the literature. DS, AM, AA, KS, VB, VD, AL, LZ, IP, and VB performed the experiments. All authors read and approved the final manuscript.

FUNDING

This reported study was funded by RFBR, project no. 17-00-00359 (including nos. 17-00-00356 and 17-00-00358) and Russian Science Foundation (19-14-00173 – model of the brain ischemia used for animals and mitochondrial study).

ACKNOWLEDGMENTS

We would like to thank Dr. Grigori Enikolopov for kindly providing the nestin-GFP mouse line. We thank Lubov Davydova for preparation of rS1/9 microparticles.

SUPPLEMENTARY MATERIAL

The Supplementary Material for this article can be found online at: https://www.frontiersin.org/articles/10.3389/fcell.2020.00823/full#supplementary-material

REFERENCES

An, B., Tang-Schomer, M., Huang, W., He, J., Jones, J., Lewis, R. V., et al. (2015). Physical and biological regulation of neuron regenerative growth and network formation on recombinant dragline silks. *Biomaterials* 48, 137–146. doi: 10.1016/j.biomaterials.2015.01.044

Arvidsson, A., Collin, T., Kirik, D., Kokaia, Z., and Lindvall, O. (2002). Neuronal replacement from endogenous precursors in the adult brain after stroke. *Nat. Med.* 8, 963–970. doi: 10.1038/nm747

Baklaushev, V. P., Bogush, V. G., Kalsin, V. A., Sovetnikov, N. N., Samoilova, E. M., Revkova, V. A., et al. (2019). Tissue engineered neural constructs composed of neural precursor cells, recombinant spidroin and PRP for neural tissue regeneration. *Sci. Rep.* 9:3161. doi: 10.1038/s41598-019-39341-9

Bang, O. Y., and Kim, E. H. (2019). Mesenchymal stem cell-derived extracellular vesicle therapy for stroke: challenges and progress. *Front. Neurol.* 10:211. doi: 10.3389/fneur.2019.00211

Bast, T., Pezze, M., and McGarrity, S. (2017). Cognitive deficits caused by prefrontal cortical and hippocampal neural disinhibition. *Br. J. Pharmacol.* 174, 3211–3225. doi: 10.1111/bph.13850

Benner, E. J., Luciano, D., Jo, R., Abdi, K., Paez-Gonzalez, P., Sheng, H., et al. (2013). Protective astrogenesis from the SVZ niche after injury is controlled by Notch modulator Thbs4. *Nature* 497, 369–373. doi: 10.1038/nature12069

Bergmann, O., Spalding, K. L., and Frisén, J. (2015). Adult neurogenesis in humans. *Cold Spring Harb. Perspect. Biol.* 7:a018994. doi: 10.1101/cshperspect.a018994

Bernal, A., and Arranz, L. (2018). Nestin-expressing progenitor cells: function, identity and therapeutic implications. *Cell. Mol. Life Sci.* 75, 2177–2195. doi: 10.1007/s00018-018-2794-z

Bogush, V. G., Sokolova, O. S., Davydova, L. I., Klinov, D. V., Sidoruk, K. V., Esipova, N. G., et al. (2009). A novel model system for design of biomaterials based on recombinant analogs of spider silk proteins. *J. Neuroimmune. Pharmacol.* 4, 17–27. doi: 10.1007/s11481-008-9129-z

Borlongan, C. V. (2019). Concise review: stem cell therapy for stroke patients: are we there yet? *Stem Cells Transl. Med.* 8, 983–988. doi: 10.1002/sctm.19-0076

Bradke, F., Fawcett, J. W., and Spira, M. E. (2012). Assembly of a new growth cone after axotomy: the precursor to axon regeneration. *Nat. Rev. Neurosci.* 13, 183–193. doi: 10.1038/nrn3176

Brewer, G. J. (1995). Serum-free B27/neurobasal medium supports differentiated growth of neurons from the striatum, substantia nigra, septum, cerebral cortex, cerebellum, and dentate gyrus. *J. Neurosci. Res.* 42, 674–683. doi: 10.1002/jnr.490420510

Burda, J. E., and Sofroniew, M. V. (2014). Reactive gliosis and the multicellular response to CNS damage and disease. *Neuron* 81, 229–248. doi: 10.1016/j.neuron.2013.12.034

Chen, H. I., Attiah, M., Baltuch, G., Smith, D. H., Hamilton, R. H., and Lucas, T. H. (2014). Harnessing plasticity for the treatment of neurosurgical disorders: an overview. *World Neurosurg.* 82, 648–659. doi: 10.1016/j.wneu.2014.02.003

Cheng, A., Wan, R., Yang, J.-L., Kamimura, N., Son, T. G., Ouyang, X., et al. (2012). Involvement of PGC-1α in the formation and maintenance of neuronal dendritic spines. *Nat. Commun.* 3:1250. doi: 10.1038/ncomms2238

Chin, Y., Kishi, M., Sekino, M., Nakajo, F., Abe, Y., Terazono, Y., et al. (2013). Involvement of glial $P2Y_1$ receptors in cognitive deficit after focal cerebral stroke in a rodent model. *J. Neuroinflammation* 10:95. doi: 10.1186/1742-2094-10-95

Churchwell, J. C., and Kesner, R. P. (2011). Hippocampal-prefrontal dynamics in spatial working memory: interactions and independent parallel processing. *Behav. Brain Res.* 225, 389–395. doi: 10.1016/j.bbr.2011.07.045

de Oliveira Bristot, V. J., de Bem Alves, A. C., Cardoso, L. R., da Luz Scheffer, D., and Aguiar, A. S. (2019). The role of PGC-1α/UCP2 signaling in the beneficial effects of physical exercise on the brain. *Front. Neurosci.* 13:292. doi: 10.3389/fnins.2019.00292

Enikolopov, G., Overstreet-Wadiche, L., and Ge, S. (2015). Viral and transgenic reporters and genetic analysis of adult neurogenesis. *Cold Spring Harb. Perspect. Biol.* 7:a018804. doi: 10.1101/cshperspect.a018804

Faiz, M., Sachewsky, N., Gascón, S., Bang, K. W. A., Morshead, C. M., and Nagy, A. (2015). Adult neural stem cells from the subventricular zone give rise to reactive astrocytes in the cortex after stroke. *Cell Stem Cell.* 17, 624–634. doi: 10.1016/j.stem.2015.08.002

Filippov, V., Kronenberg, G., Pivneva, T., Reuter, K., Steiner, B., Wang, L.-P., et al. (2003). Subpopulation of nestin-expressing progenitor cells in the adult murine hippocampus shows electrophysiological and morphological characteristics of astrocytes. *Mol. Cell. Neurosci.* 23, 373–382. doi: 10.1016/s1044-7431(03)00060-5

Gao, X., Enikolopov, G., and Chen, J. (2009). Moderate traumatic brain injury promotes proliferation of quiescent neural progenitors in the adult hippocampus. *Exp. Neurol.* 219, 516–523. doi: 10.1016/j.expneurol.2009.07.007

George, J. H., Nagel, D., Waller, S., Hill, E., Parri, H. R., Coleman, M. D., et al. (2018). A closer look at neuron interaction with track-etched microporous membranes. *Sci. Rep.* 8:15552. doi: 10.1038/s41598-018-33710-6

Gopalakrishnan, A., Shankarappa, S. A., and Rajanikant, G. K. (2019). Hydrogel scaffolds: towards restitution of ischemic stroke-injured brain. *Transl. Stroke Res.* 10, 1–18. doi: 10.1007/s12975-018-0655-6

Hagihara, H., Toyama, K., Yamasaki, N., and Miyakawa, T. (2009). Dissection of hippocampal dentate gyrus from adult mouse. *J. Vis. Exp.* 33:1543. doi: 10.3791/1543

Hoover, W. B., and Vertes, R. P. (2007). Anatomical analysis of afferent projections to the medial prefrontal cortex in the rat. *Brain Struct. Funct.* 212, 149–179. doi: 10.1007/s00429-007-0150-4

Hopkins, A. M., Laporte, L. D., Tortelli, F., Spedden, E., Staii, C., Atherton, T. J., et al. (2013). Silk hydrogels as soft substrates for neural tissue engineering. *Adv. Funct. Mater.* 23, 5140–5149. doi: 10.1002/adfm.201300435

Jin, J., and Maren, S. (2015). Prefrontal-hippocampal interactions in memory and emotion. *Front. Syst. Neurosci.* 9:170. doi: 10.3389/fnsys.2015.00170

Johari, N., Moroni, L., and Samadikuchaksaraei, A. (2020). Tuning the conformation and mechanical properties of silk fibroin hydrogels. *Eur. Polym. J.* 134:109842. doi: 10.1016/j.eurpolymj.2020.109842

Kempermann, G., Kuhn, H. G., and Gage, F. H. (1997). More hippocampal neurons in adult mice living in an enriched environment. *Nature* 386, 493–495. doi: 10.1038/386493a0

Kiryushko, D., Berezin, V., and Bock, E. (2004). Regulators of neurite outgrowth: role of cell adhesion molecules. *Ann. N.Y. Acad. Sci.* 1014, 140–154. doi: 10.1196/annals.1294.015

Knoth, R., Singec, I., Ditter, M., Pantazis, G., Capetian, P., Meyer, R. P., et al. (2010). Murine features of neurogenesis in the human hippocampus across the lifespan from 0 to 100 years. *PLoS One* 5:e8809. doi: 10.1371/journal.pone.0008809

Krishnaji, S. T., Bratzel, G., Kinahan, M. E., Kluge, J. A., Staii, C., Wong, J. Y., et al. (2013). Sequence–Structure–Property relationships of recombinant spider silk proteins: integration of biopolymer design, processing, and modeling. *Adv. Funct. Mater.* 23, 241–253. doi: 10.1002/adfm.201200510

Lazutkin, A., Podgorny, O., and Enikolopov, G. (2019). Modes of division and differentiation of neural stem cells. *Behav. Brain Res.* 374:112118. doi: 10.1016/j.bbr.2019.112118

Lee, T.-K., Ahn, J. H., Park, C. W., Kim, B., Park, Y. E., Lee, J.-C., et al. (2020). Pre-treatment with laminarin protects hippocampal ca1 pyramidal neurons and attenuates reactive gliosis following transient forebrain ischemia in Gerbils. *Mar. Drugs* 18:52. doi: 10.3390/md18010052

Lewicka, M., Hermanson, O., and Rising, A. U. (2012). Recombinant spider silk matrices for neural stem cell cultures. *Biomaterials* 33, 7712–7717. doi: 10.1016/j.biomaterials.2012.07.021

Licht, T., Sasson, E., Bell, B., Grunewald, M., Kumar, S., Kreisel, T., et al. (2020). Hippocampal neural stem cells facilitate access from circulation via apical cytoplasmic processes. *eLife* 9:e5213. doi: 10.7554/eLife.52134

Magaz, A., Faroni, A., Gough, J. E., Reid, A. J., Li, X., and Blaker, J. J. (2018). Bioactive silk-based nerve guidance conduits for augmenting peripheral nerve repair. *Adv. Healthc. Mater.* 7:e1800308. doi: 10.1002/adhm.201800308

Maness, P. F., and Schachner, M. (2007). Neural recognition molecules of the immunoglobulin superfamily: signaling transducers of axon guidance and neuronal migration. *Nat. Neurosci.* 10, 19–26. doi: 10.1038/nn1827

Mignone, J., Peunova, N., and Enikolopov, G. (2016). Nestin-based reporter transgenic mouse lines. *Methods Mol. Biol.* 1453, 7–14. doi: 10.1007/978-1-4939-3786-8_2

Moisenovich, M. M., Plotnikov, E. Y., Moysenovich, A. M., Silachev, D. N., Danilina, T. I., Savchenko, E. S., et al. (2019). Effect of silk fibroin on neuroregeneration after traumatic brain injury. *Neurochem. Res.* 44, 2261–2272. doi: 10.1007/s11064-018-2691-8

Moisenovich, M. M., Pustovalova, O., Shackelford, J., Vasiljeva, T. V., Druzhinina, T. V., Kamenchuk, Y. A., et al. (2012). Tissue regeneration in vivo within recombinant spidroin 1 scaffolds. *Biomaterials* 33, 3887–3898. doi: 10.1016/j.biomaterials.2012.02.013

Moisenovich, M. M., Pustovalova, O. L., Arhipova, A. Y., Vasiljeva, T. V., Sokolova, O. S., Bogush, V. G., et al. (2011). *In vitro* and *in vivo* biocompatibility studies of a recombinant analogue of spidroin 1 scaffolds. *J. Biomed. Mater. Res. A* 96, 125–131. doi: 10.1002/jbm.a.32968

Moreau, F., Patel, S., Lauzon, M. L., McCreary, C. R., Goyal, M., Frayne, R., et al. (2012). Cavitation after acute symptomatic lacunar stroke depends on time, location, and MRI sequence. *Stroke* 43, 1837–1842. doi: 10.1161/STROKEAHA.111.647859

Moretti, A., Ferrari, F., and Villa, R. F. (2015). Neuroprotection for ischaemic stroke: current status and challenges. *Pharmacol. Ther.* 146, 23–34. doi: 10.1016/j.pharmthera.2014.09.003

Nakagomi, T., Molnár, Z., Nakano-Doi, A., Taguchi, A., Saino, O., Kubo, S., et al. (2011). Ischemia-induced neural stem/progenitor cells in the pia mater following cortical infarction. *Stem Cells Dev.* 20, 2037–2051. doi: 10.1089/scd.2011.0279

Nakata, M., Nakagomi, T., Maeda, M., Nakano-Doi, A., Momota, Y., and Matsuyama, T. (2017). Induction of perivascular neural stem cells and possible contribution to neurogenesis following transient brain ischemia/reperfusion injury. *Transl. Stroke Res.* 8, 131–143. doi: 10.1007/s12975-016-0479-1

Nih, L. R., Gojgini, S., Carmichael, S. T., and Segura, T. (2018). Dual-function injectable angiogenic biomaterial for the repair of brain tissue following stroke. *Nat. Mater.* 17, 642–651. doi: 10.1038/s41563-018-0083-8

Nilssen, E. S., Doan, T. P., Nigro, M. J., Ohara, S., and Witter, M. P. (2019). Neurons and networks in the entorhinal cortex: a reappraisal of the lateral and medial entorhinal subdivisions mediating parallel cortical pathways. *Hippocampus* 29, 1238–1254. doi: 10.1002/hipo.23145

Nosenko, M. A., Moysenovich, A. M., Zvartsev, R. V., Arkhipova, A. Y., Zhdanova, A. S., Agapov, I. I., et al. (2018). Novel biodegradable polymeric microparticles facilitate scarless wound healing by promoting re-epithelialization and inhibiting fibrosis. *Front. Immunol.* 9:2851. doi: 10.3389/fimmu.2018.02851

Obernier, K., and Alvarez-Buylla, A. (2019). Neural stem cells: origin, heterogeneity and regulation in the adult mammalian brain. *Development* 146:dev156059. doi: 10.1242/dev.156059

Park, K., and Biederer, T. (2013). Neuronal adhesion and synapse organization in recovery after brain injury. *Future Neurol.* 8, 555–567. doi: 10.2217/fnl.13.35

Park, Y. R., Sultan, M. T., Park, H. J., Lee, J. M., Ju, H. W., Lee, O. J., et al. (2018). NF-κB signaling is key in the wound healing processes of silk fibroin. *Acta Biomater.* 67, 183–195. doi: 10.1016/j.actbio.2017.12.006

Pous, L., Deshpande, S. S., Nath, S., Mezey, S., Malik, S. C., Schildge, S., et al. (2020). Fibrinogen induces neural stem cell differentiation into astrocytes in the subventricular zone via BMP signaling. *Nat Commun* 11:630. doi: 10.1038/s41467-020-14466-y

Qu, J., Xin, L., Xu, X., Zhang, F., Zuo, B., and Zhang, H. (2010). "Tussah silk fibroin excels silk fibroin from the domesticated silkworm in supporting the development of neurons," in *6th World Congress of Biomechanics (WCB 2010). August 1-6, 2010 Singapore* IFMBE Proceedings, eds C. T. Lim and J. C. H. Goh (Heidelberg: Springer), 1574–1577. doi: 10.1007/978-3-642-14515-5_401

Reiner, O., and Sapir, T. (2018). A coated sponge: toward neonatal brain repair. *Cell Stem Cell* 22, 3–4. doi: 10.1016/j.stem.2017.12.007

Salehi, S., Koeck, K., and Scheibel, T. (2020). Spider silk for tissue engineering applications. *Molecules* 25:737. doi: 10.3390/molecules25030737

Sandhir, R., Onyszchuk, G., and Berman, N. E. J. (2008). Exacerbated glial response in the aged mouse hippocampus following controlled cortical impact injury. *Exp. Neurol.* 213, 372–380. doi: 10.1016/j.expneurol.2008.06.013

Scarpulla, R. C. (2011). Metabolic control of mitochondrial biogenesis through the PGC-1 family regulatory network. *Biochim. Biophys. Acta* 1813, 1269–1278. doi: 10.1016/j.bbamcr.2010.09.019

Seki, T., and Arai, Y. (1999). Temporal and spacial relationships between PSA-NCAM-expressing, newly generated granule cells, and radial glia-like cells in the adult dentate gyrus. *J. Comp. Neurol.* 410, 503–513. doi: 10.1002/(sici)1096-9861(19990802)410:3<503::aid-cne11>3.0.co;2-h

Shimada, I. S., LeComte, M. D., Granger, J. C., Quinlan, N. J., and Spees, J. L. (2012). Self-renewal and differentiation of reactive astrocyte-derived neural stem/progenitor cells isolated from the cortical peri-infarct area after stroke. *J. Neurosci.* 32, 7926–7940. doi: 10.1523/JNEUROSCI.4303-11.2012

Shimada, I. S., Peterson, B. M., and Spees, J. L. (2010). Isolation of locally derived stem/progenitor cells from the peri-infarct area that do not migrate from the lateral ventricle after cortical stroke. *Stroke* 41, e552–e560. doi: 10.1161/STROKEAHA.110.589010

Sigurdsson, T., and Duvarci, S. (2015). Hippocampal-prefrontal interactions in cognition, behavior and psychiatric disease. *Front. Syst. Neurosci.* 9:190. doi: 10.3389/fnsys.2015.00190

Silachev, D. N., Shram, S. I., Shakova, F. M., Romanova, G. A., and Myasoedov, N. F. (2009). Formation of spatial memory in rats with ischemic lesions to the prefrontal cortex; effects of a synthetic analog of ACTH(4-7). *Neurosci. Behav. Physiol.* 39, 749–756. doi: 10.1007/s11055-009-9197-4

Volkov, A. V., Muraev, A. A., Zharkova, I. I., Voinova, V. V., Akoulina, E. A., Zhuikov, V. A., et al. (2020). Poly(3-hydroxybutyrate)/hydroxyapatite/alginate scaffolds seeded with mesenchymal stem cells enhance the regeneration of critical-sized bone defect. *Mater. Sci. Eng.C* 114:110991. doi: 10.1016/j.msec.2020.110991

Wang, Y., Luo, W., and Reiser, G. (2008). Trypsin and trypsin-like proteases in the brain: proteolysis and cellular functions. *Cell. Mol. Life Sci.* 65, 237–252. doi: 10.1007/s00018-007-7288-3

Wang, Y., Tan, H., and Hui, X. (2018). Biomaterial scaffolds in regenerative therapy of the central nervous system. *Biomed. Res. Int.* 2018:7848901. doi: 10.1155/2018/7848901

Watson, B. D., Dietrich, W. D., Busto, R., Wachtel, M. S., and Ginsberg, M. D. (1985). Induction of reproducible brain infarction by photochemically initiated thrombosis. *Ann. Neurol.* 17, 497–504. doi: 10.1002/ana.410170513

Wei, G.-J., Yao, M., Wang, Y.-S., Zhou, C.-W., Wan, D.-Y., Lei, P.-Z., et al. (2013). Promotion of peripheral nerve regeneration of a peptide compound hydrogel scaffold. *Int. J. Nanomed.* 8, 3217–3225. doi: 10.2147/IJN.S43681

Wobst, H., Schmitz, B., Schachner, M., Diestel, S., Leshchyns'ka, I., and Sytnyk, V. (2015). Kinesin-1 promotes post-golgi trafficking of NCAM140 and NCAM180 to the cell surface. *J. Cell. Sci.* 128, 2816–2829. doi: 10.1242/jcs.169391

Conflict of Interest: The authors declare that the research was conducted in the absence of any commercial or financial relationships that could be construed as a potential conflict of interest.

Copyright © 2020 Moisenovich, Silachev, Moysenovich, Arkhipova, Shaitan, Bogush, Debabov, Latanov, Pevzner, Zorova, Babenko, Plotnikov and Zorov. This is an open-access article distributed under the terms of the Creative Commons Attribution License (CC BY). The use, distribution or reproduction in other forums is permitted, provided the original author(s) and the copyright owner(s) are credited and that the original publication in this journal is cited, in accordance with accepted academic practice. No use, distribution or reproduction is permitted which does not comply with these terms.

frontiers in Cell and Developmental Biology

ORIGINAL RESEARCH
published: 09 September 2020
doi: 10.3389/fcell.2020.00698

Extracellular Vesicles Released by Tumor Endothelial Cells Spread Immunosuppressive and Transforming Signals Through Various Recipient Cells

Tatiana Lopatina[1], Enrica Favaro[1], Ludmila Danilova[2,3], Elana J. Fertig[2], Alexander V. Favorov[2,3], Luciane T. Kagohara[2], Tiziana Martone[4], Benedetta Bussolati[5], Renato Romagnoli[6], Roberto Albera[7], Giancarlo Pecorari[7], Maria Felice Brizzi[1], Giovanni Camussi[1] and Daria A. Gaykalova[2,8]*

[1] Department of Medical Sciences, University of Turin, Turin, Italy, [2] Department of Oncology, The Sidney Kimmel Comprehensive Cancer Center, Johns Hopkins University School of Medicine, Baltimore, MD, United States, [3] Laboratory of System Biology and Computational Genetics, Vavilov Institute of General Genetics, Moscow, Russia, [4] Department of Neuroscience "Rita Levi Montalcini", University of Turin, Turin, Italy, [5] Department of Molecular Biotechnology and Health Sciences, University of Turin, Turin, Italy, [6] General Surgery 2U, Liver Transplantation Center, AOU Città della Salute e della Scienza di Torino, University of Turin, Turin, Italy, [7] Division of Otorhinolaryngology, Department of Surgical Sciences, University of Turin School of Medicine, Turin, Italy, [8] Department of Otolaryngology – Head and Neck Surgery, Johns Hopkins University School of Medicine, Baltimore, MD, United States

OPEN ACCESS

Edited by:
Pavel Makarevich, Lomonosov Moscow State University, Russia

Reviewed by:
Ciro Tetta, Unicyte AG, Switzerland
Tatiana Shtam, Petersburg Nuclear Physics Institute (RAS), Russia
Olga Evgenievna Bryzgunova, Institute of Chemical Biology and Fundamental Medicine (RAS), Russia

***Correspondence:**
Tatiana Lopatina
tatiana.lopatina@unito.it

Specialty section:
This article was submitted to Stem Cell Research, a section of the journal Frontiers in Cell and Developmental Biology

Received: *18 May 2020*
Accepted: *09 July 2020*
Published: *09 September 2020*

Citation:
Lopatina T, Favaro E, Danilova L, Fertig EJ, Favorov AV, Kagohara LT, Martone T, Bussolati B, Romagnoli R, Albera R, Pecorari G, Brizzi MF, Camussi G and Gaykalova DA (2020) Extracellular Vesicles Released by Tumor Endothelial Cells Spread Immunosuppressive and Transforming Signals Through Various Recipient Cells. Front. Cell Dev. Biol. 8:698. doi: 10.3389/fcell.2020.00698

Head and neck squamous cell carcinoma (HNSCC) has a high recurrence and metastatic rate with an unknown mechanism of cancer spread. Tumor inflammation is the most critical processes of cancer onset, growth, and metastasis. We hypothesize that the release of extracellular vesicles (EVs) by tumor endothelial cells (TECs) induce reprogramming of immune cells as well as stromal cells to create an immunosuppressive microenvironment that favor tumor spread. We call this mechanism as non-metastatic contagious carcinogenesis. Extracellular vesicles were collected from primary HNSCC-derived endothelial cells (TEC-EV) and were used for stimulation of peripheral blood mononuclear cells (PBMCs) and primary adipose mesenchymal stem cells (ASCs). Regulation of ASC gene expression was investigated by RNA sequencing and protein array. PBMC, stimulated with TEC-EV, were analyzed by enzyme-linked immunosorbent assay and fluorescence-activated cell sorting. We validated *in vitro* the effects of TEC-EV on ASCs or PBMC by measuring invasion, adhesion, and proliferation. We found and confirmed that TEC-EV were able to change ASC inflammatory gene expression signature within 24–48 h. TEC-EV were also able to enhance the secretion of TGF-β1 and IL-10 by PBMC and to increase T regulatory cell (Treg) expansion. TEC-EV carry specific proteins and RNAs that are responsible for Treg differentiation and immune suppression. ASCs and PBMC, treated with TEC-EV, enhanced proliferation, adhesion of tumor cells, and their invasion. These data indicate that TEC-EV exhibit a mechanism of non-metastatic contagious carcinogenesis that regulates tumor microenvironment and reprograms immune cells to sustain tumor growth and progression.

Keywords: extracellular vesicles, tumor endothelial cells, tumor immune editing, T regulatory (T reg) cells, head and neck cancer

INTRODUCTION

Tumor angiogenesis, the formation of new blood vessels within a tumor, is one of the crucial steps of tumor growth and progression (Folkman, 1985). TECs are the cells lining the tumor-associated blood vessels (Dudley, 2012). Recent data suggest that TEC play a critical role in tumor growth and metastasis (Osawa et al., 2013; Yadav et al., 2015), and show characteristics of cancer stem cells (Dudley et al., 2008). TEC could regulate tumor microenvironment since they have direct contact with blood cells and vessel stromal cells. This regulation is mediated via production of increased levels of growth factors and cytokines, as well as via release of EV. EV are membrane vesicles containing a specific set of proteins, lipids, and nucleic acids, which could incorporate into recipient cells via cell surface receptors and regulate their gene expression (Quesenberry et al., 2015).

Extracellular vesicles are essential regulators of inflammation and angiogenesis (Baruah and Wary, 2019). Cancer requirement of inflammation is now widely described for almost all types of cancer since immune cells infiltrate tumor stroma and contribute to cancer development. EV secreted by tumor cells were shown to play an essential role in tumor niche establishment, metastasis (Hoshino et al., 2015), and regulation of immune reaction and inflammation (Ye et al., 2014; Grange et al., 2015). EV could activate immune cells by binding their surface receptors, such as MHC class I and II, CD47, TLR4, and others (Robbins et al., 2016).

Extracellular vesicles stimulate immune cells to express cytokines and growth factors critical for angiogenesis, TGF-β1, TNF-α, IL-6, and others (Roma-Rodrigues et al., 2014). Therefore, inflammation and angiogenesis are interdependent; moreover, those processes share participating immune cells and signaling pathways (Mamlouk and Wielockx, 2013; Szade et al., 2015).

Head and neck squamous cell carcinoma is the fifth most common cancer worldwide and has a high recurrence and metastasis rate (Argiris et al., 2008). It was shown that EV from HNSCC cells could inhibit T-cell proliferation and differentiation of pro-inflammatory cells Th1 and Th17 (Ye et al., 2014). HNSCC-derived EV are enriched in tumor antigens and potentially promote tumor progression (Principe et al., 2013). At present, limited information is available on the cellular and molecular functions of TEC from HNSCC and EV released by those cells (Rodriguez Zorrilla et al., 2019; Xie et al., 2019). Studying the TEC-EV molecular composition and specific functions in tumor development can define novel mechanisms of cancer immune editing, help developing novel therapeutic targets, and determine diagnostic signatures to be used for non-invasive liquid biopsies.

Here we investigated the role of EV released by TEC from HNSCC in the reprogramming of non-tumor cells, such as PBMCs or mesenchymal stem cells from adipose tissue (ASCs). Those cells underwent induction and contributed to tumor development by the secretion of growth factors and cytokines. This study characterized the regulation of the immune response by TEC-EV and showed the pro-tumorigenic functions of non-tumor cells after induction with TEC-EV.

Abbreviations: ACTB, actin beta 1; ASCs, adipose stem cells; CD14, cluster of differentiation 14; CD31, cluster of differentiation 31; CD47, cluster of differentiation 47; CD73, cluster of differentiation 73; CD90, cluster of differentiation 90; CD105, cluster of differentiation 105; CD163, cluster of differentiation 163; CD206, cluster of differentiation 206; CM, conditioned medium; Ctr, control; DMEM, Dulbecco's modified Eagle medium; DMSO, dimethyl sulfoxide; ELISA, enzyme-linked immunosorbent assay; EVs, extracellular vesicles; FACS, fluorescence-activated cell sorting; FBS, fetal bovine serum; HLA, human leukocyte antigen; HMEC, human dermal microvascular endothelium; HNSCC, head and neck squamous cell carcinoma; IFN-γ, interferon gamma; IL-6, interleukin 6; IL-10, interleukin 10; lncRNA, long non-coding RNA; MALAT1, metastasis associated lung adenocarcinoma transcript 1; MHC, major histocompatibility complex; PBMC, peripheral blood mononuclear cell; PBS, phosphate-buffered saline; RNA, ribonucleic acid; RT-PCR, reverse transcription polymerase chain reaction; TECs, tumor endothelial cells; TGF-β1, transforming growth factor beta-1; Th1, T helper type 1; Th17, T helper type 17; TLR4, toll-like receptor 4; TNF-α, tumor necrosis factor alpha; Treg, T regulatory cells; Trtm, treatment; VEGF, vascular endothelial growth factor.

MATERIALS AND METHODS

Ethics Approval and Consent to Participate

Overall, we received the ethics approval for the isolation of human cells, such as TEC and tumor cells from HNSCC patients, as well as ASC from non-neoplastic patients. HNSCC tissues were isolated under approved protocol from the Ethics Committee of A.O.U. Città della Salute e della Scienza di Torino, Turin, Italy (CS2/1255 – Protocol number 0050416, May 16, 2019). ASC isolation was approved by the Ethics Committee of A.O.U. Città della Salute e della Scienza di Torino, Turin, Italy (CS/100 – Protocol number 12175, February 4, 2014). Adipose tissue was obtained from patients of non-neoplastic elective abdominal surgery. Informed consent was obtained from all patients according to the Helsinki Declaration. Laboratory researchers had no direct contact with the participants in the present study (patients' anonymity was guaranteed).

TEC Isolation

TEC were isolated from tumor tissue samples of HNSCC patients (stage IV). Specimens were finely minced and digested by incubation in DMEM medium with 220 U/mL collagenase I (Sigma) for 1 h at 37°C. After washings the cells in DMEM with 10% FBS (Lonza), endothelial cells were isolated from this filtered cells suspension using magnetic beads conjugated with anti-CD105 Ab (**Supplementary Table S1**) from magnetic cell-sorting MACS system (Miltenyi Biotech). TECs were grown in the complete EndoGro medium (Millipore) supplemented with 2% FBS, as previously described (Grange et al., 2006). Expression of CD31 by the isolated cells was confirmed by FACS analysis on the passages #1 and #4. TEC were used at 8–18 passages. TEC were functionally evaluated to form vessel-like structures at 4, 8, and 18 passages (see below).

Tumor cells were isolated from the specimens of four HNSCC male patients (mean age 62 ± 5) without sorting and cultured in MSCBM complete medium (Lonza). Tumor cells do not form vessel-like structures on Matrigel and have fibroblast-like morphology. The cells were allowed to undergo 8–18 passages before being used in the experiments.

ASC Isolation

Adipose mesenchymal stem cells exhibit diverse inflammatory and secretory features depending on patient' age, health, metabolism, and body size (Efimenko et al., 2014; Louwen et al., 2018). We used ASCs isolated from subcutaneous abdominal tissue of non-obese five male patients, submitted to non-neoplastic elective abdominal surgery (mean age 60 ± 8). Those adipose tissues were washed in sterile PBS and were minced into pieces of 2 mm in diameter. ASCs were isolated by enzyme digestion with 220 U/mL collagenase I type (Worthington Biochemical), and 40 U/mL dispase (Invitrogen Corporation) in DMEM, FBS deprived, and containing 100 units/ml penicillin, 0.1 mg/ml streptomycin, and 0.25 μg/ml amphotericin B (antibiotic/antimycotic solution, Sigma). The tissue was digested at 37°C for 30 min with constant mixing. Enzyme activity was neutralized with an equal volume of DMEM, containing 10% FBS. The digested suspension was centrifuged at 900 *g* for 10 min to obtain a high-density stromal vascular fraction pellet. The cell pellet was resuspended in MSCBM complete medium (Lonza) and cultured at 37°C in 5% CO_2 incubator. After 2 days, the medium with detached cells was changed, and the adherent cells were cultivated until 100% confluence. ASC characterization was performed by FACS analysis for the positive expression of mesenchymal markers (CD105, CD73, CD90), and negative expression of hematopoietic markers (CD31) and by differentiation into adipogenic, osteogenic, and chondrogenic phenotypes as previously described (Kalinina et al., 2015). For our experiments, we used cells after 2–8 passages.

PBMC Isolation

The fresh PBMC was isolated from 15 healthy donors. Their heparinized blood samples were used for the density gradient centrifugation. PBMC were seeded in 6 well plates at a density of 10×10^6 cells per well in 2 ml of serum-free AIM V medium.

TEC-EV Isolation

To isolate EV from TEC, TEC were washed with FBS-deprived DMEM and cultured in this medium for 18 h. The obtained conditioned medium was centrifuged for 30 min at 3000 *g* to remove cell debris and then filtered using 0.22 μm filters (MillexGP). The supernatants were then ultracentrifuged for 3 h at 100,000 *g* and 4°C using the Beckman Coulter Optima L-100K Ultracentrifuge with the rotor type 45 Ti 45000RPM. Minimum of 67 ml of conditioned medium was used for ultracentrifugation (maximum volume for the tubes). From this volume we extracted $0.5–2 \times 10^{11}$ EV. The EV pellet was resuspended in DMEM supplemented with 1% of dimethyl sulfoxide (DMSO) then stored at −80°C until further use.

ASC Stimulation With TEC-EV

To stimulate ASC with TEC-EV, we changed the complete growth medium of ASC culture to FBS-deprived DMEM. We added TEC-EV to the ASC culture to obtain the final concentration 10×10^3 EV/cell. ASC were incubated with TEC-EV for 24 or 48 h to obtain ASCind. As a control, ASC were incubated with the equal volume of DMEM with 1% DMSO for 0, 24, or 48 h. After incubation, the cells were harvested, lysed by QIAzol Lysis Reagent and used for RNA isolation by RNAeasy kit (Qiagen), following manufacturer's instructions.

EV Isolation From Stimulated and Non-stimulated ASC

ASCind (stimulated for 24 h with TEC-EV) were used for isolation of their EV (ASCind-EV). Non-stimulated ASC were used for control EV isolation (ASC-EV). After 24 h-incubation with or without TEC-V, the growth medium of ASC was changed to FBS-deprived DMEM for the additional 24 h. We isolated EV from ASC conditioned medium as described for TEC-EV. From one ultracentrifuge tube (67 ml of conditioned medium) we extracted $1–5 \times 10^{10}$ EV.

PBMC Stimulation With EV

To stimulate PBMC with different EV (TEC-EV, ASC-EV, and ASCind-EV), we added EV to PBMC in the concentration of 1×10^3 EV/cell for 48 h. After 48 h of incubation, the cultured PBMC and conditioned media were harvested for FACS, RT-PCR, and ELISA. For the T regulatory cell (Tregs) detection, PBMC were analyzed 5 days after incubation with EV.

PBMC Consumption of EV

To demonstrate the intake of TEC-EV by PBMC, TEC-EV were labeled with PKH26GL green fluorescent cell linker (Sigma) dye for 30 min at 37°C and then washed and ultracentrifuged at 100,000 *g* for 1 h at 4°C. These labeled EV were added to PBMCs (1×10^3 EV/cell) for different times (10, 30 min, 1, 3, or 24 h). The consumption of EV by PBMCs was evaluated by FACS (CytoFlex, Beckman Coulter).

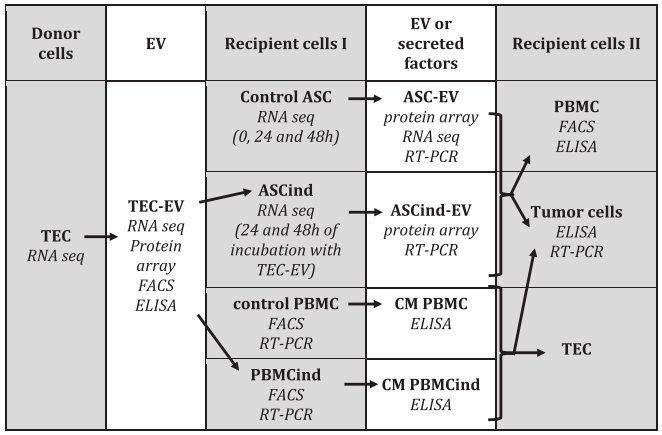
Vessel-Like Formation Assay

To verify the endothelial origin of TEC (donor cells, **Table 1**), or measure the angiogenesis (recipient cells II, **Table 1**), we have completed the vessel-like formation assay. For that, we seeded the cells onto Matrigel-coated wells in a 24-well plate (25×10^3 cells per well), and cultured TEC in DMEM medium without FBS. In case of recipient cells II, 50% of the medium was replaced by the conditioned medium (CM) from the control PBMC or PBMCind. After incubation for 6 h, phase-contrast images (magnification, × 100) were recorded, and the total length of the network structures was measured using LAS software (Leica). In the case of recipient cells II, the total length per field was calculated in five random fields and expressed relative to CM PBMC control. Data were expressed as mean ± SEM.

Adhesion Assay

In this experiment, we measured PBMC or tumor cells adhesion on the endothelium. As a source of endothelial cells, we used HMEC (ATCC, PCS-110-010) cultured in EBM complete medium (Lonza). During the adhesion assay, all cell types (PBMC, endothelial cells, and tumor cells) were stimulated by the same EV to imitate the physiological conditions of EV circulation in the tumor blood vessels. HMEC seeded in 24-well plate were allowed to grow until 100% confluence. Those

TABLE 1 | Scheme of the study.



In gray columns – cells used for the study, in white – EV (or conditioned media from PBMC). In bold – samples' abbreviation used in text, in italic – methods for molecular composition analysis used for the sample.

100% confluent HMECs were stimulated with control ASC-EV or ASCind-EV in concentration 10×10^3 EV/cell overnight. At the same time, PBMC or tumor cells were stimulated with the same EV (in the concentration 10×10^3 EV/cell or 1×10^3 EV/cell for tumor cells or PBMC respectively). Next day, tumor cells and PBMC were labeled with PKH26GL red fluorescent cell linker (Sigma) according the manufacturer's instructions. Labeled PBMC (2×10^5 cells) or tumor cells (1×10^3) resuspended in 0.5 ml of EBM complete medium were added to each well of confluent and stimulated HMEC for 1 h incubation at 37°C. The non-adherent cells were removed by supernatant aspiration and two additional washing steps with PBS. Adherent cells were counted by digital analysis (Leica application suite V4.9). Four independent experiments were performed in duplicates; the results are expressed as mean of cells counted in 10 fields. The non-stimulated cells (HMEC, PBMC, or tumor cells) were used as negative controls.

Tumor Cell Proliferation

The proliferation of tumor cells was measured by BrdU incorporation using Cell Proliferation ELISA BrdU (colorimetric) kit (Roche, #11647229001) according to the manufacturer's instructions. Tumor cells were cultured in DMEM deprived FBS and were stimulated by 50% diluted conditioned medium from control PBMC or PBMCind. Tumor cells were stimulated with such medium for 72 h.

Tumor Cell Invasion

The effect of ASC-EV on tumor cell invasion was detected by the Transwell assay (COSTAR transwell, Corning Incorporated). Tumor cells were resuspended in DMEM (serum-free) and seeded into the upper compartment of an invasion chamber (50×10^3 cells per well) containing a polycarbonate membrane with an 8 μm pore size, which was coated with a layer Matrigel (MatrigelTM, Becton Dickinson). ASC-EV or ASCind-EV were added to the cells into the concentration 5×10^8 EV/well. DMEM with 10% of FBS was used as the attractant and added to the bottom well. After 24 h of incubation, the invasive cells migrated through the Matrigel to the bottom side of the membrane. The migrated cells were stained with Mayer dye and counted. Every experiment was repeated six times.

RNA Sequencing and Analysis of TEC-EV

Four TEC-EV samples were collected from the same TEC culture on different cell passages and were used for RNA sequencing using Lexogen[1] service (Vienna, Austria). From 1×10^{11} of EV was extracted around 30 μg of RNA. The service included the comparison of RNA carried by TEC-EV with RNA carried by ASC-EV by DeSeq2. The top 1000 up-regulated genes in TEC-EV relative to ASC-EV ($p_{adj} < 0.1$) were used in the Panther classification system[2] for functional clustering.

RNA Sequencing of ASC Stimulated With TEC-EV

RNA from treated and non-treated cells was extracted using the mirVana miRNA Isolation Kit (Ambion, Forster City, CA, United States). RNA sequencing was performed, as previously described (Guo et al., 2017). Briefly, samples were required to achieve an RNA Integrity Number (RIN) of at least 7.0. A stranded RNA library was prepared using the Illumina TruSeq stranded total RNA seq poly A + Gold kit (San Diego, CA, United States), and then ribosomal RNA reduction was performed from 400 ng of total RNA and purified with AMPure XP magnetic beads.

Sequencing was performed using the HiSeq 2500 platform sequencer (Illumina) and the TruSeq Cluster Kit, resulting in approximately 80 million paired reads per sample. Next, the RNA sequencing data were normalized based on the version 2 protocols developed by TCGA (Cancer Genome Atlas Network, 2015). The alignment was performed using MapSplice2 version 2.0.1.9 (Wang et al., 2010) to the GRCh37/hg19 genome assembly. Gene expression values were quantified from RNA sequencing data using RSEM version 1.2.9 (Li and Dewey, 2011) and upper quantile normalized. We found patterns on this data by performing CoGAPS analysis on log transformed, upper quantile normalized data (Fertig et al., 2010). This analysis identified five patterns in the dataset, which were associated with biological pathways by applying the CoGAPS gene set statistic to Hallmark pathways (Liberzon et al., 2015) in MSigDB version 5.2. CoGAPS patterns are visualized by creating a heatmap of the gene expression values for patternMarker genes that are uniquely associated with each process (Stein-O'Brien et al., 2018).

Protein Array of EV

Protein composition of EV was identified by AAH-BGL-100004 Human L1000, Glass Slide array (RayBiotech). To extract protein peptides, EV were lysed by 2x Cell Lysis Buffer (RayBiotech, Inc.) and ultrasonicated 30 s at 4°C (Microson Ultrasonic cell disruptor; 47 kHz frequency and 185 Watt peak power). The protein concentration was measured by BCA Protein Assay Kit (Thermo Fisher). One μg of total protein was used for the

[1]www.lexogen.com

[2]http://www.pantherdb.org

protein array according to manufacturer instructions. This array provides detection of 1000 secreted proteins. For each set of EV, we performed two technical repeats. Only proteins, consistently detected in both replicates were used for functional clustering by Panther classification system[2].

Real-Time PCR Analysis

Total RNA from stimulated and non-stimulated PBMC, and from EV released by ASC controls and ASCind, was extracted using RNAeasy kit (Qiagen). Approximately 200 ng of RNA was reverse transcribed into complementary DNA (cDNA) using miScript II RT Kit (Qiagen) according to manufacturer's protocol.

The analysis of the TGF-β1 and MALAT1 RNA expression, as well as the expression of endogenous controls, ACTB and 18S RNA, was performed using miScript SYBR Green PCR kit (Qiagen). Specific primers for RT-PCR (TGF-β1 forward CTAATGGTGGAAACCCACAACG, reverse TATCGCCAGGAATTGTTGCTG; MALAT1 forw ard CCCCTGGGCTTCTCTTAACA, reverse GCTAGATCAAA AGGCACGGG; ACTB forward CATGTACGTTGCTATCCA GGC, reverse CTCCTTAATGTCACGCACGAT, 18S RNA forward AGAAACGGCTACCACATCCA, reverse CCC TCCAATGGATCCTCGTT) were obtained from primer bank[3]. Used real-time cycler conditions were following: PCR initial activation step 15 min 95°C; 40 steps of Denaturation (94°C, 15 s), Annealing (60°C, 15 s), Extension (72°C, 15 s); fluorescence data collection after Extention of every cycle; melting curve data between 60 and 95°C. The RT-PCR was performed on the QuantStudio 12K Flex real-time PCR instrument (Applied Biosystems). The differential expression analysis was performed using Expression Suite Software (Thermo Fisher), using endogenous controls.

Fluorescence-Activated Cell Sorting

Fluorescence-activated cell sorting was used to define surface protein markers on cells and EV. A pool of approximately 5×10^{10} cells or EV dissolved in 100 μl was incubated with the particular antibody (**Supplementary Table S1**) for 30 min at room temperature. Then the final volume was increased until 300 μl and FACS analysis was performed using CytoFlex from Beckman Coulter. To detect EV we used Violet Side Scatter (VSSC) that permit to detect even smaller vesicles, as the refraction index of EVs is inversely proportional to the size of the vesicle. We were able to select the population of EV using CD63, CD81, and Annexin V as positive controls. The median fluorescence intensity (MFI) was corrected for background and gated based on their respective fluorescence intensity as per manufacturer's instructions. The FITC, PerCP, or PE non-immune isotypic IgG were used as a negative control.

ELISA Assay

ELISA assay was performed using DuoSet® ELISA Development Systems (R&D Systems) according to manufacturer instructions. Briefly, the suspension of EV or cells was mixed with RIPA buffer and ultrasonicated. Then, 30 μg of total protein was used for ELISA. TEC-EV were analyzed using kits specific to IGF1, IL-1β, TGF-β1, and VEGF. PBMC or tumor cells were analyzed using kits specific to IFN-γ, IL-6, IL-10, TGF-β1, TNF-α, and VEGF.

Statistical Analysis

All reported p-values were calculated using pair-wise Student's t-test, comparing a condition of interest with its corresponding control. p-Value < 0.05 was considered as significant.

RESULTS

The Study Flow

We performed two rounds of EV collection and used them for stimulation of the recipient cells, as described in **Table 1**. The study was started from the isolation of the TEC (donor cells) and TEC-EV collection and characterization. TEC-EV were analyzed by RNA sequencing, protein array, FACS, and ELISA and were used for stimulation of two types of recipient cells I (ASCs and PBMC). ASCs induced with TEC-EV (ASCind) were analyzed by RNA sequencing at 24 and 48 h after the stimulation. Non-stimulated control ASCs and TEC were also analyzed by RNA sequencing for comparative analysis. PBMC stimulated with TEC-EV (PBMCind) were analyzed by ELISA and FACS to demonstrate activation and differentiation. At the second round, control ASCs or ASCind were used for EV collection (ASC-EV or ASCind-EV), which were used for stimulation of the recipient cells II (tumor cells or PBMC).

EV Characterization

TEC-EV, ASC-EV, and ASCind-EV were analyzed using Nanoparticle Tracking Analysis (Malvern Instruments, Ltd.) and transmission electron microscopy. Mean size of EV evaluated by electron microscopy was 90 nm (± 20); we did not detected vesicles bigger than 100 nm o smaller than 30 nm. According to Western blot all types of EV expressed CD63 and CD81 exosome markers but not endoplasmic reticulum calnexin (**Supplementary Figure S1**).

Protein and RNA Composition of TEC-EV

To study the molecular composition of TEC-EV, we ran RNA sequencing and protein array on TEC-EV. Analysis of RNA sequencing of TEC-EV revealed that TEC-EV contained mRNA from inflammation, interleukin signaling, TGF-β1, and T and B cell activation pathways (**Figure 1**, left). According to RNA sequencing data TEC-EV are enriched with TGF-β1 mRNA and long non-coding RNA MALAT1. TGF-β1 is a mediator of immunosuppression and Treg differentiation (Taylor et al., 2006; Konkel et al., 2017), while the MALAT1 was described as a downstream mediator of TGF-β1 effect in immunosuppression (Yang et al., 2016; Masoumi et al., 2019).

Analysis of TEC-EV proteins showed enrichment of similar signaling pathways relevant to inflammation (**Figure 1**, right). Comparison of gene lists, revealed by RNA sequencing and

[3]https://pga.mgh.harvard.edu/primerbank/

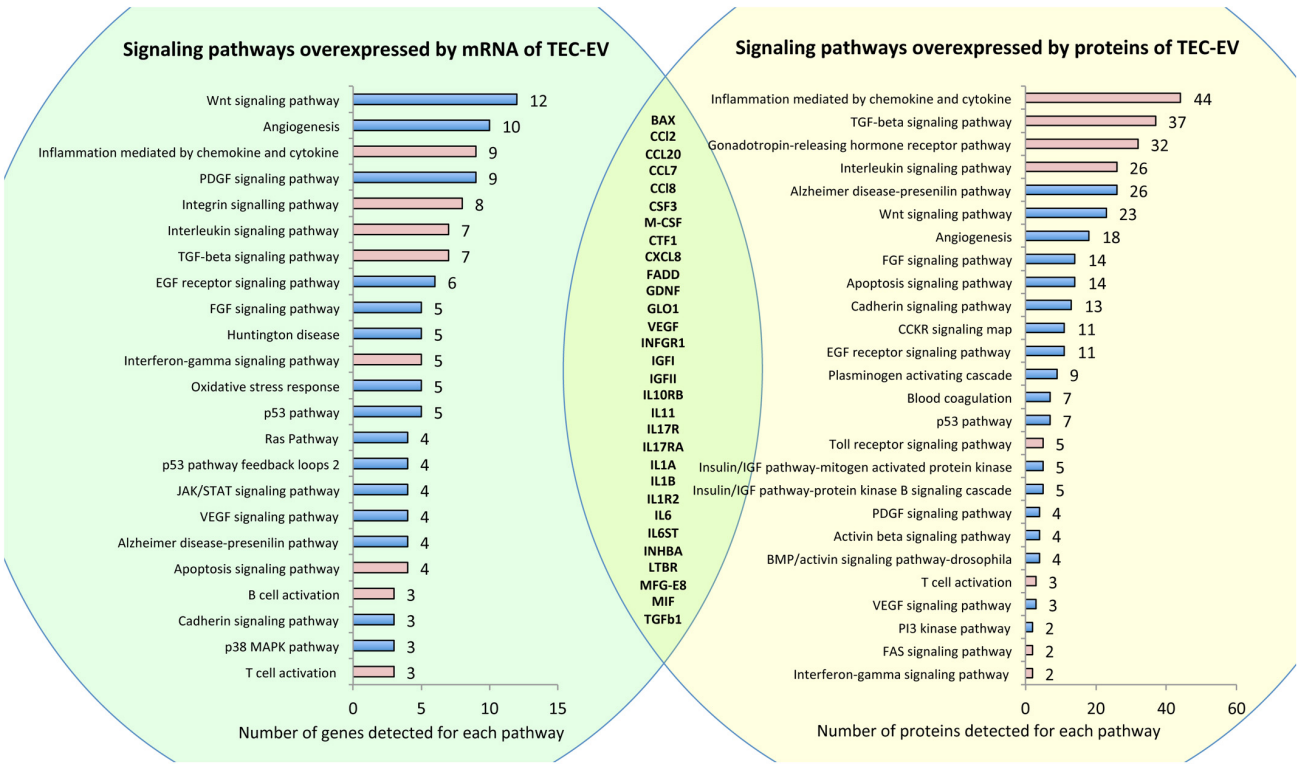


FIGURE 1 | RNA and protein composition of TEC-EV. Left panel (in green) shows pathways overrepresented by mRNAs detected by RNA sequencing of TEC-EV. Right panel (in yellow) shows pathways overrepresented by proteins, detected by protein array in TEC-EV. Pathways relevant to inflammation are marked in pink. In the intersection, there is a list of genes present in TEC-EV at both mRNA and protein levels.

by protein array, confirmed that TEC-EV carry mRNA and proteins of genes relevant to inflammation (**Figure 1**, intersection of the circles), such as interleukins and their receptors IL-1a/b, IL1R2, IL6, IL10RB, IL11, IL6ST, IL13RA1, IL17R, IL7RA, IL17RA, chemokines CCL2, CCL7, CCL8, CXCL8, CCL20, growth factors TGF-a, TGF-β1, GDNF, VEGFa, M-CSF, CSF3, IGFI, IGFII, CTF1, and others (MFG-E8, BAX, FADD, GLO1, INHBA, IFNA/BR1, IFNGR1, and MIF). Using ELISA, we further confirmed the enrichment of TEC-EV with TGF-β1, IL-1β, IGF1, and VEGF.

Fluorescence-activated cell sorting analysis of TEC-EV showed the surface representation of HLA class I, HLA G, CD47, TLR4, VE-cadherin, CD44, CD63, CD81, ICAM, VCAM, and CD31 proteins. Interestingly, TEC-EV were negative for CD45, CD279, CD274, and HLA-DR (**Supplementary Figure S2**).

The molecular composition of TEC-EV suggests that they are enriched with transcripts and proteins of different immune pathways, and therefore can potentially regulate immune reaction.

TEC-EV Activated PBMC and Stimulated T Regulatory Cell Formation

To study the direct effect of TEC-EV on immune cells, we stimulated PBMC (**Table 1**, recipient cell I, **Figure 2A**) with the EV in serum-free medium, and analyzed the changes in proliferation, differentiation, and cytokine expression.

First, we demonstrated the uptake of TEC-EV by PBMC. We added TEC-EV, labeled with PKH67GL green fluorescent dye, to freshly isolated PBMC and performed FACS analysis at different time points. TEC-EV were absorbed faster by monocytes since after 3 h more than 70% of these cells were fluorescent, while lymphocytes even after 24 h were < 40% positive (**Supplementary Figure S3**).

Interestingly, when we isolated monocytes and lymphocytes from the total PBMC population to perform a separated stimulation with TEC-EV, TEC-EV were hardly able to support the viability of separated cells in serum-free medium, and we did not see any changes in proliferation and cytokine secretion. Therefore, we performed all following experiments on total PBMC population.

Using FACS analysis, we compared the PBMC induced with TEC-EV (PBMCind) with its unstimulated control (ctrPBMC). The analysis showed that TEC-EV activated monocytes, according to enhanced expression of CD14 and CD69 (**Supplementary Figure S4**).

TEC-EV increased the expression of CD25, the marker of proliferation, in both monocytes and lymphocytes (fold change 3.5 for monocyte fraction, and 1.6 for lymphocytes, $p < 0.05$, **Supplementary Figure S4**). These

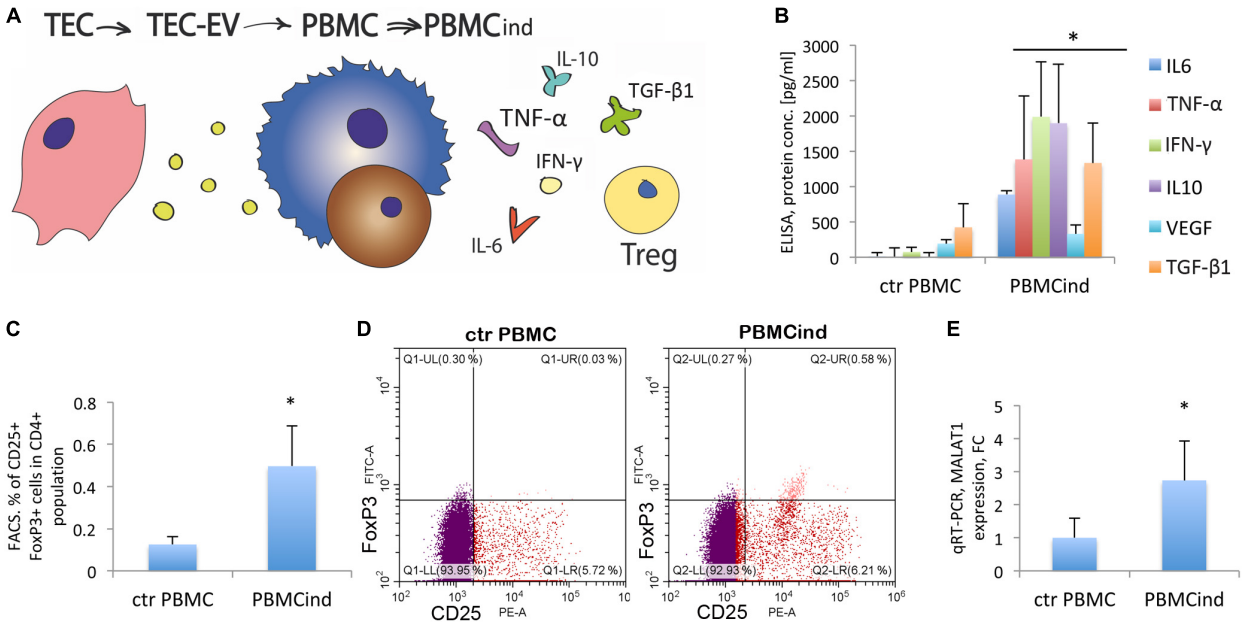


FIGURE 2 | PBMC stimulation with TEC-EV. **(A)** Scheme of the experiment: TEC- EV were isolated from TEC and used for the induction of PBMC (PBMCind). After that, PBMCind and control non-stimulated PBMC (ctr PBMC) were analyzed by FACS, PCR, and ELISA. **(B)** Diagram of the PBMC cytokine secretion: IL-6, IFN-γ, TNF-α, and IL-10, as well as TGF-β1 and VEGF are secreted significantly more by PBMCind than control PBMC. **(C)** Diagram of Treg formation by PBMCind. **(D)** Representative FACS dot-plots of double-positive FoxP3$^+$ (FITC) and CD25$^+$ (PE) cells (up-right quarter, Q2), selected from CD4$^+$ cells. **(E)** Diagram of MALAT1 expression in control PBMC and PBMCind. Data are represented as mean (SD), *$p < 0.05$ vs. PBMC, $n = 15$.

data suggest that TEC-EV stimulated the proliferation of both cell types in PBMC.

We have also evaluated the role of TEC-EV on the differentiation of the PBMC cells. Thus, TEC-EV increased the expression of CD163 (fold change 2.6, $p = 0.03$) and CD206 (fold change 4.3, $p = 0.05$) in monocyte fraction. These data suggest that TEC-EV could induce differentiation of monocytes into immunosuppressive macrophages type M2. Also, TEC-EV significantly increased the expression of CD274 (PD-L1) in monocyte fraction (fold change 4.4, $p = 0.05$, **Supplementary Figure S4**).

ELISA analysis of cytokine expression in PBMCind showed a significant increase of IFN-γ, TNF-α, IL-6, VEGF, IL-10, and TGF-β1 expression relative to unstimulated controls (**Figure 2B**). TGF-β1 plays an essential role in u formation. Indeed, TEC-EV stimulation significantly increased the population of Tregs (CD4$^+$CD25$^+$FoxP3$^+$) in PBMCind (fold change 3.96, $p = 0.049$) (**Figures 2C,D**). We also showed that PBMC treatment with TEC-EV increased the expression of MALAT1 in PBMCind (fold change 2.7, $p = 0.04$, **Figure 2E**). Its increased expression could be relevant for both M2-type differentiation of macrophages and Treg formation (Masoumi et al., 2019). All of these results suggest that TEC-EV induce an immunosuppressive phenotype (formation of Treg and CD206$^+$, CD163$^+$ monocytes) in PBMC via influence on monocytes and lymphocyte proliferation and differentiation.

PBMC Induced With TEC-EV Stimulate Tumor Cell Proliferation and Angiogenesis *in vitro*

To demonstrate the functional activity of the PBMC induced with TEC-EV, we used the conditioned medium from PBMCind for stimulation of tumor cells and TEC (**Table 1**, recipient cells II, **Figure 3A**).

Conditioned medium from PBMCind enhanced the pro-angiogenic properties of TEC *in vitro* (fold change 1.8, $p = 0.001$ **Figures 3B,C**). That also correlated with the increased production of VEGF, IL-6, and TGF-β1, the effectors of tumor angiogenesis (**Figure 2B**). Moreover, conditioned medium from PBMCind stimulated the proliferation of tumor cells (fold change 1.4, $p = 0.04$, **Figure 3D**).

According to these results, we suggested that stimulated PBMC stimulated the growth of tumor mass and its angiogenesis.

TEC-EV Regulate Gene Expression in ASCs

To study if TEC-EV induce immunosuppressive phenotype in stromal cells, we analyzed the effect of TEC-EV on gene regulation in ASCs directly (**Table 1**, recipient cells I), since adipose tissue is present in close proximity of primary head and neck tumors. For this reason, we induced ASCs with TEC-EV (ASCind) for 24 and 48 h. We compared ASCind and its unstimulated controls with the donor TEC cells. The gene expression in each experiment was analyzed by RNA sequencing (**Figure 4**) and was used to define gene expression

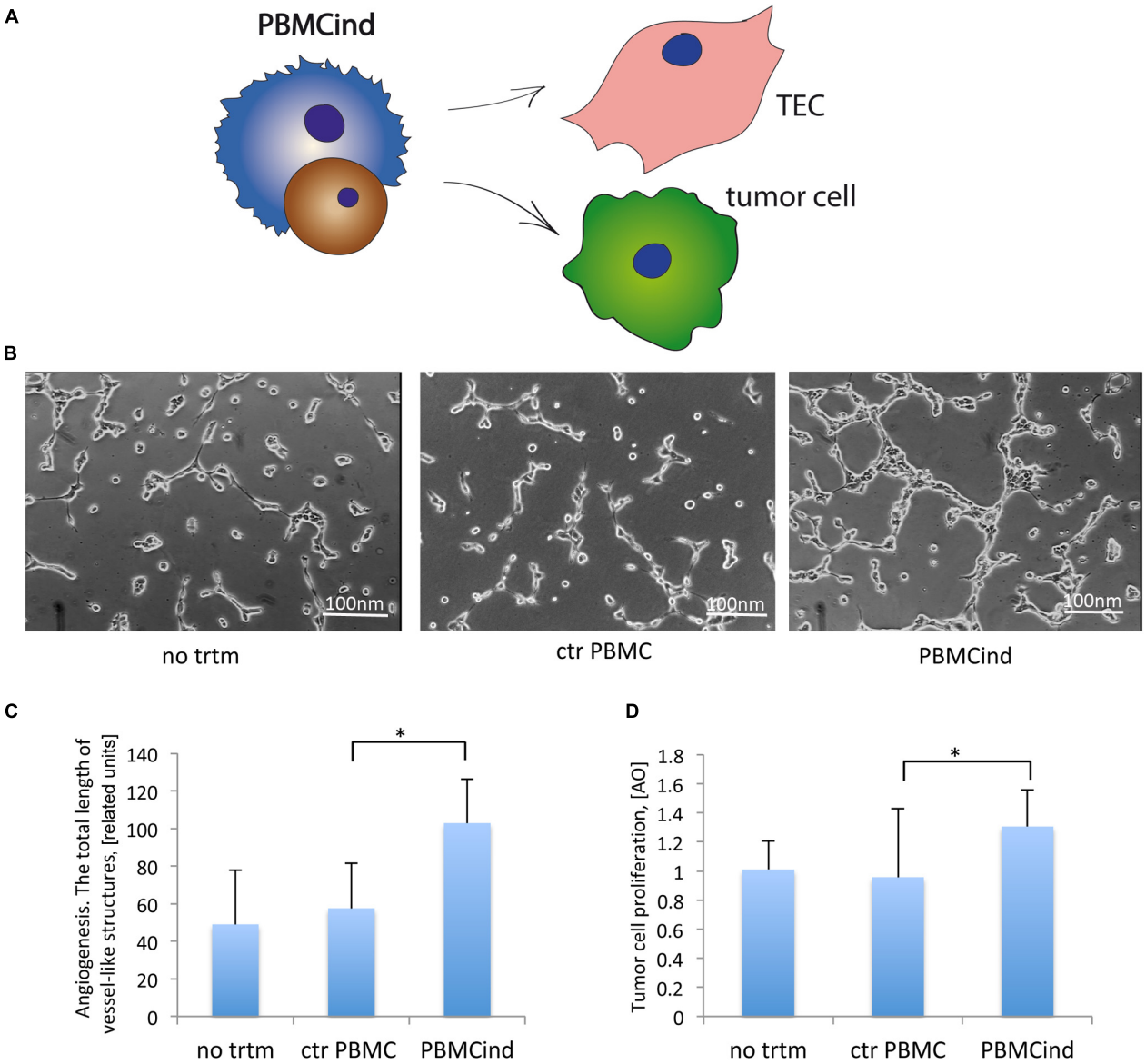


FIGURE 3 | PBMCind regulated tumor cell growth and function. **(A)** Scheme of the experiment: conditioned medium from control PBMC and PBMCind were used to stimulate TEC or tumor cells, then angiogenesis *in vitro* and proliferation were measured. As negative control were used TEC or tumor cells without any treatment (no trtm). **(B)** Representative images of angiogenesis *in vitro* by TEC, stimulated with conditioned medium obtained from control PBMC or PBMCind. **(C)** Diagram of the total length of vessel-like structures formed *in vitro* by TEC, stimulated with conditioned medium from control PBMC or PBMCind. **(D)** Diagram of stromal cell proliferation. Data are represented as mean (SD), $*p < 0.05$ vs. CM PBMC CONTROL, $n = 6$.

signatures of acquired cancerization of ACS by the Bayesian matrix factorization algorithm (CoGAPS) (Fertig et al., 2010).

The CoGAPS analysis demonstrated the coherent down-regulation of a set of genes after the exposure of ACS to TEC-EV (**Figures 4B,C**). Such downregulation correlated with the overall nature of HNSCC, known for its tumor suppressor-driven biology. This pattern contains genes that are highly expressed in control ASCs, not expressed in TEC, and down-regulated in ASCs after TEC-EV stimulation (**Figure 4B**). These genes play a role in pathways involved in tumor immune response (INFLAMMATORY_RESPONSE, COMPLEMENT, IL6_JAK_STAT3_SIGNALING) and in fatty acid metabolism pathway (FATTY_ACID_METABOLISM). These data suggest immunosuppression and transdifferentiation of ASC after TEC-EV induction.

ASCind-EV Activated PBMC and Stimulated Tregs Formation

To demonstrate if tumorigenic induction could be passed from TEC through ASCs to secondary cells by EV, we collected EV released by ASCind (ASCind-EV) or control

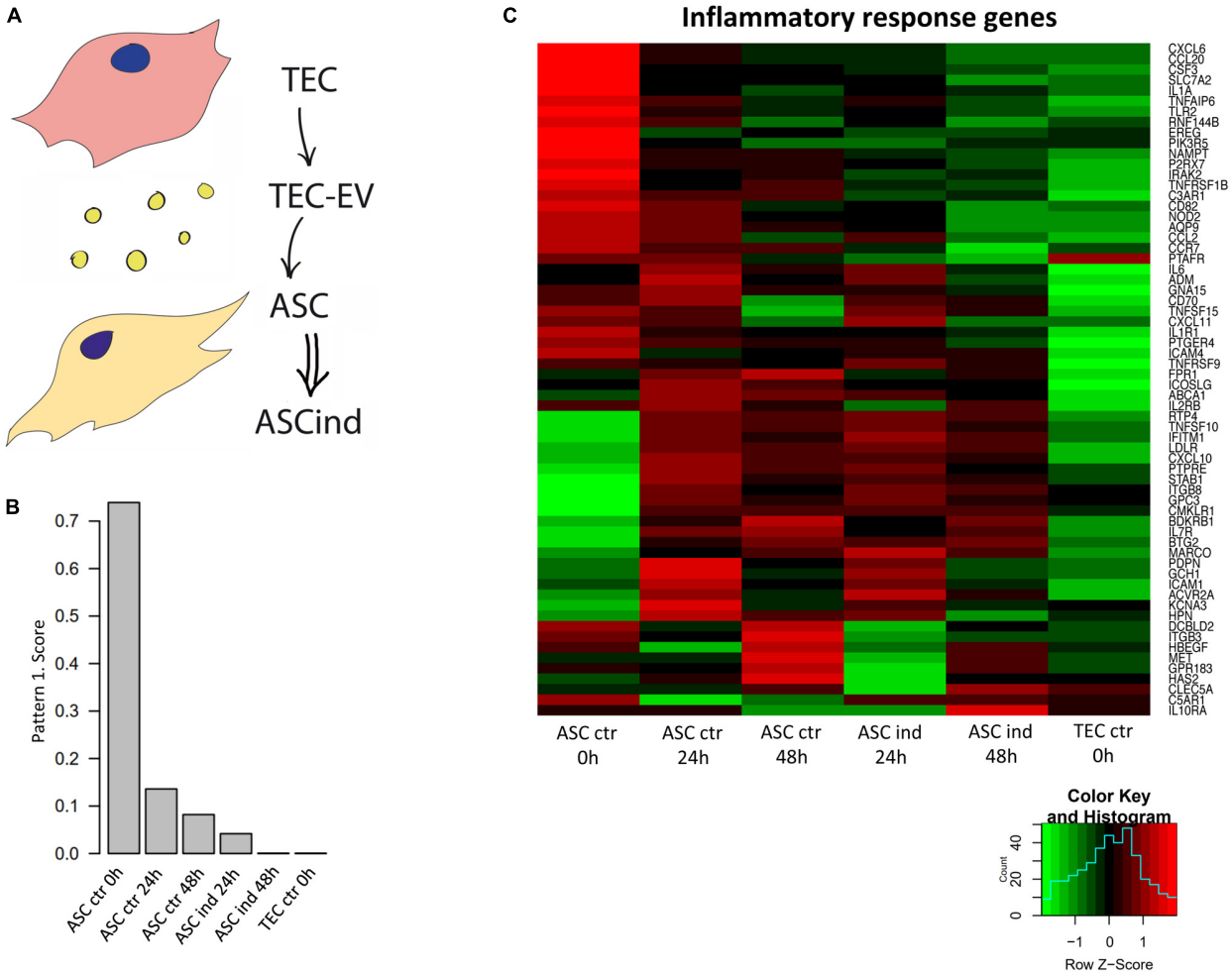


FIGURE 4 | TEC-EV influence on ASCs. **(A)** Scheme of the experiment: TEC-EV were used for the induction of ASC (ASCind). **(B)** Diagram of the relative expression of genes from pattern 1, obtained after analysis of RNA sequencing data of ASCs stimulated with TEC-EV during 24 and 48 h. **(C)** Gene expression heatmap of the inflammatory response group. ASCs at time point 0 h were taken as control (ASC ctr 0 h), also TEC were taken as control cells (TEC ctr). ASCs, induced during 24 and 48 h (ASCind 24 h and ASCind 48 h) were analyzed in parallel with non-stimulated ASCs at the same time points (ASC ctr 24 and ASC ctr 48 h respectively).

ASCs (ASC-EV) and used these EV for stimulation of the recipient cells II (PBMC) (**Table 1**, recipient cells II, **Figure 5A**).

The ASCind-EV and ASC-EV were characterized by protein array. The protein level of CXCL2, CXCL5, FGF2, PGF, MMP1, MMP3, CCL2, CCL7, S100A12, PRL, NID1, IL-10, TGF-α, and TGF-β1-5 was increased in ASCind-EV relative to control ASC-EV (**Supplementary Figure S5A**). Many of those proteins are involved in tumor growth.

ASCind-EV had an increased level of lncRNA MALAT1 (**Supplementary Figure S5B**). ASCind-EV significantly increased the secretion of IL-6 by and expression of MALAT1 in PBMC (**Figures 5B,C**). This strongly correlated with the increased expression of both IL-6 and MALAT1 in PBMC after TEC-EV stimulation (**Figures 2B,E**).

Functionally, PBMC adhesion on endothelium increased after the stimulation with ASCind-EV (**Figure 5D**). Moreover, ASCind-EV increase the formation of Treg relative to control ASC-EV (**Figure 5E** and **Supplementary Figure S6**).

These findings suggest that ASC once stimulated with TEC-EV could induce an immunosuppressive phenotype of PBMC through the released ASCind-EV.

ASCind-EV Stimulate Tumor Cells

To study the effect of ASCind-EV on tumor stroma, we stimulated tumor cells with the ASC-EV or ASCind-EV and analyzed their biological activity (**Table 1**, recipient cells II, **Figure 6A**). Tumor cell stimulation with ASCind-EV led to a significant increase of TGF-β1 expression and secretion (**Figures 6B,C**). Also, the expression of MALAT1 was significantly enhanced in tumor cells after the stimulation with ASCind-EV (**Figure 6B**). This strongly correlates with the increased expression of both TGF-β1 and MALAT1 in ASCind (**Supplementary Figure S5**).

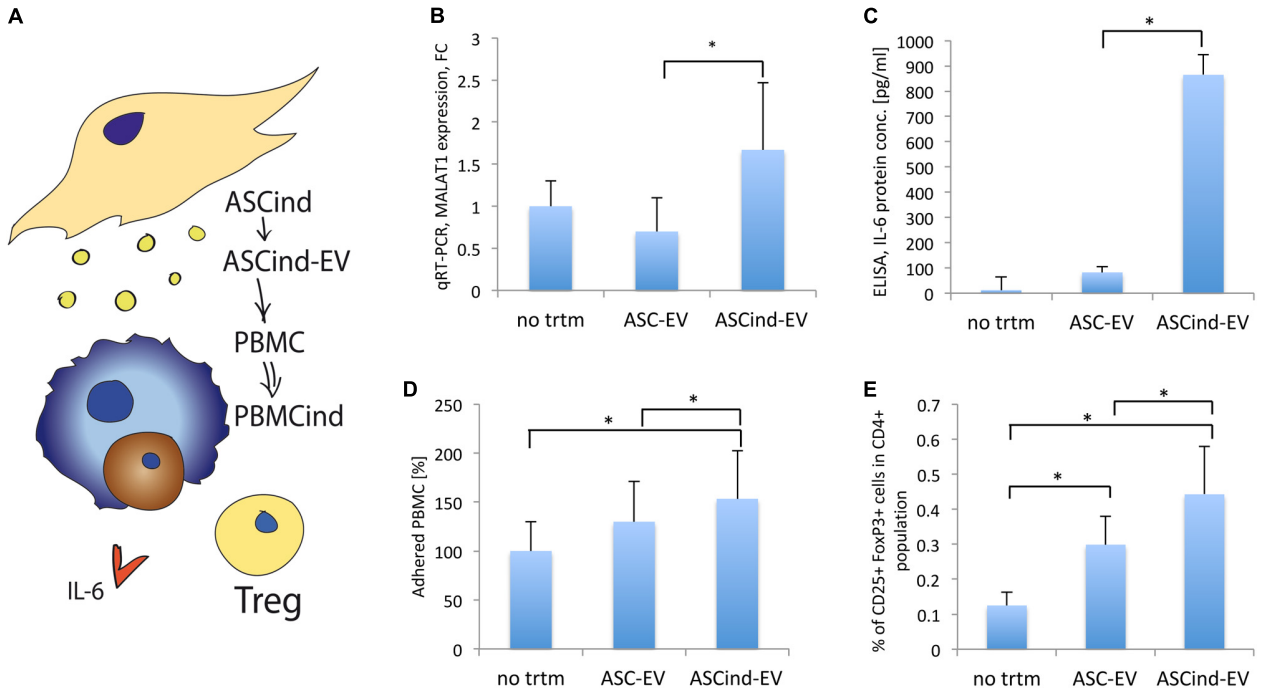


FIGURE 5 | The influence of the ASCind on PBMC activity. **(A)** Scheme of the experiment: ASCind-EV were used for stimulation of PBMC, after that ELISA and FACS analysis of the stimulated PBMC were performed. **(B)** Diagram of MALAT1 expression in PBMC stimulated with control ASC-EV or ASCind-EV respect to non-treated PBMC (mean (SD), $*p < 0.05$ vs. ASC-EV, $n = 8$). As negative control were used PBMC without any treatment (no trtm). **(C)** Diagram of IL-6 secretion by PBMC, stimulated or not with ASC-EV and ASCind-EV [mean (SD), $*p < 0.05$ vs. ASC-EV, $n = 8$]. **(D)** Diagram of the PBMC adhesion on endothelium after stimulation with ASC-EV or ASCind-EV [mean (SD), $*p < 0.05$ vs. ASC-EV, $n = 8$]. **(E)** Diagram of Treg formation by PBMC, stimulated with ASC-EV or ASCind-EV [mean (SD), $*p < 0.05$, $n = 6$].

Tumor cell invasion and adhesion on endothelium (**Figures 6D–F**) were also increased, suggesting the increased capacity of tumor cells to invade from circulation to tissue after being stimulated with ASCind-EV.

These findings suggest that ASC once stimulated with TEC-EV induce the migration of tumor cells from the bloodstream that could be relevant to subsequent metastasis.

DISCUSSION

In our study, we showed that TEC-EV could transmit their oncogenic signals, and this process represents a contagious carcinogenesis. Unlike the metastatic spread of tumor cells, this mechanism regulates tumor microenvironment and reprograms immune cells to sustain tumor growth and progression. In the present study for the first time, we showed the pro-tumorigenic functions of the surrounding non-tumor cells. Such data correlates with previous knowledge that cancerous EV reprogram the immune and stromal cells of the microenvironment to enhance tumor growth, angiogenesis, migration, and tumor tolerance by immune cells (Grange et al., 2015; Hoshino et al., 2015).

Extracellular vesicles, released from tumor cells, including breast cancer (Lombardo et al., 2018), renal carcinoma (Lopatina et al., 2019b), leukemia (Paggetti et al., 2015) and others (Guo et al., 2019), participate in the formation of tumor-promoting pre-metastatic niches (Hoshino et al., 2015). Unfortunately, similar studies for HNSCC are limited. In this work, we explored the role of cancer-derived EV on the local microenvironment of HNSCC tissues and the mechanism of spread of the pro-oncogenic signals. We have shown that this effect is achieved through stromal and immune cells.

A short-time (24 h) stimulation of the recipient cells I (PBMC or ASCs) with TEC-EV changed the gene expression of these cells into pro-oncogenic direction. Thus, TEC-EV regulate gene expression of ASC and decrease their immune reaction. On the other hand, TEC-EV also activate PBMC, regulate cytokine secretion, stimulate Treg cell formation, and activate immunosuppression. Moreover, PBMC can get further immunomodulated by EV from the induced ASCs. Therefore, TEC acting through TEC-EV have both direct and indirect effect on the immune system. This non-metastatic spread of tumor signals to the healthy surrounding cells leads to the carcinogenesis. Furthermore, stimulated PBMC and ASC can carry out the induced pro-oncogenic signals to tumor tissues, enhancing proliferation, adhesion, and invasion of tumor cells, and angiogenesis of TEC. This process makes tumor-surrounding immune and adipose cells function in favor of tumor development and amplify the pro-oncogenic stimulus.

The immune system plays an important role in tumor development. We have shown that EV are get absorbed mainly

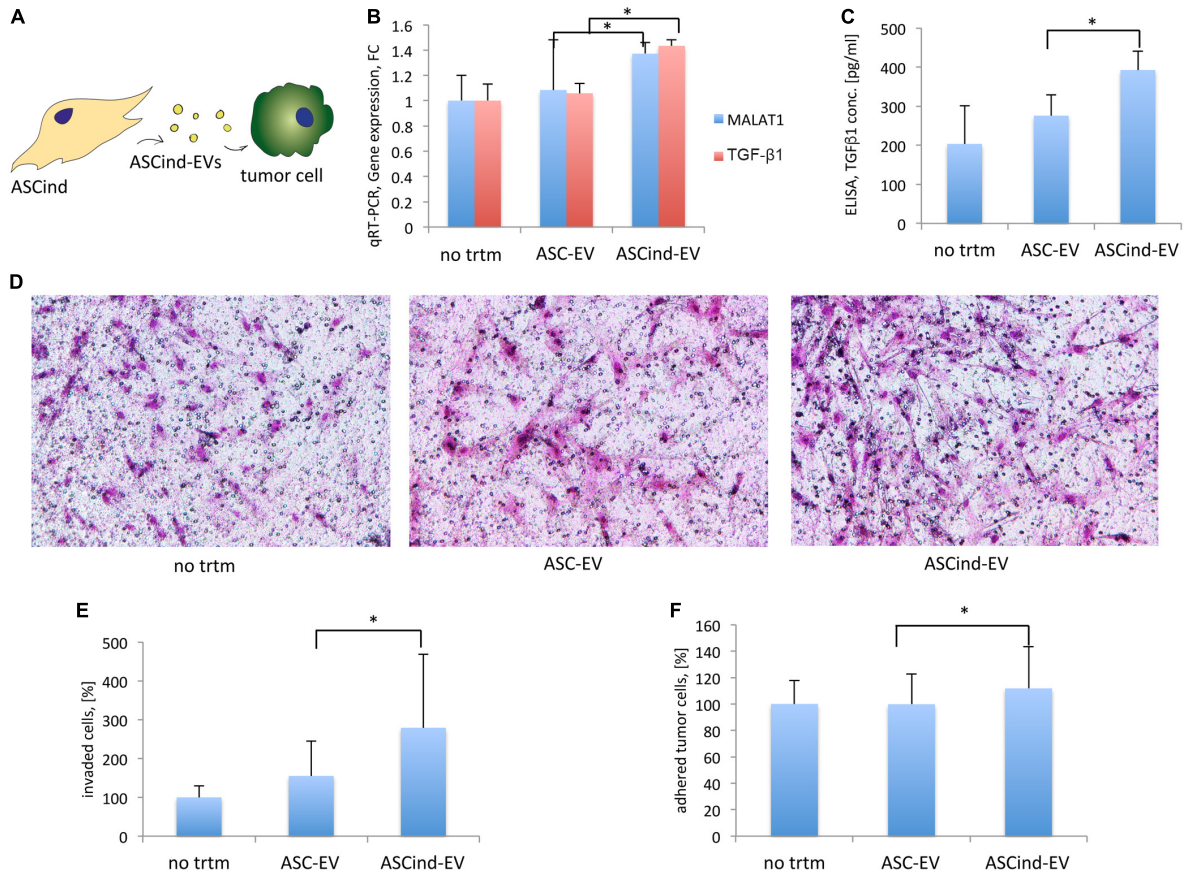


FIGURE 6 | The influence of the ASCind on tumor cell activity and functions. **(A)** Scheme of the experiment: ASCind-EV were used for stimulation of tumor cells, after that tumor cell gene expression and secretory activity, adhesion, and invasion were measured. **(B)** Diagram of the MALAT1 and TGF-β1 gene expression in tumor cells stimulated with ASC-EV or ASCind-EV [mean (SD), $*p < 0.05$, $n = 6$]. As negative control were used tumor cells without any treatment (no trtm). **(C)** Diagram of TGF-β1 secretion by tumor cells stimulated with ASC-EV or ASCind-EV [mean (SD), $*p < 0.05$ vs. ASC-EV, $n = 6$]. **(D)** Representative images on tumor cell invasion. Ability to invade into Matrigel was quantified by counting the number of invaded cells under a phase-contrast microscope. **(E)** Diagram on tumor cell invasion. **(F)** Diagram of the tumor cell adhesion on endothelium [mean (SD), $*p < 0.05$ vs. ASC-EV, $n = 6$].

by monocytes, as well as by lymphocytes. These data is strongly supported by the known internalization of EV by macrophages (Imai et al., 2015). Moreover, our data strongly correlated with the described role of different stromal non-tumor cells, such as endothelial cells (Yu et al., 2010), fibroblasts (Knuchel et al., 2015), mesenchymal stem cells (Lee and Hong, 2017), adipose-derived stem cells (Wei et al., 2015), in the regulation of growth and progression of tumors.

Obesity is considered to be another risk factor for cancer progression (Abd Elmageed et al., 2014). Chronic inflammation links obesity and tumor development, sharing plenty of molecular mechanisms. Recent studies have shown that ASCs can be easily induced into tumor direction (Razmkhah et al., 2018). Moreover, HNSCC is often laid within close proximity of adipose tissue (Tan et al., 2015; Gama et al., 2017). We presume that the inflammatory status and biodiversity of each sample of ASC did not affect the results of our study, since we demonstrated the immunosuppressive effect of ASCind-EV in comparison with control ASC-EV, collected from the same ASC culture.

The immunosuppressive function of EV during cancer formation was recently reported for head and neck cancer development (Ludwig et al., 2017). Thus, EV from the plasma of patients with the stages III/IV HNSCCs exhibit active immune suppression functions through the synthesis of adenosine and stimulation of Treg (Maybruck et al., 2017; Theodoraki et al., 2018), by inducing apoptosis of $CD8^+$ T cells and suppression of $CD4^+$ T-cell proliferation (Ludwig et al., 2017), by inducing immunosuppressive phenotype of $CD8^+$ cells (Maybruck et al., 2017) and carrying immunosuppressive proteins, such as PD-1, PD-L1, Fas, FasL, CTLA-4, TRAIL, CD73, COX2, TGFβ-LAP (Ludwig et al., 2017). These data can explain a high speed of HNSCC cancer formation and its high rate of cancer recurrence. The recurrence rate for HNSCC is 25–48%, and sometimes up to 67% and especially higher for the late-stages III–IV tumors (Schwartz et al., 2000).

We delineated the genes expression signatures for the acquired cancerization of ASCs, by the CoGAPS [Coordinated Gene Activity in Pattern Sets, algorithm (Fertig et al., 2010)]. This algorithm was applied to the gene expression time-course data

of ASC stimulated with TEC-EV. CoGAPS was previously used to successfully delineate the time-course data of therapeutic response in breast and HNSCC (Hill et al., 2016; Stein-O'Brien et al., 2018). In our case, it detected the critical role of inflammatory response gene set to respond to TEC-EV stimuli within 24 h (**Figure 4**).

Tumor and adjacent non-tumor cells in its microenvironment, consisting of heterogenic malignant, stromal, and immune cells, are found in continuous reciprocal communication. The induction of non-tumor cells toward the oncogenic direction by squamous tumor cells was first described as field cancerization in 1953 (Slaughter et al., 1953). From that time, the gene expression reciprocal regulation of the adjacent tumor and non-tumor cells was demonstrated to almost all types of cancer (Curtius et al., 2018). The recent single-cell analysis of HNSCC showed that stromal and immune cells had consistent gene expression across patients, whereas malignant cells varied their expression signatures (Puram et al., 2017). We showed how TEC could regulate gene expression of PBMC and ASC through EV, making them favor tumor development. In particular, we showed that TEC-EV increased expression of TGF-β1 and MALAT1 in target cells. According to the published data, TGF-β1 is involved not only in immune suppression in tumor microenvironment (Takahashi et al., 2017), but also promotes heterogeneity and cancer stem cell formation (Oshimori et al., 2015) and epithelial-mesenchymal transition (Horiguchi et al., 2012), supporting our findings. Therefore, TEC-EV stimulated target cells to secret TGF-β1 necessary for tumor cell differentiation and immune surveillance escape.

The higher expression of MALAT1 was detected in PBMC and in ASC-EV after direct stimulation with TEC-EV, as well as in PBMC and tumor cells after stimulation with ASCind-EV. MALAT1 was shown as a circulating biomarker of head and neck cancer (He et al., 2017). TGF-β1 could activate the transcription of MALAT1 (Wang et al., 2018), and MALAT1 in its turn could activate the transcription of LTBP3, a gene that regulates the bioavailability of TGF-β (Li et al., 2014). We have shown that TEC-EV could enhance the secretion of both MALAT1 and TGF-β1 within ASCind-EV, and that ASCind-EV could induce their expression by tumor cells, play a role in Treg formation, and stimulate their immunosuppressive activity. This transfer of MALAT1 could be one of the possible molecular mechanisms that regulate tumor microenvironment. Future studies are needed to understand those mechanisms.

In vitro we have shown the immunosuppressive effects of EV derived from TEC of HNSCC, and transfer of these effects through non-tumor cells, suggesting, that TEC-EV can reprogram non-tumor cells into an oncogenic phenotype in short time. These data need the *in vivo* confirmation, and we plan to investigate the influence of TEC-EV on tumor growth and tumor niche formation using laboratory *in vivo* models (Grange et al., 2011). Such prospective work will also help us to define the role of TEC-EV on the CoGAPS inflammatory cell pattern in mice. Since EV, in general, have complex structures with highly specific and diversified molecular composition, it is challenging to identify the molecular mechanism of its action. We are going to down-regulate the MALAT1 expression in TEC to see the molecular changes in TEC-EV and their effect on Treg formation and TGF-β1 production by target PBMC.

Overall, our data suggest that tumor tissues trigger many self-promoting mechanisms that amplify the pro-oncogenic signals, with a specific role of TEC, which line tumor blood vessels, and their EV in this process. Moreover, our data suggest that TEC might be essential targets for the development of cancer therapy.

DATA AVAILABILITY STATEMENT

The datasets presented in this study can be found in online repositories. The names of the repository/repositories and accession number(s) can be found in the article/ **Supplementary Material**.

ETHICS STATEMENT

The studies involving human participants were reviewed and approved by Ethics Committee of A.O.U. Città della Salute e della Scienza di Torino. The patients/participants provided their written informed consent to participate in this study.

AUTHOR CONTRIBUTIONS

TL and DG: conception and design. TL, EF, EJF, and LK: development of methodology. LK, EJF, BB, RR, RA, and GP: acquisition of data (acquired and managed patients, provided facilities, etc.). TL, EJF, AF, LD, and DG: analysis and interpretation of data (e.g., statistical analysis, biostatistics, computational analysis). TL, LD, AF, MB, GC, and DG: writing, review, and/or revision of the manuscript. MB and GC: administrative, technical, or material support (i.e., reporting or organizing data, constructing databases). All authors contributed to the article and approved the submitted version.

FUNDING

This work was supported by NIH R01DE027809 and JHU Catalyst Award (DG). Additional funding was provided by P30 CA006973 (LD, AF, and EJF), R50 CA243627 (LD), R01 CA177669 (EJF). This work was also supported by Associazione Italiana per la Ricerca sul Cancro (AIRC) project IG 12890 (GC), project IG 2015.17630 (MB), and project IG2015 16973 (BB) and by Russian Basic Research Foundation grant RBRF 17-00-00208 (LD and AF). This manuscript has been released as a pre-print at ISEV2019 Abstract Book (Lopatina et al., 2019a).

SUPPLEMENTARY MATERIAL

The Supplementary Material for this article can be found online at: https://www.frontiersin.org/articles/10.3389/fcell.2020.00698/full#supplementary-material

REFERENCES

Abd Elmageed, Z. Y., Yang, Y., Thomas, R., Ranjan, M., Mondal, D., Moroz, K., et al. (2014). Neoplastic reprogramming of patient-derived adipose stem cells by prostate cancer cell-associated exosomes. *Stem Cells* 32, 983–997. doi: 10.1002/stem.1619

Argiris, A., Karamouzis, M. V., Raben, D., and Ferris, R. L. (2008). Head and neck cancer. *Lancet* 371, 1695–1709.

Baruah, J., and Wary, K. K. (2019). Exosomes in the regulation of vascular endothelial cell regeneration. *Front. Cell Dev. Biol.* 7:353. doi: 10.3389/fcell.2019.00353

Cancer Genome Atlas Network (2015). Comprehensive genomic characterization of head and neck squamous cell carcinomas. *Nature* 517, 576–582. doi: 10.1038/nature14129

Curtius, K., Wright, N. A., and Graham, T. A. (2018). An evolutionary perspective on field cancerization. *Nat. Rev. Cancer* 18, 19–32. doi: 10.1038/nrc.2017.102

Dudley, A. C. (2012). Tumor endothelial cells. *Cold Spring Harb. Perspect. Med.* 2:a006536.

Dudley, A. C., Khan, Z. A., Shih, S. C., Kang, S. Y., Zwaans, B. M., Bischoff, J., et al. (2008). Calcification of multipotent prostate tumor endothelium. *Cancer Cell* 14, 201–211. doi: 10.1016/j.ccr.2008.06.017

Efimenko, A., Dzhoyashvili, N., Kalinina, N., Kochegura, T., Akchurin, R., Tkachuk, V., et al. (2014). Adipose-derived mesenchymal stromal cells from aged patients with coronary artery disease keep mesenchymal stromal cell properties but exhibit characteristics of aging and have impaired angiogenic potential. *Stem Cells Transl. Med.* 3, 32–41. doi: 10.5966/sctm.2013-0014

Fertig, E. J., Ding, J., Favorov, A. V., Parmigiani, G., and Ochs, M. F. (2010). CoGAPS: an R/C++ package to identify patterns and biological process activity in transcriptomic data. *Bioinformatics* 26, 2792–2793. doi: 10.1093/bioinformatics/btq503

Folkman, J. (1985). Tumor angiogenesis. *Adv. Cancer Res.* 43, 175–203.

Gama, R. R., Song, Y., Zhang, Q., Brown, M. C., Wang, J., Habbous, S., et al. (2017). Body mass index and prognosis in patients with head and neck cancer. *Head. Neck* 39, 1226–1233. doi: 10.1002/hed.24760

Grange, C., Bussolati, B., Bruno, S., Fonsato, V., Sapino, A., and Camussi, G. (2006). Isolation and characterization of human breast tumor-derived endothelial cells. *Oncol. Rep.* 15, 381–386.

Grange, C., Tapparo, M., Collino, F., Vitillo, L., Damasco, C., Deregibus, M. C., et al. (2011). Microvesicles released from human renal cancer stem cells stimulate angiogenesis and formation of lung premetastatic niche. *Cancer Res.* 71, 5346–5356. doi: 10.1158/0008-5472.can-11-0241

Grange, C., Tapparo, M., Tritta, S., Deregibus, M. C., Battaglia, A., Gontero, P., et al. (2015). Role of HLA-G and extracellular vesicles in renal cancer stem cell-induced inhibition of dendritic cell differentiation. *BMC Cancer* 15:1009. doi: 10.1186/s12885-015-2025-z

Guo, T., Sakai, A., Afsari, B., Considine, M., Danilova, L., Favorov, A. V., et al. (2017). A Novel functional splice variant of AKT3 defined by analysis of alternative splice expression in HPV-Positive oropharyngeal cancers. *Cancer Res.* 77, 5248–5258. doi: 10.1158/0008-5472.can-16-3106

Guo, Y., Ji, X., Liu, J., Fan, D., Zhou, Q., Chen, C., et al. (2019). Effects of exosomes on pre-metastatic niche formation in tumors. *Mol. Cancer* 18:39.

He, B., Zeng, J., Chao, W., Chen, X., Huang, Y., Deng, K., et al. (2017). Serum long non-coding RNAs MALAT1, AFAP1-AS1 and AL359062 as diagnostic and prognostic biomarkers for nasopharyngeal carcinoma. *Oncotarget* 8, 41166–41177. doi: 10.18632/oncotarget.17083

Hill, S. M., Heiser, L. M., Cokelaer, T., Unger, M., Nesser, N. K., Carlin, D. E., et al. (2016). Inferring causal molecular networks: empirical assessment through a community-based effort. *Nat. Methods* 13, 310–318.

Horiguchi, K., Sakamoto, K., Koinuma, D., Semba, K., Inoue, A., Inoue, S., et al. (2012). TGF-beta drives epithelial-mesenchymal transition through deltaEF1-mediated downregulation of ESRP. *Oncogene* 31, 3190–3201. doi: 10.1038/onc.2011.493

Hoshino, A., Costa-Silva, B., Shen, T. L., Rodrigues, G., Hashimoto, A., Tesic, M. M., et al. (2015). Tumour exosome integrins determine organotropic metastasis. *Nature* 527, 329–335. doi: 10.1038/nature15756

Imai, T., Takahashi, Y., Nishikawa, M., Kato, K., Morishita, M., Yamashita, T., et al. (2015). Macrophage-dependent clearance of systemically administered B16BL6-derived exosomes from the blood circulation in mice. *J. Extracell. Ves.* 4:26238. doi: 10.3402/jev.v4.26238

Kalinina, N., Klink, G., Glukhanyuk, E., Lopatina, T., Efimenko, A., Akopyan, Z., et al. (2015). miR-92a regulates angiogenic activity of adipose-derived mesenchymal stromal cells. *Exp. Cell Res.* 339, 61–66. doi: 10.1016/j.yexcr.2015.10.007

Knuchel, S., Anderle, P., Werfelli, P., Diamantis, E., and Ruegg, C. (2015). Fibroblast surface-associated FGF-2 promotes contact-dependent colorectal cancer cell migration and invasion through FGFR-SRC signaling and integrin alphavbeta5-mediated adhesion. *Oncotarget* 6, 14300–14317. doi: 10.18632/oncotarget.3883

Konkel, J. E., Zhang, D., Zanvit, P., Chia, C., Zangarle-Murray, T., Jin, W., et al. (2017). Transforming growth factor-beta signaling in regulatory T cells controls T helper-17 cells and tissue-specific immune responses. *Immunity* 46, 660–674. doi: 10.1016/j.immuni.2017.03.015

Lee, H. Y., and Hong, I. S. (2017). Double-edged sword of mesenchymal stem cells: cancer-promoting versus therapeutic potential. *Cancer Sci.* 108, 1939–1946. doi: 10.1111/cas.13334

Li, B., and Dewey, C. N. (2011). RSEM: accurate transcript quantification from RNA-Seq data with or without a reference genome. *BMC Bioinformatics*. 12:323. doi: 10.1186/1471-2105-12-323

Li, B., Chen, P., Qu, J., Shi, L., Zhuang, W., Fu, J., et al. (2014). Activation of LTBP3 gene by a long noncoding RNA (lncRNA) MALAT1 transcript in mesenchymal stem cells from multiple myeloma. *J. Biol. Chem.* 289, 29365–29375. doi: 10.1074/jbc.m114.572693

Liberzon, A., Birger, C., Thorvaldsdottir, H., Ghandi, M., Mesirov, J. P., and Tamayo, P. (2015). The molecular signatures database (MSigDB) hallmark gene set collection. *Cell Syst.* 1, 417–425. doi: 10.1016/j.cels.2015.12.004

Lombardo, G., Gili, M., Grange, C., Cavallari, C., Dentelli, P., Togliatto, G., et al. (2018). IL-3R-alpha blockade inhibits tumor endothelial cell-derived extracellular vesicle (EV)-mediated vessel formation by targeting the beta-catenin pathway. *Oncogene* 37, 1175–1191. doi: 10.1038/s41388-017-0034-x

Lopatina, T., Favaro, E., Danilova, L., Fertig, E., Favorov, A., Martone, T., et al. (2019a). The mechanism of non-metastatic contagious carcinogenesis. *ISEV* 339.

Lopatina, T., Grange, C., Fonsato, V., Tapparo, M., Brossa, A., Fallo, S., et al. (2019b). Extracellular vesicles from human liver stem cells inhibit tumor angiogenesis. *Int. J. Cancer* 144, 322–333. doi: 10.1002/ijc.31796

Louwen, F., Ritter, A., Kreis, N. N., and Yuan, J. (2018). Insight into the development of obesity: functional alterations of adipose-derived mesenchymal stem cells. *Obes. Rev.* 19, 888–904. doi: 10.1111/obr.12679

Ludwig, S., Floros, T., Theodoraki, M. N., Hong, C. S., Jackson, E. K., Lang, S., et al. (2017). Suppression of lymphocyte functions by plasma exosomes correlates with disease activity in patients with head and neck cancer. *Clin. Cancer Res.* 23, 4843–4854. doi: 10.1158/1078-0432.ccr-16-2819

Mamlouk, S., and Wielockx, B. (2013). Hypoxia-inducible factors as key regulators of tumor inflammation. *Int. J. Cancer* 132, 2721–2729. doi: 10.1002/ijc.27901

Masoumi, F., Ghorbani, S., Talebi, F., Branton, W. G., Rajaei, S., Power, C., et al. (2019). Malat1 long noncoding RNA regulates inflammation and leukocyte differentiation in experimental autoimmune encephalomyelitis. *J. Neuroimmunol.* 328, 50–59. doi: 10.1016/j.jneuroim.2018.11.013

Maybruck, B. T., Pfannenstiel, L. W., Diaz-Montero, M., and Gastman, B. R. (2017). Tumor-derived exosomes induce CD8(+) T cell suppressors. *J. Immunother. Cancer* 5:65.

Osawa, T., Ohga, N., Akiyama, K., Hida, Y., Kitayama, K., Kawamoto, T., et al. (2013). Lysyl oxidase secreted by tumour endothelial cells promotes angiogenesis and metastasis. *Br. J. Cancer* 109, 2237–2247. doi: 10.1038/bjc.2013.535

Oshimori, N., Oristian, D., and Fuchs, E. (2015). TGF-beta promotes heterogeneity and drug resistance in squamous cell carcinoma. *Cell* 160, 963–976. doi: 10.1016/j.cell.2015.01.043

Paggetti, J., Haderk, F., Seiffert, M., Janji, B., Distler, U., Ammerlaan, W., et al. (2015). Exosomes released by chronic lymphocytic leukemia cells induce the

transition of stromal cells into cancer-associated fibroblasts. *Blood* 126, 1106–1117. doi: 10.1182/blood-2014-12-618025

Principe, S., Hui, A. B., Bruce, J., Sinha, A., Liu, F. F., and Kislinger, T. (2013). Tumor-derived exosomes and microvesicles in head and neck cancer: implications for tumor biology and biomarker discovery. *Proteomics* 13, 1608–1623. doi: 10.1002/pmic.201200533

Puram, S. V., Tirosh, I., Parikh, A. S., Patel, A. P., Yizhak, K., Gillespie, S., et al. (2017). Single-cell transcriptomic analysis of primary and metastatic tumor ecosystems in head and neck cancer. *Cell* 171, 1611–1624.e1624.

Quesenberry, P. J., Aliotta, J., Deregibus, M. C., and Camussi, G. (2015). Role of extracellular RNA-carrying vesicles in cell differentiation and reprogramming. *Stem Cell Res. Ther.* 6:153.

Razmkhah, M., Mansourabadi, Z., Mohtasebi, M. S., Talei, A. R., and Ghaderi, A. (2018). Cancer and normal adipose-derived mesenchymal stem cells (ASCs): do they have differential effects on tumor and immune cells? *Cell Biol. Int.* 42, 334–343. doi: 10.1002/cbin.10905

Robbins, P. D., Dorronsoro, A., and Booker, C. N. (2016). Regulation of chronic inflammatory and immune processes by extracellular vesicles. *J. Clin. Invest.* 126, 1173–1180. doi: 10.1172/jci81131

Rodriguez Zorrilla, S., Garcia Garcia, A., Blanco Carrion, A., Gandara Vila, P., Somoza Martin, M., Gallas Torreira, M., et al. (2019). Exosomes in head and neck cancer. Updating and revisiting. *J. Enzyme Inhib. Med. Chem.* 34, 1641–1651. doi: 10.1080/14756366.2019.1662000

Roma-Rodrigues, C., Fernandes, A. R., and Baptista, P. V. (2014). Exosome in tumour microenvironment: overview of the crosstalk between normal and cancer cells. *Biomed. Res. Int.* 2014:179486.

Schwartz, G. J., Mehta, R. H., Wenig, B. L., Shaligram, C., and Portugal, L. G. (2000). Salvage treatment for recurrent squamous cell carcinoma of the oral cavity. *Head. Neck* 22, 34–41. doi: 10.1002/(sici)1097-0347(200001)22:1<34::aid-hed6>3.0.co;2-3

Slaughter, D. P., Southwick, H. W., and Smejkal, W. (1953). Field cancerization in oral stratified squamous epithelium; clinical implications of multicentric origin. *Cancer* 6, 963–968. doi: 10.1002/1097-0142(195309)6:5<963::aid-cncr2820060515>3.0.co;2-q

Stein-O'Brien, G., Kagohara, L. T., Li, S., Thakar, M., Ranaweera, R., Ozawa, H., et al. (2018). Integrated time course omics analysis distinguishes immediate therapeutic response from acquired resistance. *Genome Med.* 10:37.

Szade, A., Grochot-Przeczek, A., Florczyk, U., Jozkowicz, A., and Dulak, J. (2015). Cellular and molecular mechanisms of inflammation-induced angiogenesis. *IUBMB Life* 67, 145–159. doi: 10.1002/iub.1358

Takahashi, H., Sakakura, K., Kudo, T., Toyoda, M., Kaira, K., Oyama, T., et al. (2017). Cancer-associated fibroblasts promote an immunosuppressive microenvironment through the induction and accumulation of protumoral macrophages. *Oncotarget* 8, 8633–8647. doi: 10.18632/oncotarget.14374

Tan, X., Nelson, H. H., Langevin, S. M., McClean, M., Marsit, C. J., Waterboer, T., et al. (2015). Obesity and head and neck cancer risk and survival by human papillomavirus serology. *Cancer Causes Control* 26, 111–119. doi: 10.1007/s10552-014-0490-3

Taylor, A., Verhagen, J., Blaser, K., Akdis, M., and Akdis, C. A. (2006). Mechanisms of immune suppression by interleukin-10 and transforming growth factor-beta: the role of T regulatory cells. *Immunology* 117, 433–442. doi: 10.1111/j.1365-2567.2006.02321.x

Theodoraki, M. N., Hoffmann, T. K., Jackson, E. K., and Whiteside, T. L. (2018). Exosomes in HNSCC plasma as surrogate markers of tumour progression and immune competence. *Clin. Exp. Immunol.* 194, 67–78. doi: 10.1111/cei.13157

Wang, K., Singh, D., Zeng, Z., Coleman, S. J., Huang, Y., Savich, G. L., et al. (2010). MapSplice: accurate mapping of RNA-seq reads for splice junction discovery. *Nucleic Acids Res.* 38:e178. doi: 10.1093/nar/gkq622

Wang, Y., Wu, C., Zhang, C., Li, Z., Zhu, T., Chen, J., et al. (2018). TGF-beta-induced STAT3 overexpression promotes human head and neck squamous cell carcinoma invasion and metastasis through malat1/miR-30a interactions. *Cancer Lett.* 436, 52–62. doi: 10.1016/j.canlet.2018.08.009

Wei, H. J., Zeng, R., Lu, J. H., Lai, W. F., Chen, W. H., Liu, H. Y., et al. (2015). Adipose-derived stem cells promote tumor initiation and accelerate tumor growth by interleukin-6 production. *Oncotarget* 6, 7713–7726. doi: 10.18632/oncotarget.3481

Xie, C., Ji, N., Tang, Z., Li, J., and Chen, Q. (2019). The role of extracellular vesicles from different origin in the microenvironment of head and neck cancers. *Mol. Cancer* 18:83.

Yadav, A., Kumar, B., Yu, J. G., Old, M., Teknos, T. N., and Kumar, P. (2015). Tumor-associated endothelial cells promote tumor metastasis by chaperoning circulating tumor cells and protecting them from Anoikis. *PLoS One* 10:e0141602. doi: 10.1371/journal.pone.0141602

Yang, S., Yao, H., Li, M., Li, H., and Wang, F. (2016). Long non-coding RNA MALAT1 mediates transforming growth factor beta1-induced epithelial-mesenchymal transition of retinal pigment epithelial cells. *PLoS One* 11:e0152687. doi: 10.1371/journal.pone.0152687

Ye, S. B., Li, Z. L., Luo, D. H., Huang, B. J., Chen, Y. S., Zhang, X. S., et al. (2014). Tumor-derived exosomes promote tumor progression and T-cell dysfunction through the regulation of enriched exosomal microRNAs in human nasopharyngeal carcinoma. *Oncotarget* 5, 5439–5452. doi: 10.18632/oncotarget.2118

Yu, D. C., Chen, J., and Ding, Y. T. (2010). Hypoxic and highly angiogenic non-tumor tissues surrounding hepatocellular carcinoma: the 'niche' of endothelial progenitor cells. *Int. J. Mol. Sci.* 11, 2901–2909. doi: 10.3390/ijms11082901

Conflict of Interest: The authors declare that the research was conducted in the absence of any commercial or financial relationships that could be construed as a potential conflict of interest.

Copyright © 2020 Lopatina, Favaro, Danilova, Fertig, Favorov, Kagohara, Martone, Bussolati, Romagnoli, Albera, Pecorari, Brizzi, Camussi and Gaykalova. This is an open-access article distributed under the terms of the Creative Commons Attribution License (CC BY). The use, distribution or reproduction in other forums is permitted, provided the original author(s) and the copyright owner(s) are credited and that the original publication in this journal is cited, in accordance with accepted academic practice. No use, distribution or reproduction is permitted which does not comply with these terms.

frontiers in Cell and Developmental Biology

ORIGINAL RESEARCH
published: 22 September 2020
doi: 10.3389/fcell.2020.555378

Mesenchymal Stromal Cell-Produced Components of Extracellular Matrix Potentiate Multipotent Stem Cell Response to Differentiation Stimuli

Ekaterina Novoseletskaya[1,2†], Olga Grigorieva[1†], Peter Nimiritsky[1,2], Nataliya Basalova[1,2], Roman Eremichev[1], Irina Milovskaya[3], Konstantin Kulebyakin[1,2], Maria Kulebyakina[2], Sergei Rodionov[4], Nikolai Omelyanenko[4] and Anastasia Efimenko[1,2]*

[1] Institute for Regenerative Medicine, Medical Research and Education Center, Lomonosov Moscow State University, Moscow, Russia, [2] Faculty of Medicine, Lomonosov Moscow State University, Moscow, Russia, [3] Faculty of Biology, Lomonosov Moscow State University, Moscow, Russia, [4] N.N. Priorov National Medical Research Center of Traumatology and Orthopedics, Moscow, Russia

OPEN ACCESS

Edited by:
Andrei S. Chagin, Karolinska Institutet (KI), Sweden

Reviewed by:
Chao-Ling Yao, Yuan Ze University, Taiwan
Naichen Cheng, National Taiwan University Hospital, Taiwan

***Correspondence:**
Anastasia Efimenko
efimenkoan@gmail.com

[†] These authors have contributed equally to this work

Specialty section:
This article was submitted to Stem Cell Research, a section of the journal Frontiers in Cell and Developmental Biology

Received: *24 April 2020*
Accepted: *31 August 2020*
Published: *22 September 2020*

Citation:
Novoseletskaya E, Grigorieva O, Nimiritsky P, Basalova N, Eremichev R, Milovskaya I, Kulebyakin K, Kulebyakina M, Rodionov S, Omelyanenko N and Efimenko A (2020) Mesenchymal Stromal Cell-Produced Components of Extracellular Matrix Potentiate Multipotent Stem Cell Response to Differentiation Stimuli. Front. Cell Dev. Biol. 8:555378. doi: 10.3389/fcell.2020.555378

Extracellular matrix (ECM) provides both structural support and dynamic microenvironment for cells regulating their behavior and fate. As a critical component of stem cell niche ECM maintains stem cells and activates their proliferation and differentiation under specific stimuli. Mesenchymal stem/stromal cells (MSCs) regulate tissue-specific stem cell functions locating in their immediate microenvironment and producing various bioactive factors, including ECM components. We evaluated the ability of MSC-produced ECM to restore stem and progenitor cell microenvironment *in vitro* and analyzed the possible mechanisms of its effects. Human MSC cell sheets were decellularized by different agents (detergents, enzymes, and apoptosis inductors) to select the optimized combination (CHAPS and DNAse I) based on the conservation of decellularized ECM (dECM) structure and effectiveness of DNA removal. Prepared dECM was non-immunogenic, supported MSC proliferation and formation of larger colonies in colony-forming unit-assay. Decellularized ECM effectively promoted MSC trilineage differentiation (adipogenic, osteogenic, and chondrogenic) compared to plastic or plastic covered by selected ECM components (collagen, fibronectin, laminin). Interestingly, dECM produced by human fibroblasts could not enhance MSC differentiation like MSC-produced dECM, indicating cell-specific functionality of dECM. We demonstrated the significant integrin contribution in dECM-cell interaction by blocking the stimulatory effects of dECM with RGD peptide and suggested the involvement of key intracellular signaling pathways activation (pERK/ERK and pFAK/FAK axes, pYAP/YAP and beta-catenin) in the observed processes based on the results of inhibitory analysis. Taken together, we suppose that MSC-produced dECM may mimic stem cell niche components *in vitro* and maintain multipotent progenitor cells to insure their effective response to external differentiating stimuli upon activation. The obtained data provide more insights into the possible role of MSC-produced ECM in stem and progenitor cell regulation within their niches. Our results are also useful for the developing of dECM-based cell-free products for regenerative medicine.

Keywords: extracellular matrix, decellularization, mesenchymal stromal cells, stem cell niche, progenitor

INTRODUCTION

The extracellular matrix (ECM) is a complex three-dimensional network of interlaced fibrillar proteins, proteoglycans, multiple matrix protein macromolecules, anchored growth factors, and other bioactive components (Gattazzo et al., 2014; Mouw et al., 2014; Theocharis et al., 2016). Extracellular matrix provides physical support for cells and modulates cell functional activity, proliferation, adhesion, migration, acquisition of a specialized phenotype and its maintenance (Gattazzo et al., 2014; Humphrey et al., 2014). Tissue-specific ECM appears as a result of the unique composition and topography and provides a distinctive cell microenvironment in various tissue compartments, including stem cell niches (Gattazzo et al., 2014; Ahmed and Ffrench-Constant, 2016; Chermnykh et al., 2018; Novoseletskaya et al., 2019). Different ECM components may support stem cells and regulate their fate as well as contribute to the malignization of normal cells (Iozzo and Gubbiotti, 2018). Composition of ECM produced by different cell types, the assembly of these macromolecules into a functional three-dimensional structure and its role in cell differentiation, tissue morphogenesis and physiological tissue remodeling were intensively studied for several decades (Lu et al., 2011; Bonnans et al., 2014; Leavitt et al., 2016). However, despite the currently accepted important contribution of ECM to the regulation of these processes, the mechanisms of complex effects exerted by ECM produced by specific cells are poorly understood.

It is well-known that mesenchymal stem/stromal cells (MSCs) play a key role in the processes of tissue repair and regeneration, mostly due to the production of soluble bioactive molecules, extracellular vesicles and ECM, which components are predominantly produced within MSC secretome (Kalinina et al., 2015; Keshtkar et al., 2018; Gomez-Salazar et al., 2020). They also include small subpopulation of stem and progenitor cells that can differentiate in adipogenic, osteogenic, chondrogenic, and some other lineages. Presumably, stromal cell subtypes presented in heterogeneous population of MSCs have regulatory functions that at least partially mediated by produced ECM. After an injury MSC-produced ECM creates a certain basis for the restoration of tissue structure, directing the migration of other cells to the damaged zone and stimulation of blood vessels and nerves growth (Rubina et al., 2009; Mauney et al., 2010; Ode et al., 2010; Lopatina et al., 2019a,b). Emerging ECM provides cell attachment and prevents their death as well as regulates the fate of stem and progenitor cells in regenerating tissue (Gattazzo et al., 2014).

One of the most promising approach to model ECM-based cell microenvironment is a decellularization of extracellular matrices provided bioactive and biocompatible materials consisting of a complex assembly of fibrillar proteins, matrix macromolecules and associated growth factors that often recapitulates the composition and organization of the original ECM microenvironments and creates the necessary microenvironment for the activity of cells *in vitro* or *in vivo* (Rana et al., 2017; Dzobo et al., 2019; Heath, 2019; Novoseletskaya et al., 2019; Ebrahimi Sadrabadi et al., 2020). To stimulate the production of ECM components MSCs can be cultured in 3D conditions such as cell multilayers, or cell sheets. Decellularization of cell sheets provides the preparation of ECM with a composition of protein components close to the native structure and composition (Cheng et al., 2014; Sart et al., 2020). Different decellularizing agents might be used including detergents, enzymes, apoptosis inductors, etc., and an effective combination should be adjusted based on required conservation of ECM structure and effectiveness of DNA removal (Gilpin and Yang, 2017; Hoshiba, 2017; Shakouri-Motlagh et al., 2017; Cramer and Badylak, 2019; Heath, 2019).

Several studies have shown the capacity of dECM to maintain the multipotent state of both MSCs (Lai et al., 2010) and hematopoietic stem cells (Prewitz et al., 2013). Concerning that ECM is one of the key components of the stem cell microenvironment that plays an important role in the regulation of stem cell self-maintenance and differentiation, dECM could be helpful for studying molecular interactions between stem/progenitor cells and ECM and establishing the role of cell-specific ECM in these processes. In the present study we developed the optimized preparation protocol of dECM produced by human MSCs with retained structure and composition. The obtained material was biocompatible, non-cytotoxic, non-immunogenic, and had the capacity to maintain cell growth. Then we evaluated the ability of dECM to restore stem and progenitor cell microenvironment *in vitro* and analyzed the possible mechanisms of its effects.

MATERIALS AND METHODS

Cell Lines

ASC52telo, human telomerase reverse transcriptase (hTERT) immortalized adipose derived mesenchymal stem cells (ATCC® SCRC-4000™) (hTERT-MSCs) were received from ATCC®. hTERT-MSCs were used to assemble cell sheets and to obtain decellularized ECM (dECM). Primary MSC cell lines were isolated from subcutaneous adipose tissue human MSCs (hMSCs) and fibroblast cell lines were isolated from dermis (hFibroblast). All primary cell lines were obtained from healthy donors and preserved in the biobank of the Institute for Regenerative Medicine, Medical Research and Education Center, Lomonosov MSU, collection ID: MSU_MSC_AD, MSU_FB. The institutional local ethic committee (Ethic Committee of Lomonosov Moscow State University, IRB00010587) approved the collection of biomaterials from donors (protocol #4, date of approval 04.06.2018), and all donors provided the informed consent. Mesenchymal stem cells of all types were cultivated in AdvanceSTEM™ media (HyClone, United States) supplemented with 10% Mesenchymal Stem Cell Growth AdvanceSupplement™ (HyClone, United States), 1% penicillin/streptomycin solution (HyClone, United States), 1% GlutaMAX-1 (Gibco, United States). Dermal fibroblasts were cultivated in DMEM low glucose (Gibco, United States) supplemented with 10% fetal bovine serum (FBS; HyClone, United States), 1% penicillin/streptomycin solution (HyClone, United States), 1% GlutaMAX-1 (Gibco, United States). Cell

culture conditions composed an atmosphere of 5% CO_2 at 37°C. Culture medium was changed every 3 days.

Human promonocyte THP-1 cell line were cultivated in RPMI1640 media (Gibco, United States) supplemented with 10% FBS (Gibco, United States), 1% penicillin/streptomycin solution (HyClone, United States), 1% GlutaMAX-1 (Gibco, United States), 1% HEPES (Gibco, United States), 0.0001% β-mercaptoethanol (Sigma, United States) under an atmosphere of 5% CO_2 at 37°C.

Preparation of MSC-Produced dECM

hTERT-MSCs were seeded on tissue culture polystyrene (plastic) plates at a density of 50,000 cells per ml and were cultured for 2 weeks. To remove cellular components cell sheets were treated with either 0.5% 3-[(3-cholamidopropyl)dimethylammonio]-1-propanesulfonate (CHAPS) or 0.1% sodium deoxycholate dissolved in Phosphate-buffered saline (PBS), then washed 3–5 times with sterilized Hank's Balanced Salt Solution (HBSS; Paneco, Russia), and incubated with DNase I (50 U/ml, SciStore, Russia) at 37°C for 30 min. To obtain higher efficiency of decellularization protocol, cell sheets were treated with 500 nM rotenone (Sigma, Germany) to induce apoptosis 24 h before use of detergents.

Apoptosis induction in hTERT-MSCs was evaluated by flow cytometry. Cell suspension was labeled with annexin V (Invitrogen, United States) and 7-Aminoactinomycin D (7-AAD) (BioLegend, United States) and analyzed using cytometer MoFlo (Dako Cytomation, United States). The number of live cells in hTERT-MSCs cell sheets after the incubation with rotenone was estimated by the amount of adenosine triphosphate (ATP) using the ATPlite 1 step kit (PerkinElmer, United States), according to the manufacturer's instructions.

Analysis of dECM Structure and Composition

Samples of hTERT-MSCs cell sheets and dECM were fixed in 10% neutral formalin, then they were washed in distilled water and dehydrated in alcohols of ascending concentration, a mixture of alcohol-acetone and then pure acetone. Samples were dried at the critical point using Quorum K350 (Quorum gala instrument gmbh, Germany) or HCP-2 (Hitachi, Japan) was used. The samples were mounted on a special aluminum table with conductive carbon glue, sprayed with gold or platinum-palladium alloy in the spraying unit Quorum Q150TS (Quorum gala instrument gmbh, Germany) or IB-3 Ion Coater (EIKO, Japan) and observed with scanning electron microscope S 3400N (Hitachi, Japan).

The structure of dECM was evaluated in Dulbecco's Phosphate-Buffered Saline (DPBS) solution using a direct two-photon laser confocal scanning microscope A1rMP+ (Nikon, Japan) with NIR Apo 60x Oil λS DIC N2 lens. A titanium-sapphire laser Chameleon Vision II (Coherent, United States) with tunable wavelength in the range of 700–1000 nm, pulse repetition frequency of 80 MHz and pulse duration of 140 FS was used as a source of laser radiation. The excitation of the signal in this work was carried out at a wavelength of 760 nm. The signal was recorded simultaneously in three spectral channels: in the wavelength range $300 < \lambda 1 < 400$ nm (encoded in blue in the images), in the range $458 < \lambda 2 < 492$ nm (encoded in green), and in the range $492 < \lambda 3 < 593$ nm (encoded in yellow). Processing of the images was performed in the program NIS-Elements (Nikon, Japan).

Type I collagen, fibronectin and laminin in the deposited ECM were investigated by immunohistochemical labeling. First, the deposited ECM after decellularization were detached from the plastic and placed in Tissue-Tek® O.C.T. Compound (Sakura® Finetek, United States) freezing medium. After sample polymerization the 8 μm cryosections were prepared using Leica CM1950 cryostat (Germany). The sections were fixed with 4% paraformaldehyde (Panreac, Spain) at room temperature for 30 min and then samples were incubated with 0.2% triton X100 (Sigma, United States) solution at room temperature for 10 min. Further, the samples were incubated with 1% bovine serum albumin (BSA, Sigma, United States) and 10% normal goat serum (Abcam, United Kingdom) solution at room temperature for 1 h. Subsequently, the samples were incubated with rabbit polyclonal primary antibodies: anti-collagen I (ab34710), anti-fibronectin (ab2413) and anti-laminin (ab11575) (Abcam, United Kingdom) in 1% BSA solution at +4° overnight. Samples were then incubated with goat-anti-rabbit secondary antibodies (A11034, A11037, Invitrogen, United States) at room temperature for 1 h. Cell nuclei were labeled with DAPI (DAKO, United States). Another approach included labeling ECM components of cell sheets or dECM attached to plastic. Samples were fixed with 4% paraformaldehyde (Panreac, Spain) at room temperature for 10 min and were processed as described above. hMSCs seeded on plastic or dECM were treated as described above using anti-β1-antibody (303001, Biolegend, United States). Samples were analyzed with a Leica DM6000B fluorescent microscope equipped with a Leica DFC 360FX camera (Leica Microsystems GmbH, Germany).

Evaluation of Residual DNA Content

The amount of DNA in hTERT-MSCs cell sheets or dECM was measure using PicoGreen assay kit (Life Technologies, United States) according to the manufacturer's instructions. Each sample was lysed in 500 ml of ExtractRNA (Eurogen, Russia) (analogous reagent as TRIzol, TRI Reagent) for 10 min at room temperature. The lysates were diluted 50 times with TE buffer solution. Dissolved lysate was placed in a 96-well plate with PicoGreen dye (1:1). The plate was incubated in the dark for 10 min and then the optical density was measured with a plate spectrophotometer EnVision Multilabel Plate Readers (PerkinElmer, United States).

In vitro Time-Lapse Evaluation of MSC Proliferation With IncuCyte ZOOM System

hTERT-MSCs were seeded in a 12-wells plate, covered with dECM (15,000 cells per ml). The plate was placed in the IncuCyte® ZOOM Live Cell Analysis System (Essen Bioscience, United States) and time-lapse shooting was carried out every

4 h for 4 days. The device's built-in software allows to estimate the area occupied by cells by applying a "mask" to the obtained images and thus calculating the percentage of cell culture confluency. The increase in confluence directly correlates with the increase in the number of cells, which allows us to judge the growth rate of cell culture by calculated parameters.

To analyze the proliferation rate of hTERT-MSCs, cells were seeded on culture plastic or dECM and cultured for 4 days. Cell number was examined by MTT test (Paneco, Russia) on day 1 and 4. Optical density was measured with the plate spectrophotometer EnVision Multilabel Plate Reader (Perkin Elmer, United States).

Immunogenic Properties of dECM

Immunogenic examination was evaluated through the ability of dECM to induce macrophage differentiation. When tissue is injured, monocytes appear in the damaged area after a few hours, where they begin to differentiate into macrophages. Thus, during the entire healing process, macrophages are one of the main regulators of repair, with a powerful paracrine effect. A distinctive feature of the line of monocytes-macrophages is plasticity, which turns them into an adaptive component of innate immunity (Locati et al., 2013). *In vitro* monocyte activation test (MAT) is widely used to assess the pyrogenic activity of medical materials and detect substances that activate human monocytes to release cytokines (Borton and Coleman, 2018). THP-1 is a human leukemia monocytic cell line, which has been extensively used to study monocyte/macrophage functions, mechanisms, signaling pathways, and nutrient and drug transport. This cell line has become a common model to estimate modulation of monocyte and macrophage activities (Chanput et al., 2014). THP-1 are regarded as a simplified model of human macrophages when investigating relatively straightforward biological processes, such as polarization and its functional implications (Tedesco et al., 2018). To perform MAT for investigating immunogenic properties of prepared dECM, THP-1 were added to a 12-well plate on plastic or dECM (500,000 cells per well) with or without 50 ng/ml phorbol ester (phorbol-12-myristate-13-acetate, PMA) (Sigma, United States). Cells were cultured for 7 days, then conditioned medium was collected and centrifuged at 300 *g* for 10 min. The concentration of IL-6, IL-8, IL-10, IL-12p70, MCP-1 was analyzed in supernatants using enzyme-linked immunoassay (ELISA; R&D, United States) according to the manufacturer's instructions. The optical density of the samples was measured at wavelengths of 450 and 525 nm with a flatbed spectrophotometer EnVision Multilabel Plate Reader (PerkinElmer, United States).

Colony-Forming Unit Assay

To determine the ability of dECM to support MSC colony formation, colony-forming unit (CFU) assay was performed. MSCs were seeded on plastic or dECM at low density (400 cells per well in 6-well culture plate) and cultured for 2 weeks, then fixed with a solution of 4% paraformaldehyde and stained with crystal violet (Sigma, United States) for 30 min at room temperature. The nuclei we additionally stained with DAPI. The number and average size of colonies as well as area of cell growth and cell number were counted in each well.

Adipogenic, Osteogenic, and Chondrogenic Differentiation of MSCs

Cell differentiation was performed using the StemPro Adipogenesis Differentiation Kit (Gibco, United States), StemPro Osteogenesis Differentiation Kit (Gibco, United States) and StemPro Chondrogenesis Differentiation Kit (Gibco, United States) according to the manufacturer's instructions. Briefly, hMSCs were seeded in 12-well plates in the density of 120,000 cells per well (and in 48-well plates in the density of 30,000 cells per well) on dECM produced by hTERT-MSCs or dermal fibroblasts, on plastic or on plastic covered by ECM structural proteins [recombinant human fibronectin or recombinant human laminin or type I collagen (IMTEK, Russia)] according to the manufacturer's recommendation for cell culture. Then cells were and cultured for 24 h in the full growth media. After 24 h the media has been replaced by differentiation induction media. The media was changed every 3 days. Four or 10 days after induction samples were fixed with 4% paraformaldehyde for 30 min. Visualization of mineral deposits by osteoblasts was performed with Alizarin red solution from Mesenchymal Stem Cell Osteogenesis Kit (Chemicon, United States), lipid drops in adipocytes were stained with Oil Red O solution from Mesenchymal Stem Cell Adipogenesis Kit (Chemicon, United States) according to the manufacturer's instructions. Chondrogenic differentiation was observed with staining 0.1% Toluidine blue (Sigma, United States) solution in 1% Sodium chloride, pH 2.3. For quantification, all of dyes were extracted with DMSO (AplliChem, United States), and the absorbance at 530 nm (Oil Red O), at 560 (Alizarin Red) and at 608 nm (Toluidine blue) was measured on a flatbed spectrophotometer EnVision Multilabel Plate Reader (PerkinElmer, United States).

Real-Time RT-PCR

Total RNA was extracted from 120×10^3 cells (∼90% confluence) using the RNeasy Mini Kit (Qiagen, United Kingdom) following the manufacturer's protocols. The cDNA was synthesized with 300 ng of total RNA using the MMLV Reverse Transcription Kit (Eurogen, Russia). The temperature mode was supported by Mastercycler® nexus gradient (Eppendorf, Germany). cDNA was used for qPCR with qPCRmix-HS SYBR + LowROX (Eurogen, Russia) according to the manufacturer's protocols. Gene expression analysis was performed with the relative quantification method. Quantification and normalization of expression levels of the target genes and the reference gene (RPLP0) were calculated using the comparative threshold cycle (CT) method. RPLP0 is one of the most stable expression housekeeping gene during hMSCs differentiation into the canonical lineages (Ragni et al., 2013). The primers were designed in-house using the NCBI Primer Designing Tool,[1] selecting only the primers spanning an exon–exon junction and producing

[1] http://www.ncbi.nlm.nih.gov/tools/primer-blast/

a PCR amplificate with length between 63 and 199 base pairs (**Supplementary Table 1**).

Real-time PCR data were analyzed using the ΔC_T method for evaluating the expression of master genes and markers of adipogenic and osteogenic differentiation normalized to housekeeping gene (RPLP0) in dynamics, as well as analysis of pluripotency gene expression and integrin expression profile. We applied the $2^{-\Delta\Delta CT}$ method to evaluate the level of target gene expression in experimental samples relative to untreated control samples (without differentiation induction) in integrin-blocking assays.

Inhibitor Analysis and Integrin-Blocking Assays

hMSCs were seeded in 48-well plates in the density of 30,000 cells per well for differentiation experiment and in six-well plates in the density of 300,000 per well for western blot assay, on plastic or on dECM produced by hTERT-MSCs. Then cells were cultured for 24 h in the full growth media. After 24 h the media has been replaced by media, consist of growth media with one of the next signaling inhibitors: inhibitor of the Src family of protein tyrosine kinases (PP2) (529573, Sigma, United States), PD 98059 selective & reversible inhibitor of MAP Kinase Kinase (MEK; 513000, Sigma, United States), Akt Inhibitor VIII, Akti-1/2 (Akti) (124018, Sigma, United States) and dobutamine hydrochloride (DBN) as inhibitor of YAP nuclear translocation (DBN) (ab120768) (Abcam, United Kingdom) (Bao et al., 2011). All inhibitors were added to the final concentration of 10 mkM (Kim and Kim, 2010; Hu et al., 2014; Shin et al., 2019), except for DBN up to 20 mkM (Lorthongpanich et al., 2019). Therefore, 0.1% DMSO was used as a vehicle control in all experiments. After another 24 h, signaling inhibition was evaluated using Western blot. In another case, the medium was changed to induction medium for inhibition of signaling during differentiation of cell for 4 days. On the 4th day, the cells were fixed and the studied as described in section "Adipogenic, Osteogenic, and Chondrogenic Differentiation of MSCs."

hMSCs were incubated with cycle-RGD-TPP peptide (kindly provided by Elena Markvicheva, Institute of bioorganic chemistry of RAS, Moscow, Russian Federation), which blocked the connection of integrins with ECM proteins consisted RGD sequence. Ñycle-RGD-TPP was used at the empirically adjusted concentration of 40 μM. Cell suspension were incubated during 10 min under cell culture conditions in solution of Ñycle-RGD-TPP. hMSCs were then seeded onto surfaces in the density of 120,000 cells per well in culture media or differentiation media, while peptide still present and not allowed to attach for 4 days.

Western Blotting and Dot-Blotting

Proteins were extracted using cell lysis buffer [62.5 mM Tris-HCl (pH 6.8), 7.5% glycerol, 2% SDS, 0.0125% Bromophenol blue and 1.25% β-mercaptoethanol] supplemented with a protease inhibitor cocktail (Roche, South San Francisco, CA, United States) and HaltTM phosphatase inhibitor cocktails (Thermo Fisher Scientific, United States). Nuclear and cytoplasmic extracts were obtained as described by Longobardi and Blasi (2003). About 500×10^3 cells (∼100% confluence) were washed twice with cold phosphate-buffered saline, separated by centrifugation (200 *g* 5 min + 4°C), collected with 150 μl of cold buffer A (10 mM HEPES, pH 7.9, 10 mM KCl, 1.5 mM $MgCl_2$, 0.5 mM dithiothreitol, 0.5 mM phenylmethylsulfonyl fluoride) into an Eppendorf tube, left 10 min on ice, and lysed by the addition of 0.3% Triton X-100. The nuclei were collected by centrifugation (14,000 *g* 5 min + 4°C). The supernatant was transferred to a new tube, and 0.11 volume of buffer B was added (0.3 M HEPES, pH 7.9, 1.4 M KCl, 30 mM $MgCl_2$), incubated for 30 min at 4°C, and centrifuged (14,000 *g* 5 min + 4°C). The resulting supernatant was denoted as cytoplasmic extract. Nuclear extracts were prepared by resuspending the pelleted nuclei in 30 μL of buffer C (20 mM HEPES, pH 7.9, 25% glycerol (v/v), 0.42 M NaCl, 1.5 mM $MgCl_2$, 0.5 mM dithiothreitol, 0.2 mM EDTA, 0.5 mM phenylmethylsulfonyl fluoride) for 30 min on ice. The extract was cleared by centrifugation (14,000 *g* 5 min + 4°C). Protein concentration was determined using a Bradford protein assay.

Polyacrylamide gel electrophoresis was performed according to the standard protocol (Laemmli, 1970). After electrophoretic separation by 12% SDS-polyacrylamide gel electrophoresis, proteins were electroblotted onto polyvinylidene fluoride (PVDF) membranes (Millipore Immobilon-P) according to the method described by Towbin et al. (1979), or the gel was stained with a Coomassie Blue Silver suspension as described in Candiano et al. (2004). The membranes were blocked with Tris-buffered saline containing 0.1% Tween-20 (TBST) and 5% BSA for 30 min at room temperature. For target protein detection following primary antibodies were used: anti-collagen I (ab34710), anti-fibronectin (ab2413), anti-laminin (ab11575) (Abcam, United Kingdom), Anti-ERK1 + ERK2 antibody (Abcam; ab17942), Anti-Erk1 (pT202/pY204) + Erk2 (pT185/pY187) antibody (Abcam, ab4819), Anti-Active-β-Catenin (Anti-ABC) (Merck Millipore, 05-665), Anti-β-Catenin Antibody (Merck Millipore, 6734), YAP Antibody (Cell signaling technology, 4912), Phospho-YAP (Ser127) Antibody (Cell signaling technology, 4911), Phospho-FAK (Tyr397) Antibody (Cell signaling technology, 3283), FAK Antibody (Cell signaling technology, 3285), Phospho-Akt (Ser473) Antibody (Cell signaling technology, 9271), Akt (pan) (C67E7) Antibody (Cell signaling technology, 4691), p-c-Src (Tyr 419)(Santa Cruz Biotechnology, sc-101802), Anti-Vinculin antibody (Merck Millipore, V4139), histone H3 (Cell Signaling Technology, 4499) for nuclear fraction and GAPDH for total and cytoplasmic fractions (14C10) (Cell Signaling Technology, 2118). Membranes were incubated with antibodies overnight at 4°C with slight shaking. Thereafter, the membranes were washed in TBST buffer and further incubated with an HRP-conjugated antibody (goat anti-rabbit IgG; IMTEK) for 2 h at room temperature. To visualize the protein bands an enhanced chemiluminescence system (Bio-Rad ECL Clarity Max detection kits with the ChemiDoc Imaging System Bio-Rad, United States) was used. Semi-quantitative evaluation of the bands was performed by densitometry.

The relative levels of FAK, p-FAK, ERK1/2, p-ERK1/2, YAP, and pYAP were determined by normalizing them to the level of the housekeeping protein GAPDH, the relative level of active b-catenin in nuclear fraction was normalized to histone H3 protein.

Quantitative analysis of proteins of interest (collagen-1, fibronectin, laminin) was carried out by the method of dot-immunoenzyme analysis (dot-ELISA): lysed samples were dispensed and dried per 1 μl in two parallels on nitrocellulose membrane surface. Then immunodetection by the above protocol for Western blotting was carried out. The proteins of interest were visualized using the Clarity Max ECL chemoluminescence kit (Bio-Rad, United States). In addition, in parallel with the lysate samples, samples with a known concentration of a specific protein of interest were titrated with 1: 2 dilution factor and processed in the same way to construct a calibration curve. Quantitative calculations were performed using ImageJ application (NIH, Bethesda, MD, United States). Briefly, measured chemiluminescence levels were used to calculate the concentrations of the proteins of interest using a calibration curves, and then the calculated amounts were normalized on total protein amounts in corresponding samples measured using Amido Black dye (Sigma Aldrich, United States).

Statistical Data Processing

Statistical data processing was performed using the program GraphPad Prizm 8.0. Values are expressed as mean ± SD for normally distributed data and as median and percentiles (25–75%) for non-normal data. If normality of data were confirmed (according to the Kolmogorov–Smirnov test and Shapiro–Wilk's W test), comparison of independent groups was performed by Student's *t*-test, *F*-test, Tukey's multiple comparisons test; if the data were not confirmed comparison was performed by Mann–Whitney test, Dunn's multiple comparisons test, two-stage linear step-up procedure of Benjamini, Krieger and Yekutieli. Multiple comparisons were made using one-way ANOVA for normally distributed data and otherwise by Kruskall–Wallis test. Differences were considered statistically significant at the significance level of $p < 0.05$. Significant differences marked by *(p value < 0.05), **(p value < 0.005), ***(p value < 0.0005) and ****(p value < 0.0001).

RESULTS

Preparation of MSC-Produced dECM

To promote ECM production, we cultured hTERT-MSCs as cell sheets for two weeks. Cells produced and formed ECM proteins (**Figures 1A,C**). Based on our previous results and literature data the following detergents for decellularization were selected: zwitter-ion detergent – CHAPS and ion detergent – sodium deoxycholate. Ionic detergents, such as sodium deoxycholate, are actively use for the decellularization of organs and tissues (Rana et al., 2017; Dzobo et al., 2019; Heath, 2019; Ebrahimi Sadrabadi et al., 2020; Sart et al., 2020). On the other side, this type of detergents can contribute the leaching of a significant part of the ECM from the cell sheet. Despite the properties of ionic detergents, as example sodium deoxycholate is FDA approved for medical use. Another perspective type of detergents for the decellularization of tissue and organs is zwitter-ionic surfactants (CHAPS). These surfactants also effective remove cell compartment, at the same time they do not denature proteins (Tsuchiya et al., 2014, 2016; Sengyoku et al., 2018), which makes them the most promising agent for the decellularization of cell sheets.

In addition, we hypothesized that pre-incubation of hTERT-MSCs cell sheets with rotenone (apoptotic inductor) may increase the efficiency of decellularization. As a promising approach for decellularization we examined one of the inductors of apoptosis (rotenone). Rotenone is a strong inhibitor of the mitochondrial complex I, which disrupt electron transfer within the mitochondrial respiratory chain leads to the formation of reactive oxygen species and thereby induces oxidative stress and apoptosis in cells. After detergent treatment and several washings cell sheets were incubated with DNase I in the empirically adjusted concentration (50 U/ml) selected from the tested interval 50–200 U/ml. Examples of obtained dECM are shown in **Figure 1B,D,E**.

The following combinations of decellularization agents were tested: CHAPS with DNAse I, rotenone with CHAPS and DNAse I, sodium deoxycholate with DNAse I, rotenone with sodium deoxycholate and DNAse I (**Figure 1**). Rotenone effectively induced apoptosis both in hTERT-MSCs suspension and hTERT-MSCs cell sheets (**Supplementary Figure S1**), although we did not find any improvement in decellularization efficiency based on residual DNA in dECM after the pretreatment with rotenone.

Decellularization efficiency was estimated by residual DNA as a percentage of the original DNA content in the cell sheets (**Figure 2**). Execution of all tested protocols effectively removed DNA (80 ± 5% efficiency). At the same time, using sodium deoxycholate led to better removal efficiency (**Figure 2E**), but the amount of residual matrix in this biomaterial was lower and its structure was substantially damaged compared to CHAPS-based protocols (**Figure 1D** and **Supplementary Figure S3**). Unexpectedly, there were no benefits of the protocols included incubation with rotenone concerning the decellularization efficiency (**Supplementary Figures S2**, **3**). In all dECM samples we detected basic ECM structural proteins such as type I collagen and fibronectin via IHC analysis (**Supplementary Figure S2**). Another ECM protein laminin was found in low quantity. Better results were obtained when the treatment of CHAPS and DNAse I was used for decellularization: structural ECM proteins and their three-dimensional patterns were preserved which was confirmed by immunohistochemical analysis (**Figure 3**).

Biochemical assessment of matrix structure demonstrated that the total amount of protein decreased during decellularization (**Figure 3G**), but as a result of the procedure, the samples were enriched with ECM components (**Figures 3H,I**). The most represented component of ECM was fibronectin, and laminin was the second most represented component. Type I collagen was obviously not the major type of collagen produced by these cells

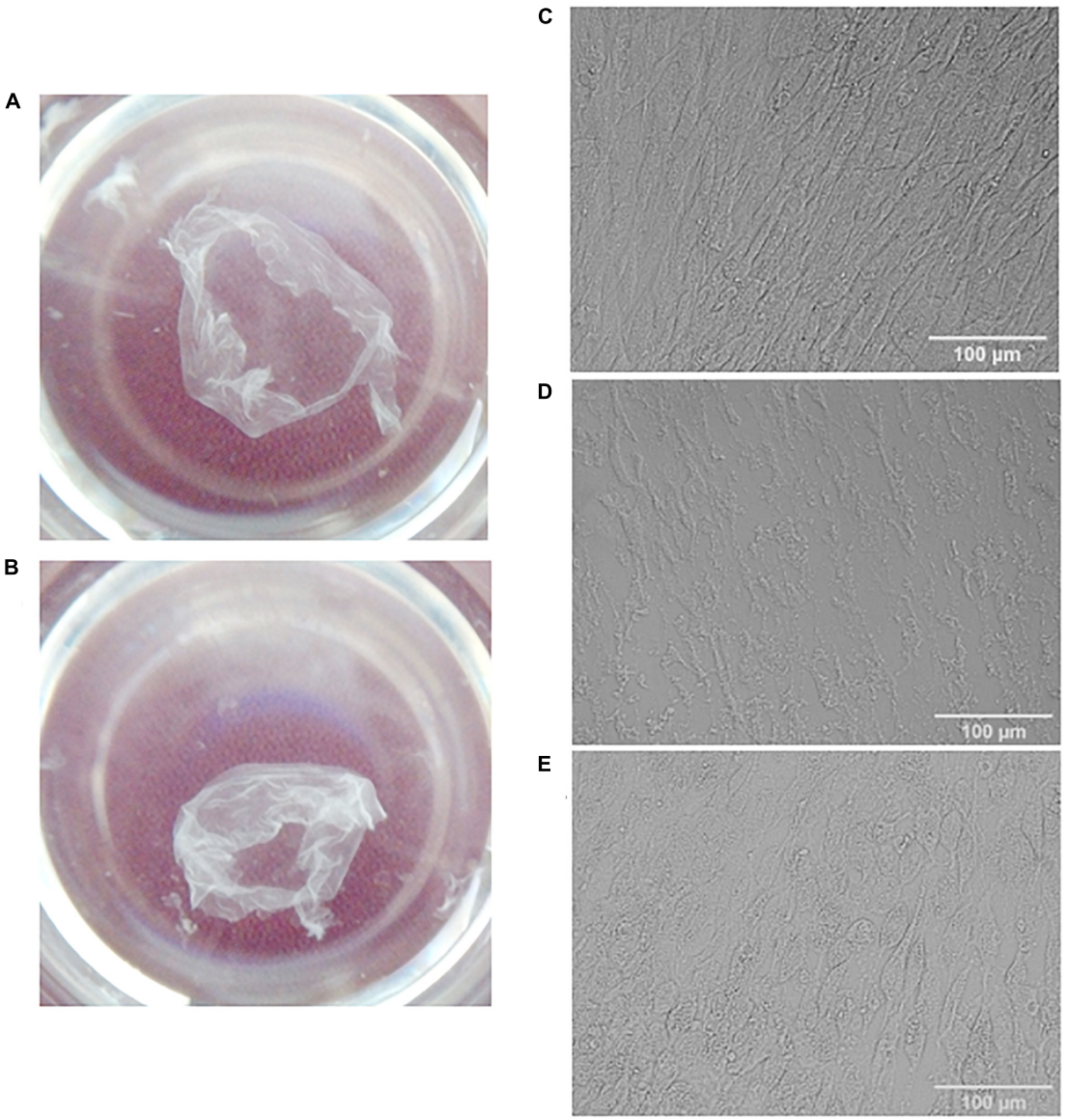


FIGURE 1 | Visualization of MSC cell sheets **(A,C)** and decellularized cell sheets **(B,D,E)**. General view **(A,B)** and representative microphotographs of a cell sheet **(C)**, dECM prepared with sodium deoxycholate and DNAse I treatment **(D)** or with additional pre-incubation with rotenone **(E)**. Pictures were obtained using differential interference contrast (DIC) microscopy (objective magnification, ×10).

in this approach, but its amount also increased relative to the total protein after decellularization.

The microstructure of dECM was also studied using scanning electron microscopy (SEM) and two-photon laser microscopy. Decellularization of hTERT-MSCs cell sheets with sodium deoxycholate led to the destruction of protein network and mesh-like structure of ECM (**Figure 1D** and **Supplementary Figures S3D,I**). In contrast, preincubation with CHAPS for 10 min resulted to the better preservation of ECM (**Supplementary Figures S2B,G**), whereas a shorter preincubation for 3 min had kept the efficiency of decellularization (**Figures 4B,D,F**) and allowed to get a tight dimensional array with a scattered ECM cell debris and matrix-bounded vesicles (**Figures 4D,F**).

Two-photon laser microscopy allows to find out whether fibrillar proteins such as type I and II collagens are present in ECM. However, comparison of cell sheets and dECM using two-photon laser microscopy did not reveal the presence of any fibrillar proteins nor in hTERT-MSCs cell sheets, neither in dECM (**Figures 4G,H**).

To evaluate the proliferation and adhesion rate of hTERT-MSCs seeded on dECM, cells were placed in the Incucyte ZOOM system. Time-lapsed shooting showed that hTERT-MSCs adhered

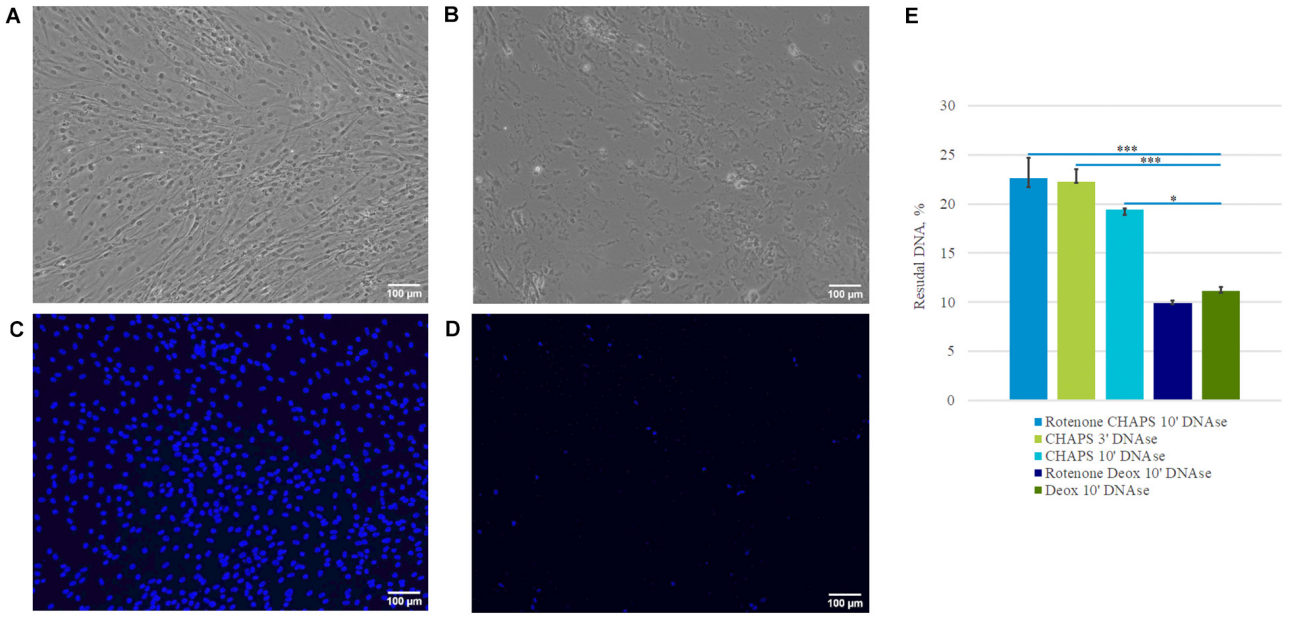


FIGURE 2 | Effectiveness of decellularization accessed by the percentage of residual DNA. Representative microphotographs of a cell sheet **(A,C)**, dECM prepared with CHAPS and DNAse I treatment **(B,D)**. Pictures were obtained using phase-contrast **(A,B)** and fluorescence microscopy **(C,D)** – (blue is DAPI) (objective magnification, ×10). Examination of DNA content in dECM prepared by different methods was performed using PicoGreen assay and normalized to DNA content in the cell sheets **(E)**. The quantitative data are represented as median (25%, 75%), *(p value < 0.05), ***(p value < 0.0005).

to dECM surface and proliferated during the entire period of the experiment. MTT test was performed to quantify hTERT-MSCs proliferation rate. We found significantly higher hTERT-MSCs proliferation activity if cultured on dECM obtained with CHAPS + DNAse I treatment comparing to other protocols (**Figure 5**). Taken together, prepared hTERT-MSCs-produced dECM is a biocompatible and non-cytotoxic material, which can maintain cell survival and proliferation. The protocol included the treatment with 0.5% CHAPS for 3 min with the following incubation with DNAse I was selected as the preferable decellularization method for MSC cell sheets and then was used in further research.

dECM Modulate the Differentiation of THP-1 to Macrophages

Since none of the existing methods of decellularization provides complete DNA removal from the sample, there is an opportunity of potential immunogenicity of the residual DNA *in vivo*.

To test immunogenic properties of dECM, we used the monocytes to macrophages differentiation *in vitro* model. As monocytes we used THP-1 cell line which represents human promonocytes cells. We cultured THP-1 on plastic or dECM during a week with or without 50 ng/ml PMA. To evaluate the macrophage activation, the levels of pro-inflammatory and anti-inflammatory cytokines in the cell-conditioned medium were analyzed using ELISA for the determination of IL-6, IL-8, IL-10, IL-12, and MCP-1.

Phorbol-12-myristate-13-acetate stimulation led to the activation of THP-1, attachment of cell suspension to plastic/dECM surface and spreading which are typical signs of macrophage differentiation. Respectively, we observed the increased level of pro-inflammatory cytokines in conditioned media such as IL-6 (465.7 pkg/ml), MCP-1 (7.6 ng/ml), and IL-8 (1.5 µg/ml). We observed low levels of secreted IL-10 which correlates with classical pro-inflammatory macrophage polarization.

Decellularized ECM itself did not stimulate THP-1 activation and differentiation as followed from cellular morphology and low levels of secreted factors [IL-6 (6 pkg/ml), IL-8 (242.7–452.3 pkg/ml), MCP-1 (85–112 pkg/ml)], IL-10 (no secretion was observed), and IL-12 (no secretion was observed). At the same time, macrophages cultured on dECM with PMA secreted 2.8-times less MCP-1 and 1.4-times less IL-6 than macrophages cultured on plastic in the presence of PMA (**Figure 6**).

Thus, the stimulation of THP-1 by PMA resulted in differentiation toward classically activated macrophages M1. The investigated dECM did not stimulate macrophage differentiation and even reduced the concentration of pro-inflammatory factors in conditioned media. We concluded the absence of immunogenicity of dECM in our model. The decrease of IL-6 and MCP-1 secretion during cultivation of macrophages on dECM may consider as an anti-inflammatory effect, although this statement requires further investigations.

Evaluation of dECM Influence on the Colony Formation and Stemness Maintenance

We tested the ability of dECM to stimulate the formation of colonies by multipotent hMSCs comparing to cultural plastic in CFU assay. hMSCs were seeded on plastic or dECM and

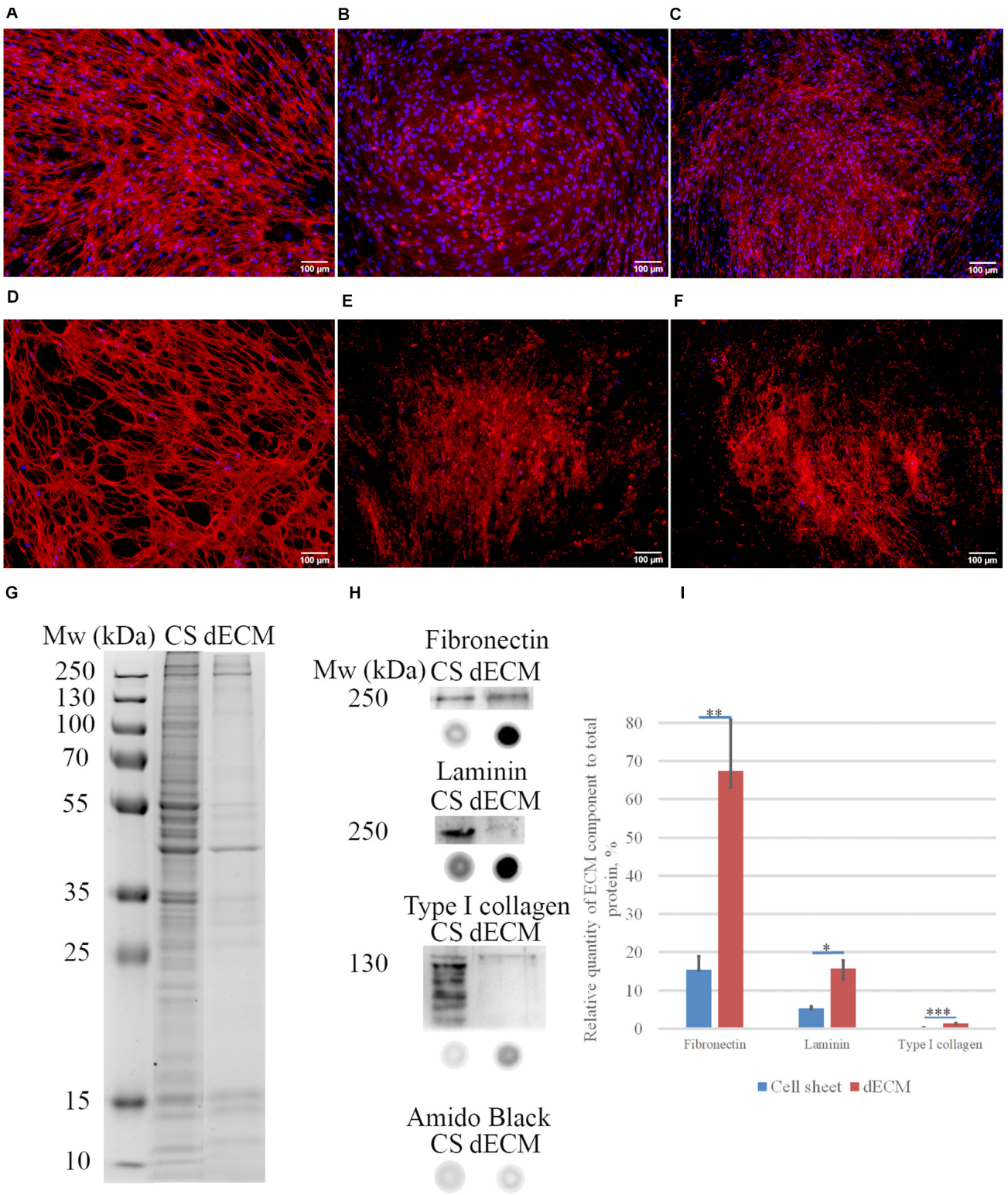


FIGURE 3 | Expression of ECM proteins [fibronectin **(A,D)**, laminin **(B,E)**, type I collagen **(C,F)**] in MSC cell sheets and dECM evaluated by immunohistochemistry without permeabilization (objective magnification, ×10). Control immunostaining with isotype IgG is presented in **Supplementary Figure S4**. Silverstain analysis of electrophoretically separated proteins in cell sheet (CS) and dECM **(G)**. Immunoblot analysis of total fibronectin, total laminin and type I collagen expression levels in CS and dECM **(H)**. Also, dot-blot results performed **(H)**, and data analysis of quantity expression is shown **(I)**. The quantitative data are represented as median (25%, 75%), *(p value < 0.05), **(p value < 0.005), ***(p value < 0.0005).

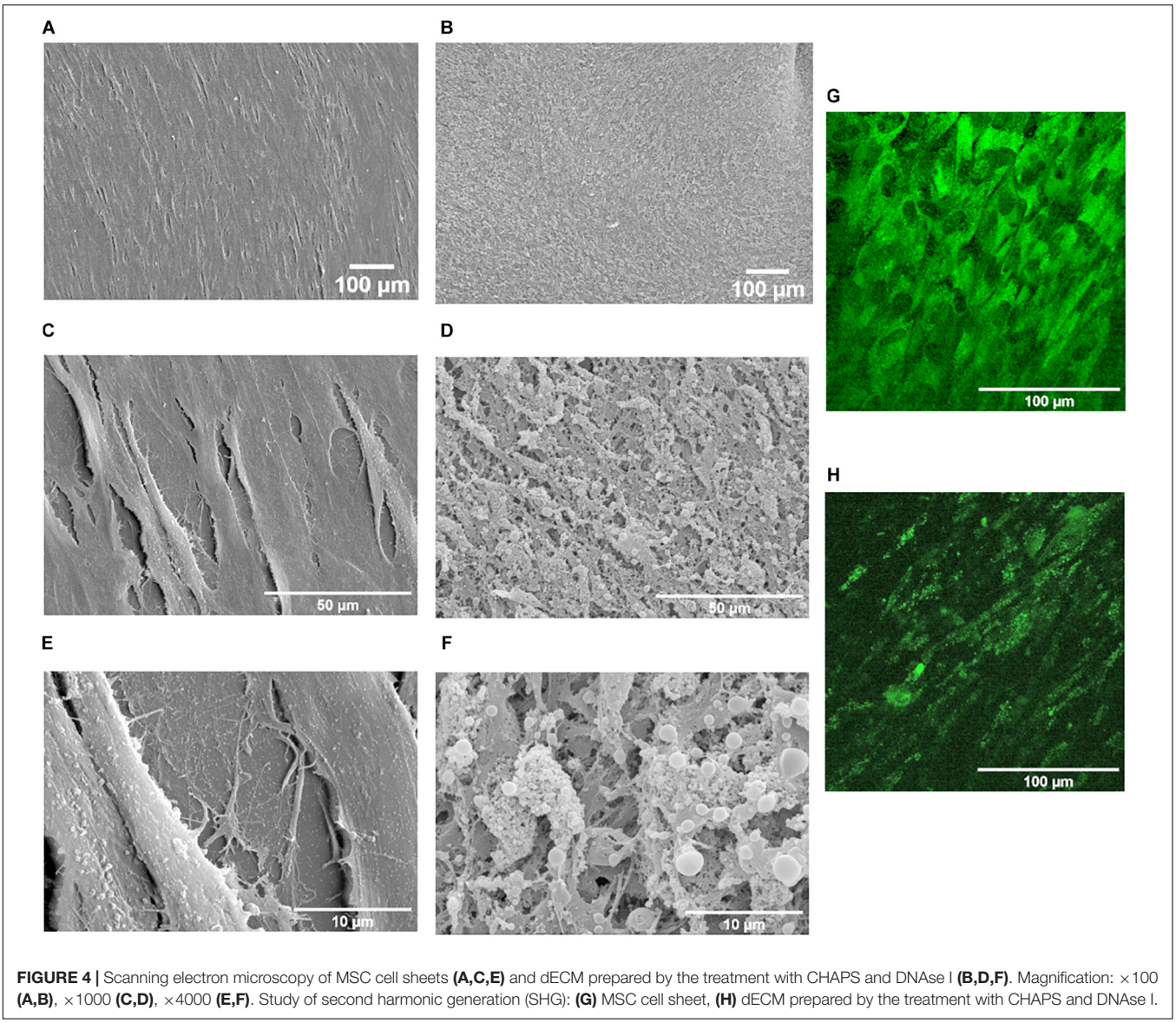


FIGURE 4 | Scanning electron microscopy of MSC cell sheets **(A,C,E)** and dECM prepared by the treatment with CHAPS and DNAse I **(B,D,F)**. Magnification: ×100 **(A,B)**, ×1000 **(C,D)**, ×4000 **(E,F)**. Study of second harmonic generation (SHG): **(G)** MSC cell sheet, **(H)** dECM prepared by the treatment with CHAPS and DNAse I.

after 10 days of cultivation we evaluated the number of formed colonies. CFU assay showed that the number of clonogenic precursors were comparable in both cases (we observed 3% CFU on plastic vs 2.5% CFU on dECM), although it should be noted that the size of a single colony was significantly larger if hMSCs were cultured on dECM (**Figures 7A,B,C**). To exclude the influence of cell adhesion, a thorough analysis of cell morphology (**Figures 7D–I**) was performed, and it was shown that despite the larger area of colonies on the dECM, the area of each cell individually did not increase (**Figure 7F**). On the contrary, the area of cells on plastic was statistically significantly larger, although the number of cells was smaller (**Figures 7F,I**). It is likely that the native matrix formed by the cells themselves provides a division-friendly geometric and functional substrate for cell growth. Analysis of mRNA level of pluripotency genes (*NANOG, OCT4, SOX2*) in hMSCs did not show any substantial differences between plastic and dECM, however, *SOX2* expression was slightly increased in hMSCs cultured on dECM (**Figures 7J,K,L**). Thus, hTERT-MSCs-produced dECM does not significantly affect the number of stem cells and expression of pluripotency genes supporting "stemness" of cultured cells. However, it probably promotes active proliferation even at the level of a single progenitor cell.

dECM Stimulates Inducible Differentiation of Primary MSCs

MSCs derived from adipose tissue represent heterogenic cell population with a number of multipotent cells capable to be induced to differentiate into adipocytes, osteocytes and chondrocytes. This property underlies some of the regenerative effects of MSCs *in vivo*. We tested the ability of dECM to modulate induced differentiation of these cells into the adipogenic and osteogenic lineages *in vitro* to evaluate a possible

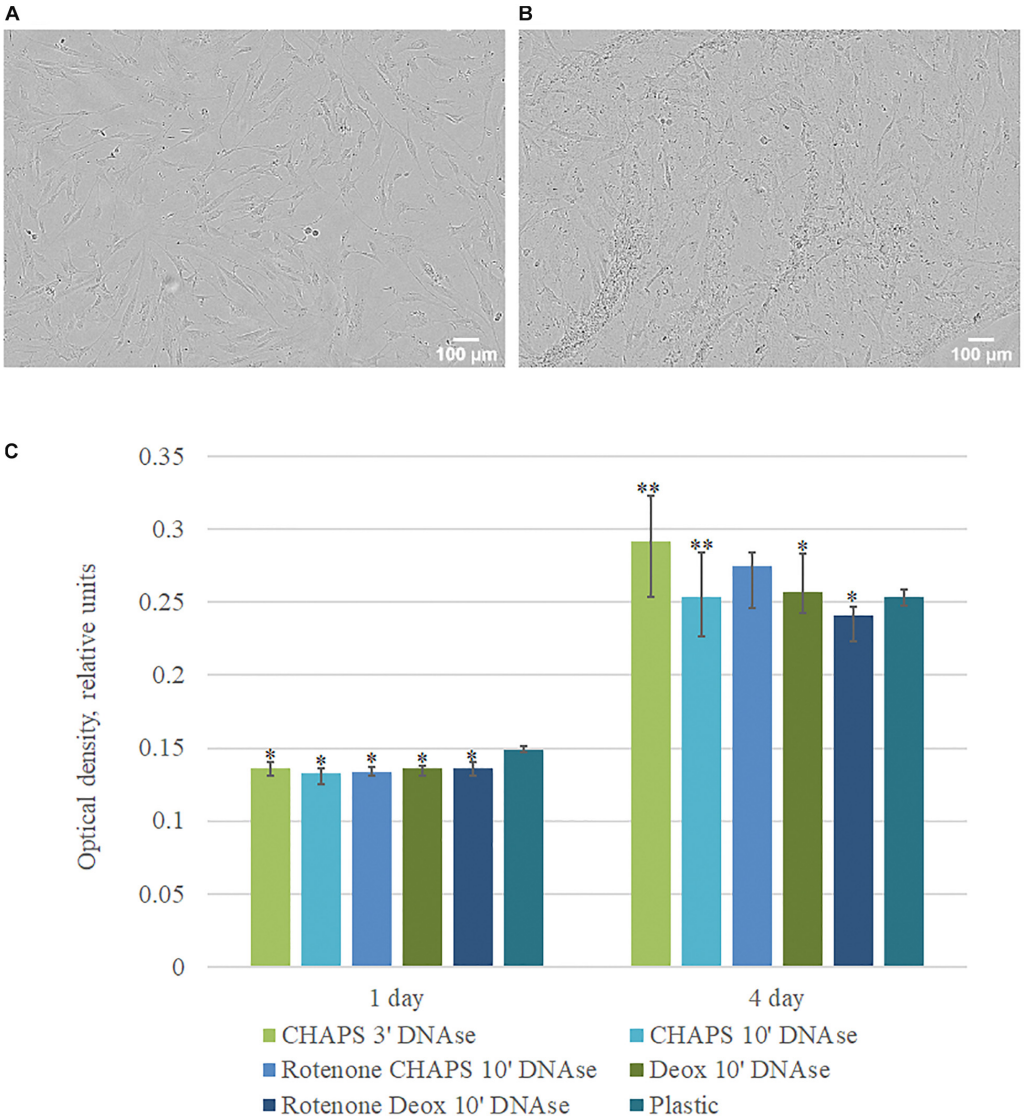


FIGURE 5 | Proliferation activity of hMSCs cultured on plastic and dECM. **(A,B)** Representative microphotographs of hMSCs cultured on plastic **(A)** and dECM **(B)** for 4 days (phase contrast, objective magnification – ×10), **(C)** MTT assay of hMSCs cultured on plastic and dECM for 1 and 4 days. The quantitative data are represented as median (25%, 75%). Significant differences marked by *(p value < 0.05), **(p value < 0.005) compared to cells cultured on plastic.

role of MSC-produced ECM in this process. hMSCs were cultured on dECM derived from hTERT-MSCs or fibroblasts, or on plastic covered with type I collagen, fibronectin or uncovered for 10 days under inductive conditions and then were stained with OilRed for adipocytes and Alizarin Red for osteocytes (**Figures 9**, **10**). We observed that dECM derived from hTERT-MSCs significantly accelerated both adipogenic and osteogenic differentiation of hMSCs compared with the differentiation of cells cultured in different conditions. The difference was detectable even on the 4th day while the greatest differences were observed on the 10th day. At the same moment hMSC cultured on the plastic shown just the first signs of differentiation (**Figures 8A–D, 9, 10**). Differentiation was confirmed by real-time PCR. Although due to the high level of variability, mRNA level of marker genes for adipogenic (*PPARγ*, *ADIPOQ*) and osteogenic (*BGLAP, RUNX2*) differentiation only tended to have higher level in cells cultured on dECM compared to plastic (**Figures 8E–I**). Importantly, we found that dECM effectively promoted differentiation of hMSC into adipogenic and osteogenic lineages within specific induction culture conditions at the very early stages (day 4 after induction of differentiation) compared not only to plastic, but also to plastic covered by selected ECM components (fibronectin, or type I collagen or laminin) presented in dECM (**Figures 9–11**). Interestingly, dECM produced by human fibroblasts and processed using the same protocol couldn't enhanced hMSC differentiation like hTERT-MSCs-produced dECM, indicating cell-specific functionality of dECM.

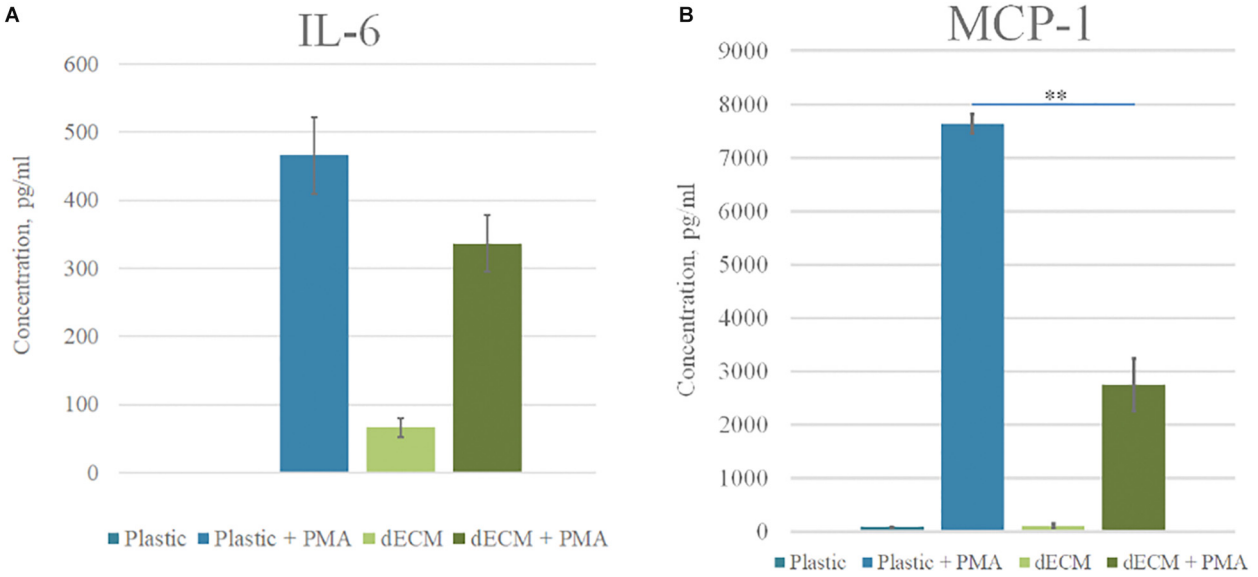


FIGURE 6 | Cytokine profile of monocytes cultured on plastic and dECM. Level of IL-6 **(A)** and MCP-1 **(B)** secreted by monocytes/macrophages with or without PMA treatment measured by ELISA are presented. The quantitative data are represented as median (25%, 75%), **(p value < 0.005).

Attachment to dECM Modulates Specific Cell Signaling Pathways in hMSCs

To reveal the possible mechanisms of the observed dECM-mediated effects on hMSC differentiation, we analyzed the changes in the intercellular signaling pathways in hMSCs cultured on dECM. The outside-in signals from ECM are transferred due to the interaction of cell surface with chemical ECM components (mainly by integrins) as well as by the sensing of ECM stiffness, fiber orientation or other mechanical forces by cells. To check if hMSCs were able to form contacts with dECM via integrins and sense mechanical characteristics of their microenvironment, we analyzed the activation of key signaling pathways in hMSCs after the culture on plastic or dECM by immunoblotting (**Figure 12**). The phosphorylation level of focal adhesion kinase (FAK) was increased in hMSCs seeded on dECM compared to plastic which indicated the upregulation of integrin signaling due to binding of cell surface integrins to ECM proteins and confirmed the functionality of prepared dECM. Moreover, we observed the increase of downstream FAK target phosphorylation like ERK 1/2 (p42/p44) after attaching of hMSCs to dECM. Hippo effectors YAP/TAZ are known as on–off mechanosensing switches for ECM, so we examined pYAP and YAP expression in hMSCs and found the slight elevation of both protein forms in cells cultured on dECM. On the other hand, interplay between hMSCs differentiation and adhesion may be mediated by b-catenin signaling (Takada et al., 2009). We observed the reduction of active β-catenin level in nuclear fraction of hMSCs on dECM compared to cells cultured to plastic (**Figure 11**). This may be a result of increased recruitment of b-catenin to the forming cell–matrix contacts which are known to compete with nuclear factors for β-catenin (Brembeck et al., 2004).

dECM Supports hMSC Differentiation Through Src-PI3K-AKT-Dependent Cell Signaling Pathway

Despite the fact that our preliminary results demonstrated the classical activation of the ERK signaling cascade for cell interaction with ECM (Mecham, 2011), the Src-PI3K-AKT signaling pathway was revealed to be critical for rapid activation of differentiation on dECM (**Figure 13 Supplementary Figure S7**). First, the cells that were cultured on dECM were extremely sensitive to the Src inhibitor. This was manifested in a strong change of the morphology of cells and in formation of spheroid-like structures. A similar process was observed during inhibition of FAK of ectomesenchymal multipotent stem cells when in cell culture dishes coated with poly-L-lysine (Beck et al., 2014). In the presence of Src inhibitor the ability of dECM to promote hMSC differentiation significantly decreased (**Figure 13**). At the same time, the addition of MEK and DBN inhibitors did not in have any effect on the phenomena we observed. As for the Acti inhibitor, it did not change the cell morphology, but it did inhibit the dECM-mediated stimulation of hMSC differentiation, which we observed earlier. PI3K/Akt signaling is a key pathway required for human MSC osteogenesis (Baker et al., 2015). These facts suggest that the Src-PI3K-AKT signaling pathway plays an important role in stimulating cell differentiation in the activated microenvironment.

Interaction of hMSCs With dECM via Integrins May Modulate Cell Differentiation

Considering the significant activation of pFAK/FAK signaling pathway in hMSCs cultured on dECM we evaluated the impact

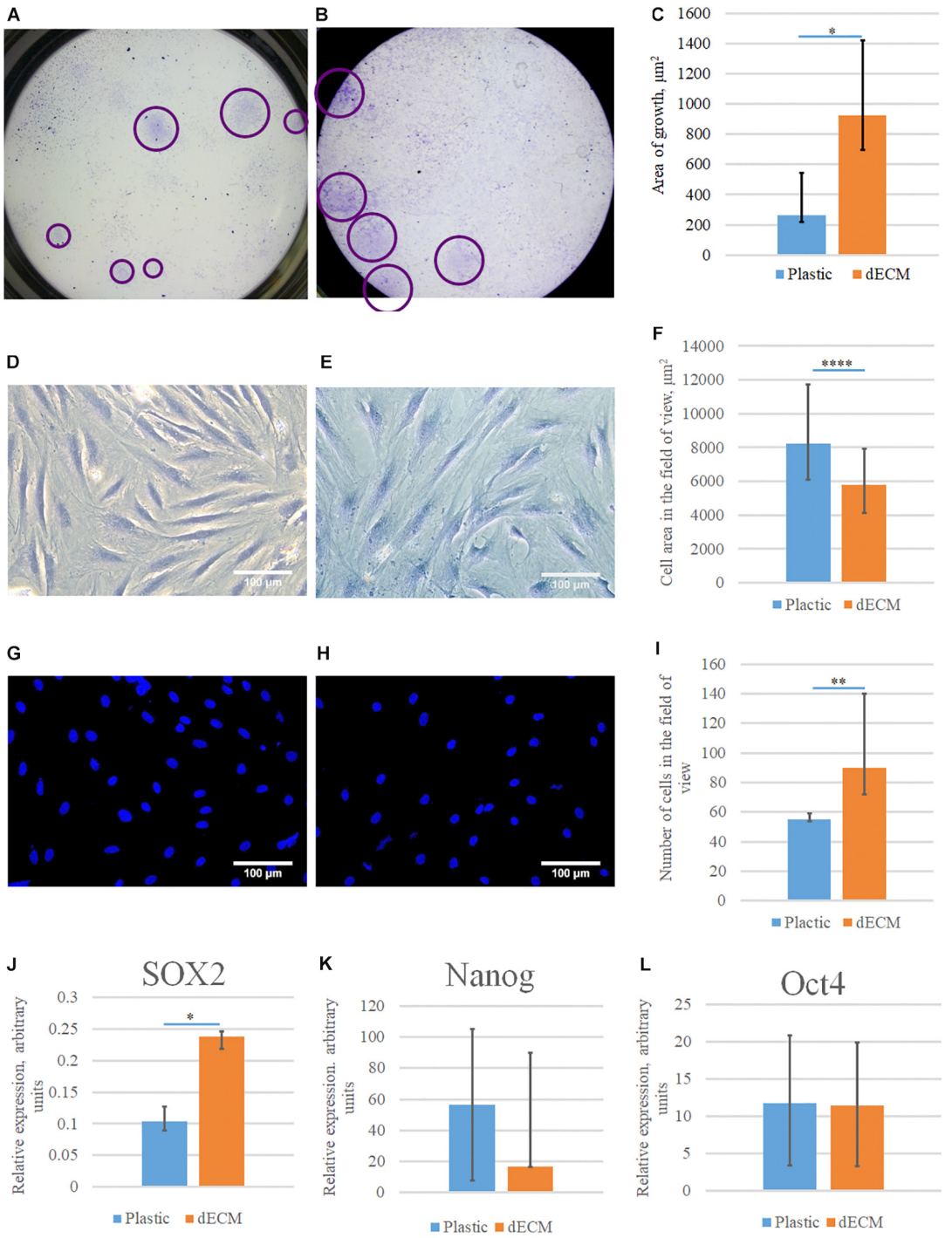


FIGURE 7 | Evaluation of the colony formation and stemness maintenance of hMSCs cultured on plastic or dECM. CFU-F assay was performed for hMSCs cultured on plastic **(A,D,G)** or dECM **(B,E,H)**, quantification of differences between cell colony sizes, cell area in field of view or number of cells in the field of view are demonstrated on diagrams **(C,F,I)**. Relative expression of pluripotency genes *SOX2* **(J)**, *NANOG* **(K)**, and *POU5F1* (Oct4) **(L)** in hMSCs measured by real-time PCR normalized to housekeeping gene (RPLP0). The quantitative data are represented as median (25%, 75%), *(p value < 0.05), **(p value < 0.005), ****(p value < 0.0001).

of integrin-mediated interactions into the stimulation of hMSCs differentiation. We observed the expression of the wide range of integrin genes including α2, α3, α4, α5, αV, α6, α8, β1, β4, β5, β7 subunits in hMSCs (**Figure 14A**), although we didn't find any significant differences between mRNA levels of these genes in hMSCs cultured on plastic vs dECM, except the

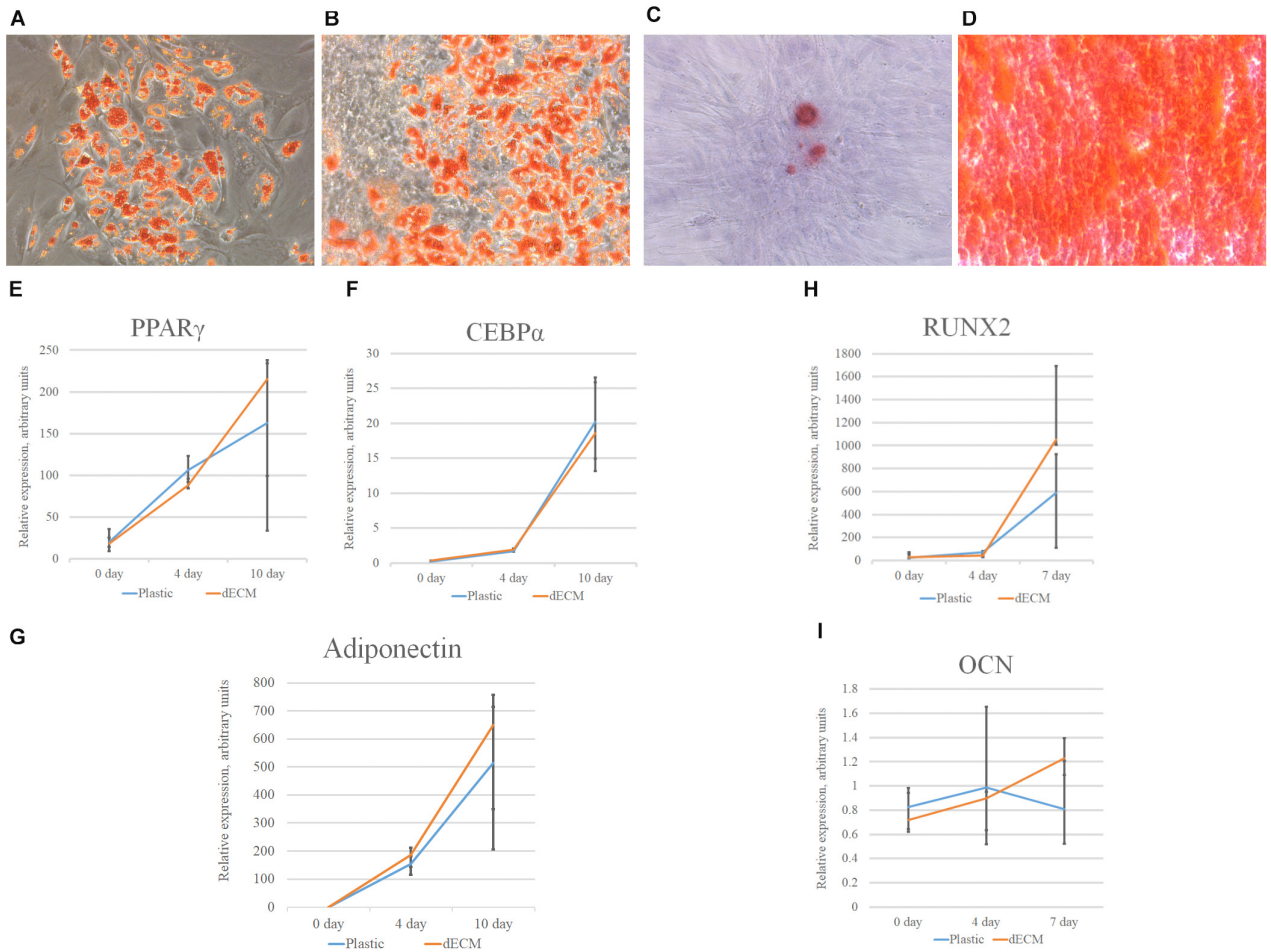


FIGURE 8 | Induction of adipogenic and osteogenic differentiation of hMSCs cultured on plastic **(A,C)** or dECM **(B,D)** for 10 days assessed by cytochemical staining with Oil Red **(A,B)** or Alizarin Red **(C,D)** and expression of adipogenic [PPARγ(*PPARG*) **(E)**, CEBPα(*CEBPA*) **(F)**, adiponectin (*ADIPOQ*) **(G)**] or osteogenic [*RUNX2* **(H)**, osteocalcin(*OCN*) **(I)**] differentiation markers measured by real-time PCR normalized to housekeeping gene (RPLP0). Objective magnification, ×10. The quantitative data are represented as median (25%, 75%).

expression of α2 and β7 subunits which was slightly higher in hMSC cultured on dECM. High expression level was observed for *ITGAV, ITGA8, ITGB1* and *ITGB5*, while we confirmed β1 subunit expression on hMSCs using immunohistochemical analysis (**Figures 14B,C**). Possible combinations of αVβ1, αVβ5, α8β1 probably play important role in interaction of heterogeneous hMSCs population with ECM components such as fibronectin and vitronectin which in most cases involves RGD sequence. To evaluate the impact of this type of cell-ECM interaction, we blocked it with RGD-peptide, which prevents binding of integrins to RGD-containing ECM proteins, during the induction of adipogenic or osteogenic differentiation. The optimal concentration of RGD peptide was selected based on the preliminary experiments when ability of RGD concentration to prevent adherence for 4 days. We also confirmed that addition of RGD peptide couldn't activate pFAK/FAK signaling pathway in hMSCs by contrast with attachment to fibronectin (**Figure 14D**). Importantly, in the presence of RGD peptide the expression of the master-gene for adipogenic differentiation *PPARγ* and *CEBPα* significantly inhibited on the 4th day after the differentiation induction (**Figures 14E,F**). Correspondingly, the addition of RGD peptide during the induction of osteogenic differentiation significantly decreased mRNA level of *RUNX2*, which is considered as master-gene of this process and was markedly induced by induction medium (**Figure 14G**), while the level of *BGLAP* as well as *ADIPOQ* mRNA did not change (data not shown) in hMSC cultured on dECM during osteogenic and adipogenic differentiation, respectively.

DISCUSSION

The rapid development of cell-based technologies leads to the transition from artificial biomaterials to modulation of regenerative processes involving organism endogenous resources and mimicking the natural healing processes. One of the perspective approaches is a reconstitution of cellular microenvironment, or niche. Niche is a specialized

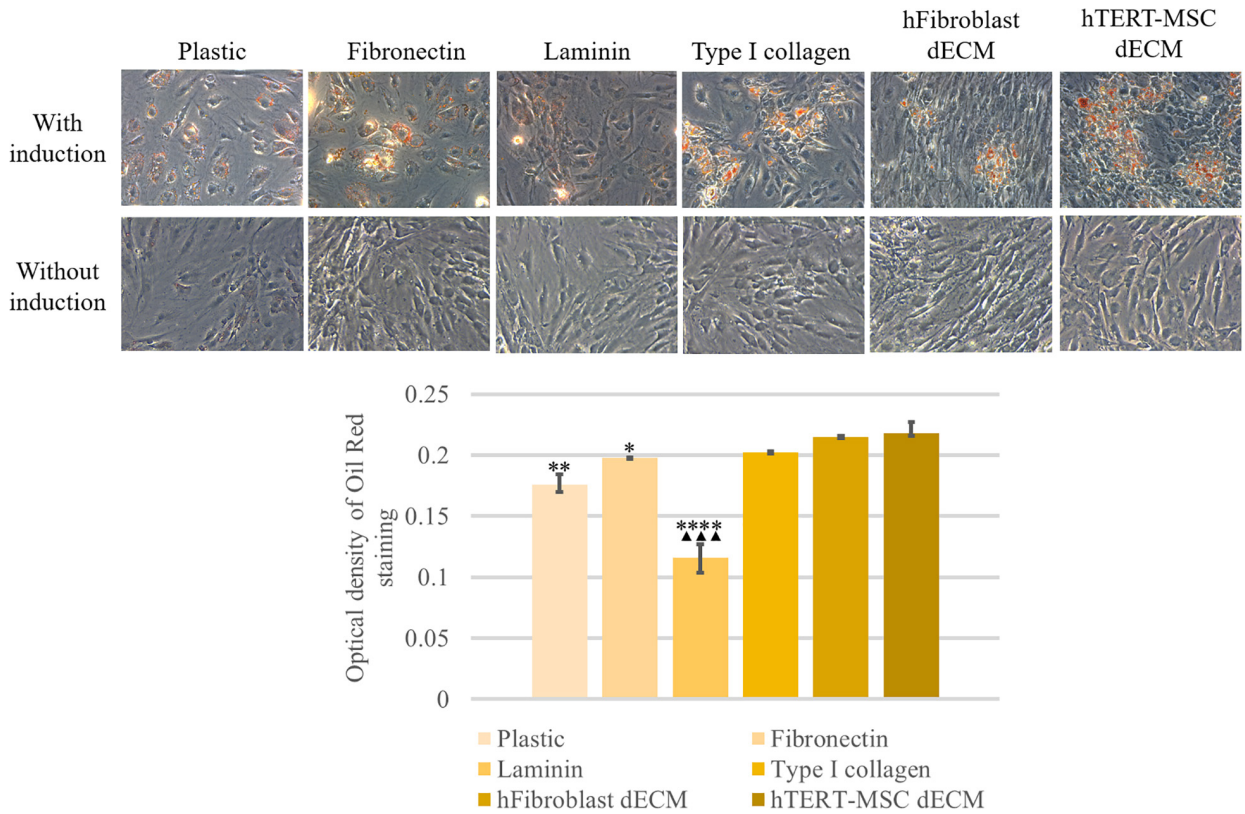


FIGURE 9 | Induction of adipogenic differentiation of hMSCs cultured on plastic, plastic covered by fibronectin, or laminin, or type I collagen and dECM produced by human fibroblasts or MSCs for 4 days assessed by histological staining with Oil Red. Objective magnification, ×20. The dye was extracted, and Oil Red O staining was quantified by measuring the optical density at 530 nm **(lower panel)** ($n = 4$). The quantitative data are represented as median (25%, 75%), *(p value < 0.05), **(p value < 0.005), ****(p value < 0.0001) compared to cells cultured on hTERT-MSC dECM and ▲▲▲(p value < 0.0005) compared to cells cultured on hFibroblast dECM.

cell microenvironment which refers to the extrinsic physical and functional factors that feedback to mediate cell behavior (Schofield, 1978). Only being in the specific niche a cell can retain its properties (Nimiritsky et al., 2018; Andreotti et al., 2019; Pastuła and Marcinkiewicz, 2019; Lee et al., 2020). Tissue damage leads to the disturbing of niches, which can be the reason why tissue or organ cannot recover completely. Many approaches are aimed to creating a biomaterial similar to the natural microenvironment (Donnelly et al., 2018; Hagbard et al., 2018; Thomas et al., 2018; Shrestha and Yoo, 2019). The difficulty lies in the selection of niche components that could be crucial for reconstruction of naïve microenvironment. Thus, ECM is an important niche component in regulation of cell behavior, including cell adhesion, proliferation and differentiation (Cramer and Badylak, 2019; Padhi and Nain, 2020). The effects of selected ECM components may depend on their molecular weight (Garantziotis and Savani, 2019; Wahart et al., 2019) and tissue specificity (Smith and Gerecht, 2018; Padhi and Nain, 2020).

The development and application of dECM matrices, prepared both by decellularization of tissues or whole organs and cell-based constructs, has grown rapidly in the fields of cell biology, tissue engineering and regenerative medicine in recent years (Hoshiba, 2017; Rana et al., 2017; Shakouri-Motlagh et al., 2017; Parmaksiz et al., 2020; Riis et al., 2020; Sart et al., 2020). The source of cells producing ECM is of great importance for realizing its functional role (Cramer and Badylak, 2019). Among other cell types MSCs represent a promising source of multipotent adult stem and progenitor cells for cell therapy and tissue engineering (Lukomska et al., 2019; Gomez-Salazar et al., 2020). They play an important role in maintenance of hematopoietic stem cell niche and are considered as a critical stem cell niche component in different tissues (Kfoury and Scadden, 2015). Accumulating evidence indicated that MSC regenerative effects are mostly mediated by their ability to produce a wide range of bioactive molecules such as growth factors (Chen et al., 2019; Dilogo and Fiolin, 2019; Seetharaman and Srivastava, 2019) and cytokines (Selich et al., 2019), extracellular vesicles (Keshtkar et al., 2018; Gowen et al., 2020) as well as ECM components (Kalinina et al., 2015; Ragelle et al., 2017; Rolandsson Enes et al., 2017; Devaud et al., 2018). Extracellular matrix production by MSCs is enhanced if cells are cultured as cell sheets which can be used as cell-derived matrices after decellularization. MSC-produced dECM has recently emerged as a promising substrate for the improved expansion of different cells (Chen et al., 2007; Lai et al., 2010; Ng et al., 2014; Wu et al., 2016). It was

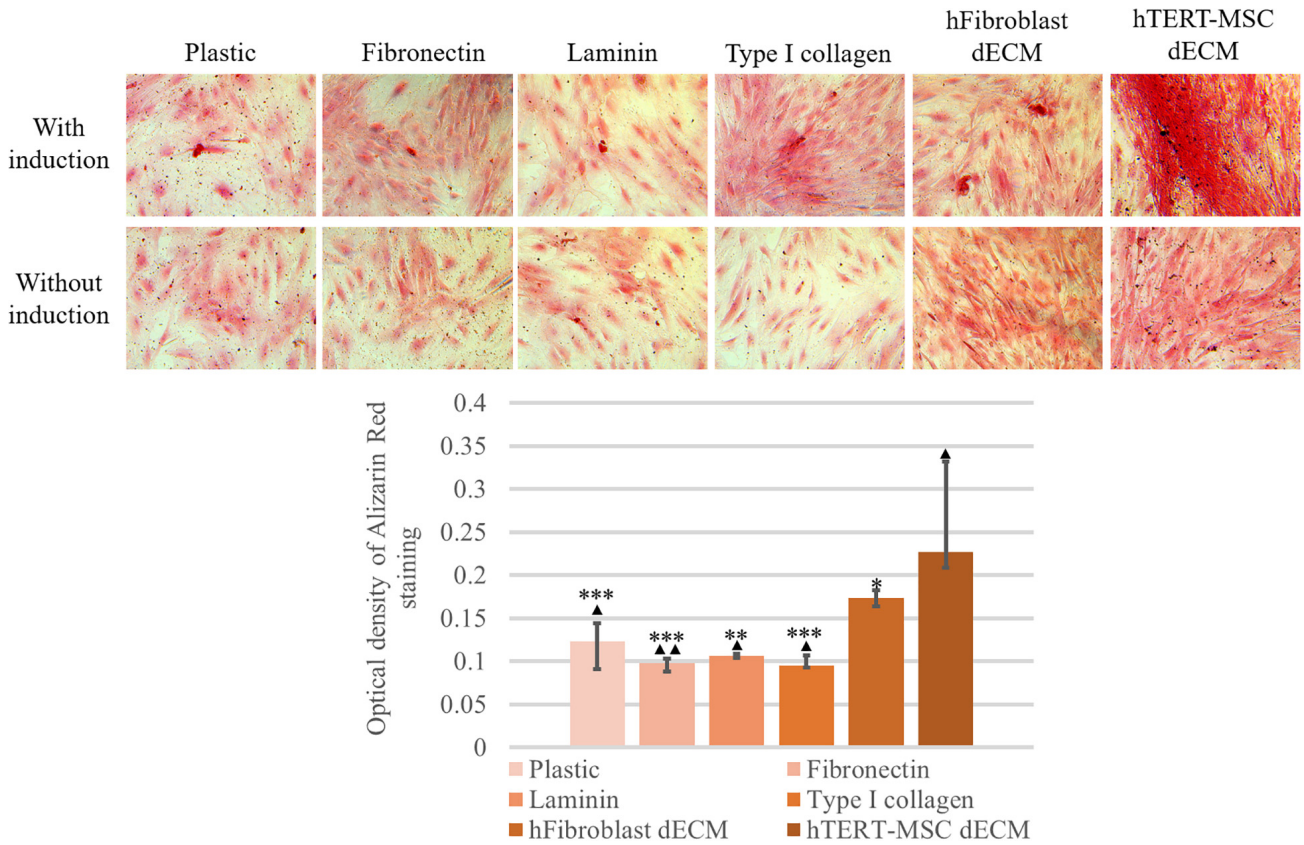


FIGURE 10 | Induction of osteogenic differentiation of hMSCs cultured on plastic, plastic covered by fibronectin, or laminin, or type I collagen and dECM produced by human fibroblasts or MSCs for 4 days assessed by histological staining with Alizarin Red. Objective magnification, ×20. The dye was extracted, and Alizarin Red staining was quantified by measuring the optical density at 560 nm **(lower panel)** ($n = 6$). The quantitative data are represented as median (25%, 75%), *(p value < 0.05), **(p value < 0.005), ***(p value < 0.0005) compared to cells cultured on hTERT-MSC dECM and ▲(p value < 0.05), ▲▲(p value < 0.005) compared to cells cultured on hFibroblast dECM.

shown that MSCs cultured on these surfaces exhibited improved proliferation capacity, maintenance of phenotype, and increased differentiation potential (Shakouri-Motlagh et al., 2017; Sart et al., 2020). However, the mechanisms of these effects remained to be poor understood.

In the current study we have tested several agents for decellularization of hTERT-MSCs cell sheets (detergents, enzymes, apoptosis inductors). It should be noted that cellular sheets as structures do not have such a potent ECM as in the formed organs, it is necessary to carefully select the agents for decellularization to preserve the functional biologically active substances and to form the more correct model of cell microenvironment *in vitro* (Gilpin and Yang, 2017). Our experimental findings allowed to select the optimized protocol of hTERT-MSCs cell sheet decellularization using the combination of brief incubation with CHAPS and the following DNAse I treatment with high efficiency of DNA removal and preservation of ECM proteins, including fibronectin, type I collagen and laminin. We did not reveal the presence of fibrillar proteins in native cell sheets or in dECM by two-photon microscopy. However, according to other authors, fibrillar proteins could be found in the cell layers produced by the primary isolated bone marrow and adipose tissue-derived MSCs (Marinkovic et al., 2016) which might be explained by methodological differences.

Residual DNA in dECM may be immunogenic for cell culture or cause immune response when injected *in vivo*. However, in our study prepared dECM did not stimulate THP-1 macrophage differentiation which was evaluated by cell attachment to the substrate and specific cytokine profile.

The maintenance of stemness is one of the crucial functions of stem cell niche. As MSCs are involved in niche functioning *in vivo* it is important to understand if they perform this particularly via production and organization of ECM. We tested this hypothesis by analyzing the expression of pluripotency genes (*NANOG, OCT4, SOX2*) in hMSCs and colonies formed by multipotent cells within heterogeneous population of hMSCs cultured on plastic or dECM in CFU assay. Interestingly, we revealed that not the number of colonies, but their average size increased if hMSCs were cultured on dECM, and these findings were confirmed by the data obtained by others (Rao Pattabhi et al., 2014). Correspondingly, there were no substantial differences between hMSCs cultured on plastic or dECM in pluripotency

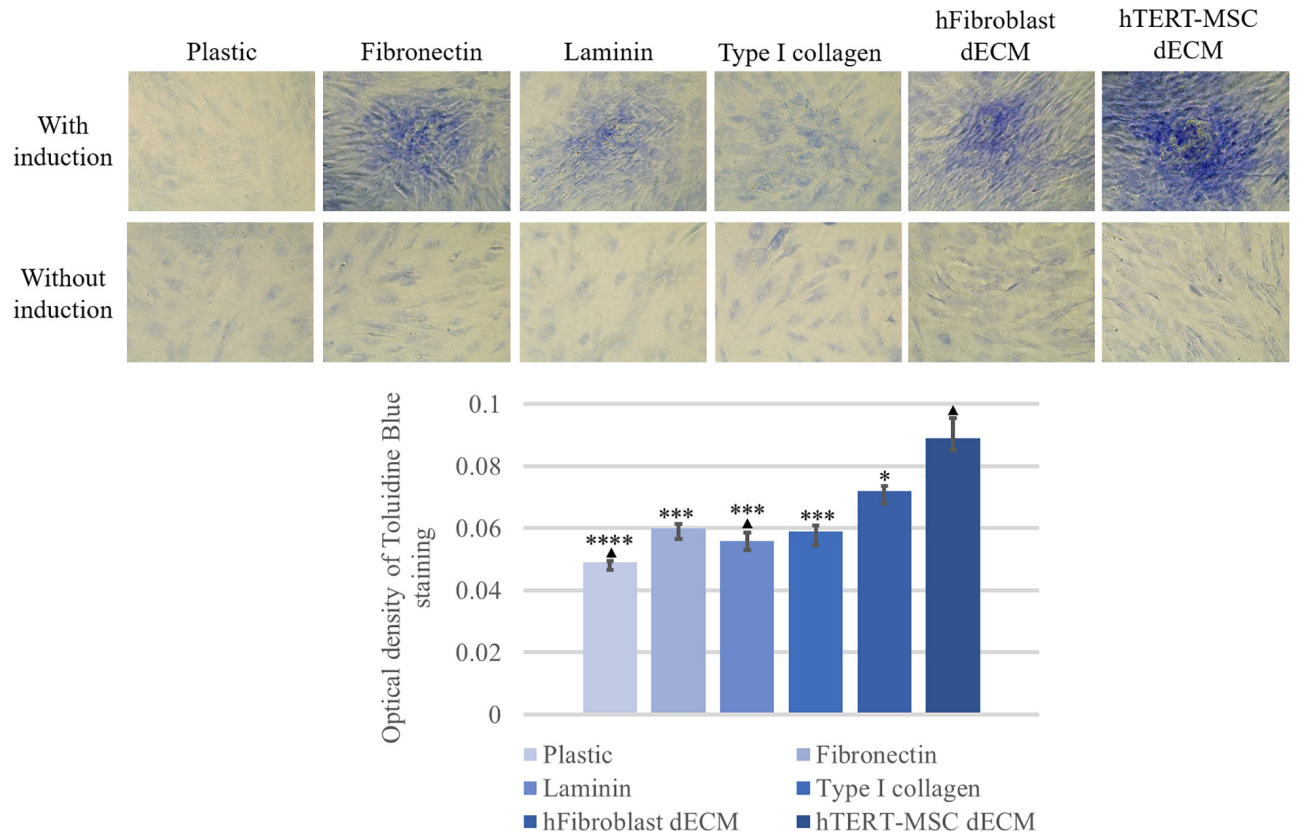


FIGURE 11 | Induction of chondrogenic differentiation of hMSCs cultured on plastic, plastic covered by fibronectin, or laminin, or type I collagen and dECM produced by human fibroblasts or MSCs for 4 days assessed by histological staining with Toluidine Blue. Objective magnification, ×20. The dye was extracted, and Toluidine Blue staining was quantified by measuring the optical density at 608 nm **(lower panel)** ($n = 6$). The quantitative data are represented as median (25%, 75%), *(p value < 0.05), ***(p value < 0.0005) compared to cells cultured on hTERT-MSC dECM and ▲(p value < 0.05) compared to cells cultured on hFibroblast dECM.

gene expression, although *SOX2* expression was slightly increased in hMSCs cultured on dECM. Thus, dECM may not improve the number of multipotent cells, but increased significantly clonal expansion of progenitors, and these findings were confirmed by the data obtained by others (Rakian et al., 2015; Ji et al., 2018). We also observed that the proliferative rate of total hMSCs population slightly increased on dECM comparing to plastic, which can be explained by selective stimulation of proliferation of multipotent progenitor cells wherein not the proliferation of differentiated cells.

The development of complex tissues, including various cell types and their spatial organization, depends on a consistent series of decisions about cell fate, which begins with the fertilization of a single cell. Although growth factors are usually regarded as the major extracellular ligands that control these decisions, ECM and intercellular adhesion provide equally important instructions for controlling gene expression and the fate of all cells. Integrins play central role to all these aspects of determining the fate of a cell. They transmit signals into the cell via adhesion complexes, which include several types of specialized cell interaction sites with ECM, including focal complexes, focal adhesions, fibrillar adhesions, and podosomes (Zaidel-Bar et al., 2007). Moreover, they recruit both adapters (such as paxillin, p130Cas, integrin-linked kinase, and guanine nucleotide metabolism factors), as well as enzymes (like protein kinases FAK, Src and Jnk, Rho-family GTPases and lipid kinases) that trigger signaling pathways controlling decisions about cell fate, such as survival, growth, migration, and differentiation (Giancotti and Tarone, 2003; Lo, 2006).

Cell differentiation is a result of certain combinations of transcription factor activity that cause cell type-specific gene expression patterns. Specific inductors can act alone or in complex with integrins as it was described for oligodendrocyte differentiation (Baron et al., 2005). According to our data, hMSCs plated on dECM turn on the integrin-mediated signaling via phosphorylation of FAK and downstream ERK signaling. This type of signals could be considered as pro-survival, pro-mitogenic and contributing to cell differentiation. We observed that hMSCs demonstrated rapid differentiation rate into three different lineages cultured on dECM vs plastic; moreover, this effect exhibited at the very early stages after induction and unlikely related to the differences in stiffness as it was not reproduced for hMSCs cultured on plastic covered by selected single ECM proteins (fibronectin, laminin or type I collagen) and dECM produced by fibroblasts in cell sheets. Using RGD peptide as an inhibitor of interactions between cell integrins and some key

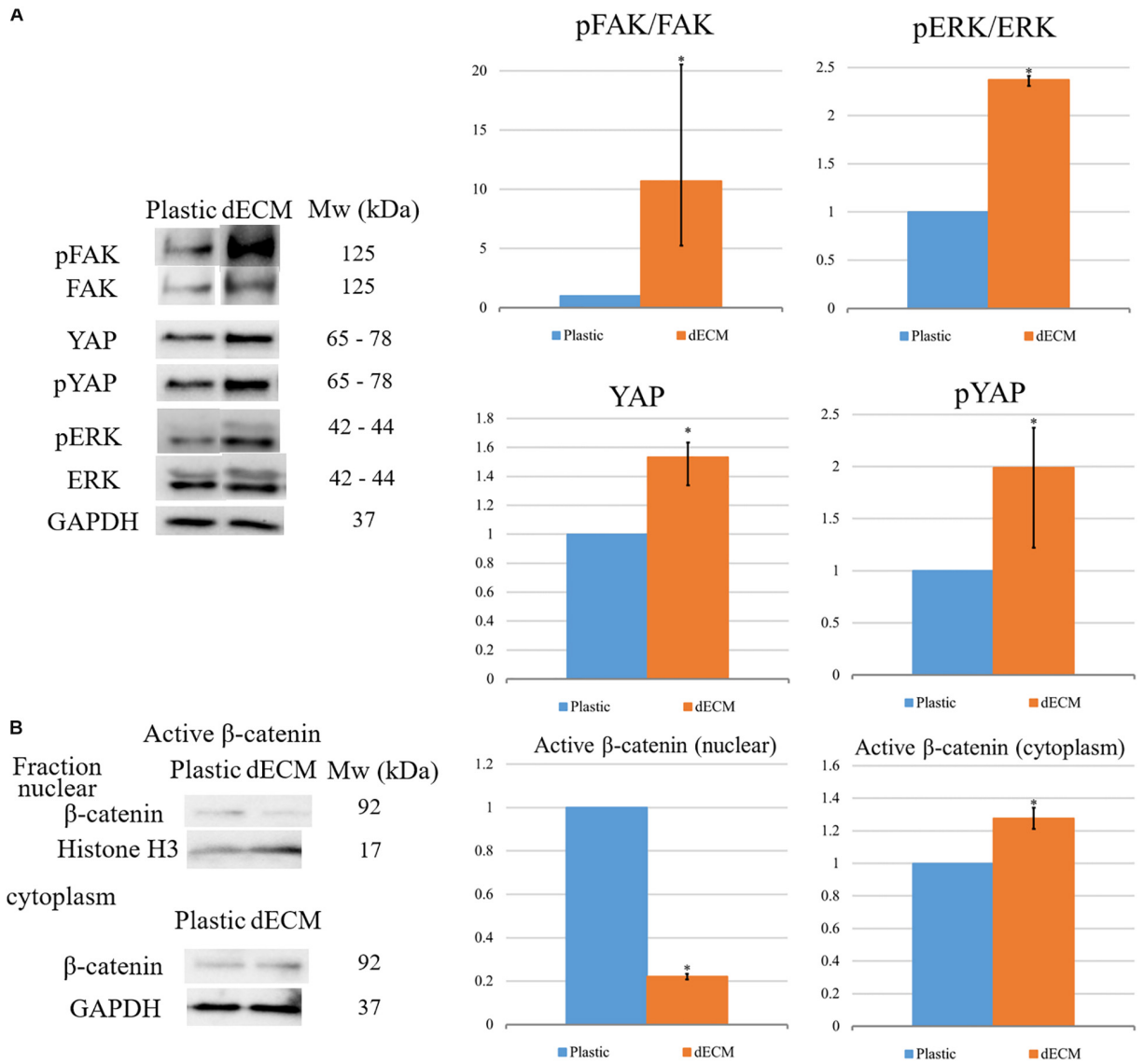


FIGURE 12 | Evaluation of differentiation-related intracellular signaling pathways activation in hMSCs cultured on plastic or dECM in total lysate of samples for targets: **(A)** Evaluation of activation of FAK, ERK, pYAP and YAP. The quantitative data are represented as folds of protein expression in hMSCs cultured on dECM vs. hMSCs cultured on plastic, data are median (25%, 75%), $*p < 0.05$; **(B)** Analysis of distribution of active β-catenin between nucleus and cytoplasm. The quantitative data are represented as folds of protein expression in hMSCs cultured on dECM vs. hMSCs cultured on plastic, data are median (25%, 75%), $*(p$ value $< 0.05)$. Figure shows representative blots, $n = 3$.

ECM proteins, we demonstrated that integrin-mediated signaling significantly contributed to the ability of dECM to support hMSC differentiation. This phenomenon may be partly mediated by the interaction of cells with fibronectin fibers. Soluble fibronectin has been shown to stimulate integrin signaling of cells. However, the presence of a filamentous structure with specific binding sites for ECM components can cause a synergistic effect of integrin signaling and growth factor signaling (Donnelly et al., 2018). When seeded on dECM, hMSCs maintained their phenotype, although in many cell types ERK signaling was induced directly by integrin adhesion (Velling et al., 2008). Probably selective switch-on of integrin-pFAK-pERK signaling in multipotent cells depends on different repertoire of integrins on cell surface comparing to stromal cell fraction. According to other author's data, stem cells may represent wide spectrum of different integrin subunits which participate in maintenance of stemness (Saller et al., 2012). Furthermore, total MSCs population exhibit a lot of integrins on cell surface (Prowse et al., 2010), which correlates with our data on integrin expression by hMSCs. Thus, a multipotent cell may express unique integrins which mediate dECM binding and ERK phosphorylation which lead to increased clonal expansion.

Additionally, we observed an important role of Src-PI3K-AKT signaling pathway in stimulation of MSC differentiation

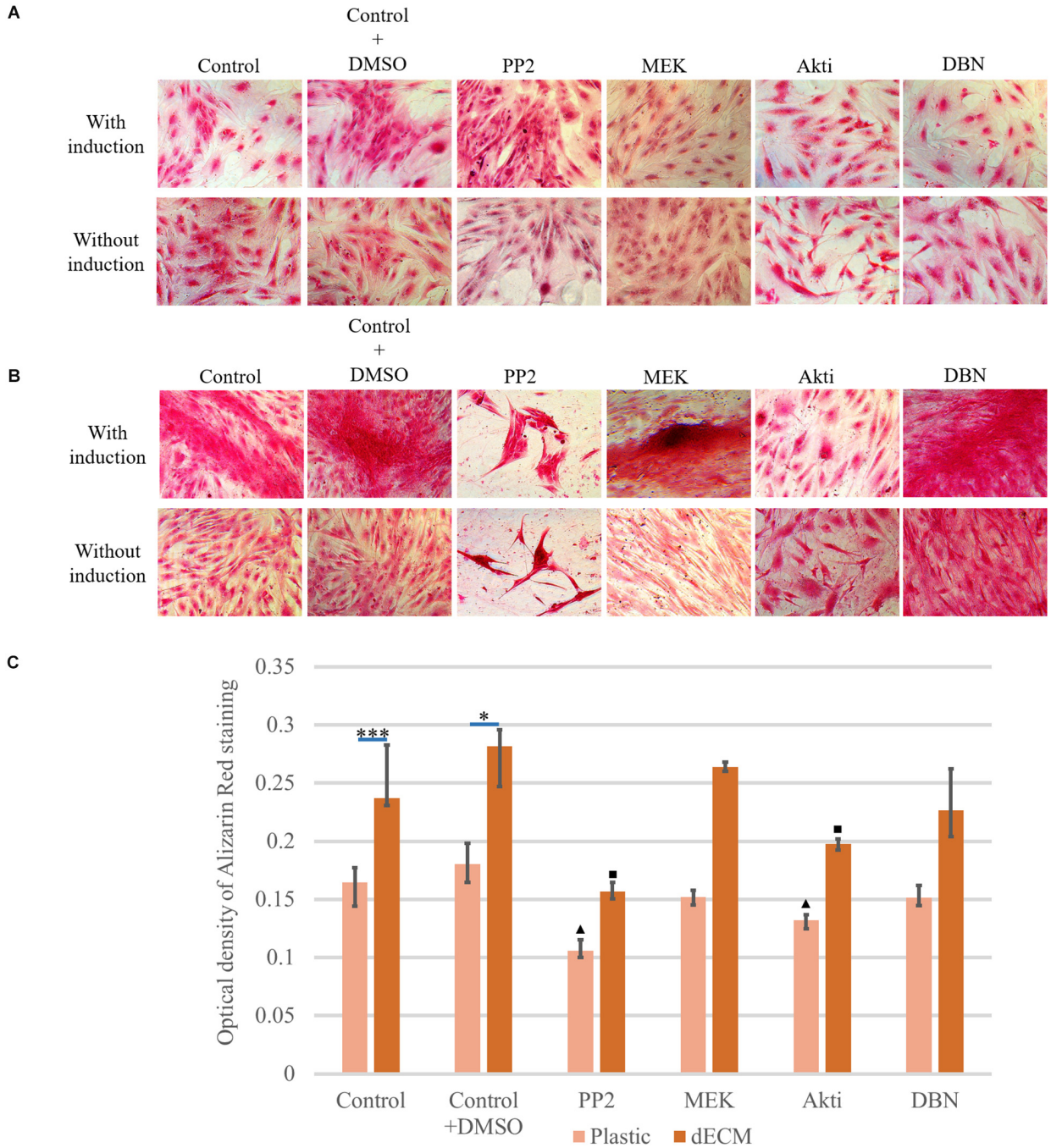


FIGURE 13 | Inhibition study of induction mechanism of osteogenic differentiation with inhibitor treatment (PP2 as Src kinase inhibitor, MEK as ERK inhibitor, Akti VIII(Akti) as protein kinase B (Akt) inhibitor and dobutamine (DBN) as YAP inhibitor) of hMSCs cultured on plastic **(A)** or dECM produced by hTERT-MSCs **(B)** for 4 days assessed by histological staining with Alizarin Red. Objective magnification, ×20. The dye was extracted, and Alizarin Red staining was quantified by measuring the optical density at 560 nm **(lower panel C)** ($n = 3$). The quantitative data are represented as median (25%, 75%), *(p value < 0.05), ***(p value < 0.0005), triangle and square signs represent the significant changes compared to the corresponding controls (p value < 0.05).

by dECM. Inhibition of Src protein kinase dramatically changed morphology of cells plated on dECM and led to formation of spheroid-like structures, as well as resulted in decreased differentiation potential. We assume that this results from the loss of contact of cells with ECM, which leads to increased formation of intercellular contacts. However, selective inhibition of Akt did not affect cell morphology but only mitigated the pro-differentiation effect of dECM, suggesting that Akt acted downstream and affected only processes of differentiation but not cell–matrix interactions.

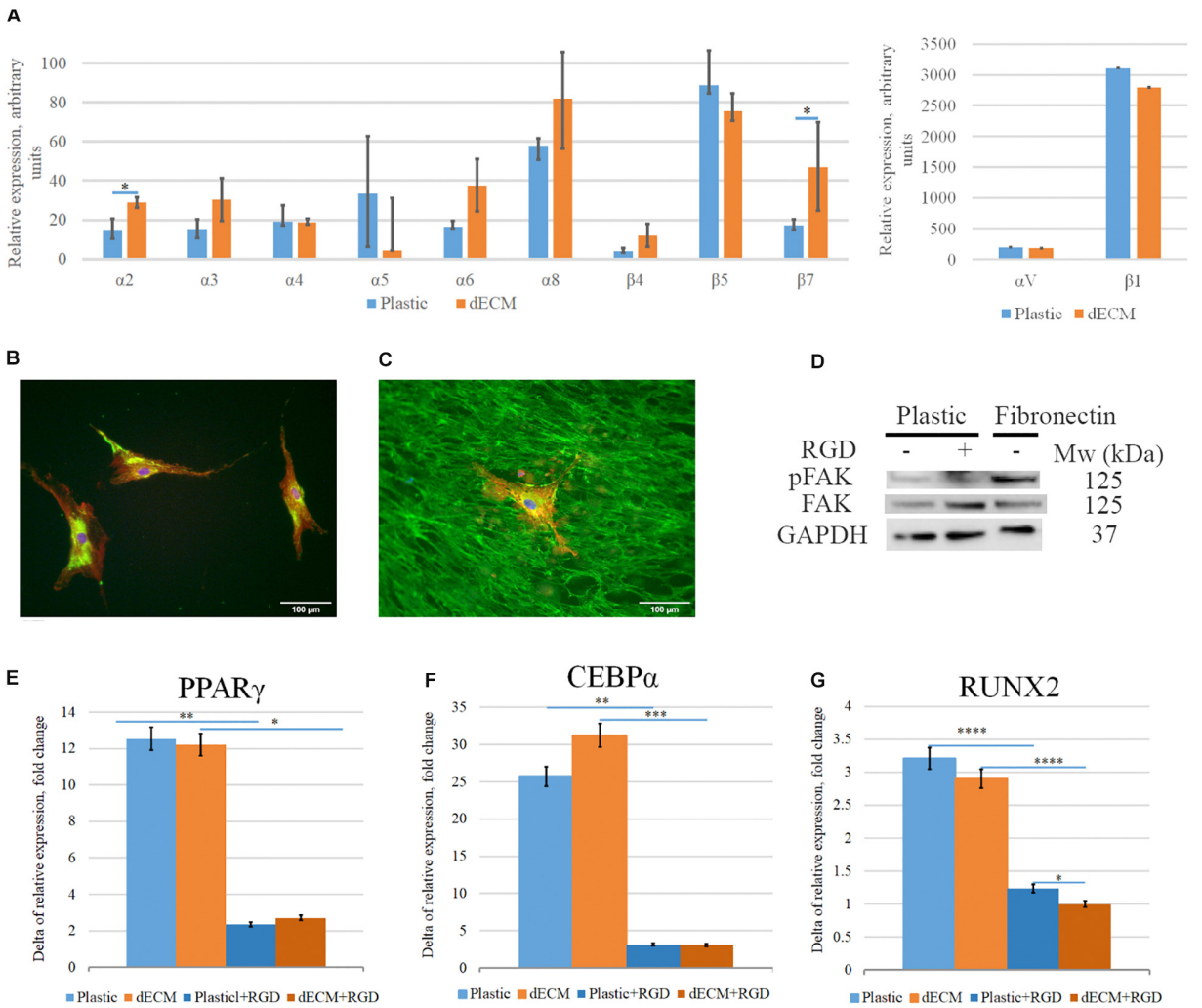


FIGURE 14 | Impact of interaction of hMSCs with dECM via integrins into dECM-mediated hMSCs differentiation stimulation. **(A–C)** Expression of integrins in hMSCs cultured on plastic **(A,B)** or dECM **(A,C)** estimated by real-time PCR **(A)** including α2(*ITGA2*), α3(*ITGA3*), α4(*ITGA4*), α5(*ITGA5*), αV(*ITGAV*), α6(*ITGA6*), α8(*ITGA8*), β1(*ITGB1*), β4(*ITGB4*), β5(*ITGB5*), β7(*ITGB7*) and immunocytochemical staining for integrin β1 subunit **(B,C)**. **(D)** Activation of pFAK/FAK signaling pathway in hMSCs in suspension (1) on the presence of RGD peptide (2) or after 1-h attachment to fibronectin (3). **(E–G)** Relative fold change of hMSC differentiation induction (4 days) measured as increased expression of differentiation markers for adipogenic [PPARγ(*PPARG*) **(E)**, CEBPα(*CEBPA*) **(F)**], and osteogenic [*RUNX2* **(G)**] differentiation by real-time PCR normalized to housekeeping gene (RPLP0) in hMSCs cultured on plastic or dECM with or without blocking of integrin interaction via RGD sequence using RGD peptide. The quantitative data are represented as median (25%, 75%), *(p value < 0.05), **(p value < 0.005), ***(p value < 0.0005), ****(p value < 0.0001).

The interaction between dECM and cells also modulated the activity of canonical Wnt/b-catenin signaling pathway in hMSCs. b-catenin, the main effector of this signaling, exists in superposition of two conditions – on the one hand, connecting E-cadherin and a-catenin in cell adhesion complex (Drees et al., 2005), on the other, it can transfer to the nucleus and act as a transcriptional activator in conjunction with its partners LEF/TCF (Behrens et al., 1996). In our experiments we observed decrease of active b-catenin content in nuclear fraction of hMSCs cultured on dECM. This phenomenon may be a result of increased recruitment of b-catenin to the forming cell–matrix contacts, which are known to compete with nuclear factors for β-catenin (Brembeck et al., 2004).

Importantly, there was no specific cell commitment to adipogenic, osteogenic or chondrogenic lineages for hMSCs as could be expected from some previously published data (Marinkovic et al., 2016). We consider this non-specific effect due to the transient activation of ERK signaling cascade in multipotent progenitor cells on dECM, which is particularly necessary for the initial stage of adipogenic differentiation (Tyurin-Kuzmin et al., 2020). Our hypothesis is also confirmed by the slight elevation of both pYAP and YAP expression in hMSCs cultured on dECM. YAP is an important effector protein in the Hippo signaling pathway that acts as a transcriptional regulator of several transcription factors activity, including RUNX, and provides the mechanosensing switches for ECM.

Increased YAP expression is essential for satellite cell activation under homeostasis in skeletal muscles, whereas pYAP gradually elevates along with the expansion and differentiation of muscle progenitor cells (Fischer et al., 2016; Eliazer et al., 2019). Other examples include progenitors in the intestinal crypt, neural progenitor cells in the neural tube and epidermal stem cells, where YAP activity promotes proliferation and blocks differentiation (Camargo et al., 2007; Cao et al., 2008; Watt et al., 2010; Schlegelmilch et al., 2011). Pancreatic exocrine cells are also converted to progenitors by transient YAP expression (Panciera et al., 2016). Recently it was shown that YAP is also crucial for modulating human MSC differentiation to adipocytes and osteoblasts (Lorthongpanich et al., 2019).

Taken together, based on all revealed changes in hMSCs cultured on dECM we suppose that specific MSC-produced ECM-mediated signaling leads to the proliferation of multipotent cells and generation of progenitors, increasing the number of cells able to be quickly and efficiently induced into a differentiation process. It is worthy to note that the cell embedded in the thickness of ECM should be able to recognize the specific signals from the outside. The diverse responses to the extrinsic stimuli may be due to the dose-dependent activities of signaling factors, or to intrinsic differences in the response of cells to a given signal—a phenomenon called differential cellular competence (Kiecker et al., 2016). We found that dECM simultaneously smoothed out the basal expression level of differentiation transcription factors in hMSCs, supported proliferation of progenitor cells and prepared the intracellular pathways for the rapid response phase. Thus, we assume that ECM secreted by MSCs could convert target cells to the competent state facilitating their responses to the specific differentiation stimuli. Whether these effects are distinctive for cultured MSCs or realizing also *in vivo*, need further investigations.

CONCLUSION

ECM represents a dynamic structure, actively remodeling throughout life. Producing of ECM components and creating of regulatory framework for the rest of cell types is one of the crucial functions of MSCs. Moreover, produced ECM does not only provide a mechanical support, but plays a decisive role in formation of cell microenvironment and regulation of cell fate, in particular within stem cell niches. Our approach of MSC cell sheet decellularization allowed us to trace the role of MSC-produced ECM in multipotent cell proliferation and differentiation. The obtained data suggest that ECM can stimulate these processes via binding of integrins with RGD sequences well-conserved in dECM samples. Thus, MSC-produced dECM largely reconstitutes composition and structure of the native matrix, so it may mimic stem cell niche components *in vitro* and maintain multipotent progenitor cells to insure their effective response to the external differentiating stimuli. MSC cell sheets and obtaining dECM from such multicellular constructions represent the promising *in vitro* models for the establishing of ECM contribution into the organization of specific cell microenvironment in various conditions. Our results also can be used for the developing of novel biomedical cell-free products based on dECM for regenerative medicine.

DATA AVAILABILITY STATEMENT

All datasets presented in this study are included in the article/**Supplementary Material**.

ETHICS STATEMENT

The studies involving human participants were reviewed and approved by Ethics Committee of Lomonosov Moscow State University, IRB00010587. The patients/participants provided their written informed consent to participate in this study.

AUTHOR CONTRIBUTIONS

EN, OG, and AE designed the study. EN performed all the experiments, except those specified below. SR provided with DIC microscopy and study of SHG. OG and RE helped sample preparation for IHC of ECM components and fluorescence microscopy. PN and OG helped with THP-1 and ELISA experiments. PN estimated the amount of ATP in samples. KK and NB helped with RT PCR for differentiation experiments. KK, MK, and IM provided western-blot. EN, OG, KK, NO, and AE provided intellectual input to the manuscript. EN, OG, KK, and AE wrote the manuscript. All authors contributed for the development of this article.

FUNDING

This reported study was funded by the Russian Foundation for Basic Research, project number 19-315-90060 (studying of the mechanisms of dECM-MSCs interactions) and 18-315-20053 (MSC-produced dECM characterization by ICH, WB, and dot-blot), by the Russian Science Foundation, grant number 19-75-30007 (exploring the dECM-mediated effects on human MSCs differentiation) and supported by Lomonosov Moscow State University Grant for Leading Scientific Schools "Depository of the Living Systems" in the frame of MSU Development Program (biomaterials). The samples preparing, in part of drying at the critical point and ion coater, was performed at the User Facility Center "Electron Microscopy in Life Sciences" of Lomonosov Moscow State University.

ACKNOWLEDGMENTS

We would like to acknowledge Natalia Alexandrushkina, Institute for Regenerative Medicine, Lomonosov MSU, Moscow, Russian Federation, for the assistance with experiments using IncuCyte ZOOM system. We gratefully acknowledge Elena Markvicheva, Institute of bioorganic chemistry of RAS, Moscow, Russian Federation, for RGD peptide and Alexander Vorotnikov,

National Medical Research Center of Cardiology, Moscow, Russian Federation, for PP2 and MEK inhibitors. Also we would like to acknowledge Anatolij Bogdanov and Konstantin Romanenko, the User Facility Center "Electron Microscopy in Life Sciences", Lomonosov MSU, for the support in sample preparation for electron microscopy.

SUPPLEMENTARY MATERIAL

The Supplementary Material for this article can be found online at: https://www.frontiersin.org/articles/10.3389/fcell.2020.555378/full#supplementary-material

FIGURE S1 | Apoptosis of hTERT-MSCs caused by rotenone. The flow cytometry data obtained for unlabeled cells **(A)** and after labeling of cells with Annexin V and 7-AAD before **(B)** and after the incubation with rotenone (500 nM) for 24 h **(C)**. Effectiveness of apoptosis induction in hTERT-MSC cell sheet using rotenone is shown on diagram **(D)**.

FIGURE S2 | Expression of ECM components such as fibronectin **(A–E)**, type I collagen **(F–J)**, laminin **(K–O)** in hTERT-MSC cell sheets **(A,F,K)** and dECM prepared by different decellularization methods: CHAPS 10' with DNAse I **(B,G,L)**, rotenone pretreatment with the following decellularization by CHAPS and DNAse I **(C,H,M)**, sodium deoxycholate with DNAse I **(D,I,N)**, rotenone pretreatment with the following decellularization by sodium deoxycholate and DNAse I **(I,J,O)** evaluated by immunohistochemistry without permeabilization (objective magnification, x40). The IgG control is presented for each sample in the corresponding column **(P–T)**.

FIGURE S3 | Scanning electron microscopy of MSC cell sheets **(A,F)** and dECM prepared by different decellularization methods: CHAPS with DNAse I **(B,G)**, rotenone pretreatment with the following decellularization by CHAPS and DNAse I **(C,H)**, sodium deoxycholate with DNAse I **(D,I)**, rotenone pretreatment with the following decellularization by sodium deoxycholate and DNAse I **(I,J)**. Magnification: x1000 **(A–E)**, x4000 **(F–J)**.

FIGURE S4 | Isotype IgG control immunocytochemical staining without permeabilization of MSC cell sheets **(A)** and dECM **(B)** for **Figure 3**.

FIGURE S5 | Isotype IgG control immunocytochemical staining without permeabilization of hMSC on dECM **(A)** and TCP **(B)** for **Figure 12**.

FIGURE S6 | Proliferation activity of activated monocytes/macrophages (THP-1) cultured on plastic and dECM. **(A)** representative microphotographs of THP-1 cultured on plastic and dECM with or without PMA treatment in the beginning and for 4 days (phase contrast, objective magnification – ×10). Additional cytokine profile of monocytes cultured on plastic and dECM. Level of IL-8 **(B)** and IL-10 **(C)** secreted by monocytes/macrophages with or without PMA treatment measured by ELISA are presented. The quantitative data are represented as median (25%, 75%).

FIGURE S7 | Inhibitor analysis of major signaling pathways in hMSC cultivated on plastic or dECM. DBN-dobutamine, Mek – MEK inhibitor PD 98059, PP2 – Src inhibitor PP2, Akti – Akt1 and Akt2 inhibitor Akti-1/2. Figure shows representative blots, n = 3.

REFERENCES

Ahmed, M., and Ffrench-Constant, C. (2016). Extracellular matrix regulation of stem cell behavior. *Curr. Stem Cell Rep.* 2, 197–206. doi: 10.1007/s40778-016-0056-2

Andreotti, J. P., Silva, W. N., Costa, A. C., Picoli, C. C., Bitencourt, F. C. O., Coimbra-Campos, L. M. C., et al. (2019). Neural stem cell niche heterogeneity. *Semin. Cell Dev. Biol.* 95, 42–53. doi: 10.1016/j.semcdb.2019.01.005

Baker, N., Sohn, J., and Tuan, R. S. (2015). Promotion of human mesenchymal stem cell osteogenesis by PI3-kinase/Akt signaling, and the influence of caveolin-1/cholesterol homeostasis. *Stem Cell Res. Ther.* 6:238.

Bao, Y., Nakagawa, K., Yang, Z., Ikeda, M., Withanage, K., Ishigami-Yuasa, M., et al. (2011). A cell-based assay to screen stimulators of the hippo pathway reveals the inhibitory effect of dobutamine on the YAP-dependent gene transcription. *J. Biochem.* 150, 199–208. doi: 10.1093/jb/mvr063

Baron, W., Colognato, H., and ffrench-Constant, C. (2005). Integrin-growth factor interactions as regulators of oligodendroglial development and function. *Glia* 49, 467–479. doi: 10.1002/glia.20132

Beck, H. C., Gosau, M., Kristensen, L. P., and Morsczeck, C. (2014). A site-specific phosphorylation of the focal adhesion kinase controls the formation of spheroid cell clusters. *Neurochem. Res.* 39, 1199–1205. doi: 10.1007/s11064-014-1298-y

Behrens, J., von Kries, J. P., Kühl, M., Bruhn, L., Wedlich, D., Grosschedl, R., et al. (1996). Functional interaction of β-catenin with the transcription factor LEF- 1. *Nature* 382, 638–642. doi: 10.1038/382638a0

Bonnans, C., Chou, J., and Werb, Z. (2014). Remodelling the extracellular matrix in development and disease. *Nat. Rev. Mol. Cell Biol.* 15, 786–801. doi: 10.1038/nrm3904

Borton, L. K., and Coleman, K. P. (2018). Material-mediated pyrogens in medical devices: applicability of the in vitro monocyte activation test. *ALTEX* 35, 453–463. doi: 10.14573/altex.1709221

Brembeck, F. H., Schwarz-Romond, T., Bakkers, J., Wilhelm, S., Hammerschmidt, M., and Birchmeier, W. (2004). Essential role of BCL9-2 in the switch between β-Catenin's adhesive and transcriptional functions. *Genes Dev.* 18, 2225–2230. doi: 10.1101/gad.317604

Camargo, F. D., Gokhale, S., Johnnidis, J. B., Fu, D., Bell, G. W., Jaenisch, R., et al. (2007). YAP1 increases organ size and expands undifferentiated progenitor cells. *Curr. Biol.* 17, 2054–2060. doi: 10.1016/j.cub.2007.10.039

Candiano, G., Bruschi, M., Musante, L., Santucci, L., Ghiggeri, G. M., Carnemolla, B., et al. (2004). Blue silver: a very sensitive colloidal coomassie G-250 staining for proteome analysis. *Electrophoresis* 25, 1327–1333. doi: 10.1002/elps.200305844

Cao, X., Pfaff, S. L., and Gage, F. H. (2008). YAP regulates neural progenitor cell number via the TEA domain transcription factor. *Genes Dev.* 22, 3320–3334. doi: 10.1101/gad.1726608

Chanput, W., Mes, J. J., and Wichers, H. J. (2014). THP-1 cell line: an in vitro cell model for immune modulation approach. *Int. Immunopharmacol.* 23, 37–45. doi: 10.1016/j.intimp.2014.08.002

Chen, X. D., Dusevich, V., Feng, J. Q., Manolagas, S. C., and Jilka, R. L. (2007). Extracellular matrix made by bone marrow cells facilitates expansion of marrow-derived mesenchymal progenitor cells and prevents their differentiation into osteoblasts. *J. Bone Miner. Res.* 22, 1943–1956. doi: 10.1359/jbmr.070725

Chen, Y. T., Tsai, M. J., Hsieh, N., Lo, M. J., Lee, M. J., Cheng, H., et al. (2019). The superiority of conditioned medium derived from rapidly expanded mesenchymal stem cells for neural repair. *Stem Cell Res. Ther.* 10, 1–15. doi: 10.1155/2018/4898152

Cheng, C. W., Solorio, L. D., and Alsberg, E. (2014). Decellularized tissue and cell-derived extracellular matrices as scaffolds for orthopaedic tissue engineering. *Biotechnol. Adv.* 32, 462–484. doi: 10.1016/j.biotechadv.2013.12.012

Chermnykh, E., Kalabusheva, E., and Vorotelyak, E. (2018). Extracellular matrix as a regulator of epidermal stem cell fate. *Int. J. Mol. Sci.* 19:1003. doi: 10.3390/ijms19041003

Cramer, M. C., and Badylak, S. F. (2019). Extracellular matrix-based biomaterials and their influence upon cell behavior. *Ann. Biomed. Eng.* 48, 2132–2153. doi: 10.1007/s10439-019-02408-9

Devaud, Y. R., Avilla-Royo, E., Trachsel, C., Grossmann, J., Martin, I., Lutolf, M. P., et al. (2018). Label-free quantification proteomics for the identification of mesenchymal stromal cell matrisome inside 3D poly(ethylene glycol) hydrogels. *Adv. Healthc. Mater.* 7:e1800534. doi: 10.1002/adhm.201800534

Dilogo, I. H., and Fiolin, J. (2019). Role of mesenchymal stem cell-conditioned medium (MSC-CM) in the bone regeneration: a systematic review from 2007-2018. *Annu. Res. Rev. Biol.* 31, 1–16. doi: 10.9734/arrb/2019/v31i230045

Donnelly, H., Salmeron-Sanchez, M., and Dalby, M. J. (2018). Designing stem cell niches for differentiation and self-renewal. *J. R. Soc. Interface* 15:20180388. doi: 10.1098/rsif.2018.0388

Drees, F., Pokutta, S., Yamada, S., Nelson, W. J., and Weis, W. I. (2005). α-Catenin is a molecular switch that binds E-Cadherin-β-catenin and regulates actin-filament assembly. *Cell* 123, 903–915. doi: 10.1016/j.cell.2005.09.021

Dzobo, K., Motaung, K. S. C. M., and Adesida, A. (2019). Recent trends in decellularized extracellular matrix bioinks for 3D printing: an updated review. *Int. J. Mol. Sci.* 20:4628. doi: 10.3390/ijms20184628

Ebrahimi Sadrabadi, A., Baei, P., Hosseini, S., and Baghaban Eslaminejad, M. (2020). "Decellularized extracellular matrix as a potent natural biomaterial for regenerative medicine," in *Advances in Experimental Medicine and Biology*, eds W. E. Crusio, H. Dong, H. H. Radeke, N. Rezaei, and J. Xiao (New York, NY: Springer). doi: 10.1007/5584_2020_504

Eliazer, S., Muncie, J. M., Christensen, J., Sun, X., D'Urso, R. S., Weaver, V. M., et al. (2019). Wnt4 from the niche controls the mechano-properties and quiescent state of muscle stem cells. *Cell Stem Cell* 25, 654–665.e4. doi: 10.1016/j.stem.2019.08.007

Fischer, M., Rikeit, P., Knaus, P., and Coirault, C. (2016). YAP-mediated mechanotransduction in skeletal muscle. *Front. Physiol.* 7:41. doi: 10.3389/fphys.2016.00041

Garantziotis, S., and Savani, R. C. (2019). Hyaluronan biology: a complex balancing act of structure, function, location and context. *Matrix Biol.* 78–79, 1–10. doi: 10.1016/j.matbio.2019.02.002

Gattazzo, F., Urciuolo, A., and Bonaldo, P. (2014). Extracellular matrix: a dynamic microenvironment for stem cell niche. *Biochim. Biophys. Acta* 1840, 2506–2519. doi: 10.1016/j.bbagen.2014.01.010

Giancotti, F. G., and Tarone, G. (2003). Positional control of cell fate through joint integrin/receptor protein kinase signaling. *Annu. Rev. Cell Dev. Biol.* 19, 173–206. doi: 10.1146/annurev.cellbio.19.031103.133334

Gilpin, A., and Yang, Y. (2017). Decellularization strategies for regenerative medicine: from processing techniques to applications. *Biomed Res. Int.* 2017:9831534. doi: 10.1155/2017/9831534

Gomez-Salazar, M., Gonzalez-Galofre, Z. N., Casamitjana, J., Crisan, M., James, A. W., and Péault, B. (2020). Five decades later, are mesenchymal stem cells still relevant? *Front. Bioeng. Biotechnol.* 8:148. doi: 10.3389/fbioe.2020.00148

Gowen, A., Shahjin, F., Chand, S., Odegaard, K. E., and Yelamanchili, S. V. (2020). Mesenchymal stem cell-derived extracellular vesicles: challenges in clinical applications. *Front. Cell Dev. Biol.* 8:149. doi: 10.3389/fcell.2020.00149

Hagbard, L., Cameron, K., August, P., Penton, C., Parmar, M., Hay, D. C., et al. (2018). Developing defined substrates for stem cell culture and differentiation. *Philos. Trans. R. Soc. B Biol. Sci.* 373:20170230. doi: 10.1098/rstb.2017.0230

Heath, D. E. (2019). A review of decellularized extracellular matrix biomaterials for regenerative engineering applications. *Regen. Eng. Transl. Med.* 5, 155–166. doi: 10.1007/s40883-018-0080-0

Hoshiba, T. (2017). Cultured cell-derived decellularized matrices: a review towards the next decade. *J. Mater. Chem. B* 5, 4322–4331. doi: 10.1039/C7TB00074J

Hu, J., Lu, J., Lian, G., Zhang, J., Hecht, J. L., and Sheen, V. L. (2014). Filamin B regulates chondrocyte proliferation and differentiation through Cdk1 signaling. *PLoS One* 9:e89352. doi: 10.1371/journal.pone.0089352

Humphrey, J. D., Dufresne, E. R., and Schwartz, M. A. (2014). Mechanotransduction and extracellular matrix homeostasis. *Nat. Rev. Mol. Cell Biol.* 15, 802–812. doi: 10.1038/nrm3896

Iozzo, R. V., and Gubbiotti, M. A. (2018). Extracellular matrix: the driving force of mammalian diseases. *Matrix Biol.* 71–72, 1–9. doi: 10.1016/j.matbio.2018.03.023

Ji, J., Zhang, D., Wei, W., Shen, B., Zhang, Y., Wang, Y., et al. (2018). Decellularized matrix of adipose-derived mesenchymal stromal cells enhanced retinal progenitor cell proliferation via the Akt/Erk pathway and neuronal differentiation. *Cytotherapy* 20, 74–86. doi: 10.1016/j.jcyt.2017.08.019

Kalinina, N., Kharlampieva, D., Loguinova, M., Butenko, I., Pobeguts, O., Efimenko, A., et al. (2015). Characterization of secretomes provides evidence for adipose-derived mesenchymal stromal cells subtypes. *Stem Cell Res. Ther.* 6:221.

Keshtkar, S., Azarpira, N., and Ghahremani, M. H. (2018). Mesenchymal stem cell-derived extracellular vesicles: novel frontiers in regenerative medicine. *Stem Cell Res. Ther.* 9:63.

Kfoury, Y., and Scadden, D. T. (2015). Mesenchymal cell contributions to the stem cell niche. *Cell Stem Cell* 16, 239–253. doi: 10.1016/j.stem.2015.02.019

Kiecker, C., Graham, A., and Logan, M. (2016). Differential cellular responses to hedgehog signalling in vertebrates-what is the role of competence? *J. Dev. Biol.* 4:36. doi: 10.3390/jdb4040036

Kim, H. J., and Kim, S. H. (2010). Tanshinone IIA enhances BMP-2-stimulated commitment of C2C12 cells into osteoblasts via P38 activation. *Amino Acids* 39, 1217–1226. doi: 10.1007/s00726-010-0557-8

Laemmli, U. K. (1970). Cleavage of structural proteins during the assembly of the head of bacteriophage T4. *Nature* 227, 680–685. doi: 10.1038/227680a0

Lai, Y., Sun, Y., Skinner, C. M., Son, E. L., Lu, Z., Tuan, R. S., et al. (2010). Reconstitution of marrow-derived extracellular matrix ex vivo: a robust culture system for expanding large-scale highly functional human mesenchymal stem cells. *Stem Cells Dev.* 19, 1095–1107. doi: 10.1089/scd.2009.0217

Leavitt, T., Hu, M. S., Marshall, C. D., Barnes, L. A., Lorenz, H. P., and Longaker, M. T. (2016). Scarless wound healing: finding the right cells and signals. *Cell Tissue Res.* 365, 483–493. doi: 10.1007/s00441-016-2424-8

Lee, D., Kim, D. W., and Cho, J. Y. (2020). Role of growth factors in hematopoietic stem cell niche. *Cell Biol. Toxicol.* 36, 131–144. doi: 10.1007/s10565-019-09510-7

Lo, S. H. (2006). Focal adhesions: what's new inside. *Dev. Biol.* 294, 280–291. doi: 10.1016/j.ydbio.2006.03.029

Locati, M., Mantovani, A., and Sica, A. (2013). Macrophage activation and polarization as an adaptive component of innate immunity. *Adv. Immunol.* 120, 163–184. doi: 10.1016/B978-0-12-417028-5.00006-5

Longobardi, E., and Blasi, F. (2003). Overexpression of PREP-1 in F9 teratocarcinoma cells leads to a functionally relevant increase of PBX-2 by preventing its degradation. *J. Biol. Chem.* 278, 39235–39241. doi: 10.1074/jbc.M304704200

Lopatina, T., Kalinina, N., Karagyaur, M., Stambolsky, D., Rubina, K., Revischin, A., et al. (2019a). Adipose-derived stem cells stimulate regeneration of peripheral nerves: BDNF secreted by these cells promotes nerve healing and axon growth de novo. *PLoS One* 6:e17899. doi: 10.1371/Journal.Pone.0017899

Lopatina, T., Kalinina, N., Karagyaur, M., Stambolsky, D., Rubina, K., Revischin, A., et al. (2019b). Correction: adipose-derived stem cells stimulate regeneration of peripheral nerves: BDNF secreted by these cells promotes nerve healing and axon growth de novo. *PLoS One* 14:e0219946. doi: 10.1371/journal.pone.0219946

Lorthongpanich, C., Thumanu, K., Tangkiettrakul, K., Jiamvoraphong, N., Laowtammathron, C., Damkham, N., et al. (2019). YAP as a key regulator of adipo-osteogenic differentiation in human MSCs. *Stem Cell Res. Ther.* 10:402.

Lu, P., Takai, K., Weaver, V. M., and Werb, Z. (2011). Extracellular matrix degradation and remodeling in development and disease. *Cold Spring Harb. Perspect. Biol.* 3:a005058. doi: 10.1101/cshperspect.a005058

Lukomska, B., Stanaszek, L., Zuba-Surma, E., Legosz, P., Sarzynska, S., and Drela, K. (2019). Challenges and controversies in human mesenchymal stem cell therapy. *Stem Cells Int.* 2019:9628536. doi: 10.1155/2019/9628536

Marinkovic, M., Block, T. J., Rakian, R., Li, Q., Wang, E., Reilly, M. A., et al. (2016). One size does not fit all: developing a cell-specific niche for in vitro study of cell behavior. *Matrix Biol.* 52–54, 426–441. doi: 10.1016/j.matbio.2016.01.004

Mauney, J., Olsen, B. R., and Volloch, V. (2010). Matrix remodeling as stem cell recruitment event: a novel in vitro model for homing of human bone marrow stromal cells to the site of injury shows crucial role of extracellular collagen matrix. *Matrix Biol.* 29, 657–663. doi: 10.1016/j.matbio.2010.08.008

Mecham, R. (2011). *The Extracellular Matrix: An Overview*. Berlin: Springer-Verlag.

Mouw, J. K., Ou, G., and Weaver, V. M. (2014). Extracellular matrix assembly: a multiscale deconstruction. *Nat. Rev. Mol. Cell Biol.* 15, 771–785. doi: 10.1038/nrm3902

Ng, C. P., Sharif, A. R. M., Heath, D. E., Chow, J. W., Zhang, C. B. Y., Chan-Park, M. B., et al. (2014). Enhanced ex vivo expansion of adult mesenchymal stem cells by fetal mesenchymal stem cell ECM. *Biomaterials* 35, 4046–4057. doi: 10.1016/j.biomaterials.2014.01.081

Nimiritsky, P. P., Sagaradze, G. D., Efimenko, A. Y., Makarevich, P. I., and Tkachuk, V. A. (2018). The stem cell niche. *Tsitologiya* 60, 575–586. doi: 10.31116/tsitol.2018.08.01

Novoseletskaya, E. S., Grigorieva, O. A., Efimenko, A. Y., and Kalinina, N. I. (2019). Extracellular matrix in the regulation of stem cell differentiation. *Biochemistry* 84, 232–240.

Ode, A., Duda, G. N., Glaeser, J. D., Matziolis, G., Frauenschuh, S., Perka, C., et al. (2010). Toward biomimetic materials in bone regeneration: functional behavior of mesenchymal stem cells on a broad spectrum of extracellular matrix components. *J. Biomed. Mater. Res. A* 95, 1114–1124. doi: 10.1002/jbm.a.32909

Padhi, A., and Nain, A. S. (2020). ECM in differentiation: a review of matrix structure, composition and mechanical properties. *Ann. Biomed. Eng.* 48, 1071–1089. doi: 10.1007/s10439-019-02337-7

Panciera, T., Azzolin, L., Fujimura, A., Biagio, D. D., Frasson, C., Bresolin, S., et al. (2016). Induction of expandable tissue-specific stem/progenitor cells through transient expression of YAP/TAZ. *Cell Stem Cell* 19, 725–737. doi: 10.1016/j.stem.2016.08.009

Parmaksiz, M., Elçin, A. E., and Elçin, Y. M. (2020). Decellularized cell culture ECMs act as cell differentiation inducers. *Stem Cell Rev. Rep.* 16, 569–584. doi: 10.1007/s12015-020-09963-y

Pastuła, A., and Marcinkiewicz, J. (2019). Cellular interactions in the intestinal stem cell niche. *Arch. Immunol. Ther. Exp.* 67, 19–26. doi: 10.1007/s00005-018-0524-8

Prewitz, M. C., Seib, F. P., von Bonin, M., Friedrichs, J., Stißel, A., Niehage, C., et al. (2013). Tightly anchored tissue-mimetic matrices as instructive stem cell microenvironments. *Nat. Methods* 10, 788–794. doi: 10.1038/nmeth.2523

Prowse, A. B. J., Doran, M. R., Cooper-White, J. J., Chong, F., Munro, T. P., Fitzpatrick, J., et al. (2010). Long term culture of human embryonic stem cells on recombinant vitronectin in ascorbate free media. *Biomaterials* 31, 8281–8288. doi: 10.1016/j.biomaterials.2010.07.037

Ragelle, H., Naba, A., Larson, B. L., Zhou, F., Prijić, M., Whittaker, C. A., et al. (2017). Comprehensive proteomic characterization of stem cell-derived extracellular matrices. *Biomaterials* 128, 147–159. doi: 10.1016/j.biomaterials.2017.03.008

Ragni, E., Viganò, M., Rebulla, P., Giordano, R., and Lazzari, L. (2013). What is beyond a QRT-PCR study on mesenchymal stem cell differentiation properties: how to choose the most reliable housekeeping genes. *J. Cell. Mol. Med.* 17, 168–180. doi: 10.1111/j.1582-4934.2012.01660.x

Rakian, R., Block, T. J., Johnson, S. M., Marinkovic, M., Wu, J., Dai, Q., et al. (2015). Native extracellular matrix preserves mesenchymal stem cell "stemness" and differentiation potential under serum-free culture conditions. *Stem Cell Res. Ther.* 6:235.

Rana, D., Zreiqat, H., Benkirane-Jessel, N., Ramakrishna, S., and Ramalingam, M. (2017). Development of decellularized scaffolds for stem cell-driven tissue engineering. *J. Tissue Eng. Regen. Med.* 11, 942–965. doi: 10.1002/term.2061

Rao Pattabhi, S., Martinez, J. S., and Keller, T. C. S. (2014). Decellularized ECM effects on human mesenchymal stem cell stemness and differentiation. *Differentiation* 88, 131–143. doi: 10.1016/j.diff.2014.12.005

Riis, S., Hansen, A. C., Johansen, L., Lund, K., Pedersen, C., Pitsa, A., et al. (2020). Fabrication and characterization of extracellular matrix scaffolds obtained from adipose-derived stem cells. *Methods* 171, 68–76. doi: 10.1016/j.ymeth.2019.07.004

Rolandsson Enes, S., Åhrman, E., Palani, A., Hallgren, O., Bjermer, L., Malmström, A., et al. (2017). Quantitative proteomic characterization of lung-MSC and bone marrow-MSC using DIA-mass spectrometry. *Sci. Rep.* 7:9316. doi: 10.1038/s41598-017-09127-y

Rubina, K., Kalinina, N., Efimenko, A., Lopatina, T., Melikhova, V., Tsokolaeva, Z., et al. (2009). Adipose stromal cells stimulate angiogenesis via promoting progenitor cell differentiation, secretion of angiogenic factors, and enhancing vessel maturation. *Tissue Eng. A* 15, 2039–2050. doi: 10.1089/ten.tea.2008.0359

Saller, M. M., Prall, W. C., Docheva, D., Schönitzer, V., Popov, T., Anz, D., et al. (2012). Increased stemness and migration of human mesenchymal stem cells in hypoxia is associated with altered integrin expression. *Biochem. Biophys. Res. Commun.* 423, 379–385. doi: 10.1016/j.bbrc.2012.05.134

Sart, S., Jeske, R., Chen, X., Ma, T., and Li, Y. (2020). Engineering stem cell-derived extracellular matrices: decellularization and biological function. *Tissue Eng. B Rev.* doi: 10.1089/ten.teb.2019.0349 [Epub ahead of print].

Schlegelmilch, K., Mohseni, M., Kirak, O., Pruszak, J., Rodriguez, J. R., Zhou, D., et al. (2011). Yap1 acts downstream of α-catenin to control epidermal proliferation. *Cell* 144, 782–795. doi: 10.1016/j.cell.2011.02.031

Schofield, R. (1978). The relationship between the spleen colony-forming cell and the haemopoietic stem cell. *Blood Cells* 4, 7–25.

Seetharaman, R., and Srivastava, A. (2019). Annals of stem cell research & therapy mesenchymal stem cells derived paracrine factors: an alternative approach in regenerative therapy. *Stem Cell Res. Ther.* 3.

Selich, A., Ha, T. C., Morgan, M., Falk, C. S., von Kaisenberg, C., Schambach, A., et al. (2019). Cytokine selection of MSC clones with different functionality. *Stem Cell Rep.* 13, 262–273. doi: 10.1016/j.stemcr.2019.06.001

Sengyoku, H., Tsuchiya, T., Obata, T., Doi, R., Hashimoto, Y., Ishii, M., et al. (2018). Sodium hydroxide based non-detergent decellularizing solution for rat lung. *Organogenesis* 14, 94–106. doi: 10.1080/15476278.2018.1462432

Shakouri-Motlagh, A., O'Connor, A. J., Brennecke, S. P., Kalionis, B., and Heath, D. E. (2017). Native and solubilized decellularized extracellular matrix: a critical assessment of their potential for improving the expansion of mesenchymal stem cells. *Acta Biomater.* 55, 1–12. doi: 10.1016/j.actbio.2017.04.014

Shin, M. S., Song, S. H., Shin, J. E., Lee, S. H., Huh, S. O., and Park, D. (2019). Src-mediated phosphorylation of BPix-b regulates dendritic spine morphogenesis. *J. Cell Sci.* 132:jcs224980. doi: 10.1242/jcs.224980

Shrestha, K. R., and Yoo, S. Y. (2019). Phage-based artificial niche: the recent progress and future opportunities in stem cell therapy. *Stem Cells Int.* 2019:4038560. doi: 10.1155/2019/4038560

Smith, Q., and Gerecht, S. (2018). Extracellular matrix regulation of stem cell fate. *Curr. Stem Cell Rep.* 4, 13–21. doi: 10.1007/s40778-018-0111-2

Takada, I., Kouzmenko, A. P., and Kato, S. (2009). Wnt and PPARγ signaling in osteoblastogenesis and adipogenesis. *Nat. Rev. Rheumatol.* 5, 442–447. doi: 10.1038/nrrheum.2009.137

Tedesco, S., De Majo, F., Kim, J., Trenti, A., Trevisi, L., Fadini, G. P., et al. (2018). Convenience versus biological significance: are PMA-differentiated THP-1 cells a reliable substitute for blood-derived macrophages when studying *in vitro* polarization? *Front. Pharmacol.* 9:71. doi: 10.3389/fphar.2018.00071

Theocharis, A. D., Skandalis, S. S., Gialeli, C., and Karamanos, N. K. (2016). Extracellular matrix structure. *Adv. Drug Deliv. Rev.* 97, 4–27.

Thomas, D., O'Brien, T., and Pandit, A. (2018). Toward customized extracellular niche engineering: progress in cell-entrapment technologies. *Adv. Mater.* 30:1703948. doi: 10.1002/adma.201703948

Towbin, H., Staehelin, T., and Gordon, J. (1979). Electrophoretic transfer of proteins from polyacrylamide gels to nitrocellulose sheets: procedure and some applications. *Proc. Natl. Acad. Sci. U. S. A.* 76, 4350–4354. doi: 10.1073/pnas.76.9.4350

Tsuchiya, T., Balestrini, J. L., Mendez, J., Calle, E. A., Zhao, L., and Niklason, L. E. (2014). Influence of PH on extracellular matrix preservation during lung decellularization. *Tissue Eng. C Methods* 20, 1028–1036. doi: 10.1089/ten.tec.2013.0492

Tsuchiya, T., Mendez, J., Calle, E. A., Hatachi, G., Doi, R., Zhao, L., et al. (2016). Ventilation-based decellularization system of the lung. *Biores. Open Access.* 5, 118–126. doi: 10.1089/biores.2016.0012

Tyurin-Kuzmin, P. A., Kalinina, N. I., Kulebyakin, K. Y., Balatskiy, A. V., Sysoeva, V. Y., and Tkachuk, V. A. (2020). Angiotensin receptor subtypes regulate adipose tissue renewal and remodelling. *FEBS J.* 287, 1076–1087. doi: 10.1111/febs.15200

Velling, T., Stefansson, A., and Johansson, S. (2008). EGFR and B1 integrins utilize different signaling pathways to activate akt. *Exp. Cell Res.* 314, 309–316. doi: 10.1016/j.yexcr.2007.08.018

Wahart, A., Hocine, T., Albrecht, C., Henry, A., Sarazin, T., Martiny, L., et al. (2019). Role of elastin peptides and elastin receptor complex in metabolic

and cardiovascular diseases. *FEBS J.* 286, 2980–2993. doi: 10.1111/febs.14836

Watt, K. I., Judson, R., Medlow, P., Reid, K., Kurth, T. B., Burniston, J. G., et al. (2010). Yap is a novel regulator of C2C12 myogenesis. *Biochem. Biophys. Res. Commun.* 393, 619–624. doi: 10.1016/j.bbrc.2010.02.034

Wu, J., Sun, Y., Block, T. J., Marinkovic, M., Zhang, Z. L., Chen, R., et al. (2016). Umbilical cord blood-derived non-hematopoietic stem cells retrieved and expanded on bone marrow-derived extracellular matrix display pluripotent characteristics. *Stem Cell Res. Ther.* 7:176.

Zaidel-Bar, R., Itzkovitz, S., Ma'ayan, A., Iyengar, R., and Geiger, B. (2007). Functional atlas of the integrin adhesome. *Nat. Cell Biol.* 9, 858–867. doi: 10.1038/ncb0807-858

Conflict of Interest: The authors declare that the research was conducted in the absence of any commercial or financial relationships that could be construed as a potential conflict of interest.

Copyright © 2020 Novoseletskaya, Grigorieva, Nimiritsky, Basalova, Eremichev, Milovskaya, Kulebyakin, Kulebyakina, Rodionov, Omelyanenko and Efimenko. This is an open-access article distributed under the terms of the Creative Commons Attribution License (CC BY). The use, distribution or reproduction in other forums is permitted, provided the original author(s) and the copyright owner(s) are credited and that the original publication in this journal is cited, in accordance with accepted academic practice. No use, distribution or reproduction is permitted which does not comply with these terms.

frontiers in Cell and Developmental Biology

ORIGINAL RESEARCH
published: 22 October 2020
doi: 10.3389/fcell.2020.558354

Influence of Human Platelet Lysate on Extracellular Matrix Deposition and Cellular Characteristics in Adipose-Derived Stem Cell Sheets

Nai-Chen Cheng[1†], Yuan-Kun Tu[2†], Ning-Hsu Lee[3] and Tai-Horng Young[3*]*

[1] Department of Surgery, National Taiwan University Hospital, National Taiwan University College of Medicine, Taipei, Taiwan, [2] Department of Orthopedics, E-Da Hospital/I-Shou University, Kaohsiung, Taiwan, [3] Institute of Biomedical Engineering, College of Medicine, College of Engineering, National Taiwan University, Taipei, Taiwan

OPEN ACCESS

Edited by:
Pavel Makarevich, Lomonosov Moscow State University, Russia

Reviewed by:
Wan Safwani Wan Kamarul Zaman, University of Malaya, Malaysia
Thierry Burnouf, Taipei Medical University, Taiwan

***Correspondence:**
Nai-Chen Cheng
nccheng@ntu.edu.tw
Tai-Horng Young
thyoung@ntu.edu.tw

† These authors have contributed equally to this work

Specialty section:
This article was submitted to Stem Cell Research, a section of the journal Frontiers in Cell and Developmental Biology

Received: 02 May 2020
Accepted: 22 September 2020
Published: 22 October 2020

Citation:
Cheng N-C, Tu Y-K, Lee N-H and Young T-H (2020) Influence of Human Platelet Lysate on Extracellular Matrix Deposition and Cellular Characteristics in Adipose-Derived Stem Cell Sheets. Front. Cell Dev. Biol. 8:558354. doi: 10.3389/fcell.2020.558354

Adipose-derived stem cell (ASC) is a valuable source of cell therapy. By stimulating extracellular matrix (ECM) secretion, ASC sheets can be fabricated with enhanced regenerative capabilities. In recent years, human platelet lysate (HPL) provides an attractive alternative to fetal bovine serum (FBS) for the *ex vivo* expansion of ASCs for clinical use. However, the effect of HPL on ASC sheet formation has not been previously determined. In this study, we compared ECM composition and cellular characteristics of ASC sheets cultured in growth medium supplemented with either FBS or HPL. HPL supplement significantly enhanced ASC proliferation without obvious change in the expression pattern of cell surface markers. We found that culturing ASCs with HPL rendered thicker cell sheets with significantly more ECM deposition, including collagen and fibronectin. Proteomic analysis of the FBS or HPL-cultured cell sheets showed diversity in ECM composition. HPL-cultured ASC sheets exhibited up-regulation of interleukin-6 and an anti-inflammatory cytokine, C1q/tumor necrosis factor-related protein-3. Conditioned medium of HPL-cultured ASC sheets significantly enhanced fibroblast migration and tube formation of endothelial cells *in vitro*, while it inhibited the migration of macrophages toward stimulated macrophages *in vitro*. TGF-β1-stimulated fibroblasts cultured in ASC sheet-conditioned medium showed down-regulation of α-*SMA* and *TGF-β1*. By adding an anti-hepatocyte growth factor (HGF) neutralizing antibody in conditioned medium, we indicated that an anti-fibrosis effect of HPL-cultured ASC sheets is partially mediated through the increased secretion of HGF. Moreover, chick embryo chorioallantoic membrane (CAM) assay showed comparable capillary density after applying either FBS or HPL-cultured ASC sheets, both of which were significantly higher than the control. In conclusion, robust ECM formation with altered ECM composition was noted in ASC sheets cultured in HPL-supplemented medium. Their immunomodulatory and pro-angiogenesis capabilities were largely maintained. Our findings paved the way to elucidate the potential of HPL-cultured ASC sheets for clinical application in tissue regeneration.

Keywords: adipose-derived stem cell, cell sheet, extracellular matrix, human platelet lysate, fetal bovine serum, angiogenesis

INTRODUCTION

Cell therapy with mesenchymal stem cells (MSCs) has become a promising therapeutic approach for regenerative medicine. The abundance and easy accessibility of adipose-derived stem cell (ASC) have made it a promising candidate for MSC-based therapies. However, transplantation of dissociated ASCs is frequently associated with early cell death with limited therapeutic effects, and cell sheet engineering of ASCs holds promise in treating many diseases, including myocardial infarctions, skin wounds, hind limb ischemia, esophageal strictures, and oral ulcers (Sukho et al., 2018). We have successfully stimulated extracellular matrix (ECM) secretion of ASCs and fabricated cell sheets by applying a long-acting form of ascorbic acid, L-ascorbic acid 2-phosphate (A2-P), in the culture medium (Yu et al., 2014). With this approach, native ECM secreted by the cells was preserved, and ASCs could be harvested as a contiguous cell sheet with intact cell-to-cell connections. Enhanced expression of stemness markers, including Oct4, Sox2, and Nanog, was found in ASCs within the cell sheets. ASC sheets also possess the necessary paracrine factors to improve skin wound healing and decrease scar formation (Yu et al., 2018).

The aforementioned studies employed fetal bovine serum (FBS) for ASC culture during cell sheet fabrication. However, due to the risks of xeno-immunization against bovine antigens, transmission of zoonotic diseases, and potential limits of availability, it was necessary to find suitable human alternatives for the manufacture of ASC sheets to meet clinical therapeutic purposes (Mackensen et al., 2000; Horwitz et al., 2002; Schallmoser and Strunk, 2013; Barro et al., 2020). Human platelet lysate (HPL) contains a number of mitogenic growth factors, including fibroblast growth factor (FGF), endothelial growth factor (EGF), platelet-derived growth factors (PDGF), vascular endothelial growth factor (VEGF), and transforming growth factor (TGF; Fekete et al., 2012; Chen et al., 2018). The platelet lysates have demonstrated the advantages to replace FBS for culturing fibroblasts, endothelial cells or tumor cell lines (Burnouf et al., 2016; Schallmoser et al., 2020). A series of reports have shown that both allogeneic and autologous HPL are superior to FBS for stimulation of MSC proliferation (Schallmoser and Strunk, 2009; Naaijkens et al., 2012; Barro et al., 2019). Moreover, MSCs expanded in HPL-supplemented culture medium preserved their immune-privileged capabilities, including the suppression of T cell proliferation and activation (Flemming et al., 2011).

The highly stimulatory effect of HPL on cell proliferation enabled large-scale expansion of ASC for clinical use, yielding a great advantage when compared with the standard FBS culture method (Cowper et al., 2019; Gao et al., 2019). Besides enhancing the proliferative activity, HPL was also shown to promote ASC differentiation into osteoblasts and chondrocytes compared to FBS (Gao et al., 2019). HPL was suggested to alter the ASC behavior and function via multiple signaling pathways (Kakudo et al., 2019). A previous study showed that HPL can benefit cell behavior and ECM production, thus optimizing the conditions for cell sheet production in periodontal ligament stem cells (Tian et al., 2018). Since the application of HPL in fabricating ASC sheets had not been reported in the literature, it was therefore intriguing to explore the effect of replacing FBS with HPL on the microenvironment fabricated within ASC sheets. To elucidate the potential clinical application of HPL-cultured ASC sheets, we also examined their cellular function regarding wound healing, immunomodulation and angiogenesis.

MATERIALS AND METHODS

Isolation and Culture of Human ASCs

Adipose-derived stem cells were isolated from the subcutaneous fat tissue of four non-smoking, non-diabetic female donors with an average age of 45 years (32–57 years) and an average body mass index of 24.6 (21.0–26.6) as described previously (Wu et al., 2020). The study protocol has been approved by the Research Ethics Committee of National Taiwan University Hospital, and the informed consent has been obtained from each donor of adipose tissue. This study was conducted in accordance to the institutional biosafety standards. Small pieces of subcutaneous fat tissue were finely minced and washed using phosphate-buffered saline (PBS; Omics Biotechnology, Taipei, Taiwan), followed by treatment with collagenase type I (Gibco, Carlsbad, CA, United States) for 60 min. FBS (Hyclone, Logan, UT, United States) was added to inhibit collagenase activity before the cell suspension was filtered and centrifuged. Pellets were suspended and plated with Dulbecco's modified Eagle's medium (DMEM)/F-12 (Hyclone) and supplemented with 10% FBS, 1% penicillin–streptomycin (Biological Industries, Kibbutz Beit Haemek, Israel), and 1 ng/mL fibroblast growth factor-2 (FGF2; R&D systems, Minneapolis, MN, United States). The cells were cultured in a 5% CO2 humidified atmosphere at 37 °C, and the medium was changed every 2–3 days. Upon reaching 90% confluence, the cells were detached using 0.05% trypsin-ethylenediaminetetraacetic acid (EDTA) (Biological Industries) and re-plated until the third or fourth passage for various experiments. The cells have been previously tested to exhibit differentiation capabilities toward osteogenic, chondrogenic and adipogenic lineages (Tsai et al., 2019). Isolated human ASCs were pooled to become a single population based on the comparable surface marker expression and differentiation potential presented in each ASC clone.

Flow Cytometry Analysis and Population Doubling Assay

Commercially available HPL (UltraGRO^{TM}, Helios BioScience, Atlanta, GA) was used for ASC culture supplement. ASCs were cultured in DMEM-high glucose (DMEM-HG; Hyclone) supplemented with 10% FBS, 5% HPL, 2% HPL or 1% HPL and subjected to flow cytometry analysis to determine the cell surface antigen expression. The cells were incubated with the following antibodies: human monoclonal antibodies against CD31 (BD Pharmingen, San Jose, CA, United States), CD44, CD34, CD73, CD90, and CD166 (all from BioLegend, San Diego, CA, United States). The samples were analyzed using a flow cytometer (FACSVerse; BD Biosciences, Franklin Lakes, NJ, United States) in which 10,000 cells were counted per sample. Positive cells were determined as the proportion of the population with higher fluorescence than 95% of the isotype

control. Moreover, ASCs were seeded in 10 cm culture dishes and supplemented with 10% FBS, 5% HPL, 2% HPL, or 1% HPL. After 7 days, the cells were lifted, counted with Scepter 2.0 Cell Counter (Millipore, Billerica, MA, United States), and the population doubling time was calculated by the following formula:

$$\text{Doubling Time}\,(\text{h}) = 168 \times \ln 2 / \ln\left(\text{Ne}/N_0\right)$$

N_0 is the seeding cell number at the beginning of the incubation time (1.6×10^4 cells per dish). Ne is the cell number at the end of the incubation time.

Differentiation of Human ASCs

Adipose-derived stem cells were cultured in DEME-HG supplemented with 10% FBS or 5% HPL. When the cells reached 80% confluence, the medium was changed to respective induction medium. Adipogenic differentiation was induced by DEME-HG supplemented with 10% FBS or 5% HPL, 1% penicillin/streptomycin, 500 μM 3-isobutyl-1-methylxanthine, 1 μM dexamethasone, 10 μM insulin, and 400 μM indomethacin (all from Sigma). Osteogenic differentiation was induced by DMEM-HG supplemented with 10% FBS or 5%HPL, 1% penicillin/streptomycin, 10 nM dexamethasone, 50 μM A2-P, 10 nM 1α,25-dihydroxyvitamin D3, and 10 μM β-glycerophosphate (all from Sigma). ASCs were fixed in 4% paraformaldehyde and stained with Oil Red O (Sigma) for adipogenesis assay or Alizarin Red S (Sigma) for osteogenesis assay on day 14.

Fabrication of ASC Sheets

To create cell sheets, ASCs were seeded at a density of 2.5×10^3 cells/cm^2. The culture medium consisted of DMEM-HG supplemented with 10% FBS or 5% HPL, 1% penicillin/streptomycin, and 250 μM A2-P. The culture medium was refreshed every 2∼3 days. The cell number within ASC sheets was estimated by measuring double-strand DNA (dsDNA) content of the ASCs. On day 7 and 14, DNA content was measured fluorometrically using the Quant-iT Picogreen dsDNA Reagent and Kits (Invitrogen, Carlsbad, CA, United States) according to the manufacturer's protocol (excitation wavelength, 485 nm; emission wavelength, 535 nm). The cell number within each well was estimated using a calibration curve. Cell sheets were peeled off from the culture plates for further analysis on day 14.

Microscopic Images and Histology

For the electron microscopic study, cell sheets fabricated in 10% FBS or 5% HPL were washed thoroughly and fixed in 4% paraformaldehyde in PBS for 20 min. The cell sheets were dehydrated by gradual change of concentrated ethanol, followed by lyophilization. The specimens were then sputter coated with platinum and examined using a scanning electron microscope (JSM-6700F, JOEL, Tokyo, Japan). A second harmonic generation microscopic system was also used to examine the ASC sheets as previously described (Wu et al., 2019). A wavelength-tunable Ti:Sapphire laser pumped by a diode-pumped solid-state laser (Spectra Physics, Mountain View, CA, United States) was used as the excitation source. The 880 nm output laser system was guided toward a modified upright microscope (BX51WI, Olympus, Tokyo, Japan). The excitation source was beam expanded and reflected toward the focusing objective by a primary dichroic beamsplitter (Semrock, Rochester, NY, United States). To optimize image quality without laser ablation, the laser power was set at about 70 mW on the tissue section. The non-linear autofluorescence signals were spectrally separated by bandpass filters of 434/17 nm and 510/84 nm (Semrock).

As for the histological analysis, FBS or HPL-cultured ASC sheets were fixed in 4% paraformaldehyde and then paraffin-embedded. Sections were cut perpendicular to the surface of the cell sheet with a thickness of 5 μm. Paraffin-embedded sections were de-parafinized, rehydrated, and stained with hematoxylin and eosin (H&E, Sigma) or Masson's trichrome (Sigma). The thickness of cell sheets was determined using ImageJ. Three ASC sheets from each group were used, and five high-power fields in each section were randomly selected, followed by three measurements of sheet thickness per field.

Ribonucleic Acid (RNA) Isolation and Quantitative Polymerase Chain Reaction (qPCR)

Total RNA was extracted from FBS or HPL-cultured monolayer ASCs and ASC sheets using a RNeasy Mini Kit (Qiagen, Valencia, CA, United States) according to the manufacturer's protocols. After the RNA was isolated, complementary DNA (cDNA) was synthesized from the RNA using High-Capacity cDNA Reverse Transcription Kits (Applied Biosystems, Foster City, CA, United States). Real-time qPCR was performed with FastStart Universal SYBR Green Master (Roche, Indianapolis, IN, United States) using CFX Connect Real-Time PCR Detection System (Bio-Rad, Hercules, CA, United States). The expression level was analyzed and normalized to glyceraldehyde 3-phosphate dehydrogenase (GAPDH) for each cDNA sample. The relative quantity (RQ) of gene expression was calculated by relative quantification based on threshold cycle number. The sequences of the gene-specific primers are shown in **Supplementary Table S1**.

Western Blot, ELISA, and Total Collagen Assay

The expression of collagen 1α1, fibronectin, laminin, and hepatocyte growth factor (HGF) was determined in FBS or HPL-cultured ASC sheets by western blot analysis. Briefly, ASC sheets were lysed in radioimmunoprecipitation assay buffer (Pierce Biotechnology, Rockford, IL, United States). After centrifugation, the protein content was determined in the supernatants by a bicinchoninic acid protein quantification kit (Pierce Biotechnology). Protein samples were added to sample buffer and boiled for 10 min. Proteins were separated by 7% sodium dodecyl sulfate polyacrylamide gel electrophoresis (SDS-PAGE) and blotted onto polyvinylidene difluoride membranes. Western blot was performed using anti-collagen 1α1 (R&D Systems, AF6220), anti-fibronectin (R&D Systems, MAB19182), anti-laminin (R&D Systems, AF4187), and anti-HGF (R&D

Systems, AF-294-NA). Moreover, quantification of secreted HGF in the conditioned medium from FBS or HPL-cultured ASC sheets was performed using an ELISA kit for human HGF (Quantikine; R&D Systems). Data were expressed as the secreted factor per 10^5 cells at the time of harvest.

Collagen content during the ASC sheet fabrication process was also assessed by Sircol collagen assay (Biocolor, Newtownabbey, United Kingdom). After 5 days of culture, cells in each well were detached by HyQtase (Hyclone) treatment and discarded, and the remaining ECM was digested with 5 mg/ml pepsin (Roche) overnight. Then 0.5 ml Sircol dye reagent was added into each well and agitated to form collagen-dye complex, followed by centrifugation and dye release by alkali treatment. The absorbance of the released dye was measured by a spectrometer (Infinite F200; Tecan, San Jose, CA, United States) at 570 nm.

Proteomic Analysis of the ASC Sheet ECM Samples

Fetal bovine serum or HPL-cultured ASC sheets were decellularized with 0.5% Triton X-100 at 37°C for 10 min, and 0.3% ammonium hydroxide at 37°C for 5 min. The sheets were then treated with 240 U/ml of DNase-I for 1 h at 37°C as previously described (Lin et al., 2012). Decellularization was confirmed by 4',6-diamidino-2-phenylindole (DAPI; Santa Cruz, Santa Cruz, CA, United States) staining under a fluorescence microscope. Protein samples were separated by SDS-PAGE, followed by in-gel digestion, then subjected to liquid chromatography-tandem mass spectrometry (LC-MS/MS). Proteins were then identified and quantified by proteomics softwares. The detailed experimental protocol is provided in the **Supplementary Material**.

ASC Sheet-Conditioned Medium for Fibroblast Culture

Conditioned media were harvested from ASC sheets cultured in 10% FBS or 5% HPL after culturing for 24 h. Terminally differentiated human fibroblasts (Hs68) were seeded into a 24-well culture plate with a small rectangular culture inserts (Ibidi, Gräfelfing, Germany) placed at the center of each well. The seeding density was 2×10^4 cells/well, and the cells were incubated in DMEM-HG supplemented with 10% FBS and 1% penicillin/streptomycin for 4 h to allow attachment. Then the inserts were removed, creating a rectangular cell-free zone in each well. After washing twice with PBS, the medium was changed to the collected conditioned medium of FBS or HPL-cultured ASC sheets. Serum-free DEME-HG was employed as a control group. Time-lapse microscopic images were taken with a time interval of 60 min for 12 h using an inverted microscope, and *in vitro* migration of fibroblasts into the cell-free zone was quantified using ImageJ.

The effect of ASC sheet-conditioned medium on Hs68 cell proliferation was also examined. Hs68 fibroblasts were seeded at a density of 2×10^4 cells/well in 24-well culture plates. After cell attachment, the medium was replaced with the conditioned medium of FBS or HPL-cultured ASC sheets. On days 1, 4, 7, alamar blue solution (AbD Serotec, Kidlington, United Kingdom) was directly added into the culture wells, and the plate was further incubated at 37°C for 24 h. The fluorescence signals are measured at an excitation wavelength at 560 nm and an emission wavelength at 590 nm by a spectrometer. Moreover, Hs68 cells were stimulated with 20 ng/mL TGF-β1 for 24 h to test the anti-fibrosis effect of ASC sheet-conditioned media. Subsequently, the medium was replaced by the conditioned medium from FBS or HPL-cultured ASC sheets supplemented with 20 ng/mL TGF-β1. In two groups, anti-human HGF neutralizing antibody (5 μg/mL; Sigma, H0652) was also added in the ASC sheet-conditioned media. After 40 h, Hs68 cells were harvested for analysis of *TGF-β1* and α-smooth muscle actin (*α-SMA*) gene expression.

ASC Sheet-Conditioned Medium for Macrophage Chemotaxis Assay

The influence of conditioned medium derived from monolayer ASCs and ASC sheets on the chemotaxis of mouse macrophage J774A1 cells (Bioresource Collection and Research Center, Hsinchu, Taiwan) was determined using transwell inserts with 8-μm pores (Corning). J774A1 cells which had been stimulated by lipopolysaccharide (LPS; 0.1 μg/mL) for 4 h were seeded in the lower wells at a density of 3×10^5 cells/well. The upper wells were seeded with unstimulated macrophages at a density of 1×10^5 cells/well, and the medium was replaced with the conditioned media of FBS or HPL-cultured monolayer ASCs or ASC sheets. After 24 h of culture in conditioned medium, macrophage migration through the transwell membrane was assessed through crystal violet (Sigma) staining of the lower surface of the membrane. The stained cells in the acquired microscopic images were quantified using ImageJ.

ASC Sheet-Conditioned Medium for *in vitro* Tube Formation Assay

Human umbilical vein endothelial cells (HUVECs) were seeded on μ-slide (Ibidi) at a density of 8,000 cells/well, which were previously coated with Matrigel (Corning, Lowell, MA, United States). HUVECs were treated with the conditioned medium of FBS or HPL-cultured ASC sheets. All conditioned medium was mixed with equal volume of endothelial growth medium 2 (EGM2; PromoCell, Heidelberg, Germany) and applied for HUVEC culture. A basal medium mixed by equal volume of DMEM-HG and endothelial basal medium (EBM, PromoCell) served as a negative control, while EGM2 was used as a positive control. Formation of tube-like structures was visualized by a phase-contrast microscope at 6 h, and the images were analyzed using ImageJ.

Angiogenesis Assay in Chick Embryo

The chick embryo chorioallantoic membrane (CAM) model is a well-established *in ovo* assay for studying angiogenesis (Cheng et al., 2017). Briefly, fertilized chicken eggs were incubated at 37°C with 70% humidity. On day 3, a circular window was made on the air chamber, and the embryo viability was evaluated. On day 7, FBS or HPL-cultured ASC sheets attached to polyester membranes (Corning) as carriers were placed onto

the CAM through the open window. The opening window in the shell was then sealed with Tegaderm (3M) to prevent dehydration and contamination, and the eggs were returned to the incubator at 37°C for another 3 days. On day 10, the embryos were infused with 4% paraformaldehyde and placed at −80°C overnight. ASC sheets and adjacent CAM tissues were removed and transferred to 6-well plates containing 4% paraformaldehyde. The CAM specimens were photographed, and the blood vessels were quantified by measuring the capillary area and length, as well as counting the number of capillary branch points and nodes using ImageJ.

Statistical Analysis

All investigations were confirmed by at least three independent experiments. All measurements are presented as the means ± standard deviation. Statistical significance was evaluated using an independent-sample Student's t-test or one-way ANOVA. Tukey's post hoc test was used when the group of interest was compared to all other groups in the experiment. All statistical analyses were performed using GraphPad Prism 7 (La Jolla, CA, United States), and statistically significant values were defined as $p < 0.05$.

RESULTS

Characterization of FBS and HPL-Cultured ASCs

Human ASCs cultured with 10% FBS, 5% HPL, 2% HPL or 1% HPL were harvested for flow cytometry analysis. The surface epitopes of HPL-treated ASCs were similar to those of ASCs undergoing FBS treatment. These ASCs were negative for hematopoietic markers CD31 and CD34, and they were positive for MSC-related markers CD44, CD73, CD90, and CD166 (**Figure 1A**). Population doubling time estimated by cell number calculation demonstrated higher ASC proliferative activity under HPL culture condition (1% HPL: 43.0 ± 0.9 h, 2% HPL: 32.1 ± 0.6 h, 5% HPL: 28.6 ± 0.5 h vs. 10% FBS: 58.0 ± 3.0 h, $p < 0.01$, respectively; **Figure 1B**). Since significant statistical difference was found among the population doubling time of the 1, 2, and 5% HPL groups, 5% HPL was chosen to be used in the subsequent experiments. Moreover, 10% FBS or 5% HPL-treated ASCs maintained their adipogenic and osteogenic differentiation capabilities after application of appropriate induction media, as demonstrated by histology staining specific for oil and calcium, respectively (**Figure 1C**).

HPL Enhanced Cell Sheet Formation

Cell number within FBS or HPL-cultured ASC sheets were estimated by dsDNA assay, revealing significantly more cells in the HPL group relative to the FBS group on either day 7 or 14 of culture (**Figure 2A**). Under electron microscope, HPL-cultured cell sheets appeared to exhibit more matrix, and it was difficult to distinguish the cellular boundary on the sheet surface (**Figure 2B**). Comparing to FBS-cultured ASC sheets, abundant collagen deposition was noted in the HPL-cultured ASC sheets under second harmonic imaging microscopy (**Figure 2C**). Cell sheets were also peeled off from the tissue culture plates and subjected to histological examination of their cross sections. H&E staining showed 2 or 3 layers of ASCs within the FBS-cultured cell sheets, while 3 to 4 layers of ASCs could be observed in the HPL-cultured cell sheets. Masson's trichrome staining demonstrated abundant ECM formation within the interstitial voids of the HPL-cultured ASC sheets (**Figure 2D**). Moreover, quantitative measurement of the thickness of the cell sheets revealed significantly thicker sheet formation in the HPL group (13.4 ± 0.5 μm vs. 21.8 ± 0.6 μm, $p < 0.005$; **Figure 2E**).

Real-time qPCR analysis revealed 2.1 ± 0.3-fold up-regulated collagen 1α1 (*COL1A1*), 2.1 ± 0.2-fold up-regulated fibronectin (*FN1*) and 2.3 ± 0.2-fold up-regulated laminin (*LAMA1*) genes in HPL-cultured ASC sheets relative to FBS-cultured monolayer ASCs, and significantly more transcripts of these genes were also noted when compared to the HPL-cultured monolayer ASCs (**Figure 3A**). Relative to FBS-cultured ASC sheets, HPL-treated ASC sheets exhibited significant higher collagen contents as determined by Sircol collagen assay ($p < 0.005$; **Figure 3B**). Western blot results also revealed enhanced collagen 1α1 and fibronectin expression in HPL-cultured ASC sheets (**Figure 3C**). Through proteomic analysis, we further identified 63 unique proteins in FBS-cultured ASC sheets and 83 unique proteins in HPL-treated ASC sheets (**Figure 3D** and **Supplementary Table S2**).

Conditioned Medium Enhanced Fibroblast Migration and Proliferation

Incubated in conditioned medium of FBS or HPL-cultured ASC sheets, Hs68 fibroblasts were subjected to *in vitro* cell migration assay (**Figure 4A**). The migrated fibroblasts covered a significantly larger portion of wound area in the group of HPL-cultured ASC sheet (FBS sheet: 59.0 ± 13.0% vs. HPL sheet: 94.52 ± 1.5% at 12 h, $p < 0.005$; **Figure 4B**). Moreover, alamar blue assay revealed significantly higher Hs68 cell proliferation when cultured with conditioned medium from HPL-sheets at days 4 and 7 ($p < 0.01$ and $p < 0.005$ relative to the FBS group at each day; **Figure 4C**).

Immunomodulatory Gene Expression in HPL-Cultured ASC Sheets

In order to fully understand the immunomodulatory capabilities associated with FBS or HPL-cultured ASC sheets, we examined the expression of immunomodulation-related genes, including interleukin-6 (*IL6*), tumor necrosis factor-α-induced protein 6 (TSG-6; *TNFAIP6*), C1q/tumor necrosis factor-related protein-3 (*CTRP3*), and indoleamine 2,3-dioxygenase (*IDO-1*). Relative to the FBS monolayer culture condition, FBS-cultured ASC sheets showed significant up-regulation of *CTRP3* (11.8 ± 1.7-fold, $p < 0.005$), while HPL-cultured ASC sheets exhibited significant up-regulation of both *IL-6 and CTRP3* (2.1 ± 0.6-fold, $p < 0.05$ and 13.7 ± 4.0-fold, $p < 0.005$, respectively; **Figure 5A**).

Moreover, we collected conditioned medium of FBS or HPL-cultured monolayer ASCs or ASC sheets and applied in a transwell experimental setting of macrophage culture

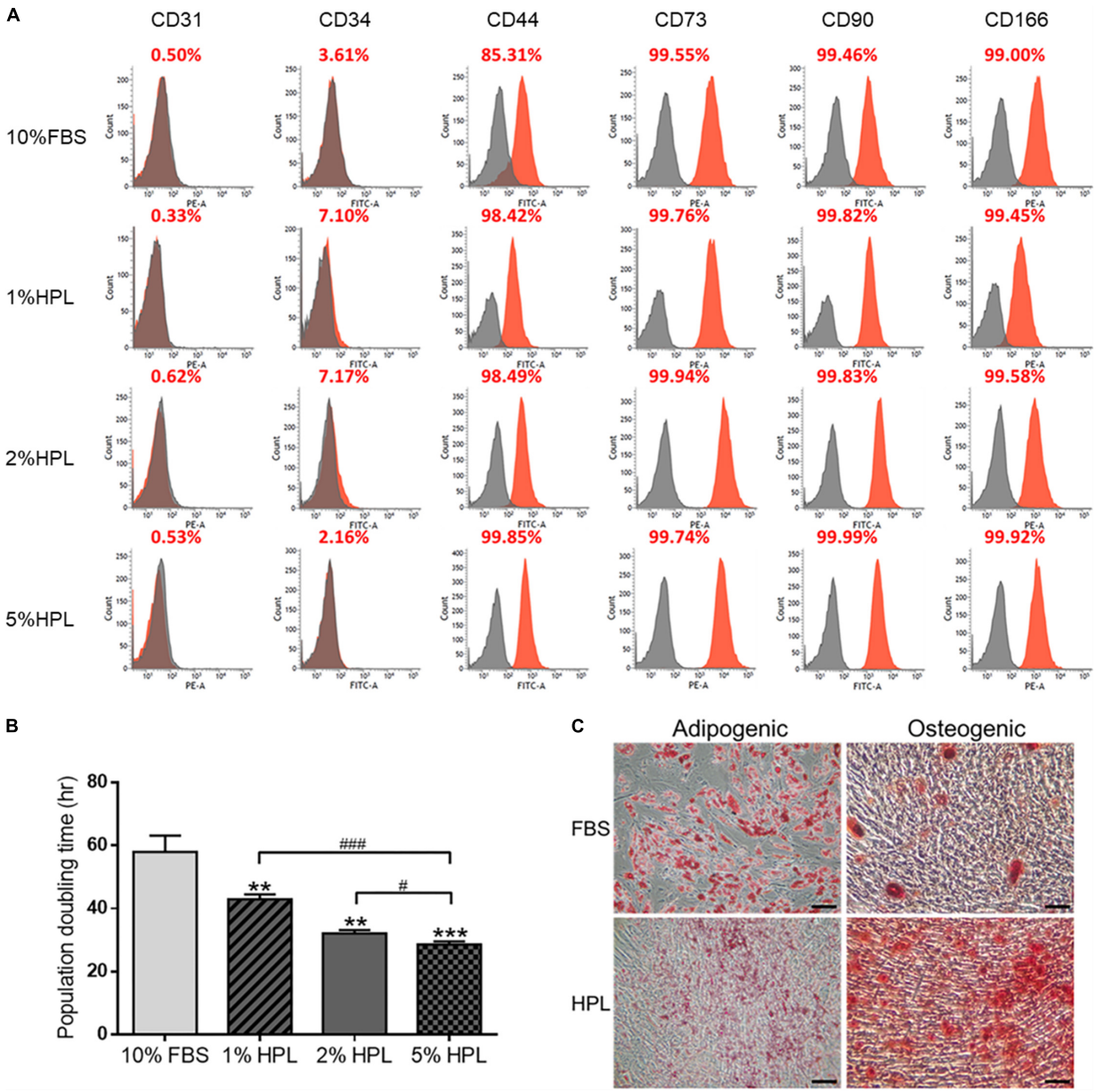


FIGURE 1 | Phenotypic characteristics of adipose-derived stem cells (ASCs) cultured in medium supplemented with fetal bovine serum (FBS) or different concentrations of human platelet lysate (HPL). **(A)** Representative flow cytometry results of ASC surface antigens shown as the proportion relative to a positive control. **(B)** Population doubling time of ASCs cultured with FBS or different concentrations of HPL ($n = 3$; $^{*}p < 0.05$; $^{**}p < 0.01$; $^{***}p < 0.005$ from 10% HBS, $^{\#}p < 0.05$; $^{\#\#}p < 0.01$; $^{\#\#\#}p < 0.005$ between the indicated groups). **(C)** Microscopic images of FBS or HPL-cultured ASCs cultured in adipogenic and osteogenic induction medium for 14 days. Adipocytes and osteocytes were stained by Oil Red O and Alizarin red, respectively (scale bar = 100 μm).

in vitro. The chemotaxis of macrophages toward LPS-stimulated macrophages was examined, and the number of migrated cells on the undersurface of the transwell membrane was estimated. Relative to the groups using monolayer ASC-conditioned media, the migrated cell number was significantly lower in the presence of ASC sheet-conditioned media relative to the control ($p < 0.005$ respectively). Among them, the FBS and HPL-cultured ASC sheet-conditioned medium groups exhibited no significant difference in the number of migrated cells (**Figure 5B**).

Expression of Angiogenic Growth Factors in HPL-Cultured ASC Sheets

The relative mRNA expression of several angiogenic growth factors, including VEGF-A, VEGF-C, HGF, and FGF2, was analyzed by real-time qPCR. Relative to the FBS monolayer culture group, down-regulation of *VEGF-C* and *FGF2*

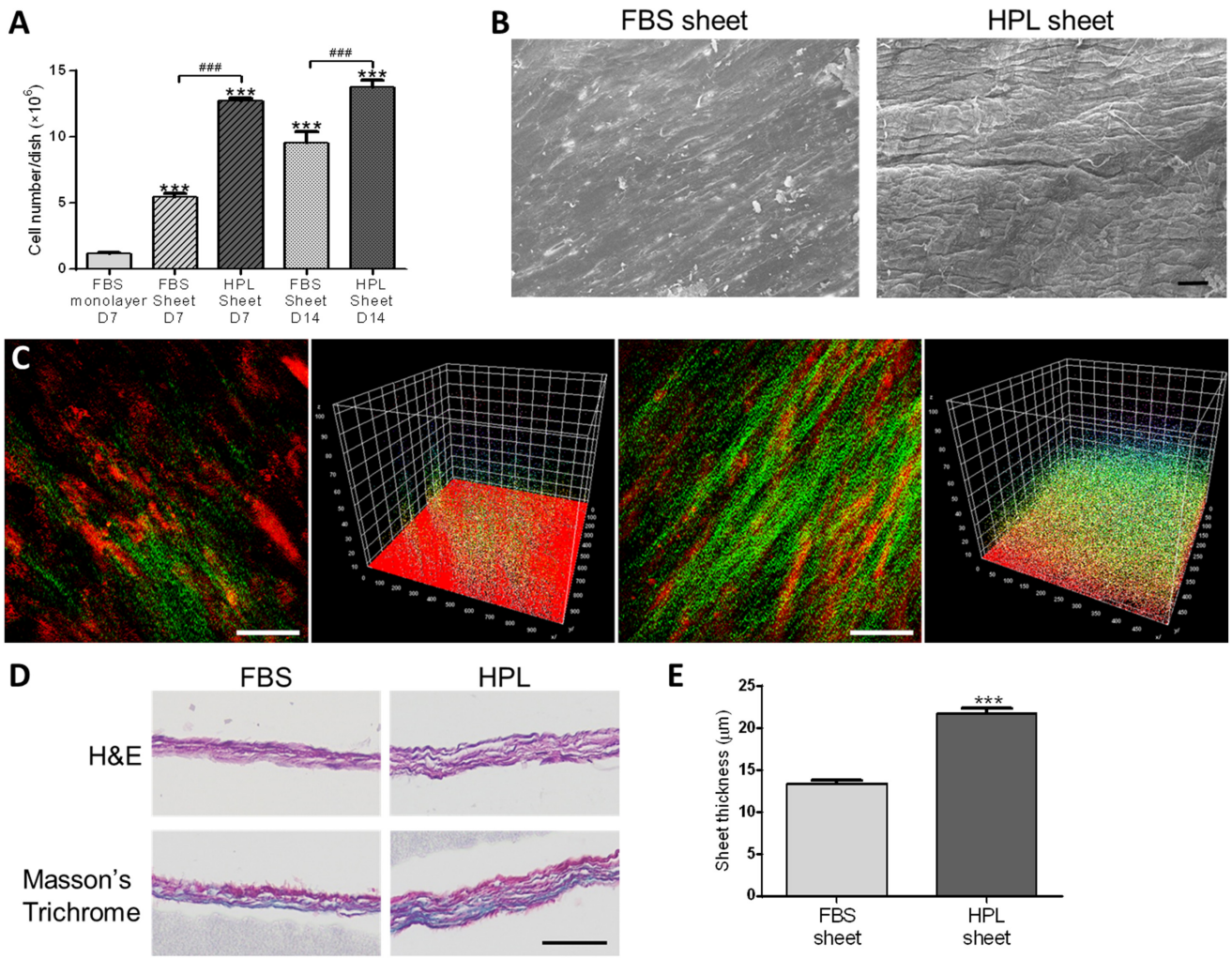


FIGURE 2 | Cell sheet formation of fetal bovine serum (FBS) or human platelet lysate (HPL)-cultured adipose-derived stem cells (ASCs). **(A)** Representative scanning electron microscopic images of FBS or HPL-cultured ASC sheets (scale bar = 50 μm). **(B)** Cell number estimated by double-strand DNA (dsDNA) quantification assay (n = 3). **(C)** Second harmonic generation images of FBS or HPL-cultured ASC sheet after 7 days of culturing (scale bar = 50 μm). **(D)** Hematoxylin and eosin (H&E) and Masson's Trichrome staining of cross section after 14 days of FBS or HPL-cultured ASC sheets (scale bar = 50 μm). **(E)** Thickness of the ASC sheets measured in histological images (n = 6; ***p < 0.005 from the control, ###p < 0.005 between the indicated groups).

was noted in HPL treatment or sheet formation groups. *VEGF-A* transcript number was significantly lower in the FBS or HPL-cultured ASC sheets, while up-regulation of *HGF* was noted in both groups. Compared to FBS-cultured ASC sheets, the HPL counterpart exhibited a significantly higher expression level of *HGF* (9.4 ± 1.4-fold vs. 15.4 ± 1.1-fold, $p < 0.005$; **Figure 6A**). ELISA analysis of HGF levels in human ASC sheet-conditioned media confirmed higher content of HGF released from HPL-cultured ASC sheets (FBS sheet: 84.2 ± 13.5 pg/10^5 cells vs. HPL sheet: 660.0 ± 47.1 pg/10^5 cells, $p < 0.005$; **Figure 6B**). Western blot analysis also showed more HGF expression in HPL-cultured ASC sheets compared to the FBS-cultured sheets (**Figure 6C**). Significant down-regulation of α-*SMA* and *TGF-β1* was noted in *TGF-β1*-stimulated Hs68 fibroblasts treated by conditioned medium of either FBS or HPL-cultured ASC sheets. Moreover, the down-regulation of α-*SMA* was partially reversed in Hs68 fibroblasts after supplementing anti-HGF neutralizing antibody in the conditioned medium of HPL-cultured ASC sheets (**Figure 6D**).

Tube Formation Assay of Endothelial Cells

Conditioned media harvested from FBS or HPL-cultured ASC sheets were used for HUVEC culture, and the endothelial cells began to form a vascular network structure within 4 h (**Figure 7A**). The *in vitro* tube formation of HUVECs was quantified by counting the total number of branching nodes and meshes per power field. Relative to the group receiving conditioned medium of FBS-cultured ASC

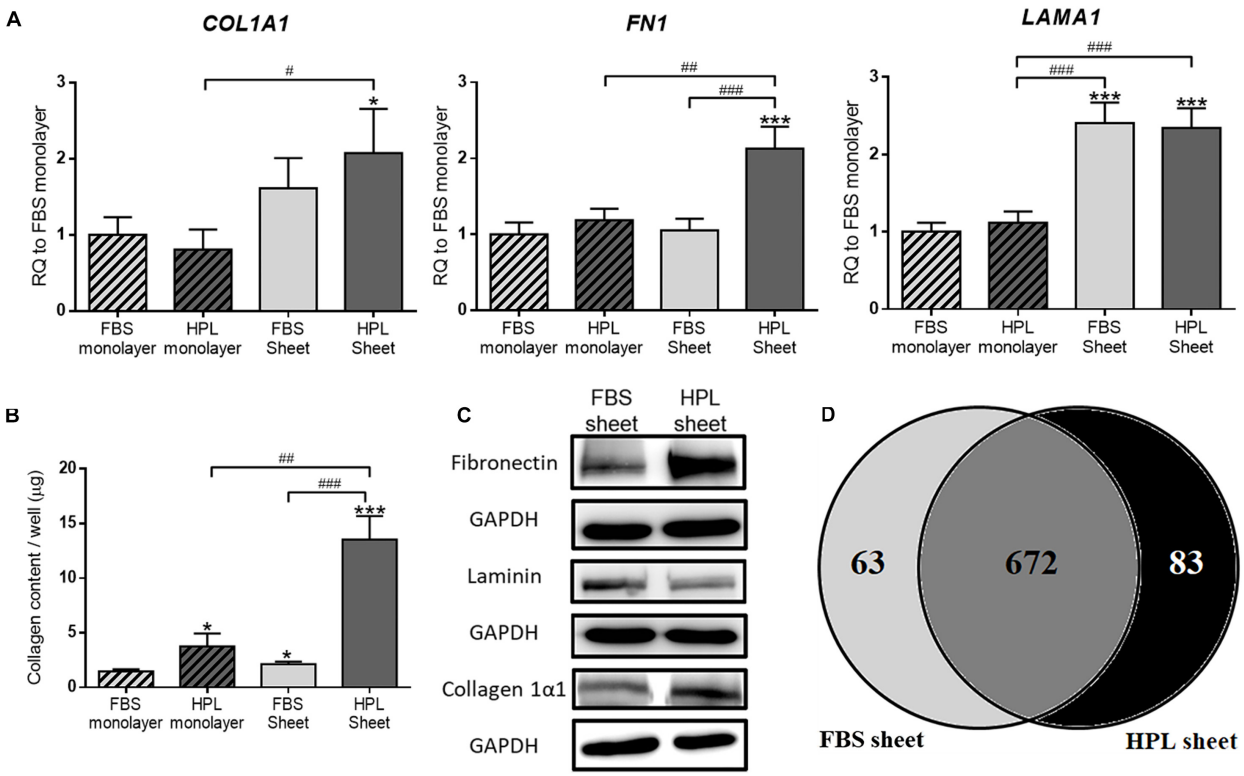


FIGURE 3 | Extracellular matrix (ECM) deposition in fetal bovine serum (FBS) or human platelet lysate (HPL)-cultured adipose-derived stem cell (ASC) sheets. **(A)** Gene expression of collagen 1α1 (*COL1A1*), fibronectin (*FN1*), and laminin (*LAMA1*) in ASCs under different culture condition ($n = 3$). **(B)** Sircol assay of ASCs cultured under different culture condition ($n = 3$). **(C)** Western blot analysis of the expression of the ECM proteins in FBS or HPL-cultured ASC sheets. **(D)** Venn diagram of the number of proteins detected on LC/MS in the ECM of ASC sheets cultured with FBS and HPL, respectively (*$p < 0.05$; **$p < 0.01$; ***$p < 0.005$ from control, $^{\#}p < 0.05$; $^{\#\#}p < 0.01$; $^{\#\#\#}p < 0.005$ between the indicated groups).

sheets, the HPL group exhibited significantly more tube-like structures (176.2 ± 6.9 vs. 249.3 ± 23.3 for nodes; 8.0 ± 0.3 vs. 17.4 ± 2.9 for meshes, $p < 0.01$, respectively; **Figure 7B**).

ASC Sheets Enhanced Angiogenesis in CAM Assay

We examined the capillary formation on CAM to investigate the angiogenesis potential of FBS or HPL-cultured ASC sheets (**Figure 8A**). After implantation of FBS or HPL-cultured ASC sheets on CAMs, the capillary area proportion around the sheets was estimated to be significantly higher relative to the control (FBS sheet: 13.2 ± 0.6%, HPL sheet: 13.6 ± 0.7% vs. control: 6.8 ± 1.6%, $p < 0.005$, respectively; **Figure 8B**). Total capillary length around the sheets on CAMs was also estimated to be significantly longer relative to the control (FBS sheet: 607 ± 77 μm per power field, HPL sheet: 568 ± 45 μm per power field vs. control: 242 ± 41 μm per power field; $p < 0.005$, respectively). Similarly, placing ASC sheets on CAMs also yielded significantly more capillary branch points or nodes per power field ($p < 0.005$ respectively; **Figure 8B**).

DISCUSSION

By preserving the cellular junctions and endogenous ECM, cell sheets recreate cellular microenvironments *in vitro*, mimicking the inherent chemical, mechanical, and biological properties of cellular niche. Therefore, cell sheet fabrication is deemed beneficial for ASC-based regenerative therapies (Sukho et al., 2018). In our previous studies, transferable ASC sheets can be generated by employing A2-P in the culture medium, and they exhibited enhanced biological function to promote wound healing and decrease scar formation. We also revealed the important role of endogenous ECM in the enhanced stemness of ASCs within cell sheets (Yu et al., 2014, 2018). Given the application of ASC sheets in clinical settings, they would ideally be generated without using xenogeneic supplements such as FBS. HPL has been shown to surpass xenogeneic FBS in terms of bio-safety, while maintaining the potential of ASCs for proliferation, differentiation and immunomodulation (Cowper et al., 2019; Kakudo et al., 2019). Therefore, adopting HPL is a viable alternative for ASC sheet fabrication, which can facilitate the translation of this technology into clinical treatments. By comparing the ASC sheets cultured with FBS or HPL, this study revealed prominent differences in the abundance of ECM and the composition of the microenvironment deposited *in vitro*.

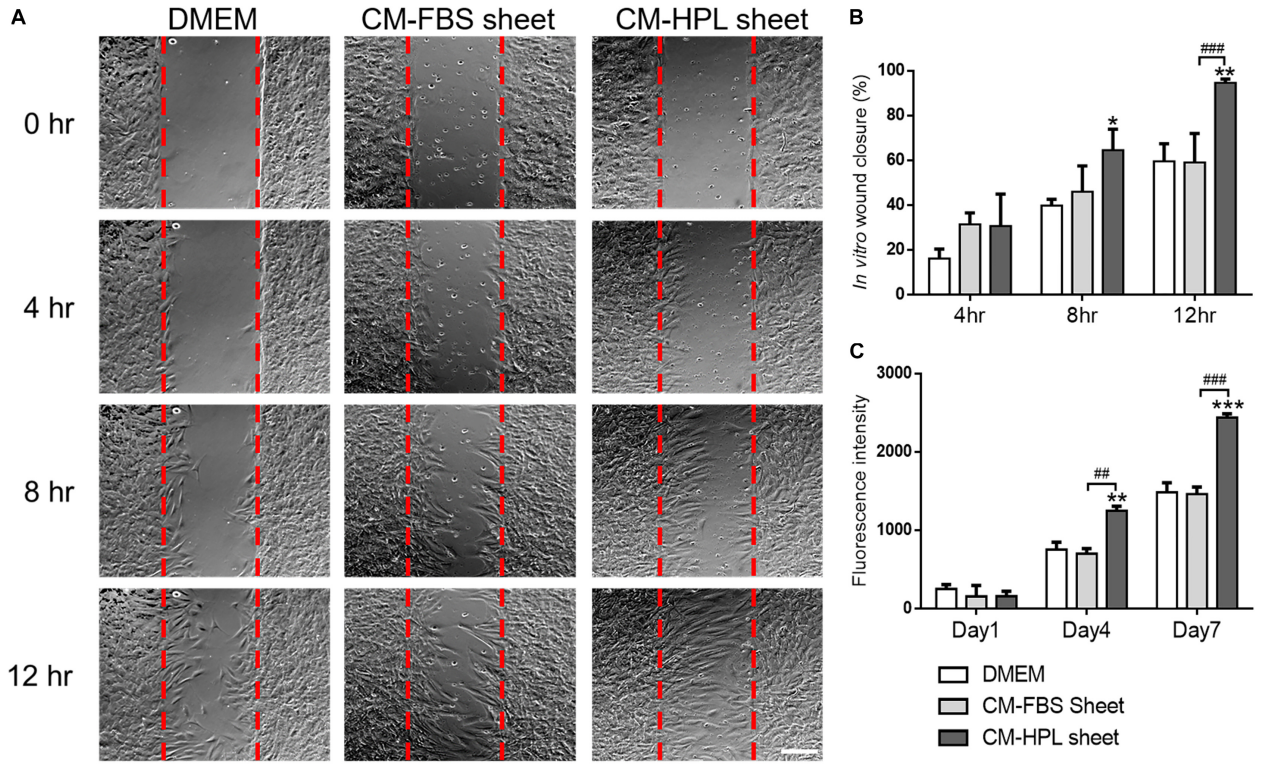


FIGURE 4 | Effect of conditioned medium (CM) collected from fetal bovine serum (FBS) or human platelet lysate (HPL)-cultured adipose-derived stem cell (ASC) sheets on migration and proliferation of HS68 fibroblasts. **(A)** Representative microscopic images of *in vitro* cell migration assay. Serum free Dulbecco's modified Eagle's medium (DMEM) was employed as the control group (scale bar = 200 μm). Red dotted lines represent the initial borders of the cell-free zone. **(B)** Quantification of the wound closure percentage of Hs68 fibroblasts. **(C)** Alamar blue assay for estimating Hs68 cell proliferation ($n = 3$; $^{*}p < 0.05$; $^{**}p < 0.01$; $^{***}p < 0.005$ from DMEM control, $^{\#}p < 0.05$; $^{\#\#}p < 0.01$; $^{\#\#\#}p < 0.005$ between the indicated groups).

Human platelet lysate prepared from human platelets has been increasingly suggested to replace FBS in clinically oriented MSC expansion applications, allowing efficient cell propagation under animal serum-free conditions for clinical use (Cowper et al., 2019; Pasztorek et al., 2019; Schallmoser et al., 2020). Although autologous blood is a reliable resource for producing HPL, requesting each patient to donate his/her blood during the long-term *in vitro* cell expansion process is certainly not cost effective. Therefore, large scale and standardized manufacturing of allogeneic HPL products from platelets of human blood donors for cell culture is a more practical option (Glovinski et al., 2017), and the potential risk of viral contamination should be judiciously evaluated during the manufacturing process (Burnouf et al., 2019). The expression of cell surface markers and adipogenic/osteogenic differentiation capabilities were maintained after replacing FBS with HPL for ASC culture. In a collaborative work, we have previously shown that HPL promoted human ASC differentiation into osteoblasts and chondrocytes compared to FBS (Gao et al., 2019). With 5% HPL employed in this study, the proliferative activity of ASCs was significantly increased relative to 10% FBS. The finding was in line with a previous study showing that 5% HPL was the optimal concentration for culturing human ASCs (Kakudo et al., 2019). Consequently, significantly more cells were found within the ASC sheets fabricated with HPL relative to the FBS-cultured cell sheets.

Histology of the cell sheet cross sections revealed significantly thicker HPL-cultured cell sheets relative to the FBS-cultured counterparts, comprising of several layers of ASCs with abundant ECM formation within the interstitial voids of the cells. Abundant deposition of ECM molecules, including collagen and fibronectin, was also found in the HPL-cultured ASC sheets. We previously demonstrated that A2-P-induced ECM synthesis was crucial for stemness enhancement of ASCs within cell sheets, indicating the importance of the microenvironment formulated by the ASC-secreted ECM (Yu et al., 2014). ECM signals are transduced into cells by cell surface receptors, thereby affecting various cellular functions. Stem cell fate determination by the surrounding ECM may be mediated through physical cell support and control of cell shape and geometry as a function of surface topography, substrate stiffness, and biochemical signaling (Engler et al., 2006). Stem cell-derived ECM was found to display a specific and unique matrisome signature, leading to differential survival and gene-expression profiles among the cell types (Ragelle et al., 2017). In this study, in addition to the different expression quantities of several important ECM proteins, mass spectrometry-based proteomic analysis further revealed that some proteins were found exclusively in the FBS or HPL-cultured ASC sheets. By

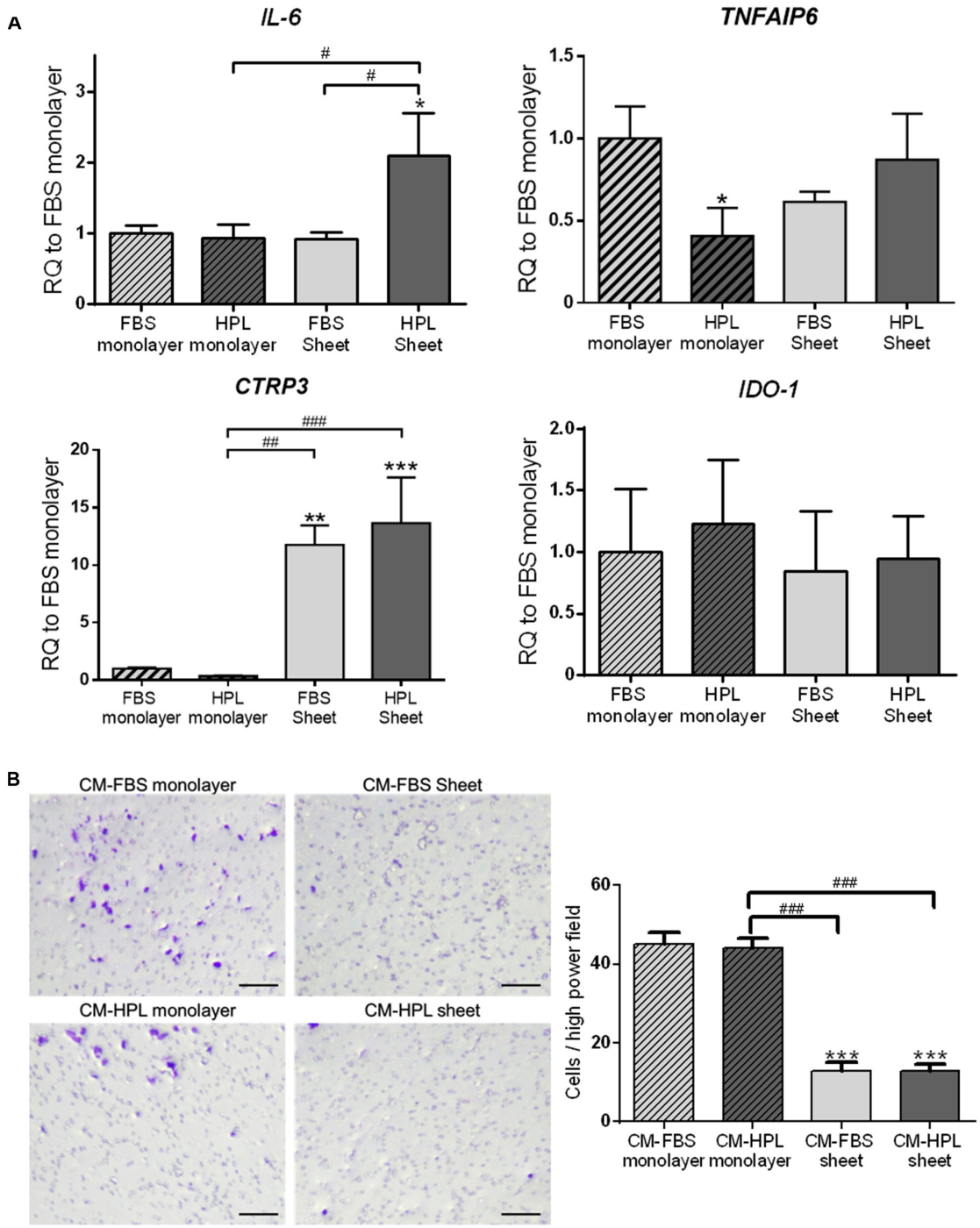


FIGURE 5 | Expression of immunomodulatory factors in fetal bovine serum (FBS) or human platelet lysate (HPL)-cultured ASC sheets and their influence on macrophage migration. **(A)** Real-time quantitative polymerase chain reaction (qPCR) measurements for immunomodulatory genes in monolayer and ASC sheets during *in vitro* culture. **(B)** Migration of macrophages toward lipopolysaccharide (LPS)-stimulated mouse macrophages was significantly inhibited by conditioned medium (CM) of FBS or HPL-cultured ASC sheets ($n = 3$; $^{*}p < 0.05$; $^{**}p < 0.01$; $^{***}p < 0.005$ from FBS monolayer group, $^{\#}p < 0.05$; $^{\#\#}p < 0.01$; $^{\#\#\#}p < 0.005$ between the indicated groups).

allowing interactions of cells with the surrounding ECM to adapt to their native morphology, the cell-derived ECMs can influence the resident cells in a different manner (Cheng et al., 2012). Therefore, certain differences are expected between the cellular phenotype and biological function of ASCs in different microenvironment of FBS or HPL-cultured cell sheets.

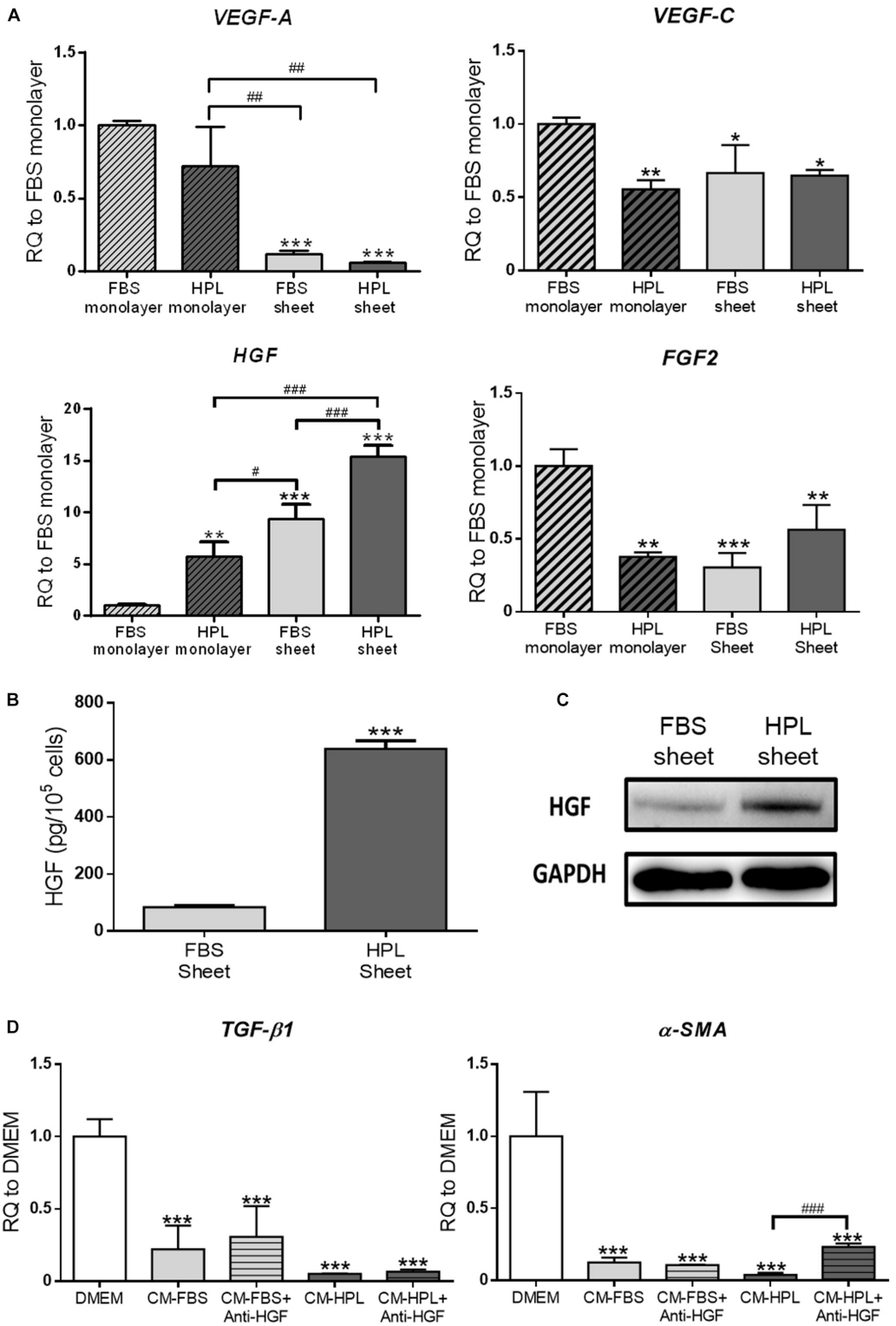


FIGURE 6 | Enhanced secretion of hepatocyte growth factor (HGF) from adipose-derived stem cell (ASC) sheets cultured in human platelet lysate (HPL). **(A)** Gene expression of several angiogenic growth factors in ASCs under different culture condition ($n = 3$; $^{*}p < 0.05$; $^{**}p < 0.01$; $^{***}p < 0.005$ from fetal bovine serum (FBS) monolayer group, $^{\#}p < 0.05$; $^{\#\#}p < 0.01$; $^{\#\#\#}p < 0.005$ between the indicated groups). **(B)** Release of HGF from FBS or HPL-cultured ASC sheets as determined by ELISA ($n = 3$; $^{***}p < 0.005$ from FBS sheet). **(C)** Western blot analysis of HGF expression in FBS or HPL-cultured ASC sheets. **(D)** Gene expression of *TGF-β1* and α-*SMA* in TGF-β1-stimulated Hs68 fibroblasts treated by different conditioned medium (CM) with or without anti-HGF neutralizing antibody ($n = 3$; $^{***}p < 0.005$ from Dulbecco's modified Eagle's medium (DMEM) group; $^{\#\#\#}p < 0.005$ between the indicated groups).

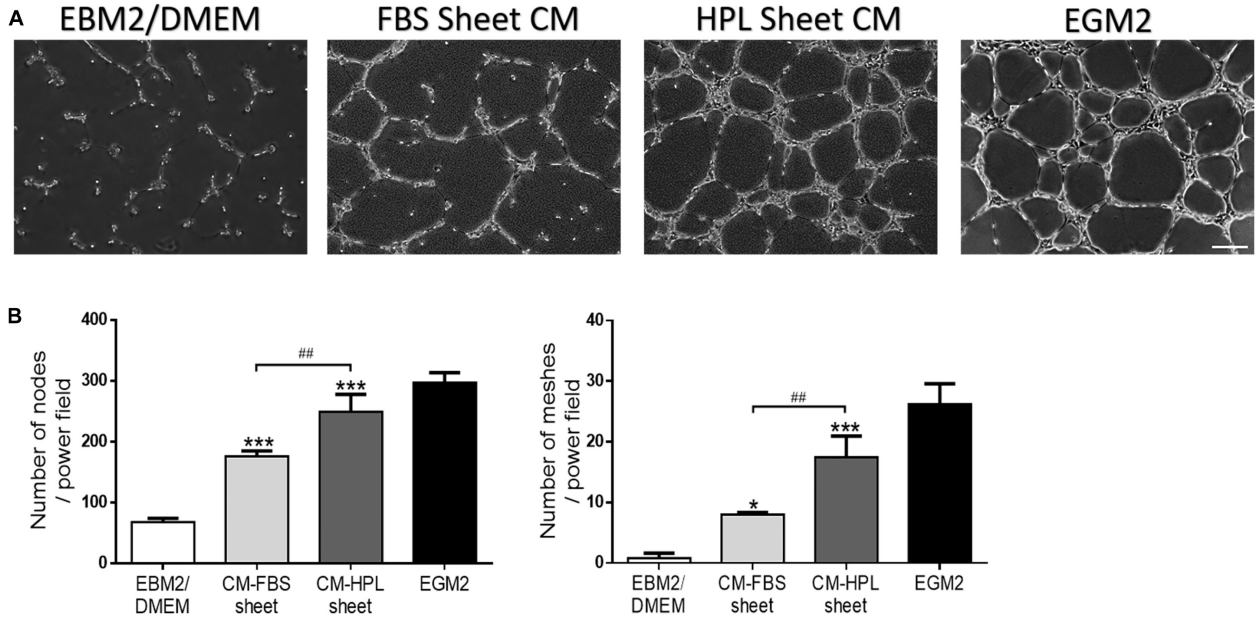


FIGURE 7 | Effect of conditioned medium (CM) collected from fetal bovine serum (FBS) or human platelet lysate (HPL)-cultured adipose-derived stem cell (ASC) sheets on the *in vitro* tube formation of Human umbilical vein endothelial cells (HUVECs). **(A)** Representative microscopic images of endothelial cells after incubation with conditioned medium. HUVECs cultured in endothelial growth medium 2 (EGM2) served as a positive control, and those in EBM2/DMEM was a negative control (scale bar = 200 μm). **(B)** Number of branching nodes and meshes per power field were compared among different groups. Values are presented as means ± SD ($n = 3$; $^{*}p < 0.05$; $^{**}p < 0.01$; $^{***}p < 0.005$ from EBM2/DMEM control, $^{\#}p < 0.05$; $^{\#\#}p < 0.01$; $^{\#\#\#}p < 0.005$ between the indicated groups).

We previously demonstrated that FBS-cultured ASC sheets enhanced skin wound healing, and the neodermis possessed a highly organized collagen structure (Yu et al., 2018). In this study, HPL-cultured ASC sheets were found to be more effective in stimulating the migration and proliferation of fibroblasts *in vitro*, indicating their potential application in wound healing. Moreover, an anti-scarring effect of the ASC sheets-conditioned medium was evidenced by the down-regulation of *TGF-β1* and α-*SMA* in TGF-β1-stimulated fibroblasts. After an anti-human HGF neutralizing antibody was added in the conditioned medium of HPL-cultured ASC sheets, partial reverse of the α-*SMA* down-regulation was observed in TGF-β1-stimulated fibroblasts. The finding indicates that HPL-cultured ASC sheets inhibit the differentiation of fibroblasts toward α-SMA-expressing myofibroblasts partially through the increased secretion of HGF. Similarly, Ma et al. recently demonstrated that ASC-secreted HGF effectively inhibits fibrosis-related factors and regulates ECM remodeling in hypertrophic scar fibroblasts (Ma et al., 2020).

The immunomodulatory function of ASCs has been recognized to play important roles for their therapeutic activity (Prockop and Oh, 2012). In an inflammatory microenvironment, ASCs can profoundly affect the function of various effector cells involved in the adaptive and innate immune reaction, including T-cells, B-cells, natural killer (NK) cells, monocytes, macrophages, dendritic cells, neutrophils, and mast cells (Prockop and Oh, 2012; Hsu et al., 2013). The specific molecular mechanisms involved in the immune regulatory properties of ASCs are associated with both cell contact-dependent mechanisms and soluble inducible factors. ASCs release an array of cytokines that exert potent immunomodulatory effects capable of regulating multiple signaling pathways and cell types that contribute to the pathogenesis of inflammatory or immune-related diseases (Zimmermann and Mcdevitt, 2014). Particularly, MSCs cultivated in 3D structure are sensitive to medium supplemented with HPL, resulting in changes in actin filament formation, mitochondrial dynamics and membrane elasticity that can have an impact on the immunomodulatory function of MSCs (Pasztorek et al., 2019). IL-6 is a regulator of inflammation, and previous reports have shown that IL-6 released from ASCs can increase proliferation of several types of cells (Lu et al., 2016; Pu et al., 2019). Since IL-6 was up-regulated in HPL-cultured ASC sheets, but not in the FBS counterparts, this finding may help to explain the stimulatory effects of conditioned medium of HPL-cultured ASC sheets on the migration and proliferation of fibroblasts *in vitro*. TSG-6 has been identified as an important component of paracrine-mediated MSC immunomodulation (Lee et al., 2014), but the ASC sheets and FBS-cultured monolayer ASCs in the present study exhibited no significant difference in the gene expression of TSG-6. However, FBS or HPL-cultured ASC sheets were found to exhibit significant up-regulation of *CTRP3* relative to monolayer ASCs. CTRP3 was found to inhibit the C-C motif ligand 2 release by macrophages *in vitro* and subsequently reduced the chemotaxis of unstimulated macrophages (Yu et al., 2018). In this study, we confirmed that conditioned medium of HPL-cultured ASC sheets significantly inhibited the migration of macrophages toward LPS-stimulated macrophages *in vitro*, suggesting HPL-cultured ASC sheets

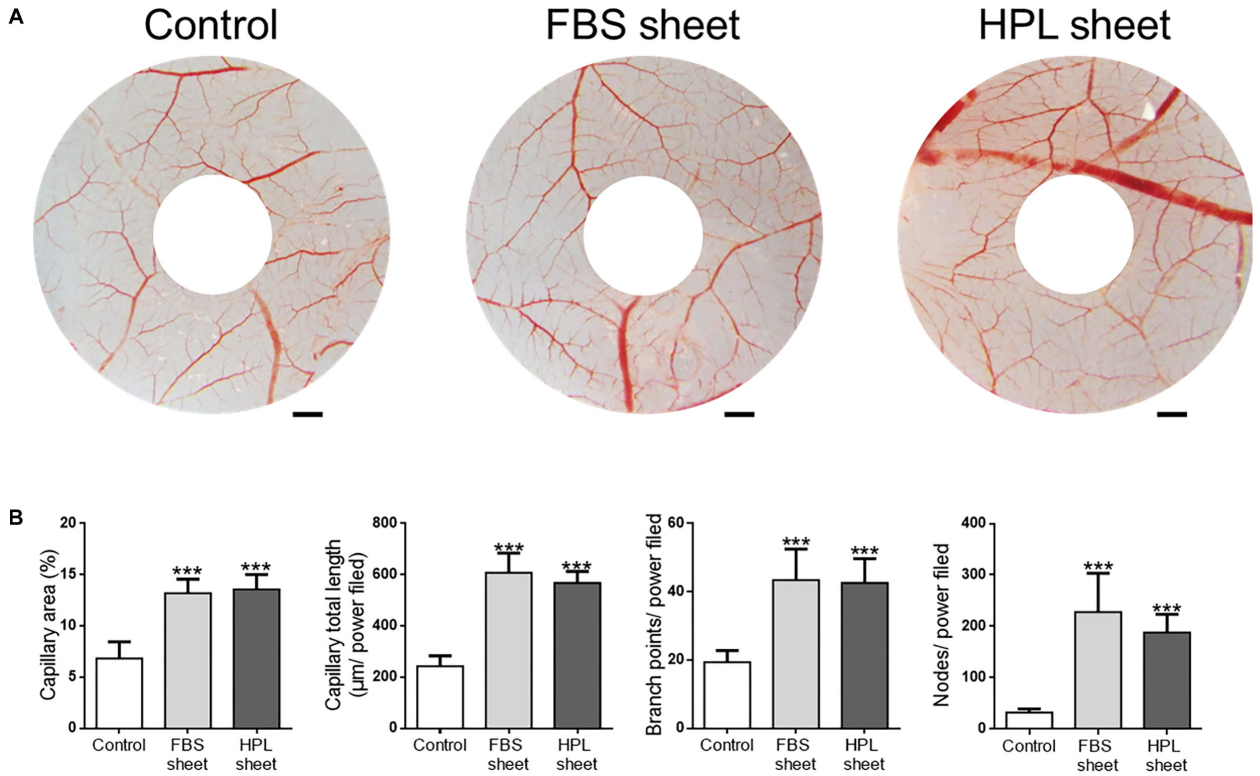


FIGURE 8 | Chick embryo chorioallantoic membrane (CAM) assay. **(A)** Photographs of CAMs after treatment with fetal bovine serum (FBS) or human platelet lysate (HPL)-cultured adipose-derived stem cell (ASC) sheets, which were loaded on the CAMs of day 7 chick embryos. After 72 h of incubation, CAMs were excised and photographed (scale bar = 2 mm). **(B)** Blood vessel formation on CAMs was quantified by measuring the area covered by capillaries and the total capillary length. The number of capillary branch points and nodes per power field were also counted (image analysis performed on 10 random fields per sample, $n = 3$; $^{***}p < 0.005$ from control).

can decrease local inflammation by inhibiting macrophage recruitment to the injury site.

Blood flow is required to supply oxygen and nutrition, and to remove waste throughout the process of tissue regeneration. Capillary angiogenesis is therefore vital for promoting regeneration in ischemic tissues. ASCs have been shown to secrete multiple cytokines or growth factors that can promote angiogenesis. Among them, VEGF has been considered to play an important role in ASC-mediated angiogenesis. However, down-regulation of VEGF has been noted in ASCs after sheet formation (Makarevich et al., 2015). After replacing FBS with HPL during the sheet fabrication process, down-regulation of VEGF-A and VEGF-C persisted, but significant up-regulation of HGF was noted. In this study, ELISA also revealed a significantly higher HGF concentration in the conditioned medium of HPL-cultured ASC sheets. HGF production is important for ASC potency by mediating the proangiogenic, prosurvival, and repair promotion activities of ASCs (Cai et al., 2007). A recent clinical trial also demonstrated the effectiveness of topical HGF injection in promoting healing of ischemic ulcers in lower limbs (Gu et al., 2019). Moreover, IL-6 released by ASCs can also stimulate angiogenesis and enhanced recovery after ischemia-reperfusion injury (Pu et al., 2017), suggesting *IL-6* up-regulation in HPL-cultured ASC sheets may also contribute to angiogenesis. Therefore, co-culturing HUVECs with conditioned medium of HPL-cultured ASC sheets revealed more tube-like structure formation of the endothelial cells, indicating the potential of these cell sheets in promoting angiogenesis. By quantification of the capillary area and length in the CAM assay, we confirmed that HPL-cultured ASC sheets significantly promoted angiogenesis, though no significant difference was found between the FBS and HPL-cultured cell sheets.

In summary, we successfully fabricated ASC sheets using HPL as a substitute for xenogeneic FBS, resulting in thicker cell sheets with more abundant ASC-derived ECM deposition. The composition of ECMs within cell sheets was modified by replacing FBS with HPL for ASC culture, affecting the characteristics and function of the resident cells. HPL-cultured ASC sheets more effectively promoted fibroblast migration and proliferation, and they also inhibited the differentiation of fibroblasts into α-SMA-expressing myofibroblasts upon TGF-β1 stimulation *in vitro*. Moreover, FBS and HPL-cultured ASC sheets both inhibited the chemotaxis of unstimulated macrophages, which was possibly mediated through the significant up-regulation of CTRP3. Relative to their FBS counterpart, more HGF was found to release from HPL-cultured ASC sheets, and the angiogenic potential of HPL-cultured ASC sheets was maintained both *in vitro* and *in vivo*. The results of this study

demonstrated a promising approach to fabricate ASC sheets with HPL for clinical use. Further animal studies are required to fully extrapolate the cellular function resulting from the altered microenvironment within the HPL-cultured ASC sheets.

DATA AVAILABILITY STATEMENT

The datasets generated in this study can be found in online repositories. The names of the repository/repositories and accession number(s) can be found in the article/ **Supplementary Material**.

ETHICS STATEMENT

The study protocol has been approved by the Research Ethics Committee of National Taiwan University Hospital, and the informed consent has been obtained from each donor of adipose tissue.

AUTHOR CONTRIBUTIONS

N-CC conceived and designed the experiments, wrote the manuscript, participated in performing the experiments and analyzing the data. Y-KT contributed to the study design, practical work, and manuscript revision. N-HL took part in performing the experiments and analyzing the data. T-HY conceived and designed the experiments and made the final approval of the version to be published. All authors contributed to the article and approved the submitted version.

FUNDING

This research was supported by the Ministry of Science and Technology, Taiwan (MOST 109-2314-B-002-267 and 109-2628-B-002-048), National Taiwan University Hospital (109-S4476), and E-Da Hospital-National Taiwan University Hospital Joint Research Program (108-EDN05 and 109-EDN07).

ACKNOWLEDGMENTS

The authors thank Prof. Sung-Jan Lin and Dr. Yueh-Feng Wu (National Taiwan University) for professional support and help. The authors also acknowledge the technical assistance of the staff at the Eighth Core Lab of National Taiwan University Hospital.

SUPPLEMENTARY MATERIAL

The Supplementary Material for this article can be found online at: https://www.frontiersin.org/articles/10.3389/fcell.2020.558354/full#supplementary-material

REFERENCES

Barro, L., Nebie, O., Chen, M.-S., Wu, Y.-W., Koh, M. B., Knutson, F., et al. (2020). Nanofiltration of growth media supplemented with human platelet lysates for pathogen-safe xeno-free expansion of mesenchymal stromal cells. *Cytotherapy* 22, 458–472. doi: 10.1016/j.jcyt.2020.04.099

Barro, L., Su, Y. T., Nebie, O., Wu, Y. W., Huang, Y. H., Koh, M. B., et al. (2019). A double-virally-inactivated (intercept–solvent/detergent) human platelet lysate for in vitro expansion of human mesenchymal stromal cells. *Transfusion* 59, 2061–2073. doi: 10.1111/trf.15251

Burnouf, T., Barro, L., Nebie, O., Wu, Y.-W., Goubran, H., Knutson, F., et al. (2019). Viral safety of human platelet lysate for cell therapy and regenerative medicine: moving forward, yes, but without forgetting the past. *Trans. Apher. Sci.* 58:102674. doi: 10.1016/j.transci.2019.102674

Burnouf, T., Strunk, D., Koh, M. B., and Schallmoser, K. (2016). Human platelet lysate: replacing fetal bovine serum as a gold standard for human cell propagation? *Biomaterials* 76, 371–387. doi: 10.1016/j.biomaterials.2015.10.065

Cai, L., Johnstone, B. H., Cook, T. G., Liang, Z., Traktuev, D., Cornetta, K., et al. (2007). Suppression of hepatocyte growth factor production impairs the ability of adipose-derived stem cells to promote ischemic tissue revascularization. *Stem Cells* 25, 3234–3243. doi: 10.1634/stemcells.2007-0388

Chen, L. W., Huang, C. J., Tu, W. H., Lu, C. J., Sun, Y. C., Lin, S. Y., et al. (2018). The corneal epitheliotrophic abilities of lyophilized powder form human platelet lysates. *PLoS One* 13:e0194345. doi: 10.1371/journal.pone.0194345

Cheng, N. C., Lin, W. J., Ling, T. Y., and Young, T. H. (2017). Sustained release of adipose-derived stem cells by thermosensitive chitosan/gelatin hydrogel for therapeutic angiogenesis. *Acta Biomater.* 51, 258–267. doi: 10.1016/j.actbio.2017.01.060

Cheng, N. C., Wang, S., and Young, T. H. (2012). The influence of spheroid formation of human adipose-derived stem cells on chitosan films on stemness and differentiation capabilities. *Biomaterials* 33, 1748–1758. doi: 10.1016/j.biomaterials.2011.11.049

Cowper, M., Frazier, T., Wu, X., Curley, L., Ma, M. H., Mohuiddin, O. A., et al. (2019). Human platelet lysate as a functional substitute for fetal bovine serum in the culture of human adipose derived stromal/stem cells. *Cells* 8:724. doi: 10.3390/cells8070724

Engler, A. J., Sen, S., Sweeney, H. L., and Discher, D. E. (2006). Matrix elasticity directs stem cell lineage specification. *Cell* 126, 677–689. doi: 10.1016/j.cell.2006.06.044

Fekete, N., Gadelorge, M., Fürst, D., Maurer, C., Dausend, J., Fleury-Cappellesso, S., et al. (2012). Platelet lysate from whole blood-derived pooled platelet concentrates and apheresis-derived platelet concentrates for the isolation and expansion of human bone marrow mesenchymal stromal cells: production process, content and identification of active components. *Cytotherapy* 14, 540–554. doi: 10.3109/14653249.2012.655420

Flemming, A., Schallmoser, K., Strunk, D., Stolk, M., Volk, H.-D., and Seifert, M. (2011). Immunomodulative efficacy of bone marrow-derived mesenchymal stem cells cultured in human platelet lysate. *J. Clin. Immunol.* 31, 1143–1156. doi: 10.1007/s10875-011-9581-z

Gao, Y., Ku, N. J., Sung, T. C., Higuchi, A., Hung, C. S., Lee, H. H., et al. (2019). The effect of human platelet lysate on the differentiation ability of human adipose-derived stem cells cultured on ecm-coated surfaces. *J. Mater. Chem. B* 7, 7110–7119. doi: 10.1039/c9tb01764j

Glovinski, P. V., Herly, M., Mathiasen, A. B., Svalgaard, J. D., Borup, R., Talman, M. M., et al. (2017). Overcoming the bottleneck of platelet lysate supply in large-scale clinical expansion of adipose-derived stem cells: a comparison of fresh versus three types of platelet lysates from outdated buffy coat-derived platelet concentrates. *Cytotherapy* 19, 222–234. doi: 10.1016/j.jcyt.2016.10.014

Gu, Y., Cui, S., Wang, Q., Liu, C., Jin, B., Guo, W., et al. (2019). A randomized, double-blind, placebo-controlled phase ii study of hepatocyte growth factor in the treatment of critical limb ischemia. *Mol. Ther.* 27, 2158–2165. doi: 10.1016/j.ymthe.2019.10.017

Horwitz, E. M., Gordon, P. L., Koo, W. K., Marx, J. C., Neel, M. D., Mcnall, R. Y., et al. (2002). Isolated allogeneic bone marrow-derived mesenchymal cells engraft and stimulate growth in children with osteogenesis imperfecta:

implications for cell therapy of bone. *Proc. Natl. Acad. Sci. U.S.A.* 99, 8932–8937. doi: 10.1073/pnas.132252399

Hsu, W. T., Lin, C. H., Chiang, B. L., Jui, H. Y., Wu, K. K., and Lee, C. M. (2013). Prostaglandin E2 potentiates mesenchymal stem cell-induced IL-10+IFN-γ+CD4+ regulatory T cells to control transplant arteriosclerosis. *J. Immunol.* 190, 2372–2380. doi: 10.4049/jimmunol.1202996

Kakudo, N., Morimoto, N., Ma, Y., and Kusumoto, K. (2019). Differences between the proliferative effects of human platelet lysate and fetal bovine serum on human adipose-derived stem cells. *Cells* 8:1218. doi: 10.3390/cells8101218

Lee, R. H., Yu, J. M., Foskett, A. M., Peltier, G., Reneau, J. C., Bazhanov, N., et al. (2014). TSG-6 as a biomarker to predict efficacy of human mesenchymal stem/progenitor cells (hMSCs) in modulating sterile inflammation in vivo. *Proc. Natl. Acad. Sci. U.S.A.* 111, 16766–16771. doi: 10.1073/pnas.1416121111

Lin, H., Yang, G., Tan, J., and Tuan, R. S. (2012). Influence of decellularized matrix derived from human mesenchymal stem cells on their proliferation, migration and multi-lineage differentiation potential. *Biomaterials* 33, 4480–4489. doi: 10.1016/j.biomaterials.2012.03.012

Lu, J. H., Wei, H. J., Peng, B. Y., Chou, H. H., Chen, W. H., Liu, H. Y., et al. (2016). Adipose-derived stem cells enhance cancer stem cell property and tumor formation capacity in lewis lung carcinoma cells through an interleukin-6 paracrine circuit. *Stem Cells Dev.* 25, 1833–1842. doi: 10.1089/scd.2016.0163

Ma, J., Yan, X., Lin, Y., and Tan, Q. (2020). Hepatocyte growth factor secreted from human adipose-derived stem cells inhibits fibrosis in hypertrophic scar fibroblasts. *Curr. Mol. Med.* 20, 558–571. doi: 10.2174/1566524020666200106095745

Mackensen, A., Drager, R., Schlesier, M., Mertelsmann, R., and Lindemann, A. (2000). Presence of IgE antibodies to bovine serum albumin in a patient developing anaphylaxis after vaccination with human peptide-pulsed dendritic cells. *Cancer Immunol. Immunother.* 49, 152–156. doi: 10.1007/s002620050614

Makarevich, P. I., Boldyreva, M. A., Gluhanyuk, E. V., Efimenko, A. Y., Dergilev, K. V., Shevchenko, E. K., et al. (2015). Enhanced angiogenesis in ischemic skeletal muscle after transplantation of cell sheets from baculovirus-transduced adipose-derived stromal cells expressing VEGF165. *Stem Cell Res. Ther.* 6:204. doi: 10.1186/s13287-015-0199-6

Naaijkens, B. A., Niessen, H. W., Prins, H. J., Krijnen, P. A., Kokhuis, T. J., De Jong, N., et al. (2012). Human platelet lysate as a fetal bovine serum substitute improves human adipose-derived stromal cell culture for future cardiac repair applications. *Cell Tissue Res.* 348, 119–130. doi: 10.1007/s00441-012-1360-5

Pasztorek, M., Rossmanith, E., Mayr, C., Hauser, F., Jacak, J., Ebner, A., et al. (2019). Influence of platelet lysate on 2D and 3D amniotic mesenchymal stem cell cultures. *Front. Bioeng. Biotechnol.* 7:338. doi: 10.3389/fbioe.2019.00338

Prockop, D. J., and Oh, J. Y. (2012). Mesenchymal stem/stromal cells (mscs): role as guardians of inflammation. *Mol. Ther.* 20, 14–20. doi: 10.1038/mt.2011.211

Pu, C. M., Chen, Y. C., Chen, Y. C., Lee, T. L., Peng, Y. S., Chen, S. H., et al. (2019). Interleukin-6 from adipose-derived stem cells promotes tissue repair by the increase of cell proliferation and hair follicles in ischemia/reperfusion-treated skin flaps. *Mediat. Inflamm.* 2019:2343867. doi: 10.1155/2019/2343867

Pu, C. M., Liu, C. W., Liang, C. J., Yen, Y. H., Chen, S. H., Jiang-Shieh, Y. F., et al. (2017). Adipose-derived stem cells protect skin flaps against ischemia/reperfusion injury via IL-6 expression. *J. Invest. Dermatol.* 137, 1353–1362. doi: 10.1016/j.jid.2016.12.030

Ragelle, H., Naba, A., Larson, B. L., Zhou, F., Prijic, M., Whittaker, C. A., et al. (2017). Comprehensive proteomic characterization of stem cell-derived extracellular matrices. *Biomaterials* 128, 147–159. doi: 10.1016/j.biomaterials.2017.03.008

Schallmoser, K., Henschler, R., Gabriel, C., Koh, M. B. C., and Burnouf, T. (2020). Production and quality requirements of human platelet lysate: a position statement from the working party on cellular therapies of the international society of blood transfusion. *Trends Biotechnol.* 38, 13–23. doi: 10.1016/j.tibtech.2019.06.002

Schallmoser, K., and Strunk, D. (2009). Preparation of pooled human platelet lysate (PHPL) as an efficient supplement for animal serum-free human stem cell cultures. *J. Vis. Exp.* 32:1523. doi: 10.3791/1523

Schallmoser, K., and Strunk, D. (2013). Generation of a pool of human platelet lysate and efficient use in cell culture. *Methods Mol. Biol.* 946, 349–362. doi: 10.1007/978-1-62703-128-8_22

Sukho, P., Cohen, A., Hesselink, J. W., Kirpensteijn, J., Verseijden, F., and Bastiaansen-Jenniskens, Y. M. (2018). Adipose tissue-derived stem cell sheet application for tissue healing in vivo: a systematic review. *Tissue Eng. Part B Rev.* 24, 37–52. doi: 10.1089/ten.TEB.2017.0142

Tian, B.-M., Wu, R.-X., Bi, C.-S., He, X.-T., Yin, Y., and Chen, F.-M. (2018). Human platelet lysate supports the formation of robust human periodontal ligament cell sheets. *J. Tissue Eng. Regen. Med.* 12, 961–972. doi: 10.1002/term.2511

Tsai, C. C., Hong, Y. J., Lee, R. J., Cheng, N. C., and Yu, J. (2019). Enhancement of human adipose-derived stem cell spheroid differentiation in an in situ enzyme-crosslinked gelatin hydrogel. *J. Mater. Chem. B* 7, 1064–1075. doi: 10.1039/c8tb02835d

Wu, Y. F., Wang, C. Y., Yang, T. L., Tsao, P. N., Lin, S. J., and Tan, H. Y. (2019). Intravital multiphoton microscopic imaging platform for ocular surface imaging. *Exp. Eye Res.* 182, 194–201. doi: 10.1016/j.exer.2019.02.016

Wu, Y. K., Tu, Y. K., Yu, J., and Cheng, N. C. (2020). The influence of cell culture density on the cytotoxicity of adipose-derived stem cells induced by L-ascorbic acid-2-phosphate. *Sci. Rep.* 10:104. doi: 10.1038/s41598-019-56875-0

Yu, J., Tu, Y. K., Tang, Y. B., and Cheng, N. C. (2014). Stemness and transdifferentiation of adipose-derived stem cells using L-ascorbic acid 2-phosphate-induced cell sheet formation. *Biomaterials* 35, 3516–3526. doi: 10.1016/j.biomaterials.2014.01.015

Yu, J., Wang, M. Y., Tai, H. C., and Cheng, N. C. (2018). Cell sheet composed of adipose-derived stem cells demonstrates enhanced skin wound healing with reduced scar formation. *Acta Biomater.* 77, 191–200. doi: 10.1016/j.actbio.2018.07.022

Zimmermann, J. A., and Mcdevitt, T. C. (2014). Pre-conditioning mesenchymal stromal cell spheroids for immunomodulatory paracrine factor secretion. *Cytotherapy* 16, 331–345. doi: 10.1016/j.jcyt.2013.09.004

Conflict of Interest: The authors declare that the research was conducted in the absence of any commercial or financial relationships that could be construed as a potential conflict of interest.

Copyright © 2020 Cheng, Tu, Lee and Young. This is an open-access article distributed under the terms of the Creative Commons Attribution License (CC BY). The use, distribution or reproduction in other forums is permitted, provided the original author(s) and the copyright owner(s) are credited and that the original publication in this journal is cited, in accordance with accepted academic practice. No use, distribution or reproduction is permitted which does not comply with these terms.

frontiers in Cell and Developmental Biology

ORIGINAL RESEARCH
published: 25 November 2020
doi: 10.3389/fcell.2020.554984

The Bone-Forming Properties of Periosteum-Derived Cells Differ Between Harvest Sites

Lisanne C. Groeneveldt[1,2,3,4,5], Tim Herpelinck[1,2], Marina Maréchal[1,2], Constantinus Politis[3,4], Wilfred F. J. van IJcken[5,6], Danny Huylebroeck[5,7], Liesbet Geris[1,2,8,9], Eskeatnaf Mulugeta[5] and Frank P. Luyten[1,2,7]*

[1] Prometheus, Division of Skeletal Tissue Engineering, KU Leuven, Leuven, Belgium, [2] Skeletal Biology and Engineering Research Center, KU Leuven, Leuven, Belgium, [3] OMFS IMPATH Research Group, Department of Imaging and Pathology, KU Leuven, Leuven, Belgium, [4] Oral and Maxillofacial Surgery, University Hospitals Leuven, Leuven, Belgium, [5] Department of Cell Biology, Erasmus University Medical Center, Rotterdam, Netherlands, [6] Center for Biomics, Erasmus University Medical Center, Rotterdam, Netherlands, [7] Department of Development and Regeneration, KU Leuven, Leuven, Belgium, [8] Biomechanics Research Unit, GIGA-R In Silico Medicine, Université de Liége, Liège, Belgium, [9] Biomechanics Section, KU Leuven, Leuven, Belgium

OPEN ACCESS

Edited by:
Pavel Makarevich, Lomonosov Moscow State University, Russia

Reviewed by:
Andrea Banfi, University of Basel, Switzerland
Andrei S. Chagin, Karolinska Institutet (KI), Sweden

***Correspondence:**
Liesbet Geris
liesbet.geris@kuleuven.be

Specialty section:
This article was submitted to Stem Cell Research, a section of the journal Frontiers in Cell and Developmental Biology

Received: *23 April 2020*
Accepted: *22 October 2020*
Published: *25 November 2020*

Citation:
Groeneveldt LC, Herpelinck T, Maréchal M, Politis C, van IJcken WFJ, Huylebroeck D, Geris L, Mulugeta E and Luyten FP (2020) The Bone-Forming Properties of Periosteum-Derived Cells Differ Between Harvest Sites. Front. Cell Dev. Biol. 8:554984. doi: 10.3389/fcell.2020.554984

The development of alternatives for autologous bone grafts is a major focus of bone tissue engineering. To produce living bone-forming implants, skeletal stem and progenitor cells (SSPCs) are envisioned as key ingredients. SSPCs can be obtained from different tissues including bone marrow, adipose tissue, dental pulp, and periosteum. Human periosteum-derived cells (hPDCs) exhibit progenitor cell characteristics and have well-documented *in vivo* bone formation potency. Here, we have characterized and compared hPDCs derived from tibia with craniofacial hPDCs, from maxilla and mandible, respectively, each representing a potential source for cell-based tissue engineered implants for craniofacial applications. Maxilla and mandible-derived hPDCs display similar growth curves as tibial hPDCs, with equal trilineage differentiation potential toward chondrogenic, osteogenic, and adipogenic cells. These craniofacial hPDCs are positive for SSPC-markers CD73, CD164, and Podoplanin (PDPN), and negative for CD146, hematopoietic and endothelial lineage markers. Bulk RNA-sequencing identified genes that are differentially expressed between the three sources of hPDC. In particular, differential expression was found for genes of the HOX and DLX family, for *SOX9* and genes involved in skeletal system development. The *in vivo* bone formation, 8 weeks after ectopic implantation in nude mice, was observed in constructs seeded with tibial and mandibular hPDCs. Taken together, we provide evidence that hPDCs show different profiles and properties according to their anatomical origin, and that craniofacial hPDCs are potential sources for cell-based bone tissue engineering strategies. The mandible-derived hPDCs display - both *in vitro* and *in vivo* - chondrogenic and osteogenic differentiation potential, which supports their future testing for use in craniofacial bone regeneration applications.

Keywords: cell differentiation, mandible, maxilla, mesenchymal stromal cells, osteogenesis, periosteum, tibia, transcriptome

INTRODUCTION

The development of effective treatments for large bone defects incurred by trauma, osteonecrosis or tumor resection remains a challenge, which is further complicated by factors such as infections and congenital abnormalities. Currently, autografts are considered as the standard treatment of these bone defects, however, this approach requires large volumes of bone. In addition, it also requires a second surgical site where donor tissue is harvested, thereby introducing donor site morbidity (including pain) and potential major complications (in up to 10% of the cases; Arrington et al., 1996). These include vascular injuries or deep infection in the donor site, and the possibility of herniation of abdominal contents in case an iliac crest graft is used. Furthermore, usually these donor sites provide insufficient quantities of tissue for filling large bone defects and, in addition, poor vascularization of the tissue graft can lead to necrosis (Meijer et al., 2008).

Bone tissue engineering presents an opportunity for the repair of large bone defects, with the engineered constructs classically being composed of appropriate cells that are able to proliferate and differentiate, and growth factors to instruct cell differentiation in a 3D environment that provides some biomechanical support (Leijten et al., 2015). Skeletal stem and progenitor cells (SSPCs), often referred to as mesenchymal stromal cells (MSCs), whereas these originate from various tissues including bone marrow, adipose tissue, gingiva, dental pulp and the periosteum, are being assessed for their potential in bone tissue engineering. Recently, a *bona fide* human skeletal stem cell characterized by a $PDPN^{+}$ $CD146^{-}$ $CD73^{+}$ $CD164^{+}$ signature was identified (Chan et al., 2018). This stem cell population demonstrates significant amplification properties in response to fracture. Similarly, periosteum-derived cells (PDCs) undergo a rapid expansion to assist in callus formation (Colnot et al., 2012), suggesting the presence of a stem or progenitor cell population among PDCs.

Depending on their tissue of origin, differences in the properties of SSPCs regarding cellular proliferation, differentiation and senescence, as well as cytokine release and gene/mRNA expression profiles have been documented (Dominici et al., 2006; Kern et al., 2006; Tsai et al., 2007). Although bone marrow-derived SSPCs (BM-SSPCs) are osteogenic *in vitro* and form bone tissue *in vivo,* the bone forming cells in a long bone fracture forming the callus are predominantly PDCs (Colnot et al., 2012). Furthermore, periosteum forms a larger callus with a higher mineral content compared to bone marrow (Guichet et al., 1998), and cells in the periosteum display higher proliferation following injury (Brighton and Hunt, 1997). Ultimately, some data suggests that PDCs contain a higher bone regenerative potential than BM-SSPCs (Duchamp de Lageneste et al., 2018). For these reasons PDCs are increasingly studied as a clinically relevant source for bone tissue engineering purposes (Nakahara et al., 1991; De Bari et al., 2006; van Gastel et al., 2012; Owston et al., 2019; Bolander et al., 2020).

The anatomical location and other types (e.g., developmental molecular signatures) of positional information are important factors when studying *in vivo* bone formation (Leucht et al., 2008). During development, facial cartilage and bone are predominantly derived from cranial neural crest, unlike long bones, such as the tibia, that originate from limb skeletal precursors derived from the somatic layer of the lateral plate mesoderm (Noden, 1982; Couly et al., 1993). In the neural plate stage embryo, neural crest and placodal cells develop in the future cranial region at the border of the neural plate with the non-neural ectoderm under the influence of FGF signaling together with precisely dosed Wnt and/or BMP signaling. The actions of these signals converge on specific gene families of Msh-type homeobox (MSX1, MSX2), distal-less homeobox (DLX) and paired domain (PAX) transcription factors (Villanueva et al., 2002; Tribulo et al., 2003; Meulemans and Bronner-Fraser, 2004; Green et al., 2015). The cranial neural crest cells extensively migrate to the pharyngeal arches and form multiple ectomesenchymal cell types including thymus cells, odontoblasts, osteoblastic, adipogenic and chondrogenic cells, muscle cells and neuronal ganglia (Green et al., 2015). Craniofacial bone tissue has a higher turnover rate, "ages" more slowly, and has higher levels of osteoblastic markers compared to appendicular skeletal bone tissue such as that from tibia (Aghaloo et al., 2010). Furthermore, substantial differences in structure and bone biology exist between maxillary and mandibular bone tissue. Maxillary bone tissue arises by intramembranous ossification and consists of trabecular bone surrounded by a thin cortical layer, has low bone density and mineral content, and is highly vascularized. Mandibular bone tissue develops by both endochondral ossification and intramembranous ossification. It consists of lamellar bone tissue that is surrounded by a thick cortical layer, has a high mineral content and bone density, and shows more centralized vascularization (Park et al., 2008; Lindhe et al., 2013). In a first step to assess the implications of these differences on tissue regeneration strategies, Leucht et al. (2008) performed cross-grafting of tibial periosteum onto craniofacial defects and vice versa, and further have shown that embryonic origin and homeobox gene expression influenced the regeneration potential. Despite these well-known differences in bone origin, structure and biology – and their effect on tissue regeneration strategies – many bone tissue engineering therapies intended for use in maxillofacial context continue using the same cell source as their long bone counterparts.

In this study, we built on the work of Leucht et al. (2008), toward clinical translation. We investigate the molecular differences of *in vitro* expanded periosteal cells from maxilla and mandibula in the context of their potential use as cell source for maxillofacial tissue engineering applications, using tibial hPDCs as benchmark. Cell surface markers, growth curves, trilineage differentiation potential, gene/mRNA expression and *in vivo* bone formation were assessed. We show that craniofacial PDCs meet essential criteria of SSPCs (Chan et al., 2018). In addition, *in vitro* differentiation and the mRNA profiling by bulk RNA-sequencing (RNA-seq) show that hPDCs exhibit different properties depending on their retrieval site.

MATERIALS AND METHODS

Isolation and Culture of hPDCs

Periosteal samples (5 × 10 mm) were obtained from the posterior areas of the maxilla and mandible of 16- to 30-year-old healthy patients who underwent bimaxillary orthognathic surgery, after informed consent was obtained (Belgian registration number B322201731127). The tibial samples were harvested by orthopedic surgeons as described previously (Eyckmans and Luyten, 2006). These samples were digested in medium consisting of Dulbecco's modified Eagle's medium (DMEM) supplemented with 10% Fetal Bovine Serum (FBS; Thermo Fisher Scientific, Waltham, MA, United States) and 1% antibiotics-antimycotics solution (100 units penicillin/ml, 100 μg streptomycin/ml and 0.25 μg amphotericin-B/ml; Invitrogen), from here on referred to as DMEM-complete (DMEM-C), in addition of 4,400 units per 10 ml Collagenase type-IV (Gibco) under constant agitation for 16 h. Cells were from then on cultured in DMEM-C. Population doublings (PD) of these human PDCs (hPDCs) were calculated upon passaging using the formula $\log_2(n_2) - \log_2(n_1)$, with n_1 representing the number of cells seeded in the dish/flask and n_2 the number of cells obtained after trypsinization (TrypLE, Thermo Fisher Scientific) of cells from the same dish/flask at 90% confluency.

Cellular Senescence

For detection of senescent cells, 10^5 cells were plated per well in a 6-well plate in DMEM-C. After one day, the cells were fixed using 4% paraformaldehyde (PFA) for 5 min, rinsed using PBS and stained with 2 ml/well filtered (0.22 μm; Millex-GP) staining solution consisting of 36 mM citric acid, pH 6.0 (Sigma Aldrich), 4.5 mM potassium ferricyanide (Merck), 0.14 M NaCl, 1.8 mM $MgCl_2$ (Merck) and 1 mg/ml X-gal (Biotium). After 6 h, the cells were imaged using a Primovert inverted microscope (Zeiss).

Cell Proliferation

For detection of proliferating cells, staining for incorporated EdU was performed using the Click-iT™ EdU Alexa Fluor™ 555 Imaging Kit (Thermo Fisher Scientific) according to the manufacturer's protocol. In short, 10^5 cells/well were seeded in a 6-well plate in DMEM-C. The following day, medium was replaced with DMEM-C containing 10 μM EdU, followed by an incubation of 72 h. Next, cells were fixated using 3,7% formaldehyde in PBS (VWR) for 15 min, rinsed twice with 3% bovine serum albumin (BSA, Sigma Aldrich) in PBS and lysed with 0.5% Triton X-100 in PBS (Sigma Aldrich) for 20 min. This was followed by adding the Click-iT reaction cocktail for 30 min in absence of light, quick washing steps of 1 min using subsequently 3% BSA dissolved in PBS and later on in PBS, addition of the Hoechst solution for 30 min in a 1:2,000 dilution in PBS and final washing steps using PBS for 1 min.

Cell Metabolism

Cell metabolism was measured by using 3-(4,5-dimethylthiazol-2-yl)-2,5-diphenyltetrazolium bromide (MTT) assay. Living cells contain the mitochondrial reductase enzyme, which reduces MTT toward formazan forming salt crystals. By measuring the amount of reduction of MTT toward formazan, the cell metabolism was measured. This was done by removing remaining MTT and solubilizing of the salt crystals in order to get with the different quantities of salt crystals corresponding differences in color intensity (Mosmann, 1983). Tests were performed as technical replicates 6 times per donor at 6, 9, and 12 weeks of culture. 10,000 cells were seeded in a 24-well plate in 0.5 ml DMEM-C. After 1 day, DMEM-C was replaced with DMEM containing 250 μg MTT/ml (Sigma Aldrich). After 4 h, medium and remaining MTT were removed and 1 ml absolute ethanol was added to each well in order to solubilize the salt crystals. These solutions were transferred to a 96-well plate and absorbance was read at 570 and 670 nm with a Synergy HT reader (BioTek). In order to calculate the metabolic rate, the background absorbance (at 670 nm) was subtracted from the absorbance at 570 nm and corrected for the blank values which were obtained by performing all steps on wells containing no cells.

Flow Cytometry

10^6 cells were at passage 6 washed in 500 μl PBS + 1% FBS and incubated at the following dilutions with anti-CD90-APC (1:250), anti-CD164-PE (1:250), anti-CD45-FITC (1:1,000), anti-CD31-FITC (1:1,000), anti-CD235ab-FITC (1:1,000; all from BioLegend), anti-CD146-BV711 (1:250), anti-CD73-BV395 (1:250) and anti-PDPN-BV510 (1:100; all from BD Bioscience) in 200 μl PBS + 1% FBS for 15 min in a dark area. The cells were then washed twice with 1% FBS in PBS. For compensation controls, UltraComp eBeads Compensation Beads (Thermo Fisher Scientific) were used. Gating was performed using Fluorescence-Minus-One (FMO) controls. Fluorescence measurement was performed on a FACS Calibur (BD Biosciences) using 100,000 events.

Differentiation of hPDCs

Human periosteum-derived cells were primed for adipogenic, osteogenic and chondrogenic differentiation for 14, 21, and 7 days, respectively. Analysis was performed by staining with Oil Red O, Alizarin Red and Alcian Blue, respectively.

For adipogenic differentiation of hPDCs, cells were cultured in 24-well plates at a density of 19,000 cells/well in 0.5 ml DMEM-C. After 2 days, the medium was changed for adipogenic differentiation medium, i.e., Minimum Essential Medium Eagle - alpha modification (α-MEM; Invitrogen supplemented with 10% FBS, 1% antibiotics-antimycotics solution, 1 μM dexamethasone + 10 μg/ml human insulin (Sigma Aldrich), 100 μM indomethacin (Sigma Aldrich) and 25 μM 3-isobutyl-1-methylxanthine (Sigma Aldrich). The cells were cultured in a humidified atmosphere at 5% CO2 and 37°C for 14 days and medium was replaced every 2 days. Lipid droplets were stained by Oil Red O. Cells in monolayer were washed in PBS and fixed for 30 min at room temperature in 10% formaldehyde (VWR) diluted in PBS. Next, cells were washed with Milli-Q water and rinsed in 60% isopropanol (VWR) diluted in Milli-Q water. Cells were allowed to dry completely and then stained with 0.2% Oil Red O (Sigma Aldrich) in Milli-Q water for 60 min. These cells

were then washed with Milli-Q water before obtaining pictures using the Primovert microscope (Zeiss).

For osteogenic differentiation of hPDCs, cells were cultured in 24-well plates at a density of 8,550 cells per well in 0.5 ml DMEM-C, first allowing them to proliferate. After 1 day, medium was then changed for osteogenic medium consisting of DMEM-C supplied with 100 nM dexamethasone (Sigma Aldrich), 10 mM β-glycerophosphate disodium salt hydrate (Sigma Aldrich) and 50 μg/ml L-ascorbic acid 2-phosphate (Sigma Aldrich). Cells were cultured in a humidified atmosphere at 5% CO_2 and 37°C for 21 days, during which this medium was replaced every 3 days. Cells in monolayer were washed in PBS, fixed with methanol at −20°C (Fisher Scientific), stored for 1 h at 4°C, and washed again with PBS. Cells were stained for 1 h with a 2% Alizarin-S stain (Sigma Aldrich) in Milli-Q water with pH adjusted to 4.2 (Merck) while the plate was placed on a shaker for constant agitation. After staining, cells were washed with Milli-Q water. Pictures were made using a Discovery.v8 SteREO microscope (Zeiss).

For chondrogenic differentiation of hPDCs, the cells were cultured in micromasses. Micromasses containing 200,000 cells in 10 μl DMEM-C after centrifugation at 260 RCF for 10 min were added to individual wells of 24-well plates. After 2 h, an extra 0.5 ml of DMEM-C was added to each well. After 1 day, this medium was replaced by chondrogenic inductive medium (DMEM-F12 (Invitrogen) containing 2% FBS, antibiotics-antimycotics solution, 1x ITS + premix universal culture supplement (Corning), 100 nM dexamethasone, 10 μM Y27632 (Axon Medchem), 50 μg/ml L-ascorbic acid 2-phosphate, 40 μg/ml proline (Sigma Aldrich) and 10 ng/ml transforming growth factor-β1 (TGFβ1; PeproTech). These cells were cultured under humidified conditions at 37°C and 5% CO_2 for 7 days; medium was replaced every 2 days. Sulfated glycosaminoglycans in the micromasses were stained by Alcian Blue (Roth). The cells were rinsed with PBS and fixed with excess ice-cold methanol for 1 h at 4°C. This methanol was removed and cells were rinsed with Milli-Q water prior to adding 0.1% Alcian Blue staining solution (in 0.1 M HCl at pH 2.4) for 1 h on a shaker. Alcian Blue stain was removed and the cells were rinsed with Milli-Q water before pictures were made using the Discovery.v8 SteREO microscope (Zeiss). At days 1 (control), 3, 5 and 7, micromasses were also obtained for confirmation of chondrogenic differentiation by RT-qPCR. Micromasses were individually lysed in 350 μl RLT buffer (Qiagen) containing 1% β-mercaptoethanol (Sigma Aldrich) and homogenized by thoroughly pipetting up and down. Samples were directly placed on ice and frozen at −80°C until further processing.

RNA Isolation, cDNA Synthesis and Quantitative PCR

RNA was isolated from biological duplicates when a cumulative PD∼10 was reached for RT-qPCR and at PD∼16 for RNA-seq analysis. 10^6 cells were rinsed twice in PBS and centrifuged at 260 RCF for 10 min. After removing the supernatant, the cell pellet was lysed by adding 350 μl RLT buffer (Qiagen) containing 1% β-mercaptoethanol (Sigma Aldrich) and homogenized by thoroughly pipetting up and down. Samples were directly placed on ice and frozen at −80°C until further processing. The Qiagen RNeasy mini kit was used to isolate RNA according to the manufacturer's instructions. cDNA was obtained by reverse transcription of 500 ng of total RNA, using the RevertAid H Minus First Strand cDNA Synthesis Kit, 1 mM oligo (dT)20 and random hexamer primers (Thermo Fisher Scientific).

RT-qPCR was performed on expanded cells without stimulation for differentiation for RNA encoding alkaline phosphatase (*ALPL*), osteocalcin (*BGLAP*), osteopontin (*SPP1*), peroxisome proliferator activated receptor gamma (*PPARG*), collagen type-X (*COL10A1*), SRY (sex determining region Y)-box 9 (*SOX9*) and vascular endothelial growth factor receptor 1 (*VEGFR*-1). On chondrogenically differentiated cells, the expression of aggrecan (*ACAN*), *Col10A1* and Runt-related transcription factor 2 (*RUNX2*) were defined. Samples were processed and measured in technical duplicates on a Step-One-Plus PCR machine (Applied Biosystems) using a Sybr Green detection system (Life Technologies) according to the manufacturer's instructions, and normalized using glyceraldehyde 3-phosphate dehydrogenase (*GAPDH*) as a housekeeping gene. The respective primer sequences are listed in the **Supplementary Table S1**.

RNA-Sequencing and Data Analysis

RNA-seq samples were obtained from three donors for the maxillary samples (HP417, HP421, and HP424), four donors for mandibular samples (HP418, HP422, HP425, and HP427), and three tibial donors (HP415, HP420, and HP423). RNA-seq samples were prepared from hPDCs at cumulative PD∼16 in technical duplicates (A and B) and cDNA libraries were generated using the Illumina TruSeq Stranded mRNA Library Prep Kit. These libraries were then sequenced (50 bp length) according to the Illumina TruSeq Rapid v2 protocol in 5 runs, 2 lanes each run, on an Illumina HiSeq 2500 sequencer. Low quality reads and contaminants (e.g., sequence adapters) were removed using Trimmomatic (Bolger et al., 2014). Sequences that passed the quality assessment were aligned to the GRCh38 genome using HiSat2 (version 2.1.0) (Kim et al., 2015). Transcript abundance level (transcript count) was generated using HTSeq (version 0.9.1) (Anders et al., 2015). The transcript counts were further processed using R (version 3.4.0). Data normalization and removal of batch effect was performed using the EDASeq R package (Risso et al., 2011) and RUVseq package (Remove Unwanted Variation from RNA-Seq package). Differential expression analysis was performed using the edgeR R package (Robinson et al., 2010), using the negative binomial generalized linear model approach. Differentially expressed genes with false discovery rate (FDR) $\leq$ 0.05 after Benjamini-Hochberg correction for multiple testing and expression level greater than 1 count per million (CPM) were retained and used for further processing, gene ontology and pathway analysis. Gene enrichment analysis was performed using metascape (Zhou et al., 2019). The RNA

sequencing data is deposited at NCBI with GEO accession number GSE149167.

In vivo Bone Formation

After proliferation, 10^6 cells suspended in 25 µl of DMEM-C were seeded on NuOss scaffolds (21 mm^3; ACEuropa). One hour after seeding, an additional 5 ml of DMEM-C was added. After overnight incubation at 37°C and 5% CO2, scaffolds were randomly implanted subcutaneously over the available mice in triplicates with a maximum of 4 for each mouse at the shoulder and the back in the limb region of 8-week-old female NMRI$^{nu/nu}$ mice (Janvier). All animal procedures were approved by the local ethical committee for Animal Research (KU Leuven). The animals were housed according to the guidelines of the Animal Facilities at Leuven (KU Leuven). Explants were harvested after 8 weeks.

Bone formation was analyzed using the Phoenix NanoTom S CT system (GE measurement) at a voltage of 60 kV and a current of 200 mA. An aluminium filter of 1 mm was used to filter out the low energetic radiation. CTAn and Batch Manager Software programs (Bruker micro-CT, Kontich, Belgium) were used for 3-D quantification of the bone volume and calcium phosphate (CaP) grains of the NuOss scaffold. A three-level automatic Otsu segmentation algorithm was used to segment the newly formed bone tissue and CaP-grains from the background in combination with manually chosen thresholds. Noise was reduced by removing black and white speckles smaller than 200 voxels and a closing operation of 2 voxels was performed to solidify the resulting structure, providing binarized images suitable for the 3-D analysis. Percentage of bone was calculated with respect to total explant volume (Kerckhofs et al., 2013). After decalcification in EDTA, dehydration through a series of graded ethanol baths, embedding in paraffin and sectioning, histological stainings were performed. Staining with hematoxylin and eosin (H&E) was done by a dip in Hematoxylin-solution for 2 min, followed by a wash in H_2O and subsequently a staining in 1% Eosin (Klinipath, Duiven, Netherlands) for 7 min (Bolander et al., 2016). For Alcian Blue staining, samples were rehydrated, stained for 30 min in 0.5% Alcian Blue (Roth) solution in 1 M HCl (pH = 1). Nuclear Fast Red (Vector) was used for staining of the nuclei during 5 min. For staining with Safranin O, samples were dipped in acidic alcohol (1% HCl in 70% ethanol). Next, they were placed in Fast Green (Klinipath) for 3 min, dipped in 1% acetic acid and then stained in 0.1% Safranin O (Sigma Aldrich) for 10 min. Masson's trichrome staining was performed using Bouin's solution (Sigma Aldrich) as mordant followed by 5-minute-dips in Weigert's Iron Hematocxylin Solution, Biebrich Scarlet-Acid Fuchsin, Phosphotungstic/Phosphomolybdic Acid Solution and Aniline Blue Solution (all from Sigma Aldrich), followed by a dip in 1% acetic acid for 2 min. The sections were cleared in HistoClear (National-Diagnostics) and mounted in Pertex (Histolab). Pictures were made using the IX83 microscope (Olympus).

Statistical Analysis

Statistical analysis for cellular senescence, quantitative PCR and *in vivo* bone formation was performed using the Kruskal-Wallis test. In case $p < 0.05$ for Kruskal-Wallis, a two-sided Wilcoxon test was performed to make comparisons for the qPCR validation of the RNA-seq data and to analyze cellular senescence, proliferation and metabolism rate. Student's *t*-test was used to make comparisons for the chondrogenically differentiated micromasses. The Bonferroni correction was used to correct for multiple testing. All statistical analyses were performed in R (version 3.6.0). Results were considered statistically significant at $p < 0.05$. Data are presented as mean values ± standard deviation (SD) or 95% confidence interval (CI) when stated.

RESULTS

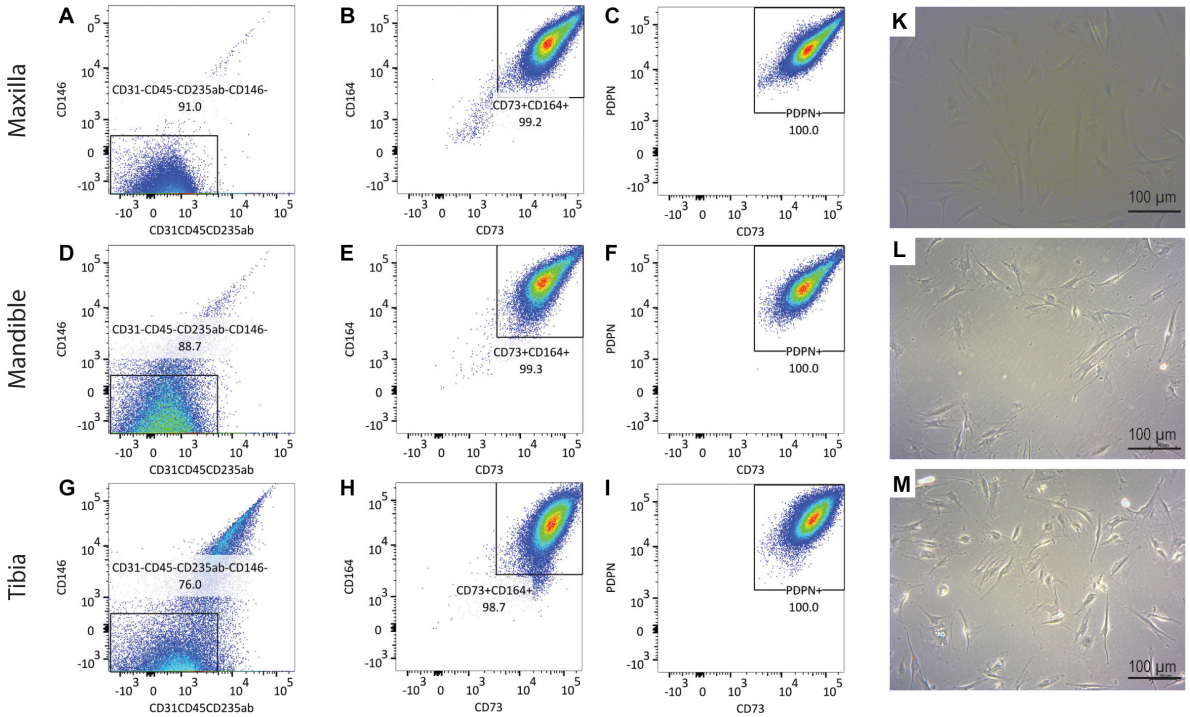
Characterization of the Isolated and Expanded Human Periosteum-Derived Cells

Flow cytometric analysis was performed on culture expanded hPDCs to confirm the presence of SSPCs (**Figures 1A–I**). 88.9% of the maxillary hPDCs were positive (+) for CD73, CD164 and PDPN, while negative for CD31, CD45, CD235ab, and CD146 (**Figure 1J**). In contrast, 87.7% of the mandibular cells and 62.0% of the tibial hPDCs met the SSPC criteria. All cells were selected based on their capacity to adhere to plastic (**Figures 1K–M**).

Alcian Blue-positive micromasses from maxillary and mandibular and tibial hPDCs indicated their ability to differentiate toward the chondrogenic lineage (**Figures 2A–C**; controls in **Figures 2D–F**). Adipogenic differentiation of hPDC cultures in monolayer was verified by staining with Oil Red O, for hPDCs obtained from the three different origins (**Figures 2G–I**; controls in **Figures 2J–L**). Calcium phosphate formed by osteogenic primed cells in monolayer was stained by Alizarin Red (**Figures 2M–O**; controls in **Figures 2P–R**) and showed mineral deposition by the hPDCs, independent of their origin. Additional RT-qPCR on chondrogenically differentiated micromasses at days 1 (control), 3, 5, and 7 showed that *RUNX2* (**Figure 2U**) and *COL10A1* (**Figure 2T**) were expressed at higher levels after chondrogenic differentiation in comparison to undifferentiated micromasses at day 1. Also *ACAN* was expressed from day 5 at statistically significantly higher levels compared to the controls (**Figure 2S**). These results indicated that plastic-adherent hPDCs derived from maxilla and mandible could be expanded, and that these cultured hPDCs were positive for acknowledged SSPC surface markers and able to differentiate toward three different cell types.

Human PDCs Can Be Expanded for 2 Months

We have tested the ability to expand hPDCs obtained from maxilla versus mandible and tibia. The proliferation rates of hPDCs during *in vitro* expansion under the culture conditions used, measured in cumulative population doublings (CPDs), were similar and independent of their origin (**Figures 3A,B**). After 6, 9 and 12 weeks of expansion, staining with X-gal for



J

	Single cells	CD31- CD45- CD235ab- CD146-	CD73 + CD164 +	PDPN+	Single cells fulfilling SSPC criteria
Maxilla	95.6%	89.7%	99.1%	100%	88.9%
Mandible	92.0%	89.1%	98.7%	100%	87.7%
Tibia	96.1%	65.8%	94.2%	100%	62.0%

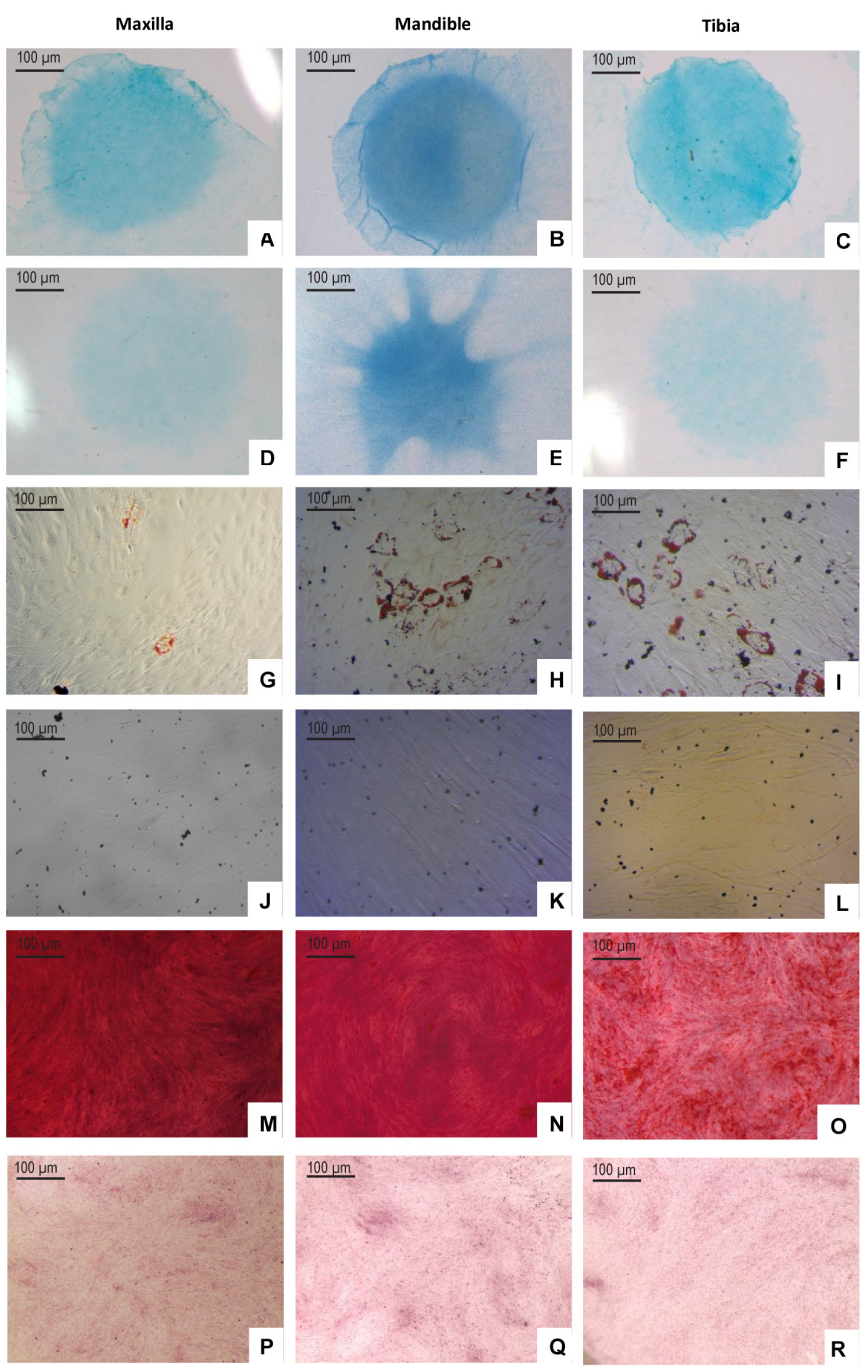
FIGURE 1 | (A) Flow-cytometric analysis of periosteal-derived cells obtained from maxilla **(A–C)**, mandible **(D–F)** and tibia **(G–I)**. Gating is performed using FMO's for each run. $n = 3$. 100.000 events were read for each sample. **(J)** Summary of flow-cytometric analysis, $n = 3$ for each origin. SA-β-gal staining on periosteal cells derived from maxilla **(K)**, mandible **(L)**, and tibia **(M)** demonstrating no precipitation of X-gal.

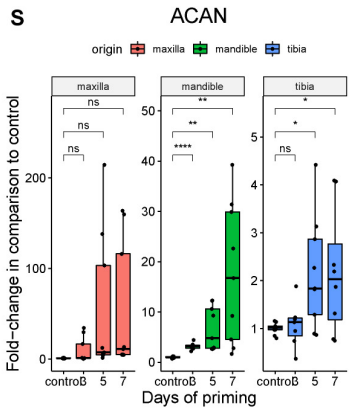
senescence-associated β-Galactosidase was performed. During the first 9 weeks the average rates of such cells remained below 5%. After 12 weeks significantly higher rates were found, up until 28% of the cells ($p = 0.045$; **Figure 3C**). Quantification of proliferation was measured by staining for incorporated EdU, again after expansion for 6, 9 and 12 weeks. About 75% of the cells were EdU + after 6 and 9 weeks of expansion (**Figure 3D**) with a significantly higher proliferation rate for maxillary hPDCs after 6 weeks in comparison to mandibular and tibial hPDCs.

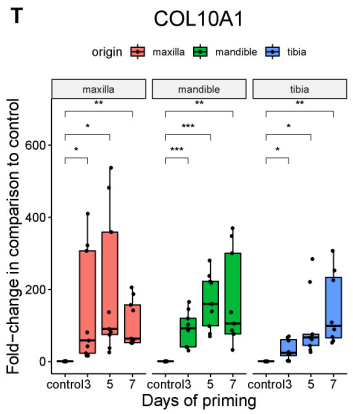
Assessing cellular metabolic activity using the MTT colorimetric assay, we saw a trend toward lower mitochondrial metabolic rates in tibia-derived hPDCs, however, no statistically significant differences were found between the maxillary, mandibular and tibia-derived hPDCs (**Figure 3E**). Furthermore, no decline in the metabolic activity was observed after 12 weeks. From this, we conclude that hPDCs, regardless of their tissue source, can be expanded during at least 9 weeks, with an expected yield of about 350 million cells after 50 days of proliferation. This yield is sufficient for typical applications in bone tissue engineering (Lammens et al., 2020).

In vitro Analysis of Marker Genes on Expanded hPDCs From 3 Different Origins

In order to investigate further the differences in mRNA profiles between the respective *in vitro* expanded hPDCs, we performed RT-qPCR on acknowledged marker genes for bone. These include *ALP*, a marker of osteogenic differentiation; *BGLAP*, coding for a protein secreted in bone solely by osteoblasts; and *SPP1*, a gene expressed by multiple cell types including osteoblasts and osteoclasts. The steady-state transcripts of *ALP* are higher in maxillary compared to mandibular ($p = 0.025$) and tibial hPDCs ($p = 0.0013$) (**Figure 4A**), whereas *BGLAP* transcripts showed no statistically significant differences (**Figure 4B**). *SPP1* was upregulated for tibia-derived cells when compared







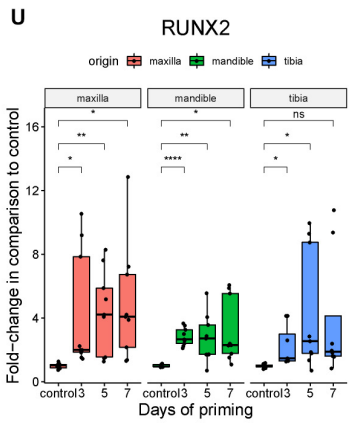


FIGURE 2 | Alcian Blue staining of chondrogenically differentiated hPDCs obtained from maxilla, mandible and tibia **(A–C)** and cells cultured in DMEM-C **(D–F)**. Oil Red O staining of adipogenically differentiated hPDCs **(G–I)** and cells cultured in DMEM-C as controls **(J–L)**. Cells stained with Alizarin Red staining to detect calcium phosphate deposition of osteogenically differentiated hPDCs **(M–O)** and controls cultured in DMEM-C **(P–R)**. RT-qPCR performed at days 1 (control), 3, 5 and 7 for the chondrogenic genes *RUNX2*, *COL10A1* and *ACAN* showed as fold-change compared to the control after correction for GAPDH, $n = 3$ in biological triplicates. $^{*}p \leq 0.05$, $^{**}p \leq 0.01$, $^{***}p \leq 0.001$, $^{****}p \leq 0.0001$ **(S–U)**.

to hPDCs from mandible ($p = 0.014$; **Figure 4C**). For the adipogenic receptor *PPARG* no differences were seen that are statistically significant (**Figure 4D**). *SOX9* was upregulated in both maxillary and mandibular cells compared to tibial hPDCs ($p = 0.03$ and $p = 0.008$, respectively; **Figure 4E**). *VEGFR-1* transcripts were higher in maxillary compared to tibial ($p = 0.007$) and mandibular hPDCs ($p = 0.04$) (**Figure 4F**). Also for *COL10A1* an upregulation was seen for maxillary hPDCS

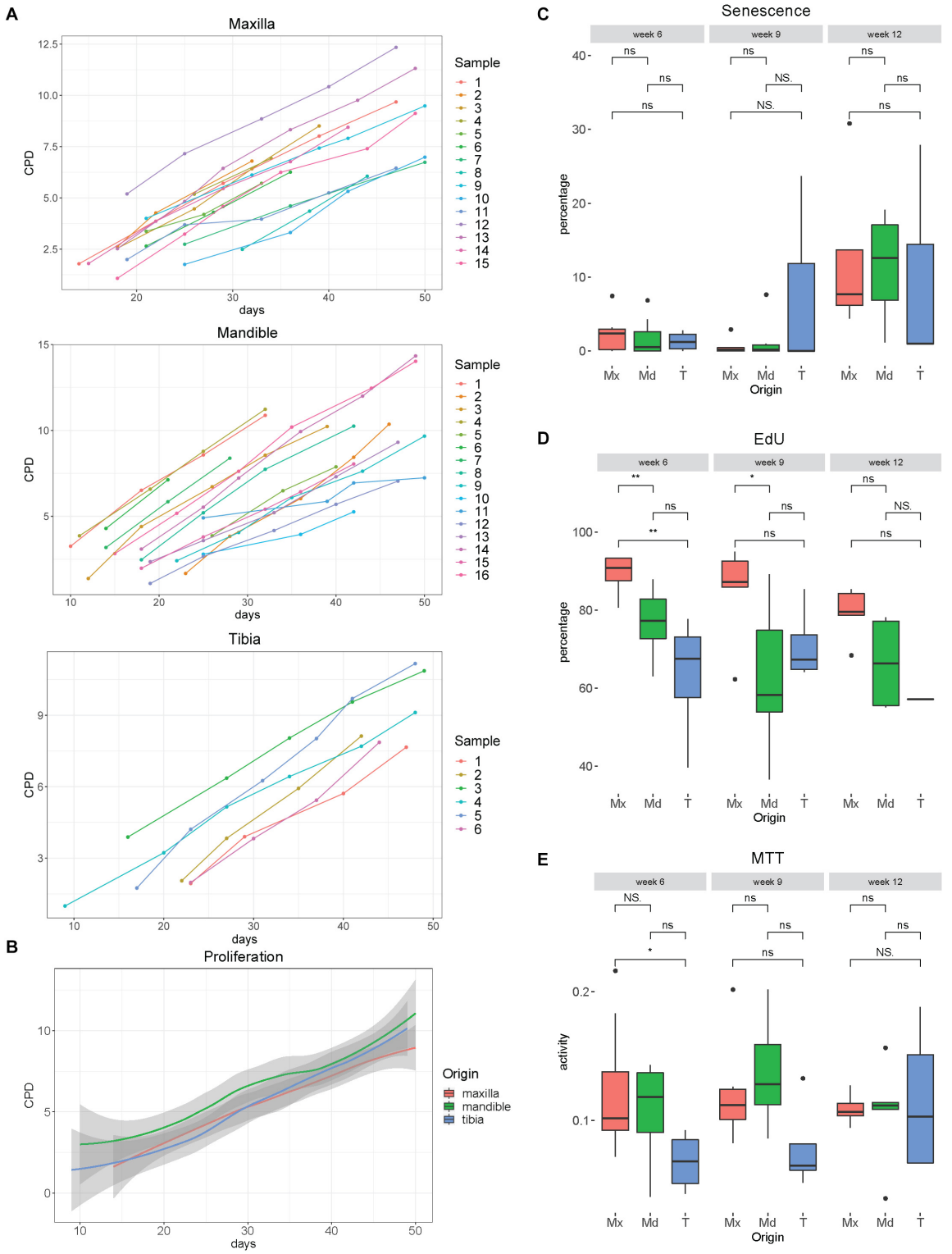


FIGURE 3 | (A) Proliferation curves of hPDCs obtained from maxilla, mandible and tibia, wherein the X-bar displays the time in days and the vertical axis the cumulative population doublings (CPD). **(B)** Mean proliferation curves of hPDCs from maxilla (red), mandible (green) and tibia (blue), with confidence interval showed in gray. **(C)** Percentage of SA-β-gal staining-positive cells at 6, 9 and 12 weeks of expansion in DMEM-C. **(D)** Proliferation-capacity of hPDCs showed by the percentage of EdU-positive cells after 6, 9, and 12 weeks of expansion in DMEM-C. **(E)** Metabolic activity shown by MTT-test of hPDCs obtained from maxilla (Mx), mandible (Md) and tibia (T) after 6, 9 and 12 weeks of expansion in DMEM-C. $^{*}p \leq 0.05$, $^{**}p \leq 0.01$.

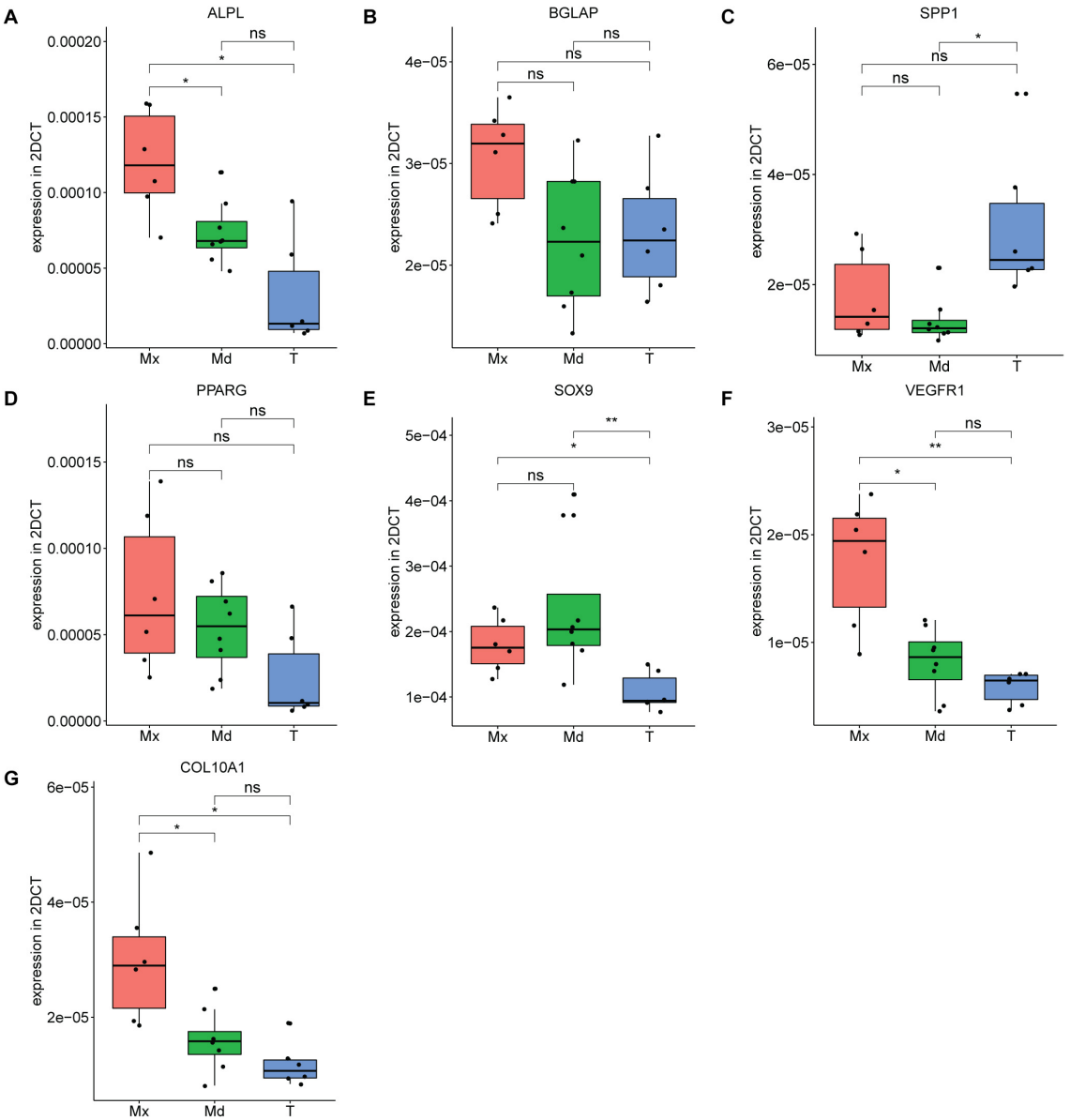


FIGURE 4 | Expression level of ALPL **(A)**, BGLAP **(B)**, SPP1 **(C)**, PPARG **(D)**, SOX9 **(E)** VEGFR-1 **(F)** and COL10A1 **(G)** of hPDCs from maxilla (Mx), mandible (Md) and tibia (T) after expansion in DMEM-C at PD = 10, $n = 3$ in biological duplicates for each origin corrected for GAPDH. $^{*}p \leq 0.05$, $^{**}p \leq 0.01$, $^{***}p \leq 0.001$, $^{****}p \leq 0.0001$.

compared to mandibular and tibial hPDCs ($p = 0.016$ and 0.013, respectively, **Figure 4G**).

Bulk RNA-Seq of Cultured Adult hPDCs Reveals Differences That Reflect Different Embryonic Origins

We have also performed bulk RNA-seq on expanded cells. Principal component analysis (PCA; **Figure 5A**) and the hierarchical clustering (dendrogram in **Figure 5B**) show that the differences in anatomical origin of the hPDCs are reflected in bulk mRNA expression differences. To capture the genes that contribute to this distinction, we have performed differential gene expression analysis between the hPDCs. 780 differentially expressed genes (DEGs; FDR < 0.05, log fold change > 1) were identified between tibial and maxillary hPDCs. 291 of these were down-regulated and 489 up-regulated in maxilla-derived hPDCs. Between mandible and tibia-derived hPDCs 841 DEGs were identified, with 361 genes down- and 480 genes up-regulated in mandibular hPDCs (**Figure 5C** and **Supplementary Tables S2**, **S3**). In these comparisons only around 33% of the DEGs are common between maxilla and mandible derived hPDCs compared to tibial hPDCs, attesting to the large difference that exists between

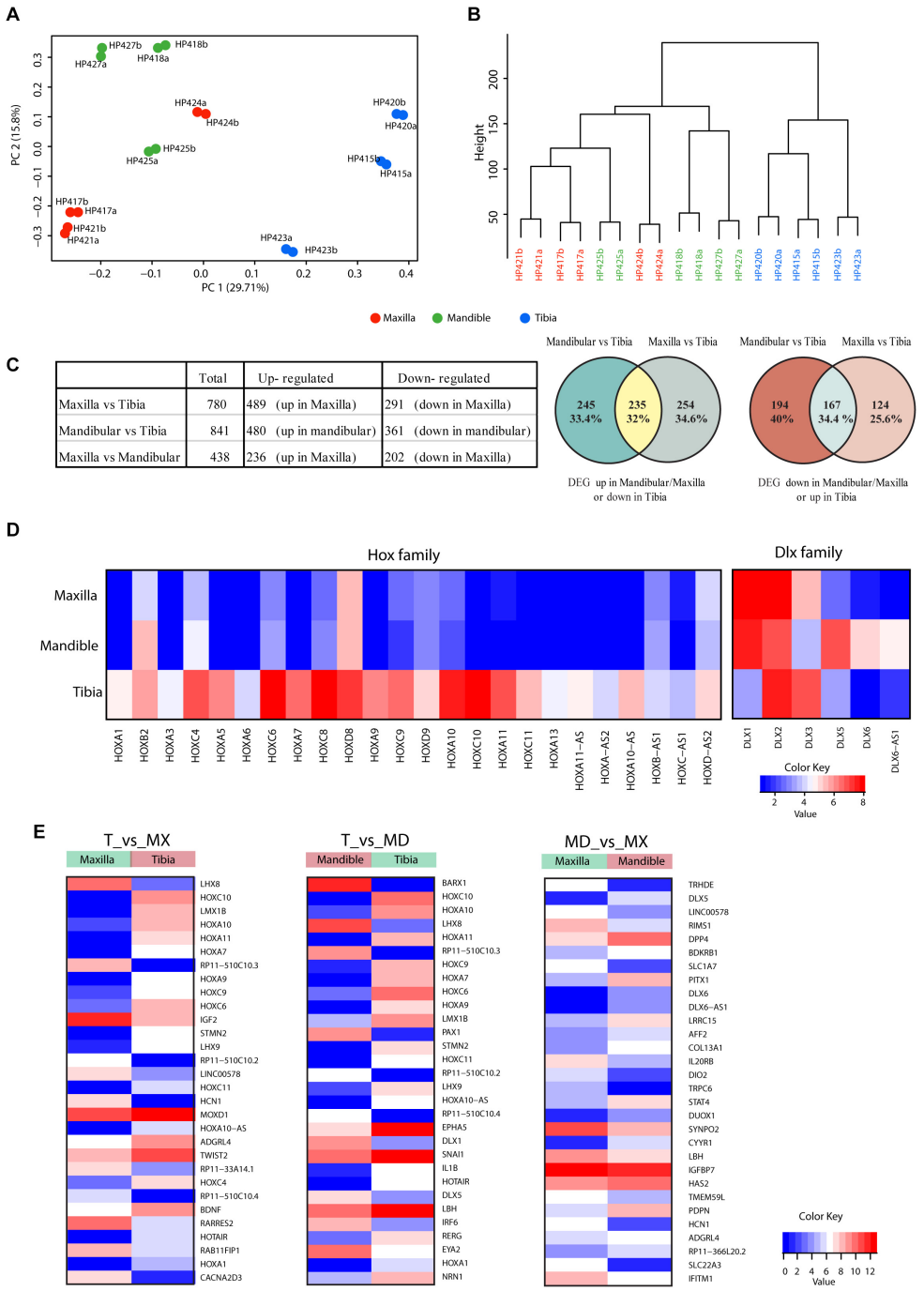


FIGURE 5 | (A) Principal component analysis of RNA-sequencing on hPDCs obtained from maxilla (red), mandible (green) and tibia (blue). Each dot represents the sample mean from a single donor. **(B)** Cluster dendrogram based on RNA-sequencing results. **(C)** Table showing the number of differentially expressed genes and venn diagrams of differentially expressed genes between maxillary, mandibular and tibial hPDCs based on RNA-seq. **(D)** Heatmap of Hox and DLX family genes based on RNA-seq data. **(E)** Heatmap of the 30 most differentially expressed genes in the comparisons maxilla (Mx) vs. tibia (T), mandible (Md) vs. T and Mx vs. Md.

maxilla and mandible-derived hPDCs. Finally, the comparison between mandibular and maxilla-derived hPDCs identified 438 DEGs; 236 of these genes were up-, and 202 genes were down-regulated in maxilla-derived hPDCs (**Figure 5C** and **Supplementary Table S4**).

Next, we performed gene enrichment analysis on the DEGs to capture the biological processes and molecular functions that show significant changes. Genes that show up- and down-regulation in both maxillary and mandibular hPDCs, compared to tibial hPDCs, are involved in skeletal system development,

extracellular structure organization, vascular development and related pathways (**Supplementary Figures S1**, **S2**). Upregulated genes in tibia showed more significant enrichment in bone development related pathways (**Supplementary Figures S1**, **S2**). In the comparison between maxillary and mandibular hPDCs, genes that are up-regulated in mandibular (and also down-regulated in maxillary) were enriched for terms related to skeletal system development, bone remodeling, ossification (**Supplementary Figure S3**). This reflects the chondrogenic and osteogenic differentiation potential of mandible-derived hPDCs compared to maxillary hPDCs. Down-regulated genes in mandibular (and also up-regulated in maxillary) were involved for terms that are not related to bone development (**Supplementary Figure S3**).

The list of DEGs also pointed to differences among HOX- and DLX-family genes between craniofacial and tibial hPDCs. The majority of the HOX-family genes showed upregulation in tibial hPDCs. However, some HOX genes (*HOXC8*, *HOXD8*, *HOXC9*, *HOXD9*, and *HOXA10*) showed also higher expression in craniofacial hPDCs (**Figure 5D**). From the DLX family, *DLX1* was highly expressed in craniofacial and tibial hPDCs, and *DLX5* in mandibular hPDCs.

The RNA-seq data were validated by RT-qPCR by taking the top-10 DEGs in the 3 comparisons (**Figure 5E** and **Supplementary Table S5**). Expression of *HOXA11,* encoding a transcription factor regulating positional cell identity along the anterior-posterior (AP) axis of embryonic segments (Liatsikos et al., 2010; Raines et al., 2015), was elevated in tibial compared to maxillary and mandibular hPDCs (p = 0.007 for both; **Figure 6A**). Also, significantly higher expression values of *HOXA7*, *HOXA10*, *HOXC10*, and the *HOX* transcript antisense RNA (*HOTAIR*) were obtained for tibial hPDCs compared to those from the craniofacial area, which confirmed the RNA-seq results (**Figures 6B–E**). We conclude that tibia-derived periosteal cells isolated from patients still express genes that are involved in AP patterning in the embryo. *DLX1,* encoding a transcriptional regulator and a downstream target of multiple transforming growth factor beta (TGF-β) family members (Mimura et al., 2016), was more highly expressed in mandibular compared to tibial hPDCs (p = 0.007; **Figure 6F**). *DLX5* is an early-BMP responsive gene and encodes a transcription factor involved in osteoblast differentiation (Li et al., 2008). This gene was more strongly expressed by mandibular compared to tibial hPDCs (p = 0.013; **Figure 6G**). *DLX6*, often proposed as paralog of *DLX1* (Li et al., 2008), did not show any statistically significant difference (**Figure 6H**), but the antisense RNA encoded by *DLX6* (*DLX6-AS1*), was down-regulated in mandibular compared to tibial hPDCs (p = 0.007; **Figure 6I**). The latter is in accordance with the trend toward a higher expression of *DLX6* in mandibular hPDCs.

BARX1 is expressed during tooth development and neural crest-derived craniofacial mesenchymal tissues, but is also known for its inhibiting interaction on canonical Wnt signaling (Woo et al., 2011; Lin et al., 2019). Expression of *BARX1* was higher in mandibular compared to tibial hPDCs (p = 0.007; **Figure 6J**). *LHX8* encodes a transcription factor that plays a role in the development of the palate, in oogenesis and neuronal differentiation (Choi et al., 2008; Flandin et al., 2011; Cesario et al., 2015). However, *LHX8* is also known to stimulate the proliferation of MSCs, while a drop in *LHX8* expression level combined with increased levels of BMP2 promotes osteogenesis (Wang et al., 2019). For *LHX8* higher expression was found in maxillary compared to tibial hPDCs (p = 0.013; **Figure 6K**). *PAX1*, a target of Shh signaling that plays a role in axial skeletogenesis (Wallin et al., 1994), showed a trend toward down-regulation in hPDCs originating from the mandible, compared to those from tibia (**Figure 6L**). *PAX1* also positively regulates the chondrogenic marker genes *SOX5*, *ACAN*, *COL2A1*, and WW domain-containing protein 2 (*WWP2*) (Takimoto et al., 2019). *COL13A1* encodes the alpha-chain of one of the non-fibrillar collagens and has previously been implicated in bone mass and bone formation rate (Ylönen et al., 2005), but did not show any statistically significant differences (**Figure 6M**). *DPP4* plays an important role in glucose metabolism. Administration of inhibitors against DPP4 results in an increase in bone mass by upregulation of IL-10 expression and subsequent stimulation of chondrocyte hypertrophy (Jung et al., 2013; Wang et al., 2018). *DPP4* was expressed less by maxillary compared to mandibular hPDCs (p = 0.015; **Figure 6N**). *GPC3,* an antagonist of *DPP4* and involved in limb patterning and skeletal development via BMP4 (Paine-Saunders et al., 2000), did not show statistically significant differences, but an opposing trend to *DPP4* (**Figure 6P**). No statistically significant differences were found for the G-protein coupled receptor *GPRC5C* (**Figure 6O**). *VEGFB*, involved in angiogenesis and endothelial cell physiology (Hagberg et al., 2010), showed an upregulated trend in maxillary compared to tibial and mandibular hPDCs (**Figure 6Q**). In total, we could confirm, using RT-qPCR and after Bonferroni-correction, statistically significant differences in expression for 11 out of the 30 DEGs selected from the RNA-seq lists.

In vivo Bone Formation

We assessed whether after 8-weeks bone formation in scaffolds seeded with tibial hPDCs did occur; for this, we used Nano-CT analysis of ectopically implanted scaffolds (**Figures 7A,B**). No *in vivo* mineralized tissue was detected with maxilla-derived hPDCs, whereas it was present, as a positive control, in constructs seeded with tibial hPDCs (p = 0.04326) at an average of 0.0736 mm^3 bone tissue (**Figures 7A,B**). Importantly, bone formation by mandibular hPDCs was detected in 6 out of the 12 retrieved constructs, averaging 0.06 mm^3 bone tissue in those 12 constructs. Staining with hematoxylin/eosin (HE) confirmed that the mineralized tissue seen on CT-scans was indeed bone tissue (**Figures 7C–E**). Staining of cartilage with Alcian Blue showed more staining in scaffolds seeded with mandibular hPDCs (Figures F–H). Staining for bone tissue with Masson's Trichrome confirmed the results obtained from both HE and Alcian Blue staining (Figures I–K).

DISCUSSION

Research toward cell-based bone tissue-engineering recently focused strongly on the properties of SSPCs and proposed

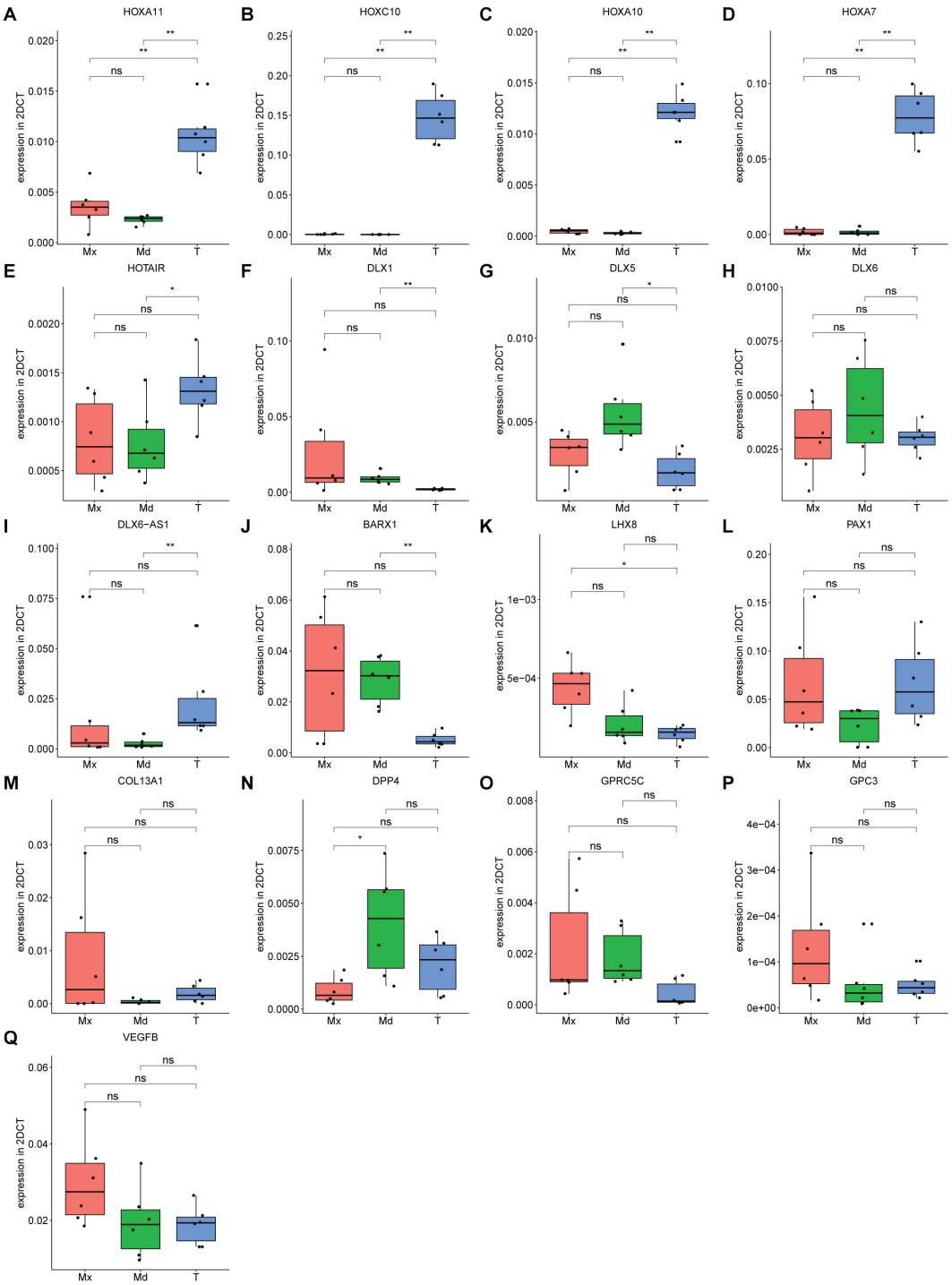
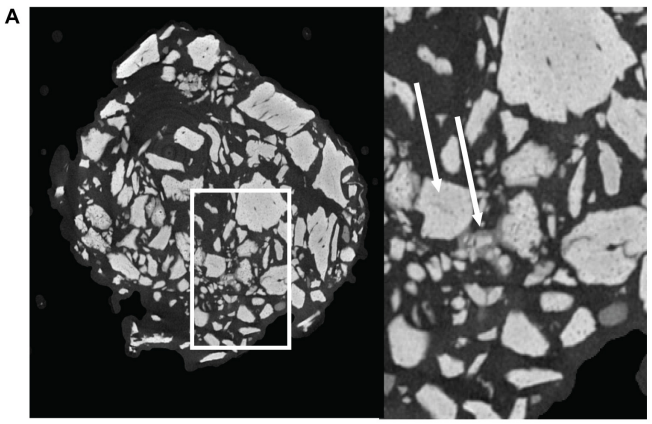


FIGURE 6 | (A–Q) Expression level of genes found in top 10 from RNA-sequencing for each comparison, forming in total a top 30 list, confirmed on maxillary (Mx), mandibular (Md) and tibial (T) hPDCs obtained from different donors at PD = 10, $n = 3$ in biological duplicates for each origin corrected for GAPDH. $^{*}p \leq 0.05$, $^{**}p \leq 0.01$.

hPDCs as candidate cells (Roberts et al., 2015; Bolander et al., 2020). We have documented the differences between PDCs obtained from different anatomical locations (maxilla, mandible and tibia, respectively) *in vitro* and also *in vivo*. FACS on *in vitro* expanded cells scored them as CD73+, CD164+, and PDPN+, each marker associated with SSPC identity, whereas they were negative for hematopoietic lineage markers. The latter is important, for the presence of one or more hematopoietic



B

	Mean	SD
Maxilla		
Mandible	1,10%	1,44%
Tibia	1,72%	1,14%

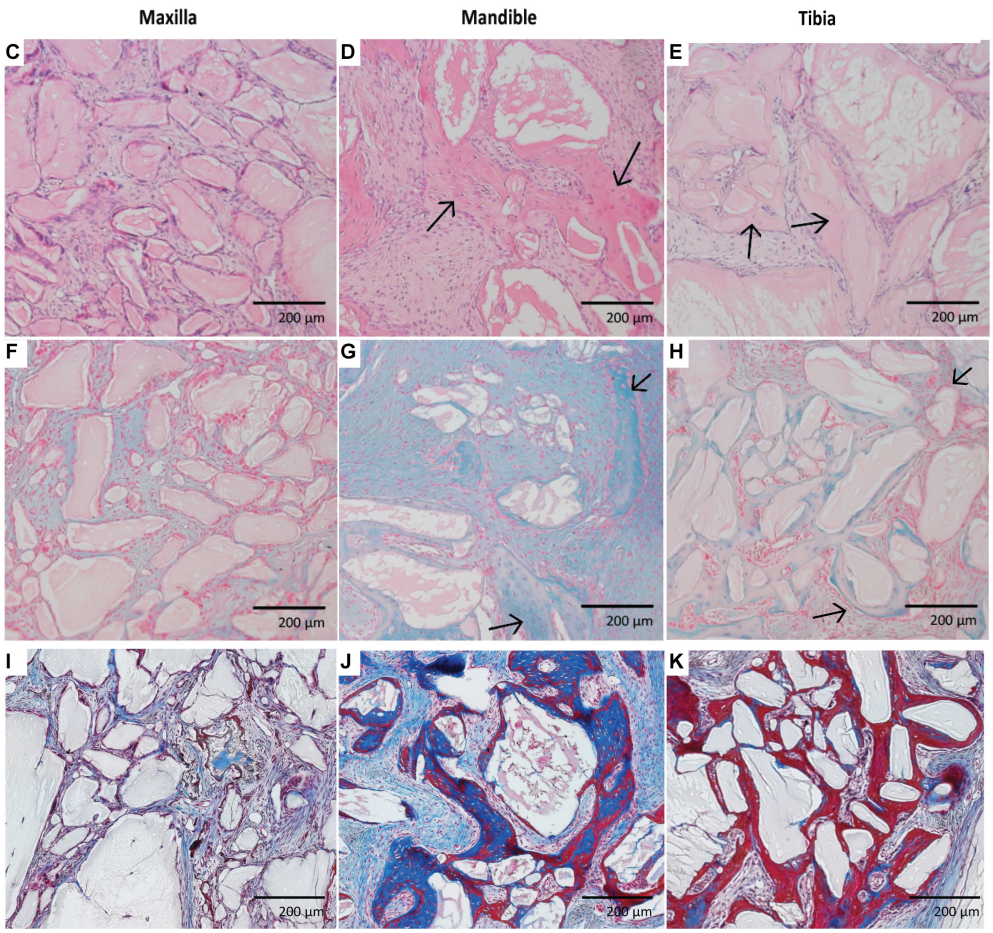


FIGURE 7 | Nano-CT imaging of scaffolds seeded with hPDCs obtained after 8 weeks of ectopic implantation with scaffold grains in light gray (white arrow) and mineralized tissue in dark gray (white dashed arrow). **(A)** Volumetric percentage of mineralized tissue in each cell construct. **(B)** Histological imaging of those cell constructs stained with Hematoxylin & Eosin **(C–E)**, Alcian Blue **(F–H)** with bony tissue pointed by black arrows and Masson's Trichrome **(I–K)**.

markers on SSPCs was shown by others to underlie further cellular differentiation accompanied by loss of stem cell state (van Lochem et al., 2004). We concluded that 88% of our *in vitro* expanded craniofacial cells fulfilled the applied SSPC criteria, and 62% of our *in vitro* expanded tibial hPDCs, but also acknowledged the limited relevance of these markers for stem cell function (Ambrosi et al., 2019). Our hPDCs were able to proliferate *in vitro* at comparable rates to each other, they did not display senescence during 9 weeks of culture, and were able to differentiate at CPD∼8 to osteogenic, chondrogenic and adipogenic lineages. *ALPL* and *BGLAP* displayed higher mRNA expression *in vitro* cultured hPDCs obtained from maxilla

compared to tibia, which could underlie the higher *in vitro* osteogenic potential of maxilla-derived hPDCs. For *in vivo* endochondral bone formation, the mandibular hPDCs showed a higher potential, possibly due to higher *SOX9* expression by these cells *in vitro*, again compared to tibial hPDCs. The steady-state mRNA levels of *VEGFR-1*, encoding a receptor that is normally upregulated during vascularization in healing of fractured bones, were highest in maxillary hPDCs compared to the other ones. This can be of interest when scaling-up tissue engineering constructs that have diffusion limits of oxygen and nutrients, since cell death or apoptosis in the center of the implant has been reported if good vascularization is not achieved quickly (Potier et al., 2007; Giannoni et al., 2010).

RNA-seq and further validation by RT-qPCR on separate *in vitro* cultured samples thus reveal notable differences in gene expression between hPDCs obtained from the three sites. These are represented mostly by the higher expression of HOX and DLX family genes steering skeletal system and other connective tissue development, but also co-determine extracellular matrix organization, collagen formation, and responses to growth factors. Overall, these sets of genes are irrefutably relevant to *in vivo* bone regeneration and form a solid basis for future experiments that aim at improving bone tissue engineering applications. *HOXA7*, *HOXA10*, *HOXC10*, and *HOTAIR* were each upregulated in tibial hPDCs compared to those from the craniofacial area. Hence, tibia-derived periosteal cells isolated from adult patients still express genes that are involved in several other processes, including anterior-posterior patterning in the embryo, or these genes also have additional functions in cell differentiation. Leucht et al. (2008) grafted periosteum from the tibia onto craniofacial bone defects (and vice versa) and demonstrated that *HOXA11*$^{+}$ cells maintain their HOX status after changing the environment, but *HOXA11*-negative cells can start to express *HOXA11* after changing the environment. In this study, the change of environment, which *in vitro* expansion is, could explain the presence of low expression of HOX genes by hPDCs obtained from the maxilla and mandible. *DLX1* was expressed at a higher level in maxilla-derived hPDCs. This could explain the higher osteogenic potential of these cells *in vitro*. *DLX5* acts as an early BMP-responsive transcriptional activator driving osteoblastic differentiation of cells, while *DLX6* has been proposed as paralog of *DLX1* (Li et al., 2008). These results suggest favoring the use of mandibular hPDCs in craniofacial applications, since *DLX5* and *DLX6* where both up-regulated in these cells. However, *PAX1*, a target of Shh signaling, but also positively regulating the chondrogenic effector or marker genes *SOX5*, *ACAN*, *COL2A1*, and *WWP2* (Wallin et al., 1994; Takimoto et al., 2019), was expressed at higher levels in tibial hPDCs. Taken together, hPDCs obtained from maxilla, mandible and tibia showed different gene/mRNA expression profiles, including of relevant effector or marker genes, which could lead to different direct or endochondral bone forming properties. This could be exploited in bone tissue engineering strategies for various anatomical locations. For a number of selected genes, based on RNA-seq, we also could not reproduce the results by RT-qPCR. We hypothesize that this is due to our use of different donors throughout these comparisons, which made the validation more stringent.

Analysis of hPDC-seeded scaffolds showed bone formation 8 weeks after ectopic implantation when seeded with tibial and mandibular cells, but unexpectedly not with maxilla-derived hPDCs. For the latter, cells show *in vitro* upregulation of osteogenic genes compared to tibia-derived cells. We hypothesize that maxilla-derived periosteal cells are less prone for endochondral bone formation when the cells are not stimulated by growth factors. Also local environmental cues influence the ability of these cells to form bone, as demonstrated previously through periosteal grafting experiments (Leucht et al., 2008). In addition, the choice of the carrier or any coincidence in view of the generally observed biological variability of the *in vivo* ectopic bone formation assays, could account for the documented difference (Ji et al., 2018).

To our knowledge, *in vivo* results of ectopic bone formation using *in vitro* expanded maxilla-derived periosteal cells have not been reported yet. Additional work is needed to investigate if priming of hPDCs prior to implantation could be optimized for craniofacial-derived hPDCs, as was shown for tibial hPDCs (Bolander et al., 2016). The effects of priming tibia-derived periosteal cells with different concentrations of calcium in the medium on their bone-forming capacities *in vivo*, and when using calcium phosphate scaffolds, have been documented previously (Chai et al., 2012). Mandibular periosteal cells, obtained from the region near the wisdom tooth, yield more bone tissue *in vivo* when co-cultured with CD34^{+} endothelial progenitors obtained from the umbilical cord, while a trend toward a better osteogenic potential of mandibular periosteum-derived cells cultured using cyclic tension force has also been reported (Lee et al., 2014, 2017). For tibia-derived periosteal cells, the effects of different calcium phosphate scaffolds on *in vivo* bone formation capacities of such cells was also reported (Kerckhofs et al., 2016). Others have stated the importance of the combination of mesenchymal lineage-derived cells with type of scaffold (Mattioli-Belmonte et al., 2015), but this has not yet been explored with maxilla and/or mandible-derived cells. Furthermore, many features of scaffolds contribute to the *in vivo* outcome, including bio-compatibility, porosity, pore size, surface properties, osteo-inductivity and mechanical properties (Salgado et al., 2004). In addition, the predictability and robustness of the *in vivo* formed bone construct as well as possible differences in the speed of bone formation, and bone formation in an orthotopic environment altogether, should also be evaluated and/or improved in order to prepare translation toward the clinic (Geris and Papantoniou, 2019).

We hypothesized that location and tissue of origin are relevant for successful bone repair when using *in vitro* expanded cell-based tissue engineering constructs. hPDCs from different anatomical locations may be interesting sources, but would display different properties and possibly differences in outcome with regard to bone healing *in vivo*. Therefore, we focused on documenting (dis)similarities between *in vitro* expanded periosteum-derived cells from tibia, maxilla and mandible. Progenitor cells from different anatomical sources indeed differ in their transcriptomic signature and *in vivo* differentiation

potential (Sacchetti et al., 2016). We have shown that *in vitro* expanded hPDCs obtained from these respective sites do not differ in their capacities to proliferate *in vitro* under the experimental conditions used. However, the cells showed differences in gene expression profiles and *in vivo* bone formation. So, different properties, including embryonic origin and (epi)genetic priming laid down within functionally similar cell types, located at different anatomical sites, can be retained during *ex vivo* expansion. This then influences the functional outcome, here demonstrated by different skeletogenic potential of SSPCs. It remains to be investigated if these observed differences are critical for clinical outcomes, including remodeling of tissue over time, and for which indications.

DATA AVAILABILITY STATEMENT

The datasets presented in this study can be found in online repositories. The names of the repository/repositories and accession number(s) can be found below: https://www.ncbi.nlm.nih.gov/geo/, GSE149167.

ETHICS STATEMENT

The studies involving human participants were reviewed and approved by Ethics Committee Research UZ/KU Leuven. Written informed consent to participate in this study was provided by the participants or their legal guardian. The animal study was reviewed and approved by KU Leuven Animal Ethics Committee.

AUTHOR CONTRIBUTIONS

LG contributed to conception, design, and data acquisition, drafted and critically revised the manuscript. TH contributed to the data analysis and critically revised the manuscript. MM and FL contributed to conception, design supported in case of problems, and critically revised the manuscript. CP contributed to conception and critically revised the manuscript. WI contributed to data acquisition, initial data analysis, and critically revised the manuscript. DH and EM contributed to conception, design, data acquisition, data analysis, interpretation of results, and critically revised the manuscript. LG contributed to conception, supported in case of problems and critically revised the manuscript. All authors gave final approval and agree to be accountable for all aspects of the work.

FUNDING

This work was supported by the Department of Cell Biology primary funding at Erasmus MC, BIG project funding by Erasmus University, Rotterdam, Netherlands Organization for Health Research and Development ZonMW (EM), KU Leuven Special Research Fund (C24/17/077), OMFS-Impath research department at KU Leuven and Research Foundation - Flanders through doctoral grants 1193020N (LG) and 1S80019N (TH). The X-ray computed tomography images have been generated on the X-ray computed tomography facilities of the KU Leuven, financed by the Hercules Foundation (project AKUL 09/001: Micro-and nano-CT for the hierarchical analysis of materials).

ACKNOWLEDGMENTS

We thank Stijn Bellinkx, Melanie Van den Broeck, Orely Vanborren and Janne Vleminckx for their practical support during the experiments. We also thank Carla Geeroms for acquisition of μCT-scans, Samuel Ribeiro Visei for his help with the FACS experiment and Kathleen Bosmans for her help during implantation experiments. We would also thank Louca Verbeeck and Samuel Ribeiro Visei for their help during analysis of FACS data, and Mirjam van den Hout for help with RNA-seq.

SUPPLEMENTARY MATERIAL

The Supplementary Material for this article can be found online at: https://www.frontiersin.org/articles/10.3389/fcell.2020.554984/full#supplementary-material

Supplementary Figure 1 | Gene ontology terms for up- and downregulated genes between hPDCs obtained from maxilla and tibia.

Supplementary Figure 2 | Gene ontology terms for up- and downregulated genes between hPDCs obtained from mandible and tibia.

Supplementary Figure 3 | Gene ontology terms for up- and downregulated genes between hPDCs obtained from maxilla and mandible.

Supplementary Table 1 | Primer sequences used for RT-qPCR.

Supplementary Table 2 | List of up- and downregulated genes of hPDCs obtained from maxilla compared to tibial hPDCs.

Supplementary Table 3 | List of up- and downregulated genes of hPDCs obtained from mandible compared to tibial hPDCs.

Supplementary Table 4 | List of up- and downregulated genes of hPDCs obtained from mandible compared to maxillary hPDCs.

Supplementary Table 5 | Primer sequences of selected top-30 genes after RNA-sequencing, used for RT-qPCR.

REFERENCES

Aghaloo, T. L., Chaichanasakul, T., Bezouglaia, O., Kang, B., Franco, R., Dry, S. M., et al. (2010). Osteogenic potential of mandibular vs. long-bone marrow stromal cells. *J. Dent. Res.* 89, 1293–1298. doi: 10.1177/0022034510378427

Ambrosi, T. H., Longaker, M. T., and Chan, C. K. F. (2019). A revised perspective of skeletal stem cell biology. *Front. Cell. Dev. Biol.* 7:189. doi: 10.3389/fcell.2019.00189

Anders, S., Pyl, P. T., and Huber, W. (2015). HTSeq–a Python framework to work with high-throughput sequencing data. *Bioinformatics* 31, 166–169. doi: 10.1093/bioinformatics/btu638

Arrington, E. D., Smith, W. J., Chambers, H. G., Bucknell, A. L., and Davino, N. A. (1996). Complications of iliac crest bone graft harvesting. *Clin. Orthop. Relat. Res.* 329, 300–309. doi: 10.1097/00003086-199608000-00037

Bolander, J., Herpelinck, T., Chaklader, M., Gklava, C., Geris, L., and Luyten, F. P. (2020). Single-cell characterization and metabolic profiling of in vitro cultured human skeletal progenitors with enhanced in vivo bone forming capacity. *Stem Cells Transl. Med.* 9, 389–402. doi: 10.1002/sctm.19-0151

Bolander, J., Ji, W., Geris, L., Bloemen, V., Chai, Y. C., Schrooten, J., et al. (2016). The combined mechanism of bone morphogenetic protein- and calcium phosphate-induced skeletal tissue formation by human periosteum derived cells. *Eur. Cell Mater.* 31, 11–25. doi: 10.22203/ecm.v031a02

Bolger, A. M., Lohse, M., and Usadel, B. (2014). Trimmomatic: a flexible trimmer for Illumina sequence data. *Bioinformatics* 30, 2114–2120. doi: 10.1093/bioinformatics/btu170

Brighton, C. T., and Hunt, R. M. (1997). Early histologic and ultrastructural changes in microvessels of periosteal callus. *J. Orthop. Trauma* 11, 244–253. doi: 10.1097/00005131-199705000-00002

Cesario, J. M., Landin Malt, A., Deacon, L. J., Sandberg, M., Vogt, D., Tang, Z., et al. (2015). Lhx6 and Lhx8 promote palate development through negative regulation of a cell cycle inhibitor gene, p57Kip2. *Hum. Mol. Genet.* 24, 5024–5039. doi: 10.1093/hmg/ddv223

Chai, Y. C., Roberts, S. J., Desmet, E., Kerckhofs, G., van Gastel, N., Geris, L., et al. (2012). Mechanisms of ectopic bone formation by human osteoprogenitor cells on CaP biomaterial carriers. *Biomaterials* 33, 3127–3142. doi: 10.1016/j.biomaterials.2012.01.015

Chan, C. K. F., Gulati, G. S., Sinha, R., Tompkins, J. V., Lopez, M., Carter, A. C., et al. (2018). Identification of the human skeletal stem cell. *Cell* 175, 43–56.e21. doi: 10.1016/j.cell.2018.07.029

Choi, Y., Ballow, D. J., Xin, Y., and Rajkovic, A. (2008). Lim homeobox gene, lhx8, is essential for mouse oocyte differentiation and survival. *Biol. Reprod.* 79, 442–449. doi: 10.1095/biolreprod.108.069393

Colnot, C., Zhang, X., and Knothe Tate, M. L. (2012). Current insights on the regenerative potential of the periosteum: molecular, cellular, and endogenous engineering approaches. *J. Orthop. Res.* 30, 1869–1878. doi: 10.1002/jor.22181

Couly, G. F., Coltey, P. M., and Le Douarin, N. M. (1993). The triple origin of skull in higher vertebrates: a study in quail-chick chimeras. *Development* 117, 409–429.

De Bari, C., Dell'Accio, F., Vanlauwe, J., Eyckmans, J. I, Khan, M., Archer, C. W., et al. (2006). Mesenchymal multipotency of adult human periosteal cells demonstrated by single-cell lineage analysis. *Arthritis Rheum.* 54, 1209–1221. doi: 10.1002/art.21753

Dominici, M., Le Blanc, K., Mueller, I., Slaper-Cortenbach, I., Marini, F., Krause, D., et al. (2006). Minimal criteria for defining multipotent mesenchymal stromal cells. The international society for cellular therapy position statement. *Cytotherapy* 8, 315–317. doi: 10.1080/14653240600855905

Duchamp de Lageneste, O., Julien, A., Abou-Khalil, R., Frangi, G., Carvalho, C., Cagnard, N., et al. (2018). Periosteum contains skeletal stem cells with high bone regenerative potential controlled by Periostin. *Nat. Commun.* 9:773. doi: 10.1038/s41467-018-03124-z

Eyckmans, J., and Luyten, F. P. (2006). Species specificity of ectopic bone formation using periosteum-derived mesenchymal progenitor cells. *Tissue Eng.* 12, 2203–2213. doi: 10.1089/ten.2006.12.2203

Flandin, P., Zhao, Y., Vogt, D., Jeong, J., Long, J., Potter, G., et al. (2011). Lhx6 and Lhx8 coordinately induce neuronal expression of Shh that controls the generation of interneuron progenitors. *Neuron* 70, 939–950. doi: 10.1016/j.neuron.2011.04.020

Geris, L., and Papantoniou, I. (2019). The third era of tissue engineering: reversing the innovation drivers. *Tissue Eng. Part A* 25, 821–826. doi: 10.1089/ten.TEA.2019.0064

Giannoni, P., Scaglione, S., Daga, A., Ilengo, C., Cilli, M., and Quarto, R. (2010). Short-time survival and engraftment of bone marrow stromal cells in an ectopic model of bone regeneration. *Tissue Eng. Part A* 16, 489–499. doi: 10.1089/ten.TEA.2009.0041

Green, S. A., Simoes-Costa, M., and Bronner, M. E. (2015). Evolution of vertebrates as viewed from the crest. *Nature* 520, 474–482. doi: 10.1038/nature14436

Guichet, J. M., Braillon, P., Bodenreider, O., and Lascombes, P. (1998). Periosteum and bone marrow in bone lengthening: a DEXA quantitative evaluation in rabbits. *Acta Orthop. Scand.* 69, 527–531. doi: 10.3109/17453679808997792

Hagberg, C. E., Falkevall, A., Wang, X., Larsson, E., Huusko, J., Nilsson, I., et al. (2010). Vascular endothelial growth factor B controls endothelial fatty acid uptake. *Nature* 464, 917–921. doi: 10.1038/nature08945

Ji, W., Kerckhofs, G., Geeroms, C., Marechal, M., Geris, L., and Luyten, F. P. (2018). Deciphering the combined effect of bone morphogenetic protein 6 and calcium phosphate on bone formation capacity of periosteum derived cells-based tissue engineering constructs. *Acta Biomater.* 80, 97–107. doi: 10.1016/j.actbio.2018.09.046

Jung, Y. K., Kim, G. W., Park, H. R., Lee, E. J., Choi, J. Y., Beier, F., et al. (2013). Role of interleukin-10 in endochondral bone formation in mice: anabolic effect via the bone morphogenetic protein/Smad pathway. *Arthritis Rheum.* 65, 3153–3164. doi: 10.1002/art.38181

Kerckhofs, G., Chai, Y. C., Luyten, F. P., and Geris, L. (2016). Combining microCT-based characterization with empirical modelling as a robust screening approach for the design of optimized CaP-containing scaffolds for progenitor cell-mediated bone formation. *Acta Biomater.* 35, 330–340. doi: 10.1016/j.actbio.2016.02.037

Kerckhofs, G., Sainz, J., Wevers, M., Van de Putte, T., and Schrooten, J. (2013). Contrast-enhanced nanofocus computed tomography images the cartilage subtissue architecture in three dimensions. *Eur. Cell Mater.* 25, 179–189. doi: 10.22203/ecm.v025a13

Kern, S., Eichler, H., Stoeve, J., Klüter, H., and Bieback, K. (2006). Comparative analysis of mesenchymal stem cells from bone marrow, umbilical cord blood, or adipose tissue. *Stem Cells* 24, 1294–1301. doi: 10.1634/stemcells.2005-0342

Kim, D., Langmead, B., and Salzberg, S. L. (2015). HISAT: a fast spliced aligner with low memory requirements. *Nat. Methods* 12, 357–360. doi: 10.1038/nmeth.3317

Lammens, J., Maréchal, M., Delport, H., Geris, L., Oppermann, H., Vukicevic, S., et al. (2020). A cell-based combination product for the repair of large bone defects. *Bone* 138:115511. doi: 10.1016/j.bone.2020.115511

Lee, J. H., Hah, Y. S., Cho, H. Y., Kim, J. H., Oh, S. H., Park, B. W., et al. (2014). Human umbilical cord blood-derived CD34-positive endothelial progenitor cells stimulate osteoblastic differentiation of cultured human periosteal-derived osteoblasts. *Tissue Eng. Part A* 20, 940–953. doi: 10.1089/ten.TEA.2013.0329

Lee, J. M., Kim, M. G., Byun, J. H., Kim, G. C., Ro, J. H., Hwang, D. S., et al. (2017). The effect of biomechanical stimulation on osteoblast differentiation of human jaw periosteum-derived stem cells. *Maxillofac. Plast. Reconstr. Surg.* 39:7. doi: 10.1186/s40902-017-0104-6

Leijten, J., Chai, Y. C., Papantoniou, I., Geris, L., Schrooten, J., and Luyten, F. P. (2015). Cell based advanced therapeutic medicinal products for bone repair: Keep it simple? *Adv. Drug Deliv. Rev.* 84, 30–44. doi: 10.1016/j.addr.2014.10.025

Leucht, P., Kim, J. B., Amasha, R., James, A. W., Girod, S., and Helms, J. A. (2008). Embryonic origin and Hox status determine progenitor cell fate during adult bone regeneration. *Development* 135, 2845–2854. doi: 10.1242/dev.023788

Li, H., Marijanovic, I., Kronenberg, M. S., Erceg, I., Stover, M. L., Velonis, D., et al. (2008). Expression and function of Dlx genes in the osteoblast lineage. *Dev. Biol.* 316, 458–470. doi: 10.1016/j.ydbio.2008.01.001

Liatsikos, S. A., Grimbizis, G. F., Georgiou, I., Papadopoulos, N., Lazaros, L., Bontis, J. N., et al. (2010). HOX A10 and HOX A11 mutation scan in congenital malformations of the female genital tract. *Reprod. Biomed. Online* 21, 126–132. doi: 10.1016/j.rbmo.2010.03.015

Lin, X., Yang, H., Wang, L., Li, W., Diao, S., Du, J., et al. (2019). AP2a enhanced the osteogenic differentiation of mesenchymal stem cells by inhibiting the formation of YAP/RUNX2 complex and BARX1 transcription. *Cell Prolif.* 52:e12522. doi: 10.1111/cpr.12522

Lindhe, J., Bressan, E., Cecchinato, D., Corrá, E., Toia, M., and Liljenberg, B. (2013). Bone tissue in different parts of the edentulous maxilla and mandible. *Clin. Oral Implants Res.* 24, 372–377. doi: 10.1111/clr.12064

Mattioli-Belmonte, M., Teti, G., Salvatore, V., Focaroli, S., Orciani, M., Dicarlo, M., et al. (2015). Stem cell origin differently affects bone tissue engineering strategies. *Front. Physiol.* 6:266. doi: 10.3389/fphys.2015.00266

Meijer, G. J., de Bruijn, J. D., Koole, R., and van Blitterswijk, C. A. (2008). Cell based bone tissue engineering in jaw defects. *Biomaterials* 29, 3053–3061. doi: 10.1016/j.biomaterials.2008.03.012

Meulemans, D., and Bronner-Fraser, M. (2004). Gene-regulatory interactions in neural crest evolution and development. *Dev. Cell* 7, 291–299. doi: 10.1016/j.devcel.2004.08.007

Mimura, S., Suga, M., Okada, K., Kinehara, M., Nikawa, H., and Furue, M. K. (2016). Bone morphogenetic protein 4 promotes craniofacial neural crest induction from human pluripotent stem cells. *Int. J. Dev. Biol.* 60, 21–28. doi: 10.1387/ijdb.160040mk

Mosmann, T. (1983). Rapid colorimetric assay for cellular growth and survival: application to proliferation and cytotoxicity assays. *J. Immunol. Methods* 65, 55–63. doi: 10.1016/0022-1759(83)90303-4

Nakahara, H., Goldberg, V. M., and Caplan, A. I. (1991). Culture-expanded human periosteal-derived cells exhibit osteochondral potential in vivo. *J. Orthop. Res.* 9, 465–476. doi: 10.1002/jor.1100090402

Noden, D. M. (1982). "Patterns and organization of craniofacial skeletogenic mesenchyme: a perspective," in *Factors and Mechanisms Influencing Bone Growth*, eds A. D. Dixon and B. G. Sarnat (New York, NY: Alan R. Liss).

Owston, H. E., Ganguly, P., Tronci, G., Russell, S. J., Giannoudis, P. V., and Jones, E. A. (2019). Colony formation, migratory, and differentiation characteristics of multipotential stromal cells (MSCs) from clinically accessible human periosteum compared to donor-matched bone marrow MSCs. *Stem Cells Int.* 2019:6074245. doi: 10.1155/2019/6074245

Paine-Saunders, S., Viviano, B. L., Zupicich, J., Skarnes, W. C., and Saunders, S. (2000). glypican-3 controls cellular responses to Bmp4 in limb patterning and skeletal development. *Dev. Biol.* 225, 179–187. doi: 10.1006/dbio.2000.9831

Park, H. S., Lee, Y. J., Jeong, S. H., and Kwon, T. G. (2008). Density of the alveolar and basal bones of the maxilla and the mandible. *Am. J. Orthod. Dentofacial Orthop.* 133, 30–37. doi: 10.1016/j.ajodo.2006.01.044

Potier, E., Ferreira, E., Meunier, A., Sedel, L., Logeart-Avramoglou, D., and Petite, H. (2007). Prolonged hypoxia concomitant with serum deprivation induces massive human mesenchymal stem cell death. *Tissue Eng.* 13, 1325–1331. doi: 10.1089/ten.2006.0325

Raines, A. M., Magella, B., Adam, M., and Potter, S. S. (2015). Key pathways regulated by HoxA9,10,11/HoxD9,10,11 during limb development. *BMC Dev. Biol.* 15:28. doi: 10.1186/s12861-015-0078-5

Risso, D., Schwartz, K., Sherlock, G., and Dudoit, S. (2011). GC-content normalization for RNA-Seq data. *BMC Bioinformatics* 12:480. doi: 10.1186/1471-2105-12-480

Roberts, S. J., van Gastel, N., Carmeliet, G., and Luyten, F. P. (2015). Uncovering the periosteum for skeletal regeneration: the stem cell that lies beneath. *Bone* 70, 10–18. doi: 10.1016/j.bone.2014.08.007

Robinson, M. D., McCarthy, D. J., and Smyth, G. K. (2010). edgeR: a Bioconductor package for differential expression analysis of digital gene expression data. *Bioinformatics* 26, 139–140. doi: 10.1093/bioinformatics/btp616

Sacchetti, B., Funari, A., Remoli, C., Giannicola, G., Kogler, G., Liedtke, S., et al. (2016). No identical mesenchymal stem cells at different times and sites: human committed progenitors of distinct origin and differentiation potential are incorporated as adventitial cells in microvessels. *Stem Cell Reports* 6, 897–913. doi: 10.1016/j.stemcr.2016.05.011

Salgado, A. J., Coutinho, O. P., and Reis, R. L. (2004). Bone tissue engineering: state of the art and future trends. *Macromol. Biosci.* 4, 743–765. doi: 10.1002/mabi.200400026

Takimoto, A., Kokubu, C., Watanabe, H., Sakuma, T., Yamamoto, T., Kondoh, G., et al. (2019). Differential transactivation of the upstream aggrecan enhancer regulated by PAX1/9 depends on SOX9-driven transactivation. *Sci. Rep.* 9:4605. doi: 10.1038/s41598-019-40810-4

Tribulo, C., Aybar, M. J., Nguyen, V. H., Mullins, M. C., and Mayor, R. (2003). Regulation of Msx genes by a Bmp gradient is essential for neural crest specification. *Development* 130, 6441–6452. doi: 10.1242/dev.00878

Tsai, M. S., Hwang, S. M., Chen, K. D., Lee, Y. S., Hsu, L. W., Chang, Y. J., et al. (2007). Functional network analysis of the transcriptomes of mesenchymal stem cells derived from amniotic fluid, amniotic membrane, cord blood, and bone marrow. *Stem Cells* 25, 2511–2523. doi: 10.1634/stemcells.2007-0023

van Gastel, N., Torrekens, S., Roberts, S. J., Moermans, K., Schrooten, J., Carmeliet, P., et al. (2012). Engineering vascularized bone: osteogenic and proangiogenic potential of murine periosteal cells. *Stem Cells* 30, 2460–2471. doi: 10.1002/stem.1210

van Lochem, E. G., van der Velden, V. H., Wind, H. K., te Marvelde, J. G., Westerdaal, N. A., and van Dongen, J. J. (2004). Immunophenotypic differentiation patterns of normal hematopoiesis in human bone marrow: reference patterns for age-related changes and disease-induced shifts. *Cytometry B Clin. Cytom.* 60, 1–13. doi: 10.1002/cyto.b.20008

Villanueva, S., Glavic, A., Ruiz, P., and Mayor, R. (2002). Posteriorization by FGF, Wnt, and retinoic acid is required for neural crest induction. *Dev. Biol.* 241, 289–301. doi: 10.1006/dbio.2001.0485

Wallin, J., Wilting, J., Koseki, H., Fritsch, R., Christ, B., and Balling, R. (1994). The role of Pax-1 in axial skeleton development. *Development* 120, 1109–1121.

Wang, W., Huang, D., Ren, J., Li, R., Feng, Z., Guan, C., et al. (2019). Optogenetic control of mesenchymal cell fate towards precise bone regeneration. *Theranostics* 9, 8196–8205. doi: 10.7150/thno.36455

Wang, X., Zheng, P., Huang, G., Yang, L., and Zhou, Z. (2018). Dipeptidyl peptidase-4(DPP-4) inhibitors: promising new agents for autoimmune diabetes. *Clin. Exp. Med.* 18, 473–480. doi: 10.1007/s10238-018-0519-0

Woo, J., Miletich, I., Kim, B. M., Sharpe, P. T., and Shivdasani, R. A. (2011). Barx1-mediated inhibition of Wnt signaling in the mouse thoracic foregut controls tracheo-esophageal septation and epithelial differentiation. *PLoS One* 6:e22493. doi: 10.1371/journal.pone.0022493

Ylönen, R., Kyrönlahti, T., Sund, M., Ilves, M., Lehenkari, P., Tuukkanen, J., et al. (2005). Type XIII collagen strongly affects bone formation in transgenic mice. *J. Bone Miner Res.* 20, 1381–1393. doi: 10.1359/JBMR.050319

Zhou, Y., Zhou, B., Pache, L., Chang, M., Khodabakhshi, A. H., Tanaseichuk, O., et al. (2019). Metascape provides a biologist-oriented resource for the analysis of systems-level datasets. *Nat. Commun.* 10:1523. doi: 10.1038/s41467-019-09234-6

Conflict of Interest: The authors declare that the research was conducted in the absence of any commercial or financial relationships that could be construed as a potential conflict of interest.

Copyright © 2020 Groeneveldt, Herpelinck, Maréchal, Politis, van IJcken, Huylebroeck, Geris, Mulugeta and Luyten. This is an open-access article distributed under the terms of the Creative Commons Attribution License (CC BY). The use, distribution or reproduction in other forums is permitted, provided the original author(s) and the copyright owner(s) are credited and that the original publication in this journal is cited, in accordance with accepted academic practice. No use, distribution or reproduction is permitted which does not comply with these terms.

frontiers in Cell and Developmental Biology

ORIGINAL RESEARCH
published: 09 April 2021
doi: 10.3389/fcell.2021.572727

The Duo of Osteogenic and Angiogenic Differentiation in ADSC-Derived Spheroids

Anastasiya A. Gorkun[1,2], Daria P. Revokatova[1,3], Irina M. Zurina[1,2], Denis A. Nikishin[3,4], Polina Y. Bikmulina[5], Peter S. Timashev[2,5,6,7], Anastasiya I. Shpichka[5], Nastasia V. Kosheleva[1,2,5], Tamara D. Kolokoltsova[1] and Irina N. Saburina[1]*

[1] FSBSI Institute of General Pathology and Pathophysiology, Moscow, Russia, [2] Institute for Regenerative Medicine, Sechenov University, Moscow, Russia, [3] Faculty of Biology, Lomonosov Moscow State University, Moscow, Russia, [4] Koltzov Institute of Developmental Biology of Russian Academy of Sciences, Moscow, Russia, [5] World-Class Research Center "Digital Biodesign and Personalized Healthcare," Sechenov University, Moscow, Russia, [6] Chemistry Department, Lomonosov Moscow State University, Moscow, Russia, [7] Department of Polymers and Composites, N.N.Semenov Federal Research Center for Chemical Physics, Russain Academy of Sciences, Moscow, Russia

Bone formation during embryogenesis is driven by interacting osteogenesis and angiogenesis with parallel endothelial differentiation. Thence, all *in vitro* bioengineering techniques are aimed at pre-vascularization of osteogenic bioequivalents to provide better regeneration outcomes upon transplantation. Due to appearance of cell–cell and cell–matrix interactions, 3D cultures of adipose-derived stromal cells (ADSCs) provide a favorable spatial context for the induction of different morphogenesis processes, including vasculo-, angio-, and osteogenesis and, therefore, allow modeling their communication *in vitro*. However, simultaneous induction of multidirectional cell differentiation in spheroids from multipotent mesenchymal stromal cells (MMSCs) was not considered earlier. Here we show that arranging ADSCs into spheroids allows rapid and spontaneous acquiring of markers of both osteo- and angiogenesis compared with 2D culture. We further showed that this multidirectional differentiation persists in time, but is not influenced by classical protocols for osteo- or angio-differentiation. At the same time, ADSC-spheroids retain similar morphology and microarchitecture in different culture conditions. These findings can contribute to a better understanding of the fundamental aspects of autonomous regulation of differentiation processes and their cross-talks in artificially created self-organizing multicellular structures. This, in turn, can find a wide range of applications in the field of tissue engineering and regeneration.

Keywords: osteogenesis, agiogenesis, spheroid, 3D culture, tissue engineering, adipose-derived stromal cells (ADSCs)

OPEN ACCESS

Edited by:
Andrei S. Chagin, Karolinska Institutet (KI), Sweden

Reviewed by:
Anastasia Efimenko, Lomonosov Moscow State University, Russia
Natalia Kalinina, Lomonosov Moscow State University, Russia

****Correspondence:***
Anastasiya A. Gorkun
stgork@gmail.com

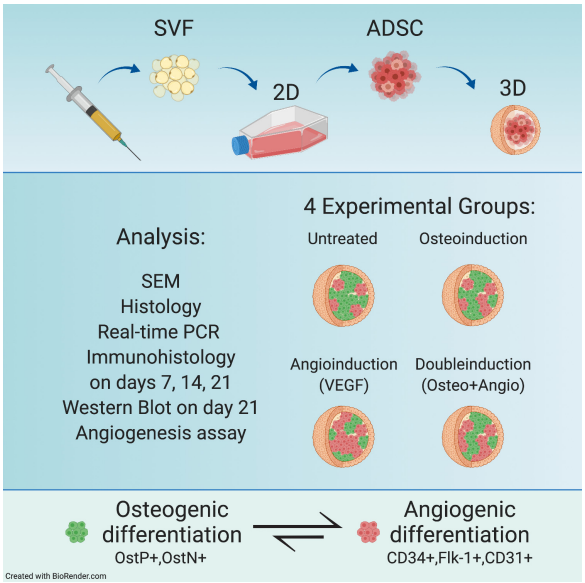
Specialty section:
This article was submitted to Stem Cell Research, a section of the journal Frontiers in Cell and Developmental Biology

Received: *15 June 2020*
Accepted: *25 February 2021*
Published: *09 April 2021*

Citation:
Gorkun AA, Revokatova DP, Zurina IM, Nikishin DA, Bikmulina PY, Timashev PS, Shpichka AI, Kosheleva NV, Kolokoltsova TD and Saburina IN (2021) The Duo of Osteogenic and Angiogenic Differentiation in ADSC-Derived Spheroids. Front. Cell Dev. Biol. 9:572727. doi: 10.3389/fcell.2021.572727

INTRODUCTION

Numerous studies have shown that multipotent mesenchymal stromal cells (MMSCs) from various sources can supply factors supporting tissue regeneration into the local microenvironment. In particular, angiogenesis and osteogenesis can be stimulated through the secretion of specific cytokines, such as epidermal growth factor (EGF), basic fibroblast growth factor (bFGF), platelet-derived growth factor (PDGF), vascular endothelial growth factor (VEGF), keratinocyte growth factor (KGF), and angiopoietins (Chen et al., 2009; Langenbach et al., 2013; Yamaguchi et al., 2014). Clinical efficacy and availability of these cells have already been shown for treating bone defects at various locations (Corre et al., 2013).



GRAPHICAL ABSTRACT

It has long been recognized that osteogenesis and angiogenesis, including endothelial differentiation, are coupled and coordinated during bone formation (Schipani et al., 2009; Grosso et al., 2017). Therefore, it is crucial to create pre-vascularized structures since diffusion only allows osteoblasts to exchange gases and nutrients at distances not exceeding 200 μm (Muschler et al., 2004). In ideal tissue-engineered bone tissue constructions, functionality and structure, as well as regulation of both osteogenesis and vasculogenesis, should be combined, which could potentially solve the problem of obtaining massive artificial vascularized bone tissue fragments *in vitro*. Bioengineering is considered to be the most promising strategy for replacing or reconstructing large-scale defects (Song et al., 2016). According to the literature, there are different methods currently used to obtain vascularized bone tissue-engineered constructions (Laschke and Menger, 2012; Duttenhoefer et al., 2013; Roux et al., 2015). Different approaches were used to achieve vascularization: cells are immobilized on the substrate and co-cultured in monolayer or hydrogels (Annabi et al., 2014; Rohringer et al., 2014; Holnthoner et al., 2015).

One way to solve the problem of vasculogenesis in bone tissue is to use a combination of MMSCs with human umbilical vein endothelial cells (HUVEC) (Inglis et al., 2016; Strassburg et al., 2016) or peripheral blood cells (Holnthoner et al., 2015). Many groups work on the design and architecture of substrates or constructions, as well as the optimization of biologically active materials (Lovett et al., 2009; Sakaguchi et al., 2013; Holnthoner et al., 2015; Song et al., 2016). Combining biomaterials with 3D cultures is another possible strategy, e.g., a two-step digital light-processing technique for fabricating a bone-mimetic 3D hydrogel construct based on octacalcium phosphate (OCP), HUVEC spheroids, and gelatin methacrylate (GelMA) hydrogels (Anada et al., 2019).

Studies have shown that of different MMSC populations, adipose-derived stromal cells (ADSCs) have an advantage in terms of angio- and vasculogenesis since they contain not only a population of multipotent cells but also a vascular fraction that can contribute to the rapid restoration of blood supply to the damaged area (Marra and Rubin, 2012; Thery et al., 2015). Another unique feature of ADSCs is their ability to enhance angiogenesis through paracrine stimulation (Kalinina et al., 2015; Zhang et al., 2016). Altogether, this makes ADSCs a convenient cell source widely used in vascular regeneration-related studies for recreation of an angiogenic niche by using native (Cerino et al., 2017) as well as genetically modified ADSCs (Makarevich et al., 2015, 2018).

It is now widely accepted that 3D culturing of cells in the form of spheroids or organoids is a "bridge" between monolayer cultures and native tissues (Pampaloni et al., 2007). In 3D culture, cells acquire emergent functionality via multilevel interactions through cell junctions, microvesicle exchange, and extracellular matrix (ECM), which altogether provides the regulation of their collective behavior as well as restoration of initial cellular phenotype and functional activity (Repin et al., 2014; Zurina et al., 2018, 2020). Indeed, it was shown that such arrangements within spheroids as intercellular junctions and cell–matrix interactions result in the appearance of a local microenvironment, which facilitates proper cellular differentiation (Lee et al., 2016; Muller et al., 2019). In the case of ADSCs, cultivation in the form of spheroids allows, among other things, endothelial (Park et al., 2014; Gorkun et al., 2018; Saburina et al., 2018) and osteogenic differentiation (Gurumurthy et al., 2017; Saburina et al., 2018). However, simultaneous induction of multidirectional cell differentiation in MMSC-derived spheroids has not been considered earlier.

Thus, in this work, we aimed to explore the possibility of simultaneous induction of both angiogenic and osteogenic differentiation of ADSC employing spheroid culture system. The aim is to establish a platform where interactions between angiogenesis and osteogenesis can be easily manipulated and studied, employing high-throughput approaches.

MATERIALS AND METHODS

The study was conducted on the primary culture of human adipose-derived stromal cells (ADSCs). Adipose tissue fragments were collected from three donors (without chronic diseases, age 25–60) undergoing liposuction after receiving their written, informed consent. All the procedures were performed under local anesthesia and aseptic conditions and were approved by the Local Ethical Committee of Sechenov University (#07–17 from 13.09.2017, Moscow, Russia) while performed in accordance with the Helsinki Declaration.

The culture of human umbilical vein endothelial cells (HUVEC) was kindly provided by the "Collection of cell cultures for biotechnological and biomedical researches (of general biological and biomedical applications)" of the Koltzov Institute of Developmental Biology of Russian Academy of Sciences.

2D Culture of Human Adipose-Derived Stromal Cells

Biopsy samples were placed in a sterile transport container with DMEM/F-12 (BioLoT, Russia), L-glutamine (2 mM; BioLoT, Russia), and gentamicin (50 μg/ml; PanEco, Russia) and delivered to the laboratory.

Tissue samples were washed in Hank's solution (BioLoT, Russia) containing antibiotics (1% penicillin–streptomycin, 400 U/ml of gentamicin; PanEco, Russia), minced mechanically, and digested with collagenase type I (0.07% solution) and dispase (0.025% solution) (PanEco, Russia) for 25 min at + 37°C. After incubation, DMEM/F-12 with 10% fetal clone serum (FCS; HyClone, United States) was added to the samples, and they were centrifuged for 5 min at 400 *g*. The pellet was resuspended in medium and filtered through a nylon filter to remove large tissue fragments. The cell suspension, together with small tissue fragments, was transferred to Petri dishes and cultured in complete growth medium consisting of DMEM/F-12 (1:1; BioLoT, Russia) supplemented with 2 mM L-glutamine, 100 U/ml of gentamicin (PanEco, Russia), 10% FCS (HyClone, United States), 1% 100 × ITS-G (insulin–transferrin–selenium) (BioLoT, Russia), 20 ng/ml of bFGF (ProSpec, Israel), and 15 U/ml of heparin (PanEco, Russia). ADSCs were cultured under standard conditions (37°C, 5% CO_2). The medium was replaced every 3 days. As soon as cultures reached 90–95% confluence, the monolayer was treated with versene (BioLoT, Russia) and 0.25% trypsin solutions (BioLoT, Russia). The cells were passaged in a fresh portion of growth medium to new Petri dishes. Cell morphology and character of growth were controlled daily under an Olympus CKX-41 inverted phase-contrast microscope. Cells were cultured up to passage 4.

Immunophenotyping of Human Adipose-Derived Stromal Cells in 2D Culture

The monolayer ADSC cultures at the fourth passage were immunophenotyped by the following surface marker proteins of multipotent mesenchymal stromal cells (Dominici et al., 2006; Haasters et al., 2009): CD105-PerCP-Cy5.5, CD90-FITC (BD Stemflow Positive cocktail, BD Bioscience, United States), CD73-PE, CD19-PE, CD29-PE, CD44-PE, CD31-PE (Miltenyi Biotec, Germany), CD45-PE, CD34-PE, CD14-PE, CD11b-PE, HLA-DR-PE (BD Stemflow Negative cocktail, BD Bioscience, United States), and CD146-PE (Biolegend, United States). Mouse isotypic controls IgG2a, IgG1 (Miltenyi Biotec, Germany), and unstained cells were used as controls.

Cells were washed from the complete growth medium with versene solution (BioLot, Russia), treated with 0.25% trypsin solution (BioLot, Russia), transferred to 15-ml tubes, and centrifuged (7 min, 400 *g*). The pellet was resuspended in PBS (pH 7.4) with 1% serum and incubated in the dark (15 min, 25°C) with antibodies (10 μl of antibodies per 1×10^6 cells) conjugated with fluorescent labels [fluorescein isothiocyanate (FITC), phycoerythrin (PE), Cyanine 5.5 (Cy5.5)]. Stained cells were centrifuged (5 min, 400 *g*), and the pellet was resuspended in 1 ml of PBS containing 1% FCS in tubes for flow cytometry. The samples were analyzed on a SONY SH800 cell sorter (Sony biotechnology, United States).

To reveal the capacity for osteogenic and angiogenic cell differentiation, ADSC monolayers were incubated with osteoinductive medium and VEGF (see detailed protocol below) for 21 days. After day 21, cells were seeded on coverslips. Then coverslips were fixed in 4% PFA for 20 min at +4°C. Samples were then washed in cold PBS (PanEco, Russia) and stained with antibodies against osteopontin (Abcam, United Kingdom) and VEGFR2 Flk-1 (Thermo Scientific, United States) (see detailed protocol below).

3D Cultivation and Differentiation of Human Adipose-Derived Stromal Cells

Agarose multiwell plates were prepared from a 2% agarose solution (A-6013, Sigma-Aldrich, Germany) on a DMEM/F12 mixture (1:1) supplemented with 75 μg/ml gentamicin using 3D PetriDish molds (Microtissues^{TM}, United States). Agarose plates were stored at +4°C in DMEM/F12 medium.

Cells at the fourth passage were treated with versene (BioLoT, Russia) and 0.25% trypsin (BioLoT, Russia) solutions to obtain cell suspension, transferred to 15-ml tubes, and centrifuged (7 min, 400 *g*). The resulting pellet was resuspended in the full growth medium to a concentration of 3.3×10^6 cells/ml. Of the resulting suspension, 150 μl was transferred to non-adherent agarose plates. After an hour, 2 ml of complete growth or induction medium was added to the wells. Every microplate allowed us to collect up to 256 spheroids for further high-throughput analysis.

Spheroids were divided into four experimental groups: (1) Untreated spheroids with the regular growth medium; (2) Osteo group with the osteoinductive medium; (3) Angio group with the VEGF-supplemented growth medium; (4) Double group with the medium containing all components necessary for both osteo- and angiogenic differentiation.

For osteogenic differentiation, spheroids were cultivated in the complete growth medium supplemented with 100 nM dexamethasone (Sigma-Aldrich, Germany), 20 mM β-glycerophosphate (Sigma-Aldrich, Germany), and 0.05 mM ascorbic acid (Sigma-Aldrich, Germany).

Angiogenic differentiation was induced by adding 10 ng/ml of vascular endothelial growth factor VEGF (Sci-Store, Russia) to the complete growth medium. For double induction, all components necessary for both osteo- and angiogenic differentiation were added to the complete growth medium. The medium was replaced every 2 days. Cells in all groups were cultured under 3D conditions for 7, 14, and 21 days. For real-time PCR experiments, spheroids after 1 day in 3D culture were also included in the analysis.

Immunocytochemical Staining of Spheroids From Human Adipose-Derived Stromal Cells

Immunocytochemical staining was performed on 3D cell cultures fixed with methanol for 12 h. Before staining, spheroids were washed from 100% methanol at room temperature sequentially in 80%, 60%, 40%, and 20% methanol solutions and in PBS

for 10 min. Antigen retrieval procedure was used for CD31 staining: the samples were incubated with Tris-EDTA buffer (pH = 9) for 20 min at + 95°C. After washing, the samples were incubated in 250 μl of a solution of primary antibodies in PBS with 10% serum and 0.1% Tween-20 (24 h at +4°C). We used primary antibodies against vimentin (Abcam, R&D Systems, United States), CD31 (Thermo Scientific, United States), VEGFR2 Flk-1 (Thermo Scientific, United States), collagen type I (Abcam, United Kingdom), osteocalcin (R&D Systems, United States), and osteopontin (Abcam, United Kingdom). All antibodies were used at 1/500 dilution. Samples were then washed with PBS and incubated in 250 μl of a solution of secondary species-specific antibodies conjugated with fluorochromes Alexa Fluor 488 and Alexa Fluor 594 (ThermoScientific, United States). All antibodies were used at 1/500 dilution. The nuclei were stained with 2 μg/ml of intercalating dye Hoechst 33258 (Serva, Germany) or DAPI (Abcam, United Kingdom). The preparations in the mounting medium were covered with coverslips and examined under an Olympus Fluoview FV10I laser confocal scanning microscope (Olympus, Japan) in visible and UV light.

Quantitative Analysis of Collagen and Vimentin Fiber Alignment

The fibers' alignment and angles, stained with antibodies against vimentin and collagen type I, were measured on confocal images with the available software CurveAlign (UW–Madison[1]) in MatLab. Collagen type I and vimentin alignment measure the similarity of the orientations of cytoskeleton fibers in a defined area, calculated as the mean resultant vector length in circular statistics (Berens, 2009). The alignment coefficient ranged from 0.0 to 1.0, where higher alignment coefficients indicate fibers in a given image or regions of interest (ROI) to be more aligned. Measurement was performed using the curvelet fiber representation (CFR) mode of fiber analysis method (Liu et al., 2017). The diagrams representing angle distribution were built using Maple software.

Scanning Electron Microscopy

For scanning electron microscopy (SEM), the samples were fixed with glutaraldehyde (3% solution in PBS) overnight at +4°C. Samples were then washed thrice with PBS and fixed in OsO_4 (1% solution in PBS) for 1 h at room temperature. Then spheroids were washed thrice with PBS and dehydrated with ethanol (50% and 70%; twice for 5 min each). The samples were stored at +4°C in 70% ethanol. The samples were then further dehydrated with ethanol (80%—twice for 5 min; 96%—twice for 5 min) and acetone (5 min). Then we dried the samples at the critical point, covered them with golden particles in vacuum, and studied the replica using a CamScan-S2 scanning electron microscope (Cambridge Instruments, United Kingdom).

Histology

Spheroids were collected and fixed in 4% PFA for 20 min at +4°C. Samples were then washed in cold PBS (PanEco, Russia), embedded in the HistoGel™ (Richard-Allan Scientific™, USAHG-4000-012), dehydrated in graded alcohol concentrations, and embedded in paraffin. Paraffin sections of 5-μm thickness were cut, deparaffinized, rehydrated, and stained with hematoxylin/eosin (H&E) (Sigma-Aldrich, Germany) to assess overall spheroids' morphology.

Analysis of Gene Expression by Real-Time Polymerase Chain Reaction

Spheroids were fixed in a 500-μl lysis mixture [1 ml of lysis buffer (Thermo Scientific, United States), 20 μl mercaptoethanol] and pipetted until spheroids were completely lysed. Samples were stored at −80°C.

GeneJET PCR purification kit (Thermo Scientific, United States) was used to isolate total RNA according to the manufacturer's instructions. Then RNA was treated with DNase I to remove the genomic DNA. Samples were incubated overnight at −20°C in acetate, 0.5 μl of glycogen, and 96% ethanol to reprecipitate RNA, and then centrifuged for 20 min at 14,000 *g*. The supernatant was removed, and RNA concentration was measured using a Nanodrop 8000 spectrophotometer (Thermo Scientific, United States).

M-MLV reverse transcriptase (Evrogen, Russia) and random hexanucleotides (Evrogen, Russia) were used to synthesize cDNA. The obtained samples were used to the analyze gene expression listed in **Table 1**. For PCR reaction, commercial mixtures qPCRmix and SYBR + LowROX (Eurogen, Russia) were used. The sequences of the used primers are presented in **Table 1**. Synthetic oligonucleotides used as primers (Eurogen, Russia) were selected using PrimerSelect programs (DNA STAR, United States) based on sequential values obtained in the international NCBI database. Real-time PCR was performed using the 7500 Real-Time PCR Amplifier System (Applied Biosystems, United States); analysis of the results was performed in StepOne™ and StepOnePlus™ Software v2.3 (Applied Biosystems, United States). We used RPS18 (ribosomal protein) to normalize mRNA expression, which was specifically selected from eight commonly used genes for spheroids as the most stable. The selection was performed based on absolute quantification of reference gene expression for days 1, 7, 14, and 21 as in the protocol described previously (Nikishin et al., 2018). The absence of primer dimers was evaluated using the melting curves.

3D Angiogenesis Assay

To evaluate the spheroids' ability to form a capillary-like network, they were encapsulated within PEGylated fibrin hydrogels as previously described (Gorkun et al., 2018). PEGylated fibrin hydrogel was prepared according to the previously developed protocol (Shpichka et al., 2020). Briefly, fibrinogen was covalently bonded with polyethylene glycol (PEG) using O,O′-bis[2-(N-succinimidyl-succinylamino)ethyl]polyethylene glycol (PEG-NHS; Sigma-Aldrich, Germany) at a molar ratio of 5:1 (PEG-NHS: fibrinogen). The reaction mixture was incubated at 37°C for 2 h. The spheroids suspension was distributed in fibrinogen solution, and then the thrombin

[1]http://loci.wisc.edu/software/curvealign

TABLE 1 | List of primers used in the research.

Primers	Primer sequence (5′-3′)	Primer description	Length (nt)	Tm (°C)
hCD31_For	TTG TCT CCC GCT GGT TTT G	hCD31	19	58.2
hCD31_Rev	ATT GGC ATT TGG GAC TTG AT		23	56.9
hCD34 _For	CCT TGC AAC ATC TCC CAC TAA A	hCD34	22	59.8
hCD34 _Rev	CCC TCT CCC CTG TCC TTC TT		20	61.5
hCol1a1_For	ACC GAG GCC TCC CAG AAC	hCol1a1	18	62.4
hCol1a1_Rev	GTG CAG CCA TCG ACA GTG AC		20	60.3
hFlk1_For	TGG TCA GGC AGC TCA CAG TC	hFlk1	20	61.2
hFlk1_Rev	CCG GTT CCC ATC CTT CAA TA		20	57.2
hOsx_For	CAC TGC CCC ACC CCT TAG	hOsx	18	60.7
hOsx_Rev	CTT CCC CAC CCA TTC TTC A		19	57.6
hRunx2_Fow	TGT CAT GGC GGG TAA CGA	hRunx2	18	58.7
hRunx2_Rev	TTG GGG AGG ATT TGT GAA GAC		21	60.4
hBmp2_For	ACG AGG TCC TGA GCG AGT TC	hBmp2	20	61.2
hBmp2_Rev	ACC TGA GTG CCT GCG ATA CA		20	59.6
hRPS18_For	ACGCCGCCGCTTGTG CT	hRPS18	17	71.0
hRPS18_Rev	AGTTCTCCCGCCCTC TTGGTGA	hRPS18	22	70.4

solution was added (fibrinogen to thrombin ratio 1:1). This mixture immediately formed a gel.

Spheroids from all four groups were cultured in gels for 7 days, in complete growth medium supplemented with 10 ng/ml of VEGF, changed every 2 days. The process of tubule growth was monitored using a CKX41 inverted phase-contrast microscope (Olympus, Japan).

Immunocytochemistry of Spheroids in Fibrin Gel

Spheroids in fibrin gel were fixed in 4% paraformaldehyde (+4°C, overnight), washed thrice in PBS, permeabilized by 0.2% Triton X-100 (in PBS) for 10 min, and blocked with 5% goat serum in PBS. Samples were then incubated (+4°C, overnight) in the mix of PBS+0.1% Tween-20+5% goat serum with primary antibodies against CD31 (ab119339; Abcam), fibronectin (MA5-11981; Abcam), CD34 (ab54208; Abcam), and vimentin (ab92547; Abcam). After three times washing with PBST (PBS+0,1% tween), samples were then incubated in 250 μl of a solution of secondary species-specific antibodies conjugated with fluorochromes Alexa Fluor 488 and Alexa Fluor 594 (ThermoScientific, United States). All antibodies were used at 1/500 dilution. The nuclei were stained with 2 μg/ml of intercalating dye Hoechst 33258 (Serva, Germany) or DAPI (Abcam). The preparations in the mounting medium were covered with coverslips and examined under LSM 880 laser confocal scanning microscope (ZEISS, Germany) in visible and UV light.

Western Blot

Spheroids were homogenized in RIPA buffer with protease inhibitor cocktail. Protein concentration was measured by the BCA Pierce™ BCA Protein Assay Kit (Thermo Scientific). Samples were denatured in Laemmli sample buffer consisting of 2% SDS, 10% glycerol, 5% mercaptoethanol, 62.5 mM Tris (pH 6.8), and 0.004% bromophenol blue. Proteins were separated by 10% sodium dodecyl sulfate polyacrylamide gel electrophoresis (SDS-PAGE) and then electrophoretically transferred onto Immuno-Blot® PVDF Membrane (Bio-Rad). The membrane was washed with PBS buffer + Tween-20 and then blocked with 5% BSA for 1 h and incubated overnight at 4°C with primary monoclonal antibodies against CD31 (ab119339, Abcam), osteopontin (ab8448, Abcam), and ACTB (Sigma-Aldrich A5441; 1:5,000). After washing five times in PBST, the membranes were incubated for 1 h at room temperature with peroxidase-conjugated secondary polyclonal goat antibodies anti-rabbit IgG (Jackson ImmunoResearch Laboratories 111–035–144; 1:50,000) and anti-mouse IgG (Jackson ImmunoResearch Laboratories 115-035-003; 1:50,000). After washing five times in PBST, conjugated antibodies were visualized using enhanced chemiluminescence in 0.1 M Tris–HCl, pH 8.5, 12.5 mM luminol, 2 mM coumaric acid, and 0.09% H_2O_2.

Expression levels were compared with HSP90 expression, since its expression remains stable both at the transcriptional level, as well as at the level of protein synthesis (Nikishin et al., 2018).

Statistics

Statistical analysis of fibril alignment and PCR results was performed, and graphs were created using the Prism 8.0 GraphPad software package. The significant difference of data was confirmed via two- and three-way analysis of variance (ANOVA), Tukey's test, and paired samples *t*-test for the *p*-value less than 0.05. At least five measurements of three independent samples (from three different donors) of each kind were collected; data are reported as the means ± SEM.

RESULTS

Verifying Adipose-Derived Stromal Cells as Those Showing Specific Characteristics of Multipotent Mesenchymal Stromal Cell

Upon expansion in culture for four passages, the ADSCs displayed surface markers specific for the multipotent mesenchymal stem cells including CD29 (98.86 ± 0.07%),

CD44 (99.95 ± 0.45%), CD105 (98.15 ± 0.91%), CD90 (91.94 ± 4.02%), CD73 (99.99 ± 0.01%) although not CD146 (0.02 ± 0,01%) (see also **Figure 1**). Double and triple multiparametric analysis showed 99.97 ± 3.57% of double CD73/CD90 cells, 99.97 ± 3.16% of CD90/CD105 cells, and 99.98 ± 0.82% CD73/CD105 cells. At the same time, the levels of markers for endothelial cells, endothelial progenitors, and blood cells (HLA-DR, CD11b, CD14, CD19, CD34, CD31, and CD45) were approaching zero (**Figure 1**) indicating that there were no such cells in the culture.

ADSCs Are Capable of Dual Spontaneous Osteo- and Angiogenic Differentiation in 3D but Not 2D Culture

Next, we set to explore the possibility to promote simultaneous differentiation of these cells toward osteogenic and angiogenic directions.

Morphologically, ADSCs presented a homogeneous cellular population highly adhesive to the plastic, actively proliferating with spindle-shaped morphology (**Figure 2A**) and expression of collagen type I and vimentin as detected by immunohistochemistry (**Figure 2B**). Altogether with the described phenotype (see **Figure 1**), these features strongly indicate that the obtained ADSCs satisfy the classical characteristics of MMSCs.

At normal 2D culture conditions, ADSCs did not show any specific markers of osteoblasts (osteopontin) or endothelial cells (Flk1) (**Figure 2C**; see also FACS data for CD146, CD31, and CD34 in **Figure 1**). A combination of classical osteoinductive medium (see section "MATERIALS AND METHODS" for details) with VEGF (angioinductive agent) caused elevation of osteopontin, but not Flk-1 (**Figure 2D**). Arrangements of ADSCs into compact 3D spheroids (**Figure 2E**) immediately caused spontaneous and strong upregulation osteogenic markers osteopontin and osteocalcin as well as endothelial markers Flk-1 and CD31 (**Figures 2G,H**) and maintained expression of collagen I and vimentin on day 7 (**Figure 2F**).

However, RT-PCR revealed upregulation of osteogenic marker Runx2, but no BMP2, Osterix, (**Figure 2I**, qRT-PCR: 2D, 1 day in 3D), as well as angiogenic marker CD31, but not CD34 and Flk1 (**Figure 2J**, qRT-PCR) on day 1 in 3D culture.

Thus, these data indicate that arranging ADSCs in spheroids abruptly promotes expression of both osteo- and angiogenic markers compared with 2D cultures, thereby indicating a capacity for spontaneous dual osteo- and angiogenic differentiation in 3D.

Adipose-Derived Stromal Cell Spheroids Subjected to Osteo- and Angio-Differentiation Maintain a Consistent Phenotype

We further set to assess if this duo differentiation capacity is regulated by standard differentiation protocols toward osteogenic lineage or angiogenic lineage. For this purpose, the spheroids were cultivated in the presence of either standard osteogenic differentiation medium (dexamethasone, b-glycerophosphate, and ascorbic acid; called below *Osteo* group), standard angiogenic inductor VEGF (*Angio* group), or a combination of both (*Double* group). We matured spheroids in culture for 21 days and followed specific marker expression dynamics over this period. A clear trend was observed toward neither osteogenic nor angiogenic differentiation with time (**Figure 3**).

The immunocytochemical analysis of these spheroids revealed a high level of expression of an early marker of osteogenesis–osteopontin (OstP) in all groups (**Figure 3A**). At the same time, expression of osteocalcin (OstC), a late osteogenesis marker, was not as abundant as of OstP but present in all groups (**Figure 3B**). The markers of early endothelial cell differentiation (Flk-1) and mature endothelial cells (CD31) were more abundant in Angio and Double groups (**Figures 3A,C**). Angiogenesis assay demonstrated that spheroids from all groups were able to grow tubule-like structures in PEGylated fibrin gel in the presence of VEGF within 7 days (**Figure 3D**), and the cells forming these tubule-like structures were positive for CD34 (**Figure 3E**). Western blot analysis revealed a similar amount of osteopontin (OstP) and CD34 in all groups as housekeeping protein HSP90 (**Figure 3F**).

These observations suggest that osteogenic differentiation within spheroids is rather spontaneous and independent on the presence of dexamethasone, b-glycerophosphate, and ascorbic acid. At the same time, angiogenic differentiation may be promoted in the presence of VEGF. To further elaborate on these observations, we have performed quantification of marker gene expression in spheroids using real-time PCR. Analysis of angiogenic markers (CD34, CD31, Flk1) did not reveal a time-dependent trend, elevation of angiogenic markers in either Angio or Double groups (**Figures 4A–C**). Similarly, expression of osteogenic markers (BMP2, Osterix, Runx2) did not demonstrate any time-dependent trend, but rather temporal fluctuations, e.g., elevation of osterix in Osteo group on day 7, but not on days 14 or 21 of culture (**Figures 4D–F**).

During this maturation process, the spheroids acquired a very smooth surface composed of a few layers of hexagonal-shaped cells tightly attached to each other (**Figures 5A–C**), whereas the central core had solitary scattered cells surrounded by abundant extracellular matrix including collagen type I (**Figure 5D**).

In all groups for all donors tested, ADSC spheroids maintained identical, external, and internal morphology with electron microscopy (**Figures 5A,B**) as well as histology with hematoxylin and eosin staining of their sections (**Figure 5C**). High expression levels of collagen type I (Col1) and vimentin (Vim) were noticed in all the groups (**Figure 5D**), and the levels of collagen type I (gene *COL1A1*) were further verified by RT-PCR (**Figure 5E**). There was mild but significant increase in the level of *COL1A1* on day 7 and day 21 of culture in both Osteo and Double groups compared with the untreated control (**Figure 5E**). We next explored alignment of collagen fibrils (CF) and vimentin filaments (VF), which revealed a general stability of random orientation indicated by a low coefficient (< 0.4) of anisotropy in all groups (**Figure 5F**). Angle's frequency analysis showed a similar distribution of fibril orientation with rare significant differences between groups (**Figure 5G**).

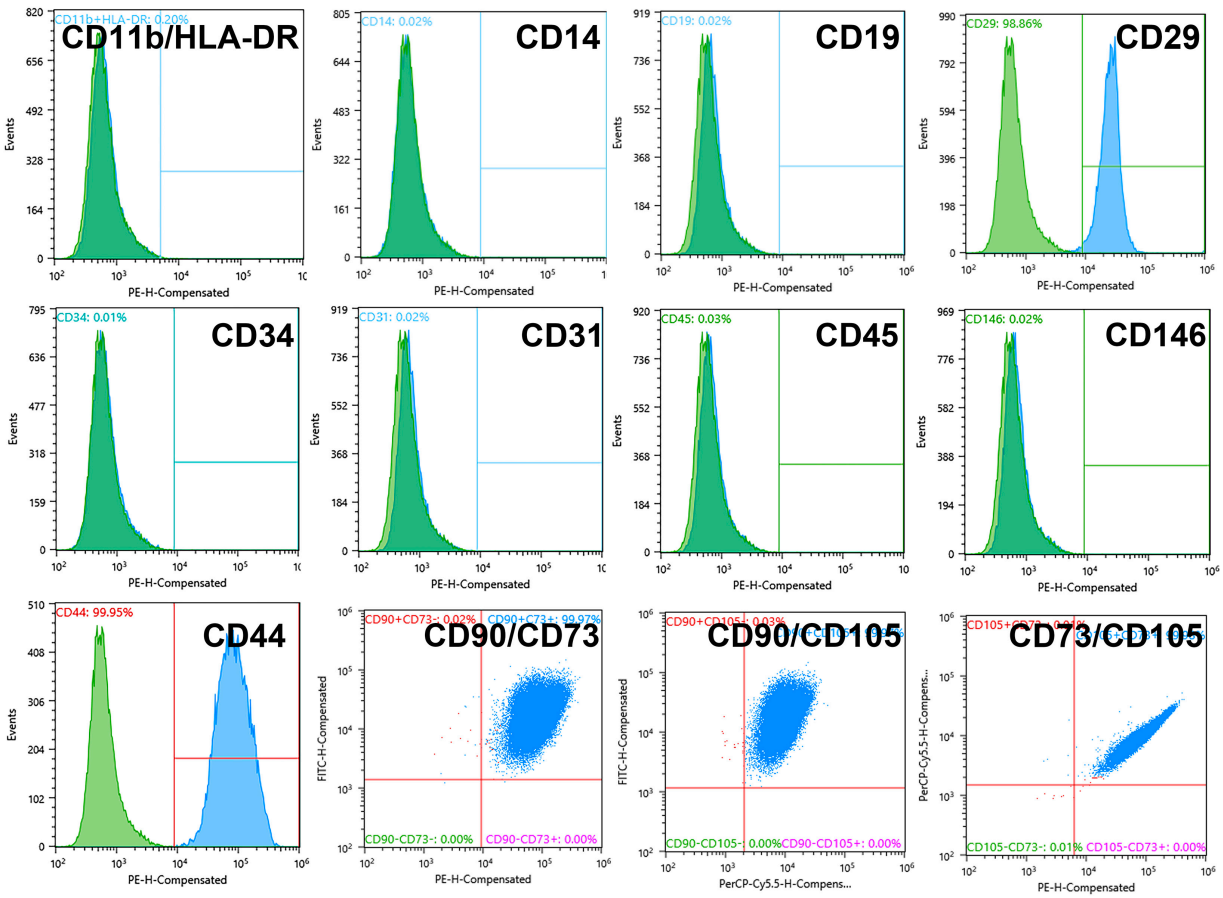


FIGURE 1 | Adipose-derived stromal cell (ADSC) 2D culture showed a standard multipotent mesenchymal stromal cell (MMSC) phenotype at Passage 4 (before 3D cultivation). Negative marker levels: 0.02% of CD11b/HLA-DR cells, 0.02% of CD14 cells 0.02% of CD19 cells, 0.03% of CD45 cells, 0.01% of CD34 cells, 0.02% of CD31 cells, 0.02% of CD146 cells; positive marker levels: 98.86% of CD29 cells, 99.95% of CD44 cells, 91.94% of CD90 cells, 98.15% of CD105 cells, 99.99% of CD73 cells. The blue-filled histograms indicate the positively stained cells, while the green-filled histograms indicate the isotype-matched antibody controls. *Flow cytometry.*

These data stay in line with immunohistochemical and PCR analysis and altogether suggest that despite double osteo- and angiogenic differentiation, this occurs in 3D cultures spontaneously and is not regulated by standard protocols developed for 2D cultures.

DISCUSSION

We showed that adipose-derived stromal cells (ADSCs) with standard characteristics of multipotent mesenchymal stromal cells (MMSC) form spheroids of similar morphology and microarchitecture in different culture conditions creating microenvironment favorable for spontaneous and induced multidirection cell differentiation.

Adipose derived stromal cells belong to the broad family of MMSCs characterized by spindle-shaped morphology, molecular heterogeneity, multilineage differentiation, and secretion of numerous immunomodulatory and cytokine factors (Pittenger et al., 2019). ADSCs obtained from different donors satisfied the standard criteria of MMSCs (Hass et al., 2011) and showed the absence of endothelial cells, endothelial progenitors, blood cells, or osteoblasts in 2D culture. Additionally, as classic MMSCs, ADSCs showed a positive response to osteoinductive stimuli resulting in osteopontin expression and did not respond to angiogenic factors in monolayer. Herein, cells from different donors expressed collagen type I and vimentin, which have been previously shown to be typical for MMSCs from different sources (Konno et al., 2013; Amable et al., 2014).

When cultured in 3D, the situation changes drastically and assembling ADSCs into spheroids results in rapid and spontaneous upregulation of markers specific for both osteogenic and angiogenic differentiation. We suspect that spontaneous dual differentiation may be facilitated by the novel characteristics of cells' microenvironment, which may, in turn, lead to changes in epigenetic landscape and/or increased stemness of MMSCs (Jauković et al., 2020). Indeed, several studies showed that cells in MMSC-derived spheroids, regardless of the source tissue, undergo spontaneous reprogramming including upregulation of pluripotent factors such as Sox2, NANOG, Oct4, and TERT

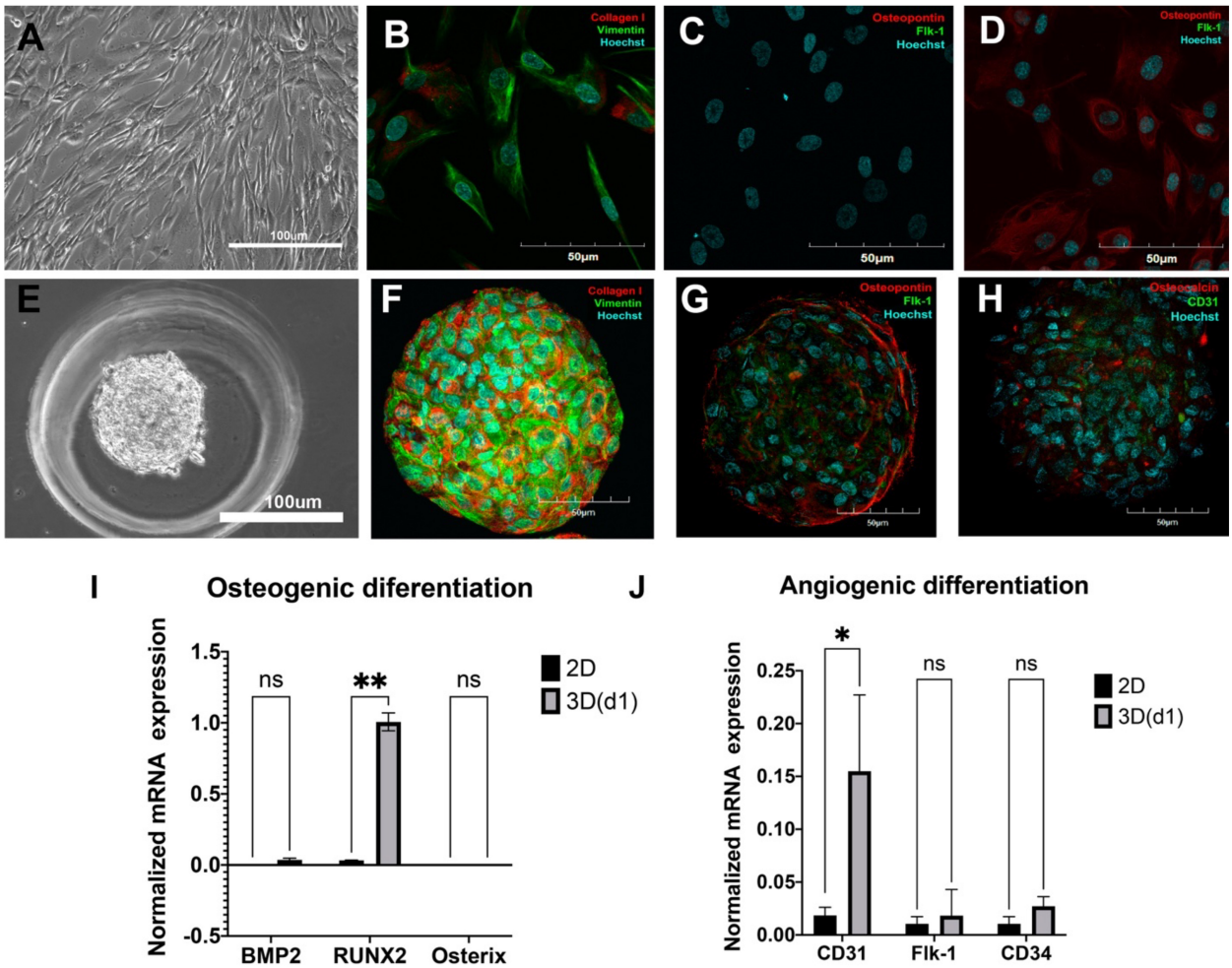


FIGURE 2 | Spontaneous osteogenic and angiogenic differentiation of adipose-derived stromal cells (ADSCs) in 3D but not in 2D culture. **(A)** Cells were elongated and spindle shaped with a wave pattern of spreading. *Light Phase-Contrast Microscopy, scale bar 100 μm*. **(B)** ADSCs expressed vimentin (green) and collagen type I (red) in 2D culture. **(C)** Monolayer ADSC culture did not express osteopontin (red)/Flk-1(green). **(D)** After being cultured in the presence of osteogenic and angiogenic inducers, ADSCs in monolayer cultures started expressing osteopontin (red) but not Flk-1 (green). **(B–D)** The nuclei were counterstained with Hoechst 33258 (blue). *Laser Scanning Confocal Microscopy, scale bars 50 μm*. **(E)** ADSC aggregated into compact spheroid on day 1. *Light Phase-Contrast Microscopy, scale bar 100 μm*. **(F)** ADSCs expressed vimentin (green) and collagen type I (red) in 3D culture. **(G)** ADSC spheroid expressed osteopontin (red)/Flk-1(green) on day 7. **(H)** ADSC spheroid expressed osteocalcin (red) and CD31(green) on day 7. **(F–H)** The nuclei were counterstained with Hoechst 33258 (blue). *Laser Scanning Confocal Microscopy, scale bars 50 μm*. **(I)** Mean (± SEM) osteogenic gene (*BMP2*, *Runx2*, *Osterix*) expression levels (normalized to housekeeping genes) for 2D and 3D (day 1) cultures. **(J)** Mean (± SEM) angiogenic gene (*CD31*, *Flk-1*, *CD34*) expression levels (normalized to housekeeping genes) for 2D and 3D (day 1) cultures. Statistical analysis was performed by paired samples t-test, $^{*}p < 0.05$, $^{**}p < 0.01$.

(Cheng et al., 2012; Guo et al., 2014; Zhou et al., 2017). It was also shown that the differentiation process starts earlier and involves more cells in spheroids than in monolayer culture, which has been shown for osteogenic (Guo et al., 2014) and adipogenic (Wang et al., 2009) differentiation. Whether this is attributed to changes in cell epigenetic/stemness remains to be elucidated.

ADSC-derived spheroids maintained a similar structure under various differentiation conditions with the layered surface and the ECM-enriched core. This is consistent with the previously described morphology for MMSC-derived spheroids (Bellotti et al., 2016; Cesarz and Tamama, 2016; Kosheleva et al., 2017). Undoubtedly, these data imply morphogenesis going on in a similar way for all groups, including the untreated group.

The consistency of morphological processes was also confirmed by similar high expression and orientation of collagen type I fibrils and vimentin filaments (**Figure 5**). Their low degree of alignment (coefficient of anisotropy < 0.4) and distribution characterized non-mature tissue with the absence of mineralization in ADSC-derived spheroids and their high elastic properties (Georgiadis et al., 2016), which accorded primarily transverse orientation that is specific for Type I osteon (Bromage et al., 2003).

These results are matched with previous findings that MMSC-derived spheroids are characterized by increased ECM synthesis and changes in cytoskeleton organization and cell polarity. These novel mechanical properties provide a dynamic spatial context

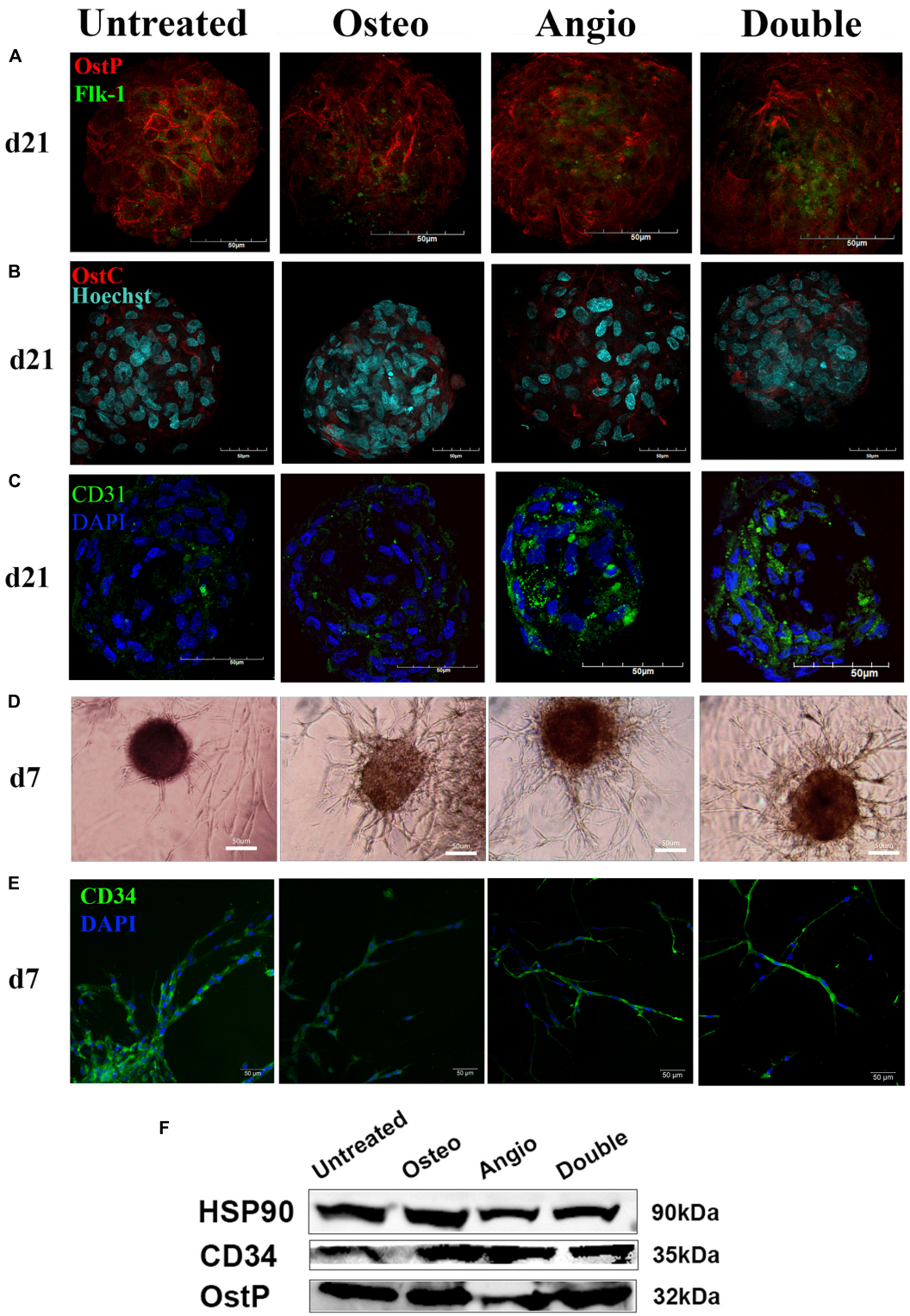


FIGURE 3 | ADSC-derived spheroids showed similar expression of osteogenic (osteopontin, osteocalcin) and endothelial markers (Flk-1, CD31, CD34) with a similar for all groups capacity of angiogenesis in PEGylated fibrin gel. **(A)** The similar distribution of OstP (red) and Flk-1 (green) in spheroids for all groups on day 21. **(B)** The similar distribution of OstC (red) in spheroids for all groups on day 21. **(C)** Spheroids showed expression of PECAM1 (CD31) in all groups on day 21. **(D)** All groups showed an ability to form tubule-like structures in fibrin gels on day 7. **(E)** CD34-positive cells migrated from spheroids through fibrin gel and formed tubules on day 7. *Laser Scanning Confocal Microscopy, scale bar 50 μm. Light Phase-Contrast Microscopy, scale bar 50 μm.* **(F)** Similar expression of osteopontin (OstP) and CD34 compared with the housekeeping protein HSP90 in all groups on day 21 (blots were cropped and presented).

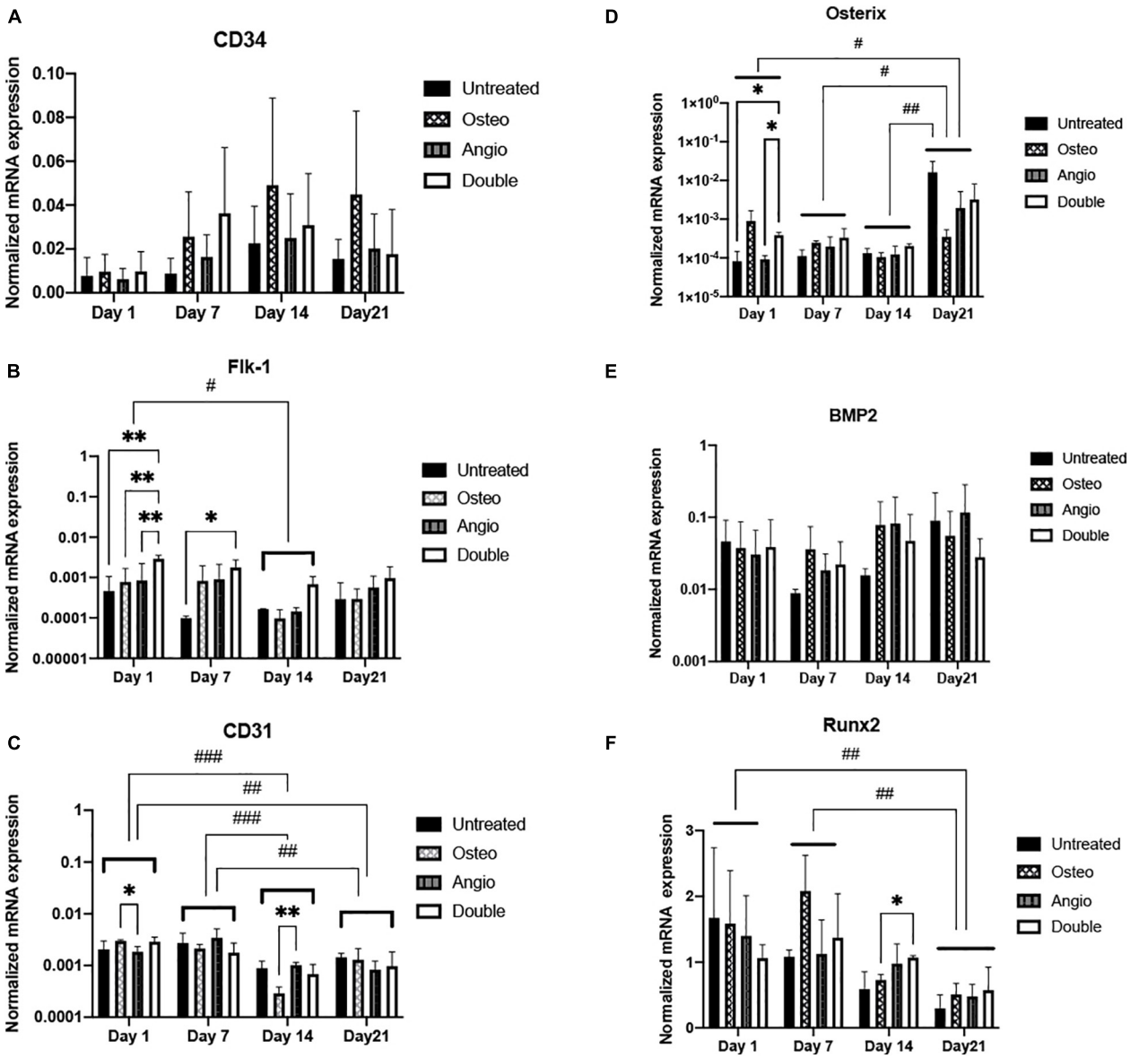


FIGURE 4 | All groups of ADSC-derived spheroids showed different dynamics of gene expression in angiogenic and osteogenic differentiation. **(A)** Expression of *CD34* gene (early angiogenic differentiation marker) showed non-significant increase in all groups toward day 21. **(B)** *Flk-1* (VEGF receptor 2 gene) expression decreased significantly in all groups on day 14 compared with that on day 1. **(C)** *CD31* (mature endothelial cell marker) gene expression was significantly downregulated on days 14 and 21 compared with days 1 and 7. **(D)** *Osterix* marker showed a significantly increasing gene expression dynamics toward day 21. **(E)** All groups maintained consistent *BMP2* gene expression. **(F)** *Runx2* gene expression drastically regressed during 3D cultivation. Histograms represent mean (± SEM) gene expression levels (normalized to housekeeping genes). Two-way ANOVA describes significant differences between groups of the same time point (*$p < 0.05$, **$p < 0.01$). Three-way ANOVA describes significant differences between time points (#$p < 0.05$, ##$p < 0.01$, ###$p < 0.001$).

of cell–matrix and cell–cell interactions and lead to a significant rearrangement of physical forces acting on each cell within the 3D spheroid. Enhanced ECM secretion also provides a favorable environment for local growth factor and cytokine enrichment, supporting autocrine signaling (Bartosh et al., 2010).

Based on the described patterns of gene expression, the untreated group revealed spontaneous osteogenic and endothelial differentiation. However, most osteogenic and endothelial genes' expression showed a lower trend in the untreated group compared with the groups with induction, which indicates the influence of VEGF and osteoinductive factors. On the other hand, patterns of gene expression dynamics during 3D cultivation were consistent among all groups. Immunohistochemical analysis of osteopontin, osteocalcin, CD31, and Flk-1 expression in all groups confirmed spontaneous osteogenesis and angiogenesis in ADSC spheroids (**Figure 3**). In general, the levels of expression of osteogenic markers significantly exceeded the levels of angiogenic marker expression

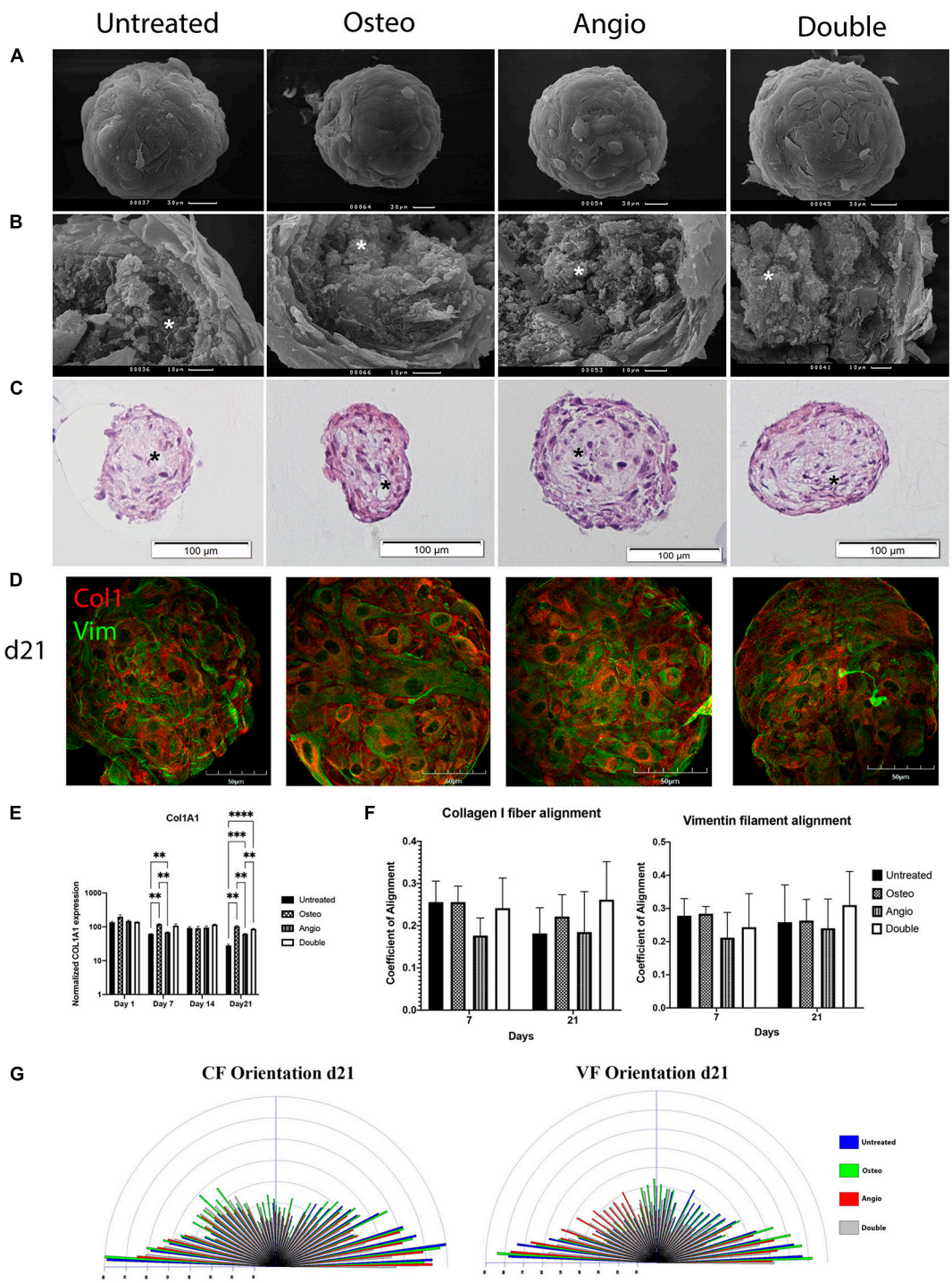


FIGURE 5 | Untreated and treated ADSC-derived spheroids developed identical morphology by day 21 in 3D culture. **(A)** ADSCs aggregated in compact spheroids with a smooth surface formed by hexagonal-shaped cells; scale bar 30 μm. **(B)** Cracked spheroids revealed the layered structure of the surface and the central core composed of fibrils and bundles of extracellular matrix labeled by white asterisks; scale bar 10 μm. *Scanning electron microscopy*. **(C)** Histological H&E staining confirms that the surface of spheroids was formed by a few layers of cells and shows that the core had cavities labeled by black asterisks; scale bar 100 μm. *Bright-field microscopy*. **(D)** The distribution of Col1 (red) and Vim (green) in spheroids on day 21. *Laser Scanning Confocal Microscopy, scale bar 50 μm*. **(E)** Mean (± SEM) *COL1A1* gene expression levels (normalized to housekeeping genes), two-way ANOVA, $^{**}p < 0.01$, $^{***}p < 0.001$, $^{****}p < 0.0001$. **(F)** Col1 fibrils and Vim filament alignment coefficients. **(G)** The distribution and frequency of angles of collagen type I fibrils and vimentin filament orientation.

that indicates predominance of osteogenic differentiation, which is consistent with previously observed MMSC's potency to osteogenesis in spheroid (Imamura et al., 2020). Angiogenesis by $CD34^+$ cells observed in all groups in PEGylated fibrin gel is confirming this observation and stays in line with the earlier study showing appearance of $CD34^+$ cells in ADSC-derived spheroids (Bellagamba et al., 2018).

At the same time, we could not facilitate consistent either osteo- or angiogenic differentiation utilizing standard differentiation conditions. This can be attributed to the need for distinct differentiation protocols for 3D cultures. Alternatively, the complex interactions between various cell sub-types or cell–matrix interactions counterbalance the induced differentiation processes. We believe that more specific and more direct approaches are needed to simultaneously modulate multidirectional differentiation. Indeed, it has been shown that VEGF affect not only angiogenesis but may also influence osteogenesis (Lattanzi and Bernardini, 2012). Similarly, glucocorticoids used for standard osteogenic differentiation are also known to influence angiogenesis (Chen et al., 2018).

CONCLUSION

In this study, we show that 3D culture promotes spontaneous multidirectional differentiation of ADSCs. Specifically, adipose tissue-derived MMSC-like cells acquire a capacity for spontaneous osteogenesis and partial endothelial-like differentiation when cultured in the form of spheroids. At the same time, standard osteogenic and angiogenic exogenic factors were not capable of influencing cell differentiation within spheroids in a persistent and time-dependent manner. We also show that ADSC-derived spheroids maintain stable morphology in different cultural conditions.

Our results open new approaches for *in vitro* generation of bioequivalents of vascularized bone tissue fragments and allow rapid and high-throughput analysis of interactions between osteogenic and angiogenic differentiation lineages. This opens a wide range of possibilities in both fundamental and applied research in the area of bone tissue development and regeneration.

DATA AVAILABILITY STATEMENT

The original contributions presented in the study are included in the article/supplementary material, further inquiries can be directed to the corresponding author/s.

ETHICS STATEMENT

Adipose tissue fragments were collected from the patients undergoing liposuction after receiving their written informed consent. All the procedures were performed under local anesthesia and aseptic conditions and were approved by the Local Ethical Committee of Sechenov University (#07–17 from 13.09.2017, Moscow, Russia) while performed in accordance with the Helsinki Declaration.

AUTHOR CONTRIBUTIONS

AG, IZ, and IS contributed to the conception and the design of the study. DR and IZ wrote the first draft of the manuscript. AG, DR, and IZ prepared the submitted version of the study. DR and IZ performed 2D and 3D cell cultivation and collected samples for further analysis. AG and PB accomplished the flow cytometry and immunocytochemical staining. DR and DN performed the PCR and WB of all samples. IZ and AS performed the angiogenesis assay. IZ and NK provided the SEM, confocal microscopy, and statistical analysis. TK, PT, and IS supervised the study and edited the manuscript. All authors contributed to the manuscript revision, read and approved the submitted version.

FUNDING

This work was supported by the Russian Federation President grant MK-3776.2019.4 (all parts concerning spheroids' characteristics) and The Special Federal Programme of the Russian Federation Government, Research Project No. 0520-2019-0026 (2D and 3D cell culturing). The part of the study with flow cytometry, angiogenesis assay, and confocal microscopy of spheroids within fibrin gels was funded by RFBR, Project No. 20-02-00712.

ACKNOWLEDGMENTS

Part of the work using confocal microscopy of spheroids was performed at the Faculty of Biology in Lomonosov Moscow State University (Equipment Complex for Tissue-engineering Technologies, Visualization and Microsurgery; ID: 9351669). Part of the work using the methods of electron microscopy was performed using the equipment of the Electron Microscopy Laboratory of the Lomonosov Moscow State University with the financial support of the Ministry of Education and Science of the Russian Federation. We are grateful to Adam Jorgensen for his assistance regarding the use of CurveAlign software, Dr. N. E. Leontiev for the graphical visualization of Angle's frequency distribution, and Dr. N. Mahajan for reviewing the description of real-time PCR results. -

REFERENCES

Amable, P. R., Teixeira, M. V. T., Carias, R. B. V., Granjeiro, J. M., and Borojevic, R. (2014). Protein synthesis and secretion in human mesenchymal cells derived from bone marrow, adipose tissue and Wharton's jelly. *Stem Cell Res. Ther.* 5:53. doi: 10.1186/scrt442

Anada, T., Pan, C.-C., Stahl, A. M., Mori, S., Fukuda, J., Suzuki, O., et al. (2019). Vascularized bone-mimetic hydrogel constructs by 3D bioprinting to

promote osteogenesis and angiogenesis. *Int. J. Mol. Sci.* 20:1096. doi: 10.3390/ijms20051096

Annabi, N., Tamayol, A., Uquillas, J. A., Akbari, M., Bertassoni, L. E., Cha, C., et al. (2014). 25th anniversary article: rational design and applications of hydrogels in regenerative medicine. *Adv. Mater.* 26, 85–124. doi: 10.1002/adma.201303233

Bartosh, T. J., Ylöstalo, J. H., Mohammadipoor, A., Bazhanov, N., Coble, K., Claypool, K., et al. (2010). Aggregation of human mesenchymal stromal cells (MSCs) into 3D spheroids enhances their antiinflammatory properties. *Proc. Natl. Acad. Sci. U. S. A.* 107, 13724–13729. doi: 10.1073/pnas.1008117107

Bellagamba, B. C., Grudzinski, P. B., Ely, P. B., Nader, P. D. J. H., Nardi, N. B., and Da Silva Meirelles, L. (2018). Induction of expression of CD271 and CD34 in mesenchymal stromal cells cultured as spheroids. *Stem Cells Int.* 2018:7357213. doi: 10.1155/2018/7357213

Bellotti, C., Duchi, S., Bevilacqua, A., Lucarelli, E., and Piccinini, F. (2016). Long term morphological characterization of mesenchymal stromal cells 3D spheroids built with a rapid method based on entry-level equipment. *Cytotechnology* 68, 2479–2490. doi: 10.1007/s10616-016-9969-y

Berens, P. (2009). CircStat: a MATLAB toolbox for circular statistics. *J. Stat. Softw.* 31, 1–21.

Bromage, T. G., Goldman, H. M., McFarlin, S. C., Warshaw, J., Boyde, A., and Riggs, C. M. (2003). Circularly polarized light standards for investigations of collagen fiber orientation in bone. *Anat. Rec. B New Anat.* 274, 157–168. doi: 10.1002/ar.b.10031

Cerino, G., Gaudiello, E., Muraro, M. G., Eckstein, F., Martin, I., Scherberich, A., et al. (2017). Engineering of an angiogenic niche by perfusion culture of adipose-derived stromal vascular fraction cells. *Sci. Rep.* 7:14252.

Cesarz, Z., and Tamama, K. (2016). Spheroid culture of mesenchymal stem cells. *Stem Cells Int.* 2016:9176357. doi: 10.1155/2016/9176357

Chen, C.-W., Montelatici, E., Crisan, M., Corselli, M., Huard, J., Lazzari, L., et al. (2009). Perivascular multi-lineage progenitor cells in human organs: regenerative units, cytokine sources or both? *Cytokine Growth Factor Rev.* 20, 429–434. doi: 10.1016/j.cytogfr.2009.10.014

Chen, Y., Chen, S., Kawazoe, N., and Chen, G. (2018). Promoted angiogenesis and osteogenesis by dexamethasone-loaded calcium phosphate nanoparticles/collagen composite scaffolds with microgroove networks. *Sci. Rep.* 8:14143. doi: 10.1038/s41598-018-32495-y

Cheng, N. C., Wang, S., and Young, T. H. (2012). The influence of spheroid formation of human adipose-derived stem cells on chitosan films on stemness and differentiation capabilities. *Biomaterials* 33, 1748–1758. doi: 10.1016/j.biomaterials.2011.11.049

Corre, P., Merceron, C., Vignes, C., Sourice, S., Masson, M., Durand, N., et al. (2013). Determining a clinically relevant strategy for bone tissue engineering: an "all-in-one" study in nude mice. *PLoS One* 8:e81599. doi: 10.1371/journal.pone.0081599

Dominici, M., Le Blanc, K., Mueller, I., Slaper-Cortenbach, I., Marini, F. C., Krause, D. S., et al. (2006). Minimal criteria for defining multipotent mesenchymal stromal cells. The international society for cellular therapy position statement. *Cytotherapy* 8, 315–317. doi: 10.1080/14653240600855905

Duttenhoefer, F., Lara de Freitas, R., Meury, T., Loibl, M., Benneker, L. M., Hermann, M., et al. (2013). 3D scaffolds co-seeded with human endothelial progenitor and mesenchymal stem cells: evidence of prevascularisation within 7 days. *Eur. Cell. Mater.* 26, 64–65.

Georgiadis, M., Müller, R., and Schneider, P. (2016). Techniques to assess bone ultrastructure organization: orientation and arrangement of mineralized collagen fibrils. *J. R. Soc. Interface* 13:20160088. doi: 10.1098/rsif.2016.0088

Gorkun, A. A., Shpichka, A. I., Zurina, I. M., Koroleva, A. V., Kosheleva, N. V., Nikishin, D. A., et al. (2018). Angiogenic potential of spheroids from umbilical cord and adipose-derived multipotent mesenchymal stromal cells within fibrin gel. *Biomed. Mater.* 13:044108. doi: 10.1088/1748-605X/aac22d

Grosso, A., Burger, M. G., Lunger, A., Schaefer, D. J., Banfi, A., and Di Maggio, N. (2017). It takes two to tango: coupling of angiogenesis and osteogenesis for bone regeneration. *Front. Bioeng. Biotechnol.* 5:68. doi: 10.3389/fbioe.2017.00068

Guo, L., Zhou, Y., Wang, S., and Wu, Y. (2014). Epigenetic changes of mesenchymal stem cells in three-dimensional (3D) spheroids. *J. Cell. Mol. Med.* 18, 2009–2019. doi: 10.1111/jcmm.12336

Gurumurthy, B., Bierdeman, P. C., and Janorkar, A. V. (2017). Spheroid model for functional osteogenic evaluation of human adipose derived stem cells. *J. Biomed. Mater. Res. A* 105, 1230–1236. doi: 10.1002/jbm.a.35974

Haasters, F., Prall, W. C., Anz, D., Bourquin, C., Pautke, C., Endres, S., et al. (2009). Morphological and immunocytochemical characteristics indicate the yield of early progenitors and represent a quality control for human mesenchymal stem cell culturing. *J. Anat.* 214, 759–767. doi: 10.1111/j.1469-7580.2009.01065.x

Hass, R., Kasper, C., Böhm, S., and Jacobs, R. (2011). Different populations and sources of human mesenchymal stem cells (MSC): a comparison of adult and neonatal tissue-derived MSC. *Cell Commun. Signal.* 9:12.

Holnthoner, W., Hohenegger, K., Husa, A., Muehleder, S., Meinl, A., Peterbauer-Scherb, A., et al. (2015). Adipose-derived stem cells induce vascular tube formation of outgrowth endothelial cells in a fibrin matrix. *J. Tissue Eng. Regen. Med.* 9, 127–136. doi: 10.1002/term.1620

Imamura, A., Kajiya, H., Fujisaki, S., Maeshiba, M., Yanagi, T., Kojima, H., et al. (2020). Three-dimensional spheroids of mesenchymal stem/stromal cells promote osteogenesis by activating stemness and Wnt/β-catenin. *Biochem. Biophys. Res. Commun.* 523, 458–464. doi: 10.1016/j.bbrc.2019.12.066

Inglis, S., Christensen, D., Wilson, D. I., Kanczler, J. M., and Oreffo, R. O. C. (2016). Human endothelial and foetal femur-derived stem cell co-cultures modulate osteogenesis and angiogenesis. *Stem Cell Res. Ther.* 7:13.

Jauković, A., Abadjieva, D., Trivanović, D., Stoyanova, E., Kostadinova, M., Pashova, S., et al. (2020). Specificity of 3D MSC spheroids microenvironment: impact on MSC behavior and properties. *Stem Cell Rev. Rep.* 16, 853–875. doi: 10.1007/s12015-020-10006-9

Kalinina, N., Kharlampieva, D., Loguinova, M., Butenko, I., Pobeguts, O., Efimenko, A., et al. (2015). Characterization of secretomes provides evidence for adipose-derived mesenchymal stromal cells subtypes. *Stem Cell Res. Ther.* 6:221.

Konno, M., Hamabe, A., Hasegawa, S., Ogawa, H., Fukusumi, T., Nishikawa, S., et al. (2013). Adipose-derived mesenchymal stem cells and regenerative medicine. *Dev. Growth Differ.* 55, 309–318.

Kosheleva, N. V., Ilina, I. V., Kozhina, K. V., Zurina, I. M., Roskova, A. E., Gorkun, A. A., et al. (2017). Cellular model based on laser microsurgery of cell spheroids to study the repair process. *Russ. J. Dev. Biol.* 48, 56–64. doi: 10.1134/S1062360417010076

Langenbach, F., Naujoks, C., Smeets, R., Berr, K., Depprich, R., Kübler, N., et al. (2013). Scaffold-free microtissues: differences from monolayer cultures and their potential in bone tissue engineering. *Clin. Oral Investig.* 17, 9–17. doi: 10.1007/s00784-012-0763-8

Laschke, M. W., and Menger, M. D. (2012). Vascularization in tissue engineering: angiogenesis versus inosculation. *Eur. Surg. Res.* 48, 85–92. doi: 10.1159/000336876

Lattanzi, W., and Bernardini, C. (2012). "Genes and molecular pathways of the osteogenic process," in *Osteogenesis*, ed. Y. Lin (Rijeka: InTech), 21–55.

Lee, J. H., Han, Y.-S., and Lee, S. H. (2016). Long-duration three-dimensional spheroid culture promotes angiogenic activities of adipose-derived mesenchymal stem cells. *Biomol. Ther. (Seoul)* 24:260. doi: 10.4062/biomolther.2015.146

Liu, Y., Keikhosravi, A., Mehta, G. S., Drifka, C. R., and Eliceiri, K. W. (2017). Methods for quantifying fibrillar collagen alignment. *Methods Mol. Biol.* 1627, 429–451. doi: 10.1007/978-1-4939-7113-8_28

Lovett, M., Lee, K., Edwards, A., and Kaplan, D. L. (2009). Vascularization strategies for tissue engineering. *Tissue Eng. Part B Rev.* 15, 353–370.

Makarevich, P. I., Boldyreva, M. A., Gluhanyuk, E. V., Efimenko, A. Y., Dergilev, K. V., Shevchenko, E. K., et al. (2015). Enhanced angiogenesis in ischemic skeletal muscle after transplantation of cell sheets from baculovirus-transduced adipose-derived stromal cells expressing VEGF165. *Stem Cell Res. Ther.* 6:204.

Makarevich, P. I., Dergilev, K. V., Tsokolaeva, Z. I., Boldyreva, M. A., Shevchenko, E. K., Gluhanyuk, E. V., et al. (2018). Angiogenic and pleiotropic effects of VEGF165 and HGF combined gene therapy in a rat model of myocardial infarction. *PLoS One* 13:e0197566. doi: 10.1371/journal.pone.0197566

Marra, K. G., and Rubin, J. P. (2012). The potential of adipose-derived stem cells in craniofacial repair and regeneration. *Birth Defects Res. C Embryo Today* 96, 95–97.

Muller, S., Ader, I., Creff, J., Leménager, H., Achard, P., Casteilla, L., et al. (2019). Human adipose stromal-vascular fraction self-organizes to form vascularized adipose tissue in 3D cultures. *Sci. Rep.* 9:7250.

Muschler, G. F., Nakamoto, C., and Griffith, L. G. (2004). Engineering principles of clinical cell-based tissue engineering. *J. Bone Joint Surg. Am.* 86, 1541–1558.

Nikishin, D. A., Filatov, M. A., Kiseleva, M. V., Bagaeva, T. S., Konduktorova, V. V., Khramova, Y. V., et al. (2018). Selection of stable expressed reference genes in native and vitrified/thawed human ovarian tissue for analysis by qRT-PCR and Western blot. *J. Assist. Reprod. Genet.* 35, 1851–1860. doi: 10.1007/s10815-018-1263-9

Pampaloni, F., Reynaud, E. G., and Stelzer, E. H. K. (2007). The third dimension bridges the gap between cell culture and live tissue. *Nat. Rev. Mol. Cell Biol.* 8, 839–845. doi: 10.1038/nrm2236

Park, I. S., Chung, P. S., and Ahn, J. C. (2014). Enhanced angiogenic effect of adipose-derived stromal cell spheroid with low-level light therapy in hind limb ischemia mice. *Biomaterials* 35, 9280–9289. doi: 10.1016/j.biomaterials.2014.07.061

Pittenger, M. F., Discher, D. E., Péault, B. M., Phinney, D. G., Hare, J. M., and Caplan, A. I. (2019). Mesenchymal stem cell perspective: cell biology to clinical progress. *NPJ Regen. Med.* 4:22. doi: 10.1038/s41536-019-0083-6

Repin, V. S., Saburina, I. N., Kosheleva, N. V., Gorkun, A. A., Zurina, I. M., and Kubatiev, A. A. (2014). 3D-technology of the formation and maintenance of single dormant microspheres from 2000 human somatic cells and their reactivation in vitro. *Bull. Exp. Biol. Med.* 158, 137–144. doi: 10.1007/s10517-014-2709-4

Rohringer, S., Hofbauer, P., Schneider, K. H., Husa, A.-M., Feichtinger, G., Peterbauer-Scherb, A., et al. (2014). Mechanisms of vasculogenesis in 3D fibrin matrices mediated by the interaction of adipose-derived stem cells and endothelial cells. *Angiogenesis* 17, 921–933. doi: 10.1007/s10456-014-9439-0

Roux, B. M., Cheng, M., and Brey, E. M. (2015). Engineering clinically relevant volumes of vascularized bone. *J. Cell. Mol. Med.* 19, 903–914. doi: 10.1111/jcmm.12569

Saburina, I. N., Gorkun, A. A., Fidarov, A. F., Kolokol'tsova, T. D., Zurina, I. M., Kosheleva, N. V., et al. (2018). Induction of vasculo- and osteogenesis in spheroids formed by adipose-derived stromal cells. *Bull. Exp. Biol. Med.* 166, 163–169. doi: 10.1007/s10517-018-4306-4

Sakaguchi, K., Shimizu, T., Horaguchi, S., Sekine, H., Yamato, M., Umezu, M., et al. (2013). In vitro engineering of vascularized tissue surrogates. *Sci. Rep.* 3:1316.

Schipani, E., Maes, C., Carmeliet, G., and Semenza, G. L. (2009). Regulation of osteogenesis-angiogenesis coupling by HIFs and VEGF. *J. Bone Miner. Res.* 24, 1347–1353. doi: 10.1359/jbmr.090602

Shpichka, A. I., Konarev, P. V., Efremov, Y. M., Kryukova, A. E., Aksenova, N. A., Kotova, S. L., et al. (2020). Digging deeper: structural background of PEGylated fibrin gels in cell migration and lumenogenesis. *RSC Adv.* 10, 4190–4200. doi: 10.1039/c9ra08169k

Song, T.-Q., Ge, B.-J., Chen, H.-L., Yang, X.-W., and Yuan, F. (2016). Osteogenesis of bone marrow mesenchymal stem cells on nano-hydroxyapatite/bacterial cellulose coposite scaffolds in rats. *Int. J. Clin. Exp. Pathol.* 9, 9775–9785.

Strassburg, S., Nienhueser, H., Björn Stark, G., Finkenzeller, G., and Torio-Padron, N. (2016). Co-culture of adipose-derived stem cells and endothelial cells in fibrin induces angiogenesis and vasculogenesis in a chorioallantoic membrane model. *J. Tissue Eng. Regen. Med.* 10, 496–506. doi: 10.1002/term.1769

Thery, A., Bléry, P., Malard, O., Pilet, P., Sourice, S., Corre, P., et al. (2015). Role of the stromal vascular fraction from adipose tissue in association with a phosphocalcic scaffold in bone regeneration in an irradiated area. *J. Craniomaxillofac. Surg.* 43, 1169–1176. doi: 10.1016/j.jcms.2015.05.014

Wang, W., Itaka, K., Ohba, S., Nishiyama, N., Chung, U., Yamasaki, Y., et al. (2009). 3D spheroid culture system on micropatterned substrates for improved differentiation efficiency of multipotent mesenchymal stem cells. *Biomaterials* 30, 2705–2715. doi: 10.1016/j.biomaterials.2009.01.030

Yamaguchi, Y., Ohno, J., Sato, A., Kido, H., and Fukushima, T. (2014). Mesenchymal stem cell spheroids exhibit enhanced in-vitro and in-vivo osteoregenerative potential. *BMC Biotechnol.* 14:105. doi: 10.1186/s12896-014-0105-9

Zhang, Y., Yu, M., and Tian, W. (2016). Physiological and pathological impact of exosomes of adipose tissue. *Cell Prolif.* 49, 3–13. doi: 10.1111/cpr.12233

Zhou, Y., Chen, H., Li, H., and Wu, Y. (2017). 3D culture increases pluripotent gene expression in mesenchymal stem cells through relaxation of cytoskeleton tension. *J. Cell. Mol. Med.* 21, 1073–1084. doi: 10.1111/jcmm.12946

Zurina, I. M., Gorkun, A. A., Dzhussoeva, E. V., Kolokoltsova, T. D., Markov, D. D., Kosheleva, N. V., et al. (2020). Human melanocyte-derived spheroids: a precise test system for drug screening and a cellular module for tissue engineering. *Front. Bioeng. Biotechnol.* 8:540. doi: 10.3389/fbioe.2020.00540

Zurina, I. M., Shpichka, A. I., Saburina, I. N., Kosheleva, N. V., Gorkun, A. A., Grebenik, E. A., et al. (2018). 2D/3D buccal epithelial cell self-assembling as a tool for cell phenotype maintenance and fabrication of multilayered epithelial linings in vitro. *Biomed. Mater.* 13:054104. doi: 10.1088/1748-605X/aace1c doi: 10.1088/1748-605x/aace1c

Conflict of Interest: The authors declare that the research was conducted in the absence of any commercial or financial relationships that could be construed as a potential conflict of interest.

Copyright © 2021 Gorkun, Revokatova, Zurina, Nikishin, Bikmulina, Timashev, Shpichka, Kosheleva, Kolokoltsova and Saburina. This is an open-access article distributed under the terms of the Creative Commons Attribution License (CC BY). The use, distribution or reproduction in other forums is permitted, provided the original author(s) and the copyright owner(s) are credited and that the original publication in this journal is cited, in accordance with accepted academic practice. No use, distribution or reproduction is permitted which does not comply with these terms.

frontiers in Cell and Developmental Biology

ORIGINAL RESEARCH
published: 28 June 2021
doi: 10.3389/fcell.2021.685494

Novel Functional Genes Involved in Transdifferentiation of Canine ADMSCs Into Insulin-Producing Cells, as Determined by Absolute Quantitative Transcriptome Sequencing Analysis

Pengxiu Dai, Jiakai Li, Yijing Chen, Luwen Zhang, Xinke Zhang, Jinglu Wang, Guixiang Qi and Yihua Zhang*

Shaanxi Branch of National Stem Cell Engineering and Technology Centre, College of Veterinary Medicine, Northwest A&F University, Yangling, China

OPEN ACCESS

Edited by:
Pavel Makarevich, Lomonosov Moscow State University, Russia

Reviewed by:
Ivan B. Filippenkov, Institute of Molecular Genetics (RAS), Russia
Jangwook P. Jung, Louisiana State University, United States

***Correspondence:**
Yihua Zhang
zyh19620207@163.com

Specialty section:
This article was submitted to Stem Cell Research, a section of the journal Frontiers in Cell and Developmental Biology

Received: *25 March 2021*
Accepted: *31 May 2021*
Published: *28 June 2021*

Citation:
Dai P, Li J, Chen Y, Zhang L, Zhang X, Wang J, Qi G and Zhang Y (2021) Novel Functional Genes Involved in Transdifferentiation of Canine ADMSCs Into Insulin-Producing Cells, as Determined by Absolute Quantitative Transcriptome Sequencing Analysis. Front. Cell Dev. Biol. 9:685494. doi: 10.3389/fcell.2021.685494

The transdifferentiation of adipose-derived mesenchymal stem cells (ADMSCs) into insulin-producing cells (IPCs) is a potential resource for the treatment of diabetes. However, the changes of genes and metabolic pathways on the transdifferentiation of ADMSCs into IPCs are largely unknown. In this study, the transdifferentiation of canine ADMSCs into IPCs was completed using five types of procedures. Absolute Quantitative Transcriptome Sequencing Analysis was performed at different stages of the optimal procedure. A total of 60,151 transcripts were obtained. Differentially expressed genes (DEGs) were divided into five groups: IPC1 vs. ADSC (1169 upregulated genes and 1377 downregulated genes), IPC2 vs. IPC1 (1323 upregulated genes and 803 downregulated genes), IPC3 vs. IPC2 (722 upregulated genes and 680 downregulated genes), IPC4 vs. IPC3 (539 upregulated genes and 1561 downregulated genes), and Beta_cell vs. IPC4 (2816 upregulated genes and 4571 downregulated genes). The gene ontology (GO) and Kyoto Encyclopedia of Genes and Genomes (KEGG) enrichment analysis of DEGs revealed that many genes and signaling pathways that are essential for transdifferentiation. *Hnf1B*, *Dll1*, *Pbx1*, *Rfx3*, and *Foxa1* were screened out, and the functions of five genes were verified further by overexpression and silence. *Foxa1*, *Pbx1*, and *Rfx3* exhibited significant effects, can be used as specific key regulatory factors in the transdifferentiation of ADMSCs into IPCs. This study provides a foundation for future work to understand the mechanisms of the transdifferentiation of ADMSCs into IPCs and acquire IPCs with high maturity.

Keywords: adipose-derived mesenchymal stem cells, transdifferentiation, insulin producing cells, novel genes, Absolute Quantitative Transcriptome Sequencing Analysis

INTRODUCTION

Diabetes encompasses a group of lifelong metabolic diseases, and common drug therapies are not able to cure it. Long-term use of drugs and the continuous injection of insulin greatly reduce the patient's quality of life, and strengthening of treatment increases risk of hypoglycemic coma and can even be life-threatening (Cattin, 2016; Harreiter and Roden, 2019; Petersmann et al., 2019). Thus, a safe and effective treatment for diabetes and its complications is urgently needed. At first, islet transplantation was considered as an excellent approach for curing diabetes, but its clinical application was greatly limited by lack of islet donor sources, low islet survival rate *in vitro* and immune rejection after transplantation (Bruni et al., 2014; Gamble et al., 2018; Rickels and Robertson, 2019). Therefore, the search for insulin-producing cells (IPCs) from other sources to replace islet transplantation has become an active area of research.

Adipose-derived mesenchymal stem cells (ADMSCs) are abundant in sources, are easily isolated and cultivated, exhibit pluripotent differentiation potential and show low immunogenicity after transplantation, serving as ideal seed cells for the treatment of diabetes and its complications (Kim et al., 2010; Zhang et al., 2016; Takemura et al., 2019; Wada and Ikemoto, 2019; Tokuda et al., 2020). Numerous small molecule compounds, growth factors, activators, and inhibitors can transdifferentiate ADMSCs into IPCs and improve IPCs survival and ability to release insulin *in vitro* (Dayer et al., 2017; Anjum et al., 2018; Ikemoto et al., 2018; Shahjalal et al., 2018; Pavathuparambil Abdul Manaph et al., 2019; Ghoneim et al., 2020). The overexpression of *Pdx1*, *Neurog3*, *MafA*, and *Pax4* can improve transdifferentiation efficiency and insulin secretion (Limbert et al., 2011; Xu et al., 2017; Zhu et al., 2017; Dayer et al., 2019). However, various transdifferentiation methods have not been systematically compared with one another, leaving various methods in a chaotic state, and opinions on transdifferentiation efficiency vary. Moreover, the changes of genes and metabolic pathways on the transdifferentiation of ADMSCs into IPCs is largely unknown. Thus, ADMSCs transdifferentiate into functional mature beta cells need more research.

In this study, canine ADMSCs were transdifferentiated into IPCs by five types of procedures, the optimal procedure was determined through comparison. Absolute Quantitative Transcriptome Sequencing Analysis was performed at different stages of the optimal procedure to study the changes in genes and metabolic pathways during the transdifferentiation process for the first time. The datasets obtained provided important reference value for the study of the transdifferentiation of ADMSCs into IPCs, islet development and canine genes pool. Five functional genes were screened out. The functions of these genes were verified by overexpression and silencing. This study provides a foundation for future work to understand the mechanisms of the transdifferentiation of ADMSCs into IPCs and acquire IPCs with high maturity.

MATERIALS AND METHODS

Animal

All the dogs (Beagle, Female, 2–5 years old) were purchased from Northwest Agriculture and Forestry University Animal Laboratories (Xian, China). All of the dogs were reared, obtained, and housed in accordance with our institute's laboratory animal requirements, the dogs were kept in cages in a feeding room without purification equipment at a temperature of 18–25°C, humidity of 40–60%, airflow value of 0.13–0.18 m/s, ventilation rate of 10–20 times per hour, light normal, noise below 60 dB, and all procedures and the study design were conducted in accordance with the Guide for the Care and Use of Laboratory Animals (Ministry of Science and Technology of China, 2006) and were approved by the Animal Ethical and Welfare Committee of Northwest Agriculture and Forest University (Approval No: 2020002).

Isolation and Culture of Canine ADMSCs

Canine inguinal adipose tissue was obtained by aseptic surgery. The adipose tissue was minced using a sterile scissors and placed in a 50-mL sterile tube with triple volume of 0.1% type I collagenase (Sigma, Ronkonkoma, NY, United States) solution, the tube was transferred to shaker at 180 r/min, 37 °C for 60 min (Raposio et al., 2017). α-MEM Medium [MEM Alpha Modification Medium (Gibco, Waltham, MA, United States) supplemented with 10% fetal bovine serum (Zeta Life, Menlo Park, CA, United States), 100 U/mL penicillin (Sigma, Ronkonkoma, NY, United States), 0.1 mg/mL streptomycin (Sigma, Ronkonkoma, NY, United States) and 0.5 μg/mL Mycoplasma Removal Agent (MP Biomedicals, Irvine, CA, United States)] was used to stop digestion, the tube was centrifuged at 1000 r/min for 5 min, and the upper suspension and floating fat were discarded (Zuk et al., 2001; Vieira et al., 2010). Cells were resuspended in the α-MEM Medium, the suspension was filtered by 200-mesh sieves and centrifuged at 1000 r/min for 5 min, and the supernatant was discarded. Cells were resuspended in α-MEM Medium, transferred to a 60-mm cell culture dish (ThermoFisher Scientific, Waltham, MA, United States), and cultured in a carbon dioxide incubator at 37 °C, 5% CO2 (Palumbo et al., 2015). When the cells grew to 90%, they were digested with trypsin (Gibco, Waltham, MA, United States) and passaged at a ratio of 1:3.

Identification of Canine ADMSCs

The fourth-generation canine ADMSCs were inoculated into 96-well plates at 5×10^2 cells per well for a total of 44 wells. Contents were taken from four wells every day, and the MTT Cell Proliferation Assay Kit (ThermoFisher Scientific, Waltham, MA, United States) was used to determine the proliferation of cells with continuous determination for 11 days.

The fourth-generation canine ADMSCs were adjusted to 2×10^6 cells/mL suspension; 100 μL cell suspension was transferred into a flow cytometry tube and 5 μL CD13-FITC, CD29-FITC, CD31-FITC, CD44-FITC, CD45-PE, CD73-FITC, CD90-PE, CD105-PE, and CD235a-FITC fluorescent antibodies

(BD Biosciences, San Jose, CA, United States) were added. Cells were incubated without light for 15 min and flow cytometry (CytoFLEX, Beckman Coulter, :Brea, CA, United States) was used for detection.

Dog Adipose-derived Stem Cell Adipogenic/Osteogenic/Chondrogenic Differentiation Basal Medium (CAXMD-90031[1] /CAXMD-90021[2]/CAXMD-90041,[3] Cyagen, China) were used to induce canine ADMSCs into adipocytes/osteocytes/chondrocytes. The differentiated cells were stained with Oil Red O, Alizarin Red, and Alcian Blue, respectively.

Isolation of Canine Pancreatic Islets

Canine pancreatic islets were isolated by collagenase V (Sigma-Aldrich, Burlington, MA, United States) digestion and purified by centrifugation on a Ficoll density gradient (Borot et al., 2013). Purified islets were incubated (37°C, 5% CO_2) in DMEM medium (Gibco, Waltham, MA, United States) supplemented with 10% fetal bovine serum (Zeta Life, Menlo Park, CA, United States), 100 U/mL penicillin (Sigma, Ronkonkoma, NY, United States), 0.1 mg/mL streptomycin (Sigma, Ronkonkoma, NY, United States), and 0.5 μg/mL Mycoplasma Removal Agent (MP Biomedicals, Irvine, CA, United States).

Transdifferentiation of ADMSCs Into IPCs

Based on published studies, appropriate modifications to transdifferentiation procedures were developed. Finally, we used five types of procedures (**Figure 1** and **Supplementary Material 1**) to transdifferentiate canine ADMSCs into IPCs for screening. In the initial study, the procedure 1 (Sun et al., 2007; Mohamed et al., 2016), the procedure 2 (Zhang et al., 2010), and the procedure 3 (Wang et al., 2020) can transifferentiated mesenchymal stem cells into IPCs, the procedure 4 (Pagliuca et al., 2014), and the procedure 5 (Rezania et al., 2012, 2014) can transdifferentiated induced pluripotent stem cells into IPCs. The canine ADMSCs were plated in six-well plates, and the cells were transdifferentiated when the cell density reached 75%. After transdifferentiation, cells morphology was observed, the numbers of islet-like cells were counted, and their diameters were measured. The cells were stained with dithizone using the Dithizone dyeing solution (PB9012, Coolaber, China).

RT-qPCR

The expression of islet β-cell related genes and differentially expressed genes (DEGs) was detected by RT-qPCR in cells (Nolan et al., 2006). Canine ADMSCs were used as the control group, and *GADPH* was used as the reference gene. The TaKaRa MiniBEST Universal RNA Extraction Kit (TaKaRa, Japan) was used to extract RNA from cells. The PrimeScript™ RT Master Mix (Perfect Real Time) (TaKaRa, Japan) was used to prepare cDNA. Reactions were conducted according to the Maxima SYBR Green/ROX qPCR Master Mix (ThermoFisher Scientific, Waltham, MA, United States) manual, and RT-qPCR was performed using the Step One Plus Real-Time PCR System (Applied Biosystems, Bedford, MA, United States). Three biological replicates and three technical replicates were used to determine the Ct values. The expression levels of the tested genes were determined from the Ct values, as calculated by $2^{-\Delta\Delta Ct}$ (Livak and Schmittgen, 2001).

Glucose-Stimulated Insulin Secretion

Cells were washed with PBS 3 times, 5 mM glucose was added, the cells were incubated for 30 min, and the supernatant was collected. Next, cells were washed three times in PBS and incubated in 25 mM glucose for 30 min, and supernatants were collected. Finally, cells were washed three times in PBS and incubated in 5 mM glucose and 30 mM KCl for 30 min, and the supernatant was collected. Cell masses were dispersed into single cells, and cells were counted. Supernatant samples containing secreted insulin were processed using the Human/Canine/Porcine Insulin Quantikine ELISA Kit (R&D Systems, Minneapolis, MN, United States). The glucose stimulation index (SI), which measures the sensitivity of IPCs to glucose, was obtained by dividing the amount of insulin secreted at the high glucose (25 mM) level by the amount of insulin secreted at the low glucose (5 mM) level.

Absolute Quantitative Transcriptome Sequencing Analysis

Among the five procedures, the optimal procedure was selected. Absolute Quantitative Transcriptome Sequencing Analysis (Kivioja et al., 2011) was performed on the cells obtained by the optimal transdifferentiation procedure. Cells were collected at 5 days (IPC1), 11 days (IPC2), 19 days (IPC3), 25 days (IPC4) of transdifferentiation. Canine ADMSCs were used as a negative control, and canine pancreatic islets were used as a positive control. Two biological replicates were completed for each sample.

Total RNA was extracted using TRIzol® reagent (Invitrogen, Waltham, MA, United States) following the manufacturer's protocol. mRNA was enriched, and cDNA was synthesized and connected to adapters using unique molecular identifiers (UMIs). Illumina Sequencing Platform HiSeq 2500 was used for sequencing, and the sequencing length was PE150 (Sequencing was conducted by LC Sciences, LLC.). Removal of duplicates and data error correction were performed based on genome location and UMI tagging (FastQC 0.10.1, RSeQC 2.3.9, UMI_tools 0.5.4). High quality clean reads were generated from the assembly library by filtering. HISAT2 2.0.4 (Daehwan et al., 2015) was performed to align high-quality reads with the *Canis lupus familiaris* genome,[4] and the alignment rate was calculated. StringTie 1.3.4d (Pertea et al., 2015) was used for transcript splicing and merging. Gene expression was calculated by the fragments per kilobase per million (FPKM) method (Roberts, 2011). And edgeR (Robinson et al., 2010) was used for transcript quantification. The DEGs were selected with

[1]https://www.cyagen.com/cn/zh-cn/product/msc-adipogenic-differentiation-media-CAXMD-90031.html?from=34

[2]https://www.cyagen.com/cn/zh-cn/product/msc-osteogenic-differentiation-media-CAXMD-90021.html?from=33

[3]https://www.cyagen.com/cn/zh-cn/product/msc-chondrogenic-differentiation-media-CAXMD-90041.html?from=35

[4]https://www.ncbi.nlm.nih.gov/genome/?term=Canis%20lupus%20familiaris

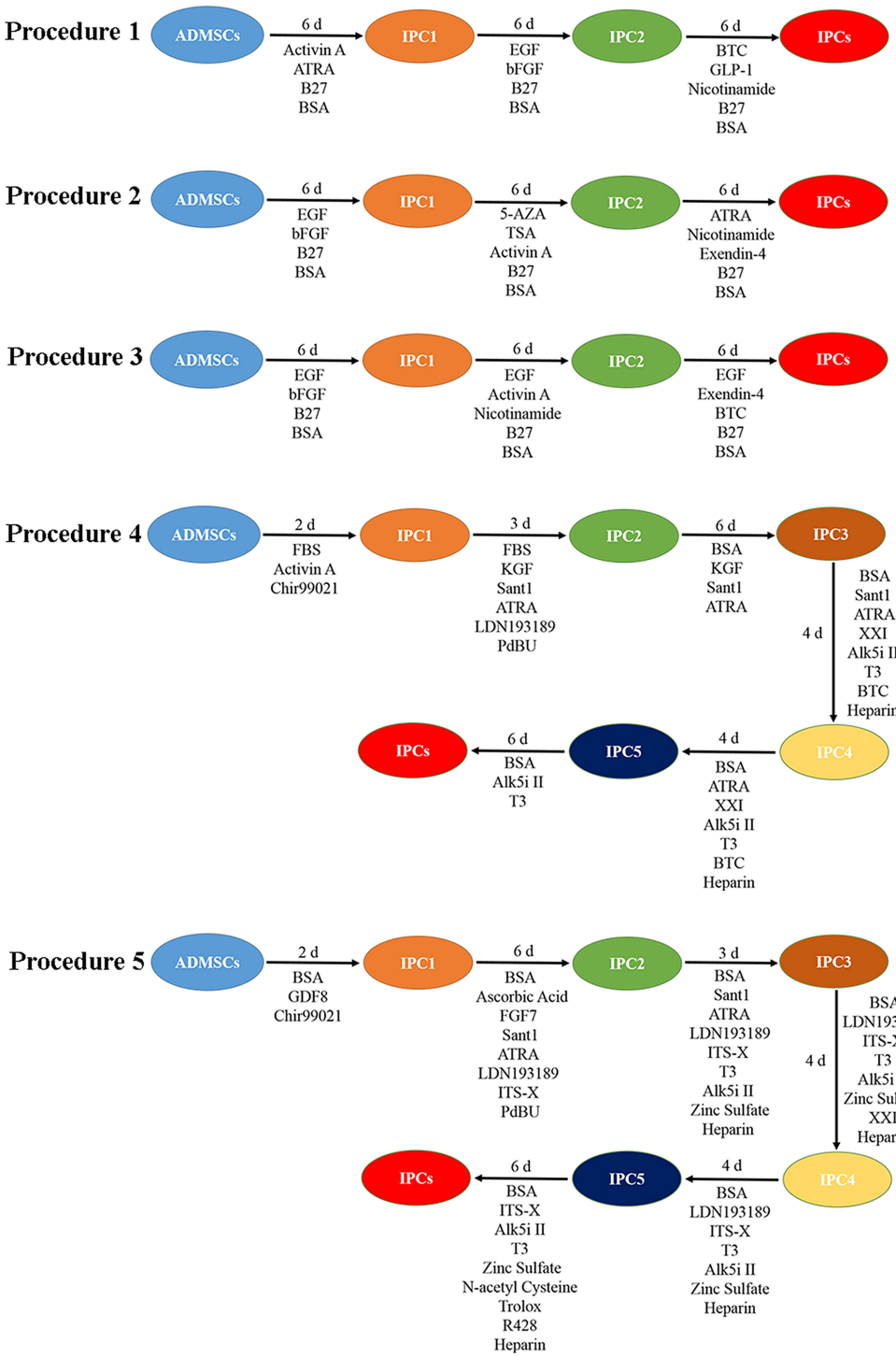


FIGURE 1 | The five types of procedures.

log2 (fold change) $\geq$ 2 or log2 (fold change) = -2 and the p-value = 0.05 by R package–edgeR (Robinson et al., 2010). If too many genes meet this p-value condition, use the q-value (the fold discovery rate p-value correction) = 0.05 for further screening (Flenniken and Andino, 2013). In many cases, it's more rigorously corrected and there are fewer differential genes. The R pheatmap toolkit[5] was used for hierarchical clustering analysis. We used GOseq (Young et al., 2010) for

[5]https://cran.rstudio.com/web/packages/pheatmap/index.html

gene ontology (GO) enrichment analysis,[6] Kyoto Encyclopedia of Genes, and Genomes (KEGG)[7] for KEGG enrichment analysis in the DEGs.

Adenovirus-Mediated Gene Overexpression

The cDNA sequences for genes were synthesized by Wuhan Gene Create Biological Engineering Co., Ltd. (Wuhan, China). The cDNA for each gene was PCR-amplified and inserted into *pAdTrack-CMV* previously digested with *BglII*/*Hin*dIII using the In-Fusion HD cloning kit (Takara, Japan) (Sleight et al., 2010). The resulting plasmid was linearized with *Pme*I, and then homologous recombination was performed with *pAdeasy-1* in *E. coli BJ5183*. The recombinant plasmid with *Pac*I linearization was used to transfect AAV-293 cells to produce recombinant adenovirus particles using the Advanced DNA RNA transfection reagent (Zeta Life, Menlo Park, CA, United States). RT-qPCR (Nolan et al., 2006) and Western-blot (following the Elabscience Western blot detection kit operation manual) were used to detect the expression of target gene. The canine ADMSCs were transfected with the recombinant adenovirus particles.

Immunofluorescent Staining

Cells were fixed with 4% paraformaldehyde for 10 min and washed with PBS three times. Next, the cells were permeabilized for 15 min with 0.1% Triton X-100 (Sigma, Ronkonkoma, NY, United States) and washed with PBS three times. Cells were blocked with goat serum for 30 min and incubated with primary antibodies (1:600; Abcam, United Kingdom) at 4°C overnight. After washing with PBS three times, cells were incubated with secondary antibodies (1:600; Abcam, United Kingdom) for 1 h at 37°C in the dark, and again washed with PBS three times. Nucleus counterstaining was performed with 10 μg/mL Hoechst 33342 (Sigma, Ronkonkoma, NY, United States). Fluorescence images were obtained with an inverted fluorescence microscope (Sunny Optical Technology Company Limited, ICX41, China).

siRNA-Mediated Gene Silencing

Fluorescein-labeled siRNA (Small interfering RNA) was synthesized and purified by Gene Pharma Co., Ltd. (Shanghai, China). Each gene was designed with three siRNAs. In the process of transdifferentiation, the canine ADMSCs were transfected with siRNAs using the Advanced DNA RNA transfection reagent (Zeta Life, Menlo Park, CA, United States). RT-qPCR (Nolan et al., 2006) was used to detect the silencing efficiency of siRNAs and the one with the highest silencing efficiency was selected. The gene was silenced every 7 days throughout the transdifferentiation to keep it silent.

Statistical Analysis

Assays were repeated three times. One-way analysis of variance (ANOVA) was used for the statistical comparisons among groups. The tests were performed using IBM SPSS Statistics 25 software (SPSS Inc., Chicago, IL, United States).

[6]http://geneontology.org

[7]http://www.kegg.jp/kegg

RESULTS

Canine ADMSC Isolation, Culture, and Identification

The fourth-generation isolated cells showed long spindle type and adherent growth (**Supplementary Figure 2A**) and proliferated rapidly in the 3–7 day after adherent growth, exhibiting logarithmic growth (**Supplementary Figure 2B**). The cells were tested by flow cytometry, and the expression levels of CD13, CD29, CD44, CD73, CD90, and CD105 were positive. Expression levels for CD31, CD45, and CD235a were negative (**Supplementary Figure 2C**). In osteogenic differentiation, the cells grew in clusters; Alizarin Red staining showed red-stained calcified nodules. In chondrogenic differentiation, the cells gathered and grew, and blue staining was observed after Alcian Blue staining. In adipogenic differentiation, large areas of fat droplets were observed by Oil Red O staining (**Supplementary Figure 2D**). These results prove that the isolated cells were canine ADMSCs.

Transdifferentiation of ADMSCs Into IPCs

The canine ADMSCs were transdifferentiated into IPCs using five types of procedures. In procedure 1, the cells did not form into clusters, and no obvious islet-like cells were found. In procedures 2, 3, 4, and 5, the cells agglomerated into a spherical shape, with obvious islet-like cells; the resulting islet-like cells were scarlet with dithizone staining (**Figure 2A**). There were also differences in the number of cell cluster from procedures 2, 3, 4, and 5, among which the number of procedure 5 cells was the greatest, reaching $123 \pm 10.72/10^6$ canine ADMCS, with a cell cluster of 99.75 ± 8.26 μm in diameter and an average of 110.50 ± 18.81 cells per cell cluster (**Figure 2B**). For procedure 1, after stimulation with low glucose (5 mM), high glucose (25 mM), 5 mM glucose, and 30 mM KCl, the secretion of insulin was significantly lower than values for procedures 2, 3, 4, and 5. The secretion of insulin was the highest in procedure 5, with 53.13 ± 3.39 IU/10^5 cells in low glucose, 125.23 ± 4.35 IU/10^5 cells in high glucose and 127.02 ± 4.66 IU/10^5 cells in 5 mM glucose and 30 mM KCl; the second highest level of insulin secretion was observed for procedure 4, but all these values lower than for the mature islet cells group (**Figure 2C**). The glucose SI after procedure 1 was significantly lower than values for procedures 2, 3, 4, and 5; the SI of procedure 5 was 2.36 ± 0.11, showing the most favorable response to glucose stimulation (**Figure 2D**).

The RT-qPCR was performed on the cells (the primers are provided in **Supplementary Table 1** at **Supplementary Material 3**). As shown in **Figure 3**, the expression level of each gene (Canine ADMSCs were used as the control group, and *GADPH* was used as the reference gene, the relative expression of the genes calculated by $2-^{\Delta\Delta Ct}$) was elevated following procedure 5 and significantly different from values for procedures

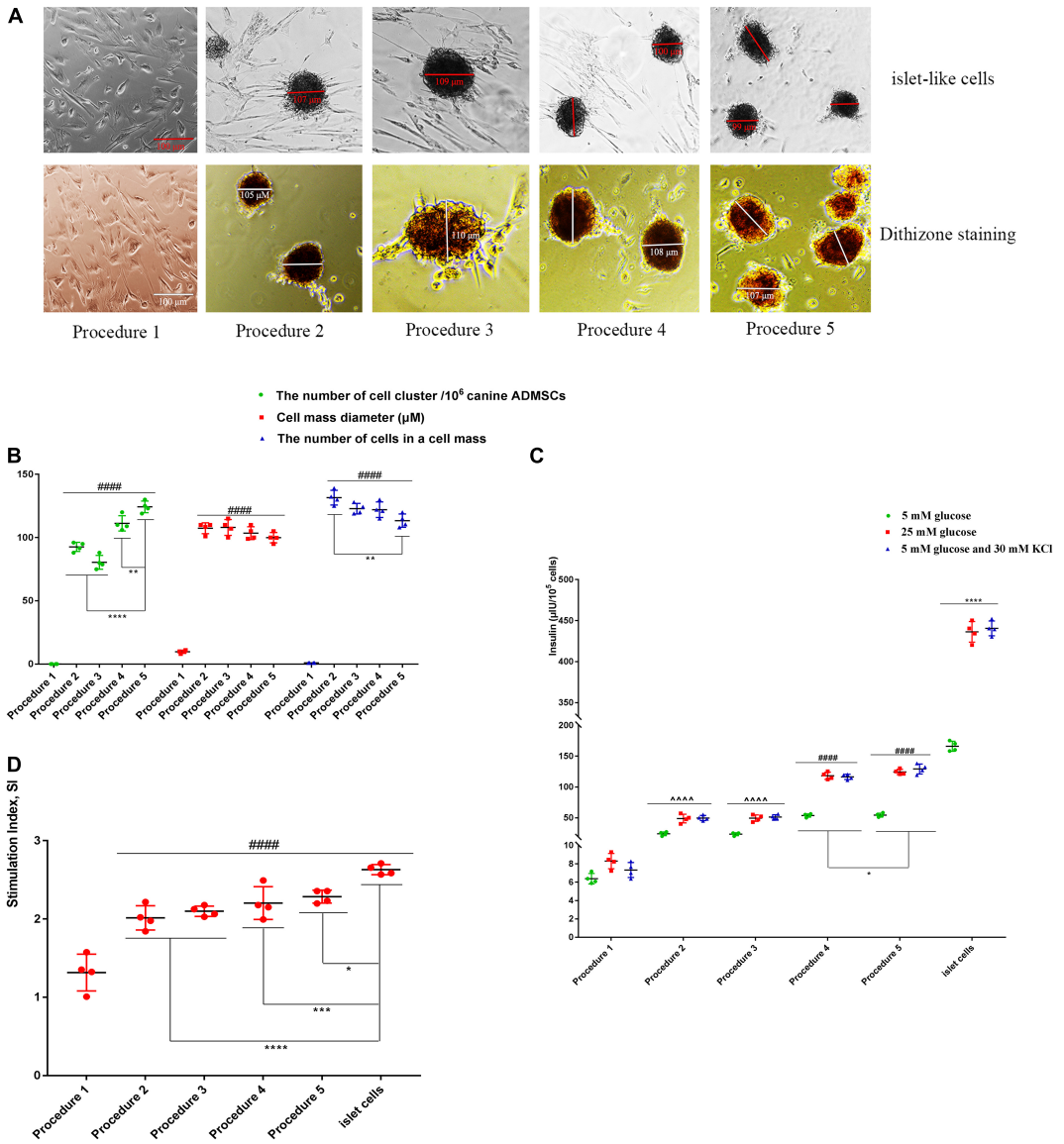


FIGURE 2 | The transdifferentiation of ADMSCs into IPCs using five types of procedures. **(A)** The cellular morphology and dithizone staining. **(B)** The number of cell cluster of procedures 2, 3, 4, 5 was significantly more than inducing procedures 1 (####$p < 0.0001$). There were also differences in the number of cell cluster in procedures 2, 3, 4, and 5 (****$p < 0.0001$; **$p < 0.01$) ($n = 4$). **(C)** After the stimulation of low glucose (5 mM), high glucose (25 mM), 5 mM glucose, and 30 mM KCl, the secretion of insulin in procedure 1 was significantly lower than that of procedures 2 and 3 (^^^^$p < 0.0001$). The secretion of insulin in procedure 4 and 5 was higher than that of procedures 2 and 3 (####$p < 0.0001$), procedure 5 is higher than procedure 4 (*$p < 0.05$), but they were all lower than the mature islet cells group (****$p < 0.0001$) ($n = 4$). **(D)** The glucose Stimulation Index (SI) of procedure 1 was significantly lower than that of procedures 2, 3, 4, 5, and mature islet cells (####$p < 0.0001$), procedure 5 is highest in five types of procedures (****$p < 0.0001$; ***$p < 0.001$; *$p < 0.05$) ($n = 4$).

1, 2, 3, and 4. The expression levels for procedures 1, 2, 3, 4, and 5 were significantly lower than those in mature islet cells.

According to the above results, procedure 5 exhibited the highest transdifferentiation efficiency.

Quality Control of Sequencing Data and Genes Expression Level Analysis

Absolute Quantitative Transcriptome Sequencing Analysis was performed for the four stages of procedure 5 (divided into IPC1, IPC2, IPC3, and IPC4). Canine ADMSCs were used as a negative control (divided into ADSC) and mature canine islet cells as a positive control (divided into Beta_cell). After sequencing, the raw reads were saved in FASTQ format. **Supplementary Table 1** in **Supplementary Material 4** lists the data quality throughout the data analysis process. After data processing, highly reliable data were aligned to the canine reference genome to obtain comprehensive transcript information (**Supplementary Table 2** in **Supplementary Material 4**). The regional distribution aligned with the reference genome is shown

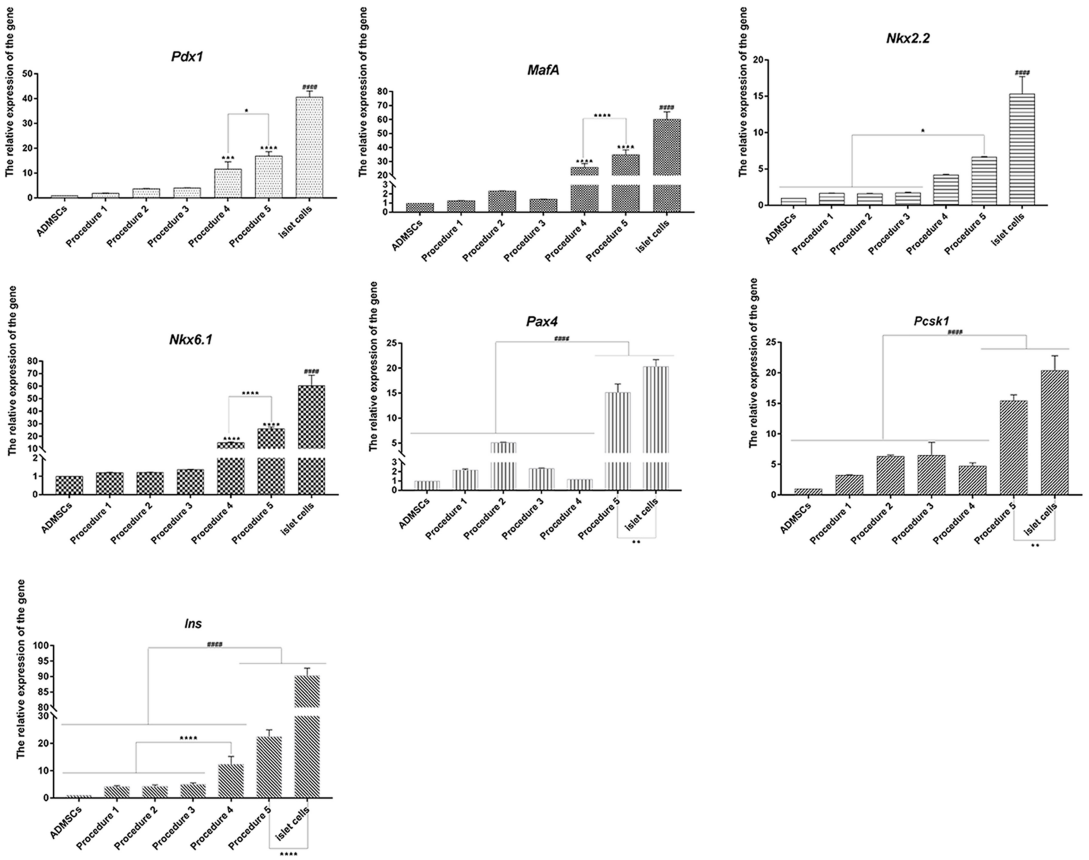


FIGURE 3 | RT-qPCR analysis. The expression level of each gene in procedure 5 was elevated, which was significantly higher than procedures 1, 2, 3, and 4, there is no difference between procedures 1, 2, and 3. The expressions of *Pdx1*, *MafA*, *Nkx6.1*, and *Ins* in procedure 4 were significantly higher than those in procedure 1, 2, and 3 (****$p < 0.0001$; ***$p < 0.001$; **$p < 0.01$; *$p < 0.05$). The expression level of all genes in procedure 1, 2, 3, 4, and 5 was significantly lower than that of mature islet cells (####$p < 0.0001$).

in **Supplementary Material 5**. The result of genes expression level analysis (Transcriptome expression profile and Gene expression profiling) was shown in Supplementary Material 6, a total of 60,151 transcripts were obtained.

The problem of oncological transformation of stem cells is acute in the development of molecular stem cell technologies. In this study, tumor markers, such as *Cd133*, *A2b5*, *Ssea-1* were not expressed, and *Myc* had low expression in ADSC, IPC1, IPC2, IPC3, IPC4, and Beta_cell.

Differential Expression Genes Analysis and Clustering Analysis

The DEGs screening conditions for the DEGs were log2 (fold change) ≥ 2 or log2 (fold change) $= -2$ with the *p*-value set at = 0.05. The fold discovery rate *p*-value correction (FDR, *q*-value) is also provided in the results. DEGs were divided into five groups: IPC1 vs. ADSC (1169 up-regulated genes and 1377 down-regulated genes, *p*-value = 0.05; 1166 up-regulated genes and 1376 down-regulated genes, *q*-value = 0.05), IPC2 vs. IPC1 (1323 up-regulated genes and 803 down-regulated genes, *p*-value = 0.05; 1319 up-regulated genes and 799 down-regulated genes, *q*-value = 0.05), IPC3 vs. IPC2 (722 up-regulated genes and 680 down-regulated genes, *p*-value = 0.05; 721 up-regulated genes and 678 down-regulated genes, *q*-value = 0.05), IPC4 vs. IPC3 (539 up-regulated genes and 1561 down-regulated genes, *p*-value = 0.05; 537 up-regulated genes and 1525 down-regulated genes, *q*-value = 0.05), and Beta_cell vs. IPC4 (2816 up-regulated genes and 4571 down-regulated genes, *p*-value = 0.05; 2815 up-regulated genes and 4472 down-regulated genes, *q*-value = 0.05) (**Supplementary Material 7**). The volcanic diagram of each differentially expressed gene analysis group is shown in **Figure 4A**. After FPKM values of DEGs were transformed to *Z* values, a clustering diagram was drawn (**Figure 4B**). Venn diagrams was constructed to compare the spectra of DEGs with each other (**Figure 4C**).

Pdx1 (*p*-value = 0.00, *q*-value = 0.00), *Nkx6.1* (*p*-value = 0.00, *q*-value = 0.00), *Nkx2.2* (*p*-value = 0.00, *q*-value = 0.00), *Pax4* (*p*-value = 0.00, *q*-value = 0.00), and *Ins* (*p*-value = 0.00, *q*-value = 0.00), which are critical for islet β-cell development and insulin secretion, were also screened for DEGs; *MafA* was not differentially expressed in this study (**Supplementary Material 7**). DEGs analysis and cluster analysis showed obvious

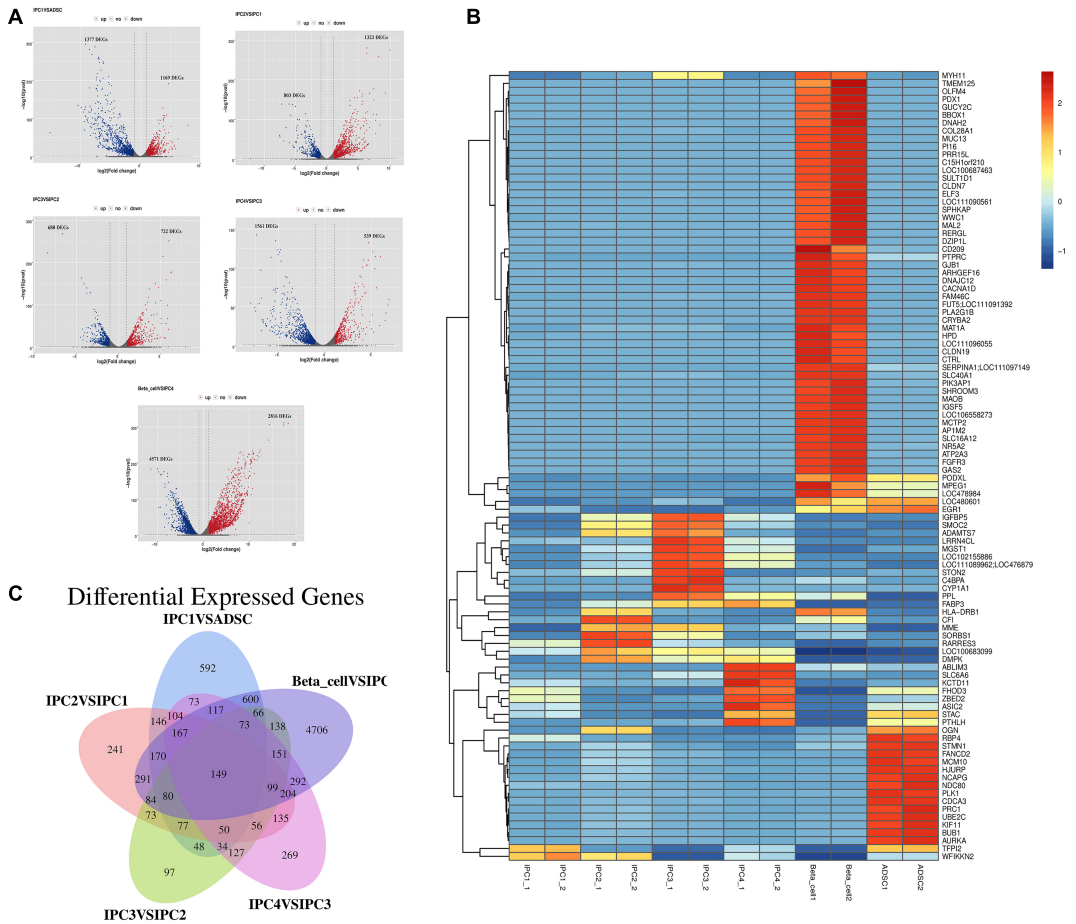


FIGURE 4 | Differential expression genes analysis and clustering analysis. **(A)** Volcanic maps of the DEGs. Blue dot and green dot represent that the expression level of genes has difference, the black dot represents no difference. **(B)** Clustering analysis. The abscissa is the sample, and the ordinate is the genes. Different colors indicate different gene expression level, and the color ranges from blue to white to red, indicating low to high expression levels. **(C)** Venn diagrams was constructed to compare the spectra of DEGs with each other.

differences in cell genes expression appears from canine ADMSCs to IPC4, and there were significant differences between IPC4 and islet cells. These results suggest that at the end of each transdifferentiation phase, the cells gene expression undergo corresponding changes.

GO Functional Enrichment Analysis and KEGG Pathways Enrichment Analysis

Supplementary Material 8 and **Figure 5A** show the GO enrichment analysis for all DEGs. The fold discovery rate *p*-value correction (FDR, *q*-value) is also provided in the results. There were 47 GO Terms enriched by over 100 DEGs (*p*-value = 0.05 and *q*-value = 0.05), 26 GO Terms enriched by over 200 DEGs (*p*-value = 0.05 and *q*-value = 0.05). **Supplementary Material 9A** shows the GO enrichment analysis of each group. According to the size of *p*-values and *q*-values, the 20 most significant GO terms were selected as dot plots (**Figure 5B**), **Supplementary Material 9B** shows the 20 most significant GO terms for each group.

In GO Functional Enrichment Analysis, we identified 126 DEGs involved in endocrine pancreas development (*p*-value = 0.34, *q*-value = 0.93), pancreas morphogenesis (*p*-value = 0.42, *q*-value = 0.93), pancreas development (*p*-value = 0.45, *q*-value = 0.93), branching involved in pancreas morphogenesis (*p*-value = 0.42, *q*-value = 0.93), regulation of insulin secretion involved in cellular response to glucose stimulus (*p*-value = 0.02, *q*-value = 0.73), insulin secretion (*p*-value = 0.15, *q*-value = 0.93), positive regulation of insulin secretion involved in cellular response to glucose stimulus (*p*-value = 0.16, *q*-value = 0.93), insulin secretion involved in cellular response to glucose stimulus (*p*-value = 0.17, *q*-value = 0.93), positive regulation of insulin secretion (*p*-value = 0.16, *q*-value = 0.93), regulation of insulin secretion (*p*-value = 0.33, *q*-value = 0.93). In IPC1VSADSC, there are 18 DEGs were enriched in these GO Terms, In IPC2VSIPC1, IPC3VSIPC2, IPC4VSIPC3, and Beta_cellVSIPC4, there were 15 DEGs, 14 DEGs, 19 DEGs, and 90 DEGs were enriched in these GO Terms, respectively. See **Supplementary Material 10** for specific DEGs names, these DEGs are involved in pancreatic islet cell development,

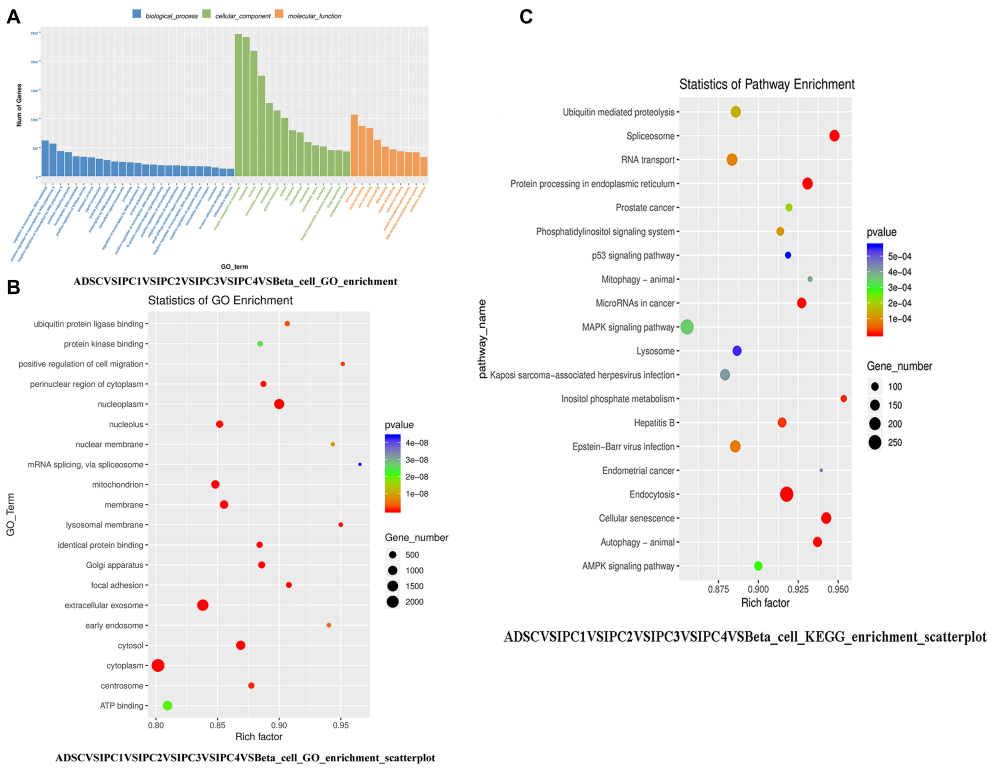


FIGURE 5 | The GO functional enrichment analysis and KEGG pathways enrichment analysis. **(A)** The GO enrichment analysis of all DEGs. **(B)** The 20 most significant GO terms in GO functional enrichment analysis of DEGs. The horizontal axis represents the enrichment degree (Rich factor), the vertical axis represents the GO Term of enrichment. Dot size indicates the number of DEGs enriched in a GO term. The dot color represents different *P*-values; Rich factor means the number of DEGs belonging to a certain GO term. The higher the Rich factor is, the higher the GO enrichment degree will be. **(C)** The 20 most significant KEGG pathways in KEGG Pathways Enrichment Analysis of DEGs.

insulin secretion. These DEGs may play important roles in the transdifferentiation of canine ADMSCs into IPCs *in vitro*.

In this study, scatterplots were used to visually demonstrate KEGG pathway enrichment results of DEGs. The 20 KEGG pathways with the most significant expression were selected according to *p*-values and *q*-values (**Figure 5C**). **Supplementary Material 11** shows the 20 most significant KEGG pathways for each group. There were 23 KEGG Pathways enriched by over 100 DEGs (*p*-value = 0.05 and *q*-value = 0.05), 3 KEGG Pathways enriched by over 200 DEGs (*p*-value = 0.05 and *q*-value = 0.05) (**Supplementary Material 12**).

In KEGG Pathways Enrichment Analysis, we found that there were 143 DEGs, 74 DEGs, 23 DEGs, and 26 DEGs enriched, respectively, for Insulin signaling pathway (*p*-value = 0.01, *q*-value = 0.06), Insulin secretion (*p*-value = 0.42, *q*-value = 0.80), Maturity onset diabetes of the young (*p*-value = 0.15, *q*-value = 0.39), and Type I diabetes mellitus (*p*-value = 0.99, *q*-value = 1.00). In IPC1VSADSC, there are 31 DEGs were enriched in these KEGG Pathways, In IPC2VSIPC1, IPC3VSIPC2, IPC4VSIPC3, and Beta_cellVSIPC4, there were 49 DEGs, 28 DEGs, 39 DEGs, and 178 DEGs were enriched in these KEGG Pathways, respectively (see **Supplementary Material 12** for specific DEGs names). These DEGs can regulate the development of pancreatic islet cells and the production of insulin. These DEGs may be important for transdifferentiation of canine ADMSCs into IPCs *in vitro*.

Pdx1, *Nkx6.1*, *Nkx2.2*, *MafA*, and *Pax4* have been shown to play an important role in the transdifferentiation of mesenchymal stem cells to IPCs (Limbert et al., 2011; Bahrebar et al., 2015; Li et al., 2017; Zhang et al., 2019; Aigha and Abdelalim, 2020). In this study, the aim was to explore what other factors, except for these key regulatory factors, play a role in the transdifferentiation of mesenchymal stem cells to IPCs. So we decided to filter out these genes and look for new regulatory genes instead. In this study, gene functional analysis was performed on the genes involved in the development of pancreatic islet β-cells, DEGs listed from GO functional enrichment analysis and KEGG pathways enrichment analysis, we screened a total of 51 genes according to the significance of difference, the expression level at each stage and the function of genes (**Supplementary Material 13**). Protein interaction network analysis was performed (**Supplementary Material 14**), we found that FOXO1, FOXA1, SOX17, HNF1A, HNF1B, INSM1, NR5A2, GCK, PBX1, ONECUT1, ONECUT2, PTF1A, and RFX6 can form a protein interaction network with PDX1, NKX6.1, NKX2.2, MAFA, NGN3, and PAX4. Although WNT5A, TCF7L2, BMP4, RFX3, and DLL1 cannot interact with PDX1, NKX6.1, NKX2.2, MAFA, NGN3, and PAX4, it does interact with FOXA1, SOX17, NR5A2, ONECUT1, HNF1A,

HNF1B, and GCK, that is, it indirectly interacts with PDX1, NKX6.1, NKX2.2, MAFA, NGN3, and PAX4. The 18 genes (*Foxo1*, *Foxa1*, *Sox17*, *Hnf1a*, *Hnf1b*, *Insm1*, *Nr5a2*, *Gck*, *Pbx1*, *Onecut1*, *Onecut2*, *Ptf1a*, *Wnt5a*, *Tcf7l2*, *Bmp4*, *Rfx3*, *Dll1*, *and Rfx6*) are referred to as novel functional genes. The 18 novel functional genes were separately overexpressed in canine ADMSCs. Novel functional genes were further screened by RT-qPCR validation (Canine ADMSCs were used as the control group, and GADPH was used as the reference gene, the relative expression of the genes calculated by 2ˆ-△△Ct). Relative to other genes, the *Foxa1*, *Hnf1b*, *Dll1*, *Pbx1*, *and Rfx3* can significantly stimulate the expression of islet β-cell development cascade regulation genes (**Supplementary Material 15**). The *Foxa1*, *Hnf1b*, *Dll1*, *Pbx1*, and *Rfx3* were used in subsequent studies.

RT-qPCR Verification of Absolute Quantitative Transcriptome Sequencing

In this study, 12 DEGs were selected from the above DEGs, and the Absolute Quantitative Transcriptome Sequencing Analysis results were verified by RT-qPCR (primers listed in **Supplementary Table 2** at **Supplementary Material 3**). In Absolute Quantitative Transcriptome Sequencing, we used the PRKM results (**Supplementary Material 6**). In RT-qPCR, we used the relative expression of the genes (Canine ADMSCs were used as the control group, and *GADPH* was used as the reference gene, calculated by $2^{-\Delta\ \Delta\ Ct}$) (**Supplementary Material 16**). The results of RT-qPCR were consistent with the gene expression trend in the Absolute Quantitative Transcriptome Sequencing, and the Absolute Quantitative Transcriptome Sequencing results were correct.

Preparation of Adenovirus Venom

Foxa1, *Hnf1b*, *Dll1*, *Pbx1*, and *Rfx3* overexpression adenovirus particles were prepared to verify the roles of these five genes in the differentiation of canine ADMSCs into IPCs. Five genes were amplified by PCR (primers listed in **Supplementary Table 3** in **Supplementary Material 3**), and five overexpressed single-gene adenovirus shuttle vectors were constructed (*pADTrcak-CMV-Foxa1*, *pADTrcak-CMV-Hnf1b*, *pADTrcak-CMV-Dll1*, *pADTrcak-CMV-Pbx1*, and *pADTrcak-CMV-Rfx3*). And the recombinant vectors were *pAdeasy-Foxa1*, *pAdeasy-Hnf1b*, *pAdeasy-Dll1*, *pAdeasy-Pbx1*, and *pAdeasy-Rfx3*. The linearized recombinant vectors were packaged as adenoviruses by AAV-293 cells, and the adenovirus particles were obtained; the virus titers were 6×10^9, 5.5×10^9, 7.5×10^9, 6×10^9, and 7×10^9 TU/mL, respectively. The expression of the target genes and proteins was verified by RT-qPCR (primers listed in **Supplementary Table 4** in **Supplementary Material 4**) and Western-blot (**Supplementary Material 17**). The results showed that the adenovirus particles could successfully express the target proteins.

Functional Verification of the *Foxa1*, *Hnf1b*, *Dll1*, *Pbx1*, and *Rfx3*

The canine ADMSCs were infected with the adenovirus particles according to the multiplicity of infection MOI = 100. Two days after canine ADMSCs were infected, positive cells were screened according to green fluorescence. The cells were cultured for 2 days and transdifferentiated with procedure 5 (grouped into FOXA1 + Procedure 5, HNF1B + Procedure 5, DLL1 + Procedure 5, PBX1 + Procedure 5, RFX3 + Procedure 5) with normal cell passage during transdifferentiation. After 25 days of transdifferentiation, the cells were observed.

The cells of five groups grew in clusters, showing the appearance of islets. The green fluorescence carried by adenoviruses had disappeared, the cells were stained with dithizone and were able to be dyed red (**Figure 6A**), indicating that the cells could express insulin. The cells of five groups under the stimulus of glucose were able to secrete insulin, and insulin secretion was higher than procedure 5 (**Figure 6B**). The overexpression of *Foxa1*, *Hnf1b*, *Dll1*, *Pbx1*, *Rfx3* were further able to improve the effect of transdifferentiation, insulin secretion. Among these, the overexpression of *Foxa1*, *Pbx1*, and *Rfx3* exhibited the most significant effects. The glucose SI exceeded 2.5 for five groups, higher than for procedure 5, indicating that cells were able to respond to glucose stimulation (**Figure 6C**). Immunofluorescence staining of insulin and c-peptide showed that the cells were insulin and c-peptide positive (**Figure 6D**). The expression of islet-specific transcription factors was detected by RT-qPCR (primers listed in **Supplementary Table 1** in **Supplementary Material 3**); the overexpression of *Foxa1*, *Hnf1b*, *Dll1*, *Pbx1*, *Rfx3* were able to significantly stimulate high expression of *Pdx1*, *MafA*, *Nkx6.1*, *Nkx2.2*, and *Ins* genes with higher levels of expression than for procedure 5, indicating that the overexpression of these five genes could further stimulate the expression of islet cascade regulatory genes and improve transdifferentiation efficiency (Canine ADMSCs were used as the control group, and *GADPH* was used as the reference gene, the relative expression of the genes calculated by 2ˆ-△△Ct) (**Figure 7**). The results described above indicate that the overexpression of *Foxa1*, *Hnf1b*, *Dll1*, *Pbx1*, and *Rfx3* was able to increase transdifferentiation efficiency and improve maturity of IPCs; *Foxa1*, *Pbx1*, and *Rfx3* exerted the most significant effects.

siRNA-Mediated Genes Silencing

Each gene was designed with three siRNAs (**Supplementary Table 5** in **Supplementary Material 3**), and the one with the highest silencing efficiency was selected. The canine ADMSCs were transfected with the siRNAs every 7 days. After transfection, cells were induced with procedure 5 (grouped into: FOXA1 SiRNA + Procedure 5, HNF1B SiRNA + Procedure 5, DLL1 SiRNA + Procedure 5, PBX1 SiRNA + Procedure 5, RFX3 SiRNA + Procedure 5).

After *Foxa1*, *Hnf1b*, *Dll1*, *Pbx1*, and *Rfx3* were separately silenced, the cells showed aggregation, but numbers of clusters were significantly less than those of the non-silenced groups (**Figure 8A**). When the cells were subjected to the glucose stimulation test, it was found that the ability of the cells to secrete insulin decreased compared with the non-silenced groups; secretion declined significantly with FOXA1 siRNA, PBX1 siRNA, and RFX3 siRNA, indicating that the transdifferentiation efficiency of the cells was reduced after genes silencing (**Figure 8B**). Decreases in the glucose SI indicated reduced

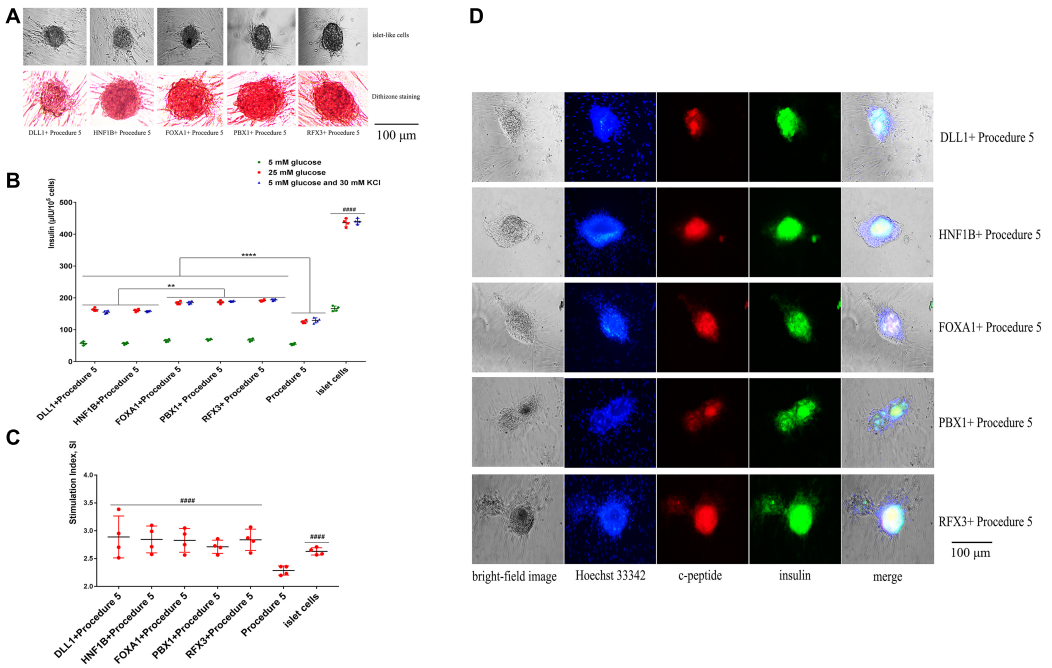


FIGURE 6 | Functional verification of the *Foxa1*, *Hnf1b*, *Dll1*, *Pbx1*, and *Rfx3*. **(A)** The cells agglomerated into a spherical shape, with obvious islet-like cells. The cells were stained with dithizone, and the cells could be dyed red. **(B)** After the stimulation of low glucose (5 mM), high glucose (25 mM), 5 mM glucose, and 30 mM KCl, the secretion of insulin in procedure 5 was significantly lower than that of genes overexpression groups (****$p < 0.0001$). The secretion of insulin in FOXA1 + Procedure 5, PBX1 + Procedure 5, and RFX3 + Procedure 5 was highest (**$p < 0.01$), but they were all lower than the mature islet cells group (####$p < 0.0001$) ($n = 4$). **(C)** The glucose stimulation index of genes overexpression is greater than 2.5, and higher than procedure 5 (####$p < 0.0001$) ($n = 4$). **(D)** Immunofluorescence staining of insulin and c-peptide showed that the cells were insulin and c-peptide positive. Green was insulin, red was c-peptide, and Hoechst 33342 made the nucleus blue.

sensitivity to glucose with FOXA1 siRNA, PBX1 siRNA, and RFX3 siRNA (**Figure 8C**). The expression of islet-specific transcription factors was detected by RT-qPCR (Canine ADMSCs were used as the control group, and *GADPH* was used as the reference gene, the relative expression of the genes calculated by 2ˆ-△△Ct) (primers listed in **Supplementary Table 1** in **Supplementary Material 2**), and it was found that the expression of *Pdx1*, *MafA*, *Nkx6.1*, *Nkx2.2*, *Pax4*, *Pcsk1*, and *Ins* genes was reduced when *Foxa1*, *Hnf1b*, *Dll1*, *Pbx1*, and *Rfx3* genes were separately silenced compared with the non-silenced groups. FOXA1 siRNA, PBX1 siRNA, and RFX3 siRNA decreased most significantly (**Figure 8D**). These results indicate that *Foxa1*, *Hnf1b*, *Dll1*, *Pbx1*, and *Rfx3* were silenced, and the transdifferentiation efficiency and IPC maturity were depressed, the transdifferentiation efficiency most significantly decreasing after the silencing of *Foxa1*, *Pbx1*, and *Rfx3*.

DISCUSSION

Transdifferentiation of Canine ADMSCs Into IPCs

Retinoic acid and fibroblast growth factor are essential for pancreatic development, at present, most procedures include agonists for these signaling pathways (Bhushan et al., 2001; Molotkov et al., 2005). However, bone morphogenetic protein (BMP) signaling has been shown to promote choice of liver destiny rather than pancreas development (Wandzioch and Zaret, 2009). Accordingly, several procedures involve BMP inhibitors. However, it has also been suggested that BMP inhibitors should be eliminated because they have been shown to promote premature endocrine differentiation and damage PDX1/NKX6.1 positive cells (Russ et al., 2015). Studies have shown that histone deacetylase inhibitors could significantly improve the morphological grading and insulin secretion of islet cells (Ikemoto et al., 2018). There has also been no consensus on whether other pathway regulators, such as epidermal growth factor (EGF) or protein kinase C (PKC) agonists, should be included in procedures (Rezania et al., 2014; Nostro et al., 2015; Russ et al., 2015).

In this study, we systematically compared five procedures, each of which used different regulators, including agonists and inhibitors of various signaling pathways, transdifferentiation steps, and transdifferentiation times. In procedure 1, cells unable to respond to glucose stimulation, and no islet-like cells appeared in procedure 1. In procedures 2 and 3, insulin secretion and glucose SI were significantly higher than for procedure 1. Procedures 1, 2, and 3 need to be improved to further improve insulin secretion and cell maturity. Insulin secretion and glucose SI were highest in procedures 4 and 5, procedure 5 is higher than procedure 4. In inducing procedures 2, 3, 4, and 5, insulin secretion increased with increasing formation of islet-like cells,

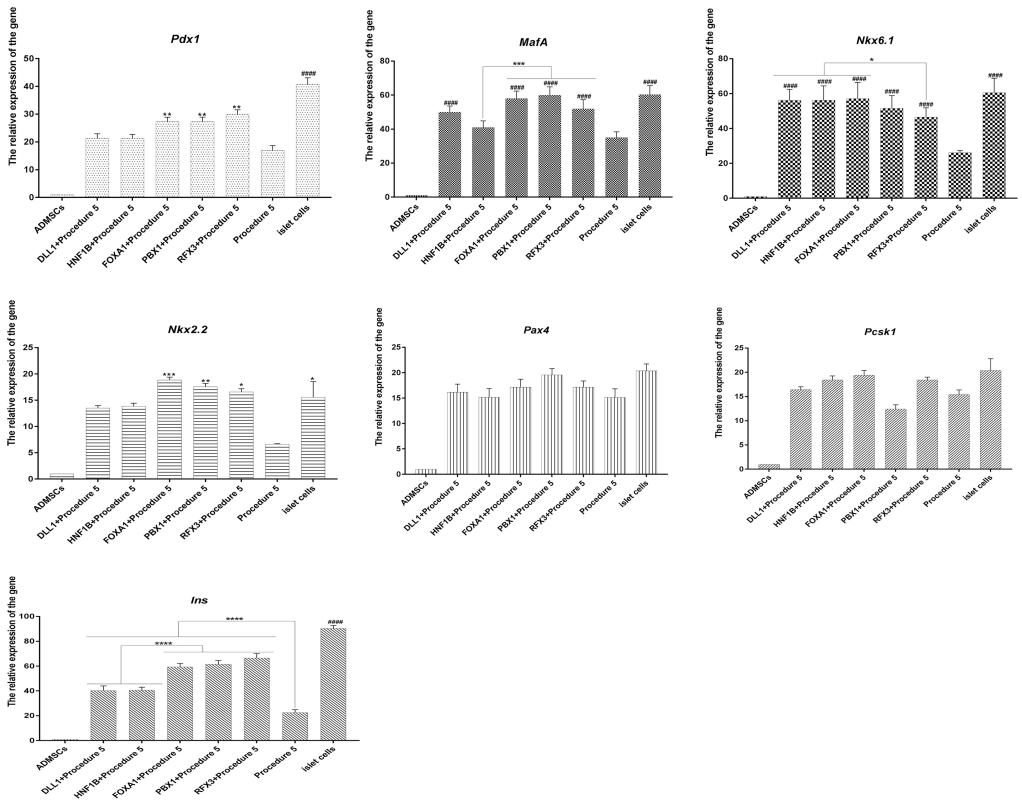


FIGURE 7 | RT-qPCR analysis. The overexpression of *Foxa1*, *Hnf1b*, *Dll1*, *Pbx1*, *Rfx3* can significantly stimulate high expression of islet cascade regulatory genes, with higher expression level than procedure 5. After *Foxa1*, *Pbx1*, and *Rfx3* were overexpressed, the expression of *Pdx1*, *Ins*, and *Nkx2.2* was significantly higher than that of the unexpressed group and *Hnf1b and Dll1* overexpressed groups. There was no significant difference in the expression of *Pax4* and *Pcsk1* (####$p < 0.0001$; ****$p < 0.0001$; ***$p < 0.001$; **$p < 0.01$; *$p < 0.05$).

this suggests that cell formation contributes to the maturation of cells. With respect to cell cluster diameter and the number of cells that a cell cluster contains, a bigger cell cluster is not more favorable. The results in this study showed that the transdifferentiation effect improved as the cell number and diameter of the cell cluster decreased, showing greater insulin secretion, but the optimal cell cluster diameter and number; i.e., the threshold values, are unknown and require further study. In the original study, procedure 1, 2, and 3 can transdifferentiate mesenchymal stem cells into IPCs, and procedure 4, and 5 can transdifferentiate pluripotent stem cells into IPCs. However, in this study, the transdifferentiation efficiency of procedures 4 and 5 was higher than that of procedures 1, 2, and 3, indicating that further modification of procedures 1, 2, and 3 was required, and that the transdifferentiation procedure suitable for induced pluripotent stem cells was also suitable for mesenchymal stem cells, and better efficiency could be obtained. Although procedure 5 achieved a good induction efficiency, it still lagged far behind the insulin secretion capacity of mature islet β-cells, which was caused by the limitations of *in vitro* culture conditions. No matter how perfect the *in vitro* conditions were, they could not be completely the same as the complex *in vivo* development environment. In addition, the transdifferentiation procedures in this study was carried out in two-dimensional mode, which had a certain impact on the efficiency of transdifferentiation. In 2019, Mohammad Foad Abazari et al., found that the expression levels of *Ins*, *Glut2*, and *Pdx1* genes in cells induced by three-dimensional culture were significantly higher than those in cells cultured by two-dimensional culture (Abazari et al., 2020). In the following studies, we will conduct transdifferentiation in three-dimensional mode to explore the changes in genes and metabolic pathways during the transdifferentiation of ADMSCs to IPCs in three-dimensional mode.

In this study, the optimal transdifferentiation procedure (procedure 5) was determined through comparison with various detection methods, and this laid a good foundation for quantitative Absolute Quantitative Transcriptome Sequencing to generate better genetic datasets and identify novel functional genes.

Absolute Quantitative Transcriptome Sequencing in Transdifferentiation of Canine ADMSCs Into IPCs

How is the transdifferentiation of ADMSCs into islet cells different from the maturation process of natural islet cells? What new transcription factors are involved in regulation besides Pdx1,

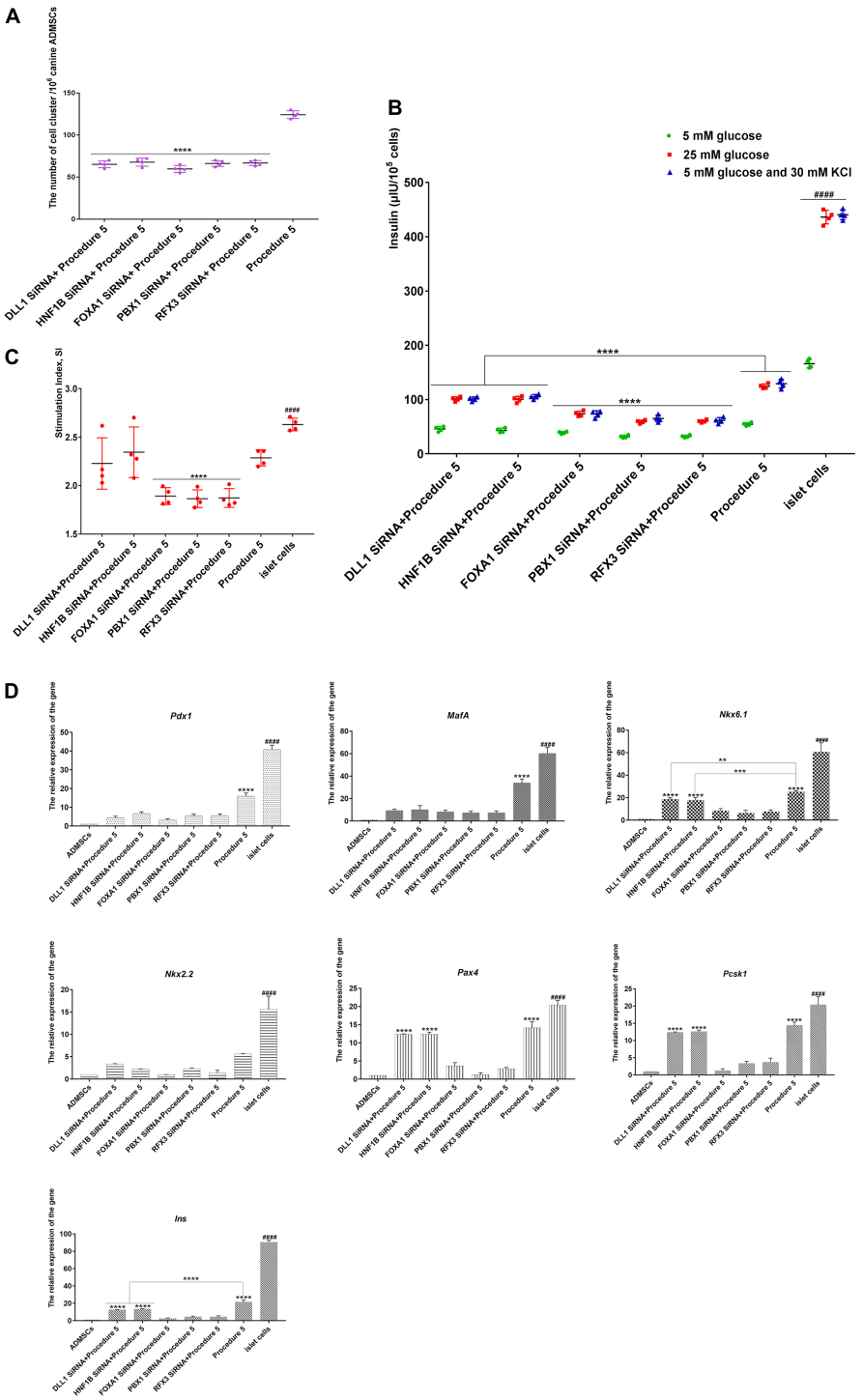


FIGURE 8 | SiRNA-mediated genes silencing. **(A)** After SiRNA infects canine ADMSCs, the numbers of cluster in gene silencing groups were significantly less than that of the non-silenced group (****$p < 0.0001$) ($n = 4$). **(B)** After the stimulation of low glucose (5 mM), high glucose (25 mM), 5 mM glucose, and 30 mM KCl, the secretion of insulin in procedure 5 was significantly higher than that of genes silence groups (****$p < 0.0001$). The secretion of insulin in FOXA1 SiRNA + Procedure 5, PBX1 SiRNA + Procedure 5, and RFX3 SiRNA + Procedure 5 was lowest (****$p<0.0001$), they were all lower than the mature islet cells group (####$p < 0.0001$) ($n = 4$). **(C)** The glucose stimulation index of FOXA1 SiRNA + Procedure 5, PBX1 SiRNA + Procedure 5, and RFX3 SiRNA + Procedure 5 was lower than procedure 5, DLL1 SiRNA + Procedure 5, HNF1B SiRNA + Procedure 5 (****$p < 0.0001$), islet cells group was highest (####$p < 0.01$) ($n = 4$). **(D)** The silence of *Foxa1*, *Hnf1b*, *Dll1*, *Pbx1*, *Rfx3* can reduce expression of islet cascade regulatory genes. Islet cascade regulatory genes were most significantly decreased when *Foxa1*, *Pbx1*, *Rfx3* genes were silenced separately compared with the non-silenced group. After *Foxa1*, *Pbx1*, and *Rfx3* were silenced, the expression of *Nkx6.1*, *Pax4*, *Ins*, and *Pcsk1* was significantly lower than that of the *Hnf1b and Dll1* silencing groups. There was no significant difference in the expression of *Nkx2.2* (****$p < 0.0001$; ***$p < 0.001$; **$p < 0.01$). The expression of all genes was lower than the mature islet cells group (####$p < 0.0001$).

Nkx6.1, Ngn3, and other transcription factors that are known to play an important role.

In 2019, a study evaluated three transdifferentiation procedures, sequenced the resulting pancreatic progenitor cells with mRNA and ATAC, and compared them with a human embryonic pancreatic population. This study defined a common transcriptional and epigenetic signature of PPs, including several genes not previously involved in pancreatic development (Wesolowska-Andersen et al., 2020). In 2020, Wang et al., completed the transdifferentiation of BMSCs into IPCs process and achieved the transcriptome profiling of five samples with two biological duplicates. A total of 11,530 DEGs were revealed in the profiling data. In KEGG enrichment analysis, DEGs are mainly concentrated in tight junction, protein digestion and absorption, pancreatic secretion, focal adhesion, ECM-receptor interaction, Rap1 signaling pathway, and cell cycle, etc. In GO enrichment analysis, DEGs are mainly concentrated in the categories of nucleus, extracellular region, intracellular membrane-bound organelle, the regulation of transcription, regulation of RNA biosynthetic process, carbohydrate metabolic process, single-organism carbohydrate metabolic process and small GTPase-mediated signal transduction, et al. *Sstr2*, *Rps6ka6*, and *Vip* they pick up may regulate decisive genes during the development of transdifferentiation of insulin producing cells (Wang et al., 2021). In this study, Absolute Quantitative Transcriptome Sequencing was used to detect the changes of genes and metabolic pathways during the transdifferentiation of canine ADMSCs into IPCs *in vitro* for the first time. In this sequencing, we obtained a large genetic database, which provided a certain reference for the study of ADMSCs transdifferentiating into IPCs, islet development, and canine gene pool. A total of 15,561 DEGs were revealed in the profiling data, 4031 more DEGs were found than the study by Wang et al. The *Sstr2*, *Rps6ka6*, and *Vip* selected by Wang et al., showed no specificity in this study and were not selected. In GO and KEGG enrichment analysis, the signal pathways and functions enriched by DEGs were also different compared with those studied by Wang et al. Only a few signal pathways were the same. The transcriptome data of the two studies are partly the same, but also partly different. The main reasons are as follows: The first is the comparison between BMSCs and ADMSCs, the second is the application of Absolute Quantitative Transcriptome Sequencing technology, in Absolute Quantitative Transcriptome Sequencing, UMI technology is used to tag each sequence segment to eliminate interference with the quantitative accuracy of the transcriptome by PCR amplification to the maximum extent and to obtain more accurate quantitative analysis results (Kivioja et al., 2011; Islam et al., 2014). And the third is the difference of transdifferentiation procedures. The transdifferentiation procedures (the procedure 3 in this study) used in the study of Wang et al., were found in this study to be of low transdifferentiation efficiency, but this study compared the transdifferentiation procedures. The optimal procedure (procedure 5) was selected for Absolute Quantitative Transcriptome Sequencing. The transcriptome data in this study were more accurate. In procedure 5, after the first stage, we obtained 2546 DEGs; in the second stage, we obtained 2126 DEGs; in the third and fourth stages, we obtained 1402 and 2100 DEGs, respectively; and after transdifferentiation, relative to mature islets cells, we obtained 7387 DEGs. These results suggest that at the end of each transdifferentiation phase, the cells underwent corresponding changes and transdifferentiated toward IPCs, but a large gap with mature islet cells remained. Through GO functional enrichment analysis, we obtained 126 DEGs, and through KEGG pathway enrichment analysis, we obtained 266 DEGs and 18 pathways, all of which are related to islet development and insulin secretion. These data can be further mined and validated. Subsequently, through further bioinformatics analysis such as with protein interaction networks, we identified 18 genes as novel functional genes, which are of great significance for subsequent research.

Novel Functional Genes Can Improve the Transdifferentiation Efficiency

In this study, we obtained 18 novel functional genes, and through verification, we found that 5 novel functional genes may be the key regulators of ADMSCs transdifferentiation into IPCs. Studies have shown that *Foxa1 Hnf1b*, *Dll1*, *Pbx1*, and *Rfx3* plays an important role in the regulatory network that controls the generation of pancreatic endocrine cell lines in model animals (Kim et al., 2002; Ait-Lounis et al., 2010; Gao et al., 2010; De Vas et al., 2015; Rubey et al., 2020). However, the roles of these genes in the transdifferentiation of ADMSCs into IPCs *in vitro* and whether these genes are key regulatory factors remain unknown. Therefore, the functioning of these five novel genes was verified by gene overexpression and silencing.

In overexpression experiments, the results showed that these five genes played an important role in the transdifferentiation of canine ADMSCs into IPCs. They can further improve insulin secretion and glucose SI, significantly improve the transdifferentiation efficiency and IPC maturity, with the most significant effects with *Foxa1*, *Pbx1*, and *Rfx3*. At the same time, the expression of islet development cascade regulation genes was significantly increased, but the specific direct or indirect effects need more research to verify. The solution of these problems can clarify the mechanism of these five genes improving transdifferentiation efficiency. After silencing these five genes, respectively, the transdifferentiation efficiency decreased to varying degrees, with silencing of *Foxa1*, *Pbx1*, and *Rfx3* genes showing significant decrease. This finding may be observed because *Dll1* and *Hnf1b*, when silenced, stimulate cascade regulatory gene expression in other ways; however, after *Foxa1*, *Pbx1*, and *Rfx3* were silenced, no other compensation appeared. This finding also proves the importance of *Foxa1*, *Pbx1*, and *Rfx3* in the transdifferentiation of ADMSCs into IPCs.

The above results prove that the five novel functional genes screened by us are of great significance in transdifferentiating ADMSCs into IPCs *in vitro*; *Foxa1*, *Pbx1*, and *Rfx3* are especially essential in the transdifferentiation of ADMSCs into IPCs and can be used as specifically key regulatory factors. In this study, after the overexpression/silencing of *Foxa1*, *Pbx1*, and *Rfx3*, we continued to conduct *in vitro* induction to explore the role of these three genes in the transdifferentiation of ADMSCs to IPCs.

We will continue to explore the effects of *Foxa1*, *Pbx1*, and *Rfx3* on the function of mature islet β cells in future studies.

CONCLUSION

In this study, canine ADMSCs were transdifferentiated into IPCs using five types of procedures, and the optimal procedure was determined. Many genes and signaling pathways were identified may play an important role in transdifferentiation of ADMSCs into IPCs in Absolute Quantitative Transcriptome Sequencing Analysis. *Hnf1B*, *Dll1*, *Pbx1*, *Rfx3*, and *Foxa1* were found to play important roles in ADMSCs transdifferentiating into IPCs. *Foxa1*, *Pbx1*, *Rfx3* exerted the most significant effects and can be used as specific key regulatory factors in the transdifferentiating of ADMSCs into IPCs. This study establishes a foundation for the further acquisition of IPCs with high maturity.

DATA AVAILABILITY STATEMENT

The datasets presented in this study can be found in online repositories. The names of the repository/repositories and accession number(s) can be found in the article/ **Supplementary Material 18**.

ETHICS STATEMENT

The animal study was reviewed and approved by the Animal Ethical and Welfare Committee of Northwest Agriculture and Forest University (Approval No: 2020002).

AUTHOR CONTRIBUTIONS

PD: methodology, data curation, writing—original draft, writing-review, and editing. JL: methodology, data curation, and writing—original draft. YC: data curation and writing—original draft. LZ: data curation and writing—original draft. XZ: data curation. JW: data curation. GQ: data curation. YZ: funding acquisition, project administration, supervision, writing—review, and editing. All authors contributed to the article and approved the submitted version.

FUNDING

This work was supported by the National Natural Science Foundation of China (Grant No. 31872529), the Natural Science Foundation of Shaanxi Province (Grant No. 2019JZ-16), and the Program of Shaanxi Province Science and Technology Innovation Team (Grant No. 2019TD-036).

ACKNOWLEDGMENTS

We thank one or more of the highly qualified native English-speaking editors at AJE, for editing this manuscript for proper English language, grammar, punctuation, spelling, and overall style.

SUPPLEMENTARY MATERIAL

The Supplementary Material for this article can be found online at: https://www.frontiersin.org/articles/10.3389/fcell.2021.685494/full#supplementary-material

Supplementary Material 1 | Five types of procedures.

Supplementary Material 2 | Canine ADMSC isolation, culture, and identification.

Supplementary Material 3 | All tables.

Supplementary Material 4 | Quality control of sequencing data and the alignment with the reference genome.

Supplementary Material 5 | The regional distribution aligned with the reference genome.

Supplementary Material 6 | The result of genes expression level analysis.

Supplementary Material 7 | DEGs.

Supplementary Material 8 | GO Functional Enrichment Analysis of DEGs.

Supplementary Material 9 | The 20 most significant GO terms for each group.

Supplementary Material 10 | DEGs involved in pancreatic development and insulin secretion.

Supplementary Material 11 | The 20 most significant KEGG pathways for each group.

Supplementary Material 12 | Enrichment Analysis of KEGG Pathways of DEGs.

Supplementary Material 13 | Functional analysis.

Supplementary Material 14 | Protein interaction network analysis.

Supplementary Material 15 | Five novel functional genes (Foxa1, Hnf1b, Dll1, Pbx1, Rfx3) were screened by validation.

Supplementary Material 16 | RT-qPCR Verification of Absolute Quantitative Transcriptome Sequencing.

Supplementary Material 17 | The expression of the target genes and proteins was verified by RT-qPCR and Western-blot.

Supplementary Material 18 | The names of the repository/repositories and accession number(s).

REFERENCES

Abazari, M. F., Nasiri, N., Nejati, F., Zare Karizi, S., Amini Faskhodi, M., Saburi, E., et al. (2020). Comparison of human-induced pluripotent stem cells and mesenchymal stem cell differentiation potential to insulin producing cells in 2D and 3D culture systems in vitro. *J. Cell Physiol.* 235, 4239–4246. doi: 10.1002/jcp.29298

Aigha, I. I., and Abdelalim, E. M. (2020). NKX6.1 transcription factor: a crucial regulator of pancreatic β cell development, identity, and proliferation. *Stem Cell Res. Ther.* 11:459. doi: 10.1186/s13287-020-01977-0

Ait-Lounis, A., Bonal, C., Seguín-Estévez, Q., Schmid, C. D., Bucher, P., Herrera, P. L., et al. (2010). The transcription factor Rfx3 regulates beta-cell differentiation, function, and glucokinase expression. *Diabetes* 59, 1674–1685. doi: 10.2337/db09-0986

Anjum, M. S., Mehmood, A., Mahmood, F., Ali, M., Tarrar, M. N., Khan, S. N., et al. (2018). In vitro preconditioning of insulin-producing cells with growth factors improves their survival and ability to release insulin. *J. Biosci.* 43, 649–659. doi: 10.1007/s12038-018-9796-8

Bahrebar, M., Soleimani, M., Karimi, M. H., Vahdati, A., and Yaghobi, R. (2015). Generation of islet-like cell aggregates from human adipose tissue-derived stem cells by lentiviral overexpression of PDX-1. *Int. J. Organ Transplant. Med.* 6, 61–76.

Bhushan, A., Itoh, N., Kato, S., Thiery, J. P., Czernichow, P., Bellusci, S., et al. (2001). Fgf10 is essential for maintaining the proliferative capacity of epithelial progenitor cells during early pancreatic organogenesis. *Development (Cambridge, England)* 128, 5109–5117. doi: 10.1242/dev.128.24.5109

Borot, S., Crowe, L. A., Parnaud, G., Ris, F., Meier, R., Giovannoni, L., et al. (2013). Quantification of islet loss and graft functionality during immune rejection by 3-tesla MRI in a rat model. *Transplantation* 96, 438–444. doi: 10.1097/TP.0b013e31829b080f

Bruni, A., Gala-Lopez, B., Pepper, A. R., Abualhassan, N. S., and Shapiro, A. J. (2014). Islet cell transplantation for the treatment of type 1 diabetes: recent advances and future challenges. *Diabetes Metab. Syndr. Obes.* 7, 211–223. doi: 10.2147/DMSO.S50789

Cattin, L. (2016). [Diabetes mellitus: etiology, pathophysiology and clinical classification]. *Giornale Italiano Nefrol.* 33:gin/33.S68.6.

Daehwan, K., Ben, L., and Salzberg, S. L. (2015). HISAT: a fast spliced aligner with low memory requirements. *Nat. Methods* 12, 357–360. doi: 10.1038/nmeth.3317

Dayer, D., Tabandeh, M. R., Moghimipour, E., Hashemi Tabar, M., Ghadiri, A., Allah Bakhshi, E., et al. (2019). MafA overexpression: a new efficient protocol for in vitro differentiation of adipose-derived mesenchymal stem cells into functional insulin-producing cells. *Cell J.* 21, 169–178.

Dayer, D., Tabar, M. H., Moghimipour, E., Tabandeh, M. R., Ghadiri, A. A., Bakhshi, E. A., et al. (2017). Sonic hedgehog pathway suppression and reactivation accelerates differentiation of rat adipose-derived mesenchymal stromal cells toward insulin-producing cells. *Cytotherapy* 19, 937–946. doi: 10.1016/j.jcyt.2017.05.003

De Vas, M. G., Kopp, J. L., Heliot, C., Sander, M., Cereghini, S., and Haumaitre, C. (2015). Hnf1b controls pancreas morphogenesis and the generation of Ngn3+ endocrine progenitors. *Development (Cambridge, England)* 142, 871–882. doi: 10.1242/dev.110759

Flenniken, M. L., and Andino, R. (2013). Non-specific dsRNA-mediated antiviral response in the honey bee. *PLoS One* 8:e77263. doi: 10.1371/journal.pone.0077263

Gamble, A., Pepper, A. R., and Bruni, A. (2018). The journey of islet cell transplantation and future development. *Islets* 10, 80–94. doi: 10.1080/19382014.2018.1428511

Gao, N., Le Lay, J., Qin, W., Doliba, N., Schug, J., Fox, A. J., et al. (2010). Foxa1 and Foxa2 maintain the metabolic and secretory features of the mature beta-cell. *Mol. Endocrinol. (Baltimore, Md.)* 24, 1594–1604. doi: 10.1210/me.2009-0513

Ghoneim, M. A., Refaie, A. F., Elbassiouny, B. L., Gabr, M. M., and Zakaria, M. M. (2020). From mesenchymal stromal/stem cells to insulin-producing cells: progress and challenges. *Stem Cell Rev. Rep.* 16, 1156–1172. doi: 10.1007/s12015-020-10036-3

Harreiter, J., and Roden, M. (2019). [Diabetes mellitus-definition, classification, diagnosis, screening and prevention (Update 2019)]. *Wien. Klin. Wochenschr.* 131, 6–15. doi: 10.1007/s00508-019-1450-4

Ikemoto, T., Feng, R., Shimada, M., Saito, Y., Iwahashi, S., Morine, Y., et al. (2018). A new 2-Stp acceleration protocol using a histone deacetylase inhibitor to generate insulin-producing cells from adipose-derived mesenchymal stem cells. *Pancreas* 47, 477–481. doi: 10.1097/MPA.0000000000001017

Islam, S., Zeisel, A., Joost, S., La Manno, G., Zajac, P., Kasper, M., et al. (2014). Quantitative single-cell RNA-seq with unique molecular identifiers. *Nat. Methods* 11, 163–166. doi: 10.1038/nmeth.2772

Kim, S. C., Han, D. J., and Lee, J. Y. (2010). Adipose tissue derived stem cells for regeneration and differentiation into insulin-producing cells. *Curr. Stem Cell Res. Ther.* 5, 190–194. doi: 10.2174/157488810791268717

Kim, S. K., Selleri, L., Lee, J. S., Zhang, A. Y., Gu, X., Jacobs, Y., et al. (2002). Pbx1 inactivation disrupts pancreas development and in Ipf1-deficient mice promotes diabetes mellitus. *Nat. Genet.* 30, 430–435. doi: 10.1038/ng860

Kivioja, T., Vähärautio, A., Karlsson, K., Bonke, M., Enge, M., Linnarsson, S., et al. (2011). Counting absolute numbers of molecules using unique molecular identifiers. *Nat. Methods* 9, 72–74. doi: 10.1038/nmeth.1778

Li, H. T., Jiang, F. X., Shi, P., Zhang, T., Liu, X. Y., Lin, X. W., et al. (2017). In vitro reprogramming of rat bmMSCs into pancreatic endocrine-like cells. In vitro cellular & developmental biology. *Animal* 53, 157–166. doi: 10.1007/s11626-016-0087-0

Limbert, C., Path, G., Ebert, R., Rothhammer, V., Kassem, M., Jakob, F., et al. (2011). PDX1- and NGN3-mediated in vitro reprogramming of human bone marrow-derived mesenchymal stromal cells into pancreatic endocrine lineages. *Cytotherapy* 13, 802–813. doi: 10.3109/14653249.2011.571248

Livak, K. J., and Schmittgen, T. D. (2001). Analysis of relative gene expression data using real-time quantitative PCR and the 2(-Delta Delta C(T)) Method. *Methods (San Diego, Calif.)* 25, 402–408. doi: 10.1006/meth.2001.1262

Mohamed, G. A., Hala, A. A., Mahmoud, E. A., Nashwa, E. M., and Sherry, K. M. (2016). Differentiation of bone marrow-derived mesenchymal stem cells in diabetic patients into islet-like insulinproducing cells: a new era in the treatment of diabetes. *Egypt. J. Pathol.* 36, 87–94. doi: 10.1097/01.XEJ.0000484379.67282.f8

Molotkov, A., Molotkova, N., and Duester, G. (2005). Retinoic acid generated by Raldh2 in mesoderm is required for mouse dorsal endodermal pancreas development. *Dev. Dyn.* 232, 950–957. doi: 10.1002/dvdy.20256

Nolan, T., Hands, R. E., and Bustin, S. A. (2006). Quantification of mRNA using real-time RT-PCR. *Nat. Protocols* 1, 1559–1582. doi: 10.1038/nprot.2006.236

Nostro, M. C., Sarangi, F., Yang, C., Holland, A., Elefanty, A. G., Stanley, E. G., et al. (2015). Efficient generation of NKX6-1+ pancreatic progenitors from multiple human pluripotent stem cell lines. *Stem Cell Rep.* 4, 591–604. doi: 10.1016/j.stemcr.2015.02.017

Pagliuca, F. W., Millman, J. R., Gürtler, M., Segel, M., Van Dervort, A., Ryu, J. H., et al. (2014). Generation of functional human pancreatic β cells in vitro. *Cell* 159, 428–439. doi: 10.1016/j.cell.2014.09.040

Palumbo, P., Miconi, G., Cinque, B., La Torre, C., Lombardi, F., Zoccali, G., et al. (2015). In vitro evaluation of different methods of handling human liposuction aspirate and their effect on adipocytes and adipose derived stem cells. *J. Cell. Physiol.* 230, 1974–1981. doi: 10.1002/jcp.24965

Pavathuparambil Abdul Manaph, N., Sivanathan, K. N., Nitschke, J., Zhou, X. F., Coates, P. T., and Drogemuller, C. J. (2019). An overview on small molecule-induced differentiation of mesenchymal stem cells into beta cells for diabetic therapy. *Stem Cell Res. Ther.* 10:293. doi: 10.1186/s13287-019-1396-5

Pertea, M., Pertea, G. M., Antonescu, C. M., Chang, T. C., Mendell, J. T., and Salzberg, S. L. (2015). StringTie enables improved reconstruction of a transcriptome from RNA-seq reads. *Nat. Biotechnol.* 33, 290–295. doi: 10.1038/nbt.3122

Petersmann, A., Müller-Wieland, D., Müller, U. A., Landgraf, R., Nauck, M., Freckmann, G., et al. (2019). Definition, classification and diagnosis of diabetes mellitus. *Exp. Clin. Endocrinol. Diabetes* 127, S1–S7. doi: 10.1055/a-1018-9078

Raposio, E., Simonacci, F., and Perrotta, R. E. (2017). Adipose-derived stem cells: Comparison between two methods of isolation for clinical applications. *Ann. Med. Surg.* 20, 87–91. doi: 10.1016/j.amsu.2017.07.018

Rezania, A., Bruin, J. E., Arora, P., Rubin, A., Batushansky, I., Asadi, A., et al. (2014). Reversal of diabetes with insulin-producing cells derived in vitro from human pluripotent stem cells. *Nat. Biotechnol.* 32, 1121–1133. doi: 10.1038/nbt.3033

Rezania, A., Bruin, J. E., Riedel, M. J., Mojibian, M., Asadi, A., Xu, J., et al. (2012). Maturation of human embryonic stem cell-derived pancreatic progenitors into functional islets capable of treating pre-existing diabetes in mice. *Diabetes* 61, 2016–2029. doi: 10.2337/db11-1711

Rickels, M. R., and Robertson, R. P. (2019). Pancreatic islet transplantation in humans: recent progress and future directions. *Endocr. Rev.* 40, 631–668. doi: 10.1210/er.2018-00154

Roberts, A. (2011). Improving RNA-Seq expression estimates by correcting for fragment bias. *Genome Biol.* 12:R22. doi: 10.1186/gb-2011-12-3-r22

Robinson, M. D., McCarthy, D. J., and Smyth, G. K. (2010). edgeR: a bioconductor package for differential expression analysis of digital gene expression data. *Bioinformatics* 26, 139–140. doi: 10.1093/bioinformatics/btp616

Rubey, M., Chhabra, N. F., Gradinger, D., Sanz-Moreno, A., Lickert, H., Przemeck, G. K. H., et al. (2020). DLL1- and DLL4-Mediated notch signaling is essential

for adult pancreatic islet homeostasis. *Diabetes* 69, 915–926. doi: 10.2337/db19-0795

Russ, H. A., Parent, A. V., Ringler, J. J., Hennings, T. G., Nair, G. G., Shveygert, M., et al. (2015). Controlled induction of human pancreatic progenitors produces functional beta-like cells in vitro. *EMBO J.* 34, 1759–1772. doi: 10.15252/embj.201591058

Shahjalal, H. M., Abdal Dayem, A., Lim, K. M., Jeon, T. I., and Cho, S. G. (2018). Generation of pancreatic β cells for treatment of diabetes: advances and challenges. *Stem Cell Res. Ther.* 9:355. doi: 10.1186/s13287-018-1099-3

Sleight, S. C., Bartley, B. A., Lieviant, J. A., and Sauro, H. M. (2010). In-fusion BioBrick assembly and re-engineering. *Nucleic Acids Res.* 38, 2624–2636. doi: 10.1093/nar/gkq179

Sun, Y., Chen, L., Hou, X. G., Hou, W. K., Dong, J. J., Sun, L., et al. (2007). Differentiation of bone marrow-derived mesenchymal stem cells from diabetic patients into insulin-producing cells in vitro. *Chin. Med. J.* 120, 771–776. doi: 10.1097/00029330-200705010-00007

Takemura, S., Shimizu, T., Oka, M., Sekiya, S., and Babazono, T. (2019). Transplantation of adipose-derived mesenchymal stem cell sheets directly into the kidney suppresses the progression of renal injury in a diabetic nephropathy rat model. *J. Diabetes Investig.* 11, 545–553. doi: 10.1111/jdi.13164

Tokuda, K., Ikemoto, T., Saito, Y., Miyazaki, K., Yamashita, S., Yamada, S., et al. (2020). The fragility of cryopreserved insulin-producing cells differentiated from adipose-tissue-derived stem cells. *Cell Transplant.* 29:963689720954798. doi: 10.1177/0963689720954798

Vieira, N. M., Brandalise, V., Zucconi, E., Secco, M., Strauss, B. E., and Zatz, M. (2010). Isolation, characterization, and differentiation potential of canine adipose-derived stem cells. *Cell Transplant.* 19, 279–289. doi: 10.3727/096368909X481764

Wada, Y., and Ikemoto, T. (2019). The differences in the characteristics of insulin-producing cells using human adipose-tissue derived mesenchymal stem cells from subcutaneous and visceral tissues. *Sci. Rep.* 9:13204. doi: 10.1038/s41598-019-49701-0

Wandzioch, E., and Zaret, K. S. (2009). Dynamic signaling network for the specification of embryonic pancreas and liver progenitors. *Science (New York, N.Y.)* 324, 1707–1710. doi: 10.1126/science.1174497

Wang, J., Dai, P., Gao, D., Zhang, X., Ruan, C., Li, J., et al. (2020). Genome-wide analysis reveals changes in long noncoding RNAs in the differentiation of canine bmscs into insulin-producing cells. *Int. J. Mol. Sci.* 21:5549. doi: 10.3390/ijms21155549

Wang, J., Dai, P., Zou, T., Lv, Y., Zhao, W., Zhang, X., et al. (2021). Transcriptome analysis of the transdifferentiation of canine BMSCs into insulin producing cells. *BMC Genomics* 22:134. doi: 10.1186/s12864-021-07426-3

Wesolowska-Andersen, A., Jensen, R. R., Alcántara, M. P., Beer, N. L., Duff, C., Nylander, V., et al. (2020). Analysis of differentiation protocols defines a common pancreatic progenitor molecular signature and guides refinement of endocrine differentiation. *Stem Cell Rep.* 14, 138–153. doi: 10.1016/j.stemcr.2019.11.010

Xu, L., Xu, C., Zhou, S., Liu, X., Wang, J., Liu, X., et al. (2017). PAX4 promotes PDX1-induced differentiation of mesenchymal stem cells into insulin-secreting cells. *Am. J. Trans. Res.* 9, 874–886.

Young, M. D., Wakefield, M. J., Smyth, G. K., and Alicia, O. (2010). Gene ontology analysis for RNA-seq: accounting for selection bias. *Genome Biol.* 11, R14–R14. doi: 10.1186/gb-2010-11-2-r14

Zhang, J., Zhou, S., Zhou, Y., Feng, F., Wang, Q., Zhu, X., et al. (2016). Adipose-derived mesenchymal stem cells (ADSCs) with the potential to ameliorate platelet recovery, enhance megakaryopoiesis, and inhibit apoptosis of bone marrow cells in a mouse model of radiation-induced thrombocytopenia. *Cell Transplant.* 25, 261–273. doi: 10.3727/096368915X688155

Zhang, T., Wang, H., Wang, T., Wei, C., Jiang, H., Jiang, S., et al. (2019). Pax4 synergistically acts with Pdx1, Ngn3 and MafA to induce HuMSCs to differentiate into functional pancreatic β-cells. *Exp. Ther. Med.* 18, 2592–2598. doi: 10.3892/etm.2019.7854

Zhang, Y., Shen, W., Hua, J., Lei, A., Lv, C., Wang, H., et al. (2010). Pancreatic islet-like clusters from bone marrow mesenchymal stem cells of human first-trimester abortus can cure streptozocin-induced mouse diabetes. *Rejuvenation Res.* 13, 695–706. doi: 10.1089/rej.2009.1016

Zhu, Y., Liu, Q., Zhou, Z., and Ikeda, Y. (2017). PDX1, Neurogenin-3, and MAFA: critical transcription regulators for beta cell development and regeneration. *Stem Cell Res. Ther.* 8:240. doi: 10.1186/s13287-017-0694-z

Zuk, P. A., Zhu, M., Mizuno, H., Huang, J., Futrell, J. W., Katz, A. J., et al. (2001). Multilineage cells from human adipose tissue: implications for cell-based therapies. *Tissue Eng.* 7, 211–228. doi: 10.1089/107632701300062859

Conflict of Interest: The authors declare that the research was conducted in the absence of any commercial or financial relationships that could be construed as a potential conflict of interest.

Copyright © 2021 Dai, Li, Chen, Zhang, Zhang, Wang, Qi and Zhang. This is an open-access article distributed under the terms of the Creative Commons Attribution License (CC BY). The use, distribution or reproduction in other forums is permitted, provided the original author(s) and the copyright owner(s) are credited and that the original publication in this journal is cited, in accordance with accepted academic practice. No use, distribution or reproduction is permitted which does not comply with these terms.

frontiers in Cell and Developmental Biology

ORIGINAL RESEARCH
published: 20 September 2021
doi: 10.3389/fcell.2021.723057

Characterized the Adipogenic Capacity of Adipose-Derived Stem Cell, Extracellular Matrix, and Microenvironment With Fat Components Grafting

Wenqing Jiang[1†], Junrong Cai[1†], Jingyan Guan[1], Yunjun Liao[1], Feng Lu[1], Jingjing Ma[2], Jianhua Gao[1‡] and Yuteng Zhang[1*‡]*

[1] Department of Plastic and Cosmetic Surgery, Nanfang Hospital, Southern Medical University, Guangzhou, China,
[2] Department of Plastic Surgery, Sir Run Run Shaw Hospital, School of Medicine, Zhejiang University, Hangzhou, China

OPEN ACCESS

Edited by:
Yu-Chen Hu,
National Tsing Hua University, Taiwan

Reviewed by:
Hong Ouyang,
Sun Yat-sen University, China
Alice Busato,
University of Verona, Italy

***Correspondence:**
Jianhua Gao
doctorgaojianhua@outlook.com
Yuteng Zhang
doctoryuteng@gmail.com

[†] These authors have contributed equally to this work and share first authorship

[‡] These authors have contributed equally to this work and share last authorship

Specialty section:
This article was submitted to Stem Cell Research, a section of the journal Frontiers in Cell and Developmental Biology

Received: 09 June 2021
Accepted: 31 August 2021
Published: 20 September 2021

Citation:
Jiang W, Cai J, Guan J, Liao Y, Lu F, Ma J, Gao J and Zhang Y (2021) Characterized the Adipogenic Capacity of Adipose-Derived Stem Cell, Extracellular Matrix, and Microenvironment With Fat Components Grafting. Front. Cell Dev. Biol. 9:723057. doi: 10.3389/fcell.2021.723057

Background: Autologous fat grafting has been a widely used technique; however, the role of adipose-derived stem cells (ASCs), extracellular matrix (ECM), and microenvironment in fat regeneration are not fully understood.

Methods: Lipoaspirates were obtained and processed by inter-syringe shifting to remove adipocytes, yielding an adipocyte-free fat (Aff). Aff was then exposed to lethal dose of radiation to obtain decellularized fat (Df). To further remove microenvironment, Df was rinsed with phosphate-buffered saline (PBS) yielding rinsed decellularized fat (Rdf). Green fluorescent protein (GFP) lentivirus (LV-GFP)-transfected ASCs were added to Df to generate cell-recombinant decellularized fat (Crdf). Grafts were transplanted subcutaneously into nude mice and harvested over 3 months.

Results: Removal of adipocytes (Aff) didn't compromise the retention of fat grafts, while additional removal of stromal vascular fraction (SVF) cells (Df) and microenvironment (Rdf) resulted in poor retention by day 90 (Aff, 82 ± 7.1% vs. Df, 28 ± 6.3%; $p < 0.05$; vs. Rdf, 5 ± 1.2%; $p < 0.05$). Addition of ASCs to Df (Crdf) partially restored its regenerative potential. Aff and Crdf exhibited rapid angiogenesis and M2-polarized macrophages infiltration, in contrast to impaired angiogenesis and M1-polarized inflammatory pattern in Df. GFP + ASCs participated in angiogenesis and displayed a phenotype of endothelial cells in Crdf.

Conclusion: Adipose ECM and microenvironment have the capacity to stimulate early adipogenesis while ECM alone cannot induce adipogenesis *in vivo*. By directly differentiating into endothelial cells and regulating macrophage polarization, ASCs coordinate early adipogenesis with angiogenesis and tissue remodeling, leading to better long-term retention and greater tissue integrity.

Keywords: fat grafting, adipogenesis, adipose-derived stem cell, extracellular matrix, microenvironment

INTRODUCTION

Autologous fat grafting has increasingly been applied to promote volume augmentation and facilitate tissue regeneration, and progress in this field has been rapid (Strong et al., 2015; Khouri, 2017). However, the retention rate of mass volume engraftment remains suboptimal, and complications are unpredictable (Yoshimura and Coleman, 2015; Groen et al., 2016; Lv et al., 2020). Due to the interdependent dynamic changes of various components during grafting, the technique for ideal fat grafting remains controversial.

The "cell replacement theory" describes three different outcomes from the periphery to the center of the graft: survival, regeneration, and necrosis. As transplant volume increases, the most central adipocytes in the graft undergo ischemic necrosis (Kato et al., 2014; Mashiko and Yoshimura, 2015). The necrotic and regenerative ratios of the transplanted tissue will determine the final tissue retention and morphotype (Dong et al., 2015). To improve regenerative outcomes, it is essential to elucidate the detailed mechanisms underlying the components of fat grafts.

Adipocytes constitute about 90% of graft volume (Rotondo et al., 2016). Severe ischemia and hypoxia after avascular grafting limit the function of these cells, and most undergo apoptosis before re-vascularization. By contrast, nucleated stromal cells, especially adipose-derived stem cells (ASCs), are capable of surviving extreme circumstances and actively contributing to tissue regeneration (Suga et al., 2010). Studies of ASCs have revealed that these cells have a variety of functions, including enhanced proliferation, migration, and paracrine angiogenic cytokines, which make them more likely to survive the hypoxic insult of transplantation and expedite vascularization (Kang et al., 2014). In conjunction with supplemental ASCs or SVF, the cell-assisted lipotransfer (CAL) technique has had promising effects on retention and graft quality, yielding considerably higher residual volumes and less necrotic tissue (Kolle et al., 2013; Toyserkani et al., 2016; Zhou et al., 2016). Together, these results suggest that ASCs have tremendous potential for promoting fat regeneration.

Meanwhile, the extracellular matrix (ECM) and microenvironment of adipose tissue also play an essential role in fat regeneration (Flynn, 2010; Wu et al., 2012; Sano et al., 2014). Recent studies illustrated the adipoinduction potential and prospective volume retention rate of Allograft Adipose Matrix (AAM) (Giatsidis et al., 2019). Kokai et al. (2019) applied AAM allogenetically in a clinical trial; the material achieved a 44 ± 16% retention rate after 24 weeks *in vivo* by inducing host-derived vascular invasion and adipose regeneration (Kokai et al., 2019). This study showed for the first time that AAM promotes adipose regeneration. Moreover, in a murine model, by significantly improving recellularization and angiogenesis, ASC-seeded decellularized adipose matrix improved long-term retention after transplantation (Turner et al., 2012; Han et al., 2015; Trivanovic et al., 2018). However, the role of each component of fat tissue in fat grafting is still unclear. Elucidating the relationship among ASCs, ECM and microenvironment will provide insight into the essential elements of adipose regeneration and contribute to the development of adipose transplantation procedures.

In this study, we used different mechanical processes to alter the components in fat tissue and test the relevant fat products' retention rate. Inter-syringe shifting and centrifugation were used to remove most adipocytes, but preserved the SVF cells and original ECM (Yao et al., 2017). By further eliminating the SVF cells in the fat tissue, radiation is applied to the fat tissue and resulted in a cell-free adipose tissue which is mainly comprised of ECM and the soluble proteins (microenvironment) (Jonathan et al., 1999; Favaudon et al., 2014). This product is furthered rinsed to remove the soluble proteins to explore the role of microenvironment in fat tissue. By removing different components in fat tissue step by step, it is possible to assess the orchestration among ASCs, ECM, and microenvironment after fat grafting.

MATERIALS AND METHODS

Preparation of Adipocyte-Free Fat (Aff), Decellularized Fat (Df), and Rinsed Decellularized Fat (Rdf)

Human lipoaspirates were obtained using standard Coleman methods from 11 healthy women, with mean ± SD age of 33.4 ± 6.3 years and mean ± SD body mass index of 23.2 ± 1.9 kg/m2. To remove adipocytes, fat was mechanically emulsified by shifting between two regular syringes. The emulsified fat was then centrifuged to remove the upper layer of oil. The lower layer was used as Aff. To remove SVF cells, the prepared Aff was subjected to lethal radiation at a rate of 300 cGy/min for 40 min using the 6 MV photon beam of the Varian 23EX linear accelerator (Varian Medical Systems, Palo Alto, CA, United States) and the resulted product was termed as Df. To remove the soluble proteins, the prepared Df was rinsed three times with PBS and centrifuged at 1,200 *g* for 3 min to obtain Rdf.

Scanning Electron Microscopy

Samples were fixed with 2% glutaraldehyde in 0.1 M phosphate buffer, postfixed in 1% osmium tetroxide in the same buffer for 1 h, dehydrated in increasing concentrations of acetone, critical-point dried, fixed to stubs with colloidal silver, sputtered with gold using a MED 010 coater, and examined under an S-3000N scanning electron microscope (Hitachi, Ltd., Tokyo, Japan).

Isolation and Culture of Adipose-Derived Stem Cells

Adipocyte-free fat and decellularized fat were washed with PBS and digested with 0.075% type I collagenase (Sigma-Aldrich, St. Louis, MO, United States). After inactivation of collagenase activity, the cell suspension was filtered through a 40 μm cell strainer (BD Biosciences, San Jose, CA, United States) and centrifuged at 1,200 *g* for 3 min. Red blood cell lysis buffer (Leagene Biotech, Beijing, China) was used to remove erythrocytes. The cells were then collected by removal of supernatant, and then resuspended in human adipose-derived

mesenchymal stem cell complete medium (Cyagen, Santa Clara, CA, United States). Cell viability was investigated 72 h after culture using the Live/Dead assay kit (Invitrogen, Carlsbad, CA, United States).

Recombination of Green Fluorescent Protein-Transfected Adipose-Derived Stem Cells to Decellularized Fat (Cell-Recombinant Decellularized Fat)

LV vectors containing green fluorescent protein (GFP) were constructed and designated as LV-GFP (GeneChem, Shanghai, China). ASCs isolated from Aff were transfected with LV-GFP at a multiplicity of infection (MOI) of 80 in the presence of Polybrene (6 μg/ml) for 8 h. After 12 h, the supernatant was replaced with culture medium. Crdf was generated by mixture of 5 × 105 transfected cells per 1 ml Df by gentle shaking.

Graft Model in Nude Mice

All animal experiments were approved by the Nanfang Hospital Institutional Animal Care and Use Committee and performed according to the guidelines of the National Health and Medical Research Council (People's Republic of China). Nude mice (aged 6–8 weeks) were housed in individual cages with a 12 h light/dark cycle and provided with standard food and water *ad libitum*. Both dorsal flanks of each mouse were injected subcutaneously with 0.3 ml Aff, Df, Rdf, or Crdf using a 1 ml syringe with a blunt infiltration cannula. Each recipient site was numbered and assigned to the four groups randomly. The grafts were injected in a hemispherical shape. Five animals in each group were sacrificed at 7, 15, 30, 60, and 90 days after injection. At the time of sacrifice, the grafts were harvested and carefully separated from surrounding tissue, and their volumes were measured. Each harvested sample was assessed histologically and immunohistochemically.

Histologic Examination

Tissue samples were fixed in 4% paraformaldehyde (BD Biosciences), dehydrated, and embedded in paraffin. Tissue blocks were sectioned for staining with hematoxylin and eosin staining or Masson's trichrome staining, examined under a BX51 microscope (Olympus, Tokyo, Japan), and imaged using a DP71 digital camera (Olympus). Total collagen content was reported as the percentage of the total tissue area positively stained with aniline blue, as determined using ImageJ (National Institutes of Health, Bethesda, MD, United States) software.

Immunofluorescence Staining

Sample sections were stained with the following primary antibodies: rat anti-mouse Mac2 (1:200; Cedarlane Corp., Burlington, ON, Canada), rabbit anti-mouse CD206 (1:300; Abcam, Cambridge, MA, United States), goat anti-mouse perilipin-1 (1:200; Abcam), rat anti-mouse CD31 (1:200; Invitrogen, North Ryde, NSW, Australia), and rabbit anti-human alpha-smooth muscle actin (α-SMA) (1:200; Abcam). After washing, the samples were incubated with donkey anti-rat-555 immunoglobulin G (1:200; Abcam), donkey anti-goat-594 immunoglobulin G (1:200; Abcam) and donkey anti-rabbit-488 immunoglobulin G (1:200; Abcam) secondary antibodies. Nuclei were stained with DAPI (Sigma). The samples were examined under a TCS SP2 confocal microscope (Leica Microsystems GmbH, Wetzlar, Germany). Leica LAS AF software was used for images analysis.

Enzyme-Linked Immunosorbent Assay (ELISA)

Enzyme-linked immunosorbent assay assays (Enzyme-linked Biotechnology, Shanghai, China) were performed to detect the levels of vascular endothelial growth factor (VEGF), basic fibroblast growth factor (bFGF), and transforming growth factor-β1 (TGFβ1) within Aff, Df or Rdf. Briefly, 1 ml of freshly prepared sample was mixed with 1 ml PBS and centrifuged at 1,200 *g* for 3 min. Extracted media were collected and subjected to sandwich ELISA assay.

Quantitative Reverse Transcription Polymerase Chain Reaction (RT-PCR)

Fat tissue was excised, snap-frozen in liquid nitrogen, and stored at −80°C. Total RNA was extracted using TRIzol Reagent (Invitrogen) according to the manufacturer's protocol. All primers shown in **Table 1** designed for this study were determined through established GenBank sequences. The level of target gene was normalized to the housekeeping gene glyceraldehyde 3-phosphate dehydrogenase (GAPDH) and analyzed with the ABI PRISM 7500 Sequence Detection System with the SYBR Green PCR Master Mix (Sigma).

Statistical Analysis

Data were expressed as mean ± SEM and analyzed by repeated-measures analysis of variance. Independent *t*-tests were used to compare the two groups of mice at single time points, and one-way analysis of variance was used to compare the groups at all time points. A value of $p < 0.05$ was considered statistically significant.

TABLE 1 | Primer sequences for real-time RT-PCR.

Gene	Forward	Reverse
IL-10	5′ -AGTGGAGCAGGTGAAGAGTG-3′	5′ -TTCGGAGAGAGGTACAAACG-3′
PPARγ	5′ -AGAACCTGCATCTCCACCTT-3′	5′ -ACAGACTCGGCACTCAATGG-3′
bFGF	5′ -AGCGGCTCTACTGCAAGAAC-3′	5′ -CCGTCCATCTTCCTTCATAG-3′
LPL	5′ -AAGAAAACCCCAGCAAGGCA-3′	5′ -TAGCCCAGATTGTTACAGCGA-3′
C/EBPβ	5′ -CAAGCTGAGCGACGAGTACA-3′	5′ -TCAGCTCCAGCACCTTGTG-3′
GAPDH	5′ -ACCCAGAAGACTGTGGATGG-3′	5′ -CACATTGGGGGTAGGAACAC-3′

RESULTS

Removal of Adipose Components in Fat

Stepwise mechanical processes were conducted to fat to obtain Aff, Df, Rdf (**Figure 1A**). Scanning electron microscopy revealed that most of the adipocytes were removed in Aff, Df, and Rdf (**Figure 1B**). Freshly prepared Df and Rdf were examined using Live/Dead and TUNEL staining to measure irradiation-induced cell death and apoptosis relative to that in fresh Aff. The results revealed that after isolation from grafts and culture for 72 h, SVF cells in Df and Rdf exhibited a fragmented and shrunken cell morphology with slow proliferation activity relative to Aff. Df and Rdf had significantly lower cell viability, with most of cells undergoing cell death after 72 h; by contrast, no cell death was observed in Aff (**Figure 1C**). The levels of VEGF, bFGF and TNFβ1 did not significantly differ between the Aff and Df groups, while significantly decreased in Rdf (**Figure 1D**). Due to the irradiation, more apoptotic cells were observed in the Df group and Rdf group than in the Aff group on day 1 after grafting (**Figure 1E**).

Removal of Stromal Vascular Fraction and Microenvironment Impairs Graft Retention

In the next experiments, we harvested Aff, Df, and Rdf at different time points (**Figure 2A**). The Aff and Df grafts showed a similar appearance and texture from days 0 to 90, both covered with a thin, well-vascularized fibrous capsule. While Rdf grafts appeared to be less integrate after day 30 with a

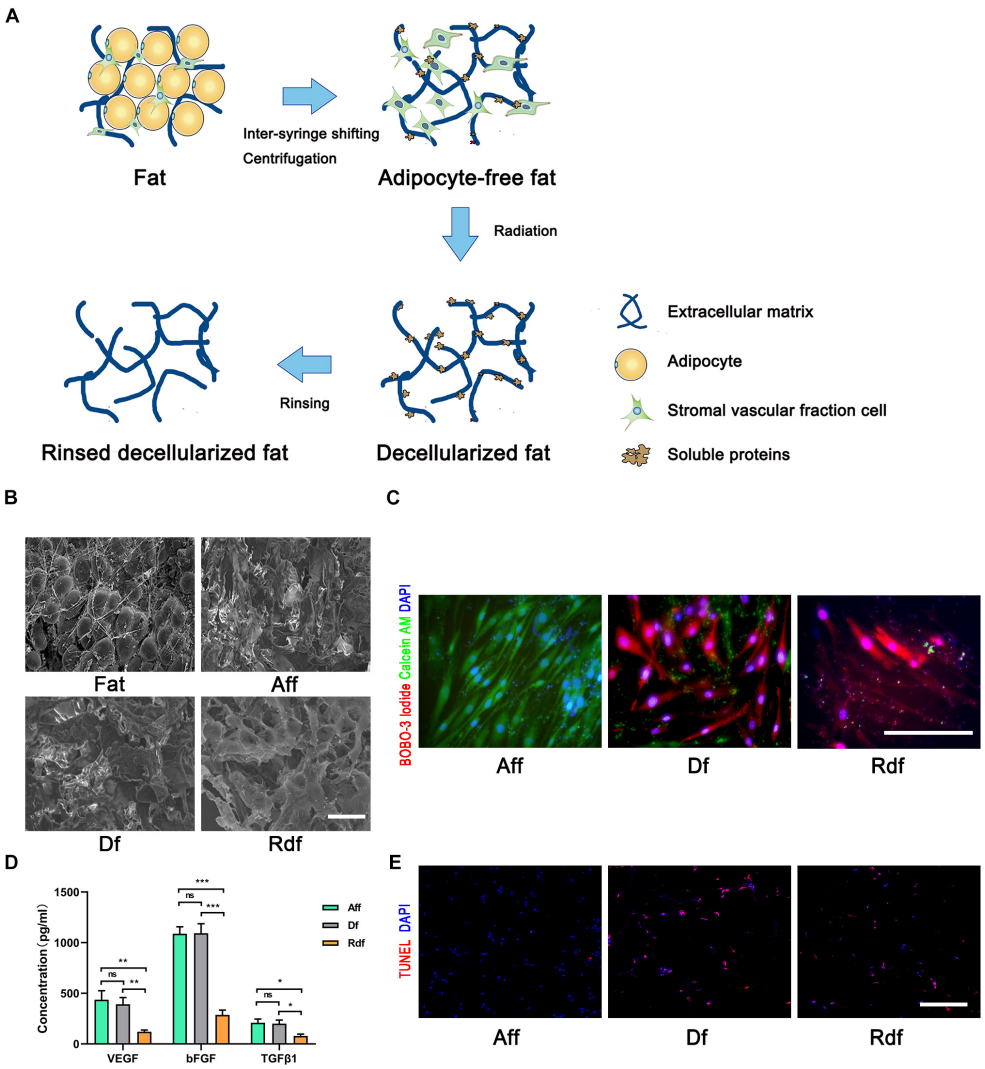


FIGURE 1 | Removal of adipose components in fat. **(A)** Illustration showing stepwise procedures eliminating adipose components in fat. **(B)** Scanning electron microscopy views of fat, Aff, Df, and Rdf. **(C)** Live/Dead assay staining measuring SVF cell death of Aff, Df, and Rdf after 72 h of culture. **(D)** ELISA analyses levels of VEGF, bFGF and TNFβ1 in Rdf compared with Aff and Df (*$p < 0.05$, **$p < 0.01$, ***$p < 0.001$, ns = statistically non-significant). $n = 3$ independent experiments. **(E)** TUNEL staining to investigate cell apoptosis of Aff, Df, and Rdf on post-grafting day 1. Scale bar = 100 μm.

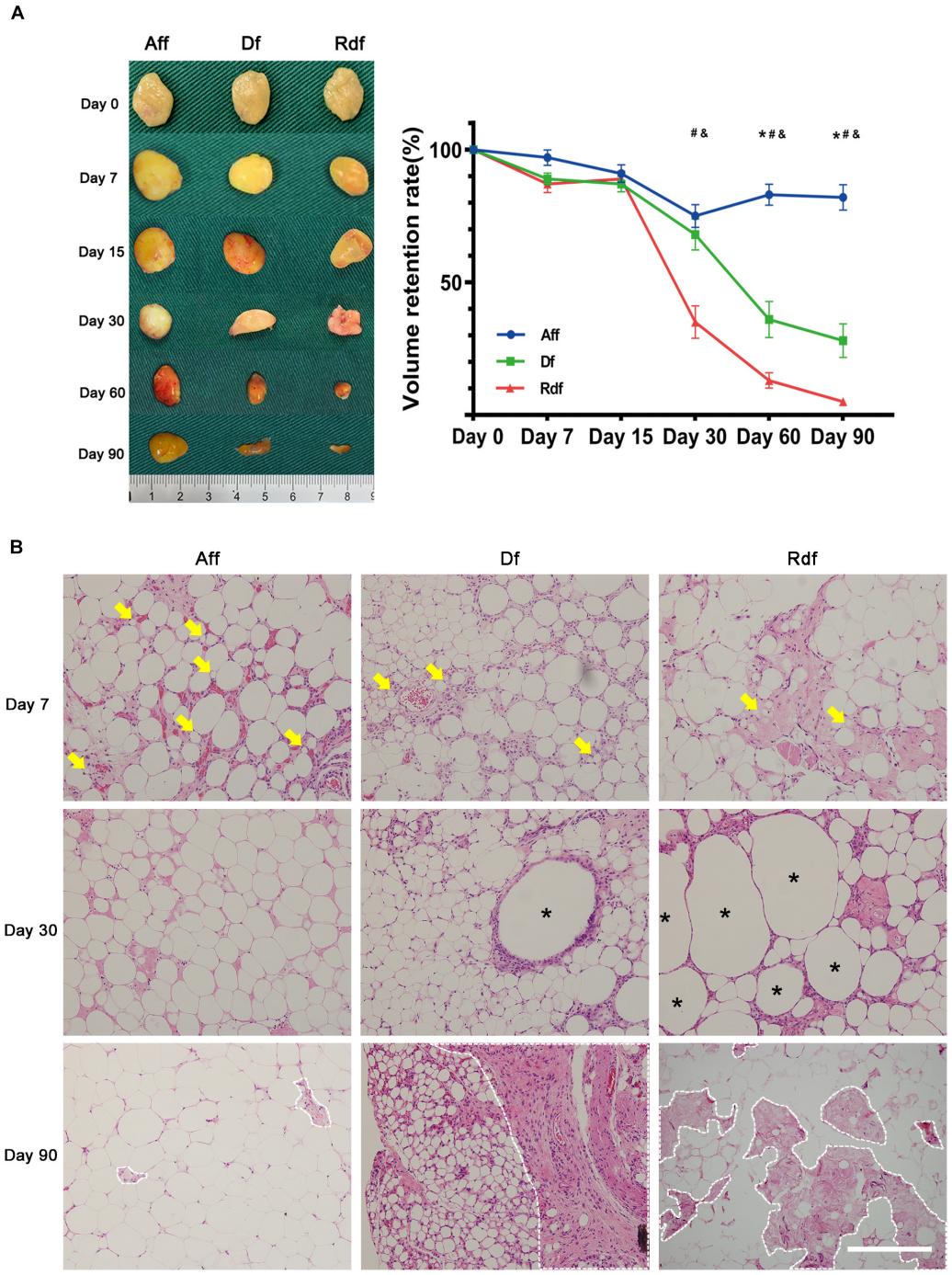


FIGURE 2 | Removal of SVF and microenvironment impairs graft retention. **(A)** Graft appearance and retention rates over time. Quantification of graft volume, showing significantly higher retention rates in the Aff group versus Df (*$p < 0.05$) or versus Rdf (#$p < 0.05$) at later time points. The retention rate of Df was significantly higher than Rdf on days 30, 60, and 90 (&$p < 0.05$). $n = 5$ mice. **(B)** Histological changes in Aff, Df, and Rdf grafts on post-operative day 7, 30, and 90. Some small preadipocytes with multiple intracellular lipid droplets (arrows) were observed as early as day 7. Large amounts of necrotic tissue and large oil cysts (asterisks) were observed in the interior zone of Df and Rdf groups on day 30. Severe fibrosis was observed in the Df and Rdf groups on day 90 (dotted line). Scale bar = 100 μm.

sharp decline in volume. The volumes of the Aff and Df grafts remained relatively constant before day 30 (**Figure 2A**, left panel). Quantification of graft volume indicated that the volume of Aff decreased over the first 30 days and maintained its volume afterward. The volume of Df and Rdf decreased markedly from days 15 to 90. On day 90, Aff had the highest retention rate

(82 ± 7.1% vs. Df, 28 ± 6.3%; *$p < 0.05$; vs. Rdf, 5 ± 1.2%; #$p < 0.05$). The retention rate of Df was significantly higher than Rdf on day 90 (28 ± 6.3% vs. 5 ± 1.2%; &$p < 0.05$) (**Figure 2A**, right panel).

Histologic analysis showed that both the superficial and central areas of the Aff group contained large numbers of small preadipocytes (arrows), extensive well-vascularized connective tissue, and infiltrated cells on day 7 after transplantation (**Figure 2B**). By day 30, Aff developed large numbers of mature adipocytes showing a normal adipose structure. By contrast, although a few small preadipocytes appeared within peripheral area of the Df graft, some large oil cysts (asterisks) hadn't been completely absorbed by day 30. Df exhibited large proportion of fibrotic area (dotted line) with intensive cell infiltration in the interior zone on day 90. As in the Rdf group, small-sized preadipocytes were barely found at the early stage after grafting. Large proportion of graft were occupied by necrotic tissue and large oil cysts on day 30. By day 90, the central areas of Rdf exhibited deconstructed adipose morphology with appearing of tissue debris, severe fibrosis and little cell infiltration. Quantification of the percentage of the fibrosis area showed significantly higher levels of fibrosis in the Df and Rdf group on day 90 (*$p < 0.05$) (**Supplementary Figure 1**).

Impaired Angiogenesis and Adipogenesis in Decellularized Fat and Rinsed Decellularized Fat

Immunostaining of CD31/perilipin revealed the earliest angiogenesis in Aff on day 7 (**Figure 3A**). At the time when angiogenesis was observed, the Aff graft did not exhibit an obvious necrotic area but instead arose plenty of early-differentiated preadipocytes (arrows) with a distinctive multiple perilipin + lipid droplet morphology. By day 30, Aff developed large number of small-sized immature adipocytes, which grew and matured by day 90. By contrast, limited vascular fractions were observed in Df and Rdf. In coordination with angiogenesis, Df exhibited limited adipogenesis with appearing of regional small adipocytes in the periphery. Central area remained perilipin- by day 90. Moreover, Rdf had the poorest adipogenesis with only a few perilipin + adipocytes displayed in the graft. Large area was CD31- and perilipin-. The mean number of vessels per high-power field (HPF) in Aff was significantly higher than that in the Df and Rdf group at post-operative day 7 (Aff, 28.6 ± 2.53 vs. Df, 12.4 ± 1.97 vs. Rdf, 9.8 ± 1.89, *$p < 0.05$) (**Figure 3B**). Quantification of adipocytes revealed that adipogenesis on day 7 was best in Aff, still prominent in Df, and weakest in Rdf (52.2 ± 3.91 vs. 22.4 ± 3.08 vs. 7.2 ± 2.13, *$p < 0.05$) (**Figure 3C**). Quantitative polymerase chain reaction (qPCR) analysis assay showed that adipogenic relative genes, peroxisome proliferator-activated receptor gamma (PPARγ), lipoprotein lipase (LPL), and CCAAT/enhancer-binding protein beta (C/EBPβ), of both Aff and Df groups were significantly higher than that in the Rdf group (*$p < 0.05$). Compared with the Df group, the expression of PPARγ and LPL was significantly higher in the Aff group (*$p < 0.05$) (**Figure 3D**).

Adipose-Derived Stem Cell Supplementation Rescue Poor Adipogenesis and Reverse M1 Inflammation in Decellularized Fat

To explore the regenerative ability of supplemented ASCs, CD31/perilipin immunofluorescent staining was applied to determine the angiogenesis and adipogenesis in Crdf versus Df (**Figure 4A**). With ASC supplementation, Crdf contained a few more CD31 + spots on day 7 compared with the Df group. By day 90, Crdf developed appreciable number of small-sized adipocytes scattered in both interior and periphery of the graft. By contrast, Df exhibited regional adipogenesis mostly at the periphery of the graft. Quantification of adipocytes indicated improved adipogenesis in the Crdf group compared with that in the Df group (Df, 18.8 ± 3.08 vs. Crdf, 39.6 ± 4.18, *$p < 0.05$) (**Figure 4B**). The mean number of vessels was significantly higher in Crdf than that in the Df group at post-operative day 7 (22.8 ± 1.98 vs. Df, 12.4 ± 1.97, *$p < 0.05$). To evaluate the adipogenic and angiogenic capacity of the supplemented ASCs, PPARγ and bFGF were assessed by quantitative RT-PCR. Results showed that PPARγ and bFGF mRNA expression was significantly higher in the Crdf group (*$p < 0.05$). A higher level of interleukin-10 (IL-10) expression was also observed in the Crdf group (*$p < 0.05$) (**Figure 4C**).

By day 7, immunofluorescence staining revealed that macrophages in the Crdf group tended to be M2-polarized (Mac2 + /CD206 +) (white arrow), whereas Mac2 + /CD206- M1 macrophages were predominant in Df grafts (**Figure 4D**). Quantification of the M2 macrophage indicated significantly higher percentage of M2 macrophage infiltration in Crdf than Df (39.13 ± 3.1 vs. Df 15.65 ± 2.72, *$p < 0.05$) (**Figure 4E**). By day 90, prolonged Mac2 + macrophage infiltration was observed in Df compared with Crdf (**Figure 4F**). Quantification of macrophage infiltration revealed that the number of macrophages in Df was significantly higher than that in Crdf (606.4 ± 20.98 vs. Df, 213.5 ± 14.22, *$p < 0.05$) (**Figure 4G**).

Adipose-Derived Stem Cells in Cell-Recombinant Decellularized Fat Differentiate Into Vascular Endothelium

We examined the fluorescence signals of GFP-transfected ASCs in the Crdf group by immunofluorescence staining (**Figure 5**). Colocalization of GFP + ASCs with CD31 + endothelium was observed in the graft (white arrow). αSMA + pericytes were not colocalized with ASCs, indicating that ASCs were mainly involved in endothelium formation during vascularization. Similarly, no GFP + /perilipin + adipocytes were detected in the Crdf group, indicating that the ASCs had undergone minimal adipogenic differentiation.

DISCUSSION

Our previous study demonstrated that mechanical destruction and removal of adipocytes from the fat graft did not compromise

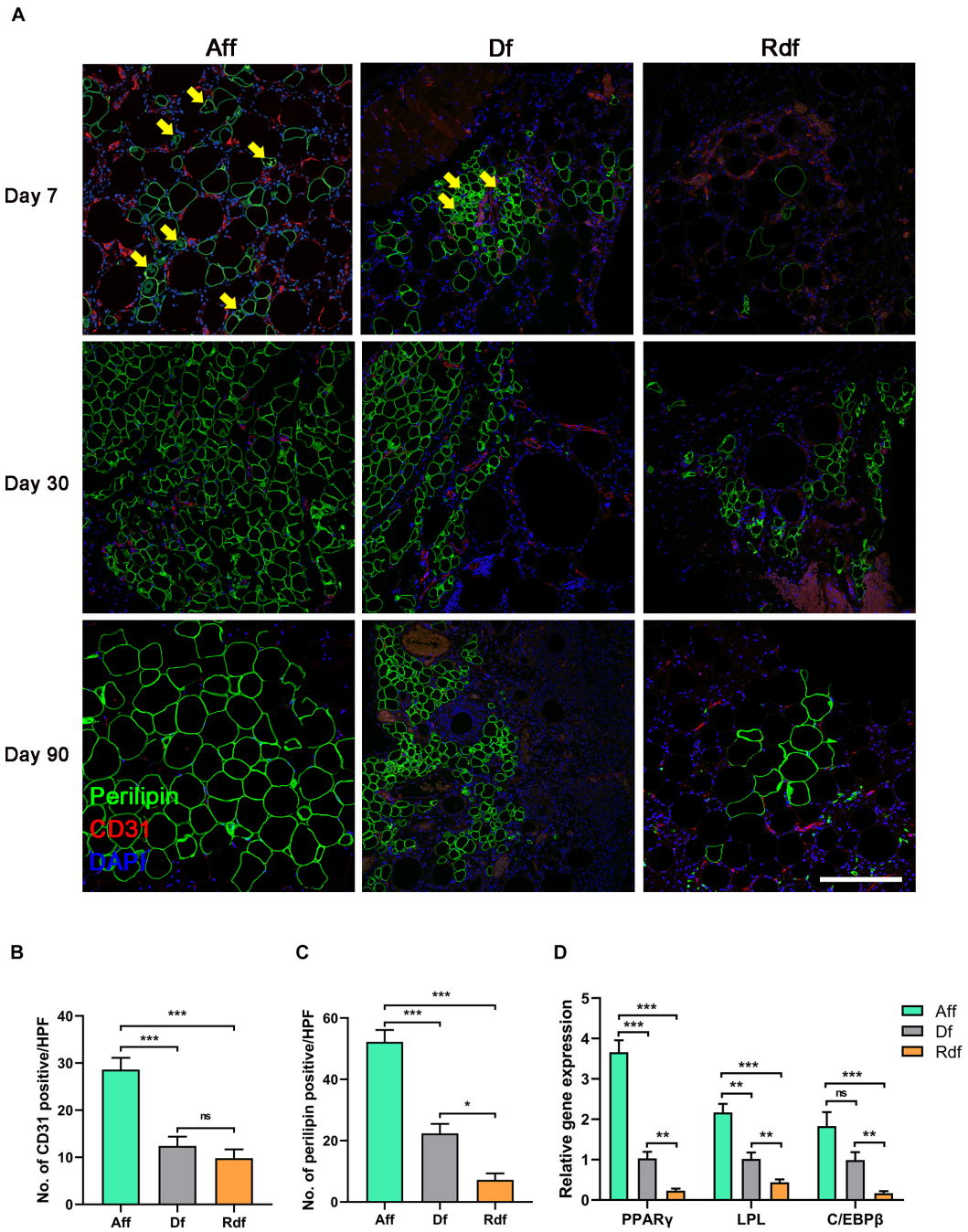


FIGURE 3 | Impaired angiogenesis and adipogenesis in Df and Rdf. **(A)** Representative immunofluorescence staining of perilipin (green) and CD31 (red) in Aff, Df, and Rdf grafts on post-operative day 7, 30, and 90. Early-differentiated preadipocytes (arrows) were identified in Aff and Df on day 7. Quantification of **(B)** CD31-positive area and **(C)** perilipin-positive area in grafts on post-operative day 7 per high power field (*$p < 0.05$, ***$p < 0.001$, ns = statistically non-significant). **(D)** Relative transcription of PPARγ, LPL, and C/EBPβ (**$p < 0.01$, ***$p < 0.001$, ns = statistically non-significant). $n = 3$ independent experiments with 5 samples each group. Scale bar = 100 μm.

the retention rate or the adipogenic potential (Zhang et al., 2018). To our surprise, the removal of adipocytes decreased the inflammatory level in the fat and enhanced adipogenesis (Zhang et al., 2018). Other studies revealed that the apoptosis of adipocytes is conductive to induce inflammatory infiltration and caused oil cysts after fat grafting (Lancaster and Langley, 2014; Nishimoto et al., 2016). These results suggested that adipocytes are not the key element for adipose regeneration after fat grafting, and the other components should make great contribution to adipogenesis. This is the first study of the regenerative ability of ASCs, ECM, and microenvironment exclusively after transplantation.

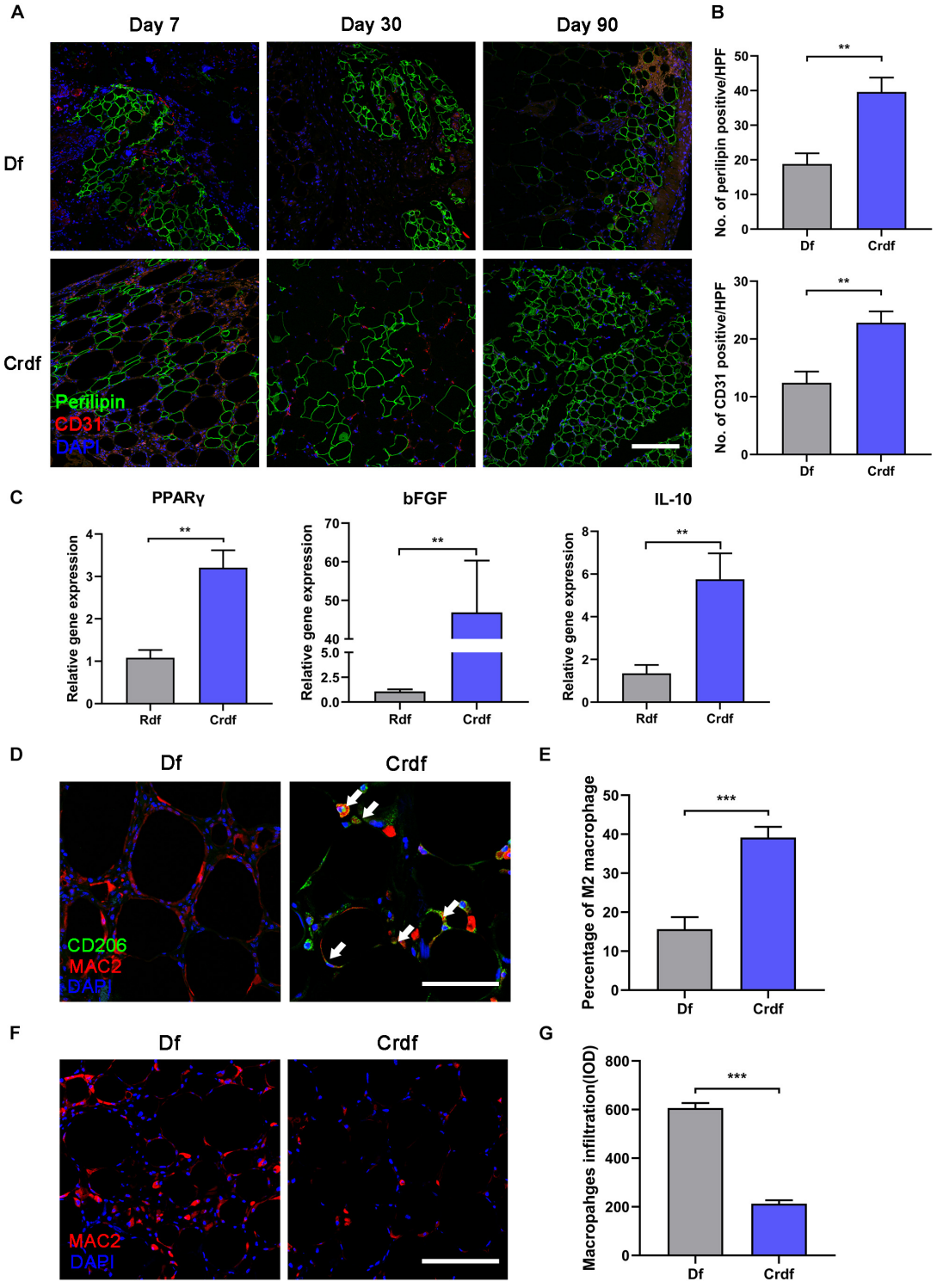


FIGURE 4 | ASC supplementation rescue poor adipogenesis and reverse M1 inflammation in Df. **(A)** Representative immunofluorescence staining of perilipin (green) and CD31 (red) in Df and Crdf on post-operative day 7, 30, and 90. **(B)** Quantification of perilipin-positive area and CD31-positive area in grafts on post-operative day 30 per high power field. (**$p < 0.01$). **(C)** Relative transcription of PPARγ, bFGF, and IL-10 (**$p < 0.01$). **(D)** Representative immunofluorescence staining of CD206 (green) and Mac2 (red) in Df and Crdf on post-operative day 7. **(E)** Quantification of percentage of CD206 + /Mac2 + M2 macrophage in Mac2 + macrophage in grafts on post-operative day 7 per high power field (***$p < 0.001$). **(F)** Representative immunofluorescence staining of Mac2 (red) in Df and Crdf on post-operative day 90. **(G)** Quantification of Mac2 + macrophage infiltration in grafts on post-operative day 90 (***$p < 0.001$). $n = 3$ independent experiments with 5 samples each group. Scale bar = 100 μm.

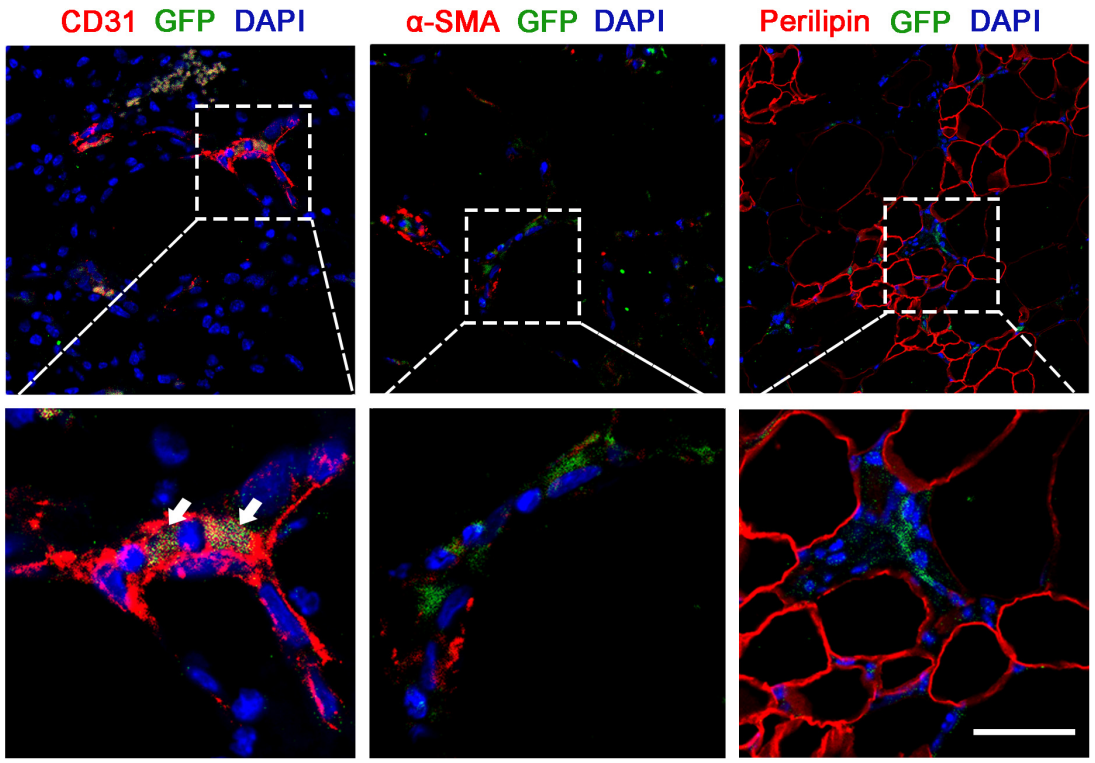


FIGURE 5 | ASCs in Crdf differentiate into vascular endothelium. GFP fluorescence in conjunction with CD31, αSMA, and perilipin immunofluorescence were applied to identify the transformation of supplemented GFP + ASCs. Scale bar = 50 μm.

The results suggested that the long-term retention rate was significantly higher for Aff and Df grafts than for Rdf grafts (82 ± 7.1% vs. Df, 28 ± 6.3%; $^{*}p < 0.05$; vs. Rdf, 5 ± 1.2%; $\#p < 0.05$). At the early stage of transplantation, adipogenesis was observed in all groups except the Rdf group. Initial adipose regeneration developed further in Aff and Crdf grafts, but not in Df grafts. At 90 days post-grafting, Df exhibited large amounts of necrotic tissue and large oil cysts in the interior zone. The regenerative mode of Df was characterized by impaired angiogenesis and M1 macrophage infiltration, whereas M2 macrophage infiltration and active angiogenesis were observed in Aff and Crdf. In addition, ASCs directly participated in vessel formation and exhibited an endothelial phenotype.

Previous studies demonstrated that decellularized adipose matrix (DAM) has the potential to induce adipogenesis (Flynn, 2010; Turner et al., 2012; Trivanovic et al., 2018). While transplantation of DAM leads to severe fibrotic tissue morphology, with pronounced M1 macrophage infiltration (Turner et al., 2012). Moreover, another study suggests that the adipose induction potential of DAM can be influenced by the preparation methods (Brown et al., 2011). Because the preparation of DAM requires full clearance of antigens, the adipose tissue in this study underwent multiple and prolonged procedures that may influence the preservation of soluble protein. Soluble growth factors, which are the important constituents of microenvironment, had a positive role in promoting long-term preservation of DAM (Chun et al., 2019). Using supplemental bFGF, Zhang et al. (2016) reported fat regeneration and long-term retention of DAM 12 weeks after transplantation. To minimize damage to the adipose ECM and soluble microenvironment, we applied a mechanical process and radiation to remove all viable cellular components, thereby preserving the native ECM and microenvironment. As with DAM, Df could also induce adipogenesis with the appearance of scattered perilipin + immature adipocytes at the early stage of grafting. While further removing soluble protein, adipogenesis was barely found in Rdf transplantation, indicating that retention of the abundant extracellular microenvironment within the adipose ECM may be the key to inducing fat regeneration.

Many studies had shown that without adipose-inductive scaffolds and microenvironment, transplantation of ASCs does not generate adipose tissue (Acil et al., 2014; Kurzyk et al., 2019). However, we found that they played an important role in activating the adipoinduction potential of the ECM and microenvironment. After supplementation of Df with ASCs, Crdf had higher long-term retention rate and greater tissue integrity than Df. The number of CD31 + endothelial cells was significantly higher for Crdf than for the Df group indicating improved angiogenesis.

Moreover, Crdf induced transient M2-polarized macrophages infiltration, in contrast to the chronic M1 macrophages in the Df group. Previous studies had shown that rapid inflammatory responses could activate chemotaxis of host-derived mesenchymal stem cells and promote angiogenesis in

the early stage of grafting (Zhan and Lu, 2017; Cai et al., 2018). While persistent high levels of macrophage infiltration inhibit adipogenesis and cause severe fibrosis (Cai et al., 2017a,b). M2 polarization of macrophages help decreases inflammation and promotes tissue remodeling via secretion of anti-inflammatory and angiogenic cytokines (Jetten et al., 2014). Increasing the proportion of M2-type macrophages can facilitate better long-term retention and tissue texture in fat grafting (Dong et al., 2013). Collectively, these results suggest that ASCs can decrease fibrosis and create a better microenvironment for adipogenesis.

GFP-ASC tracing revealed that ASCs presented in the stromal area and participated mainly in formation of vascular endothelium rather than adipocytes or pericytes. In a previous study, adipocytes were derived from the graft (Doi et al., 2015), and another study showed that donor ASCs could develop into newly differentiated adipocytes (Hong et al., 2018), which seems to contradict our results. Those authors used a CAL model to identify the role of ASCs, whereas we used Df + ASC model. Different cellular components were used in these models, which might explain the differences in our results. We removed all SVF cells from the transplanted fat, whereas Hong's model preserved native SVF cells. Both studies confirmed that ASCs could develop into endothelial cells and may incorporate the host blood supply (Laschke et al., 2009), thereby accelerating the revascularization of the graft. These findings suggest that ASCs serve as vascular endothelium to extend the range of adipogenesis within the graft; however, further studies are required to determine the detailed interactions between grafted ASCs and neonatal adipose precursors.

Figure 6 summarizes the adipogenesis outcomes with or without supplemented ASCs of Df based on the results of this study. Removing all cellular components through mechanical processes and irradiation, the adipose ECM and microenvironment are capable of initiating adipogenesis. However, the sustained predominance of M1 inflammation and limited angiogenesis led to poor adipogenesis and severe fibrosis in the graft. By shifting to an M2-dominated milieu and differentiating into vascular endothelium, ASCs promote angiogenesis and adipogenesis, thereby facilitating complete reconstruction of adipose tissue.

In addition, it is worth mentioning that the Aff, which contained SVF instead of ASCs as its cellular component, had a higher long-term retention rate than Crdf (data not presented). This indicated that other cells in SVF may also contribute to adipose reconstruction. Many studies have reported that regulatory T-cells (Treg) are involved in resolving inflammation resolution during tissue repair by controlling neutrophils, inducing macrophage polarization, and regulating helper T-cells (Weirather et al., 2014; Dombrowski et al., 2017). Further

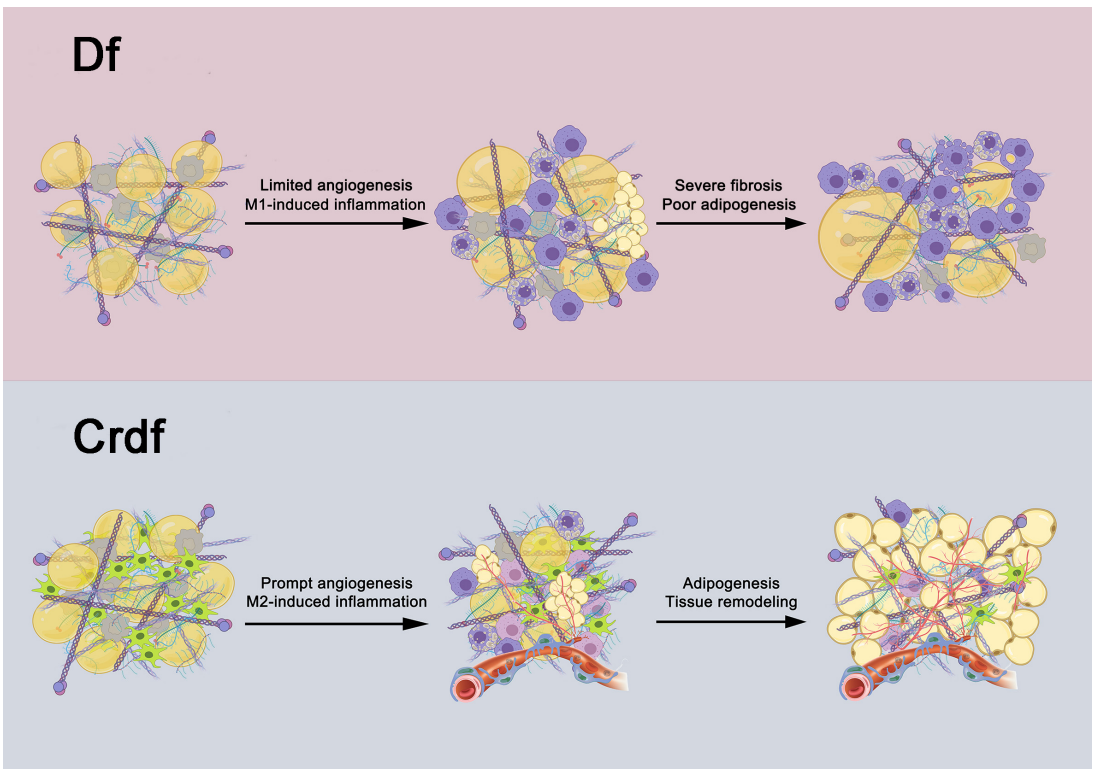


FIGURE 6 | Potential role of ASCs in fat regeneration. After all adipocytes and SVF cells within the graft are removed, adipogenesis can be induced by the transplanted adipose ECM and the microenvironment in Df. However, the sustained presence of M1 inflammation and slow angiogenesis leads to poor adipogenesis and severe fibrosis. Supplementation with ASCs in Df can drive M1 macrophages into M2 polarization as well as develop into endothelial cells of vessels, which promote inflammation resolution and enhance angiogenesis, collectively contribute to mature adipogenesis.

characterization of the cellular components involved in adipose regeneration is required to enabling sophisticated adipose induction strategy.

CONCLUSION

This preliminary animal study demonstrated that grafting of adipose ECM and microenvironment have the capacity to stimulate early adipogenesis *in vivo*. Whereas insufficient graft vascularization and chronic M1 inflammation lead to fibrosis and necrosis outcome. Further removal of microenvironment lost the capacity of inducing adipogenesis. By directly differentiating into endothelial cells and regulating M2 polarization of macrophage, supplementation of ASCs increased the long-term retention rate and had a greater tissue integrity after transplantation.

DATA AVAILABILITY STATEMENT

The original contributions presented in the study are included in the article/**Supplementary Material**, further inquiries can be directed to the corresponding authors.

ETHICS STATEMENT

The animal study was reviewed and approved by the Nanfang Hospital Institutional Animal Care and Use Committee.

AUTHOR CONTRIBUTIONS

YZ and JiaG: conception and design, financial support, and final approval of the manuscript. WJ and JC: conception and design, manuscript writing, assembly of data, and data analysis and interpretation. JinG and YL: assembly of data. FL and JM: data analysis and interpretation. All authors contributed to the article and approved the submitted version.

FUNDING

This work was supported by National Nature Science Foundation of China (81971852, 81772101, 81901976, 81901975, 81871573, 81801932, and 81801933) and Natural Science Foundation of Zhejiang Province of China (LQ19H150002).

SUPPLEMENTARY MATERIAL

The Supplementary Material for this article can be found online at: https://www.frontiersin.org/articles/10.3389/fcell.2021.723057/full#supplementary-material

Supplementary Figure 1 | Masson's trichrome staining of Aff, Df, and Rdf grafts. **(A)** On day 90, thick fibrous tissue was observed in Df and Rdf grafts. By contrast, Aff grafts showed reduced collagen accumulation and normal adipose tissue structure. **(B)** Quantification of fibrosis areas in the grafts, showing that the levels of fibrosis were significantly higher in the Df and Rdf group on day 90 ($p < 0.05$). $n = 5$ mice. Scale bar = 100 μm.

REFERENCES

Acil, Y., Zhang, X., Nitsche, T., Moller, B., Gassling, V., Wiltfang, J., et al. (2014). Effects of different scaffolds on rat adipose tissue derived stroma cells. *J. Craniomaxillofac. Surg.* 42, 825–834. doi: 10.1016/j.jcms.2013.11.020

Brown, B. N., Freund, J. M., Han, L., Rubin, J. P., Reing, J. E., Jeffries, E. M., et al. (2011). Comparison of three methods for the derivation of a biologic scaffold composed of adipose tissue extracellular matrix. *Tissue Eng. Part C Methods* 17, 411–421. doi: 10.1089/ten.TEC.2010.0342

Cai, J., Feng, J., Liu, K., Zhou, S., and Lu, F. (2018). Early macrophage infiltration improves fat graft survival by inducing angiogenesis and hematopoietic stem cell recruitment. *Plast. Reconstr. Surg.* 141, 376–386. doi: 10.1097/PRS.0000000000004028

Cai, J., Li, B., Liu, K., Feng, J., Gao, K., and Lu, F. (2017a). Low-dose G-CSF improves fat graft retention by mobilizing endogenous stem cells and inducing angiogenesis, whereas high-dose G-CSF inhibits adipogenesis with prolonged inflammation and severe fibrosis. *Biochem. Biophys. Res. Commun.* 491, 662–667. doi: 10.1016/j.bbrc.2017.07.147

Cai, J., Li, B., Liu, K., Li, G., and Lu, F. (2017b). Macrophage infiltration regulates the adipose ECM reconstruction and the fibrosis process after fat grafting. *Biochem. Biophys. Res. Commun.* 490, 560–566. doi: 10.1016/j.bbrc.2017.06.078

Chun, S. Y., Lim, J. O., Lee, E. H., Han, M. H., Ha, Y. S., Lee, J. N., et al. (2019). Preparation and characterization of human adipose tissue-derived extracellular matrix, growth factors, and stem cells: a concise review. *Tissue Eng. Regen. Med.* 16, 385–393. doi: 10.1007/s13770-019-00199-7

Doi, K., Ogata, F., Eto, H., Kato, H., Kuno, S., Kinoshita, K., et al. (2015). Differential contributions of graft-derived and host-derived cells in tissue regeneration/remodeling after fat grafting. *Plast. Reconstr. Surg.* 135, 1607–1617. doi: 10.1097/PRS.0000000000001292

Dombrowski, Y., O'Hagan, T., Dittmer, M., Penalva, R., Mayoral, S. R., Bankhead, P., et al. (2017). Regulatory T cells promote myelin regeneration in the central nervous system. *Nat. Neurosci.* 20, 674–680. doi: 10.1038/nn.4528

Dong, Z., Fu, R., Liu, L., and Lu, F. (2013). Stromal vascular fraction (SVF) cells enhance long-term survival of autologous fat grafting through the facilitation of M2 macrophages. *Cell. Biol. Int.* 37, 855–859. doi: 10.1002/cbin.10099

Dong, Z., Peng, Z., Chang, Q., Zhan, W., Zeng, Z., Zhang, S., et al. (2015). The angiogenic and adipogenic modes of adipose tissue after free fat grafting. *Plast. Reconstr. Surg.* 135, 556e–567e. doi: 10.1097/PRS.0000000000000965

Favaudon, V., Caplier, L., Monceau, V., Pouzoulet, F., Sayarath, M., Fouillade, C., et al. (2014). Ultrahigh dose-rate FLASH irradiation increases the differential response between normal and tumor tissue in mice. *Sci. Transl. Med.* 6, 245r–293r. doi: 10.1126/scitranslmed.3008973

Flynn, L. E. (2010). The use of decellularized adipose tissue to provide an inductive microenvironment for the adipogenic differentiation of human adipose-derived stem cells. *Biomaterials* 31, 4715–4724. doi: 10.1016/j.biomaterials.2010.02.046

Giatsidis, G., Succar, J., Waters, T. D., Liu, W., Rhodius, P., Wang, C., et al. (2019). Tissue-engineered soft-tissue reconstruction using noninvasive mechanical preconditioning and a shelf-ready allograft adipose matrix. *Plast. Reconstr. Surg.* 144, 884–895. doi: 10.1097/PRS.0000000000006085

Groen, J. W., Negenborn, V. L., Twisk, J. W., Ket, J. C., Mullender, M. G., and Smit, J. M. (2016). Autologous fat grafting in cosmetic breast augmentation: a systematic review on radiological safety, complications, volume retention, and patient/surgeon satisfaction. *Aesthet. Surg. J.* 36, 993–1007. doi: 10.1093/asj/sjw105

Han, T. T., Toutounji, S., Amsden, B. G., and Flynn, L. E. (2015). Adipose-derived stromal cells mediate in vivo adipogenesis, angiogenesis and inflammation in decellularized adipose tissue bioscaffolds. *Biomaterials* 72, 125–137. doi: 10.1016/j.biomaterials.2015.08.053

Hong, K. Y., Yim, S., Kim, H. J., Jin, U. S., Lim, S., Eo, S., et al. (2018). The fate of the adipose-derived stromal cells during angiogenesis and adipogenesis after

cell-assisted lipotransfer. *Plast. Reconstr. Surg.* 141, 365–375. doi: 10.1097/PRS.0000000000004021

Jetten, N., Verbruggen, S., Gijbels, M. J., Post, M. J., De Winther, M. P., and Donners, M. M. (2014). Anti-inflammatory M2, but not pro-inflammatory M1 macrophages promote angiogenesis in vivo. *Angiogenesis* 17, 109–118. doi: 10.1007/s10456-013-9381-6

Jonathan, E. C., Bernhard, E. J., and McKenna, W. G. (1999). How does radiation kill cells? *Curr. Opin. Chem. Biol.* 3, 77–83. doi: 10.1016/s1367-5931(99)80014-3

Kang, S., Kim, S. M., and Sung, J. H. (2014). Cellular and molecular stimulation of adipose-derived stem cells under hypoxia. *Cell. Biol. Int.* 38, 553–562. doi: 10.1002/cbin.10246

Kato, H., Mineda, K., Eto, H., Doi, K., Kuno, S., Kinoshita, K., et al. (2014). Degeneration, regeneration, and cicatrization after fat grafting: dynamic total tissue remodeling during the first 3 months. *Plast. Reconstr. Surg.* 133, 303e–313e. doi: 10.1097/PRS.0000000000000066

Khouri, R. K. (2017). Current clinical applications of fat grafting. *Plast. Reconstr. Surg.* 140, 466e–486e. doi: 10.1097/PRS.0000000000003648

Kokai, L. E., Schilling, B. K., Chnari, E., Huang, Y. C., Imming, E. A., Karunamurthy, A., et al. (2019). Injectable allograft adipose matrix supports adipogenic tissue remodeling in the nude mouse and human. *Plast. Reconstr. Surg.* 143, 299e–309e. doi: 10.1097/PRS.0000000000005269

Kolle, S. F., Fischer-Nielsen, A., Mathiasen, A. B., Elberg, J. J., Oliveri, R. S., Glovinski, P. V., et al. (2013). Enrichment of autologous fat grafts with ex-vivo expanded adipose tissue-derived stem cells for graft survival: a randomised placebo-controlled trial. *Lancet* 382, 1113–1120. doi: 10.1016/S0140-6736(13)61410-5

Kurzyk, A., Ostrowska, B., Swieszkowski, W., and Pojda, Z. (2019). Characterization and optimization of the seeding process of adipose stem cells on the polycaprolactone scaffolds. *Stem Cells Int.* 2019:1201927. doi: 10.1155/2019/1201927

Lancaster, G. I., and Langley, K. G. (2014). Endogenous, adipocyte-derived lipids signal the recruitment of proinflammatory immune cells. *Diabetes* 63, 1844–1846. doi: 10.2337/db14-0303

Laschke, M. W., Vollmar, B., and Menger, M. D. (2009). Inosculation: connecting the life-sustaining pipelines. *Tissue Eng. Part B Rev.* 15, 455–465. doi: 10.1089/ten.TEB.2009.0252

Lv, Q., Li, X., Qi, Y., Gu, Y., Liu, Z., and Ma, G. E. (2020). Volume retention after facial fat grafting and relevant factors: a systematic review and meta-analysis. *Aesthetic Plast. Surg.* 45, 506–520. doi: 10.1007/s00266-020-01612-6

Mashiko, T., and Yoshimura, K. (2015). How does fat survive and remodel after grafting? *Clin. Plast. Surg.* 42, 181–190. doi: 10.1016/j.cps.2014.12.008

Nishimoto, S., Fukuda, D., Higashikuni, Y., Tanaka, K., Hirata, Y., Murata, C., et al. (2016). Obesity-induced DNA released from adipocytes stimulates chronic adipose tissue inflammation and insulin resistance. *Sci. Adv.* 2:e1501332. doi: 10.1126/sciadv.1501332

Rotondo, F., Romero, M. D., Ho-Palma, A. C., Remesar, X., Fernandez-Lopez, J. A., and Alemany, M. (2016). Quantitative analysis of rat adipose tissue cell recovery, and non-fat cell volume, in primary cell cultures. *PeerJ* 4:e2725. doi: 10.7717/peerj.2725

Sano, H., Orbay, H., Terashi, H., Hyakusoku, H., and Ogawa, R. (2014). Acellular adipose matrix as a natural scaffold for tissue engineering. *J. Plast. Reconstr. Aesthet. Surg.* 67, 99–106. doi: 10.1016/j.bjps.2013.08.006

Strong, A. L., Cederna, P. S., Rubin, J. P., Coleman, S. R., and Levi, B. (2015). The current state of fat grafting: a review of harvesting, processing, and injection techniques. *Plast. Reconstr. Surg.* 136, 897–912. doi: 10.1097/PRS.0000000000001590

Suga, H., Eto, H., Aoi, N., Kato, H., Araki, J., Doi, K., et al. (2010). Adipose tissue remodeling under ischemia: death of adipocytes and activation of stem/progenitor cells. *Plast. Reconstr. Surg.* 126, 1911–1923. doi: 10.1097/PRS.0b013e3181f4468b

Toyserkani, N. M., Quaade, M. L., and Sorensen, J. A. (2016). Cell-assisted lipotransfer: a systematic review of its efficacy. *Aesthetic Plast. Surg.* 40, 309–318. doi: 10.1007/s00266-016-0613-1

Trivanovic, D., Drvenica, I., Kukolj, T., Obradovic, H., Okic Djordjevic, I., Mojsilovic, S., et al. (2018). Adipoinductive effect of extracellular matrix involves cytoskeleton changes and SIRT1 activity in adipose tissue stem/stromal cells. *Artif. Cells Nanomed. Biotechnol.* 46(Suppl. 3), S370–S382. doi: 10.1080/21691401.2018.1494183

Turner, A. E., Yu, C., Bianco, J., Watkins, J. F., and Flynn, L. E. (2012). The performance of decellularized adipose tissue microcarriers as an inductive substrate for human adipose-derived stem cells. *Biomaterials* 33, 4490–4499. doi: 10.1016/j.biomaterials.2012.03.026

Weirather, J., Hofmann, U. D., Beyersdorf, N., Ramos, G. C., Vogel, B., Frey, A., et al. (2014). Foxp3+ CD4+ T cells improve healing after myocardial infarction by modulating monocyte/macrophage differentiation. *Circ. Res.* 115, 55–67. doi: 10.1161/CIRCRESAHA.115.303895

Wu, I., Nahas, Z., Kimmerling, K. A., Rosson, G. D., and Elisseeff, J. H. (2012). An injectable adipose matrix for soft-tissue reconstruction. *Plast. Reconstr. Surg.* 129, 1247–1257. doi: 10.1097/PRS.0b013e31824ec3dc

Yao, Y., Dong, Z., Liao, Y., Zhang, P., Ma, J., Gao, J., et al. (2017). Adipose extracellular matrix/stromal vascular fraction gel: a novel adipose tissue-derived injectable for stem cell therapy. *Plast. Reconstr. Surg.* 139, 867–879. doi: 10.1097/PRS.0000000000003214

Yoshimura, K., and Coleman, S. R. (2015). Complications of fat grafting: how they occur and how to find, avoid, and treat them. *Clin. Plast. Surg.* 42, 383–388. doi: 10.1016/j.cps.2015.04.002

Zhan, W., and Lu, F. (2017). Activated macrophages as key mediators of capsule formation on adipose constructs in tissue engineering chamber models. *Cell. Biol. Int.* 41, 354–360. doi: 10.1002/cbin.10731

Zhang, S., Lu, Q., Cao, T., and Toh, W. S. (2016). Adipose tissue and extracellular matrix development by injectable decellularized adipose matrix loaded with basic fibroblast growth factor. *Plast. Reconstr. Surg.* 137, 1171–1180. doi: 10.1097/PRS.0000000000002019

Zhang, Y., Cai, J., Zhou, T., Yao, Y., Dong, Z., and Lu, F. (2018). Improved long-term volume retention of SVF-gel grafting with enhanced angiogenesis and adipogenesis. *Plast. Reconstr. Surg.* 141, 676e–686e. doi: 10.1097/PRS.0000000000004312

Zhou, Y., Wang, J., Li, H., Liang, X., Bae, J., Huang, X., et al. (2016). Efficacy and safety of cell-assisted lipotransfer: a systematic review and meta-analysis. *Plast. Reconstr. Surg.* 137, 44e–57e. doi: 10.1097/PRS.0000000000001981

Conflict of Interest: The authors declare that the research was conducted in the absence of any commercial or financial relationships that could be construed as a potential conflict of interest.

Publisher's Note: All claims expressed in this article are solely those of the authors and do not necessarily represent those of their affiliated organizations, or those of the publisher, the editors and the reviewers. Any product that may be evaluated in this article, or claim that may be made by its manufacturer, is not guaranteed or endorsed by the publisher.

Copyright © 2021 Jiang, Cai, Guan, Liao, Lu, Ma, Gao and Zhang. This is an open-access article distributed under the terms of the Creative Commons Attribution License (CC BY). The use, distribution or reproduction in other forums is permitted, provided the original author(s) and the copyright owner(s) are credited and that the original publication in this journal is cited, in accordance with accepted academic practice. No use, distribution or reproduction is permitted which does not comply with these terms.

Frontiers in
Cell and Developmental Biology

Explores the fundamental biological processes of life, covering intracellular and extracellular dynamics.

The world's most cited developmental biology journal, advancing our understanding of the fundamental processes of life. It explores a wide spectrum of cell and developmental biology, covering intracellular and extracellular dynamics.

Discover the latest Research Topics

See more →



Frontiers

Avenue du Tribunal-Fédéral 34
1005 Lausanne, Switzerland
frontiersin.org

Contact us

+41 (0)21 510 17 00
frontiersin.org/about/contact